Iron Ore

Related titles

Fundamentals of Metallurgy,
(ISBN 978-1-85573-927-7)

Direct Strip Casting of Metals,
(ISBN 978-1-84569-049-6)

Creep-resistant Steels
(ISBN 978-1-84569-178-3)

Woodhead Publishing Series in Metals and Surface Engineering: Number 66

Iron Ore

Mineralogy, Processing and Environmental Sustainability

Edited by

Liming Lu

AMSTERDAM • BOSTON • CAMBRIDGE • HEIDELBERG
LONDON • NEW YORK • OXFORD • PARIS • SAN DIEGO
SAN FRANCISCO • SINGAPORE • SYDNEY • TOKYO
Woodhead Publishing is an imprint of Elsevier

Woodhead Publishing is an imprint of Elsevier
80 High Street, Sawston, Cambridge, CB22 3HJ, UK
225 Wyman Street, Waltham, MA 02451, USA
Langford Lane, Kidlington, OX5 1GB, UK

Copyright © 2015 Elsevier Ltd. All rights reserved.

No part of this publication may be reproduced, stored in a retrieval system or transmitted in any form or by any means electronic, mechanical, photocopying, recording or otherwise without the prior written permission of the publisher.

Permissions may be sought directly from Elsevier's Science & Technology Rights Department in Oxford, UK: phone (+44) (0) 1865 843830; fax (+44) (0) 1865 853333; email: permissions@elsevier.com. Alternatively you can submit your request online by visiting the Elsevier website at http://elsevier.com/locate/permissions, and selecting Obtaining permission to use Elsevier material.

Notice
No responsibility is assumed by the publisher for any injury and/or damage to persons or property as a matter of products liability, negligence or otherwise, or from any use or operation of any methods, products, instructions or ideas contained in the material herein. Because of rapid advances in the medical sciences, in particular, independent verification of diagnoses and drug dosages should be made.

ISBN 978-1-78242-156-6 (print)
ISBN 978-1-78242-159-7 (online)

British Library Cataloguing-in-Publication Data
A catalogue record for this book is available from the British Library

Library of Congress Control Number: 2015939621

For information on all Woodhead Publishing publications visit our website at http://store.elsevier.com/

List of Contributors

A. Babich RWTH Aachen University, Aachen, Germany

B. Beven Fortescue Metals Group Limited, Pilbara, WA, Australia

W.J. Bruckard CSIRO Mineral Resources Flagship, Clayton South, VIC, Australia

J.M.F. Clout Ironist Pty Ltd, Nedlands, WA, Australia

C. Crisafio Fortescue Metals Group Limited, Pilbara, WA, Australia

A. Deev CSIRO Mineral Resources Flagship, Clayton South, VIC, Australia

E. Donskoi CSIRO Mineral Resources Flagship, Pullenvale, QLD, Australia

R.B. Dwyer CSIRO Land and Water Flagship, Wembley, WA, Australia

M.J. Fisher-White CSIRO Mineral Resources Flagship, Clayton South, VIC, Australia

N. Haque CSIRO Mineral Resources Flagship, Clayton South, VIC, Australia

G.W. Heyes CSIRO Mineral Resources Flagship, Clayton South, VIC, Australia

R.J. Holmes CSIRO Mineral Resources Flagship, Clayton South, VIC, Australia

O. Ishiyama Nippon Steel & Sumitomo Metal Corporation, Futtsu, Chiba-Pref., Japan

S. Jahanshahi CSIRO Mineral Resources Flagship, Clayton South, VIC, Australia

A. Jankovic Metso Process Technology & Innovation, Pullenvale, QLD, Australia

I. Lau CSIRO Mineral Resources Flagship, Bentley, WA, Australia

C. Laukamp CSIRO Mineral Resources Flagship, Bentley, WA, Australia

X. Li University of Science and Technology Liaoning, Anshan, Liaoning, China

R.R. Lovel CSIRO Mineral Resources Flagship, Clayton South, VIC, Australia

L. Lu CSIRO Mineral Resources Flagship, Pullenvale, QLD, Australia

J.R. Manuel CSIRO Mineral Resources Flagship, Pullenvale, QLD, Australia

E. Maré Fortescue Metals Group Limited, Pilbara, WA, Australia

J.G. Mathieson CSIRO Mineral Resources Flagship, Clayton South, VIC, Australia

N.J. McSweeney CSIRO Land and Water Flagship, Wembley, WA, Australia

T. Norgate CSIRO Mineral Resources Flagship, Clayton South, VIC, Australia

T.C. Ooi Fortescue Metals Group Ltd, East Perth, WA, Australia

J. Pan Central South University, Changsha, Hunan, China

A. Poliakov CSIRO Mineral Resources Flagship, Pullenvale, QLD, Australia

E. Ramanaidou CSIRO Mineral Resources Flagship, Bentley, WA, Australia

S.M. Rea CSIRO Land and Water Flagship, Wembley, WA, Australia

D. Senk RWTH Aachen University, Aachen, Germany

L.K. Smith CSIRO Mineral Resources Flagship, Clayton South, VIC, Australia

M.A. Somerville CSIRO Mineral Resources Flagship, Clayton South, VIC, Australia

G.J. Sparrow CSIRO Mineral Resources Flagship, Clayton South, VIC, Australia

R. Stace University of Nottingham, Nottingham, UK

I.Ž. Tonžetić Indigo Research Laboratories, Johannesburg, South Africa

J.P.R. de Villiers University of Pretoria, Pretoria, South Africa

M. Wells CSIRO Mineral Resources Flagship, Bentley, WA, Australia

D. Xiong SLon Magnetic Separator Ltd, Ganzhou, China

D. Zhu Central South University, Changsha, Hunan, China

Woodhead Publishing Series in Metals and Surface Engineering

1 **Nickel and chromium plating**
J. K. Dennis and T. E. Such
2 **Microbiologically influenced corrosion handbook**
S. Borenstein
3 **Surface engineering casebook**
Edited by J. S. Burnell-Gray and P. K. Datta
4 **Duplex stainless steels**
Edited by R. Gunn
5 **Engineering coatings**
S. Grainger and J. Blunt
6 **Developments in marine corrosion**
Edited by J. P. Blitz and C. B. Little
7 **Fundamental and applied aspects of chemically modified surfaces**
J. P. Blitz and C. B. Little
8 **Paint and surface coatings**
Edited by R. Lambourne and T. A. Strivens
9 **Surfacing: Core research from TWI**
TWI
10 **Recommended values of thermophysical properties for selected commercial alloys**
K. C. Mills
11 **Corrosion of austenitic stainless steels**
Edited by H. S. Katal and B. Raj
12 **Fundamentals of metallurgy**
Edited by S. Seetharaman
13 **Energy absorption of structures and materials**
G. Lu and T. X. Yu
14 **The Hatfield memorial lectures: Developments in iron and steel processing**
Edited by P. R. Beely
15 **Laser shock peening**
K. Ding and L. Ye
16 **Structural shear joints**
G. T. Hahn, C. A. Rubin and K. A. Iyer
17 **Direct strip casting of metals and alloys**
M. Ferry
18 **Surface coatings for protection against wear**
Edited by B. G. Mellor
19 **Handbook of gold exploration and evaluation**
E. MacDonald
20 **The cold spray materials deposition process**
Edited by V. K. Champagne

21 The SGTE casebook: Thermodynamics at work: Second Edition
Edited by K. Hack
22 Belt conveying of minerals
E. D. Yardley and L. R. Stace
23 Techniques for corrosion monitoring
Edited by L. Yang
24 Creep-resistant steels
Edited by F. Abe
25 Developments in high temperature corrosion and protection of materials
Edited by W. Gao
26 Mineral wool: Production and properties
B. Sirok and B. Blagojevic
27 High-performance organic coatings
Edited by A. S. Khana
28 Hydrometallurgy: Principles and applications
T. Havlik
29 Corrosion control in the aerospace industry
Edited by S. Benavides
30 Multiaxial notch fatigue
L. Susmel
31 Titanium alloys
W. Sha and S. Malinox
32 Advances in marine antifouling coatings and technologies
Edited by C. Hellio and D. M. Yebra
33 Maraging steels
W. Sha and W. Gao
34 Surface engineering of light alloys
Edited by H. Dong
35 Sintering of advanced materials
Edited by Z. Z. Fang
36 Managing wastes from aluminium smelter plants
B. Mazumber and B. K. Mishra
37 Fundamentals of aluminium metallurgy
Edited by R. Lumley
38 Electroless copper and nickel-phosphorus plating
W. Sha and X. Wu
39 Thermal barrier coatings
Edited by H. Xu and H. Guo
40 Nanostructured metals and alloys
Edited by S. H. Wang
41 Corrosion of magnesium alloys
Edited by G. L. Song
42 Shape memory and superelastic alloys
Edited by Y. Yamauchi and I. Ohkata
43 Superplasticity and grain boundaries in ultrafine-grained materials
A. L. Zhilyaev and A. I Pshenichnyuk
44 Superplastic forming of advanced metallic materials
Edited by G. Guiliano
45 Nanocoatings and ultra-thin films
Edited by A. S. H. Makhlouf and I. Tiginyanu

46 Stress corrosion cracking
Edited by V. S. Raja and T. Shoji
47 Tribocorrosion of passive metals and coatings
Edited by D. Landolt and S. Mischler
48 Metalworking fluids (MWFs) for cutting and grinding
Edited by V. P Astakhov and S. Joksch
49 Corrosion protection and control using nanomaterials
Edited by V. S. Saji and R. Cook
50 Laser surface modification of alloys for corrosion and erosion resistance
Edited by C. T. Kowk
51 Gaseous hydrogen embrittlement of materials in energy technologies Volume 1: The problem, its characterisation and effects on particular alloy classes
Edited by R. P. Gangloff and B. P. Somerday
52 Gaseous hydrogen embrittlement of materials in energy technologies Volume 2: Mechanisms, modelling and future developments
Edited by R. P. Gangloff and B. P. Somerday
53 Advances in wrought magnesium alloys
Edited by C. Bettles
54 Handbook of metal injection molding
Edited by D. Heaney
55 Microstructure evolution in metal forming processes
Edited by J. Lin and D. Balint
56 Phase transformations in steels Volume 1: Fundamentals and diffusion-controlled transformations
Edited by E. Pereloma and D. V. Edmonds
57 Phase transformations in steels Volume 2: Diffusionless transformations, high strength steels, modelling and advanced analytical techniques
Edited by E. Pereloma and D. V. Edmonds
58 Corrosion prevention of magnesium alloys
Edited by G. L. Song
59 Fundamentals of magnesium alloy metallurgy
Edited by M. Pekguleryuz, K. Kainer and A. Kaya
60 Advances in powder metallurgy
Edited by I. Chang
61 Rare earth-based corrosion inhibitors
Edited by M. Forsyth and B. Hinton
62 Thermochemical surface engineering of steels
Edited by E. J. Mittemeijer and M. A. J. Somers
63 Underground pipeline corrosion: Detection, analysis and prevention
Edited by M. Orazem
64 Handbook of smart coatings for materials protection
Edited by A. S. H. Makhlouf
65 Future development of thermal spray coatings: Types, designs, manufacture and applications
Edited by N. Espallargas
66 Iron ore: mineralogy, processing and environmental sustainability
Edited by L. Lu

Preface

As a pyrometallurgist who has specialized in raw material preparation and ironmaking processes, I have always been keen on understanding iron ore, its mineralogy, and upstream processes. This has provided me with a full appreciation of the phenomena occurring during the downstream processing of iron ore, such as sintering, pelletizing, and ironmaking. Over the years, I have had many opportunities to work with mineralogists and process engineers from different iron ore producers, who have been keen to understand downstream iron ore processes. In fact this has become increasingly important at a time when the market is so demanding and competitive with a strong focus on tailoring products to better suit their end users. However, it appears there are no modern books covering the broad area of technologies used throughout the iron ore supply chain. It is this experience that motivated me to organize contributions and edit this new book on iron ore. I believe it will prove to be a valuable reference book on a subject that has not been covered in a single publication.

While the iron ore industry is sometimes viewed as a simple quarrying operation, the industry is fiercely competitive internationally and has been over the years under considerable pressure to improve productivity and reduce its environmental footprint. This is particularly so for the steel industry. From 1992 to 2012, the world has seen drastic increases in iron ore production from about 925 Mt per annum to 2.93 Bt per annum and crude steel production from approximately 506 Mt per annum to 1.124 Bt per annum. These massive increases have been underpinned by the development and deployment of leading edge technologies. While there are excellent books on individual facets of the iron ore supply chain, most of these books were published in the 1970s and 1980s. There have been significant technological developments since then.

This new book aims to provide all involved in the various stages of the iron ore supply chain, from those who initiate the development of a resource to those involved in the various end-user market areas, with information on the latest practices and expert views on the research and technology development trends. Following an introductory overview of the global iron ore industry, this book is thematically divided into the following four sections:

- Characterization of iron ore using advanced analytical tools.
- Recent advances in iron ore extraction, comminution, classification, and physical and physicochemical as well as biotechnological separation techniques.
- Detailed insight into iron ore agglomeration and blast furnace ironmaking technologies.
- Environmental issues and low-emission technologies related to iron ore production and utilization.

The chapters in this book have been carefully prepared by a wide range of internationally renowned experts and summarize the current status of these areas as well as the new technologies being developed to underpin the future of the iron ore industry.

Finally, I would like to thank all those who have contributed to the preparation of the book, particularly Dr. Ralph Holmes from CSIRO. I sincerely hope it becomes a valuable source of information to industry professionals and academics working in the genesis, geology, geometallurgy, exploration, mining, processing, and marketing of iron ores and those who are interested in the science and technology of ironmaking processes.

Dr. Liming Lu
The Commonwealth Scientific and
Industrial Research Organisation (CSIRO)
Brisbane, Australia
January 28, 2015

Introduction: overview of the global iron ore industry

1

R.J. Holmes[1], *L. Lu*[2]
[1]CSIRO Mineral Resources Flagship, Clayton South, VIC, Australia
[2]CSIRO Mineral Resources Flagship, Pullenvale, QLD, Australia

1.1 Introduction

1.1.1 World steel and iron ore production

Steel is an alloy of iron and carbon that is vital to the global economy. Its unique combination of strength, formability, versatility, recyclability, and low cost, make it an ideal material for the construction industry, shipbuilding, motor vehicle manufacture, railway construction, bridge building, heavy industry, machinery manufacture, and engineering applications. Based on the World Steel Association statistics shown in Figure 1.1, the world's crude steel production has almost doubled since 2000. Compared with the 94% increase in world crude steel production between 2000 and 2013, China's increase in crude steel production over the same period has been almost 540% accounting for more than 86% of the additional production.

Iron ore is the primary raw material from which metallic iron is extracted to make steel. To meet the rapid increase in crude steel production, the last decade has seen major expansions in world iron ore production. As evident in Figure 1.2, the world's iron ore production has increased from 1.043 Bt in 2001 to 2.93 Bt in 2012. China is the largest iron ore-producing country, producing about 1.3 Bt in 2012, about 45% of the world's iron ore production, followed by Australia and Brazil with their combined production of 919 Mt in 2012.

1.1.2 World iron ore trade

Turning to iron ore exports and imports, the tonnages are summarized in Table 1.1 for 2012 and 2013 (BREE). China is also the largest iron ore-importing country and imported about 65% of the world's seaborne iron ore in 2013, followed by Japan (11%), Europe (10%), and Korea (6%) as shown in Figure 1.3. These imports are clear indicators of iron ore consumption and that the Asian countries continue to drive the expansion of the international iron ore industry. In terms of tonnages, the rapid rise in iron ore imports into China from about 50 Mt/a in 2000 to around 745 Mt/a in 2012 is shown in Figure 1.4, with imports in 2013 being about 820 Mt/a, largely from Australia, Brazil, South Africa, Canada, and India. The three largest iron ore producers in the world are Vale in Brazil and Rio Tinto and BHP Billiton with operations primarily in Australia. Between them, these companies are responsible for about 74% of the world's seaborne trade in iron ore (see Table 1.1).

Iron Ore. http://dx.doi.org/10.1016/B978-1-78242-156-6.00001-0
© 2015 Elsevier Ltd. All rights reserved.

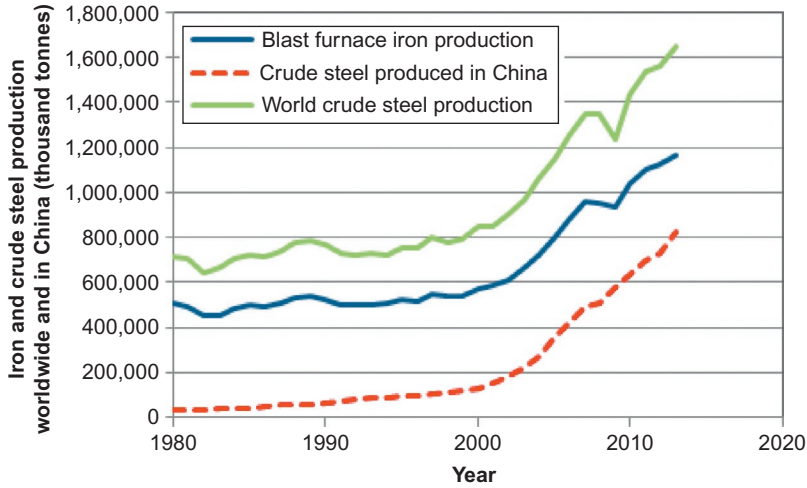

Figure 1.1 Iron and crude steel production worldwide and in China since 1980. *Source:* Worldsteel Association.

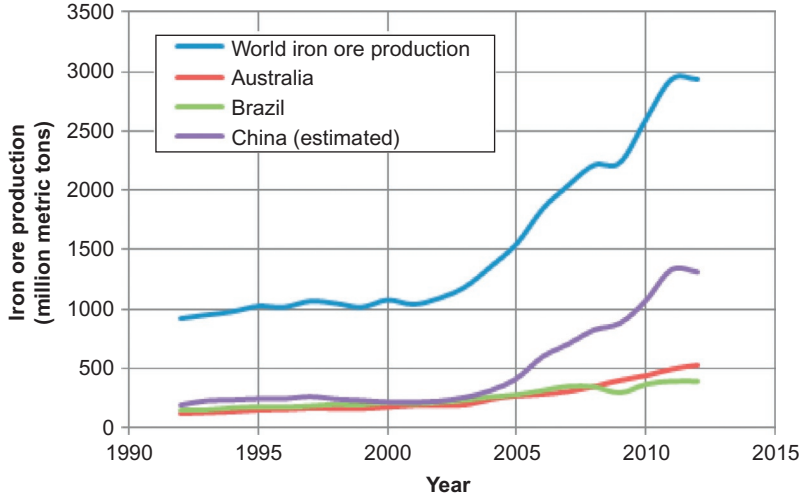

Figure 1.2 World iron ore production since 1992 (USGS). *Note: Million metric tons = million tonnes*.

1.1.3 World iron ore reserves and resources

The production of iron ore in the main iron ore-producing countries is generally backed up by substantial iron ore reserves that are technically and economically feasible to extract. As summarized in Table 1.2, Australia has the largest reserves in terms of both unprocessed (crude) ore and iron content, followed very closely by Brazil with slightly higher in situ iron grades. Russia is also well placed with respect to its iron ore reserves and in situ grade, but clearly, China is less well endowed. While the

Table 1.1 World iron ore trade

	2012 (Mt)	2013 (Mt)
Iron ore imports		
China	745	820
Japan	131	136
The European Union	121	128
South Korea	66	63
Iron ore exports		
Australia	492	579
Brazil	327	330
India (net exports)	16	9
Canada	35	36
South Africa	54	48
World trade	1154	1225

Sources: Australian Government Bureau of Resources and Energy Economics (BREE), Bloomberg, United National Conference on Trade and Development (UNCTAD).

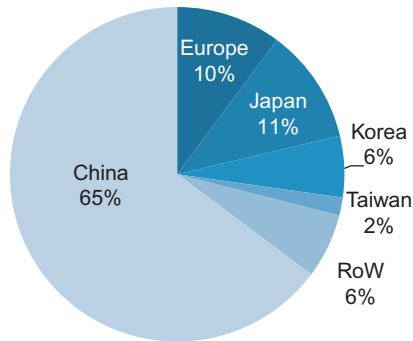

Figure 1.3 Distribution of world seaborne iron ore trade by destination in 2013 (RoW: rest of the world).

tonnages of unprocessed ore in China are substantial and similar to Russia, they are significantly lower in grade, so the contained iron is only about half that for Russia. This is obviously a long-term issue for China given its current iron ore production rate and need for raw materials to feed its steel industry. India will also face long-term supply issues given the scope for economic development and its rapidly rising population.

In addition to the reserves of iron ore in the main producing countries listed in Table 1.2, they also have substantial resources of iron ore that have reasonable prospects for eventual economic extraction. Not shown in Table 1.2 are the reserves and resources currently under development and evaluation in a number of countries in West Africa (see Figure 1.5), including Guinea, Sierra Leone, Liberia, Cameroon, and the Democratic Republic of Congo. The region hosts a number of world-class

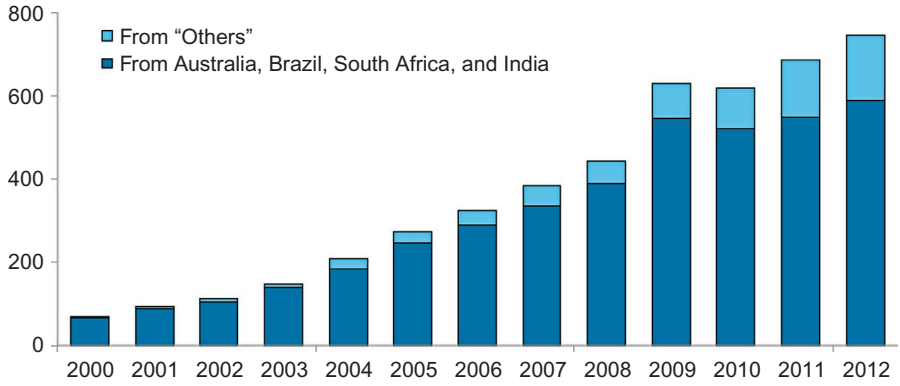

Data: CRU, GTIS. Note: "Others" excludes Australia, Brazil, South Africa, and India.

Figure 1.4 Rapid rise of iron ore imports (Mt/a) into China from 2000 to 2012.

Table 1.2 Estimated iron ore reserves in 2013 in the main iron ore-producing countries

		Iron ore reserves (Mt)	
Rank	**Country**	**Unprocessed ore**	**Iron content**
1	Australia	35,000	17,000
2	Brazil	31,000	16,000
3	Russia	25,000	14,000
4	China	23,000	7200
5	India	8100	5200
6	Venezuela	4000	2400
7	Canada	6300	2300
8	Ukraine	6500	2300
9	Sweden	3500	2200
10	The United States	6900	2100
11	Iran	2500	1400
12	Kazakhstan	2500	900
13	South Africa	1000	650
	Other countries	14,000	7100

Source: US Geological Survey (2014).

high-grade hematitic iron ore deposits, including the high-grade Simandou deposit (see Figure 1.6), and recent investment by the major iron ore companies indicates that West Africa is likely to be the next major global iron ore province. The geologic formations are similar to those found in the Carajás system in Brazil, which is consistent with the view that the South American and African continents were once joined as a single land mass prior to separation due to continental drift (see Figure 1.7). Approximate estimates of the iron ore resources in the main iron ore-rich West African countries are provided in Table 1.3, together with annual production tonnages where applicable.

Figure 1.5 Guinea, Sierra Leone, and Liberia in West Africa showing the location of Simandou.

Figure 1.6 High-grade Simandou deposit in Guinea.

1.2 Iron ore mining operations by country

Iron ore production from the top 20 iron ore-producing countries in million tonnes per annum (Mt/a) in recent years is summarized in Table 1.4, with the major iron ore-producing countries shown in Figure 1.8. The key mining operations in the top 10 iron ore-producing countries as well as Sweden are discussed below.

1.2.1 China

China is currently the largest producer, consumer, and importer of iron ore, producing more than 1.3 Bt and importing about 820 Mt in 2013. Driven by the rapid increase in demand for iron ore over the last decade for steel production in China, domestic iron ore production increased dramatically from approximately 231 Mt in 2002 to 1310 Mt

Figure 1.7 Reconstruction of the South American and African continents prior to separation due to continental drift.

Table 1.3 Estimated iron ore resources in key iron ore-rich West African countries

Country	Project	Iron ore resources (Mt)	Iron ore production (Mt/a)
Guinea	Simandou	2400	–
Sierra Leone	Marampa	864	5.4
	Tonkolili	12,800	20[a]
Liberia	Nimba	182	–
	Putu	2370	–
Cameroon/ Democratic Republic of Congo	Mbalam-Nabeba	775	–
Democratic Republic of Congo	Mayoko-Moussondji	917	–
Total		20,308	

[a]Production milestone in 2013.

Table 1.4 Iron ore production from the top 20 iron ore-producing countries

Rank	Country	Iron ore production (Mt/a)	Year
1	China	1320	2013
2	Australia	579	2013
3	Brazil	398	2013
4	India	152	2013
5	Russia	102	2013
6	Ukraine	80	2013
7	South Africa	67	2013
8	The United States	52	2013
9	Canada	40	2013
10	Iran	37	2013
11	Venezuela	30	2013
12	Sweden	26	2013
13	Kazakhstan	25	2013
14	Mexico	14.5	2011
15	Chile	12.6	2011
16	Mauritania	12.0	2011
17	Peru	10.5	2011
18	Malaysia	7.7	2011
19	North Korea	5.3	2011
20	Turkey	4.5	2011

Sources: Australian Government Bureau of Resources and Energy Economics (BREE), Indian Bureau of Mines, and http://en.wikipedia.org/wiki/List_of_countries_by_iron_ore_production.

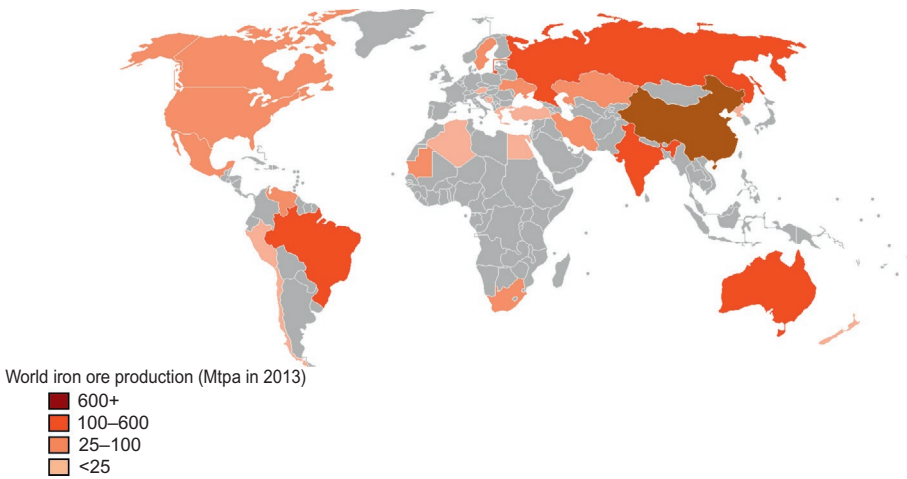

Figure 1.8 Major iron ore-producing countries.
Source: http://en.wikipedia.org/wiki/List_of_countries_by_iron_ore_production.

in 2012 as shown in Figure 1.2 and to 1320 Mt in 2013 (see Table 1.4). Over the same period, Figure 1.4 shows that China's iron ore imports also increased dramatically from about 110 Mt in 2002 to 745 Mt in 2012 (see Table 1.1) and subsequently to 820 Mt in 2013 (see Table 1.4).

China is endowed with crude ore reserves of about 23 Bt according to the US Geological Survey (USGS), although the China Geological Survey estimate is considerably higher at more than 70 Bt. However, China's reserves are relatively low-grade, averaging about 31% Fe, and hence contain only 7.2 Bt of iron according to USGS estimates. Unlike other major iron ore-producing countries, China exploits a wide range of different ore types, including magnetite, hematite, V-Ti magnetites, limonite, siderite, and other complex polymetallic ore types. Figure 1.9 shows the relative proportions of these different iron ore types in the proved reserves in China. Magnetite is the most predominant ore type, accounting for approximately 64% of China's reserves, followed by hematite, V-Ti magnetite, siderite, limonite, and other complex ore types.

The major "iron ore" provinces in China and the corresponding iron ore formations and mining areas are summarized in Table 1.5. These formations host 80% of China's total reserves, the largest contributors being the eastern Liaoning formation, the eastern part of the northern margin of the North China platform, and the iron ore formations along the Xikang-Yunnan axis. However, the ore deposits are often polymetallic and vary in iron grade from less than 30% Fe up to about 52% Fe as shown in Table 1.6, which presents significant processing challenges.

Iron ore is produced in most of China's provinces as shown in Figure 1.10, except for Tianjin, Shanghai, Ningxia, and Tibet. The provinces of Hebei, Sichuan, and Liaoning are the key iron ore provinces, producing about 520, 160, and 150 Mt of iron ore, respectively, in 2012. These provinces are followed by Shanxi and Inner Mongolia, which produced 81.3 and 80.5 Mt of iron ore, respectively, in 2012. As shown in Figure 1.11, these five provinces accounted for about 77% of China's domestic iron ore production.

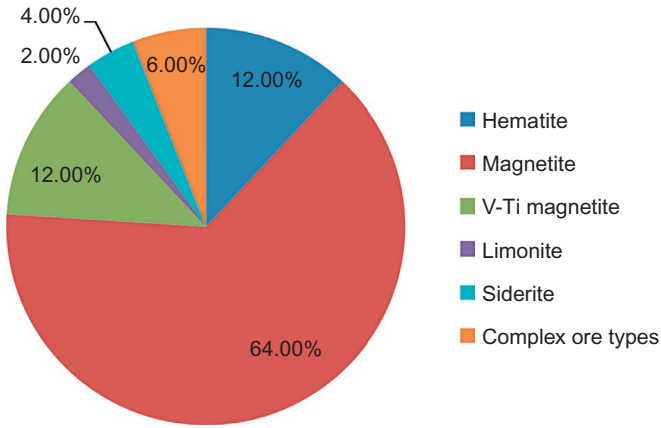

Figure 1.9 Occurrence of different iron ore types in China's proved reserves.
Source: Li.

Table 1.5 Major iron ore provinces, formations, and mining areas in China

Iron ore province	Formation	Mining area	Rank	Percentage of total reserves
Eastern China	Eastern Liaoning	Anshan-Benxi	1	23.2
	Eastern part of the northern margin of the North China platform	Eastern Hebei-Miyun/Huairou-Zhangjiakou/Xuanhua	2	13.5
	Shanxi band	Lvliang	4	8.3
	Southern margin of the North China block	Handan/Xingtai	6	4.2
	West Shandong including the Huaibei group	Luzhong	7	3.9
	North China fault depression/basin	Xuchang-Huoqiu	8	3.8
	Western section of the north margin of the North China platform	Baotou/Baiyunebo	9	3.6
Yangtze	Formations along the Xikang-Yunnan axis	Panzhihua/Xichang	3	12.7
	Middle and downstream region of the Yangtze River	Daye, Anqing-Fanchang, Nanjing/Wuhu	5	6.1
South China	Hainan	Hainan	10	0.7
Total				80.0

The top 10 iron ore-producing companies in China in 2012 are listed in Table 1.7. There are three types of iron ore producers, namely, the captive mines of steel mills, independent mining companies, and private mining companies, with the first two types of iron ore companies in Table 1.7 being state-owned enterprises. Unlike Australia and Brazil, Table 1.7 shows that only about 8% of the iron ore concentrate produced in China is generated by the top 10 producers, so China's iron ore production is spread widely across a large number of companies with relatively small operations compared to the other major iron ore-producing countries.

Due to the low-grade and polymetallic nature of most of China's iron ore deposits, considerable beneficiation is required at almost all mining operations to produce concentrates that are high enough in grade for subsequent sintering and pelletizing to provide raw materials for the country's steel industry. In many instances, China's iron ore mines are designed to recover more than just the iron minerals from the ore. For example, the processing plants for the V-Ti magnetite ores separate the primary process stream into separate streams for subsequent extraction of iron and vanadium/titanium.

Table 1.6 Average in situ analyses of key iron ore deposits in China

Deposit	Average grade
Qidashan deposit in Liaoning Province	31.2% Fe, 56% SiO_2, 0.3% S, and 0.0090–0.03% P
Panzhihua V-Ti-magnetite deposit in Sichuan Province	33% Fe, 11% TiO_2, and 0.3% V_2O_3
Tieshan (Daye deposit in Hubei)	52.1% Fe, 0.57% Cu, 0.24% Co, 2.68% S, and 0.04% P
Aoshan deposit in Anhui Province	28.9% Fe, 0.21% V_2O_5, 1.68% S, and 0.8% P
Huimin deposit in Yunnan Province	*Limonite*: 40% Fe, 0.17–1.43% P, and 0.01–0.61% S *Siderite*: 25–35% Fe, 0.2–2.8% P, and 0.4–20% S *Magnetite*: 45–50% Fe and 0.4–1.3% P
Daxigou deposit in Shanxi Province	28% Fe, 1.4% S, 0.04% S, 0.29–1.05% Cu, and 41.2% $BaSO_4$
Guanzhuang deposit in Hubei Province	38.7% Fe, 11.6% SiO_2, 0.11% S, and 0.42% P
Beiyunebo deposit in Inner Mongolia Province	33–35% Fe, 0.4–0.8% F, 1.2–1.9% S, 0.4–0.8% P, 0.6–2% Mn, 0.07–0.25% Nb_2O_5, and 3–6% total rare earths
Shilu deposit in Hainan Province	52.1–43% Fe, 0.05% S, 0.017% P, and 19.3% SiO_2

Figure 1.10 Location of Chinese provinces.

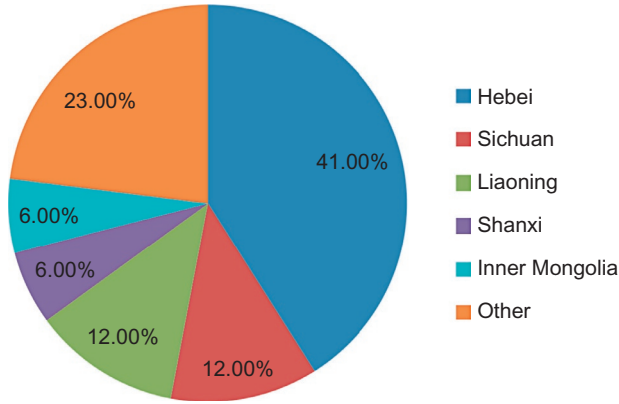

Figure 1.11 Iron ore production in the key Chinese provinces in 2012.

Table 1.7 Top 10 iron ore-producing companies in China in 2012

Company	Province	ROM ore production (Mt)	Concentrate production (Mt)
Panzhihua Iron and Steel	Sichuan	40.9	13.3
Ansteel	Liaoning	39.6	13.8
Hebei Iron and Steel Group	Hebei	36.0	7.2
Baogang Group	Inner Mongolia	31.4	9.3
TISCO	Shanxi	21.2	6.2
Benxi Iron and Steel Company	Liaoning	21.0	7.4
Sichuan Tranvic Group	Sichuan	18.7	6.2 (estimated)
Shougang Group	Hebei	13.3	4.8
Masteel	Anhui	11.1	2.9
Shandong Iron and Steel Group	Shandong	9.2	3.7
Total		242.4	74.8
% Total domestic production		18.0	8.1

An example of an integrated mine and beneficiation plant in Liaoning Province is shown in Figure 1.12. A range of beneficiation methods are used depending on the chemistry and mineralogy of the ore deposit, including low-intensity magnetic separation (LIMS) for recovering magnetite (see Figure 1.13), wet high-intensity magnetic separation (WHIMS) for hematite recovery (see Figure 1.14), and both forward flotation and reverse flotation, respectively, for recovering the iron minerals and removing the gangue (see Figure 1.15).

1.2.2 Australia

Australia has been a major iron ore exporter for more than 40 years and is approaching the end of a period of unprecedented expansion triggered by China's demand for iron ore. A major focus now is optimizing mining operations and extracting the maximum tonnage from the infrastructure that has been constructed. Outside China, Australia is currently the

Figure 1.12 Iron ore mine and the associated beneficiation plant in China's Liaoning Province.

Figure 1.13 Low-intensity magnetic separators (LIMS) for beneficiating ore in China's Sichuan Province.

largest producer of iron ore, producing and exporting 579 Mt in 2013 (Tables 1.1 and 1.4) with crude ore reserves of about 35 Bt containing 17 Bt of iron (Table 1.2).

The iron ore export industry in Australia began with the lifting of the export embargo in December 1960 (O'Leary, 1993) followed by the discovery and development of large iron ore resources in the Pilbara region of Western Australia, which currently accounts for over 95% of Australia's iron ore production (see Figure 1.16). This required significant infrastructure development in a challenging arid environment, and Goldsworthy Mining Ltd, which was later acquired by BHP Billiton, was the first company to ship iron ore to Japan in 1965. This was followed by first shipments by Hamersley Iron Pty Limited in 1966 and Mount Newman Mining Co. Pty Ltd

Figure 1.14 SLon WHIMS used for recovering hematite in China.

Figure 1.15 Flotation cell in a beneficiation plant in Sichuan Province.

(now BHP Billiton Iron Ore) in 1969. By 1970, combined iron ore exports from the Pilbara region had risen to 36 Mt/a, which was a major achievement at the time given the technologies and resources available and, by 1990, reached around 105 Mt/a of direct shipping ore (DSO) primarily from the high-grade Brockman iron formation.

The growth in Australia's iron ore industry has continued at an impressive rate and exports of lump and sinter fines reached more than 579 Mt/a in 2013, the major producers currently being Rio Tinto, BHP Billiton, and Fortescue Metals Group (FMG) in the Pilbara region (see Figure 1.17), with smaller contributions from Atlas Iron, Hancock Prospecting via its Hope Downs mine (joint venture with Rio Tinto), and BC Iron (Holmes, 2013). Other producers include Mount Gibson Iron and Gindalbie Metals Ltd in the midwest region north of Perth (sinter fines and magnetite concentrate) and Cliffs Natural Resources in the Yilgarn region east of Perth (sinter fines). In addition,

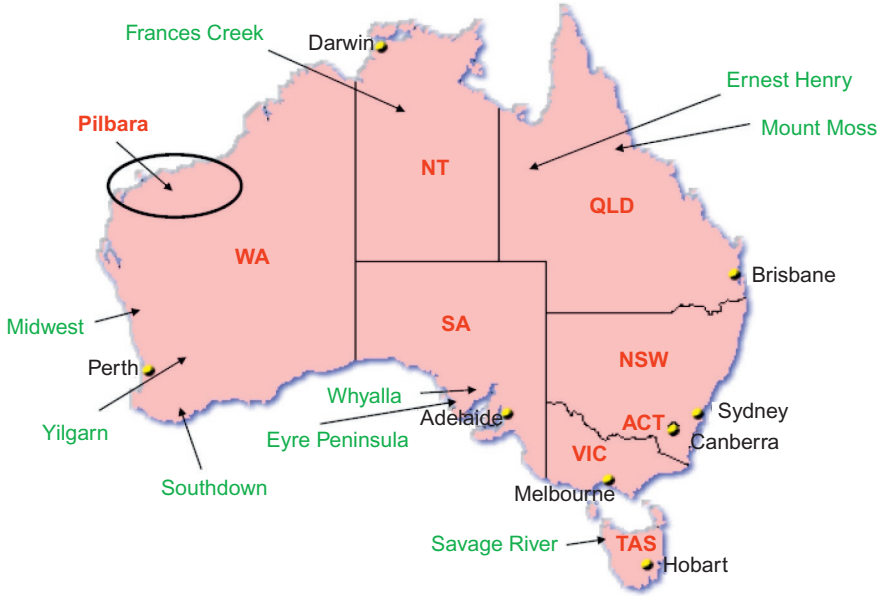

Figure 1.16 Location of Australia's main iron ore resources and operations.

Figure 1.17 Iron ore operations in the Pilbara region of Western Australia, where "blue squares" signify current iron ore operations/projects, "blue text" signifies existing operations or projects under development, and "red text" signifies proposed or potential projects.

CITIC Pacific Mining's Sino Iron project in the Pilbara exports magnetite concentrate, Arrium Mining on the Eyre Peninsula in South Australia (Whyalla) produces magnetite pellets for internal consumption and exports sinter fines, Grange Resources in Tasmania exports magnetite pellets, and until recently Territory Resources in the Northern Territory (Frances Creek) exported sinter fines. There have also been minor contributions (magnetite ore and concentrate) from Ernest Henry Mining and Mt Moss Mining in Queensland depending on the market conditions. A summary of production tonnages in 2013 from the main Australian iron ore producers is provided in Table 1.8.

Major changes in the nature of Australia's iron ore reserves and resources have also taken place in parallel with the massive expansion of the iron ore industry. New ore types such as hematite/goethite ores from deposits in the Marra Mamba iron formation, pisolitic ore from channel iron deposits (CIDs), and detrital ores from detrital iron deposits (DIDs) now either are being mined or are under development to increase export tonnages and supplement the reserves of the traditional premium-grade Brockman ores from world-class mines such as Mount Whaleback (see Figure 1.18) and Mount Tom Price that have underpinned the iron ore export industry since its inception in the 1960s. These new ore types contain a lot more goethite, can be lower in grade, and in some cases require processing to optimize resource utilization. The research work conducted by CSIRO and the Australian iron ore industry over the last 15 years was critical to the introduction and placement of these new ore types in the market.

Table 1.8 Summary of production tonnages from the main Australian iron ore producers in 2013

Company	Operations	Products	Approximate tonnage (Mt/a)
Rio Tinto Iron Ore	Pilbara	Lump and fines	246
BHP Billiton Iron Ore	Pilbara	Lump and fines	187
Fortescue Metals Group (FMG)	Pilbara	Lump and fines	81
Cliffs Natural Resources	Koolyanobbing and Mount Jackson	Lump and fines	11
Arrium Mining	Middleback Ranges	Fines and concentrate	12
Atlas Iron	Pardoo, Wodgina, Abydos, and Mt Webber	Fines	10
BC Iron	Nullagine	Fines	5
Mount Gibson Iron	Tallering Peak and Koolan Island	Fines	8.8
Gindalbie Metals Ltd	Karara in the midwest region	Fines and concentrate	4.1
Grange Resources	Savage River and Port Latta	Pellets	1.5
Territory Resources	Frances Creek	Fines	2.2
CITIC Pacific Mining	Pilbara	Concentrate	1

Sources: Company 2013 Annual reports and websites.

Figure 1.18 BHP Billiton's Mount Whaleback mine in the Pilbara region of Western Australia.

Rio Tinto is currently the largest producer and exporter of iron ore from Australia, shipping hematite/goethite and pisolite ores (Brockman, Marra Mamba, CID, and DID) from operations at Mount Tom Price, Paraburdoo, Eastern Ranges, Channar, Marandoo, Brockman, Nammuldi, Yandi, Mesa J, Mesa A, West Angelas, and Hope Downs through its ports at Parker Point (see Figure 1.19), East Intercourse Island, and Cape Lambert. Current production capacity is 290 Mt/a, with plans to expand production to 360 Mt/a over the next few years.

BHP Billiton Iron Ore (2013) is the next largest producer, currently exporting hematite, hematite/goethite, and pisolite ores from operations at Mount Whaleback; satellite ore bodies 18, 23, 24, 25, 20, and 30; Jimblebar; Area C; and Yandi (see Figure 1.20) via berths at Nelson Point and Finucane Island in the Port Hedland inner harbor. Current production capacity is 220 Mt/a with plans to expand to 270 Mt/a.

The third largest producer is FMG (2013), currently exporting hematite/goethite ore from Cloudbreak and Christmas Creek and hematite/goethite and pisolite ores from the company's recently established Solomon Hub via its Herb Elliott Port in Port Hedland. Production in 2013 was just over 80 Mt/a, with infrastructure in place to expand to 155 Mt/a.

The iron ore mines in Australia are all opencut and the ore is usually extracted by conventional drill and blast mining methods. However, because some of the ore is soft and free digging, surface miners are used at a number of mines, particularly in FMG's operations. Australia traditionally produces DSOs with minimum processing often involving a number of stages of crushing and screening to produce lump and sinter fines products, which are stockpiled and blended on-site and/or at the port prior to export. However, the new more complex ore types now under development often require additional processing to achieve the required grade. Consequently, various nonmagnetic physical separation methods such as scrubbers, jigs, spirals, hydrocyclones, and heavy medium drums and cyclones are used. While magnetic separation is also used for the hematitic ores, performance is limited due to the nature of the ores. Concentrators are located at Rio Tinto's Mount Tom Price and Paraburdoo (see Figure 1.21) operations,

Figure 1.19 Rio Tinto's Parker Point port in the Pilbara region of Western Australia.

Figure 1.20 BHP Billiton's Yandi operation in the Pilbara region of Western Australia.

at BHP Billiton's Mount Whaleback mine (see Figure 1.22), and at FMG's Cloudbreak and Christmas Creek mine sites (see Figure 1.23).

1.2.3 Brazil

Brazil is the world's second largest iron ore producer outside China. The iron ore deposits in Brazil are largely located in the Amazon basin in the state of Pará and in the "Iron Quadrangle" in the state of Minas Gerais. The largest iron ore mine is Carajás located in the state of Pará (see Figure 1.24), which is wholly owned and operated by Vale, while the second largest is the Samarco Alegria mine located in the state of Minas Gerais, which is owned and operated as a 50:50 joint venture between Vale and BHP Billiton. Vale is the largest single producer with total iron ore reserves of about

Figure 1.21 Beneficiation plant employing desliming hydrocyclones at Rio Tinto's Paraburdoo operation in the Pilbara region of Western Australia.

Figure 1.22 Beneficiation plant employing heavy media drums, spirals, and heavy media cyclones at BHP Billiton's Mount Whaleback operation in the Pilbara region of Western Australia.

14 Bt in terms of iron content and is also the largest iron ore producer in the world on a company basis, producing about 300 Mt of iron ore and 39 Mt of iron ore pellets in 2013, which accounted for more than 80% of Brazil's total iron ore exports.

The other significant iron ore mining operators in Brazil are Samarco with an annual pellet production of about 22 Mt, MMX Mineração e Metálicos S.A. with an annual production capacity of about 10 Mt, and Companhia Siderúrgica Nacional (CSN) with an annual production capacity of about 28 Mt. In addition, Usiminas operates four mines at Serra Azul in the state of Minas Gerais, which have a combined production capacity of 12 Mt/a to feed the company's steel mills in Brazil. The approximate production tonnages in 2013 are summarized in Table 1.9.

Figure 1.23 Beneficiation plant employing desanding cyclones and spirals at FMG's Cloudbreak operation in the Pilbara region of Western Australia.

Figure 1.24 Vale's Carajás mine in the state of Para in Brazil.

Vale's iron ore resources and reserves can be quite high-grade, the reserves at the Carajás mine in the northern system in particular consisting of about 18 Bt of hematite ore with an average iron ore content of around 65–66% Fe compared with 62–63% Fe for the Rio Tinto and BHP Billiton mines in Australia. While this can be an advantage for Vale and Brazil, the geographic proximity of Australia to the major Chinese market offsets Brazil's grade advantage. In order to address Brazil's shipping disadvantage, Vale has started using very large bulk ore carriers (Valemax) capable of shipping cargoes of more than 400,000 tonne to reduce transport costs (see Figure 1.25). On the other hand, the iron ore reserves in the state of Minas Gerais in the southern and southeastern systems contain high levels of itabirite and have average iron contents of 35–50% Fe. Itabirite is a banded-quartz hematite and consequently requires beneficiation, usually using a combination of cyclones and reverse flotation, to achieve shipping grades of around 63% Fe.

The iron ore operations of Vale are spread across four systems, namely, the northern, southeastern, southern, and midwestern systems, as shown in Figure 1.26. The northern system comprises the high-grade Carajás mine, which produces lump ore,

Table 1.9 Approximate production of the main Brazilian iron ore and pellet producers in 2013

Company	Iron ore production (Mt)	Pellet production (Mt)	Total production (Mt)
Vale	300	39	339
CSN	28		28
Samarco		22	22
Usiminas	12		12
MMX Mineração e Metálicos S.A.	10		10

Sources: Vale (2013) and http://www.thomaswhite.com/global-perspectives/iron-steel-industry-in-brazil-in-a-sweet-spot/.

Figure 1.25 A 400,000 tonne Valemax ore carrier being loaded at Vale's Port of Tubarão in Brazil.

sinter fines, pellet feed, and special feed for direct reduction. The products are shipped through Terminal de Ponta da Madeira, with pellets being produced in the São Luís pelletizing plant prior to shipment. The mines in the southeastern system are located in the Iron Quadrangle in the state of Minas Gerais and include the Itabira, Minas Centrais, and Mariana mines. The products include sinter fines, lump ore, and pellet feed, which are railed to the Port of Tubarão near Vitória for export, with the pellet feed being pelletized in one of the eight Vale or joint venture straight-grate pellet plants prior to export. The southern system mines are also located in the Iron Quadrangle and comprise four mines and beneficiation plants in the Minas Itabirito complex, three mines and a beneficiation plant in the Vargem Grande complex, and four mines and three beneficiation plants in the Paraopebas complex. The products include sinter fines, lump ore, pellet feed, and a special product called hematitinha used primarily by Brazilian pig iron producers. Due to the high levels of itabirite in the ores in the southern and southeastern systems, these ores are beneficiated. Cyclones coupled with reverse flotation are commonly used to remove the silica gangue for

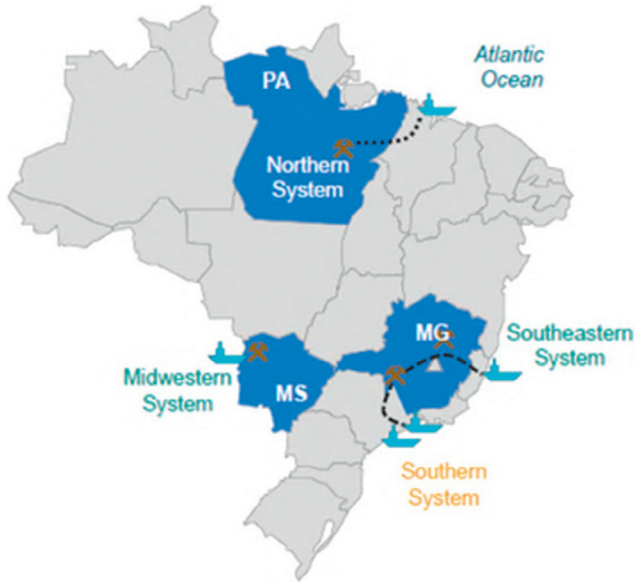

Figure 1.26 Location of the northern, southeastern, southern, and midwestern systems of Vale's iron ore operations in Brazil.

the itabiritic ores in the southeastern and southern systems. Finally, the midwestern system comprises the small, but high-grade, Corumbá and Urucum mines producing lump ore and sinter fines. The iron ore production from each of these Vale Systems is summarized in Table 1.10, while production from each of Vale's pellet plants is summarized in Table 1.11, noting that the Tubarão I and II and São Luis pellet plants were shut down in 2013 due to a drop in market demand for pellets.

Samarco operates the Alegria mine in Minas Gerais as a joint venture between BHP Billiton and Vale with ore reserves totaling 2.1 Bt. The ore is beneficiated in the Germano concentrator and pumped as a slurry down a 400 km pipeline to Ponta Ubu where it is dewatered and pelletized in one of four straight-grate pelletizing machines (see Figure 1.27). Following a recent expansion, the pelletizing capacity is now 30.5 Mt/a.

1.2.4 India

India produced about 150 Mt of iron ore in 2013, with reserves estimated at around 8.1 Bt containing 5.2 Bt of iron (Table 1.2). The major economic deposits of iron ore in India are distributed across five broad zones, as shown in Figure 1.28:

- Zone A: Singhbhum in Jharkhand and Cuttack in Odisha
- Zone B: Dantewada and Durg in Chhattisgarh and Chandrapur and Gadchiroli in Maharashtra
- Zone C: Bellary-Hospet iron belt in Karnataka
- Zone D: Goa and Ratnagiri in Maharashtra and North Karnataka
- Zone E: Metamorphosed BIF along the west coast in Karnataka and Kerala

Table 1.10 Iron ore production from Vale's northern, southeastern, southern, and midwestern systems

	2012 (Mt)	2013 (Mt)
Northern system		
Carajás	106.8	104.9
Southeastern system		
Itabira	37.7	34.0
Mariana	37.2	37.7
Minas Centrais	40.7	37.8
Southern system		
Minas Itabirito	31.8	31.0
Vargem Grande	26.6	21.9
Paraopebas	25.9	26.0
Midwestern system		
Corumbá	4.6	4.5
Urucum	1.8	2.0
Total	309.0	299.8

Source: Vale (2013).

Table 1.11 Pellet production from Vale's pellet plants

	2012 (Mt)	2013 (Mt)
Southeastern system		
Nibrasco	8.8	9.0
Kobrasco	4.4	4.3
Hispanobras	4.4	3.9
Itabrasco	4.1	4.4
Tubarão I and II	4.7	0
Southern system		
Fabrica	3.6	3.8
Vargem Grande	4.5	5.3
São Luis	3.5	0
Total	37.8	30.7

Source: Vale (2013).

The nature of the iron mineralization in each of the five zones in India is presented in Table 1.12, with the first four zones (A–D) accounting for the hematite/goethite mineralization and zone E accounting predominantly for the magnetite mineralization. The most common names used in India to describe iron ore types are banded

Figure 1.27 Samarco's pelletizing complex at Ponta Ubu in Brazil.

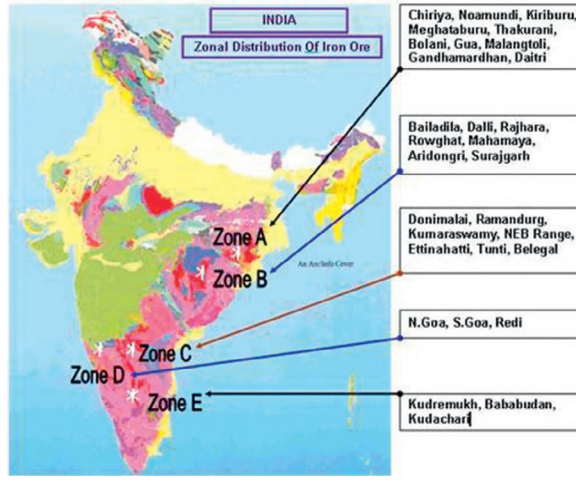

Figure 1.28 Location of the five prominent iron ore zones (A–E) in India.
Source: Mineral Index Map 1.3.M.

hematite quartzite (BHQ), banded hematite jasper (BHJ), and banded magnetite quartzite (BMQ).

Almost all the current iron ore production in India comes from the hematite/goethite reserves (BHQ/BHJ). While there are also substantial magnetite resources in India, they are not exploited because they are located in the environmentally and ecologically sensitive areas of the Western Ghats, which is a UNESCO World Heritage Site in India and one of the eight "hottest hotspots" of biological diversity in the world.

Iron ore production is primarily spread across six Indian states, that is, Jharkhand, Odisha (formerly Orissa), Madhya Pradesh, Chhattisgarh, Karnataka, and Goa, the largest producing state in 2012–2013 being Odisha (47%), followed by Chhattisgarh (21%),

Table 1.12 Characteristics of Indian iron mineralization in zones A–E

Zone	Location	Mines	Mineralization
A	Bonai iron ranges in Jharkhand and Odisha and in adjoining areas in eastern India	Chiria, Noamundi, Kiriburu, Meghatuburu, Thakurani, Gua, Taldih, Bilani, Joda, Daitari, Khondbond, and Gandhamardan	BHQ/BHJ formations as massive ore (58–66% Fe), laminated ore, shaley ore, blue dust (66–68% Fe), and lateritic ores (56–60% Fe). The hematite occurs intimately associated with limonite and goethite, while the lateritic ores contain numerous cavities filled with limonite, goethite, and ochreous material
B	North-south trending linear belt in Central India in the states of Chhattisgarh, Madhya Pradesh, and east Maharashtra	Bailadila, Dalli-Rajhara, Mahamaya, Aridongri, Rowghat, and Surajgarh	Mainly laminated and massive high-grade hematite ore (64–68% Fe), associated with BHQ. Predominantly hard and compact hematite with minor amounts of limonite and goethite. The associated gangue minerals are quartz, clay, ferruginous shale, etc.
C	Bellary-Hospet region of Karnataka	Donimalai and Ramdurga	BHQ/BHJ intercalation with ferruginous shale, consisting of long, narrow, and scattered patches of hematite with intervening shale bands containing 58–64% Fe. The hematite contains minor amounts of magnetite, martite, specularite, and goethite with quartz and clay as the main impurities
D	Goa and west Maharashtra	North and south Goa and Reddi	Predominantly (~80%) fine blue dust (63–64% Fe), fines (59% Fe), and lump ore (57–58% Fe). Goethite/limonite and clay/gibbsite occur with banded ferruginous quartzite and ferruginous phyllite
E	Magnetite deposits of Karnataka	Kudremukh, Baba Budan Hills, and Kodachadri	Thick bands and lenses of hematite/magnetite in BHQ/BMQ formations (57–62% Fe). The associated gangue is mainly quartz

Source: Indian Bureau of Mines, Iron and Steel—Vision 2020.

Figure 1.29 SAIL iron ore mining operations in India.

Jharkhand (13%), Goa (8%), and Karnataka (8%). Unlike Australia and Brazil, the iron ore mines in India are numerous and relatively small in size (see Figure 1.29), with 270 mines in 2012–2013 reporting iron ore production figures. Ownership of the mining companies in India spans both the public sector responsible for 39% of production and the private sector responsible for the remaining 61% of production, with the state-owned National Mineral Development Corporation (NMDC) being the largest iron ore producer (~21%), followed by the state-owned Steel Authority of India (SAIL) (~16%) and Tata Steel Limited (12%) from the private sector. The five leading producers, namely, NMDC, SAIL, Tata Steel Limited, Rungta Mines Limited, and Sarda Mines Private Limited, have a total of 22 mines, which accounted for 58% of the total iron ore production in India in 2012–2013.

India is almost completely self-sufficient with respect to iron ore, but the current reserves have a limited life of 15–20 years at the present rate of steel production. Hence, with the high-grade reserves under threat of depletion despite revision of the threshold value for iron ore reserves to 35–45% Fe depending on the ore type, it is now obligatory for the mining industry to look at exploitation of the huge resources/reserves of low/lean-grade iron ores in India, which in the past would have been left undeveloped. Furthermore, a 30% export duty has been imposed on high-grade iron ore exports aimed at preserving India's high-grade iron ore reserves/resources for domestic use. This export duty, together with a royalty rate of 15%, mining bans, mine closures, and expiry of leases, has had a huge impact on India's iron ore production and exports over the last 5 years. According to the Indian Bureau of Mines, iron ore production in India in 2009–2010 was 218 Mt, but this dropped to 152 Mt in 2013–2014 (see Table 1.4). The reduction in exports has been even more dramatic, falling from over 105 Mt in 2008–2009 to only about 15 Mt in 2013–2014 as indicated in Table 1.13.

Sintering and pelletizing are encouraged in India to increase the utilization of iron ore fines. Hence, India has an installed sintering capacity of around 40 Mt/a (2010 figures) and an installed pelletization capacity of around 30 Mt/a (2010 figures), although sinter production and pellet production are significantly below these figures. A summary of the installed pelletizing capacity in 2010 is provided in Table 1.14.

Table 1.13 India's iron ore exports since 2008–2009

Year	Iron ore exports (Mt/a)
2008–2009	105.9
2009–2010	117.4
2010–2011	97.7
2011–2012	61.7
2012–2013	18.7
2013–2014	15.1

Source: Federation of Indian Mineral Industries and Ore Team.

Table 1.14 Installed pelletizing capacity in India in 2010

Company	Feedstock	Production capacity (Mt/a)
SAIL[a]	Gua fines	4.0
SAIL	Taldih and Kalta fines	2.0
Tata Steel Minerals Canada	Noamundi fines	6.0
Jindal Steel	Barbil fines and fines from various other mines	10.0
Essar	Odisha fines	10.0
KIOCL[b]	Bellary and Donimalai fines	4.0
NMDC	Bailadila and Bacheli slimes	2.0
NMDC	Donimalai slimes	1.2

[a] Steel Authority of India Limited.
[b] Formerly Kudremukh Iron Ore Company.
Source: Indian Bureau of Mines, Iron and Steel — Vision 2020.

1.2.5 Russia

Russia produced 102 Mt of iron ore in 2013, making it the fifth largest iron ore producer after China, Australia, Brazil, and India. The country's iron ore reserves are estimated to be about 25 Bt containing approximately 14 Bt of iron, with almost 60% of the reserves located in the Kursk Magnetic Anomaly in European Russia. Hence, more than half of Russia's iron ore production comes from this area, with the remaining production coming from the Urals and Siberia.

The largest iron ore producer in Russia is Metalloinvest (2013), producing about 37% of the iron ore concentrate and sinter fines and 57% of the iron ore pellets in Russia in 2013. The company has the two largest iron ore mining and processing operations in the country, which are located in Lebedinsky and Mikhailovsky (see Figure 1.30). The Lebedinsky mine is shown in Figure 1.31.

The other major iron ore producer in Russia is Severstal (2013), which has iron ore mining and processing complexes at Karelsky Okatysh and Olcon in northwest Russia. The company produces about 20% of Russia's iron ore pellets. The iron ore

Figure 1.30 Location of Metalloinvest's iron ore operations in Russia.

Figure 1.31 Metalloinvest's Lebedinsky iron ore mine in Russia.

fines, concentrate and pellet production by Metalloinvest and Severstal, which constitutes the major part of Russia's output, is summarized in Table 1.15.

1.2.6 Ukraine

Ukraine produced 80 Mt of iron ore products in 2013, with estimated iron ore reserves of about 6.5 Bt containing 2.3 Bt of iron. There are four major iron ore regions in Ukraine, namely, Kryvyi Rih, Kerch, Kremenchuk, and Bilozerka (see Figure 1.32), most of the mines being deep open pits or underground mines with average grades of 45–55% Fe. The largest iron ore basin is Krivoy Rog in the Dnepropetrovsk region

Table 1.15 Iron ore fines, concentrate, and pellet production by Metalloinvest and Severstal in 2013

Company	Product	Production tonnage (Mt/a)
Metalloinvest	Concentrate and sinter fines	38.4
	Pellets	22.6
Severstal	Concentrate	4.6
	Pellets	10.8

Source: Metalloinvest and Severstal Annual reports (2013).

Figure 1.32 Ukraine's major iron ore resources are located in the Krivoy Rog Basin in central Ukraine, including the Black Iron project under development near Kryvyi Rih.

between Kremenchuk and Zaporizhzhya in central Ukraine, where the majority of the ore reserves are located, including the new Black Iron project under development near Kryvyi Rih. The mining and beneficiation plants in the area generate 80–90% of all Ukraine's iron ore fines, concentrate, and pellet production.

The two top iron ore-producing companies in Ukraine are Metinvest and Ferrexpo, with the Poltava mine operated by Ferrexpo in the Kremenchuk region being the country's largest mine extracting and processing 30 Mt/a of run-of-mine (ROM) iron ore. Ferrexpo was Ukraine's largest iron ore exporter in 2013, shipping more than 10.8 Mt of iron ore products, that is, about 28% of the country's total exports. Closely following was Metinvest, which exported 10.7 Mt in 2013 through its Severny, Tsentralny,

and Inguletsky iron ore mining operations and beneficiation plants. In total, Ukraine exported 37.7 Mt of iron ore products in 2013, comprising roughly equal tonnages of concentrate and pellets.

1.2.7 South Africa

Based on USGS estimates, South Africa produced about 67 Mt of iron ore in 2013, the estimated iron ore reserves in the country being 1 Bt containing 650 Mt of iron. The majority of South Africa's iron ore reserves are located in the Northern Cape adjacent to the Kalahari Desert (see Figure 1.33). The two main iron ore-producing companies in South Africa are Kumba Iron Ore, a subsidiary of Anglo-American, and Assmang, which is a joint venture between African Rainbow Minerals and Assore. The ore bodies being mined are renowned for their dense hematitic ore types, and high-grade products are produced using both dense medium separation (DMS) and jigs. In both cases, the lump and fine products from the Kumba Iron Ore and Assmang mines in the Northern Cape are railed to a deepwater port located at Saldanha Bay in the Western Cape for export (see Figure 1.34). Kumba Iron Ore also has a smaller Thabazimbi mine in Limpopo Province, which produces high-grade ore that is low in contaminants for internal consumption in South Africa.

Kumba Iron Ore operates two mines in the Northern Cape, namely, the original Sishen mine opened in 1947 (see Figure 1.35) and the more recent Kolomela mine about 80 km south of Sishen. In 2013, iron ore production from the Sishen and Kolomela mines was 30.9 and 10.8 Mt, respectively, that is, a total of 41.7 Mt, while production from the small Thabazimbi mine was a modest 0.6 Mt.

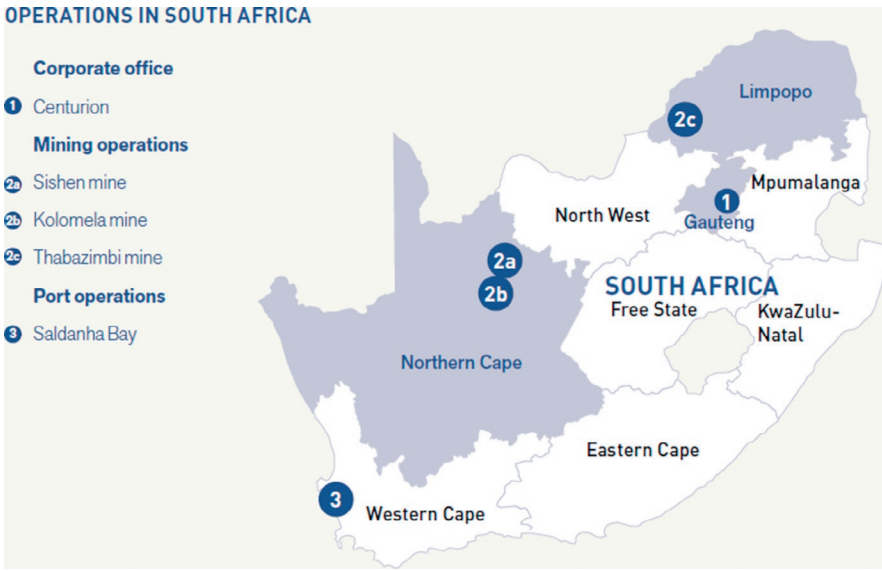

Figure 1.33 Location of Kumba Iron Ore operations in South Africa.

Figure 1.34 Iron ore shiploading at Saldanha Bay in South Africa.

Figure 1.35 Kumba Iron Ore's Sishen mine in the Northern Cape, South Africa.

Assmang has two operating mines at Beeshoek and Khumani. The Beeshoek mine near Postmasburg was established in 1964 and uses jigs to upgrade the ore. However, production from the mine has been declining in recent years and was around 5 Mt in 2012. The new Khumani mine is located about 60 km north of the Beeshoek mine adjacent to Kumba Iron Ore's Sishen mine and produced about 10 Mt in 2012. The Khumani mine is quite cost-competitive due to the low stripping ratio and the reported quality is among the best in South Africa.

Both Kumba Iron Ore and Assmang's iron ore products are railed to Saldanha for export through Transnet's rail system. Stockpiling and loading at Saldanha are also handled by Transnet with South African exports of iron ore totaling about 48 Mt in 2013.

1.2.8 The United States

The United States produced about 52 Mt of iron ore in 2013, with estimates of iron ore reserves being about 6.9 Bt containing around 2.1 Bt of iron. The country's major iron ore operations are in Michigan and Minnesota located in the Lake Superior district (see Figure 1.36) and account for the majority of the country's iron ore production. The ores mined are largely hard low-grade taconite-type ores containing 25–30% Fe with varying proportions of hematite and magnetite, which require beneficiation and pelletizing prior to use. Magnetite is the main iron mineral recovered using crushing and grinding, followed by magnetic separation and in some instances flotation to produce a magnetite concentrate. In some cases, hematite is also recovered as a separate concentrate when it is economic.

The USGS reported that 11 iron ore mines (10 open pits and 1 reclamation operation), 9 concentrators, and 9 pellet plants were in operation in 2013. Eight of the mines operated by the three major iron ore producers in the United States, namely, Cliffs Natural Resources, ArcelorMittal, and US Steel, accounted for most of the production, although part of the combined capacity was idled during the year and construction of a planned taconite mine in Minnesota was delayed until 2015 due to reduced demand. Cliffs Natural Resources, which operates the Empire, Tilden, Hibbing Taconite, Northshore, and United Taconite mines (see Figures 1.37 and 1.38), is the country's leading iron ore producer and accounts for 57% of the total pellet

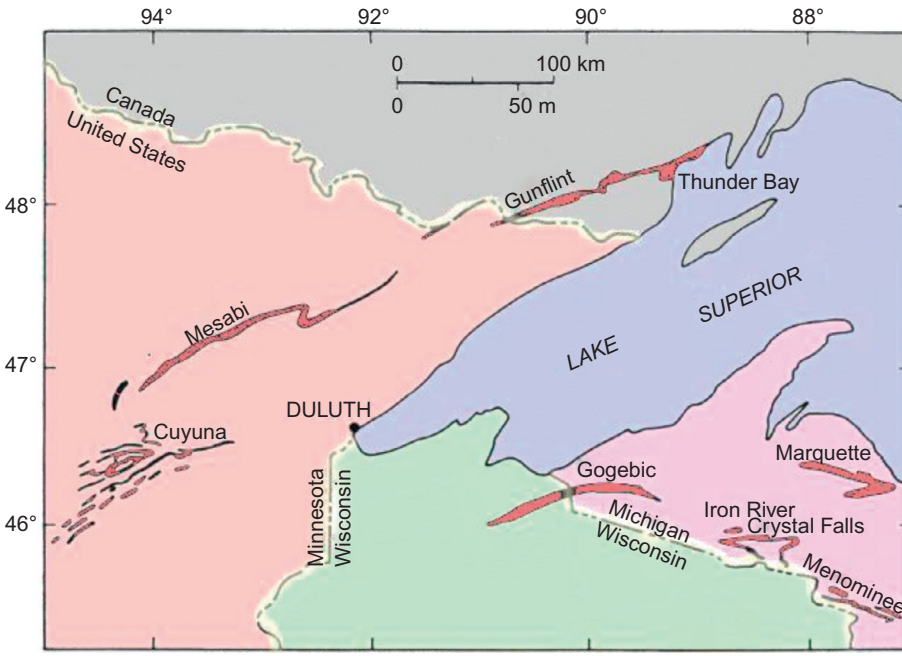

Figure 1.36 Location of iron ore deposits in Michigan and Minnesota in the United States.

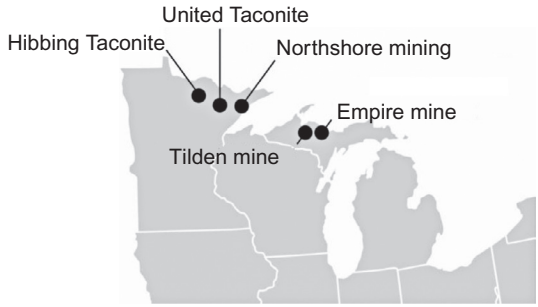

Figure 1.37 Cliffs Natural Resources' iron ore operations in the United States.

Figure 1.38 Hibbing taconite mining operations in the United States.

production. A summary of pellet production from the main operations in the United States is provided in Table 1.16. Small tonnages of iron nuggets (169 Kt in 2012) are also produced using the ITmk3® process.

In addition to the iron ore operations in Michigan and Minnesota, the historic Iron Mountain mine in southwestern Utah was reopened in 2010 after being closed for more than 10 years. The mine is owned and operated by CML Metals Corporation and is located near the northern fringes of the Mojave Desert. The ore is mined at about 47% Fe and then crushed and ground to about 150 µm to liberate the magnetite, which is recovered using magnetic separation followed by reverse flotation to reduce the silica content. About 2.1 Mt of high-grade concentrate was produced in 2013, most of which was exported.

1.2.9 Canada

Canada produced about 40 Mt of iron ore in 2013, the reserves being about 6.3 Bt containing around 2.3 Bt of iron. Virtually all Canada's iron ore production comes from western Labrador and northeastern Quebec within a geologic region known as

Table 1.16 Pellet production by the main operations in the United States in 2013

Operation	Production tonnage (Mt)
Minntac	16.1
Keetac	5.6
Hibbing Taconite	7.7
Tilden	7.5
Empire	3.0
Northshore	3.9
United Taconite	5.2
Minorca	2.8
Total	51.8

Sources: United States Steel Corporation (2013) and Cliffs Natural Resources (2013).

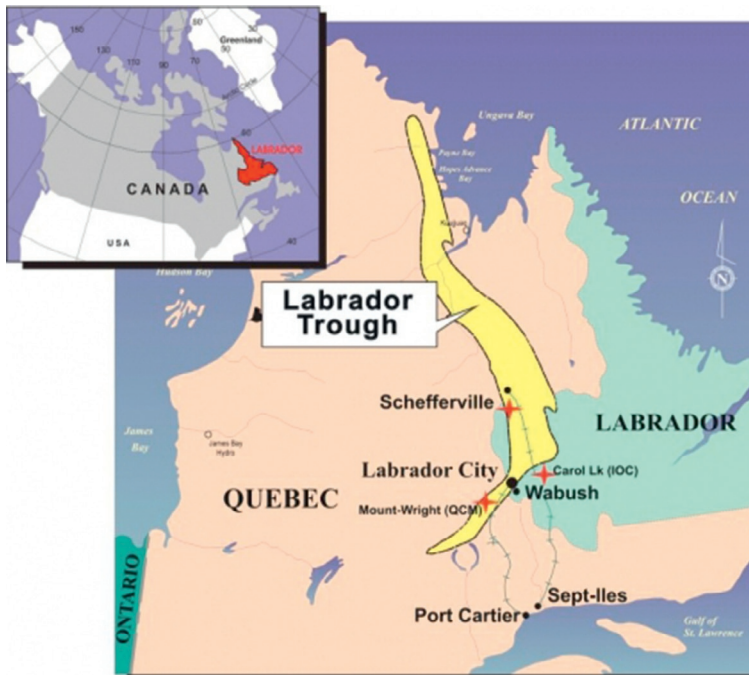

Figure 1.39 Location of the Labrador Trough and mining operations in western Labrador and northeastern Quebec in Canada.

the Labrador Trough (see Figure 1.39). Hematite and magnetite are key ore types, including coarse-grained specular hematite, with lesser amounts of goethite and limonite (see Figure 1.40).

The largest iron ore producers in Canada are located in the Labrador City-Wabush area, with Iron Ore Company of Canada (IOC—a joint venture with Rio Tinto as the

Figure 1.40 Coarse-grained specular hematite (dark material) present in the iron ore deposits in the Labrador Trough, Canada.
Source: Newfoundland and Labrador Geological Survey (2012).

Figure 1.41 Humphrey main pit in IOC's Carol Lake operation in Canada.
Source: Newfoundland and Labrador Geological Survey (2012).

majority shareholder) producing 4.2 Mt of concentrate and 9.9 Mt of pellets at its Carol Lake operation (see Figure 1.41), ArcelorMittal producing 15 Mt of concentrate and pellets at its Mont-Wright Mining Complex operation, and Cliffs Natural Resources producing 8.7 Mt of concentrate at its Wabush and Bloom Lake operations in 2013 for shipping and pelletizing at Pointe-Noire near Sept-Îles. The ore at these operations is mined at 30–40% Fe and beneficiated using gravity separation, especially spirals, and magnetic separation as required. In addition, DSO is produced from mines in the Schefferville area by Labrador Iron Mines (LIM), New Millennium Iron Corporation, and Tata Steel Minerals Canada, key mines being the James mine and the Timmins

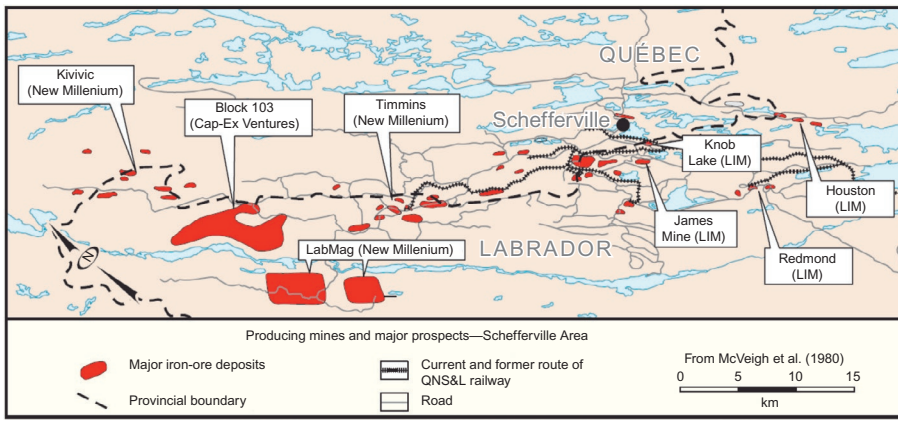

Figure 1.42 Location of DSO and taconite iron ore deposits in the Schefferville area in Canada.

mine (see Figure 1.42). The products are railed to deepwater ports at Sept-Iles, Port Cartier, and Pointe-Noir at the mouth of the Saint Lawrence seaway for shipping to customers.

1.2.10 Iran

Iran produced 37 Mt of iron ore in 2013, which was less than production of about 48 Mt in 2012. The iron ore reserves in Iran are about 2.5 Bt containing 1.4 Bt of iron. The two largest iron ore mines in Iran are the Chadormalu mine in central Iran about 180 km northeast of Yazd and the Gol Gohar iron ore mine in the Kerman province in southeastern Iran (see Figure 1.43), which together account for 80% of Iran's iron ore production. The Chadormalu mine is the largest (see Figure 1.44), the ROM ore (see Figure 1.45) being beneficiated and pelletized to produce about 9.5 Mt/a of iron ore pellets, followed by Gol Gohar (see Figure 1.46) producing about 7.2 Mt/a of pellets from its pellet plant near Sirjan. Other producers are Iran Central Iron Ore (5.3 Mt/a pellets) and the Gohar Zamin iron ore mine, which is being expanded to produce 10 Mt/a of concentrate and 10 Mt/a of pellets. Nearly all of Iran's iron ore exports go to China, with 22.4 Mt shipped in 2013.

1.2.11 Sweden

Sweden produced approximately 25 Mt of iron ore products in 2013, comprising about 23 Mt of pellets and 2 Mt of concentrate, with iron ore reserves of about 3.5 Bt of magnetite ore containing around 2.2 Bt of iron. LKAB is Sweden's largest iron ore producer and operates two underground iron ore mines at Kiruna and Malmberget and an opencut mine at Svappavaara (see Figure 1.47). The Kiruna mine (see Figure 1.48) is the largest underground iron ore mine in the world and ore is extracted by means of sublevel caving where gravity is exploited to get ore to fall into development drifts for

Figure 1.43 Map of Iran showing the location of Yazd and Kerman.

Figure 1.44 Chadormalu iron ore mine in Iran.

subsequent transport by ore loaders, trains, and hoists to the surface. Every day, about 76,000 tonnes of ore are mined and brought to the surface in the Kiruna mine. Future iron ore reserves are located under the current Kiruna town, so plans are in place to relocate the town to enable safe mining of this ore.

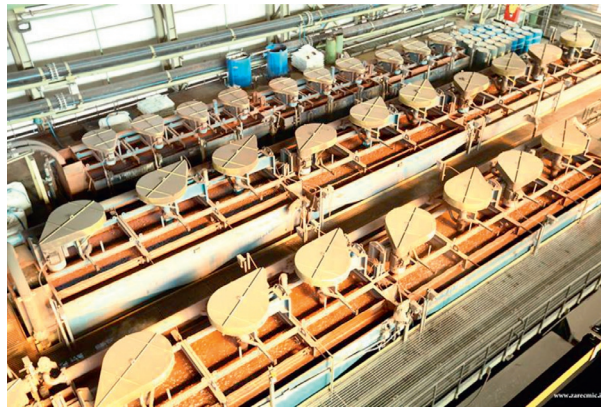

Figure 1.45 Flotation banks in the Chadormalu iron ore concentrator in Iran.

Figure 1.46 Gol Gohar iron ore operation in Iran.

The ore extracted from LKAB's three mines is ground in autogenous and ball mills to liberate the magnetite, which is the principal iron mineral, although some areas may contain hematite as well. The iron minerals are recovered using magnetic separation, which is followed by flotation to remove phosphorus contained in apatite that is present in the ore. Most of the concentrate is then pelletized in one of LKAB's pellet plants at Kiruna, Malmberget, and Svappavaara. The products (pellets and concentrate) from the three operations are finally railed to Narvik in Norway (see Figure 1.49), which is ice-free all year, or to Luleå in Sweden for shipping to LKAB customers.

While LKAB is by far the major iron ore producer in Sweden, it is not the only producer. Northland Resources is developing iron ore operations near the border between Sweden and Finland and produced about 1 Mt from its Tapuli mine in 2013, which was railed to Narvik for shipping.

Figure 1.47 Location of LKAB's iron ore operations in northern Sweden.

Figure 1.48 Kiruna town in Sweden with LKAB's iron ore operations in the background.

1.3 Technology status and challenges

While the iron ore mining industry is sometimes viewed as a simple quarrying operation, the industry is fiercely competitive internationally and is under considerable pressure at present to reduce costs due to the recent major fall in iron ore prices. Consequently, the level of technology adopted by the industry is high and often quite advanced. Examples of recent leading-edge developments to reduce operating costs include the introduction of driverless trucks at a number of Australian Pilbara operations and in the longer-term driverless trains, as well as the use of surface miners

Figure 1.49 LKAB pellet and concentrate loading berth at Narvik in Norway.

instead of the conventional drill and blast mining method where the ore is free digging. The development and implementation of technologies for remote control of mining and processing operations in Australia and Sweden are also undoubtedly at the leading edge in terms of technology applications in the iron ore mining industry. Both Rio Tinto and BHP Billiton have recently opened remote operation centers in Perth, Australia, which for the first time enable the total supply chain to be visualized and largely controlled in real time, enabling metropolitan-based operators to make timely decisions and improve productivity while simultaneously removing them from a high risk location. These facilities utilize leading-edge technologies for haul truck control and management, train control and control of fixed plant in mine and port operations, and CCTV and radio systems to communicate with remote sites. New sensing technologies for downhole logging, in situ analysis on the drill rig, drill core logging, face analysis, and online analysis are also utilized. Another example of automation is the introduction of robotic sample preparation and analysis laboratories around the world, once again with the long-term objective of reducing operating costs and making the workplace safer and less laborious. Other developments to reduce costs and improve the grade and recovery of concentrates included stirred milling for fine grinding, microscreening to remove gangue minerals, coarse and fine particle flotation, and the application of biotechnologies.

Despite these leading-edge developments, substantial challenges still face the international iron ore industry over the next 10–20 years as reserves of high-grade ore around the world continue to fall and alternative ore types need to be developed to replace them, including progressively lower-grade hematite/goethite ores, magnetite ores, and polymetallic ores such as those currently being exploited in China that are low in grade, complex in mineralogy, and fine in grain. These ores will require crushing and grinding to liberate the valuable minerals followed by concentration processes such as gravity separation, magnetic separation, flotation, leaching, and bioprocessing to produce high-grade products suitable for subsequent downstream processing. Consequently, there will be a continuous need to improve grinding and separation efficiencies to maximize productivity and reduce production costs, as well as reduce

the production of waste products, water consumption, greenhouse and other gaseous emissions, and environmental impact. More specifically, some of the key challenges facing the iron ore industry are as follows:

- Development of more efficient mining methods, for example, to maximize lump production from the new ore types that tend to be more highly hydrated and more friable than the traditional high-grade ores
- Reduction of energy consumption in grinding ores prior to beneficiation, particularly for magnetite and polymetallic ores
- Development of more efficient beneficiation processes for removing gangue components such as alumina, silica, and phosphorus while minimizing the loss of iron units
- Development of economic dewatering and drying processes for the new ore types due to their high porosity as mining moves progressively below the water table in some countries, particularly Australia
- Minimizing water consumption in arid environments during beneficiation of low-grade ores, particularly in India
- Development of dry processing methods for beneficiation of iron ore where water is scarce
- Continuous improvement and development of methods for counteracting the adverse effect of increasing alumina content on sinter quality and productivity
- Reduction of toxic emissions in sintering and pelletizing iron ores, including dioxins, and reducing CO_2 emissions and carbon footprints
- Minimization of dust generation during handling and processing due to ever-increasing environmental constraints
- Mine site rehabilitation to mitigate the environmental, social, and economic impacts on local communities

The following chapters in this book summarize the current status of many of these areas and the new technologies being developed to underpin the future of the iron ore industry.

1.4 Iron ore outlook

The recent unprecedented expansion of the iron ore industry triggered by China's growth and need for steel for building and infrastructure development appears to have peaked, and iron ore prices have fallen nearly 40% to less than US$80 per tonne in September 2014 from around US$130 per tonne (CFR China) in January 2014 and even more from their historic high of more than US$180 per tonne (CFR China) around 2011 (see Figure 1.50). This drop in iron ore price is attributed to a cooling of the Chinese economy and an oversupply of iron ore from the major iron ore producers. This has put considerable pressure on the higher-cost iron ore producers to reduce costs, and even the major producers such as BHP Billiton, Rio Tinto, Vale, FMG, and Kumba Iron Ore at the lower end of the cost curve (see Figure 1.51) are reducing staff levels and operating costs to improve profit margins, a key focus being on maximizing productivity. However, analysis of per capita steel consumption in China shows that consumption levels are still well below those of other developed countries in the world, so the major iron ore companies are still optimistic about the future outlook for the iron ore industry and are continuing to invest, albeit at a more moderate rate.

Figure 1.50 Fluctuation in iron ore prices from 2010 to 2014.

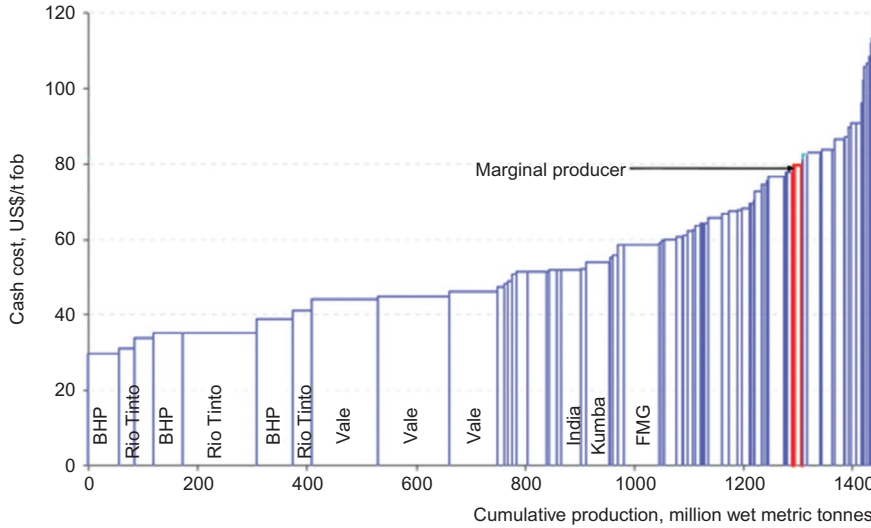

Figure 1.51 Cash cost for iron ore production for the major producers outside China in 2013–2014.
Source: CRU Ltd, Morgan Stanley Research.

Notwithstanding this, it is expected that there will be casualties among the high-cost producers, particularly those that have recently entered the iron ore market with high start-up costs and debt levels. Clearly, the large iron ore suppliers with world-class assets, scale of production, high efficiency, and good cost structures are in a more secure financial position at the current low prices. The iron ore price is expected to gradually recover from the current low when the high-cost producers drop out and production levels better match market demand. However, the highs of $US130 per tonne and above are unlikely to be repeated any time soon.

References

BHP Billiton, 2013. Annual report.
Cliffs Natural Resources, 2013. Annual report.
Fortescue Metals Group, 2013. Annual report.
Holmes, R.J., 2013. Overview of the Australian iron ore industry. In: Rankin, W.J. (Ed.), Australasian Mining and Metallurgical Operating Practices. The Australasian Institute of Mining and Metallurgy: Melbourne, Australia, pp. 1379–1384.
Iron and Steel—Vision 2020, Indian Bureau of Mines, Ore Dressing Section (Indian Bureau of Mines, Nagpur) (2011).
Li, H. Rock and Mineral Analysis, Vol. 32, No. 1, pp. 128–130.
McVeigh, H.G., Elliott, R.A., Neal, H.E., Rolling, F.J., 1980. Potential for further iron ore development in Newfoundland and Labrador. Hatch Associates Ltd. Unpublished report (for Department of Mines and Energy, Government of Newfoundland and Labrador), 175 pp.
Metalloinvest, 2013. Annual report.
Newfoundland and Labrador Geological Survey—Mineral Commodities Series, No. 7, 2012.
O'Leary, M.A., 1993. Overview of the iron ore industry—twenty-five years of iron ore developments in Australia. In: Monograph 19—The Sir Maurice Mawby Memorial Volume. The Australasian Institute of Mining and Metallurgy: Melbourne, Australia, p. 231.
Severstal, 2013. Annual report.
United States Steel Corporation, 2013. Annual report.
US Geological Survey, 2014. Mineral Commodity Summaries, February 2014.
Vale, 2013. Annual report.

Mineralogical, chemical, and physical characteristics of iron ore

2

J.M.F. Clout[1], *J.R. Manuel*[2]
[1]Ironist Pty Ltd, Nedlands, WA, Australia
[2]CSIRO Mineral Resources Flagship, Pullenvale, QLD, Australia

2.1 Introduction

Iron is estimated to make up 32.07% of the Earth's mass and its elemental abundance varies between about 5% of the Earth's crust and as much as 80% of the planet's core (Morgan and Anders, 1980). It is therefore not surprising that there are a number of commonly occurring iron minerals and many iron ore deposits found at the surface of the Earth. Morris (1985) suggested that just one of the iron-enrichment deposit types alone, derived from iron formations, represents the largest and most concentrated accumulation of any single metalliferous element in the Earth's crust. The term "iron ore" is used here as an economic term to refer to iron-bearing deposits and products that have been, are being, or could be expected to be exploited economically for their iron content. Any uneconomic iron accumulations are simply referred to as "iron mineralization."

2.2 Mineralogy

2.2.1 Common iron ore and gangue minerals

Details of the common iron ore and associated gangue minerals found in many iron ore deposits and iron ore products are given in Table 2.1. The three most common iron ore minerals are magnetite, hematite (the spelling "hematite" is preferred here over "haematite"), and goethite, which together account for an estimated >99% of the iron minerals contained in world seaborne-traded iron ores in 2012.

Magnetite (Fe_3O_4) is a common iron ore mineral in iron ore deposits of metasedimentary and magmatic origin. Magnetite has an inverse spinel structure and is partly altered in near-surface environments to hematite or kenomagnetite (Waychunas, 1991).

Hematite is commonly thought to form from oxidation of magnetite in the near-surface environment although Ohmoto (2003) demonstrated that the transformation of magnetite to hematite or vice versa can also be achieved via a pH shift without a redox reaction. Martite is a commonly used textural term to denote hematite pseudomorphs after primary magnetite where the octagonal outlines of many of the original magnetite grains are preserved (Morris, 1985). The term "kenomagnetite" was introduced by Morris (1980, 1985) to describe metal-deficient spinel phases between magnetite and maghemite.

Iron Ore. http://dx.doi.org/10.1016/B978-1-78242-156-6.00002-2
© 2015 Elsevier Ltd. All rights reserved.

Table 2.1 Common iron ore and gangue mineral definitions

	Chemical formula	Description
Ore mineral		
Hematite	Fe_2O_3	Iron oxide
Magnetite	Fe_3O_4	Primary iron oxide
Goethite	FeOOH	Most abundant iron oxyhydroxide with three subtypes: yellow ochreous has excess water and chemical impurities; brown, the most common variant, is stoichiometric; while vitreous is glassy and contains 2–9% $SiO_2 + Al_2O_3$, either as an impurity or as submicron inclusions of quartz
Maghemite[a]	$Fe^{3+}[Fe^{3+}_{1.67}[\ ]_{.33}]O_4$	Intermediate iron oxide
"Kenomagnetite"[b]	$Fe_{3-x}(\ )_xO_4$	Intermediate metal-deficient phase between magnetite and maghemite
"Martite"	Fe_2O_3	Hematite that has replaced primary magnetite
"Hydrohematite"[c]	$Fe_{(2-x)/3}(OH)_xO_{3-x}$	A defect solid solution where OH^- ions replace oxygen
Gangue mineral		
Quartz	SiO_2	Common oxide of silicon
Kaolinite	$Al_4(Si_4O_{10})(OH)_8$	Clay
Gibbsite	$Al(OH)_3$	Clay
Minnesotaite[d]	$(Mg,Fe)_3Si_4O_{10}(OH)_2$	Common Fe-Mg silicate in iron formations
Stilpnomelane	$(K,Na,Ca)_{0.6}(Mg,Fe^{2+},Fe^{3+})_6Si_8Al(O,OH)_{27}2–4H_2O$	Common silicate in iron formations
"Chlorite"[e]	$(Fe,Al,Mg)_3(Si,Al)_2O_5(OH)_4$	Silicate
Pyrite	FeS_2	Iron sulfide
Pyrolusite	MnO_2	Manganese dioxide
Siderite	$FeCO_3$	Fe-carbonate
Ankerite	$Ca(Fe, Mg, Mn)(CO_3)_2$	Ca-Fe-Mg-Mn carbonate

( ) represents cation vacancies. Formulae are from Deer et al. (1992) unless indicated otherwise.
[a] From Waychunas (1991).
[b] From Morris (1985).
[c] From Wolska and Szajda (1985).
[d] From Miyano (1987).
[e] From Klein and Bricker (1977).

Goethite is an iron oxyhydroxide (α-FeOOH), believed to be the most common iron ore mineral in sedimentary and near-surface, altered metasedimentary iron ore deposits. The three most common forms of goethite are brown, yellow ochreous, and dark brown vitreous goethites (Table 2.1). Many seaborne-traded iron ores are mixtures of hard brown goethite and yellow ochreous goethite with hematite (Figure 2.1). The yellow ochreous form of goethite is often incorrectly referred to as "limonite." Limonite is a discredited mineral name according to the Commission on New Minerals and

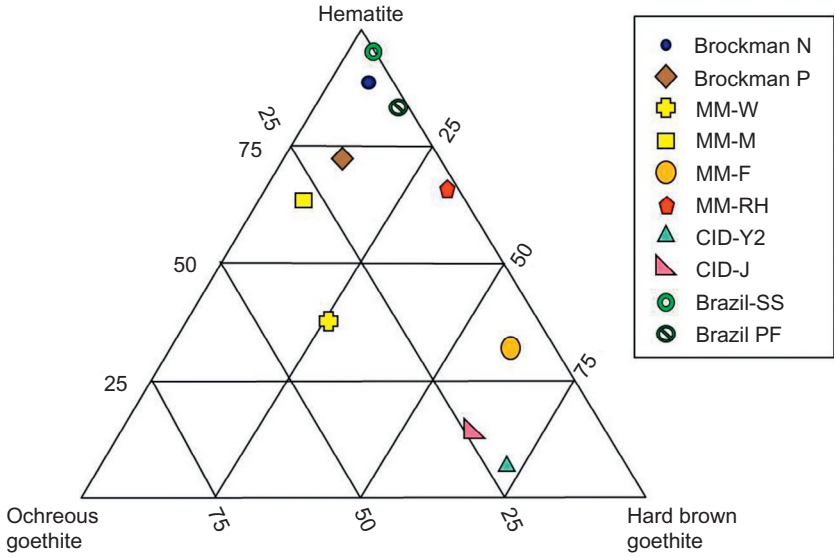

Figure 2.1 Ternary mineralogy plot for various seaborne-traded iron ore products from Western Australia (Pilbara) and Brazil. Note the normative mineralogy has been calculated from assay and normalized to 100%, with goethite abundance calculated from loss on ignition at 371 °C and goethite type and abundance confirmed from polished section microscopy. From Clout and Fitzgerald (2011).

Mineral Names of the International Mineralogical Association (Nickel and Nichols, 1991) and its continued use should therefore be discouraged. Yellow ochreous goethite often contains amorphous material and high (2–9%) levels of Al_2O_3 and SiO_2, although there is some debate on the extent to which the latter two oxides are present as submicron inclusions of contaminant minerals or substituted as elemental Al and Si into the crystal lattice.

Maghemite occurs more commonly in alluvial deposits, typically iron-rich conglomerates and gravels, but elsewhere may partly replace magnetite in weathered iron ores.

Hydrohematite ($Fe_{(2-x)/3}(OH)_xO_{3-x}$) is a defect solid solution structure where OH^- ions replace oxygen atoms and charge balance is achieved by octahedral Fe^{3+} ion vacancies (Wolska and Szajda, 1985; Wolska and Schwertmann, 1989). The presence of hydrohematite is often inferred, but its presence is difficult to prove, especially where colloform goethite is interpreted to have been partially dehydrated to hematite.

While, in rare cases, in some countries, iron may be extracted from the iron-bearing minerals pyrite and siderite, they are not considered here to be economically viable iron ore minerals since they result in unacceptable environmental emissions of SO_x and CO_2, respectively, during subsequent agglomeration and high-temperature processing.

Quartz is by far the most common iron ore gangue mineral overall, whereas clays (kaolinite and gibbsite) predominate in weathered supergene altered and near-surface exposures of ore deposits, while minnesotaite and stilpnomelane are the most common silicate minerals in unweathered iron formation deposits. There are many other major to minor gangue minerals associated with iron ore deposits including many different

silicates (including amphiboles and chlorites), carbonates (siderite and ankerite), sulfides (e.g., pyrite), and oxides (e.g., pyrolusite).

Morris (1980, 1985, 1987) recognized that while the mineralogy of many iron ore deposits is relatively simple, the ore textures are typically quite complicated and are directly related to deposit ore genesis. Furthermore, Clout (2005) provided evidence that it is these complex textures and not mineralogy alone that control metallurgical process performance from crushing to screening, beneficiation and agglomeration (sintering or pelletizing) of fine ores or concentrates, and lump burden behavior in the blast furnace. Differences in iron ore chemistry, texture, mineralogy, and physical properties are directly related to iron deposit types.

2.2.2 Iron ore deposits

2.2.2.1 Deposit types

There are many different types of iron ore deposits that have been historically important for the production of iron ores and other types of metalliferous deposits where iron ore is produced as a by-product, but none are as significant as the iron formation iron ores (Clout and Simonson, 2005). Iron formation-hosted iron ore deposits account for the majority of current world production and resources of iron ore, followed by the important channel iron deposits (CIDs) that filled Tertiary river channels (Morris and Ramanaidou, 2007), Kiruna-type iron oxide-apatite ores (Harlov et al., 2002), and certain types of Cu-Fe skarn (e.g., Daye, People's Republic of China (PRC), Du Yan, 1996; Apurimac-Cusco porphyry-skarn belt, Hapugoda et al., 2009) and rare-earth deposits (Bayan Obo, PRC) (Clout and Simonson, 2005; Williams et al., 2005; Table 2.2). Gutzmer and Beukes (2009) estimated that over 95% of all iron ore deposits exploited today are of sedimentary origin, originating as chemical precipitates from ocean water, of which the iron formation-hosted iron ore deposits are the most abundant example. There are also many other less significant but still substantial past, present, and potential future sources of iron including terrestrial detrital iron deposits (DIDs) (McKenna and Harmsworth, 1998), which form alluvial fans derived from iron formation ores; detrital marine placer deposits typically referred to as “iron sands”; oolitic goethite deposits of Minette/Salzgitter type; iron oxide Cu-Au (IOCG) deposits (e.g., Ernest Henry); and contact metamorphic ores formed by replacement of carbonate rocks in the aureoles of granitoid intrusions (Clout and Simonson, 2005; Williams et al., 2005; Gutzmer and Beukes, 2009). While IOCG deposits are believed to account for only a small amount of current world iron ore production, the amount of contained Fe as magnetite (e.g., Candelaria) or hematite (e.g., Olympic Dam) is speculated to approach that of some of the largest iron formation iron ore deposits (Williams et al., 2005).

Each of the iron ore deposit types in Table 2.2 has characteristic run-of-mine (ROM) and product ore mineralogy (e.g., Figure 2.1), gangue mineralogy (Table 2.3), ore textures, chemical composition, and product physical properties. Given the great number and diversity of iron ore deposits, this chapter will deal largely with the mineralogical and geologic characteristics of the most common sources of iron ore, the iron formation-hosted iron ores, and CIDs, with far less attention to all other iron ore deposit types.

Table 2.2 **Iron ore deposit types**

Classification	Subtype	Characteristics	Deposit examples
Iron formation-hosted	Unenriched	Magnetite with silicate gangue	See Table 2.4
	Martite-goethite	Martite-brown ± ochreous goethite	
	High-grade hematite	Hematite with minor quartz, kaolinite	
Channel iron deposit (CID)	Low Al_2O_3	Pisolitic goethite with minor hematite cores and brown to ochreous cement	Australia: Yandicoogina Junction, Yandi, Bonnie Creek
	High Al_2O_3		Australia: Robe Mesa J, Mesa A, Kings
Detrital	Terrestrial detrital deposits	Hematite-goethite conglomerates and gravels derived by erosion of iron formation or iron formation-hosted mineralization	Australia: Brockman 2, Marillana
	Marine deposits "iron sands"	Marine deposits of titanomagnetite-rich sediments, typically occurring as beach sand deposits associated with erosion of young volcanic terrains	New Zealand: Waikato North Head, Tahāroa Indonesia: Jogjakarta
Fe oxide	Iron apatite	High-grade magnetite-apatite	Sweden: Kiruna, Malmberget
	Kiruna-type		The United States: Pea Ridge Peru: El Romeral
	Fe skarns	Magnetite skarn deposits	Chile: El Laco PRC: Daye Russia: Magnitaya Gora
Fe-Ti-V oxide deposits	Anorthosite Complexes	Titanomagnetite-rich layers in gabbro or ferrodiorite	South Africa: Bushveld Igneous Complex Mozambique: Tete
	Flood basalts	Titanomagnetite in flood basalts in large igneous provinces	Australia: Windimurra PRC: Panzhihua, Hongge, Baima, Xinjie
Oolitic Fe		Sedimentary oolitic ironstone	Germany: Minette, Salzgitter Australia: Hodgson Downs/Roper River PRC: Exi Canada: Peace River The United States: Clinton
Iron oxide Cu-Au		Fe oxide-copper-gold ("IOCG"), some with associated light rare-earth elements. Either hematite or magnetite is the main Fe oxide	Australia: Olympic Dam, Ernest Henry Chile: La Candelaria PRC: Bayan Obo

Based on Clout and Simonson (2005), Williams et al. (2005), Gutzmer and Beukes (2009), Pang et al. (2010), Song et al. (2013), Petruk (1977), and this chapter.

Table 2.3 **Modal mineralogy of some typical iron ores.**

Deposit type	Source	Deposit type	Hematite	Hydrohem.	Magnetite	Goethite	Och. goethite	Quartz	Kaolinite	Gibbsite	Nontronite	Olivine	Ti-augite	Cum.-grun.	Hornbl.	Plag.	Biotite	Chlorite	Chrysotile	Dolomite	Apatite	Ilmenite	Pyrite	Others
BIF	4	IF			28			29						18	11		13			1				
HG hematite	4	IF	63.6	3.5		12.0	15.0	0.9	5.0															
M-G	4	IF	39.0	2.6		30.2	22.8		2.1															
Carajás	4	IF	90.7		0.6	5.2	1.9		1.2															
SSF	4	IF	90.5		1.4	2.3	1.3	3.9	0.6															
CID	4	IF	0.7	12.2		58.6	28.0		0.6															
Exi	*2	Oolite	61					20										2			2			15
Peace River	3	Oolite				45		5			45										5			
Panzhihua ROM	*1	Fe-Ti-V	3.5		30.6				3.6			16.2	13.1			15.8		4.2	3			6.1	0.7	0.9

Results are from quantitative XRD analysis, expressed as weight percent
Hydrohem., hydrohematite; Och. goethite, ochreous goethite; Cum.-grun., cummingtonite-grunerite series; Hornbl., hornblende; Plag., plagioclase.
Sources: *1, Dahe, 2004; *2, interpreted from Song et al., 2013; 3, Petruk, 1977; 4, J Clout and J Manuel, unpublished information.

2.2.2.2 Iron formation-hosted iron ore deposits

Iron formation-hosted iron ore deposits account for the majority of current world production and >31,000 Mt of high-grade hematite resources of iron ore (Gutzmer and Beukes, 2009; Dalstra and Guedes, 2004). Iron formations have been divided into three subtypes (Gutzmer and Beukes, 2009) on the basis of texture and geologic age of the iron formation host:

- Banded iron formations (BIFs) are further subdivided into the typically thinner >2.75 Ga Algoma-type BIF and the thick and laterally extensive Hamersley-type BIF at 2.0–2.75 Ga. Both were deposited below wave base on shelf platforms of the first stable cratons.
- Granular iron formations (GIFs) are 1.8–2.1 Ga in age, are of smaller lateral extent, are believed to have been deposited above wave base, and contain coarser banding, along with granules and oolites of iron oxides and chert.
- Rapitan iron formations (RIFs) are much younger at 0.8–0.6 Ga and associated with glaciomarine sediments that contain bands of disseminated magnetite (e.g., Rapitan, Canada; Braemar iron formation, South Australia).

The Hamersley-type BIFs host the largest known BIF-hosted iron ore deposits worldwide, while the GIFs host smaller deposits in the Lake Superior region. Little has so far been mined from the lower-grade RIF deposits.

BIF and GIF deposits can be subdivided into three classes: (1) unenriched primary iron formation with typically 30–45 wt% Fe; (2) martite-goethite ore formed by supergene processes, with abundant hydrous iron oxides containing 56–63 wt% Fe; and (3) high-grade hematite ores thought to be of supergene-modified hypogene or metamorphic origin with 60–68 wt% Fe (Table 2.4; Morris, 1985; Beukes et al., 2002; Clout and Simonson, 2005).

Archaean and Proterozoic iron formations with 30–45 wt% Fe are mined in the United States, Australia and Canada, and especially in the PRC, the latter where ~1300 Mt was mined as ROM ore in 2011 and beneficiated to a ~64–67 wt% Fe product (Sha and Wang, 2013). The majority (>85%) of the 700 Mt of iron ore imported into the PRC during 2011 (Sha and Wang, 2013) is believed to be of iron formation-hosted iron ore with typical ore mineralogy given in Figure 2.1.

High-grade hematite ores are subdivided into hematite, including itabirite-derived residual ore, and microplaty hematite replacement ore. Itabirite is oxidized, metamorphosed, and heterogeneously deformed BIF that contains iron ore deposits formed by supergene leaching of gangue minerals and residual accumulation of hematite (Dorr, 1969; Spier et al., 2003). Microplaty hematite replacement ore consists of a three-dimensional network of 10–200 μm plates of hematite with interstitial voids, formed from replacement of silicate and carbonate bands in the iron formation (Morris, 1985). Individual high-grade hematite iron ore deposits range from a few million tonnes to over 2 billion tonnes at >64 wt% Fe, although most fall within the range of 200–500 Mt.

In general terms, the largest iron ore deposits are found where paleoenvironmental conditions permitted the accumulation of the largest iron formations. For example, the Carajás and Quadrilátero Ferrífero (Iron Quadrangle) provinces in Brazil and the Hamersley province in Western Australia are among the largest iron formations on Earth and account for the bulk of the world's iron resources, in the form of iron

Table 2.4 Iron formation-hosted iron ore deposit classifications for selected current and some future mines with either published resources or reserves

Classification	Subtype	Current and future mines
Unenriched iron formation, BIF, GIF, and RIF	Magnetite	PRC: Diao Juntai, Gong Chang Ling, Chita Shan, Dashihe The United States: Empire, Hibbing, Northshore (Mesabi Iron Range) Australia: Karara, Mount Gibson, Koolanooka, Tallering Peak (Yilgarn Craton), Balmoral (Pilbara Craton), Razorback Ridge (RIF)
	Hematite	Canada: Wabush, Mont Wright, Carol Lake, Bloom Lake, Fire Lake, Fire Lake North The United States: Tilden PRC: Dong'anshan, Hainan Island
Martite-goethite		Australia: Marandoo, West Angelas, Orebody 29, Area C mine, Hope Downs, Christmas Creek, Ophthalmia Range, Rhodes Ridge, Paraburdoo, Eastern Ranges, Section 6 and 7, Firetail, Nyidinghu (Pilbara Craton), Koolyanobbing, Mount Jackson, and Mount Windarling (Yilgarn Craton)
High-grade hematite	Microplaty hematite	Australia: Mount Whaleback, Mount Tom Price, Paraburdoo, Channar, Yarrie, Giles Mini (Pilbara Craton); Iron Duke, Iron Knight, Iron Duchess (Gawler Craton) Brazil: Carajás district: N1 to N9, including N4E, S11–S45 India: Goa, Noamundi, Aridongri district Guinea: Simandou, Mount Nimba Republic of Congo: Badondo South Africa: Thabazimbi Ukraine: Krivoy Rog district
	Hematite	Australia: Cockatoo Island (GIF) Brazil: Quadrilátero Ferrífero District: Águas Claras, Alegria, Andrade, Baú, Brucutú, Cauê, Córrego do Feijão, Córrego do Meio, Capanema, Conceição, Casa de Pedra, Fábrica, Fazendão, Morro Agudo, Matuca, Ouro Fino, Pico, Pires, Retiro das Almas, Tamanduá, and Timbopeba PRC: Hainan South Africa: Sishen-Beeshoek, Sierra Leone: Marampa Cameroon: Mbarga Republic of Congo: Mbalam-Nabeba

The majority of the deposits are BIF-hosted, except those marked as GIF or RIF.
Modified from Clout and Simonson (2005).

formation-hosted high-grade iron ore. High-grade economic bodies do not form, however, without subsequent events that upgrade the iron formation, typically increasing grade from 30 wt% Fe in an unenriched iron formation to 56–68 wt% Fe in martite-goethite and high-grade hematite ores.

2.2.2.3 Iron formation ore textures and mineralogy

Many of the primary mesobands and microbands of the parent BIF are preserved during the formation of the martite-goethite and high-grade hematite ores (Figure 2.2; Morris, 1985; Clout and Simonson, 2005). This preservation results from replacement of chert and carbonate bands by hematite (in the case of high-grade microplaty hematite ores) or goethite (in martite-goethite ores) or residual accumulation of martite as the result of leaching out of chert and carbonate bands, which once contained disseminated magnetite. Magnetite-rich bands in the iron formation were oxidized to martite and/or replaced by secondary hematite in ore, whereas Al-rich silicate bands have been leached and partly replaced by clays to form "shale"-like bands. The shale-like mesobands should not be considered as epiclastic sedimentary rocks, but rather the Al-rich residue of supergene leaching and weathering of Al-rich silicate mesobands that originated as a mixture of fine volcaniclastic material and chemical precipitates (Ewers and Morris, 1981; Pickard et al., 2004). In martite-goethite ores, chert- and carbonate-dominant bands have

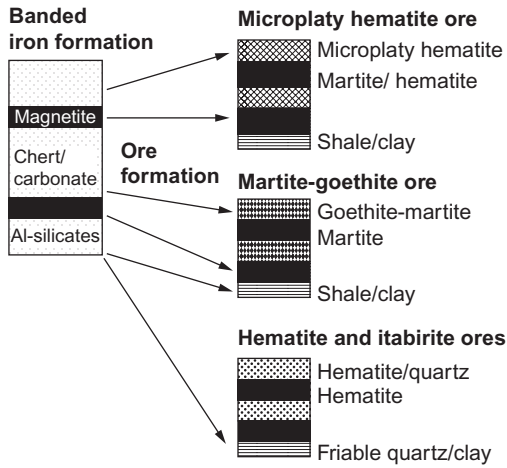

Figure 2.2 Simplified summary of ore relationships to primary banding in BIF for high-grade hematite and martite-goethite iron ores. For microplaty hematite ores, microplaty hematite = cross-hatching, martite/hematite = black bands and shale/clay bands = horizontal line work; for martite-goethite ores, martite-hematite = black bands, after original BIF magnetite = black bands, BIF chert or carbonate bands are replaced by goethite-disseminated martite (black squares); for itabirite and other leached hematite and hematite-goethite ores, BIF chert or carbonate bands now hematite (stipple) or friable hematite-residual quartz, magnetite bands replaced by hematite/martite (black bands), and Al-silicate bands by shale (clays). Note similar replacement relationships also apply to granular iron formation (GIF). Modified from Clout and Simonson (2005) and Clout (2005).

been leached out and replaced by goethite so that the overall iron content is enriched. Disseminated magnetite in BIF chert and carbonate bands is oxidized to martite in martite-goethite ores. In the microplaty hematite ores, a network of fine (0.2–0.01 mm) microplates of hematite has completely replaced chert and carbonate-dominant bands. For the metamorphosed itabirite-derived ores from the Quadrilátero Ferrífero and deposits like Mbarga in southeast Cameroon, as well as Nabeba in the northwest Republic of Congo (Longley et al., 2013), residual concentration of hematite, specular hematite, and martite has been achieved by leaching out of silicate- or carbonate-rich bands. In the less strongly leached itabirite-derived ore, some remnant friable quartz may be present with residual hematite or "specular" hematite and martite. Specular hematite or "specularite" is defined as coarse-grained hematite with a splendent metallic luster, evident from reflecting "mirrorlike" grains visible to the naked eye (Morris, 1985). Specular hematite should not be confused with the much finer-grained microplaty hematite, micaceous hematite, or hematite specimens with marked schistosity.

Although the main ore minerals in many iron ore deposits are hematite and goethite and the overall mineralogy is quite simple, ore textures and their spatial distribution and modification across individual deposits are typically complex (Clout, 2002).

2.2.2.4 Unenriched iron formation ores

Unenriched primary iron formation is a major source of iron ore in many parts of the world, especially the PRC and North America and includes both magnetite- and hematite-rich iron formations. In North America, the term taconite is used to describe magnetite- and hematite-rich BIF-GIF ore with >30 wt% Fe (James, 1954; Neal, 2000). In Australia, Africa, and Brazil, little unenriched iron formation ore has been mined to date due to the presence of significant resources of direct-ship or easily beneficiated high-grade hematite and martite-goethite ores.

Where observed, the geology and mineralogy of the iron formation ores are similar to the surrounding uneconomic iron formation facies (Table 2.5), except that the ore zone contains more abundant and coarser-grained magnetite (Figure 2.3a) or hematite, less gangue inclusions in magnetite, or a higher percentage of iron oxide meso-/microbands compared to silicate or carbonate-rich mesobands (Figure 2.3b). Iron formation ores are commonly located in greenschist- to amphibolite-facies terrain, with the higher metamorphic-grade associated with coarser magnetite grain size and more discrete grains of gangue (Neal, 2000). Sub- to lower greenschist-facies iron formations such as those in Australia and Brazil are commonly uneconomic, since the magnetite either is very fine (Figure 2.3c) or contains very fine inclusions of gangue, which require expensive fine grinding to liberate prior to beneficiation. Many iron formation ores contain a weathered cap of hard hematite or hematite-goethite underlain by friable hematite-quartz ("saprolite") (Figure 2.4). In some cases, the thin hematite-goethite cap may be economic to process (e.g., Tallering Peak mine, Western Australia, and the now depleted high-grade supergene-upgraded ore above taconite ore in the Great Lakes region).

In the United States, significant resources of Lake Superior-type BIF-GIF taconite have been mined from Michigan (Empire and Tilden) and Minnesota (Hibbing and North Shore), with Fe-grade ores as low as 30–35 wt% (Graber and Sundberg, 2002).

Table 2.5 Names and idealized compositions of the iron-bearing mineral characteristic of each of James' (1954, 1966) four mineralogical facies of unenriched, unmetamorphosed iron formations

Mineral facies	Principal iron-rich mineral(s)	Chemical formula
Oxide	Hematite	Fe_2O_3
	Magnetite	Fe_3O_4
Silicate	Greenalite[a]	$Fe_3Si_2O_5(OH)_4$
	Minnesotaite[a]	$(Mg,Fe)_3Si_4O_{10}(OH)_2$
	Stilpnomelane	$(K,Na,Ca)_{0.6}(Mg,Fe^{2+},Fe^{3+})_6Si_8$ $Al(O,OH)_{2.7}2–4H_2O$
	"Chlorite"[b]	$(Fe,Al,Mg)_3(Si,Al)_2O_5(OH)_4$
	Riebeckite	$Na_2Fe^{2+}{}_3Fe^{3+}{}_2Si_8O_{22}(OH)_2$
Carbonate	Siderite	$FeCO_3$
	Ankerite	$Ca(Fe,Mg,Mn)(CO_3)_2$
Sulfide	Pyrite	FeS_2

Formulae are from Deer et al. (1992) unless indicated otherwise.
[a] From Miyano (1987).
[b] From Klein and Bricker (1977).

Although magnetite is commonly the main ore mineral in the iron formation, other ore minerals include hematite-siderite (Tilden mine) and minor goethite near the surface. Key gangue minerals include quartz, iron carbonates (siderite and ankerite), and iron silicates (minnesotaite, greenalite, stilpnomelane, and cummingtonite) (Table 2.5).

The Anshan district, located in the Archaean Anshan-Liaoning granite-greenstone belt in the southern part of the Liaoning province in the northeast of the PRC, has a history of iron formation mining dating back to the middle Tang Dynasty of the seventh century. The Gongchangling deposit is typical of a number of >500 Mt BIF ore deposits (25–35 wt% Fe) in the Anshan district, with significant production of 35 Mt of magnetite concentrates in 2004 (Bofei, 2005). The Gongchangling deposit is located within a steeply dipping greenschist- to amphibolite-facies metavolcano-sedimentary sequence. The main ore mineral is magnetite, although it has been oxidized to martite near the surface. The gangue mineralogy is quite complex and includes quartz, stilpnomelane, chlorite, muscovite, eastonite, alumino-greenalite, almandine, grunerite, cummingtonite, calcite, albite, epidote, and hornblende as independent or composite bands. Cummingtonite, grunerite, riebeckite, and arfvedsonite are indicators of high-grade ore, whereas different varieties of hornblende are indicators of low-grade ore.

2.2.2.5 Martite-goethite supergene ores

The martite-goethite ores are generally accepted as the products of recent supergene leaching and replacement of BIF (Morris, 1980, 1985). Martite-goethite ores are characterized by a predominance (>50%) of goethite over martite and well-preserved bedding from the primary iron formation. The typical distribution between goethite types and hematite is shown in Figure 2.1 for martite-goethite and other iron formation

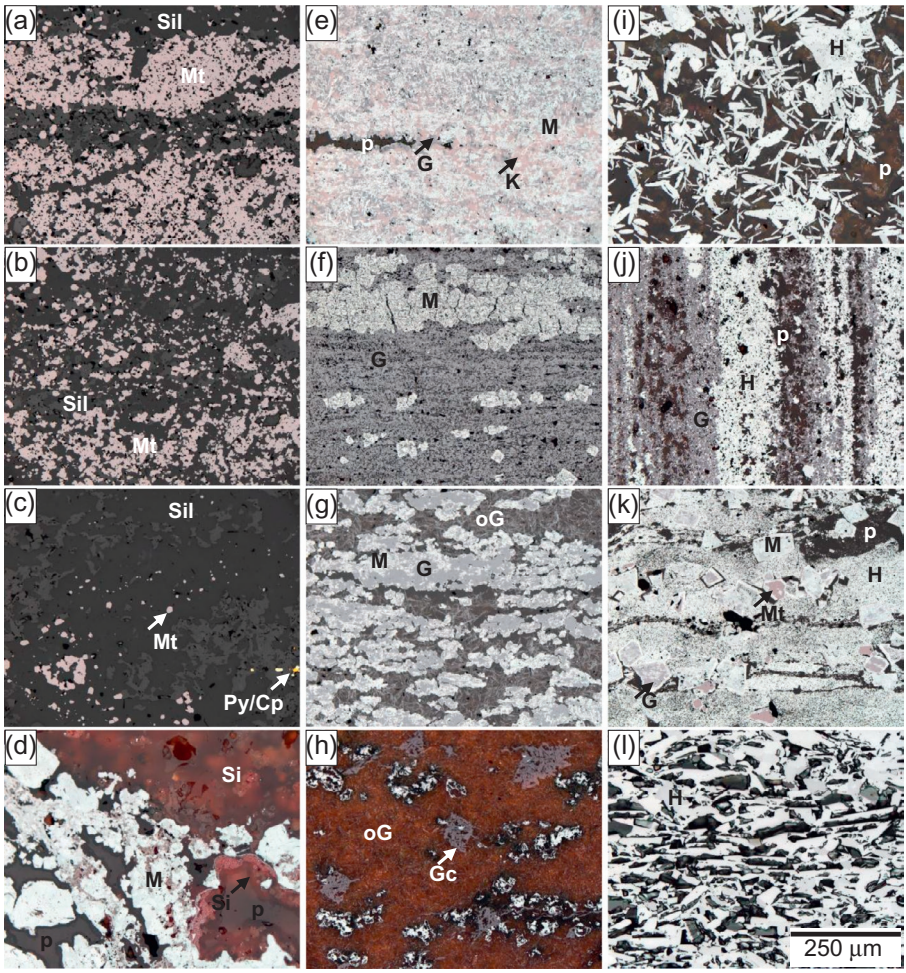

Figure 2.3 (a) coarser-grained magnetite (Mt)/chert-silicate-carbonate (Sil) BIF; (b) fine-grained BIF; (c) chert-amphibole band with fine magnetite and pyrite (Py)/chalcopyrite (Cp) grains; (d) Martite-secondary amorphous silica (Si) hardcap; (e) hard martite (M)-goethite (G) ore with remnant kenomagnetite (K); (f) primary martite-goethite ore; (g) porous martite-goethite ore with martite and dense goethite replacing magnetite, and microporous, ochreous goethite (oG) replacing silicates; (h) goethite-martite ore with goethite preserving carbonate (Gc) and silicate (oG) primary BIF textures; (i) characteristic hematite (H) microplates; (j) fine microplaty hematite infilled with goethite; (k) martite (and goethite) replacing magnetite, with fine microplaty hematite infill; (l) specular hematite (microporous). N.B. p = pore (epoxy-filled or open). N.B. a,b,c,g,k 100x; d,e,h,i,j,l 200x; f 50x magnification; scale bar correct for 100x.

ores. About 90% of the pre-mining iron formation-hosted resource for the Hamersley province is of Phanerozoic supergene martite-goethite ore (Morris, 2002). Some of the best examples of martite-goethite ores (Table 2.4) are hosted in the 2.60 Ga Marra Mamba Iron Formation in the Pilbara Craton of Western Australia (Trendall et al., 1998) and include the Marandoo, Area C, and West Angelas deposits (Harmsworth

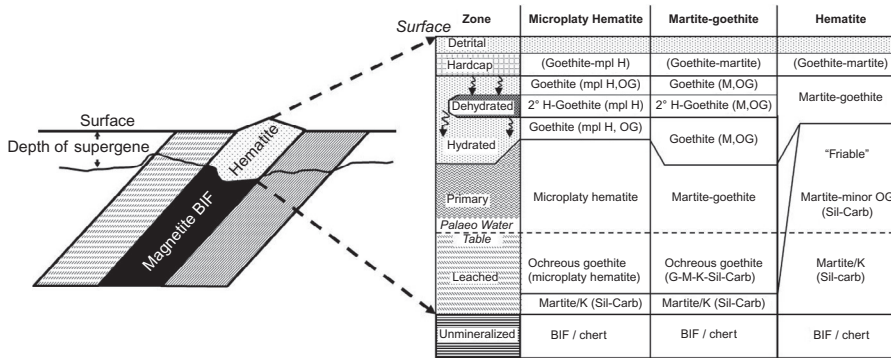

Figure 2.4 Stylized cross section through a typical iron formation deposit showing vertical mineralogical zonation (right) of typical supergene alteration. In areas of deep supergene leaching, the martite/kenomagnetite "friable" zone in itabirite-hematite ores and martite-goethite or goethite-martite ore may be very thick while the cemented martite-goethite hydrated "cap" may be thin. Vertical scale = horizontal scale, and depth of supergene alteration is 5–150 m. Modified from Clout (2005). mplH, microplaty hematite; H, hematite; M, martite; OG, ochreous goethite; K, kenomagnetite; Sil, silicates; predominantly quartz; Carb, carbonates. Wiggly arrows show groundwater movement direction. (), leached.

et al., 1990). Significant martite-goethite mineralization is also well developed in the stratigraphically higher Brockman Iron Formation (e.g., Ophthalmia Range, Rhodes Ridge, Paraburdoo, Eastern Ranges, and Section 6 and 7 deposits).

In Pilbara martite-goethite ores, martite has replaced magnetite microbands (Figure 2.3e) and magnetite disseminated in silicate/carbonate microbands (Figure 2.3f), preserving the original outline of banding in the BIF (Figure 2.3f–g). Preservation of banding has also occurred due to iron enrichment where silicate/carbonate microbands have been replaced by either brown goethite (Figure 2.3f) or yellow ochreous goethite (Figure 2.3g). Ochreous goethite has pseudomorphed delicate brushlike silicate textures (Figure 2.3h) and carbonate rhombs (Figure 2.3h) from silicate-carbonate BIF.

Preservation of primary BIF layering in Pilbara martite-goethite ores is common, with magnetite micro- to mesobands pseudomorphed by martite and silicate/carbonate micro- to mesobands replaced by goethite (Figure 2.5). In the hard martite-goethite ore, coarse-grained (1–4 mm) martite is intergrown with goethite and few pores remain (Figure 2.3e). Moderate leaching of martite-goethite hard ore has resulted in either porous martite (M in Figure 2.3f) or martite-ochreous goethite ore (M-oG in Figure 2.5f). In what was once chert with disseminated magnetite, hard brown goethite typically replaces silicate or carbonate with magnetite replaced by martite (Figure 2.5g). Friable, ochreous goethite-martite ore may consist of alternating bands of ochreous goethite replacing ex-silicate/carbonate microbands and martite grains replacing original magnetite microbands (Figure 2.3g and h). The gangue occurs mainly as thin (<2 m) kaolinite-rich shale mesobands, whereas quartz is largely secondary and restricted to the weathered, macroporous, brown to vitreous goethite surface hardcap (Figure 2.5h).

Many high-grade hematite deposits in the Quadrilátero Ferrífero and Carajás districts of Brazil also contain a recent thin (<30 m) goethite-martite hardcap and goethitic "canga,"

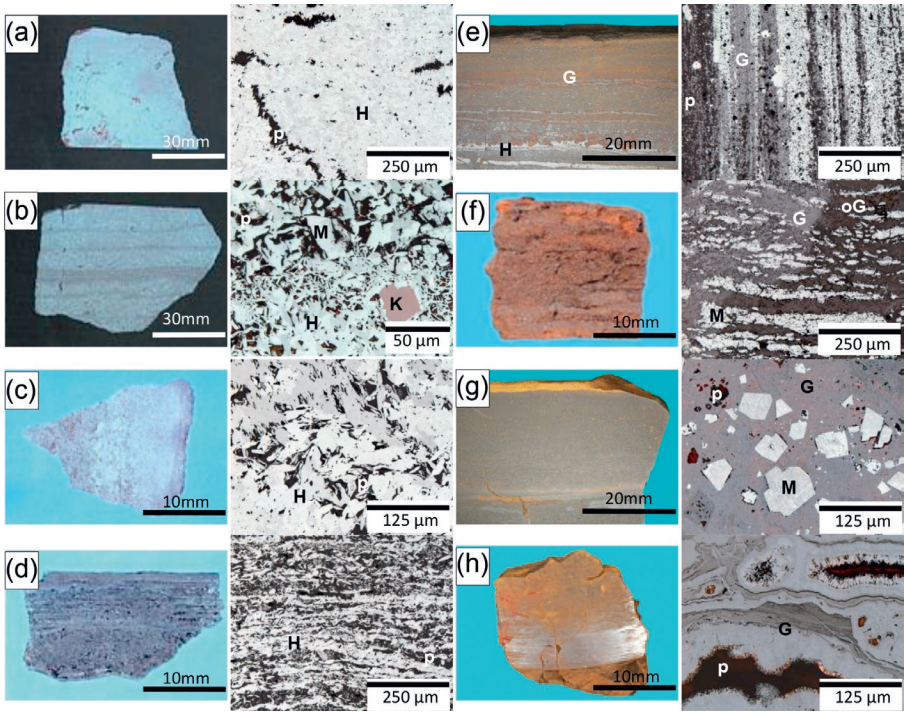

Figure 2.5 Typical hand specimen and corresponding reflected light photomicrographs of various high-grade microplaty hematite ores (a-e) and martite-goethite ores (f-h). Samples are: (a) dense hematite ore with interlocking grains and macropores; (b) martite-hematite ore, preserving primary BIF layering and remnant kenomagnetite; (c) hard, microplaty hematite; (d) microporous, laminated microplaty hematite (minor goethite); (e) laminated, fine-grained microplaty hematite-goethite ore with goethite replacing BIF silicate/carbonate; (f) variably leached martite-goethite with more resistant (lighter colour) brown goethite and microporous (darker) zones, martite after primary BIF magnetite layers and goethite after silicate/carbonate; (g) hard goethite-martite with euhedral martite grains pseudomorphed after magnetite; goethite preserving outlines of carbonates. A thin, yellow ochreous goethite layer is visible at the upper surface of the hand specimen; (h) intermediate, brown/'earthy' goethite, photomicrograph showing secondary colloform/crystalline void infill. K = kenomagnetite, M = martite, H = microplaty hematite, G = goethite, oG = ochreous goethite, p = pore. N.B. photomicrographs a,d,e,f 100x; c,g,h 200x; b 500x magnification. Handspecimen scale: Specimen b is 75 mm across from left to right and the photograph of specimen a is at the same scale. Field width for the photographs of specimens c, d, f and h is 30 mm and for e and g, 50 mm.

a term to describe loose detrital material and cemented martite-hematite conglomerate at the surface. However, the hardcap and canga may also derive from goethite replacement of gangue in BIF or supergene ore during recent weathering (Spier et al., 2003).

2.2.2.6 High-grade hematite ores

The high-grade (>60 wt% Fe) hematite ores, which include martite-hematite and microplaty hematite-martite replacement ores, have quite variable characteristics (Table 2.6).

Table 2.6 Summary of mineralogical characteristics of key iron formation-hosted high-grade hematite deposits

District	Reserves Gt (1000 Mt)	Host rock	Main ore type	Accessory ore types
Sishen, South Africa	0.17	Asbestos Hills Subgroup	Hard massive hematite, laminated hematite (60–66% Fe)	Specular hematite
Quadrilátero Ferrífero, Brazil	3.3	Caué Itabirite (35–41% Fe)	Friable hematite (64–68% Fe)	Specular hematite, magnetite, dolomite-itabirite (32% Fe)
Carajás, Brazil	18.0	Carajás Formation (35–38% Fe)	Friable hematite (66–68% Fe)	Brecciated hematite-dolomite, laminated hematite-dolomite (45% Fe)
Hamersley, Australia	3.5	Brockman iron formation (34% Fe)	Hard-friable hematite (64–68% Fe)	Magnetite-siderite-apatite, hematite-ankerite-apatite (44–68% Fe)
Krivoy Rog, Ukraine	4.7	Saksagan suite (36% Fe)	Hematite (64% Fe)	Magnetite/ magnetite-specular hematite, magnetite-carbonate, magnetite-amphibole (50–57% Fe)
Bailadila, India	1.5	Bailadila group (35% Fe)	Hard hematite (64–68% Fe)	–
Thabazimbi, South Africa	0.3	Penge Iron Formation (36% Fe)	Hard hematite (65% Fe)	Brecciated hematite-calcite (45% Fe), laminated hematite-dolomite (42% Fe), hematite-talc

All percent values on weight basis.
Modified from Dalstra and Guedes (2004), Carney and Miene (2002), and Clout and Simonson (2005).

Hematite ores: The hematite ores are composed of residual martite and/or hematite thought to be derived from iron formation by leaching of gangue, leading to residual concentration of the iron minerals. For the most part, hematite ores contain very little (<15%) goethite, except in the surface hardcap, and may include some hematite of interpreted hypogene origin (e.g., Quadrilátero Ferrífero hard and high-grade ores).

The high-grade Sishen hematite deposit (1690 Mt at 64.8 wt% Fe; Carney and Miene, 2002) in South Africa occurs immediately beneath a major regional erosional unconformity and grades downward into unmineralized BIF (Beukes, 1986; Beukes et al., 2002). Beukes et al. (2002) and Carney and Miene (2002) described two major supergene ore types and their relative abundances: (1) hard, microcrystalline, massive

(58% of the total resource) and laminated (18%) martite ores and (2) conglomeratic (detrital) ores (16%). Breccia ores (8%) are present and comprise very angular and poorly sorted fragments of laminated and massive ores (Carney and Miene, 2002). The microcrystalline, laminated martite ore preserves original textures and banding of the precursor BIF and is interpreted as a product of supergene residual concentration of martite. However, localized coarse, specular hematite infill of secondary pores and veinlets crosscuts both laminated and conglomeratic ores and suggests some secondary iron remobilization.

The Quadrilátero Ferrífero hosts major (~17,500 Mt at >64 wt% Fe) soft, high-grade hematite and/or martite deposits, with resources of ~10,000 Mt averaging 66–68 wt% Fe. They are thought to have formed in part by residual concentration due to supergene leaching of carbonate and quartz from hard itabirite (meta-BIF) protore with about 40 wt% Fe (Guild, 1953, 1957; Dorr, 1965; Rosière and Chemale, 1991; Pires, 2002; Ribeiro et al., 2002; Guedes et al., 2002; Beukes et al., 2002; Spier et al., 2003; Rosière and Rios, 2004). However, only 15% of the total resource is of hard, high-grade ore, which forms smaller pods and lenses within the dominant (85% of total resource) soft, high-grade supergene residual ores (Spier et al., 2003). Itabirite in the Quadrilátero Ferrífero has been deeply leached to depths of up to 500 m beneath the surface.

At the Águas Claras mine (~288 Mt), in the Quadrilátero Ferrífero district, the ore consists of pods of hard, high-grade hematite ore within dominant soft, high-grade supergene ore, with thin goethitic hardcap (Spier et al., 2003). The soft, high-grade (>64 wt% Fe) ore mainly consists of residual martite, granular hematite, and locally foliated, tabular hematite crystals (specularite; Figure 2.3l) with rare gangue consisting of dolomite, chlorite, talc, and apatite (Pires, 2002; Spier et al., 2003).

At least four principal textural types of high-grade hematite ore are recognized in the Quadrilátero Ferrífero, including (1) thin-bedded, laminated, and banded; (2) foliated, micaceous, and schistose, from high-strain domains; (3) minor brecciated; and (4) massive/compact (Rosière et al., 2001; Pires, 2002; Rosière and Rios, 2004). Although the ores are best known for a foliated specular hematite texture (Figure 2.3l), the most common texture is martite after magnetite. The friable, hematite-rich low-grade (40–58 wt% Fe) itabirite ore is composed of liberated hematite and quartz gangue and so is widely used as low-grade concentrator feed to produce a high-grade (>65 wt% Fe) concentrate (Spier et al., 2003).

In the Pico Mine, south of Águas Claras, high-grade ore and iron-rich itabirite are hosted within siliceous itabirite (Spier et al., 2003). The soft, high-grade ores are well laminated and highly porous (30–45 vol%) and consist of microbands formed by aggregates of martite and hematite that alternate with highly porous martite-hematite microbands (Spier et al., 2003).

2.2.2.7 *Microplaty hematite ore*

The high-grade replacement microplaty hematite ores are characterized by ubiquitous microplates of hematite (Figure 2.3i) and variable hardness and porosity; they occur with or without martite. The Mount Tom Price deposit in the Pilbara Craton

of Western Australia is an example of high-grade microplaty hematite ore, with the original resource being 900 Mt at 63.9 wt% Fe of low-phosphorus (0.053 wt% P) ore (Harmsworth et al., 1990; Bitencourt et al., 2002). The microplaty hematite ore at Mount Tom Price varies from hard to medium, massive hematite/martite-microplaty hematite to friable ores and powdery and highly leached blue dust ore (Clout, 2002). Alternating hard, medium, and friable hematite/martite micro- and mesobands persist laterally over a few meters (Figure 2.5d). Porous microplaty hematite mesobands (Figure 2.5b) commonly alternate with hard and dense, interlocking mosaic-textured hematite (Figure 2.5b) or residual martite (Figure 2.5a and d). Although the microplates of hematite interlock in the harder ore types (Figure 2.3i), they just touch at their tips in the friable porous ore types. At shallow (0–40 m) depths below the present land surface, the pores between hematite microplates may be filled with secondary goethite (Figures 2.3j and 2.5e), which may be partly dehydrated back to hematite (Clout, 2002). The blue dust ore consists largely of 0.2–0.03 mm corroded and leached plates of hematite and minor porous martite.

The Mount Whaleback deposit is the largest iron ore accumulation in Australia, originally having in excess of 1800 Mt of resources at 64 wt% Fe. It lies in a faulted outlier of the Hamersley Group (Harmsworth et al., 1990). As with Mount Tom Price, the ore is largely developed in the Dales Gorge Member as medium to hard, microplaty hematite-martite. Ore is developed to a lesser extent in the Joffre Member as softer, fissile, microplaty hematite ore with locally more goethite or as highly leached blue dust, microplaty hematite ore.

A third example of high-grade microplaty hematite ore is the deposits of the Carajás district, Brazil, that contain ~17,500 Mt ore with >64 wt% Fe hosted by the Carajás Formation (Guedes et al., 2002; Beukes et al., 2002; Rios et al., 2004; Silva et al., 2004). High-grade ore occurs as tabular bodies of friable to soft hematite that contain smaller lenses of hard hematite. The friable hematite ore occurs both as powdery hematite, almost devoid of internal structure, and as millimeter-thick bands of fine-grained hematite. In the N4 mine, Guedes et al. (2002) documented idioblastic martite surrounded by very fine-grained (~10 μm) microplaty hematite (Figure 2.3k). The hard hematite ore bodies with >66 wt% Fe contain microplaty hematite and occur mainly near the contact with the underlying metavolcanic rocks, where they are surrounded by an aureole of hydrothermal carbonate alteration. Relict BIF bedding is generally preserved in the hard ore, with dense hematite alternating with porous hematite.

2.2.2.8 Channel iron deposits

CIDs are iron-rich channel-bound fluvial rocks ranging from fine siltstones to gravelly mudstones and fine gravel with subordinate pebbles to boulder conglomerates (Morris and Ramanaidou, 2007). CID mineralization has previously been referred to as "pisolite" or "limonite" deposits. The economic portion of a CID is typically of granular goethite with minor hematite and consists of 2–10 mm diameter rounded pisoids and small (0.25–2 mm) rounded ooids (Figure 2.6). The ooids (Figure 2.6a and b) consist of a simple or complex nucleus surrounded by cortex whereas the less abundant pisoids (Figure 2.6c) consist of goethite replacements of regolith particles. CID ore is typically composed of brown or

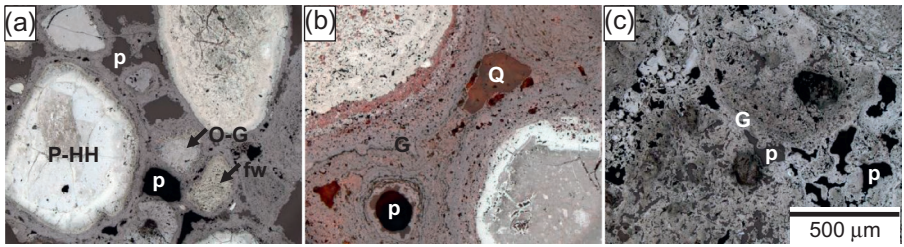

Figure 2.6 Reflected light photomicrographs of CID ore: (a) Hydrohematite (HH) / goethite (G) pisoids (P) and ooids (O) cemented by goethite, N.B. fossil wood fragment (fw); (b) detail of goethite matrix cement, with embedded quartz (Q); (c) pisoids with a matrix of goethitised infill; darker areas aluminous. p = macropore. a,c 50x; b 200x magnification; scale bar correct for 50x.

yellow ochreous goethite pelletoids (ooids and pisoids), some of which may be partly dehydrated to hematite (white) or hydrohematite (HH), ferruginized fossil wood/charcoal fragments, micro- and macropores, and minor goethitic matrix (Figure 2.6a). The main gangue minerals present include quartz, often including the chalcedonic variety (Figure 2.6b), and clays, which include kaolinite (e.g., Yandi) or gibbsite (e.g., Bonnie Creek).

2.2.2.9 Iron sands

Titanomagnetite is an unconventional source of iron ore processed in less than 15 steel mills in the world, most notably in the PRC, Russia, South Africa, and New Zealand. In 2009, only 2.6% of steel produced in the world was derived from titanomagnetite, with the most notable sources being titanomagnetite iron sand producers from Indonesia and New Zealand (Buckrell, 2011). Iron sands typically consist of 100–300 µm diameter grains predominantly of magnetite, intergrown with very fine exsolved lamellae of ilmenite. Typical gangue includes minor quartz, augite, and feldspar.

2.2.2.10 Iron ore classification

The "ore group" iron ore textural classification scheme (Table 2.7 and Figures 2.7 and 2.8) has been developed to link ore texture to downstream processing performance including lump/fines ratio, beneficiation, blast furnace lump physical and metallurgical properties, or fine ore sintering quality (Clout, 2002). The Ore Group scheme defines textural groupings on the basis of similarities in mineralogy, ore texture, porosity, mineral associations, and hardness. Groups are also distinguished by what mineral forms the matrix and what is interstitial. Ore groups are the basic building blocks of iron ores. Textural characteristics are visible in hand specimen or under the petrographic microscope. Textures are often liberated from each other in both lump ore (−40 mm) and fine ore (−6.3 to 0.06 mm). The scheme follows a logical classification tree in the decision-making process (Figure 2.8) that can be defined numerically, measured objectively, and classified using automated optical image analysis (Donskoi et al., 2013). It groups together similar, but not perfectly, identical examples, with distinct processing characteristics. The scheme is easily adaptable to the introduction of new categories through the decision tree process and coding using three- or four-letter codes (Table 2.8).

Table 2.7 The ore group textural classification scheme major groupings and distribution in BIF-derived deposits

Group	Dominant mineralogy	Porosity	Origin	BIF-derived deposit subtype		
				Microplaty hematite	Martite-goethite	Detrital iron deposit
1	Dense martite-hematite	Very low	Primary	✓	✓	
2	Microplaty hematite	Medium-high	Primary	✓		
3	Martite-goethite	Medium	Primary		✓	
4	Goethite-martite	High	Primary		✓	✓
5	Dense hematite-martite-hydrohematite	Low	Dehydration	✓	✓	✓
6	Dense martite-goethite	Low	Hydration	✓	✓	✓
7	Dense goethite-martite	Medium	Hydration		✓	
8	Microplaty hematite-goethite	Medium	Hydration	✓		
9	Brown goethite	Medium	Hydration	✓	✓	✓
10	Ochreous goethite	Very high	Hydration-primary	✓	✓	✓
11	Vitreous goethite	Medium	Hydration	✓	✓	✓

From Clout (2002).

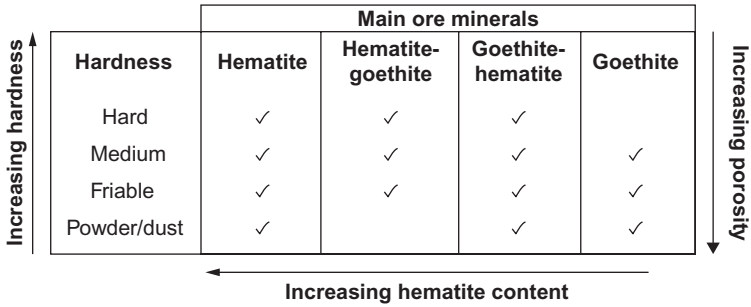

Figure 2.7 Simplified iron ore classification scheme matrix. Note that hematite here can refer to either martite or microplaty hematite or both. Goethite may be the typical brown, hard or the yellow, ochreous variety.

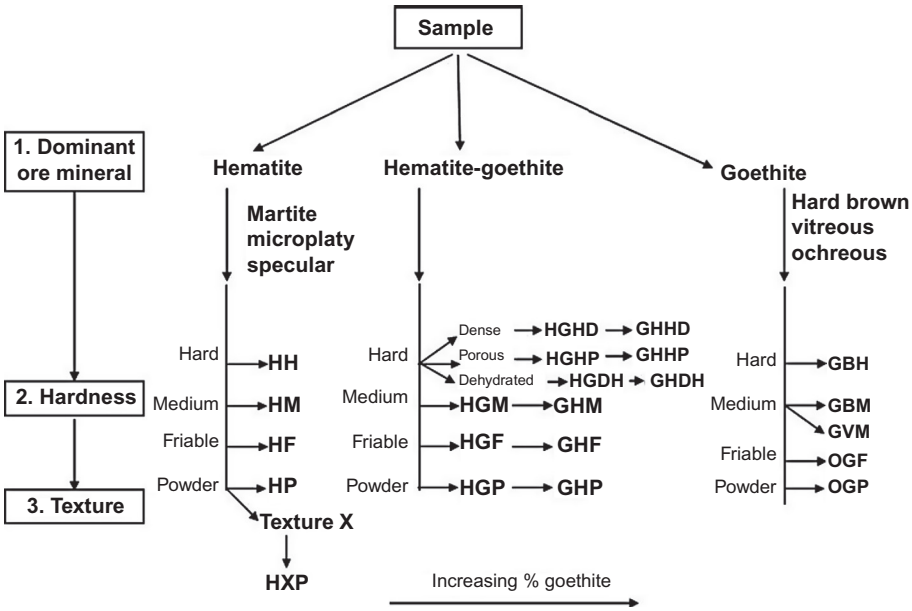

Figure 2.8 The Iron Ore Group classification tree showing dominant mineral type, hardness, and texture steps. H, hematite; G, goethite; GB, brown goethite; OG, ochreous yellow goethite; GV, vitreous goethite; D, dense; P, porous; DH, dehydrated hematite. Modified from Clout (2002).

The main ore texture groups (Table 2.7) include dense hematite (Figure 2.5a), dense martite-hematite (Figure 2.5b), microplaty hematite (Figures 2.3i and 2.5c and d), microplaty hematite-goethite (Figures 2.3j and 2.5e), martite-goethite (Figure 2.3g), goethite-martite (Figures 2.3f and 2.5g), and goethite-rich (Figures 2.3h and 2.5h). Different types of hematite are subdivided into martite, microplaty, specular, "TextureX," and undifferentiated. TextureX is nanometer-sized platy hematite, typically has a deep red color, and is powdery (Trudu et al., 2004).

The distinction between martite-goethite and goethite-martite textures is on the basis that the first mineral listed forms the matrix or supporting structure, while the latter is interstitial. Each group can be further subdivided into physically hard to softer subcategories.

The ore textural groups can be divided into those associated with primary replacement of BIF (groups 1–4; Figures 2.3e–l and 2.5a–e) and secondary textures interpreted to have resulted from more recent modification by near-surface hydration or goethitization (groups 6–10; Figure 2.5g and h) or dehydration (group 5) and surface hard-capping (Figure 2.3d) processes (group 11) (Table 2.7).

Analogous ore textural groups have been documented from iron ore deposits in Australia, Brazil, and Africa (Clout, 2002, 2005). The principles of the ore group classification scheme formed the basis for the material-type classification used by Rio Tinto Iron Ore for logging of drill holes and geologic mapping (Box et al., 2002; Clout, 2002). In addition, recent automated optical microscopy techniques have enabled far more detailed, objective ore group abundance and porosity information to be collected than is possible with visual logging or SEM-based analysis (Donskoi et al., 2013).

2.3 Chemical composition

Iron ores and concentrate products have an apparent wide range in chemical composition, especially for Fe (56–67%) and the main contaminant oxides SiO_2 (0.6–5.7%) and Al_2O_3 (0.6–3.7%) (Table 2.8). However, if the analysis is normalized to correct for loss on ignition (crystal-bound water) during sintering or pelletizing, the calcined fine ore values vary within a remarkably narrow range of 1.9–9.3% for ($SiO_2 + Al_2O_3$) and 64.1–68.1% for Fe.

The chemical composition of direct-ship and beneficiated iron ores can be divided into high-grade hematite ores, with 64–67% Fe and low SiO_2 and Al_2O_3, largely from Brazil and West Africa (e.g., Simandou); a number of Australian and other iron ores with ~60–62% Fe; high-LOI martite-goethite Australian ores; and high-LOI Australian CID iron ores.

Magnetite and hematite concentrates are generally higher in grade (64–67% Fe) with low contaminants or >67% Fe with very low contaminants when used for direct reduction purposes, reflecting more extensive beneficiation, typically with fine grinding followed by magnetite separation and sometimes also with reverse flotation or gravity concentration to reduce silica content.

The chemical composition of many fine iron ore products continues to decline with time as higher-grade reserves are replaced with lower-grade reserves for both direct-ship and beneficiated products. It is expected that this trend of declining iron ore product grades is most likely to continue well into the future. Lower-grade direct-ship products are likely to be slowly replaced in the future with beneficiated fine ores and magnetite concentrates derived from BIF.

Clout (1998) identified a number of common gangue minerals and elements that may have a negative impact on downstream processing (Table 2.9). While high levels

Table 2.8 Chemical composition of some typical fine iron ores and concentrates

Name	Dep. type	Analyte dry weight %												
		Fe_{Total}	FeO	SiO_2	Al_2O_3	TiO_2	Mn	CaO	MgO	Na_2O	K_2O	P	S	LOI_T
African H-1	IF	64.7		4.0	1.49	0.065	0.015	0.11	0.02	0.15	0.25	0.063	0.014	0.6
Australian HG	IF	61.2	0.10	4.6	2.23	0.090	0.10	0.11	0.08	0.03	0.02	0.086	0.022	5.0
Australian MG	IF	57.5	0.05	5.7	2.5	0.130	0.80	0.15	0.10	0.03	0.03	0.055	0.035	8.3
Australian CID	CID	58.3		4.7	1.56	0.072	0.07	0.05	0.04	0.03	0.01	0.040	0.013	9.0
Brazilian H1	IF	67.0		0.9	0.95		0.50					0.033	0.006	1.6
Brazilian H2	IF	66.0		3.6	0.70		0.20	0.09	0.04			0.027	0.005	0.9
Brazilian HC	IF	67.3		0.6	0.63	0.020	0.25	0.01	0.05			0.032	0.008	1.9
Indian H	IF	61.6		4.6	2.37		0.05	1.01	0.10			0.050	0.045	4.0
Chinese MtC1	IF	64.9		4.1	0.54		0.10	1.20	2.32			0.015	0.051	0.0
Chinese MtC2	IF	66.3		2.6	2.01	0.01	0.03	1.44	0.83			0.020	0.300	1.0
Iron sand	Pl	56.6		4.1	3.76	7.70						0.154		

Analysis by XRF, except LOI, which is by TGA. H, hematite; M, martite; Mt, magnetite; C, concentrate.
Data sources: J Clout and J Manuel, unpublished information.

Table 2.9 Effect of deleterious gangue and minor/trace elements on downstream process performance

Deleterious phase/ element	Geologic control	Process stage	Effects
Sideritic carbonates	Carbonate BIF or hydrothermal carbonate alteration, extent of replacement/ leaching	Sintering and pelletizing	Lowers strength of sinter and pellets due to increased porosity once carbonates are calcined (CO_2 driven off above 1000 °C)
Clays (>5%)	Shale bands and Al-silicate content of BIF host	Sintering and pelletizing	Lowers strength of sinter and pellets due to increased melt viscosity due to Al_2O_3
Alkalis (e.g., K_2O >0.09% and Na)	K_2O: BIF micas and stilpnomelane Na: hypersaline groundwater	Sintering, pelletizing, BF	Lowers melt temperature, corrosion of BF refractory bricks
P (>0.08%)	Apatite in BIF, extent of supergene leaching of P	Metal production	Removal cost
Base metals (e.g., Zn and Pb >100 ppm) and heavy metals	BIF host, hydrothermal source	BF, sintering	Removal costs, especially reprocessing of base and heavy metal-rich dusts
Al_2O_3 (>2.8%)	Shale bands and Al-silicate content of BIF host	Sintering, BF	Higher levels progressively increase melt viscosity and hence increase fuel rates
SiO_2 (>5%)	BIF and shale, extent of supergene leaching	Sintering, BF	Increases the amount of slag. Increased use of limestone since the ratio of CaO/SiO_2 must be fixed
Mn (>0.9%)	Remobilization of Mn from impure dolomite above or below mineralization, carbonate BIF	Steelmaking	Although some types of steel require Mn, excess levels require dilution with low Mn-bearing ores to maintain steel properties

Continued

Table 2.9 Continued

Deleterious phase/ element	Geologic control	Process stage	Effects
Cu (>100 ppm)	BIF host, hydrothermal source	Sintering, steelmaking	Catalyzes dioxin formation during sintering, must be diluted with low Cu ores to maintain steel quality
Cl (>500 ppm)	Hypersaline groundwater	Sintering, BF	Increased dioxin (toxic) and NO_x emissions, reduces efficiency of electrostatic dust precipitators and increases BF refractory wear
S (>0.08%)	BIF host, organic S in hardcap or near-surface martite-goethite	Sintering, BF	Increased SO_x emissions and higher MgO levels required to partition S into BF slag
Ti (>1.0%)	Shale bands, ilmenite from intrusives, or iron sand	Sintering and pelletizing	Lower physical strength of pellets and sinter

BF, blast furnace.
Modified from Clout (1998).

of one or more of the deleterious elements may limit the ability to use the product, dilution through blending at the steel mill is often a valuable strategy to enable use of what might otherwise seem to be an unacceptable iron ore. Dilution during blending will often limit but not eliminate the adverse effects of a deleterious element.

2.4 Physical properties

2.4.1 Relative hardness

There are a number of terms used frequently to describe the physical properties of iron ores that are not commonly used for other commodities, especially relative physical hardness. The relative physical hardness of high-grade hematite and martite-goethite ores varies considerably within a deposit and is a function of ore texture and the extent of secondary leaching of martite, goethite, and microplaty hematite, which produces

internal porosity (Clout, 2002). Iron ores are commonly described throughout the international iron ore industry in terms of decreasing relative physical hardness from hard to medium, friable, and finally powder or dust (Figure 2.7). Hardness is clearly independent of mineralogy alone with, for example, hematite-only ores varying from powdery to very hard. Ores that are of high to medium hardness have low porosity with physically strong, interlocking textures of martite, hematite, martite-goethite, or martite-microplaty hematite. Friable is the term used to describe ore that can be easily broken up by hand, commonly into centimeter-scale prisms defined by joint planes and fissile bedding. Friable ore is more porous than medium hardness ore. Soft is the term used where the ore can be dug in situ by hand or with a shovel, is composed of 0.05–1.0 mm particles, and is very porous, but typically not dusty. Powdery or dusty ore contains an appreciable proportion of particles less than 0.01 mm in diameter. Blue dust is a term used in Australia and India to describe distinctly blue-gray, fine-grained (0.005–0.2 mm) powdery ore composed of leached martite and/or microplaty hematite. TextureX is typically deep red and powdery and consists of nanometer-sized plates of hematite.

The hardness and related characteristics of ore are obviously important factors in its grinding and beneficiation, as well as the amount of lump ore obtained, as it often attracts a premium price over fine ore. Lump ore is defined as having a nominal particle size of 31.5–6.3 mm, whereas particles less than 6.3 mm are known as sinter fines.

2.4.2 Lump material-handling properties

The iron ore lump obtained from ROM crushing and screening plants will continue to break down into −6.3 mm particles during material handling from the product screen to stockpiles, port, and customer. Drop test conditioning of diamond drill core and crusher lump samples has been developed to simulate material handling and plant stockpiling (Clout et al., 2007). The outcomes of the lump simulations in Figure 2.9 indicate that most of the breakage of lump to −6.3 mm fines occurs after the first significant drop height; thereafter, the lump consistently shows the same lower rate of breakage to the extent of testing. Breakage functions can be developed, like the curves in Figure 2.7, for specific iron ores and their hardness categories and then used in subsequent plant engineering design and lump degradation modeling. Different iron ores will show different breakdown characteristics, with very hard iron ores showing a slower rate of breakdown, whereas friable lump breaks down so rapidly that it is unlikely to be economically viable as a lump product (e.g., Figure 2.9, ROM 15 –Friable).

2.4.3 ROM properties for crushing

2.4.3.1 Uniaxial compressive strength

Uniaxial compressive strength (UCS) is a key physical test relevant to iron ore crusher design and rock geomechanics for mining. Tests are typically performed on intact lengths of NQ, HQ, or PQ diamond drill core and record the maximum axial load

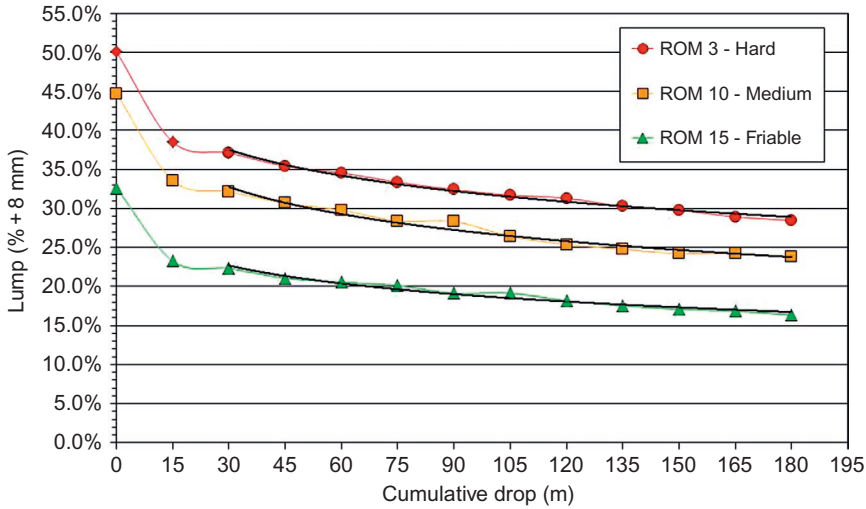

Figure 2.9 Simulation of lump yield with cumulative mechanical breakdown in material handling from crusher to port. Lump yield for various hardness types derived from crushing and screening of run-of-mine (ROM) feed.
Modified from Clout et al. (2007).

sustained at the point of failure. The International Society for Rock Mechanics (ISRM) standard terminology for UCS is very low (<5 MPa), low (5–25 MPa), moderate (25–50 MPa), medium (50–100 MPa), high (100–250 MPa), and very high (>250 MPa). UCS for most iron ores varies between low to medium, with BIF and hard hematite ores in the high to very high range (Table 2.10). Powdery to friable iron ores usually do not present as a single piece of diamond drill core and so cannot be tested.

2.4.3.2 Impact crushability

Bond impact crushability work index (CWi) (Bond, 1963) results reported for iron ores vary from hard iron ore (17.7 kWh/t) to medium hardness iron ore (11.3 kWh/t) and friable iron ore (6.3 kWh/t) (Table 2.11; Clout et al., 2007). The CWi for hard iron ores typically overlaps with those reported for BIF ("taconite") iron ores while the range in values in Table 2.11 covers that for different types of iron ores and materials reported earlier by Bond (1963), with some relevant data in Table 2.12.

2.4.4 Particle specific gravity

Particle specific gravity (SG) for natural crushed iron ores varies between 4.1 and 4.6 g/cm^3 for friable to medium hardness and 4.7–4.9 g/cm^3 for hard, high-grade hematite (Table 2.12). Natural supergene-leached iron ores typically contain abundant micropores and inclusions of gangue, which reduce particle SG compared to that expected from more theoretical mineral SG values (e.g., Deer et al., 1992). In contrast, particles in high-grade hematite and magnetite concentrates contain few micropores or inclusions of gangue and hence typically have higher particle SGs, in the range of 4.6–4.9 g/cm^3.

Table 2.10 UCS ranges for Australian iron ores and hard rocks for comparison, from O'Connor et al. (2000)

Rock/ore type	UCS (MPa)
Friable hardness iron ore	20–35
Medium hardness iron ore	110–200
Hard iron ore	200–500
Penryn granite	132
Nuneaton quartzite	139
Cliffe Hill diorite	275

2.4.5 Material-handling properties

Table 2.11 Bond impact crushability work index (CWi) ranges for an Australian iron ore

Rock/ore type	CWi (kWh/t)
Friable hardness iron ore	6.3
Medium hardness iron ore	11.3
Hard iron ore	17.7
Cloudbreak mine average[a]	12.5

[a] Average from 15 samples each of about 10 tests.
From Clout et al. (2007).

Table 2.12 Bond abrasion index (Ai) and impact crushability work index (CWi) results for Australian iron ores and waste rocks compared with other rocks

Material	SG (g/cm^3)	CWi (kWh/t)	P80 (mm)	Ai (g)
Friable waste	2.6–3.4		4.14	0.007
Shale*	2.62	9.9	11.7	0.021
Limestone*	2.7	12.7	12.8	0.024
Friable iron ore	4.1–4.6		13.53	0.243
Medium iron ore	4.2–4.6		15.46	0.365
Mt Coot-tha Quarry	2.6		14.88	0.368
Granite*	2.72	16.6	14.6	0.388
Hard waste rock	3.1–3.5		12.53	0.430
Hematite–specular*	3.29	15.40		
Hard iron ore	4.7–4.9		16.16	0.458
BIF/taconite iron ore*	3.37	16.3	–	0.624
Quartzite*	2.7	17.4	–	0.775
Alumina*	3.9	17.5	15.8	0.891

Modified from O'Connor et al (2000) and those marked "*" are from Bond (1963).

2.4.5.1 Abrasion properties

The Bond abrasion index (Ai) is used as a measure of the relative abrasivity of different rock materials on metal and is important to understand for process plant design and operation in crushing, screening, and especially grinding (Bond, 1963). Iron ores are moderate to strongly abrasive with Ai values typically higher than shale and limestone, with hard iron ore and BIF forming a range between those of granite and quartzite (Table 2.12).

2.4.5.2 Frictional properties

The coefficient of dynamic friction is typically measured using a standard soil shear box (Kezdi, 1980). Cut drill core samples of different hardness are held in a rigid sample holder with an applied weight on top while a horizontal shear force is applied. Typical values of the coefficient of dynamic friction for different relative hardness of iron ores are given in Table 2.13.

The static coefficient of friction is important for design of material handling facilities including bin wall angles. The angle at which a particle starts to slip down an inclined plane is the angle of static friction, θ, or angle of repose. The coefficient of static friction μ_s is defined as

$$\mu_s = \tan\theta$$

The angle of repose is measured using a variable inclined plane capable of being fitted with different wear-resistant materials.

The static coefficient of friction typically increases with decreasing particle size and in a similar manner for hard, medium, and friable iron ores (Figure 2.10). The static coefficient of friction for bulk iron fine ores typically increases with increasing moisture content until it reaches a maximum, beyond which the coefficient declines rapidly in response to material becoming saturated with moisture (Figure 2.11).

Table 2.13 Coefficient of dynamic friction for particle-particle interaction as a function of iron ore particle relative hardness

Relative hardness type	Coefficient of dynamic friction
Hard/medium	0.28
Medium/medium	0.35
Hard/medium	0.36
Hard/soft	0.43
Soft/medium	0.51
Soft/soft	0.61

From O'Connor et al. (2000).

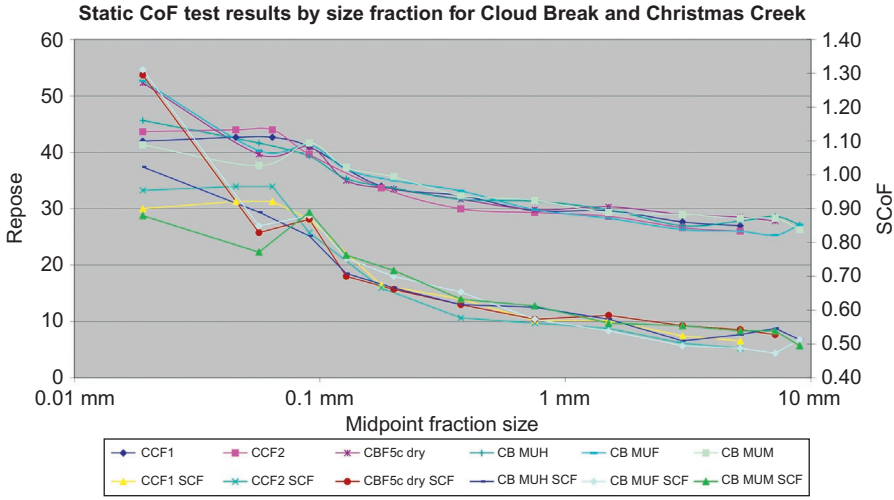

Figure 2.10 Angle of repose (left vertical axis, upper trend) and static coefficient of friction (right vertical axis, lower trend) results for Cloudbreak (CB) and Christmas Creek (CC) fine ores at varied size fractions and 0% moisture. NB MUF, friable; MUM, medium; MUH, hard; CBF 5c, bulk fine ore; CCF1 and CCF2, bulk fine ore. Stainless steel-inclined surface.

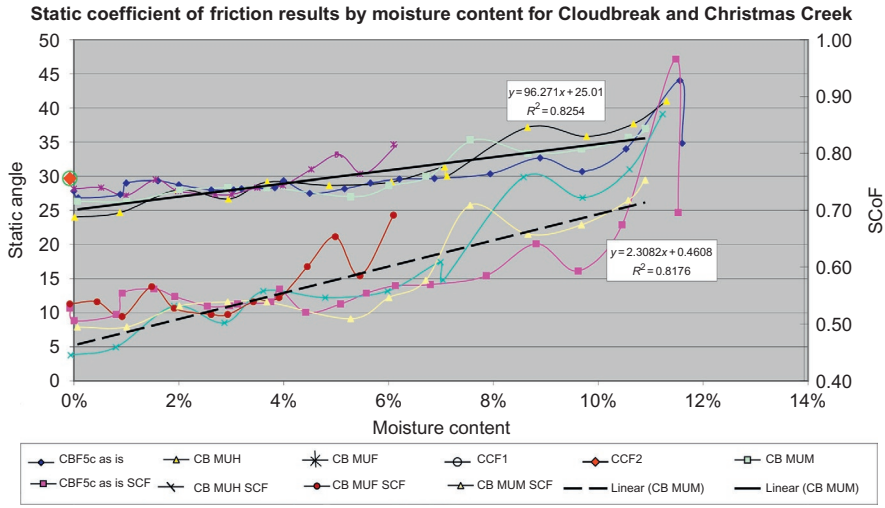

Figure 2.11 Angle of repose (left vertical axis, upper trend) and static coefficient of friction (right vertical axis, lower trend) results for Cloudbreak (CB) at varying moisture levels (0–12%) and Christmas Creek (CC) at 0%. Labels per Figure 2.10. Stainless steel-inclined surface.

2.4.5.3 Bulk density

Three types of bulk density are often determined, including in situ bulk density of rock masses usually measured from diamond drill cores, loose bulk density of iron ore products measured in the laboratory for use in conveyor design, and compacted bulk density, also measured in the laboratory, using a slight compaction force to simulate storage in a stockpile or bin. Loose bulk density typically decreases with increasing moisture due to increased voidage resulting from granulation.

There is a wide range in loose bulk densities between different fine ores, concentrates, and lumps, with concentrates generally having higher values and lump ores with lower values (Table 2.14).

2.4.6 Product particle size

Fine iron ores and concentrate products have characteristic particle size distributions, which, like their chemical analyses, inevitably change with time (Figure 2.12). The majority of fine iron ores have P_{100} of 12 mm with P_{50} of 1.0 mm of average coarseness, $P_{50} > 1.0$ mm signifying a coarse ore, and $P_{50} < 1.0$ mm a finer than average fine ore.

Magnetite and hematite concentrates have a typical P_{80} range of 45–120 µm, with P_{80} of 45–60 µm most common for pellet feed applications (Figure 2.12; "Chinese MtC"). Concentrates with P_{80} within the range of 120–500 µm are usually too coarse to use directly for pellet making so must be either sintered or reground to make pellet feed.

2.4.7 Relationship between ore properties and process performance

For typical iron ores, downstream processing performance is far more complex and dependent on ore group, from crushing and beneficiation to the final metallization stage in the blast furnace, compared to either base metals or gold. While the effects

Table 2.14 Loose bulk density as a function of different iron ore types, and hematite and magnetite concentrates for pellet feed, measured at nominally 0% moisture

Ore type	Loose bulk density (t/m³)	
	Fine ore	Lump
CID	1.55–1.81	1.85
Martite-goethite	1.70–1.95	1.65–1.80
Hematite	2.0–2.6	2.1–2.3
High-grade hematite	1.85–2.58	
Hematite concentrate	2.31	
Magnetite concentrate	2.5–2.7	

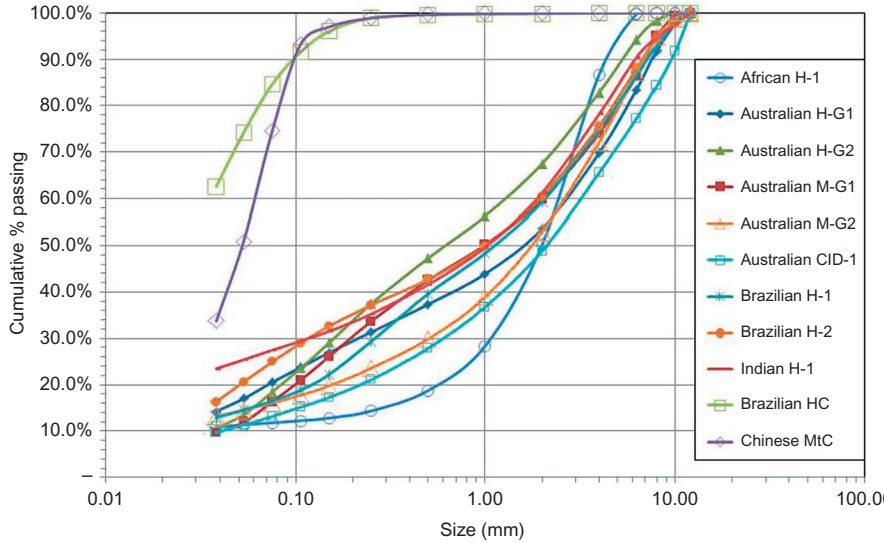

Figure 2.12 Typical particle size distributions for fine iron ores together with one hematite and one magnetite concentrate example. H, hematite; G, goethite; M, martite; C, concentrate; Mt, magnetite.

of deleterious minor and trace elements on downstream process performance are well known (Table 2.9), the effects of ore textures are poorly understood.

2.4.7.1 Prediction of blast furnace lump quality

The effects of lump ore group (texture, mineralogy, porosity, and hardness) will be initially seen in mine lump yield and then directly in lump high-temperature performance in the blast furnace. CSIRO has for a number of years conducted extensive metallurgical testing of different lump ore groups from many different iron ore deposits from Australia and around the world. This detailed work, together with collaborative industry studies (e.g., Box et al., 2002), has built up a picture of the relationship between ore groups and their lump metallurgical characteristics, as defined by industry standard tests used to characterize lump burden behavior in the blast furnace (Figure 2.13). The laboratory tests include tumble index (TI, % −6.3 mm), abrasion index (AI, % −0.5 mm), decrepitation index (DI, % −5.0 mm), reduction degradation index (RDI, % −3.15 mm), and reducibility index (RI) (Figure 2.13). TI and AI (ISO 3271) are designed to measure lump resistance to physical breakdown during transportation, DI (ISO 8371) is a measure of lump resistance to thermal shock in the upper part of the blast furnace, RDI (ISO 4696) simulates physical breakdown during reduction, while RI (ISO 7215) is a measure of the ease with which iron oxides can be reduced (Figure 2.13).

The common ore textural types in lump ores can be assigned relative metallurgical characteristics, based on previous CSIRO test result experience (Table 2.15; Clout, 2002).

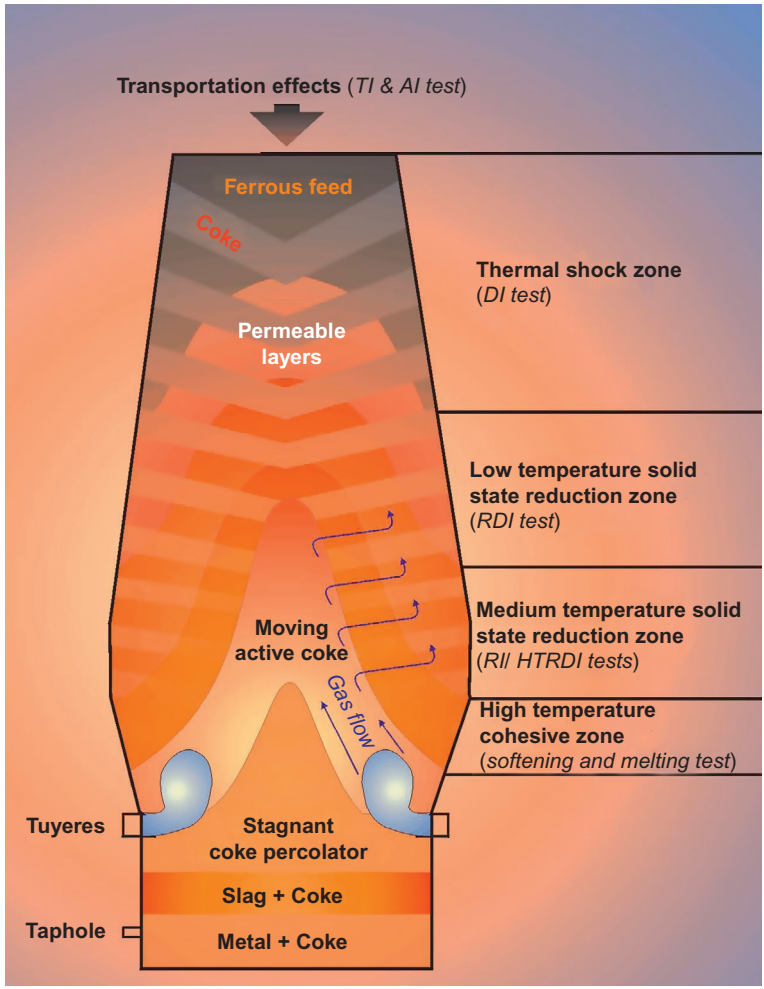

Figure 2.13 Schematic cross-section through the blast furnace showing key zones and standard industry laboratory tests designed to simulate the respective zone.

The lump properties of ore textural groups appear to be relatively consistent within and between the iron ore deposits examined, with minor quality differences largely due to differences in porosity (leaching).

Key controls on lump metallurgical quality include the following:

1. TI is interpreted to be largely a function of physical hardness, with less porous and dense martite-hematite textures being of higher TI and more porous, soft, goethite-bearing textures being of lower TI.
2. AI is essentially the complement of TI, with more porous and/or goethitic ores having higher AI.

Table 2.15 Relative lump metallurgical qualities of common iron ore textural groups

Ore group	Tumble index	Abrasion index	Decrepitation index	Reduction degradation index	Reducibility index
1. Dense martite-hematite (VL)	High	Low	Low	Low	Medium
2. Microplaty hematite (M-H)	Low-medium	High-medium	Very low	Medium-high	High
3. Martite-goethite (M)	Medium	Medium	Medium	Medium	Medium
4. Goethite-martite (H)	Low-medium	High-medium	Medium	Medium	High
5. Dense hematite/M/hydrohem. (L)	Very high	Low	Very high	Low	Medium
6. Dense martite-goethite (L)	High	Low	High	Medium	Medium
7. Dense goethite-martite (M)	Medium	Medium	High	Medium	Medium
8. Microplaty hematite-goethite (M)	Medium	Medium	Medium	High	High
9. Brown goethite (L-M)	Medium	Medium	Low-medium	Low	High
10. Ochreous goethite (VH)	Low	High	Low	High	Very high
11. Vitreous goethite (M)	Medium	Medium	Medium	Medium	High

M, martite; H, hematite, under the ore group; (), porosity; VL, very low; L, low; M, medium; H, high; VH, very high.
Modified from Clout (2002).

3. DI appears to be highest where thermal shock results in rapid evolution of mineral structural water, especially where goethite is locked within dense/low, open-porosity hematite/hydrohematite or where dense goethite is present.
4. RDI tends to be high where there is a finely porous structure and the minerals have few thick/solid interconnections.
5. High lump reducibility is interpreted to be due to more porous ore textures and is highest for porous, goethitic textures and lowest for very dense kenomagnetite.

2.4.7.2 Lump DI and ore groups

The relationship between lump DI and the ore group classification scheme has been compared with more conventional geologic classification schemes at a number of different mines, using single-particle DI tests. The tests are based on a modified ISO 8371 test and use oven predried particles (12 h at 105 °C) that are then heated in a muffle furnace in separate crucibles to 700 °C for 30 min, slowly cooled, and then screened at either 5.0 or 6.3 mm.

In the two iron ore deposits examined, the ore groups had a characteristic range in DI (Figure 2.14) with groups containing minor goethite in dense hematite/martite having the highest DI, followed by those with moderate porosity, while highly porous groups had the lowest DI (Figure 2.15). It is also evident from Figure 2.16 that a common simplistic assumption, that DI is controlled by the abundance of goethite, is not valid.

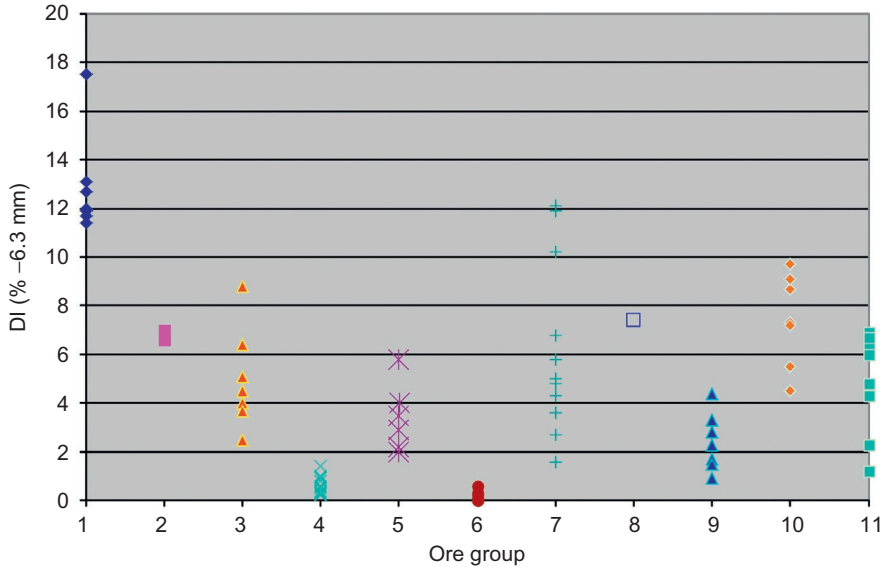

Figure 2.14 DI (% –6.3 mm) versus ore group classification types 1–11. Each data point represents the result of a single-particle DI test.

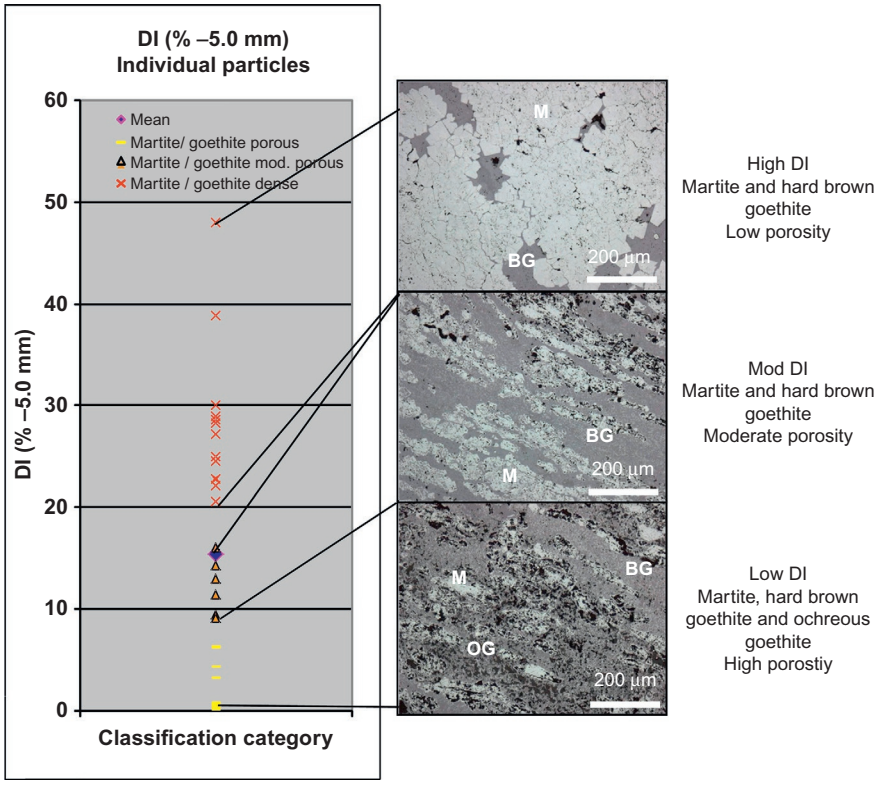

Figure 2.15 Relationship between ore group textures and DI in a single classification category. Each data point represents the result of a single-particle DI test.

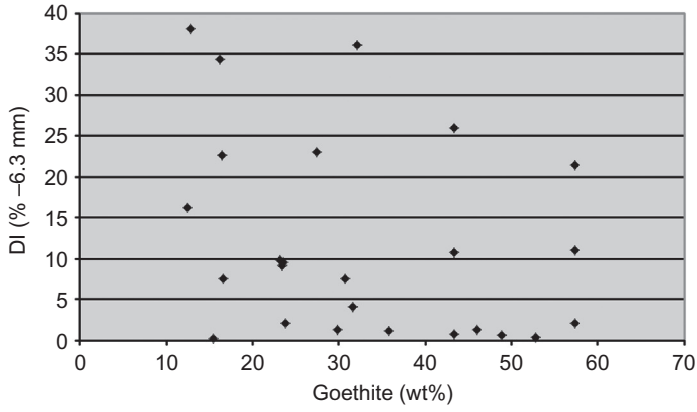

Figure 2.16 DI versus goethite modal abundance (measured by LOI at 371 °C), mine B. Each data point represents the result of a single-particle DI test.

2.5 Future trends

While the basic mineralogical understanding of iron ores is well established, there is a considerable lack of knowledge of the more detailed crystal structure, chemistry, magnetic, and physical mineral properties between the end members and variants of many iron-bearing ore minerals. For example, the crystal structural differences between brown goethite and yellow ochreous goethite are poorly understood, as are the so-called intermediate phases between magnetite and hematite (e.g., kenomagnetite). It is expected that research in this area alone will ultimately help contribute to improved beneficiation processes and hence potentially improved Fe recovery.

The average Fe grade of seaborne-traded iron ore products has slowly declined over the last ten years as reserves of higher-grade hematite ores have been progressively depleted and replaced by lower Fe-grade deposits. The trend has been underlined by a steady depletion of natural, so-called high-grade hematite "direct-ship ores" (DSOs), to be replaced by lower Fe-grade DSO, different types of beneficiated iron ores (hematite and hematite-goethite), and fine concentrates (magnetite and minor hematite) derived from BIF through fine grinding and beneficiation. It is thought that this trend of declining ore reserve Fe grade and an increase in beneficiated lower Fe-grade iron ores and magnetite and hematite concentrates will continue over the next 20 years, in the absence of any major new iron ore exploration discoveries.

References

Beukes, N.J., 1986. The Transvaal sequence in Griqualand west. In: Anhaeusser, C.R., Maske, S. (Eds.), Mineral Deposits of Southern Africa, vol. 1. Geological Society of South Africa, Johannesburg, pp. 819–828.

Beukes, N.J., Gutzmer, J., Mukhopadhyay, J., 2002. The geology and genesis of high-grade hematite iron ore deposits. In: Proceedings of Iron Ore 2002 Conference, Perth, Western Australia, AusIMM, 7/2002, pp. 23–29.

Bitencourt, R., Mackenzie, P., Gordon, J., Morey, B., 2002. High-grade optimisation and improved grade control practices in Mount Tom Price. In: Proceedings of Iron Ore 2002 Conference, Perth, Western Australia, AusIMM, 7/2002, pp. 261–277.

Bofei, J., 2005. Outputs of China major iron ore mines in Jan–Dec 2004, China Metallurgical Newsletter, Metallurgical Council of China Council for the Promotion of International Trade, 7, 20 p.

Bond, F.C., 1963. Metal wear in crushing and grinding. In: 54th Annual Meeting of the American Institute of Chemical Engineers, 12/1963.

Box, J., Phillips, J., Clout, J.M.F., 2002. Use of geological material types for predicting iron ore product characteristics. In: Proceedings 1st Japan-Australia Symposium on Iron and Steelmaking, Fuwa-Ward Symposium, Kyoto University, ISIJ, April 4–5, 2002.

Buckrell, D., 2011. New Zealand iron sands. Report to the Resources Group of the Energy and Communications, Branch of the Ministry of Economic Development, New Zealand, 31p.

Carney, M.D., Miene, P.J., 2002. A geological comparison of the Sishen and Sishen South (Welgevonden) iron ore deposits, Northern Cape Province, South Africa. In: Proceedings of Iron Ore 2002 Conference, Perth, Western Australia, AusIMM, 7/2002, pp. 145–151.

Clout, J.M.F., 1998. The effects of ore petrology on downstream processing performance: a review. In: Proceedings of Mine to Mill 1998 Conference, AusIMM, Brisbane, Australia, pp. 43–50.

Clout, J.M.F., 2002. Upgrading processes in BIF-derived iron ore deposits—implications for ore genesis and downstream processing. In: Proceedings of Iron Ore 2002 Conference, Perth, Western Australia, AusIMM, 7/2002, pp. 237–242.

Clout, J.M.F., 2005. Iron formation-hosted iron ores in the Hamersley Province of Western Australia. In: Proceedings of Iron Ore 2005 Conference, Perth, Western Australia, AusIMM, 8/2005, pp. 9–19.

Clout, J.M.F., Simonson, B.M., 2005. Precambrian iron formations and iron formation-hosted iron ore deposits. In: Hedenquist, J.W., Thompson, J.F.H., Goldfarb, R.J., Richards, J.P. (Eds.), One Hundredth Anniversary Volume 1905–2005. In: Economic Geology, Society of Economic Geologists, Littleton, Colorado, pp. 643–679.

Clout, J.M.F., Maré, E., Ilich, B., Brandli, R., Bradley, M., 2007. Simulation of product size distributions of a Marra Mamba iron ore—comparison of conventional drill and blast versus surface miner product at the Cloud Break deposit. In: Proceedings of Iron Ore 2007 Conference, Perth, Western Australia, AusIMM, 6/2007, pp. 235–240.

Clout, J.M.F., Fitzgerald, B., 2011. The Roy Hill Project, Perth Western Australia. In: Proceedings of Iron Ore 2011 Conference, Perth, Western Australia, AusIMM, 6/2011, pp. 3–10.

Dahe, X., 2004. SLon magnetic separators applied in the ilmenite processing industry. Phys. Sep. Sci. Eng. 13 (3–4), 119–126.

Dalstra, H.J., Guedes, S., 2004. Giant hydrothermal hematite deposits with Mg-Fe metasomatism: a comparison of the Carajás, Hamersley, and other iron ores. Econ. Geol. 99, 1793–1800.

Deer, W.A., Howie, R.A., Zussman, J., 1992. An Introduction to the Rock-Forming Minerals, second ed. Longman Scientific and Technical, London, 696 p.

Donskoi, E., Poliakov, A., Manuel, J.R., Peterson, M.J., Hapugoda, S., 2013. Industrial strength optical image analysis system—Mineral4/Recognition4. In: Proceedings of Iron Ore 2013 Conference, Perth, Western Australia, AusIMM, 6/2013, pp. 227–241.

Dorr II, J.v.N., 1965. Nature and origin of the high-grade hematite ores of Minas Gerais, Brazil. Econ. Geol. 60, 1–46.

Dorr II, J.v.N., 1969. Physiographic, stratigraphic and structural development of the Quadrilátero Ferrífero, Minas Gerais. In: U. S. Geological Survey Professional Paper 641-A, 110p.

Du Yan (Eds.), 1996. Handbook of Ferrous Metal Mines in China. Metallurgical Industry Press, Beijing, pp. 557–560, 318–324.

Ewers, W.E., Morris, R.C., 1981. Studies of the Dales Gorge member of the Brockman iron formation, Western Australia. Econ. Geol. 76, 1929–1953.

Graber, R.G., Sundberg, C.R., 2002. Evolution of iron ore characterisation techniques—a North American perspective. In: Proceedings of Iron Ore 2002 Conference, Perth, Western Australia, AusIMM, 7/2002, pp. 195–199.

Guedes, S.C., Rosière, C.A., Barley, M., Lobato, L., 2002. Carbonate alteration associated with Carajás high-grade hematite deposits, Brazil. In: Proceedings of Iron Ore 2002 Conference, Perth, Western Australia, AusIMM, 7/2002, pp. 63–66.

Guild, P.W., 1953. Iron deposits of the Congonhas District, Minas Gerais, Brazil. Econ. Geol. 48, 639–676.

Guild, P.W., 1957. Geology and mineral resources of the Congonhas District Minas Gerais, Brazil. U. S. Geological Survey Professional Paper 290, 90p.

Gutzmer, J., Beukes, N.J., 2009. Iron and manganese ore deposits: mineralogy, geochemistry, and economic geology. In: Geology, vol. 4. Eolss Publishers Co. Ltd/UNESCO, Oxford, United Kingdom. The summary is available from: http://www.eolss.net/sample-chapters/c01/e6-15-06-03.pdf.

Hapugoda, S., Peterson, M.J., Manuel, J.R., 2009. Mineralogical and textural characterisation of iron ore from a Peruvian magnetite-haematite skarn prospect. In: Proceedings of Iron Ore 2009 Conference, Perth, Western Australia, AusIMM 7/2009, pp. 105–112.

Harlov, D.E., Andersson, U.B., Förster, H.J., Nyström, J.O., Dulski, P., Broman, C., 2002. Apatite-monazite relations in the Kiirunavaara magnetite-apatite ore, Northern Sweden. Chem. Geol. 191, 47–72.

Harmsworth, R.A., Kneeshaw, M., Morris, R.C., Robinson, C.J., Shrivastava, P.K., 1990. BIF-derived iron ores of the Hamersley Province. In: Hughes, F.E. (Ed.), Geology of the Mineral Deposits of Australia and Papua New Guinea, Volume 1. In: AusIMM Monograph, vol. 14. The Australasian Institute of Mining and Metallurgy, Carlton, Victoria, Australia, pp. 617–642.

James, H.L., 1954. Sedimentary facies of iron-formation. Econ. Geol. 49, 235–293.

James, H.L., 1966. Chemistry of the iron-rich sedimentary rocks. U. S. Geological Survey Professional Paper, 440-W, 61 p.

Kezdi, A., 1980. Handbook of Soil Mechanics. Elsevier Scientific Publishing Company, New York, pp. 130–137.

Klein, C., Bricker, O.P., 1977. Some aspects of the sedimentary and diagenetic environment of Proterozoic banded iron-formation. Econ. Geol. 72, 1457–1470.

Longley, R.S., Kitto, P.L., Thornett, S.E., 2013. Exploration history of the Mbalam iron project. In: Proceedings of Iron Ore 2013 Conference, Perth, Western Australia, AusIMM, 6/2013, pp. 107–115.

McKenna, D.M., Harmsworth, R.A., 1998. Brockman No. 2 detritals (B2D) iron ore deposit. In: Berkman, D.A., Mackenzie, D.H. (Eds.), Geology of Australian and Papua New Guinean Mineral Deposits. In: AusIMM, Monograph, vol. 2. The Australasian Institute of Mining and Metallurgy, Carlton, Victoria, Australia, pp. 375–380.

Miyano, T., 1987. Diagenetic to low-grade metamorphic conditions of Precambrian iron-formations. In: Appel, P.W.U., LaBerge, G.L. (Eds.), Precambrian Iron-Formations. Theophrastus Publications, Athens, Greece, pp. 155–186.

Morgan, J.W., Anders, E., 1980. Chemical composition of Earth, Venus, and Mercury. Proc. Natl. Acad. Sci. U. S. A. 77 (12), 6973–6977.

Morris, R.C., 1980. A textural and mineralogical study of the relationship of iron ore to banded iron formation in the Hamersley iron province of Western Australia. Econ. Geol. 75, 184–209.

Morris, R.C., 1985. Genesis of iron ore in banded iron-formation by supergene and supergene-metamorphic processes—a conceptual model. In: Wolf, K.H. (Ed.), Handbook of Strata-bound and Stratiform Ore Deposits, vol. 13. Elsevier, Amsterdam, pp. 73–235.

Morris, R.C., 1987. Iron ores derived by the enrichment of banded iron-formation. In: Hein, J.R. (Ed.), Siliceous Sedimentary Rock-Hosted Ores and Petroleum. Van Nostrand Reinhold Co., New York, NY, pp. 231–267.

Morris, R.C., 2002. Iron ore genesis and post-ore metasomatism at Mount Tom Price. In: Proceedings of Iron Ore 2002 Conference, Perth, Western Australia, AusIMM, 7/2002, pp. 3–13.

Morris, R.C., Ramanaidou, E.R., 2007. Genesis of the channel iron deposits (CID) of the Pilbara region, Western Australia. Aust. J. Earth Sci. 54, 733–756.

Neal, H.E., 2000. Iron ore deposits of the Labrador Trough. Explor. Min. Geol. 9 (2), 113–121.

Nickel, E.H., Nichols, M.C., 1991. Mineral Reference Manual. Chapman and Hall, New York, 250 p.

O'Connor, M.T., Norrman, R., Clout, J.M.F., Boland, J.N., 2000. Frictional properties of Australian iron ores. Trans. Mech. Eng. ME24 (1), 47–52.

Ohmoto, H., 2003. Nonredox transformations of magnetite-hematite in hydrothermal systems. Econ. Geol. 98, 157–161.

Pang, K.W., Zhou, M.F., Qi, L., Shellnutt, G., Wang, C.Y., Zho, D., 2010. Flood basalt-related Fe–Ti oxide deposits in the Emeishan large igneous province, SW China. Lithos 119, 123–136.

Petruk, W., 1977. Mineralogical characteristics of an oolitic iron deposit in the Peace River District, Alberta. Can. Mineral. 15, 3–13.

Pickard, A.L., Barley, M.E., Krapez, B., 2004. Deep-marine depositional setting of banded iron formation: sedimentological evidence from interbedded clastic sedimentary rocks in the early Palaeoproterozoic Dales Gorge Member of Western Australia. Sediment. Geol. 170, 37–62.

Pires, F.R.M., 2002. Distribution of hard hematite ore at the Quadrilátero Ferrífero, Minas Gerais, Brazil and its possible genetic significance. In: Proceedings of Iron Ore 2002 Conference, Perth, Western Australia, AusIMM, 7/2002, pp. 71–76.

Ribeiro, D.T., Pires, F.R.M., Carvalho, R.M., 2002. Supergene iron ore and disorder. In: Proceedings of Iron Ore 2002 Conference, Perth, Western Australia, AusIMM, 7/2002, pp. 81–89.

Rios, F.J., Lobato, L.M., Rosière, C.A., Silva, R.C.F., Souza, A.S., 2004. Resultados preliminares do estudo metalogenético do minério hematítico de alto teor do depósito de ferro N5—Carajás, utilizando microscopia e microtermometria de infravermelho [ext. abs.]. In: Simpósio Brasileiro de Exploração Mineral, Anais. Ouro Preto, Minas Gerais, CD-ROM.

Rosière, C.A., Chemale Jr., F., 1991. Textural and structural aspects of iron ores from Iron Quadrangle, Brazil. In: Pagel, M., Leroy, J.L. (Eds.), Source, Transport and Deposition of Metals. Society for Geology Applied to Mineral Deposits Anniversary Meeting, 25th, Nancy, Proceedings, pp. 485–489.

Rosière, C.A., Rios, F.J., 2004. The origin of hematite in high grade iron ores based on infrared microscopy and fluid inclusion studies: the example of the Conceição mine, Quadrilátero Ferrífero, Brazil. Econ. Geol. 99, 611–624.

Rosière, C.A., Siemes, H., Quade, H., Brokmeier, H.-G., Jansen, E., 2001. Microstructures, textures and deformation mechanisms in hematite. J. Struct. Geol. 23, 1429–1440.

Sha, Y., Wang, Z., 2013. The Chinese iron and steel industry response to the challenges of iron ore supply. In: Proceedings of Iron Ore 2013 Conference, Perth, Western Australia, AusIMM, 6/2013, pp. 7–14.

Silva, R.C.F., Lobato, L.M., Rosière, C.A., Guedes, S.C., Monteiro, A., Meireles, H., Matias, P.H., 2004. Estudos petrográficos microscópicos, geoquímicos e geocronológicos em jaspilitos e minério de ferro dos depósitos N1, N4W, N4E e N5E, Província Mineral Carajás [ext. abs.]. In: Simpósio Brasileiro de Exploração Mineral, Anais. Ouro Preto, Minas Gerais, CD-ROM.

Song, S.X., Campos-Toro, E.F., Zhang, Y.M., Lopez-Valdivieso, A., 2013. Morphological and mineralogical characterizations of oolitic iron ore in the Exi region, China. Int. J. Miner. Metall. Mater. 20 (2), 113–118.

Spier, C.A., Oliveria, S.M., Rosière, C.A., 2003. Geology and geochemistry of the Águas Claras and Pico iron mines, Quadrilátero Ferrífero, Minas Gerais, Brazil. Mineral. Deposita 38, 751–774.

Trendall, A.F., Nelson, D.R., De Laeter, J.R., Hassler, S.W., 1998. Precise zircon U-Pb ages from the Marra Mamba Iron Formation and the Wittenoom Formation, Hamersley Group, Western Australia. Aust. J. Earth Sci. 45, 137–142.

Trudu, A.G., Clout, J.M.F., Young, J.M., 2004. Nanometre size iron oxides in Australian iron ores. Implications for mineral processing. In: ICAM 2004, Brazil, 4 p.

Waychunas, G.A., 1991. Crystal chemistry of oxides and oxyhydroxides. In: Lindsley, D.H. (Ed.), Oxide Minerals: Petrologic and Magnetic Significance. In: Ribbe, P.H. (Ed.), Reviews in Mineralogy, vol. 25. Mineralogical Society of America, Washington, pp. 11–68 (Chapter 2).

Williams, P.J., Barton, M.D., Johnson, D.A., Fontbote, L., Haller De, A., Mark, G., Oliver, N.H.S., Marschik, R., Williams, P.J., Barton, M.D., Johnson, D.A., Fontbote, L., Haller De, A., Mark, G., Oliver, N.H.S., Marschik, R., Williams, P.J., Barton, M.D., Johnson, D.A., Fontbote, L., Haller De, A., Mark, G., Oliver, N.H.S., Marschik, R., 2005. Iron oxide copper-gold deposits: geology, space-time distribution, and possible modes of origin. Society of Economic Geologists, Econ. Geol. One hundredth Anniversary Volume, 371–405.

Wolska, E., Schwertmann, U., 1989. Nonstoichiometric structures during dehydroxylation of goethite. Z. Kristallogr. 189, 223–237.

Wolska, E., Szajda, W., 1985. Structural and spectroscopic characteristics of synthetic hydrohematite. J. Mater. Sci. 20, 4407–4412.

XRD analysis and evaluation of iron ores and sinters

3

J.P.R. de Villiers[1], *L. Lu*[2]
[1]University of Pretoria, Pretoria, South Africa
[2]CSIRO Mineral Resources Flagship, Pullenvale, QLD, Australia

3.1 Introduction

The iron and steel industry is confronted by decreasing grades and increased impurity levels and a buildup of lower-grade discard material that needs to be upgraded. In modern blast furnaces, stronger, more reactive sinters are required for a high productivity. To address these problems, knowledge of the phases and their impurity levels is necessary so that the most appropriate measures can be devised.

X-ray powder diffraction (XRD) has a unique capability to distinguish between different phases on the basis of their crystal structure and their chemistry. This has been extensively utilized following the development of suitable instrumentation and has led to the characterization and examination of powdered or fine-grained materials for their phase composition. The compilation of the data into a database of known diffraction patterns has led to widespread acceptance of the X-ray powder diffraction method for phase identification. A major limitation however was the lack of quantitative capability.

With the development of fast detectors, modern accurate instrumentation, and advanced software, X-ray diffraction analysis has undergone a revival. It is used increasingly in the field of mineral processing to characterize minerals, to track their behavior, and to optimize the performance of metallurgical processes. It is fast, requiring no special sample preparation, apart from fine grinding, and together with statistical methods such as cluster analysis, can provide valuable information to the process engineer. It is usually the first method, together with X-ray fluorescence and microanalysis, to be used for the characterization of iron ores and products arising from their processing. SEM methods used for mineral quantification are not well suited for the distinction of hematite and magnetite in ores and especially in sinters, so again, XRD is the method of choice for phase quantification.

All mineral processing operations treat minerals (not elements), and as such, their identity, their properties, and their behavior in these processes are of importance. The minerals can also vary spatially across an ore body, and it is therefore necessary to characterize the ores and to measure their distribution in order to optimize mining and mineral processing operations.

In high-temperature processes, the behavior of the feedstock is of importance in the calculation of phase equilibria, slag formation, and mass and energy balances. In all

Iron Ore. http://dx.doi.org/10.1016/B978-1-78242-156-6.00003-4
© 2015 Elsevier Ltd. All rights reserved.

these calculations, the phase compositions and their quantities are important variables to be used in thermodynamic modeling of the processes. In iron ore sinters and pellets, the identity of the bonding phase is of importance, and this influences the strength and reducibility of the feedstock in the subsequent blast furnace operation.

In this contribution, after a short theoretical analysis, the applications of the method will be discussed, followed by practical applications in iron ore processing.

3.2 Principles of powder X-ray diffraction

Powder X-ray diffraction (XRD) analysis uses a monochromatic beam of X-rays to irradiate a sample with the X-ray source and detector making variable angles with normally a flat sample. The diffracted X-rays from the crystal planes in the powdered phases that will be measured by a detector will show up as peaks of variable intensities at specific diffraction angles. Each phase or mineral will have a unique diffraction pattern that is a function of its crystal structure, its crystallite size, and its lattice strain, if present.

The intensity I_{hkl} of a diffraction peak is a function of a number of factors and is expressed in abbreviated form as the following equation:

$$I_{hkl} = S \times M_{hkl} \times LP \times A \times P_{hkl} \times \left|F_{hkl}\right|^2$$

where S is the scale factor that equates the experimental diffraction pattern to the calculated pattern. It is a function of the crystal structure of the phase and the quantity of the phase in a mixture, M_{hkl} is a multiplicity factor that depends on the number of times that symmetrically equivalent reflections overlap in a diffraction pattern, LP is a combined term depending on the geometry of diffraction and the partial polarization of the X-ray beam, A is a correction for the absorption of the X-ray beam, P_{hkl} is the preferred orientation correction term that corrects for possible deviations from the random orientation of crystallites in the sample due to their shape, F_{hkl} is the structure factor that is defined by the crystal structure.

The structure factor is a function of the scattering power of the constituent atoms and their positions and is given by

$$F_{hkl} = \sum_{n=1}^{N} f_n \mathrm{e}^{2\pi i(hx+ky+lz)}$$

where f_n is the atomic scattering factor of the nth atom; $x, y,$ and z is the position of the nth atom.

The temperature factor B, also called the Debye–Waller factor, is an additional factor affecting the intensity so that $f_n = f_0 \mathrm{e}^{\left(-B\frac{\sin\theta}{\lambda}\right)^2}$ for each atom position for each phase.

The diffraction peaks are further affected by instrumental and sample effects that cause broadening so that the combination of all these gives the peak profiles that are observed in the experimental diffraction pattern.

This discussion on the theory of X-ray diffraction analysis is kept to a minimum, since this can be sourced from a number of excellent references by Klug and Alexander (1974), Jenkins and Snyder (1996), Pecharsky and Zavalij (2005), and references therein. The latter reference is a very useful modern treatise on the elements of powder diffraction. The real purpose of this contribution is to describe the versatility of the method and its application in iron ore processing.

The diffraction patterns of a very large number of phases and minerals are tabulated in a database (Powder Diffraction File, issued by the International Centre for Diffraction Data (ICDD)) consisting mainly of interplanar d-spacings and intensities of the diffracting planes. The diffraction pattern of the phase being investigated can then be compared with those of the phases in the database to identify it and to get an approximation of its quantity in a mixture of phases. Figure 3.1 shows a schematic diagram of the most common geometry used in modern XRD equipment. The X-ray beam from the X-ray source is directed onto a flat sample, while the source and detector scan increasing angles towards the vertical. A set of slits ensure that the beams are focused. In modern instruments, a solid-state strip detector is used that increases measurement speed almost a hundredfold compared with the older point detectors.

The output consists of a list of angles and their intensities collected from the sample being investigated. A typical XRD pattern of a goethitic iron ore is shown in Figure 3.2. The positions of the peaks calculated from crystal structure data are shown as vertical lines. For example, the mineral content of a goethite containing iron ore can readily be identified and quantified by XRD with a 10 min scan. Much additional information relating to the element distribution in the various minerals can be obtained when using powder XRD together with mineral compositions obtained by SEM analysis.

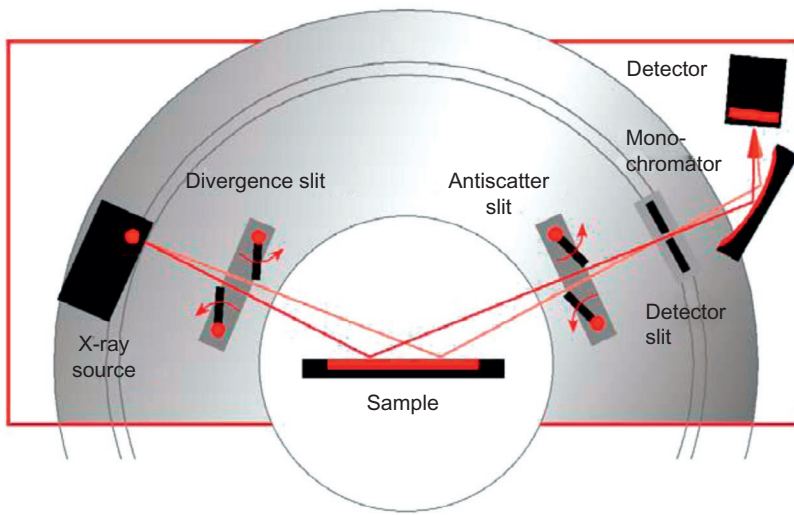

Figure 3.1 The Bragg–Brentano geometry used in modern diffractometers. Courtesy of Bruker AXS.

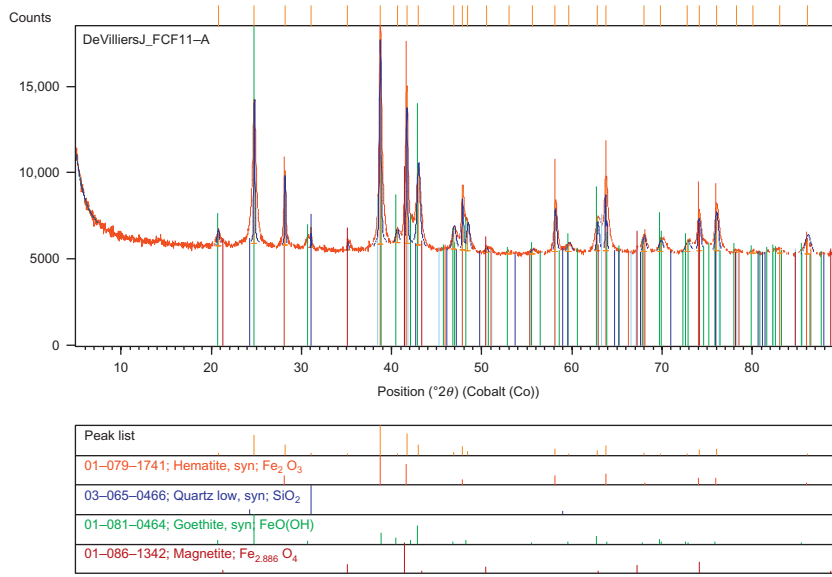

Figure 3.2 XRD pattern of an iron ore sample, showing the peak positions of the major minerals. Extensive peak overlap is apparent.

3.3 Rietveld analysis

With the advent of modern fast computers, the fitting of the experimental XRD pattern with that of the calculated one has become possible, and the method is being used for the structure refinement of unknown phases and for the quantification of phases or minerals in a mixture. The experimental XRD pattern is compared with the pattern calculated from the crystal structures of the constituent phases, and a measure of the goodness-of-fit and difference curve are calculated. This is done for every analysis step in the diffraction pattern. The least squares method then calculates a number of scale factors that are directly proportional to the relative amounts of the phases. A number of discrepancy factors are also calculated. A useful treatise of the method is given in the monograph edited by Young (1993). Discussions on phase quantification using the method are given in numerous articles, for example, by Madsen et al. (2001).

Necessary inputs for Rietveld analysis are the following:

- An aligned X-ray diffractometer, calibrated with an internal standard
- An experimental XRD pattern, measured in steps of at least 0.02 degrees 2ϑ
- Accurate cell dimensions, space group, and atomic positions for each phase
- A sample, micronized to a particle size of approximately 10–15 µm
- Sample rotation, essential to lessen the effects of preferred orientation
- Suitable software for the analysis

Rietveld software programs are designed to describe the peak profiles as accurate as possible. The XRD peaks can either be fitted to some analytic function describing the peaks (usually some variant of a Gaussian or Lorentzian distribution that has limited

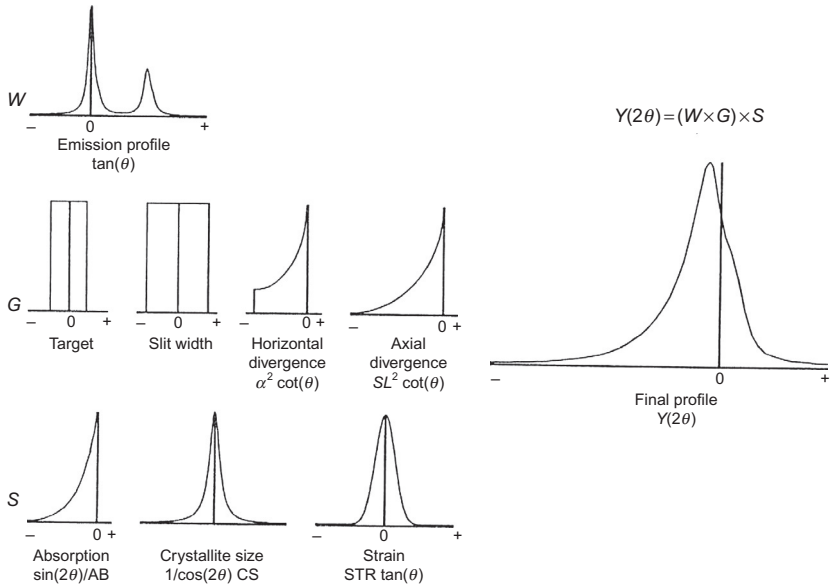

Figure 3.3 Convolution of the various parameters that influence the peak shapes showing their contribution to the final peak shape.
Courtesy of Bruker AXS.

physical meaning) or be calculated using the so-called fundamental parameters. Normally, for software using the fundamental parameters approach, the instrumental parameters for the diffractometer must be determined using a suitable standard. This is shown pictorially in Figure 3.3. As can be seen, the diffraction peaks are based on the convolution (folding) of the X-ray emission profile, *W*, the instrumental parameters, *G*, and the sample parameters, *S*. The X-ray emission profile is a given for a specific radiation and is taken from previous determinations. The instrumental parameters are determined once for a specific instrument using a well-characterized XRD standard such as LaB_6. Once these are fixed, then only the sample characteristics such as the crystallite sizes, the lattice strain, and the relative amounts of the phases are refined. So, in Figure 3.3, the parameters *W* and *G* are essentially fixed, leaving only the sample parameters *S* to be refined.

For quantitative analysis, Hill and Howard (1987) had derived simple relationships on which the Rietveld method relies for quantification without or with an internal standard. These are given as

$$W_P = \frac{S_P (ZMV)_P}{\sum_{i=1}^{n} S_i (ZMV)_i} \quad \text{without an internal standard, assuming no amorphous phase present,}$$

and

$$W_{P'} = \frac{W_S S_P (ZMV)_P}{S_s (ZMV)_s} \quad \text{with an internal standard}$$

where W_P is the relative mass fraction of phase p in a mixture of n phases, $W_{P'}$ is the absolute mass fraction of phase p in a mixture, W_S is the mass fraction of standard s, S_P is the Rietveld scale factor for phase p, S_s is the Rietveld scale factor for the standard, Z is the number of formula units per cell for phase i, M is the mass of the formula unit for phase i, V is the cell volume for phase i.

If an amorphous phase is present and an internal standard was added, its mass fraction is given as

$$W_{\mathrm{Am}} = \frac{1 - \frac{W_{is}}{W_{Rc}}}{100 - W_{is}}$$

where W_{Am} is the mass% amorphous phase, W_{is} is the weighed mass% standard, and W_{Rc} is the Rietveld determined mass% of standard.

In some investigations, the full crystal structures of one or more phases are not known, and Scarlett and Madsen (2006) had developed a method of quantification (PONKCS), used in conjunction with the Rietveld method. In this case, the pure phase or a known quantity of the phase is used to calibrate the method. The method shows great promise even in cases where the crystal structures are well known, because effects such as microabsorption that can seriously affect phase quantification are mitigated.

The Rietveld method matches the XRD pattern calculated from the crystal structure data with the experimental pattern using a nonlinear least squares fitting technique. The fit minimizes the following function:

$$R = \sum_{i=1}^{n} w_i \left(Y_i^{\mathrm{obs}} - Y_i^{\mathrm{calc}} \right)^2$$

where Y^{obs} and Y^{calc} are the observed and calculated intensities for every step of the XRD pattern and w is a weighting factor.

The profile residual is given as

$$R_{wp} = \left[\frac{\sum_{i=1}^{n} w_i \left(Y_i^{\mathrm{obs}} - Y_i^{\mathrm{calc}} \right)^2}{\sum_{i=1}^{n} w_i \left(Y_i^{\mathrm{obs}} \right)^2} \right]^{1/2}$$

A note of caution must be expressed here; often, samples containing transition elements exhibit high background counts, especially when modern strip detectors together with adjustable slits are used. This can give rise to low R_{wp} values because of the predominant background (Y^{obs} includes the background). This might therefore not necessarily reflect a good fit.

Typical parameters that are obtained from a Rietveld refinement are the following:

- Crystallographic information of the phases, that is, the crystal structures can be refined.
- The lattice parameters of the phases. These can be used to calculate compositions in solid solutions.

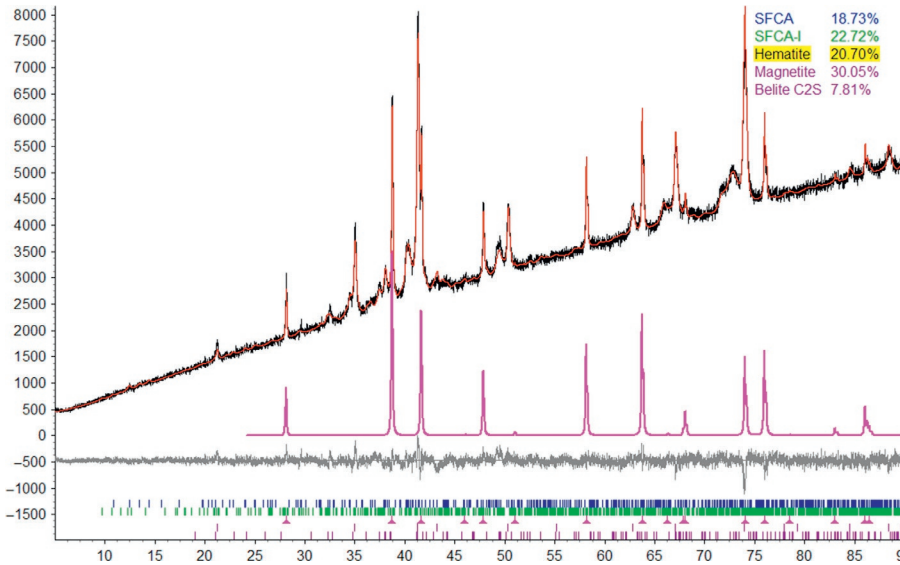

Figure 3.4 Rietveld analysis of an iron ore sinter showing the calculated pattern (red) superimposed on the experimental pattern. The difference pattern is shown below the calculated pattern of hematite. The peak positions of the different phases are also shown. The quantities of the different phases are shown in the upper right-hand corner.

- Relative quantities for the constituent phases.
- Amorphous content if an internal standard is used.
- Crystallite sizes of the phases.
- Lattice strain of the phases. This is a rather broad term that includes stacking disorder, dislocations, and strain.

A typical Rietveld analysis of an iron ore sinter is shown in Figure 3.4. In this case, the calculated pattern of the hematite phase is also shown together with the difference curve (between experimental and calculated intensities). This should be horizontal and featureless without any residual peaks.

3.4 Sources of error in XRD analysis

Mineral quantification is the most widely used application of Rietveld analysis, and it is applied to numerous cases, especially in geometallurgy and mineral processing. However, despite its successes, the method still suffers from the following shortcomings that can affect its accuracy and precision:

- Preferred orientation of minerals with a pronounced habit such as micas and amphiboles. The mineral grains orient themselves in the sample holder in response to their shape, and therefore, the diffraction peaks from the preferentially oriented planes are artificially enhanced. Methods have been devised to correct for this effect but are still inadequate in some cases.

- Microabsorption effects in samples containing phases with variable density. This effect is due to the absorption of the diffracted X-rays by the minerals with bigger mass absorption coefficients. This effect is especially prevalent if CuKα radiation is used for the examination of iron-containing minerals and phases.
- XRD cannot easily detect or quantify minerals with less than ~1% abundance because of relatively poor peak to background ratios. The method is therefore restricted to quantification of ores containing major amounts of valuable minerals. Fortunately, iron ores and sinters fall in this class, and therefore, XRD is particularly suited for their evaluation.
- Quantitative phase analysis by XRD can also be seriously in error because of the presence of undetected phases or minerals and the presence of amorphous material. These are by definition difficult to detect, and therefore, the results must always be validated by independent means such as microanalysis of the phases and chemical analysis. This will be discussed later.

3.5 Applications of cluster analysis

Cluster analysis is a statistical procedure that discriminates between sets of closely related XRD scans from different samples. It then separates the similar samples into different groups using statistical criteria. No information is given as to what the differences between groups entail: only that they are different. The procedure is especially useful in ore body evaluation to discriminate between different ore types and in sinter evaluation to examine differences between sinters prepared using different recipes or operational variables such as suction and cooling rates. Once the different clusters have been identified, they can then be examined in greater detail to establish what the differences are and what they mean in terms of ore quality or sinter properties such as tumble index or reduction disintegration indices. The principal components are combinations of features in the diffraction patterns, and no information is given regarding what these components represent in terms of mineral identities or quantities. This must be deduced by the investigator upon closer evaluation.

For an example of the application of cluster analysis to iron ore evaluation and grade control, the reader is referred to the contribution by Paine et al. (2012), who evaluated a large number of iron ore samples from an iron ore deposit.

In sinters, ongoing studies have identified differences according to different recipes and also differences between size fractions, to be discussed later. Figure 3.5 shows the differences between different clusters of sinter samples as small spheres of different colors. For each of the clusters, the XRD patterns of the samples representing the cluster are also given so that the characteristics of each cluster can be deduced more easily.

3.6 Applicability of XRD analysis

The XRD method is not universally applicable to all minerals in ore deposits. This is true for all ores where the economic minerals occur as minor or trace phases. Due to their low signal to background ratio and the extensive overlap of the diffraction peaks, they show relatively high detection limits as compared to elemental analysis. However, for all ores where the economically important phases are the predominant

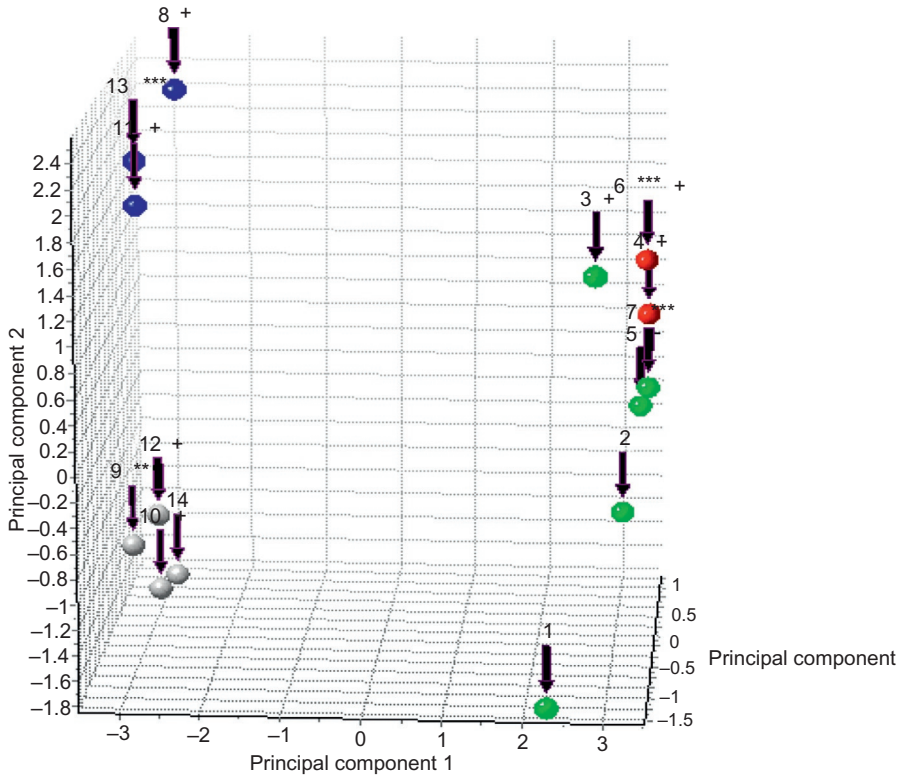

Figure 3.5 Clustering of sinter samples using XRD patterns as input. The different clusters are shown on a 3-dimensional plot. The biggest differences between samples are manifested along principal component 1, which is a combination of a number of features in the diffraction patterns.

ones, such as iron, aluminum, phosphate, and fluorite ores, XRD is widely used. Since the method is one of the few that detect and quantify minerals, it can be used to measure the different minerals in iron ores. This can lead to better classification of ores and eventually to causes of elemental variation in them.

In iron ore sinters, the presence of different phases reflects differences in sinter constituent mixtures and different temperatures and reductant additions during sintering. This can be of use in the development of stronger, more reducible sinters of the desired basicity.

3.7 Use of mass balancing in iron ore analysis

Mass balancing is important in not only assessing the accuracy of XRD and mineral analysis but also evaluating the suitability of ores for upgrading and beneficiation. The bulk chemical composition is calculated from the XRD and mineral analyses (by microprobe or SEM analysis) and is compared with the actual chemical analysis

(by XRF or ICP analysis). This shows the contribution that each mineral makes to the elemental abundances. A percentage deviation is calculated, which is an indication of the accuracy of the analysis. Smaller deviations indicate a higher likelihood that the XRD and phase compositions are correct. An example of such a calculation of a high-alumina iron ore is given in Table 3.1.

3.8 The principal minerals and phases

The minerals occurring in all major iron ores is given in Table 3.2, together with their formulas and most important elemental impurities. These impurities, especially aluminum and magnesium in the main iron-bearing minerals, hematite, magnetite, and goethite, are important factors to consider in the upgrading of low-grade iron ores.

In sinters, the main phases that form are listed in Table 3.3. Important are the main impurities that affect the electron backscatter intensities of especially magnetite and hematite, inhibiting their quantification using SEM-based methods.

3.9 XRD for the characterization of Iron ores

3.9.1 Iron ore characterization

Variations in iron ores can be traced and mapped using cluster analysis and XRD quantification. Paine et al. (2012) evaluated a large number of iron ore samples from an iron ore deposit. Using cluster analysis and mineral quantification, the ores could be classified into defined theoretical grade blocks, which included high grade, high grade with minor gibbsite, high-grade beneficiation, low-grade beneficiation, low-grade other, and waste. As a result, material with a propensity for higher degrees of beneficiation was identified and delimited.

For iron ore beneficiation, the mineral quantities in the ores is essential to establish the degree of upgrading that can be achieved. In a study of the removal of aluminum in goethitic iron ores, mass balance calculations assisted greatly to assess the maximum amount of Al that can be removed without appreciable iron loss, mainly from the goethite. This is shown graphically in Figure 3.6, which shows that 68% of the Al in the sample is distributed in goethite. The goethite also contains 60% of the iron in the sample and cannot be removed. Therefore, if Al is to be removed, only kaolinite and gibbsite can be eliminated without major iron loss, and only as little as 22% of the Al can be removed by flotation or other methods.

3.9.2 Lattice constant refinement for the evaluation of hematite and goethite

Lattice constant refinement can be used to assess the substitution of impurity elements, especially in fine-grained goethite and hematite, as determined by Schulze (1984) and Stanjek and Schwertmann (1992), respectively.

Table 3.1 **Mass balance comparing XRD and mineral analysis**

	Mass balance calculation—Fe ore FCF11-A									
Mass balance	**Fraction(XRD)**	**SiO_2**	**Al_2O_3**	**TiO_2**	**Fe_2O_3**	**LOI**	**P_2O_5**	**K_2O**		
Annite	0.21	0.06	0.02	0.00	0.09	0.00	0.00	0.03		
Gibbsite	0.17	0.00	0.11	0.00	0.00	0.06	0.00	0.00		
Goethite	60.48	2.49	3.09	0.81	47.80	6.29	0.00	0.00		
Hematite	32.78	0.33	0.46	0.00	31.99	0.00	0.00	0.00		
Kaolinite	2.17	1.00	0.85	0.00	0.00	0.30	0.00	0.00		
Magnetite	3.82	0.00	0.01	0.00	3.94	0.00	0.00	0.00		
Quartz	0.38	0.38	0.00	0.00	0.00	0.00	0.00	0.00		
Total	100.01	4.27	4.54	0.81	83.83	6.64	0.00	0.04	100.12	R(%)
XRF Analysis		3.59	4.54	0.69	82.58	7.44	0.11	0.00	98.95	3.03

Table 3.2 Principal minerals occurring in sedimentary iron ores

Mineral name	Formula	Impurities
Hematite	Fe_2O_3	Al_2O_3 and OH
Magnetite	Fe_3O_4	MgO and Al_2O_3
Goethite	FeOOH	Al_2O_3 and adsorbed P_2O_5
Greenalite	$(Fe^{2+},Fe^{3+})_{2-3}Si_2O_5OH_4$	MgO
Stilpnomelane	$K(Fe^{2+},Mg,Fe^{3+})_8(Si,Al)_{12}(O,OH)_{27}\times n(H_2O)$	
Kaolinite	$Al_2Si_2O_5(OH)_4$	Almost pure
Annite	$KFe_3^{2+}AlSi_3O_{10}(OH,F)_2$	
Gibbsite	$Al(OH)_3$	Almost pure
Quartz	SiO_2	Pure

Table 3.3 Predominant phases in iron ore sinters

Phase	Formula	Impurities
Hematite	Fe_2O_3	Al_2O_3
Magnetite	Fe_3O_4	CaO, MgO, and Al_2O_3
SFCA (silico-ferrite of Ca and Al)	$(Ca,Mg)_3(Fe,Al)_{10}SiO_{20}$	MnO
SFCA-I	$Ca_3(Fe,Al)_{17}O_{28}$	MnO
SFCA-II	$Ca_5(Fe,Al)_{29}O_{48}$	MnO
Larnite (C2S)	Ca_2SiO_4	FeO

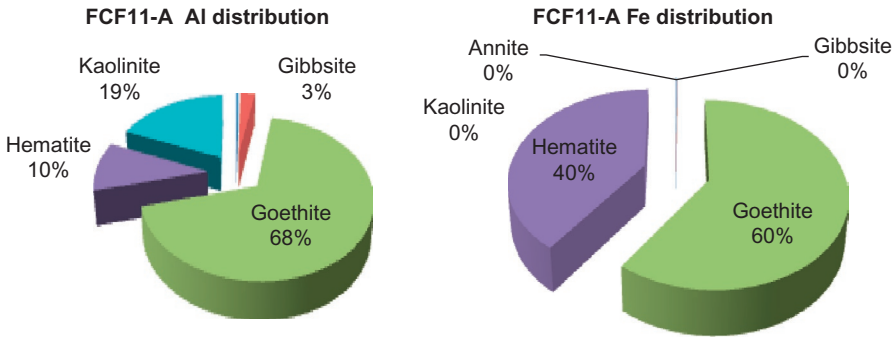

Figure 3.6 Distribution of Al and Fe in the different phases in a goethite-rich iron ore.

The hematite unit cell parameters are affected by Al and OH substitution:

$$a = 5.0359 - 0.00183\text{Al} + 0.00175\text{LOI}$$

$$c = 13.740 - 0.00512\text{Al} + 0.0130\text{LOI}$$

Table 3.4 Calculation of Al and OH contents in hematite and Al contents in goethite using the unit cell parameters of the two phases

	Hematite			Goethite		
Sample	**X(Al)-h**	**X (OH)**	**LOI(%)**	***c***	**Mol % Al**	**X(Al)-g**
FCF 11-A	0.039	0.023	0.42	3.0154	5.22	0.052
FCF 11-B	0.022	0.042	0.78	3.0187	3.28	0.033
FCF 11-C4	0.032	0.054	1.01	3.0201	2.50	0.025
FCF 11-D4	0.027	0.034	0.62	3.0180	3.73	0.037
FCF 11-D4	0.058	0.042	0.78	3.0178	3.80	0.038

OH substitution affects mainly the *c* parameter:

$$\Delta c = 0.00841 + 0.0130\text{LOI}$$

The goethite cell parameters are affected mainly by Al substitution:

$$\%\text{Al} = 1730 - 572 * c$$

The procedure was elegantly included in the Rietveld refinement procedure by Knorr and Neumann (2011) and Neumann et al. (2014).

The use of XRD can therefore give a quick assessment of the extent of Al and OH substitution in hematite and the amount of Al substitution in goethite. This was done for five goethite-rich iron ores and is shown in Table 3.4.

3.10 XRD in sintering and pelletizing

3.10.1 Fundamental studies of sinter phases and reactions

Reliable quantification using Rietveld analysis rely critically on accurate crystal structures of minerals and sinter phases. Fortunately, the structures of the important binding phases SFCA, SFCA-I, and SFCA-II have been determined by Mumme and coworkers (Hamilton et al., 1989; Mumme et al., 1998; Mumme, 2003). Sugiyama et al. (2005) determined the structures of Mg-rich SFCA. Recently, the crystal structures of SFCA and aluminium free SFC have been redetermined by Liles and de Villiers (2015).

3.10.2 Sinter reactions

Important laboratory studies of reactions in sinter mixtures have been conducted at high temperature at controlled oxygen partial pressures using both laboratory and synchrotron X-ray sources by Scarlett et al. (2004) and Webster et al (2012). Critical reactions and formation temperatures of the various phases have been established.

These serve as important benchmarks for the interpretation of the reactions taking place in course-grained mixtures in experimental sinter pots and commercial sinter plants.

Reactions that take place during sintering and pelletizing can be easily followed by XRD. The extent of sintering can be assessed by the SFCA/hematite ratio; this is not possible by using chemical analysis. The redox conditions prevailing during sintering (reductant addition) can be assessed by the magnetite/hematite ratio. Presently, this is determined chemically using the FeO content. The relation between the XRD peak intensities and the FeO content was established by Bonvin et al. (2000) and by Konig et al. (2012).

The reactions that occur during initial combustion, at maximum temperature, and during cooling can be established by interrupting the sinter reactions in a sinter box using water quenching. Figure 3.7 shows the diffraction patterns of samples collected from top to bottom in a quenched sinter pot. This shows that hematite at the bottom of the sinter pot essentially disappears at the flame front (F4 and F5) with the formation of magnetite and that secondary hematite (and SFCA) again forms during cooling and oxidation by air at the top of the sinter bed.

3.10.3 Phase chemistry of sinter screen fractions

Figure 3.5 shows an essential difference between clusters along principal component 1. This difference is between size fractions of sinters. Hematite is concentrated in the samples of −5 mm fractions that cluster on the left side of the diagram. This is also shown in Figure 3.8. The production of sinter fines is probably due to the formation of secondary or granular hematite, a product that contributes to the degradability of sinters.

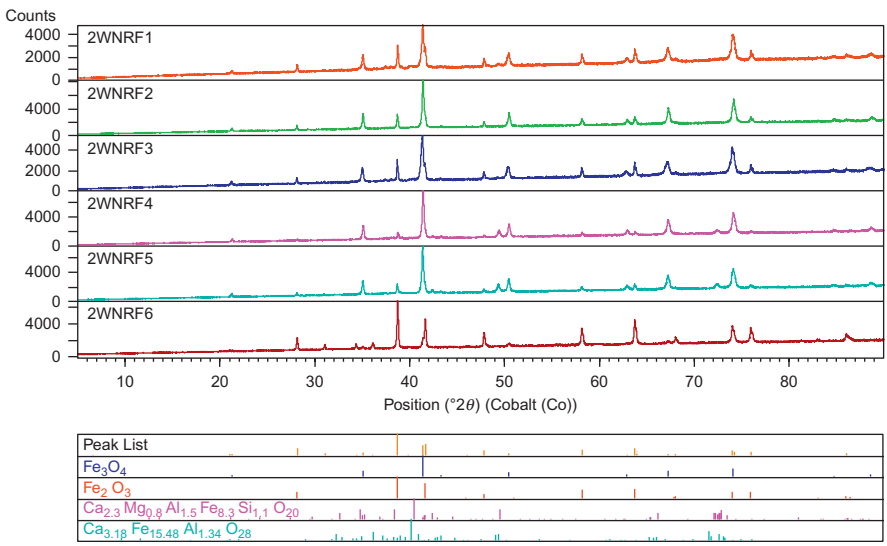

Figure 3.7 Changes in the phase composition from top to bottom in a water-quenched sinter pot.

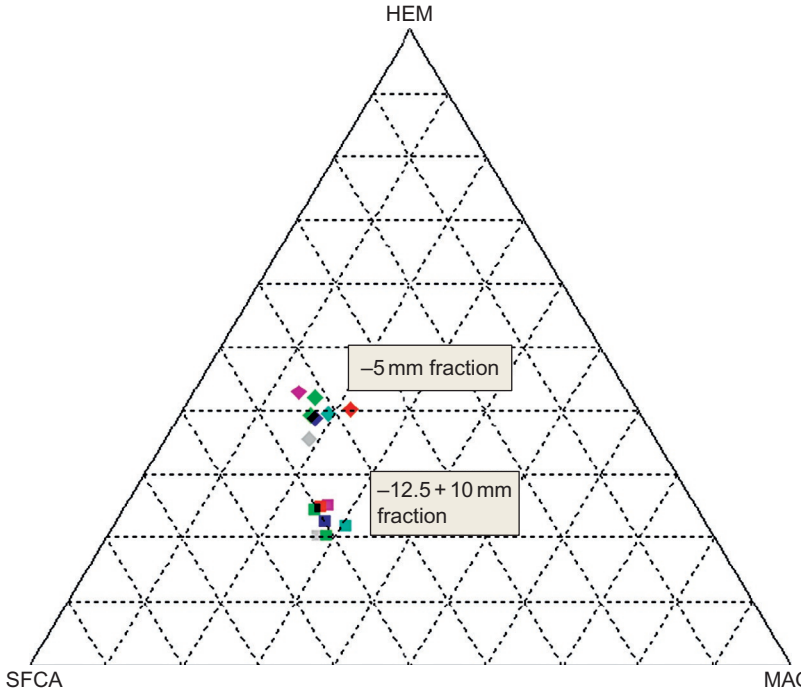

Figure 3.8 Triangular plot showing that the −5 mm fraction is enriched in hematite.

3.11 Summary and conclusions

The use of XRD and the Rietveld method have resulted in the development of fast and reliable methods of phase quantification in the iron ore industry. Compared with other methods, it is still the most reliable method for phase quantification, and it has the potential to make important contributions to our knowledge regarding the effect of phase relations on the properties of sinters. Several applications of the method have been discussed in some detail.

New developments will necessarily attempt to relate phase composition to sinter strength and reducibility, and increased use of cluster analysis can identify important relations between these parameters.

References

Bonvin, D., Yellepeddi, R., Buman, A., 2000. Applications and perspectives of a new innovative XRF-XRD spectrometer in industrial process control. Adv. X-Ray Anal. 42, 126–136.

Hamilton, J.D.G., Hoskins, B.F., Mumme, W.G., Borbridge, W.E., Montague, M.A., 1989. The crystal structure and crystal chemistry of $Ca_{2.3}Mg_{0.8}Al_{1.5}Fe_{9.3}O_{20}$ (SFCA): solid solution limits and selected phase relationships of SFCA in the SiO_2-Fe_2O_3-CaO(-Al_2O_3) system. N. Jb. Mineral. (Abh.) 161, 1–26.

Hill, R.J., Howard, C.J., 1987. Quantitative phase analysis from neutron powder diffraction data using the Rietveld method. J. Appl. Crystallogr. 20, 467–474.

Jenkins, R., Snyder, R.L., 1996. Introduction to X-ray Powder Diffractometry. John Wiley, New York.

Klug, H.P., Alexander, L.E., 1974. X-ray Diffraction Procedures for Polycrystalline and Amorphous Materials, second ed. John Wiley, New York.

Knorr, K., Neumann, R., 2011. Advances in quantitative X-ray mineralogy—mixed crystals in bauxite. In: Proceedings of the 10th International Congress for Applied Mineralogy (ICAM), TRONDHEIM, Norway, pp. 377–384.

Konig, U., Gobbo, L., Reiss, C., 2012. Quantitative XRD for ore, sinter, and slag characterization in the steel industry. In: Proceedings of the 10th International Congress for Applied Mineralogy (ICAM), pp. 385–393.

Liles, D.C., de Villiers, J.P.R., 2015. Refinement of iron ore sinter phases: a silico-ferrite of calcium and aluminium (SFCA) and an Al-free SFC, and the effect on phase quantification by X-ray diffraction. Acta Crystallogr. accepted for publication.

Madsen, I.C., Scarlett, N.V.Y., Cranswick, L.M.D., Lwin, T., 2001. Outcomes of the International Union of Crystallography Commission on powder diffraction Round Robin on quantitative phase analysis: samples 1a to 1h. J. Appl. Crystallogr. 34 (4), 409–426.

Mumme, W.G., 2003. The crystal structure of SFCA-II, $Ca_{5.1}Al_{9.3}Fe^{3+}_{18.7}Fe^{2+}_{0.9}O_{48}$, a new homologue of the aenigmatite structure type, and structure refinement of SFCA type, $Ca_2Al_5Fe_7O_{20}$. Implications for the nature of the "ternary phase solid solution" previously reported in the $CaO\text{-}Al_2O_3$-iron oxide system. N. Jb. Mineral. (Abh.) 178, 307–335.

Mumme, W.G., Clout, J.M.F., Gable, R.W., 1998. The crystal structure of SFCA-I, $Ca_{3.18}Fe^{3+}_{14.66}Al_{1.34}Fe^{2+}_{0.82}O_{28}$, a homologue of the aenigmatite structure type, and new crystal structure refinements of β-CFF, $Ca_{2.99}Fe^{3+}_{14.30}Fe^{2+}_{0.55}O_{25}$ and Mg-free SFCA, $Ca_{2.45}Fe^{3+}_{9.04}Al_{1.74}Fe^{2+}_{0.16}O_{20}$. N. Jb. Mineral. (Abh.) 173, 93–117.

Neumann, R., Avelar, A.N., da Costa, G.M., 2014. Refinement of the isomorphic substitutions in goethite and hematite by the Rietveld method, and relevance to bauxite characterisation and processing. Miner. Eng. 55, 80–86.

Paine, M., König, U., Staples, E., 2012. Application of rapid X-ray diffraction (XRD) and cluster analysis to grade control of iron ores. In: Proceedings of the 10th International Congress for Applied Mineralogy (ICAM), pp. 495–501.

Pecharsky, V.K., Zavalij, P.Y., 2005. Fundamentals of Powder Diffraction and Structural Characterization of Materials. Springer, New York.

Scarlett, N.V.Y., Madsen, I.C., 2006. Quantification of phases with partial or no known crystal structures. Powder Diffract. 21 (4), 278–284.

Scarlett, N.V.Y., Madsen, I.C., Pownceby, M.I., Christensen, A.N., 2004. In situ X-ray diffraction analysis of iron ore sinter phases. J. Appl. Crystallogr. 37, 362–368.

Schulze, D.G., 1984. The influence of aluminium on iron oxides. VIII. Unit cell dimensions of Al-substituted goethites and estimation of Al from them. Clays Clay Miner. 32 (1), 36–44.

Stanjek, H., Schwertmann, U., 1992. The influence of aluminium on iron oxides. Part XVI: hydroxyl and aluminium substitution in synthetic hematites. Clays Clay Miner. 40 (3), 347–354.

Sugiyama, K., Monkawa, A., Sugiyama, T., 2005. Crystal structure of the SFCAM phase. $Ca_2(Ca,Fe,Mg,Al)_6(Fe,Al,Si)_6O_{20}$. ISIJ Int. 45 (4), 560–568.

Webster, N.A.S., Pownceby, M.I., Madsen, I.C., Kimpton, J.A., 2012. Silico-ferrite of calcium and aluminum (SFCA) iron ore sinter bonding phases: new insights into their formation during heating and cooling. Metall. Mater. Trans. B 43B, 1344–1357.

Young, R.A. (Ed.), 1993. The Rietveld method. In: IUCr Monographs on Crystallography. Oxford University Press, Oxford, New York.

Automated optical image analysis of natural and sintered iron ore

4

E. Donskoi, A. Poliakov, J.R. Manuel
CSIRO Mineral Resources Flagship, Pullenvale, QLD, Australia

4.1 Introduction: Overview of optical image analysis technique

The utilization of optical microscopy for the characterization of rocks and minerals started over 150 years ago. One of the first researchers in optical mineral characterization area was Henry Clifton Sorby, who developed the basic techniques of petrography, using the polarizing microscope to study the structure of thin rock sections (Sorby, 1858).

Measurement of ore mineral reflectance with microchemical techniques used for mineral identification started in the early twentieth century (Murdoch, 1916), and, after intensive work by many mineralogists, the Table of Quantitative Data was produced by Commission on Ore Microscopy in 1962 (Gray and Millman, 1962; Criddle and Stanley, 1993). This table contained reflectance data of different minerals for four wavelengths, which significantly helped with mineral identification.

In modern optical mineral analysis, the information required extends well beyond basic mineral identification and qualitative description. The main goal in optical microscopic characterization of iron and other ores is to obtain information, which will assist in the determination of the downstream processing route of such ores (Donskoi et al., 2007, 2008a, 2012, 2013a). This information may include mineral abundances; mineral association and liberation characteristics; dimensional characteristics of particles and grains such as size distribution, shape, and elongation; surface roughness; porosity, microdiscontinuities, and density; presence of different textures; reciprocal position of mineral grains; and other morphological and morphometric characteristics. A typical modern automated microscopy system with moving stage based on a Zeiss Axioplan microscope is shown in Figure 4.1.

There are two methods of imaging in optical microscopy: it can be performed in transmitted and reflected light. In transmitted light microscopy (Hunt et al., 2010; Rath et al., 2012), minerals are imaged in polished thin sections, usually around 30 μm thick. As a general rule, transmitted light is used for imaging nonopaque objects such as biological cells or for minerals, which do not remain opaque when ground to a thickness of the order of 30 μm. On the other hand, minerals that have significant metallic bonding (e.g., native elements, sulfides, and oxides, including iron oxides) do not transmit a significant amount of light, even in thin sections. Also, when structural or textural elements of the mineral being studied are typically smaller than the section thickness, they may interfere or obscure each other. This is why reflected light microscopy is usually used for the study of iron ore.

Iron Ore. http://dx.doi.org/10.1016/B978-1-78242-156-6.00004-6
© 2015 Elsevier Ltd. All rights reserved.

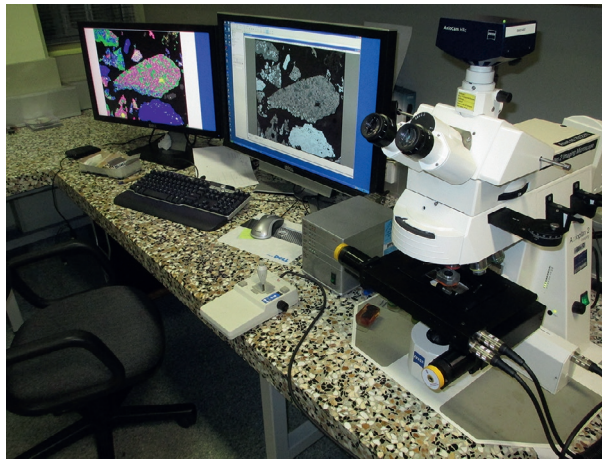

Figure 4.1 A typical automated microscopy system with moving stage (Zeiss Axioplan microscope).

In reflected light microscopy of iron ore and iron ore sinter, each sample (typically one size fraction when studying ore fines) is mixed with liquid epoxy resin and allowed to settle. Large iron ore or sinter pieces are also usually embedded in epoxy, which simplifies the polishing procedure and significantly improves polishing quality. Unmounted polished samples are also used sometimes but are difficult to prepare to the high standard of surface quality required for image analysis, being prone to scratching and relief in particular. It may also be difficult to achieve a horizontal surface position when placing such samples under the microscope. After the resin hardens, most often, the bottom part of the block is cut perpendicular to the settling (vertical) direction and then undergoes very fine polishing (Bonifazi, 1995). Examples of typical epoxy blocks with embedded iron ore fines, sinter, and coke are shown in Figure 4.2. In bigger samples of iron ore or sinter, the internal porosity might not be fully filled with epoxy so after the block is cut and/or plane ground to the desired level, it may backfilled with epoxy and then polished.

When the sample consists of iron ore fines, the sample has to be thoroughly mixed with epoxy in order to obtain a uniform layer. However, during block solidification, particles settle in liquid epoxy and may significantly segregate due to their different specific gravities (SGs). In iron ore, the difference can be very significant, for example, the SG of porous kaolinite gangue can be around $1.4\,g\,cm^{-3}$, whereas nonporous magnetite has SG $5.2\,g\,cm^{-3}$. Partial segregation by density may also occur during the mixing process. Figure 4.3 shows the difference in mineral composition for different locations within a polished block (the top layers of the block are the deepest layers during settling; the whole width of the settled sample is around 1 mm) for iron ore fines in the $-150+106\,\mu m$ size fraction. It can be seen that the difference is quite significant. In this example, the concentration of particles composed of heavier minerals (hematite) is higher closer to the top of the block, whereas particles of lighter minerals (ochreous goethite and kaolinite) are concentrated closer to the bottom, as it can be

Figure 4.2 Typical epoxy blocks with iron ore fines, sinter, and coke to be used in reflected light microscopy.

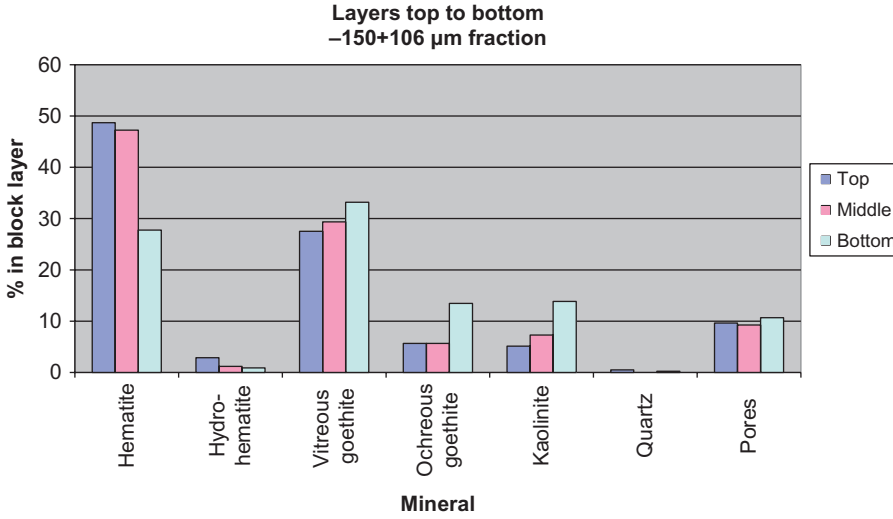

Figure 4.3 Average presence of iron ore minerals in different layers of thin 1 mm settled sample in epoxy polished block.

expected. This effect can significantly distort the information about the sample when the polished surface is perpendicular to the settling direction. To avoid this distortion, sectioning can be carried out parallel to the settling direction (i.e., perpendicular to the bottom of the block), with the resulting half blocks then reset in another epoxy block and the longitudinal cross sections polished. Data for images from all layers equally represented should be taken into account in final statistics. Such an approach, however, increases the time and cost of sample preparation. Some researchers grind the

block to the middle of the fines layer parallel to the bottom with the aim to overcome the settling effect. Still, as Figure 4.3 shows, the mineral composition in the middle layer may also be significantly different from the average mineral composition.

The imaging of polished blocks can be performed under normal reflected light, under reflected plane polarized light (Danti et al, 1993), or under circular polarized light (Higgins, 2010; Gomes et al, 2013). The recognition of different minerals is based on the difference between mineral reflectivities (amount of light reflected) in different color channels (red, green, and blue). For the purpose of further discussion, reflectivity with no color channel specified will refer to grayscale reflectivity, or the average reflectivity in all three channels, and color will mean the perceived color of the mineral resulting from nonequal reflectivities in different channels. It should be noted that crystals of the same mineral (e.g., hematite) may have different brightness and color within the same block, especially when imaged under polarized light (Gomes et al., 2010; Iglesias et al., 2011). Still, the difference in reflectivity and color between minerals is usually much higher than between different grains of the same mineral. However, reflectivity ranges of different minerals can significantly overlap, which makes it difficult to reliably differentiate one mineral from another by standard optical image analysis (OIA) methods. This is particularly the case for differentiating between nonopaque minerals and between nonopaque minerals and epoxy in reflected light.

Earlier image analysis systems such as VideoPro (Danti et al., 1993) had rather limited capabilities in differentiating objects with similar reflectivity. They only used 256 gradations in reflectivity scale (either grayscale or separate color channels) so even objects distinguishable by human eye sometimes could not be distinguished by the OIA system (Bonifazi, 1995). In contrast, modern systems can easily recognize differences in reflectivity not noticeable by the human eye. Many of them can recognize more than 16,000 reflectivity levels. This capability makes it possible to identify different grains of the same mineral or even some nonopaque minerals such as apatite, amphibole, calcite, and garnet (Lane et al., 2008). However, for OIA of iron ores, differentiation of nonopaque minerals is still quite a significant problem due to the similarity between the reflectivities of epoxy and nonopaque minerals. Several different approaches to this issue have been proposed. Lane et al. (2008) suggested covering polished blocks with carbon and performing extra light polishing, which can reveal minerals while leaving the epoxy covered. Unfortunately, for iron ore minerals, this method does not work due to the porous condition of the majority of iron ore minerals. Another approach to the identification of nonopaque minerals, proposed by Poliakov and Donskoi (2014), is based on identification of relief and will be discussed later in this chapter.

Even though different researchers studying iron ore and sinter on different mineral systems may be performing different tasks, the general steps in image collection and further digital image processing (Donskoi et al., 2013a) are the same and consist of the following:

Image acquisition, where the researcher initially has to prepare the imaging system (microscope, digital camera, and moving stage) for reliable and consistent acquisition

of images. Make sure the imaging surface is prepared up to standard (automated image analysis requires high quality of polishing) and decide what area should be imaged, which magnification should be used, and how many images should be acquired to fulfill the task and obtain a reliable set of data (a discussion on which can be found in Section 4.3.7). Prior to image acquisition, it is also very important to perform a system calibration with reflectivity standards, which means setting the microscope into a predefined imaging mode. Calibration should also include shading correction, which compensates for inherent variations in illumination in different areas of the image (Pirard, 2004).

Image improvement, where the image is modified to enable the best possible processing. This step usually includes operations such as noise removal, image sharpening (or blurring), correction of brightness and contrast, and also cropping of image margins in order to avoid possible misidentifications on image edges, due to nonuniform illumination, and to remove uneven borders caused by stitching of elementary images. Once the image is fully prepared, the steps of automated identification of constituents of the imaged object are performed.

Automated segmentation of imaged objects. Images may include more than one object, for example, when iron ore fines are imaged, a single object (e.g., a large particle) or part of an object (e.g., an image on the boundary of a particle or pellet). These objects must be segmented from epoxy.

Automated differentiation of different minerals (see Section 4.3.1). To perform this stage of the process correctly, it is very important to have a good understanding of the major minerals comprising the studied object. For this purpose, it is very useful (and sometimes mandatory, e.g., if chemical composition has to be calculated as a result of image analysis) to image the sample under the optical microscope and after that to perform electron probe microanalysis (EPMA) at different points of interest identified from the optical images. This operation ensures that all areas visually perceived as one mineral are actually the same mineral and not a set of different minerals with the same reflectivity. EPMA can also give an understanding of stoichiometry (or variable chemistry) of studied minerals. It should be noted that in iron ores, the composition of single minerals can be quite variable, due to element substitution (e.g., Si and Al in magnetite) and/or crystallographic lattice defect structures (e.g., resulting from substitution of hydroxyl groups for oxygen in hydrohematite). EPMA can show quite a wide range of compositions (e.g., with different oxygen content) for a single mineral within the same ore, related to ore genesis.

Automated object separation. If the task is textural classification or calculation of mineral association and liberation values, touching objects (particles) can significantly distort the correct information about the sample. Procedures for object separation can be quite comprehensive and computationally time consuming.

Porosity identification. Correct identification of porosity is extremely important and can significantly affect the final mineral abundance values, which in turn will affect many other values (textural, association, liberation, etc.).

Identification of nonidentified areas. Some areas may be identified as parts of the imaged objects but not identified as any mineral (or identified as more than one

mineral). The presence of such areas can sometimes be very significant, especially for microporous textures or for other fine textures where different minerals connect with each another.

Reidentification of misidentified areas. Certain areas can be misidentified based on their reflectivity alone. For example, small pores in magnetite can have reflectivity similar to that of vitreous goethite (FeO(OH)). However, experience shows that such juxtaposition is extremely unlikely. Reidentification of such areas can provide significant improvement in correct mineral mapping of studied images.

Correction of mineral identification on boundaries, for example, between different minerals or between minerals and epoxy. Usually such misidentifications occur only in the very thin boundary layer and correction of the layer to the depth of one to two pixels fully solves the problem.

Manual check and correction of final mineral map. It is always wise to check the results of automated processing for several images. In case of erroneous results, some manual image corrections (or mineral map correction) might be needed. The majority of image analysis packages provide such a manual correction capability to the user. However, modern analysis tasks require processing of sometimes hundreds of images, so manual editing is not practical. If automated processing shows persistent problems, some cardinal process changes should be considered instead of manual editing, such as reimaging of the sample (possibly at higher magnification) or processing of the whole set of images with different processing conditions (also known as "analysis profile"; see Section 4.3.7).

Measurements. After mineral maps based on initial image are finalized, all segmented objects are measured. The results of measurements can be further statistically processed. Alternatively, information about every object can be recorded into a database (Donskoi et al., 2013a), and further calculations can be performed outside the image processing software. For example, the Recognition4 program of the CSIRO Mineral4 OIA software suite independently performs textural classification, calculation of mineral liberation, and association data and other statistical processing.

Information obtained from polished sections is two-dimensional information, which can be significantly different from the actual facts about three-dimensional objects. In general, the information about mineral abundances is known not to be biased with sufficient statistical representation. However, liberation, association, and textural classification can be significantly distorted.

As an example of the effect caused by only consideration of a 2-D surface, Figure 4.4 shows three nonliberated particles sectioned during epoxy block preparation. All three particles consist of approximately the same amount of regularly shaped hematite (white) and goethite (shaded). The first particle is sectioned through the hematite area (Figure 4.4a1), so the visible polished section (Figure 4.4b1) consists only of hematite. The second particle is sectioned through both minerals so the section consists of both minerals (Figure 4.4b2). The third particle is sectioned through goethite, and so the visible section (Figure 4.4b3) is goethite only. This example demonstrates that even when all particles in a sample are nonliberated,

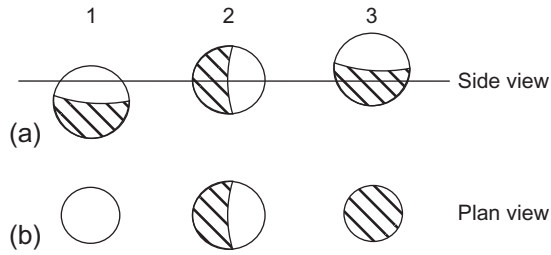

Figure 4.4 Possible sectioning of nonliberated particles during block polishing: (a) sectioning of three similar two-mineral particles—side view and (b) corresponding particle sections—two particles appear as fully liberated and only the one in the middle is not liberated.

two-dimensional imaging will show some of them as fully liberated. It should be noted that for real samples, the bias from 3-D to 2-D transformation (known as stereological error; King and Schneider, 1998) is not as high as in the example shown in Figure 4.4 but can still be significant. It should also be noted that for particles with textural features significantly smaller than the particle size, stereological error is also very small. To correct stereological error, many stereological methods have been developed (King and Schneider, 1998; Lin et al., 1995; Leigh et al., 1997; Fandrich et al., 1998). The simplest and most commonly used (although less precise) method removes small sections from consideration. The idea is very obvious, as the smaller the section is, the poorer its representation of the whole particle texture, so after removing small particle sections, there are more representative sections left. This method is sometimes called large section stereological correction.

4.2 Mineralogical characteristics of iron ore and sinter

4.2.1 Iron ores

The most valuable iron ore minerals are the iron oxides and oxyhydroxides, which comprise the great majority of resources mined for use in steelmaking. Although the mineralogy of the main iron-bearing minerals relevant to this discussion is relatively simple, the ores themselves are often texturally complex. In contrast, associated gangue mineralogy may be very complex but will not be considered in detail in this discussion.

The major iron-bearing minerals are magnetite (Fe_3O_4), hematite (α-Fe_2O_3), vitreous goethite (FeO(OH)), and ochreous goethite ($FeO(OH)\cdot n(H_2O)$). Limonite (or limonitic) is often used as a general term to describe goethitic ores, particularly those with abundant ochreous goethite, but is not recognized mineralogically and therefore will not be used further here. Hydrohematite ($Fe_{1.8333}(OH)_{0.5}O_{2.5}$) (Clout, 2003), maghemite (γ-Fe_2O_3), and siderite ($FeCO_3$) are among other phases commonly recognized, generally in secondary abundance, although siderite is a primary component in some economic deposits.

Due to substitution by nonferrous elements (commonly including Si, Al, Mn, and Ti), as well as different degrees of oxidation and hydration, the same mineral in different ores (or even within the same ore) may have a range of chemical compositions. Perhaps, the most commonly observed example of a nonstoichiometric composition is that of Fe-deficient magnetite ($Fe_{3-x}(\cdot)_xO_4$), known as kenomagnetite (Morris, 1980).

Iron ores can vary significantly in hardness, and their color may also vary from silver/blue to dark gray/black, red, brown, and bright yellow in hand specimen, depending on the mineralogy, size (color of ultra-fines is different from lumps for the same minerals) and the amount and distribution of porosity. Under the reflecting optical microscope, hematite has the highest reflectivity of the iron oxides, normally calibrated to white, unless other associated, higher reflectivity phases such as pyrite or pyrolusite need to be correctly represented. Hematite displays distinct pleochroism under plane polarized light (white to light gray), depending on grain orientation, which can be useful in determining grain structure where grains are strongly intergrown. Reflectivity decreases with decreasing Fe content and associated increasing OH^- content and Al and Si impurity substitution. Siderite ($FeCO_3$) is distinguished by lower reflectivity (dark gray) than any of the iron oxides/oxyhydroxides.

The appearance of these minerals may be completely different under the reflecting microscope from that observed in hand specimen. The appearance of minerals under the reflecting microscope depends primarily on their reflectivity and color. It also depends significantly on the light source, its polarization, intensity, and color temperature. Thus, so for reliable comparison, standard imaging conditions should be chosen. All images presented in this section were produced in plane polarized light after light source calibration, where readings in all three color channels were equalized during imaging of a cubic zirconia (ZrO_2) reflectivity standard.

Figure 4.5 is a reflected light photomicrograph showing kenomagnetite (K), hematite (martite) (H), hydrohematite (HH), and vitreous goethite (vG) present in certain iron ore. The presence of the various iron oxide types indicates that the ore has been subject to different degrees of oxidation and hydration. In this sample, remnant kenomagnetite, which has a pinkish color in optical photomicrographs, is present. Often, kenomagnetite is intergrown with hematite, which develops from magnetite by oxidation, an example of which can be seen in this figure. Hydrohematite is also present. It has slightly lower reflectivity than hematite and a bluish shade. Kenomagnetite is also present adjacent to vitreous goethite (gray), which is not a common association, as magnetite is unstable under conditions favoring goethite formation.

Iron ore with maghemite (bluish) and magnetite (brownish) is shown in Figure 4.6. A very fine intergrowth of magnetite/maghemite with white hematite is evident around grain boundaries, where oxidation has penetrated into magnetite along cleavage planes.

Goethitic ores represent one of the major iron ore resources, and these ores typically have a low percentage of kenomagnetite and maghemite due to oxidizing conditions

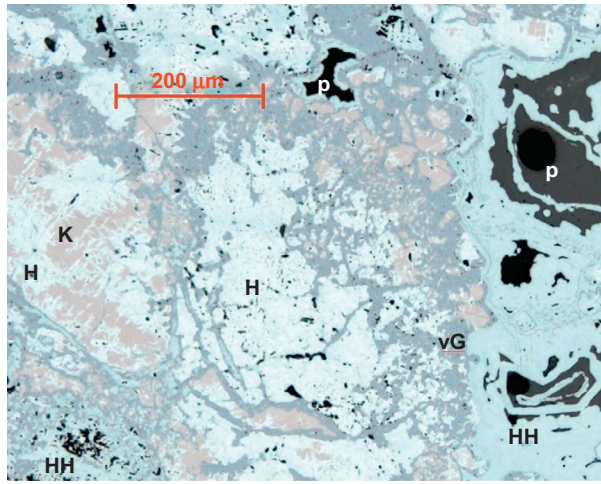

Figure 4.5 Reflected light photomicrograph of an iron ore sample showing kenomagnetite (K), hematite (martite) (H), hydrohematite (HH), and vitreous goethite (vG) in association (p = pore).

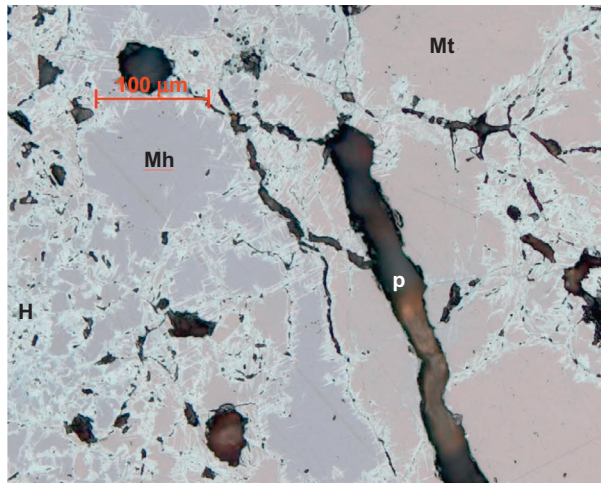

Figure 4.6 Reflected light photomicrograph of magnetite (Mt), maghemite (Mh), and hematite (H) (p = pore/void).

and high contents of ochreous and vitreous goethite. Figure 4.7 shows an example of such ore where the major phases are represented by the iron oxyhydroxides: hydrohematite and vitreous and ochreous goethite, with minor retained martite (hematite formed by magnetite oxidation but retaining the cubic crystal form of magnetite). Ochreous goethite is typically darker than vitreous goethite, with a yellow-brown hue due to high microporosity and internal reflections. The latter are both evident under

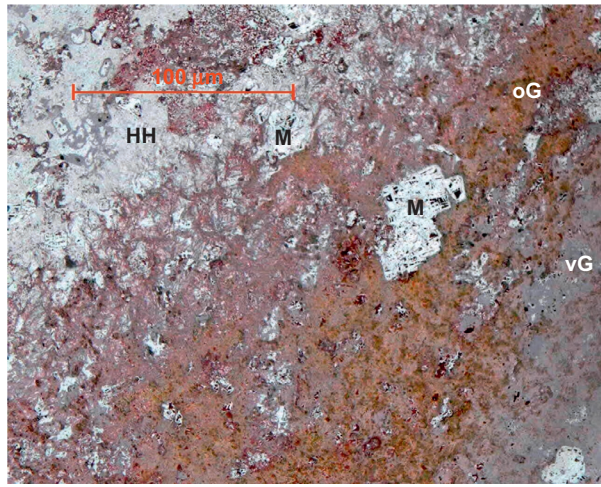

Figure 4.7 Reflected light photomicrograph of martite (M), hydrohematite (HH), and vitreous goethite and ochreous goethite (vG and oG, respectively).

plane polarized light at higher magnifications. Note the slightly lower reflectivity of hydrohematite, compared with martite, and its amorphous morphology and intimate intergrowth with goethite. Also, significant variation in the color for the same mineral (especially ochreous goethite) can be seen. This is connected with different degrees of element substitution (e.g., Si or Al), different degrees of oxidation and hydration, and deferent degrees of micro-/nanoporosity presence.

4.2.2 Sinter

Low-temperature (<1300 °C) iron ore sinter is an agglomerate of unmelted and partially melted nuclei particles (+1 mm) and a matrix bonding phase produced from the melting of fine ore (−1 mm) and flux particles, with the majority of melt formation occurring in the granule adhering fines layer. The majority of nuclei are hematitic, but they can also be any other unreacted particles such as flux or aluminosilicate gangue that may also act as nuclei during granulation. The composition of the melt phase and resulting sinter matrix mineralogy (upon cooling) can be locally variable, but the main phases are hematite and/or magnetite; complex ferrite phases such as magnesioferrite, silicoferrite of calcium and aluminum (SFCA), and silicoferrite of calcium (SFC); and silicate phases such as undifferentiated glass and larnite (dicalcium silicate) or clinopyroxene (Pownceby and Clout, 2000, 2003).

A typical image of sinter acquired at 50× magnification is provided in Figure 4.8. The large white areas are hematite nuclei, which retain original microporosity and are largely unreacted in this case, although well bonded to the surrounding magnetite/SFCA matrix. There also is plenty of fine hematite (both primary-unmelted and secondary-precipitated from the melt), especially in the right bottom corner, disseminated within magnetite (brown-purple) and SFCA (gray). Even though magnetite

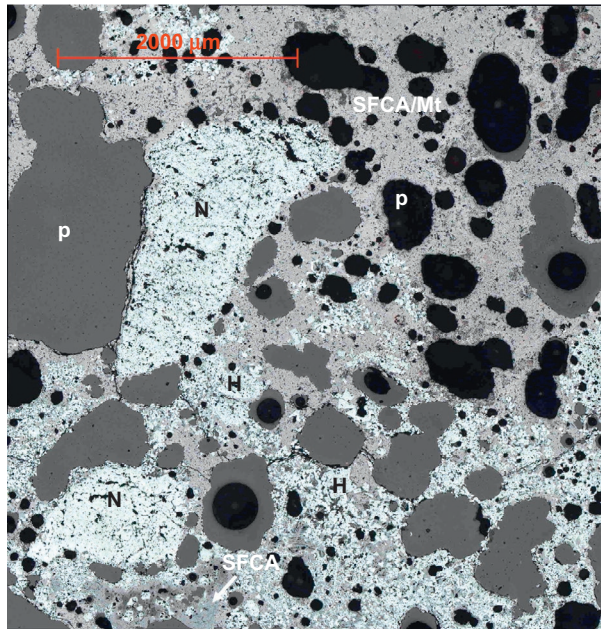

Figure 4.8 Reflected light photomicrograph of sinter (magnification x50) showing major phases of sinter: hematite nuclei (N) and matrix (formed from melt) predominantly consisting of magnetite (Mt), primary/secondary hematite (H), and SFCA (p = pore).

areas look quite uniform, they may include lots of fine SFCA and glass, and much higher magnification (at least 200×) is needed to distinguish them.

A photomicrograph of another sinter sample taken at 200× magnification is given in Figure 4.9. It shows why high magnification is required for proper sinter characterization, as some of the features in the image are less than 1 µm in size. This figure demonstrates all of the major components of sinter: hematite, magnetite, glass, larnite, and SFCA. It can be seen that a significant amount of SFCA has formed by precipitation from the melt between magnetite grains and that magnetite and SFCA appearances are very close to each other so at lower magnification, they may look as one phase.

There are three different major morphologies of SFCA: prismatic (Sasaki and Hida, 1982), acicular (McAndrew and Clout, 1993), and dendritic (Ahsan et al, 1983). The overall number of SFCA forms described by different authors is quite high, in particular because quite often, they use different terms for the same SFCA type. However, the major types mentioned in the literature and used by industry are fibrous (which actually has platy morphology, also called SFCA I) (Mumme et al, 1998), columnar (which has prismatic morphology), and dense (where the SFCA crystals are intergrown, with undetermined morphology). Figure 4.10 provides examples of fibrous and columnar types and Figure 4.11 demonstrates dense SFCA.

Even though the larnite area in Figure 4.9 looks dark, the actual larnite is very similar in reflectivity and color to glass. Larnite is distinguished from glass by its needle-like

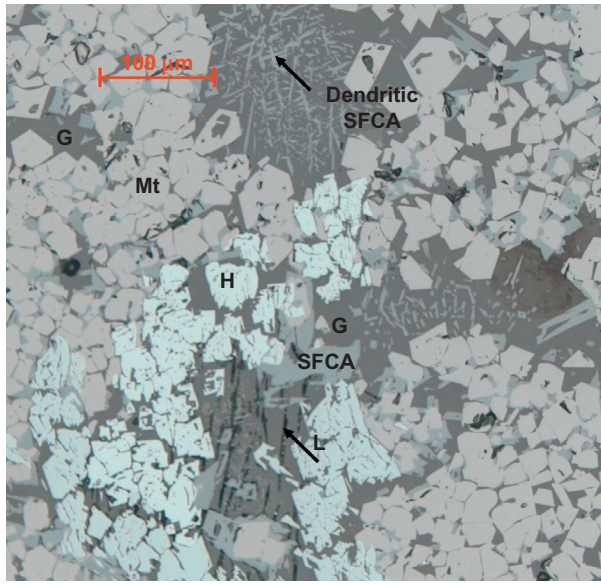

Figure 4.9 Reflected light photomicrograph of high-temperature (completely melted) iron ore sinter (magnification x200) showing major phases: secondary hematite (H), secondary magnetite (Mt), glass (G), larnite (L), and SFCA.

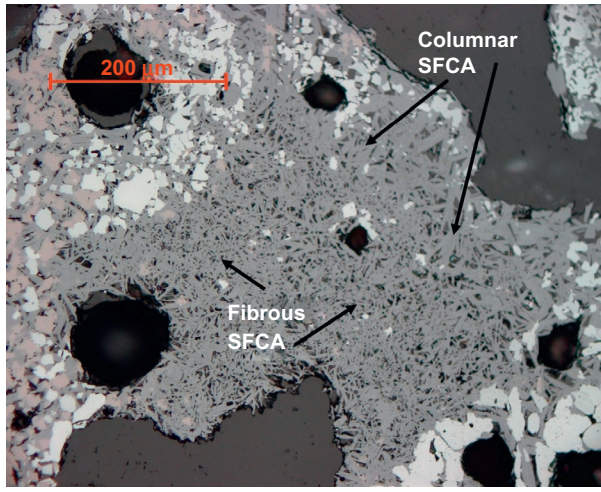

Figure 4.10 Photomicrograph of sinter (magnification x200) showing different types of SFCA: SFCA I (platy) and columnar SFCA (prismatic).

shape. The additional problem with imaging larnite is that it is water-soluble, so it is easily washed out during grinding/polishing, unless particular care is taken. Figure 4.9 therefore shows not larnite, as such, but rather pores in the block left after polishing. To properly image larnite, the sample should be polished in alcohol rather than water.

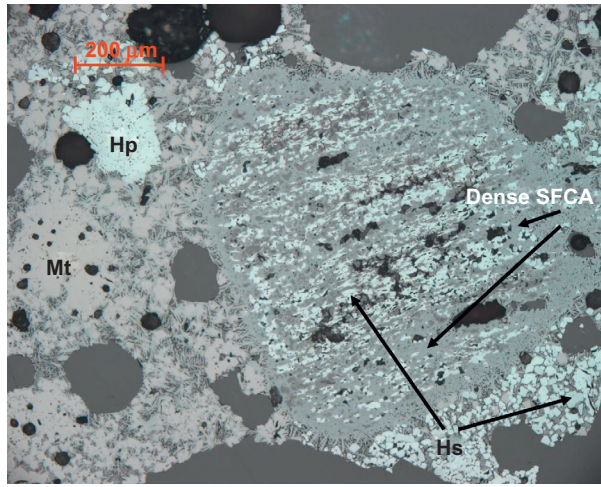

Figure 4.11 Photomicrograph of sinter (magnification ×100) showing dense type of SFCA, primary hematite (Hp) and secondary hematite (Hs), and secondary magnetite (Mt).

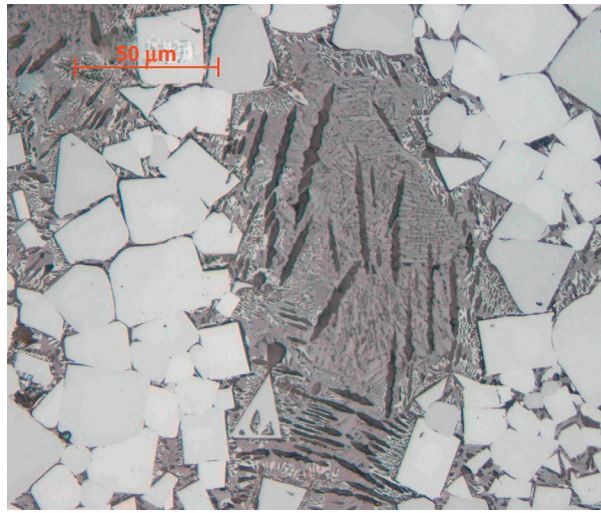

Figure 4.12 High-magnification reflected light photomicrograph of sinter (magnification ×500) showing preserved larnite needles. The dark borders are due to relief of larnite compared to the surrounding dendritic SFCA/hematite and glass.

Figure 4.12 shows a photomicrograph of a sinter block polished with ethanol-based suspension and lubricant, preserving larnite. Even though magnification is very high and the resolution is close to the limiting capabilities of optical microscopy, the image also shows some very fine textural features that obviously require much higher magnification to be seen in detail. This clearly indicates that even very high optical resolution

cannot always provide full textural characterization of sinter structure. In the majority of cases, however, 200× magnification provides sufficient resolution, and correlation between the results obtained by OIA and by other ore or sinter characterization methods (e.g., SEM, XRD, and XRF) is very high (Donskoi et al, 2014).

4.3 Automated optical image analysis (OIA)

4.3.1 Automated identification of particles and opaque minerals

The application of automated OIA to iron ore can be subdivided into three different scenarios depending on the relative size of the imaged objects and the image itself. The most complex situation occurs when multiple objects (particles) appear in one image. This is typical when a certain size fraction of iron ore or sinter fines is analyzed and the size of the particles is significantly less than the image size. A different situation takes place when a large piece of ore or sinter is analyzed under high magnification. In this case, a single image covers only a small part of the object area, and all images are taken within the boundary of the object. The third scenario is when different areas of an object (e.g., an inhomogeneous sinter lump) are of specific interest, and so some images may contain part of the object (boundary area) and epoxy. In all these scenarios, the solid part of the object(s) should be initially identified. It is technically possible to avoid this step by allowing each mineral to be identified individually and after that obtaining the map of the whole solid part as the sum of all individual mineral maps. The danger of such an approach is that the areas of nonidentified minerals or certain intermediary areas between minerals can be lost, not be identified at all, or be misidentified (most commonly as porosity).

There are many possible methods for discrimination of particle sections or minerals (Gonzalez and Woods, 2008), including edge detection, region growing, and thresholding. One of the major methods for whole particle identification is dynamic thresholding, which refers to adaptive gray value segmentation where a low pass filter is applied to the input image and then the low-pass-filtered image is subtracted from the input image (Donskoi et al., 2010). As a result, small structures (or rather their nonporous part) are segmented against a varying background. This method is rarely used for individual mineral identification due to its low color differentiation.

The major method of identification of the solid part of imaged objects, or individual minerals, is intensity thresholding (Otsu, 1979). An example of hematite thresholding segmentation is shown in Figure 4.13.

The reflectivity histogram of the sample is used to perform thresholding (some authors call it the intensity histogram, e.g., Seul et al., 2000). On the histogram, the *x*-axis represents the reflectivity value and the *y*-axis the number of image pixels with such reflectivity. In Figure 4.13b, the reflectivity histogram for the image in Figure 4.13a is shown next to the image displaying partial hematite segmentation. Two distinct peaks can be seen on this histogram. The left, taller, and broader peak corresponds to epoxy,

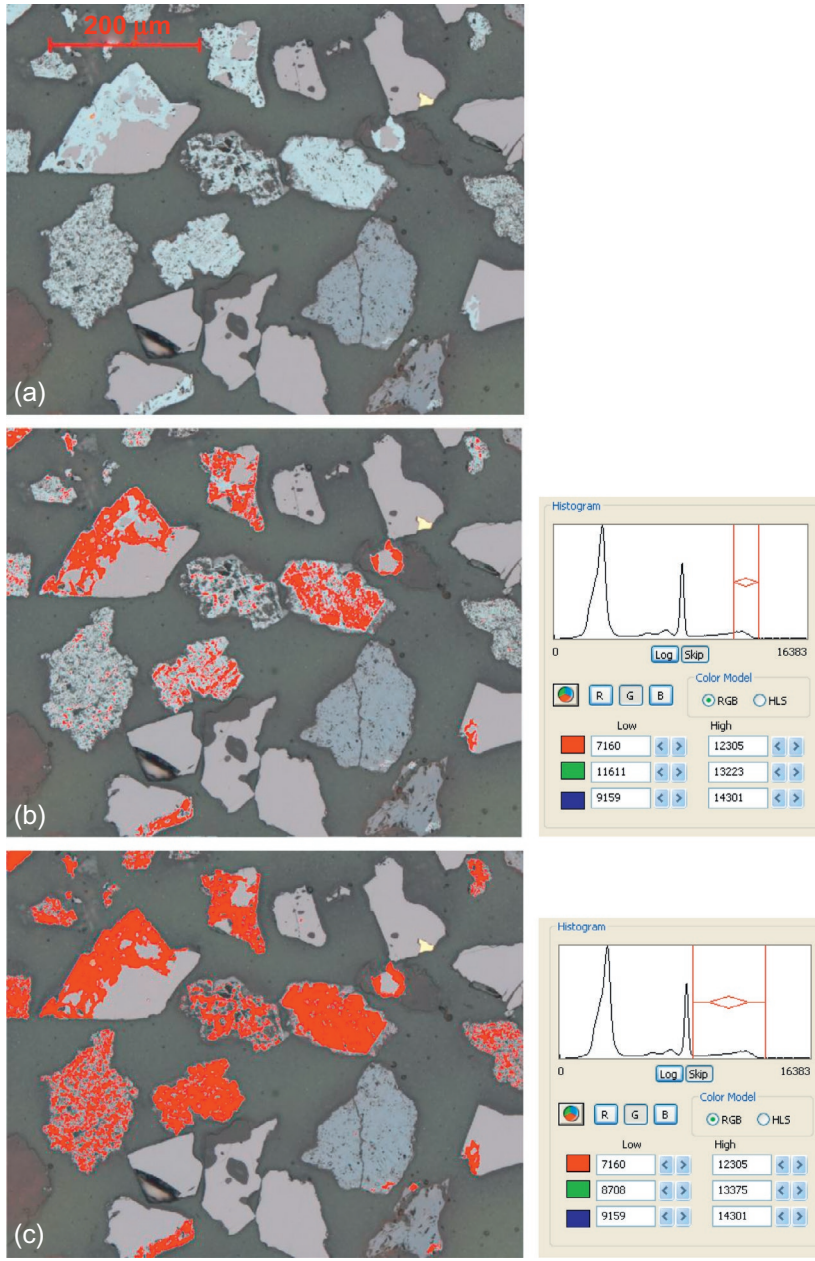

Figure 4.13 Thresholding of hematite during image analysis: (a) original image; (b) partial identification of hematite (segmentation of the brightest part); and (c) full identification. (Reflectivity histograms show green channel values and represent screenshots from Zeiss AxioVision software.)

and the second peak to the right corresponds to magnetite. To perform thresholding of a certain mineral, the reflectivity range corresponding to this mineral has to be chosen. The low but broad "hill" to the right of the magnetite reflectivity peak corresponds to hematite. In Figure 4.13b, only the brighter (higher reflectivity) part of hematite is chosen. While hematite associated with magnetite is already mostly segmented, the amount of identified hematite in porous particles is less than half the total hematite in such particles. Figure 4.13c shows segmentation of nearly all hematite in this image, excluding some hematite in porous particles, which has lower reflectivity due to interference with microporosity. In later sections on identification of unidentified areas and automated correction of mineral maps, the issue of correct identification of such darker areas will be discussed.

In Figure 4.13, the effect of thresholding in only one color channel (green) has been shown. However, thresholding very often should be performed in all three color channels to improve phase discrimination. The interference between reflectivities of different minerals can significantly affect the quality of mineral segmentation.

Figure 4.14a shows two ellipses inside that each point corresponds to a certain reflectivity combination in two color channels, red (y-axis) and green (x-axis). The areas of these ellipses correspond to all possible color reflectivity values for two different minerals. For the sake of simpler demonstration, in this and further examples, only two color channels are taken into account, whereas in reality, all three channels (red, green, and blue) may have to be considered. If thresholding is only performed using the red channel (assuming the other two channels are fully selected for the whole reflectivity range), it can be seen from Figure 4.14a that mineral 1 and mineral 2 will not be discriminated one from the other, because by selecting mineral 2 thresholds from L2R (low, second mineral, red channel) up to H2R, mineral 1 will also be fully thresholded. So it is obvious that segmentation of these two minerals requires using another channel, green in this example.

Figure 4.14a shows one possible scenario for choosing thresholding ranges for the green channel, where the highest value of selected reflectivity for the first mineral (H1G) is lower than the lowest value for the second mineral (L2G). This way, it is guaranteed that no pixels belonging to mineral 2 are identified as mineral 1 and vice versa. In this scenario, no misidentification occurs; however, pixels in both minerals corresponding

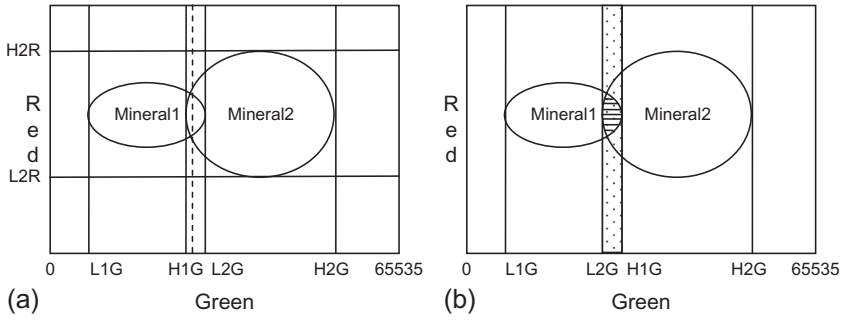

Figure 4.14 Thresholding segmentation of two minerals. L1G and L2G represent the lower thresholds for minerals 1 and 2 in the green channel, respectively, while H1G and H2G represent the upper thresholds. (a) H1G less than L2G; (b) L2G less than H1G.

to the ellipse area between the H1G and L2G thresholds are not identified at all. The second scenario is when H1G is higher than L2G, such that all mineral 1 pixels are identified during mineral 1 thresholding, likewise for mineral 2. In this situation, pixels that correspond to the reflectivities in the shaded area in Figure 4.14b are identified as belonging to both minerals. The most suitable choice in this scenario is probably to choose H1G equal to L2G (the dashed line in Figure 4.14a). However, even in this case, parts of the areas of minerals (with reflectivity higher than H1G = L2G for mineral 1 and with reflectivity less than this value for mineral 2) will not be identified correctly. Such situations, when even after some compromise decision in choosing thresholds is taken, some pixels in the image are still not identified and misidentified or are identified as two or more minerals, are not unusual. This is especially true when minerals such as porous hematite, vitreous goethite, kenomagnetite, and hydrohematite are present in the studied ore simultaneously. Handling of such areas (not identified at all or identified as two or more minerals) will be discussed later in Section 4.3.5.

In reality, the reflectivity area corresponding to one mineral can be significantly different from the simplistic example shown in Figure 4.14. Much more probable is the situation when the reflectivity area of certain mineral is closer to an ellipse with axes not parallel to the axes of the graph (see Figure 4.15a). If an attempt is made to segment all points of the mineral under this scenario, quite a significant additional

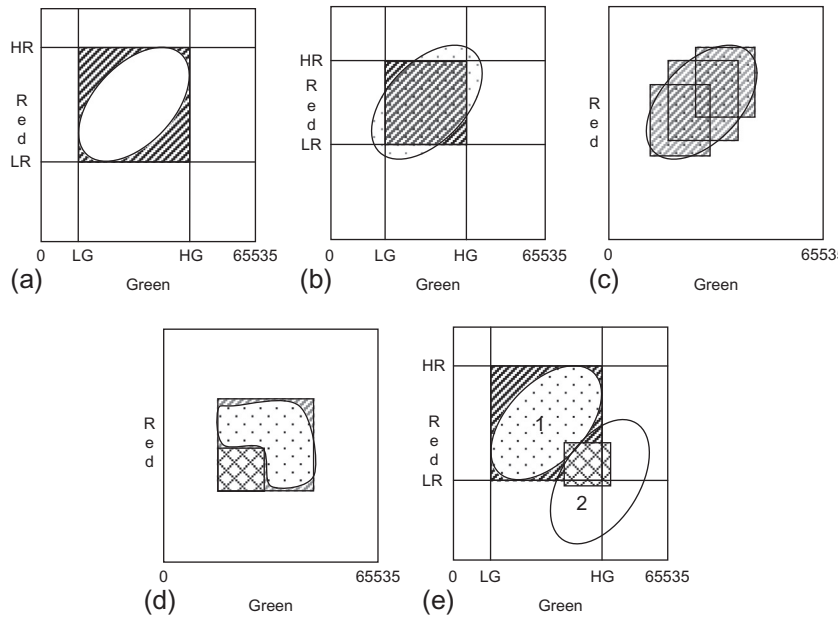

Figure 4.15 Different scenarios for thresholding of mineral reflectivity areas: (a) all points corresponding to the mineral are thresholded, giving the possibility of significant misidentification; (b) only part of the mineral reflectivity area is thresholded to reduce misidentification; (c) application of a multithresholding procedure where different individual thresholding steps are added together; and (d and e) application of a multithresholding procedure to a complex mineral reflectivity area where one thresholded area is subtracted from another.

reflectivity area (shaded) will also be chosen, and it is quite probable that reflectivity areas of other minerals will overlap with the shaded area. Reduction of the thresholded area (Figure 4.15b) will result in a situation where some points of the mineral of interest are not identified (dotted areas), while some areas not belonging to the mineral may still be discriminated. In an ideal situation, the analysis software should be able to identify minerals based not on minimum and maximum thresholds in color channels ("boxed" identification) but rather on the specific position, orientation, and shape of their reflectivity areas in the reflectivity space (in the example, an ellipse on the reflectivity plane). However, no commercially available software package has such a capability. The approach suggested by Donskoi et al. (2013a) is to generate an approximation of complex reflectivity areas by performing several thresholdings, that is, multithresholding. In this work, the authors reported segmentation of a mineral whose reflectivity area partially overlapped with the reflectivity area of epoxy. Figure 4.15c shows a multithresholding approximation of an elliptical reflectivity area achieved by combining three different individual thresholding steps. In this example, the whole mineral reflectivity area is overlapped by some minor, extra differentiated areas. Another capability of multithresholding allows the removal of a portion of a mineral reflectivity area where it interferes with another mineral. Two scenarios are shown in Figure 4.15d and e in which a reflectivity area corresponding to a smaller cross shaded square is removed from the initial mineral thresholding area corresponding to a larger shaded square. The targeted mineral reflectivity area in these cases is represented by a dotted area. In Figure 4.15d, the reflectivity area of the mineral has a complex shape, while in Figure 4.15e, the use of extra removal thresholding significantly reduces misidentification caused by interference with another mineral reflectivity area.

The examples in Figure 4.15 demonstrate some possible scenarios for mineral reflectivity areas and their thresholding. Mineral identification for real ores can be much more complicated when even complex thresholding by itself cannot differentiate two or more different minerals. This situation also can occur when discrimination of different textural forms of the same mineral is needed. In these cases, the capability of some software packages to identify different textures can be utilized (see Donskoi et al., 2011, 2013a). The presence of textural information is sometimes very important for the prediction of downstream processes (Donskoi et al., 2006, 2008b, 2009). Figure 4.16 shows an example where a textural identification module in CSIRO Mineral4/Recognition4 software helps to differentiate microplaty hematite from martite.

4.3.2 Automated identification of nonopaque minerals

As discussed in the previous section, the majority of iron-bearing and gangue minerals in iron ore can be identified using RGB thresholding, sometimes requiring a combination of several individual thresholding steps and/or textural segmentation. This is true, however, only for opaque minerals, which are nontransparent substances and are different in their grayscale reflectivity, color (if responses are different in red, blue, and green channels), and texture. This makes it possible to distinguish them from objects with different reflectivities, which could be other minerals and/or mounting epoxy.

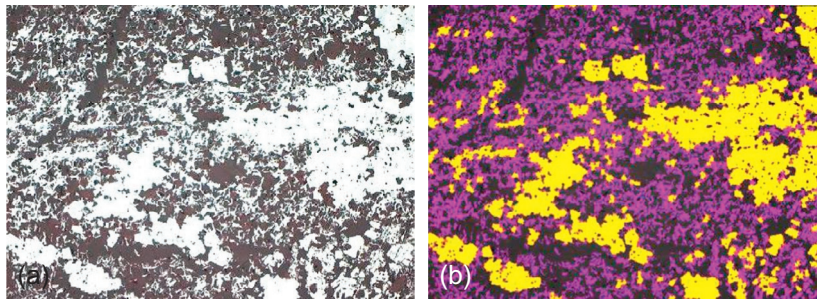

Figure 4.16 Differentiation of microplaty hematite and martite by CSIRO Mineral4/Recognition4 OIA package: (a) original reflected light photomicrograph and (b) mineral map (microplaty hematite, magenta; martite, yellow; porosity, black).

There is another nonopaque class of minerals that are transparent or semitransparent in visible light. As a result, what is typically seen where such minerals are mounted in the epoxy block is the out-of-focus underlying epoxy so that the area occupied by the mineral is close in reflectivity to the epoxy. Automated differentiation of the nonopaque mineral from epoxy therefore becomes a difficult task.

The issue of identifying minerals with reflectivities close to that of epoxy has always been a challenge for traditional OIA (Launeau et al., 1994; Neumann and Stanley, 2008). Of course, if the reflectivity of a mineral in a given sample is close to that of epoxy by coincidence, the choice of a different epoxy or the use of a color additive can help to resolve the problem. This is not the case for nonopaques as very often, they simply exhibit the reflectivity of the underlying epoxy, possibly modified slightly with the hue of the mineral. As mentioned earlier, the recent improvements in camera sensitivities and computing power have made it possible to segment some nonopaque minerals, for example, apatite and garnet, using RGB thresholding (Lane et al., 2008). In iron ore studies, however, the most important nonopaque mineral, also one of the most abundant gangue minerals in many types of iron ores, is quartz. So far, any attempts to reliably discriminate quartz using RGB thresholding have been unsuccessful. Although quartz is present in different types of iron ores, it is particularly abundant in magnetite ores. Therefore, the recent increased focus on magnetite resources makes the ability of OIA to identify quartz quite significant. Although quartz will be the main focus of discussion in this section, it should be kept in mind that the discussion is applicable to other nonopaque minerals as well.

It is important to note that quartz, although fully transparent, is not invisible as such and experienced mineralogists can usually identify between quartz grains and infill reasonably easily. Firstly, the border between quartz and epoxy is more or less visible in the vast majority of cases. Also, even though quartz itself is transparent, it also has some thickness; therefore, the underlying structure is out of focus when imaged. That is likely to result in the appearance looking slightly different to epoxy resin. The difference may become more prominent if the epoxy shows some texture, for example, when additives such as finely ground pigment are used. Combined together, these two factors give quartz grains some visibility that can be easily discriminated by a trained human brain.

Unfortunately, the "slightly different appearance of quartz" mentioned above, even though it provides some possibility of distinguishing quartz by RGB thresholding, is not enough for its reliable automated identification. One reason is that no object in an image, whether mineral or epoxy, has a single defined reflectivity. As described earlier, every mineral (as well as epoxy) has a reflectivity range that in a digital image corresponds to a statistical set of differently colored pixels that belong to the same mineral. When the reflectivity ranges of two minerals are significantly different, even though they may slightly overlap, they can be mostly differentiated by thresholding, especially using multiple color channels. In case of quartz and epoxy, however, the reflectivity ranges overlap very significantly.

Figure 4.17a–c shows an attempt to identify quartz by RGB thresholding. Note that in this sample, epoxy impregnated with dye has been used to make the quartz

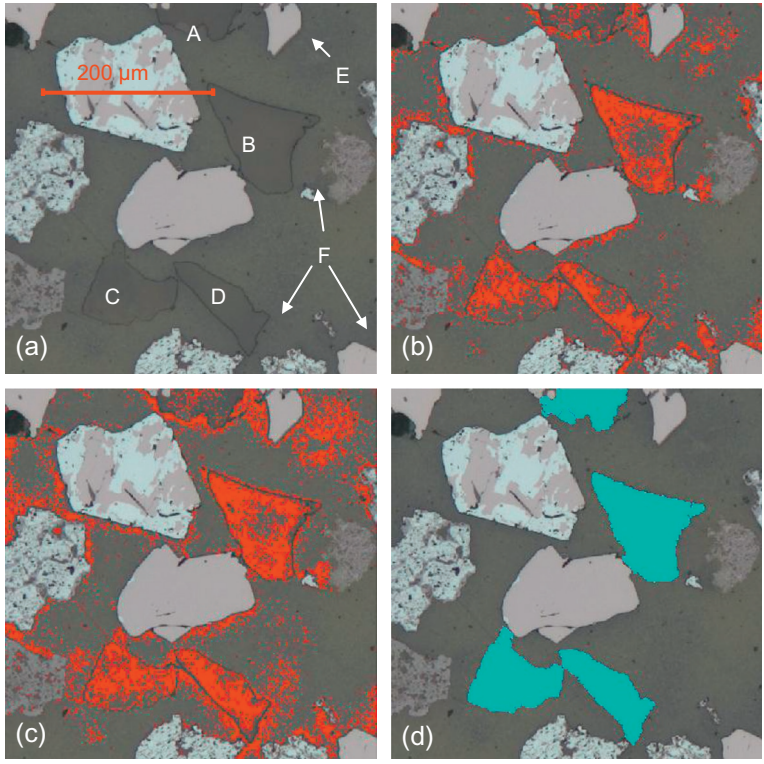

Figure 4.17 Identification of quartz in an iron ore sample: (a) original photomicrograph, quartz particles marked with A, B, C, and D, and "shadows" in epoxy marked with E and F; (b) attempted RGB thresholding, quartz significantly underestimated, and some false readings in the epoxy; (c) attempt to identify more quartz by RGB thresholding—quartz still underestimated, very significant false readings in the epoxy; and (d) border-based identification of quartz grains by CSIRO Mineral4 OIA software (Donskoi et al., 2013a; Poliakov and Donskoi, 2014).

grains stand out to the observer's eye more prominently. The figure shows two attempts (Figure 4.17b and c) to threshold quartz; however, the reflectivity of significant areas within epoxy also matches areas inside quartz grains. Epoxy is not uniform in reflectivity, and there always are individual pixels that match the reflectivity of quartz. Figure 4.17b shows that even in quartz-only regions that are noticeably different from the main epoxy body are identified by thresholding, there are also individual pixels of "quartz" identified within the epoxy. It might be possible to remove these individual pixels by scrap or erosion cleanup; however, quartz itself is also significantly underestimated by RGB thresholding and even more of it will be lost during cleanup. It should also be noted that the false readings tend to form clusters, most of them close to other particles, both quartz and opaque. Most likely, this is caused by the fact that there are parts of particles immediately underneath the epoxy that are visible as "shadows," which slightly change the epoxy appearance. If an attempt is made to increase quartz discrimination by thresholding, as in Figure 4.17c (note—it is still not all quartz!), the shadows become much more prominent and solid, so they can no longer be removed by cleanup and will provide significant false readings.

A number of approaches have been suggested in the past in order to improve quartz identification. Some of the techniques, such as thin section imaging (Hunt et al., 2010), provide reliable identification of quartz but require complex sample preparation and acquisition techniques. Such techniques are also of limited use for iron ore fines analysis because of the section thickness being too high compared to the typical size of the textural elements. The approach with repolishing carbon-coated blocks by Lane et al. (2008) is also a valid technique for quartz identification in certain ores. However, its applicability to iron ores containing highly porous minerals is limited. Attempts to use more traditional single-image analysis by careful selection of mounting resin have so far proved unsuccessful (Neumann and Stanley, 2008). It is also possible to use an ultrafine-textured epoxy to distinguish quartz (that does not display such texture) through textural identification capability of CSIRO Mineral4 OIA software. However, this method is still under development by CSIRO, the main problem being the creation of a uniform microtexture within the epoxy.

Poliakov and Donskoi (2014) had recently developed another method where Mineral4 software utilizes a principle different from RGB thresholding, namely, the identification of nonopaque minerals, predominantly quartz in iron and manganese ores, based on their visible borders or relief. This technique relies on the optical relief effect that is caused by the difference between the refractive indices of nonopaque minerals and mounting media (Phillips, 1971), whereby the border between quartz and epoxy is reasonably well defined in some epoxies. Even more important, as the refractive index of quartz (1.544) is known in advance, it is possible to specifically select an epoxy with a different refractive index, for example, Struers EpoFix (1.578), to ensure the contrast in relief is sufficient. Although in general EpoFix provides good border visibility, for some quartz grains, the borders are less prominent, most likely based on crystal orientation due to the extraordinary refractive index of quartz being higher (1.553) or possibly on the lower physical relief that also contributes to grain visibility. Still, in general, the visibility of quartz borders in EpoFix is acceptable for the purpose of further image analysis. In practice, the visibility of borders is better under lower

magnification, when increased area of light beam result in more peripheral illumination. Figure 4.17d shows an example of a quartz-bearing iron ore sample with quartz identified by Mineral4 using a border-based mechanism (Poliakov and Donskoi, 2014). It can be seen that the method provides very reasonable identification of quartz particles. In order to provide this identification, sophisticated algorithms have been applied to the image. A brief description of the algorithms follows.

Figure 4.18a shows a photomicrograph of a quartz particle cross section in a polished epoxy block. Even though the epoxy is less textured than in Figure 4.17a, the particle is still clearly identifiable by a human observer, mostly because of the easily recognizable border around the particle. The large continuous epoxy area around the particle provides a clear reference point, confirming that the area isolated inside the border must be a particle embedded in epoxy. It is reasonable to assume that a computer algorithm can perform the identification in exactly the same way. There

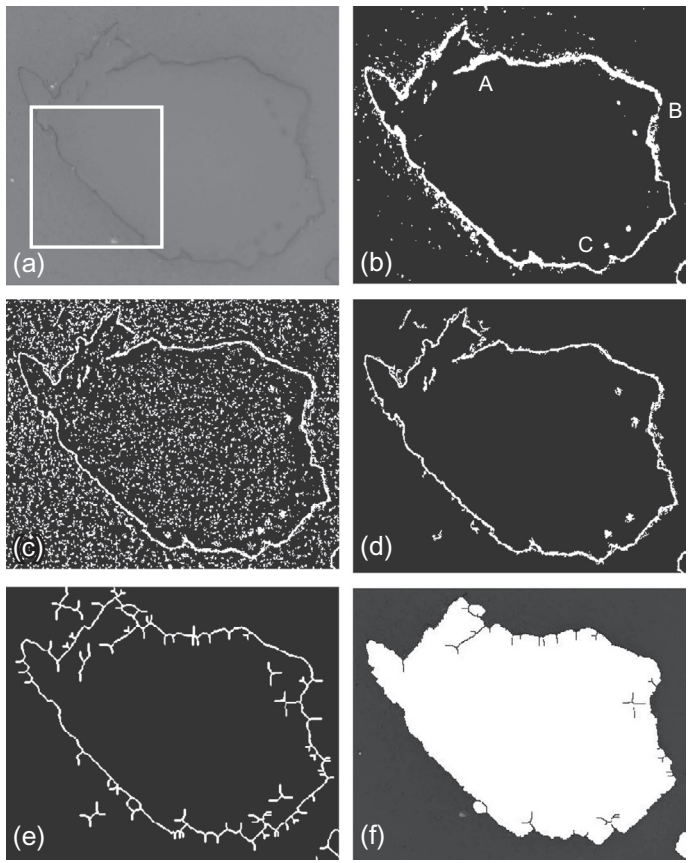

Figure 4.18 Border-based identification of a quartz particle: (a) original photomicrograph, digitally enhanced for better border visibility; (b) attempt at RGB thresholding of the border with very careful threshold selection—note thick borders (A) and clearly visible breaks (B, C); (c) dynamic thresholding with standard settings before cleanup; (d) dynamic thresholding after cleanup; (e) final border identification; and (f) border-based identification of quartz.

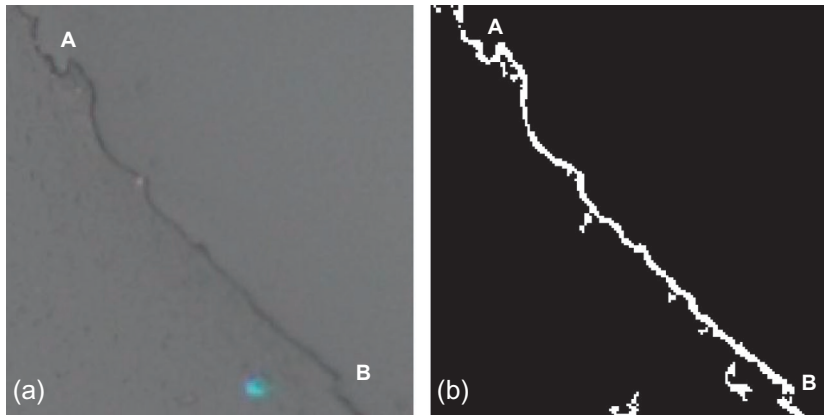

Figure 4.19 Closer view of the white square from Figure 4.18a: (a) original photomicrograph, digitally enhanced for better border visibility—note loss of reference and visible border breaks at A and B; and (b) after dynamic thresholding and cleanup, border breaks at A and B still to be closed.

is, however, a simple way to demonstrate some of the possible issues by selecting a smaller area within the image, which roughly corresponds to the same sample being imaged at higher magnification; see Figure 4.19a. First of all, it can now be seen that the border is not as prominent, uniform, and continuous as it looks like under lower magnification. Secondly, in the absence of an obviously bigger epoxy body, it is hard to decide which of the two image areas separated by the border in Figure 4.19a belongs to epoxy and quartz. Note that both issues can prevent the quartz area from correct recognition. If the border is not fully closed, the two areas are connected, so a software algorithm will recognize both areas as essentially being the same area. If there is no clear reference to the main body of the epoxy, the algorithm can mistakenly attribute quartz to epoxy and vice versa. Note that reference can be lost not only at high magnification but also in the presence of an ambiguous pattern of touching particles or nonuniformities of the polished block itself, for example, scratches.

The set of algorithms developed by CSIRO for the Mineral4 OIA software nonopaque identification module attempts to address both these issues, as well as a number of others that can have detrimental effects on automated nonopaque mineral identification, such as cracked or highly textured nonopaque areas. As a result, the module provides very good automated identification (up to 95% of all areas with a negligible amount of false readings) in samples where quartz particles are reasonably well liberated and are relatively small compared to the overall image area (this is typical for textural classification studies) and the sample is free from adhering ultrafines (properly wet-sized) and not too dense (to avoid ambiguous patterns of touching particles). Careful selection of analysis parameters provides good results even where some of the conditions are not met.

To provide good initial recognition of quartz borders, dynamic thresholding, which looks for gradients rather than RGB reflectivity values, is used. Figure 4.18b–d demonstrates why dynamic thresholding has been chosen. In the presence of particle "shadows," RGB thresholding (Figure 4.18b) can return very thick "borders," making it hard to recognize where the actual border is and potentially creating false

connections between particles. At the same time, RGB thresholding is not very efficient at recognizing the low visibility border portions. While dynamic thresholding (Figure 4.18c–d) provides much better borders, it may still leave some of the borders unclosed (Figure 4.19b). In order to overcome this issue, a procedure called "border improvement," which attempts to grow the borders and close the gaps, is applied. Once all borders are identified and refined (Figure 4.18e), the image area not occupied by known opaque minerals is subdivided into a number of smaller areas, some of which correspond to epoxy and others to quartz. A number of tests based on the sizes, shapes, and known neighbors of these areas are then applied to assign them to either epoxy or quartz. Figure 4.18f shows such identification for a simple single-particle case.

It should be noted that, even though the algorithm provides reasonable segmentation of quartz and other nonopaque minerals in a number of cases, CSIRO is working on further improvements of the algorithm, such as combining the border-based approach with RGB thresholding of nonopaque areas. Although RGB thresholding by itself is less precise and reliable, it can provide useful extra identification in complex cases. It should also be noted that the ability of this method to identify quartz is limited by the fact that it cannot automatically distinguish a quartz grain, fully locked inside a particle, from a pore (Donskoi et al., 2011). There are possible mechanisms to compensate for this, such as declaring all pores above a certain size as quartz inclusions if this can be confirmed by sample petrology. Still, in order to better identify quartz in a sample, other analysis options, such as SEM, are required.

4.3.3 Automated particle separation

Particle sections in a photomicrograph often touch each other, and if they are not separated during image analysis, they will be considered as one particle (Figure 4.20). If image analysis is only aimed at estimating mineral abundances, touching particles

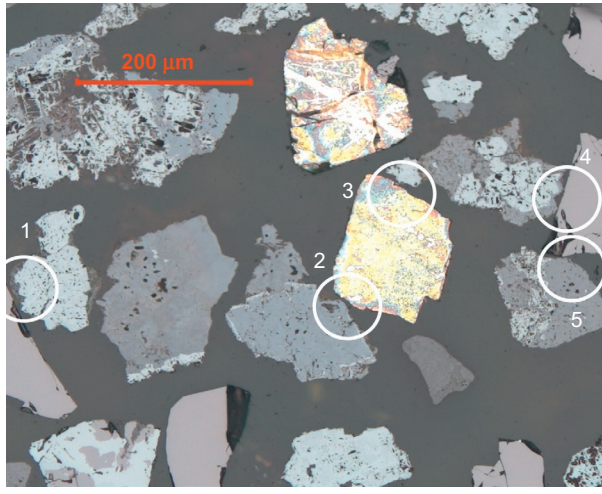

Figure 4.20 Iron ore photomicrograph with touching particles (shown by white circle areas).

are not a problem. However, if the task is to obtain liberation and association data or to perform particle classification, ignoring the problem of touching particles can significantly alter the final result. As correct liberation and association characteristics, as well as classification data of a studied ore, provide valuable insights into the potential benefits and optimal route for processing, it is important for analysis software to properly address the issue of particle separation.

Figure 4.20 shows a typical image where several ore particles touch each other. Particles touching each other in circled area 2 consist predominantly of vitreous goethite and pyrite. The first is a valuable mineral, whereas pyrite is considered gangue due to its sulfur content. If during OIA these two particles are not separated, they will be reported as one particle: half vitreous goethite and half pyrite, in reality not present in the sample. The actual situation in this particular image is even worse. There are multiple particles touching each other (areas 2, 3, 4, and 5), and without separation, all of them may be identified as one large, composite particle with characteristics (size, density, mineral composition, texture, etc.) completely different from those of the individual touching particles.

Separation of grains or particles during automated image analysis is quite a challenging task. The main approaches to perform separation are based on either erosion–dilation cycles or watershed segmentation. However, several other methods have been recently developed. Among these, Filho et al. (2013) used optimal path forest operations, Faessel and Courtois (2009) used a gap-filling method applied to the skeleton of the image background, and Van Den Berg et al. (2002) used a method that creates intersections between grain sections if the angle of the contact wedges in the outline of touching grain sections is smaller than a user-defined threshold value.

Among erosion–dilation cycle methods, the work by Shatadal et al. (1995), using mathematical morphology to develop the algorithm for disconnecting connected kernel regions, is notable. Generally, such methods include steps such as the creation of a binary map of the objects and the progressive erosion of this binary map, followed by dilation, thus avoiding connections between growing regions (known as ultimate dilation). In this case, the boundary between growing regions is used as the mask for the separation of original objects at the final stage. The main deficiencies of erosion–dilation methods is that they fail when touching objects form a long connection between them, when objects contain relatively small parts or parts connected to them with narrow necks, or when objects in the image are significantly different in size.

More robust methods of particle separation, which are the most popular, are the methods based on watershed segmentation described in detail by Russ (1998). In watershed segmentation, an image is considered as a topographic relief map in which the height of a pixel is proportional to its brightness. An analogy between the topographic peaks and the adjacent catchment basins is used here. If such topographic relief starts to be filled with water, due to runoff from rain, the water will start to flood the surface from each minimum, until all puddles nearly meet each other at the boundary between basins, without mixing. A barrier between basins protecting the water from different puddles from mixing is considered as the separation line between adjacent catchment basins (Russ, 1998). In iron ore studies, the objects to be separated are usually brighter than the surrounding epoxy so the inverted image should be used for watershed calculations.

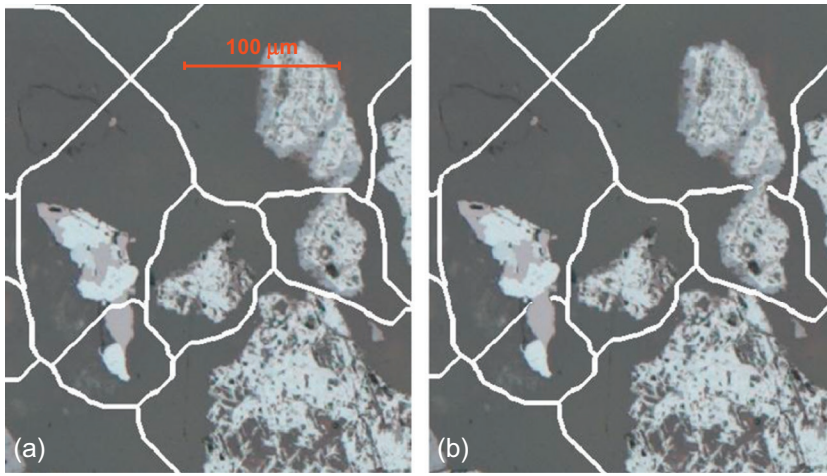

Figure 4.21 Example of watershed separation approach in a photomicrograph of iron ore particles: (a) application of standard watershed procedure; and (b) application of modified watershed separation used in CSIRO Mineral4/Recognition4 optical image analysis package (Donskoi et al., 2010, 2013a).

The utilization of standard watershed algorithms usually oversegments the objects to be separated and results in a large number of erroneous separations. In particular, it tends to oversegment objects within complex shapes containing large concavities. Figure 4.21a shows a section of a photomicrograph imaging particles of iron ore where two elongated particles have been mistakenly separated by a standard watershed procedure.

Different modifications of the watershed separation procedures have been developed to avoid such oversegmentation. Qin et al. (2013) used an extended-maxima transform for touching corn kernels. Derivaux et al. (2010) used a fuzzy supervised classification procedure and a genetic algorithm in order to build the elevation map used in the watershed. Couprie et al. (2009) added graph cuts, random walker, and shortest path optimization algorithms to their watershed procedure to be applied to seeded image segmentation.

In their application to iron ore particle section separation during automated image analysis, Donskoi et al. (2010, 2013a) used an approach significantly different to those mentioned above. The majority of approaches to modified watershed algorithm apply the modifications before the watershed is drawn. Such modifications often rely on the known properties of objects to be separated: shape, size distribution, relative position, etc. Mineral particle sections to be separated usually have very different shapes and sizes and quite roughened surfaces. That makes it difficult to develop an algorithm that will take into account all peculiarities of particle sections in advance. Donskoi et al. (2010) proposed an algorithm where a standard watershed procedure (from Zeiss AxioVision software; AxioVision, 2006–2009) is applied, but all subsequent separations performed by the watershed algorithm are automatically analyzed and those deemed erroneous are automatically removed (see Figures 4.21b and 4.22c).

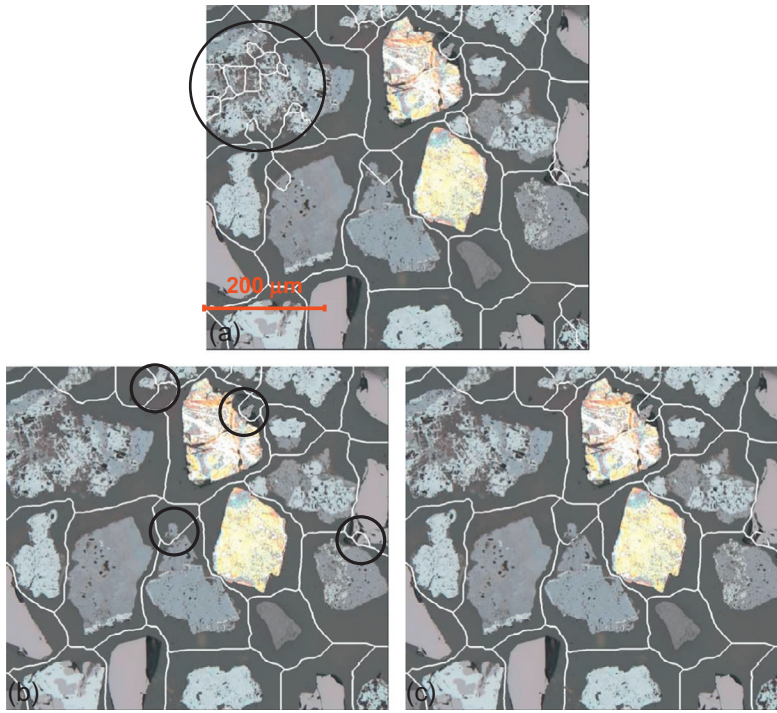

Figure 4.22 Application of watershed separation to the image from Figure 4.20: (a) direct application of the watershed algorithm without filling of porosity, segmenting porous particles; (b) direct application of watershed algorithm with filling of porosity, protruding elements in black circles cut off; and (c) application of modified watershed separation used in CSIRO Mineral4/Recognition4 optical image analysis package—all wrong separations in circled areas automatically removed (Donskoi et al., 2010, 2013a).

One of the most important steps before the watershed algorithm is applied is the filling of all pores. Figure 4.22a shows the result of watershed algorithm application without filling the pores. It can be seen that the porous particle in the black circle has been highly segmented. In contrast, Figure 4.22b shows the direct result of watershed algorithm application with porosity prefilled. Several protruding elements (in black circles) are cut off from the particle sections. Finally, Figure 4.22c shows application of a modified watershed algorithm (Donskoi et al., 2010) where all erroneous separations have been automatically removed.

To conclude this section, it is worth mentioning that from the mineral association, liberation, and textural classification point of view, if there is a choice between the software failing to separate some particles or the software generating some false separations, the preference should be given to extra separations. It is quite probable that even if a particle is erroneously divided, the pieces will still keep similar textures and mineral abundances to the parent particle, so the information will not be significantly affected by erroneous sectioning. In the case of missing separation, however,

the resulting pseudoparticle may report properties that do not exist in the sample at all. It is therefore advised against being too conservative when selecting settings for automated separation.

4.3.4 Automated porosity identification

The importance of correct automated identification of porosity is difficult to overestimate. Different iron ore mineral components have quite different densities and natural porosity ranges (Donskoi et al., 2008a). For instance, quartz and magnetite usually have very low porosity, while ochreous goethite and kaolinite are usually highly porous. Consider an OIA output showing that a certain iron ore consists of volume of 40% nonporous hematite and 60% goethite with 30% porosity. If the density of hematite is 5.1 g cm^{-3} (slightly below the 5.26 g cm^{-3} of pure crystalline hematite) and that of goethite 3.7 g cm^{-3} (roughly the average between ~3.1 and 3.3 g cm^{-3} for ochreous and ~4.1 and 4.3 g cm^{-3} for vitreous goethite), the calculated weight percentages of these minerals, with porosity taken into account, will be 56.8% hematite and 43.2% goethite, giving an overall density of 3.59 g cm^{-3}. If porosity is not taken into account, the calculated percentages will be 47.9% hematite and 52.1% goethite, with an overall density of 4.26 g cm^{-3}—a major difference. This example shows how important is the correct identification of porosity and the effect of wrong identification of porosity on mineral abundances and particle density evaluation. It should be noted that correct identification of porosity is also very important for textural identification and classification.

Porosity can be thresholded in the same way as any other mineral. The choice of threshold can significantly affect the result (Moreira et al., 2012). Another, more common procedure for segmentation of porosity is filling of voids after all minerals (or solid parts of a characterized object) are identified. This approach identifies porosity enclosed within particles (closed porosity). However, porosity connected with the particle surface (open porosity) can also be very significant, especially for very porous materials. Usually this porosity is identified by the following procedure: the overall mineral map of a particle is closed with a significant closing coefficient, resulting in the closure of the open pores. After this procedure, the mineral map is filled and the difference between the filled map and the original one is identified as closed porosity. Such identification strongly depends on the choice of closing coefficient (which makes it subjective) and also has side effects, as surface concavities may also be filled. Figure 4.23 shows identification of closed and open porosity in a porous hematitic particle. As can be seen from Figure 4.23b, where only internal porosity is identified, and Figure 4.23c, showing porosity connected with background (epoxy), the relative amount of the latter is very significant, so it definitely should be segmented in this case. Figure 4.23d shows that if cleaning is not performed, surface concavities are also filled after the closing procedure, and these areas are then identified as porosity, which should normally be avoided (Figure 4.23e).

OIA shows that the particle in Figure 4.23a has 55.5% porosity and a calculated density of 2.27 g cm^{-3}. The amount of closed porosity measured is 29.4% and open porosity, 26.1%. If open porosity was not taken into account, the reported porosity

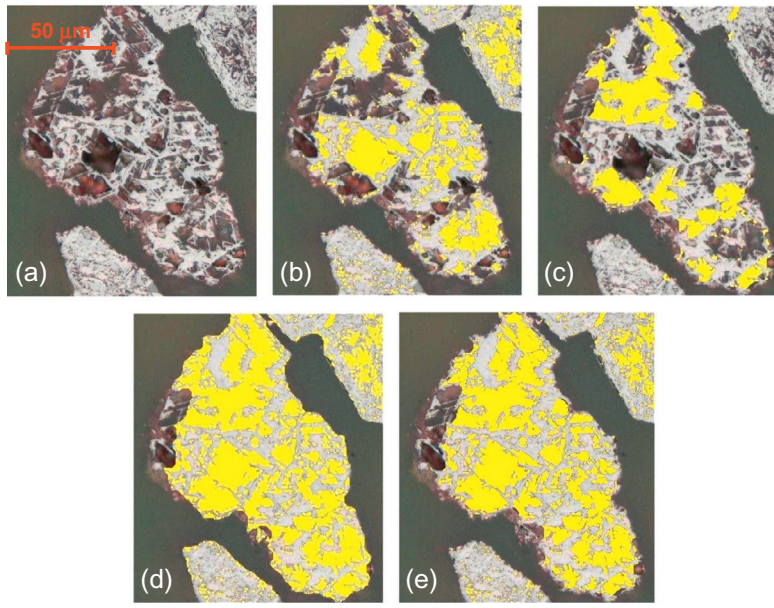

Figure 4.23 Identification of porosity in a porous hematitic particle: (a) original image; (b) internal (closed) porosity only; (c) porosity connected to epoxy (open porosity) only; (d) closed and open porosity without cleaning; and (e) closed and open porosity with cleaning.

would be 39.8% and the calculated density, 2.89 g cm^{-3}. Such a significant overestimation of density can seriously affect mineral abundance calculations and the prediction of particle behavior during downstream processing (e.g., hydrocycloning and gravity separation). It also should be noted that if the open porosity is not taken into account, the measured perimeter of the particle can significantly increase, which results in a significant overestimation of its shape factor. In this case, the shape factor calculated when open porosity is taken into account is 6.0 while otherwise rising to 49.9. (In reality, even a value of 6 is an overestimate of shape factor for this particle and is caused by the very rough surface of the particle. After appropriate smoothing of the surface is performed, the shape factor drops to 2.5.)

Part of the porosity (especially microporosity) is also segmented during the mineral map correction stage and will be discussed in Sections 4.3.5 and 4.3.6.

4.3.5 Automated identification of unidentified areas

As shown earlier, after mineral segmentation, some areas of imaged objects may not be identified as any mineral or may be identified as two or more minerals. A very detailed discussion has been provided in Section 1.3.1 on how the choice of thresholding for minerals with interfering reflectivity areas can result in both types of problematic identifications.

One of the ways to avoid the creation of areas identified as belonging to more than one mineral (and therefore to partially simplify the thresholding procedure) is to exclude mineral areas identified at each stage of the thresholding process from subsequent mineral identifications. Of course, this approach can only be used when the identification of minerals to be excluded is perfect (i.e., guaranteed to be free from misidentifications), which is not often the case. For the purpose of further discussion, areas which were identified as belonging to more than one mineral will also be referred to as unidentified areas from here on, as they are treated in the same manner.

Unidentified areas quite often are small areas on the boundary between minerals and epoxy, either on the outside boundary of imaged objects or on the internal boundary of porosity filled with epoxy. Such areas may occur in microporous areas or within pores that were not properly filled with epoxy. Unidentified areas can also be caused by reflection from minerals underneath the epoxy (inside pores or outside imaged objects) but very close to the polished surface. Nonidentification also can occur on boundaries between different minerals or grains of the same mineral. If microtextures are not present, all minerals are segmented with reasonable quality, and there is no significant overlap between the reflectivities of different minerals, the percentage of unidentified areas is usually not high and is around 1–2% of the overall solid area. However, in the presence of the conditions listed above, the percentage of such areas can be quite significant. If the percentage of these unidentified areas is not large, the image processing approaches discussed below should be used to allocate them to identified phases. If the percentage of unidentified areas is large, reidentification of thresholds or additional textural identification of minerals (Donskoi et al., 2013a) for better segmentation of minerals should be considered. Reimaging of the sample at higher magnification usually reduces the percentage of unidentified areas. However, there is always a compromise between factors such as magnification, image size, and the capability of a system to collect and process large images (many systems allow collection of mosaic images, where a matrix of several elementary images is combined into one large image), the required number of imaged objects, and processing time. A significant increase in imaging magnification may not be practical and may not eliminate unidentified areas completely.

Different approaches may be used to automatically identify unidentified areas. Firstly, the positions of thresholds for individual minerals can be automatically corrected to reduce the percentage of unidentified areas. Secondly, the reflectivity of every pixel in such areas can be assessed against mineral thresholds, and, depending on its RGB values, every pixel can be attributed to the closest (from the reflectivity point of view, in all three channels) mineral match. Finally, neighboring identified pixels can be analyzed, and unidentified pixels can be assigned to one of the neighboring minerals. The last two methods can be weighted and taken into account at the same time.

Photomicrograph of an iron ore fines made at magnification 200× is shown in Figure 4.24. The major minerals present are magnetite, hematite, and vitreous

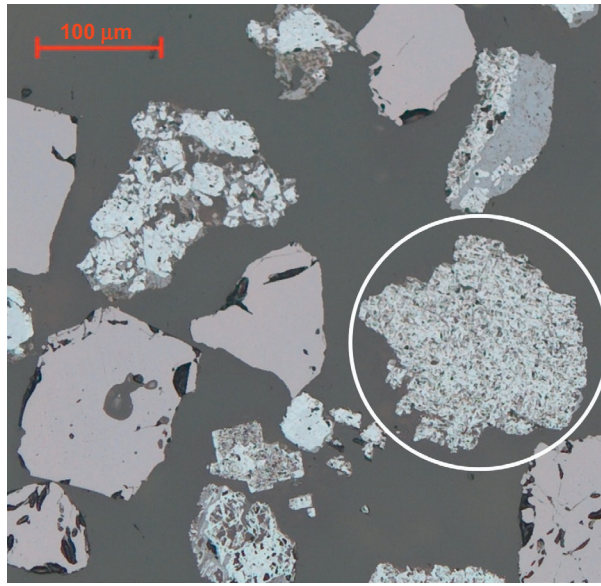

Figure 4.24 Photomicrograph of an iron ore fines from the −150 + 106 µm size fraction at magnification 200×.

goethite, with minor ochreous goethite and silicate. The highly microporous hematitic particle marked with a white circle will be specifically discussed. Normally, the interference between the reflectivity ranges of these minerals is quite small. However, the presence of microporosity significantly extends the reflectivity of hematite to the darker part of the reflectivity spectrum, so its interference with vitreous goethite and magnetite reflectivity becomes much stronger.

Figure 4.25 shows the mineral map for the image in Figure 4.24 obtained from mineral thresholding by the CSIRO Mineral4 OIA software (Donskoi et al., 2010, 2013a). An enlarged map of the hematitic particle is also given. It should be mentioned that in this case, the thresholding was performed very carefully by multiple thresholding as discussed in Section 4.3.1, and the result is very close to the best possible segmentation. However, even after thorough thresholding, there are still various small unidentified areas; in this image, white represents areas not identified as any mineral and red, areas identified as two or more minerals. The enlarged image of the hematitic particle also shows numerous areas identified as magnetite, vitreous, and ochreous goethite. Analysis of an image of the same particle taken at magnification 500× (Figure 4.26) shows that the actual amount of goethite in this particle is very small, and it is only present in a few spots such as the one in encircled area. More than 99% of this particle is actually pure hematite and porosity. A comparison of the mineral map given in Figure 4.25 with the original image confirms that the vast majority of unidentified and misidentified areas occur where hematite interferes with microporosity.

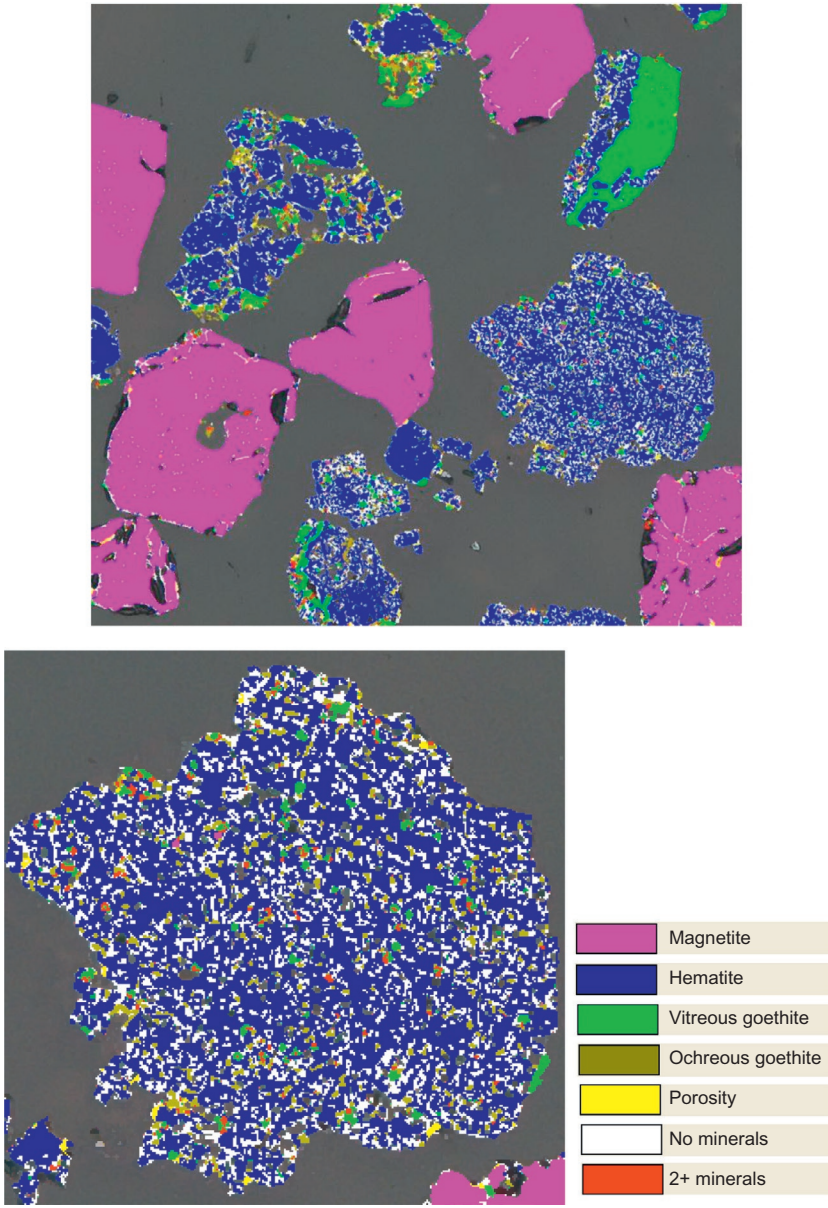

Figure 4.25 Mineral map for the image in Figure 4.24 obtained from mineral thresholding only.

Figure 4.27 shows unidentified areas after their identification (see Donskoi et al., 2010, 2013a). The general correlation is obvious—most previously unidentified areas are identified as the major mineral (or porosity) in this particular location (see color coding in Figure 4.25). A very good example of that can be seen in the enlarged image of a hematitic-goethite particle also given in Figure 4.27. However, some unidentified

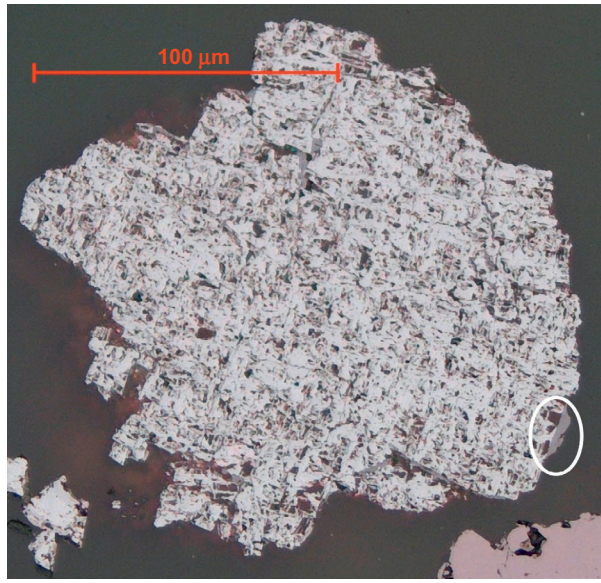

Figure 4.26 Image of the hematitic particle in Figure 4.24 taken at magnification 500× (small area of vitreous goethite encircled).

areas can be identified wrongly due to the presence of misidentified areas after thresholding. In the enlarged image of hematite particle in Figure 4.27, some former unidentified areas were identified as vitreous goethite. These spots, together with originally misidentified "vitreous goethite" areas, are reidentified in the next stage of image processing (Section 4.3.6).

4.3.6 Automated correction of mineral maps

While correction of unidentified areas is based on actual details of the image such as threshold-based mineral maps, automated correction of mineral maps obtained after thresholding and identification of unidentified areas, on the contrary, depends on the operator's experience. An experienced operator, for example, knows that small pores in magnetite can be thresholded as vitreous or ochreous goethite. In reality, it is very unusual to find fine inclusions of goethite within magnetite and the darker spots, when studied under high resolution, usually prove to be pores. Another example of optical or digital artifacts that require correction is thin rims of goethite that may appear around pores in hematite after thresholding. Higher magnification shows that there actually are no rims and they appear only because of the interference between porosity and hematite on the phase boundary.

Figure 4.28 shows the mineral map for the image in Figure 4.24 obtained after identification of unidentified minerals and before automated correction. It shows some ochreous goethite inclusions within magnetite particles and quite a significant amount of fine vitreous and ochreous goethite within microporous hematite. As discussed

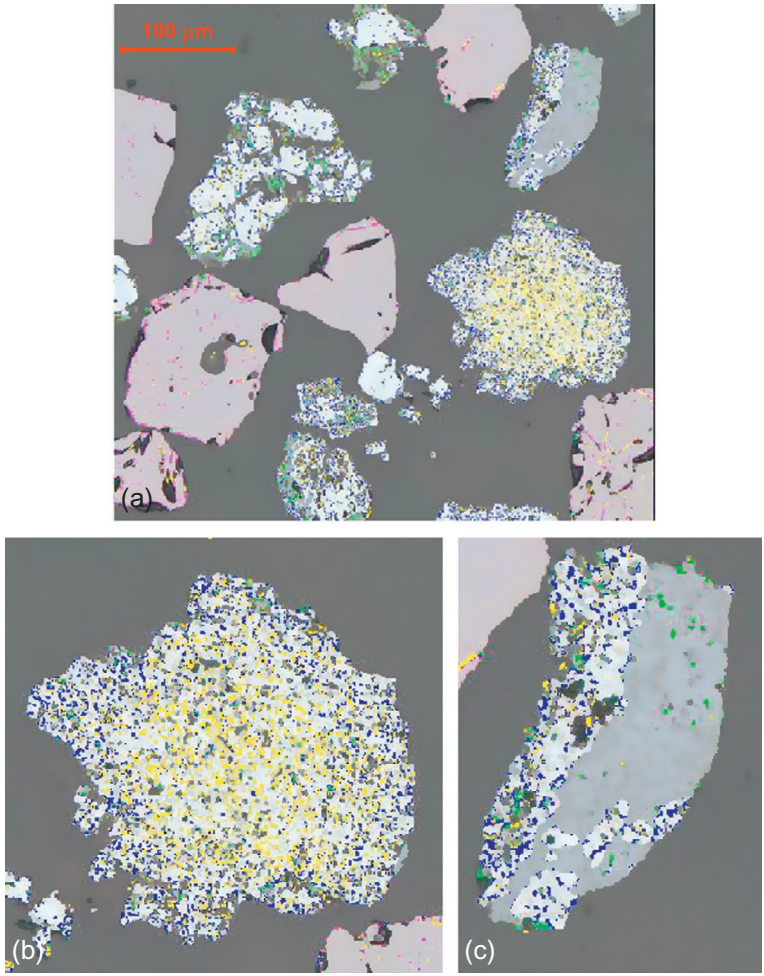

Figure 4.27 Previously unidentified areas after identification: (a) whole image; (b) detail of hematite particle; and (c) detail of hematite–goethite particle.

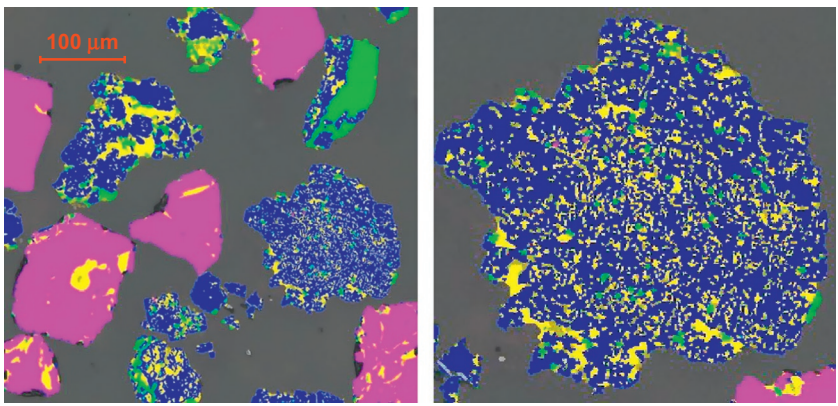

Figure 4.28 Mineral map after identification of unidentified minerals but before automated correction (for color coding, see Figure 4.25).

above, this fine goethite is the result of interference between porosity and hematite. Such areas should be reidentified, attributing them partially to hematite and partially to porosity, and it is quite important to perform reidentification of such areas correctly. Typically, the brighter pixels in such areas should go to hematite and the darker pixels to porosity. The boundary between the two can be identified experimentally (from direct porosity measurement of a similar sample) or from imaging of the same particle at higher magnification.

Depending on the boundary value, the measured porosity for the same particle can be significantly different, especially for microporous structures. Taking the hematitic particle from Figure 4.24 as an example, if all goethite areas to be reidentified are transferred to porosity during reidentification, the total porosity will be 28.8% of the particle area. On the contrary, if settings strongly discriminating against porosity are used during identification of unidentified areas and automated correction of the mineral map, the total porosity will be only 9.6% (see Figure 4.29). Furthermore, if porosity connected to epoxy is not identified, the percentage will drop even further to 8.6%.

Similar reidentification can be performed for false goethite inclusions in magnetite, with the difference that such inclusions can normally be converted directly to pores. There are other scenarios when darker minerals not normally found inside lighter minerals may show up after thresholding because of interference with pores, and they also can be taken care of by comprehensive analysis software.

During the final stage of automated correction of mineral maps, some possible misidentifications on boundaries between two minerals and between minerals and epoxy are corrected. Usually such misidentifications appear within very thin (1–2 pixel) layers and can be easily corrected by dilation/erosion procedures. Final, automatically obtained mineral map for the image in Figure 4.24 is shown in Figure 4.30. The porosity calculated for the hematitic particle of interest after this final identification is 23.0%.

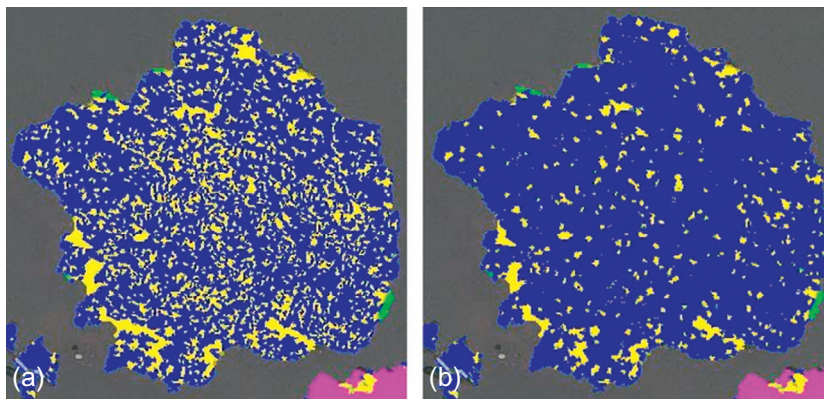

Figure 4.29 Identification of porosity in the hematitic particle in Figure 4.24: (a) maximization of porosity identification and (b) minimization of porosity during identification of unidentified areas and automated correction of mineral map (porosity connected with epoxy is still present).

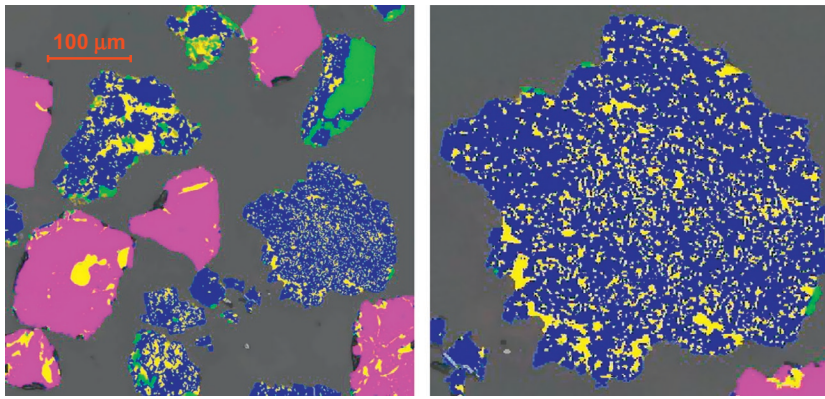

Figure 4.30 Final mineral map developed by CSIRO Mineral4 OIA software for the image in Figure 4.24.

4.3.7 Automated image processing

In the previous sections, it has been shown that automated OIA incorporates many powerful techniques allowing reliable identification of various iron-bearing and gangue minerals as well as porosity in mineralogical samples. Along with those techniques, it is also important to discuss the automation process itself because proper organization and utilization of automation is one of the key elements that make OIA a valuable, reliable, and cost-effective tool for research and industrial applications.

First of all, quantitative OIA in the mineral industry is very rarely applied to isolated individual images, especially if the subject of analysis is iron ore fines or sinter. In most cases, it takes many images to be analyzed in order to obtain reliable, representative, and statistically significant information. Dozens and even hundreds of individual images (depending on magnification and size of the image) can be collected from a standard 30 mm round block with a sample of an iron ore fine size fraction imaged at proper resolution. The actual number of images in one study can vary significantly, but as a general principle, the set of images should contain enough objects of interest for the study to become representative and statistically significant. If, for example, ore particles are being studied in order to determine the abundance of certain textural or liberation classes in the ore and the properties of such classes, multiple particles from each class should be present. For example, if a particular class comprises 1% of the overall sample, there will be approximately 10 particles of that class in a set of 1000 particles, giving enough data for at least some statistical estimation. Therefore, if classes represented by less than 1% of the total sample are not important, 1000 imaged particle sections is a suitable choice. In fact, 1000 particles are typically used for analysis, which can possibly mean hundreds of images. Of course, the actual number of particles and corresponding images may vary depending on the sample being studied and the task. In particular, the magnification used for imaging is normally determined by the size of typical textural features that have to be clearly recognizable. It should be mentioned that for studies of parameters such as mineral liberation, association, or textural classification, particle sections significantly smaller than the size of the studied size fraction are not recommended for consideration because of possible

lack of representability. The exclusion of small particle sections from consideration is known as “large section stereological correction” (Lin et al., 1995). Image analysis software is usually able to perform such exclusion. Similarly, particle sections cut by the image frame are known to not truly represent particle shape and dimensions and are also likely to miss some details, so they are often excluded as well. If the imaged particles are very large compared to the individual image (the order of image size), the loss of particles due to filtering of particles cut by the frame can be very significant. This loss can be decreased by using stitched mosaic images, but due to computational limitations, as the individual image size grows, the processing time also grows in a nonlinear manner up to the point where the composite images may be too large to process.

A single image may sometimes require a lengthy adjustment of analysis parameters during different stages of image processing in order to achieve good identification of minerals. Importantly, this adjustment does not have to be repeated for every image in a set of images obtained during a single acquisition session, because it should be generally suitable for all other images as well. We assume here that, once acquisition parameters such as illumination, exposure time and color balance have been set up at the beginning of an acquisition session, they won't change during the session. The list of parameters used to analyze the first image can be recorded as an analysis profile, which is a computer-readable file containing all processing parameter values. These values can then be reapplied to other images in the set automatically without further adjustment. Similarly, they can be usefully applied to other sets of images of the same ore, provided that image acquisition was performed under exactly the same conditions, that is, a standard calibration procedure has been performed prior to image acquisition, as described later.

It should be noted that an individual image does not necessarily have all the features typical for a given sample, so the initial profile setup should normally be verified against several other images and refined if necessary. Once that has been done, the profile can be used in fully automated mode. It is still recommended to perform a check of all or randomly chosen results of fully automated image processing to make sure there is no systematic identification error caused by a sample feature not discovered during profile development. Image analysis software that generates particle and mineral maps for processed images can help the operator make such visual checks reasonably easily, as shown in Figure 4.31.

If a systematic error is encountered, there are two possible approaches to handling it. If the image analysis software supports manual editing of images and the number of misidentifications is relatively low, it is possible to fix the errors manually. It should be noted that image analysis software normally produces reports for a whole set rather than individual images; therefore, manual editing is only viable if the software also supports reassembling of reports after editing. Alternatively, further refinement of the analysis profile is required based on the problematic images, followed by a full reprocessing of the set. In certain cases, manual editing is a reasonable option, especially if the errors are hard to correct in any other way. Still, it requires a significant amount of tedious work for the operator; it also makes it hard or impossible to reproduce the analysis unless the software can record all the manual edits. On the other hand, full reprocessing may take some time, but, in fully automated mode, operator intervention is only required during profile refinement.

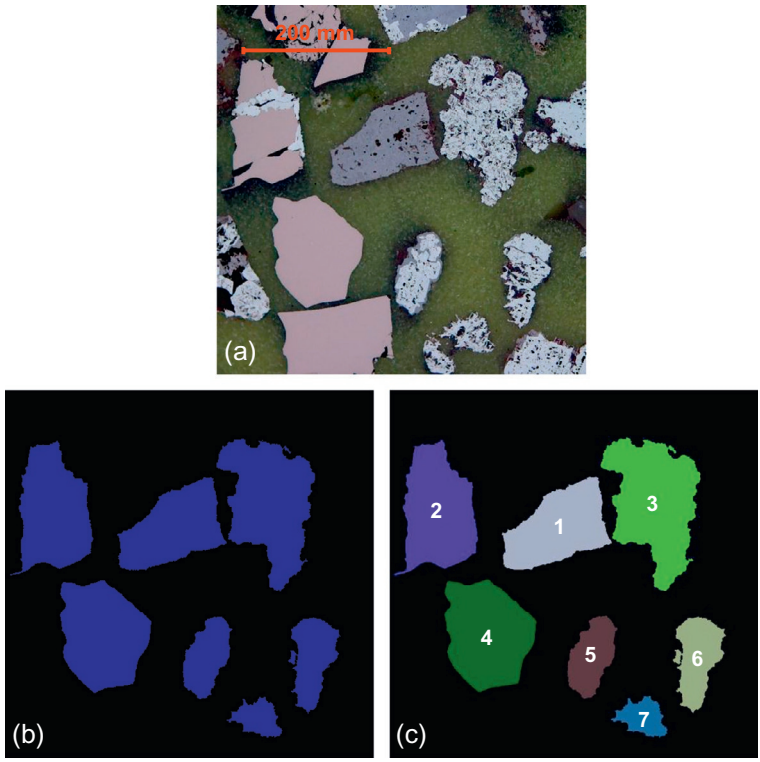

Figure 4.31 Image of iron ore and associated images recorded during processing to help with review of results: (a) original image; (b) measured minerals; and (c) numbered individual particles. Particles on frame in this example were excluded from consideration.

Another reason for preference of profile refinement is the fact that a quality profile can be reused not only for one ore sample but also for any similar samples in the future, thus saving vast amounts of time. Of course, a profile developed for one ore should again be verified against several images from the new ore. It should be emphasized that to fully utilize this possibility, the images in different sets must be taken at exactly same conditions of illumination in all three color channels. This can be achieved by adopting a calibration procedure that is performed prior to image acquisition. A typical calibration procedure requires a uniform calibration sample, or possibly multiple samples, of known reflectivity. By adjusting camera settings such as exposure and color balance, the operator makes sure that the reflectivity peak of the calibration sample matches the recorded RGB values. Light sources, especially incandescent bulbs, are known to change their brightness slightly over time and also require time to stabilize when their intensity is adjusted. Therefore, a good calibration procedure requires the light source to be brought to the desired intensity some time prior to calibration and also includes recalibration at regular time intervals during acquisition to confirm that the imaging conditions (brightness and color channel balance) have not

drifted. It should be noted, though, that nonthreshold profile settings (e.g., the parameters used for cleanup, particle separation, and mineral reidentification and corrections) can normally be reused even without proper calibration, but the thresholds, of course, will need to be adjusted in this case. It is therefore suggested to follow the calibration procedure for all acquisitions.

The calibration procedure should also include shading correction, used to compensate for nonuniformities of the light field such as vignetting, that is, progressive concentric decrease of illumination from the center to the edges of the image. A defocused uniform reflectivity sample such as the standard described above can also be used to obtain a white reference image, which is later applied to the acquired images to compensate for such nonuniformities (Pirard, 2004). Modern acquisition software can usually perform the compensation automatically once a white reference image has been taken. Without shading correction, the difference in illumination across the imaged area makes proper thresholding hard or even impossible. Intensity calibration and shading correction must be repeated after every change of objective.

Figure 4.32 provides an example of such a calibration procedure. In this example, by changing camera settings (exposure and color balance), the operator tries to achieve a situation where the maximum of the reflectivity peak of the calibration standard coincides with a prerecorded threshold. Figure 4.32a shows the peak maximum as below the threshold, which results in most pixels in the calibration image being selected by thresholding (red in Figure 4.32b), which, along with peak position itself, indicates poor calibration. Once camera settings are adjusted, so there is a match between the peak and the threshold (Figure 4.32c), the result of the thresholding will be a random pattern of selected and nonselected pixels, indicating good calibration (Figure 4.32d). Note that a nonrandom pattern, such as shown in Figure 4.32e, most likely indicates incorrect preparation of the calibration sample (not flat, dirty, and not properly defocused) or a bad shading correction. Both these issues, if encountered, should be addressed to achieve a successful calibration.

Analysis profiles are usually different for different objective magnifications, as both the amount of light coming through the objective and various size-related parameters change between magnifications. Different types of ores being studied are also likely to require different profiles. For example, the reflectivity of ochreous goethite may be different, depending on the composition and porosity; some types of ores also don't contain certain minerals that can therefore be excluded from profiles to speed up processing and improve the quality of recognition of the remaining minerals. A well-established mineralogical characterization laboratory will have an extensive library of profiles for different magnifications, ore types, mosaic settings, etc.; as a result, most samples can be processed either straight away after acquisition or with minimal adjustments.

Another important factor to be taken into consideration is the ability of image acquisition and image analysis software to perform tasks in batch mode without operator intervention. As discussed, automated image analysis of a set of acquired images consists of two stages. The first stage, the preliminary stage of profile development or selection and adjustment, depending on the complexity of task and the availability of already recorded profiles, may take from minutes to hours. The second stage, the

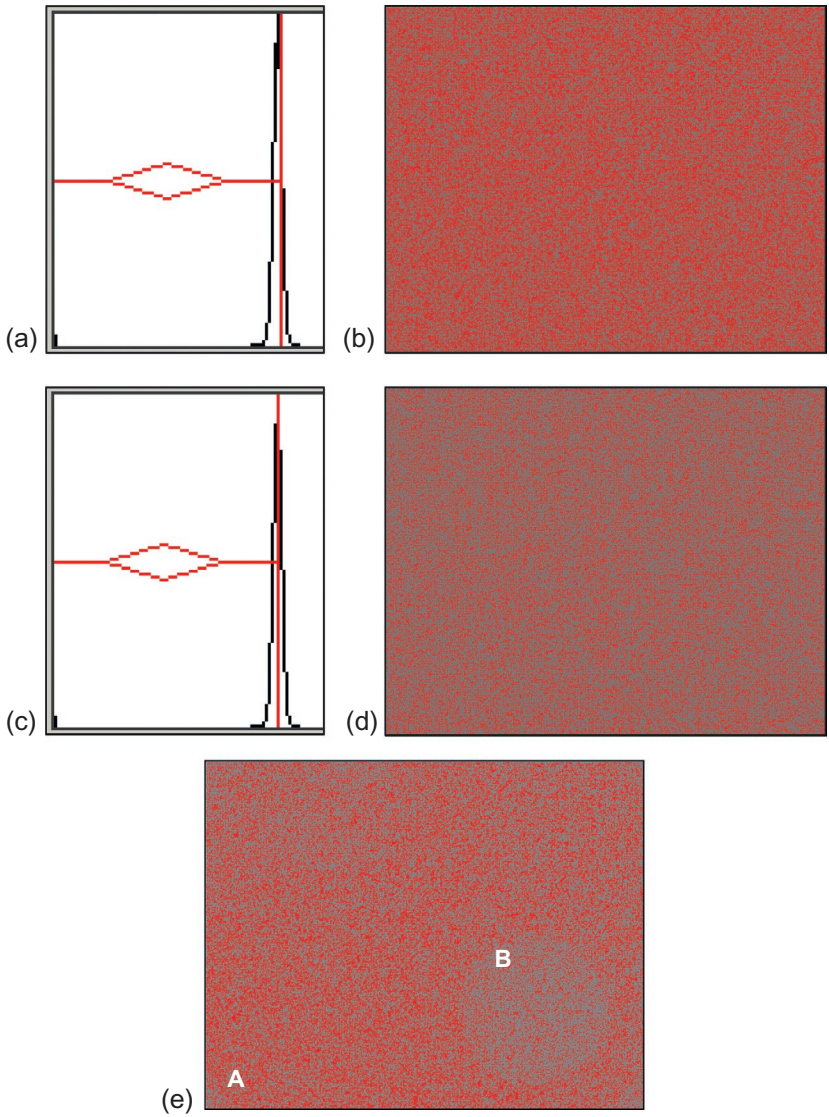

Figure 4.32 Example of calibration procedure—the maximum of the reflectivity peak of the calibration standard in the histogram (black) must coincide with the prerecorded value (red): (a) reflectivity peak (black) to the left of the desired value (red); (b) most pixels in calibration image are selected by thresholding (red); (c) reflectivity peak coincides with the desired value; (d) about half of calibration image pixels selected forming a random pattern—the desired outcome; and (e) an example of bad shading correction, showing nonuniform corners (A) and traces of dirt (B). NB: Only one color channel used for demonstration—images obtained within Zeiss AxioVision software.

actual analysis, can take hours or in some cases even days, depending on the set size. During the automated analysis stage, operator involvement is usually not required. The system can actually be set up to wait for certain operator input before finalizing processing of every image, but this is inefficient and is therefore rarely used in full-scale processing. Once the set analysis is over, the operator's input is required again. That breaks the operator's working time into chunks, the length of which is not well known in advance. As a result, either the operator or the workstation is idle for some time during the day. On the contrary, if the workflow is organized in such a way that the operator can perform the setup for multiple sets of images and then let the system perform the analysis unattended, possibly overnight, utilization of both the operator and the system, and therefore overall productivity, can be much higher. For example, the CSIRO Mineral4 OIA software allows batch processing of up to 20 groups, and each group can in turn contain up to 20 image sets that share the same analysis profile. Each set normally corresponds to one polished block and may consist of hundreds of images. The ability to process many sets in unattended mode (e.g., over the weekend) can provide a significant boost in productivity (Donskoi et al., 2013a). A similar increase in productivity can also be achieved during image acquisition if that can be performed in batch mode as well.

Once the processing is completed, the measured data are recorded in some predefined format and can be either used directly for reporting or processed further to extract more complex information such as statistical dependencies. One typical way is to output raw particle or full image data in the format of a particle database and then use standard or specialized software for further data analysis and report generation. For example, in the CSIRO OIA package, the Recognition4 component is used to automatically classify measured objects and calculate statistics for every class, mineral liberation, and association, as well as many other sample characteristics. At the same time, the image analysis software can have strong built-in reporting functionality as well and output preprocessed and collated data in the way most useful for the operator, for example, in Microsoft Excel or Word file format.

4.4 Application of automated OIA to natural and sintered iron ore

After an image has been fully analyzed and final mineral maps are obtained, they can be measured. Based on the measurements, useful information about every image, or every object in the image, can be calculated. If an operator works with an individual image, they can often observe the information directly during the analysis session. However, if statistical processing of information from many images is needed, the information from each image usually has to be saved in a database. For example, Figure 4.33 shows several images from a sample of Brockman ore with some addition of martite/kenomagnetite ore (BM1 sample).

The typical purposes of such processing are to obtain mineral abundances, textural classification, mineral liberation, and association data for the sample. Table 4.1 gives

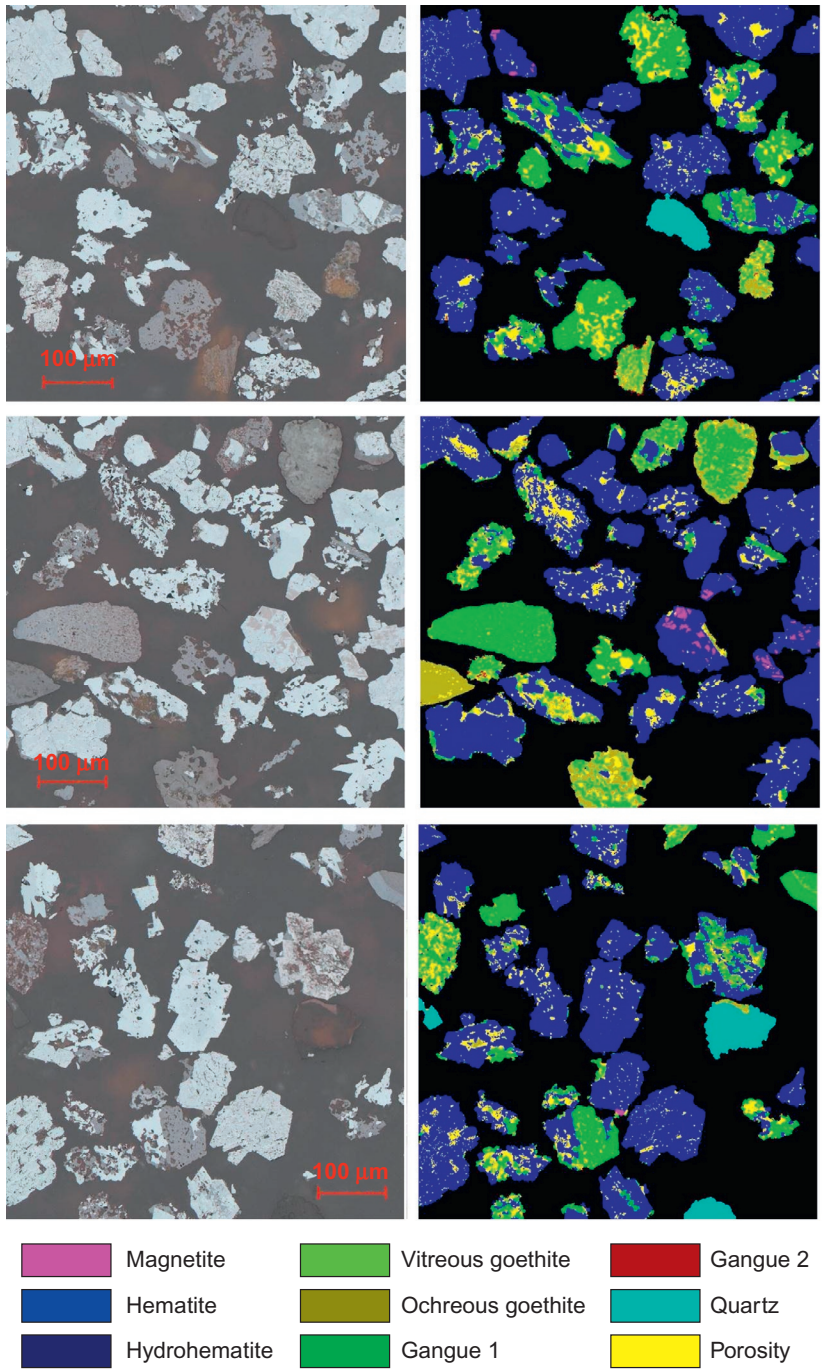

Figure 4.33 Images from BM1 sample and their corresponding mineral maps, including color coding.

Table 4.1 **Modal analysis for the BM1 sample, including XRD results**

	Occurrence	Area (μm²)	Volume (%)	Surface (%)	Density	Weight (%)	XRD (wt%)
Kenomagnetite	1344	266,870	2.19	3.69	5.10	2.96	3.5
Hematite	1728	6,978,127	57.24	56.47	4.80	72.92	73.0
Hydrohematite	255	9390	0.08	0.05	4.70	0.10	
Vitreous goethite	1489	2,315,777	18.99	23.14	4.00	20.17	21.8
Ochreous goethite	1249	212,400	1.74	2.42	3.60	1.66	
Kaolinite	756	89,677	0.74	1.39	2.60	0.51	1.1
Quartz	93	291,026	2.39	1.73	2.65	1.68	1.0
Pores	1988	2,028,334	16.64	11.10	0.00	0.01	n/a

NB: XRD results for hematite include hydrohematite and for goethite represent combined vitreous and ochreous goethite content.

an example of a "modal analysis" table, which is the CSIRO Mineral4/Recognition4 output of calculations from image analysis of the BM1 sample. Only particle sections with areas more than 2500 μm^2 were included in calculations, which represented 72.4% of all particle sections identified by image analysis (1990 out of 2749).

The data in the density column correspond to the known actual densities of minerals, corrected by taking into account fine porosity not recognizable by OIA. Generally, it depends on the specific ore, due to the presence of submicron porosity in different minerals. The last column presents XRD results for this sample. It can be seen that the results of OIA and XRD are in very good agreement.

Liberation analysis tables usually show how each mineral or group is liberated against the rest of the minerals in the sample. The example given below for BM1 shows how the set of minerals, consisting of kenomagnetite, hematite, and hydrohematite (set A), is liberated from the remaining minerals: vitreous goethite, ochreous goethite, kaolinite, and quartz (set B). Table 4.2 gives information for the group of selected particles as in the previous example (area greater than 2500 μm^2). In this table, the whole group is subdivided into 11 classes based on the total weight percentage of set A minerals in particles falling within a certain range of values (0–5% for class 1, 5–15% for class 2, and so on). Table 4.2 shows that most of the sample belongs to only three liberation classes. The first such class has less than 5% of set A minerals by weight, therefore corresponding to liberated set B minerals, and includes 330 particles (see row N). The second class (221 particles) has between 85% and 95% of set A minerals per particle, and the third class (999 particles) corresponds to liberated set A minerals with more than 95 wt% set A. Liberation output also gives mineral composition for every class calculated by weight and by volume. For example, it can be seen that the liberation class from 0% to 5% has on average 81.1% of vitreous goethite, which is a valuable mineral and should have been included in set A if the purpose of liberation studies was to determine liberation of valuable iron-bearing minerals from minerals carrying the majority of alumina and silica (inclusion of ochreous goethite depends on its actual composition). Recognition4 software is fully flexible in choosing the sets of minerals for liberation studies. The liberation table also gives area percentage of grade class (Ar%), its average grade by weight (AvG), weight percentage of grade class (Wht%), average SG, distribution by total iron (FeD), average total iron in class (FeG), recovery of set A minerals (Rec), cumulative recovery (C Rec) and cumulative yield (C Yld), and also the number and percentage of particles in each class (N, N%).

Figure 4.34 shows a liberation histogram for all particles and for the group of selected particles (area greater than 2500 μm^2). The 0–5% liberation class is larger for all particles than for selected particles. That results from the fact that all particles include the small particle sections that statistically are supposed to have better liberation than large particles. The 95–100% liberation class is also larger for all particles, but not significantly so.

Mineral association analysis for the BM1 sample is shown in Table 4.3. Columns corresponding to certain minerals show what percentage of this mineral is associated with another mineral named in the corresponding row (Donskoi et al., 2007). The cells with the same mineral in a column and a row express the percentage of the fully liberated mineral. The table shows that there are no particles consisting only of

Table 4.2 Liberation analysis table for BM1 sample, showing liberation of kenomagnetite, hematite, and hydrohematite (set A) from vitreous goethite, ochreous goethite, kaolinite, and quartz (set B)

Grade	0–5	5–15	15–25	25–35	35–45	45–55	55–65	65–75	75–85	85–95	95–100
Ar%	15.22	2.55	1.93	2.65	1.49	3.48	1.61	2.62	4.58	11.48	52.39
AvG%	0.51	8.50	19.85	30.11	40.43	49.89	60.90	70.37	81.16	91.07	99.07
Wht%	12.64	2.25	1.74	2.40	1.38	3.29	1.54	2.62	4.64	11.92	55.58
SG	3.07	3.08	3.26	3.12	3.23	3.46	3.26	3.42	3.54	3.74	4.19
FeD	10.19	2.03	1.62	2.21	1.28	3.14	1.48	2.63	4.69	12.30	58.43
FeG	52.43	58.73	60.47	59.76	60.46	61.95	62.51	65.33	65.78	67.13	68.39
Rec	0.09	0.25	0.46	0.95	0.73	2.16	1.24	2.42	4.95	14.28	72.46
C Rec	0.09	0.34	0.79	1.75	2.48	4.64	5.88	8.30	13.25	27.54	100.00
C Yld	100.00	99.91	99.66	99.21	98.25	97.52	95.36	94.12	91.70	86.75	72.46
By weight											
KMg	0.09	0.98	2.73	4.13	1.53	2.98	2.26	3.99	3.85	3.63	3.44
Hem	0.42	7.51	17.02	25.83	38.72	46.54	58.58	66.16	77.23	87.10	95.58
HHm	0.00	0.01	0.10	0.14	0.18	0.36	0.06	0.22	0.07	0.33	0.05
VG	81.11	81.20	75.15	60.49	52.25	44.17	32.66	26.56	15.70	7.20	0.65
OG	6.93	8.54	3.41	5.63	2.74	2.41	2.28	2.25	1.37	0.70	0.08
Kln	1.83	0.50	0.29	0.85	1.36	0.46	1.21	0.36	0.41	0.47	0.18
Qtz	9.60	1.25	1.29	2.92	3.21	3.07	2.94	0.46	1.36	0.56	0.02
Por	0.01	0.01	0.01	0.01	0.01	0.01	0.01	0.01	0.01	0.01	0.00
By volume											
KMg	0.06	0.59	1.74	2.53	0.97	2.02	1.44	2.67	2.67	2.67	2.83
Hem	0.27	4.82	11.57	16.79	26.06	33.51	39.73	47.07	56.96	67.90	83.41
HHm	0.00	0.00	0.07	0.09	0.12	0.27	0.04	0.16	0.05	0.26	0.04
VG	62.17	62.48	61.28	47.17	42.20	38.16	26.59	22.67	13.90	6.74	0.68
OG	5.91	7.30	3.09	4.88	2.46	2.31	2.07	2.14	1.35	0.72	0.09
Kln	2.16	0.59	0.37	1.01	1.70	0.61	1.51	0.48	0.55	0.68	0.30
Qtz	11.11	1.46	1.59	3.44	3.92	4.00	3.61	0.59	1.82	0.79	0.03
Por	18.33	22.76	20.30	24.10	22.58	19.12	25.01	24.22	22.69	20.24	12.62
N	330	59	47	52	32	57	33	67	93	221	999
N%	16.58	2.96	2.36	2.61	1.61	2.86	1.66	3.37	4.67	11.11	50.20

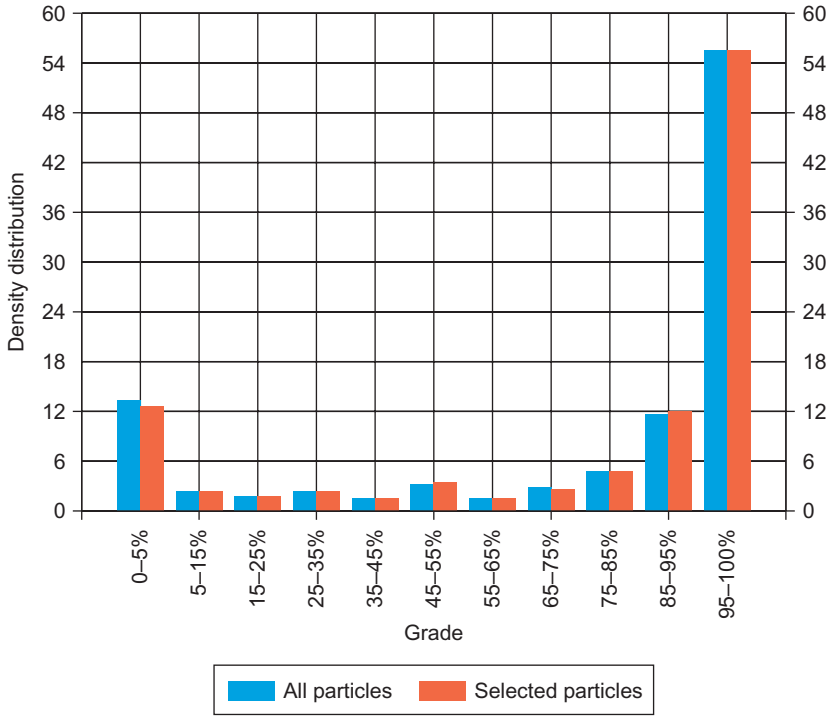

Figure 4.34 Liberation of kenomagnetite, hematite, and hydrohematite (set A) from vitreous goethite, ochreous goethite, kaolinite, and quartz (set B) for all particles and selected groups of particles (area greater than 2500 μm^2) for BM1 sample.

kenomagnetite, hydrohematite, ochreous goethite, and kaolinite, whereas almost 26% of hematite is liberated (25.96%), almost 74% of ochreous goethite is associated with vitreous goethite (73.98%), and more than 85% of kenomagnetite is associated with hematite. Such tendencies can be confirmed in Figure 4.33 even though only a small portion of the sample is shown there.

The unique capability of Mineral4/Recognition4 software (Donskoi et al., 2007, 2008a,b, 2009) that is also very important for downstream processing performance prediction is the capability to automatically classify particles to different textural classes. Particles within the same class have similar mineralogy, porosity, and density and so are expected to behave similarly during the same processing. This means that understanding of the behavior of certain textural particle classes during specific processing steps and knowledge of the abundance of each textural class in the sample will give the power to predict the behavior of such a sample in the process.

The information corresponding to the textural classification of BM1 sample (particle area greater than 2500 μm^2) is given in Tables 4.4 and 4.5. Only the seven largest textural classes are given (altogether 20 textural classes have been identified in this sample). Table 4.4 gives the major characteristics of analyzed particles such as the

Table 4.3 Mineral association analysis for BM1 sample (particles selected with selection criterion "Total Area > 2500 μm²")

	KMg	Hem	HHm	VG	OG	Kln	Qtz
Kenomagnetite	0.00	31.02	19.32	3.72	1.08	0.82	0.40
Hematite	85.68	25.96	50.04	41.18	18.15	34.74	19.93
Hydrohematite	0.27	0.10	0.00	0.11	0.03	0.18	0.00
Vitreous goethite	12.51	32.87	24.42	5.88	73.98	16.38	17.26
Ochreous goethite	0.90	2.03	0.76	43.88	0.00	5.32	2.97
Kaolinite	0.29	6.16	5.47	3.15	3.38	0.00	46.40
Quartz	0.35	1.86	0.00	2.08	3.38	42.57	13.04

Table 4.4 **Major classes in textural classification of BM1 sample—general parameters**

Mineralogy	Texture/ hardness	No. of part	Frequency (%)	Area (%)	Weight (%)	Mean Fe total	Mean SG	Mean mineral area	Mean shape factor	Mean elongation
Dense hematite	Very hard	604	30.35	30.52	36.1	68.44	4.46	6163.6	2.53	1.69
Microplaty hematite/ martite	Medium	438	22.01	22.12	22.4	67.95	3.82	6160.1	2.99	1.78
Goethite-martite	Hard	125	6.28	6.33	6.05	62.87	3.6	6178.2	3.07	1.77
Vitreous goethite	Dense	153	7.69	6.54	6.31	59.7	3.64	5212.3	2.45	1.75
Martite-goethite	Medium	177	8.89	9.19	8.99	66.44	3.69	6330.9	3.24	1.71
Martite-goethite	Soft	77	3.87	3.85	2.86	65.24	2.79	6107.5	3.25	1.54
Vitreous–ochreous goethite	Soft	168	8.44	7.89	6.13	58.67	2.93	5727.7	2.89	1.72

Table 4.5 **Major classes in textural classification of BM1 sample—mineral composition**

Mineralogy	Texture/ hardness	KMg (area)	Hem (area)	HHm (area)	VG (area)	OG (area)	Kln (area)	Qtz (area)	Pores (%) (area)	Total (%) (area)
Dense hematite	Very hard	3.49	88.35	0.042	0.65	0.08	0.26	0	7.13	100
Microplaty hematite/ martite	Medium	1.69	75.93	0.042	1.35	0.19	0.63	0.37	19.81	100
Goethite-martite	Hard	2.01	26.81	0.22	52.8	1.93	0.57	0.19	15.48	100
Vitreous goethite	Dense	0.18	0.84	0.002	86.94	2.61	0.32	0.22	8.89	100
Martite-goethite	Medium	2.41	58.81	0.11	16.88	1.14	0.34	0.43	19.88	100
Martite–goethite	Soft	2.9	38.95	0.025	15.45	3.65	0.51	0.31	38.21	100
Vitreous–ochreous goethite	Soft	0.13	0.94	0	64.66	7.36	0.56	0.33	26.02	100

total number of particles in the textural class; calculated percentage of these particles by number, area, and weight; calculated average total iron; calculated average density; average area; calculated average shape factor; and calculated average elongation. Recognition4 also gives coefficients of variation for the average numbers, not included here. Table 4.5 provides mineral composition of every texture class, in this example by area, but output by weight is also possible.

It can be seen that the largest textural class in this sample was "dense hematite—very hard" (604 particles out of 1990, 36.1% by weight; see Table 4.4). A significant number of these low-porosity hematitic particles can be seen in Figure 4.33. Some of these particles also include magnetite and that is why mean total iron content for these particles is very high (68.44%). Average percentage of hematite by area in this textural class is 88.4%, with 3.5% of kenomagnetite and a low 7.1% porosity. This explains why this textural class has very high hardness. For comparison, "soft" textures such as "martite-goethite—soft" and "vitreous-ochreous goethite—soft" have average porosity determined by OIA at 38.2% and 26.0% correspondingly.

The second largest textural class is "microplaty hematite/martite—medium" (438 particles out of 1990, 22.4% by weight; see Table 4.4). In comparison with "dense hematite—very hard," this class has less kenomagnetite (1.69%), less hematite (75.93%), more goethite (1.54%), and significantly more porosity (19.8%).

The example shows that extended information about every textural class, such as that given in Tables 4.4 and 4.5, allows better understanding of the whole sample and the use of this information in modeling of "virtual feed" (Donskoi et al., 2008a) for downstream processing prediction.

The statistical processing and output for the BM1 sample shown in this section are only a small part of the whole sample characterization that can be performed in powerful image analysis packages such Mineral4/Recognition4. Description of the extended output can be found in publications by Donskoi et al. (2007a, 2010, 2013a).

Figure 4.35 shows another sample (RM1) that is a typical Marra Mamba fine ore. This ore type may have (depending on deposit) a significant amount of hydrohematite (dark blue in color mineral maps). Particles containing hydrohematite are highlighted by white ellipses in Figure 4.35a and c. Particle 2 in Figure 4.35a has an outer layer of ochreous goethite, underneath that a layer of vitreous goethite and then a layer of hydrohematite. That corresponds to the direction in which oxidation/hydration developed. Particle 1 also shows that certain areas of hydrohematite are associated with large pores.

The whole RM1 sample had 3979 particles. After removing sections less than 10,000 μm^2 in area, 2460 were left. Mineral compositions for the selected particles obtained from OIA and from XRD are shown in Table 4.6. Here, the difference between XRD and OIA is much more prominent compared to the BM1 sample. Several reasons can be suggested: The normalization of XRD results for crystalline material to 100%, densities used for the calculation of mineral abundances that may require correction, and the presence of structures with very small embedded crystals not identifiable by image analysis (e.g., very often, kaolinite contains submicron crystals of ochreous goethite and vice versa).

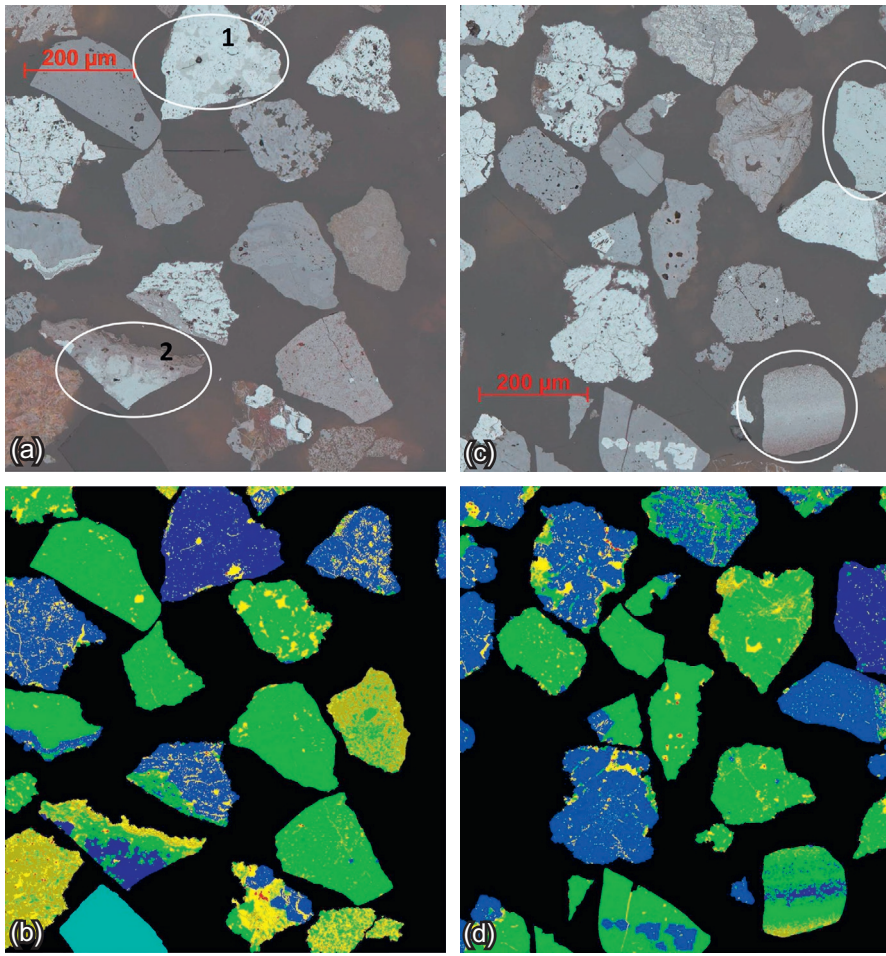

Figure 4.35 Images and their mineral maps for RM1 sample (see Figure 4.33 for color coding).

Another application of OIA is to characterize iron ore sinter. To study the behavior of ore fines during sintering or to study the reaction of certain fine ore blends with certain textural types of nucleus particles, compacted cylindrical tablets may be prepared (Ware et al., 2013; Clout and Manuel, 2003; Dehghan-Manshadi et al., 2014). These tablets are fired in a laboratory tube furnace using particular heating profiles and atmosphere depending on the study. This technique is often called "compact sintering," and it allows the study of reaction rates, degree of assimilation, sinter matrix structure, mineralogy, etc., without expensive pot grate sintering. The fired tablets can even be tumbled to measure tumble index as the percentage above 2.0 mm retained, which would characterize compact sinter strength.

One of the criteria in the estimation of sinter quality and the degree of reaction between melted sinter fines (matrix) and larger nuclei particles is the amount of hematite crystallized from the melt (secondary hematite) and hematite that has not reacted

Table 4.6 **Modal analysis for RM1 sample (selected particles with selection criterion "Total Area > 10,000 μm²")**

	Occurrence	Area	Volume (%)	Surface (%)	Density	Weight (%)	XRD (wt%)
Hematite	1954	22,122,665	39.53	38.61	4.8	49.24	52.8
Hydrohematite	1310	521,984.56	0.93	0.61	4.7	1.14	
Vitreous goethite	2375	23,694,581	42.34	46.84	4	43.95	44.4
Ochreous goethite	2317	2,721,146.7	4.86	6.08	3.6	4.54	
Kaolinite	1855	549,527.32	0.98	1.35	2.6	0.66	1.1
Quartz	44	379,445.75	0.68	0.66	2.65	0.47	1.6
Pores	2457	5,973,263.4	10.67	5.85	0	0	0

(primary hematite). Usually the amounts of these types of hematite are estimated by manual point counting. An experienced petrographer/mineralogist examines a set of points under the reflecting microscope and determines and records minerals in each position. Subjective decisions are made about the type of the hematite observed, based on morphology. Standard OIA cannot automatically distinguish between primary and secondary hematites because it is based on the reflectivity of identified phases, and as both types are essentially the same mineral, the reflectivity is also the same. However, textural identification performed by Mineral4/Recognition4 allows segmentation between these phases.

One grain of crushed compact sinter made from hematitic ore is shown in Figure 4.36. Dark blue areas on the mineral map correspond to secondary hematite, and light blue corresponds to primary hematite. It can be seen that primary hematite (large nucleus) is almost unreacted, while secondary hematite consists of small crystals strongly associated with SFCA and magnetite, which also crystallized from the melt.

A strong advantage of automated OIA of iron sinter in comparison with manual point counting is its robust identification of glass. Figure 4.37 shows a compact sinter

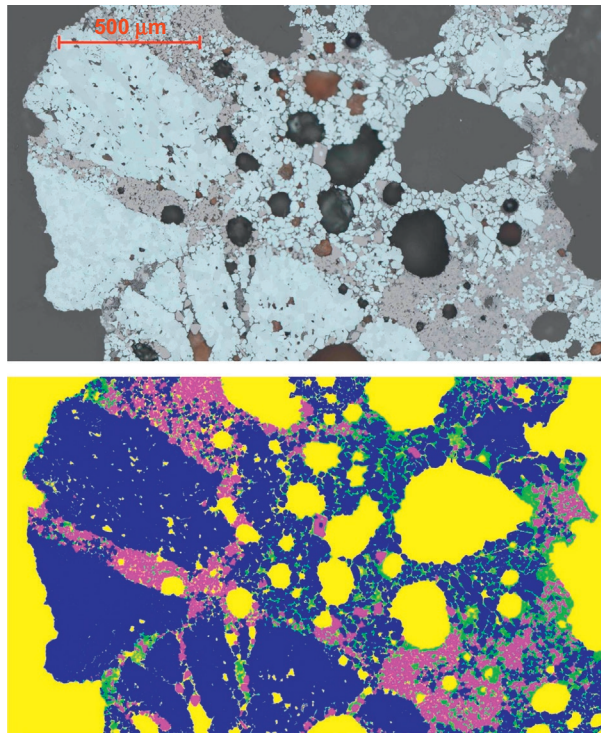

Figure 4.36 Photomicrograph and automatically created mineral map of compact sinter grain containing primary and secondary hematite (primary hematite, light blue; secondary hematite, dark blue; magnetite, magenta; SFCA, green; glass, cyan; porosity and epoxy, yellow).

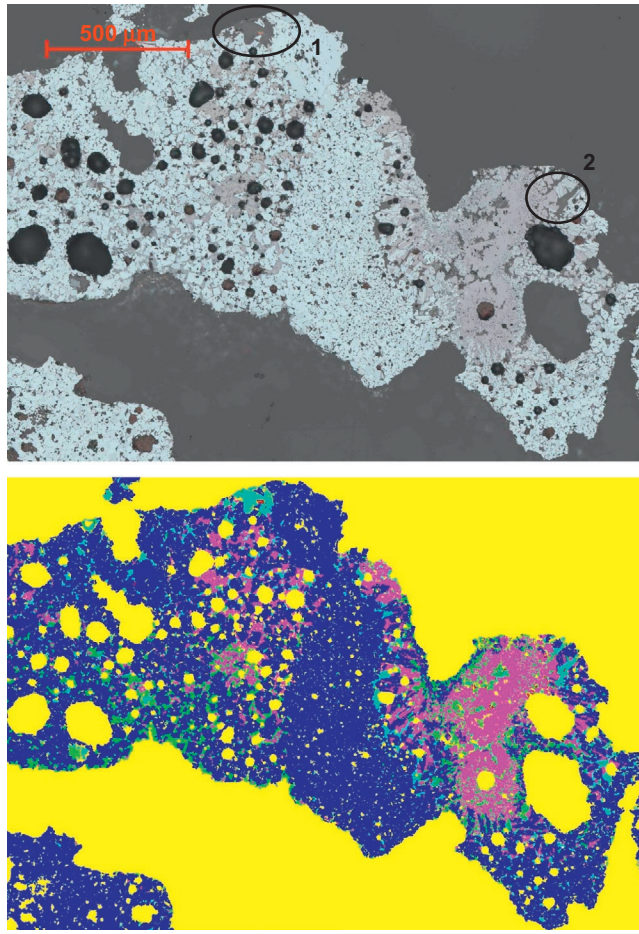

Figure 4.37 Photomicrograph and automatically created mineral map of compact sinter grain containing a significant amount of glass (for color coding, see Figure 4.36).

grain with a significant amount of glass (cyan). Figure 4.38 shows an enlarged part of this grain from the bottom right corner of Figure 4.37. When glass has a significant, clearly seen boundary with epoxy (e.g., area 1 of Figure 4.37), a mineralogist can easily distinguish these two phases. However, if the boundary between glass and epoxy is very small (area 2 of Figure 4.37) or glass occupies the entire pore (area 1 of Figure 4.38), it is almost impossible for the human eye to distinguish it from epoxy. On the other hand, OIA in modern systems can recognize more than 16,000 levels of reflectivity, so automated OIA segments glass from epoxy very reliably.

Another important factor in the underestimation of glass and other phases with small dimensions during manual point counting is caused by the fact that the visible border of such phases covers a statistically significant portion of the phase area. When the reticle (the crosswire used for point counting) happens to stop within or touching the border, the point will almost certainly be counted as the major phase because its presence

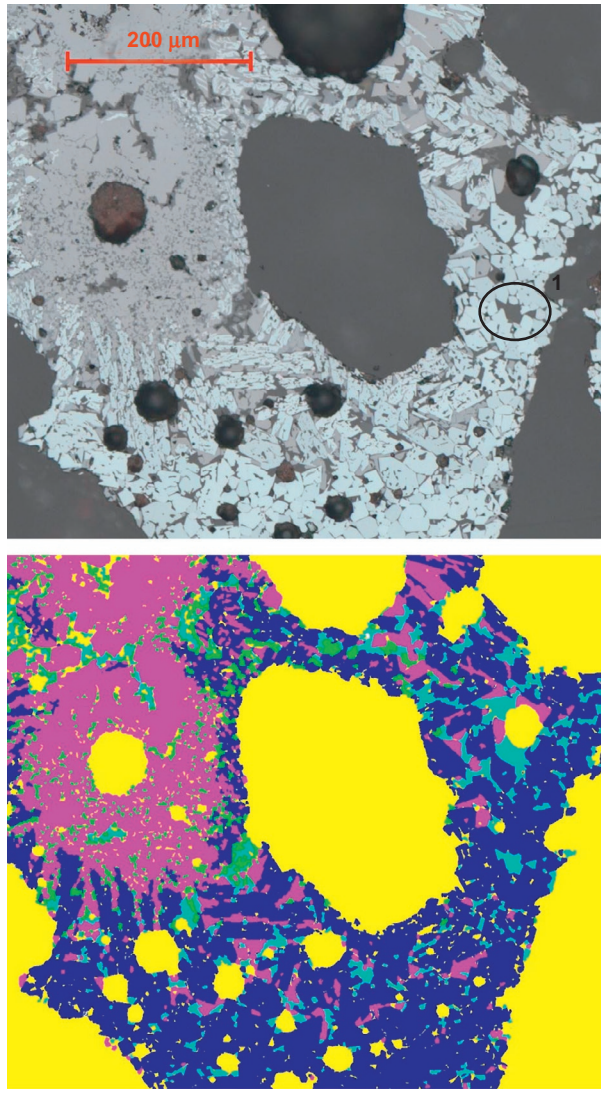

Figure 4.38 Enlarged bottom-right part of the grain shown in Figure 4.37 (for color coding, see Figure 4.36).

around the center of reticle is more prominent. It is therefore a systematic difference in results between manual point counting and automated OIA that OIA reports the amount of glass in sinter 20–40% more than manual point counting.

Apart from glass identification, which is difficult to confirm visually, the rest of automated mineral identification in this sinter fully corresponds to visual. Overall Mineral4/Recognition4 can give very comprehensive characterization of structures such as sinter and coke (Donskoi et al., 2013b). For porosity characterization, it includes porosity

abundance and size distribution, elongation, shape factor, equivalent circle diameter, convexity, concavity, and solidity for every pore as well as the average values. Similar information can be reported for each mineral. The characterization of solids also includes the calculation of average wall thickness and the presence of one mineral (or porosity) within another. The software also characterizes the connections between different phases, which includes the average abundance of connected walls, the average connected wall thickness, the average length of voids or another mineral in the boundary, and the smoothness of the boundaries.

It is important to notice that modern image analysis packages such as Mineral4/Recognition4 can import and process images in various formats and from different sources, so they are not limited to optical microscopy but can also take input from the scanning electron microscope, Raman microscopy, or any other imaging facility. This chapter, however, has focused on OIA of iron ores and sinters. It has been demonstrated that optical imaging and analysis of iron minerals is very reliable, fast, and cheap and can identify a wide spectrum of iron oxides and oxyhydroxides, thus making OIA a powerful tool in the characterization of iron ore mineralogy.

References

Ahsan, S.N., Mukherjee, T., Whiteman, J.A., 1983. Structure of fluxed sinter. Ironmak. Steelmak. 10, 54–64.

AxioVision [Computer software], 2006–2009. V 4.8.0.0, Carl Zeiss Imaging Solutions Gmbh.

Bonifazi, G., 1995. Digital multispectral techniques and automated image-analysis procedures for industrial ore modelling. Miner. Eng. 8 (7), 779–794.

Clout, J.M.F., 2003. Upgrading processes in BIF-derived iron ore deposits: implications for ore genesis and downstream mineral processing. Trans. Inst. Min. Metall., Sect. B Appl. Earth Sci. 112, 89–96.

Clout, J.M.F., Manuel, J.R., 2003. Fundamental investigations of differences in bonding mechanisms in iron ore sinter formed from magnetite concentrates and hematite ores. Powder Technol. 130 (1), 393–399.

Couprie, C., Grady, L., Najman, L., Talbot, H., 2009. Power watersheds: a new image segmentation framework extending graph cuts, random walker and optimal spanning forest. In: 2009 IEEE 12th International Conference on Computer Vision, pp. 731–773.

Criddle, A.J., Stanley, C.J., 1993. Quantitative Data File for Ore Minerals, third ed. Chapman and Hall, London.

Danti, K.J., Cross, K.C., Halsall, C., 1993. A high performance, low cost image analysis system for IBM compatible computers: practical applications in mineral processing and geology. In: Programme and Abstracts, International Congress on Applied Mineralogy '93, Mineralogy in the Service of Mankind, Fremantle, WA, pp. 47–49.

Dehghan-Manshadi, A., Manuel, J., Hapugoda, S., Ware, N., 2014. Sintering characteristics of titanium containing iron ores. ISIJ Int. 54 (10), 2189–2195.

Derivaux, S., Forestier, G., Wemmert, C., Lefvre, S., 2010. Supervised image segmentation using watershed transform, fuzzy classification and evolutionary computation. Pattern Recogn. Lett. 31 (15), 2364–2374.

Donskoi, E., Suthers, S.P., Campbell, J.J., Raynlyn, T., Clout, J.M.F., 2006. Prediction of hydrocyclone performance in iron ore beneficiation using texture classification. In: XXIII International Mineral Processing Congress, Istanbul 2006, pp. 1897–1902.

Donskoi, E., Manuel, J.R., Clout, J.M.F., Zhang, Y., 2007. Mathematical modeling and optimization of iron ore sinter properties. Isr. J. Chem. 47, 373–379.

Donskoi, E., Suthers, S.P., Campbell, J.J., Raynlyn, T., 2008a. Modelling and optimization of hydrocyclone for iron ore fines beneficiation—using optical image analysis and iron ore texture classification. Int. J. Miner. Process. 87, 106–119.

Donskoi, E., Holmes, R.J., Manuel, J.R., Campbell, J.J., Poliakov, A., Suthers, S.P., Raynlyn, T., 2008b. Utilization of iron ore texture information for prediction of downstream process performance. In: 9th International Congress for Applied Mineralogy, pp. 687–693.

Donskoi, E., Manuel, J.R., Lu, L., Holmes, R.J., Poliakov, A., Raynlyn, T., 2009. Advances in mathematical modelling of sintering performance of iron ore fines. In: Iron Ore 2009, Perth, WA, Australia, pp. 341–349.

Donskoi, E., Poliakov, A., Manuel, J.R., Raynlyn, T.D., 2010. Advances in optical image analysis and textural classification of iron ore fines. In: XXV International Mineral Processing Congress—IMPC2010, Brisbane, Australia, pp. 2823–2836.

Donskoi, E., Manuel, J., Austin, P., Poliakov, A., Peterson, M., Hapugoda, S., 2011. Comparative study of iron ore characterisation by optical image analysis and QEMSCAN(TM). In: Iron Ore 2011, Perth, WA, Australia, pp. 213–222.

Donskoi, E., Collings, A.F., Poliakov, A., Bruckard, W.J., 2012. Utilisation of ultrasonic treatment for upgrading of hematitic/goethitic iron ore fines. Int. J. Miner. Process. 114–117, 80–92.

Donskoi, E., Poliakov, A., Manuel, J., Peterson, M., Hapugoda, S., 2013a. Industrial strength optical image analysis system—Mineral4/Recognition4. In: Iron Ore 2013, August 12–14, 2013, Perth, WA, Australia, pp. 227–241.

Donskoi, E., Poliakov, A., Lu, L., 2013b. Advances in optical image analysis of coke structure. In: 10th Australian Coal Science Conference, November 18–19, 2013, Brisbane, pp. 17.

Donskoi, E., Manuel, J., Austin, P., Poliakov, A., Peterson, M., Hapugoda, S., 2014. Comparative study of iron ore characterisation using a scanning electron microscope and optical image analysis. Trans. Inst. Min. Metall., Sect. B Appl. Earth Sci. 122 (4), 217–229.

Faessel, M., Courtois, F., 2009. Touching grain kernels separation by gap-filling. Image Anal. Stereol. 28, 195–203.

Fandrich, R.G., Schneider, C.L., Gay, S.L., 1998. Two stereological correction methods: allocation method and kernel transformation method. Miner. Eng. 11 (8), 707–715.

Filho, I.M., Spina, T.V., Falcão, A.X., Vidal, A.C., 2013. Segmentation of sandstone thin section images with separation of touching grains using optimum path forest operators. Comput. Geosci. 57, 146–157.

Gomes, O.D.F.M., Paciornik, S., Iglesias, J.C.A., 2010. A simple methodology for identifying hematite grains under polarized reflected light microscopy. In: Proceedings of 17th International Conference on Systems, Signals and Image Processing—IWSSIP 2010. EdUFF, Rio de Janeiro, pp. 428–431.

Gomes, O.D.F.M., Iglesias, J.C.A., Paciornik, S., Vieira, M.B., 2013. Classification of hematite types in iron ores through circularly polarized light microscopy and image analysis. Miner. Eng. 52, 191–197.

Gonzalez, R.C., Woods, R.E., 2008. Digital Image Processing, third ed. Pearson Education, Inc., London, FL, 954p.

Gray, I.M., Millman, A.P., 1962. Reflection characteristics of ore minerals. Econ. Geol. 57, 325–349.

Higgins, M.D., 2010. Imaging birefringent minerals without extinction using circularly polarized light. Can. Mineral. 48, 231–235.

Hunt, J., Berry, R., Walters, S., 2010. Using mineral maps to rank potential processing behaviour. In: 25th International Mineral Processing Congress, 2010, Brisbane, pp. 2899–2905.

Iglesias, J.C.A., Gomes, O.D.M., Paciornik, S., 2011. Automatic recognition of hematite grains under polarized reflected light microscopy through image analysis. Miner. Eng. 24 (12), 1264–1270.

King, R.P., Schneider, C.L., 1998. Stereological correction of linear grade distributions for mineral liberation. Powder Technol. 98 (1), 21–37.

Lane, G.R., Martin, C., Pirard, E., 2008. Techniques and applications for predictive metallurgy and ore characterization using optical image analysis. Miner. Eng. 21, 568–577.

Launeau, P., Cruden, A.R., Bouchez, J.L., 1994. Mineral recognition in digital images of rocks: a new approach using multichannel classification. Can. Mineral. 32, 919–933.

Leigh, G.M., Lyman, G.J., Gay, S.L., 1997. Computer-based examination of self-contained, flexible stereological correction procedures. Powder Technol. 92 (2), 101–110.

Lin, D., Gomes, C.O., Finch, J.A., 1995. Comparison of stereological correction procedures for liberation measurements. Trans. Inst. Min. Metall. 104, C155–C161.

McAndrew, J., Clout, J.M.F., 1993. The nature of SFCA and its importance as a bonding phase in iron ore sinter. In: Proceedings of the 4th China–Australia Symposium on the Technology of Feed Preparation for Ironmaking, Dampier, pp. 1–15.

Moreira, A.C., Appoloni, C.R., Mantovani, I.F., Fernandes, J.S., Marques, L.C.b., Nagata, R., Fernandes, C.P., 2012. Effects of manual threshold setting on image analysis results of a sandstone sample structural characterization by X-ray microtomography. Appl. Radiat. Isot. 70 (6), 942–945.

Morris, R.C., 1980. A textural and mineralogical study of the relationship of iron ore to banded iron-formation in the Hamersley iron province of Western Australia. Econ. Geol. 75, 184–209.

Mumme, W.G., Clout, J.M.F., Gable, R.W., 1998. The crystal structure of SFCA-I, $Ca_{3.18}Fe^{3+}_{14.66}Al_{1.34}Fe^{2+}_{0.82}O_{28}$, a homologue of the aenigmatite structure type, and new crystal structure refinements of β-CFF, $Ca_{2.99}Fe^{3+}_{14.30}Fe^{2+}_{0.55}O_{25}$ and Mg-free SFCA, $Ca_{2.45}Fe^{3+}_{9.04}Al_{1.74}Fe^{2+}_{0.16}Si0.6O_{20}$. Neues Jahrb. Mineral. Abh. 173, 93–117.

Murdoch, J., 1916. Microscopical Determination of the Opaque Minerals. John Wiley & Sons, New York, 165p.

Neumann, R., Stanley, C.J., 2008. Specular reflectance data for quartz and some epoxy resins—implications for digital image analysis based on reflected light optical microscopy. In: 9th International Congress for Applied Mineralogy, Brisbane, pp. 703–705.

Otsu, N., 1979. Threshold selection method from gray-level histograms. IEEE Trans. Syst. Man Cybern. 9 (1), 62–66.

Phillips, W.R., 1971. Mineral Optics: Principles and Techniques. Freeman, San Francisco.

Pirard, E., 2004. Multispectral imaging of ore minerals in optical microscopy. Mineral. Mag. 68 (2), 323–333.

Poliakov, A., Donskoi, E., 2014. Automated relief-based discrimination of non-opaque minerals in optical image analysis. Miner. Eng. 55, 111–124.

Pownceby, M.I., Clout, J.M.F., 2000. Phase relations in the Fe-rich part of the system Fe_2O_3 (-Fe_3O_4)-CaO-SiO_2 at 1240-1300°C and $pO_2 = 5x10^{-3}$ atm: implications for iron ore sinter. Trans. Inst. Min. Metall. Sect. C 109, C36–C48.

Pownceby, M.I., Clout, J.M.F., 2003. Importance of fine ore chemical composition and high temperature phase relations: applications to iron ore sintering and pelletising. Trans. Inst. Min. Metall. Sect. C 112, C44–C51.

Qin, Y., Wang, W., Liu, W., Yuan, N., 2013. Extended-maxima transform watershed segmentation algorithm for touching corn kernels. Adv. Mech. Eng. 2013, Article number 268046.

Rath, B., Rao, G.V., Sharma, S.K., 2012. Mineralogy and liberation studies of sub grade iron ore from Bacheli, Bailadila sector, India. In: 26th International Mineral Processing Congress, IMPC 2012, pp. 4463–4471.

Russ, J.C., 1998. The Image Processing Handbook, third ed. CRC Press LLC in cooperation with IEEE Press, Boca Raton, FL, 771p.

Sasaki, M., Hida, Y., 1982. Considerations on the properties of sinter from the point of sintering reaction. Tetsu to Haganè 68, 563–571.

Seul, M., O'Gorman, L., Sammon, M.J., 2000. Practical Algorithms for Image Analysis: Description, Examples and Code. Cambridge University Press, USA, 295p.

Shatadal, P., Jayas, D.S., Bulley, N.R., 1995. Digital image analysis for software separation and classification of touching grains: I. Disconnect algorithm. Trans. Am. Soc. Agric. Eng. 38 (2), 635–643.

Sorby, H.C., 1858. On the microscopical structure of crystals indicating the origin of minerals and rocks. J. Geol. Soc. 14, 453–500.

Van Den Berg, E.H., Meesters, A.G.C.A., Kenter, J.A.M., Schlager, W., 2002. Automated separation of touching grains in digital images of thin sections. Comput. Geosci. 28 (2), 179–190.

Ware, N., Manuel, J., Raynlyn, T., Lu, L., 2013. Melting behaviour of hematite and goethite fine ores and its potential impact on sinter quality. In: Proceedings of AusIMM, Iron Ore 2013, 12–14 August, 2013, Perth, WA, Australia, pp. 485–486.

Quantitative analysis of iron ore using SEM-based technologies

5

I.Ž. Tonžetić
Indigo Research Laboratories, Johannesburg, South Africa

5.1 Introduction

Improved characterization of lower-grade iron ores is becoming more critical owing to the depletion of world high-grade iron ore reserves. The mineralogy and gangue minerals of the lower-grade iron ores are found to affect the quality of pretreated agglomerates of fine ore (sinters and pellets), which are making up a growing proportion of blast-furnace feedstock (currently ~70 % in East Asia).

The understanding of lower-grade iron ore mineralogy and the subsequent characterization of lower-grade iron ore are therefore becoming increasingly important to the efficient processing of the ores and the optimization of downstream smelting processes.

Using scanning electron microscope (SEM)-based technologies to characterize and quantitatively analyze iron ores and iron ore mineralogy dates back to the invention of the technology in the late 1950s to the early 1960s. The emphasis shifted from the chemical analysis of penalty elements on microprobe systems to quantitative mineralogy on automated mineralogical systems (auto-SEMs) only relatively recently (early 1990s). However, auto-SEMs consistently struggled to differentiate between the most common iron oxides present within iron ore, those being magnetite (Fe_3O_4) and hematite (Fe_2O_3), since auto-SEMs traditionally used energy-dispersive spectroscopic (EDS) technology for Fe quantification and furthermore ran at low X-ray counts. Assay reconciliation, by comparing the amount of Fe measured from chemical analyses against the calculated amount of Fe in a sample based on its mineralogy, was thus essential for these systems, in gaining some kind of grasp on the amount of hematite/magnetite in an ore body up until about 2008 and often required further X-ray diffraction (XRD) analysis for confirmation, which with the advent of Rietveld analysis has become more quantitative in recent years.

Improved beam, system, and vacuum stabilities and in some instances stretched brightness/contrast signals resulted in better, more consistent backscattered electron (BSE) imaging, which allowed for better magnetite/hematite discrimination. With the arrival of an appropriate level of hematite/magnetite distinction came the ability to use the input of theoretical densities to predict the performance of various mechanisms of density separation, mostly sink-float or washability analysis (B. Ntsoelengoe, 2011, personal communication). Also, with an appreciation of the different chemistries distinguishing acicular SFCAs from columnar/tabular SFCAs, the analysis of iron ore sinters in these systems was relooked at from about 2010 (Tonžetić and Dippenaar, 2011).

Iron Ore. http://dx.doi.org/10.1016/B978-1-78242-156-6.00005-8
© 2015 Elsevier Ltd. All rights reserved.

With this came the realization that auto-SEMs, in one form or another, could be used for mineralogical quantification through the project flow cycle, from exploration (where bulk ore mineralogy was most important), to mining (recently geometallurgical modeling), to processing (concentrator/mining products), to utilization (sinter and pellets; Table 5.1). Auto-SEMs even found application in the characterization of iron ore mine overburden, consisting mostly of pedocrete (Tonžetić, 2012). This proved vital since it had a direct bearing on the calculations of the amount of overburden occurring over the deposit, which in turn related directly to the cost of the overburden removal (usually calculated on mass/density and not volume). Of specific note was the occurrence of swelling clays (smectite) that had a direct bearing on the volume of overburden encountered, though XRD is still a better technique for clay mineral speciation since many clay minerals have similar chemistry but different lattice structures.

5.2 Principles of SEM-based technologies

5.2.1 Introduction to the principle of scanning electron microscopy

The scanning electron microscope (often abbreviated SEM) is the electron beam analog of a reflected light microscope. Quantum theory dictates that all matter/energy exhibits a dual nature, possessing both wave and particle (quantum) properties. It should then come as no surprise that electrons can be used in a very similar manner to light by creating an electron beam from an electron source (called an "electron gun") in a vacuum environment. The relationship of particles (in this instance, electrons) to waves can be expressed through the de Broglie wavelength equation:

$$\lambda = h / p$$

where λ is the wavelength, h is Planck's constant, and p is the momentum (mass × velocity) of the traveling body/quanta.

All this demonstrates that electrons can be refracted, reflected, absorbed, and transmitted just like light.

In addition, primary electrons (from the electron gun) can generate characteristic X-rays from electrons being displaced in the atomic orbitals of the sample being analyzed (conservation of energy principle), which can be detected with X-ray detectors and are characteristic of chemical elements present within the minerals being analyzed. The electrons that are "reflected" are called "backscattered electrons" (Figure 5.1). Generated secondary electrons (primarily a surface phenomenon) can also be used to generate images (but not for any kind of mineralogical quantification). Even though certain iron ore minerals may cathodoluminescence (give off light) in the presence of an electron beam, cathodoluminescence is not currently employed for iron ore mineral characterization. It may however provide a further means to separate distinct grains from the same minerals, which happen to be touching, in the future.

Table 5.1 The possible uses of auto-SEMs in a project lifecycle

Project flow	Exploration ⇒	Ore characterization/ geometallurgical modeling ⇒	Mining/concentrator products ⇒	Sinters/pellets ⇒
Auto-SEM use	Bulk mineralogy Microlithotyping Grain size analysis Textural analysis Fe deportment	Density separation Sink-float analysis/washability prediction (grade-recovery) Bulk mineralogy Bandwidth determination Clast size determination	Bulk Mineralogy Liberation Analysis Grain Size Analysis Fe Deportment “Locking” Analysis	SFCA[a] Differentiation Bulk Mineralogy

[a] Silicoferrite of calcium and aluminum, a product of sintering low-grade fine iron ore to create a feed for blast furnaces. For more information, see Tonžetić and Dippenaar (2011).

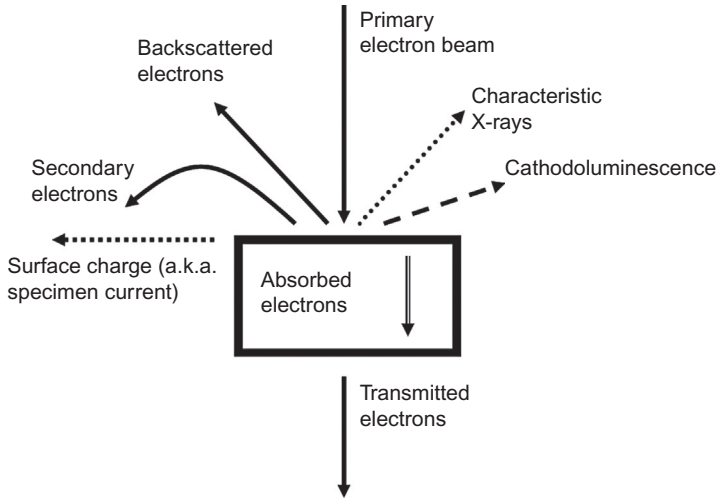

Figure 5.1 Diagram of electron beam–specimen interaction.

To summarize, the SEM uses essentially two characteristics of materials to identify minerals.

5.2.1.1 The average atomic number of a mineral or substance

This translates to its BSE grayscale value (in the range 0–255). Occasionally, it is heard in industry that this relates to the "density" of a mineral although this is not technically true, since magnetite appears brighter in SEMs than hematite, even though it is less dense. It does however have a slightly higher average atomic number (compare the ratio of Fe to O in the two minerals and one will readily see this to be the case—Fe having a higher atomic number than O). The confusion arises out of very dense substances typically appearing "white" in analyses or calibration procedures.

5.2.1.2 Characteristic X-ray spectra of minerals

It is the measurement of characteristic chemical X-ray spectra that makes any SEM (with attached X-ray detectors) essentially a chemical tool that uses stoichiometry (the measurement of characteristic chemical ratios in compounds and minerals—albeit approximately) to characterize minerals and materials.

5.2.2 Sample preparation principles

Conventional sample preparation techniques include the setting of samples in epoxy resin within (typically) 30 mm diameter mounts. The addition of graphite ensures particle separation. Depending on the sample holder and instrument type, 7–16 samples can be accommodated at any one time. Larger rock chips and even cores or slabs have been known to be measured in these systems; however, these are often related to on-site special core/rock/slab holder engineering capabilities. In the case of slabs and drill

core, since most iron ore is sedimentary in origin, great care must be taken to ensure that the area for cutting is in profile across bedding planes to maximize the discrimination of any textural features.

5.2.3 Various SEM-based technologies

5.2.3.1 Electron probe microanalysis

In the late 1940s, focused static electron beams or probes (with the aid of optical microscopes to aid in finding the points of interest) began to be used to excite characteristic X-ray spectra (Hillier, 1947). With the addition of highly specialized wavelength-dispersive spectrometers and after the introduction of raster beam scanning, these initial instruments evolved into the first electron probe microanalysis (EPMA) machines or the electron microprobes of today. The birth of these "microprobe" instruments would allow for the development of average atomic number, fluorescence, and adsorption correction factors (ZAF correction factors) that would also be in use for later EDS and would pave the way for the development of SEMs in analysis applications. These X-ray detectors specifically looked for the "wavelengths" or peaks of specific chemical elements with specific detectors looking for specific elements. They were used to determine the chemistry of analyzed points or "spots" and exercised a precision that still has not been matched by auto-SEM energy-dispersive X-ray detectors. In terms of terminology, the instrument is called an "electron microprobe," the X-ray detectors perform "wavelength-dispersive spectroscopy," and the whole analysis is termed "electron probe microanalysis." Duncumb (1999) gave a detailed and anecdotal review of the history of EPMA. Rao et al. (2009) presented an example of how microprobe data can be used to help characterize an iron ore.

5.2.3.2 Automated mineralogical (auto-SEM) technologies

All current auto-SEM technologies are automated image analysis systems based on SEMs as platform instruments with EDS detectors attached, the signals from which are integrated according to the specific instrument. Furthermore, these EDS detectors are usually run at low count totals to speed up analysis times and measurements. Historically (pre-2008), up to four light-element EDS X-ray detectors could be attached to any single system. However, since the analysis speeds have substantially increased (analysis times have decreased), these numbers of EDS detectors are no longer needed or used on most machines. All elements heavier than carbon can be identified confidently although stoichiometric oxygen determinations can still prove problematic, especially with low count spectra. For that reason, oxygen abundance is usually based on the calculation of oxide mass percentages based on the analysis of the relevant cations. Additionally, with the ubiquitous presence of carbon in both the mounting media and carbon coating (which helps to ensure conducting specimens, which in turn ensure consistent specimen currents and hence consistent BSE values—with calibration), carbon may seem more abundant than it actually is. All these instruments have the ability to simultaneously utilize both BSE brightness and energy-dispersive (EDS) X-ray spectra in the creation of digital mineral images. However, the rule sets

(SIP files in the case of QEMSCAN, standard files in the case of MLA, and recipes in the case of Mineralogic (R)) seldom account for both methods of mineral identification due to historical paradigms. All these instrument paradigms have much to do with the chamber/detector geometry and the traditional SEM setup of the developing companies. Off-line data mining (which includes the off-line replaying or reanalysis of datasets after mineral identification rules have been changed) and graph plotting are possible with all the systems.

Differences in the values of quantities between auto-SEMs and other technologies do occur, since the auto-SEM classification of minerals is based mostly on chemical composition while traditional classification through XRD is based on crystal structure. Also, whereas point-counting results (from light microscopes) are typically presented in terms of area percent and XRD results are typically presented in terms of weight percent, auto-SEM results are typically presented in terms of both area and weight percent (calculated based on input density values since auto-SEMs cannot measure density directly).

Since most auto-SEMs prefer flat surfaces for measurement (like light microscopes) to avoid X-ray shadowing and the proper application of ZAF correction factors in the EDS analysis, cognizance should be made of the fact that the morphological interpretations of sections have limited value as evidenced in Figure 5.2. Light microscopes suffer from the same limitation. Historically, this is what has limited SFCA characterization on auto-SEM systems (though the same argument/limitation should be used for light microscopes that have traditionally studied sinters).

5.2.3.3 Auto-SEMs with specific regard to iron ore analysis

For all SEM-based systems, potential difficulties in analysis occur when phases of similar chemistry have similar average atomic numbers (i.e., similar BSE intensities) making distinctions difficult. While albite and quartz have similar average atomic numbers, they are readily distinguishable due to their unique chemistries. Conversely, while pyrite and pyrrhotite have similar chemistries, they are distinguishable due to their unique

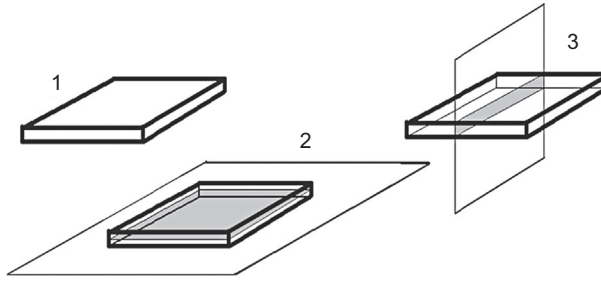

Figure 5.2 Morphological classification dependence on sectioning. (1) Original unsectioned crystal. (2) Planar sectioning of crystal. The gray area illustrates a tabular interpretation of sectioning. (3) Cross-sectioning of crystal. The gray area illustrates an acicular interpretation of sectioning. Note how the same crystal can be classified differently according to its morphology as determined by the obliquity of its sectioning.

average atomic numbers. Problem minerals therefore encountered in analysis may include hematite and magnetite since they share similar chemistries and similar average atomic numbers. Goethite may also be problematic in identification, though it usually contains sufficient impurities to help differentiate it from hematite, in auto-SEM systems. It is therefore important to note that auto-SEM distinctions between magnetite and hematite are dependent on a number of factors, specifically the surface characteristics of the iron oxides being measured (scratching, plucking, dipping beneath mounting media, porosity, carbon coating thickness, etc.) and the degree of ionic substitution being encountered in the iron oxides (in particular Mg, Ca, Al, and Mn).

Iron oxide discrimination on auto-SEM systems can furthermore be influenced by BSE stabilizers (also known as BSE amplifiers) on certain systems, gun alignment (essentially whether the electron beam is coming down the column unhindered with no shadowing of the beam), and magnification field sizes. Furthermore, stage height (working distance) focus primarily determines grayscale, while beam focus has an effect on BSE grayscale averaging (and the image focus itself). Appropriate third point BSE calibration standards and increased beam dwell times (i.e., giving the electron beam more time on a specific point to make an identification) improve discrimination. Image analysis and processing can do away with certain artifacts of analysis. Auto-SEM instruments make use of their own paradigms to reduce or eliminate some of the abovementioned problems, though no single instrument eliminates all of them.

Figure 5.3 presents images of an electron microprobe hematite standard measured in a QEMSCAN system with different measurement parameters. The following sections look more closely at the instrument types and varieties. Table 5.2 highlights their differences.

5.2.3.4 QEMSCAN

QEMSCANs were previously produced by Intellection on Carl Zeiss EVO platforms (Pirrie et al., 2004; Gottlieb et al., 2000; Sutherland and Gottlieb, 1991). Currently, QEMSCANs use FEI Quanta and field emission gun (FEG) platforms for their operation. QEMSCAN instrumentation uses computer grayscale BSE imaging in conjunction with a custom-designed X-ray spectral window database to identify phases of interest. The QEMSCAN technique tends to produce X-ray maps, whereby EDS X-ray spectra are collected at predefined beam-stepping intervals, at lower magnifications/higher field sizes (because of historically poor imaging). Because of its emphasis on X-ray collection, it is a preferred method for characterizing solid solutions (where BSE grayscale is not amenable to species differentiation), finely intergrown, chemically complex textures, and silicates, since EDS analyses are taken every couple of microns (typically between 1 and 20 μm). In recent years, QEMSCAN has focused on collecting X-ray elemental concentration data (rather than data on X-ray spectral windows) although QEMSCAN systems still favor superior X-ray collection.

5.2.3.5 MLA

Previously manufactured by JKTech (the technology transfer company for the Sustainable Minerals Institute housed in the Julius Kruttschnitt Mineral Research Centre of the University of Queensland, Australia) on FEI Quanta platforms, MLAs

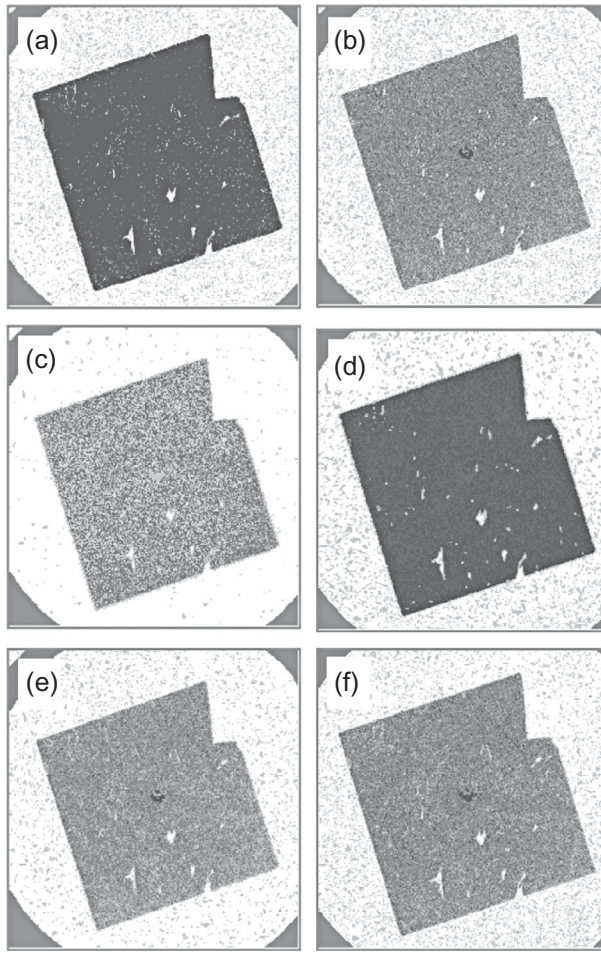

Figure 5.3 Hematite standard measured in a QEMSCAN system with different measurement parameters. Light gray = interpreted goethite; dark gray = interpreted magnetite; medium gray = interpreted hematite. (a) Inappropriate third point calibration; (b) appropriate third point calibration; (c) stage (−1 mm); (d) stage (+1 mm); (e) focus (−1 mm); (f) focus (+1 mm).

are now manufactured wholesale by FEI (Figueroa et al., 2011). MLA instrumentation uses a best-fit model to compare collected EDS X-ray spectra with a spectral library. The MLA technique tends to produce X-ray centroid measurements, whereby single EDS X-ray spectra are collected for common BSE grayscale levels, at higher magnifications/lower field sizes and is thus a preferred technique for small grain sizes and high-resolution imaging. The MLA favors superior imaging over EDS collection. In recent years, MLA data have been made compatible with QEMSCAN iDiscover/iExplorer software, since it is more versatile for data interrogation and processing. A novel feature of the MLA system is the ability to produce initial spectral collection surveys where type spectra are collected for common BSE grayscales. The approach

Table 5.2 Basic auto-SEM comparison among different platforms

	QEMSCAN	MLA	Mineralogic	TIMA
Historic SEM platform	Oxford LEOs/ Carl Zeiss EVOs	FEI Quanta	N/A	N/A
Current SEM platform	FEI Quanta/ FEG	FEI Quanta/ FEG	Carl Zeiss EVO	TESCAN MIRA FEG/VEGA
EDX detection	Oxford/Bruker SDD	Bruker SDD	Bruker/Oxford SDD	PulseTor SDD
Number of detectors (historical)	4	1	N/A	N/A
Number of detectors (current)	Up to 4	Up to 4	Up to 4	Up to 4
Traditional mode of measurement	X-ray mapping	X-ray centroiding	N/A	N/A
Current mode of measurement	X-ray mapping/X-ray centroiding	X-ray centroiding/ X-ray mapping	X-ray centroiding/ X-ray mapping	X-ray mapping
Mineral ID	Species identification protocol	Standard file matching	Mineral recipe identification	Mineral classification rules/profiles
Accommodation of 30mm sample blocks	9–16	14	9–16 (Customizable)	7 (Customizable)
Consistent specimen current for BSE calibration	Yes	No (range very narrow)	No	?
Spectral matching	First match	Best fit	Priority/first match (best fit if priorities are equal)	?
Iron oxide distinction	Arbitrary yet consistent BSE cutoff	BSE histogram peak separation	Correlative microscopy	?
Typical X-ray count rates	1000	1000	>3000 (Variable)	?

of the MLA system typically means that most systems use single-spectral libraries and are also more beginner/user friendly than QEMSCANs.

5.2.3.6 Mineralogic (R)

The Mineralogic (R) (and TIMA, discussed below) auto-SEMs are the newest automated mineral analyzers on the market. The Mineralogic (R) system is manufactured by Carl Zeiss and favors image processing and image analysis that occurs during the automeasurement to discriminate between the sample and mounting media (Hill, 2014). Unlike the QEMSCAN and MLA systems, analysis times are requested and not analysis counts. The analysis involves a parallel two-stream approach where image processing/image analysis forms one stream (and is in the control of the operator unlike traditional auto-SEM technologies) and energy-dispersive X-ray analysis forms a second stream (similar to more traditional technologies). The X-ray analysis and image analysis can then be recombined to form a higher-order classification. This may allow for mineral variety classifications in the future whereby, for instance, a hematite spectral assignation occurring in a mineral grain of a specific shape might be called specularite, theoretically. The Mineralogic (R) system also allows for a degree of correlative microscopy whereby it is possible to "georeference" or correlate images from different technologies (light microscopy, cathodoluminescence, secondary electron images, etc.) with those seen in the auto-SEM to facilitate mineral identification (especially magnetite/hematite distinction).

5.2.3.7 TESCAN integrated mineral analyzer

TESCAN integrated mineral analyzer (TIMA) is currently manufactured by TESCAN (Kralova, 2013). Unlike traditional technologies, the TIMA has opted for PulseTor SDDs. The relationship between TESCAN and PulseTor has allowed for an unprecedented degree of integration between the systems making X-ray/SEM communication more seamless than traditional technologies. This in practice means fewer communication "bugs" and failures ("crashes") compromising automated runs.

5.3 Application of automated SEM-based technologies to ore characterization

After an ore is measured but before it can be interrogated, most auto-SEMs typically employ a step that entails rudimentary image processing. For the QEMSCAN and MLA, this occurs after measurement and before reporting. For the Mineralogic (R) system, however, this occurs during measurement but typically only after it has been instructed to do so with an appropriate recipe.

The image processing, in all cases, entails one, more, or some of the following steps:

- Touching particle processing (getting rid of or splitting touching particles).
- Erroneous pixel processing (getting rid of slimes, unwanted artifacts, and dust contamination; in short, getting rid of any undesirables).

- Mixed spectral resolution often referred to as "boundary phase processing" (getting rid of or reclassifying mixed spectra occurring at boundaries between mineral grains of different composition).
- Granulating (through erosion/dilation algorithms; typically used to extract grains of economic interest for further processing).
- Field stitching (used for large particulates/slabs/cores that take up more than a single field of view during measurement).

5.3.1 Textural analysis

The state of the art for the latest auto-SEM technologies, in terms of textural analysis, is mostly visual, although iDiscover (QEMSCAN software) does allow for categorizing particles or grains on *x*- and *y*-axes creating what are termed image grids. The properties that can be used to create those categories (things like shape factor) are, however, somewhat limited. The MLA and Mineralogic (R) systems have far more categories for interrogating shape. However, they lack the flexibility of being able to create image grids. Textural images of conglomerate, measured with a QEMSCAN system, are presented in Figure 5.6.

5.3.2 Mineral abundance

Table 5.3 presents a typical example of how mineral abundance is presented in auto-SEM analyses. Usually these data are presented in terms of mass percent. All auto-SEM systems allow for first-order mineral identification (the SIP files, standard files, and mineral identification recipes mentioned above) and first-order groupings where mineral densities (and other mineral qualities) are assigned and second-order groupings are simplified to make data interpretation easier and more relevant. So, in terms of work flow, a QEMSCAN system may identify a "zircon" and a "metamict zircon" from its SIP files, group these together in a primary mineral list (first-order grouping), and further group these along with other minerals in an "others" grouping (secondary mineral list) if there is not enough zircon to warrant specifying it in a mineral abundance table.

5.3.3 Magnetite/hematite distinction

The analysis of iron oxides in automated mineralogy is primarily based on grayscale values that are directly proportional to an average atomic number. It can thus occur that, with atomic substitution (for instance, Mg or Ca for Fe), the average atomic number of magnetite can be lowered, resulting in a lower grayscale value, with a resultant overestimation of hematite and an underestimation of magnetite. A pure hematite or magnetite standard can be used as a third point calibration for both the QEMSCAN and MLA systems although QEMSCAN typically uses copper as a third standard while MLA uses chalcopyrite (Figueroa et al., 2011). Using a synthetically or artificially pure standard might not negate these misidentifications always, since in naturally occurring hematite, Fe can be substituted with Al, for instance, and in naturally occurring

Table 5.3 **A typical example of the bulk mineral abundance for conglomeratic iron ores**

Id	Hematite	Quartz	Feldspar	Mica	Chlorite/ clay	Phosphates	Pyrite	Others	Total
C1	40.9	57.0	0.0	0.2	1.1	0.4	0.0	0.3	100.0
C2	55.8	0.0	0.0	40.8	2.1	0.3	0.0	0.9	100.0
C3	74.1	20.2	0.1	1.5	2.3	1.4	0.0	0.4	100.0
C4	97.0	0.0	0.0	1.0	1.5	0.2	0.0	0.4	100.0
C5	33.0	0.0	0.0	0.2	63.2	0.1	0.0	3.4	100.0
C6	94.0	0.0	0.0	0.0	5.4	0.1	0.0	0.5	100.0
C7	78.5	0.0	0.0	15.9	1.5	0.3	0.0	3.8	100.0
C8	60.2	14.8	0.0	1.7	22.5	0.3	0.0	0.4	100.0

magnetite, Fe can be substituted with Ca and Mg. Using a properly characterized standard from a specific ore deposit may correct for this, bearing in mind that grayscales can still be affected by mineral–mineral or mineral–background edge effects, particle relief (minimized with appropriate polishing techniques), and porosity.

5.3.4 Lithotyping/microlithotyping

The use of filters or categorizers and especially the creation of image grids (based on whether particles are intuitively of a certain type) in iDiscover software allow for the creation of rules that can separate particles into lithotypes, or rather "microlithotypes." Mineralogic (R) also allows for the very basic creation of expressions, usually the addition of the quantity of two different minerals in an analysis, which are used to classify particles during the measurement into defined microlithotypes. Since there is no consistency between how QEMSCAN, MLA, and Mineralogic (R) (or any other of the auto-SEMs) create these expressions, none of them can be moderated into standard types that would correspond with geologic definitions of lithotypes. The software of the various auto-SEMs also allows for very basic plotting of properties on ternary diagrams, with the three axes being limited to the particle properties that can be extracted from the relevant software suites.

5.3.5 Grain size

Since beam-stepping intervals (in the case of X-ray mapping) or pixel sizes (in the case of X-ray centroiding) are always known and since this information can be counted for contiguous classified pixels in mineral grains, grain size can be readily calculated for mineral grains. Most particle/grain sizes are usually recalculated and reported as equivalent circular diameter (ECD) values though this not necessarily always correct or meaningful especially in the case of hematite bands in a banded iron formation (BIF). An extracted hematite band converted to an ECD is meaningless. What must also always be remembered is that the grain size calculated is very much dependent on the magnification calibration of the individual instrument (and this is usually dependent on the skill of the instrument service engineer).

5.3.6 Liberation, locking, and association

Historically, mineral liberation has been used as a proxy for the "processability" of a particular mineral, since the many properties of minerals that could allow for concentration and processing could not be directly measured from auto-SEM instrumentation. Thus, the poor liberation of a mineral of interest in a tailings sample (and consequent high liberation of a concentrate) was indicative of a feed that was properly concentrated or processed. The high liberation of a tailings sample (and consequent poor liberation of a concentrate) would be indicative of poor processing. High liberation of a feed sample also suggested that it would be easily processed and poor liberation of a feed sample would suggest difficulties in further processing. However, liberation has been characterized differently by different mineralogists, companies,

authors, etc., since different processing mechanisms are amenable to different mineral properties and ore textures. Thus, a gravity or density separation procedure would necessitate liberation characterization based on the area percent of a mineral of interest in a particle, whereas a leaching concentration procedure would necessitate liberation characterization based on the free surface area percent (exposure on a particle surface) of a mineral of interest in a particle. This latter, free surface area percent liberation is called, by some authors, "locking" although the term "locking" is also applied to minerals of interest sorted according to their association in an image grid with other minerals, once all liberated mineral grains have been removed from an analysis. Here, association is typically represented as the occurrence of "binary" particles where if a particle constitutes more than 80% hematite and quartz, for instance, then it is classified as a hematite-quartz binary particle. These associations are subsequently quantified. To avoid confusion, the proper use of the term association, it is felt, should be restricted to the property of "adjacency," where two minerals are associated, if they are adjacent to one another. The number of occurrences of adjacency (as long as it is specified as left-right pixel occurrences, top-down pixel occurrences, or both) can be counted and converted into a percentage, and this would quantify an association between two minerals of interest.

Liberation is typically divided into categories based on 10% subdivisions of the area percent occurrence of a mineral of interest (for instance, hematite) within a particle. Thus, particles are separated into 0–10%, 10–20%, 20–30%, etc., categories and plotted on 3D charts with size fractions, liberation categories, and their weighting (mass percent) being plotted on three axes, based firstly on "unnormalized discrete" values (values that add up to the absolute amount of hematite in the total sample) to "normalized head (absolute)" values (hematite is normalized to 100% for the total sample) to "normalized fraction (relative)" values (hematite is normalized to 100% per size fraction). These normalizations allow for the cumulative plotting of liberation values on common graphs and allow for the direct comparison of liberation between different samples, size fractions, etc. These liberation categories are usually further simplified by grouping them in 20% categories. Thus, particles in the 0–20% class are usually called "locked," 20–40% are "lower-grade middlings," 40–60% are "medium-grade middlings," 60–80% are "high-grade middlings," and 80–100% are "liberated." Some workers suggest also using "0%" (gangue) and "100%" (fully liberated) categories though since we are dealing with the 2D analysis of surfaces in auto-SEMs, these categories are strictly speaking invalid since we cannot make assumptions about the occurrence of hematite below (and eroded "above") the surface that has been analyzed.

As can be seen, the liberation characterization of minerals of interest in auto-SEM systems is hardly trivial. Though with the direct input of mineral characteristics (such as electrostatic affinity, "floatability," and magnetic susceptibility) into auto-SEM analytical programs and the understanding of particle characteristics (area percent liberation vs. surface area percent liberation) that make minerals amenable to processing, the reliance on liberation (as is currently conventionally used) may be reduced in the future, with more of a direct reliance on the "calculated processability" of an ore.

5.4 Characterization of natural and sintered iron ore using QEMSCAN

The following applications of automated mineralogy in iron ore are based in large part on the papers of Tonžetić and Dippenaar (2011) and Tonžetić et al. (2012).

Tonžetić et al. (2012) used granulation on conglomeratic ores to extract hematite clasts from matrix to obtain clast size distributions (Figure 5.4). Image erosion (eroding particle and grain edges one pixel at a time for a specified number of iterations) was used to separate touching clasts and clasts from matrix in especially monomictic (clasts of a singular mineral composition) and clast-supported (sensu stricto orthoconglomerates) ores. Dilation was attempted to restore the clasts to their original size. Granulation was further applied to sections of BIFs to facilitate the measurement of band widths, as seen in Figures 5.5 and 5.6.

A clast size distribution (quantified according to mass % hematite) was constructed for these conglomeratic ores (Figure 5.7). This allowed for a certain degree of ideal grind size prediction to liberate hematite clasts from matrix (Tonžetić et al., 2012). Plotting these clast sizes cumulatively allowed for the relative ranking of conglomerates in terms of clast size (Figure 5.8).

Similarly, hematite microbandwidth distributions were constructed using granulation functions for BIFs, though there was no need for erosion functions to be used in the image processing, to separate bands adequately. It was assumed that the bedding bands were laterally continuous and thus that stereological corrections were not necessary for accurate size determinations. An example of a microbandwidth distribution is presented in Figure 5.9.

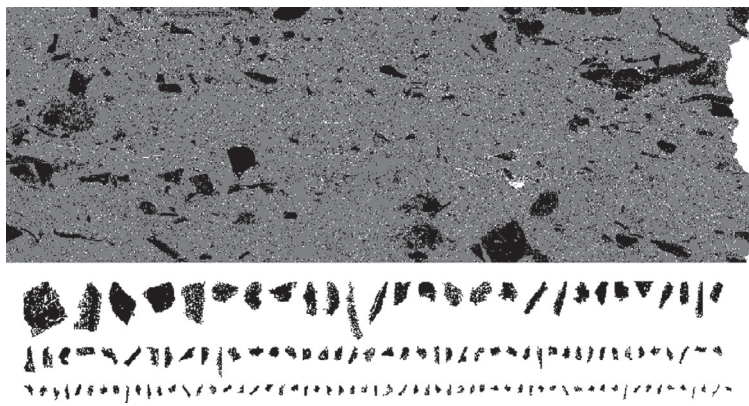

Figure 5.4 Image of originally measured slab and subsequent granulation of dark gray/black hematite clasts with erosion and dilation operations having subsequently been applied. White represents (vugular) macroporosity.

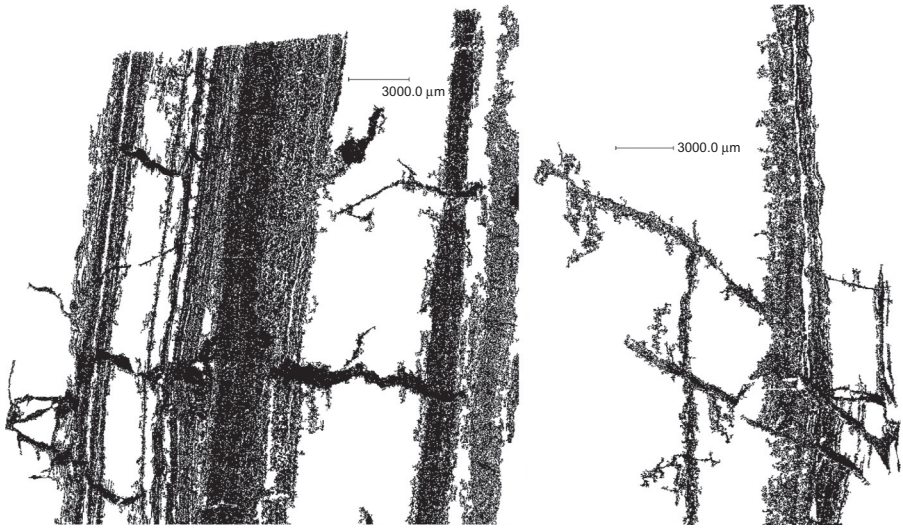

Figure 5.5 Hematite granulation applied to BIF samples. Note the interconnectivity across hematite bands, which suggest the fracturing and remobilization of hematite.

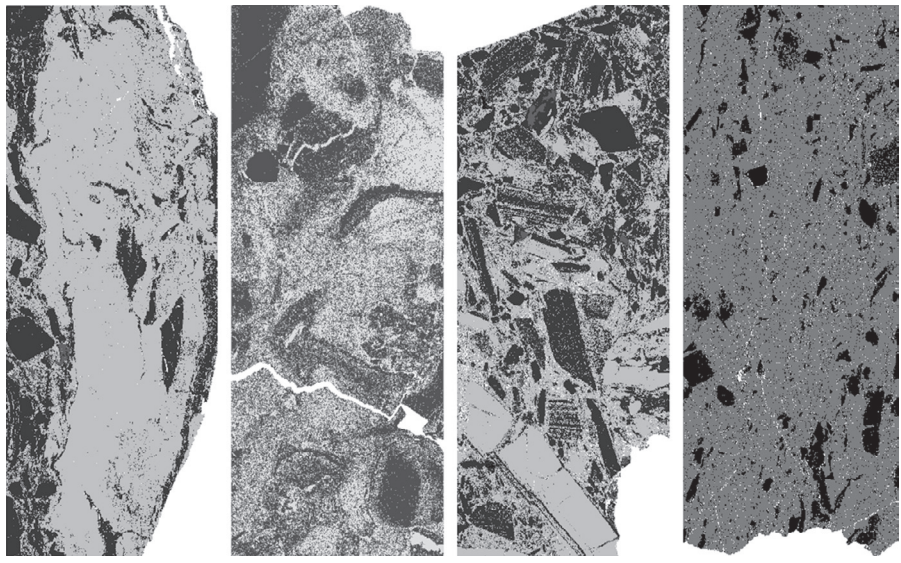

Figure 5.6 Example textures of conglomerates. Samples are approximately 9 cm × 4 cm.

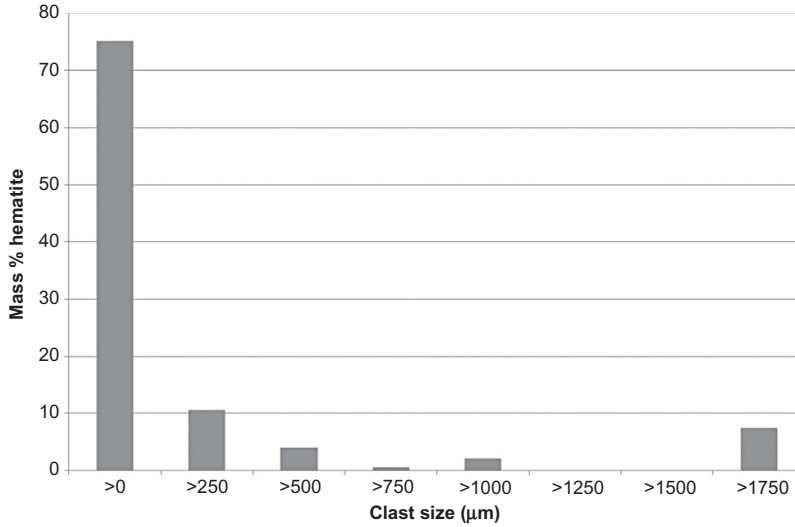

Figure 5.7 Example of a clast size distribution histogram for a conglomeratic ore.

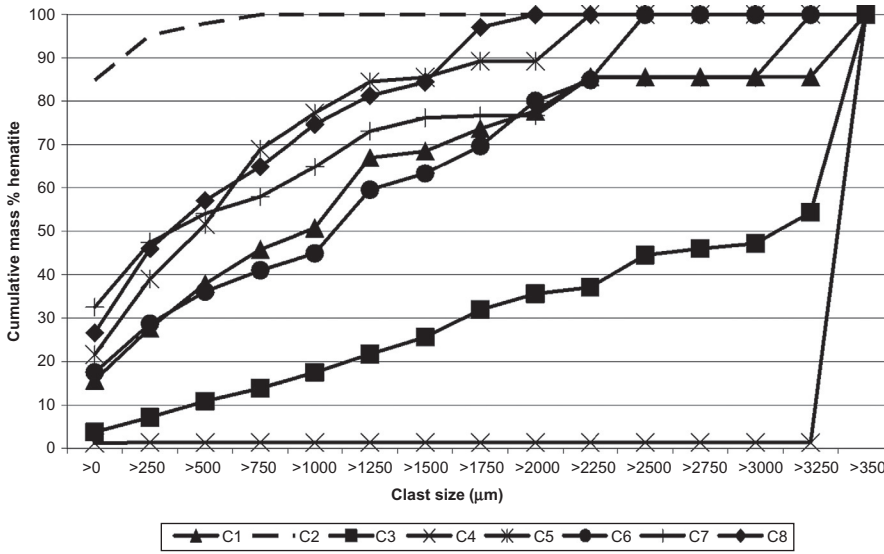

Figure 5.8 Cumulative clast size distributions for hematite in theoretical conglomerates. Note prevalence of bimodal distributions indicating the occurrence of matrix versus clasts. C4 (concave up, bottom right) would rank higher for clast size distribution than say C2 (concave down, top left).

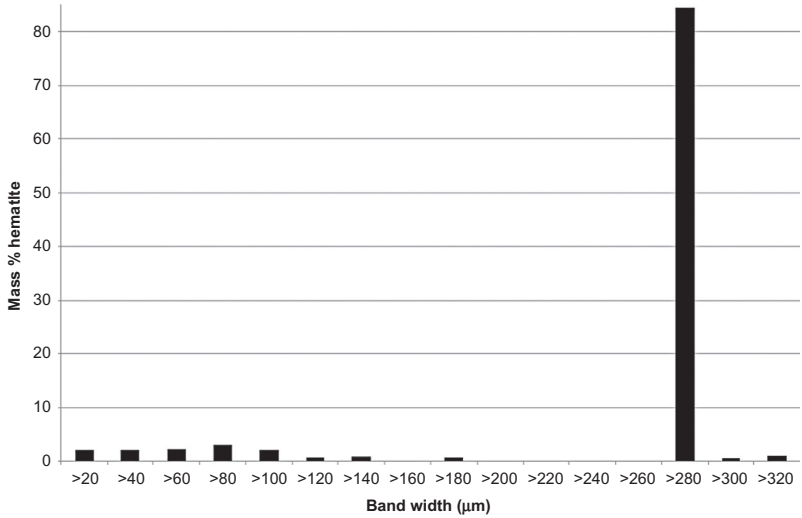

Figure 5.9 Example of a microband size distribution histogram for a BIF-type ore.

Hematite microbandwidths typically returned values on the micron scale, since macrobands of hematite are typically contaminated with microlaminations of quartz, which is to be expected when macroscopic hematite band transition to macroscopic quartz bands. Put differently, microscopically, it was evident that there were hematite microlayers present in quartz and *vice versa* for all the BIF samples analyzed. There was thus a disconnect between the size of hematite bands seen in hand specimens (suggested by the geologist) and the small hematite bands measured within the auto-SEM. Hematite macrobandwidth compositions were thus defined according to hematite mass percent thresholds and acted as a bridging concept between microscopic hematite bandwidths and macroscopic hand specimen bandwidths. Figure 5.10 presents a hematite macroband profile as a function of hematite composition for 500 µm intervals. Unfortunately, this complicated the definition and delineation of hematite bands since one could define the occurrence of hematite bands on the amount of hematite present within those bands. As such, in Figure 5.10, if one suggested that a hematite band must contain at least 50 mass% hematite (corresponding to ~35% Fe grade), then there are only two hematite bands that can be accounted for in the sample even though there is clearly a third histogram peak between the two larger hematite bands (and that can be seen in a textural map of the sample in Figure 5.11). This does however allow for minimum and maximum bandwidths to be defined as outlined in Table 5.4. Microbandwidth distributions have implications for product grade (quality). Macrobandwidth distributions, based on bandwidth compositions, have implications for tonnage (hematite quantity).

The paper of Tonžetić and Dippenaar (2011) presents the first real attempt at trying to solve the silicoferrite quantification problem on an automated SEM mineralogical

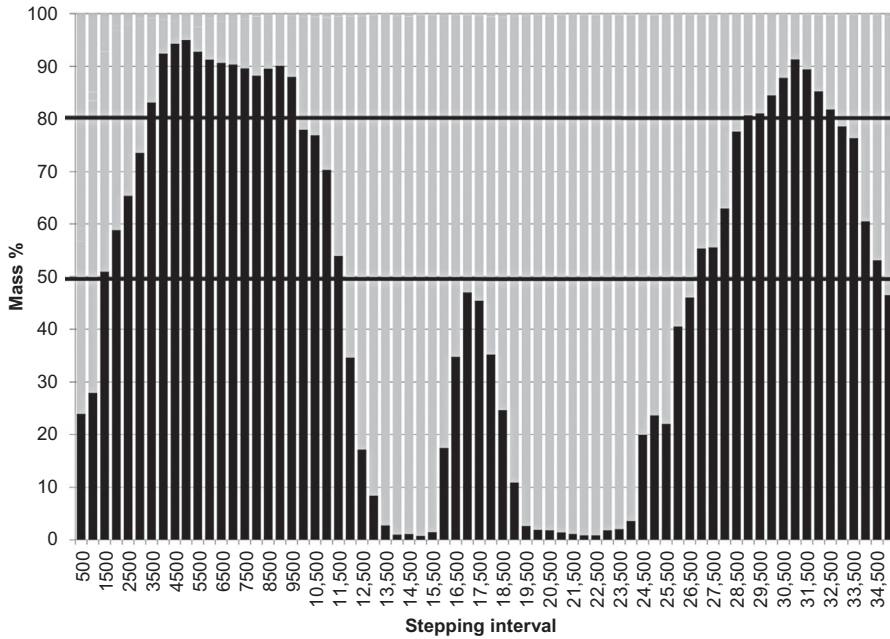

Figure 5.10 Demonstration of the subjectivity of defining band widths for sample B7 with the occurrence of quartz microbands. Hematite composition is black while quartz is light gray.

system. Point-counting and XRD results provided for quantification baselines, bearing in mind the inherent pitfalls that could be (and in some cases indeed were) found in these types of abundance analyses. Table 5.6 presents a basic comparison of mineral distinction between QEMSCAN and point-counting techniques. Table 5.7 presents modal results of QEMSCAN against point-counting. Both these tables put in context difficulties that can be encountered in both techniques when it comes to mineral identification, for instance, Loo (1998) suggested that it is virtually impossible to differentiate "magnesioferrite" from magnetite under optical microscope point-counting conditions, whereas a magnesium X-ray signature is essential for QEMSCAN identification and is readily measured. Table 5.8 presents a comparison of QEMSCAN results with the Topas and Autoquan results (both XRD methods of measurement). In Table 5.8, an increase in magnetite is seen with an increase in magnesium (consistent with Hsieh and Whiteman, 1993 and Oluwadare, 2007), with the increase being more pronounced in the QEMSCAN results (as evidenced by the magnetite to hematite ratio). High aluminum appears to promote SFCA formation as seen by the high SFCA to calcium ferrite ratio (consistent with Oluwadare, 2007), with the results once again being more prominent for the QEMSCAN analysis. The QEMSCAN results also suggested the preferential formation or stabilization of hematite with an increase in aluminum (consistent with Oluwadare, 2007). Tonžetić and Dippenaar (2011) discussed extensively possible reasons for the differences encountered in the SFCA modal abundances between the various technologies but pointed to vague and inconsistent

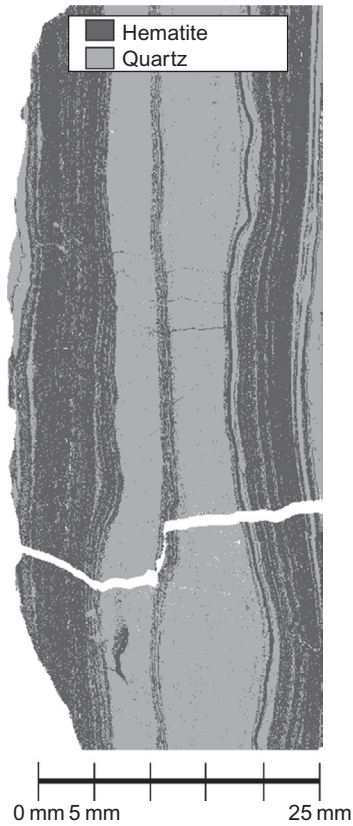

Figure 5.11 An example of a BIF measured within a QEMSCAN system. White represents (vugular) macroporosity.

Table 5.4 An example of bandwidth specifications for sample above as defined by hematite mass % cutoffs

	Hematite cutoff at 50%		Hematite cutoff at 80%	
Sample	**Min**	**Max**	**Min**	**Max**
B7	8 mm	10.5 mm	4 mm	6.5 mm

definitions of SFCAs in the literature and the dependence on morphological classification schemes resulting in a plethora of confusing SFCA synonyms. They pointed out that chemical distinction schemes (which can be used by QEMSCAN) are supported by Scarlett et al. (2004) and Pimenta and Seshadri (2002). The paper also found Al-deficient, pure SFCs and Mg analogs of SFCA. In summary, the paper showed a rough agreement between QEMSCAN and XRD results, with less agreement between QEMSCAN and point-counting results.

Table 5.5 Potential auto-SEM measurement errors

(1) Sample preparation error (1.1) Riffling/splitting/measuring/subsizing/ adequate sample error (1.2) Density segregation/settling error (1.2.1) Associated with the addition of graphite (1.2.2) Associated with density settling in epoxy resin (1.2.3) "Bubble" error (formation of bubbles in substrate) (1.3) Polishing/plucking/smearing/scratching error	(2) Measuring error (2.1) Reproducibility (data) and repeatability (instrument) (2.2) Statistical error (2.2.1) Particle count error (2.2.2) Measurement parameter error (line spacing, beam-stepping interval, field size/magnification errors, etc.) (2.3) Block rotation error (2.4) X-ray peak overlap error (2.5) First-order mineral identification error	(3) Data interpretation error (3.1) First-order grouping error (3.1.1) Density assignation error (3.1.2) Mineral assay assignation error (3.2) Second-order grouping error

Table 5.6 A comparison of mineral distinction between QEMSCAN and point-counting techniques

Mineral	QEMSCAN (EDS-SEM microscopy)	Point-counting (reflective light microscopy)
Magnetite	Fe and O signals *above* threshold grayscale value (85 ∩ 89 depending on deconvolution of BSE histogram)	Gray against hematite
Magnesioferrite	Mg, Fe, and O signals	Mottled appearance in magnetite of slightly different gray (reflectance is between hematite and magnetite)
Calciomagnetite	Fe and O signals with *low*-Ca signatures	Indistinguishable from magnesioferrite
Hematite	Fe and O signals *below* threshold grayscale value (85 ∩ 89 depending on deconvolution of BSE histogram)	White against magnetite
Calcium ferrite	Fe and O signals with *high*-Ca signatures	"Acicular" morphology (dependent on sectioning)
SFCA	Ca, Si, Fe, and O signals that may contain Al	"Tabular" morphology (dependent on sectioning)
Calcium silicates	Ca, Si, and O signals (which may be differentiated according to Ca/Si)	Only differentiable in polished thin section
Glass	Everything else (though differentiable into chemical subgroups)	Everything else (when distinguishable from calcium silicates)

All auto-SEMs allow for the input of standard mineral density values into their analytic programs. It is therefore possible to calculate the average density of any given measured particle by adding together the area fractions of minerals occurring in a particle multiplied by their appropriate inputted densities. It is then possible to place these minerals into density classes or categories and to plot a mass percentage histogram. This is enough to gauge a rough idea of ideal heavy liquid separation parameters for dense liquid separation, though by itself gives no idea of grade. If the increasing cumulative percentage of iron is plotted along the same axes, along with the decreasing cumulative percentage of any major gangue element (usually silicon), the grade (and amount of deleterious element concentration) of a given concentrate can be predicted if dense media separation is carried out at a specified dense liquid cutoff. Conversely, if a specific grade of concentrate is required, it can be found on the graph and the appropriate density of liquid needed can be selected (Richardson and Morrison, 2003).

Table 5.7 Comparison of QEMSCAN (QS) results against point-counting (PC) results (area %)

	Sample 1		Sample 2		Sample 3		Sample 4	
Mineral	**QS**	**PC**	**QS**	**PC**	**QS**	**PC**	**QS**	**PC**
Magnetite	6.3	12.8	3.2	7.8	9.4	7.0	5.8	8.1
Magnesioferrite	0.8	16.7	0.9	22.3	0.8	21.3	0.5	18.1
Calciomagnetite	13.0	0.0	11.5	0.0	12.5	0.0	12.4	0.0
Hematite	27.6	21.0	32.1	25.9	24.9	20.5	30.3	21.2
Calcium ferrite	30.4	11.3	29.3	6.4	30.7	6.2	33.0	14.9
SFCA[a]	18.4	35.2	17.4	32.7	16.5	40.8	14.8	35.9
Calcium silicates	0.4	0.0	1.0	0.0	0.3	0.0	0.1	0.0
Glass	3.1	3.0	4.6	4.9	4.9	4.2	3.1	1.8
Total	100.0	100.0	100.0	100.0	100.0	100.0	100.0	100.0

[a] Silicoferrite of calcium and aluminum.

Table 5.8 Comparison of QEMSCAN (QS) results against XRD Topas and Autoquan (AQ) (weight %) with additional chemistry

Name	Sample 8			Sample 9			Sample 10		
Aluminum	1.0			1.0			1.1		
Magnesium	0.7			1.4			1.4		
Mineral	**QS**	**TP**	**AQ**	**QS**	**TP**	**AQ**	**QS**	**TP**	**AQ**
Magnetite	35.3	35.5	39.3	48.0	40.7	42.1	37.2	50.6	51.7
Hematite	22.2	34.7	33.3	11.2	24.9	25.2	25.5	24.3	24.6
Calcium ferrite	15.5	9.4	7.0	14.2	10.5	11.7	9.5	7.9	6.0
SFCA	20.1	12.6	12.8	19.1	12.8	11.5	18.5	10.0	11.0
Ca silicates/glass/ others	6.9	7.8	7.6	7.5	11.1	9.5	9.3	7.2	6.7
Total	100.0	100.0	100.0	100.0	100.0	100.0	100.0	100.0	100.0
SFCA/CF[a]	1.3	1.3	1.8	1.3	1.2	1.0	1.9	1.3	1.8
Mag/Hem[b]	1.6	1.0	1.2	4.3	1.6	1.7	1.5	2.1	2.1

[a] CF, calcium ferrite.
[b] Ratio of total magnetite to hematite (total magnetite = magnesioferrite + calciomagnetite + magnetite).

5.5 Summary

The relative strengths and weaknesses of automated SEM-based technologies for the characterization of iron ore samples, compared with manual techniques, are summarized below.

5.5.1 Advantages (strengths)

While most auto-SEMs are not entirely operator-independent, they, to a large extent, allow for the automatic collection of data once a measurement run has been initiated. They are accurate once they have been "taught" what they need to know (though this usually resides within the intellectual property of the operator or purchaser, this does allow for a certain competitive advantage to be gained from purchasing an auto-SEM and "training" it to do very specific measurements). Auto-SEMs are quick with typical point analyses occurring in the region of milliseconds and measurement runs per sample block typically being resolved within 1–4 h. There is no doubt that these techniques are repeatable. Their consistency between testing runs is unparalleled. They remove the tedium of manual analyses often associated with microprobes and more complicated instrumentation. While being expensive (in the order of 0.6–1.2 million US$), they are by no means the most expensive of analytic equipment and can be cost-efficient since they can be run automatically after business hours and during weekends. The fact that they can be left to run by themselves also means that they are time-efficient in that operating mineralogists and metallurgists can be preoccupied with other duties while their instruments are running.

The statistically valid data that are generated by these instruments run into the thousands to millions of analysis points per measurement (approximately 10,000 times greater number of analysis points than those obtained by point-counting) and most can record and monitor variation during measurement to allow for project management and quality control. The generation of these statistics means that work previously considered impractical is now possible and that one is more likely to simply measure for the sake of empirical experiment. Any single particle, collected and measured, can be treated as a single particle or as part of a set of particles. As a single particle, its properties are not hidden in a plethora of tables, modal results, and bulk data. These auto-SEMs can, in a sense, be both holistic and atomistic.

5.5.2 Disadvantages (weaknesses)

As has already been mentioned, for all SEM-based systems, potential difficulties in analysis occur when phases of similar chemistry have similar average atomic numbers (i.e., similar BSE intensities). These difficulties are minimized with appropriate standards, best practice methodologies including the stretching of contrast and the use of multiple measures in combination (BSE, X-ray information, elemental ratios, etc.) to increase confidence in analyses.

Further, there are a number of difficulties associated with automated image analysis including the delineation of hematite clasts against hematite matrix

compositions in these automated analysis systems. The occurrence of hematite clasts in hematite matrices makes clast boundaries indistinguishable in auto-SEM systems. Furthermore, if monomictic hematite clasts are clast-supported (sensu stricto orthoconglomerates), then even if they are easily distinguished from a siliceous matrix, they will still be touching one another and thus not easily be resolved into separate clasts. The extensive image processing capabilities (specifically the watershedding capabilities) of the Mineralogic (R) suite might allow for a superior granulation that could allow for the separation of grains of the same minerals that happen to be touching.

Furthermore, the sources and extent of error in auto-SEM analysis have yet to be properly studied and characterized but can broadly be grouped into three categories (not including error introduced during sampling and where the onus is not on the instrumentation to correct or quantify but on the samplers to be representative of their sampling):

(1) Sample preparation error (such as inaccurate sizing/weighing, density settling, and incorrect polishing procedures).
(2) Measuring error (including data reproducibility and instrument repeatability).
(3) Data interpretation error (such as inappropriate mineral groupings and incorrect densities)

Far be it from the scope of this chapter to elaborate on the possible causes of these errors, for each of the above, the reader will briefly be made aware of where errors can creep into an analysis by point form in Table 5.5 (for more information, consult the references at the end of this chapter and the author). Measurement errors are usually less significant than sample preparation errors because, to a certain extent, they can be compensated for in the mineral identification rule sets and can also, once again to a certain extent, be corrected for in data processing by experienced operators. So, for instance, boundary or edge effects can be accommodated for in mineral identification rule sets by accounting for the presence of carbon (among other elements) from epoxy resin and graphite fillers. Also, any unidentified (mixed spectral or "boundary") phases can be resolved into legitimate mineral entries by various data-processing strategies (Tonžetić, 2014). More grave errors usually creep in with sample preparation (relief artifacts, bubbles, plucking, smearing, scratching, etc.) and inexperienced auto-SEM operators attempting to compensate too much for instrument physics (for instance, by increasing mineral identification windows to limits that will catch multiple different minerals within a single entry).

5.6 Future trends

Doubtless, auto-SEMs will get faster, "smarter," be more accurate, and be more automated in the future, the speculation of which lies in the "how." "Faster" no doubt lies in the improved performance of EDX spectrometers. In a single generation, liquid nitrogen detectors were eclipsed by SDDs (silicon drift detectors), which were 4 times quicker and doubtless will get faster in the future in terms of analysis speeds.

In terms of accuracy, detector quality is sure to improve and may in the future approach the same level of elemental differentiability as WDS detectors though this will probably require the writing of some very smart rules or code that operate in the background of auto-SEM runs.

Smarter auto-SEMs will no doubt entail an improved query language especially for textural evaluation, so that an operator mineralogist can bring up or "return" any particles of interest that obey or observe any quality that has been measured directly or calculated indirectly by inference. Many auto-SEM software programmers have maintained (and doubtless will always maintain) that the data are "all there"… It's just a question of bringing it out. Forays into this area have already been made with most auto-SEMs being able to at least accept additional data characteristics of minerals other than the ubiquitous density (values such as flotation indices). Smarter query languages or even smarter measurement variables may in the future allow for the distinction of mineral varieties based on their morphologies or textures. So, for instance, specularitic varieties of hematite may be distinguished from martitic varieties of hematite based on shape factor (compactness, aspect ratios, etc.) or even their association with pores (porosity). A smarter (or at least more integrative) approach in the future may allow for the possible incorporation of cathodoluminescence (or any other analysis method resulting in a multispectral approach) as a tool in grain segmentation or even further identification of minerals in iron ores (and other commodities). Correlative microscopy that would combine SEM and optical approaches (and even XRM) to overcome issues associated with the differentiation of phases with similar chemistry and BSE values (magnetite and hematite) can most definitely add value to iron ore quantification. This approach would not be far removed from the integrative geographic information system (GIS) approach in common use for "macro" (large-scale) geographic mapping.

More automated "one-button" approaches have already been developed by some of the auto-SEM companies though great care and caution should be exercised with these instruments to ensure valid datasets. As always quicker, less-intensive measurement setup of samples (and subsequently less operator-intensive data processing and interpretation) should allow the mineralogist more time to solve complicated problems associated with mine, processing plant, or exploration surveys.

Some have speculated that X-ray microtomography may replace auto-SEMs in the near future. This is unlikely. In all likelihood, XRMs will be treated in a complementary fashion with XRMs providing critical three-dimensional information to ores through the mapping of attenuation coefficients, analogous to 2D BSE grayscales (proportional to average atomic number), with these attenuation coefficients being regularly compared, correlated, and validated with auto-SEM X-ray data. The main impedances to XRMs completely replacing auto-SEMs (in the near future) are as follows:

– Their reliance on attenuation coefficients. One cannot directly gain access to X-ray information within a core/sample. Just like auto-SEMs have overlapping BSE grayscales between minerals, XRMs have overlapping attenuation coefficients. So only in very simplistic samples would it be possible to separate minerals in an ore through attenuation coefficients. Once a suitable attenuation coefficient of a specific value has been identified, one would

still have to figure out exactly what mineral is being looked at through nondestructive means (commonly by using an auto-SEM).
- Price. XRMs are currently far more expensive than auto-SEMs.
- Memory. The data created by XRMs are currently prohibitively large for large-volume scans (gigabytes of data produced at approximately tens of micron resolution for approximately cm^3 volumes).
- Resolution. XRM resolution is generally low (also to do with the size of data created by an analysis—the higher the resolution, the more prohibitive the memory usage).

There is however much scope for XRMs being used in a complementary fashion to auto-SEMs.

References

Duncumb, P., 1999. Quantitative analysis with the electron microprobe. The first 50 years and beyond (Plenary Lecture). Fifteenth International Congress on X-Ray Optics and Microanalysis (ICXOM), Antwerp, Belgium, August 24–27, 1998. J. Anal. At. Spectrom. 14, 357–366.

Figueroa, G., Moeller, K., Buhot, M., Gloy, G., Haberlah, D., 2011. Advanced discrimination of hematite and magnetite by automated mineralogy. In: 10th International Congress for Applied Mineralogy proceedings, Trondheim, pp. 197–204.

Gottlieb, P., Wilkie, G., Sutherland, D., Ho-Tun, E., Suthers, S., Perera, K., Jenkins, B., Spencer, S., Butcher, A., Rayner, J., 2000. Using quantitative electron microscopy for process mineralogy applications. J. Mineral. 52, 24–25.

Hill, E., 2014. ZEISS Mineralogic Mining—Ore Process Optimization. Carl Zeiss White Paper.

Hillier, J., 1947. Electron probe analysis employing X-ray spectrography (Patent No. 2,418,029).

Hsieh, L.-H., Whiteman, J.A., 1993. Effect of raw material composition on the mineral phases in a lime-fluxed sinter. ISIJ Int. 33, 462–473.

Kralova, V., 2013. Automated mineral analysis in SEM for rapid evaluation of mineralogical samples. In: 51st Annual Conference of the Microscopy Society of Southern Africa Technical Forum Proceedings, Pretoria, South Africa, pp. 25.

Loo, C.E., 1998. Some progress in understanding the science of iron ore sintering. In: ICSTI/Ironmaking Conference Proceedings.

Oluwadare, G.O., 2007. Roles of alumina and magnesia on the formation of SFCA in iron ore sinters. Trends Appl. Sci. Res. 2 (6), 483–491.

Pimenta, H.P., Seshadri, V., 2002. Characterisation of structure of iron ore sinter and its behaviour during reduction at low temperatures. Ironmak. Steelmak. 29 (3), 169–174.

Pirrie, D., Butcher, A.R., Power, M.R., Gottlieb, P., Miller, G.L., 2004. Rapid quantitative mineral and phase analysis using automated scanning electron microscopy (QemSCAN); potential applications in forensic geosciences. In: Forensic Geoscience: Principles, Techniques and Applications. Geological Society, London, pp. 123–136 (Special Publications No. 232).

Rao, D., Kumar, T., Rao, S., Prabhakar, S., Raju, G., 2009. Mineralogy and geochemistry of a Low grade iron ore sample from Bellary-Hospet Sector, India and their implications on beneficiation. J. Miner. Mater. Charact. Eng. 8 (2), 115–132.

Richardson, J.M., Morrison, R.D., 2003. Metallurgical balances and efficiency. In: Fuerstenau, M.C., Han, K.N. (Eds.), Principles of Mineral Processing. Society for Mining, Metallurgy and Exploration (SME), Colorado, pp. 363–365.

Scarlett, N.V.Y., Pownceby, M.I., Madsen, I.C., Christensen, A.N., 2004. Reaction sequences in the formation of silico-ferrites of calcium and aluminium in iron ore sinter. Metall. Mater. Trans. 35B, 929–936.

Sutherland, D.N., Gottlieb, P., 1991. Application of automated quantitative mineralogy in mineral processing. Miner. Eng. 4 (7–11), 753–762.

Tonžetić, I.Ž., 2012. The characterization of surface overburden (pedocretes) at the Sishen Mine, South Africa. In: FEI User Group 2012, Stellenbosch, South Africa.

Tonžetić, I.Ž., 2014. Mixed spectral signature resolution with Zeiss Mineralogic Mining. In: Carl Zeiss Lunch & Learn Workshop, Johannesburg, South Africa.

Tonžetić, I.Ž., Dippenaar, A., 2011. An alternative to traditional iron-ore sinter phase classification. Miner. Eng. 24 (12), 1258–1263.

Tonžetić, I.Ž., Duncan, M., Bramdeo, S., 2012. The ore characterisation of different hematitic iron ores. In: Process Mineralogy 2012 Proceedings, Cape Town, South Africa.

Characterization of iron ore by visible and infrared reflectance and, Raman spectroscopies

6

E. Ramanaidou, M. Wells, I. Lau, C. Laukamp
CSIRO Mineral Resources Flagship, Bentley, WA, Australia

6.1 Introduction

In the last decade, there has been massive growth in iron ore production around the world fuelled by the high demand from China (Table 6.1). This boost in demand has encouraged iron ore mining companies to ramp up production rates in current mines and to open up new deposits. Mining companies are now confronted with the challenge of characterizing increasing volumes of iron ore (Ramanaidou and Wells, 2014). Faster and smarter analyses of iron ore diamond cores, drill chips, and mine faces are required to provide rapid and detailed characterization of ore and gangue minerals for mine development and process optimization. Hyperspectral drill core logging technologies (Ramanaidou et al., 2008; Ramanaidou and Wells, 2011a, 2013; Schodlok and Ramanaidou, 2011; Haest et al., 2012a,b) are now routinely used by iron ore companies to provide objective mineralogical and ore type information on diamond cores and drill chips. Mine face systems, such as CSIRO point analysis scanning robot (Ramanaidou et al., 2002), CSIRO OARS system (Fraser et al., 2006), and NEO HySpex and Specim hyperspectral cameras, have been used successfully to map iron ore mine faces (Melkumyan and Murphy, 2010; Ramanaidou and Wells, 2011a; Murphy and Monteiro, 2013). Multispectral and hyperspectral images generated from the ASTER satellite (Fujisada et al., 1998; Yamaguchi et al., 1999) and HyMap airborne (Reston and Cocks, 1998) systems are also very valuable for the exploration of iron ore (Duuring et al., 2012) and the monitoring of iron ore dust near port and cities (Ong et al., 2003).

Raman spectroscopy provides complementary information to infrared spectroscopy for online systems and is also valuable for *in situ* mineralogical characterization of magnetite, hematite, goethite, and quartz. Importantly, the common iron ore oxide minerals, such as goethite, hematite, and magnetite, and commonly associated gangue minerals, such as quartz and carbonates, are unique and all strongly Raman-active (e.g., De Faria et al., 1997; Bersani et al., 1999; Chamritski and Burns, 2005). Representative Raman spectra for the main iron oxide minerals of economic interest and of selected gangue phases show that the distinct nature of the spectra allows unequivocal identification and quantification of the key iron oxides and gangue minerals.

Iron Ore. http://dx.doi.org/10.1016/B978-1-78242-156-6.00006-X
© 2015 Elsevier Ltd. All rights reserved.

Table 6.1 **Iron ore production (Mt) by country between 2004 and 2013**

	2004	2005	2006	2007	2008	2009	2010	2011	2012	2013	Crude ore (CO)	Iron content (IC)	IC/CO
Australia	234	262	275	299	342	394	433	480	521	530	35,000	17,000	0.49
Brazil	262	281	318	355	355	300	370	390	398	398	31,000	16,000	0.52
Canada	29	30	34	33	31	32	37	37	39	40	6300	2300	0.37
China	320	420	601	707	824	880	1070	1200	1310	1320	23,000	7200	0.31
India	121	152	181	202	220	245	230	240	144	150	8100	5200	0.64
Iran	18	19	26	32	32	33	28	30	37	37	2500	1400	0.56
Kazakhstan	20	19	22	24	23	22	24	24	26	35	2500	900	0.36
Mauritania	10	11	11	12	11	10	11	11	12	14	1100	700	0.64
Mexico	11	12	11	11	12	12	14	14	14	14	700	400	0.57
Russia	97	97	102	105	100	92	101	100	105	102	25,000	14,000	0.56
South Africa	39	40	41	42	49	55	59	55	63	67	1000	650	0.65
Sweden	22	23	23	25	24	18	25	25	23	26	3500	2200	0.63
Ukraine	66	69	74	78	73	66	78	80	82	80	6500	2300	0.35
United States	55	54	53	52	54	27	49	54	54	52	6900	2100	0.30
Venezuela	19	21	22	21	21	15	14	16	27	30	4000	2400	0.60
Other countries	37	42	67	47	47	43	48	50	75	55	12,000	6200	0.52
Total	1360	1552	1861	2045	2218	2244	2591	2806	2930	2950	170,000	81,000	0.48

6.2 Principles of reflectance and Raman spectroscopies

The last decade witnessed a strong development of spectroscopic methods in the field of mineralogy. For instance, reflectance and Raman spectroscopies are now used to characterize the mineralogy of many geologic samples. Reflectance spectroscopy, in the visible and infrared wavelength range (Figure 6.1), is a fast and cost-effective technique to acquire accurate and quantitative mineralogy, which can be automated to enable mineralogical characterization of large volumes of iron ore, diamond core, and chip trays. Raman spectroscopy complements infrared spectroscopy at a finer scale (Ramanaidou and Wells, 2011a; Wells and Hogan, 2013) and provides mineralogical characterization of iron oxides and quartz in thin sections (Ramanaidou et al., 2008).

6.2.1 Reflectance spectroscopy

Reflectance spectroscopy is the study of the interaction of light, either reflected or scattered and as a function of wavelength, with solid matter such as minerals and rocks. The photons of the incident radiation are reflected from the surface, while some penetrate the mineral(s) and are finally absorbed (Clark et al., 1990).

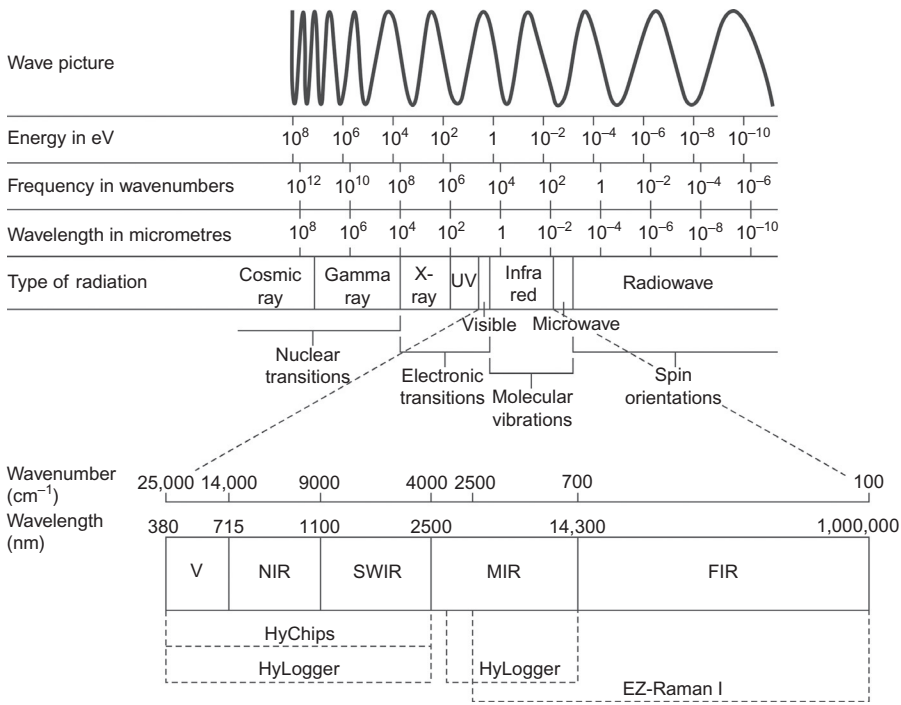

Figure 6.1 Electromagnetic spectrum defining the different types of radiation and the wavelength associated with each radiation. The wavelengths detected by the HyLogging™ system 1 and HyLogging™ system 3 and the EZ Raman are also added.

Visible and near infrared light (380–1000 nm) is energetic enough to redistribute electrons in a molecule (Harris and Bertolucci, 1989), and as a result, it is called electronic spectroscopy. These electronic processes involve transfer of electrons from low to high energy states within orbitals (crystal field) or from ligands (OH groups) to cations (charge transfer effects), producing broad absorption features, in particular for iron oxides such as hematite and goethite (Singer, 1981).

In the lower energy, infrared part of the electromagnetic spectrum, light is absorbed by vibrational modes of molecules, where the frequency of vibration is largely dependent on the bond length of the infrared active molecule. The vibrational modes of the molecules can be used to characterize the investigated material using vibrational spectroscopy (Harris and Bertolucci, 1989). All bonds vibrate with different motions (stretching and bending); therefore, an individual bond commonly absorbs at more than one IR frequency (Figure 6.2). The bending and stretching of fundamental vibrations produce overtones and combination tones at lower wavelengths or higher frequencies in particular in the shortwave infrared region between 1000 and 2500 nm in which OH-bearing minerals (for instance, smectite, kaolinite, talc, and serpentine) have very strong absorption features at 1400 and 2100–2450 nm.

The spectral signature of a mineral is dependent on a number of parameters, including electronic and/or vibrational processes, absorption coefficient, refractive index, scattering

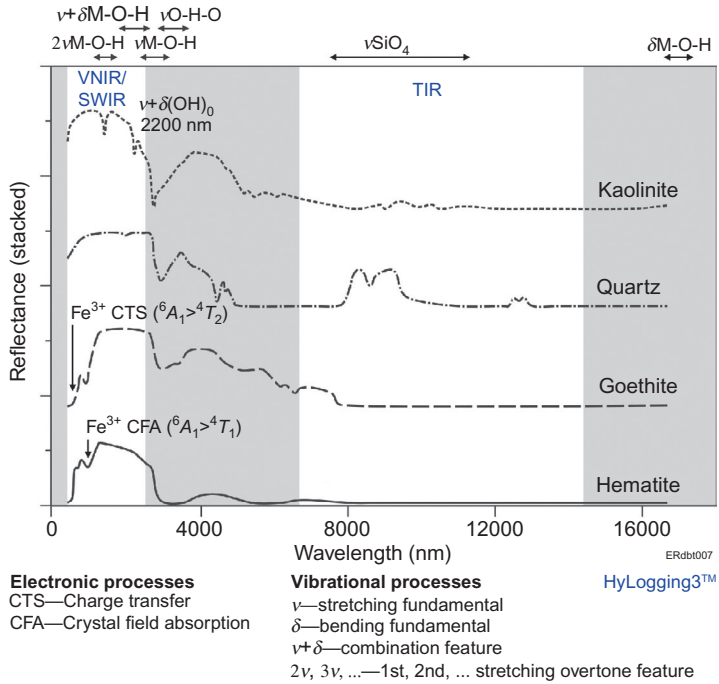

Figure 6.2 Spectral signatures and locations of the electronic and vibrational processes for goethite, quartz, hematite, and kaolinite across the VNIR, SWIR, and MIR.

effects, diffuse and/or specular reflection, volume and/or surface scattering, and single or multiple volume scattering. Spectral variation is caused by the mineralogy, composition, crystallinity, water, particle size effects, mixtures, and orientation of the sample.

6.2.2 Raman spectroscopy

Raman spectroscopy, named after one of its discoverers (Raman and Krishnan, 1928) as cited by McMillan and Hofmeister (1988), is a technique that examines molecular vibrational and rotational modes within a system using inelastically scattered visible or near-infrared (NIR) radiation. A detailed discussion of Raman theory, instrumentation, and its applications has been presented in a number of articles (McMillan and Hofmeister, 1988; Schrader, 1995) and the references contained therein. A later recent review by Das and Agrawal (2011) focused more on the advancement of Raman spectroscopy in a number of fields, particularly in the area of materials science for characterizing polymers and superconductors/semiconductors. More recently still, as well as describing in some detail the theory behind the Raman effect, the significant contribution of Dubessy et al. (2012) covers recent development of Raman instrumentation, as well as detailed applications of the technique across a number of fields. As such, the method is only summarily described below.

A monochromatic radiation reacting with material surface is either almost completely reflected or scattered by molecules exposed at the surface without a change in wavelength. This is termed Rayleigh scattering, and the change in frequency is denoted as $0\,cm^{-1}$. For a small proportion of the radiation, the wavelength of the incident light is modulated by the energy or vibrational frequency of the chemical bonds within the molecules. Energy (E) and frequency (υ) are related through the equation, $E=h\upsilon$, where h is Planck's constant. Therefore, the energy (e) or spatial frequency of the scattered radiation is given as the vibrational frequency of the incident light $\pm$ the vibrational frequency of the molecular bond (McMillan and Hofmeister, 1988). For active vibrational modes, Raman lines occur at anti-Stokes ($E+e$) and Stokes ($E-e$) energies, with Stokes Raman-shifted frequencies denoted with positive wavenumber values (McMillan and Hofmeister, 1988). Usually in Raman excitation experiments, the incident laser (i.e., Rayleigh scattered radiation) and anti-Stokes Raman-shifted frequencies are filtered out, so that only the more intense Stokes Raman-shifted frequencies are detected and recorded.

6.3 Technologies

6.3.1 Reflectance spectroscopy instrumentations

6.3.1.1 Field spectroradiometer

Analytical spectral devices (ASD, now PANalytical) field spectroradiometers, such as the FieldSpec Pro FR and the FieldSpec 3 and 4, cover the wavelength range between 350 and 2500 nm. The spectral resolution is 3 nm at 700 nm, 8.5–10 nm at 1400, and 6.5–12 nm at 2100 nm. The scanning time is around 0.1 s. There are three detectors: a 512 element Si photodiode array for the 350–1000 nm range and two separate,

TE-cooled, graded index InGaAs photodiodes for the 1000–2500 nm range. A fiber-optic cable was used to collect the reflected radiation. A reference reflectance standard made from compressed polytetrafluoroethylene commercially available as Spectralon or Fluorilon to name a few and the illumination source was a quartz halogen lamp.

6.3.1.2 Hyperspectral drill core and chip scanning system

A handful of hyperspectral drill core and chip scanning systems are currently in use in the iron ore industry and include (1) the CSIRO-developed (Figure 6.3a) point analyzer "HyLogging™ systems" (Ramanaidou et al., 2004, 2008; Huntington et al., 2006; Wells and Ramanaidou, 2007; Ramanaidou and Wells, 2011a; Schodlok and Ramanaidou, 2011; Haest et al., 2012a,b) and also the addition of a Raman spectrometer (Figure 6.3c); (2) the hyperspectral core imager Mark III from Corescan called HCI-3 System™ (Figure 6.3b), which provides not only a full spectral image from 450 to 2500 nm at a 0.5 mm pixel resolution but also a surface topography image, thanks to an array of laser beams and a high-resolution digital camera; (3) a hyperspectral

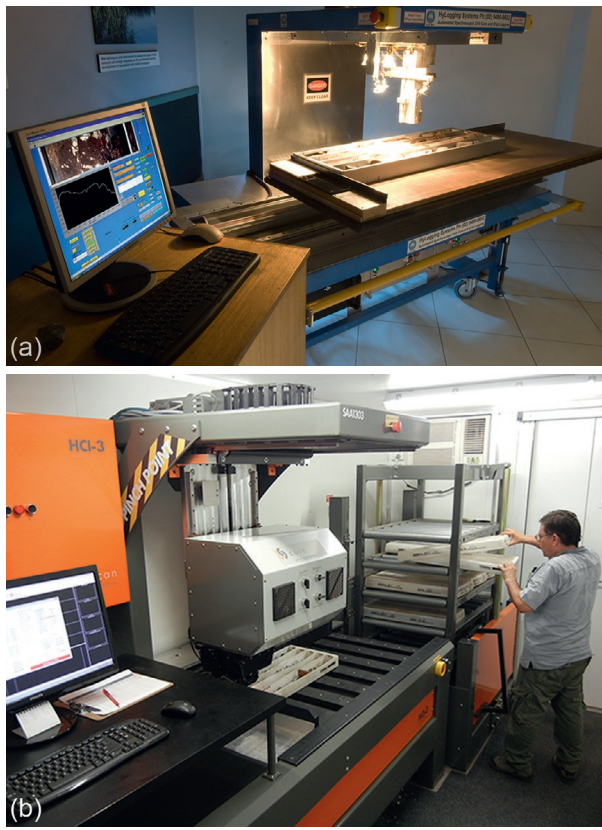

Figure 6.3 (a) HyLogging™ system 1 or HyChips; (b) Corescan HCI-3 System; (c) HyLogging™ system 1 with Raman spectrometer; (d) NEO HySpex hyperspectral camera.

Figure 6.3 Continued

imaging system from NEO HySpex (Figure 6.3d), which provides a full spectral image from 400 to 2500 nm; and (4) SisuROCK from Specim, which provides a spectral image from 970 to 2500 nm with the possibility of adding VNIR or RGB sensors and thermal infrared capability.

The two currently available "HyLogging™ systems" are respectively labeled 1 and 3. The HyLogging™ system 1(Figure 6.3a), now commercialized by FLSmidth, includes an automated tray handling system, an ASD (FieldSpec 3 or TerraSpec 4 spectrometer) measuring at a given step interval of generally 10–20 mm with a 10 mm sample size, an automated illumination setup, and safety processes. The system provides a high-resolution digital image of rocks or chips (Ramanaidou et al., 2004; Huntington et al., 2006; Haest et al., 2012a,b). The HyLogging™ system 3 is designed to continuously log drill core spatially and spectrally in the 380–2500 nm and 6000–14,500 nm wavelength ranges. The system includes a robotic *x*/*y* table for core/chip tray translation, a laser profilometer that measures core height at 0.2 mm resolution, a high-resolution (0.1 mm)

digital line scan camera, and three coupled spectrometers (a silicon-detector grating spectrometer for the 380–1072 nm interval, an InSb-detector Fourier transform infrared (FTIR) spectrometer for the 1072–2500 nm interval, and another FTIR spectrometer with an HgCdTe photoconductive detector for the 6000–14,500 nm interval). The data are processed using The Spectral Geologist (TSG™), and mineralogical data are available within seconds after measurement in the data format compatible for input into 3D mine planning and exploration software applications.

6.3.1.3 Face mapping system

The ability to map iron ore mine faces for estimating the mineralogy and associated grade and ore types is important for efficient mine planning and was first trialed by CSIRO using a prototype system: CSIRO point analysis scanning robot (Ramanaidou et al., 2002). Hyperspectral imaging systems were also assessed for a similar application and include systems such as the CSIRO OARS system (Fraser et al., 2006), NEO HySpex (Figures 6.3d and 6.4), and Specim hyperspectral cameras (Melkumyan and Murphy, 2010; Ramanaidou and Wells, 2011a; Murphy and Monteiro, 2013).

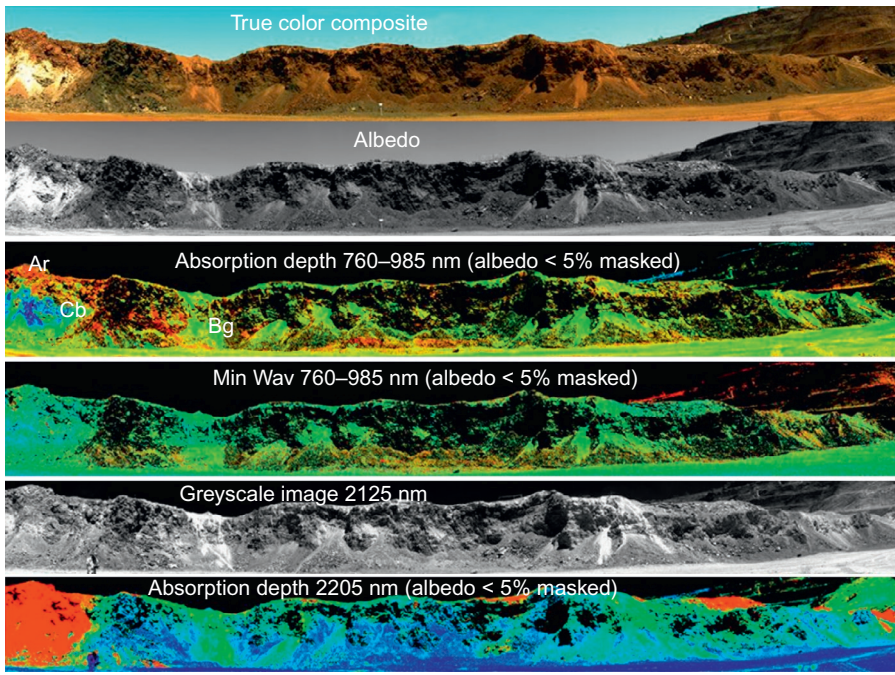

Figure 6.4 Hyperspectral image of an iron ore mine face in Ramanaidou and Wells (2011a) using a NEO HySpex camera. From top to bottom, true color composite; albedo or average of the total reflectance; absorption depth between 760 and 985 nm corresponding to the amount of iron oxide (with Ar: red spectrum at 900 nm; Bg: green spectrum at 880 nm; Cb: blue spectrum at 873 nm); grayscale image and absorption at 2205 nm corresponding to the amount of kaolinite on the mine face.

6.3.1.4 Remote sensing technology

Imaging spectroscopy has a number of applications in the iron ore resources sector, ranging from exploration (Duuring et al., 2012) to the detection of hazardous minerals (e.g., asbestos; cf. Swayze et al., 2009) that can be associated with, for example, banded iron formation-derived ores. Optical remote sensing technologies can be subdivided into multispectral and hyperspectral systems according to the resolution and sampling interval of their spectral range. ASTER (Advanced Spaceborne Thermal Emission and Reflection Radiometer; Yamaguchi et al., 1999) is a spaceborne, multispectral imaging spectrometer that collects 14 bands across the VNIR, SWIR, and MIR. The full width at half maximum (FWHM) properties and wavelength locations of the ASTER bands are sufficient to identify iron oxides, clay minerals, and anhydrous silicates (e.g., quartz) in the three respective wavelength regions. However, the spatial resolution decreases from 15 m in the VNIR to 30 m in the SWIR and 90 m in the MIR compromises the ability to perform detailed mapping, especially, of silicate minerals. Duuring et al. (2012) demonstrated how to apply ASTER data for mapping banded iron formation (BIF), intercalated mafic igneous rocks, and possibly hypogene alteration, using a combination of band ratios that identified iron oxides, mafic minerals, and other silicates. Also Landsat TM, another spaceborne, multispectral system, has been used to map iron oxides at Earth's surface (Rowan et al., 1991), but it has no capability to distinguish other major mineral groups.

A more detailed image of iron oxide mineralogy and associated mineral assemblages from Earth's surface was obtained with airborne hyperspectral systems, such as HyMap. HyMap acquires 128 spectral bands across the VNIR and SWIR at bandwidths of 10–20 nm. The spatial resolution of the collected data ranges from 3 to 15 m and depends largely on the flight height of the aircraft. Haest et al. (2012a, 2013) processed airborne hyperspectral data to map a paleochannel system that hosts a channel iron deposit (CID) by characterizing major mineral phases, including hematite, goethite, Al clays, Fe clays, and carbonates.

Numerous spaceborne hyperspectral sensors are scheduled for launch in the next 5 years (e.g., EnMAP; Stuffler et al., 2007), which will enhance the spatial and mineralogical resolution necessary for advanced iron ore exploration and resource evaluation.

6.3.2 Raman spectroscopy instrumentations

Commonly, lasers with wavelengths between 514 and 1100 nm are used as the incident radiation source for Raman excitation experiments (McMillan and Hofmeister, 1988; Schrader, 1995). The ease of the optical manipulation of light in this wavelength range has resulted in the development of combined Raman and optical microscopy systems. Consequently, Raman spectroscopy offers the following advantages: It requires minimal sample preparation, it is nondestructive and rapid, and, most importantly, analyses can be made *in situ* on either unprepared materials or samples prepared as thin sections and mounted blocks.

6.3.2.1 Portable Raman spectroscope

A high-resolution portable EZRaman-I Series (battery-powered) with a high-sensitivity TE-cooled (−50 °C) CCD spectrometer, with a 785 nm frequency stabilized laser

(Figure 6.3c), uses a narrow line width diode laser with shutter control and an optical fiber probe (Wells and Ramanaidou, 2013). Its spectral range varies between 100 and 2200 cm^{-1}. The average optical resolution is 6 cm^{-1} at a working distance of 7 mm.

6.3.2.2 Raman microscope

The Raman microscope, a HORIBA Scientific LabRAM HR Evolution, is fitted with a 1800 lines/mm dispersion grating, a 150 µm slit, and a Peltier-cooled CCD detector at 230 K and a 14 mW helium–neon laser at 785 nm.

Areas suitable for Raman analysis are initially selected by the examination of polished thin sections under a binocular, optical microscope, as being representative of the main iron oxide types (i.e., goethite, hematite/martite, and magnetite). Focusing of the laser beam on the areas selected for analysis was through a 50 times magnification lens, to produce a spot size of approximately 2 µm at the sample surface.

Laser power at the sample surface was 2.25 mW, with spectra acquired over a 30 s excitation period. These scanning conditions are selected to prevent any thermal-induced damage to the samples by the laser beam. Thermal transformation (e.g., goethite to hematite) and oxidation (e.g., magnetite to hematite) can be induced where greater laser excitation power and/or long acquisition times are employed, as previously reported by De Faria et al. (1997) and Shebanova and Lazor (2003a).

6.4 Reflectance and Raman spectroscopies of iron ore minerals

The spectral regions of reflectance and Raman spectroscopies relevant to iron ore mineralogy are listed in Table 6.2. Most of the direct-shipping ores (DSO) produced around the world, such as iron ores in Australia and Brazil (Ramanaidou and Wells, 2014), are dominated by hematite and goethite with small amounts of deleterious minerals such as kaolinite, gibbsite, and quartz. The banded iron-formation iron ores are dominated by gangue minerals such as carbonates, silicates and iron minerals consisting mainly of magnetite with a total content of around 30%. These ores need processing by such techniques as crushing, magnetic separation, and sometimes flotation to produce a magnetite concentrate of economic grade (>≈60% Fe).

6.4.1 Reflectance spectroscopy of iron ore minerals

The full (350–16,700 nm) reflectance spectra of the main minerals occurring in DSO including hematite, goethite, kaolinite, gibbsite, and quartz are displayed in Figure 6.5.

6.4.1.1 Magnetite and maghemite

In the VNIR, magnetite and maghemite display low reflectance, around 2% for the former and 11% for the latter (Figure 6.6). In the 6000–14,000 nm wavelength region, magnetite reflects poorly, but its reflectance baseline shows an increase toward longer

Table 6.2 Reflectance and Raman spectra relevant to diagnostic iron ore mineralogy (w, weak; Y, yes; –, no)

Minerals	Chemical formula	Reflectance			Raman
		VNIR	SWIR	MIR	
Magnetite	Fe_3O_4	W	–	–	Y
Maghemite	α-Fe_2O_3	W	–	–	Y
Kenomagnetite	$Fe^{2+}_{1-y}\left(Fe^{+}_{2}Fe^{3+}_{1+2/3\,y[\cdot]y/3}\right)O_4$	W	–	–	Y
Hematite/martite	α-Fe_2O_3	Y	–	–	Y (Al)
Goethite	α-FeOOH	Y	–	Y	Y (Al)
Quartz	SiO_2	–	–	Y	Y
Siderite	$FeCO_3$	–	Y	Y	Y
Magnesiosiderite	$(Mg_{0.35}Fe_{0.65})CO_3$	–	Y	Y	Y
Dolomite–ankerite series	$(Ca,Mg)(CO_3)_2$ to $Ca(Fe,Mg,Mn)(CO_3)_2$	–	Y	Y	Y
Stilpnomelane	$K(Fe^{2+},Mg,Fe^{3+})_8(Si,Al)_{12}(O,OH)_{27}\cdot n(H_2O)$	–	Y	Y	–
Minnesotaite (Fe talc)	$(Fe^{2+},Mg)_3Si_4O_{10}(OH)_2$	–	Y	Y	–
Greenalite (Fe serpentine)	$(Fe^{2+},Fe^{3+})_2\ 3Si_2O_5OH_4$	–	Y	Y	–
Pyrite	FeS_2	W	–	W	–
Riebeckite	$(Mg,Fe,\ Al)_6(Si,Al)_4(OH)_8$	–	Y	Y	–
Ferriannite	$(K_2Fe^{2+}6Fe^{3+})_2Si_6O_{20}(OH)_4$	–	Y	Y	–
Cummingtonite	$(Mg,Fe)_7(Si_4O_{11})2(OH)_2$	–	Y	Y	–
Grunerite	$Fe_7Si_8O_{22}(OH)_2$	–	Y	Y	–
Tremolite	$Ca_2Mg_5Si_8O_{22}(OH)_2$	–	Y	Y	–
Ferroactinolite	$Ca_2(Fe^{2+})_5Si_8O_{22}(OH)_2$	–	Y	Y	–
Chlorite (e.g., chamosite, ripidolite)	$(Fe^{2+},Mg)_5Al(AlSi_3O_{10})$	–	Y	Y	Y
Kaolinite	$Al_2Si_2O_5(OH)_4$	Y	Y	Y	–
Gibbsite	$Al(OH)_3$	Y	Y	Y	Y
Montmorillonite	$(Na,Ca)_{0.3}(Al,Mg)_2Si_4O_{10}(OH)_2\ n(H_2O)$	–	Y	Y	–
Beidellite	$Na_{0.5}Al_2(Si_3.5Al_{0.5})O_{10}(OH)_2\cdot n(H_2O)$	–	Y	Y	–
Saponite	$(Ca,Na)_{0.3}(Mg,Fe^{2+})_3(Si,Al)_4O_{10}(OH)_2\ 4(H_2O)$	–	Y	Y	–
Nontronite	$Na_{0.3}Fe^{3+}\ 2(Si,Al)\ 4O\ 10(OH)_2\ n(H_2O)$	–	Y	Y	–

wavelengths with such a low degree that magnetite can only be indirectly indicated by a significant vertical offset in the spectrum (Schodlok and Ramanaidou, 2011). Work on vibrational spectroscopy of magnetite has been carried out, for example, by numerous studies (e.g., Gasparov et al., 2000; Lane et al., 2002; Liese, 1967; Chamritski and Burns, 2005; Ebad-Allah et al., 2009).

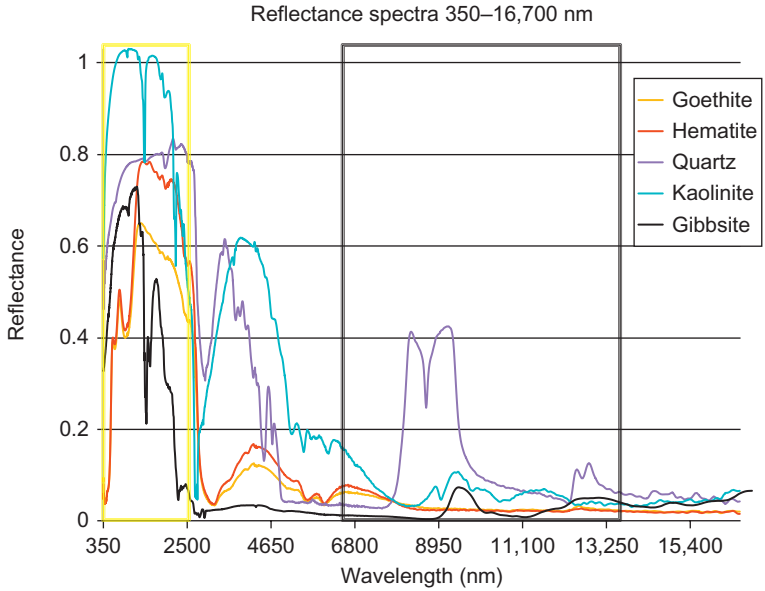

Figure 6.5 Full reflectance spectra of the dominant minerals in DSO (yellow box and black boxes correspond to the wavelength of the HyLogging™ system 1 (yellow box only) and HyLogging™ system 3 (both boxes).

6.4.1.2 Goethite and hematite

In the VNIR region, ochreous and vitreous goethites exhibit a better defined absorption shoulder (~520 nm) at a shorter wavelength compared with the hematitic samples: microplaty hematite and martite (Ramanaidou et al., 2008). The absorption at 700 nm is also more marked for the goethites than the hematitic samples. The microplaty hematite displays an even stronger shift to longer wavelengths (Figure 6.6). The major diagnostic absorption peak for ferric oxide occurs at 900 nm and is correlated to the hematite–goethite ratio (Cudahy and Ramanaidou, 1997; Ramanaidou et al., 2008). The steeper reflectance ramp between 1000 and 1400 nm is typical of vitreous goethite when compared to ochreous goethite (Ramanaidou et al., 2008; Haest et al., 2012b).

In the 6000–14,500 nm wavelength region, goethite shows two prominent reflectance peaks between 11,200–11,400 and 12,400–12,600 nm (Figure 6.5), due to fundamental OH bending vibrations (Cambier, 1986; Glotch et al., 2004; Glotch and Rossman, 2009; Kustova et al., 1992a; Prasad et al., 2006; Ruan et al., 2002; Farmer, 1974). The microplaty hematite spectrum displays a weak absorption at 6500 nm and shows an increase in reflectance between 6000 and 7500 nm and a decrease beyond 7500 nm; the decrease allows the detection of hematite in spectral mixtures (Schodlok and Ramanaidou, 2011).

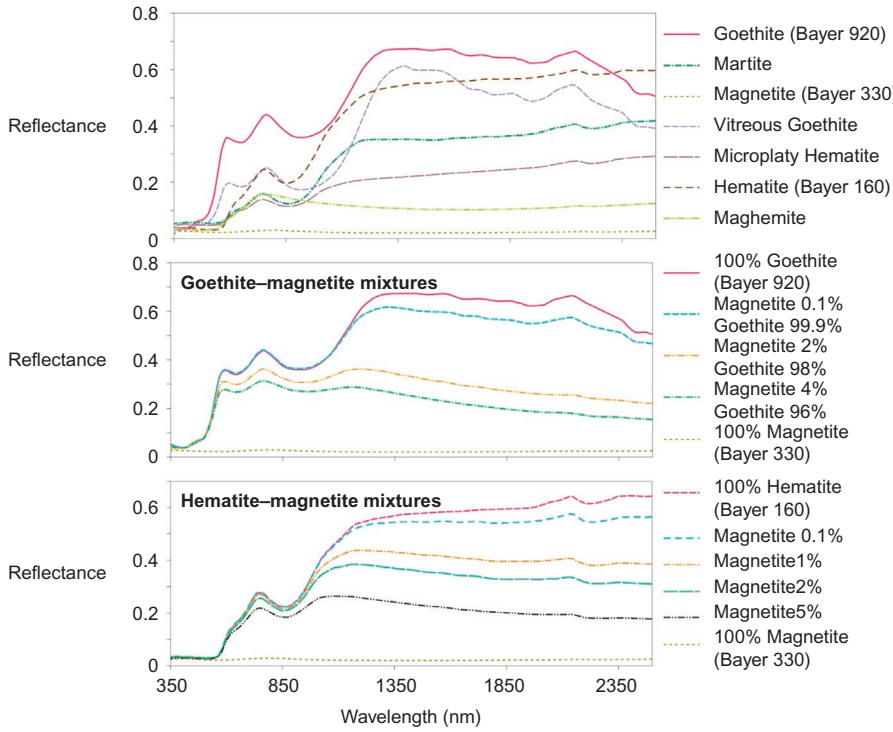

Figure 6.6 Reflectance of iron oxides and oxyhydroxides and their mixtures in the VNIR–SWIR wavelength regions.
Modified from Ramanaidou et al. (2008).

6.4.1.3 *Binary mixtures of iron oxides*

To simulate the natural variations that occur in iron ores, binary mixtures were measured, including magnetite–goethite and magnetite–hematite mixtures (Figure 6.6) and maghemite–goethite, maghemite–hematite, and hematite–goethite mixtures (Figure 6.7). Magnetite drastically influences the reflectance of the spectra, with strong diminution of the albedo, in particular in the SWIR part of the spectrum. However, the wavelength at minimum reflectance of the large ferric absorption near 900 nm is unaffected by the addition of up to 5% magnetite. The addition of up to 5% maghemite produces the same effect as that of magnetite (Ramanaidou et al., 2008).

The reflectance spectra of the binary hematite–goethite mixtures (Figure 6.7) show that the 600 nm shoulder of the goethite spectrum becomes an inflection point at 636 nm in the hematite spectrum. In this particular binary mixture, the minimum wavelength varies from 861 nm for hematite to 918 nm for goethite. The wavelength of the crystal field absorption peak is an excellent proxy for the hematite/hematite + goethite ratio (Figure 6.8). The effect of particle size has to be taken into account for the quantification of the iron oxides as it plays an important role in spectral behavior as shown for goethite in Figure 6.9.

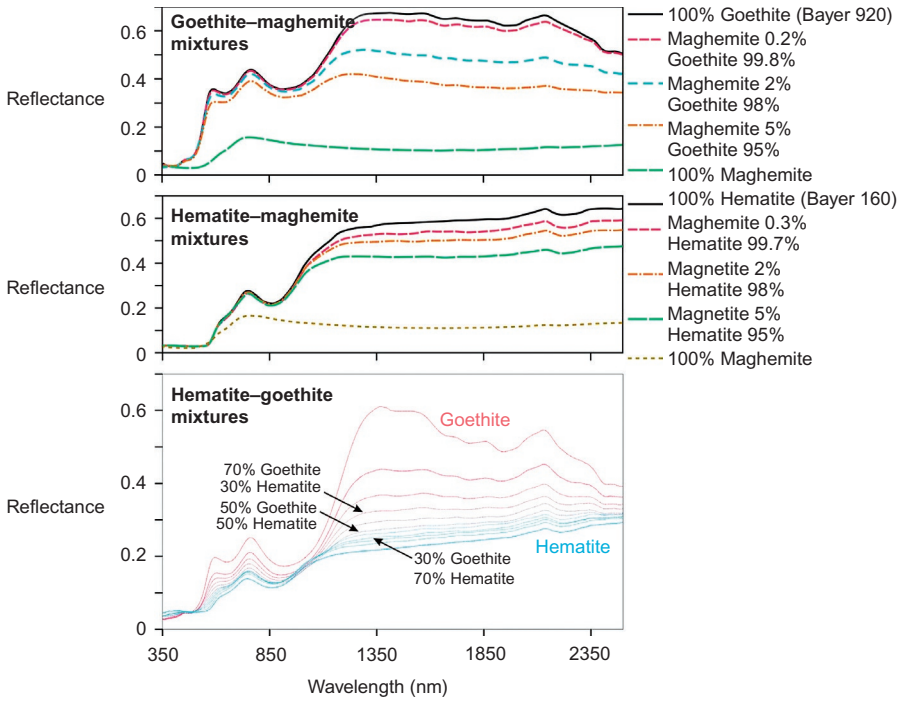

Figure 6.7 Reflectance of iron oxides and oxyhydroxide mixtures in the VNIR–SWIR wavelength regions.
Modified from Ramanaidou et al. (2008).

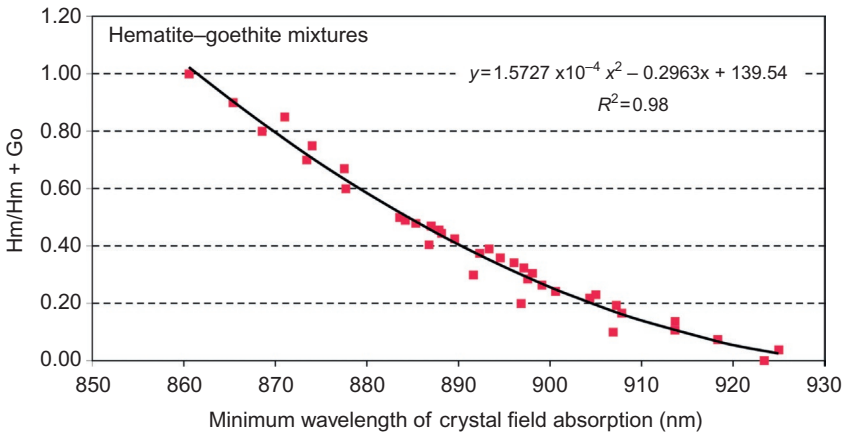

Figure 6.8 Scatterplot of the hematite/hematite + goethite ratio of the minimum wavelength of the crystal field absorption.
Modified from Ramanaidou et al. (2008).

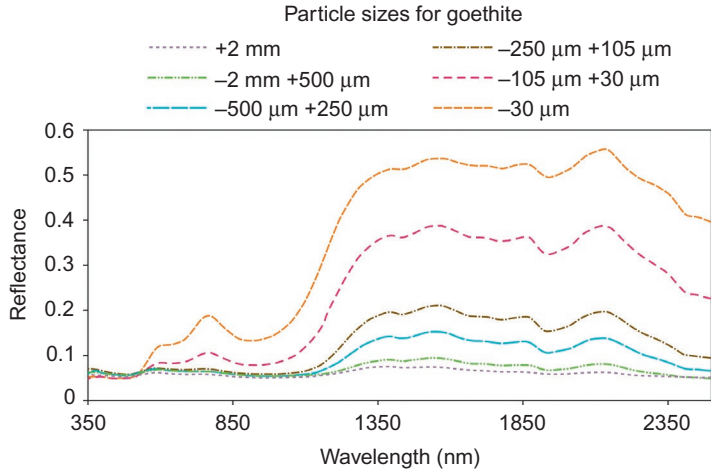

Figure 6.9 Influence of particle size on the spectral behavior of goethite in the VNIR–SWIR wavelength regions.
Modified from Ramanaidou et al. (2008).

6.4.1.4 Gangue minerals

Typical gangue or deleterious minerals associated with iron ore deposits (Table 6.2) have characteristic absorption features at various frequencies of the infrared part of the electromagnetic spectrum. Because of their respective chemical composition, these mineral-specific absorption features cluster in distinct wavelength ranges (Figures 6.2 and 6.5), including

(1) 1300–1600 nm: overtone (2ν) region of structural hydroxyl groups in hydroxyl-bearing minerals
(2) 1900–2500 nm: combination ($\nu + \delta$) region of structural hydroxyl groups in hydroxyl-bearing minerals, overlapping with the carbonate (Figure 6.10) complexes ($3\nu CO_3$)
(3) 2500–3000 nm: hydroxyl stretching fundamentals (νO–H)
(4) 6000–7000 nm (Figure 6.10): CO_3 groups in carbonates
(5) 7500–14,000 nm: Si–O stretching fundamentals in silicates (νSi–O and δO–H)
(6) >14,000: bending fundamentals (δSi–O, δO–H, and δM–O)

For the hydroxyl-bearing silicates, only the hydroxyl-related combination bands in the SWIR region are described in detail, as these minerals can be well characterized in the SWIR alone and in the mid-infrared or MIR. The reader is also referred to the some critical literature summarizing the spectral signatures of major rock-forming minerals (Farmer, 1974; Clark et al., 1990).

6.4.1.4.1 Quartz

In the VNIR, quartz has no diagnostic absorption and only influences the albedo. However, in the MIR wavelength range, quartz has a diagnostic spectral feature at 8627 nm between 8000 and 10,000 nm as a result of asymmetrical stretching vibrations of the Si–O bond (Mustard and Hays, 1997; Ninomiya, 2002; Pitman et al., 2005; Ramsey et al., 1999; Rivard et al., 1993; Wald and Salisbury, 1995; Wenrich and Christensen, 1996; Smith et al.,

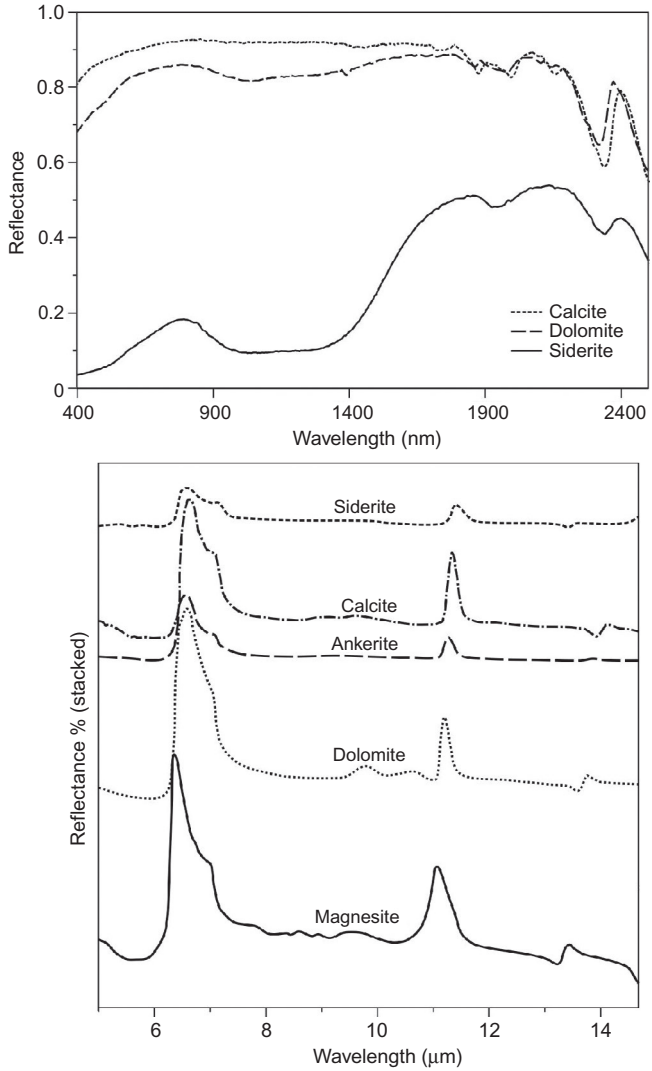

Figure 6.10 VNIR and SWIR (left) and MIR (right) reflectance spectra of carbonates.

2013; Farmer, 1974; Hunt and Logan, 1972; Spitzer and Kleinman, 1961). This feature is still present when the sample is pulped (Salisbury et al., 1991) and can be used to estimate its relative abundance on the base of its relative depth. Weaker features occur between 12,300 and 13,230 nm as a result of symmetrical stretching vibrations of the Si–O bond.

6.4.1.4.2 Clay minerals

Aluminum-bearing clay minerals, classified as dioctahedral phyllosilicates, comprise a large group of minerals including the kaolin group minerals, Al smectites, and white micas that can occur with different types of iron ore deposits. All of

them show diagnostic absorption features in the SWIR and MIR, with considerable overlap due to their similarities in crystal structure and related infrared functional groups.

In the SWIR, kaolin group minerals show a characteristic doublet consisting of a major feature fixed at around 2206 nm associated with a secondary feature between 2160 and 2180 nm (Frost and Johansson, 1998). This doublet can be decomposed into four absorption bands, with the three short wavelength ones related to stretching vibration of the inner hydroxyl groups ($\nu + \delta Al_2OH_i$, i.e., hydroxyl groups bond to the tetrahedral layer) and the major long wavelength one related to stretching vibrations of the outer hydroxyl group ($\nu + \delta Al_2OH_o$) (Frost and Johansson, 1998). Changes in the shape of this characteristic doublet are related to changes in the structure and crystallinity of the kaolin group minerals (Cudahy, 1997, and references therein). Kaolin can also display a weak to medium absorption feature at 2238 nm related to $\nu + \delta(AlFe^{3+})_2OH$, where its intensity increases with increasing ferric iron content. Three more weak combination bands in kaolin group minerals are located around 2317, 2355, and 2380 nm, respectively.

Dioctahedral 2:1 phyllosilicates (10 Å phase) comprise white micas such as paragonite, muscovite, phengite, celadonite, and smectites, such as nontronite and montmorillonite. The dominant absorption feature of these Al–O–H-bearing phyllosilicates in the SWIR ($\nu + \delta Al_2OH$) is located at around 2200 nm. However, smectites and mica-like minerals of the same octahedral composition show a different location of the OH-absorption bands, located at shorter wavelengths (~2200 nm) for smectites and longer wavelengths (~2220 nm) for illite (Crowley and Vergo, 1988; Martinez-Alonso et al., 2002). A second diagnostic absorption feature of white micas is located at 2350 nm, which is absent in smectites and can, therefore, be used to differentiate these two mineral groups.

6.4.1.4.3 Chlorite

Chlorites are trioctahedral 2:1:1 phyllosilicates (14 Å phase) and show characteristic SWIR absorption features at around 2250 and 2340 nm. In the SWIR, chlorites show a shift of the $\nu + \delta(Mg,Fe^{2+})_2OH$ from about 2248 nm for the clinochlore (Mg-rich) to 2261 nm for the chamosite (Fe-rich) end member (McLeod et al., 1987; Bishop et al., 2008). Also, the $\nu + \delta(Mg,Fe^{2+})_3OH$ (inner OH of 2:1 talc layer) at 2340 nm can shift according to the Mg/Fe^{2+} of chlorite.

6.4.1.4.4 Talc

Talc belongs to the group of trioctahedral 2:1 phyllosilicates (9 Å phase). The general composition of talc can be expressed as $Si_4O_{10}M_3(OH)_2$ with a Mg-only occupation of the M sites in the talc *sensu stricto* end member and replacement of Mg by ferrous iron in minnesotaite. In SWIR spectra of pure talc, a characteristic doublet can be observed in the 2300 nm wavelength region that comprises the combination of the stretching at 2720 nm (Petit et al., 2004), with the bending at 15,384 and 14,492 nm, respectively. The two resulting absorption bands are located at 2300 and 2279 nm, respectively, overlapping with the Mg-rich end members of the actinolite and hornblende series, due to their structural similarity. Also the third major absorption band of talc, located

at about 2380 nm, overlaps with Mg-rich amphiboles, such as tremolite. To distinguish talc from these amphiboles, a weak but diagnostic absorption feature at 2080 nm can be used, which is diagnostic only for talc (Laukamp et al., 2012).

6.4.1.4.5 Amphiboles

Major SWIR absorption features of amphiboles in the 2320 and 2380 nm wavelength region are hydroxyl-related combination bands, overlapping with di- and trioctahedral phyllosilicates containing ferric iron, as well as talc and kaolinite. A doublet around 2320 nm can be observed, for example, in Mg-rich end members of the actinolite series (i.e., tremolite), whereas actinolites of an intermediate Mg/Fe^{2+} ratio show a broad feature (actinolite/hornblende) in the same wavelength range. Crocidolite, the fibrous variety of the sodic amphibole riebeckite, is carcinogenic and is common in Australian BIF. The spectral features of amphiboles occur (1) from 8300 to 12,500 nm as a result of dominated Si-O stretching vibration features and weak broad features by Al−O stretching bands and (2) from 12,500 to 16,300 nm as a result of Si−O−Si or Si−O−Al deformation bands (Gillet et al., 1989; Ishida et al., 2008; Andrut et al., 2000; Farmer, 1974). The majority of work on amphibole OH vibration fundamentals was used to estimate cation site positions or quantify chemical compositions (Della Ventura et al., 2005, 2008; Jenkins et al., 2003; Iezzi et al., 2003, 2010; Ishida and Hawthorne, 2001, 2006; Hofmeister and Bowey, 2006; Laukamp et al., 2012).

6.4.1.4.6 Carbonates

Carbonates have several diagnostic absorption features in the SWIR, which all show considerable changes in location and shape, mainly depending on the amount of Mg, Fe, and Mn replacing Ca. The main diagnostic absorption feature in the SWIR ($3\nu 3CO_3$; for summary, see Gaffey, 1986) is located between 2300 and 2340 nm and shows a characteristic left-hand asymmetry pointing to a secondary, smaller feature on the short wavelength limb of the major feature, probably centered in the 2230–2275 nm wavelength region. With increasing amounts of Mg and Fe, such as in dolomite or siderite, the $3\nu 3CO_3$ shifts to shorter wavelengths (Gaffey, 1986). Two further minor features at 1990 and 1870 nm always appear as pairs in carbonates, and, though decreasing in intensity with increasing Mg or Fe content, they display a shift to shorter wavelengths with increasing replacement of Ca by Mg and Fe.

As a result of the asymmetrical C−O stretch vibrations, carbonates diagnostic spectral features are well defined by two strong reflectance peaks between 6000 and 7000 nm and between 11,000 and 12,000 nm. A weaker reflectance peak between 13,400 and 14,200 nm occurs as the result of the bending vibrations of the C−O bond within the CO_3 molecule (Figure 6.10). The wavelength position of the features shifts with the nature of the cation and the bond strength to the CO_3 anion (Gaffey, 1985, 1987; Hunt and Salisbury, 1971; Lane and Christensen, 1997; Ninomiya, 2002; Weir and Lippincott, 1962; Dubrawski et al., 1989a,b; Farmer and Warne, 1978). The individual diagnostic spectral features extracted here are 13,400–13,600 nm for siderite, 13,600–13,950 nm for ankerite/dolomite, and 1395–14,002 nm for calcite.

6.4.1.5 Application of reflectance spectroscopy to iron ore characterization

Schodlok and Ramanaidou (2011) have produced algorithms also called scripts that provide mineralogy and composition in the MIR wavelength range (Figure 6.11) for minerals such as quartz, riebeckite, carbonates. Similarly, to complement those of Schodlok and Ramanaidou (2011), Haest et al. (2012b) developed a series of scripts for the extraction of spectral information in the VNIR and SWIR ranges that can be used in iron ore to generate mineral abundance and composition not only for hematite, goethite, and kaolinite but also for ochreous and vitreous goethite.

6.4.2 Raman spectroscopy of iron ore minerals

The typically small sample area measured during Raman experiments, with spot measurements made in the range 2–5 μm in diameter, means that characterization of iron ore mineralogy can be facilitated at scales beyond that of most other conventional techniques, such as X-ray diffraction (XRD), and demonstrates the power of the technique for *in situ*, fine-scale identification and semiquantification of iron ore mineralogy.

The measured Raman spectra for the main economic ore minerals in Figure 6.12 are similar to spectra reported in the literature for these oxides, for example, Figures 6.1–6.3 reported in De Faria et al. (1997) and Bersani et al. (1999). Depending on the crystal orientation of the sample relative to the detector, enhancement or suppression of particular bands compared to others in the spectrum can occur (e.g., Bersani et al., 1999). For example, magnetite theoretically displays five phonon lines, but typically, only three are recorded (e.g., Das and Hendry, 2011). This may be related to the nature of the mineral surface being analyzed. For example, Bersani et al. (1999) noted that excitation of external surfaces of magnetite displayed five bands, whereas analysis of freshly fractured surfaces excited only three bands. This is less of a problem for multigranular grains, as is usually the case for goethite whose "grains" are typically multidomainic in nature.

Wavelength positions (cm^{-1}) of resolved Stokes Raman lines for the main iron ore oxide phases (e.g., hematite, goethite, magnetite, maghemite, and kenomagnetite) were reviewed and tabulated by Ramanaidou et al. (2008). More recent studies examined other common but, from an iron ore perspective, less common iron oxides, such as lepidocrocite, and akaganeite, and tabulated the Raman lines for these Fe-bearing phases (e.g., Hanesch, 2009; Das and Hendry, 2011). Based on the publically available data, wavenumbers of diagnostic phonon lines for a range of iron oxides/oxyhydroxides are presented in Table 6.3 and Table 6.4. The wavenumber values for each of the iron oxide phases presented in Table 6.3 should be used as a guide only for identification purposes. Shifts in the phonon line position or broadening of phonon lines may occur due to changes in crystallinity or composition. For example, an increase in the average oxidation state of iron in magnetite can shift the main Raman band (from about 665 to 670 cm^{-1}) to higher wavenumbers as reported by van der Weerd et al. (2004), Muralha et al. (2011), and Gomez-Nubla et al. (2013). In addition, broadening of the main phonon lines of goethite at 300 and 390 cm^{-1}

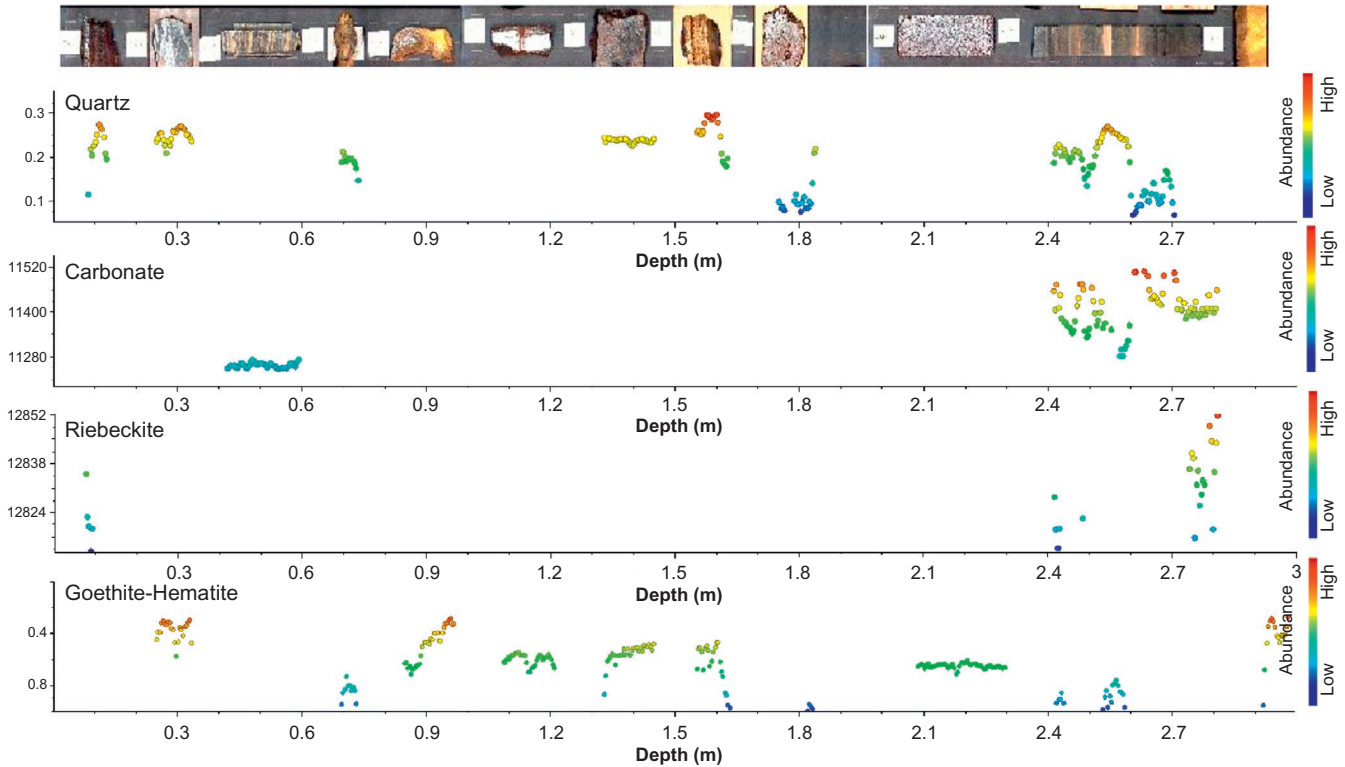

Figure 6.11 MIR Mapping result of twelve iron ore samples. Histogram plots of the mineral abundance and occurrence for quartz, carbonate, riebeckite, goethite, and hematite.

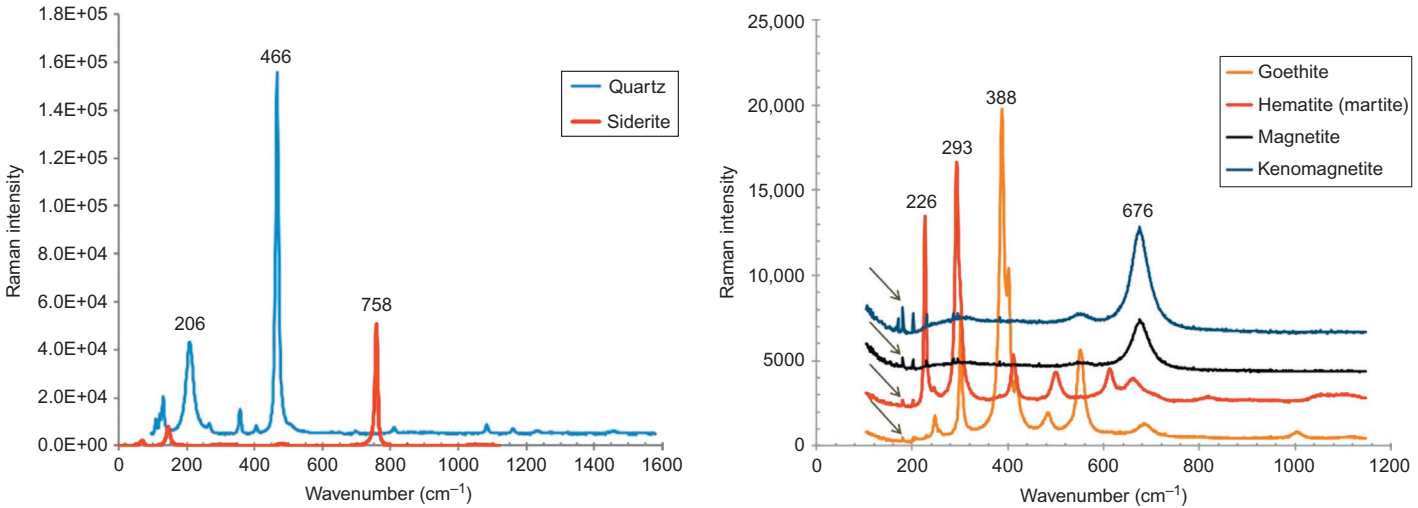

Figure 6.12 Left: Raman spectra of quartz and the Fe carbonate (siderite); some of the diagnostic phonon lines with their corresponding wavenumbers have been labeled. Spectra were taken from the RRUFF site (http://rruff.info/), with quartz as specimen #RU40031 from Spruce Claim, King County, Washington (the United States), and siderite as specimen #R040034 from Příbram, Czech Republic. Spectra have been vertically offset to enable a clearer comparison. Right: Raman spectra of goethite, hematite, magnetite, and kenomagnetite. Spectra were measured from representative examples of the main, high-grade iron ore types mined in Western Australia. Details of the Raman instrumentation used are given in Ramanaidou et al. (2008). Some of the diagnostic phonon lines with their corresponding wavenumber values have been labeled. Spectra have been vertically offset to enable a clearer comparison of each mineral. Peaks in the Raman spectra (arrowed) are spikes due to background or instrument noise.

Table 6.3 **Summary of Raman bands for iron oxides**

Iron oxide	Raman bands														References
Goethite															
						550	474	414	397		298				Thibeau et al. (1978)
									390		298				Keiser et al. (1982)
			685			550	480	420	390		300		245		Ohtsuka et al. (1986)
						557–560	470–489		385–397		300–308		250		Thierry et al. (1988)
									393		300				Johnston (1990)
		995	680			547	469		390		294		245		Synthetic (ferrous iron system)
		995	679			548	476		396	385	297		243		Synthetic (ferric iron system)
		993	685			550	479			385	299		243		De Faria et al. (1997)
		997	663			548	480	417	399	386	303		244		Ramanaidou et al. (2008)
		998	683			549	480	417	398	387	300		246		Ramanaidou et al. (2008)
			680–690			556	480			388–397	300				Ramanaidou et al. (2008)
				657	610–611	556	482–486		392/409		294/300		247		Ramanaidou et al. (2008)

Hematite																
					612		501	414			298	293	245	227		Thibeau et al. (1978)
	1320				615		500	415				295	245	225		Ohtsuka et al. (1986)
					613			423–410			302		249			Thanos (1986)
					613		500	412			299		247	225		Thierry et al. (1988)
					612		500	413			298	293	245	226		Thierry et al. (1988)
								406			296			223		Johnston (1990)
	1320				614		496	412			300	294	246	228		Massey et al. (1990)
					613		498	412			299	293	247	225		De Faria et al. (1997)
		816–820	707	660	611	552	497	411			298	293	244	226		Ramanaidou et al. (2008) (martite)
		820		660–663	612–613		498	411			298	293	245	226		Ramanaidou et al. (2008) (hematite)
Magnetite																
			667													Keiser et al. (1982)
			663	616												Thibeau et al. (1978)

Continued

Table 6.3 Continued

Iron oxide	Raman bands														References
			665		540										Ohtsuka et al. (1986)
		706	666		570		490		336						Graves et al. (1988)
			676		550			420*	320		298*				Thierry et al. (1988)
			670		550										Thierry et al. (1988)
			669		540			415*	319		294*				Odziemkowski et al. (1994)
			668		538		450–490		306					193	Shebanova and Lazor (2003b)
			663		534	513			302						De Faria et al. (1997)
			672		549				310						Ramanaidou et al. (2008)
Maghemite															
	1440	715	670		645	515		395	345		300*		265		Ohtsuka et al. (1986)
		740			650	505		380	350				263	193	Thierry et al. (1988)
Kenomagnetite															
			675		547				308						Ramanaidou et al. (2008)

*Excitation bands reported for magnetite are most likely due to small amounts of hematite.

Table 6.4 **Diagnostic Raman bands for the main iron oxides of economic interest in iron ore**

Mineral	Raman bands (cm^{-1})										
Goethite	993–997	679–685		547–560	470–486		**385–399**	298–308		243–247	
Hematite (form)											
Martite			612–618		500	414–421		298–302	293–295	245–256	**225–227**
Single crystal			613			423–410		302		249	
Polycrystal			611–614		496–501	406–412		296–300	292–294	244–247	**223–228**
Magnetite (form)											
		663–667		540							
Theoretical	706	**666**		570	490			336			
Polycrystal		**663–676**		534–550	450–490			302–320			
Kenomagnetite		**675**		547				308			
Maghemite	**715–740**	670	**645–665**		505–515		380–395	345–350		263–265	

Bands highlighted in bold are the most intense bands recorded for each phase.

has been related to increasing Al substitution in goethite (Ramanaidou et al., 1996; Liu et al., 2013).

Raman spectra have been reported for commonly occurring Al-bearing gangue minerals such as kaolinite (e.g., Michaelian, 1986; Frost et al., 1988) and gibbsite (e.g., Ruan et al., 2001). Diagnostic Raman lines for quartz, siderite, goethite, hematite, magnetite and kenomagnetite are shown in Figure 6.12.

6.4.2.1 *Application of Raman spectroscopy to iron ore characterization*

The combination of the very strong and diagnostic Raman response to ore mineralogy and the utility of the technique, particularly the nondestructive nature of the method, has seen the application of Raman spectroscopy across a wide range of disciplines, wherever fine-scale identification and characterization of iron oxides and related mineralogy have been required. Such diverse applications have included archeometry (e.g., Bikiaris et al., 2000; Neff et al., 2004; de Lucas et al., 2006; Baraldi et al., 2007), biomineralization studies (e.g., Lee et al., 2002), pedology (e.g., Trolard et al., 1997), thermal analysis (e.g., Kustova et al., 1992b), and planetary science (e.g., Wiens et al., 2005; Chevrier and Mathe, 2007; Dreyer and Mungas, 2007).

Of more relevance to the iron ore and steel-making industries is the use of the technique in corrosion investigations of iron electrode surfaces (Johnston, 1990; Ocampo et al., 2006) and high-temperature oxidation studies of iron and stainless steel, such as during early (Muralha et al., 2011) and modern-day, hot rolling operations (Inoue et al., 1990; Chattopadhyay et al., 2005; Marciuš et al., 2012). Using a combination of techniques such as XRD, Mossbauer, and Raman, Marciuš et al. (2012) established that high-temperature oxidation of iron was initiated with the formation of wüstite ($Fe_{1-x}O$) and proceeds through the transformation of intermediate magnetite, to hematite as the final oxidation product. This has implications in the efficiency of the pickling treatment of hot-rolled steel where the metallography of the oxide scale formed is dependent on the steel composition and can significantly influence residency time of the steel in the acid bath (Raman et al., 1998; Chattopadhyay et al., 2005).

Other studies have applied the technique to characterizing by-products of steel hot rolling processing such as mill scale, which may be used as a source of iron oxides of pigment quality (Legodi and de Waal, 2007), and to characterizing the mineralogy of steel mill scale iron waste to assist in the evaluation of its use as an alternative by-product in, for example, road construction and cement production (Gomez-Nubla et al., 2013).

However, it is only relatively recently that studies have applied the technique directly to iron ore characterization. A number of recent studies have used Raman spectroscopy to aid characterization of the middle Eocene ironstones of the Bahariya depression, Western Desert, Egypt (e.g., Salama et al., 2012), and used Raman spectroscopy to aid facies characterization of the three main ore types (black Mn-bearing muds, yellow-brown ironstones of microbial origin, and lateritic iron ores) of the region (Baioumy et al., 2013; Ciobotă et al., 2012; Salama et al., 2012). Raman spectroscopy

confirmed the occurrence of well-preserved organic material in the stromatolitic and ooidal–oncoidal facies Bahariya ores (e.g., Ciobotă et al., 2012; Salama et al., 2012). Detection of carotenoids, proteins, lipids, and celluloses as biomarkers for organisms such as bacteria, fungi, or algae and other organic compounds of an inferred marine origin provided evidence that the formation of ferriferous oncoids and ooids was microbially mediated (Ciobotă et al., 2012; Salama et al., 2012).

More recent work by Baioumy et al. (2013) used a combination of techniques to elucidate the nature of high-Mn iron ores, with MnO content up to 13.9 wt%, of the Bahariya depression. These authors concluded that a combination of XRD and Raman spectroscopy provided the best strategy, compared to previous investigations which used only Raman spectroscopy (e.g., Salama et al., 2012), for distinguishing the various Mn minerals in the Bahariya ironstones. Ciobotă et al. (2012), Salama et al. (2012), and Baioumy et al. (2013) identified a number of Mn-bearing minerals in the Bahariya ironstones, which occur as a range of Mn oxides (e.g., bixbyite, $(Mn,Fe)_2O_3$, and cryptomelane, $(Mn,K)_8O_6$) and hydroxides (e.g., pyrochroite, $Mn(OH)_2$), and classified these into three groups on the basis of similarities in their Raman spectra. Such Mn-bearing minerals tend to display their main Raman bands in the 500–650 cm^{-1} region (Ciobotă et al., 2012), away from the main excitation lines of goethite and hematite which occur in the wavenumber range 200–400, and so avoid peak overlap that may interfere with their identification.

As well as providing mineralogical information, Raman spectroscopy can also yield information regarding iron oxide chemistry where calibration against a suitable, representative set of standards of known composition is made. As previously mentioned, substitution of Fe^{3+} by foreign metal cations, such as Al^{3+}, within the structures of hematite and goethite can influence the crystallinity of the oxides. This is manifested in excitation experiments as a broadening of the goethite bands (Ramanaidou et al., 1996). More directly, substitution of Fe^{3+} by cations such as Al^{3+} in the crystal structures of goethite and hematite decreases the unit-cell dimensions of these oxides (e.g., Schwertmann et al., 1979; Schwertmann and Carlson, 1994). Excitation experiments (Ramanaidou et al., 1996) of both Al-bearing goethite and Al-bearing hematite displayed a shift in position of the main phonon lines of goethite (≈390 cm^{-1}) and hematite (1320–660 cm^{-1}) with increasing Al content (Figure 6.13). Changes in the relative intensities of the O^{2-} displacement peaks at 411 and 293 cm^{-1} for synthetic Al-bearing hematite were also well correlated with Al content (Ramanaidou et al., 1996).

Later investigations of the influence of Al on the Raman spectra of synthetic goethite (Liu et al., 2013) and synthetic hematite (Zoppi et al., 2008) reported similar effects with increasing Al content and shifts in the diagnostic phonon lines of goethite and hematite. For the synthetic Al-bearing goethite produced by Liu et al. (2013), under conditions similar to those used by Ramanaidou et al. (1996), a number of Raman bands, particularly the band at 299 cm^{-1}, were linearly related to increasing Al content. For Al-substituted hematite with up to 10 mol% Al, the incorporation of Al in the structure of hematite resulted in the development of a unique band at about 430 cm^{-1} attributed to a vibration ($\upsilon 6$) involving Al^{3+} ions with the band position linearly related to increasing Al content (Zoppi et al., 2008). These authors also reported the development of a broad band at about 670 cm^{-1} with increasing Al content.

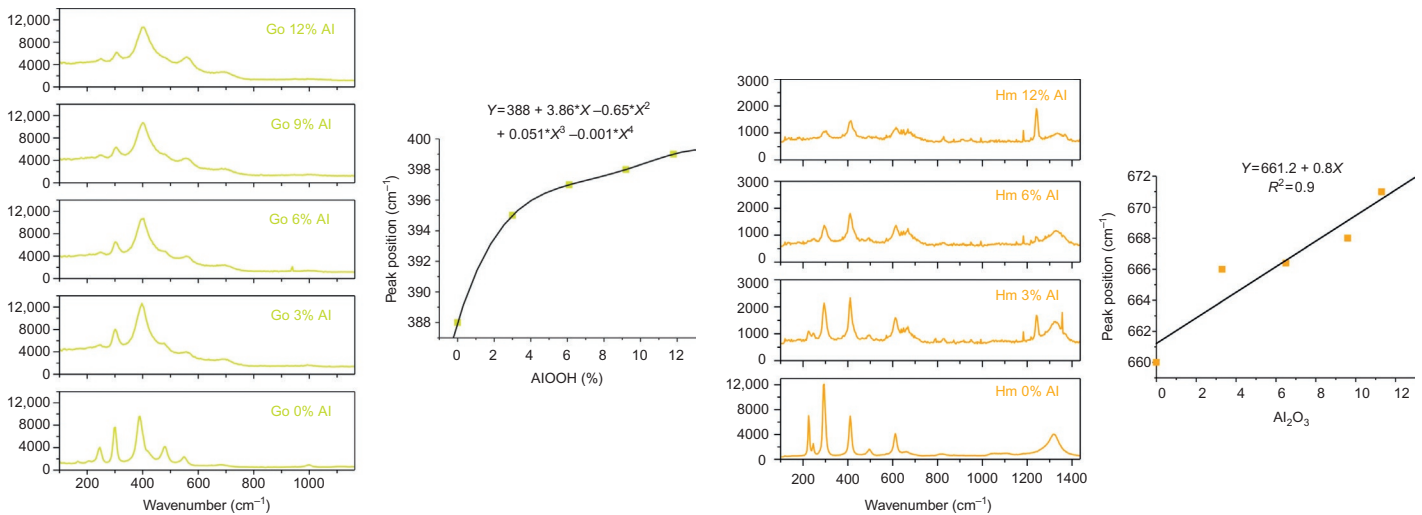

Figure 6.13 Left: Raman spectra of synthetic Al-bearing goethite showing the influence of increasing Al content on the wavelength position and broadening of the Raman bands and the relationship between Al content and the wavenumber of the band at ≈400 cm^{-1}. Al-bearing goethites were prepared by the method of Fey and Dixon (1981). Right: Raman spectra of synthetic Al-bearing hematite showing the influence of increasing Al content on the wavelength position and broadening of the Raman bands and the relationship between Al content and the wavenumber of the band at ≈670 cm^{-1}. Al-bearing hematites were prepared by the method of Wells et al. (2001).

Differences in the relationships between measured Raman shifts and Al content reported in the literature may be attributed to the different procedures used for synthesizing both Al-substituted goethite and Al-substituted hematite. For example, Al-substituted hematites studied by Zoppi et al. (2008) were prepared by calcination (~1000 °C) of mixed Fe–Al–oxalate precipitates, and these authors noted that different phonon line shifts can be observed for hematite produced at low and high temperatures, associated with differences in the morphological characteristics of hematites prepared at different temperatures. However, this may be an indirect effect with changes in the morphology of hematite reflecting recrystallization effects (e.g., sintering) toward improved structural ordering as temperature increases.

A similar influence of Al on the Raman spectra of magnetite, where solid solution of 7 wt% alumina in magnetite shifted the main A_{1g} band to higher wavenumbers toward the isostructural end-member hercynite, $FeAl_2O_4$, was reported (Muralha et al., 2011). The displacement of the main phonon line of magnetite was, in part, attributed to the presence of trace amounts of Co, Ni, and Al replacing Fe in magnetite in mill black slag (Gomez-Nubla et al., 2013) and by Ni in magnetite inclusions in early (approximately late 1830s) Russian Pt coins (van der Weerd et al., 2004). In the case of Al, further work is required with a range of iron and aluminum spinels along the magnetite–hercynite solid-solution series to determine if a Raman calibration line, similar to the empirical Vegard line relationships used to estimate goethite composition based on changes in unit-cell parameters (e.g., Schulze, 1984; Li et al., 2006), can be established to estimate the Al content of magnetite. However, van der Weerd et al. (2004) concluded that the significant shift to higher wavenumbers from 665 to 680 cm^{-1} of the main magnetite line measured in their study was more likely due to differences (i.e., an increase) in the mean oxidation state of Fe in magnetite rather than due to small variations in composition. These authors suggested that Raman spectroscopy may be a useful tool to evaluate the oxidation state of Fe in magnetite but did note the importance small compositional changes may play in the efficacy of this approach. Clearly, a thorough investigation is required to evaluate both the compositional and mean oxidation state of Fe on the Raman behavior of magnetite and the implications to the practical applications this may have.

However, during excitation experiments, care needs to be taken to prevent thermal transformation (e.g., goethite to hematite) and oxidation reactions (e.g., magnetite to hematite) that may be induced from excessive laser power and/or long acquisition times as has been previously reported (De Faria et al., 1997; Shebanova and Lazor, 2003b; Slavov et al., 2010). The irreversible transformation of magnetite, with increasing laser power, can proceed through the formation of the intermediate phase maghemite, γ-Fe_2O_3, before final conversion to hematite (Li et al., 2012) though factors, such as particle size and composition (i.e., presence of trace elements) as well as laser power under which excitation occurs, can influence the rate of transformation and the products formed. For example, oxidation of fine (<0.3 μm) particles of magnetite proceeds through the formation of metastable maghemite, whereas larger particles are oxidized directly to α-Fe_2O_3 (Shebanova and Lazor, 2003b). Similarly, maghemite can also be transformed to hematite if the laser power is too high (of the order of 1 mW) (Hanesch, 2009).

Hydrous iron oxides, such as goethite (α-FeOOH) and lepidocrocite (γ-FeOOH), and less well-ordered phases, such as ferrihydrite with a general formula, $5Fe_2O_3.9H_2O$, are particularly sensitive to transformation to their anhydrous derivatives: goethite and ferrihydrite transform to hematite, whereas lepidocrocite transforms to maghemite, γ-Fe_2O_3. de Faria and Lopes (2007) evaluated if Raman spectroscopy may be useful in discriminating hematite formed by the low-temperature transformation of goethite and poorly ordered hematite and concluded there was no distinction in the measured Raman spectra. Hence, Raman-induced formation of hematite will likely be indistinguishable from hematite found naturally within a sample. In testing a wide range of synthetic and natural iron oxides, Hanesch (2009) recommended laser power settings in the range 0.01–0.1 mW be used initially to test the stability of the material to laser-induced transformation and to minimize artificial changes to sample mineralogy.

6.5 Future trends

The utilization of reflectance spectroscopic analysis in the VNIR, SWIR, and MIR wavelength ranges is now firmly established as a technique for rapid, semiquantitative analysis of iron ore mineralogy. Previous applications have seen the technique used to quantify the hematite–goethite ratio in ore deposits (Cudahy and Ramanaidou, 1997; Ramanaidou et al., 2008), as well as to characterize the mineralogy of bedded iron deposits derived Indian and Brazilian iron ores (e.g., Costa et al., 2009; Thangavelu et al., 2011). More recently, CSIRO's automated HyLogging™ core scanning system was used to aid resource definition of the Rocklea Dome CID (Haest et al., 2012a) and was used to better define the gangue mineralogy, mainly Al-bearing phases such as kaolinite and gibbsite, at the Bonnie Creek CID (Wells and Hogan, 2013). New and fast imaging spectrometers, such as the Corescan and SisuROCK instruments, are now being used routinely and might eventually replace point analysis systems, such as the HyLogging™ systems. These systems also now provide imaging capability in the MIR range.

Ongoing research in our laboratory has focused on using the discriminatory power of Raman spectroscopy for the characterization of iron ore mineralogy either as a stand-alone technique (Ramanaidou and Wells, 2011b; Wells and Ramanaidou, 2012) or in combination with the HyLogging™ system 1 scanning platform for routine, high-volume characterization of iron ore mineralogy (Wells and Ramanaidou, 2013). The application of Raman spectroscopic imaging analysis of BIF, BID, and CID samples presented as thin sections or polished blocks confirmed the identification of the main iron oxide and gangue phases. For example, hematite, quartz and carbonate, and siderite were easily detected, with Raman measurements recorded by Ramanaidou and Wells (2011b) providing the first reported occurrence of pistomesite (high Mg-bearing siderite, containing between 30 and 50 wt% $MgCO_3$) in BIF. The success of this earlier work provided the impetus for development of a combined Raman-HyLogging™ systems for iron ore characterization that was similarly successful in detecting the main iron ore oxide and gangue minerals (Wells and Ramanaidou, 2013). However, detection of magnetite, a significant iron oxide in MID (BIF-derived magnetite iron

deposits) ores, for test samples of BIF drill core proved problematic, and further work is ongoing to optimize the scanning conditions, including laser power and excitation time versus scanning time of the core, to enable detection of magnetite.

The addition of other sensors for magnetic susceptibility, chemical analyses using X-ray fluorescence (XRF) or laser-induced breakdown spectroscopy (LIBS), and surface profiling, and high-resolution visible cameras is now being actively explored. The real breakthrough will be in the ability of fusing all the data that will provide automated information for geometallurgical characterization across the value chain.

References

Andrut, M., Gottschalk, M., Melzer, S., Najorka, J., 2000. Lattice vibrational modes in synthetic tremolite-Sr-tremolite and tremolite-richterite solid solutions. Phys. Chem. Miner. 27, 301–309.

Baioumy, H.M., Khedr, M.Z., Ahmed, A.H., 2013. Mineralogy, geochemistry and origin of Mn in the high-Mn iron ores, Bahariya Oasis, Egypt. Ore Geol. Rev. 53, 63–76.

Baraldi, P., Baraldi, C., Curina, R., Tassi, L., Zannini, P., 2007. A micro-Raman archaeometric approach to Roman wall paintings. Vib. Spectrosc. 43, 420–426.

Bersani, D., Lottici, P.P., Montenero, A., 1999. Micro-Raman investigation of iron oxide films and powders produced by sol-gel synthesis. J. Raman Spectrosc. 30, 355–360.

Bikiaris, D., Daniilia, S.X., Sotiropoulou, S., Katsimbiri, O., Pavlidou, E., Moutsatsou, A.P., Chryssoulakis, Y., 2000. Ochre-differentiation through micro-Raman and micro-FTIR spectroscopies: application on wall paintings at Meteora and Mount Athos, Greece. Spectrochim. Acta A Mol. Biomol. Spectrosc. 56, 3–18.

Bishop, J.L., Lane, M.D., Dyar, M.D., Brown, A.J., 2008. Reflectance and emission spectroscopy study of four groups of phyllosilicates: smectites, kaolinite-serpentines, chlorites and micas. Clay Miner. 43, 35–54.

Cambier, P., 1986. Infrared study of goethites of varying crystallinity and particle-size. 2. Crystallographic and morphological-changes in series of synthetic goethites. Clay Miner. 21, 201–210.

Chamritski, I., Burns, G., 2005. Infrared- and Raman-active phonons of magnetite, maghemite, and hematite: a computer simulation and spectroscopic study. J. Phys. Chem. B 109, 4965–4968.

Chattopadhyay, A., Bandyopadhyay, N., Das, A.K., Panigrahi, M., 2005. Oxide scale characterization of hot rolled coils by Raman spectroscopy technique. Scr. Mater. 52, 211–215.

Chevrier, V., Mathe, P.E., 2007. Mineralogy and evolution of the surface of Mars: a review. Planet. Space Sci. 55, 289–314.

Ciobotă, V., Salama, W., Tarcea, N., Rösch, P., El Aref, M., Gaupp, R., Popp, J., 2012. Identification of minerals and organic materials in Middle Eocene ironstones from the Bahariya Depression in the Western Desert of Egypt by means of micro-Raman spectroscopy. J. Raman Spectrosc. 43, 405–410.

Clark, R.N., King, T.V.V., Klejwa, M., Swayze, G.A., Vergo, N., 1990. High spectral resolution reflectance spectroscopy of minerals. J. Geophys. Res. 95, 12653–12680.

Costa, G.M.D., Barrón, V., Ferreira, C.M., Torrent, J., 2009. The use of diffuse reflectance spectroscopy for the characterization of iron ores. Miner. Eng. 22, 1245–1250.

Crowley, J.K., Hook, S.J., de Souza Filho, C.R., de Pereira Silva, G., Bridges, N.T., Thomson, B.J., Kargel, J.S., Brown, A.J., Ribeiro Da Luz, B., Baldwin, A., Marion, G.M., Anonymous, 2008. Spectral diversity of terrestrial banded iron formations and associated rocks: implications

for Mars remote sensing. In: Abstracts of Papers Submitted to the Lunar and Planetary Science Conference, 39, 0-Abstract 1263.
Crowley, J.K., Vergo, N., 1988. Near-infrared reflectance spectra of mixtures of kaolin-group minerals: use in clay mineral studies. Clay Clay Miner. 36, 310–316.
Cudahy, T., 1997. Pima-II spectral characteristics of natural kaolins. CSIRO, p. 62.
Cudahy, T.J., Ramanaidou, E.R., 1997. Measurement of the hematite:goethite ratio using field visible and near-infrared reflectance spectrometry in channel iron deposits, Western Australia. Aust. J. Earth Sci. 44, 411–420.
Das, R.S., Agrawal, Y.K., 2011. Raman spectroscopy: recent advancements, techniques and applications. Vib. Spectrosc. 57, 163–176.
Das, S., Hendry, M.J., 2011. Application of Raman spectroscopy to identify iron minerals commonly found in mine wastes. Chem. Geol. 290, 101–108.
de Faria, D.L.A., Lopes, F.N., 2007. Heated goethite and natural hematite: can Raman spectroscopy be used to differentiate them? Vib. Spectrosc. 45, 117–121.
De Faria, D.L.A., Silva, S.V., de Oliveira, M.T., 1997. Raman microscopy of some iron oxides and oxyhydroxides. J. Raman Spectrosc. 28, 873–878.
de Lucas, M.C.M., Moncada, F., Rosen, J., 2006. Micro-Raman study of red decorations in French faiences of the 18th and 19th centuries. J. Raman Spectrosc. 37, 1154–1159.
Della Ventura, G., Bellatreccia, F., Iezzi, G., Oberti, R., Camara, F., 2008. The P2 (sub 1)/m-C2/m phase transition in synthetic amphiboles in the system Li (sub 2) O-Na (sub 2) O-MgO-SiO (sub 2) -H (sub 2) O: a high-T FTIR study. Eur. J. Mineral. 20, 1019–1026.
Della Ventura, G., Redhammer, G.J., Iezzi, G., Hawthorne, F.C., Papin, A., Robert, J.-L., 2005. A Mössbauer and FTIR study of synthetic amphiboles along the magnesioriebeckite-ferriclinoholmquistite join. Phys. Chem. Miner. 32, 103–113.
Dreyer, C.B., Mungas, G.S., 2007. Integrated micro-LIBS, Raman spectroscopy, and microscope for space exploration. In: 38th Lunar and Planetary Science Conference, 12–16 March 2007, League City, Texas, pp. 2307–2308.
Dubessy, J., Caumon, M.-C., Rull, F., 2012. Raman Spectroscopy Applied to Earth Sciences and Cultural Heritage. European Mineralogical Union, London.
Dubrawski, J.V., Channon, A.L., Warne, S.S.J., 1989a. The effects of substitution in the dolomite-ferroan dolomite-ankerite series as illustrated by FTIR. Neues Jahrb. Mineral. Monatsh. 1989, 337–344.
Dubrawski, J.V., Channon, A.L., Warne, S.S.J., 1989b. Examination of the siderite-magnesite mineral series by Fourier transform infrared spectroscopy. Am. Mineral. 74, 187–190.
Duuring, P., Hagemann, S.G., Novikova, Y., Cudahy, T., Laukamp, C., 2012. Targeting iron Ore in banded iron formations using ASTER data: Weld Range Greenstone Belt, Yilgarn Craton, Western Australia. Econ. Geol. 107, 585–597.
Ebad-Allah, J., Baldassarre, L., Sing, M., Claessen, R., Brabers, V.A.M., Kuntscher, C.A., 2009. Infrared studies of magnetite under high pressure. High Pressure Res. 29, 500–503.
Farmer, V.C., 1974. The infrared spectra of minerals. In: Farmer, V.C. (Ed.), Monograph—Mineralogical Society, vol. 4. Mineralogical Society, London.
Farmer, V.C., Warne, S.S.J., 1978. Infrared spectroscopic evaluation of iron contents and excess calcium in minerals of the dolomite-ankerite series. Am. Mineral. 63, 779–781.
Fey, M.V., Dixon, J.B., 1981. Synthesis and properties of poorly crystalline hydrated aluminous goethites. Clay Clay Miner. 29 (2), 91–100.
Fraser, S.J., Whitbourn, L., Yang, K., Ramanaidou, E., Connor, P., Poropat, G., Soole, P., Mason, P., Coward, D., Phillips, R., 2006. Mineralogical face-mapping using hyperspectral scanning for mine mapping and control. In: 2006 Australia (AUS), AusIMM – Australasian Institute of Mining and Metallurgy, Carlton, Victoria, Australia (AUS), pp. 227–232.

Frost, R.L., Johansson, U., 1998. Combination bands in the infrared spectroscopy of kaolins—a drift spectroscopic study. Clay Clay Miner. 46, 466–477.
Frost, R.L., Tran, T.H., Rintoul, L., Kristof, J., 1988. Raman microscopy of dickite, kaolinite and their intercalates. Analyst 123, 611–616.
Fujisada, H., Sakuma, F., Ono, A., Kudoh, M., 1998. Design and preflight performance of ASTER instrument protoflight model. IEEE Trans. Geosci. Remote Sens. 36 (4), 1152–1160.
Gaffey, S.J., 1985. Reflectance spectroscopy in the visible and near-infrared (0.35–2.55 μm): applications in carbonate petrology. Geology (Boulder) 13, 270–273.
Gaffey, S.J., 1986. Spectral reflectance of carbonate minerals in the visible and near infrared (0.35–2.55 microns): calcite, aragonite, and dolomite. Am. Mineral. 71, 151–162.
Gaffey, S.J., 1987. Spectral reflectance of carbonate minerals in the visible and near infrared (0.35–2.55 μm): anhydrous carbonate minerals. J. Geophys. Res. 92, 1429–1440.
Gasparov, L.V., Tanner, D.B., Romero, D.B., Berger, H., Margaritondo, G., Forro, L., 2000. Infrared and Raman studies of the Verwey transition in magnetite. Phys. Rev. B 62, 7939–7944.
Gillet, P., Reynard, B., Tequi, C., 1989. Thermodynamic properties of glaucophane: new data from calorimetric and spectroscopic measurements. Phys. Chem. Miner. 16, 659–667.
Glotch, T.D., Morris, R.V., Christensen, P.R., Sharp, T.G., 2004. Effect of precursor mineralogy on the thermal infrared emission spectra of hematite: application to Martian hematite mineralization. J. Geophys. Res. Planets 109, E07003.
Glotch, T.D., Rossman, G.R., 2009. Mid-infrared reflectance spectra and optical constants of six iron oxide/oxyhydroxide phases. ICAUS 204, 663–671.
Gomez-Nubla, L., Aramendia, J., de Vallejuelo, S.F.O., Castro, K., Madariaga, J.M., 2013. From portable to SCA Raman devices to characterize harmful compounds contained in used black slag produced in Electric Arc Furnace of steel industry. J. Raman Spectrosc. 44, 1163–1171.
Graves, P.R., Johnston, C., Campaniello, J.J., 1988. Raman scattering in spinel structure ferrites. Mater. Res. Bull. 23, 1651–1660.
Haest, M., Cudahy, T., Laukamp, C., Gregory, S., 2012a. Quantitative mineralogy from infrared spectroscopic data. II. Three-dimensional mineralogical characterisation of the Rocklea channel iron deposit, Western Australia. Econ. Geol. 107, 229–249.
Haest, M., Cudahy, T., Laukamp, C., Gregory, S., 2012b. Quantitative mineralogy from infrared spectroscopic data. I. Validation of mineral abundance and composition scripts at the Rocklea Channel iron deposit in Western Australia. Econ. Geol. 107, 209–228.
Haest, M., Cudahy, C., Rodger, A., Laukamp, C., Martens, E., Caccetta, M., 2013. Unmixing vegetation from airborne visible-near to shortwave infrared spectroscopy-based mineral maps over the Rocklea Dome (Western Australia), with a focus on iron rich palaeochannels. Remote Sens. Environ. 129, 17–31.
Hanesch, M., 2009. Raman spectroscopy of iron oxides and (oxy)hydroxides at low laser power and possible applications in environmental magnetic studies. Geophys. J. Int. 177, 941–948.
Harris, D.C., Bertolucci, M.D., 1989. Symmetry and Spectroscopy an Introduction to Vibrational and Electronic Spectroscopy. Dover Publications, Inc., New York.
Hofmeister, A.M., Bowey, J.E., 2006. Quantitative infrared spectra of hydrosilicates and related minerals. Mon. Not. R. Astron. Soc. 367, 577–591.
Hunt, G.R., Logan, L.M., 1972. Variation of single-particle mid-infrared emission-spectrum with particle-size. Appl. Opt. 11, 142–147.
Hunt, G.R., Salisbury, J.W., 1971. Visible and near-infrared spectra of minerals and rocks. II. Carbonates. Mod. Geol. 2, 23–30.
Huntington, J., Quigley, M., Yang, K., Roache, T., Young, T., Young, C., Roberts, I., Whitbourn, L., Mason, P., 2006. A geological overview of Hylogging 18000m of core from the eastern Goldfields of Western Australia. In: 6th International Mining Geology Conference, Darwin NT.

Iezzi, G., Della Ventura, G., Camara, F., Pedrazzi, G., Robert, J.-L., 2003. ^{B}Na–^{B}Li solid-solution in a-site-vacant amphiboles: synthesis and cation ordering along the ferri-clinoferroholmquistite-riebeckite join. Am. Mineral. 88, 955–961.

Iezzi, G., Della Ventura, G., Tribaudino, M., Nemeth, P., Margiolaki, I., Cavallo, A., Gaillard, F., Behrens, H., 2010. Phase transition induced by solid solution: the (super B) Ca- (super B) Mg substitution in richteritic amphiboles. Am. Mineral. 95, 369–381.

Inoue, S., Uchida, H., Morii, M., Koterazawa, K., 1990. Characterisation by Raman spectroscopy of oxide layer formed on stainless steels. J. Jpn. Inst. Metals 54, 1376–1381.

Ishida, K., Hawthorne, F.C., 2001. Assignment of infrared OH-stretching bands in manganoan magnesio-arfvedsonite and richterite through heat-treatment. Am. Mineral. 86, 965–972.

Ishida, K., Hawthorne, F.C., 2006. Assignment of infrared OH-stretching bands in calcic amphiboles through deuteration and heat treatment. Am. Mineral. 91, 871–879.

Ishida, K., Jenkins, D.M., Hawthorne, F.C., 2008. Mid-IR bands of synthetic calcic amphiboles of tremolite-pargasite series and of natural calcic amphiboles. Am. Mineral. 93, 1112–1118.

Jenkins, D.M., Bozhilov, K.N., Ishida, K., 2003. Infrared and TEM characterization of amphiboles synthesized near the tremolite-pargasite joint in the ternary system tremolite-pargasite-cummingtonite. Am. Mineral. 88, 1104–1114.

Johnston, C., 1990. In situ laser Raman microprobe spectroscopy of corroding iron electrode surfaces. Vib. Spectrosc. 1, 87–96.

Keiser, J.T., Brown, C.W., Heidersbach, R.H., 1982. The electrochemical reduction of rust films on weathering steel surfaces. J. Electrochem. Soc. 129, 2686–2689.

Kustova, G.N., Burgina, E.B., Sadykov, V.A., Poryvaev, S.G., 1992a. Vibrational spectroscopic investigation of the goethite thermal-decomposition products. Phys. Chem. Miner. 18, 379–382.

Kustova, G.N., Burgina, E.B., Sadykov, V.A., Poryvaev, S.G., 1992b. Vibrational spectroscopic investigation of the goethite thermal decomposition products. Phys. Chem. Miner. 18, 379–382.

Lane, M.D., Christensen, P.R., 1997. Thermal infrared emission spectroscopy of anhydrous carbonates. J. Geophys. Res. 102, 25581–25593.

Lane, M.D., Morris, R.V., Mertzman, S.A., Christensen, P.R., 2002. Evidence for platy hematite grains in Sinus Meridiani, Mars. J. Geophys. Res. Planets 107(E12), 5126.

Laukamp, C., Termin, K.A., Pejcic, B., Haest, M., Cudahy, T., 2012. Vibrational spectroscopy of calcic amphiboles—applications for exploration and mining. Eur. J. Mineral. 24, 863–878.

Lee, A.P., Brooker, L.R., Bronswijk, W.V., Macey, D.J., Webb, J., 2002. Contribution of Raman spectroscopy to identification of biominerals present in teeth of *Acanthopleura rehderi*, *Acanthopleura curtisiana*, and *Onithochiton quercinus*. Biopolymers (Biospectroscopy) 72, 299–301.

Legodi, M.A., de Waal, D., 2007. The preparation of magnetite, goethite, hematite and maghemite of pigment quality from mill scale iron waste. Dyes Pigments 74, 161–168.

Li, D., O'Connor, B.H., Low, I.-M., Riessen, A.V., Toby, B.H., 2006. Mineralogy of Al-substituted goethite. Powder Diffract. 21, 289–299.

Li, Y.S., Church, J.S., Woodhead, A.L., 2012. Infrared and Raman spectroscopic studies on iron oxide magnetic nano-particles and their surface modifications. J. Magn. Magn. Mater. 324, 1543–1550.

Liese, H.C., 1967. An infrared absorption analysis of magnetite. Am. Mineral. 52, 1198–1205.

Liu, H., Chen, T., Zou, X., Qing, C., Frost, R.L., 2013. Effect of Al content of the structure of Al-substituted goethite: a micro-Raman spectroscopic study. J. Raman Spectrosc. 44, 1609–1614.

Marciuš, M., Ristic, M., Ivanda, M., Music, S., 2012. Formation of iron oxides by surface oxidation of iron plate. Croat. Chem. Acta 85, 117–124.

Martinez-Alonso, S., Rustad, J., Goetz, A., 2002. Ab initio quantum mechanical modeling of infrared vibrational frequencies of the OH group in dioctahedral phyllosilicates. Part I: methods, results and comparison to experimental data. Am. Mineral. 87, 1215–1223.

Massey, M.J., Baier, U., Merlin, R., Weber, W.H., 1990. Effects of pressure and isotopic substitution on the Raman spectrum of alpha-Fe_2O_3: identification of two-magnon scattering. Phys. Rev. B 41, 7822–7827.

McLeod, R.L., Gabell, A.R., Green, A.A., Gardavsky, V., 1987. Chlorite infrared spectral data as proximity indicators of volcanogenic massive sulphide mineralisation. In: Pacific Rim Congress 87, Gold Coast, Queensland.

McMillan, P.F., Hofmeister, A.M., 1988. Infrared and Raman spectroscopy. In: Hawthorne, F.C. (Ed.), Spectroscopic Methods in Mineralogy and Geology. In: Reviews in Mineralogy, vol. 18. Mineralogical Society of America, Washington, USA, pp. 99–159.

Melkumyan, A., Murphy, R.J., 2010. Spectral domain noise suppression in dual-sensor hyperspectral imagery using Gaussian processes. In: Wong, K.W., et al. (Eds.), ICONIP 2010, Part II, LNCS 6444, pp. 684–691, 2010. © Springer-Verlag Berlin Heidelberg 2010.

Michaelian, K.H., 1986. The Raman spectrum of kaolinite #9 at 21C. Can. J. Chem. 64, 285–294.

Muralha, V.S.F., Rehren, T., Clark, R.J.H., 2011. Characterization of an iron smelting slag from Zimbabwe by Raman microscopy and electron beam analysis. J. Raman Spectrosc. 42, 2077–2084.

Murphy, R.J., Monteiro, S.T., 2013. Mapping the distribution of ferric iron minerals on a vertical mine face using derivative analysis of hyperspectral imagery (430–970 nm). ISPRS J. Photogramm. Remote Sens. 75, 29–39.

Mustard, J.F., Hays, J.E., 1997. Effects of hyperfine particles on reflectance spectra from 0.3 to 25 µm. ICARUS 125, 145–163.

Neff, D., Reguer, S., Bellot-Gurlet, L., Dillmann, P., Bertholon, R., 2004. Structural characterization of corrosion products on archaeological iron: an integrated analytical approach to establish corrosion forms. J. Raman Spectrosc. 35, 739–745.

Ninomiya, Y., 2002. Mapping quartz, carbonate minerals and maric-ultramafic rocks using remotely sensed multispectral thermal infrared ASTER data. In: Maldague, X.P., Rozlosnik, A.E. (Eds.), Thermosense XXIV Conference, April 1–4, 2002, Orlando, FL. Spie-Int Soc Optical Engineering, pp. 191–202.

Ocampo, L.M., Mattos, O.R., Margarit-Mattos, I.C.P., Fabirs, J.D., Pereira, M.C., Rechenberg, H.R., de Faria, D.L.A., 2006. Influence of Cu and Ni on the morphology and composition of the rust layer of steels exposed to industrial environment. Hyperfine Interact. 167, 739–746.

Odziemkowski, M., Flis, J., Irish, D.E., 1994. Raman spectral and electrochemical studies of surface film formation on iron and its alloys with carbon in Na_2CO_3/$NaHCO_3$ solution with reference to stress corrosion cracking. Electrochim. Acta 39, 2225–2236.

Ohtsuka, T., Kubo, K., Sato, N., 1986. Raman spectroscopy of thin corrosion films on iron at 100 to 150° C in air. Corrosion-NACE 42, 476–481.

Ong, C.C.H., Cudahy, T.J., Caccetta, M.S., Hick, P.T., Piggott, M.S., 2003. Deriving quantitative dust measurements related to iron ore handling from airborne hyperspectral data. Min. Technol. 112, 158–163.

Petit, S., Martin, F., Wiewiora, A., De Parseval, P., Decarreau, A., 2004. Crystal-chemistry of talc: a near infrared (NIR) spectroscopy study. Am. Mineral. 89, 319–326.

Pitman, K.M., Wolff, M.J., Clayton, G.C., 2005. Application of modern radiative transfer tools to model laboratory quartz emissivity. J. Geophys. Res. Planets 110, E08003.

Prasad, P.S.R., Prasad, K.S., Chaitanya, V.K., Babu, E.V.S.S.K., Sreedhar, B., Murthy, S.R., 2006. In situ FTIR study on the dehydration of natural goethite. J. Asian Earth Sci. 27, 503–511.

Raman, C.V., Krishnan, K.S., 1928. A new type of secondary radiation. Nature 121, 151.
Raman, R.K.S., Gleeson, B., Young, D.J., 1998. Laser Raman spectroscopy: a technique for rapid characterisation of oxide scale layers. Mater. Sci. Technol. 14, 373–376.
Ramanaidou, E., Connor, P., Cornelius, A., Fraser, S., 2002. Imaging spectroscopy for iron ore mine faces. Proceedings for Iron Ore 2002, Perth 9-11th September, AusIMM Publication Series No. 7/2002, pp. 155–157.
Ramanaidou, E., Tapley, V., Bronswijk, W.V., 1996. Determination of aluminium substitution in hematite and goethite by vibrational spectroscopy. In: Proceedings of 2nd Australian Conference on Vibrational Spectroscopy, 2–4 October 1996, Queensland University of Technology, pp. 35–36.
Ramanaidou, E.R., Connor, P., Wells, M., Yang, K., Whitbourn, L., Cudahy, T., 2004. Multiscale mine imaging for enhanced ore grade definition in mining operations. In: Proceedings for the 12th Australasian Remote Sensing and Photogrammetry Conference, Fremantle.
Ramanaidou, E.R., Wells, M., Belton, D., Verrall, M., Ryan, C., 2008. Mineralogical and microchemical methods for the characterization of high-grade banded iron formation-derived iron ore. Soc. Econ. Geol. 15, 129–156.
Ramanaidou, E.R., Wells, M.A., 2011a. Hyperspectral imaging of iron ores. In: Broekmans, M. (Ed.), 10th International Congress for Applied Mineralogy (ICAM), Trondheim.
Ramanaidou, E.R., Wells, M.A., 2011b. Raman I do—Raman spectroscopy for the mineralogical characterisation of banded iron formation and iron ore. In: Iron Ore 2011. Perth: The Australasian Institute of Mining and Metallurgy.
Ramanaidou, E.R., Wells, M.A., 2013. Characterising banded iron formations—hosted iron ores using visible and near infrared spectroscopy. In: ICNIRS La Grande Motte.
Ramanaidou, E.R., Wells, M.A., 2014. 13.13—Sedimentary hosted iron ores. In: Holland, H.D., Turekian, K.K. (Eds.), In: Treatise on Geochemistry (Second Edition), vol. 13. Elsevier, Oxford, pp. 313–355.
Ramsey, M.S., Christensen, P.R., Lancaster, N., Howard, D.A., 1999. Identification of sand sources and transport pathways at the Kelso Dunes, California, using thermal infrared remote sensing. Geol. Soc. Am. Bull. 111, 646–662.
Reston, M.S., Cocks, T.D., 1998. Mapping mineralogy of the Mt. Fitton area, flinders ranges, South Australia, using HyMap airborne imaging spectrometer data. In: 9th Australasian Remote Sensing and Photogrammetry Conference, July 20–24, 1998, University of New South Wales, Sydney, Australia.
Rivard, B., Petroy, S.B., Miller, J.R., 1993. Measured effects of desert varnish on the midinfrared spectra of weathered rocks as an aid to TIMS imagery interpretation. IEEE Trans. Geosci. Remote Sens. 31, 284–291.
Rowan, L.C., Salisbury, J.W., Kingston, M.J., Vergo, N., Bostick, N.H., 1991. Evaluation of visible and near-infrared and thermal-infrared reflectance spectra for studying thermal alteration of Pierre Shale, Wolcott, Colorado. J. Geophys. Res. 96, 18047–18057.
Ruan, H.D., Frost, R.L., Kloprogge, J.T., 2001. Comparison of Raman spectra in characterizing gibbsite, bayerite, diaspore and boehmite. J. Raman Spectrosc. 32, 745–750.
Ruan, H.D., Frost, R.L., Kloprogge, J.T., Duong, L., 2002. Infrared spectroscopy of goethite dehydroxylation: III. FT-IR microscopy of in situ study of the thermal transformation of goethite to hematite. Spectrochim. Acta A Mol. Biomol. Spectrosc. 58, 967–981.
Salama, W., El Araf, M., Gaupp, R., 2012. Mineralogical and geochemical investigations of the Middle Eocene ironstones, El Bahariya Depression, Western Desert, Egypt. Gondwana Res. 22, 717–736.
Salisbury, J.W., Walter, L.S., Vergo, N., D'Aria, D.M., 1991. Infrared (2.1–25 μm) Spectra of Minerals. The Johns Hopkins University Press, Baltimore and London.

Schodlok, M.C., Ramanaidou, E.R., 2011. Mapping quartz, carbonates and riebeckite in banded iron formation iron ore drill core using CSIRO's TIR-HyLogging system. Proceedings for Iron Ore 2011, Perth 11–13 July, AusIMM Publication Series No. 6/2011, pp. 147–153.

Schrader, B., 1995. General survey of vibrational spectroscopy. In: Schrader, B. (Ed.), Infrared and Raman Spectroscopy: Methods and Applications. VCH Publishers, New York.

Schulze, D.G., 1984. The influence of aluminum on iron oxides. VIII. Unit-cell dimensions of Al-substituted goethites and estimation of Al from them. Clay Clay Miner. 32, 36–44.

Schwertmann, U., Carlson, L., 1994. Aluminum influence on iron oxides: XVII. Unit-cell parameters and aluminum substitution of natural goethites. Soil Sci. Soc. Am. J. 58, 256–261.

Schwertmann, U., Fitzpatrick, R.W., Taylor, R.M., Lewis, D.G., 1979. The influence of aluminum on iron oxides: part II. Preparation and properties of Al-substituted hematites. Clay Clay Miner. 27, 105–112.

Shebanova, O., Lazor, P., 2003a. Raman spectroscopic study of magnetite ($FeFe_2O_4$): a new assignment for the vibrational spectrum. J. Solid State Chem. 174, 424–430.

Shebanova, O.N., Lazor, P., 2003b. Raman study of magnetite (Fe_3O_4): laser-induced thermal effects and oxidation. J. Raman Spectrosc. 34, 845–852.

Singer, R.B., 1981. Near-infrared spectral reflectance of mineral mixtures: systematic combinations of pyroxenes, olivine, and iron oxides. J. Geophys. Res. B 86, 7967–7982.

Slavov, L., Abrashev, M.V., Merodiiska, T., Gelev, C., Vandenberghe, R.E., Markova-Deneva, I., Nedkov, I., 2010. Raman spectroscopy investigation of magnetite nanoparticles in ferrofluids. J. Magn. Magn. Mater. 322, 1904–1911.

Smith, M.R., Bandfield, J.L., Cloutis, E.A., Rice, M.S., 2013. Hydrated silica on Mars: combined analysis with near-infrared and thermal-infrared spectroscopy. ICARUS 223, 633–648.

Spitzer, W.G., Kleinman, D.A., 1961. Infrared lattice bands of quartz. Phys. Rev. 121, 1324–1335.

Stuffler, T., Kaufmann, C., Hofer, S., Forster, K.P., Schreier, G., Mueller, A., Eckardt, A., Bach, H., Penne, B., Benz, U., Haydn, R., 2007. The EnMAP hyperspectral imager – an advanced optical payload for future applications in Earth observation programmes. Acta Astronaut. 61, 115–120.

Swayze, G.A., Kokaly, R.F., Higgins, C.T., Clinkenbeard, J.P., Clark, R.N., Lowers, H.A., Sutley, S.J., 2009. Mapping potentially asbestos-bearing rocks using imaging spectroscopy. Geology 37, 763–766.

Thangavelu, M., Shanmugam, S., Bhattacharya, A.K., 2011. Hyperspectral radiometry to quantify the grades of iron ores of Noamundi and Joda mines, eastern India. J. Indian Soc. Remote Sens. 39, 473–483.

Thanos, I.C.G., 1986. Electrochemical reduction of thermally prepared oxides of iron and iron-chromium alloys studied by in situ Raman spectroscopy. Electrochim. Acta 31, 1585–1595.

Thibeau, R.J., Brown, C.W., Heidersbach, R.H., 1978. Raman spectra of possible corrosion products of iron. Appl. Spectrosc. 32, 532–535.

Thierry, D., Persson, D., Leygraf, C., 1988. In situ Raman spectroscopy combined with X-ray photoelectron spectroscopy and nuclear microanalysis for studies of anodic corrosion film formation on Fe-Cr single crystals. J. Electrochem. Soc. 135, 305–310.

Trolard, F., Génin, J.-M.R., Abdelmoula, M., Bourrié, G., Humbert, B., Herbillon, A., 1997. Identification of a green rust mineral in a reductomorphic soil by Mössbauer and Raman spectroscopies. Geochim. Cosmochim. Acta 61, 1107–1111.

van der Weerd, J., Rehren, T., Firth, S., Clark, R.J.H., 2004. Identification of iron oxide impurities in earliest industrial-scale processed platinum. Mater. Charact. 53, 63–70.

Wald, A.E., Salisbury, J.W., 1995. Thermal infrared directional emissivity of powdered quartz. J. Geophys. Res. 100, 24665–24675.

Weir, C.E., Lippincott, E.R., 1962. Lattice frequencies and rotational barriers for inorganic carbonates and nitrates from low temperature infrared spectroscopy. J. Res. Natl. Bur. Stand. Sect. A Phys. Chem. 66A(5), 407–434.

Wells, M.A., Hogan, P., 2013. Bonnie Creek channel iron deposits ore mineralogy—insights using the HyLogger technology. Proceedings for Iron Ore 2013, Perth Western Australia, AusIMM Publication Series No. 6/2013 321–327.

Wells, M.A., Ramanaidou, E.R., 2007. Clay quantification of channel iron deposits (CID), Pilbara, Western Australia. Proceedings for Iron Ore 2007, Perth Western Australia, AusIMM Publication Series No. 6/2007, 203–207.

Wells, M.A., Ramanaidou, E.R., 2012. Raman spectroscopic characterisation of Australian banded iron formation and iron ore. In: EGU General Assembly 2012, Vienna, Austria.

Wells, M.A., Ramanaidou, E.R., 2013. Raman spectroscopic core scanning for iron ore and BIF characterisation. In: 2013-ICAM.

Wells, M.A., Gilkes, R.J., Fitzpatrick, R.W., 2001. Properties and acid dissolution of metal-substituted hematites. Clay Clay Miner. 49 (1), 60–72.

Wenrich, M.L., Christensen, P.R., 1996. Optical constants of minerals derived from emission spectroscopy: application to quartz. J. Geophys. Res. Solid Earth 101, 15921–15931.

Wiens, R.C., Sharma, S.K., Thompson, J., Misra, A., Lucey, P.G., 2005. Joint analyses by laser-induced breakdown spectroscopy (LIBS) and Raman spectroscopy at stand-off distances. Spectrochim. Acta A Mol. Biomol. Spectrosc. 61, 2324–2334.

Yamaguchi, Y., Fujisada, H., Kudoh, M., Kawakami, T., Tsu, H., Kahle, A.B., Pniel, M., 1999. ASTER instrument characterization and operation scenario. Adv. Space Res. 23, 1415–1424.

Zoppi, A., Lofrumento, C., Castellucci, E.M., Sciau, P., 2008. Al-for-Fe substitution in hematite: the effect of low Al concentrations in the Raman spectrum of Fe_2O_3. J. Raman Spectrosc. 39, 40–46.

Iron ore extraction techniques

7

R. Stace
University of Nottingham, Nottingham, UK

7.1 Introduction

Iron is one of the major constituents of the rocks in the Earth's crust and is always present in varying degrees in sedimentary formations. It is ranked fourth in terms of the quantity of all the elements occurring (Smith, 1990) and has been mined in small quantities at a vast selection of sites in many countries to feed the localized production of iron and steel. As iron and steel production has become concentrated into ever larger centers of production, and steel has become an internationally traded commodity, so iron ore is increasingly only mined at a relatively few key sites around the world where volume of production and quality of ore dictate operational success. A seaborne trade has developed to take ore large distances in substantial quantities to meet this new pattern of demand.

Iron ore reserves are normally found within a few meters from the ground surface, and most of the major mines of the world are operating an opencut system, which requires little sophistication, except in terms of the equipment used and the quantities needed to be mined for operations to be cost effective. This chapter will look at case studies that define how mining of ore is conducted today. Examples of mining sites are described from the major mining areas of the Pilbara in Western Australia and Minas Gerais in Brazil. These are both mining sites that have fairly standard surface mining features but that, in the case of the Pilbara example chosen, also introduce a novel mining system for open-pit mines. Both are in regions remote from the users of the mined ore, and mining is entirely dependent upon good rail communications to port facilities that are required to enable ore to be taken to far distant customers.

The deep mining of iron ore is unusual in the modern era, but in northern Sweden, ore is mined from considerable depth largely aided by the application of automation and remote control equipment. Kiruna has been chosen as the example for a more detailed review of underground techniques.

However, the chapter also seeks to highlight how iron ore mining has changed in the last 60 years, and therefore, it commences by examining how iron ore mining used to be conducted and two examples of smaller scale, low grade, underground iron ore mining have been chosen from now closed operations in the United Kingdom. As these sections will show, this form of mining was a labor-intensive activity, owned by steel companies and designed to feed their local steel works. Once steel production around the world became concentrated on a small number of major centers, with an infrastructure design to import large quantities of ore, then the need for mining on this scale ended and the mines closed.

Iron Ore. http://dx.doi.org/10.1016/B978-1-78242-156-6.00007-1
© 2015 Elsevier Ltd. All rights reserved.

7.2 Iron ore mining—an historical UK context

The extraction of iron ore from reserves in the ground had been practiced in the United Kingdom from Roman times. Smith (1990) described how Roman settlement archaeological specimens were regularly retrieved from opencast workings at Thielby, north of Scunthorpe in Lincolnshire, and how more modern-day mining operations uncovered evidence of smelting activities dating from Roman times.

Ironstone bands occurred in the productive coal measures within the strata in which the workable coal seams were found, but the most productive iron ore deposits in the United Kingdom were those found in Cleveland and Lincolnshire, in a broad band that stretched further south across the United Kingdom as far as Oxfordshire. Much of the mining work was undertaken by traditional opencast methods. However, mainly in Cleveland and in the area around Scunthorpe, and occasionally elsewhere in this large reserve, underground mining was also practiced as reserves were found at a greater depth from the surface.

Goldring and Juckes (2001) had published figures for UK home iron ore production from the 1850s to the late twentieth century when mining operations ceased. They have also shown how UK imported iron ore levels varied over the same period. The UK mining industry reached an initial peak in the ten years around 1875 when 17 million tonnes per annum of ore was produced. Thereafter, there was decline followed by resurgence during the Second World War when production reached 20 million tonnes in 1942. Production again declined thereafter. By the millennium, no iron ore mining was taking place in the United Kingdom. By contrast, the total of imported ore that had never exceeded 6 million tonnes per annum before the Second World War increased to 20 million tonnes per annum by the year 2000.

Quite why this decline happened is due to a combination of circumstances. Changes in steel making techniques, the size and health of the UK steelmaking industry, and the general low quality of UK iron ore reserves all made an impact on the economics of the industry. The large steel making facilities in South Wales, on Teesside, and at Scunthorpe while being established close to iron ore mining sites were also close to port facilities where a higher quality product could be imported in sufficient quantities at a reasonable cost.

All of the UK reserves had Fe contents approaching 30%, well below that of the ores from the major producing centers of the world. These imported ores also had fewer impurities. So, in a very similar manner to the decline that happened some years later and in a more widely publicized manner to the indigenous coal mining industry, UK iron ore mining wound down and finally ceased.

This chapter seeks to examine the systems of work that were used underground in two UK iron ore mining regions to present an historical perspective. Later sections will go on to contrast these mining operations with the modern deep mining techniques applied in Sweden and the huge scale surface extraction of iron ore in Western Australia and Brazil.

In the next sections, the author has described briefly the techniques that were applied in the underground mining of iron ore in Cleveland and also the Frodingham Ironstone of North Lincolnshire.

7.2.1 Underground mining techniques in the Cleveland ironstone mines

The relationship between iron smelting and iron ore mining in Cleveland developed from the middle of the nineteenth century (Morris, 1982). The Cleveland reserve was perhaps the deepest mined iron ore activity in the United Kingdom, requiring not just drift access from the outcrop but shaft access to reserves that were in excess of 200 m below the surface at the deepest point. By the end of the nineteenth century, 40 underground mines were in operation in Cleveland. In 1908, Morris (1982) reported that 23 mines were in operation producing 6 million tonnes per annum. After the 1914–1918 war, only nine mines remained in operation with overall annual outputs of 2 million tonnes (Mt). Perrins (1953) reported that eight mines were in production in 1953, all working the Main Seam, and that in the hundred years of mining in Cleveland, some 350 Mt. of ore had been produced. The final operating mine, North Skelton, closed in 1964.

The mines were never heavily mechanized in the way that was found in the coal industry as most of the major advances in coal mine mechanization came in the early 1960s as the ironstone mines were closing. The Main Seam was one of four seams of ironstone worked at the Cleveland mines, and being up to 3.35 m thick was the most important. This was immediately underlain by the Pecton Seam that, at 0.5–1.83 m thick, allowed a total working section of 4.7 m of ironstone. As the seam was exploited to the south of the outcrop, the Main Seam became deeper, less thick, and lower in quality. These factors dictated the extent of the southward workings.

The working method employed is described by Morris (1982) as follows:

> *The method of extraction was by 'pillar and bord' working. This involved driving two parallel 3.6 m wide roadways….some 9 m apart, then joining them after 9 m or so by a 'bord' running at right angles….Passages also with bords at right angles, were driven off from the sides of the roadways every 4.5 m to 9 m and these were extended to the edge of the mining royalty…..beginning at the extremities of the mine, work now started on the extraction of the ore from the 'pillars' leaving only a 1.3 m square columns of stone to temporarily support the roof. As these became overloaded they collapsed allowing the roof to come down…..causing the ground surface to subside.*

Perrins (1953) noted that between 35% and 45% of the reserve was won from the initial extraction to the boundary but that this was increased to nearer to 90% by "taking successive lifts 12 ft wide along the pillars, a curtain of about 2 ft of ironstone being left to protect the goaf side." He goes on to explain that these curtains were then mined "to as great an extent as possible in order to induce.....the goaf to collapse."

Iron ore was won by drilling and blasting (Figure 7.1). As mining technology generally developed, so did drilling techniques and the explosives used. Smith (1990) reported that the Cleveland deposit was associated with a very strong stone roof rock (known as "dogger") allowing mine drivages to be self-supporting. However, he states that in later years where the mining had progressed to the dip, this roof beam was found to be thinner and weaker and consequently some standing support was set. He states

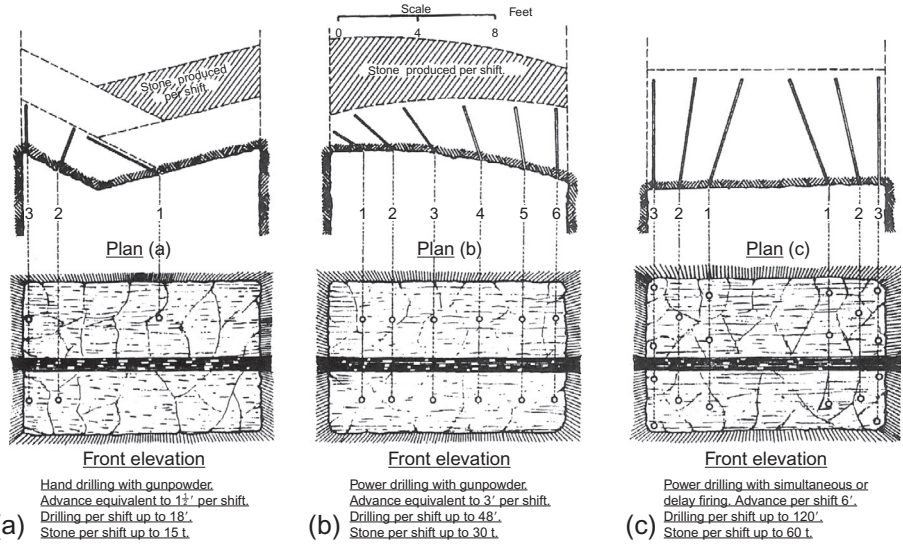

Figure 7.1 Early ironstone mining techniques.
Reproduced from Perrins (1953), with permission of the Institute of Materials, Minerals and Mining.

> *In areas where support was necessary, props and bars were set which were liable to be dislodged during blasting operations. A change was made to flat-topped steel arch supports to overcome this problem.*

While hand loading was the traditional method of loading the blasted ore during the early twentieth century, Eimco Rocker Shovels were introduced in the 1940s for this task.

The Cleveland underground ironstone mines were exceptional in noncoal mines in the United Kingdom in that they experienced methane and were therefore not classified as "naked light" mines. Perrins (1953) postulated that the source of inflammable gas was the Jet Shales that overlay the Main Seam at a distance of some 10–20 m. He reported a long history of ignitions going back into the nineteenth century and explained how shotfiring methods and materials were developed to deal with the potential for ignitions. Following a number of explosions in the early 1940s, Smith (1990) reported that larger fans were employed at the deep mines and better methods of ventilation for single entry headings sought. He notes that as mechanized drilling and loading techniques spread, output could be achieved from fewer working places and thus quantities of air delivered to each of these places were increased.

7.2.2 Underground mining techniques in the North Lincolnshire mines

The Frodingham Ironstone bed comprises a lenticular bed of ferruginous oolitic limestone that lies within the lower Lias of the Jurassic sedimentary sequence and occurs

to the east of the town of Scunthorpe in North Lincolnshire. The deposit has a thickness of some 10 m and is both over- and underlain by weak Lias clays. The beds dip gradually toward the east at a gradient of approximately 1 in 65. Smith (1990) noted that boreholes drilled 13.5 km east of the outcrop proved that this thickness was maintained at a depth of 145.5 m. However, underground mining was mainly at a depth of cover of 60–100 m. Just as with other UK ores, the iron content tends to be around the 30% level.

After experimental mining in the late 1930s, Santon drift mine was developed, and following the cessation of the hostilities, mining production commenced. Shortly afterward, a second drift mine, Dragonby, was also opened. Operations at both mines were mechanized from the outset and took advantage of the latest drilling and loading equipment in keeping with international mining practice at the time. The two mines merged in 1969.

Smith (1982) reported that Dragonby, like Santon, was initially worked on a room and pillar system with 6 m × 6 m rooms and rectangular pillars measuring 21 m × 49 m. The main development district at the mine originally consisted of five parallel roads with crosscuts at 27.5 m centers. The number of drifts increased to seven and then nine as the mine developed. In the early 1970s, all production districts consisted of seventeen parallel roads with connecting crosscuts at 21 m centers. The central roadway (with eight on each side) was chosen as the conveyor road.

Roadway heights of up to 8 m were mined with some success although the need to leave ironstone in the roof and floor meant that the normal extraction was often less than that (6–7 m) (Whittaker and Smith, 1987). The scale of these roadways and the support of the roof, especially at four-way junctions in the room and pillar layout adopted, created a number of support problems. The banded structure of the rock leading to the formation of natural roof horizons was important in the working method. Additionally, the ironstone bed was subject to vertical jointing, some of which contained water that needed to be dealt with as part of the mining method. Smith (1990) reported that ironstone left in the roof was necessary to maintain roof stability, especially when free-standing, but that it had to be at least 1.5 m thick in an 8 m wide roadway for stability to be maintained and for the clay roof strata not to be exposed by fracturing of the ironstone. Smith (1990) noted that where a 2.5 m thick roof beam was left, no falls ever occurred. In 1955, systematic roof support using rock bolts through steel straps was introduced.

The most notable feature of mining at Santon and Dragonby was the high levels of mechanization applied to mining and the scale of operations. Early mechanized mining used Joy gathering arm loaders and shuttle cars, but these were eventually replaced by diesel-driven Load-Haul-Dump (LHD) vehicles with much greater capacities loading on to a 1.2 m wide conveying system that led to the surface. Rotary drilling and blasting were the main methods of production. In the later life of the combined mine, twin boom-type roadheaders based on those used in the UK coal mines were also applied with some success although the room size had to be reduced to 6 m wide × 3.6 m high because of the limited reach of the cutting booms (Smith, 1990). Whittaker and Smith (1987) reported that, following the introduction of twin boom drilling jumbos capable of forming a 4 m long, 43 mm diameter hole in 1 min, two of these drills operating in separate district were capable of producing 20,000 ton of ore in one 5-day week.

Despite all this mechanization and subsequent modernization in mining methods, the fundamentals of low ore grades, the competition problems being faced by the iron and steel companies, and the availability of appropriately priced good quality ores on the market led to the closure of the mines in 1981.

7.3 Underground iron ore mining: Kiruna, Sweden

7.3.1 Introduction: the worldwide iron ore market

As stated in the previous sections, the mining of iron ore, at both the surface and underground, ceased in the United Kingdom toward the end of the twentieth century, not only because of the general poor quality of the ores leading to high costs of production (from the deep mines) but also due to the environmental impact of surface mining, a problem that has dominated all attempts to mine minerals by opencast methods in the densely populated United Kingdom. Additionally, iron ore mining was controlled by the iron and steel producers who themselves had faced difficult competition issues from overseas producers against a background of gluts in steel production internationally. The alternatives of higher quality imported iron ores from sources around the world became much more attractive at the surviving steel plants.

In 2013, world iron ore use was approximately 1931 Mt. This was expected to increase to 2008 Mt in 2014. The seaborne iron ore trade accounted for 58% of this production. China alone was importing some 65 Mt per month. Over 35% of iron ore production during 2012 came from the mines of three large international producing companies, Vale, Rio Tinto, and BHP Billiton (United Nations, 2013). In national terms, at the present time, China, Australia, and Brazil dominate world iron ore production and they are supplying a market dominated by the steel producers of China, Japan, and South Korea. During 2011, China was the world's largest producer of iron ore with 43% or 1200 Mt, followed by Australia with 17% or 488 Mt and Brazil with around 14% or 390 Mt of world production.

Against this background, it is, perhaps, surprising that there remain a steel making industry in Europe and furthermore a European-based supplier of iron ore to satisfy this market. Steel production in the member countries of the European Union increased by 5.3% in November 2013, compared to the previous November, to 14.25 Mt, although the eleven months total was 2.8% lower at 152.5 Mt (http://www.steelonthenet.com/plant.html). The European Iron Ore producing company of note is Luossavaara-Kiirunavaara Aktiebolag (LKAB, 2006) that operates mines in Sweden including the famous Kiruna underground mine in the north of that country.

7.3.2 Location and geology

Kiruna mine is located in northern Sweden, some 145 km north of the Arctic Circle. The magnetite–apatite orebody at Kiruna was discovered in the seventeenth century but was not worked until 1900. The orebody has the following dimensions:

- Length 4 km
- Thickness 90 m average
- A known depth in excess of 1500 m, which may be considerably deeper than originally proved
- An angle of dip between 50° and 60°

The hanging and footwall of the deposit are syenite and quartz porphyries. Below the current mining depth, the ore is thought to become of a higher grade and the orebody itself widens to 150–180 m. The iron content varies between 60% and 67% depending on the amount of phosphorus in the ore (Kurmies, 2003). This orebody is quite unlike most of the other major iron ore deposits in the world and therefore requires a hard rock mining solution for extraction.

7.3.3 Mining method: sublevel caving

Initial mining at Kiruna took the form of opencast methods, and for 65 years, all the ore was mined by surface methods to a depth of 275 m. Thereafter, mining was concentrated at the underground mine that began production in 1957 (Chadwick, 2010). Since mining began at the site over 100 years ago, LKAB has produced over 950 Mt. of ore, yet only one-third of the known ore body has been extracted. In 2008, Kiruna produced 27.5 Mt. of iron products. The operation currently employs 1800 people, of whom 400 work in the mine (http://www.mining-technology.com/projects/kiruna/).

In the life of the underground mine, ore extraction has been enabled by the development of six main locomotive horizons over that period (275, 320, 420, 540, 775, and 1045 m depths from the surface), and as future mining will go to increasing depths, a new level at 1365 m was initially planned in 2008 and the first part commissioned in 2012.

The stable rock surrounding the iron ore vein caves in a controlled fashion when blasted and is ideal for the sublevel caving system of mining. Above the 1045 m level, the mine is divided typically into 8 or 10 production sections, each with its own ore passes and ventilation systems. As stated above, the mine has been developed to depth using progressively six main haulage levels on which ore is transported from the base of vertical ore passes to the main underground crushers and then by skip, through a vertical shaft to the surface. The current haulage shafts serve the 775 m level and mine development below that level has seen a second subvertical shaft being formed.

Mining the ventilation shafts for the current production level was carried out by SIAB using Indau 500 raise borers, while Skanska Raise Drilling developed a total of 32 ore passes between the 775 and 1045 m levels using Tamrock and Robbins raise borers. Alimak developed two special units based on its RCM-6 system to reinforce the ore passes with cable bolts and shotcrete as necessary (http://www.mining-technology.com/projects/kiruna/).

Development drifts are driven right through the orebody from the footwall side and are formed between the main haulage levels, using electrohydraulic drill jumbos (Figure 7.2). The drifts can be up to 80 m long. Normal drift dimensions are 6.5 m width ×5 m height. For each charge, as many as 60 holes are drilled. Each hole is around 5 m long. Side walls and drift roof are reinforced with bolts and shotcrete (Figure 7.3). When several drifts have been driven in the same area, production

Figure 7.2 Kiruna—drilling underground.
Published with the kind permission of Luossavaara-Kiirunavaara Aktiebolag—photographer Frederic Alm.

Figure 7.3 Kiruna—reinforcement by shotcreting.
Published with the kind permission of Luossavaara-Kiirunavaara Aktiebolag—photographer Frederic Alm.

drilling can begin. During the mine life, stope tonnage has been increased by increasing the vertical distance between the sublevels from 12 m (in 1985) gradually in stages to 25 m in 1995, increasing the tonnage won from each stope to 10,000 t. This trend has continued. Chadwick (2008) reported that sublevels were being mined at 28.5 m vertical separation. This increased vertical distance also reduces drift development requirements.

LKAB has a long tradition of using three boom Sandvik Jumbo drills, especially to develop mine infrastructure and to drill production drives. Sandvik DD530 machines can mine a 5 m × 5 m tunnel. The mine was reported to require 24,500 m of drift development in 2008, an increase from 21,500 m in 2007 (Chadwick, 2008).

For production, 115 mm diameter upholes are drilled in a fan pattern of, normally, 10 holes. Drilling operations, as with so much of the mining operations at Kiruna, are remotely controlled from elsewhere underground. The fan patterns are drilled 10° off-vertical forward. The mine drills approx 1 million meters of production holes per year, with lengths of between 15 and 60 m. Each fan pattern is spaced at approximately 3 m intervals. There are normally 20 fan patterns in each 80 m drift. Accuracy of drilling is of major importance as minor deviations can lead to hole intersection in adjacent fans. Once the entire drift is drilled, hole charging with explosives can take place. This is done using an explosive that has the consistency of heavy cream and that is pumped into the holes. The explosive was specially developed for LKAB by its Kimit subsidiary, which is one of Sweden's biggest explosive producers. This process is controlled remotely. Blasting takes place every night, when around 20–30 t of explosive is detonated, each individual round bringing down 10,000 t (Chadwick, 2008, 2010, http://www.lkab.com/en/About-us/Overview/Operations-Areas/Kiruna/).

The formation of the sublevel entries and the order of their subsequent mining are constrained by the need to avoid interaction of caving or operations between adjacent sublevels both in the horizontal plain and from below. The mining entity in a sublevel is a *machine placement.* Activities in one machine placement place a restriction in an underlying or horizontally adjacent machine placement. Each contains between 1 and 3 Mt ore and waste rock (Martinez and Newman, 2011).

The production area ranges from 400 to 500 m in length measured along the strike of the vein and consists of 10 horizontal sublevels and a group of vertical ore passes. Though up to 25 electrically powered LHD (Figure 7.4) vehicles can operate simultaneously in the 10 production areas at any one time, only two or three can operate simultaneously within a shaft group because of potential congestion, cable damage, etc. (Martinez and Newman, 2011). The ore passes provide access from the sublevels to the haulage level. The LHD's load ore that has been blasted on each sublevel into the ore passes that are opened at the bottom to fill trains waiting on the main level. The

Figure 7.4 Kiruna—loader underground.
Published with the kind permission of Luossavaara-Kiirunavaara Aktiebolag—photographer Frederic Alm.

LHD vehicles that haul the ore under automatic control to the ore passes have a payload of 21.25 t (Chadwick, 2010). On the 1045 m-level main haulage, 7 × 500 t capacity ore trains, controlled remotely from the surface, collect ore from 10 groups of ore passes and deliver it on to one of four crushing stations where it is crushed to −100 mm before being hoisted to the surface (Chadwick, 2008). After primary crushing, sampling using a Morgårdshammer automatic sampler to obtain the apatite and magnetite contents, and hoisting to surface, the ore is processed in Kiruna's complex of a sorting plant, two concentrators and two pellet plants to give pellet and sinter fine products. Some ore is moved by rail to LKAB's Svappavaara plant for pelletization. Products are hauled by rail to the ports of Narvik (Norway) or Luleå for shipment.

As Kiruna mine works at deeper levels, rock support problems have increased. Swellex bolts are used in the short life (<3 years) drives. Cable bolts are used in the longer term mine infrastructure. Standard Swellex is a 100 kN bolt placed in 32–39 mm diameter boreholes. This has been superseded in more difficult areas by a bolt known as "Super Swellex." This is a 190 kN bolt placed in 51 mm diameter boreholes at lengths up to 3.05 m. The mine is also using a "SuperSwellex Mn24" bolt made from heat-treated special manganese steels. Swellex Mn 24 bolts have a breaking load of 240 kN. Bolts with lengths of 2.4 m are used in the smaller cross-sectional drifts (5 m × 5 m). Bolt spacing is normally between 1 and 1.5 m (Chadwick, 2008).

7.3.4 The 1365 m level

This new 1365 m main level and all its supporting infrastructure are being built following an investment of around $1.7 billion (http://www.mining-technology.com/projects/kiruna/). At this level, mining is planned to take place in 10 production areas each with its own access road, communications system, gravity shafts, and ore chutes. The development of this new level is intended to extend the operating life of Kiruna mine up to 2030 (Lovejoy, 2012).

The 1365 level was designed to have a mining and transport capacity of 100,000 tpd that equates to 35 Mt per annum. The new haulage system will consist of six trains, each with 20 bottom-unloading cars of 17 m^3 capacity, all automatically controlled. A new subvertical shaft has been sunk from the 775 level with a hoisting distance of 710 m. This shaft incorporates five subvertical hoists, each having a capacity of 1510 tph operating at 17 m/s winding speed (Chadwick, 2010).

During the changeover from the 1045 m level to the 1365 m level as the central focus of mining operations, there is a requirement that the existing level at 1045 m and the new level at 1365 m have to be in operation in parallel for approximately 7–8 years to maintain mine production levels.

The existing main ventilation system was constructed between 1995 and 2000 and consists of 20 raised-bored shafts (ten each for intake and return), each 3 m in diameter and 1000 m in length, down to 775 m level. The system was designed for a maximum airflow of 150 m^3/s at each shaft. Each air shaft is equipped with one variable speed axial fan. During winter, the intake air is heated on the delivery side of the fan to +1 °C to prevent buildup of ice in the shafts. This heating process is based on the use of waste heat from surface preparation facilities. When the outside temperature reaches −15 °C,

then additional heat has to be provided. Separate shafts are drilled to ventilate below the 775 m level (Mukka, 2008).

One of the unfortunate side effects of the extension of mining at Kiruna and the use of the sublevel caving method has been the realization that mining subsidence can damage large parts of the town. Arrangements are being made to move parts of the town, including key civic buildings to a position where they cannot become further affected by underground mining activity (Nilsson, 2010).

7.4 Modern-day surface mining: the Pilbara deposit

Australia has accessible resources of iron ore thought to be 37 Bt, 94% of which can be found in Western Australia adjacent to the northern coast of the state, in the region known as Pilbara, and this is where their most impressive and significant mining operations can be found (http://www-a.ga.gov.au/web_temp/1480294/75326.pdf).

Mines in Western Australia produced 474 Mt. of iron ore (97% of total national production) in 2011. Australia exported some 90% of its iron ore output to such Asian countries as China (58%), Japan (26%), the Republic of Korea (11%), and Taiwan (4%). The major operating companies are predicting that Australia will increase its production to approximately 600 Mt per annum by 2016. This is underlined by their published investment plans in the region (www.riotintoironore.com, www.bhpbilliton.com).

Mines in this region operated by two large multinational companies, BHP Billiton and Rio Tinto, have dominated the Pilbara area's output. BHP Billiton had seven iron ore mining operations and the port facilities of Nelson Point and Finucane Island, which are located within the town of Port Hedland. Rio Tinto operates an integrated network of 14 iron ore mines, three port facilities, a 1400 km rail network, and related infrastructure. However, more recently a third operating company, the Fortescue Metals Group has begun to operate a number of mines in the Pilbara region. Fortescue is said to have mining rights to an area covering 71 400 km^2.

The Pilbara mining area is huge, broadly speaking, some 500 km in extent from west to east with the furthest inland mines some 450 km from the coastal ports. The remoteness of this mining area from both Perth and the coastal ports means that workers at the mines operate in a fly-in fly-out (FIFO) system.

All the major Australian iron ore mines are opencut. The ores from the major mines in the Pilbara region are hauled from working faces to crushing and screening plants using trucks that can carry over 300 t. A typical surface mine producing between 25 and 30 Mt per annum would use between 8 and 10 loaders and some 40 trucks (www.riotintoironore.com). The ore is then transported for further treatment and blending to port sites in trains consisting of up to three locomotives and over 250 wagons. Trains of this size are over 2 km long and contain loads in excess of 25,000 t.

Most of Australia's traditional iron ore projects mine ore deposits that are enriched naturally and contain high levels of iron. The Pilbara region is rich in such hematite ore, known also as “direct shipping ore” (DSO). DSO passes through a simple crushing, screening, and blending process (beneficiation) before it is shipped for steel production. DSOs, when mined, typically have iron (Fe) content of between 56% and

64% Fe. By comparison, magnetite ore typically has a much lower iron content of between 25% and 40% Fe and in this form is unsuitable for steel making. The main iron mineral in magnetite ore is the ferrous iron oxide magnetite (Fe_3O_4). Magnetite ore requires complex processing to separate magnetite minerals from other minerals in the ore to produce an almost pure magnetite concentrate with an iron content of between 68% Fe and 70% Fe (http://www.magnetitenetwork.com.au/who-we-are/magnetite/).

The Pilbara area also has significant magnetite ore resources. Three types of iron ore are mined in the Pilbara. These are bedded iron deposits (BID—banded iron formations), channel iron deposits (CID—iron rich fluvial rocks), and detrital iron deposits (DIT—minor alluvial deposits of hematite—goethite derived from erosion of BID) (Morris and Ramanaidou, 2007).

Clout and Rowley (2010) described the development of the Cloudbreak and Christmas Creek deposits by Fortescue Metals Group. Cloudbreak mine lies some 256 km from the sea at Port Hedland. Trains are formed of 2 GE Dash 9-4400CW diesel locomotives and 230 wagons and are 2.5 km long carrying between 27,000 and 32,000 t of ore. Their paper claims that proved and probable reserves at these two mines are 1585 Mt at 58.8% Fe. The Cloudbreak and Christmas Creek deposit has a thickness of between 5 and 20 m over a total mining width along the deposit strike of 80 km and a dip extent of some 4 km. They state

> *since the ore is flat lying, thin and shallow in depth below the surface, strip mining was adopted as the mining method.....it is based on operating up to six mining pits at any one time with active mining occurring in 500 m long by 100 m wide panels.*

They write that overburden that is typically only 9–35 m thick and *"easy digging loose gravels and clays"* is removed by 650 t excavators loading in to 190 t haul trucks.

Apart from their scale of operations, what makes these mines worthy of closer examination is that the exposed ore is mined using a system of continuous surface miners built largely on the principle of the road planer by the Wirtgen group. A cutting drum with a horizontal axis, fitted with tungsten carbide tipped tools, similar in design to those used on continuous miners in the coal mining industry cuts shallow (typically 0.4 m deep) strips, 2.5 m wide (the 2500 Surface Miner (SM)). Wirtgen claim that their 2500 SM can cut at a rate of between 1200 and 2000 t per hour depending on rock hardness. Average unit production figures of between 80,000 and 100,000 tpd are claimed. The company also claims that the 2500 SM can cut rocks with an unconfined compressive strength of between 80 and 120 MPa.

Later, machines have been built with a capability of extracting 4.2 m wide strips (the 4200 SM). The company publish data that claim that 4200 SM with a 1.86 m diameter cutting head can mine a cut of up to 830 mm of rock with strengths up to 50 MPa. With a smaller drum diameter (1.5 m) and a reduced cutting depth (<650 mm), the mined rock strength can be increased. The same figures suggest that weak unconsolidated rock can be mined at the rate of over 2500 m^3/m, but stronger more solid fine-grained material would reduce production rates to less than 500 m^3/m. The company also claims that they can design and produce a special machine with

a weight of 130 t that can cut rock with a UCS of 260 MPa. The newer 4200 SM machines with a wider cutting head double the rate of production of the 2500 SM machine and enable much higher daily outputs to be recorded. It is also claimed that the operation of surface mining machines in this way allows selective cutting of target grades of ore. Figures 7.5 and 7.6 show Wirtgen surface mining machines in operation in the Pilbara mines.

The surface miners load ore directly by boom conveyor into 100 t trucks or 200 t road trains on the pit floor that take it to the preparation and loading facilities at the mine. The mine currently operates with three surface miners per pit. When mining of

Figure 7.5 Pilbara—4200 SM in action.
Published with kind permission of Wirtgen GmBH.

Figure 7.6 Pilbara—4200 SM in action.
Published with kind permission of Wirtgen GmBH.

an area is completed, the pit is filled with overburden rocks and recontoured to the original surface profile. This fill material also contains residue from the preparation facilities. Regeneration is completed by a layer of topsoil for revegetation.

Clout and Rowley (2010) claimed that the key advantages of the application of the surface miners are sixfold. Surface miners allow

- selective mining to maximize ore yields from relatively thin deposits,
- improved grade monitoring and control,
- increased lump yield and a coarser fine size distribution,
- a minimum requirement for blasting with explosives,
- elimination of the need for primary crushing and a minimization of the amount of secondary crushing,
- the mining process to leave behind very smooth pit floor profiles that are beneficial to tire life in the trucks that the miners load.

7.5 Modern day surface mining: iron ore in Minas Gerais Province, Brazil

Brazil has very large reserves of high-grade iron ores, but because these deposits were remote from world markets and because abundant reserves were more accessible elsewhere in the world, they were largely ignored until 1910.

Minas Gerais, one of the larger states of Brazil is renowned, as its name, suggests for its minerals and its mining activity. A thick pre-Cambrian sedimentary iron formation containing local concentrations of high-grade hematite ore occurs in an area of about 7000 km^2 in the *"Quadrilátero Ferrífero"* (the Iron Ore Quadrangle) of central Minas Gerais state.

Substantial mining of iron ore for shipment out of the district began only a few decades ago, although some metal was smelted locally in the early nineteenth century.

A contemporary US Geological Survey report states that overall production *to date* up to 1957 was estimated at 5,000,000 ton, *"a minute fraction of the total ore available."* The report continues to state that

> *Reserves of high-grade hematite are placed, in round figures, at 150,000,000 tons; of surficial ores of shipping grade at 100,000,000 tons. The quantity of itabirite above a depth of 1000 meters is calculated as 39,000,000,000 tons containing 20,000,000,000 tons of lumatite or 15,000,000,000 tons of metallic iron. Of this vast amount about 7,500,000,000 tons lie within 100 meters of the surface and might be extracted by opencut. Some of this material is sufficiently softened by leaching to be easily minable and can be concentrated by simple beneficiation to more than 60% iron.*
>
> *Guild (1957)*

Although there are many surface mines in this area, operated by international mining companies such as Vale, this section of the chapter will concentrate on the Casa de Pedra mine operated by Companhia Siderúrgica Nacional (CSN). Casa de Pedra lies some 80 km south of the state capital city of Belo Horizonte and some 360 km north

from the city of Rio de Janeiro. The site is approximately 1000 m above sea level. Casa de Pedra mine is a hematite-rich iron deposit of an early Proterozoic banded iron formation.

CSN is an integrated mining and steel producing company with an interest also in the rail connections to its ports on the Atlantic coast south of Rio de Janeiro. CSN manages two port terminals in Itaguaí, in the state of Rio de Janeiro: TECAR, from which the iron ore is shipped out, and Sepetiba Tecon, a container terminal. There are two railways from the mining areas to the company steel plant and TECAR. The easterly of these is called the Central Line and was built in 1950s. This goes via the steel plant. The westerly is called the Steel Railway and was built in 1975–1982. Full trains from CdP go directly from the mine on the over 400 km journey to TECAR, returning empty via the Central Line that is longer and less direct. Ore from Casa de Pedra was originally transported to a company steel works near to the coast, but in recent years (since 2007), the majority of the ore has been shipped to Asian customers, an example once again of the influence of the world-wide nature of iron and steel making and the international nature of iron ore mining operations

In the mid 1950s, the US Geological Survey reported (Guild, 1957) in Casa de Pedra mine that

> *All mining is by opencut, on three principal benches about 20 meters apart plus a few subsidiary benches. Many short adits extend into the faces. Most are connected to the bench above by raises, and are used as part of the ore-hauling system. Certain adits and their continuations past the raises were driven to explore the deposit.*
>
> *Hand-held pneumatic drills using Swedish steel bits, re-sharpened at the mine, were used at least until 1951…. Blasting was done by fuse, although simultaneous electric-cap blasting was used experimentally at least once to the writer's knowledge. Secondary blasting is done occasionally, although it is usually unnecessary as the ore breaks small enough that sledge hammers can be used. Most loading was done by hand. Several small power shovels were in use in 1951, particularly for handling the fines. Traming to the chutes or ore pockets was done largely by hand on rails which could be easily relaid, but some pneumatic-tired trucks were also used in conjunction with the shovels. Transfer from chute or pocket to the next descent was handled by trains of cars pulled by small diesel locomotives on the 1,224 level and by diesel and a few wood-burning steam locomotives on the 1,206 level. Ore thus lowered by stages to the principal chutes was loaded by gravity into one-half ton buckets and sent by aerial tramway to the railroad…… The production was about 1,000 tons per day. Top production for any one year has been about 250,000 tons.*

Casa de Pedra has been transformed into a major iron ore mine in the present day (Figures 7.7 and 7.8). There have been significant changes to the equipment being used and the volumes of ore being mined. Ore is mined from two large open pits, and a third mining area to the north of the existing mine has been developed. Total resource is now said to be 8.388 Bt, with reserves of 3.071 Bt. This is sufficient for mining to continue for a further 25 years at planned levels. Ore is currently prepared for market in a beneficiation plant at the mine site, whose products are transported 4.5 km overland by conveyor to a rail loader (Figure 7.9). When the author visited the site in 2009, there

Figure 7.7 Casa de Pedra—general view of open pit.

Figure 7.8 Casa de Pedra—general view of open pit.

Figure 7.9 Casa de Pedra—stockpiles (with primary crusher in the background).

was evidence of substantial investment in capacity and infrastructure at the mine and the rail loading site and further away at the port facilities.

Ore is currently excavated by a fleet composed of Marion 191M and P&H 1900AL electric shovels or PC 5500 Demag hydraulic shovels with wheel loaders (different brands) and then hauled by a fleet of Terex TMT3300AC (150 t), Komatsu Dresser 510E (150 t), Caterpillar CAT793 (240 t), and Terex Unit Rig (240 t) trucks out of the pit (Figure 7.10).

CSN has been expanding the Casa de Pedra mine in order to reach a total annual ore production capacity of 50 Mt. With the expansion of the Casa de Pedra mine, CSN has also consolidated its position as a significant player in the iron ore market and is,

Figure 7.10 Casa de Pedra—Terex 503 haul truck.

together with NAMISA, Brazil's second largest iron ore producer (http://www.mzweb.com.br/csn/web/arquivos/CSN_Apresentacao_20070919_eng.pdf).

7.6 Conclusions

This chapter has sought to demonstrate, using case study examples, how iron ore mining has developed from a small-scale industry feeding local steel plants on a regional or national basis to one in which only the largest and highest quality deposits can be exploited for an international market based on major steel producers, themselves addressing the needs of an international market of consumers.

Open pit mining of iron ore is fundamentally simple when compared to underground mining. While ore grades have to be maintained at high levels in order to satisfy the market, commercial advantage is gained by the application of high-capacity modern mining equipment, but volumes have to be high and costs so low to remain competitive. The mines described in Sections 7.3–7.5 of this chapter are achieving that level of competitiveness.

References

Australian iron ore reserves and production. http://www-a.ga.gov.au/web_temp/1480294/75326.pdf (accessed 26 February 2014).

Casa De Pedra mine, operated by Companhia Siderurgica Nacional (CSN). http://www.mzweb.com.br/csn/web/arquivos/CSN_Apresentacao_20070919_eng.pdf (accessed 25 June 2014).

Chadwick, J., 2008. Kiruna grows. Int. Min. 4 (6), 22–28.

Chadwick, J., 2010. Ironclad Kiruna. Int. Min. 6 (7), 9–15.

Clout, J.M.F., Rowley, W.G., 2010. The Fortescue story—from exploration to the third largest iron ore producer in Australia. Appl. Earth Sci. Trans. Inst. Min. Metall. Sect. B 119 (3), 122–130.

Goldring, D.C., Juckes, L.M., 2001. Iron Ore supplies to the United Kingdom iron and steel industry. Trans. Inst. Min. Metall. Sect. A 110 (May–August), A75–A85.

Guild, P.W., 1957. Geology and mineral resources of the Congonhas district, Minas Gerais, Brazil. US Geological Survey Professional Paper 290, US Government Printing Office, Washington, DC.

Kurmies, I., 2003. The Magnetite-Apatite Ore of the Kiruna District, Northern Sweden. Institute of Geology, University of Mining and Technology, Freiburg. www.geo.tu-freiberg.de/oberseminar/os03_04 (accessed 25 June 2014).

Luossavaara-Kiirunavaara Aktiebolag (LKAB), 2006. http://www.lkab.com/en/About-us/Overview/Operations-Areas/Kiruna/ (accessed 27 January 2014).

Lovejoy, C., 2012. Keeping up with caving. Min. Mag. 202 (6), 46–64.

Martinez, M.A., Newman, A.M., 2011. A solution approach for optimizing long- and short-term production scheduling at LKAB's Kiruna mine. Eur. J. Oper. Res. 211, 184–197.

Morris, C.H., 1982. Report on abandoned mineral workings and possible surface instability problems. County of Cleveland, Department of the County Surveyor and Engineer.

Morris, R.C., Ramanaidou, E.R., 2007. Genesis of the channel iron deposits (CID) of the Pilbara region, Western Australia. Aust. J. Earth Sci. 54, 733–756.

Mukka, L., 2008. Ventilation for Kiruna 1365. Min. Mag. 198 (6), 34–38.
Nilsson, B., 2010. Ideology, environment and forced re-location: Kiruna—a town on the move. Eur. Urban Reg. Stud. 17 (4), 433–442.
Perrins, H.J., 1953. Inflammable gas in the stratified ironstone mines of the Cleveland district of Yorkshire. Trans. Inst. Min. Eng. 113, 763–796 (1953–54).
Smith, S.F., 1982. Mining of Frodingham Ironstone with special reference to development operation and support. Paper submitted for admission to membership via the mature candidate route. IMM December 1982.
Smith, S.F., 1990. Structural Stability, Support and Excavation Aspects of Mine Openings in Stratified Iron Ore Deposits. PhD Thesis, University of Nottingham.
United Nations, 2013. The iron ore market situation—views of UNCTAD—Alexei Mojarov. www.unctad.org/commodities.
Whittaker, B.N., Smith, S.F., 1987. Stability and operational aspects of room and pillar mining in the UK sedimentary iron-ore deposits. In: Proceedings of the International Symposium on Underground Mining Methods and Technology, Nottingham, September 1986, pp. 393–402.

Developments in iron ore comminution and classification technologies

8

A. Jankovic
Metso Process Technology & Innovation, Pullenvale, QLD, Australia

8.1 Introduction

Hematite and magnetite are the most prominent iron ores. Most of the high-grade hematite iron ores (direct shipping ore (DSO)) are subjected to simple dry processes of beneficiation to meet size requirements. This involves multistage crushing and screening to obtain lump ($-31.5+6.3$ mm) and fines (approximately -6.3 mm) products. Low-grade hematite ores need to be upgraded to achieve the required iron content, which involves more complicated ore beneficiation processes. The level of comminution required for the low-grade hematite ore is similar to high-grade ores to deliver the same products, lumps and fines. In most cases, the fines product requires additional separation/desliming stages to remove fines containing a high level of clay and other waste minerals.

Although most of the current world iron ore production is represented by hematite ores, the magnetite reserves are significant and the growing demand for steel has opened the way for many new magnetite deposits to be developed. Compared to direct shipping hematite ores mined from the upper regolith, magnetite deposits require significant and different beneficiation, which typically involves grinding of the run-of-mine ore to a particle size where magnetite is liberated from its silicate matrix. The amount of energy required to produce a magnetite product suitable for sale as pellet plant feed is an order of magnitude higher than an equivalent direct shipping lump and fines hematite project.

Due to the depleting reserves of DSO ores and increasing development of low-grade hematite and magnetite deposits, the need for iron ore beneficiation is increasing. Even the DSO ores are requiring a higher level of processing as the depth of existing mines is increasing (below water table) where ores are wet and more sticky, which creates challenges for conventional crushing and screening.

This chapter reviews the current state of iron ore comminution and classification technologies. Firstly, it discusses the most commonly used crushing and screening technologies, including most common flowsheets and a short review of new trends. This is followed by review of comminution circuits and equipment for magnetite ores including most typical flowsheets and advances in comminution technology.

Iron Ore. http://dx.doi.org/10.1016/B978-1-78242-156-6.00008-3
© 2015 Elsevier Ltd. All rights reserved.

8.2 Iron ore crushing and screening

Iron ore is the raw material used to make pig iron, which is one of the main raw materials to make steel. About 98% of the mined iron ore is used to make steel either by the blast furnace—basic oxygen furnace (BF-BOF) route—or through the electric arc furnace (EAF) route. The majority of world crude steel is made from the BF-BOF route. Ores carrying very high quantities of hematite (greater than ~60% iron) are known as "natural ore" or "direct shipping ore," meaning they can be fed directly into the BF-BOF route. However, low-grade ores need to be beneficiated before they can be used to make steel. To meet the size specification required for the high-grade DSO products and liberate the gangues from the low-grade ores, run-of-mine ores are often subjected to various stages of crushing and screening operations.

8.2.1 Crushers

Crushers are machines that use a rigid surface to compress and break large rocks into smaller rocks. They come in many varieties, and a summary of different crusher types is provided in Table 8.1.

Jaw crushers are mainly used as primary crushers to produce material that can be transported by belt conveyors to the next crushing stages. The crushing process takes place between a fixed jaw and a moving jaw. The moving jaw dies are mounted on a pitman that has a reciprocating motion. The jaw dies must be replaced regularly due to wear. Figure 8.1 shows two basic types of jaw crushers: single toggle and double toggle. In the single toggle jaw crusher, an eccentric shaft is installed on the top of the crusher. Shaft rotation causes, along with the toggle plate, a compressive action of the moving jaw. A double toggle crusher has, basically, two shafts and two toggle plates. The first shaft is a pivoting shaft on the top of the crusher, while the other is an eccentric shaft that drives both toggle plates. The moving jaw has a pure reciprocating motion toward the fixed jaw. The crushing force is doubled compared to single toggle crushers and it can crush very hard ores. The jaw crusher is reliable and robust and therefore quite popular in primary crushing plants. The capacity of jaw crushers is

Table 8.1 Comparison of different crusher types

Crusher type	Typical process stage	Maximum feed size (mm)	Typical maximum product size (mm)	Typical capacities (t/h)
Gyratory crusher	Primary	1500	200–300	1200-over 5000
Jaw crusher	Primary	1400	200–300	Up to 1600
Horizontal impact crusher	Primary/ secondary	1300	200–300	Up to 1800
Cone crusher	Secondary	450	60–80	Up to 1200
Cone crusher	Tertiary	150	<30	Up to 1000

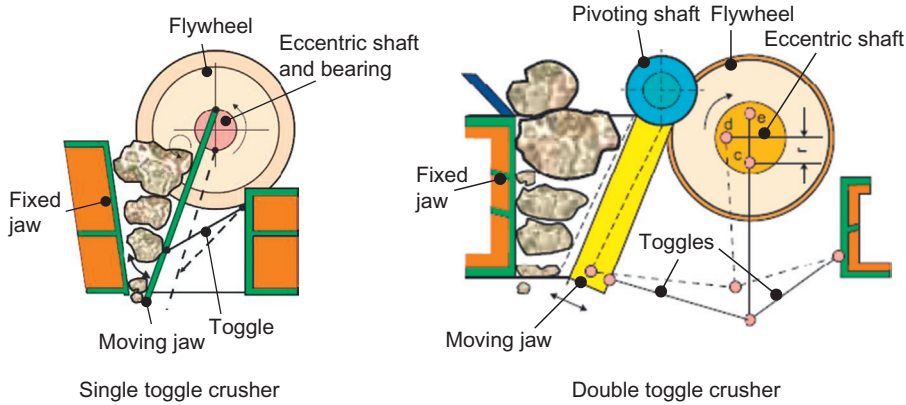

Figure 8.1 Jaw crusher schematics (Courtesy of Metso) (single toggle crusher and double toggle crusher).

limited, so they are typically used for small or medium projects up to approximately 1600 t/h. Vibrating screens are often placed ahead of the jaw crushers to remove undersize material, or scalp the feed, and thereby increase the capacity of the primary crushing operation.

Both *cone and gyratory crushers*, as shown in Figure 8.2, have an oscillating shaft. The material is crushed in a crushing cavity, between an external fixed element (bowl liner) and an internal moving element (mantle) mounted on the oscillating shaft assembly. An eccentric shaft rotated by a gear and pinion produces the oscillating movement of the main shaft. The eccentricity causes the cone head to oscillate between the open side setting (o.s.s.) and closed side setting (c.s.s.). In addition to c.s.s., eccentricity is one of the major factors that determine the capacity of gyratory and cone crushers. The fragmentation of the material results from the continuous compression that takes place between the mantle and bowl liners. An additional crushing effect occurs between the compressed particles, resulting in less wear of the liners. This is also called interparticle crushing. The gyratory crushers are equipped with a hydraulic setting adjustment system, which adjusts c.s.s. and thus affects product size distribution. Depending on cone type, the c.s.s. setting can be adjusted in two ways. The first way is by rotating the bowl against the threads so that the vertical position of the outer wear part (concave) is changed. One advantage of this adjustment type is that the liners wear more evenly. Another principle of setting adjustment is by lifting/lowering the main shaft. An advantage of this is that adjustment can be done continuously under load. To optimize operating costs and improve the product shape, as a rule of thumb, it is recommended that cones always be choke-fed, meaning that the cavity should be as full of rock material as possible. This can be easily achieved by using a stockpile or a silo to regulate the inevitable fluctuation of feed material flow. Level monitoring devices that detect the maximum and minimum levels of the material are used to start and stop the feed of material to the crusher as needed.

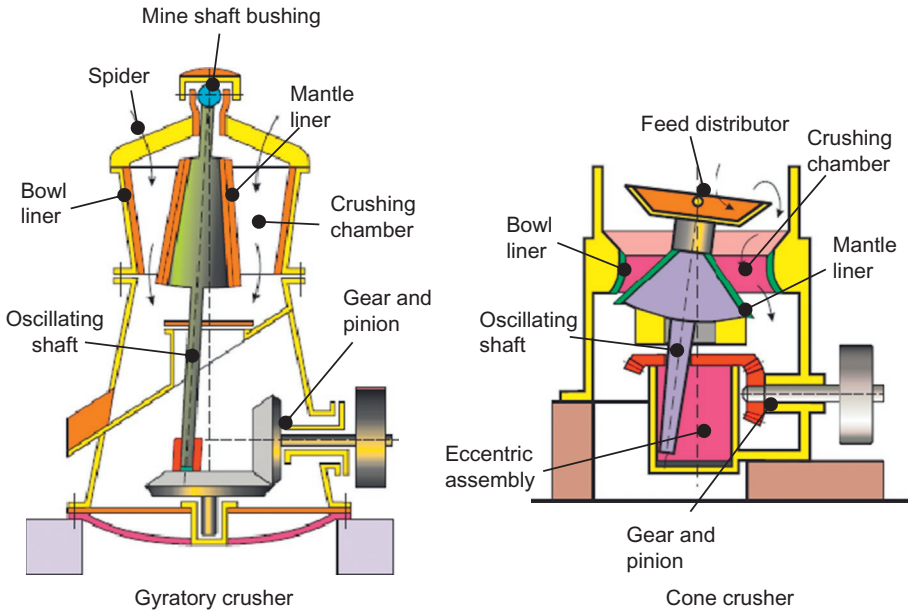

Figure 8.2 Gyratory and cone crusher schematics (Courtesy of Metso) (gyratory crusher and cone crusher).

Primary gyratory crushers are used in the primary crushing stage. Compared to the cone type crusher, a gyratory crusher has a crushing chamber designed to accept feed material of a relatively large size in relation to the mantle diameter. The primary gyratory crusher offers high capacity thanks to its generously dimensioned circular discharge opening (which provides a much larger area than that of the jaw crusher) and the continuous operation principle (while the reciprocating motion of the jaw crusher produces a batch crushing action). The gyratory crusher has capacities starting from 1200 to above 5000 t/h. To have a feed opening corresponding to that of a jaw crusher, the primary gyratory crusher must be much taller and heavier. Therefore, primary gyratories require quite a massive foundation.

The *cone crusher* is a modified gyratory crusher. The essential difference is that the shorter spindle of the cone crusher is not suspended, as in the gyratory, but is supported in a curved, universal bearing below the gyratory head or cone (Figure 8.2). Power is transmitted from the source to the countershaft to a V-belt or direct drive. The countershaft has a bevel pinion pressed and keyed to it and drives the gear on the eccentric assembly. The eccentric assembly has a tapered, offset bore and provides the means whereby the head and main shaft follow an eccentric path during each cycle of rotation. Cone crushers are used for intermediate and fine crushing after primary crushing. The key factor for the performance of a cone type secondary crusher is the profile of the crushing chamber or cavity. Therefore, there is normally a range of standard cavities available for each crusher, to allow selection of the appropriate cavity for the feed material in question.

8.2.2 Screens

Industrial screening is extensively used for size separations from 300 mm down to around 40 µm, although the efficiency decreases rapidly with fineness. Dry screening is generally limited to material above about 5 mm in size. Wet screening is common down to around 250 µm but is possible to about 40 µm. In its simplest form, a screen is a surface having many apertures, or holes, usually with uniform dimensions. Particles presented to that surface will either pass through or be retained, according to whether the particles are smaller or larger than the governing dimension of the apertures.

There are numerous different types of industrial screens available. Some of the most common are

- vibrating screens,
- static screens (grizzlies),
- trommels,
- roller screens,
- flip-flow screens,
- circular screens,
- linear screens.

The dominant screen type in industrial applications is the *vibrating screen*, of which there are many subtypes in use for coarse- and fine-screening applications. Vibrating screens have a rectangular screening surface with feed and oversize discharge at opposite ends. They are used in a variety of sizing, grading, scalping, dewatering, wet screening, and washing applications. Screens are vibrated in order to throw particles off the screening surface so that they can again be presented to the screen and to convey the particles along the screen. Vibrating motion is generally produced by vibrating mechanisms based on eccentric rotating masses with an amplitude of 1.5–5 mm and operating in a range of 700–1000 rpm. The right type of vibration also induces stratification of the feed material, which allows the finer particles to work through the layer of particles to the screen surface while causing larger particles to rise to the top. Vibrating screens of most types can be manufactured with more than one screen deck. On multiple-deck systems, the feed is introduced to the top coarse screen, the undersize falling through to the lower screen decks, thus producing a range of sized fractions from a single screen.

Inclined or circular motion screens (Figure 8.3a) are a type of vibrating screen widely used for sizing applications. A vertical circular or elliptical vibration is induced mechanically by the rotation of unbalanced weights or flywheels attached usually to a single drive shaft. The amplitude of throw can be adjusted by adding or removing weight elements bolted to the flywheels. The rotation direction can be contraflow or in-flow. Contraflow slows the material flow more and permits more efficient separation, whereas in-flow permits a greater throughput. Single-shaft screens must be installed on a slope, usually between 15° and 28° to permit flow of material along the screen.

Very coarse material is usually screened on an inclined screen called *grizzly screen* (Figure 8.3b). Grizzlies are characterized by parallel steel bars or rails set at a fixed distance apart and installed in line with the flow of ore. The gap between grizzly bars is usually greater than 50 mm and can be as large as 300 mm, with feed top size as large as 1 m. The most common use of grizzlies in mineral processing is for sizing the feed to primary and secondary crushers.

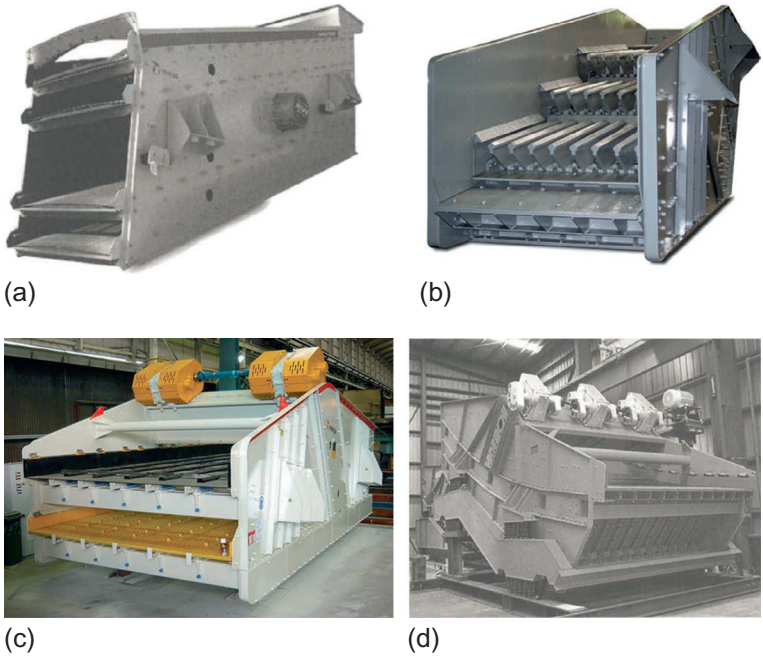

Figure 8.3 (a) Inclined four deck vibrating screen, (b) grizzly, (c) horizontal linear motion screen, and (d) banana screen.
Courtesy of Metso.

Horizontal low-head or linear vibrating *screens* (Figure 8.3c) have a horizontal or near-horizontal screening surface and therefore need less headroom than inclined screens. Horizontal screens must be vibrated with a linear or an elliptical vibration produced. The accuracy of particle sizing on horizontal screens is superior to that on inclined screens; however, because gravity does not assist the transport of material along the screen, they have lower capacity than inclined screens. Horizontal screens are used in sizing applications where screening efficiency is critical and as drain-and-rinse screens in heavy medium circuits.

Banana or multislope *screens* have become widely used in high-tonnage sizing applications where both efficiency and capacity are important. Banana screens (Figure 8.3d) typically have a variable slope of around 40–30° at the feed end of the screen, reducing to around 0–15° at the discharge end in increments of 3.5–5°. The steep sections of the screen cause the feed material to flow rapidly at the feed end of the screen. The resulting thin bed of particles stratifies more quickly and therefore has a faster screening rate for the very fine material than would be possible on a slower moving thick bed. Toward the discharge end of the screen, the slope decreases to slow down the remaining material, enabling more efficient screening of the near-size material. The capacity of banana screens is significantly greater and is reported to be up to three or four times that of conventional vibrating screens.

Rotary scrubbers are cost-effective washing units that are an integral part of a material handling system to upgrade a wide variety of primary crushed hard rock and ore, including iron ore. A rotary scrubber is a cylindrical drum with internal lifters, typically supported by trunnion rollers at either end. These high-capacity, high-retention time machines are primarily used to remove water-soluble clays, deleterious materials, and coatings from a wide variety of hard rock and ore. Rotary scrubber designs include the solid shell and combination scrubber screens and are available in a variety of diameters and lengths. Drive transmission choices include chain and sprocket, gear and pinion, or pedestal mount hydraulic motor.

8.2.3 Typical crushing and screening flowsheets

Iron ore operations commonly employ one or more stages of crushing with screening stages incorporated to remove material meeting product size specifications as soon as possible. Lump product (typically between 6 and 30 mm) attracts a premium price compared to fines product (typically less than 6 mm). Therefore, it is desirable to remove any material that falls in the lump size range as soon as it is generated and before it is broken further into the lower value fines product. Additionally, iron ore processing facilities often receive ore from various sources (such as satellite pits) with different qualities. These may be treated by different processing routes and/or blended to meet product specifications. Some examples of different iron ore crushing and screening flowsheets are provided below.

8.2.3.1 Rio Tinto iron ore processing plants

Iron ore processing by Rio Tinto in the Pilbara region of Western Australia does not involve any chemical treatment. Flowsheets for the Brockman 2 and Paraburdoo processing plants are given in Figures 8.4 and 8.5 (Kinnel, 2013). The flowsheets are relatively simple. Dry processing involves up to three crushing circuits to produce lump and fines. Wet processing is primarily aimed at the removal of clays. Key processing variables include the following:

- Feed type: if clay feed is present, the crusher will be treated as a chute. Clay is not crushable.
- Gap setting: changing the closed side setting can affect the product size distribution, product tons per hour, and bowl level.
- Crusher bowl level: maintaining a consistent bowl level can keep the crusher choke-fed, improving its operating efficiency.
- Feeder speed: feeder speed helps adjust the height of ore within the crusher bowl.
- Crusher amps: crusher current (amps) is an indication of how hard the crusher is working. A low bowl level, small gap setting, and high amps are a sign that the crusher could be working too hard. However, a high bowl level and low amps indicate the crusher is working too little. The crusher amps can also be affected by the hardness of the feed type.
- Crusher product tons per hour: the crusher product tons per hour can be affected by the gap setting. A smaller gap setting lowers the tons per hour treated by the crusher but overall could increase the amount of material produced in the desired product size fraction. This could also minimize recirculation in the system, reducing the overall power consumption.

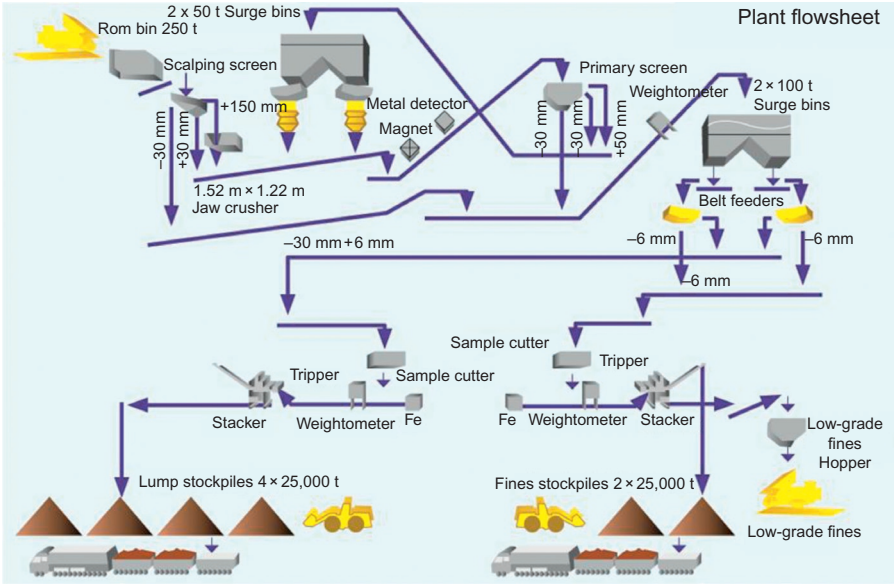

Figure 8.4 Flowsheet of the Rio Tinto Brockman 2 processing plant in Western Australia. Adopted from Kinnel (2013).

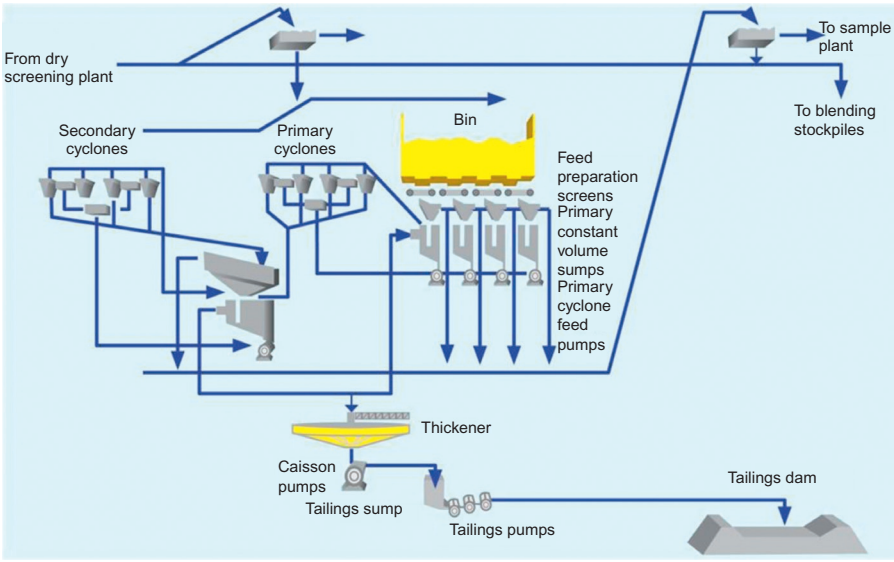

Figure 8.5 Flowsheet of the Paraburdoo processing plant in Western Australia. Adopted from Kinnel (2013).

8.2.3.2 BHP Billiton Newman iron ore handling hub

The Newman Hub ore handling facility was completed in 2010 as part of an expansion project. Here, ores received from Mt. Whaleback and the satellite operations at Orebody 18 and Wheelarra (via 49-car shuttle trains) are tertiary crushed and screened, blended to form Newman lump and fines products, and loaded onto trains for haulage to Port Hedland. Lump and fines ores from the Eastern Ridge operation at Orebody 23/25 are added to ore cars en route to the port.

A schematic flowsheet of the Newman Hub is provided in Figure 8.6 showing the ores from the three sources combined on the coarse ore stockpile (COS), which then feeds the crushing and screening plant. Blending of the three ores is an important function performed by the COS as the Newman Hub only treats the blended ore. The Newman Hub consists of five scalping screens, eight product screens, and three tertiary crushers. The top deck of the scalping screens has 46 mm × 68 mm longitudinal slots, whereas the product screen has 40 mm × 60 mm longitudinal slots. Bottom decks of both screens have longitudinal slots of 7 mm × 25 mm. The tertiary crushers are HP800s with an installed power of 590 kW and gap settings of 60 mm to minimize fines production.

The scalping screens, fed from the COS, remove as much fines (−7 mm) as possible prior to tertiary crushing. The oversize from the top decks of both the scalping screens (+46 mm) and the product screens (+40 mm) is combined and together fed to the tertiary crushers. The scalping screen middlings (−46 + 7 mm) and the tertiary crusher product are fed to the product screens. The middlings (−40 + 7 mm) from the product screens report to the lump product, while the undersize from both the scalping screens and the product screens (−7 mm) are combined and represent the fines product.

8.2.3.3 Roy Hill operation

Roy Hill is a joint venture between Ms Rinehart's Hancock Prospecting and South Korean steel giant POSCO, Japanese company Marubeni, and Taiwan's China Steel Corporation. Designed to produce 55 Mtpa (wet) of lump and fines products, a wet processing and beneficiating model has been selected, as approximately 70% of the bedded resource is below the water table and contains wet, sticky plastic clay-rich shale bands, which would be difficult to handle in a dry crushing and screening process. Lump ores produced from the processing plant will range in size from 8 to 40 mm, while fines ores produced will be less than 8 mm in size.

As shown in Figure 8.7, the proposed processing plant will include the following components: three remote primary/secondary crushing stations, overland conveying, crushed ore stockpile, wet scrubbing and screening, tertiary crushing, product screening, desanding, sampling, stockyard stacking, reclaim and train loadout, and tailings storage facilities.

The three primary and secondary crushing stations will each crush 5000 tons of ore an hour (t/h) into particles smaller than 150 mm. This material is then conveyed to a surge stockpile prior to being fed into the processing plant. When the ore is fed into the processing plant, it enters the scrubbers, before being sent to wet screening. Oversize ore that is greater than 32 mm in size is then conveyed to the tertiary crushers. Ore that is less than 32 mm but greater than 8 mm is conveyed to the lump stockpile. Ore that is finer than 8 mm but greater than 1 mm is conveyed to the fines stockpile. Any ore that is finer than 1 mm in size is conveyed to the desanding plant for beneficiating.

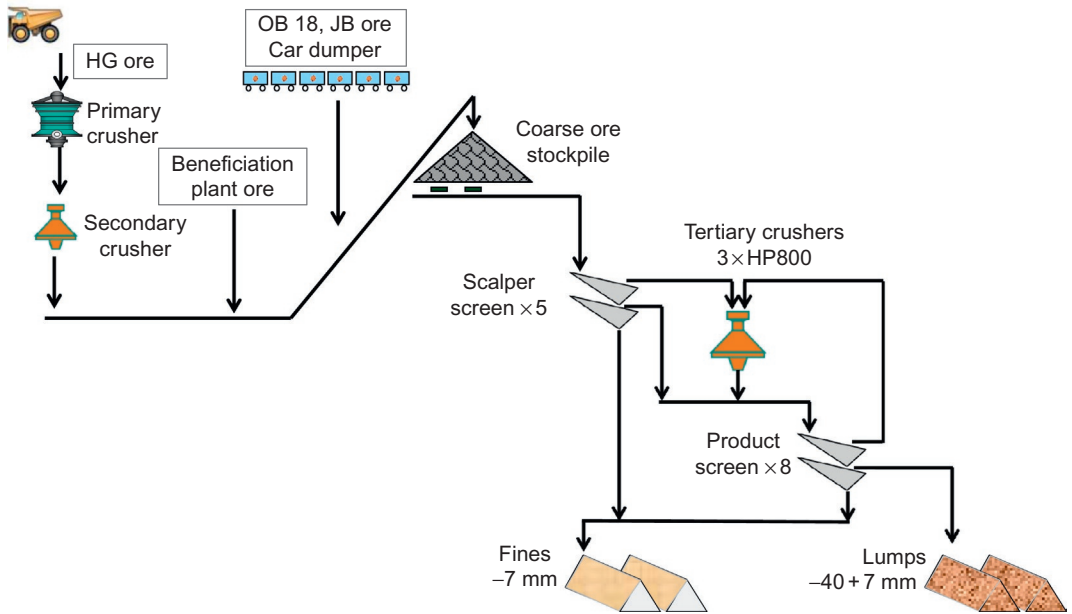

Figure 8.6 General flowsheet of the Newman Hub in Western Australia.

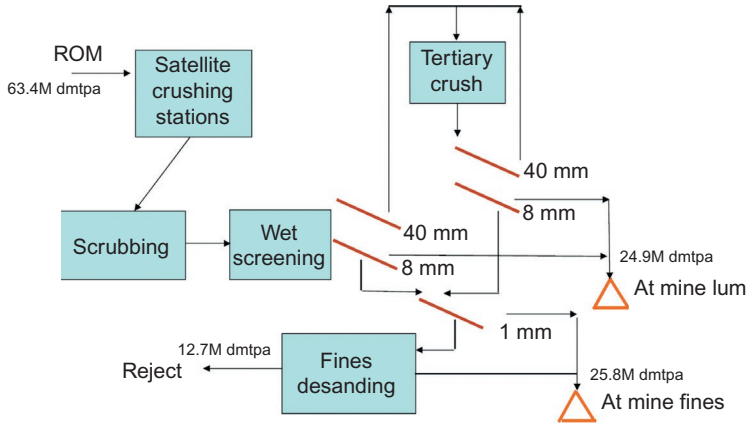

Figure 8.7 Proposed Roy Hill processing flowsheet.
Adopted from Clout and Fitzgerald (2011).

8.2.3.4 Vale S11D project

The largest iron ore company in world, Vale, is developing S11D project, located in the Amazon region of Northern Brazil (Carajás), which is expected to produce 90 million Mtpa of iron ore (Carter, 2011). In designing the innovative, modular ore crushing and screening plant for SD11, Vale was faced with the challenge of coping with the region's wet-season humidity, which potentially could reduce process efficiency. The iron ore in this area contains a large volume of fines (20–30% below 150 µm), which can be transformed by high moisture content into a sticky mass that is almost impossible to screen. Vale initially considered wet-process screening using water sprays to overcome the problem but ultimately rejected that approach as too costly. Vale has engaged Haver & Boecker Latinoamericana (HBL), which is the major supplier of vibrating screens to oil sands operations in Alberta, Canada, having delivered more than a dozen units there over the past 10 years. Those screening machines, tasked with processing up to 15,000 Mt/h of oil-sand slurry, measure 4 m wide × 11 m long and weigh more than 100 tons each. HBL engineers worked with Vale's project team to design a dry-screening setup that would enhance process efficiencies at S11D. Tests comparing the performance of elliptical-motion against linear motion screens indicated that HBL's eccentric-drive vibrating screen would achieve desired results when fed the sticky ore. Subsequently, HBL was awarded a contract valued at more than $30 million to deliver thirty 2.4 m wide × 9.4 m long double-deck eccentric screens for the S11D project over the course of a year.

8.2.4 Mobile crushing and screening plant applications for small- to medium-sized iron ore projects

There is now a new generation of mobile crushing and screening plant systems, which have been developed based on the motivation of reducing truck haulage. Newly designed mobile crushing and screening plant systems have the advantages of mobility, flexibility, economy, and reliable performance, making this system very appealing for small- to medium-sized projects or projects where a number of resources are separated

by distance. Similarly, the advantages of mobile crushers are lower capital cost (up to 30% less), higher mobility, and higher salvage value at the end of the project life. Mobile crushing plants are not suited to large long-life projects, heavy rainfall climates, or arctic climates. The design considerations, operability, and maintainability require careful consideration. The equipment selection would also be based on different criteria to fixed plant (Connelly, 2013).

8.3 Iron ore grinding and classification

Compared to direct shipping hematite ores mined from the upper regolith, magnetite deposits are much finer-grained and therefore require significant grinding to liberate the magnetite from its silicate matrix. Various magnetite ore grinding flowsheets have been implemented in the past, including

- conventional three (and four) stages of crushing followed by primary and secondary milling,
- primary crushing followed by wet SAG or AG milling and ball or pebble milling,
- air-swept AG milling (for coarse grinding).

Historically, the lowest operating cost for grinding fine-grained ores was achieved by multistage fully autogenous (AG) grinding (Koivistoinen et al., 1989) with integrated magnetic separation steps between the stages. The major benefit of fully AG grinding is the elimination of steel grinding media. In addition to reduced costs, this means the coarse magnetic separation ahead of pebble crushing does not need to discriminate between steel and magnetite. The magnetic separation step between grinding stages progressively reduces the amount of material to be ground and in many cases improves the abrasive properties of the concentrate.

Four North American subsidiaries of Cleveland-Cliffs, Inc. employ AG milling. The original AG milling circuit consisted of an AG mill followed by cobber magnetic separation of pebbles, pebble milling of the magnetic concentrate, a finisher magnetic separation stage, and silica flotation. It was installed at Empire Mines in 1963, which had six individual concentrating lines with a capacity of 1.6 Mtpa of pellets. There have been three expansions since, and in the 1990s, Empire Mines had a total of 24 individual concentrating lines and a total plant capacity of 8 Mtpa of pellets. The target grind size of the circuits varies between the 90% and 95% minus 500 mesh (32 μm) depending on the ore and operating conditions (Rajala et al., 2007). The flowsheet for a typical Empire grinding—concentrating line is shown in Figure 8.8.

LKAB's Kiruna is the world's largest, most modern underground iron ore mine. Ore is mined using sublevel caving, with sublevels spaced at 28.5 m vertically. After primary crushing and hoisting to surface, the ore is processed in Kiruna's complex consisting of a sorting plant, two concentrators, and two pellet plants to deliver pellet and sinter fines products (http://www.lkab.com/). Magnetite ore is ground using AG mills followed by cobber magnetic separation and pebble milling of the magnetic concentrate (Hahne et al., 2003). The target grind size is around 80% minus 45 μm depending on the ore and operating conditions (Tano et al., 2006).

Application of more efficient grinding technologies developed in the last 20 years, including high-pressure grinding rolls (HPGRs) for fine crushing and stirred milling

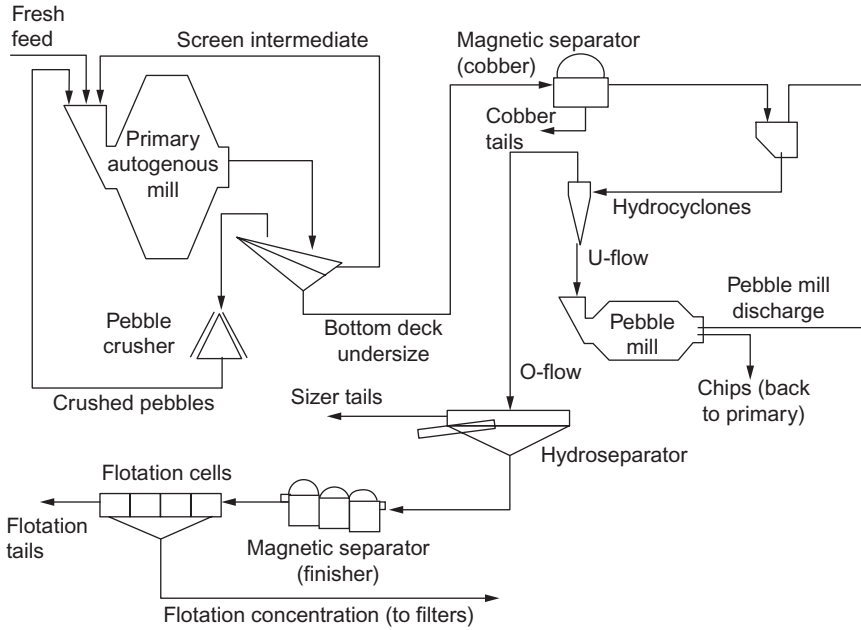

Figure 8.8 Typical Empire grinding—concentrating line (Rajala et al., 2007).

for fine grinding, has provided opportunities to further reduce the operating costs associated with grinding. At Empire Mines, an HPGR was installed for processing crushed pebbles, and its introduction has resulted in a primary AG mill throughput increase in the order of 20% (Dowling et al., 2001). Application of Vertimill® fine grinding technology at Hibbing Taconite Company enabled processing of lower-grade ores and increased the concentrate production (Pforr, 2001).

The Sino iron project, located in Cape Preston, about 100 km southwest of Karratha in the Pilbara region of Western Australia, will be the world's biggest magnetite iron ore mine when fully operational (Kalra and Delgado, 2013). The project will mine about 140 million metric tons of ore each year and the processing plant will produce approximately 80 million tons of magnetite concentrate. The ore will be crushed using four in-pit gyratory crushers before being transported to the concentrator. The crushed ore then enters the grinding circuit consisting of six grinding mill lines. Each line consists of a 12.2 m (40 ft) diameter × 11 m (36 ft) long AG mill with a 28 MW gearless motor in closed circuit with a pebble crusher and primary classifying cyclones. This is followed by a rougher magnetic concentrator and then a 7.9 m (26 ft) diameter × 13.6 m (44.6 ft) long ball mill. Each ball mill has two 7800 kW motors, giving a total of 44 MW of installed mill power in each of the six grinding lines. The final product from these large regrind ball mills using small grinding media will be approximately 28 µm. The mills will produce a fine ore stream, which enters finisher magnetic separators to produce the final concentrate. The concentrate will be thickened and stored before being pumped 25 km to the port, where it is filtered to reduce moisture. From there, the concentrate will be loaded on ships for use in steelmaking (Figure 8.9).

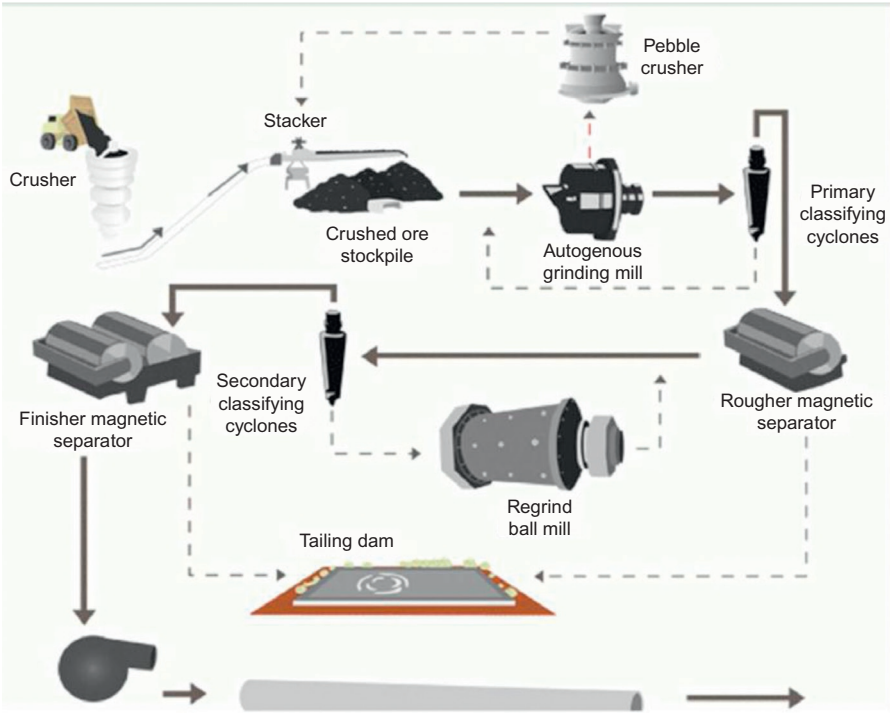

Figure 8.9 Conceptual flowsheet of Sino iron magnetite concentration plant. Modified from Kalra and Delgado (2013).

8.3.1 Grinding equipment

Grinding is the final stage of comminution, performing size reduction at finer sizes than crushers. Size reduction is achieved by a combination of impact breakage, abrasion, and attrition. After grinding, the state of the solid material is changed: the grain size, the grain surface, and the grain shape. The grinding of solid matters occurs under exposure of mechanical forces that break the structure by overcoming of the interior bonding forces. There are many different types of grinding mills and many types of materials processed in them.

8.3.2 Tumbling mills

The term "tumbling mill" encompasses many different grinding devices used in the industry. Any mill consisting of a drum that rotates on a horizontal axis, which grinds or pulverizes material mixed with a grinding media such as steel balls, can be classified as a tumbling mill. Different types of tumbling mill are characterized with respect to dry or wet operation, particle size range, grinding media type and size, mechanical design relationships, wear protection, etc.

8.3.2.1 Autogenous and semiautogenous mills

AG and semiautogenous (SAG) mills represent a type of tumbling mill that, under certain conditions, can replace size reduction equipment used for secondary crushing as well as primary and final grinding (Herbst, et al., 2003). The unique feature of this type of device is that the coarse ore particles themselves are used as the grinding media, not unlike a pebble mill in which the pebbles are generated naturally from the ore body. AG and SAG mills are coarse grinding devices; they consist of a tumbling drum with 25–40% volume filling of ore. They are fed with run-of-mine ore or primary crusher product that is around 250 mm. The main modes of breakage are thought to be impact breakage and abrasion.

In fully AG mills, steel grinding media is not used and coarse rocks in the feed are the only grinding media. In SAG mills, the rock grinding media is complemented with a small proportion (3–20% of mill volume) of steel balls (with diameter of ~120–150 mm). The steel ball media in an SAG mill changes the nature of the mill performance considerably compared to an AG mill. The additional charge weight due to steel media in an SAG mill must be considered in the mill design, and if an AG mill is to be converted to an SAG mill, modifications may be required.

Many circuit configurations are possible, but essentially, AG and SAG mills can be operated as a single-stage primary mill or can be followed by secondary milling in a ball, rod, pebble, or stirred mill. They are often operated in closed circuits with a trommel screen or external vibrating screen classifying the discharge. Pebble crushers are sometimes used to crush the largest pieces in the recycle stream. The product size of an AG mill depends strongly on the nature of the ore being ground. Tests must be carried out to determine the competency of the ore and its "natural" particle size. Results from pilot-plant tests are used to calculate the required mill size and motor power for the particular production capacity. Modern-day AG and SAG mills are typically larger than 12 m in diameter and are powered by electrical motors larger 20 MW (see examples shown in Figure 8.10).

8.3.2.2 Ball mills

The ball mill is a tumbling mill that uses steel balls as the grinding media. The length of the cylindrical shell is usually 1–1.5 times the shell diameter (Figure 8.11). The feed

Figure 8.10 Large SAG mill.

Figure 8.11 Ball mill external appearance and internal view.

can be dry, with less than 3% moisture to minimize ball coating, or slurry containing 20–40% water by weight. Ball mills are employed in either primary or secondary grinding applications. In primary applications, they receive their feed from crushers, and in secondary applications, they receive their feed from rod mills, AG mills, or SAG mills.

Ball mills are filled up to 40% with steel balls (with 30–80 mm diameter), which effectively grind the ore. The material that is to be ground fills the voids between the balls. The tumbling balls capture the particles in ball/ball or ball/liner events and load them to the point of fracture.

When hard pebbles rather than steel balls are used for the grinding media, the mills are known as "pebble mills." As mentioned earlier, pebble mills are widely used in the North American taconite iron ore operations. Since the weight of pebbles per unit volume is 35–55% of that of steel balls, and as the power input is directly proportional to the volume weight of the grinding medium, the power input and capacity of pebble mills are correspondingly lower. Thus, in a given grinding circuit, for a certain feed rate, a pebble mill would be much larger than a ball mill, with correspondingly a higher capital cost. However, the increase in capital cost is justified economically by a reduction in operating cost attributed to the elimination of steel grinding media.

In general, ball mills can be operated either wet or dry and are capable of producing products in the order of 100 µm. This represents reduction ratios of as great as 100. Very large tonnages can be ground with these ball mills because they are very effective material handling devices. Ball mills are rated by power rather than capacity. Today, the largest ball mill in operation is 8.53 m diameter and 13.41 m long with a corresponding motor power of 22 MW (Toromocho, private communications).

8.3.3 Classification equipment

The purpose of classification in a grinding circuit is to remove material that meets the product size requirements from the circuit and recycle oversize material back to the grinding mill for further comminution. For wet processing, the most common are the so-called hydraulic classifiers such as hydrocyclones, classifying spirals and rakes, settling cones, and others, while for dry classification of fine particles, the dominant equipment are air classifiers.

8.3.3.1 Hydrocyclone separators

The hydrocyclone, also referred to as cyclone, is a classifying device that utilizes centrifugal force to accelerate the settling rate of slurry particles and separate particles according to size, shape, and specific gravity. It is widely used in the minerals industry, with its main use in mineral processing being as a classifier, which has proved extremely efficient at fine separation sizes. It is extensively used in closed-circuit grinding operations but has found many other uses, such as desliming, degritting, and thickening.

A typical hydrocyclone (Figure 8.12a) consists of a conically shaped vessel, open at its apex, or underflow, joined to a cylindrical section, which has a tangential feed inlet. The top of the cylindrical section is closed with a plate through which passes an axially mounted overflow pipe. The pipe is extended into the body of the cyclone by a short, removable section known as the vortex finder, which prevents short-circuiting of feed directly into the overflow. The feed is introduced under pressure through the tangential entry, which imparts a swirling motion to the pulp. This generates a vortex in the cyclone, with a low-pressure zone along the vertical axis, as shown in Figure 8.12b. An air-core develops along the axis, normally connected to the atmosphere through the apex opening, but in part created by dissolved air coming out of solution in the zone of low pressure. The centrifugal force accelerates the settling rate of the particles, thereby separating particles according to size, shape, and specific gravity. Faster settling particles move to the wall of the cyclone, where the velocity is lowest, and migrate to the apex opening (underflow). Due to the action of the drag force, the slower-settling particles move toward the zone of low pressure along the axis and are carried upward through the vortex finder to the overflow.

Hydrocyclones are almost universally used in grinding circuits because of their high capacity and relative efficiency. They can also classify over a very wide range of particle sizes (typically 5–500 μm), smaller diameter units being used for finer classification. However, cyclone application in magnetite grinding circuits can cause inefficient operation due to the density difference between magnetite and waste minerals (silica).

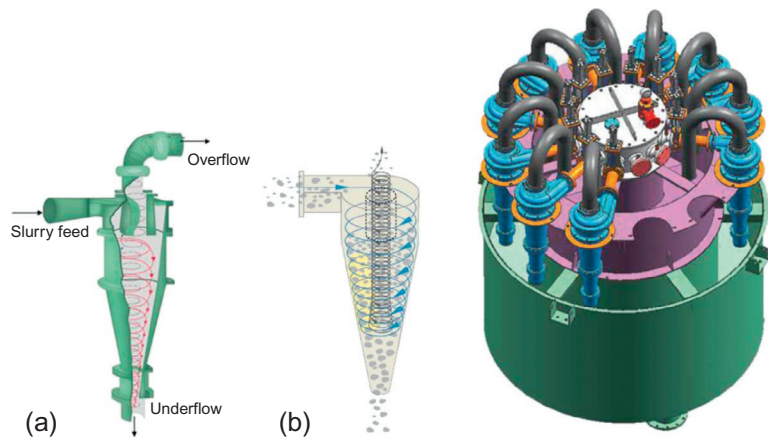

Figure 8.12 Hydrocyclone (http://www.aeroprobe.com/applications/examples/australian-mining-industry-uses-aeroprobe-equipment-to-study-hydro-cyclone) and hydrocyclone battery. Cavex hydrocyclone overvew brochure, http://www.weirminerals.com/products_services/cavex.aspx.

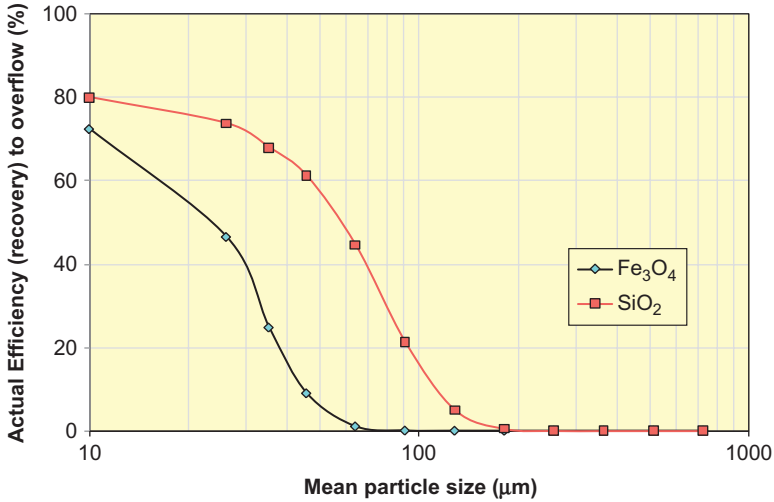

Figure 8.13 Cyclone efficiency for magnetite Fe_3O_4 and silica SiO_2—industrial survey.

Magnetite has a specific density of about 5.15, while silica has a specific density of about 2.7. In hydrocyclones, dense minerals separate at a finer cut size than lighter minerals. Therefore, liberated magnetite is being concentrated in the cyclone underflow, with consequent overgrinding of the magnetite. Napier-Munn et al. (2005) noted that the relationship between the corrected cut size (d_{50c}) and particle density follows an expression of the following form depending on flow conditions and other factors:

$$d_{50c} \propto \left(\rho_s - \rho_l\right)^{-n}$$

where ρ_s is the solids density, ρ_l is the liquid density, and n is between 0.5 and 1.0. This means that the effect of mineral density on cyclone performance can be quite significant. For example, if the d_{50c} of the magnetite is 25 µm, then the d_{50c} of silica particles will be 40–65 µm. Figure 8.13 shows the cyclone classification efficiency curves for magnetite (Fe_3O_4) and silica (SiO_2) obtained from the survey of an industrial ball mill magnetite grinding circuit. The size separation for silica is much coarser, with a d_{50c} for Fe_3O_4 of 29 µm, while that for SiO_2 is 68 µm. Due to this phenomenon, the magnetite grinding mills in closed circuits with hydrocyclones are less efficient and have lower capacity compared to other base metal ore grinding circuits.

8.4 Future trends in iron ore comminution and classification

The *in situ* grade of magnetite ores is much lower (~20–50% Fe) compared with hematite/goethite ores. Therefore, magnetite ores will always require crushing and grinding followed by magnetic separation and, in some cases, reverse flotation to produce high-grade concentrates suitable for pelletizing. Consequently, the production

costs are much higher for magnetite ore compared to hematite/goethite ore. Given the increasing cost of energy, the need to reduce greenhouse gas emissions, and the introduction of carbon taxes, there will be continual pressure to reduce the processing costs, in particular the high costs associated with grinding the ore, which typically needs to be ground finer than 50 μm to liberate the magnetite from the gangue minerals.

As magnetite ores become increasingly fine-grained, more efficient fine grinding and separation technologies are required to liberate magnetite grains from their gangue matrix. This will almost certainly determine the future of magnetite operations should iron ore prices be kept at or fall below their current levels, where only the lower-cost producers will survive.

New hematite/goethite ore types now being exploited are also slowly trending downward in grade and in the longer term will require more processing to make them attractive to overseas customers and maximize resource utilization. Efficient beneficiation processes are needed for removing gangue components such as alumina, silica, and phosphorus while minimizing the loss of iron units (Holmes, 2013). In addition, mining from deeper areas within pits tends to produce ores that are finer and wetter with a lower lump yield. This typically requires more efficient screening and less crushing. There is also a need to develop economic dewatering and drying processes for the new ore types, due to their high porosity, as mining moves progressively below the water table.

Material handling design changes have accommodated finer and damper ore types. There has been a reduction in rock box and microledge impact systems moving toward more high-angle chutes and bins with nonstick wear liners. Also, moisture control in processing facilities and of final products has addressed changes to material types and blending techniques.

This section discusses future trends in the fine grinding and separation technologies as well as HPGR technology.

8.4.1 Fine grinding technologies: stirred milling

As the product size required from tumbling ball mills becomes finer, the optimum ball size decreases. At a certain size, however, the small balls (moving under the influence of gravitational forces in a tumbling mill) can no longer provide sufficient impact force for particle fracture. Stirred mills increase the impact forces by inducing larger momentum changes than the tumbling mill. They are recognized to be more efficient than tumbling mills, especially for fine grinding applications.

The stirred mill is a fine grinding device capable of producing product particle sizes less than 1 μm. A vertical or horizontal cylindrical vessel is charged with grinding media made of steel or ceramic and the material to be ground. The charge is stirred by means of a rotating central shaft with either flights, disks, or arms extending into the charge. Different devices are stirred with different rotational speeds ranging from 20 rpm up to 2000 rpm. The most intense agitation occurs just in front and just to the rear of the moving flights or impellers. In vertical operation, slurry can be introduced into the bottom or top of the vessel. For horizontal orientations, the mill is fed under pressure at one end and discharged through a retaining ring at the other end. The stirred mill is usually used in combination with a classification device appropriate for

the small product particle size. The power intensity (energy input per unit volume) of these mills is larger than that of conventional tumbling ball mills. Values of up to 100 times greater volume-specific energy have been reported. The high power intensity is attributed to the relatively large impeller speeds. Compared with tumbling ball mills, residence times are significantly reduced in the stirred mills. This is attractive in terms of the volume of installed mills and comparatively short retention times.

8.4.1.1 Vertimill®

The Vertimill® is a vertical stirred mill that uses a helical screw to impart motion in the charge. Mechanically, the Vertimill is a very simple machine with an agitating screw suspended into the grinding chamber, supported by spherical roller bearings, and driven by a fixed speed motor through a planetary gearbox. Figure 8.14 presents a schematic diagram of the Vertimill®. The screw rotates slowly such that the ball charge and slurry are not fluidized, but settle under gravity. The screw action pulls the ball charge up the center of the mill, and the charge eventually cascades over the edge of the screw, creating a general downward flow pattern at the mill perimeter. This pattern of flow, coupled with the low velocities involved, ensures that the grinding media and particles stay in contact with one another, thus enabling the efficient transfer of the drive energy into attrition and abrasion breakage throughout the charge. The operating conditions of the Vertimill® are very similar to those of the conventional ball mill in the sense that the percentage solids of the feed should be kept in the range of between 65% and 75% by mass. The power draw of the mill is directly linked to the mass of balls within the mill. The distinct advantage that the VTM™ has over the conventional ball mill is its ability to use media smaller than 25 mm more effectively.

Figure 8.14 Schematic of the Vertimill®.

Table 8.2 Vertimill® installations in Brazilian iron ore operations (Bergerman and Delbony, 2014)

Project	Company	Ore	State	Mill type	Units	Project status
Germano	Samarco	Iron	Minas Gerais	VTM-1500	1	In operation
Conceição do Mato Dentro	Anglo American	Iron	Minas Gerais	VTM-1500	16	In construction
	Vale			VTM-200	1	R&D
Serra Azul	MMX	Iron	Minas Gerais	VTM-3000	14	In construction

In the past 20 years, more than 60 Vertimill® machines have been sold for iron ore applications, with more than 20 of those in the last 2 years alone. Table 8.2 lists examples of the Vertimill® in Brazilian iron ore applications. The Metso Vertimill® is very common in regrind applications, but the industry quickly realized its potential in coarser applications as well.

8.4.1.2 IsaMill™

The IsaMill™, as shown in Figure 8.15, is a horizontal stirred mill consisting of a series of 7–8 rotating grinding disks mounted on a cantilevered shaft that is driven through a motor and gearbox. The disks operate at tip speeds of 21–23 m/s, resulting in energy intensities of up to 300 kW/m^3. The mill is filled with suitable grinding media, and the space between each of the disks is essentially an individual grinding chamber. As a result, the mill effectively comprises eight grinding chambers in series. The media is set in motion by the action of the grinding disks, which accelerate the media radially toward the shell. Between the disks, where the media is not subjected to the high outward acceleration of the disk face, the media is forced back in toward the shaft—creating a circulation of

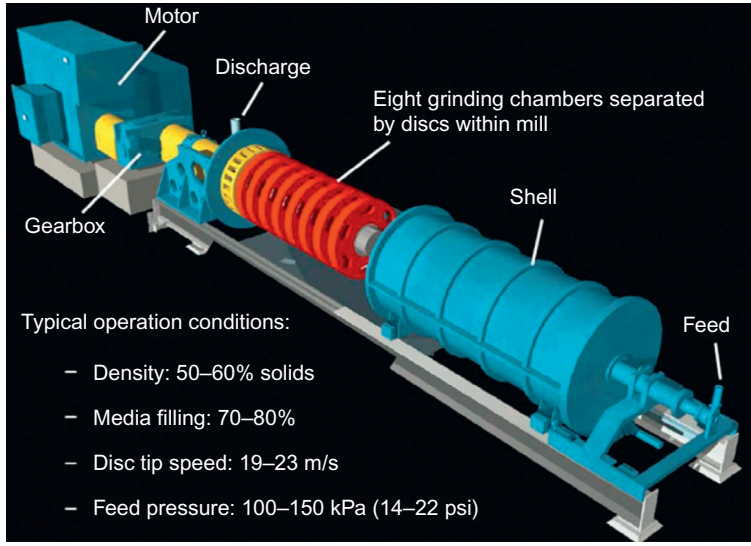

Figure 8.15 IsaMill™ layout (de Waal et al., 2012).

media between each pair of disks. Minerals are ground as a result of the agitated media, the predominant mechanism being attrition grinding (de Waal et al., 2012).

IsaMill™ operations started in 1994 at the Mount Isa Mines lead/zinc concentrator and then at MIM's McArthur River mine in 1995. These IsaMill™ machines have been used to liberate sphalerite and galena at Mount Isa and silica at McArthur River by grinding to less than 7 µm. However, the application of IsaMill™ in iron ore industry is more recent. In July 2011, the first IsaMill™ to grind magnetite was successfully commissioned at Xstrata Coppers' Ernest Henry Mine (EHM). The magnetite circuit at EHM is designed to treat 6 Mtpa and produce 1.2 Mtpa of magnetite concentrate. A 3 MW, M10,000 IsaMill™ operates in the circuit, treating magnetic rougher concentrate sizing between 150 and 200 µm and reducing it down to 40–45 µm, before it is further cleaned to produce the final grade concentrate (Larson et al., 2013). Another IsaMill™ to grind magnetite was successfully commissioned at the beginning of 2014 at Arrium Whyalla magnetite concentrator in South Australia (private communications).

8.4.2 Fine screening technologies

Derrick Corporation is considered the world leader in the supply of high-frequency screens for fine separation. Derrick introduced several significant innovations in fine screening, including the following:

- Screening surfaces such as sandwich and polyurethane to reduce blinding at fine sizes and increase open area
- A novel repulping mechanism to maximize removal of undersize particles
- Screen designs to increase the effective screen width: first with the multifeed screening machine and followed by the newest innovation, the Stack Sizer

Derrick developed polyurethane screen surfaces with high open area (as high as 45%) that will not be blinded with near-size material and last 20–30 times longer than stainless steel wire cloth. These screen surfaces are available with openings as fine as 45 µm and last for 4–12 months prior to requiring replacement depending on the abrasiveness of the material.

The Stack Sizer fine-screening machine was introduced in 2001. It has considerably greater capacity than any other type of fine wet screening machine previously available, with up to five vibrating screen decks operating in parallel for a total effective width of 5.1 m (17 ft). As shown in Figure 8.16, the decks are positioned one above the other and each deck has its own feed box. Each screen deck, consisting of two screen panels in series, is equipped with an undersize collection pan, which discharges into a common launder with a single outlet. Similarly, the oversize from each of the screen decks collects in a single hopper with a common outlet. Two Super G® vibrating motors rated at 1.9 kW (2.5 HP) each and rotating in opposite directions produce a uniform high-frequency linear motion throughout the entire length and width of all screen decks for superior oversize conveyance.

At KMAruda iron ore mine in Russia, two Stack Sizer screens fitted with 100 µm urethane panels were installed instead of hydrocyclones on one concentrator production line. Improved classification efficiency in the second-stage circuit resulted in greater line capacity and a significant reduction in specific power consumption (>50%) with the elimination of one mill. The plant recovery was also improved due to reduced overgrinding of magnetite. The grinding circuit using fines screens at KMAruda iron ore mine is illustrated in Figure 8.17.

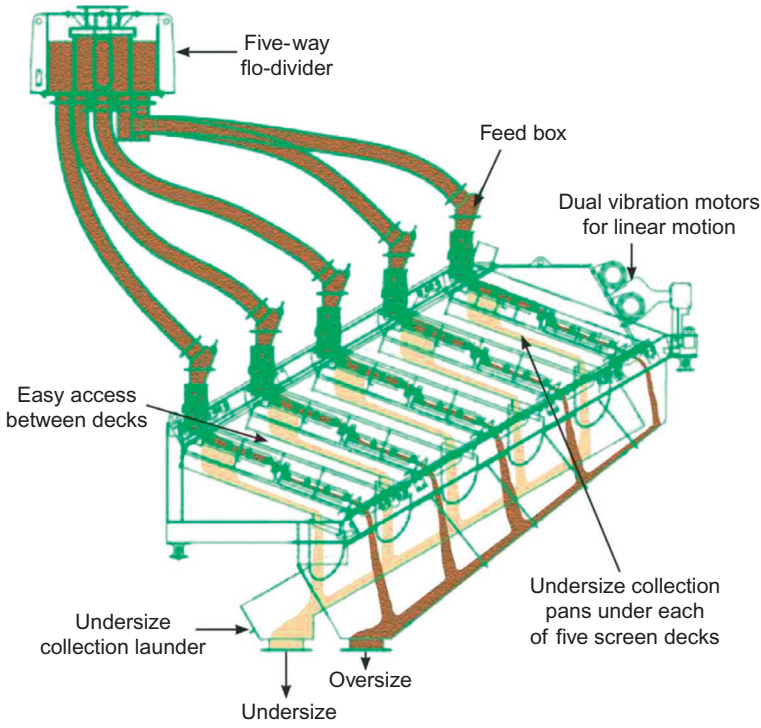

Figure 8.16 Derrick screen principle of operation.

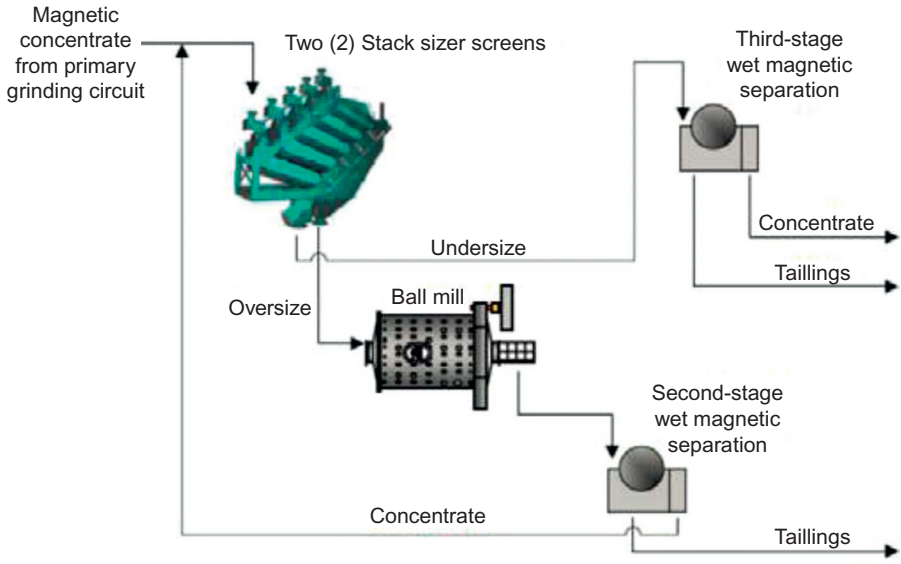

Figure 8.17 KMAruda second-stage grinding circuit with fine screen classification.

A highly efficient grinding circuit consisting of Vertimill® in closed circuit with Derrick screens will be implemented in Altay Polimetally (http://im-mining.com/2013/04/17/metso-receives-two-repeat-orders-for-altay-polimetallys-mine-in-kazakhstan/) and it was scheduled to commence operation in June 2015. The characteristics of this circuit are:

- Two (2) Vertimill® TM-4500-C
- Bond work index of 19.6 kWh/t for sulfide ore
- Bond work index of 14.1 kWh/t for oxide ore
- Feed 90% passing size (F_{90}) of 3 mm
- Capacity: 200 mtph of sulfide ore, 245.5 mtph of oxide ore per line
- Product 80% passing size (P_{80}) of 63 µm
- Closed circuit with Derrick screens
- At least 50% more energy-efficient than a conventional ball mill in closed circuit with hydrocyclones (Figure 8.18)

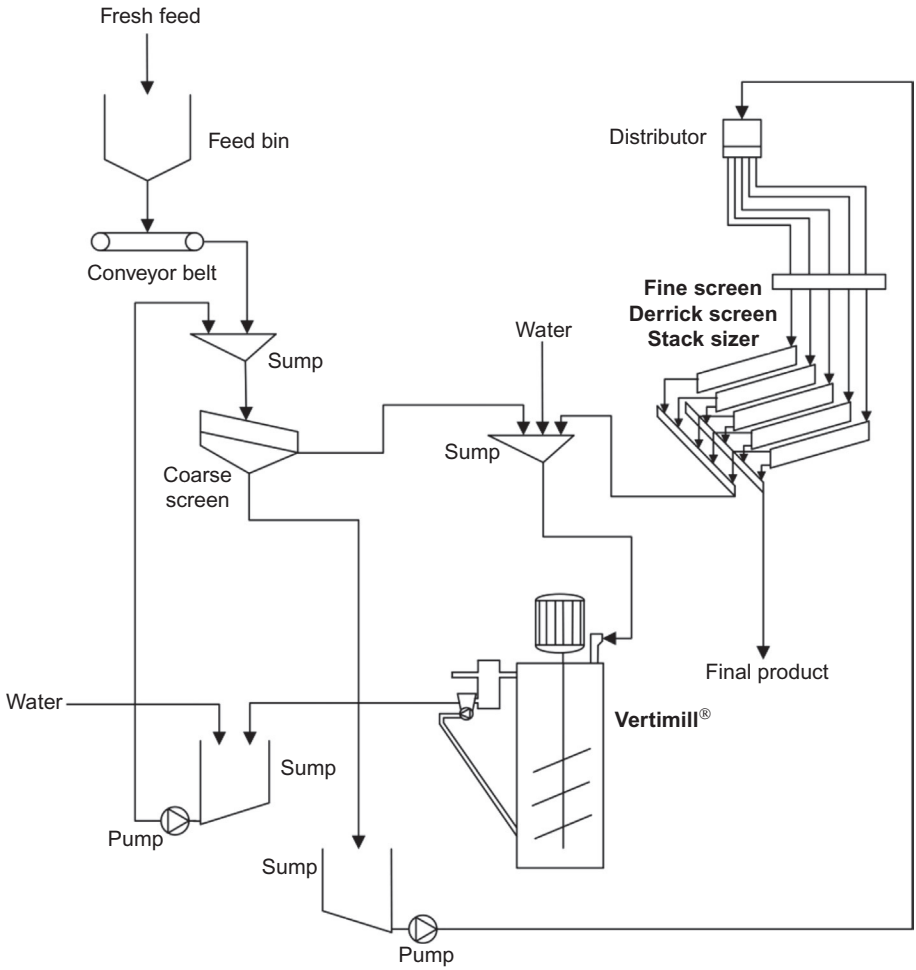

Figure 8.18 Schematic diagram of proposed flowsheet consisting of Vertimill® in closed circuit with Derrick screens.

8.4.3 Vertical roller mill

Vertical roller mills (VRM) have been around since the early 1900s and are accepted technology in the cement, power, and industrial minerals industries. However, there are very few examples of applications in the mining industry to date. The main components of a VRM are shown in Figure 8.19. Breakage in a VRM occurs by compression and in some cases shear created by two, three, four, or six rollers compacting material against the rotating disk (grinding table).

Feed material falls from the central feed chute onto the grinding table, and the centrifugal force of rotating table accelerates the material toward the grinding track where it is compressed under the grinding rollers. The table is driven by an electrical motor and the rollers rotate due to the frictional force established in the grinding bed. The grinding force is made up of the net weight of the rollers and an additional hydraulic force from the hydraulic cylinders attached to the rollers. In the conventional "air-swept" mode, air enters the mill in the lower part of the housing and passes up through the nozzle ring adjacent to the edge of the grinding table carrying the material upward to the classifier. In the modified "overflow mode," material is transported mechanically via an external conveyor to a two-stage classifier. The first stage consists of a static classifier that allows the coarse particles and some middlings to return directly to the mill. The undersize from the static classifier is treated in a dynamic classifier for final classification followed by dedusting. The coarse material from the dynamic classifier is also returned to the VRM. Pilot tests conducted by Anglo for a zinc ore demonstrated that the energy required for classification is reduced by approximately 50% in "overflow mode" compared to conventional "air-swept" classification

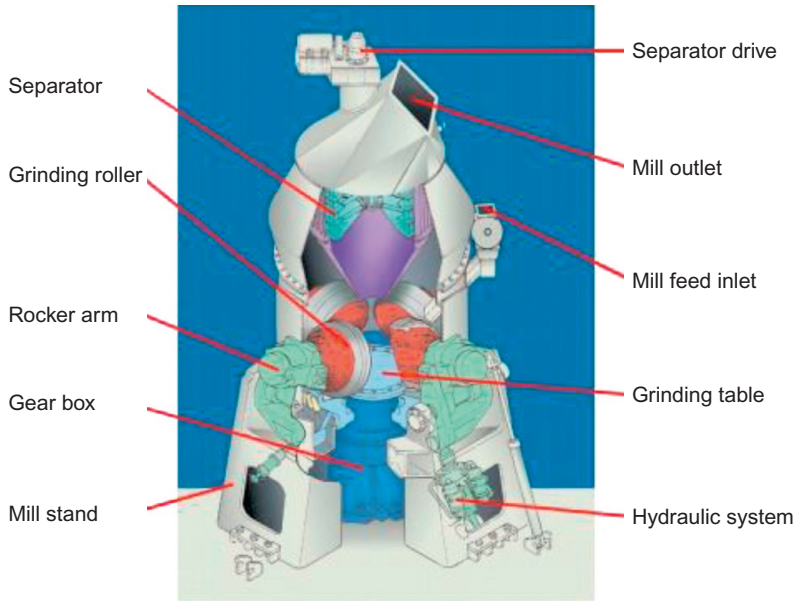

Figure 8.19 Vertical roller mill.

(Van Drunick et al., 2010). If magnetite ore is treated, middlings from the static classifier and the coarse material from the dynamic classifier could be subjected to dry magnetic separation to remove a fraction of waste material from the grinding circuit, similar to cobbing operations in conventional magnetite grinding circuits.

Several studies (Wang et al., 2009; Van Drunick et al., 2010; Valery et al., 2014) have shown that grinding with VRM technology consumes less energy than conventional SAG/ball mill processes, especially when using external material classification (i.e., overflow mode). In addition, several other advantages of VRM technology are documented, including steeper product size distribution, improved liberation, improved downstream flotation performance, the ability to handle a coarser feed size than ball mills, reduced water consumption, less wear of grinding components, no grinding media, and decoupling of the milling and downstream processes. Given the increasing demand for more energy-efficient and sustainable technologies, VRM is worthy of further consideration in mineral grinding applications.

8.4.4 High-pressure grinding rolls

HPGR technology was introduced to the mineral processing industry in the mid-1980s and has rapidly (for the mining industry) established itself as the convention in the comminution of cement, clinker, slag, iron ore, iron pellet plant feed, and diamond ore. There are now approximately over 500 machines operating in these applications. The operating history is reported to be good with few mechanical issues.

The HPGR machine is composed of two horizontally opposed rolls: one "floating" roll positioned using pneumohydraulic pistons and one roll "fixed" to the frame (Figure 8.20). The main components of the HPGR machine are the rolls, bearings, frame, pressure beams, hydraulic system, drive system, lubrication and cooling systems, feed chute, roll wear surfaces, and lateral wear protection or cheek plates.

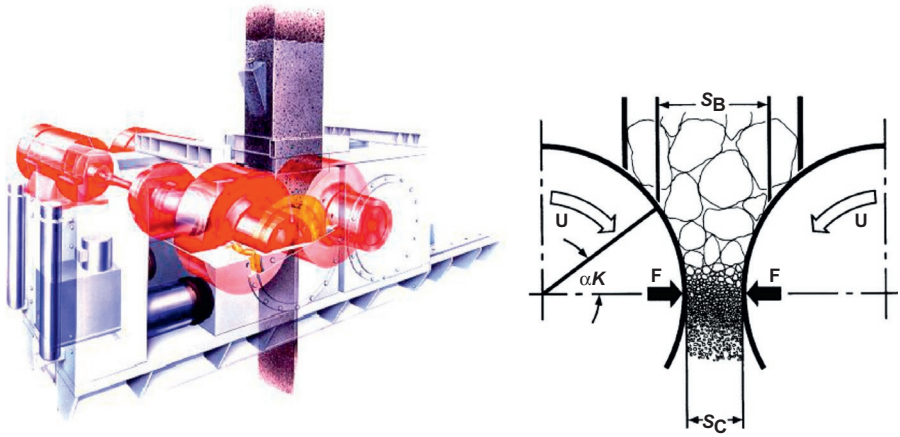

Figure 8.20 HPGR components and grinding mechanism.
Courtesy of Polysius.

The rolls must be choke-fed to ensure optimum operation. The HPGR relies on the production of a compression bed and interparticle breakage rather than the liner-rock-liner contact crushing occurring in conventional gyratory and cone crushing. The pressure applied to the rolls determines the degree of breakage and is typically between 50 and 200 MPa with the force applied to the rolls varying with roll diameter (750–20,000 kN). The roll wear-resistant liners are the principal consumable cost. The liners are typically shrink-fitted on the roll and equipped with hardened studs. The studs maintain an AG layer on the rolls to reduce liner wear when treating hard and abrasive ores. Ore is crushed between the liners and constrained by cheek plates at either end of the rolls.

HPGR can be used in different roles, from final stages of crushing to grinding applications. In iron ore operations, they are mostly used in pellet production. The reasons for the popularity of HPGR for pellet production have been presented below (Batterham and Bearman, 2005):

- Increase in Blaine (product fineness) index
- Better size distribution and shape of HPGR product compared to ball mills
- Increased quantity of ultrafines in the product, resulting in better binding of coarse particles
- More uniform pellets, resulting in significant reductions in circulating loads around balling disks and drums (reductions from 25–30% to 5–8%)
- Better moisture control and a drier filter cake resulting from improved filtration, by allowing ball mills to be operated in an open circuit and at a coarser grind
- Higher density of the pellets (average porosity decreases from 33% to 25%)
- Lower binder requirements
- Increased green ball strength, up to 50% higher than in conventional ball mills
- Reduced fuel requirements, due to improved reactivity of HPGR product
- Higher loadings and better bed permeability
- Increased productivity of indurating machine

While HPGR iron ore applications are mostly for Blaine improvement in final concentrate treatment, notable exceptions are Los Colorados in Chile, Empire Mines in the United States, Arrium Whyalla in Australia, and Zourerat in Mauritania, where the HPGRs are used as tertiary or pebble crushers.

The Los Colorados HPGR is 1.7 m diameter × 1.8 m wide and treats up to 2000 t/h in a tertiary crushing application. The feed is <63 mm from a scalping screen undersize and secondary crusher product.

The Arrium Whyalla magnetite grinding circuit is fed with <32 mm feed from a three-stage crushing plant and consists of two HPGR lines (1.4 m diameter × 1.4 m long, with two 900 kW motors) in closed circuit with a screen of 3 mm and, after the first magnetic separation stage, with another screen of 0.7 mm. The 0.7 mm screen undersize goes to a sump that feeds the cyclones, which send their overflow to the second-stage magnetic separator and the underflow to the ball mills.

The Zourerat iron ore mine has two 1.7 m diameter × 1.8 m wide HPGR units treating 1400 t/h each of aerofall mill pebbles. The feed is −25 + 1.6 mm and has a ball mill work index of 12–14 kWh/t. The iron ore has low to moderate abrasion characteristics. Figure 8.21 shows the Zourerat iron ore flowsheet.

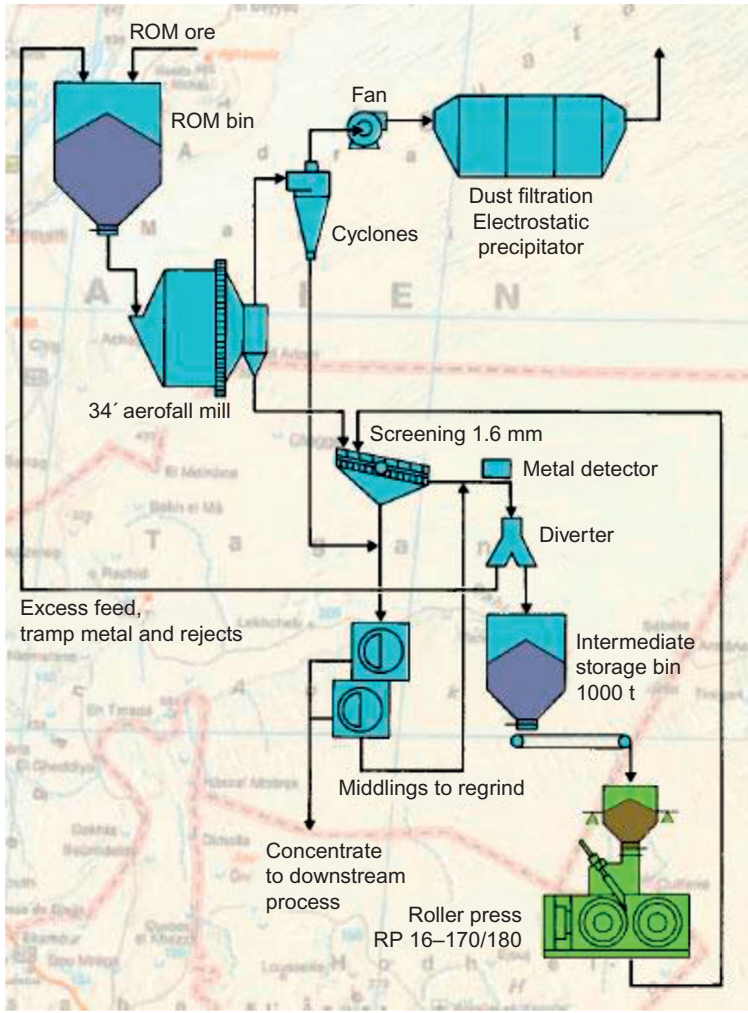

Figure 8.21 HPGR application at Zourerat iron ore mine.
Courtesy of KHD.

Including HPGR technology in a comminution circuit offers a number of advantages over conventional crusher and tumbling mill-based comminution circuits:

- Increased energy efficiency, potentially over 15% for the total grinding circuit when treating hard rock
- High-capacity crushing
- Relatively small footprint
- Reduced overgrinding and slimes production
- Reduced ball mill work indices
- Improvements in downstream comminution efficiency

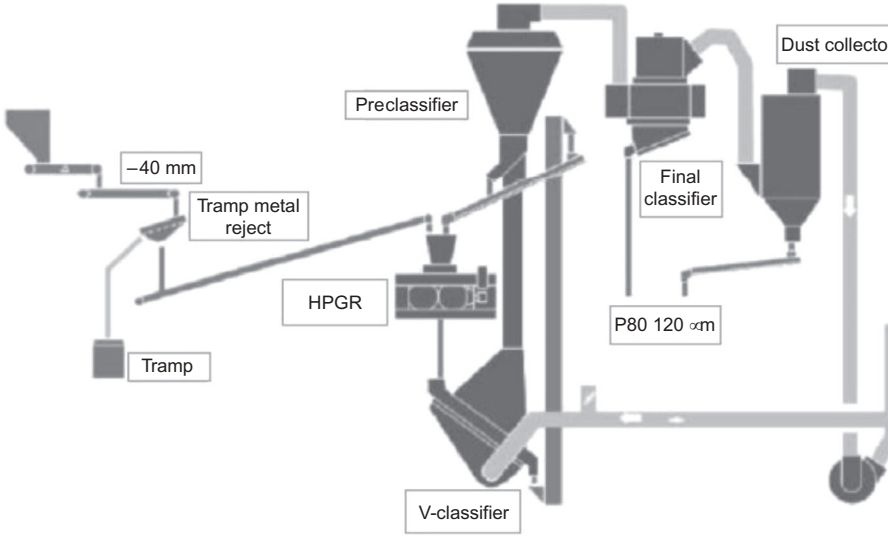

Figure 8.22 Dry grinding with HPGR in closed circuit with air classifiers. Modified from van der Meer and Strasser (2012).

- Improvements in downstream leaching recoveries
- Low comminution circuit operating costs
- Relatively consistent and steady operation

Application of HPGR in iron ore processing is expected to increase in the future. There is growing interest in dry HPGR processing in areas where water scarcity or process conditions require minimization of water consumption. Even when fine grinding is required, HPGR technology could provide dry grinding solutions by applying closed-circuit arrangements with air classification. Based on experience from cement processing, relatively high-throughput circuits can be achieved. Figure 8.22 shows the COMFLEX® plant flowsheet proposed for a 25 Mtpa magnetite ore grinding study.

Pilot-scale testing was conducted by Metso PTI in collaboration with CSIRO to evaluate the performance of a single-stage HPGR circuit in closed circuit with an air classifier. The pilot-scale testing compared two HPGR circuit options. Option A consisted of an HPGR in closed circuit with air classification to generate the final product, while option B consisted of an HPGR in closed circuit with a 2.36 mm screen followed by ball milling. These circuits were compared based on the energy consumption required to generate a product with an 80% passing size of approximately 50 µm. The test results indicate that option A with HPGR and air classifier offers a power saving of about 20–30% compared to option B. Option A also achieved a marginally finer product size, so the estimation of energy saving is conservative (Jankovic et al., 2015).

8.4.5 CAPEX and OPEX considerations

An option study was conducted for a 10 Mtpa ore processing plant to treat a consistently hard, fine-grained silica-rich magnetite ore. The emphasis was on comminution

circuit options (Jankovic and Valery, 2010). Four circuit options were considered for comparison:

OPTION 1: Primary crushing—AG milling in closed circuit with hydrocyclones and pebble crushing—rougher magnetic separation—pebble milling—cleaner magnetic separation
OPTION 2: Primary crushing—AG milling in closed circuit with hydrocyclones and pebble crushing—rougher magnetic separation—ball milling—cleaner magnetic separation—tertiary milling using stirred mills—second cleaner magnetic separation
OPTION 3: Primary crushing—closed-circuit secondary crushing—closed-circuit HPGR—rougher magnetic separation—ball milling—first cleaner magnetic separation—tertiary milling using stirred mills—second cleaner magnetic separation
OPTION 4: Primary crushing—secondary crushing—screening—open-circuit HPGR—coarse pebble milling—rougher magnetic separation—fine pebble milling—first cleaner magnetic separation—tertiary milling using AG stirred mills—second cleaner magnetic separation (see Figure 8.23)

The primary conclusion drawn from this financial evaluation is that highly energy-efficient AG processing routes with multiple separation stages (such as OPTION 4) offer significant financial benefits for fine-grained hard magnetite ores. For the ore type evaluated, the application of HPGR and stirred mill technology is indicated to reduce energy consumption by up to 25% compared to conventional flowsheets with wet tumbling mills. The reduction of energy consumption and grinding media requirements of OPTION 4 offer a significant reduction in operating cost (OPEX), which has favorable effect on net present value (NPV). A comparison of the OPEX and NPV of the four options is shown in Figure 8.24. This suggests that it is not unreasonable to expect that flowsheet selection including energy-efficient comminution technologies has the potential to vary project value in order of billion dollars for large-scale magnetite projects.

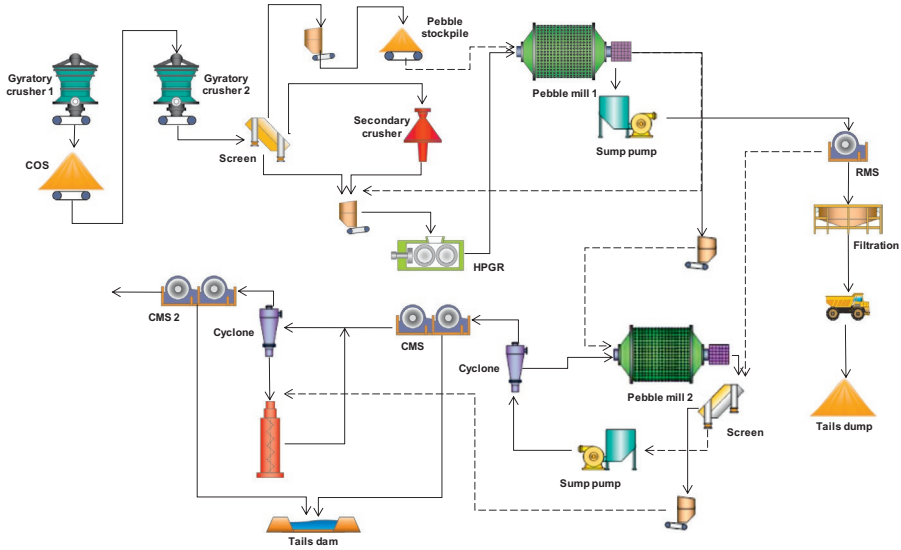

Figure 8.23 OPTION 4 highly energy-efficient magnetite processing flowsheet.

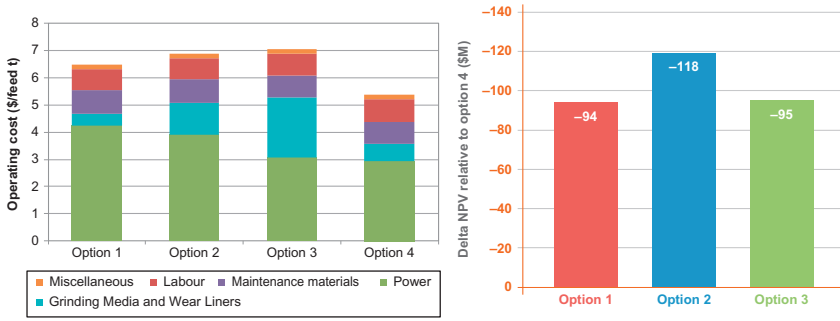

Figure 8.24 Comparison of OPEX and NPV for magnetite flowsheet options.

References

Batterham, R.J., Bearman, R.A., 2005. The role of science and technology in the future of the iron ore industry. In: Proceedings of Iron Ore Conference, Fremantle, WA, 19–21 September.

Bergerman, M.G., Delbony Jr., D., 2014. Regrind of metallic ores with Vertical Mills: an overview of existing plants in Brazil. In: Proceedings of XXVII IMPC, 20–24 October, Santiago, Chile, pp. 300–309 (Chapter 9).

Carter, R.A., 2011. Screening technology expands to meet expectations. Eng. Min. J. http://www.e-mj.com/features/1006-screening-technology-expands-to-meet-expectations.html.

Clout, J.M.F., Fitzgerald, B., 2011. The Roy Hill Project. In: Proceedings of Iron Ore Conference, Perth, WA, 11–13 July.

Connelly, D., 2013. Mobile crushing and screening plant applications for small- to medium-sized iron ore projects. In: Proceedings of Iron Ore Conference 2013, Perth, WA, Australia, 12–14 August. The Australasian Institute of Mining and Metallurgy, Melbourne.

de Waal, H., Barns, K., Monama, J., 2012. From base metals and back—IsaMills and their advantages in African base metal operations. In: 7th Base Metals Conference, SAIMM, 2–3 September, Mpumalanga, South Africa.

Dowling, E.C., Corpi, P.A., McIvor, R.E., Rose, D.J., 2001. Application of high pressure grinding rolls in an autogenous—pebble milling circuit. In: Proceedings of SAG 2001 Conference, Vancouver, BC, vol. III, pp. 194–201.

Hahne, R., Palsson, B.I., Samskog, P.O., 2003. Ore characterization for—and simulation of—primary autogenous grinding. Miner. Eng. 16, 13–19.

Herbst, J.A., Lo, Y.C., Flintoff, B., 2003. Size reduction and liberation. In: Fuerstenau, M.C. (Ed.), Principles of Mineral Processing. Society for Mining, Metallurgy, and Exploration, Inc. (SME), Littleton, CO, USA. ISBN: 0-87335-167-3 (Chapter 3).

Holmes, R.J., 2013. Overview of the Australian iron ore industry. In: Australian Mining and Metallurgical Operating Practices, third ed., AusIMM Publication, Carlton, VIC, Australia. ISBN: 978-1-921522-84-0, Monograph 28.

Jankovic, A., Valery, W., 2010. Reducing grinding energy and cost—magnetite iron ore design case study. In: Proceedings of the XIIth International Minerals Processing Symposium, Cappadocia Nevsehir, Turkey, 6–8 October.

Jankovic, A., Suthers, S., Wills, T., Valery, W., 2015. Evaluation of dry grinding using HPGR in closed circuit with an air classifier. Miner. Eng. 71, 133–138.

Kalra, R., Delgado, C., 2013. World's largest manufactured mills by CITIC HIC and installed at Sino Iron Magnetite 80 Mt/a plant in Australia. In: Proceedings of 10th International Minerals Processing Conference, Procemin 2013, October 15–18, Santiago, Chile.

Kinnel, R., 2013. Iron ore operations—Western Australia, Rio Tinto. In: Australian Mining and Metallurgical Operating Practices, third ed., AusIMM Publication, Carlton, VIC, Australia. ISBN: 978 1 921522 84 0, Monograph 28.

Koivistoinen, P., Virtanen, M., Eerola, P., Kalapudas, R., 1989. A comminution cost comparison of traditional metallic grinding, semiautogenous grinding (SAG) and two stage autogenous grinding. In: Proceedings of SAG 1989 Conference, Vancouver, BC.

Larson, M., Do, L., Siliezar, J., 2013. Enhancing magnetite returns—the benefits of IsaMilling. In: Iron Ore 2013, August 12–14, Perth, Western Australia.

Napier-Munn, T.J., Morrell, S., Morrison, R.D., Kojovic, T., 2005. Mineral Comminution Circuits – Their Operation and Optimisation. The University of Queensland, Julius Kruttschnitt Mineral Research Centre.

Pforr, B., 2001. Fine screen oversize grinding at Hibbing Taconite Company. In: SME Annual Meeting, Denver, CO, February.

Rajala, G., Suardini, G., Walqui, H., Rajala, G., Suardini, G., Walqui, H., 2007. Improving secondary grinding capacity at Empire Concentrator. In: SME Annual Meeting, Denver, CO, February 25–28.

Tano, K.T., Pålsson, B.I., Alatalo, J., Lindquist, L., 2006. The use of process simulation technology in process design when time and performance is critical. In: SME Annual Meeting, Denver, CO, February.

van der Meer, F., Strasser, S., 2012. Case study of dry HPGR grinding and classification in ore processing. In: Proceedings of 9th International Mineral Processing Conference, Procemin, 21–23 November. Santiago Chile.

Van Drunick, W., Gerold, C., Palm, N., 2010. Implementation of an energy efficient dry grinding technology into an Anglo American zinc beneficiation process. In: XXV International Mineral Processing Congress (IMPC) 2010 Proceedings, Brisbane, 6–10 September, pp. 1333–1341.

Valery, W., Jankovic, A., Runge, K., Tabosa, E., Holtham, P., Duffy, K.A., 2014. Development of a Resource and Eco-Efficient Mining Process Progress Report. Metso internal R&D project progress report, March.

Wang, J., Chen, Q., Kuang, Y., Lynch, A., Zhuo, J., 2009. Grinding process within vertical roller mills: experiment and simulation. Min. Sci. Technol. 19, 0097–0101.

Developments in the physical separation of iron ore: magnetic separation

9

D. Xiong[1], *L. Lu*[2], *R.J. Holmes*[3]
[1]SLon Magnetic Separator Ltd, Ganzhou, China
[2]CSIRO Mineral Resources Flagship, Pullenvale, QLD, Australia
[3]CSIRO Mineral Resources Flagship, Clayton South, VIC, Australia

9.1 Introduction

In the past 30 years, the world iron and steel industry has experienced significant development. This has resulted in a rapid increase in iron ore demand. The current supply of high-grade iron ores can no longer meet market needs. Low-grade deposits are therefore being developed and mined. However, these low-grade iron ores must be upgraded to a suitable Fe grade and impurity level before being charged to metallurgical furnaces. Magnetic separation technology plays an important role in upgrading such low-grade iron ores, because magnetic separators possess the combined advantages of large capacity and low operating cost and being environmentally friendly. This chapter first introduces the principles and recent advances in magnetic separation technology in processing iron ore, followed by examples of flow sheets for magnetite and oxidized ores.

9.2 Principle of magnetic separation

9.2.1 Magnetic force on particles

Different materials possess different magnetic properties by which they may be separated. Figure 9.1a shows that when a magnet is placed close to an iron ball and a ceramic ball, the iron ball will be attracted to the magnet and the ceramic ball will not. Figure 9.1b shows that when a magnet placed close to a group of mixed tiny iron and ceramic balls, most iron balls will be attracted to it, but most ceramic balls will not. The balls that are not attracted will fall due to gravity. In this way, countless different mineral particles can be separated with magnetic separators. Here, the magnetic force and gravity are the two competing forces. If the magnetic force acting on a particle is stronger than the gravitational force, the particle will move toward the magnet.

Most mineral separating processes are carried out in water or a slurry, so fluid drag forces and surface interfacial tension are also competing forces. Only if the magnetic force acting on a particle is stronger than the sum of all the competing

Iron Ore. http://dx.doi.org/10.1016/B978-1-78242-156-6.00009-5
© 2015 Elsevier Ltd. All rights reserved.

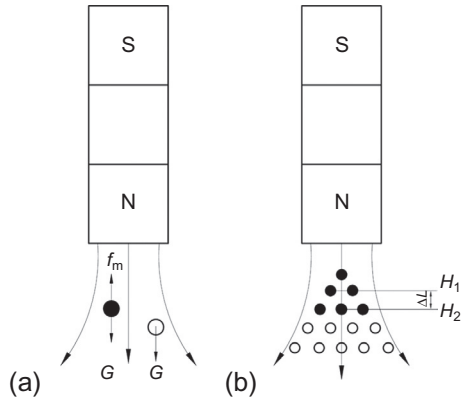

Figure 9.1 Magnetic separation between iron and ceramic balls. ●, Iron ball, ○, ceramic ball, S, south pole of magnet, N, north pole of magnet, f_m, magnetic force, G, gravity, H, magnetic field intensity.

forces will the particle move toward the magnet. The magnetic field can be provided by a permanent magnet or by energizing a coil.

The magnetic force acting on a particle can be calculated using the following equation:

$$f_m = m \cdot \chi_0 \cdot \mu_0 \cdot H \cdot \mathrm{grad}(H) \tag{9.1}$$

where f_m is the magnetic force acting on a particle (Newton), m the mass of the particle (kg), χ_0 the magnetic susceptibility of the particle (m^3/kg), μ_0 the permeability of a vacuum, $\mu_0 = 4\pi \times 10^{-7}(H/m)$, H the magnetic field intensity (A/m), grad(H) the magnetic field gradient, $\mathrm{grad}(H) = (H_2 - H_1)/\Delta L$, $\Delta L \to 0$ $(\mathrm{A/m^2})$, and ΔL the distance between any two points in the magnetic field.

From Equation (9.1), it can be concluded that the magnetic force is proportional to four key factors, that is, the mass of the particle, the magnetic susceptibility of the particle, and the intensity and gradient of the magnetic field.

In magnetic separation, as the mass and the magnetic susceptibility of the particle are fixed, only the magnetic field intensity or gradient can be varied to change the magnetic force. This is why it is extremely important to create a magnetic field of high intensity and gradient for oxidized iron ores in order to achieve higher iron recovery.

9.2.2 Magnetic susceptibilities of minerals in iron ore

Different minerals existing on earth possess different magnetic properties, ranging from strongly magnetic, weakly magnetic, zero magnetic, to antimagnetic. This can be represented by magnetic susceptibilities. The magnetic susceptibility of a mineral can be measured by comparing the weight gain in a magnetic field with a standard mineral, the magnetic susceptibility of which is known. Table 9.1 shows the magnetic susceptibility values of some iron ore-related minerals.

Table 9.1 Magnetic susceptibilities of iron ore-related minerals

Mineral	Magnetic susceptibility (10^{-6} m^3/kg)	Molecule
Magnetite	625–1156	Fe_3O_4
Martite	6.2–13.5	Fe_2O_3
Hematite	0.6–2.16	Fe_2O_3
Specularite	3.7	Fe_2O_3
Limonite	0.31–1.0	$2Fe_2O_3 \cdot 3–4H_2O$
Siderite	0.7–1.5	$FeCO_2$
Ilmenite	0.34–5	$FeTiO_3$
Quartz	0.0025–0.126	SiO_2
Feldspar	0.063	$KAlSi_3O_8$, Na $AlSi_3O_8$
Calcite	0.0038	$CaCO_3$
Spodumene	0.82	$LiAl(Si_2O_6)$
Chlorite	0.38–1.13	$(Mg, Fe)_5Al(AlSi_3O_{10})(OH)_8$
Garnet	0.79–2	$Mg_3Al_2(SO_4)_3$
Biotite	0.5–6.5	$K(Mg,Fe)_3(Si_3AlO_{10})(OH,Fe)_2$
Olivine	0.17	$(Mg, Fe)_2SO_4$
Pyrite	0.34	FeS_2
Apatite	0.007–0.142	$Ca_5(PO4)_3F$

9.2.2.1 Iron ore minerals

Based on the magnetic susceptibility values in Table 9.1, iron ore can be divided into two groups, namely, strongly magnetic iron ores, that is, magnetite (72.4% Fe), and weakly magnetic iron ores (oxidized iron ores), that is, martite (70.0% Fe), hematite (70.0% Fe), specularite (70.0% Fe), limonite (57.14–59.89% Fe), and siderite (48.2% Fe). While magnetite is naturally suitable for magnetic separation, oxidized iron ores are much more difficult to recover using magnetic separators, because their magnetic susceptibilities are only about 1% of that for magnetite.

Of the oxidized iron ores, specularite is most susceptible to magnetic fields, as it is better crystallized, followed by martite and hematite. It is therefore easier to upgrade specularite using magnetic separation, compared with martite and hematite. In contrast, limonite is less susceptible to magnetic fields and more difficult to recover using magnetic separation. Siderite contains only 48.2% Fe, and hence, it is impossible to achieve a high Fe grade for siderite concentrates. Therefore, it is very rare to mine and concentrate siderite in industry.

9.2.2.2 Gangue minerals in iron ores

In iron ore, white gangue minerals include quartz, feldspar, and calcite. The magnetic susceptibilities of white gangue minerals are close to zero. It is therefore relatively easy to separate them from iron ores by magnetic separation.

However, the magnetic susceptibilities of dark gangue minerals, such as spodumene, chlorite, garnet, biotite, and olivine, are very close to the magnetic susceptibilities of oxidized iron ores. It is therefore more difficult to separate them from oxidized iron ores by magnetic separation.

Typical harmful minerals in iron ore include pyrite and apatite, which contain the harmful elements S and P. They are also weakly magnetic. But if their magnetic susceptibilities are smaller than for oxidized iron ores, it is still possible to partially remove them from oxidized iron ores by magnetic separation.

Low-grade iron ore mined from the earth is usually composed of several minerals, desirable and undesirable. Magnetic separation means applying magnetic separators with the appropriate magnetic field intensity, magnetic field gradient, and other conditions to separate different minerals according to their differences in magnetic susceptibility.

9.3 Magnetic separators

9.3.1 Low-intensity magnetic separators

Low-intensity magnetic separators (LIMS) are widely applied to separate magnetite. Some of the typical LIMS are compared below.

9.3.1.1 Permanent magnetic drum separator

Figure 9.2 shows a permanent magnetic drum separator, which consists mainly of a permanent magnet system, a rotating drum, a separating chute, a feed tank, and a flushing pipe. For magnetite separation, the magnetic field intensity on the surface of the drum is between 0.1 and 0.4 T. However, for other applications, the intensity may reach as high as 0.8 T.

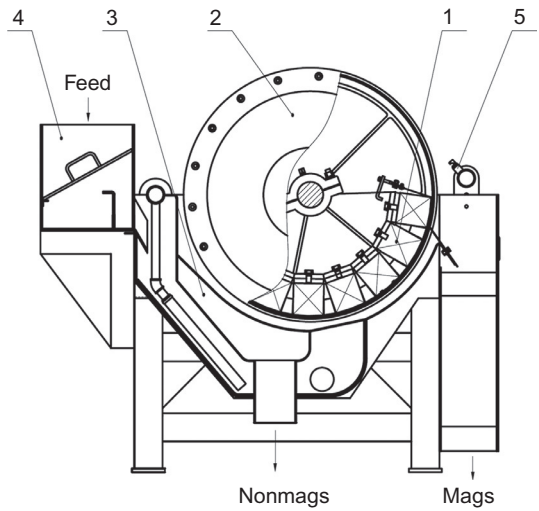

Figure 9.2 Drum permanent magnetic separator. (1) Permanent magnetic system, (2) rotary drum, (3) separating chute, (4) feed tank, (5) flushing pipe.

As shown in Figure 9.2, when the iron ore slurry passes through the separating chute, magnetite particles from the slurry are attracted by magnetic forces to the surface of the drum, while gangue minerals are dragged down by gravity and water flow. These magnetic particles are then brought by the rotating drum to the top where the magnetic field is weak and close to zero, and they are then flushed away from the drum as an iron concentrate.

There are several types of permanent magnetic drum separators used for roughing and cleaning and for fine and coarse particles. They may look different, but they all work on the same principle.

9.3.1.2 Magnetic column separator

The magnetic column separator consists of an electrically energized system, a feed box, a nonmagnetic chute, a separating column, water supply pipes, and a magnetic outlet controller (Figure 9.3).

The electrically energized magnetic column creates a low-intensity magnetic pulse (0.01–0.02 T), which can break down magnetite and gangue mineral agglomerates. When the iron ore slurry passes through the separating column, the magnetite particles are dragged by the magnetic force to the bottom of the column, and the nonmagnetic particles are brought up to the nonmagnetic chute by the moving water.

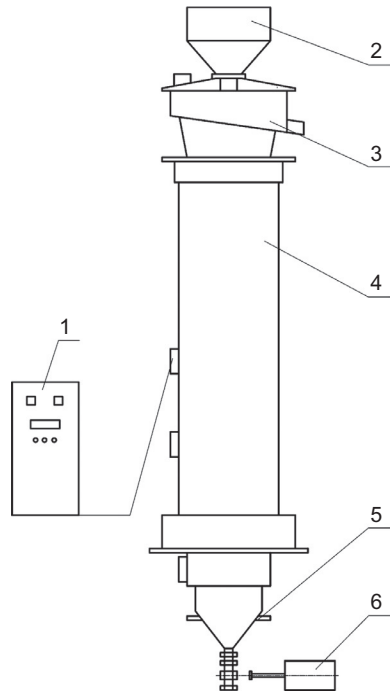

Figure 9.3 Magnetic column. (1) Electric energizing system, (2) feed box, (3) nonmagnetic chute, (4) separating column, (5) water supply pipe, (6) magnetic outlet controller.

Magnetic column separators are only used for magnetite cleaning to improve the iron grade of concentrates, but magnetic column separators consume more water than drum LIMS separators.

9.3.1.3 Magnetic thickener

The magnetic thickener consists of an awl chute, a feed tank, an overflow chute, a low-intensity permanent magnetic system located in the lower center, a water supply pipe, a magnetic outlet pipe, and an adjusting valve (Figure 9.4).

When the iron ore slurry is fed to the feed tank, magnetite particles are dragged down under the action of the magnetic force, gravity, and water, and some of the fine light gangue minerals such as quartz float up to the overflow chute.

The magnetic thickener is often used for magnetite slurry dewatering after the separation procedure. It can also reject some of the light and fine nonmagnetic minerals.

9.3.1.4 Disk magnetic scavenger

The disk magnetic scavenger consists of several disks made of permanent magnets and a device collecting the magnetic components (Figure 9.5).

When the iron ore slurry flows through the lower part of the disks, the magnetite particles are attracted to the surface of the disks by magnetic forces. These particles

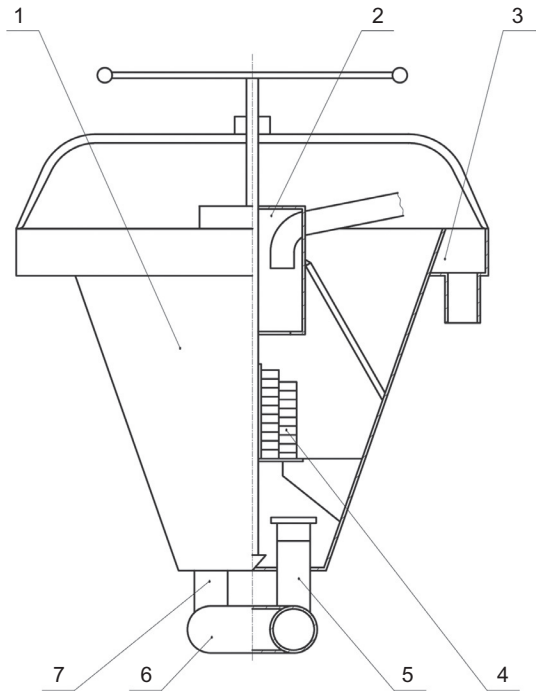

Figure 9.4 Magnetic thickener. (1) Awl chute, (2) feed tank, (3) overflow chute, (4) magnetic system, (5) water supply pipe, (6) adjusting valve.

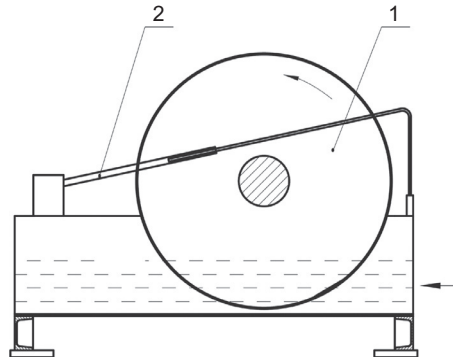

Figure 9.5 Disk magnetic scavenger. (1) Permanent magnetic disk, (2) magnetic collecting device.

are then brought up to a higher position on the disks and finally scraped off by the magnetic collection device.

The disk magnetic scavenger is used for magnetite scavenging and is usually installed on the combined tailings stream of the magnetite separation plant. It can lower the iron grade of the final tails and thus help to achieve a higher iron recovery.

9.3.2 High-intensity and high-gradient magnetic separators

Oxidized iron ores are much more difficult to upgrade by magnetic separators, because their magnetic susceptibilities are only about 1% or less of that of magnetite. In oxidized iron ore separation, it is therefore important to create magnetic fields with high intensities and high gradients to achieve higher iron recoveries.

9.3.2.1 Jones wet high-intensity magnetic separator

The Jones wet high-intensity magnetic separator (WHIMS) was developed in 1956. The structure of the Jones separator is shown in Figure 9.6 and consists mainly of an iron-core electromagnet, a vertical shaft with two (or more) separating rings, a driving system, and feeding and product collection devices. Grooved plates made of magnetic conductive iron or stainless steel serve as a magnetic matrix to enhance the field gradient of the electromagnet. The plates are vertically arranged in plate boxes that are placed around the periphery of the rotors. When the Jones magnetic separator is operating, its vertical shaft drives the separating rings with the matrix plates rotating on a horizontal plane.

When a direct electric current passes through the energizing coils, a high magnetic field with a high gradient is established in the separating zone located in the electromagnetic system, with the focused magnetic field at the teeth top of the grooved plates reaching 0.8–2 T, which is adjustable. The slurry is gravity fed onto the matrix at the leading edge of the magnetic field where the magnetic particles are captured on the teeth top of the grooved plates, while the nonmagnetic fraction passes through and is

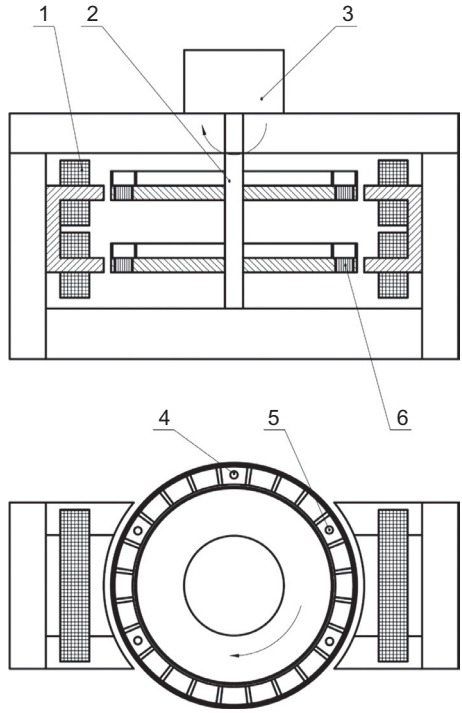

Figure 9.6 Jones wet high-intensity magnetic separator. (1) Magnetic energizing system, (2) shaft and separating rings, (3) driving system, (4) product device, (5) feed device, (6) magnetic matrix.

collected in a trough below the magnet. When the plate boxes reach the demagnetized zone half-way between the two magnetic poles, where the magnetic field changes its polarity, the magnetic field is essentially zero and the adhering magnetic particles are washed out with high-pressure water sprays.

9.3.2.2 SLon vertical ring and pulsating high-gradient magnetic separator

The SLon vertical ring and pulsating high-gradient magnetic separator (SLon magnetic separator or SLon) was developed in 1981 (Xiong et al., 1998). It has the advantages of high efficiency, high reliability, and low operating cost. Nowadays, it is one of the most popular magnetic separators used for upgrading oxidized iron ores (Xiong, 2006, 2008, 2010, 2012).

The SLon magnetic separator utilizes the combined forces of magnetic fields, pulsating fluids, and gravity to beneficiate weakly magnetic minerals. It consists of 10 main parts, including an energizing coil, a magnetic yoke, and a separating ring, as shown in Figure 9.7. The pulsating frequency and stroke are adjustable. The energizing coil is made of hollow copper tube and cooled internally with water.

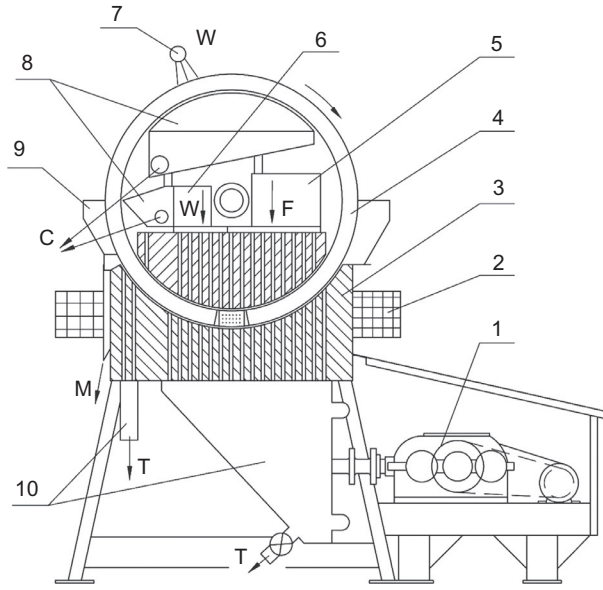

Figure 9.7 SLon vertical ring and pulsating high-gradient magnetic separator. (1) Pulsating mechanism, (2) energizing coil, (3) magnetic yoke, (4) separating ring, (5) feed box, (6) wash box, (7) magnetic flushing device, (8) magnetic collecting box, (9) middling chute, (10) nonmagnetic box. F, feed, W, water, C, concentrate (magnetic), M, middling, T, tails (nonmagnetic).

Along the periphery of the separating ring, a number of rod matrix piles made of magnetic stainless steel are located. The rods in the matrix have diameters varying from 1 to 5 mm depending on the characteristics of the iron ores to be processed. When the SLon magnetic separator is in operation, the ring with the matrix rotates around its horizontal axis.

When a direct electric current passes through the energizing coils, a high-intensity magnetic field of high gradient is established in the separating zone in the lower portion of the separating ring located in the electromagnet system, where the background field intensity is 0–1.3 T and adjustable. The intensity of the focused magnetic field on the surface of the matrix rods can reach up to 2 T. The slurry fed from the feeding boxes (on both sides of the ring) enters the matrix located in the separating zone. Magnetic particles are attracted from the slurry onto the surface of the matrix, while nonmagnetic particles pass through the matrix and enter the nonmagnetic product collecting box. When the rod matrix reaches the top of the ring where the magnetic field is close to zero, the adhering magnetic particles are washed out into the magnetic product boxes.

Since the ring rotates in the vertical plane, the flushing direction of the magnetic particles is opposite to the direction of the slurry feed relative to each matrix pile, so coarse particles can be washed out without having to pass through the entire depth of the matrix pile. The pulsating mechanism drives the slurry up and down and keeps the

particles in a loose state in the separating zone all the time. Thus, magnetic particles can be more easily recovered by the matrix, and the nonmagnetic particles can be more easily dragged out through the matrix.

The opposing flushing and pulsation help to prevent matrix clogging, and the pulsation helps to purify the magnetic product. These measures guarantee that SLon magnetic separators offer the advantages of higher grade and higher recovery of the magnetic product and more flexibility.

9.4 Typical flow sheets for iron ore separation

9.4.1 Major principles for selection of separation methods

For low-grade iron ore separation, it is very important to develop an optimized flow sheet to achieve the best iron concentrate grade and iron recovery while keeping the cost as low as possible. The major principles are as follows:

1. Before separation, the run-of-mine ore needs to be crushed and ground down to a specific particle size to liberate the minerals as much as possible. But crushing and grinding consumes a lot of energy. As the particle size becomes finer and finer, the grinding energy consumption increases exponentially. Therefore, it is likely that the gangue minerals will need to be discharged in several steps, that is, staged grinding and separation to reject the gangue minerals as early as possible and keep the mineral mass for final grinding as low as possible.
2. There are several methods that are often used in combination with concentrate iron ores, that is, magnetic separation, flotation, and gravity separation (such as jigs, spiral separators, shaking tables, and centrifugal separators). Detailed information on gravity separation and flotation technologies will be covered in Chapters 10 and 11, respectively. Magnetic separation is the most efficient separation method of these technologies. Modern magnetic separators are capable of processing up to 500 t ore/h per unit at a very low operating cost (0.3–0.5 kWh power and 2 m^3 recyclable water/t feed ore). Flotation has the advantage of good selectivity, but it often has much higher operating costs than magnetic separation. Gravity separation also has the advantage of low operating costs, but it is often implemented at a much smaller scale compared with magnetic separation.

In summary, magnetic separation should always be given priority when designing iron ore beneficiation flow sheets. For some oxidized iron ores, the selectivity of high-intensity and high-gradient magnetic separators may not be as good as other methods. Nevertheless, they can reject most of the gangue minerals if they are used at the roughing stage. This will significantly reduce the amount of ore required to be "cleaned" by flotation or gravity separation.

9.4.2 Typical separation flow sheets for magnetite ores

Magnetite is strongly magnetic, so low-intensity magnetic drum separators (drum LIMS) are widely used in processing magnetite ores. But in the final stage of separation, because the selectivity of magnetic columns or reverse flotation is better than that of drum LIMS separators, these separation technologies may be used to obtain a better concentrate iron grade.

In many magnetite iron ores, the major gangue mineral is quartz, which is harder and more difficult to grind than magnetite. In the ground product, the average size of unliberated quartz particles is usually larger than that of magnetite. Therefore, vibrating screens are usually used to screen out unliberated coarse quartz particles, which can be returned to the ball mills for regrinding.

9.4.2.1 Low-intensity magnetic drum separator flow sheet

Figure 9.8 presents a typical flow sheet for processing a magnetite ore using multiple stages of low-intensity magnetic drum separators. The ore consists predominantly of

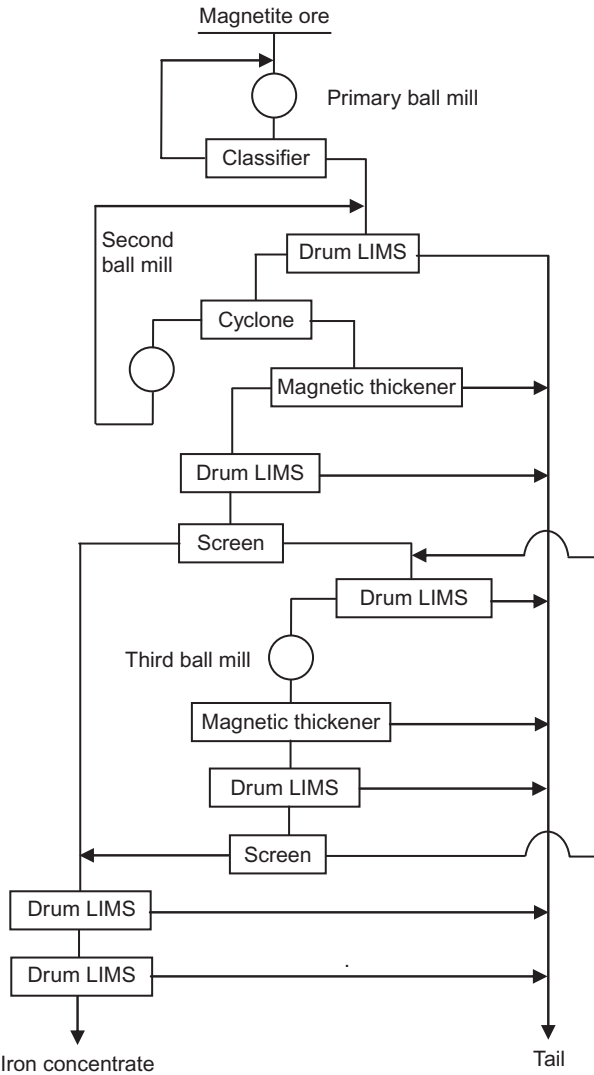

Figure 9.8 Drum low-intensity magnetic separator flow sheet.

magnetite and quartz. There are three stages of ball mill grinding and magnetic separation, using low-intensity magnetic drum separators to reject quartz as early as possible. Vibrating screens with apertures of about 150 μm are also used in the flow sheet to take out unliberated coarse quartz particles that contain mainly quartz and a small portion of magnetite, which are returned to the ball mill for regrinding. Magnetic thickeners are used for slurry dewatering and rejecting some of the light and fine gangue minerals.

The annualized plant results demonstrated that a concentrate containing 67.3% Fe can be produced from a run-of-mine ore containing 30.4% Fe using this flow sheet at a mass yield to the iron concentrate of 37.1%, an iron recovery of 81.9% (Fe in the concentrate), and a tailings grade of 8.7% Fe.

9.4.2.2 Drum LIMS and magnetic column flow sheet

Figure 9.9 presents a typical flow sheet for processing a magnetite ore using a combination of drum LIMS and magnetic columns. The ore is composed of magnetite and gangue minerals, which are mainly quartz. The flow sheet uses two stages of grinding and magnetic separation to reject quartz as early as possible. Vibrating screens with apertures of about 150 μm are again used to take out unliberated coarse quartz particles, which are returned to the ball mill for regrinding. However, in this flow sheet, magnetic columns are used instead of drum LIMS for the final cleaning stage to target a higher iron grade for the concentrate.

The annualized plant results demonstrated that an iron ore concentrate containing 68.4% Fe could be produced using the flow sheet from run-of-mine ore containing 29.1% Fe, at a mass yield to the iron concentrate of 34.8%, an iron recovery of 81.7%, and a tailings grade of 8.2% Fe.

9.4.2.3 Drum LIMS and reverse flotation flow sheet

Figure 9.10 presents a typical flow sheet for processing a magnetite ore using a combination of drum LIMS and reverse flotation. The ore is composed of magnetite and gangue minerals, which are mainly quartz. The flow sheet includes three stages of grinding and magnetic separation once again to reject quartz as early as possible. Vibrating screens are again used to take out unliberated coarse quartz particles, which are returned to the ball mill for regrinding. Reverse flotation is used in the final cleaning stage to obtain a concentrate with a higher iron grade. Because reverse flotation consumes chemical reagents used as modifiers, collectors, etc., its operating cost is higher than for a drum LIMS. At the final tailings collection point, the flow sheet includes a disk magnetic scavenger for collecting the remaining magnetite in the tailings. This helps to achieve a higher iron recovery by reducing the iron grade of the final tailings.

The annualized plant results showed that a concentrate containing 69.1% Fe could be produced using this flow sheet from a run-of-mine ore containing 30.9% Fe at a mass yield to the iron ore concentrate 35.7%, an iron recovery of 79.9%, and a tailings grade of 9.6% Fe.

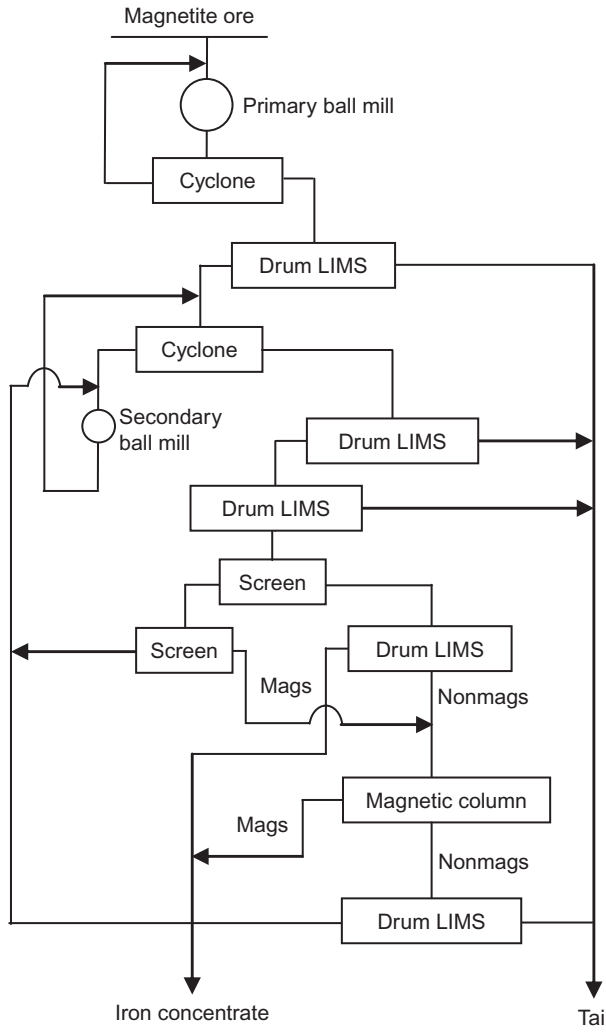

Figure 9.9 Drum LIMS and magnetic column flow sheet.

9.4.3 Typical separation flow sheets for oxidized iron ores

Oxidized iron ores are much more difficult to process using magnetic separators due to their extremely low magnetic susceptibilities. However, high-intensity and high-gradient magnetic separators have been successfully developed and used to separate oxidized iron ores. As some oxidized iron ores contain some magnetite, drum LIMS, or other separators may also be required in the processing flow sheets.

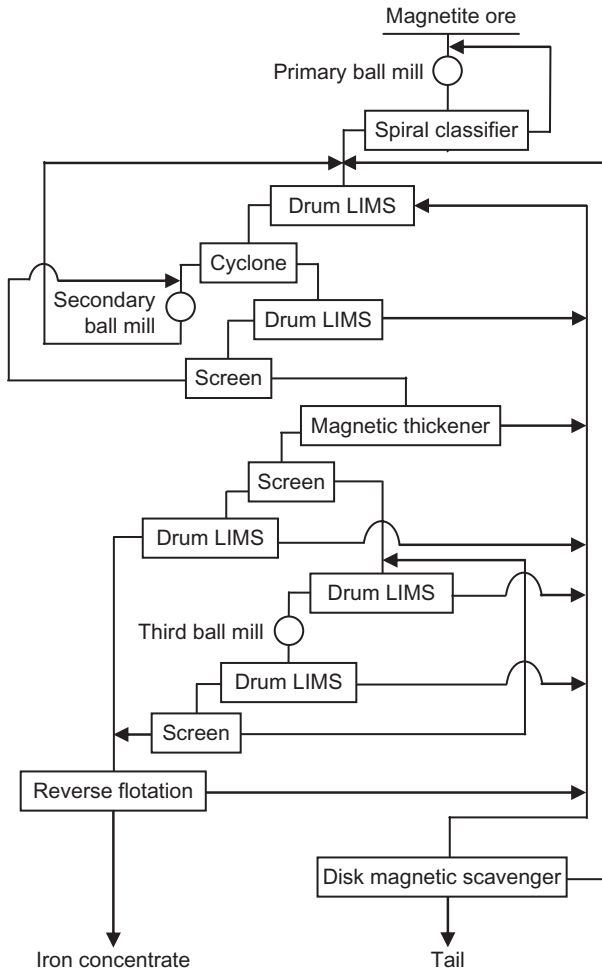

Figure 9.10 Drum LIMS and reverse flotation flow sheet.

9.4.3.1 Drum LIMS and SLon magnetic separator flow sheet

Figure 9.11 presents a typical flow sheet for processing an oxidized ore containing about 50% Fe using a combination of drum LIMS and SLon magnetite separators. The ore is mainly composed of finely crystallized hematite, a small portion of magnetite, and the gangue minerals quartz, olivine, chlorite, calcite, and pyrite. The ore is first ground using ball mills down to about 95% -75 µm. Drum LIMS are then used to take out the magnetite. SLon vertical ring and pulsating high-gradient magnetic separators are used for roughing, cleaning, and scavenging to recover the hematite. The magnetic product from the SLon scavenger and the nonmagnetic product from the SLon cleaning unit are returned to the secondary ball mill for regrinding. The magnetic products from the drum LIMS and SLon cleaning unit are combined to produce the final iron ore concentrate.

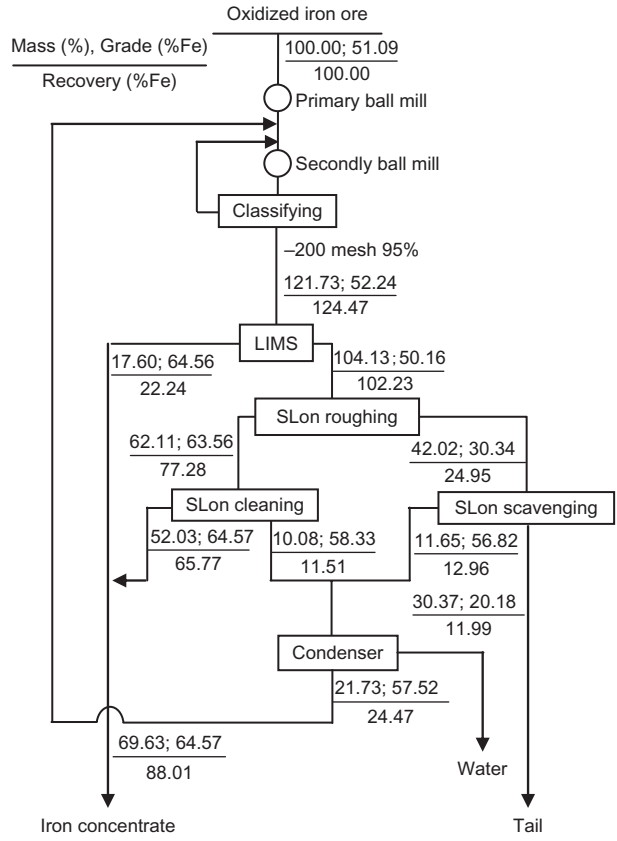

Figure 9.11 Drum LIMS and SLon magnetic separator flow sheet.

An iron ore concentrate containing 64.6% Fe can be produced using this flow sheet from a run-of-mine ore containing 51.1% Fe at a mass yield to the iron concentrate 69.6%, an iron recovery of 88.0%, and a tailings grade of 20.2% Fe.

9.4.3.2 SLon magnetic separator flow sheet to upgrade specularite

In oxidized iron ores, it is usually easier to obtain a higher-Fe grade concentrate from specularite using magnetic separation, because its grains are better crystallized. In Figure 9.12, SLon magnetic separators are used for processing a specularite ore containing about 35% Fe. The run-of-mine ore is mainly composed of specularite and quartz. The ore is first ground down to about 85% -75 μm using ball mills. SLon magnetic separators are then used for roughing and cleaning to extract the specularite particles. The magnetic component of the SLon cleaning unit is collected as the final iron ore concentrate.

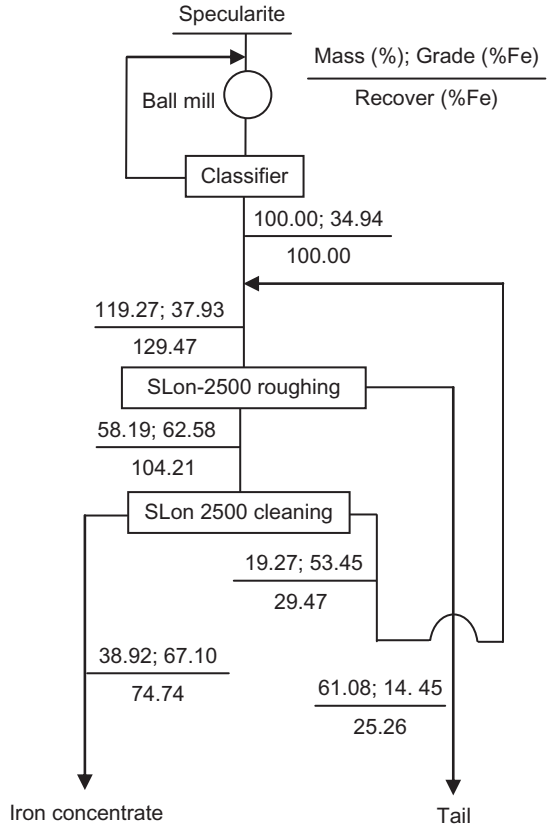

Figure 9.12 SLon magnetic separator flow sheet to separate specularite.

Plant results have demonstrated that an iron ore concentrate containing 67.1% Fe can be produced from run-of-mine ore containing 34.9% Fe, at a mass yield to the iron concentrate of 38.9%, an iron recovery of 74.7%, and a tailings grade of 14.4% Fe.

9.4.3.3 SLon magnetic separator and reverse flotation flow sheet

If the gangue mineral in an iron ore is predominantly quartz, reverse flotation is usually used in the cleaning stage to improve the concentrate grade. Figure 9.13 presents a typical flow sheet for processing an oxidized iron ore containing about 30% Fe using a combination of SLon magnetite separators and reverse flotation. The ore is mainly composed of magnetite, hematite, martite, and quartz. It is very difficult to produce a high-quality iron ore concentrate by magnetic separation alone for this type of iron ore. The ore is first ground using ball mills down to about 90% -75 μm. Drum LIMS are then used to take out the magnetite particles, while drum MIMS (0.4 T middle-intensity magnetic separators) are used to recover the martite grains. SLon magnetic separators are subsequently used to recover the

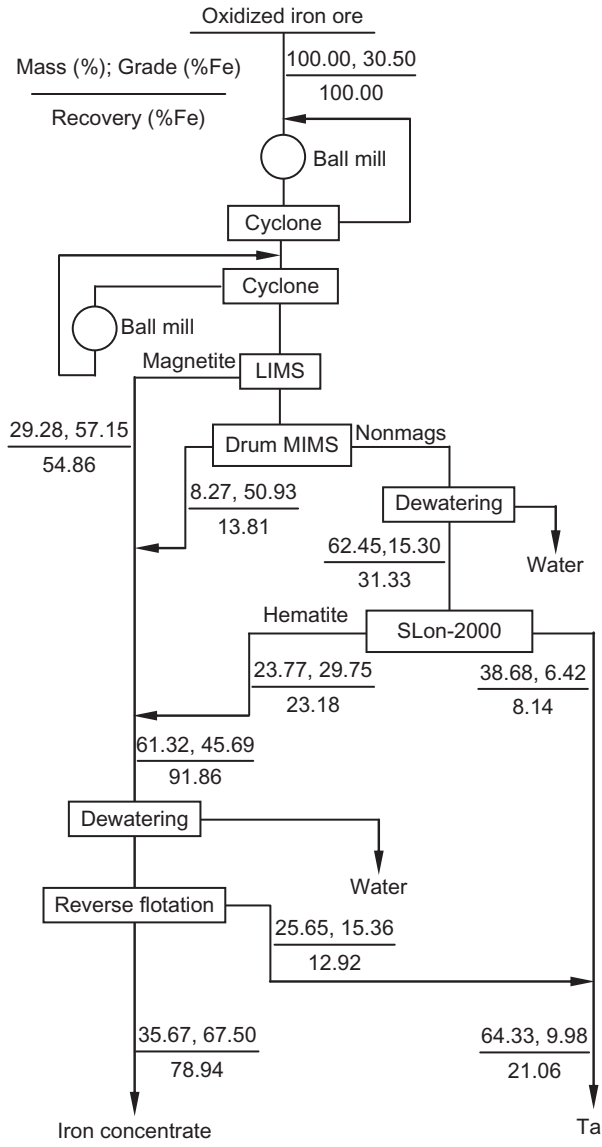

Figure 9.13 SLon magnetic separator and reverse flotation flow sheet.

hematite grains. The magnetic products from the LIMS, MIMS, and SLon are combined to generate the feed for reverse flotation, which produces the final iron ore concentrate.

From the plant operating results for this flow sheet, an iron ore concentrate containing 67.5% Fe was produced from a run-of-mine ore containing 30.5% Fe, at a mass yield to the iron ore concentrate of 35.7%, an iron recovery of 78.9%, and a tailings grade of 10.0% Fe.

9.4.3.4 *Spiral separator, SLon separator, and reverse flotation flow sheet*

The iron oxide crystal grains in most iron ores are not evenly distributed in size. Spiral separators can therefore be used to take out the coarser iron oxide grains in the primary grinding circuit to save grinding energy and help achieve a higher iron recovery. Figure 9.14 presents a typical flow sheet for processing an oxidized ore containing about 30% Fe using a combination of spiral and SLon magnetite separators and reverse flotation. This ore is mainly composed of hematite, magnetite, and quartz, and the iron oxide crystals range in size from 0.005 to 1.0 mm with an average size of about 0.05 mm. The average size of the quartz crystals is approximately 0.085 mm.

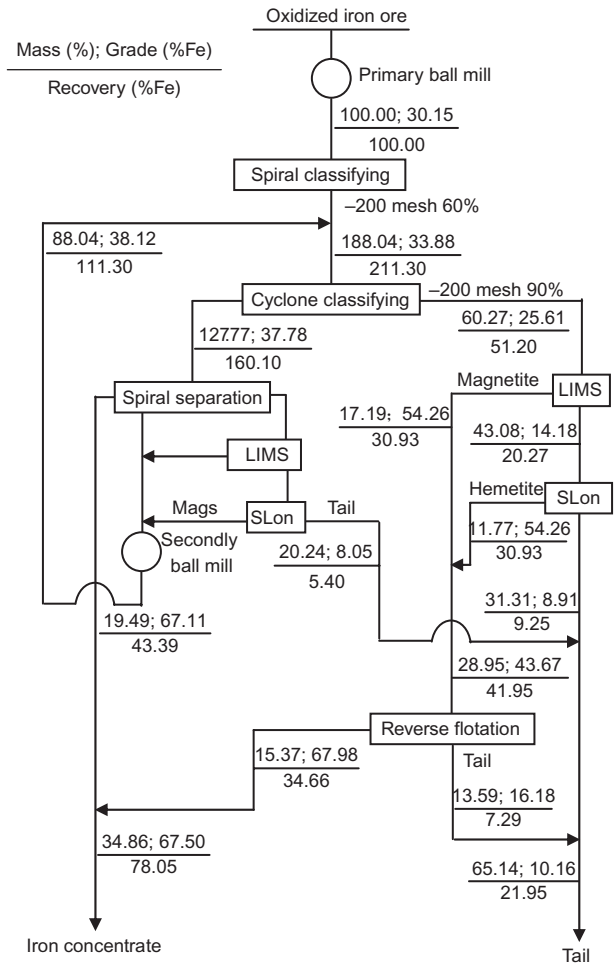

Figure 9.14 Spiral separator–SLon separator and reverse flotation flow sheet.

In the primary grinding stage of the flow sheet in Figure 9.14, the ore is first ground down to about 60% -75 μm and then classified into two size fractions, a coarse size fraction and a fine size fraction. The coarse size fraction is treated with spiral separators to recover part of the final iron ore concentrate. Then, drum LIMS and SLon magnetic separators are used to reject some of the coarse gangue minerals as final tailings. The magnetic products from the LIMS and SLon are sent back to the secondary ball mill for regrinding, and the milled product returns to the primary cyclone classifier.

The fine size fraction is about 90% -75 μm and is processed using drum LIMS separators and SLon magnetic separators in series to take out the magnetite and hematite, respectively. The magnetic products from the magnetic separators are mixed to generate the feed for reverse flotation to produce another component of the final iron ore concentrate.

The key advantage of this flow sheet lies in the fact that the spirals and SLon magnetic separators take out about 20% of the mass of the final iron concentrate and about 20% of the mass of the final tailings, respectively, from the coarse size fraction. This greatly reduces the masses being fed to the secondary ball mill and reverse flotation, thereby greatly reducing the total processing cost. From the plant results for this flow sheet, an iron concentrate containing 67.5% Fe could be produced from a run-of-mine ore containing 30.1% Fe, at a mass yield to the iron concentrate of 34.9%, an iron recovery of 78.0%, and a tailings grade of 10.2% Fe.

9.4.3.5 SLon separator and centrifugal separator flow sheet

If an oxidized iron ore contains a certain proportion of magnetite, which is associated with gangue minerals, high-intensity or high-gradient magnetic separators may not be suitable in the cleaning stage. For example, if a particle contains 1% magnetite and 99% quartz, its magnetic susceptibility can be as high as 6.25×10^{-6} m^3/kg, which is much larger than the 0.6–2.16×10^{-6} m^3/kg magnetic susceptibility of a pure hematite particle. If a SLon magnetic separator is used, the magnetic attracting force on the magnetite–quartz particle is much larger than for a pure hematite particle. Therefore, the quartz particle associated with magnetite is very easily captured into the magnetic product. Furthermore, if the magnetic product is cleaned using a SLon magnetic separator, this particle will again be captured into the magnetic product. Consequently, it is difficult to raise the concentrate iron grade by using a SLon magnetic separator in a cleaning stage.

Centrifugal separators can separate fine mineral particles according to their specific gravity, which for quartz and magnetite/hematite are 2.6 and 5.0 g/cm^3, respectively. Hence, centrifugal separator can reject quartz particles associated with magnetite. The cleaning capability of centrifugal separators is better than SLon magnetic separators for such ores. By combining the advantages of SLon magnetic separators and centrifugal separators to treat such iron ores, good separation results can be achieved.

An example where SLon magnetic separators and centrifugal separators are used in combination in a flow sheet is shown in Figure 9.15. In this case, the iron ore is composed predominantly of hematite and about 10% magnetite. The gangue minerals include quartz, feldspar, chlorite, olivine, and pyrite. Because the ore contained complex gangue minerals, reverse flotation failed in previous tests.

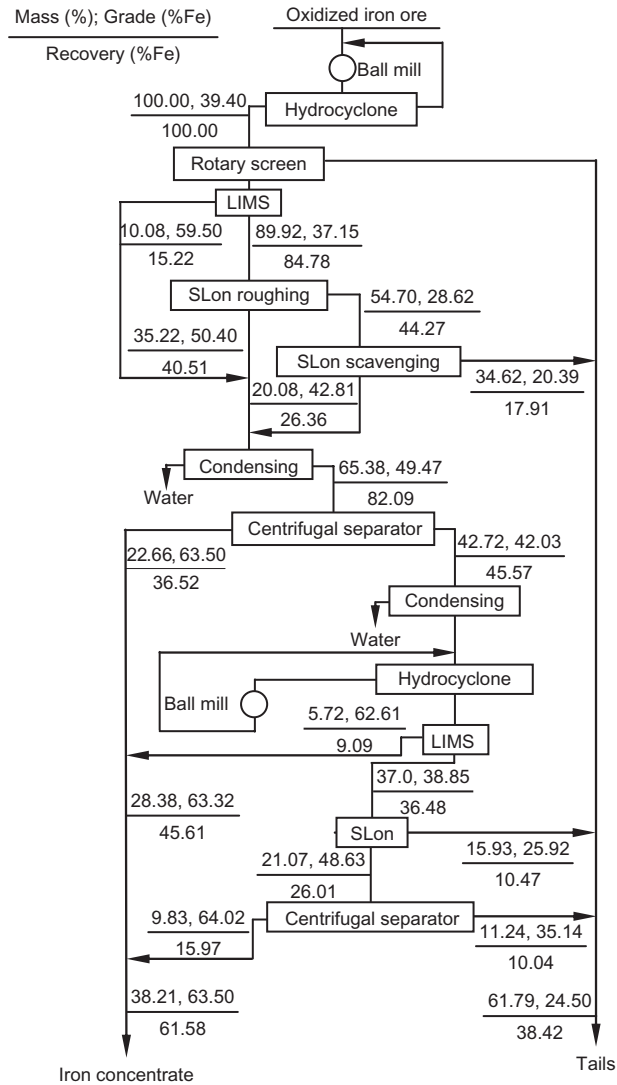

Figure 9.15 SLon separator and centrifugal separator flow sheet.

The iron ore is first ground to about 90% -75 μm. Drum LIMS are then used to take out the magnetite, while SLon magnetic separators are used for roughing and scavenging to recover the hematite. The magnetic products from the LIMS and SLon separators are combined and processed using centrifugal separators to recover part of the final iron ore concentrate. The tailings from the centrifugal separators are condensed and classified using a hydrocyclone. The underflow from the hydrocyclone goes to the secondary ball mill, while the overflow from the hydrocyclone is further processed using a LIMS to recover the magnetite as part of the final iron ore concentrate.

The nonmagnetic product from the LIMS is scavenged using a SLon magnetic separator to produce a magnetic product, which is further cleaned using centrifugal separators to generate another component of the final iron ore concentrate.

It was found from plant operating results using this flow sheet that an iron ore concentrate containing 63.5% Fe could be produced from a run-of-mine ore containing 39.4% Fe at a mass yield to the iron concentrate of 38.2%, an iron recovery of 61.6%, and a tailings grade of 24.5% Fe. The higher than usual Fe grade of the tailings is due to the presence of unrecoverable Fe in the gangue minerals.

9.4.3.6 SLon and reverse flotation flow sheet to separate specularite

Compared with the SLon magnetic separator, the operating cost of reverse flotation is much higher. The flow sheet in Figure 9.16 provides an example of how to minimize the feed to flotation to reduce the total production cost. The iron ore is composed dominantly of specularite with only about 0.5% magnetite, and the gangue mineral is mainly quartz. The run-of-mine ore contains about 32% Fe.

The ore is first ground to about 50% -75 μm in the primary ball mill. Drum LIMS are then used to take out the magnetite, while SLon magnetic separators are used for roughing and scavenging to recover the specularite. The nonmagnetic product from the scavenging SLon is discharged as the final tailings. The mass and grade of the discharged tailings are about 43% and 9.2% Fe, respectively. On the other hand, the magnetic products from the LIMS and SLon magnetic separators are fed to the secondary ball mill system, ground to about 80% -75 μm, and finally treated by drum LIMS and SLon magnetic separators for cleaning and scavenging to recover about 30% of the mass as the final iron ore concentrate, with about 15% of the mass discharged as the final tails. Because the magnetic product from the scavenging SLon, which enters the reverse flotation system for further cleaning, accounts for only about 12% of the ore mass, the flotation cost is relatively small compared to the total flow sheet cost. In this case, an iron ore concentrate containing 65.0% Fe could be produced from a run-of-mine ore containing 31.6% Fe, at a mass yield to the iron concentrate of 38.9%, an iron recovery of 80.0%, and a tailings grade of 10.4% Fe.

9.4.3.7 SLon magnetic separator to separate limonite

The magnetic susceptibilities of limonitic iron ores are the smallest of the oxidized iron ores, so they are more difficult to recover with high-intensity or high-gradient magnetic separators. Because the crystal water in limonitic ores will report to the iron ore concentrate in magnetic separation, the iron ore concentrate grade is limited to about 52% Fe.

Figure 9.17 shows an example of a flow sheet to upgrade a limonitic ore. The ore is mainly composed of limonite and quartz with a grade of about 40% Fe. The ore is first ground to about 80% -75 μm and then processed using SLon magnetic separators for roughing and scavenging. The plant operating results for this flow sheet showed that an iron ore concentrate containing 52.0% Fe could be produced from a run-of-mine ore containing 40.4% Fe, at a mass yield to the iron concentrate of 57.5%, an

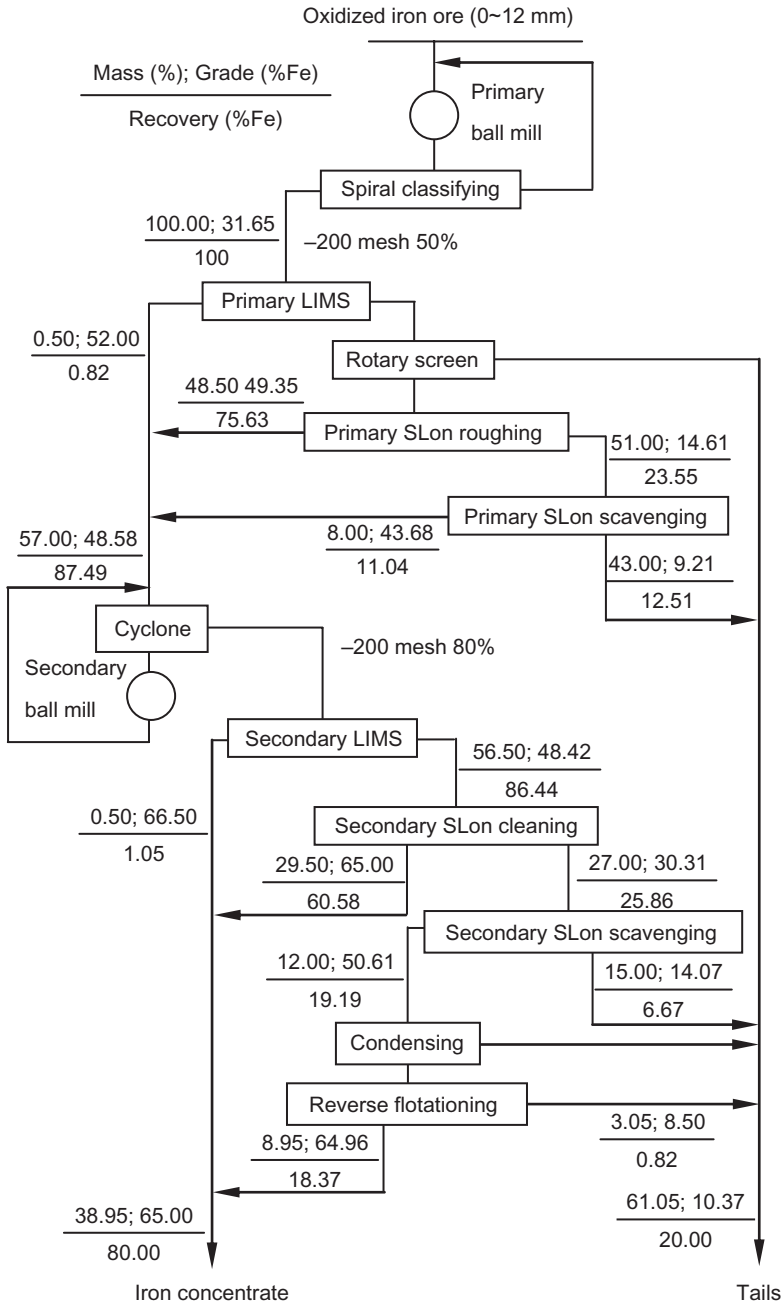

Figure 9.16 SLon and reverse flotation flow sheet to separate specularite.

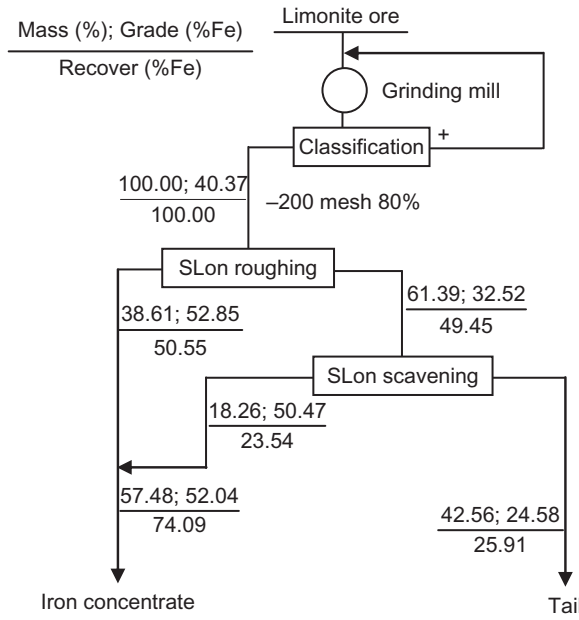

Figure 9.17 SLon magnetic separator to separate limonite.

iron recovery of 74.1%, and a tailings grade of 24.6% Fe. The higher than usual Fe grade of the tailings is due to the fact that the magnetic susceptibilities of limonitic iron ores are small and some of the fine iron ore particles are too difficult to recover using magnetic separators.

9.5 Challenges and recent advances in magnetic separation

As high-grade iron ore resources become less and less due to the rapid increase in steel production, iron ore beneficiation is becoming more and more important. The complexity of new ores also makes the task more and more difficult. Recent advances in magnetic separation are summarized below.

9.5.1 Development of large magnetic separator models

Development of large magnetic separator models can increase the ore treating capacity, reduce energy consumption, and save space. The largest permanent magnetic drum separator is 1800 mm in diameter and 5000 mm in length, and the capacity for treating magnetite ore is 250–300 ton of feed per hour.

The largest SLon vertical ring and pulsating high-gradient magnetic separator is the SLon-4000. The diameter of its separating ring is 4000 mm and the ring width

is 2000 mm, its capacity for treating oxidized iron ore being 350–550 ton of feed per hour. Its installed power is only 176 kW at a background field strength of 1.0 T, and its energy consumption is only 0.3–0.5 kWh for treating each tonne of oxidized iron ore.

9.5.2 Utilization of subeconomic iron ores

As magnetic separators progress toward larger capacity, higher efficiency, and lower operating costs, some subeconomic iron ores have been utilized in recent years. For example, magnetite iron ore containing only about 4% Fe (beach sands or ancient beach sands) to 15% Fe (iron ore formations) and oxidized iron ore of only about 10% Fe (previously mine waste) to 20% Fe (oxidized iron ore formations) are reported to be utilized. They are first crushed and the coarse particles pretreated using roll magnetic separators. The magnetic product of roll magnetic separators may reach 25–40% Fe and then is fed to mineral processing plants.

9.5.3 Development of dry magnetic separators

Most iron ore processing in the fine particle ranges is carried out on a wet basis. The alternative is dry magnetic separation, but many laboratory tests have shown that it is not as efficient as wet magnetic separation in the fine particle ranges. However, some iron ore resources are located in dry areas where adequate water supply is very difficult to obtain and hence dry processing is the only option.

Dry permanent magnetic drum separators have been developed to separate magnetite and have been used in industry. And a SLon-1000 vertical ring and vibrating high-gradient magnetic separator has been developed for dry magnetic separation. It can treat weakly magnetic minerals in the size range 0–2.0 mm and has been used in industry for upgrading roasted kaolin of 0–0.2 mm by removing the impurities of oxidized iron ore and other weakly magnetic minerals. It is a potential dry magnetic separator for oxidized iron ore beneficiation.

9.6 Summary

The majority of iron ores occurring naturally on earth are low-grade and need to be upgraded prior to use in metallurgical processes. Magnetic separation is the most important method for upgrading low-grade iron ores to high-quality iron ore concentrates because of its high capacity and low operating cost.

Iron ores are divided into two different groups according to their magnetic susceptibility, that is, strongly magnetic iron ore such as magnetite and weakly magnetic iron ores (oxidized iron ores) including martite, hematite, specularite, limonite, and siderite. In iron ore beneficiation, LIMS are used to treat magnetite ore, while high-intensity and high-gradient magnetic separators are used to treat oxidized iron ores. Because different iron ores possess different magnetic characteristics, it is very important to develop an optimized flow sheet to maximize the Fe grade of the concentrate with high Fe recovery while at the same time minimizing operating costs.

Through discussion of industrial flow sheets for iron ore beneficiation, including three flow sheets for magnetite separation and seven flow sheets for oxidized iron ore beneficiation, this chapter has demonstrated the ways that various magnetic separation technologies can be used for upgrading complex low-grade iron ores.

References

Xiong, D.H., 2006. SLon magnetic separator promoting Chinese oxidized iron ore processing industry. In: Int. Proceedings of XXIII IMPC, Istanbul, pp. 276–281.

Xiong, D.H., 2008. SLon magnetic separators applied to beneficiate low grade oxidized iron ores. In: Int. Proceedings of XXIV IMPC, Beijing, pp. 813–818.

Xiong, D.H., 2010. A new technology of applying SLon-2500 magnetic separator to recover iron concentrate from abandoned tails. In: Int. Proceedings of XXV IMPC, Brisbane, pp. 1403–1412.

Xiong, D.H., 2012. The creative technologies of SLon magnetic separators in benefiating weakly magnetic minerals. In: Int. Proceedings of XXVI IMPC, New Delhi, pp. 05866–05882.

Xiong, D.H., Liu, S.Y., Chen, J., 1998. New technology of pulsating high gradient magnetic separation. Int. J. Miner. Process. 54, 111–127.

Developments in nonmagnetic physical separation technologies for hematitic/goethitic iron ore

10

E. Maré, B. Beven, C. Crisafio
Fortescue Metals Group Limited, Pilbara, WA, Australia

10.1 Physical processing for enhanced chemical and/or physical properties

Hematitic/goethitic iron ore as a bulk commodity is normally treated at its source (mine) through relatively simple physical *ore dressing* processes of comparatively large scale to turn it into salable products prior to transportation. The overall purpose of such treatment is twofold: In the first place, iron ore needs to conform to strict sizing specifications requiring separation into different marketable products typically having size-related names like "lump" and "fines." In the second place, iron ore treatment is increasingly driven by the need to address chemistry-related grade concerns such as the levels of undesirable elements, notably silicon (Si) and aluminum (Al), and/or conversely to increase the level of the most valuable constituent, iron (Fe).

The effective sizing separation of iron ore is of primary importance, and it is achieved through the comminution and screening processes described in Chapter 8. However, the nature of iron ore is such that a certain amount of "upgrading" is inevitably associated with the sizing separation alone. For example, the "lump" component for most iron ores will naturally be of a different (normally better) chemical grade than its "fines" proportion. This chapter is concerned with the further physical separation processes applied to both coarse and fine portions for enhancing physical and/or chemical properties.

These nonmagnetic physical upgrading processes utilize differences in basic properties such as sizing, hardness, shape, density, and hydrophobicity to separate the desirable parts (salable ore) from unwanted parts (gangue or waste). Some processes may focus on only one characteristic, while the premise of others is based on a combination of the basic characteristics. As with metallurgical separation processes in general, all require appropriate liberation of the valuable ore parts through suitable comminution processes for achieving good selectivity and processing efficiency. The effectiveness of each process on its specific feed material can always be described in terms of the mass and/or chemical recoveries and the upgrading associated with the salable product(s) that it generates. As discussed later, some of these physical processes are better suited to and more effective with coarser sizes, while others only work on finer parts.

Iron Ore. http://dx.doi.org/10.1016/B978-1-78242-156-6.00010-1
© 2015 Elsevier Ltd. All rights reserved.

The most applicable physical separation processes for iron ore described in more detail in this chapter are the gravity separation techniques dense medium separation (DMS), jigging, upflow classification/hindered bed settling, and spiraling.

10.2 Dense medium separation

10.2.1 Principle

DMS is a gravity separation process. In the strictest sense, it implies separation of lower-density particles from higher-density particles at a specific separating density regardless of size, shape, and other secondary influences. In industrial reality, such simplistic gravity separation is seldom so perfectly achievable though, with appropriate design and operational care, DMS is generally able to achieve separation very close to that predicted by theoretical particle density considerations alone as size and shape play a less dominant role compared with other gravity techniques. A well-designed DMS operation can therefore be regarded as being size-independent (Bosman, 2007). It is generally more efficient in terms of separation sharpness than competing gravity processes like jigging and yet is considered the simplest of all gravity processes (Wills, 1985).

DMS machines and plants achieve the separation of different density materials in fluid media, and the terms "floats" and "sinks" are therefore often used to describe the lighter and heavier fractions. In the context of iron ore beneficiation, the separation medium is invariably made up of a suspension of very fine ferrosilicon (FeSi) particles in water that performs as a dense liquid. The lighter particles staying buoyant in the medium ("floats") are always the undesirable part, while the heavier, denser "sinks" represent the upgraded part of the ore. Iron ore beneficiation is therefore opposite to coal beneficiation where DMS is even more extensively used but where the floats represent the desired outcome. Another notable difference is that while coal DMS can use a cheaper medium made up of ground magnetite particles, the higher separation densities required in iron ore beneficiation (in the order of 3–4 kg/l) necessitate the use of relatively expensive FeSi.

10.2.2 DMS in current iron ore use

Two of the biggest DMS installations in iron ore involve the plants of Kumba Iron Ore at their Sishen mine in South Africa and of Rio Tinto at their Mount Tom Price mine in Australia.

10.2.2.1 Sishen DMS plant

Sishen crush their run of mine (ROM) to a nominal top size of 90 mm before separation into four main size fractions. The two coarsest fractions $-90+25$ mm and $-25+8$ mm are gravity fed to separate WEMCO drum sections (Figure 10.1), while the two finer fractions $-8+5$ mm and $-5+2$ mm are fed to the DMS cyclone plant

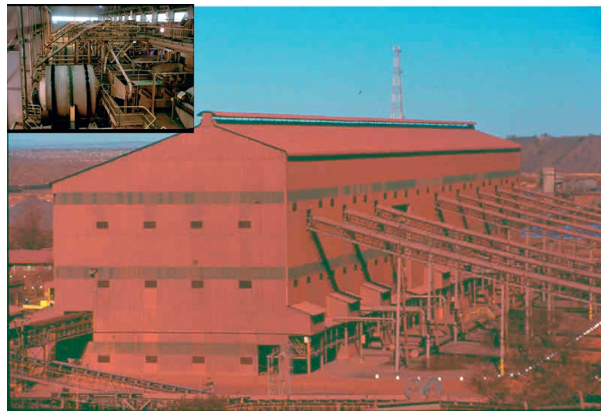

Figure 10.1 Sishen drum plant with WEMCO drums (inset).

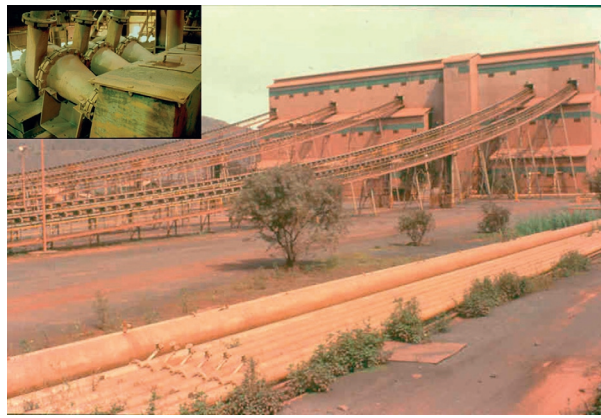

Figure 10.2 Sishen cyclone plant with 360 mm DMS cyclones (inset).

(Figure 10.2). The −2 mm material is kept out of the DMS circuits for enhanced efficiency and is rather beneficiated by non-DMS classification.

The Sishen drums are WEMCO 4 m × 4 m units with rated capacities of 650 and 450 tph in the coarse drum plant (−90 + 25 mm) and medium drum plant (−25 + 8 mm), respectively. The DMS cyclones are 360 mm with rated capacities of 340 and 190 tph per cluster of three units in the coarse cyclone plant (−8 + 5 mm) and fine cyclone plant (−5 + 2 mm), respectively.

The Sishen circuits demonstrate the typically high efficiencies expected for DMS, with E_ps (Section 10.2.3) in the region of 0.06–0.07 kg/dm^3.

Examples of the sharply defined sinks and floats of both drum and cyclone operations are shown in Figures 10.3 and 10.4.

Figure 10.3 Sishen coarse drum plant sinks (right) and floats (left).

Figure 10.4 Sishen coarse cyclone plant sinks (right) and floats (left).

10.2.2.2 Mount Tom Price DMS plant

Rio Tinto Iron Ore's low-grade ore beneficiation plant in the Pilbara was commissioned in 1979. Initial engineering, design, and construction were undertaken by KBR (Kellogg Brown and Root) and Minenco (RTIO information provided to author, 2013). The plant separates closed-circuit crushed ROM into $-31.5+6.3$ mm and $-6.3+0.5$ mm streams for feeding their DMS drum and cyclone plants, respectively (Figure 10.5).

An overhead view of the plant is shown in Figure 10.6 showing where the screening house and the two DMS buildings fit into the overall plant layout.

Like the Sishen plant, the Mount Tom Price plant utilizes ferrosilicon as dense medium. A coarser grade (65D) is used for the drum plant and a finer grade (150D) for the cyclones.

The efficiencies for the RTIO DMS plants also exhibit typically very small E_ps—in the region of 0.05–0.1 kg/dm^3.

Media recovery is by single-stage wet low-intensity magnetic separation drums (Magnapower). 200 mm densifiers are used to densify heavy media.

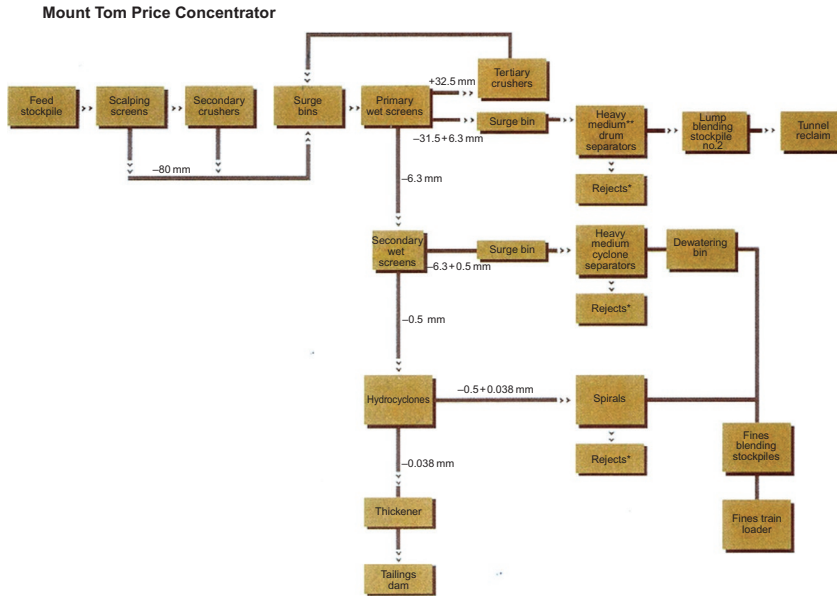

Figure 10.5 Mount Tom Price flow sheet.

Figure 10.6 Mount Tom Price DMS plants.

10.2.3 DMS performance measurement

The performance of DMS unit operations is normally expressed in terms of at least yield (sinks mass rate/feed mass rate), cut point, and efficiency.

Operational efficiency is usually best expressed in the form of a partition curve. The partition curve exercise requires known throughput rates (t/h) and plant samples that reliably represent the DMS unit operation in terms of its feed and its corresponding sinks and floats. The three samples are carefully characterized in the laboratory through a time-consuming densimetric analysis using heavy liquids of varying

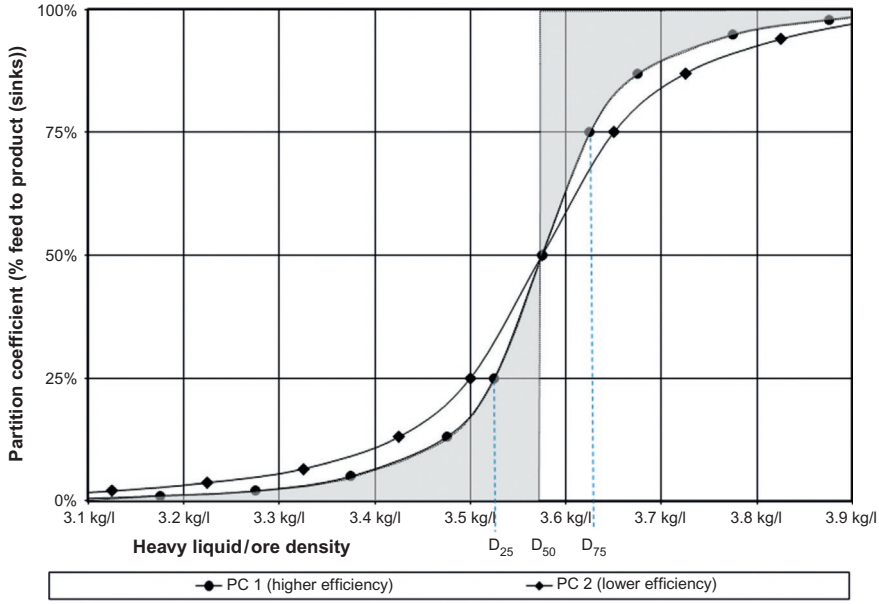

Figure 10.7 Hypothetical partition curves for a DMS unit operation.

densities. The data (rates and mass-by-density) allow the calculation of so-called partition coefficients, which in iron ore operations represent the percentages of feed material of given densities that actually report to the sinks.

An example of hypothetical DMS partition curves is shown in Figure 10.7. PC 1 shows what a higher-efficiency operation would look like compared to a less efficient operation (PC 2). In the example, PC 1 and PC 2 do not necessarily need to represent different unit operations though; they could also represent efficiencies for different sizes for a single-unit operation.

The beauty of the partition curve is that it graphically displays the deviation from the ideal separation, which in Figure 10.7 is shown by the shaded part (PC 1 only demonstrated). This inefficiency, due to misplacement, can however be expressed as an objective number—the so-called Ecart probable (E_p). The E_p is simply a selected "width" around the cut point (all measured in density units) stating the inefficiency of the operation (Napier-Munn, et al., 2009). It is calculated as follows:

$$E_p = \left(D_{75} - D_{25}\right)/2 \tag{10.1}$$

where D_{75} and D_{25} are the heavy liquid/ore densities representing the points on the curve where 75% and 25%, respectively, of the feed effectively report to sinks.

In the example, $E_{p1} = 0.05$ kg/l and $E_{p2} = 0.075$ kg/l, clearly illustrating that smaller E_ps are desirable.

The D_{50} (effective density cut point) is likewise easily read off from the partition curve.

10.2.4 DMS compared to other gravitational separation processes

The main advantage of DMS compared to its main gravitational opponent, jigging, is its higher separation efficiency, especially when excessive near-density material causes jigging to become ineffective. DMS is also more tolerant of wider feed size ranges as the opposing sinks and float movements relative to the high separating medium density of DMS are less prone to crowding than the stratification process of product and waste layers inside the water-only medium of the jigging process.

10.2.4.1 Particle size limit

In iron ore DMS circuits, the particle size limit is in the order of 0.5–1 mm. Below the limiting size, medium viscosity has too much influence on the comparatively large surface area of finer particles so that gravitational process selectivity is lost. Here, DMS is no different to jigging, however, where the practical size limit is in the same region as for DMS.

10.2.4.2 Medium density considerations

Dense medium processes are not immune to adverse medium effects influencing separation efficiency and operability. In DMS, those can include both medium viscosity and medium stability problems due to targeting medium densities that are either too high or too low. Appropriate medium densities need to consider the interaction between three main issues: percentage of slimes in the circulating medium and the sphericity and size distribution of the medium particles (Myburgh, 2006).

It is shown that these three issues need to be managed carefully to ensure medium density boundaries are not exceeded. Kumba Iron Ore therefore choose to keep very close control over the manufacture of their ferrosilicon and prefer the nitrogen-atomized variety to the more porous milled product.

10.2.4.3 Medium recovery

While DMS comes into its own when the feed is nonporous, it may not be the best choice when the material to be treated is of a porous nature. Porous ore can absorb the dense medium to an extent to render recovery of the expensive ferrosilicon very inefficient. The prevalence of porous material can therefore be enough of a deterrent to decide against the use of DMS.

As alluded to above, ferrosilicon is a major part of the operational expense of DMS processes. However, it is generally accepted that the energy costs of DMS processes are considerably lower than equivalent capacity jigging processing (Bosman, 2007). DMS plants are also generally perceived to be less capital-intensive than equivalent jigging plants.

10.3 Jigging

Jigging is a commonly used gravity separation beneficiation process. It is used extensively in the iron ore and coal industries and has undergone several technological developments over many decades.

10.3.1 Principle of jigging

Though a number of different types of jig exist, the basic concept is essentially the same for all. An ore stream is introduced into a water-filled chamber, forming a solid bed beneath the surface. As Figure 10.8 shows, the bed of ore sits on a screen deck (with or without ragging), through which water is continuously pulsed into the jig chamber.

The pulsing mechanism is a defining factor of the various jig types. The pulsing effect may be created pneumatically such as in the Baum and Batac jigs (Figure 10.9) or by mechanical means such as diaphragms and plungers as shown in the Harz and Denver jigs (Figure 10.10).

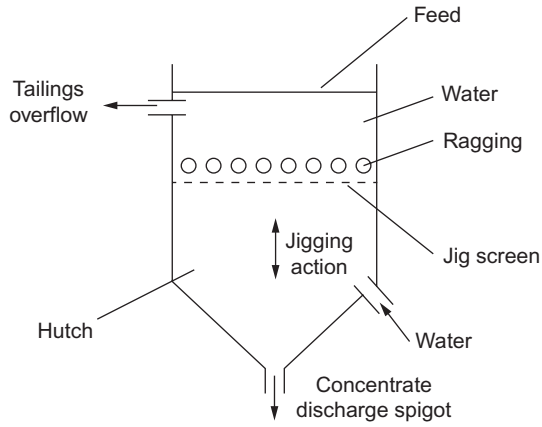

Figure 10.8 Basic jig schematic.
Source: Wills and Napier-Munn (2011).

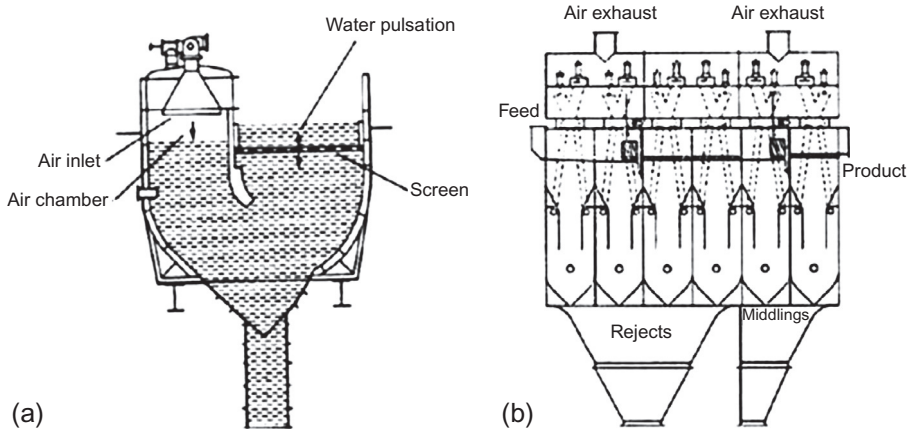

Figure 10.9 Pneumatically pulsed jigs: (a) Baum jig and (b) Batac jig.
Source: Wills and Napier-Munn (2011).

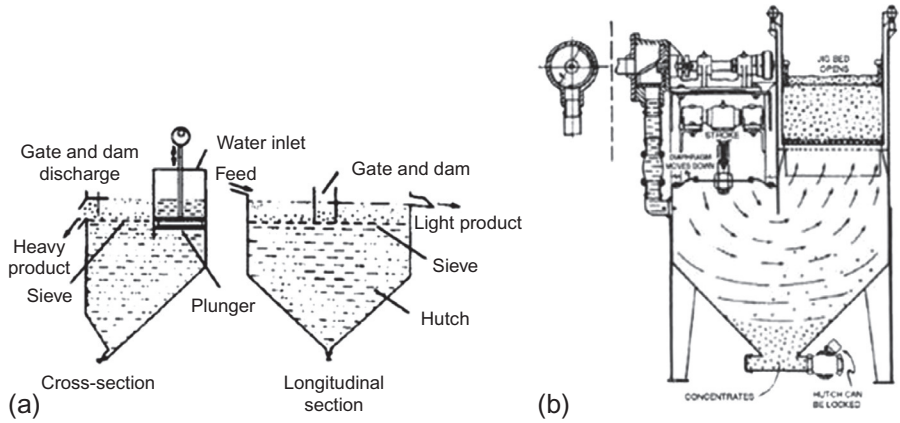

Figure 10.10 Mechanically pulsed jigs: (a) Harz and (b) Denver.
Source: Wills and Napier-Munn (2011).

The jigging cycle encompasses three distinct stages of separation, as illustrated in Figure 10.11. With each upward pulse of the water column, the bed is fluidized and particles are driven upward. The upward acceleration of each particle will vary based on individual density. Specifically, lighter particles will rise faster and heavier particles slower. Following the peak of pulsation, a stage of hindered settling commences, whereby lighter particles will settle slower and heavier particles will settle faster under the influence of gravity. It should also be noted that particle size has an influence during hindered settling, with coarser particles tending to sink faster than fine particles, given their higher terminal velocity. Finally, a period of consolidation trickling

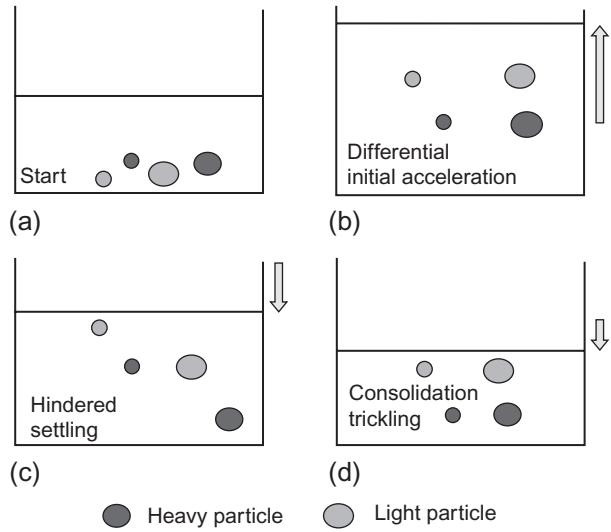

Figure 10.11 Jigging stages, with water column movement shown.
Adapted from Falconer (2003).

occurs, during which heavier fine particles are allowed to settle into interstitial spaces within the bed, in preference to lighter fines.

The combined result of these stages is rapid stratification. The higher-density (higher-grade) particles will become concentrated in the bottom layers of the bed and are extracted as a horizontal layer of product below a lighter layer of waste.

A number of parameters can be varied to fine-tune the separation process. For example, the length and frequency of each pulse are critical to ensuring adequate dilation of the bed. The appropriate settings are dependent on particle size: finer feed generally requires shorter, more frequent pulses, whereas coarser feed favors longer, less frequent pulses.

The quantity of pulsing water injected is another important variable. A minimum flow of water must be introduced to ensure that particles are adequately fluidized and that lighter particles are carried over to tails. However, excessive quantities will lead to increased high-grade fines being lost to tails. Additional process water is continuously injected into the pulsing chamber of the jig in order to replenish the water continuously exiting with the overflow and underflow streams. Recovery of water through efficient dewatering of product and tails and subsequent recovery from thickening are therefore of great importance, given the significant water circulation required for jigging.

In a conventional jig, such as allmineral's alljig, control of the cut point is achieved primarily through the concentrate layer thickness. This is the user-defined layer of extractable product within the jig bed. A hollow steel float (connected to a vertical shaft) is allowed to sit within the jig material and moves with each pulse. After each pulse, it will rest at the level in the bed at which the particle density matches its own density, that is, where it is naturally buoyant. This level becomes the measured bed layer thickness and the rate at which product is extracted is constantly controlled to keep this measurement on par with the user-defined set point. This provides streamlined control of product grade by allowing the jig bed to self-regulate in the event of fluctuating feed composition.

For example, a sudden slug of higher-grade material will cause the float to sit at a higher level. The measured layer thickness will exceed the set point and the rate of product extraction is increased until the concentrate layer falls to the set-point value. This allows the jig to accommodate for increases in useable product and prevents unnecessary losses to tails. Conversely, a sudden slug of lower-grade material will lead to the float sitting at a lower level in the jig bed. The layer thickness will be measured as less than the set point, and the rate of product extraction will automatically decrease until the concentrate layer builds to the set-point value. This will prevent low-grade material reporting to product.

10.3.2 Developments

10.3.2.1 Product extraction

Key developments in the design of the conventional jig relate to the mechanical system by which product is extracted. The commonly used method for the alljig is to have a movable bottom gate, with opening dependent on the measured layer thickness, as in Figure 10.12.

Figure 10.12a shows the jig bed in an equilibrium state, with the concentrate (dark particles) layer thickness in line with the set point. Figure 10.12b shows a slug of

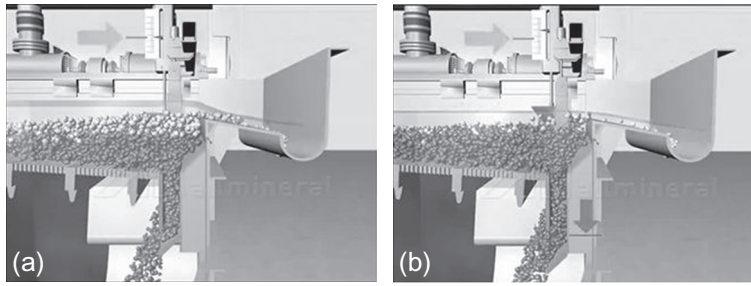

Figure 10.12 The regulation of layer thickness in the jig bed. (a) The jig bed in an equilibrium state. (b) A slug of high-grade material is introduced.
Images courtesy of allmineral.

high-grade material being introduced, forcing the concentrate layer thickness above the set point. The hydraulic gate responds by opening to allow additional product through.

Other mechanisms have been designed for the alljig to achieve the same level of control, with two such examples shown in Figure 10.13. The final segment of the jig deck can be constructed to pivot for directly controlling the opening through which product can escape. Alternatively, a "Star Gate" can be employed, with variable rotation speed to maintain the desired concentrate layer thickness.

10.3.2.2 Ragging deck

An additional development is the addition of the ragging deck. With respect to the alljig, this exists as a secondary stage of separation, handling the overflow (rejects) from the main jigging chamber. As previously discussed, hindered settling is biased toward coarser particles, which can lead to the rejection of very fine, high-grade material. The ragging deck is a means to scavenge this material from the bulk of the low-grade rejects stream.

The alljig's ragging deck is a separate chamber, immediately following the overflow weir of the main jig. Like the main chamber, its floor is a screen deck through which the solid bed is pulsed. The lower-grade particles are rewashed over a weir bar, becoming the final rejects stream. The high-grade fine particles will migrate more

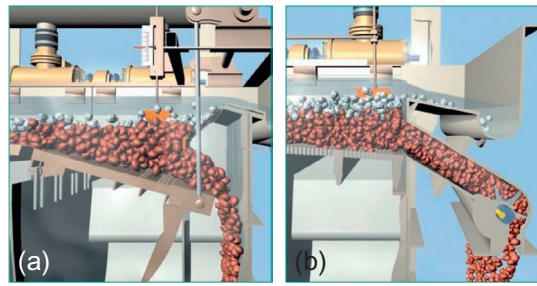

Figure 10.13 Alternative product extraction mechanisms for the allmineral alljig: (a) movable bed and (b) variable speed star gate.
Images courtesy of allmineral.

freely to the bottom layers due to the absence of competing high-grade coarse particles. The screen deck is covered with a layer of material known as ragging. The purpose of the ragging material is to provide a path for consolidation trickling, allowing the high-grade fines to escape through interstices while excluding lower-grade coarse particles. The characteristics of the ragging material used are therefore critical. The particles must be big enough to prevent them passing through the screen deck and heavy enough to not get washed out to rejects. Furthermore, the packing of the material must be such that the size of the interstices will allow the fine particles through in preference to the low-grade coarser particles. Common materials used for ragging include high-grade coarse material (Figure 10.14) or steel ball bearings.

10.3.2.3 Kelsey jig

The use of centrifugal force to improve jig separation has led to the creation of the Kelsey jig (Figure 10.15). The same pulsation technique is used as with the conventional jig; however, the jigging mechanism is rotated to create a centrifugal effect. This leads to a significant increase in the apparent gravitational field, enhancing the effect of differential acceleration and greatly improving separation efficiency. This technology is especially useful in applications involving very fine feed material or the separation of particles with very small density differences (Richards and Jones, 2004).

Figure 10.14 Ragging deck with incomplete covering of coarse ragging. Photo courtesy of Arrium Mining.

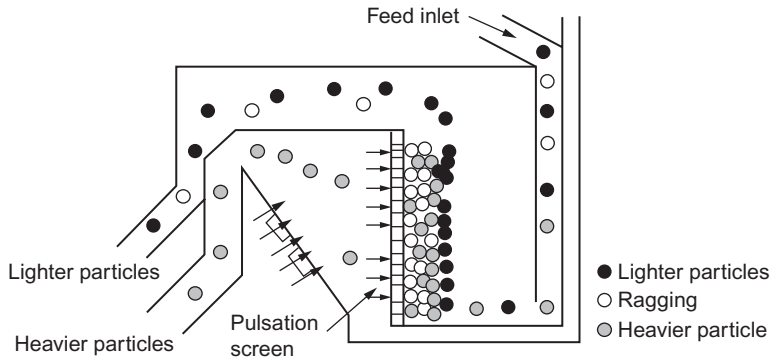

Figure 10.15 Partial cross section of a Kelsey jig.
Source: Nayak and Pal (2013).

10.3.3 Assessment of jigging

Despite being one of the oldest forms of mineral separation, jigging is still a widely used mineral beneficiation process, with its usage also extending to industries outside of mining, such as plastic recycling (Ito et al., 2010).

Jigging is a proved technique for beneficiating low-grade iron ores, creating salable product from what would ordinarily be defined as mine waste. This has been demonstrated at a number of mines worldwide. For example, testwork at the Sishen mine in South Africa has shown that ROM stocks between 50% and 60% iron can be upgraded to a salable 64% product, greatly enhancing the resource base of the mine (Pretorius and Hoffmann, 2006).

More recently, Arrium has reopened the Iron Baron mine in Whyalla, South Australia. Previously closed in the 1990s, the construction and commissioning of the low-grade hematite ore beneficiation plant have enabled the mine to once again become economically viable. The minimum 61.5% Fe product grade may now be generated from ore that was formerly segregated to waste dumps (Stanton and Bannear, 2013). Prior to this, Arrium had already been taking advantage of jigging technology for beneficiation of similar waste dumps at the Iron Duke mine site. A schematic of the beneficiation process used is shown in Figure 10.16.

Technical comparisons are often drawn between jigging and DMS as alternative methods for iron ore beneficiation. Detailed evaluation of the capital and operational costs required for jigging plants compared to equivalent dense medium circuits has been completed by Bosman (2007). Although jigging plants carry lower capital cost due to their relatively simple design, dense medium circuits generally achieve superior separation efficiency, which in many applications will justify the greater capital investment required. It should also be considered that if a wide distribution of particle size is expected in feed, multiple jigs may need to be installed, significantly increasing capital expenditure.

With respect to operational costs, a key advantage of jigging is the use of water as the separation medium, eliminating the cost of dense media such as ferrosilicon used in DMS. Moreover, the wear rates on plant equipment such as piping and pumps are likely to be lower. However, the need for large amounts of water in circulation, as

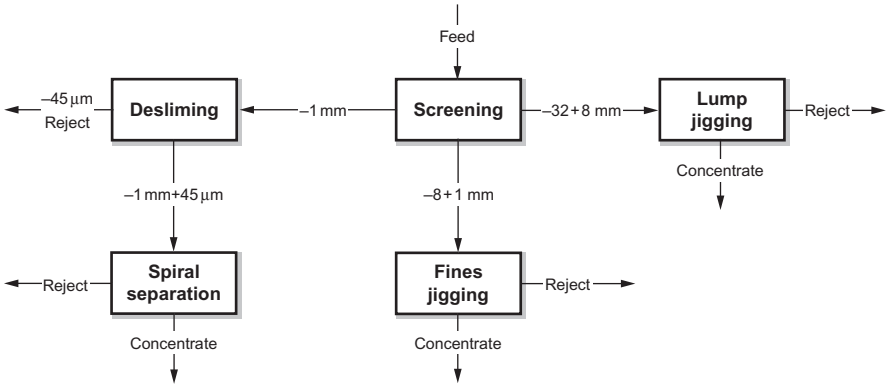

Figure 10.16 Schematic of the Arrium low-grade beneficiation plants at the Iron Baron and Iron Duke mines.
Modified from Stanton and Bannear (2013).

previously discussed, can be viewed as a disadvantage given the copious quantities of water that can be consumed if water spillage is not well controlled or water recovery is poorly done. Furthermore, jigging plants have been shown to consume significantly more power than dense medium circuits with equivalent throughput.

Like all unit operations, the feasibility of using jigs for beneficiation will vary based on the individual situation. Ore characteristics, resource availability, and logistical considerations will all be important factors to consider. Table 10.1 summarizes the advantages and disadvantages of jigging, as discussed throughout this chapter.

Table 10.1 Advantages and disadvantages of jigging

Advantages	Disadvantages
Ability to create salable product out of low-grade feed stocks	Inefficient at wide size ranges. Optimum size range is no more than 3:1
Suitable for both coarse and fine particles (as separate circuits)	Reduced water clarity negatively impacts performance
No expensive separation medium required (water or air only)	Significant water user, making highly efficient dewatering infrastructure essential
Lower wear on associated pumps and piping	Conventional jig provides less efficient separation than dense medium separation
Ability to self-regulate in line with changing feed composition	Consumes more power than an equivalent dense medium circuit
Open equipment allowed for easy visual and physical inspection	Conventional jig is less effective for −1 mm material
High capacities possible	
Separation can be improved through centrifugal force	
Various design options available to suit different applications	

10.4 Upflow classification

At finer particle sizes, screening becomes ineffective at particle separation. Upflow classifiers (also known as hydraulic classifiers) are commonly used in these scenarios, providing more effective size-based separation than conventional screening through the process of elutriation.

10.4.1 Elutriation: the driving force of upflow classification

During elutriation, particles are subjected to an upward flowing current of fluid. In doing so, differences in particle size are exploited, leading to separation into size-based underflow and overflow streams. The tendency of a particle to report to either stream is dependent on its terminal velocity, as well as the upward velocity of the fluid. Where the terminal velocity exceeds the fluid velocity, the particle will settle against the current and report to the underflow and vice versa. The volumetric flow rate of the fluid is therefore a key parameter for controlling the cut point. A basic schematic of the process is shown in Figure 10.17. The designation of the underflow and overflow streams may vary based on application. In the context of iron ore beneficiation classifier, underflow is the product, while overflow is the waste.

Despite the simplicity of the separation process, the physical principles of particle settling are quite complex and have been the subject of extensive mathematical modeling, for instance, Van Schoor, 2008. Variables such as drag force, fluid viscosity, and particle shape all have an impact on terminal velocity. However, from an operational perspective, separation in the upflow classifier can be viewed as being primarily

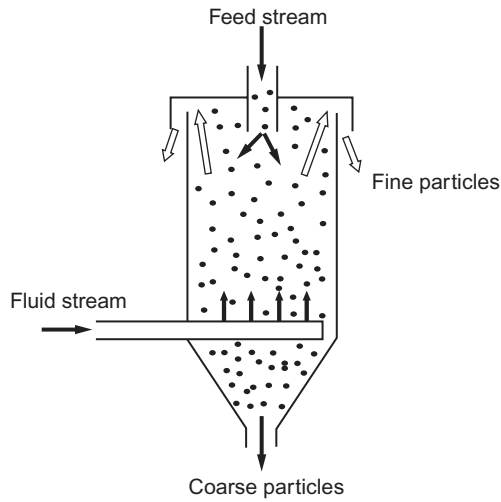

Figure 10.17 Basic upflow classifier schematic.
Modified from Rulkens and Bruning (1995).

driven by particle size with particle density having secondary influence. Specifically, for particles of identical diameter, those of higher density will settle in preference to those of lower density.

10.4.2 Developments in upflow classification

10.4.2.1 Multiple stage

A common drawback of upflow classifiers is finer high density particles of adequate grade often being sacrificed to tails due to their small size. Further beneficiation is thus required to recover these particles.

In response to this, multiple-stage classifiers have been developed to enable the separation of the feed into more than just the standard concentrate and tails. As shown in Figure 10.18, multiple stages of classification allow intermediate product streams to be generated, while the lowest-grade tails are still washed out. Consequently, downstream beneficiation of the intermediate streams becomes more efficient. In addition, as the bulk of the high-grade material is extracted in the preliminary state of classification, the required capacities of downstream operations are greatly reduced.

An example of a multiple-stage upflow classifier is the allmineral allflux shown in Figure 10.19. Consisting of two concentric separation chambers, the allflux has the ability to classify feed material into three streams: coarse product, middlings, and fine tails.

Feed is introduced to the central chamber, where the coarsest particles settle against the rising water current (commonly referred to as "teeter water") and report to the coarse concentrate stream. The remaining particles are washed out into the surrounding secondary chamber. This includes the high-grade fine particles, which, due to their sufficient density, have a greater chance to settle against the secondary teeter water current, along with the coarser lower-grade particles to become the intermediate middlings product stream. The fine, low-grade particles on the other hand are finally washed out as tails.

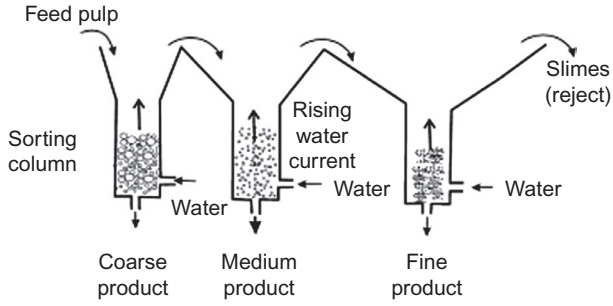

Figure 10.18 Schematic of multiple-stage elutriation circuit.
Source: Haldar (2013).

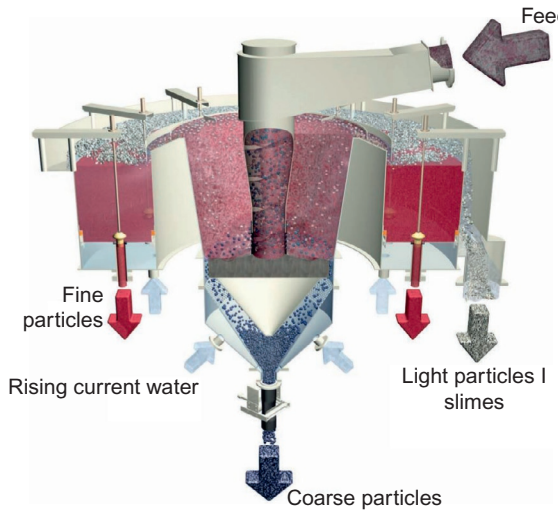

Figure 10.19 Allmineral allflux upflow classifier.
Image courtesy of allmineral.

10.4.2.2 Use with spirals

The allflux is a critical component of processes such as the desand plants used by Fortescue Metals at its Cloudbreak and Christmas Creek mines. This is a method of beneficiating the clay-rich ores characteristic of the Pilbara region, through the use of upflow classifiers in conjunction with downstream spiral concentrators (Figure 10.20).

The classifiers remove the following gangue materials that would otherwise impede the performance of the downstream spiral circuits:

- Fine clay slimes that follow the water split to the hydrocyclone underflow
- Goethite/quartz composite particles, which are difficult to remove in the spirals, due to their density being comparable to that of the higher-grade iron fines

Rejection of these particles generates an intermediate middlings product that may be more efficiently processed in the spirals (Figure 10.21). The higher-grade hematitic and goethitic particles are more easily separated from the medium-sized gangue material, and as such, only a single-stage spiral bank is required to achieve this separation (Clout, 2013).

10.4.2.3 Use with WHIMS

Iron ore processors may also employ magnetic separation for beneficiation of classifier output streams. Wet high-intensity magnetic separators (WHIMS) may be used to extract high-grade fine particles from gangue, due to the greater attraction of the former to the applied magnetic field.

In addition to beneficiating the intermediate middlings streams from the classifier, WHIMS may be used as scavenger units for classifier overflow. This enables particles of sufficient grade to be recovered that would otherwise be sacrificed to tails.

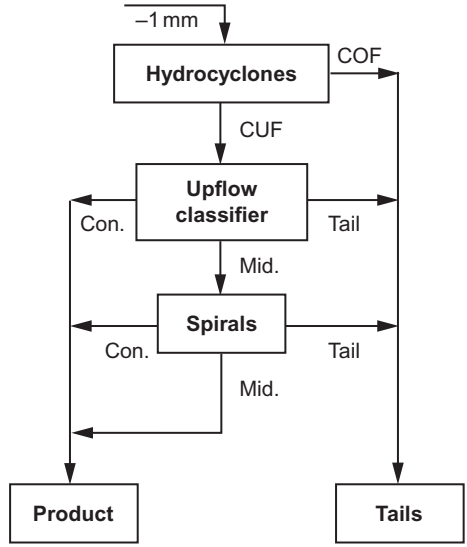

Figure 10.20 The desand process for −1 mm iron ore fines
Modified from Clout (2013).

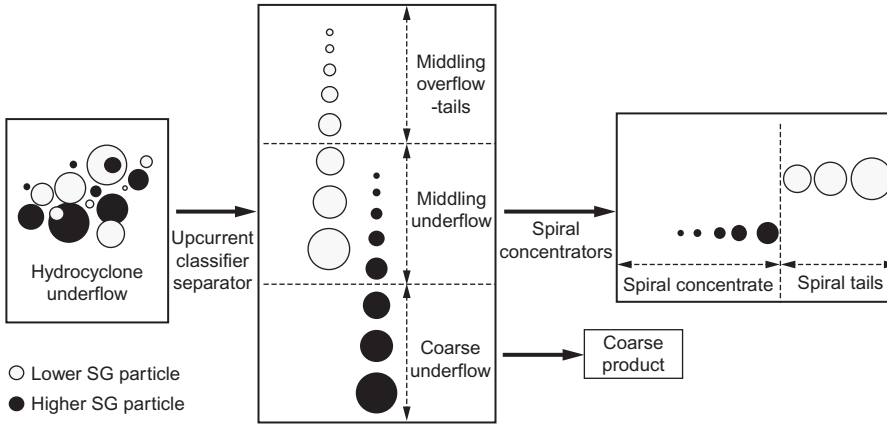

Figure 10.21 The combination of allflux and spiral concentrators.
Source: Clout (2013).

Testwork has been performed on iron ore samples from various locations to validate the use of magnetic separation following classification (Horn and Wellsted, 2011). A key example was material sourced from the Orissa state in northeastern India, with a summary of results shown in Table 10.2. The allmineral allflux and gaustec units were used to provided classification and magnetic separation, respectively.

The starting grade of the sample was a low 42% Fe. It also contained significant ultrafines with 58% passing 20 μm. This is reflected in the low yield of allflux coarse

Table 10.2 Summary of allflux and gaustec testwork on Orissa iron ore

Stream	Yield (%)	Fe (%)	SiO_2 (%)	Al_2O_3 (%)	LOI (%)
Feed (−1 mm)	–	41.6	19.9	13.8	5.58
allflux coarse concentrate	17.9	57.5	8.83	5.14	3.02
gaustec conc. from allflux middlings	10.4	59.2	6.54	4.76	3.20
gaustec conc. from allflux overflow	35.5	57.2	7.60	6.02	3.59
Combined concentrates	63.8	57.6	7.77	5.57	3.37

Source: Horn and Wellsted (2011).

concentrate; however, a notable 16% (abs) increase in iron grade was eventually achieved. The gaustec results for the middlings and overflow streams demonstrate the ability to recover additional high-grade material. With the three concentrate streams combined, an impressive yield of almost 64% was achieved with minimal decline in iron grade.

10.4.3 Assessment of upflow classification

Upflow classifiers have found extensive use in the mining industry, not only in iron ore but also for other minerals such as coal and mineral sands. As already discussed, they provide a more effective means for classification at finer particle sizes, in comparison to conventional screening. In addition, they have the ability to improve the effectiveness of downstream beneficiation units such as spirals or magnetic separators (Table 10.3).

Table 10.3 Advantages and disadvantages of upflow classifiers

Advantages	Disadvantages
Highthroughput capacity	Reduced water clarity impacts performance
Multistage separation possible for a single unit	Less suitable for +1 mm material in iron ore
Significant recoveries are possible, especially when paired with downstream processes	Significant water user, making efficient water recovery processes essential
Improved classification at fines sizes compared to screening	High-grade fines will generally be lost, unless downstream scavenging options are used
Cut point is easily varied (volumetric flow of teeter water)	
Improves the efficiency of downstream beneficiation	

10.5 Spiraling for iron ore beneficiation

Historically, the processing of hematitic iron ores relied on the mining of high-grade deposits that required only dry crushing and screening techniques to generate salable product. In recent years, however, there has been notable progression toward using dry and wet processing due to increased mining of below water table ores along with an impetus to upgrade lower-grade material.

A variety of techniques such as washing/scrubbing, jigging, hydrocycloning, dense medium, gravity separation, and flotation are currently used to treat variable ore types. Miller (2013) categorized that since 1966, iron ore physical separation processes have developed as first-, second-, third-, and fourth-generation plants involving heavy media, jigs and spiraling, washing and desliming, and more recently scrubbing.

To remain competitive, iron ore producers are more frequently driving increased product tonnages at the same or slightly reduced grade and therefore need to consider all available techniques, especially for wet fines processing.

Spirals are used all over the world to produce a variety of mineral concentrates, including iron ore fines. In some instances, several stages of spiraling may be required to achieve grade and recovery targets. These may include rougher, scavenger, cleaner, and recleaner steps. Often, spirals are used in conjunction with other fine ore technologies such as hydrocycloning and hindered settling. In some instances, such processes are used to improve feed presentation especially when ultrafines/slimes are present. Slimes are known to increase slurry viscosity, which in turn can affect the sharpness of separation. Conversely, the associated processes may be utilized to further refine spiral product.

The basic principle behind the spiral as a gravity separator is that it uses a combination of centrifugal force and fluid-related responses to effect separation. This combination causes fine heavies to segregate from coarse lights (Falconer, 2003).

10.5.1 Historical gravity separation and the advent of the modern-day spiral

The origins of spiral design can be traced back to the application of the former gravity separation equipment such as pinched sluices and Reichert cones. In both instances, valuable minerals were separated from gangue by means of wet processing techniques applying the effect of particle differentials of size, shape, and density under the influence of gravity to achieve upgrading.

Since their introduction in the 1940s, spirals have provided improved recovery of fine heavy minerals compared to the separators they replaced. Richards and Palmer stated that conventional spirals typically operate within the size range of 1–2 mm down to 75 μm (Clout, 2013). However, in some instances, feed sizes of up to 3 mm have been processed. With improvements in design, finer spirals have been manufactured to separate heavy minerals down to 30 μm. Over the years, spiral separators have been constructed from a variety of materials including cast iron, rubber tires, and asbestos cement (Holtham and Stitt, 1988). However, in the 1980s, a new generation of spirals was manufactured from fiber glass and polyurethane (Falconer, 2003). Additional materials of construction often include mild steel, aluminum, rubber, and HDPE piping.

10.5.2 Spiraling: pros and cons

As with all processing equipment, there are advantages as well as limitations associated with the use of spirals as highlighted in Table 10.4.

10.5.3 Spiral design

Modern-day spirals are factory-made from lightweight and wear-resistant materials. Often manufactured in single, double, triple, or quadruple starts, they can consist of several turns, for example, 3, 5, or 7 (Figure 10.22). Spiral capacity can vary considerably depending on the model. Often, spiral solids loading varies between 1 and 2 tph up to 9 tph per start.

Spiral banks are commonly composed of the following:

- Gravity distributor
- Spiral assembly
- Housing frame
- Product launders

Additional auxiliary equipment including feed boxes, splitters, and product collection boxes are also required. Depending on the spiral model, wash-water assemblies

Table 10.4 Spiral processing advantages and disadvantages

Advantages	Disadvantages
Low operating cost	Routine cleaning to remove debris
No reagents required	Requires stable feed to operate properly
Mechanical simplicity—no moving parts	Intolerance to ultrafines or slimes
Low cost in terms of auxiliary equipment requirements	Performance easily affected by adverse particle size, particle density differentials, solids feed rate, volumetric flow, pulp % solids, etc.
Apart from routine cleaning, it requires minimal operator supervision and training	Insufficient flow and high-density material may cause beaching resulting in inferior performance
Variable capacity designs available, for example, single, double, triple, and quadruple starts	Manual setting of splitters can be tricky and time-consuming
High capacity with multiple units. Feed rates in the 1000s tph can be achieved	Minimal online process control options available to optimize performance remotely
Many spiral models and designs available for a variety of mineral processing applications	Multispiral stages, for example, roughing, cleaning, recleaning, and scavenging, may be needed for acceptable recovery and grade
Good separation efficiencies achievable if looked after	Spiral plants generally have a large foot print area
Modern construction methods are able to utilize lightweight and durable materials	Fluid-particle dynamics are complex; therefore, modeling can be difficult and may not apply across variable feed types

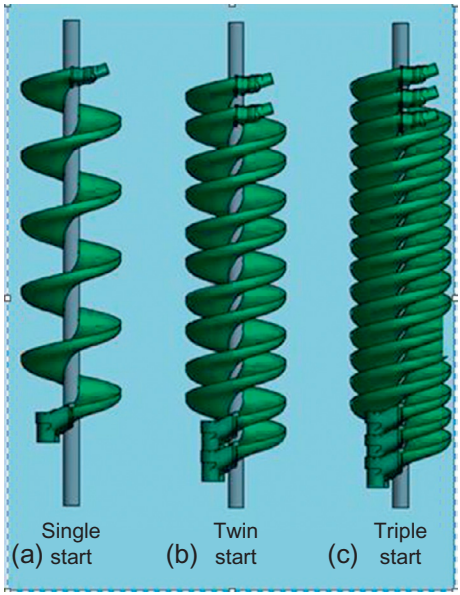

Figure 10.22 Spiral columns showing (a) single-, (b) double-, and (c) triple-start units. Image courtesy of Multotec.

may also be present. Wash water spirals such as the WW6E are often used as roughers or cleaners, whereas the SC20-7/5 HG/HC unit often finds application in cleaning and recleaning duties.

As depicted in Figure 10.23, spiral columns are often mounted in a housing frame, which provides both strength and support to the module. Above each spiral bank is a central gravity distributor (Figure 10.24), which incorporates a flanged connection allowing tie-in of a slurry feed line. At the base of the distributor is a series of outlets often coupled with wear-resistant polyurethane antisiphoning offtakes.

The primary purpose of a gravity distributor is to provide an equal distribution of pulp to each outlet feeding a given spiral start. If for whatever reason an operational requirement exists to restrict flow to one or more spirals, dart valves can be employed (Figure 10.25). In terms of the slurry distribution efficiency, there is no significant difference between the two feed options noted above—provided they are designed accordingly.

Each spiral unit has a center column about which helical troughs are mounted. Often manufactured from glass-reinforced fiber, polyurethane is later applied to provide an abrasion-resistant working surface. Mounted at the top of each spiral start is a feedbox that aids in slurry dispersal. Typically, spirals have a consistent trough profile; however, there are newer designs on the market that exhibit variable trough profiles down their length (Holtham and Stitt, 1988).

Spiral troughs are often described by a series of measurements, namely,

- pitch, the vertical distance between successive spiral turns;
- working diameter;
- number of turns;

Figure 10.23 Typical general arrangement of a spiral assembly—6-spiral bank. Image courtesy of Multotec.

- down-trough slope;
- profile.

At the bottom of each spiral is usually fitted a product collection box constructed from cast polyurethane that may contain either manual or automatic adjustable splitters. The function of a splitter is to separate spiral product into at least two streams. The resultant streams are then transferred to their respective downstream processes.

10.5.4 Operating criteria

Spiral operating criteria are very much dependent on feed material characteristics. Spirals are tolerant of moderate variations in solids concentration without a significant

Figure 10.24 Gravity distributor with flanged feed inlet and antisiphon HDPE piping. Image courtesy of Multotec.

Figure 10.25 Gravity distributor showing offtake piping and dart valves in use.

loss in performance. However, they do not handle volumetric changes as well. Typically, spirals are operated within a solids density range of between 15% and 45% w/w (Wills and Napier-Munn, 2011).

There are several factors that have been well documented to affect spiral performance including

- material feed characteristics such as size, shape, density, and porosity;
- pulp density;
- volumetric flow rate;
- solids flow rate;
- the presence of ultrafines or "slimes";
- trough profile;
- spiral pitch.

10.5.5 A theoretical perspective

The separation performance of spirals can be attributed to several quite complex interactions between solids, the flowing fluid, and surface contacts. A number of mechanisms have been used to describe the behavior observed in flowing film separators, which include spiral and wet tabling devices. Deposit transport (i.e., particles substantially remaining in contact with the trough surface) is often associated with the inner region of a spiral comprising the concentrate and middlings bands. Due to the flowing nature of the water in the outer periphery of a spiral trough, a high-velocity zone occurs in which nondeposit transfer predominates (particles remaining in suspension) (Palmer and Vadeikis, 2010).

Several mechanisms of separation have been used to describe the separation observed in spirals. These include interparticle trickling, hindered settling, differential acceleration and velocity, and fluid shear (Palmer and Vadeikis, 2010). Some or all of these mechanisms may be acting at a given time to produce a complex system that is often not well understood.

Generally, the flow patterns occurring inside a spiral trough consist of a primary component acting downward and a secondary component traversing the spiral profile (Vermaak, et al., 2008). The primary flow is associated with a region of higher density and lower pulp velocity, whereas the secondary flow pattern occurs against the outer trough wall (Figure 10.26) creating a zone of lower pulp density and higher slurry velocity (Palmer and Vadeikis, 2010). Too low a velocity may cause beaching, where material falls out of suspension, whereas too high a velocity creates zones of high turbulence that can lead to sample loss and inefficient separation.

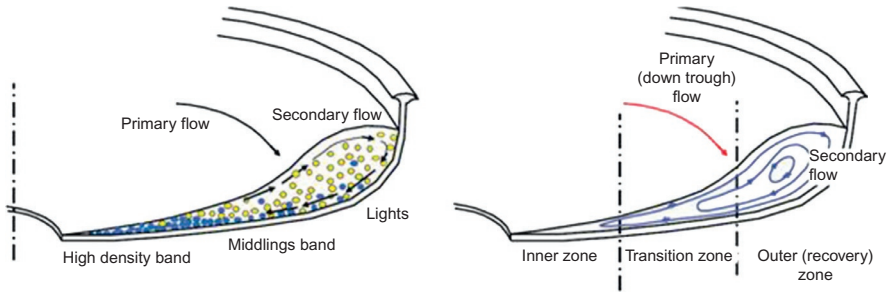

Figure 10.26 Primary and secondary flow properties on a spiral separator.
Source: Palmer and Vadeikis (2010).

10.5.6 Spiral suppliers

In Australia, there are two major spiral suppliers, namely, Multotec and Mineral Technologies. Multotec is a privately owned company that was established in South Africa in 1974. The company has offices in Canada, Chile, and Australia. Multotec fabricates spirals out of their manufacturing facility in South Africa.

An alternate supplier in the Australian market is Mineral Technologies (MT). Currently part of the Downer Group, MT has had several name changes over the years including Mineral Deposits Limited, Roche Mining MT, and CPG. Mineral Technologies' head office is located in Carrara, Queensland. Alternate international suppliers include FLSmidth Krebs, Outotec, and Metquip.

10.5.7 Spiral testwork design

Metallurgical testwork facilities worldwide offer a variety of test spirals for metallurgical evaluation. Testing can be performed on a small scale using one or more spirals for comparative evaluation, or alternatively, multistage spiral rigs can be used. Prior to selecting the optimal spiral design for a given application, the spiral performance is often assessed by means of bulk testing through a pilot plant (O'Connor and Machunter, 2006).

One method used to assess maximum separation efficiency is through the application of heavy liquid separation. In HLS, liquids of varying specific gravities are used to assess the amount and grade of recoverable material at given densities. By this means, the maximum theoretical recovery can be determined. As with most separation processes, a minimum density differential between mineral and gangue components is crucial.

When undertaking assessments of spiral performance, the following factors are often measured:

- Recovery of metal units to concentrate (e.g., Fe recovery)
- Recovery of mass to concentrate (yield)
- Establishment of grade versus recovery curves
- Separation efficiency

When evaluating spiral performance, several variables can be investigated. Often, this involves assessing performance at varying pulp density, mass loadings, and volumetric flow rates. It is important to note that optimal performance will occur over a narrow range.

10.5.8 Iron ore processing employing spirals

Various flow sheets are adopted worldwide to treat variable iron ore deposits. Current-day iron ore beneficiation flow sheets often include the use of spiral concentrators and jigging circuits in tandem to effect good recovery and material upgrade. Additional technology employed to target improved overall grade and recovery involves magnetic separation. For example, in Canada's Labrador province, several different approaches are employed to process specular hematite of which gravity separation is often the

preferred choice (Sherrell and Nevens, 2010). The flow sheets developed typically include crushing, grinding, and classification followed by three-stage spiraling.

In Brazil, the treatment of itabirites often requires gravity and magnetic separation as well as flotation to produce a salable product. In Australia, Arrium's Iron Duke Ore Beneficiation Plant, which processes ultrafine hematite, upgraded from single-stage to three-stage spiraling in 2012. At a feed grade of around 50.9% Fe, using HC33 triple-start spirals, a final concentrate of 60% Fe was produced at higher mass recovery than observed using single-stage spiraling (Selvapandian and Barr, 2013).

In India, large "lean" iron ore deposits that are composed of either low-grade *in situ* ores or iron ore slimes located in tailings storage facilities require more advanced processing routes. Sharma et al. (2010) commented that the process equipment used to process such ores were jigs, HLS (DMS), teeter bed separation, Knelson concentrators, wet tabling, magnetic separation, and froth flotation. ArcelorMittal's Mont-Wright project in Canada employs a three-stage spiral circuit with gravity distribution. The plant has a rougher spiral feed tonnage of around 10,000 tph of −1.4 mm material (written communication Craig Vadeikis-Mineral Technology, 2013).

In the Australian iron ore industry, several different physical separation processes are employed to beneficiate hematitic iron ores. At Fortescue's Chichester operations, the desand circuits (Clout, 2013) are used to beneficiate a lower-grade iron ore feed of around 54–57% Fe with significant reductions in Si and Al. The Cloudbreak and Christmas Creek flow sheets (Figure 10.20) use deslime cyclones, upflow classifiers, and rougher spirals (Figure 10.27). Desand circuit product contributes around 10% to final product, which also includes nonbeneficiated natural and crushed fines.

Figure 10.27 MG6.2 rougher spirals at Fortescue's Christmas Creek operation.

10.5.9 Recent advancements in spiral technology

There are several areas of spiral design that are being progressed including but not limited to the following:

- Improved spiral trough design
- Higher-capacity spirals
- Superior wash-water technology
- Alternate materials of constriction
- Superior manufacturing processes, for example, reverse lamination

10.5.10 Future direction

Ongoing research and development into spiral technology continues as new and improved designs are prototyped and tested. A recent development in the processing of iron ore fines has been the introduction of higher-capacity spirals. In some instances, rougher and scavenger spirals can be combined into the same unit, reducing the requirement for associated pumps and launders (Pena, 2010).

High-capacity spirals were originally developed to meet an industry need for a spiral capable of treating an increased proportion of high-density particles. The HC33 currently finds application in mineral sands, chromite, and iron ore (MT technical data sheet). Earlier spiral designs often incorporated wash-water systems. However, due to improvements in spiral separation efficiency, wash-water systems in some models are optional (Palmer and Vadeikis, 2010).

Advanced spiral designs for treating fine iron ores have progressed to a point where processing of ores down to 30 μm is possible. This type of spiral is often reserved for rougher recovery applications and is composed of a variable depth spiral trough, which ranges from just a few millimeters closest to the center column to 20 mm at the outer edge. Often, due to the low settling velocities of fine suspended solids, fine spiral separators are generally longer in length than traditional designs to allow adequate time for separation.

Attempts to understand the complex interactions occurring in spiral separators have come up against many difficulties in adequately explaining the mutual interaction between fluid flow and particles, interactions among particles themselves, and the constraints imposed by spiral geometry (Matthews, et al., 1997). Studies by Holland-Batt (1989) and Matthews et al. (1997) have commented that spiral separators possess a free surface, often consisting of shallow depths of less than 1 cm displaying regions of laminar as well as turbulent flow. The fluid phase is considered Newtonian, to possess constant physical properties, and is governed by the Reynolds-averaged turbulent Navier–Stokes equation (Matthews, et al., 1997). In Matthews et al. (1997) paper, the Lagrangian method was used to simulate particulate flow at dilute concentrations as performed on an LD9 spiral.

Computational fluid dynamic modeling consequently is an area of research that is finding increased application. Similarly to empirical modeling, CFD can be applied to predict the likely effects of changes in spiral efficiency under altered conditions. Empirical models have also been developed to fit test data (Holtham and Stitt, 1988).

Some of these models have actually been developed in-house by spiral manufacturers to predict the likely performance of their spirals under different operating conditions. The primary aim of fitting an empirical formula to original data is that computing power can be used to run multiple iterations that can correct for changing feed conditions (Fourie, 2007).

As separation efficiency will change with variations in heavy mineral loading, grade, and throughput, a model that can be used to predict performance in the event of actual changes can be a valuable tool. Models also have the optionality of accounting for the presence of recirculating loads, which are often present in spiral circuits. One method described by Fourie (2007) utilizes a modified Bézier–Spline curve to represent test data. In an attempt to account for different separation curvatures and to keep the mathematics simpler, the first and last sections of the curve are described by separate linear regressions. The center section is subsequently defined by the Bézier curve, which allows the model to be fitted to any separation curve.

References

Bosman, J., 2007. Jigging or dense medium separation—which is the best? In: Proceedings Iron Ore 2007. The Australasian Institute of Mining and Metallurgy, Melbourne, pp. 225–233.

Clout, J., 2013. Beneficiation of fine iron ores using the desand process. In: Proceedings Iron Ore 2013. The Australasian Institute of Mining and Metallurgy, Melbourne, pp. 337–347.

Falconer, A., 2003. Gravity separation: old technique/new methods. Phys. Sep. Sci. Eng. XII (1), 31–48.

Fourie, P., 2007. Modelling of separation circuits using numerical analysis. In: Proceedings of the 6th International Heavy Minerals Conference 'Back to Basics'. The Southern African Institute of Mining and Metallurgy, pp. 1–6.

Haldar, S., 2013. Mineral Exploration: Principles and Applications, first ed. Elsevier, Waltham.

Holland-Batt, A., 1989. Spiral separation: theory and simulation. Trans. Inst. Min. Metall., Sect. C 98, 46–60.

Holtham, P.N., Stitt, P.H., 1988. Developments in Australian spiral separator technology. In: Annual Conference, Sydney: Minerals and Exploration at the Crossroads: The International Outreach. The Australasian Institute of Mining and Metallurgy, Sydney, pp. 165–173.

Horn, A., Wellsted, M., 2011. Innovative beneficiation of iron ore fines with Allflux® two-stage fluidised bed classifiers and Gaustec® wet high intensity magnetic separators. In: Proceedings Iron Ore 2011. The Australasian Institute of Mining and Metallurgy, Melbourne, pp. 437–443.

Ito, M., et al., 2010. Advanced jig separation of shredded plastics. In: XXV International Mineral Processing Congress (IMPC) 2010 Proceedings. Australasian Institute of Mining and Metallurgy, Melbourne, pp. 843–850.

Matthews, B., Fletcher, C., Partridge, A., 1997. Computational simulation of fluid and dilute particulate flows on spiral concentrators. In: International Conference on CFD in Mineral & Metal Processing and Power Generation. CSIRO, Melbourne, pp. 101–108.

Miller, D., 2013. Iron ore beneficiation in Australia. In: Metallurgical Plant Design and Operating Strategies. The Australasian Institute of Mining and Metallurgy, Melbourne, p. 583.

Myburgh, H.A., 2006. The influence of the quality of ferrosilicon on the rheology of dense medium and the ability to reach higher densities. J. South Afr. Inst. Min. Metall. 106.

Napier-Munn, T.J., Gibson, G., Bessen, B., 2009. Advances in dense medium cyclone plant design. In: Tenth Mill Operators' Conference, Adelaide, SA, 12–14 October.

Nayak, N.P., Pal, B.K., 2013. Separation behaviour of iron ore fines in Kelsey centrifugal jig. J. Miner. Mater. Charact. Eng. I (3), 85–89.

O'Connor, M., Machunter, R., 2006. A review of current iron ore processing practices for −8 mm material. In: Workshop on Iron Ore Beneficiation. Indian Institute of Metals, Jamshedpur, pp. 1–5.

Palmer, M., Vadeikis, C., 2010. New developments in spirals and spiral plant operations. In: XXV International Mineral Processing Congress (IMPC) 2010 Proceedings. The Australasian Institute of Mining and Metallurgy, Melbourne, pp. 1099–1107.

Pena, C., 2010. Eco-efficient gravity separation solutions in India. In: XXV International Mineral Processing Congress (IMPC) 2010 Proceedings. Australasian Institute of Mining and Metallurgy, Melbourne, pp. 1123–1131.

Pretorius, J., Hoffmann, G., 2006. Utilisation of low grade iron ore resources to produce new products and the development of the Sishen Expansion Project ("SEP"), Sishen Iron Ore Mine, South Africa. In: DMS and Gravity Concentration Operations and Technology in South Africa. The South African Institute of Mining and Metallurgy, Johannesburg, pp. 109–132.

Richards, R., Jones, T., 2004. The Kelsey centrifugal jig—an update on technology and application. In: SME Annual Meeting. Society for Mining, Metallurgy and Exploration, Denver, pp. 4–21.

Rulkens, W., Bruning, H., 1995. Clean-up possibilities of contaminated soil by extraction and wet classification: effect of particle size, pollutant properties and physical state of the pollutants. In: van den Brink, W., Bosman, R., Arendt, F. (Eds.), Contaminated Soil '95. Kluwer Academic Publishers, Dordrecht, pp. 761–774.

Selvapandian, E., Barr, R., 2013. Managing challenges faced in the Brownfield commissioning of an ultra-fine hematite processing circuit at Arrium's iron duke ore beneficiation plant. In: Proceedings Iron Ore 2013. The Australasian Institute of Mining and Metallurgy, Melbourne, pp. 533–538.

Sharma, K., Das, T., Lahiri, K., Boral, R., 2010. Lean iron ore beneficiation in India. In: XXV International Mineral Processing Congress (IMPC) 2010 Proceedings. Australasian Institute of Mining and Metallurgy, Melbourne, pp. 3937–3946.

Sherrell, I., Nevens, M., 2010. Iron ore—mineral processing overview. In: XXV International Mineral Processing Congress (IMPC) 2010 Proceedings. Australasian Institute of Mining and Metallurgy, Melbourne, pp. 1227–1234.

Stanton, C., Bannear, M., 2013. Arrium's iron baron hematite beneficiation plant—a success from start to finish. In: Proceedings Iron Ore 2013. The Australasian Institute of Mining and Metallurgy, Melbourne, pp. 547–552.

Van Schoor, J., 2008. Settling velocities of particles in a hindered settling device. In: Proceedings MetPlant 2008. The Australasian Institute of Mining and Metallurgy, Melbourne, pp. 393–406.

Vermaak, M., Visser, H., Bosman, J., Krebs, G., 2008. A simple process control model for spiral concentrators. J. South. Afr. Inst. Min. Metall. 108 (3), 147–154.

Wills, B.A., 1985. Mineral Processing Technology, Robert Maxwell at Pergamon Press.

Wills, B.A., Napier-Munn, T., 2011. Mineral Processing Technology, seventh ed. Butterworth-Heinemann, Oxford, UK.

Developments in the physiochemical separation of iron ore

11

W.J. Bruckard, L.K. Smith, G.W. Heyes
CSIRO Mineral Resources Flagship, Clayton South, VIC, Australia

11.1 Introduction

In the beginning, there were direct shipping and smelting of iron ores. These ores were fully oxidized, consisting of high-grade hematite containing negligible sulfur and phosphorus and very low levels of other impurities. As these ores became depleted, the iron ore industry had to change to accommodate lower grades and less pure feedstock, in the form of both fully oxidized ores (hematite) and partially oxidized ores (magnetite). Now, as the quality of the available ores decreases further, the need for some sort of beneficiation is ever increasing. The ores of the future will be of even poorer quality still and the need for pretreatment will become mandatory.

Compared to base metal ores, iron ores are low-value products, and therefore, large tonnages have to be treated to make the upgrading process economically viable. This makes the flotation process, which is ideally suited for treating large tonnages of low-grade material, by far the best option for most of the ores currently being mined. However, as the characteristics of the ore bodies being mined deteriorate further and, depending on the nature of the impurities present, the best options for beneficiation may also change.

Flotation technology for the removal of impurities such as silica and aluminum oxides/silicates is well established. For sulfur, the prospects are mixed; if the sulfur is present in the form of a sulfide, then the prospects are good. As well, if the sulfur is present as a base metal sulfide, then these base metals will also be removed in parallel with the sulfur. However, if the sulfur is present as an oxide, for example, barite, then the prospects are not quite as good. For manganese, while the technology has not yet been developed, the end result may be the production of a low-manganese product and a high-manganese product. For phosphorous contamination, if the phosphorus is not present as a distinct phosphorus-containing mineral, such as apatite, a solution using flotation will not be possible. In the mean time, continuous improvement in flotation technology will contribute to it being the primary beneficiation technique for the foreseeable future.

Iron Ore. http://dx.doi.org/10.1016/B978-1-78242-156-6.00011-3
© 2015 Elsevier Ltd. All rights reserved.

11.2 Mineral properties

11.2.1 Mineralogy and occurrence

The majority of iron ores that are currently being mined are known variously as banded iron formation (BIF), taconite deposits, or itabirite deposits and were deposited about 2 billion years ago (Takenouchi, 1980). These ores constitute about 60% of the world's reserves. The BIF is a sedimentary rock with layers of iron oxides, either hematite or magnetite, banded alternately with quartz and silicates. The sediments were deposited in ancient marine environments and all were subjected to weathering and metamorphism to a greater or lesser extent.

Prior to enrichment, these sediments normally contained 20–30% Fe. Over time, the action of water leached the siliceous content and led to oxidation of the magnetite and enrichment of iron, forming hematite and goethite ore deposits. The grades of the ore and the impurity content varied with the extent of weathering and metamorphism. For example, in tropical and subtropical areas with high precipitation, high-grade deposits that require little or no beneficiation were formed. In temperate climates with less precipitation, the deposits remained as intermediate-grade deposits that require some form of beneficiation. Grade in all deposits tends to decrease with depth due to reduced enrichment by the action of water, and so upgrading is going to become increasingly important as (deeper) mining continues into the future.

The magnetic taconite deposits of the Mesabi Iron Range of Minnesota are typical BIF-type deposits. They contain quartz, silicates, magnetite, hematite, siderite, and other carbonates (Gruner, 1946). They assay about 30% Fe with about 75% of the iron in the form of magnetite and the remainder is largely iron carbonate and iron silicate minerals.

The principal separation in iron ore beneficiation, therefore, is between the iron minerals, hematite and/or magnetite, and silica, principally in the form of quartz. The use of flotation, either alone or in combination with magnetic separation, has been well established as an efficient method for rejecting silica from these iron ores. There are, however, other impurities in some deposits that also require rejection.

Aluminum-containing minerals in iron ore are detrimental to blast furnace and sinter plant operations. The two major aluminum-containing minerals in iron ore are kaolinite ($Al_2(Si_2O_5)(OH)_4$) and gibbsite ($Al(OH)_3$). Some progress has been made in using flotation to separate kaolinite from hematite.

High levels of phosphorus in iron ore attract a penalty because this makes steel brittle. In magnetite, phosphorus is often found in the form of discrete phosphate minerals, such as apatite, which can be removed by flotation. In hematite and goethite ores, however, the phosphorus tends to be incorporated into the lattice of the iron minerals, often goethite. In this case, separation by flotation is not an option. This type of phosphorus contamination needs to be rejected by chemical means.

Besides the BIF deposits, there are also smaller magmatic and contact metasomatic deposits distributed throughout the world that have been mined for magnetite. These deposits often carry impurities of magmatic origin such as sulfur, phosphorus, copper, titanium, and vanadium. While magnetic separation can reject most of these impurities, it cannot eliminate sulfur if it is present in the form of monoclinic pyrrhotite or an

oxide such as barite. Flotation may provide an option for reducing the sulfur content of magnetic concentrates when it is present in the form of metal sulfides. It is not an option for oxides such as barite.

11.2.2 Liberation

Comminution is needed for the liberation of low-grade ores so that the iron content can be upgraded by gangue removal. This necessitates grinding to such a size that the iron minerals and gangue are present as separate grains. But comminution is an expensive process and economics dictates that a compromise must be made between the cost of grinding and the ideal particle size.

Traditionally, grinding has been carried out using rod, ball, autogenous, or semiautogenous mills usually in closed circuit, that is, after grinding, the material is classified according to size with the undersized portion proceeding to the flotation circuit and the oversized portion being returned to the mill. The major benefit of fully autogenous grinding (AG) is the cost saving associated with the elimination of steel grinding media. In the last 20 years, more efficient grinding technologies, including high-pressure grinding rolls (HPGRs) for fine crushing and stirred milling for fine grinding, have provided opportunities to reduce operating costs associated with particle size reduction. A HPGR has been installed at the Empire Mine in the United States for processing crushed pebbles and its introduction has resulted in a 20% increase in primary AG mill throughput (Dowling et al., 2001). Northland Resources operates the Kaunisvaara plant in Sweden, treating magnetite ore with sulfur impurities in the form of sulfide minerals. The required P_{80} of the ore, in order to achieve adequate liberation, is 40 μm. This plant uses a vertical stirred mill after AG rather than a ball mill to achieve this fine grind size with an energy cost saving of 35% or better (Arvidson, 2013).

An important part of the comminution circuit is size classification. This can be accomplished with screens or cyclones or a combination of the two. Since cyclones classify on the basis of both particle size and specific gravity, cyclone classification in the grinding circuit directs coarse siliceous particles to the cyclone overflow. In a reverse flotation circuit, these coarser siliceous middlings can be recovered through increased collector addition but at the expense of increased losses of fine iron minerals carried over in the froth. However, if the required grind size is not so fine, then screening can be used instead of cycloning to remove the coarser particles for regrinding and, thus, produce a more closely sized flotation feed (Nummela and Iwasaki, 1986).

11.2.3 Surface and electrokinetic properties

Mineral surfaces, when brought into contact with a polar medium (such as water), acquire an electric charge as a consequence of ionization, ion adsorption, and ion dissociation. The surface charge on iron oxides and quartz is accounted for by the adsorption or dissociation of hydrogen and hydroxyl ions. Because these ions are potential determining ions for both iron oxides and quartz, control of pH is important in the flotation of these minerals since the extent of surface ionization is a function of the pH of the solution.

Table 11.1 Point of zero charge (pzc) of common iron oxide and silicate samples

Mineral	Mineral formula	pzc
Hematite	Fe_2O_3	pH 6.7
Magnetite	Fe_2O_4	pH 6.5
Cummingtonite	$(Fe,Mg)_7Si_8O_{22}(OH)_2$	pH 5.2
Quartz	SiO_2	pH 2.0–3.7
Synthetic hematite	Fe_2O_3	pH 8.1
Goethite	FeO(OH)	pH 6.7

Reproduced from Aplan and Fuerstenau (1962).

Table 11.1 shows the points of zero charge (pzc's) for some iron oxides and quartz (Aplan and Fuerstenau, 1962). This property is important when using flotation collectors that are physically adsorbed, for example, amines. The pzc's for the three iron oxides, hematite, magnetite, and goethite, are around neutral pH (~pH 7), whereas the pzc for quartz is in the acidic region (~pH 2). The pzc is the pH at which the charge on the mineral surface is zero and is usually determined by some form of acid–base titration. Surfaces of minerals can also be investigated using electrokinetic phenomena with results generally being expressed in terms of the zeta potential. The zeta potential is calculated from measured electrophoretic mobility of particles in an applied field of known strength, and the term isoelectric point (iep) refers to the pH at which the zeta potential is zero. Generally, the iep and pzc are the same if there is no adsorption of ions other than the potential determining ions H^+ and OH^-, but care should be taken with these measurements as evidenced by the variability in the literature regarding the pzc's and iep's of these minerals. For example, Kulkarni and Somasundaran (1976) determined the iep of a hematite sample to be 3.0, but the pzc of the same sample, measured using titration methods, was determined to be 7.1. These results were explained by the presence of fine silica in the hematite sample that influenced the surface properties measured by electrophoresis.

An understanding of the surface properties of minerals is utilized in the selective flotation and flocculation of minerals. For example, consider a mixture of hematite and quartz. The selectivity of the separation between hematite and quartz is related to differences in the surface charge of the two minerals. Below the iep, the mineral surfaces are positively charged and an anionic (negatively charged) collector can adsorb and render the mineral floatable; above the iep, the mineral surfaces are negatively charged and a cationic (positively charged) collector can adsorb and render the mineral floatable. From electrophoretic mobility measurements, the iep's for hematite and quartz are around pH 6.5 and 2, respectively. By choosing the correct collector type and pH, it is therefore possible to selectively float quartz from hematite with dodecylammonium chloride or float hematite from quartz with sodium dodecyl sulfate. This is illustrated in Figure 11.1 (after Iwasaki (1983)). This example is an idealized system, however, and in practice, the presence of slimes and various ions in solution will lead to variations to this model flotation behavior.

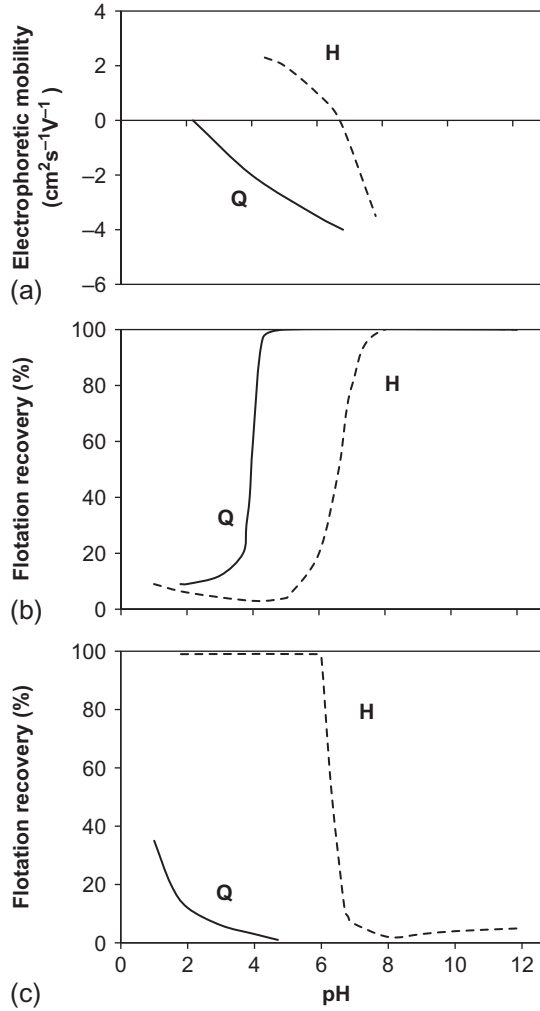

Figure 11.1 (a) Electrophoretic mobility of hematite (H) and quartz (Q) as a function of pH; (b) flotation of hematite and quartz with 10^{-4} M dodecylammonium chloride (DACl); (c) flotation of hematite and quartz with 10^{-4} M sodium dodecyl sulfate (NaDS) (Iwasaki, 1983).

11.3 Iron ore flotation

11.3.1 Separation of silica from iron ore by flotation

In the literature, there are several excellent reviews of iron ore flotation, with emphasis on the practice in North America, by Trahar (1963), Iwasaki (1983), Houot (1983), Nummela and Iwasaki (1986), Uwadiale (1992), Iwasaki (1999), Nummela (1978), and Araujo et al. (2005). Much of the early history of the iron range has been detailed by Davis (1964). A brief summary is given here; it was the impetus to develop this

resource that led to the first serious attempt to identify a flotation route for processing low-grade iron ores.

By the 1920s, the reserves of high-grade direct shipping iron ore in the United States were decreasing rapidly. At the same time, the resolve to utilize the known taconite deposits of the iron range, in the United States, was ever increasing. Some of these ores only contained magnetite as the valuable mineral and, therefore, could be (technically) treated by grinding and magnetic separation. However, other areas of the range contained ores with significant amounts of hematite, sometimes associated with magnetite and sometimes not. Generally, because of the high silica levels, the major cost in the treatment of these ores was that required for size reduction, and because of the intimate association between the silica and the iron minerals, fine grinding was needed to achieve a satisfactory level of liberation. Thus, treatment was always a compromise between tolerable grades and the cost of fine grinding. As the need to treat ores containing variable amounts of hematite increased, so too flotation became a necessary inclusion in the processing scheme.

The early beneficiation process, which relied on gravity and magnetic separation, sought to produce an iron concentrate containing a minimum of 64% iron, with about 9% silica. This was the minimum-grade product acceptable to the smelters at that time. Although much development work had been completed at the Bureau of Mines Experimental Station to show that this specification could be achieved, in practice, the prize eluded the processors. They were able to get up to about 62% iron but getting above this, on a consistent basis, proved to be impossible. After a few years, they had to give up and, reluctantly, close their processing plant down. The major impediment to their success was the intimate association between some of the magnetite and silica. For these "dusty" particles, the magnetite was contained in the silica as very fine grains that could not be liberated economically with the equipment available at that time. These particles often contained as much as 20–30% iron and therefore reported to the magnetic concentrate; but in so doing, they diluted the concentrate with their associated silica. If they could have been relegated to the tailing, the position was equally as bad because then the iron losses would have been significant. The other problem associated with magnetic separation was the tendency for much nonmagnetic material to be occluded in the magnetic concentrate, again degrading the quality of the final product. The problems seemed insurmountable at the time, and the chance of establishing a robust process seemed very slim.

However, technology is ever improving and new developments provided the answers to what had appeared as insurmountable problems. Two particular items that transformed iron ore processing were, firstly, the use of rod mills for fine grinding and, secondly, the application of the flotation process to separate values and nonvalues. Rod mills were being introduced into all phases of mineral processing and, for iron ore plants, yielded about a 6% increase in recovery, at grade, compared to size reduction equipment in prior use. And there was flotation that had many advantages over gravity and magnetic separation. The process was robust and able to treat much larger quantities. As well, it could handle a wider, and finer, range of particle sizes and provide more selective separations of various components.

From this point onward, the Bureau of Mines Experimental Station devoted a considerable amount of its effort to developing selective separation routes utilizing flotation technology.

Initial work at the Bureau of Mines Experimental Station examined separation using anionic collectors, principally fatty acids, which were cheap and readily available as a by-product from the timber industry. Anionic collectors could be used to separate iron oxides from quartz (normal flotation) or quartz from iron oxides (reverse flotation). However, because of the fine association of the valuable minerals and the gangue, it was found that, after grinding to provide adequate liberation, the presence of the very fine quartz caused a problem, whichever route was chosen.

There are several difficulties associated with the recovery of an iron oxide concentrate by normal flotation. To begin with, the presence of the slimes may lead to an excessive consumption of collector due to the high surface area of the minerals. Increasing the collector dose rate, apart from the increased cost, does not completely overcome this problem. As well, slime coatings on the valuable mineral may affect the efficiency of the separation. But the biggest problem relates to the significant dilution of the iron concentrate by silica because of the entrainment of the fine gangue (Iwasaki et al., 1962). Universally, the problem could be summarized as too much silica in the iron concentrate.

For the reverse situation, where the silica is floated from the iron oxides, there are similar problems. But, again, the biggest problem was the loss of fine iron oxides by entrainment in the froth product. Conventional desliming, as practiced in other parts of the mineral industry, also resulted in a significant loss of iron. A number of strategies to overcome this difficulty, without the need for desliming, were tested, including the use of starch to depress the fine iron oxides. During the conduct of this test work, it was noticed that the starch used actually flocculated the iron oxides but not the fine silica. This observation suggested a possible solution.

This selective flocculation allowed a means of selective separation of the fine silica from the fine iron oxides, while also providing an improved environment for the selective separation of the coarser sizes. After flocculation of the iron oxides, the silica that remained suspended could be removed by careful decantation (Frommer and Colombo, 1966; Frommer, 1968; Colombo, 1980). After the removal of the fine silica, the remaining pulp could be treated efficiently. This selective desliming allowed the development of the first robust flotation process for treating taconite ores.

After the desliming, this process route used reverse flotation to remove the silica from the finely ground ore in a froth product. In order to achieve this, using anionic collectors, the quartz had to be activated with Ca^{2+} ions at a pH of 11.5. The dispersion of the ore, which was necessary to realize efficient desliming, also required a pH of about 11 but lime could not be used. While Ca^{2+} was necessary for the activation of the quartz, this ion also functions to flocculate the pulp, whereas a dispersant was required. Thus, dispersion was achieved using sodium hydroxide and sodium silicate, followed by the addition of calcium chloride to activate the quartz before flotation with a fatty acid collector. The pH of dispersion and flotation was set at 11.5. To achieve this separation, reagent consumption was quite high: sodium hydroxide about

2 kg/t, sodium silicate about 500 g/t, starch about 1 kg/t, and fatty acid collector about 900 g/t (Frommer, 1964).

While interest in the separation of quartz from iron oxides using anionic flotation dates back to 1944 (Brown and Tartaron, 1944), the simple activation of quartz with Ca^{2+}, followed by flotation with fatty acids, had been known for many years before that (Glover, 1928). However, detailed analysis of the mechanism was elucidated by studies at the Bureau of Mines Experimental Station under the leadership of Professor S. R. B. Cooke. Using a variety of methods, including abstraction from solution, contact angle measurement, bubble pickup techniques, and batch flotation tests, he was able to identify the minimum quantity of Ca^{2+} necessary for the activation of the quartz, the optimum pH where this occurs, and the effect of added alkali metal cations such as sodium (Cooke and Digre, 1949; Cooke, 1949). This latter was important because the selective flocculation separation depended on achieving dispersion using sodium hydroxide and sodium silicate. Clearly, any interaction between sodium and calcium would affect the efficiency of the subsequent flotation separation.

There are two major issues with the process. A key to the process is proper dispersion of the ground pulp prior to the starch addition. Variations in the composition of the water used, in particular the presence of alkaline earth cations such as magnesium and calcium, affect the degree of dispersion (Heerema and Iwasaki, 1980), and therefore, the control of these ions in process waters is important. In addition, if there is a large amount of very fine (−2 μm) iron mineral in the feed, the selective flocculation step is incomplete resulting in high iron losses in the slime (Colombo, 1986).

This separation route for upgrading North American taconites was used for many years before it became uneconomic and was replaced by reverse cationic flotation. The principal reason for change was the "increasing cost of alkali to raise the pH to 11.5 and the environmental implication if any leakage occurred" (Iwasaki, pers. comm.).

The reverse cationic route is by far the most widely used iron ore flotation process. This process floats quartz with an ether amine collector at pH 10–10.5 using cornstarch to depress the iron oxides. In the early years, primary fatty amines, such as dodecylamine, were used, but these have now been replaced by the more soluble ether amines. Papini et al. (2001) compared the efficiency of several cationic collectors and found that ether amines were more efficient than primary amines and that ether monoamines were more efficient than ether diamines. Araujo et al. (2005) reported that some concentrators use a combination of ether monoamines and ether diamines. They also reported that amines are partially replaced by emulsified fuel oil in some concentrators due to the lower cost of fuel oil compared to amines. It is claimed that this reduction in amine consumption does not affect the metallurgical recovery.

Desliming is an essential step for a successful separation in the cationic flotation of iron ores for similar reasons as in the anionic flotation of iron ores (i.e., the presence of slimes leads to high reagent consumption due to their high surface area; slime coatings on the larger particles, governed by electrostatic interaction, interfere with bubble-mineral contact (Fuerstenau et al., 1958; Iwasaki et al., 1962); and misreporting of fine mineral through entrainment). The selective flocculation process developed for use with reverse anionic flotation was soon extended to incorporate reverse

cationic flotation (Colombo and Frommer, 1976; Dicks and Morrow, 1978; Colombo, 1978, 1980), and in 1975, the Tilden Mine in the United States opened using selective flocculation and reverse cationic flotation (Villar and Dawe, 1975).

Starch is used in both reverse anionic flotation and cationic flotation. Starch is not soluble in cold water and must be dissolved by a process known as gelatinization. Gelatinization may be accomplished by the use of either warm water or sodium hydroxide. Due to the hazards of using hot water in a concentrator and the associated energy costs in heating the water, most companies utilize the caustic soda route (Araujo et al., 2005). Starch can be extracted from several vegetable species such as corn, potato, wheat, and rice. In the iron ore industry, cornstarches are the most widely used. It should be pointed out that while cornstarch in the United States is actually extracted from corn, in other parts of the world, cornstarch is a generic term and can refer to starch extracted from a number of different grains.

11.3.2 Removal of impurities other than silica

In addition to silica, other impurities such as aluminum, phosphorus, and sulfur are also found in iron ores. In some cases, these impurities can be removed by flotation—strategies for the key impurities are discussed.

11.3.2.1 Aluminum removal

Since the beginning of iron ore flotation research in the 1930s, silica removal has been studied extensively while aluminum removal has received limited attention. The reverse cationic flotation route widely used in the iron ore industry is less selective for alumina–hematite separation than for quartz–hematite separation. Pradip et al. (1993) studied the flotation of an alumina-rich Indian iron ore and reported that only 60% of the iron could be recovered in reducing the aluminum content from 11.6% to 4.7%. Recently, systematic research on kaolinite, a major aluminum-containing mineral in some Australian iron ores, has been conducted at CSIRO with the aim of providing an in-depth understanding of the flotation mechanism of kaolinite in iron ore flotation and a basis for the removal of kaolinite (Ma et al., 2009; 2010; Ma and Bruckard, 2010; Ma, 2010; 2011a,b,c,d; 2012a).

Kaolinite removal in iron ore flotation is complex in that it involves three interactions, namely, interactions between kaolinite and the collector, the depressant, and the dispersant. It was found that collector interaction with kaolinite was opposite to that with silica. The pH dependence of kaolinite flotation with amine collectors is opposite to that of silica, that is, floatability decreases with increasing pH (Ma et al., 2009). It was also found that selective depression of hematite against kaolinite, with starch, largely depends on strict pH control and the level of ionic strength in the flotation pulp. In particular, the presence of calcium and magnesium ions is detrimental to kaolinite flotation (Ma, 2010). Sodium silicate, a common dispersant in iron ore flotation, was found to be inadequate to disperse kaolinite (Ma, 2011c), but a low-molecular-weight polyacrylic acid was found to fully disperse kaolinite in the presence of calcium and magnesium ions in alkaline pulps (Ma, 2011b).

In addition to kaolinite, gibbsite ($Al(OH)_3$) is also a common aluminum-containing mineral in iron ore. Separation of gibbsite from hematite and magnetite is known to be extremely difficult due to similarities in surface properties between the minerals. There are few studies on this topic and further research efforts are needed.

11.3.2.2 Phosphorus removal

In general, phosphorus is considered a penalty element in iron ore because it makes steel brittle. If the phosphorus is present in the iron ore as discrete phosphorus-containing minerals, then flotation presents a viable option for reducing the phosphorus content. For example, the LKAB concentrator in Kiruna, Sweden, treats by flotation a high phosphorus magnetite ore, which typically contains about 1% P. In this case, the phosphorus is present as apatite. The phosphorus is removed after magnetic separation by floating the apatite with a modified fatty acid collector and sodium silicate dispersant at pH 8.5–9.0 (Su et al., 1998). The main difficulty lies in optimizing the collector dosage so as to achieve acceptable P levels in the final concentrate without leaving a residual collector coating on the magnetite surfaces, which interferes with subsequent pellet production.

Some laboratory studies have been completed on the floatability of wavellite ($Al_3(PO_4)_2(OH)_3.5H_2O$), a secondary phosphate mineral present in some Brazilian ores, which have shown that cationic reverse flotation may provide a promising route for the reduction of phosphorus content in these ores (Nunes et al., 2011, 2012).

In other ores, for example, Western Australian iron ores, phosphorus exists within goethite in the form of solid solution (Graham, 1973). This form of phosphorus would be difficult to remove by physical means and necessitates the use of chemical separation.

11.3.2.3 Sulfur removal

Magnetite ores often contain sulfide minerals including pyrrhotite and pyrite. Most sulfide minerals are nonmagnetic and can be rejected by magnetic separation. Monoclinic pyrrhotite, however, in contrast to hexagonal pyrrhotite, is magnetic and is recovered in magnetic concentrates. Previous research (Cline and Rosas, 1975; Iwasaki, 1999) has shown that flotation can be used to remove pyrrhotite. The Marcona Mine in Peru uses a reverse flotation process to float pyrrhotite from the magnetite. It was found that the removal of pyrrhotite was difficult if the ore was ground in a carbon–steel mill but that its removal was readily achieved if the ore was ground in a stainless steel or porcelain mill (Cline and Rosas, 1975). These differences were attributed to electrochemical interactions between the minerals and the grinding media resulting in increased oxidation of the pyrrhotite. Marcona Mine was able to overcome these difficulties by minimizing the time between grinding and flotation and using a coarse grind, a strong collector, and an activator (Cline and Rosas, 1975).

11.3.3 Flotation equipment

Column cells have been developed over the past 30 years as an alternative to mechanically agitated flotation cells. The major operating difference between column and mechanical cells is the lack of agitation in column cells that reduces energy and

maintenance costs. Also, it has been reported that the cost of installing a column flotation circuit is approximately 25–40% less than an equivalent mechanical flotation circuit (Murdock et al., 1991). Improved metallurgical performance of column cells in iron ore flotation is reported and attributed to froth washing, which reduces the loss of fine iron minerals entrained into the froth phase (Dobby, 2002).

The Brazilian iron ore industry has embraced the use of column flotation cells for reducing the silica content of iron concentrates. Several companies, including Samarco Mineração S.A., Companhia Vale do Rio Doce (CRVD), Companhia Siderúrgica Nacional (CSN), and Minerações Brasileiras (MBR), are using column cells at present (Peres et al., 2007). Samarco Mineração, the first Brazilian producer to use column cells, installed column cells as part of a plant expansion program in the early 1990s (Viana et al., 1991). Pilot plant tests showed that utilization of a column recleaner circuit led to a 4% increase in iron recovery in the direct reduction concentrate and an increase in primary mill capacity when compared to a conventional mechanical circuit.

There are also some negative reports of the use of column cells in the literature. According to Dobby (2002), there were several failures in the application of column cells in the iron ore industry primarily due to issues related to scale-up. At CVRD's Samitri concentrator, after three column flotation stages, namely, rougher, cleaner, and recleaner, a secondary circuit of mechanical cells was still required to produce the final concentrate.

Imhof et al. (2005) detailed the use of pneumatic flotation cells to treat a magnetic separation stream of a magnetite ore by reverse flotation to reduce the silica content of the concentrate to below 1.5%. From laboratory testing, they claimed that the pneumatic cells performed better than either conventional mechanical cells or column cells. The pneumatic cells have successfully been implemented at the Compañia Minera Huasco's iron ore pellet plant.

11.3.4 Commercial flotation schemes

In Brazil, Vale process iron ore containing about 40% iron and 40% silica, using a reverse cationic flotation route. There is no desliming stage and the collector being used is from the new generation ether amines; the pH of flotation is about 10.5 and the depressant is (American) cornstarch (Ma et al., 2011). Ma et al. (2011) also suggested that for particles less than 10 µm, metal loss as a result of entrainment is over 92% in reverse cationic flotation, whereas for reverse anionic flotation, the loss is only about 40%. This result is not entirely consistent with the present understanding of the flotation mechanism and, any conclusions based on it, must be regarded as uncertain. Vieira and Peres (2007) suggested that, when using ether monoamine, the efficiency of flotation of quartz decreases rapidly for particles coarser than 150 µm. This is contrary to experience elsewhere where quartz particles as coarse as 1 mm are observed to float strongly in an oxide flotation system (Heyes and Senior, 1997).

In China, iron ore beneficiation started with the direct flotation of iron oxides using anionic collectors. However, the presence of cations, such as Ca^{2+}, in the process water reduced the selectivity of the separation and resulted in the presence of significant amounts of silica in the iron concentrate. This ultimately led to the adoption of a

reverse cationic flotation route. Currently, the trend is toward reverse anionic flotation in order to reduce the high reagent costs and the significant loss of iron in the desliming stage (Ma, 2012b).

It is interesting that the development of the Chinese processing route (and potentially the Brazilian) has gone in a different direction than that of the United States: the United States advanced from a reverse anionic route to a reverse cationic route, while the Chinese had shifted from a reverse cationic route to a reverse anionic route. While there are very little data available to provide an understanding of this dichotomy, it is possible that it is related to the mineralogy. For the US case, the ore is fine-grained and requires a very fine grind, substantially all minus 400 mesh, for liberation of the values from the nonvalues. If this is substantially finer than for other deposits, it means that the mechanism of entrainment might present a bigger problem in the United States than elsewhere. Such a problem is best dealt with by selective flocculation, and having included this stage in the process route, then the best flotation option is reverse cationic flotation.

The following commercial flotation schemes illustrate the selective flocculation and reverse cationic flotation route, the reverse anionic flotation route, and the direct anionic flotation of route.

11.3.4.1 Tilden Mine

Figure 11.2 shows the flow sheet of the Tilden concentrator in the United States that incorporates selective flocculation and reverse cationic flotation to treat a low-grade hematite ore. The ore is ground to approximately 85% passing 25 μm and dispersed using sodium silicate. Cornstarch flocculates the iron minerals, and about 15–30% of the feed weight is removed as slime while about 5% of the iron units are lost. The deslime thickener underflow, averaging 44% Fe in grade, is fed to the flotation circuit, which consists of a rougher and four scavengers. An unneutralized primary ether amine is used to float the coarser siliceous particles, with more cornstarch added as depressant for the iron minerals, to produce a final concentrate containing 64–67% Fe and less than 5% SiO_2 at a recovery of approximately 75% Fe (Colombo, 1986; Houot, 1983; Nummela and Iwasaki, 1986; Yang, 1988).

11.3.4.2 Donganshan

In recent years, reverse anionic flotation has been successfully applied in China's Anshan iron ore area. The Donganshan processing plant, one of the largest iron concentrate producers in China, uses reverse anionic flotation following gravity and magnetic separation to produce an iron concentrate with a grade of about 65% Fe at a recovery greater than 70% (Yin et al., 2010) from a feed assaying around 30% Fe. This configuration has the advantage of removing some of the slimes in the magnetic separation stage. The flotation stage uses starch as a depressant for the iron minerals; reagent RA715, an industrial sodium oleate, as collector; and calcium oxide as the activator for quartz.

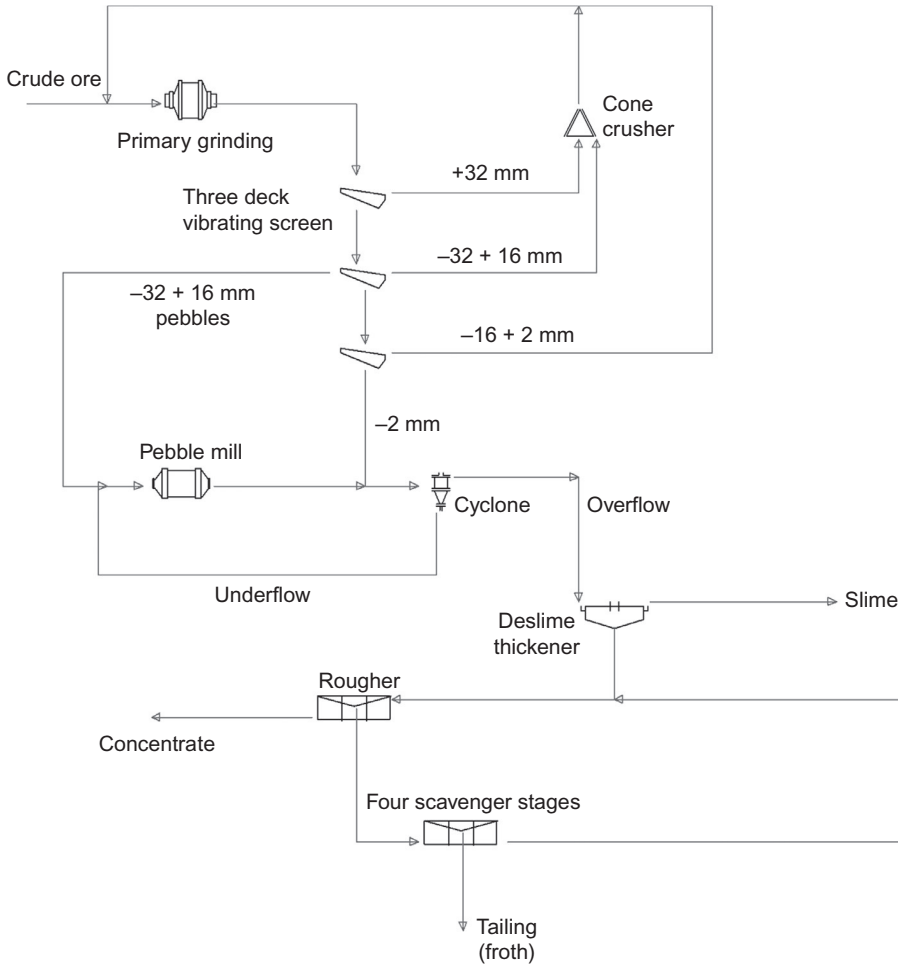

Figure 11.2 Tilden Mine (Michigan) flow sheet.

11.3.4.3 Republic

The Republic Mine in Michigan, though now closed, presents an example of the direct flotation of iron ore using anionic collectors. A schematic flow sheet is shown in Figure 11.3. The ore was ground in rod and ball mills to about −200 µm and deslimed with two stages of cycloning. A flotation stage, incorporating rougher flotation followed by two stages of cleaning, using a fatty acid reagent containing equal parts oleic and linoleic acids, produced a primary concentrate averaging 62% Fe. The primary concentrate was reground to 80% passing 44 µm and subjected to a hot flotation stage that produced a concentrate assaying 66% Fe and 4.7% SiO_2 (Nummela and Iwasaki, 1986; Houot, 1983; Yang, 1988).

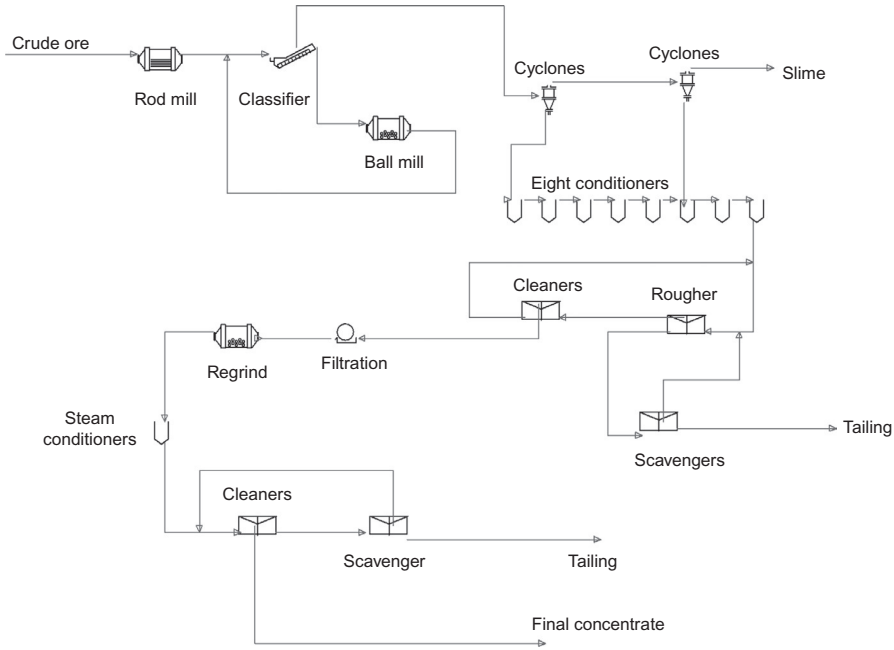

Figure 11.3 Republic Mine (Michigan) schematic flow sheet.

11.4 Key challenges and future directions

Froth flotation will remain a key unit process for the treatment of iron ores for the decades to come with the overarching challenge best described as being the need to modify and improve existing procedures and processing conditions so as to maintain an acceptable iron grade-recovery response in the face of ores and feedstock that will be finer, more complex, lower in grade, more goethitic in nature, and higher in deleterious impurities. The key impurity elements to deal with will remain silica, alumina, phosphorous, and sulfur, with kaolinite and gibbsite the most problematic gangue minerals. Improvements in flotation efficiencies alone will most likely not satisfy this challenge and improvements in the efficiency, both technical and in terms of energy savings of the unit processes that precede and follow flotation, such as crushing and grinding, magnetic separation, classification, gravity concentration, and selective flocculation, will also be needed. Moreover, novel but robust integrated flow-sheets that couple flotation with these processes will need to be developed and tested at laboratory and pilot scale.

More specifically, the focus for flotation research should be centered on four key areas, and in no particular order of priority, these should include water chemistry, reagent development, extension of the particle size range for iron ore flotation, and process control. Each of these is briefly touched on.

Water chemistry studies should include the consideration of the effects of the quality of recycled/reuse water on flotation efficiency. This water can often contain soluble salts, residual collector (e.g., amine), or depressant (e.g., starch) and can be variable

in terms of quality, pH, temperature, turbidity, ionic strength, and availability. Further, with the emerging scarcity of fresh or clean water around the globe, the need to float minerals in highly saline waters will grow and the effects of such a water regime will need to be more clearly understood for the iron ore flotation system, especially as they relate to reagent chemistry and interactions. Water chemistry issues and effects in iron ore flotation are not new but their importance and relevance will grow as the need to process in lower-quality waters increases.

In terms of reagent development, the challenge remains to develop and test new or modified reagents—not only collectors and modifiers but also dispersants and flocculants—that are more selective but still cost-competitive and environmentally friendly. For example, while cornstarch is the most widely used iron depressant in commercial iron ore flotation systems at present, a multitude of starches exist, all of which differ in terms of chain structure, type, degree of substitution, molecular size, and sensitivity to method of preparation. The degree to which these parameters effect or dictate flotation selectivity remains largely unclear. With increasing reagent costs, the need to recycle reagents should be considered and not just in relation to recycled or tailings return waters. Some recent work has been undertaken looking at bioflotation, specifically the use of bugs to produce collectors and flocculants that have a natural disposition/affinity toward a specific mineral, hence flagging the prospect of improved selectivity. While blue sky in nature for oxide flotation systems, these investigations should continue. Again, new and improved flotation reagents that herald greater selectivity are not a new topic but remain a critical area for iron ore flotation research.

Particle size effects, a key consideration in any flotation system, are more than ever especially relevant to iron ore flotation. At the fine end, in order to minimize iron unit loses to slime fractions, there will be a strong push to further reduce the lower size limit for efficient flotation. This will necessitate the need for new or modified reagent schemes and pulp chemistry regimes that can tolerate high slimes/fine levels. Along with this will be the thrust to retreat tailings and other fine or dirty iron oxide waste streams, some from different industries, to recover valuable iron units. Apart from their fine size, many of these potential feedstocks are physically and mineralogically challenging in nature, presenting another level of processing complexity. At the coarse end, improvements in the flotation of coarse silica are still needed. Amines have been shown to be effective collectors for coarse silica in some iron ore flotation systems but not in others, and in flotation systems outside of iron ore, silica/quartz has been shown to be readily floated at very coarse sizes. So, some understanding as to these inconsistencies would be beneficial.

Finally, with the explosion in the level of technical innovation in the field of sensors, data processing, and control systems, the move toward “intelligent processing” is now touching the mineral beneficiation space—flotation, including iron ore flotation, will not be exempt. There will be a need to develop slick online sensors to monitor parameters like elemental analysis, phase analysis, reagent levels, particle and bubble size, and flotation physical variables like air flow, froth depth, and turbulence, all pitched toward enabling better flotation control in terms of grade and recovery. Data from such probes, sensors, cameras, etc. will then need to be processed in real time in process control systems that still need to be affordable, robust, and as always operator friendly.

References

Aplan, F.F., Fuerstenau, D.W., 1962. Principles of non-metallic mineral flotation. In: Fuerstenau, D.W. (Ed.), Froth Flotation 50th Anniversary Volume. AIME, New York, pp. 170–214.

Araujo, A.C., Viana, P.R.M., Peres, A.E.C., 2005. Reagents in iron ores flotation. Miner. Eng. 18, 219–224. http://dx.doi.org/10.1016/j.mineng.2004.08.023.

Arvidson, Bo R., 2013. Processing high-grade concentrates from challenging low-grade iron ore deposits. Trans. Indian Inst. Met. 66 (5–6), 467–474. http://dx.doi.org/10.1007/s12666-013-0294-2.

Brown, E.H., Tartaron, F.X., 1944. Concentration of Oxidised Iron Ores. U.S. Patent 2,364,618, December 12.

Cline, W.A., Rosas, C., 1975. How Marcona floats iron sulphides from magnetite pellet feed concentrate. World Mining 28, 48–52.

Colombo, A.F., 1978. Beneficiation of fine-grained iron-bearing minerals. In: Somasundaran, P., Arbiter, N. (Eds.), Beneficiation of Mineral Fines—Problems and Research Needs. The American Institute of Mining, Metallurgical, and Petroleum Engineers, Inc., New York, pp. 237–252 (Chapter 18).

Colombo, A.F., 1980. Selective flocculation and flotation of iron bearing materials. In: Somasundaran, P. (Ed.), Fine Particles Processing, vol. 2. SME-AIME, New York, pp. 1034–1056 (Chapter 53).

Colombo, A.F., 1986. Concentration of iron oxides by selective flocculation-flotation. In: Somasundaran, P. (Ed.), Advances in Mineral Processing: A Half Century of Progress in Application of Theory to Practice. SME, Littleton, pp. 695–713.

Colombo, A.F., Frommer, D.W., 1976. Cationic flotation of Mesabi Range oxidized taconite. In: Flotation, A.M. (Ed.), Gaudin Memorial Volume, vol. 2. SME-AIME, New York, pp. 1285–1304.

Cooke, S.R.B., 1949. The flotation of quartz using calcium ion as activator. Trans. AIME 184, 306.

Cooke, S.R.B., Digre, M., 1949. Studies on the activation of quartz with calcium ion. Trans. AIME 184, 299.

Davis, E.W., 1964. Pioneering with Taconite. Minnesota Historical Society, St. Paul, 246 pp.

Dicks, M.L., Morrow, J.B., 1978. Application of the selective flocculation silica flotation process to the Mesabi Range ores. In: AIME Annual Meeting, Denver, 78 B-6, 14 pp.

Dobby, G., 2002. Column flotation. In: Mular, A.L., Halbe, D.N., Barratt, D.J. (Eds.), Mineral Processing Plant Design, Practice and Control. SME, Inc., Littleton.

Dowling, E.C., Corpi, P.A., McIvor, R.E., Rose, D.J., 2001. Application of high pressure grinding rolls in an autogenous—pebble milling circuit. In: Proceedings SAG 2001 Conference, Vancouver, vol. III, pp. 194–201.

Frommer, D.W., 1964. USBM tests on selective iron ore flotation point way to greater recoveries. Min. Eng. 16 (4), 67–71.

Frommer, D.W., 1968. Preparation of nonmagnetic taconites for flotation by selective flocculation. In: VIIIth International Mineral Processing Congress, Leningrad, D-9, pp. 464–472.

Frommer, D.W., Colombo, A.F., 1966. Process for Improved Flotation of Iron Ores by Selective Flocculation. US Patent 3,292,780, December 20.

Fuerstenau, D.W., Gaudin, A.M., Miaw, H.L., 1958. Iron oxide slime coatings in flotation. Min. Eng. 10, 792–795.

Glover, H., 1928. Flotation of some oxide and silicate minerals. Flotation Fundamentals, Part 1, Section E. Utah Eng. Exp. Sta. Tech. Paper 1, pp. 77–101.

Graham, J., 1973. Phosphorus in iron ore from the Hamersley iron formations. In: Proceedings of the Australasian Institute of Mining and Metallurgy, No. 246, pp. 41–42.

Gruner, J.W., 1946. Mineralogy and geology of the Mesabi Range. Iron Range Resources and Rehabilitation, St. Paul, Minnesota, p. 127.
Heerema, R.H., Iwasaki, I., 1980. Chemical precipitation of alkaline earth cations and its effect on flocculation and flotation of quartz. Min. Eng. 32 (10), 1510–1515.
Heyes, G.W., Senior, G.D., 1997. Alternative beneficiation of Shellsand: Pilot plant testing of a silica rejection process. Report No.: DMR-0729. CSIRO Division of Minerals, Australia.
Houot, R., 1983. Beneficiation of iron ore by flotation—a review of industrial and potential applications. Int. J. Miner. Process. 10, 183–204.
Imhof, R., Battersby, M., Parra, F., Sanchez-Pino, S., 2005. The successful application of pneumatic flotation technology for the removal of silica by reverse flotation at the iron ore pellet plant of Compania Minera Huasco, Chile. In: Centenary of Flotation Symposium, Brisbane, June, pp. 861–867.
Iwasaki, I., 1983. Iron ore flotation theory and practice. Min. Eng. 35, 622–632.
Iwasaki, I., 1999. Iron ore flotation—historical perspective and future prospect. In: Parekh, B.K., Miller, J.D. (Eds.), Advances in Flotation Technology. SME, Littleton, pp. 231–243.
Iwasaki, I., Cooke, S.R.B., Harraway, D.H., Choi, H.S., 1962. Iron wash ore slimes—some mineralogic and flotation characteristics. Trans. AIME 223, 97–108.
Kulkarni, R.D., Somasundaran, P., 1976. Mineralogical heterogeneity of ore particles and its effect on their interfacial properties. Powder Technol. 14 (2), 279–295.
Ma, M., 2010. Role of hydrolysable metal cations in starch–kaolinite interactions. Int. J. Miner. Process. 97, 100–103. http://dx.doi.org/10.1016/j.minpro.2010.09.003.
Ma, M., 2011a. Flotation mechanism of kaolinite under reverse cationic flotation conditions. In: Advances in Environmental Research, vol. 12. Nova Science, New York, pp. 197–206.
Ma, M., 2011b. Effect of a low-molecular weight polyacrylic acid on the coagulation of kaolinite particles. Int. J. Miner. Process. 99, 17–20. http://dx.doi.org/10.1016/j.minpro.2011.01.002.
Ma, M., 2011c. The dispersive effect of sodium silicate on kaolinite particles in process water: implications for iron ore processing. Clay Clay Miner. 59, 233–239. http://dx.doi.org/10.1346/CCMN.2011.0590302.
Ma, M., 2011d. Enhancement of hematite flocculation in the hematite-starch-(low-molecular-weight) polyacrylic acid system. Ind. Eng. Chem. Res. 50, 11950–11953.
Ma, M., 2012a. The significance of dosing sequence in the flocculation of hematite. Chem. Eng. Sci. 73, 51–54. http://dx.doi.org/10.1016/j.ces.2012.01.031.
Ma, X., 2012b. Froth flotation of iron ores. Int. J. Mining Eng. Min. Process. 1 (2), 56–61. http://dx.doi.org/10.5923/j.mining.20120102.06.
Ma, M., Bruckard, W.J., 2010. Effect of pH and ionic strength on starch–kaolinite interactions. Int. J. Miner. Process. 94, 111–114. http://dx.doi.org/10.1016/j.minpro.2010.01.004.
Ma, M., Bruckard, W.J., Holmes, R., 2009. Effect of collector, pH and ionic strength on the cationic flotation of kaolinite. Int. J. Miner. Process. 93, 54–58. http://dx.doi.org/10.1016/j.minpro.2009.05.007.
Ma, M., Bruckard, W.J., McCallum, D., Ma, M., Bruckard, W.J., McCallum, D., Ma, M., Bruckard, W.J., McCallum, D., 2010. Adsorption of starch on kaolinite surfaces. In: Proceedings XXV International Mineral Processing Congress, Brisbane, September.
Ma, X., Marques, M., Gontinjo, C., 2011. Comparative studies of reverse cationic/anionic flotation of Vale iron ore. Int. J. Miner. Process. 100, 179–183. http://dx.doi.org/10.1016/j.minpro.2011.07.001.
Murdock, D.J., Tucker, R.J., Jacobi, H.P., 1991. Column cells vs conventional flotation cells—a cost comparison. In: Column '91, International Conference on Column Flotation, Sudbury.
Nummela, W., 1978. Current problems in processing of fine iron ore. In: Somasundaran, P., Arbiter, N. (Eds.), Beneficiation of Mineral Fines—Problems and Research Needs. The

American Institute of Mining, Metallurgical, and Petroleum Engineers, Inc., New York, pp. 63–74 (Chapter 2).
Nummela, W., Iwasaki, I., 1986. Iron ore flotation. In: Somasundaran, P. (Ed.), Advances in Mineral Processing: A Half Century of Progress in Application of Theory to Practice. SME, Littleton, pp. 308–342.
Nunes, A.P.L., Peres, A.E.C., Araujo, A.C., Valadão, G.E.S., 2011. Electrokinetic properties of wavellite and its floatability with cationic and anionic collectors. J. Colloid Interface Sci. 361, 632–638. http://dx.doi.org/10.1016/j.jcis.2011.06.014.
Nunes, A.P.L., Pinto, C.L.L., Valadão, G.E.S., Viana, P.R.M., 2012. Floatability studies of wavellite and preliminary results on phosphorus removal from a Brazilian iron ore by froth flotation. Miner. Eng. 39, 206–212. http://dx.doi.org/10.1016/j.mineng.2012.06.004.
Papini, R.M., Brandão, P.R.G., Peres, A.E.C., 2001. Cationic flotation of iron ores: amine characterisation and performance. Miner. Metall. Process. 18 (1), 1–5.
Peres, A.E.C., Araujo, A.C., Shall, H., Zhang, P., Abdel-Khalek, N.A., 2007. Plant practice: nonsulfide minerals. In: Fuerstenau, M.C., Jameson, G., Yoon, R.-H. (Eds.), Froth Flotation—A Century of Innovation. SME, Littleton.
Pradip, Ravishankar, S.A., Sankar, T.A.P., Khosla, N.K., 1993. Beneficiation studies on alumina-rich Indian iron ore slimes using selective dispersants, flocculants and flotation collectors. In: Proceedings XVIII International Mineral Processing Congress. Australasian Institute of Mining and Metallurgy, Melbourne, pp. 1289–1294.
Su, F., Hanumantha Rao, K., Forssberg, K.S.E., Samskog, P.O., 1998. Dephosphorization of magnetite fines—part 2: influence of chemical variables on flotation kinetics. Trans. Inst. Min. Metall. C: Miner. Process. Extr. Metall. 107, C103–C110.
Takenouchi, S., 1980. Origin of iron ores. Tetsu-to-Hagane 66, 724–729.
Trahar, W.J., 1963. The flotation of iron ore. CSIRO Ore-Dressing Investigation Circular No. 7.
Uwadiale, G.G.O.O., 1992. Flotation of iron oxides and quartz—a review. Miner. Process. Extr. Metall. Rev.: Int. J. 11 (3), 129–161. http://dx.doi.org/10.1080/08827509208914209.
Viana, P.R.M., Rabelo, P.J.B., Coelho, A.G., Silva, J.P., Silva, V.C., Juliã, M.F., 1991. Column flotation for the expansion of the flotation circuit at Samarco Mineração, Brazil. In: Column '91, International Conference on Column Flotation, Sudbury.
Vieira, A.M., Peres, A.E.C., 2007. The effect of amine type, pH, and size range in the flotation of quartz. Miner. Eng. 20, 1008–1013.
Villar, J.W., Dawe, G.A., 1975. The Tilden Mine—a new processing technique for iron ore. Mining Congress J. 61 (10), 40–48.
Yang, D.C., 1988. Reagents in iron ore processing. In: Somasundaran, P., Moudgil, B.M. (Eds.), Reagents in Mineral Technology. Marcel Dekker, Inc., New York, Basel, pp. 579–644.
Yin, W.-z., Han, Y.-x., Xie, F., 2010. Two-step flotation recovery of iron concentrate from Donganshan carbonaceous iron ore. J. Cent. S. Univ. Technol. 17, 750–754. http://dx.doi.org/10.1007/s11771-010-0551-z.

Developments in chemical separation of iron ore

12

R.R. Lovel, G.J. Sparrow, M.J. Fisher-White
CSIRO Mineral Resources Flagship, Clayton South, VIC, Australia

12.1 Introduction

Major impurity elements in iron ore that can affect the quality of iron produced in a blast furnace and the efficiency of blast furnace ironmaking are silicon, aluminum, phosphorus, and sulfur. Silicon and aluminum often occur in iron ores as quartz, aluminum silicate (clay) minerals, or gibbsite. These minerals, and phosphorus when it is present as a phosphate mineral, can be removed from the iron ore by physical separation methods (Chapters 9 and 10) or flotation (Chapter 11). However, when the minerals are finely divided and difficult to liberate, chemical separation techniques may be the most suitable method for reducing impurities.

Chemical separation techniques for removing impurities from iron ores include caustic or acid leaching under a range of conditions. The leaching is usually preceded by a treatment to concentrate the impurity elements in the ore into a magnetic concentrate or to heat the ore to make the impurities more accessible to the leachant and so enhance their removal.

Phosphorus is present in iron ores as phosphorus-containing minerals (e.g., apatite) or dispersed in an iron oxide/hydroxide in the ore (e.g., in hematite in oolitic ironstone or in goethite in oolitic limonitic ores or in goethite in banded iron formations (BIFs)). Chemical separation is a prospective method for removing phosphorus from an iron ore, and this chapter focuses on the conditions and extent of phosphorus removal from the different iron ore types by chemical separation.

Caustic and acid leaching conditions for the removal of phosphate minerals from magnetite ores are discussed first, followed by leaching conditions for removal of phosphorus dispersed in oolitic ironstones. When phosphorus is dispersed in goethite in oolitic limonitic ores or in goethite within BIF, a heating treatment before a caustic or acid leach makes the phosphorus amenable to chemical separation. Most of the discussion in this chapter is concerned with the chemical separation conditions applied to lowering phosphorus levels in oolitic and BIF ores because there are massive deposits of these high-phosphorus ores that are currently underdeveloped.

Silicon, aluminum, and sulfur levels are lowered under the conditions that successfully reduce phosphorus levels. Specific results for the removal of these elements are also presented.

Iron Ore. http://dx.doi.org/10.1016/B978-1-78242-156-6.00012-5
© 2015 Elsevier Ltd. All rights reserved.

12.2 Phosphorus removal

While phosphate minerals frequently are insoluble, phosphate compounds formed with group 1 elements (e.g., H^+, Na^+, and K^+) and NH_4^+ are soluble. In iron ores, phosphorus may be present as discrete minerals or associated with an iron oxide/hydroxide mineral in the ore. Often, phosphorus occurs in several forms in the ore and the phosphorus mineralogy influences the conditions that can be used to remove it. Chemical separation methods used to produce soluble phosphorus compounds from phosphorus present as discrete minerals, and dispersed in hematite and goethite in the ores, are discussed in this section with specific examples from the literature presented. It is anticipated that the results will be indicative of outcomes for treatment of other ores with similar mineralogy.

12.2.1 Removal of phosphorus minerals from magnetite ores

The common phosphorus minerals identified in iron ores are the apatite minerals, apatite and fluorapatite ($Ca_5(PO_4)_3(OH,F,Cl)$), and the cryptocrystalline variety collophanite. Secondary phosphate minerals include wavellite ($Al_3(PO_4)_2(OH)_3.5H_2O$), vivianite ($Fe_3(PO_4)_2.8H_2O$), and minerals of the crandallite ($CaAl_3(PO_4)_2(OH)_5.H_2O$)-goyazite ($SrAl_3(PO_4)_2(OH)_5.H_2O$) series. Rare-earth phosphate minerals, xenotime (YPO_4) and monazite ($(Ce,La,Y,Th)PO_4$), have also been identified (Wells and Ramanaidou, 2011).

Hertzog (1935) investigated the solubility of natural phosphate minerals in acids and alkalis, in particular apatite and fluorapatite, dufrenite ($Fe_2(PO_4)(OH)_3$), triplite ($Fe_3Mn_3(PO_4)_2$), wavellite, and vivianite. He found that the calcium, manganese, and ferrous phosphates were soluble in inorganic acids (hydrochloric, sulfuric, and nitric acids) and organic acids (oxalic, citric, tartaric, and acetic acids), but aluminum or ferric phosphates were not. Heating the minerals at 650 °C for 15 min converted ferrous iron to the ferric state and the resultant minerals were no longer soluble in nitric acid, nor were the manganese phosphates after heating. By contrast, heating did not affect the solubility of calcium phosphate minerals in acids. Aluminum (and ferrous) phosphates had a high solubility in sodium hydroxide and potassium hydroxide.

Acids, including nitric, hydrochloric, sulfuric, and oxalic acids, have been shown to chemically separate apatite from iron ores to lower the phosphorus levels to acceptable levels. The leaching conditions depend on the acid used and the properties of the ore. Edwards et al. (2011) did report that sodium hydroxide was less effective than sulfuric acid in dissolving apatite from a magnetite ore, although no data were presented, while Engel and Heinen (1959) reported that no phosphorus was extracted from a hematite ore with 10% solutions of sodium hydroxide, sodium carbonate, sodium bicarbonate, and ammonium hydroxide.

During the period from 1964 to 1973, a plant in Sweden leached iron ore fines with nitric acid to lower phosphorus levels from 0.2% P to less than 0.05% P. However, as no recovery or recycling of the acid was used, operating costs were high and leaching was replaced by flotation to remove the apatite (Zhang and Muhammed, 1989). Forssberg and Adolfsson (1981) used hydrochloric and nitric acids, while Zhang and

Muhammed (1989) used nitric acid to remove phosphorus, in the form of fluorapatite, from Swedish magnetite ores.

Zhang and Muhammed (1989) selected nitric acid because of its low reactivity with magnetite, the main iron mineral in the ore. They considered that while hydrochloric acid formed soluble chlorocomplexes with the ferric iron, limiting the formation of insoluble ferric phosphate complexes, it had a high reactivity with magnetite, resulting in higher dissolution of iron and neutralization of acid. The use of sulfuric acid, expected to be the most economic acid, can result in the precipitation of gypsum ($CaSO_4 \cdot 2H_2O$) by reaction of the sulfate ions with the dissolved calcium ions during leaching, increasing the residual sulfur levels in the leached ore.

Zhang and Muhammed (1989) used percolation leaching with an upflow of 35% HNO_3 at ambient temperatures through a fixed bed of iron ore fines containing 64.0% Fe, followed by washing with water to remove the residual acid. A total time of 24 h was used for a percolation operation. The phosphorus level was lowered from 0.79% P to 0.04% P with a final iron content of 67.0% Fe and an associated iron loss of less than 0.5 wt% (Muhammed and Zhang, 1989). Recovery of the dissolved phosphorus as a by-product (phosphoric acid of high purity) was considered to be necessary for a cost-efficient process. Details of an integrated process to remove phosphorus from the magnetite ore by leaching with nitric acid, followed by recovery of phosphorus as phosphoric acid and regeneration of the nitric acid, were given by Muhammed and Zhang (1989) and Zhang and Muhammed (1990).

Edwards et al. (2011) removed apatite from an Australian magnetite ore with a sulfuric acid leach at pH 1 and 25 wt% solids, carried out at room temperature for 1 h. The phosphorus level was lowered from 0.536% to 0.184% P, and the iron level was increased from 59.4% to 61.8% Fe. The solution assay of the leach liquors indicated that precipitation of gypsum occurred during the leach. For the particular ore, the presence of 15% siderite ($FeCO_3$) contributed to an acid consumption of 23.7 kg H_2SO_4/t ore.

While minor amounts of collophanite were identified in a calcareous hematite ore containing 0.30–0.36% P, 36% Fe, and 12–16% CaO from Birmingham, Alabama, the form of most of the phosphorus could not be identified (Lamont et al., 1973). Flotation and reduction roasting at 700 °C followed by a magnetic separation were not effective in lowering the phosphorus content of this ore. However, an acid leach of the magnetic concentrate with hydrochloric, sulfuric, and nitric acids at 33 wt% solids for 3 min at ambient temperature did reduce phosphorus to a level of 0.06% P. It was observed that essentially, all the calcium minerals were dissolved before the acids reacted with phosphorus-containing minerals. Reoxidation of the magnetic concentrate by heating at 700–1000 °C in air for 15 min followed by leaching with hydrochloric acid resulted in increased phosphorus removal with temperature and a lower acid consumption considered by Lamont et al. (1973) to be due to the formation of acid-insoluble calcium compounds during the heating. Leach residues containing 0.03% P were obtained on heating at 900 and 1000 °C with an acid consumption of 50 kg/t concentrate. Loss of less than 0.7 wt% iron occurred in the leaching. The addition of 10% calcium chloride to the magnetic concentrate, reoxidation at 1000 °C, and leaching with hydrochloric acid resulted in leach residues with 0.05% P for an acid consumption of 25 kg/t concentrate (Lamont et al., 1973).

12.2.2 Phosphorus removal from oolitic hematite ores

Oolitic ironstones are composed of spherical or oval concentric layers of iron oxide, silica, and other minerals. The Ningxiang ore from the Hunan and Hubei provinces in China is used as the example of oolitic ironstone in which the phosphorus is associated with hematite. The removal of phosphorus from goethite in the Lisakovsky oolitic limonite ore in Kazakhstan is discussed in Section 12.2.3.

The Ningxiang ore contains 0.4–1.1% P in the form of finely dispersed collophanite in oolites and as fine apatite minerals disseminated on the edges of iron minerals and embedded in quartz and carbonate minerals. Other gangue minerals present are kaolinite, illite, and gypsum (Jiang et al., 2008; Zhu et al., 2010). Physical beneficiation including milling and screening, flotation, and magnetic separation did not lower phosphorus to acceptable levels (Zhu et al., 2010), nor did a prereduction step lead to acceptable phosphorus removal (Yin et al., 2012). However, a sulfuric acid leach after reduction and a magnetic separation did give higher phosphorus removal (Zhu et al., 2010).

Reduction of an ore sample containing 47.3% Fe and 1.59% P with coal at 800 °C for 25 min and a magnetic separation produced a concentrate with 0.81% P. Leaching the concentrate at 30 wt% solids for 2 h with sulfuric acid lowered the phosphorus content to 0.20% P for an acid consumption of 50 kg/t ore. Iron losses in the leaching were less than 1 wt% and the leach product contained 62.35% Fe. A longer leaching time was reported to result in lower phosphorus removal due to adsorption of phosphate ions onto the surfaces of the ore (Zhu et al., 2010).

From another ore sample containing 37.5% Fe and 0.88% P, Jiang et al. (2008) obtained a gravity concentrate using spirals and a shaking table containing 58.7% Fe and 0.52% P, with an iron recovery of 51.9 wt%. When the gravity concentrate was leached with 10% NaOH, 38.1 wt% of the phosphorus was removed. In contrast, 93.8 wt% of the phosphorus was removed when 2% H_2SO_4 was used. Leaching with 1% H_2SO_4 for 10 min at 10 wt% solids gave a product with 59.3% Fe and 0.066% P with an iron loss during leaching of 0.19 wt%.

Caustic and acid leaching were used by Jin et al. (2006) to remove phosphorus from a Changde iron ore sample containing 1.12% P. The phosphorus was present as apatite (22.3%), in silicate phases (9.8%), and in hematite (67.9%). Leaching 10 wt% solids with 4% NaOH at ambient temperatures for 2 h removed 28.0 wt% of the phosphorus. This was interpreted as showing that sodium hydroxide only removed phosphorus present as apatite but not phosphorus in hematite. Consequently, caustic leaching was considered to be ineffective for extraction of phosphorus from the ore. Leaching with sulfuric, hydrochloric, and nitric acids removed phosphorus present both as apatite and in the iron oxide. Acid leaching at 10 wt% solids with 1% sulfuric, hydrochloric, and nitric acids for 20 or 60 min at room temperature resulted in the removal of 91.6%, 85.0%, and 89.4% of the phosphorus, respectively. Iron losses during the acid leaching were less than 0.25 wt%.

12.2.3 Removal of phosphorus from oolitic limonite ores

The Lisakovsky iron ore deposit in Kazakhstan is a high-phosphorus oolitic limonitic ore containing about 38% Fe, in which the main iron-bearing minerals are goethite

(FeO(OH)) and other iron oxyhydroxides ("hydrogoethite"). No distinct phosphorus minerals have been identified in the ore, but Levintov et al. (2007) proposed that the phosphorus was present in hydrogoethite in the oolites. Other impurities are coarse silica embedded within the oolites and fine silica and alumina dispersed within the oolites. As the phosphorus and other impurities were finely dispersed within the oolites, little opportunity existed for the application of low-cost physical beneficiation methods to remove these impurities (Kokal et al., 2003).

To remove phosphorus, the ore was first upgraded by wet gravity and magnetic separations to produce a gravity-magnetic concentrate that was roasted to dehydrate the goethite to hematite and "open" the ore for leaching. Sulfuric acid was found to be far superior to hydrochloric acid or nitric acid in solubilizing the phosphorus (Kokal et al., 2003). Leaching a flotation concentrate containing 56.1% Fe and 0.648% P at ambient temperature for 6 h with 5% H_2SO_4 removed 40 wt% of the phosphorus along with 17 wt% of the iron. After heating the concentrate at 600 °C for 30 min, 70 wt% of the phosphorus and 30 wt% of the iron were dissolved during leaching. These high iron losses were considered to be unsatisfactory. However, after heating a gravity-magnetic concentrate at 900 °C, leaching for 18 h resulted in the removal of over 85 wt% of the phosphorus, giving a product with 0.109% P. Iron dissolution was less than 2 wt%. Increasing the acid concentration to 10% H_2SO_4 reduced phosphorus levels in the product to 0.094% P. Leaching the gravity-magnetic concentrate with 10% NaOH at 55 °C gave similar phosphorus removal with no iron dissolution (Kokal et al., 2003).

Levintov et al. (2007) reported that after roasting Lisakovsky concentrates containing 48–49% Fe and 0.6–0.8% P at 900 °C, leaching with sulfuric acid gave products with 57–58% Fe and 0.12–0.25% P. With repeated heating and leaching cycles on a concentrate, phosphorus removal increased initially but then ceased. On roasting the oolites, Levintov et al. (2007) proposed that the hydrogoethite containing the phosphorus was converted to amorphous hematite in the range of 400–700 °C. Increasing the roasting temperature to 900 °C was accompanied by significant structural and physiochemical changes with the formation of two hematite phases: one corresponding to the stoichiometric composition and the other to a solid solution of impurity components in the hematite. In the temperature range of 700–900 °C, with recrystallization of the hematite, phosphorus was segregated at the grain boundaries.

Leaching of the Lisakovsky ore at the pilot plant scale was described by Kokal et al. (2008). A gravity-magnetic concentrate containing 49.5% Fe and 0.75% P was roasted at 920 °C for 20–30 min in a rotary kiln. A magnetic separation step utilizing rare-earth magnetic separators was used to remove silica liberated during roasting. Iron recovery was 98.7 wt%. The roasted product was leached with 5% H_2SO_4 in four leach tanks, in series, using 50 wt% solids at ambient temperature. On average, a leach product containing 58.6% Fe and 0.36% P was produced from the leaching circuit operating at 26 t/h with a leaching time of 62.5 min. The best product produced contained 60.0% Fe and 0.20–0.23% P. It was considered that the residence time in the kiln at 920 °C was not sufficient to match the results achieved in the laboratory-scale testing. The leach product was used in a sinter plant.

Feld et al. (1968) patented a process for phosphorus-containing limonitic iron ores and concentrates that involved heating them with additives at 500–1200 °C for 30 min

and then leaching with 3.9–5.2% H_2SO_4, HCl, or HNO_3 at 30 °C for 5–30 min. Additives employed in an amount ranging from 5 to15 wt% were bromides, fluorides, and chlorides of alkaline earth metals, ammonia, manganese, zirconium, copper, and lithium. With chloride salts as additives, phosphorus levels were lowered in an ore sample from 0.42% P to 0.02–0.08% P, depending on the additive. Iron losses in the leach were low with recovery of over 98 wt% of the iron in the leach residue. The best additives were claimed to be calcium chloride, manganese chloride, magnesium chloride, strontium chloride, and barium chloride, with 900 °C the best heating temperature.

Ionkov et al. (2011, 2012) added alkali and alkaline earth hydroxides and oxides (NaOH, $Ca(OH)_2$, and CaO) to a Lisakovsky gravity-magnetic concentrate before heating to around 900 °C and leaching with sulfuric, hydrochloric, and nitric acids. For example, to a magnetic concentrate containing 46.4% Fe and 0.68% P, 5 wt% NaOH was added and the sample was reduced with coal at 865 °C for 1 h. The reducing roast was considered to have transformed the goethite into hematite or magnetite and promoted reaction between the phosphate anion and the alkali cations. A magnetic separation of the roasted sample removed a substantial amount of the gangue minerals and excess additives. About 50 wt% of the phosphorus was rejected during the roasting-magnetic separation step. Leaching of the roasted magnetic concentrate at ambient temperature with 10% H_2SO_4 or HCl at a pulp density of 40 wt% solids for 2 h gave leach products with 0.05% and 0.09% P, respectively. There was an iron loss of 10–15 wt% in the acid leaches and the product from the sulfuric acid leach contained 61.6% Fe. Without the addition of sodium hydroxide to the ore prior to roasting, the leach product contained 0.19% P.

12.2.4 Phosphorus removal from goethite–hematite ores

In high-phosphorus Australian goethite–hematite ores, the majority of the phosphorus is considered to be associated with the goethite fraction of the ore (Barbour, 1973; Dukino et al., 2000). Some apatite has also been identified in Western Australian ores (Graham, 1973). Apatite, wavellite, and senegalite ($Al_2(PO_4)(OH)_3{\cdot}H_2O$) have been reported to occur in Brazilian ores from the state of Minas Gerais (Araujo et al., 2003).

Texturally distinct goethite phases containing phosphorus and impurity elements, such as silicon and aluminum, have been identified in Australian iron ores. During supergene weathering, especially under acidic conditions, the original apatite is considered to have dissolved releasing phosphate ions into the groundwater. While some of this phosphorus may have reprecipitated as secondary apatite or other secondary phosphate minerals, much of the phosphorus occurring in the groundwater is considered to have been adsorbed onto the growing surfaces of gel-like precursors that crystallized as goethite during the enrichment of the ore (Dukino and England, 1997; Dukino et al., 2000). Barbour (1973) suggested a simple exchange of phosphate and hydroxyl ions on hydrated iron and aluminum oxides in Brazilian ores.

MacRae et al. (2011) had proposed that phosphorus may also be incorporated into the goethite structure by a coupled substitution mechanism between phosphorus and aluminum at the sites typically occupied by two silicon atoms, in the ochreous goethite structure. Quantum mechanical modeling (Wilson, 2013), using the B3LYP

hybrid functional, examined potential sites for the incorporation of phosphorus into the goethite structure. The calculations took into account the magnetic structure of goethite, with the antiferromagnetic ordering of the iron atoms modeled. A single phosphorus atom was placed at different sites within a $2\times1\times3$ goethite supercell (which equates to 1.5 wt% phosphorus), the atom positions and unit cell parameters were relaxed, and the energetic stability of phosphorus in different sites was calculated. The effect of an iron vacancy on the phosphorus incorporation was evaluated and the most stable configuration was found when phosphorus was coupled with an iron vacancy, with the phosphorus sitting in the goethite channel, adjacent to the vacancy in the (100) plane. In this position, there was a slight contraction of the goethite structure around the phosphorus atom, with phosphorus-oxygen bond distances calculated to be in the range of 1.54–1.58 Å, similar to the phosphorus-oxygen bond distance found in vivianite. Coupled aluminum and phosphorus incorporation was also investigated with the most stable configuration found when aluminum substituted for iron next to the phosphorus-vacancy defect.

Gooden et al. (1974) reported phosphorus was not removed from an Australian ore from the Pilbara in a caustic or acid leach. However, Fisher-White et al. (2013) were able to remove some phosphorus from an Australian Brockman Iron Formation ore sample by leaching with sodium hydroxide or sulfuric acid as shown in Table 12.1. Leaching Brockman ores containing 0.146% and 0.136% P with 20% NaOH gave leach products with 0.112% and 0.124% P, respectively. Phosphorus removal from another Brockman Iron Formation ore sample containing 0.123% P was more effective and a product with 0.08% P was obtained under the same leaching conditions. A leach of the three ores with 10% H_2SO_4 was less effective and gave products with 0.136%, 0.132%, and 0.112% P, respectively. The weight loss in the leaches was less than 4 wt%.

Mueller and Segura (1975) reported that leaching a Brazilian "earthy hematite" ore sample containing 0.16% P with 10% sodium carbonate solution at 70 or 95 °C lowered the phosphorus levels to 0.05% and 0.04% P, respectively. The addition of an equal amount of sodium carbonate prior to heating at 300 °C for 1 h was also reported by Mueller and Segura (1975) to result in the lowering of phosphorus levels from 0.16% to 0.07% P in a subsequent water leach. However, when Fonseca et al. (1994) heated a Brazilian ore sample containing 0.055% P at 100 °C for 1 h and leached in tanks without agitation for up to 1 h with 10% HCl, only 5 wt% of the phosphorus was removed, while a leach with 5% HF removed 38 wt% of the phosphorus.

Significantly better phosphorus removal was achieved from Brockman Iron Formation ore samples by leaching after a heating treatment. Fisher-White et al. (2012a,b, 2013) showed that, with increasing heating temperatures up to 1300 °C, increasing amounts of phosphorus were removed from the ores in both a caustic and an acid leach. The results in Table 12.1 show that for an ore sample containing 0.146% P heated at 300 °C and leached with 20% NaOH at the boiling point for 3 h at 25 wt% solids, a leach product with 0.079% P was obtained, while leaches with 4% NaOH gave products with 0.093% and 0.035% P after heating at 900 and 1300 °C, respectively.

Acid leaches of the Brockman Iron Formation ore sample containing 0.146% P with 10% H_2SO_4 at 60 °C and 25 wt% solids gave products with 0.107% and 0.075% P

Table 12.1 Effects of heating temperature and leaching conditions on impurity removal from Australian goethite–hematite ores

Sample	Heating temperature (°C)[a]	Leaching conditions					Leach product XRF assay data (wt%)				
		Leachant	Temp (°C)	Time (h)	Pulp density (wt%)	Weight loss (wt%)[b]	Fe	P	SiO_2	Al_2O_3	% P removed[c]
Brockman ore 1							62.0	0.146	3.07	2.27	
	–	20% NaOH	BPT	3	0.5	n.d.	65.3	0.112	1.03	0.89	27.1
	300	20% NaOH	BPT	3	25	n.d.	62.6	0.079	3.24	2.18	46.9
	900	4% NaOH	BPT	3	25	n.d.	62.4	0.093	3.21	2.11	36.7
	1300	4% NaOH	BPT	3	25	3.3	66.5	0.035	1.41	2.20	78.0
	–	10% H_2SO_4	60	3	25	1.4	63.1	0.136	3.24	2.29	8.2
	300	10% H_2SO_4	60	3	25	7.6	63.1	0.107	3.42	2.00	34.9
	900	10% H_2SO_4	60	3	25	1.7	65.8	0.075	3.21	1.45	52.0
	1300	1% H_2SO_4	60	3	25	1.0	65.4	0.037	3.26	2.23	76.2
Brockman ore 2							62.1	0.123	3.22	2.18	
	–	20% NaOH	BPT	3	0.5	n.d.	64.7	0.080	1.49	0.62	37.6
	300	4% NaOH	BPT	3	25	n.d.	63.1	0.072	3.47	1.91	42.4
	900	4% NaOH	BPT	3	25	n.d.	64.4	0.055	2.82	1.97	56.9
	1300	4% NaOH	BPT	3	0.5	4.4	66.4	0.022	1.39	2.08	83.8
	–	10% H_2SO_4	60	3	25	1.2	62.0	0.112	3.21	2.19	10.2
	300	10% H_2SO_4	60	3	25	9.6	63.3	0.078	3.26	1.92	44.8
	900	10% H_2SO_4	60	3	25	2.2	65.9	0.067	3.36	1.08	49.4
	1300	1% H_2SO_4	60	3	0.5	2.6	65.2	0.019	3.21	2.10	85.7

Brockman ore 3							56.8	0.136	6.25	3.07	
	–	20% NaOH	80	1	1.0	n.d.	61.0	0.124	2.12	1.63	15.1
	300	20% NaOH	80	1	25	3.2	61.2	0.095	3.60	2.46	35.2
	900	20% NaOH	80	1	25	4.4	63.0	0.063	2.30	2.60	59.8
	1300	4% NaOH	BPT	3	1.0	7.4	64.5	0.030	2.80	3.22	84.3
	–	10% H_2SO_4	60	1	1.0	3.9	57.4	0.132	6.17	3.13	15.4
	300	10% H_2SO_4	60	1	25	6.2	58.9	0.117	6.20	2.70	25.6
	900	10% H_2SO_4	60	1	25	1.0	62.2	0.087	6.69	2.84	42.6
	1300	1% H_2SO_4	60	3	1.0	2.0	61.3	0.059	6.85	3.22	67.4
Yilgarn ore 1							64.2	0.161	0.40	0.11	
	–	20% NaOH	BPT	3	0.5	n.d.	63.8	0.151	0.42	0.10	5.6
	350	20% NaOH	BPT	3	25	n.d.	66.5	0.092	1.18	0.15	44.8
	900	20% NaOH	BPT	3	25	n.d.	68.7	0.069	0.42	0.07	60.0
	1300	4% NaOH	BPT	3	25	1.3	69.2	0.019	0.22	0.12	89.1
	–	10% H_2SO_4	60	3	25	0.9	64.5	0.159	0.41	0.14	2.3
	350	10% H_2SO_4	60	3	25	5.8	67.0	0.137	0.34	0.09	24.5
	900	10% H_2SO_4	60	3	25	1.6	69.3	0.071	0.42	0.08	59.5
	1300	10% H_2SO_4	60	3	25	1.0	69.1	0.039	0.43	0.12	77.5

n.d., not determined.
[a]All heating times were for 1 h.
[b]Weight loss in the leach based on the solids added to the leach and the residue weight.
[c]Based on P assays for the leach residue, allowing for the weight loss in the heating and the leach.
Adapted from Fisher-White et al. (2012a,b, 2013).

after heating at 300 and 900 °C, while after heating at 1300 °C, a 1% H_2SO_4 leach gave a product with 0.037% P (Table 12.1).

Painter et al. (2010) had reported that, for roasting temperatures over the range of 450–1250 °C, the phosphorus removal from an Australian goethitic iron ore increased with the roasting temperature in a leach with 1% NaOH. When an ore containing 0.125% P was roasted in air at 450 °C for 30 min and leached with 1% NaOH, at 40 wt% solids and ambient temperature, a product with 0.101% P was obtained after 6 days in bottle roll tests.

For a goethitic ore sample from the Yilgarn iron ore province containing 0.161% P, little phosphorus was removed with either a caustic or acid leach. However, after heating at 350 and 900 °C, a 20% NaOH leach gave products with 0.092% and 0.069% P, while a 4% NaOH leach of ore heated at 1300 °C gave a product with 0.019% P. The corresponding leaches with 10% H_2SO_4 gave products with 0.137%, 0.071%, and 0.039% P, respectively (Table 12.1).

For ores heated at 300 °C, there was little weight loss in a caustic leach but the resulting fine iron oxide product was difficult to filter, while for an acid leach, the product was easier to filter but there was a weight loss of 5–10 wt% for the leaches at 25 wt% solids. In acid leaches at lower pulp densities (e.g., 0.5 wt% solids), up to 20 wt% of the solids were dissolved when removing 50–60 wt% of the phosphorus. For heating temperatures of 900 and 1300 °C, the weight losses in the acid leaches were 1–3 wt% (Fisher-White et al., 2013).

The increase in the amount of phosphorus removed in the leach with increasing heating temperature was considered by Edwards et al. (2011) and Fisher-White et al. (2012a,b, 2013) to be due to phase changes in the iron oxides in the ore during the heating. Dehydration of the goethite disrupts the crystal lattice, increasing the porosity of the sample, and these changes are considered to make the phosphorus more available for leaching. The weight loss observed in acid leaches of samples heated at 300 or 350 °C was considered to be due to the dissolution of the protohematite phase formed from the dehydroxylation of the phosphorus-containing goethite. Complete dissolution of this phase in acid solutions was considered necessary to achieve maximum phosphorus removal.

With increasing heating temperatures, a dense hematite phase is formed, phosphorus is more readily dissolved, and the leach residues contain lower levels of phosphorus. The dense hematite phase is less soluble in acid than the intermediate protohematite phase and less iron oxide is dissolved in the acid leaches of ores heated at 900 °C or higher, as discussed below.

Gooden et al. (1974) reported that heating an Australian Pilbara iron ore at 1000–1300 °C in air and then leaching with 1% H_2SO_4 at 50 °C, or 2% NaOH at 90 °C, for 1–5 h resulted in the phosphorus content being reduced from 0.11% to below 0.06% P. Similar results were obtained for pellets produced from various ores that had been fired at 1200–1300 °C (Gooden et al., 1973, 1974). When Cheng et al. (1999) leached a Western Australian iron ore lump sample (P_{80} = 5.6 mm) that had been heated to 1250 °C, and samples of pellets (produced from feed of less than 1.5 mm and less than 0.15 mm and fired at 1250 °C), with 1% H_2SO_4 at 60 °C for 5 h, the phosphorus contents were lowered from 0.126% P to 0.044%, 0.055%, and 0.042% P.

When Fonseca et al. (1994) heated a Brazilian ore containing 0.055% P at 1200 °C for 1 h and leached in tanks without agitation for up to 1 h with 10% HCl, 50 wt% of the phosphorus was removed, compared with 5 wt% when the ore was heated at only 100 °C. Peixoto (1993) also used a static leaching process to treat pellets and sinter produced from an iron ore with a thermal treatment at above 1200 °C. Pellets containing 0.029% P gave a product with 0.019% P after leaching with 10% HCl while sinter with 0.060% P was leached to a level of 0.046% P.

Gooden et al. (1974) identified a phosphorus-rich silicate phase on the surface of the solids after heating a Pilbara iron ore at 1200 °C. Fonseca et al. (1994) reported that the phosphorus migrated into silicate phases in the contour of the grains in sinter from a Brazilian ore. These phosphorus-containing silicate phases were considered to be readily dissolved in caustic and acid solutions resulting in phosphorus removal. Patrick and Lovel (2001) proposed that larnite (dicalcium silicate) is the dominant phosphorus-containing phase in iron ore sinter produced at approximately 1300 °C. Leaching of the sinter with 4% HCl at ambient temperatures for 18 h lowered the phosphorus levels from 0.13% to 0.04% P as a result of dissolution of the larnite.

When 10 wt% NaOH was added to an Australian goethite–hematite ore containing 0.146% P during a heating treatment at 275–500 °C, a leach with boiling water for 3 h at a pulp density of 0.5 wt% solids was sufficient to achieve a leached product with less than 0.075% P. Increasing the heating temperature increased the amount of phosphorus removed in the water leach, and with a heating temperature of 900 °C, the water leach product contained 0.04% P. Similar phosphorus removal was achieved with smaller sodium hydroxide additions in the heating treatment when a caustic leach replaced the water leach (Fisher-White et al., 2009, 2012a).

12.3 Removal of silicon, aluminum, and sulfur minerals

Chemical separation of impurity elements, such as silicon, aluminum, and sulfur, from iron ores often occurs in the processing to remove phosphorus from the ore. The treatments may include caustic or acid leaching of the ore, with or without a heating treatment, and magnetic separations between treatment steps.

Nitric acid leaching of Swedish magnetite ores to dissolve apatite was reported by Zhang and Muhammed (1989) to lower the alkali content significantly (potassium by 63 wt%) and the alumina level. The effect of such a treatment on the silica content was not reported but Edwards et al. (2011) did show that silica and alumina levels were lowered in a sulfuric acid leach of an Australian magnetite ore.

In an Indian hematite sample assaying 58.8% Fe, 5.74% SiO_2, and 6.65% Al_2O_3, silica and kaolinite were the major gangue minerals. A leach with 25% NaOH at 95 °C for 3 h gave a product with 2.12% SiO_2 and 1.25% Al_2O_3, and the phosphorus level was lowered from 0.15% to 0.030% P. Leaching with acid removed less silica and alumina but dissolved significant amounts of iron (Sarkar, 2011).

When a flotation concentrate produced from the Lisakovsky oolitic limonite ore was leached with 5% H_2SO_4, the silica and alumina levels were lowered by 20–25 wt%, but 17 wt% of the iron was dissolved. After heating the concentrate at 600 °C for 30 min,

28 wt% of the silica and 64 wt% of the alumina were removed, but the amount of iron dissolved increased to 30 wt%. Heating a gravity-magnetic concentrate at 900 °C and leaching with 10% H_2SO_4 did not remove any silica but a leach with 10% NaOH did remove 15 wt% of the silica. Around 15 wt% of the alumina was removed in both leaches. Less than 2 wt% of the iron was dissolved in the acid leach (Kokal et al., 2003). Magnetic separations after roasting and leaching also removed some silica.

Mueller and Segura (1975) reported data for Brazilian, Venezuelan, and Australian goethite–hematite ores showing that washing the ores with 10% Na_2CO_3 at 95 °C lowered sulfur levels from 0.052%, 0.052%, 0.037%, and 0.097% S to 0.04%, 0.01%, 0.015%, and 0.043% S, respectively.

When 10 wt% NaOH was added to Australian goethite–hematite ores and the mixture was heated to between 200 and 900 °C before a boiling water leach at 0.5 wt% solids, about 50 wt% of the silica and 60 wt% of the alumina were removed along with phosphorus (Fisher-White et al., 2009).

For leaches with 4% or 20% NaOH of unheated goethite–hematite ore and ore heated at up to 900 °C, 40–70 wt% of the silica and alumina were removed in leaches at 0.5 wt% solids. In leaches at 25 wt% solids, much less silica and alumina were removed. Acid leaching of heated and unheated ore with 10% H_2SO_4 resulted in the removal of between 20 and 50 wt% of the alumina in leaches at both 0.5 and 25 wt% solids, but virtually, no silica was removed (Fisher-White et al., 2013). With a heating temperature of 1300 °C, 45–65 wt% of the silica was removed in a caustic leach at both pulp densities, but little was removed in an acid leach. No alumina was removed in either an acid or a caustic leach of an ore heated at 1300 °C (Fisher-White et al., 2013), and it is anticipated that heating at higher temperatures leads to the formation of insoluble aluminates.

Fonseca et al. (1994) reported that 30 wt% of the alumina was dissolved from Brazilian iron ore fines in a leach with 5–20% HCl, but when they were heated at 1000 °C, less than 10 wt% of the alumina was removed in the leach. No data for silica removal were given.

Leaching of an iron ore sinter produced at 1300 °C, with 3.5% HCl, lowered silica levels from 4.99% to 3.10% as a result of dissolution of a larnite (dicalcium silicate) phase in the sinter. No data were given for alumina levels (Patrick and Lovel, 2001). Peixoto (1993) reported that 20 wt% of the silica and 10 wt% of the alumina were removed from pellets and sinter produced at 1200 °C from a Brazilian ore in a leach with 10% HCl.

12.4 Summary and future trends

In high-phosphorus iron ore deposits, the phosphorus is present either as discrete phosphate minerals (e.g., apatite) or as a phosphate in iron oxide and oxyhydroxide minerals in the ore. High impurity levels of silicon, aluminum, and sulfur in the ores are usually due to the presence of mineral impurities (e.g., quartz, kaolinite, pyrite, and gypsum).

Research indicates that there are conditions that can be used for chemical separation of phosphorus from iron ores and that other impurities often are removed along

with the phosphorus. Leaching conditions depend on the deportment of the phosphorus in the ore, the nature and levels of impurities, and end product requirements.

When phosphorus occurs as a phosphate mineral, physical separation methods may be effective in reducing phosphorus levels. However, if the minerals are finely divided and difficult to liberate or the phosphorus is incorporated with iron oxides, chemical separation techniques may be the most suitable method for removing the impurities.

When present as discrete phosphate minerals, acid leaching is effective in lowering phosphorus levels, along with silica and alumina levels in the ore. Leaching with nitric, hydrochloric, and sulfuric acids at ambient temperatures is effective (Lamont et al., 1973; Forssberg and Adolfsson, 1981; Zhang and Muhammed, 1989; Edwards et al., 2011). Acid consumption increases with the presence of carbonate minerals and other acid-soluble phases in the ore. When phosphorus levels are high, there may be an opportunity to recover a valuable phosphorus by-product, such as phosphoric acid (Forssberg and Adolfsson, 1981; Muhammed and Zhang, 1989; Zhang and Muhammed, 1990). Regeneration of acid is likely to be required for an economic process, particularly when using nitric acid as the leachant as described by Muhammed and Zhang (1989) and Zhang and Muhammed (1990). If agricultural phosphorus supply continues to tighten, the recovery of phosphorus from apatite-containing iron ores may provide a significant alternative source of phosphorus.

In oolitic and BIF ores, the phosphorus is considered to be finely dispersed in iron oxide and oxyhydroxide phases, and little is removed when the ores are leached with caustic or acid. Heating of these ores prior to leaching changes the iron oxide phase containing the phosphorus, and phosphorus removal has been shown to improve with increasing heating temperature. Heating the ore at temperatures of up to 600 °C transforms goethite to protohematite. Dissolution and dispersion of protohematite and other iron oxides during caustic and acid leaching of this heated ore expose phosphorus to the leachant and enable phosphate ions to be dissolved and removed from the ore. In a caustic leach, the resulting iron oxide product is finely dispersed and difficult to filter, while in an acid leach, significant amounts of iron are dissolved. Heating at temperatures of 700–900 °C enables the formation of a hematite phase and migration of phosphorus towards grain boundaries. Caustic and acid leaching of this heated ore can result in good phosphorus removal and the low solubility of the hematite phase results in little iron dissolution in an acid leach.

In oolitic ironstones, where the phosphorus was present as apatite or associated with the hematite in the oolitic particles, Jin et al. (2006) observed that a caustic leach dissolved the apatite in the ore, but not the phosphorus associated with the hematite. An acid leach dissolved both the apatite and phosphorus in the hematite, suggesting that an acid leach is the most likely chemical approach for removing phosphorus and other impurities from an oolitic hematite ore. It is anticipated that upgrading the ore with a reducing roast and production of a magnetite concentrate prior to leaching may be economically advantageous.

In oolitic ironstones and Australian and Brazilian high-phosphorus goethite–hematite ores, where phosphorus was mainly associated with the goethite, little phosphorus was removed by directly leaching the ore. However, increasing amounts were removed, in both caustic and acid leaches, following a heating treatment. The amount of phosphorus

removed increased with increasing heating temperature, up to 1300 °C. Silica and alumina levels in the ore could also be significantly lowered, and the final levels achieved were dependent on the treatment conditions (Fisher-White et al., 2013).

In practice, a heating temperature of 300 °C may be possible by utilizing waste heat in the operation, but the iron-containing leach liquor from an acid leach would require effluent treatment to recover iron before disposal or regeneration of the liquor. While little iron dissolved in a caustic leach, in the commercialization of a caustic leach treatment, it is expected that any solid–liquid separation would be difficult. While a specific heating facility is likely to be required to heat the ore at a temperature of 900 °C, consumption of alkali and acid in the leach is lower and little iron is dissolved in an acid leach of the heated ore (Fisher-White et al., 2012b).

Heating at 1300 °C and leaching to remove phosphorus is unlikely to be economic unless the treatment can be integrated into existing operations. Sintering a high-phosphorus ore as part of an existing integrated steel mill agglomeration step and leaching the heated product, or the return fines, may be an option for producing products with very low phosphorus levels from high-phosphorus iron ore fines. It may be possible to use static leaching or heap leaching to retain the integrity of the agglomerates.

In practice, leaching sinter return fines may be the most viable approach. Following leaching, the return fines would not require any additional drying or processing prior to reagglomeration, and the removal of silicate phases (e.g., larnite) and other contaminates may improve physical properties of the sintered product.

References

Araujo, A.C., Amarante, S.C., Souza, C.C., Silva, R.R.R., 2003. Ore mineralogy and its relevance for selection of concentration methods in processing of Brazilian iron ores. Miner. Process. Ext. Metall. (Trans. Inst. Min. Metall. Sect. C) 112, C54–C64.

Barbour, A.P., 1973. Distribution of phosphorus in the iron ore deposits of Itabira, Mina Gerais, Brazil. Econ. Geol. 68, 52–64.

Cheng, C.Y., Misra, V.N., Clough, J., Mun, R., 1999. Dephosphorisation of Western Australian iron ore by hydrometallurgical process. Miner. Eng. 12, 1083–1092.

Dukino, R.D., England, B.M., 1997. Phosphorus in Hamersley Range iron ores. In: Ironmaking Resources and Reserves Estimation. The Australasian Institute of Mining and Metallurgy, Melbourne, pp. 197–202.

Dukino, R.D., England, B.M., Kneeshaw, M., 2000. Phosphorus distribution in BIF-derived iron ores of Hamersley Province, Western Australia. Trans. Inst. Min. Metall. (Appl. Earth Sci. B) 109, B168–B176.

Edwards, C.I., Fisher-White, M.J., Lovel, R.R., Sparrow, G.J., 2011. Removal of phosphorous from Australian iron ores. In: Iron Ore 2011. The Australasian Institute of Mining and Metallurgy, Melbourne, pp. 403–412.

Engel, A.L., Heinen, H.J., 1959. Experiments in reducing the phosphorus content of a Nevada iron ore. United States Bureau of Mines, Report of Investigations, RI 5449, 8 pp.

Feld, I.L., Franklin, T.W., Lampkin, W.M., United States of America, Secretary of the Interior, 1968. Process for Removing Phosphorus from Iron Ore. US Patent 3,402,041. September 17, 1968.

Fisher-White, M.J., Lovel, R.R., Sparrow, G.J., 2009. Phosphorous removal from iron ore with a low temperature heat treatment. In: Iron Ore 2009. The Australasian Institute of Mining and Metallurgy, Melbourne, pp. 249–254.

Fisher-White, M.J., Lovel, R.R., Sparrow, G.J., 2012a. Phosphorus removal from goethitic iron ore with a low temperature heat treatment and a caustic leach. ISIJ Int. 52, 797–803.

Fisher-White, M.J., Lovel, R.R., Sparrow, G.J., 2012b. Heat and acid leach treatments to lower phosphorus levels in goethitic iron ores. ISIJ Int. 52, 1794–1800.

Fisher-White, M.J., Lovel, R.R., Sparrow, G.J., Washington, B.M., 2013. Effect of temperature on removal of phosphorus from Australian goethitic iron ores. In: Iron Ore 2013. The Australasian Institute of Mining and Metallurgy, Melbourne, pp. 373–380.

Fonseca, D.C., Souza, C.C., Araujo, A.C., 1994. Hydrometallurgical routes for the reduction of phosphorus in iron ores. In: Wilkomirsky, I., Sánchez, M., Hecker, C. (Eds.), Chemical Metallurgy, IV. Meeting of the Southern Hemisphere on Mineral Technology. Sutulov Memorial Volume, vol. III. Universidad de Concepción, Concepción, pp. 83–92.

Forssberg, E., Adolfsson, G., 1981. Entphosphorung von hochphosphorhaltigen eisenerzen durch saure laugung. Erzmetall 34 (6), 316–322 (in German).

Gooden, J.E.A., Walker, W.M., Potts, A.E., Heinzle, U.A., Australian Mineral Development Laboratories, 1973. Process for the Reduction of the Phosphorus Content of Iron Ores. Australian Patent, 457026, 17 May 1973.

Gooden, J.E.A., Walker, W.M., Allen, R.J., 1974. AMDEPHOS—A chemical process for dephosphorisation of iron ore. In: Proceedings Second National Chemical Engineering Conference. The Institution of Chemical Engineers, University of Queensland, St. Lucia, pp. 38–48.

Graham, J., 1973. Phosphorous in iron ore from the Hamersley iron formations. Proc. Australas. Inst. Min. Metall. 246, 41–42.

Hertzog, E.S., 1935. A study of the occurrence and amenability to leaching of the phosphorus compounds in some red iron ores. United States Bureau of Mines, Report of Investigations, RI 3294, 9 pp.

Ionkov, K., Gaydardzhiev, S., Correa de Araujo, A., Kokal, H., Pirson, A., Bastin, D., 2011. Dephosphorisation of limonitic concentrate by roasting, acid leaching and magnetic separation. In: Iron Ore 2011. The Australasian Institute of Mining and Metallurgy, Melbourne, pp. 445–452.

Ionkov, K., Gaydardzhiev, S., Bastin, D., Correa de Araujo, A., Lacoste, M., 2012. Removal of phosphorus through roasting of oolitic iron ore with alkaline earth additives. In: Proceedings, XXVI International Mineral Processing Congress (IMPC) 2012, New Delhi, Paper No. 389, pp. 02194–02205.

Jiang, T., Dong, H.G., Guo, Y.F., Li, G.H., Yang, Y.B., Zhang, Y.B., Li, Q., 2008. Study on beneficiation and dephosphorization of refractory oolitic hematite ore. In: Duo, W.D., Yao, S.C., Liang, W.F., Cheng, Z.L., Long, H. (Eds.), Proceedings of XXIV International Mineral Processing Congress, Science Press, Beijing, vol. 2, pp. 1755–1760.

Jin, Y.-S., Jiang, T., Yang, Y.-B., Li, Q., Li, G.-H., Guo, Y.-F., 2006. Removal of phosphorus from iron ores by chemical leaching. J. Cent. South Univ. Technol. 13 (6), 673–677.

Kokal, H.R., Singh, M.P., Naydyonov, V.A., 2003. Removal of phosphorus from Lisakovsky iron ore by a roast-leach process. In: Hyrometallurgy 2003. Proceedings of the 5th International Symposium, vol. 2. The Minerals, Metals & Materials Society, Warrendale, PA, pp. 1517–1530.

Kokal, H.R., Farias, J.M., Chop, S.V., 2008. A roasting-leaching demonstration plant for removal of phosphorus from iron ore. In: Hydrometallurgy 2008. Proceedings of the 6th International Symposium. Society for Mining, Littleton, Colorado, pp. 431–438.

Lamont, W.E., McVay, T.N., Spruiell, C.E., Feld, I.E., 1973. Phosphorus removal from Birmingham, Ala., calcareous iron ores. United States Bureau of Mines. Report of Investigations, RI 7728, 15 pp.

Levintov, B.L., Mirko, V.A., Kantemirov, M.D., Klimushkin, A.N., Naidenov, V.A., Bobir, A.V., 2007. Structure of oolitic brown iron ores and their influence on the thermochemical enrichment of Lisakovsk concentrates. Steel Transl. 37 (8), 681–685.

MacRae, C.M., Wilson, N.C., Pownceby, M.I., Miller, P.R., 2011. The occurrence of phosphorus and other impurities in Australian iron ore. In: Iron Ore 2011. The Australasian Institute of Mining and Metallurgy, Melbourne, pp. 281–289.

Mueller, D.E., Segura, M.A., Exxon Research and Engineering Company, 1975. Ore Pretreatment Process. US Patent, 3,928,024, December 23, 1975.

Muhammed, M., Zhang, Yu., 1989. A hydrometallurgical process for the dephosphorization of iron ore. Hydrometallurgy 21, 277–292.

Painter, C.L., Box, J.C., Rees, K.L., Lonergan, A.B., Technological Resources Pty. Limited, 2010. Treating Iron Ore. International Patent WO 2010/015019 A1, 11 February 2010.

Patrick, T.R.C., Lovel, R.R., 2001. Leaching dicalcium silicates from iron ore sinter to remove phosphorus and other contaminants. ISIJ Int. 41, 128–135.

Peixoto, G.B., S.A., Mineracao da Trindade-Samitri, 1993. Improvement of the Reduction Process in P Content and Other Gangues in Iron Ore and Its Agglomerates. International Patent WO 93/10271, 27 May 1993.

Sarkar, S., 2011. The removal of alumina and silica from iron rejects slime by chemical leaching. Hydrometallurgy 105, 364–369.

Wells, M.A., Ramanaidou, E.R., 2011. Occurrence and mineralogical association of phosphorus in Australian bedded iron ore deposits. In: Iron Ore 2011. The Australasian Institute of Mining and Metallurgy, Melbourne, pp. 331–336.

Wilson, N.C., 2013. CSIRO Mineral Resources Flagship, unpublished results.

Yin, J., Lv, X., Bai, C., Qiu, G., Ma, S., Xie, B., 2012. Dephosphorization of iron ore bearing high phosphorous by carbothermic reduction assisted with microwave and magnetic separation. ISIJ Int. 52, 1579–1584.

Zhang, Yu., Muhammed, M., 1989. The removal of phosphorus from iron ore by leaching with nitric acid. Hydrometallurgy 21, 255–275.

Zhang, Yu., Muhammed, M., 1990. An integrated process for the treatment of apatite obtained from dephosphorization of iron ore. J. Chem. Technol. Biotechnol. 47, 47–60.

Zhu, D., Xiao, Y., Chun, T., Chen, B., Pan, J., 2010. Upgrading and removing phosphorus from low-grade and high phosphorus containing iron ores. In: Proceedings, XXV International Mineral Processing Congress (IMPC) 2010. The Australasian Institute of Mining and Metallurgy, Melbourne, pp. 1667–1676.

Application of biotechnology in iron ore beneficiation

13

S.M. Rea[1], N.J. McSweeney[1], R.B. Dwyer[1], W.J. Bruckard[2]
[1]CSIRO Land and Water Flagship, Wembley, WA, Australia
[2]CSIRO Minerals Resources Flagship, Clayton South, VIC, Australia

13.1 Introduction

Microorganisms are used in commercial mining operations because they can attach to mineral surfaces and cause changes to the sulfide mineral surface. These changes can facilitate leaching and oxidation processes as they gain energy by oxidizing ferrous iron and/or sulfur compounds to ferric iron and protons. The ferric iron generated reduces the base metals rendering them soluble for downstream processing (bioleaching) and/or upgrades precious metals ready for further treatment (biooxidation) (Sand et al., 1995). Sulfur-oxidizing microorganisms enhance leaching by removing elemental sulfur that accumulates on the mineral surface and by generating acid. This increases both the dissolution of acid-soluble minerals and the solubility of ferric iron (Crundwell, 2003; Rohwerder et al., 2003). Microorganisms are integral to leaching and oxidation processes as in the pH range of 2–3; bacterial oxidation of ferrous iron is approximately 10^5–10^6 times faster than abiotic oxidation (Rawlings, 2002; Bosecker, 1997).

Microbial leaching is a viable commercial process. At least 15% of the world's copper supply is the direct result of microbial leaching of copper sulfide ores, and 5% of the world's gold is recovered through biooxidation (Brierley and Brierley, 2013). Commercial bioleach operations also exist for nickel, cobalt, and zinc sulfide ores (Brandl et al., 2001; Lizama et al., 2003; Olson et al., 2003). A successful bioleaching operation in Finland of a complex low-grade black schist ore is producing nickel, zinc, copper, and gold (Riekkola-Vanhanen, 2013).

As the world's supply of high-quality minerals decreases, novel ways of extracting metals and separating gangue minerals from ores are emerging. One of the promising technologies that utilizes microorganisms for ore pretreatment is biobeneficiation—the selective removal of unwanted gangue(s) from an ore by microorganisms and their metabolites (Deo and Natarajan, 1997; Natarajan and Deo, 2001; Sharma and Hanumantha Rao, 2003). Biobeneficiation can be achieved by bioflotation and bioflocculation, where microorganisms render a mineral surface more hydrophobic or hydrophilic and/or change the surface charge of the mineral. In biobeneficiation, the microorganisms and/or their metabolites can act as modifiers, collectors, and depressants (Botero et al., 2007).

Many different mineral systems have been researched, such as the biobeneficiation of phosphate ores (Zheng et al., 2001; Elmahdy et al., 2013; Merma et al., 2013) and bauxite ores (Anand et al., 1996), the bioflocculation and bioflotation of fine coal

Iron Ore. http://dx.doi.org/10.1016/B978-1-78242-156-6.00013-7
© 2015 Elsevier Ltd. All rights reserved.

(Vijayalakshmi and Raichur, 2002, 2003; Raichur et al., 1996, 1997), and the use of biocollectors for magnesite and calcite (Botero et al., 2007, 2008). The majority of research in this area has concentrated on the bioflotation and bioflocculation of sulfide minerals.

The success of commercial bioleaching operations and the deeply researched area of bioflotation reagents for sulfide ores inspired research into the applicability of bioleaching and bioflotation for oxide ores, particularly iron ore as high-grade reserves become scarce. In 20–40 years' time, all the world's quality iron ore will be gone, and only low-grade ore will be left for processing (Mudd, 2009), so more efficient and economic beneficiation techniques will be necessary. Commercial iron ore flotation systems have concentrated on the removal of quartz (silica) as the steel industry requires feedstock that is <2% SiO_2 (Ma et al., 2013).

Other impurities such as gibbsite and aluminum silicate (clay) minerals such as kaolinite are now receiving increasing attention from researchers and operators as they are considered penalty elements and must be removed prior to processing. Magnetic and hydraulic separation methods are effective where gangue minerals are discrete, but often, they are present as fine particles interspersed throughout the hematite or goethite iron ore (Ma et al., 2013). Froth flotation is then used to further upgrade the ore.

Australian iron ore is still predominantly high-grade and requires only crushing and screening before it is shipped overseas for smelting. Although most Australian iron ore is still of a high quality requiring only mechanical processing, beneficiation of Australian iron ore began in 2013 with the Gindalbie Metals group commencing operations at Karara, Western Australia (WA), with a froth flotation processing circuit to remove quartz (Netscher, 2013). This was the first commercial flotation operation for iron ore in Australia; however, froth flotation and flocculation beneficiation have been operating in Brazil and the United States for many years (Houot, 1983).

Flotation and flocculation reagents are reasonably effective in upgrading iron ore but are often expensive and environmentally hazardous. Using microorganisms or their metabolites as bioreagents, which can act as flotation and flocculation reagents for the selective separation of minerals, is a good option as they may be cheaper and more efficient at selectively separating minerals and do not introduce potentially toxic chemicals into the environment (Natarajan et al., 1997).

At the same time, as Australian and global iron ore grades are declining, global phosphorus supplies are also rapidly declining. Alternative phosphorus supplies will be required to sustain the agricultural industry in countries like Australia that have poor soils. Phosphate is an essential nutrient for all living organisms, as it is a major component of deoxyribonucleic acid (DNA). As phosphorus supplies decrease, low-grade iron ores containing medium (0.07–0.1%) or high (>0.1%) phosphorus are increasing.

Phosphorus can cause cold brittleness when making steel so penalties for iron ore with a medium or high content of phosphorus (Holmes, 2010) are applied by smelters. Microorganisms play an important role in solubilizing soil and mineral phosphates through the production of organic and inorganic acids (Whitelaw et al., 1999). This innate ability of microorganisms to transform and cycle phosphorus when it is limiting has the potential to be harnessed for bioleaching phosphorus from iron ore

(Delvasto et al., 2005). The dephosphorization of iron ore by microorganisms not only will increase the quality of the ore but also may provide an alternative source of phosphate fertilizer.

In this chapter, we will discuss how and why microorganisms adhere and change mineral surfaces and how this can be exploited for iron ore. The bioleaching of phosphate from iron ore will be examined, followed by a discussion of flotation bioreagents for sulfide ore systems, leading to a thorough review of the biobeneficiation of iron ore. The chapter will conclude with a summary of future projections dealing with the commercial viability of biomining iron ore.

13.2 Microbial adhesion to mineral surfaces

13.2.1 Adhesion mechanisms

Microorganisms will preferentially grow attached to surfaces rather than remaining in a planktonic state (free swimming). For example, Jiang et al. (2007) found that approximately 80–90% of soil bacteria are attached to solid surfaces, while Gehrke et al. (1998) determined that when mineral surface space was not limiting, >80% of cells disappeared from solution within 24 h. Microbial attachment to mineral surfaces depends on the van der Waal interactions, the surface properties of the cell (electrical charge and hydrophobicity), the production of extracellular polymeric substances, and the formation of a biofilm. However, attachment is primarily driven by the surface charge (electrostatic interactions) and the hydrophobicity of the cell (acid–base interactions) (Solari et al., 1992; Cruz et al., 2005).

Surface properties such as electrical charge and hydrophobicity are determined by the biochemical makeup of the cell surface. A useful way to determine if a microbial cell is likely to attach to a mineral surface is to determine the isoelectric point (the pH at which there is no net charge). For most microbial cells, an IEP $\leq$ 2.8 indicates that the cell surface is composed of polysaccharides that contain negatively charged phosphate and carboxyl groups (Rijnaarts et al., 1995). The soil bacteria *Mycobacterium phlei* adheres to coal and pyrite because it is negatively charged due to polysaccharides embedded in the cell wall (Raichur et al., 1996).

Other microbial cells have an outer phospholipid membrane surrounded by a thin peptidoglycan layer. The arrangement of the proteins and lipopolysaccharides on the cell surface contributes to the hydrophobicity of the cells (Dwyer et al., 2012). Many of the acidophilic bioleaching microorganisms fall into this category, including the species *Acidithiobacillus ferrooxidans*, an acidophilic, iron- and sulfur-oxidizing bacterium that uses CO_2 as a carbon source. Using *A. ferrooxidans*, Solari et al. (1992) determined that hydrophobicity, and not surface charge, was more important in promoting adhesion between bacteria and mineral surfaces. They showed that at pH 2.3–3.0, there was adhesion due to electrical attraction between the positively charged bacterial cells of *A. ferrooxidans* and negatively charged minerals. When the pH dropped below 2.2, the quartz and chalcopyrite contained in the mineral also became positively charged; however, bacterial adhesion still took place because the bacterial

hydrophobicity increased as the pH decreased. Therefore, the *A. ferrooxidans* cells overcame electrostatic repulsion to adhere to the mineral surfaces.

13.2.2 Cell surface changes due to growth conditions

Besides pH, other growth conditions affect the degree of hydrophobicity of a bacterial cell. Van der Mei et al. (1998) compiled the microbial contact angles of 142 microbial strains/species from the literature, which ranged from 15° to 110°, where 15° was hydrophilic and 110° was very hydrophobic. They intended it as a reference guide only and concluded that no generalizations could be made as growth factors and microbial species influenced the degree of hydrophobicity.

For example, the species *Candida albicans* is more hydrophobic when grown at 37 °C compared with when grown at 30 °C. Cells grown in a glucose-based medium were shown to be more hydrophobic than those grown in yeast extract medium when the incubation temperature was the same (Van der Mei et al., 1998). In addition, Liu et al. (2011) found that the cells of a strain of *A. ferrooxidans* were rendered more hydrophobic when grown on a solid substrate (pyrite) rather than on a soluble ferrous sulfate medium. The increase in hydrophobicity meant that more cells could attach to the pyrite surface.

The primary attachment of cells to mineral particles is through hydrophobic and/or electrostatic interactions; however, the production of extracellular polymeric substance (EPS) is necessary to form a biofilm and facilitate irreversible attachment. If growth conditions are unfavorable (such as deprivation of an essential nutrient or an electron acceptor), the bacterial cells can alter the functional groups expressed on the cell surface and/or in the EPS and control the composition and amount of EPS produced. These modifications can make the mineral surface more suitable for growth (Jefferson, 2004; Hermansson, 1999; Yee et al., 2000). For example, Delvasto et al. (2009) observed that oxygen deprivation caused denser colonization of an iron ore surface by a *Burkholderia* spp. when an extensive network of EPS covered the mineral surface.

Noël et al. (2010) showed that the EPS produced by mixed species of bioleaching bacteria was more extensive on the pyrite coupons provided for growth than the EPS produced by a single bioleaching species. Furthermore, iron-oxidizing species *Leptospirillum ferriphilum* and *A. ferrooxidans* attached to pyrite coupons simultaneously, while a sulfur-only-oxidizing species, *Acidithiobacillus caldus,* could not attach to the pyrite coupons without the precolonization of the surface by *L. ferriphilum* cells. These results indicated that a species capable of iron oxidation was probably necessary for primary colonization.

13.2.3 Mineral surface affects microbial adhesion

In addition to cell–mineral surface interactions and EPS production and composition, the physical structure of the mineral surface itself is also important for attachment. Microorganisms attach where the mineral surface is scratched, pitted, or cracked, and because of microbial attachment, these areas then become sites of high oxidative activity.

Some strains of the motile bacterial species *A. ferrooxidans* possess a chemosensory system where cells are attracted to oxidation sites and areas of high concentrations of ferrous/ferric ions (Sand and Gehrke, 2006) promoting attachment and growth on sulfide minerals.

13.2.4 Increasing mineral selectively by microbial adaptation

Microorganisms exposed to a mineral over time can adapt to that mineral and produce mineral-specific compounds on their cell surface and/or in their EPS. Deo and Natarajan (1999) adapted *Paenibacillus polymyxa* to corundum (alumina) by serial subculturing over time and found that the cells and their metabolites were more effective in hematite–alumina separation than cells not adapted to corundum. The same bacteria grown over time on calcite and on quartz produced more surface polysaccharides and proteins, respectively (Somasundaran et al., 2005), which increased mineral selectivity in downstream microflotation trials.

Dwyer et al. (2011) cultured *P. polymyxa* in a defined medium containing soluble growth factors in the presence and absence of kaolinite for over 2 years through serial subculturing. When both the nonadapted and adapted cells were cultured onto a medium in the presence of kaolinite (10% pulp density (w/v)), more EPS was observed attached to the surface of the kaolinite from the kaolinite-adapted than the nonadapted cells (Figure 13.1; Dwyer et al., 2013). The greater concentration of EPS produced may have resulted in an increased mineral selectivity (Deo et al., 2001) as the kaolinite may have been rendered more hydrophobic.

The ability of microorganisms to adhere to mineral surfaces and effect surface changes can be exploited for the biomining of iron ore in two ways. First, phosphate can be leached from iron ore by functional groups (bacterial metabolites) excreted by the cell, and secondly, biobeneficiation of iron ores can be selectively floated or

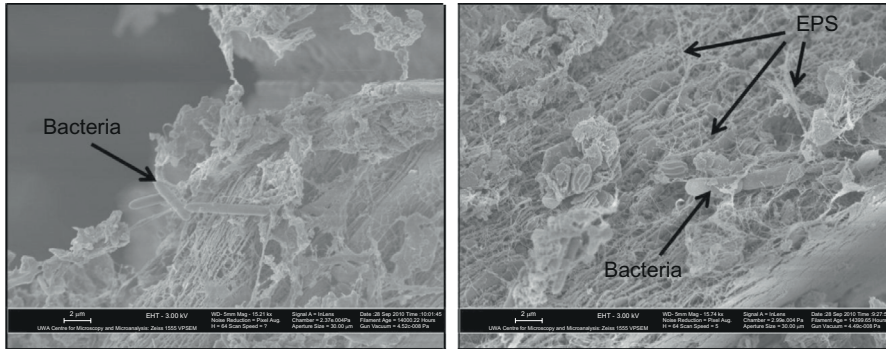

Figure 13.1 (a) Nonadapted *Paenibacillus polymyxa* cells and (b) *P. polymyxa* cells adapted to growing with kaolinite adhering to a kaolinite mineral surface. The EPS network and biofilm layer on the kaolinite mineral surface is more extensive from the cells previously adapted to kaolinite (Dwyer et al., 2013).

flocculated by bacterial cells and/or their metabolites. For iron ore biobeneficiation, the types and combinations of bacteria used and the metabolite(s) released can be modified by altering the media of growth (varying ionic strength, nutrients, carbon sources, and growth substrates), by stressful conditions, by the temperature and pH, and by the adaptation to a mineral for its selective separation from iron ore.

13.3 Bioleaching for phosphorus removal from iron ores

Dephosphorization of iron ore can be achieved through bioleaching. Different methods are needed to remove phosphorus from iron ore depending on whether it is present as a mineral (apatite) or associated with iron minerals (Edwards et al., 2011). Although most phosphorus occurs entrapped within goethite in Australian iron ores, a considerable amount is present as apatite worldwide. Microorganisms and their metabolites could be used to solubilize the phosphorus in apatite. Three different groups of microorganisms have been studied for the dephosphorization of iron ore. There are fungi, commercial bioleaching acidophilic bacteria, and the soil bacteria, which can also fix nitrogen and solubilize mineral phosphates.

13.3.1 Phosphorus bioleaching fungi

Fungi produce organic acids such as citric and oxalic acids that can solubilize phosphorus more easily from the recalcitrant iron and aluminum phosphates. Citric acid is formed via the tricarboxylic acid (TCA) cycle, which is part of aerobic respiration in all organisms (Mishra et al., 2011). Oxalic acid is produced when oxaloacetate is hydrolyzed to oxalate and acetate by the enzyme cytosolic oxaloacetase. The carboxylic anions of these organic acids compete with the phosphate for binding sites and chelate the Al^{3+} and Fe^{3+} promoting the release of phosphate into solution (Pérez et al., 2007).

A *Penicillium*-like fungus (strain F-1) isolated from garden soil produced oxalic acid and itaconic acid, which leached 28% of phosphate from an iron ore concentrate and 20% phosphate from calcium phosphate (Parks et al., 1990). This fungus may have been *Penicillium citrinum* as in a study of 36 fungal species isolated from soil, only this fungal species and *Aspergillus niger* were found to be effective at solubilizing rock phosphate (Omar, 1998). Williams and Cloete (2010) determined that *A. niger* produced citric acid to solubilize approximately 23% of phosphorus from an iron ore concentrate, which was similar to that reported by Delvasto et al. (2005), who found that a strain of *A. niger* (isolated from a high-phosphorus Brazilian iron ore) removed 20% of phosphorus rendering it acceptable for processing.

13.3.2 Commercial bioleaching acidophilic bacteria

Acidophilic bioleaching microorganisms such as *A. ferrooxidans* can solubilize phosphate in rock phosphates like fluorapatite if the acid-insoluble mineral pyrite is added. The ferrous iron in the pyrite is oxidized producing ferric iron and thiosulfate, which is

then further oxidized to tetrathionate by microorganisms to produce protons (lowering the pH) and sulfuric acid, dissolving the phosphate.

A. ferrooxidans and the heterotrophic species, *Acidiphilium cryptum*, were used together to bioleach fluorapatite with the addition of pyrite. The heterotrophic species not only used the organic matter in the rock phosphate as a carbon source for growth (organic matter is inhibitory to *A. ferrooxidans*) but also lowered the pH and increased the redox potential causing increased solubilization of the hydroxyapatite (Xiao et al., 2013). Shen et al. (2012) also found that acidophilic bioleaching microorganisms effectively bioleach phosphorus from iron ore when they added high-phosphorus iron ore and elemental sulfur to municipal wastewater to make an iron ore slurry. Apatite was the main phosphorus mineral in the iron ore and the wastewater contained native sulfur-oxidizing bacteria. The sulfur-oxidizing bacteria are not as sensitive to organic matter as the iron-oxidizing bacteria and either used the organic matter as a carbon source or were not inhibited by its presence. Between 83% and 87% of the phosphorus was bioleached from the iron ore in both experiments (Shen et al., 2012; Xiao et al., 2013).

13.3.3 Soil bacteria

Like the fungal species, many soil bacteria produce acids that solubilize calcium phosphates and apatites. The mechanism of action is different from the sulfide minerals, as the microorganisms do not gain energy from oxidizing the mineral but instead release organic and inorganic acids that act to dissolve the phosphate.

Halder et al. (1990) found that a root nodule species of *Rhizobium* solubilized ~64% of phosphorus in rock phosphate by producing 2-ketogluconic acid. Increased solubilization (>80% P) occurred when EDTA (a chelating agent) was added to the medium, which likely complexed the available Ca^{2+} ions causing the release of phosphate into solution. Microbial species of the *Rhizobium* genus were effective at leaching phosphate from hydroxyapatite or rock phosphate, but this was not a generic trait. For example, while *Burkholderia caribensis* solubilized phosphate from hydroxyapatite by the production of gluconic and acetic acids using glucose or sucrose as carbon sources, respectively, *Burkholderia cepacia* could not leach phosphorus from either hydroxyapatite or rock phosphate (Rodríguez and Fraga, 1999; Delvasto et al., 2005, 2006, 2008). Unlike *Rhizobium* spp., *B. caribensis* did not produce 2-ketogluconic acid. These studies showed that phosphate solubilization was dependent on the species (not the genera) and the carbon source supplied for growth as different acids were produced from different sugars.

13.3.4 Combination phosphorus removal

Some studies have been done to compare the effectiveness of the three groups of microorganisms alone, together or as additives to chemical leaching agents. Natarajan et al. (1997) tried both acidophilic (*Acidithiobacillus* spp.) and the soil bacteria (*P. polymyxa*) to bioleach calcite ($Ca_5(PO_4)_3$) from a bauxite ore. Both successfully dissolved the calcite; however, the bacterial metabolites from *P. polymyxa* also solubilized approximately 50% of the goethite and hematite. Delvasto et al. (2005)

found fungal-dominated cultures were more effective at dephosphorization of a high-phosphate iron ore than predominantly soil bacterial cultures, while Parks et al. (1990) found that phosphate solubilization from an iron ore could be increased from 20% (fungus metabolites alone) to 50% when HCL (a traditional leaching agent) was added in small quantities to the fungal metabolites.

13.4 Biobeneficiation of sulfide ores

13.4.1 Commercial bioleaching acidophilic bacteria

Research into the biobeneficiation of sulfide mineral systems was driven by a desire to use bioreagents to replace or augment xanthate and fatty amine collectors to upgrade the ore as these conventional collectors are expensive and environmentally damaging. In addition, there was a possibility that microorganisms and their metabolites could be used to assist or replace environmentally damaging reagents such as potassium cyanide in the desulfurization of coal tailings (Misra et al., 1996). Bioleaching microorganisms had been successfully used to bioleach the base metals from sulfide ores, but pyrite and other sulfide minerals collect in the tailings dams leading to acid mine drainage. It was possible that the same microorganisms could be used as collectors for the biobeneficiation of sulfide minerals and for the desulfurization of tailings (Patra and Natarajan, 2003).

Nagaoka et al. (1999) recorded almost complete flotation (90–99%) of five sulfide minerals (pyrite, chalcocite, molybdenite, millerite, and galena) until *A. ferrooxidans* cells were added to the mixture. The cells adhered to the pyrite causing >80% of the pyrite to settle, confirming that *A. ferrooxidans* was a selective bioflocculant of pyrite as Misra et al. (1996) had done previously. This was reinforced by Chandraprabha et al. (2004a,b) who showed that pyrite was rendered more hydrophilic than chalcopyrite and arsenopyrite with the addition of *A. ferrooxidans* cells following xanthate preconditioning.

In a similar study, preconditioning a chalcopyrite/pyrrhotite mixed ore with *A. ferrooxidans* before the addition of a xanthate collector allowed the flotation of chalcopyrite and depression of pyrrhotite (Pecina-Treviño et al., 2012). Hosseini et al. (2005) and Chandraprabha and Natarajan (2006) showed that the addition of both *A. ferrooxidans* cells and xanthate selectively depressed pyrite in a pyrite/chalcopyrite mix at both acidic and neutral pH conditions. Additionally, Hosseini et al. (2005) determined that the floatability of chalcopyrite was enhanced with cells grown on elemental sulfur instead of ferrous sulfate.

Galena was depressed and sphalerite was rendered more hydrophobic in flotation tests using *A. ferrooxidans* cells, while in bioflocculation tests, sphalerite was dispersed, while galena flocculated and settled (Santhiya et al., 2000). Govender and Gericke (2011) found that the EPS collected from a bioleaching consortium of bacteria and archaea used in conjunction with a xanthate collector floated 77% of the chalcopyrite from a chalcopyrite/pyrite mix compared to only 32% when the xanthate collector was used alone.

13.4.2 Soil bacteria

Researchers have also used soil bacteria for bioflotation and bioflocculation of mineral sulfide ores. Patra and Natarajan (2003, 2004) used *P. polymyxa* cells to selectively flocculate pyrite from a quartz/calcite mix and then selectively separated the pyrite (84% depressed) from quartz (64% floated) using bioflotation. A small quantity of amine collector (hexamine, 0.4 mM) further enhanced the floatability of quartz (91%) and further depressed pyrite (92%) after conditioning with *P. polymyxa* cells. Sharma et al. (2001) found that the surface charge of *P. polymyxa* remained the same after adaptation to galena, sphalerite, pyrite, and chalcopyrite, but the cells became more hydrophilic, particularly those adapted to chalcopyrite.

The metabolites of soil bacteria were studied to determine if they would be effective bioreagents in the biobeneficiation of sulfide ores. Patra and Natarajan (2008) rendered pyrite and chalcopyrite hydrophilic and quartz, sphalerite, and galena hydrophobic by using bacterial proteins released extracellularly as metabolites. This enabled the selective depression of the pyrite and chalcopyrite while selectively floating the quartz, sphalerite, and galena. In addition, the protein mixtures selectively flocculated the pyrite and chalcopyrite, while the quartz, sphalerite, and galena were dispersed.

Santhiya et al. (2002) used EPS polysaccharides from *P. polymyxa* in conjunction with a xanthate collector and an activator ($CuSO_4$), as well as whole cells and proteins, to selectively float sphalerite (80–90%) and depress galena (<10% floated). Without the addition of the EPS, the floatability of both in the pH range 4.5–8.5 was over 90%. Single-stranded DNA from the soil bacteria *Bacillus circulans* has also been identified as a beneficiation bioreagent, as it selectively floated approximately 85% of the sphalerite and only 30% galena in a sphalerite and galena mineral mix (Vasanthakumar et al., 2012). These results are comparable to those obtained using cells and/or their metabolites. Only approximately 50% of the sphalerite was floated when double-stranded DNA was used instead of ssDNA because dsDNA is not amphoteric (both anionic and cationic functional groups present on the cell surface), as the phosphate groups are present on the outside of the double-stranded helix, while the hydrophobic bases are within.

13.5 Biobeneficiation of iron ore

Most commercially operated iron ore flotation processes, such as the one used by Samarco in Brazil, use the reverse cationic flotation method where the process waters are basic, amine is used as a quartz/silicate collector, and starch is used as an iron depressant (Houot, 1983). As with sulfide ores, the flotation reagents can be expensive and environmentally damaging, and hence, bioreagents for upgrading iron ore have been investigated as alternatives or in addition to traditional chemical beneficiation reagents.

13.5.1 Commercial bioleaching acidophilic bacteria

Unlike mineral sulfide ores, iron ore does not provide an energy source (e.g., ferrous and sulfur compounds) for the oxidative growth of bioleaching microorganisms;

however, iron-reducing bacteria, which gain energy by the dissimilatory reduction of ferric iron to ferrous iron, may be useful in upgrading iron ore slimes. Currently, studies have focused on the use of iron-reducing bacteria and/or their metabolites for the bioremediation of contaminated environments and for the deflocculation of activated sludge (Caccavo et al., 1996) but not for the beneficiation of iron ore. In addition, *A. ferrooxidans* can respire both oxygen and ferric iron, and it could possibly be used in a reductive capacity to upgrade iron ore. Overall though, research on the biobeneficiation of iron ore has generally focused on the use of whole cells and cell metabolites of soil bacteria.

13.5.2 Soil bacteria

Initial studies for iron ore biobeneficiation focused on the floatability of hematite using *M. phlei.* When hematite was preconditioned with *M. phlei* cells and floated at pH 2.5, nearly 80% of the hematite floated. However, when the researchers tried to increase the floatability by increasing the cell concentration; large compacted flocs formed that settled rather than floated (Dubel et al., 1992; Misra et al., 1993). This was probably because hematite fines (~20 μm) were used in the experiment rather than larger particles (>53 μm) (Smith et al., 1993). The researchers also determined that the pH was critical to achieving floatability of hematite (Dubel et al., 1992; Misra et al., 1993) as adhesion of the *M. phlei* cells to the hematite decreased as pH increased. This was due to progressive proton disassociation of the anionic complexes (Omoike and Chorover, 2006). In a subsequent dewatering experiment, the hematite and cell mixture was easier to filter than the hematite alone, and although the filter cakes of both retained about 18% of water, the filter cake with hematite and cells lost 15% of its water in 20 min compared with 50 min for the control.

Caccavo et al. (1997) and Caccavo (1999) drilled down and revealed that the adsorption of the anaerobic iron-reducing *Shewanella alga* BrY to hydrous iron oxide was due to the hydrophobic proteins on the cell surface rather than the polysaccharides. The cell surface proteins competitively inhibited whole cell binding to hydrous iron oxide. Surprisingly, iron-reducing rates were similar between *S. alga* strain BrY and a mutant strain of *S. alga* (RAD20) that was deficient in cell surface proteins and did not adhere well to the ore. This finding was in contrast to previous research where cell adhesion to iron containing sludge flocs was necessary for microbial iron reduction and consequent sludge deflocculation (Caccavo et al., 1996).

Arnold et al. (1986) also found that cell adhesion was necessary to achieve high reductive dissolution of goethite by the iron-reducing bacteria *Pseudomonas* spp. 200.

The sulfate-reducing bacterium *Desulfovibrio desulfuricans* was adapted to grow with hematite and quartz anaerobically, but it did not use hematite for dissimilative growth. A mineral mix containing equal proportions of quartz and hematite was conditioned with cells adapted to growth with quartz and a silica-specific collector. At a neutral pH, approximately 88% of the quartz and only 14% of the hematite floated (Prakasan and Natarajan, 2010) indicating that the anaerobic sulfate-reducing bacteria was an effective bioreagent.

The soil bacteria *Rhodococcus opacus* was also used in a quartz–hematite mineral system because the cells are potential bioreagents due to their high hydrophobicity (contact angle 70°). In addition, the cells have a negative surface charge over a wide pH range, with an IEP of approximately pH 3.2. In their study, de Mesquita et al. (2003) determined that cells adhered to hematite over a pH range of 2–8, while very few cells adsorbed to quartz above pH 5. In subsequent flotation tests with no additional collector, approximately 72% of hematite was recovered when floating the hematite/quartz mineral mix at a neutral pH with *R. opacus* cells. A recent study (Merma et al., 2013) using *R. opacus* to selectively float apatite and depress quartz confirmed the results of de Mesquita et al. (2003) that *R. opacus* cells have a negative charge over a wide pH (3–12) with a reported IEP of pH 2.8. They achieved 90% recovery of the apatite at pH 5 after 5 min of flotation, while only 14% of the quartz floated.

A quartz–hematite mineral system where corundum (an aluminum oxide) and kaolinite (a clay mineral containing silica and alumina) were also present was conditioned for 24 h with *P. polymyxa* (Deo and Natarajan, 1998a; Deo et al., 2001). The IEP of quartz (1.7 to 3.6) and kaolinite (1.4 to 1.6) increased and that of hematite and corundum decreased (5.8–7.5 to <2.0). Deo and Natarajan (1997, 1998a) had determined in earlier papers that protein (bovine serum albumin) caused the IEP of quartz and kaolinite to increase due to the formation of cationic complexes, while starch (polysaccharides) caused the IEP of hematite, corundum, and calcite to decrease forming anionic complexes.

The extended DVLO theory (Raichur et al., 1996) examines the energies of interaction between two particles to predict adhesion but does not take into account other forces like hydrophobicity. The interaction energy for hematite and corundum and *P. polymyxa* at pH range 4.0–7.0 was negative, so adhesion occurred. At pH 4.8, the total interaction energy is at a minimum (most negative), which corresponded with the maximum in adhesion. However, in the pH 4.0–7.0 range, the interaction energy between quartz and *P. polymyxa* is positive, so adsorption of the cells on the quartz surface was low (Deo et al., 2001). The contact angles between *P. polymyxa* and hematite and corundum, as well as electrostatic interactions, decreased and the mineral surfaces became more hydrophilic.

In contrast, less cells adhered to quartz and kaolinite as contact angles increased and the surfaces became more hydrophobic (Deo et al., 2001). Flotation studies then revealed that in 1:1 mineral mixes (i.e., hematite–quartz, corundum–quartz, kaolinite–quartz, and calcite–quartz at 75–110 μm), approximately 90% of the quartz floated after 5 min conditioning time with *P. polymyxa*, which increase to 95% when a small amount of a cationic amine collector was added (Deo and Natarajan, 1997). Quartz and kaolinite were dispersed, while hematite and corundum settled when *P. polymyxa* were used in subsequent flocculation studies. In a hematite–quartz mineral mix, a separation efficiency of 95.5% was achieved at neutral pH, after 5 min conditioning time with 6×10^9 cells/min after six deliming stages (Natarajan and Deo, 2001). Overall, the research revealed that *P. polymyxa* cells were effective at selectively separating silica and alumina from iron oxide through either flotation or selective flocculation.

The metabolites of *P. polymyxa* cells were also examined by separating the protein and polysaccharide fractions to determine if they would be effective bioreagents.

Flotation tests using the fractions confirmed that when *P. polymyxa* cells were used to condition the mineral, the quartz and kaolinite became more hydrophobic and the hematite and corundum became more hydrophilic. However, using the fractions also confirmed that the proteins were responsible for the floatability of quartz and kaolinite, while the polysaccharides depress the hematite and corundum. The protein fraction excreted by *P. polymyxa* cells floated 100% of a quartz mineral, while only 4% was floated by the polysaccharide fraction. The metabolite fraction (both proteins and polysaccharides before separating the fractions) floated only 80% of the quartz indicating that the polysaccharides in the metabolite fraction depressed the quartz.

Secondary studies to determine if cells adapted to a mineral would produce compounds specific to that mineral were also undertaken. Deo and Natarajan (1999) adapted *P. polymyxa* to grow with corundum, and subsequent zeta potential measurements indicated that the IEP of unadapted cells (pH 1.5–2.0) had shifted in the adapted cells (pH 3.7). After 1 min of conditioning, 99% of the adapted cells settled, while only 90% of the unadapted settled at a neutral pH. In flocculation tests using a mineral mix of quartz, hematite, and corundum, the specific protein compounds absorbed to the corundum causing effective flocculation and separation of corundum from hematite and quartz. Deo and Natarajan (1999) also determined that adapted cells need to remain growing with the mineral as the change in cells adapted to grow with a particular mineral is not permanent (genetic) and will revert if the mineral is no longer present.

In a recent experiment, Poorni and Natarajan (2013) upgraded the whiteness and plasticity of kaolinite to a commercial grade by selective flocculation. Hematite-adapted *Bacillus subtilis* cells secreted more polysaccharides while kaolinite-adapted cells rendered the kaolinite more hydrophobic due to the expression of specific proteins. Mineral-specific *B. subtilis* cells selectively flocculated 90–95% of hematite at a neutral pH, while 80–85% of kaolinite was dispersed.

Given that bacterial cells enhance the floatability of minerals in conjunction with a collector (xanthates in sulfide ore flotation and amines and fatty acids in iron ore flotation), it is possible that the interaction between collector and cells could be used for improved environmental and economic effect. Process waters in flotation systems carry excess collectors that must be managed downstream to prevent contamination of any outflowing water supplies. Similarly, if collectors could be desorbed from the ore once flotation was completed, there would be less downstream control needed.

P. polymyxa was mixed with iron ore flotation reagents: 2 amine collectors (dodecylammonium acetate (DAA) and diamine DA-16), a fatty acid collector (sodium oleate), and a sulfide ore flotation collector (sodium isopropyl xanthate). The IEP of the cells mixed with the oleate and xanthate remained the same, but the amines caused increases in the IEP of the cells due to an increase in EPS proteins produced (Deo and Natarajan, 1998b). Given the enhanced biosorption of the amine collectors to the cells, it was not surprising that the cells and their metabolites could biodegrade the amine collectors more quickly than the oleate and xanthate. In addition, as they are organic compounds, the flotation collectors provided the carbon and nitrogen requirements for the growth of *P. polymyxa* (Deo and Natarajan, 1998b).

13.6 Future trends

Mining biotechnology will continue to expand in the future with the dwindling quality of mineral resources, higher demand for resources, and tighter restrictions by governments worldwide due to the changing climate, increasing pollution, and the necessity of creating sustainable industries for the future (Rankin, 2011). A major area of expansion will be in the processing of wastes and tailings, which are likely to contain higher metal concentrations in some situations than primary ore resources (Johnson, 2013).

Food security is already considered a worldwide problem with the expanding population, and sustaining arable land will become a greater priority. More phosphorus will need to be sourced to maintain current food crops. Using microorganisms to bioleach phosphorus from iron ore has the potential not only to upgrade the ore but also to provide an additional phosphorus resource for the agricultural industry.

All future iron ore projects worldwide will require considerable beneficiation so as to avoid economic penalties and extend the life of their resources. Detailed research has revealed that bacteria cells and their metabolites can be effective bioreagents for the specific flotation and flocculation of iron ore minerals, particularly when used in conjunction with traditional collectors and activators. The research has also revealed that the bacteria used for biobeneficiation of iron ores are similar to those capable of leaching phosphate, that is, the commercial acidophilic bioleaching bacteria and the soil bacteria.

Bioleaching microorganisms have the advantage over the soil bacteria as a carbon source does not need to be added to the process, and if any organics are present, they can be consumed by heterotrophic acidophiles (Xiao et al., 2013). However, these bacteria are not usually indigenous to an oxide environment where the pH is neutral, and the addition of these microorganisms to the native biodiversity may represent a potential environmental issue. Phosphate-solubilizing fungi and soil bacteria have been enriched from iron ore deposits (Pérez et al., 2007) and are likely to be ubiquitous to these environments; however, carbon sources would need to be added to the system for conversion to organic acids for the dephosphorization and biobeneficiation of iron ore.

Bacteria and/or their metabolites are not likely to be incorporated into current commercial beneficiation processes until a method of delivery and effective dosage is determined (Smith and Miettinen, 2006). Traditional flotation reagents like starch, amines, and xanthates are added in small concentrations compared to the concentration of cells and/or metabolites that would be needed. Freeze-dried cells as flotation collectors that are prepared in the laboratory and delivered to site may be an effective method (Smith and Miettinen, 2006), particularly if native soil bacteria from the site are used to prevent potential environmental problems. The cost of preparing freeze-dried cells and providing a carbon source on site is still likely to be prohibitive.

It is possible to genetically modify a bacterial species as a flotation or flocculation bioreagent, so that it is easier to generate and store and more effective so cell concentrations are lower. Farahat et al. (2008) modified a strain of *Escherichia coli* to carry and express a silica-induced cell surface protein (SIP). The SIP *E. coli* strain was hydrophobic and positively charged below its IEP of pH 4.5. Being amphoteric,

the surface charge of the cells was pH-dependent. In anionic flotation of quartz using sodium dodecyl sulfate as a collector, the SIP *E. coli* cells acted as a surface modifier, which increased the flotation of quartz from 28% to 85%.

Using genetically engineered bacteria in the environment could be damaging; however, using nonviable bioreagents from native soil bacteria would increase efficacy and be a cheaper proposition. The way forward for researchers could be to concentrate on one bacteria and endeavor to standardize methods for growth parameters, mass cell production, and EPS extraction prior to undertaking flotation and flocculation trials. A model microorganism would be the soil bacterium *P. polymyxa* which we have shown is highly effective in selectively separating iron oxides from associated gangues. In addition, it is relatively easy to grow, store and is a facultative anaerobe capable of iron reduction. In addition, metabolites from *P. polymyxa* have already been explored as growth promoters and antimicrobial compounds for plants (Lal and Tabacchioni, 2009). Using *P. polymxya* and ROM ore samples that have been prepared for traditional flotation (Moore, 2011) would enable researchers to target and identify the cell proteins and polysaccharides that would be effective bioreagents for commercial operations.

Acknowledgments

The authors wish to thank Liming Lu and Ka Yu Cheng for reviewing the manuscript, Kayley Usher for the scanning electron micrographs of *P. polymyxa*, and the CSIRO Mineral Resources Flagship for their financial support in this research.

References

Anand, P., Modak, J.M., Natarajan, K.A., 1996. Biobeneficiation of bauxite using *Bacillus polymyxa*: calcium and iron removal. Int. J. Miner. Process. 48, 51–60.

Arnold, R.G., DiChristina, T.J., Hoffmann, M.R., 1986. Reductive dissolution of Fe (III) oxides by *Pseudomonas* spp. 200. Biotechnol. Bioeng. 32, 1081–1096.

Bosecker, K., 1997. Bioleaching: metal solubilisation by microorganisms. FEMS Microbiol. Rev. 20, 591–604.

Botero, A.E.C., Torem, M.L., de Mesquita, L.M.S., 2007. Fundamental studies of *Rhodococcus opacus* as a biocollector of calcite and magnesite. Miner. Eng. 20, 1026–1032.

Botero, A.E.C., Torem, M.L., de Mesquita, L.M.S., 2008. Surface chemistry fundamentals of biosorption of *Rhodococcus opacus* and its effect in calcite and magnetite flotation. Miner. Eng. 2, 83–92.

Brandl, H., Bosshard, R., Wegmann, M., 2001. Computer-munching microbes: metal leaching from electronic scrap by bacteria and fungi. Hydrometallurgy 59, 319–326.

Brierley, C.L., Brierley, J.A., 2013. Progress in bioleaching: part B: applications of microbial processes by the minerals industries. Appl. Microbiol. Biotechnol. 97, 7543–7552.

Caccavo Jr., F., 1999. Protein-mediated adhesion of the dissimilatory Fe (III)-reducing bacterium *Shewanella alga* BrY to hydrous ferric oxide. Appl. Environ. Microbiol. 65 (11), 5017–5022.

Caccavo Jr., F., Frolund, B., Kloeke, F.V.O., Nielsen, P.H., 1996. Deflocculation of activated sludge by the dissimilatory Fe (III) reducing bacterium *Shewanella alga* BrY. Appl. Environ. Microbiol. 62 (4), 1487–1490.

Caccavo Jr., F., Schamberger, P.C., Keiding, K., Nielsen, P.H., 1997. Role of hydrophobicity in adhesion of the dissimilatory Fe (III)-reducing bacterium *Shewanella alga* to amorphous Fe (III) oxide. Appl. Environ. Microbiol. 63 (10), 3837–3843.

Chandraprabha, M.N., Natarajan, K.A., 2006. Surface chemical and flotation behaviour of chalcopyrite and pyrite in the presence of *Acidithiobacillus thiooxidans*. Hydrometallurgy 83, 146–152.

Chandraprabha, M.N., Natarajan, K.A., Modak, J.M., 2004a. Selective separation of pyrite and chalcopyrite by biomodulation. Colloids Surf. B 37B (3–4), 93–100.

Chandraprabha, M.N., Natarajan, K.A., Somasundaran, P., 2004b. Selective separation of arsenopyrite from pyrite by biomodulation in the presence of *Acidithiobacillus ferrooxidans*. J. Colloid Interface Sci. 276 (2), 323–332.

Crundwell, F.K., 2003. How do bacteria interact with minerals? Hydrometallurgy 71, 75–81.

Cruz, R., Lázaro, I., González, I. And, Monroy, M., 2005. Acid dissolution influences bacterial attachment and oxidation of arsenopyrite. Miner. Eng. 18, 1024–1031.

De Mesquita, L.M.S., Lins, F.F., Torem, M.L., 2003. Interaction of a hydrophobic bacterium strain in a hematite–quartz flotation system. Int. J. Miner. Process. 71 (1–4), 31–44.

Delvasto, P., Ballester, A., Muñoz, J.A., González, F., Blázquez, M.L., Garcia-Balboa, C., 2005. Exploring the possibilities of biological beneficiation of iron-ores: the phosphorus problem. In: 15th Steelmaking Conference, 5th Ironmaking Conference & 1st Environmental and Recycling Symposium IAS. Argentinean Steelmaking Institute (IAS), San Nicolas, Buenos Aires, Argentina.

Delvasto, P., Valverde, A., Ballester, A., Igual, J.M., Muñoz, J.A., Gonzáles, F., Blázquez, M.L., Garcia-Balboa, C., 2006. Characterization of brushite as a re-crystallization product formed during bacterial solubilisation of hydroxyapatite in batch cultures. Soil Biol. Biochem. 38, 2645–2654.

Delvasto, P., Valverde, A., Ballester, A., Muñoz, J.A., González, F., Blázquez, M.L., Igual, J.M., García-Balboa, C., 2008. Diversity and activity of phosphate bioleaching bacteria from a high phosphorus iron ore. Hydrometallurgy 92 (3–4), 124–129.

Delvasto, P., Ballester, A., Muñoz, J.A., Blázquez, M.L., Igual, J.M., Valverde, A., García-Balboa, C., 2009. Mobilization of phosphorus from iron ore by the bacterium *Burkholderia caribensis* FeGL03. Miner. Eng. 22 (1), 1–9.

Deo, N., Natarajan, K.A., 1997. Interaction of *Bacillus polymyxa* with some oxide minerals with reference to mineral beneficiation and environmental control. Miner. Eng. 10 (12), 1339–1354.

Deo, N., Natarajan, K.A., 1998a. Studies on interaction of *Paenibacillus polymyxa* with iron ore minerals in relation to beneficiation. Int. J. Miner. Process. 55 (1), 41–60.

Deo, N., Natarajan, K.A., 1998b. Biological removal of some flotation collector reagents from aqueous solutions and mineral surfaces. Miner. Eng. 11 (8), 717–738.

Deo, N., Natarajan, K.A., 1999. Role of corundum-adapted strains of *Bacillus polymyxa* in the separation of hematite and alumina. Miner. Metall. Process. 16 (4), 29–34.

Deo, N., Natarajan, K.A., Somasundaran, P., 2001. Mechanisms of adhesion of *Paenibacillus polymyxa* onto hematite, corundum and quartz. Int. J. Miner. Process. 62 (1–4), 27–39.

Dubel, J., Smith, R.W., Misra, M., Chen, S., 1992. Microorganisms as chemical reagents: the hematite system. Miner. Eng. 5 (3–5), 547–556.

Dwyer, R., Bruckard, W.J., Rea, S., Holmes, R.J., 2011. Bio-beneficiation of Australian iron ores-potential applications of indigenous bacteria for flotation, flocculation and

phosphorus removal. In: Proceedings Iron Ore 2011 Conference, 11–13th July, Perth, WA, Australia. The Australasian Institute of Mining and Metallurgy, Melbourne, pp. 397–402.

Dwyer, R., Bruckard, W.J., Rea, S., Holmes, R.J., 2012. Bioflotation and bioflocculation review: microorganisms relevant for mineral beneficiation. Miner. Process. Ext. Metall. 121 (2), 65–71.

Dwyer, R., Rea, S., McSweeney, N., Bruckard, W.J., Holmes, R., 2013. Microbes and their metabolites – potential iron ore flotation reagents. In: Proceedings Iron Ore 2013 Conference, 12–14th August, Perth, WA, Australia. The Australasian Institute of Mining and Metallurgy, Melbourne, pp. 369–372.

Edwards, C.I., Fisher-White, M.J., Lovel, R.R., Sparrow, G.J., 2011. Removal of phosphorus from Australian iron ores. In: Proceedings Iron Ore 2011 Conference, 11–13th July, Perth, WA, Australia. The Australasian Institute of Mining and Metallurgy, Melbourne.

Elmahdy, A.M., El-Mofty, S.E., Abdel-Khalek, M.A., Abdel-Khalek, N.A., El-Midany, A.A., 2013. Bacterially induced phosphate-dolomite separation using amphoteric collector. Sep. Purif. Technol. 102, 94–102.

Farahat, M., Hirajima, T., Sasaki, K., Aiba, Y., Doi, K., 2008. Adsorption of SIP *E. coli* onto quartz and its applications in froth flotation. Miner. Eng. 21 (5), 389–395.

Gehrke, T., Telegdi, J., Thierry, D., Sand, W., 1998. Importance of extracellular polymeric substances from *Thiobacillus ferrooxidans* for bioleaching. Appl. Environ. Microbiol. 64, 2743–2747.

Govender, Y., Gericke, M., 2011. Extracellular polymeric substances (EPS) from bioleaching systems and its application in bioflotation. Miner. Eng. 24, 1122–1127.

Halder, A.K., Mishra, A.K., Bhattacharyya, P., Chakrabartty, P.K., 1990. Solubilization of rock phosphate by *rhizobium* and *bradyrhizobium*. J. Gen. Appl. Microbiol. 36, 81–92.

Hermansson, M., 1999. The DLVO theory in microbial adhesion. Colloids Surf. B: Biointerfaces 14B (1–4), 105–119.

Holmes, R.J., 2010. CSIRO Carbon steel raw materials research. In: Singh, R., Das, A., Banerjee, P.K., Bhattacharyya, K.K., Goswami, N.G. (Eds.), Proceedings of the XI International Seminar on Mineral Processing Technology, Jamshedpur, India. pp. 527–534.

Hosseini, T.R., Kolahdoozan, M., Tabatabaei, Y.S.M., Oliazadeh, M., Noaparast, M., Eslami, A., Manafi, Z., Alfantazi, A., 2005. Bioflotation of Sarcheshmeh copper ore using *Thiobacillus ferrooxidans* bacteria. Miner. Eng. 18, 371–374.

Houot, R., 1983. Beneficiation of iron-ore by flotation—review of industrial and potential applications. Int. J. Miner. Process. 10 (3), 183–204.

Jefferson, K.K., 2004. What drives bacteria to produce a biofilm? FEMS Microbiol. Lett. 236 (2), 163–173.

Jiang, D., Huang, Q., Cai, P., Rong, X., Chen, W., 2007. Adsorption of *Pseudomonas putida* on clay minerals and iron oxide. Colloids Surf. B Biointerfaces 54, 217–221.

Johnson, D.B., 2013. Development and application of biotechnologies in the metal mining industry. Environ. Sci. Pollut. Res. 20, 7768–7776.

Lal, S., Tabacchioni, S., 2009. Ecology and biotechnological potential of *Paenibacillus polymyxa*: a minireview. Indian J. Microbiol. 49, 2–10.

Liu, H., Gu, G., Xu, Y., 2011. Surface properties of pyrite in the course of bioleaching by pure culture of *Acidithiobacillus ferrooxidans* and a mixed culture of *Acidithiobacillus ferrooxidans* and *Acidithiobacillus thiooxidans*. Hydrometallurgy 108, 143–148.

Lizama, H.M., Jensen, S.E., Stradling, A.W., 2003. Dynamic microbial populations in heap leaching of zinc sulfide ore. Miner. Eng. 25, 54–58.

Ma, M., Bruckard, W.J., Holmes, R., Gontijo, C., 2013. Impurity removal in the reverse flotation of iron ore. In: Iron Ore Conference, Perth, WA, 12–14 August, pp. 427–429.

Merma, A.G., Torem, M.L., Morán, J.J.V., Monte, M.B.M., 2013. On the fundamental aspects of apatite and quartz flotation using a gram positive strain as a bioreagent. Miner. Eng. 48, 61–67.

Mishra, M., Pradhan, M., Sukla, L.B., Mishra, B.K., 2011. Microbial beneficiation of Salem iron ore using *Penicillium purpurogenum*. Metall. Mater. Trans. B 42B, 13–19.

Misra, M., Chen, S., Smith, R.W., Raichur, A.M., 1993. *Mycobacterium phlei* as a flotation collector for hematite. Miner. Metall. Process. 10 (4), 170–175.

Misra, M., Bukka, K., Chen, S., 1996. The effect of growth medium of *Thiobacillus ferrooxidans* on pyrite flotation. Miner. Eng. 9 (2), 157–168.

Moore, P., 2011. Samarco—an iron ore pioneer. International Mining GEMS 12, 8–16.

Mudd, G.M., 2009. The sustainability of mining in Australia: key production trends and their environmental implications for the future. Research report no. RR5, Department of Civil Engineering, Monash University and Mineral Policy Institute.

Nagaoka, T., Ohmura, N., Saiki, H., 1999. A novel mineral flotation process using *Thiobacillus ferrooxidans*. Appl. Environ. Microbiol. 65 (8), 3588–3593.

Natarajan, K.A., Deo, N., 2001. Role of bacterial interaction and bioreagents in iron ore flotation. Int. J. Miner. Process. 62, 143–157.

Natarajan, K.A., Modak, J.M., Anand, P., 1997. Some microbiological aspects of bauxite mineralization and beneficiation. Miner. Metall. Process. 14 (2), 47–53.

Netscher, T., 2013. Australia's newest iron ore producer (http://gindpublic.powercreations.com.au/images/gind-veeweiyexe.pdf).

Noël, N., Florian, B., Sand, W., 2010. AFM & EFM study on attachment of acidophilic leaching organisms. Hydrometallurgy 104, 370–375.

Olson, G.J., Brierley, J.A., Brierley, C.L., 2003. Bioleaching review part B: progress in bioleaching: applications of microbial processes by the minerals industries. Appl. Microbiol. Biotechnol. 63, 249–257.

Omar, S.A., 1998. The role of rock-phosphate-solubilising fungi and vesicular-arbuscular-mycorrhiza (VAM) in growth of wheat plants fertilized with rock phosphate. World J. Microbiol. Biotechnol. 14, 211–218.

Omoike, A., Chorover, J., 2006. Adsorption to goethite of extracellular polymeric substances from *Bacillus subtilis*. Geochim. Cosmochim. Acta 70, 827–838.

Parks, E.J., Olson, G.J., Brinckman, F.E., Baldi, F., 1990. Characterization by high performance liquid chromatography (HPLC) of the solubilization of phosphorus in iron ore by a fungus. J. Ind. Microbiol. Biotechnol. 5, 1367–5435.

Patra, P., Natarajan, K.A., 2003. Microbially-induced flocculation and flotation for pyrite separation from oxide gangue minerals. Miner. Eng. 16, 965–973.

Patra, P., Natarajan, K.A., 2004. Microbially induced flotation and flocculation of pyrite and sphalerite. Colloids Surf. B Biointerfaces 36B (2), 91–99.

Patra, P., Natarajan, K.A., 2008. Role of mineral specific bacterial proteins in selective flocculation and flotation. Int. J. Miner. Process. 88 (1–2), 53–58.

Pecina-Treviño, E.T., Ramos-Escobedo, G.T., Gallegos-Acevedo, P.M., López-Saucedo, F.J., Orrantia-Borunda, E., 2012. Bioflotation of sulfide minerals with *A. ferrooxidans* in relation to copper activation and surface oxidation. Can. J. Microbiol. 58, 1073–1083.

Pérez, E., Sulbarán, M., Ball, M.M., Yarzábal, L.A., 2007. Isolation and characterisation of mineral phosphate-solubilizing bacteria naturally colonizing a limonitic crust in the south-eastern Venezuelan region. Soil Biol. Biochem. 39, 2905–2914.

Poorni, S. And, Natarajan, K.A., 2013. Biomediated separation of kaolinite and hematite using *Bacillus subtilis*. Adv. Mater. Res. 825, 223–226.

Prakasan, M.R.S., Natarajan, K.A., 2010. Microbially induced separation of quartz from hematite using sulfate reducing bacteria. Colloids Surf. B Biointerfaces 78, 163–170.
Raichur, A.M., Misra, M., Bukka, K., Smith, R.W., 1996. Flocculation and flotation of coal by adhesion of hydrophobic *Mycobacterium phlei*. Colloids Surf. B Biointerfaces 8B (1–2), 13–24.
Raichur, A.M., Misra, M., Davis, S.A., Smith, R.W., 1997. Flocculation of fine coal using synthetic and biologically derived flocculants. Miner. Metall. Process. 14 (1), 22–26.
Rankin, W.J., 2011. Towards sustainability. In: Minerals, Metals and Sustainability. CSIRO Publishing, Victoria, Australia, pp. 367–381 (Chapter 17).
Rawlings, D.E., 2002. Heavy metal mining using microorganisms. Annu. Rev. Microbiol. 56, 65–91.
Riekkola-Vanhanen, M., 2013. Talvivaara mining company—from a project to a mine. Miner. Eng. 48, 2–9.
Rijnaarts, H.H.M., Norde, W., Lyklema, J., Zehnder, A.J.B., 1995. The isoelectric point of bacteria as an indicator for the presence of cell surface polymers that inhibit adhesion. Colloids Surf. B Biointerfaces, 4, 191–197.
Rodríguez, H., Fraga, R., 1999. Phosphate solubilizing bacteria and their role in plant growth promotion. Biotechnol. Adv. 17, 319–339.
Rohwerder, T., Gehrke, T., Kinzler, K., Sand, W., 2003. Bioleaching review part A: progress in bioleaching: fundamentals and mechanisms of bacterial metal sulfide oxidation. Appl. Microbiol. Biotechnol. 63, 239–248.
Sand, W., Gehrke, T., 2006. Extracellular polymeric substances mediate bioleaching/biocorrosion via interfacial processes involving Fe^{3+} and acidophilic bacteria. Res. Microbiol. 157, 49–56.
Sand, W., Gehrke, T., Hallman, R., Schippers, A., 1995. Sulfur chemistry, biofilm, and the (in) direct attack mechanism—a critical evaluation of bacterial leaching. Appl. Microbiol. Biotechnol. 43, 961–966.
Santhiya, D., Subramanian, S., Natarajan, K.A., 2000. Surface chemical studies on galena and sphalerite in the presence of *Thiobacillus thiooxidans* with reference to mineral beneficiation. Miner. Eng. 13 (7), 747–763.
Santhiya, D., Subramanian, S., Natarajan, K.A., 2002. Surface chemical studies on sphalerite and galena using extracellular polysaccharides isolated from *Bacillus polymyxa*. J. Colloid Interface Sci. 256 (2), 237–248.
Sharma, P.K., Hanumantha Rao, K., 2003. Adhesion of *Paenibacillus polymyxa* on chalcopyrite and pyrite: surface thermodynamics and extended DLVO theory. Colloids Surf. B Biointerfaces 29, 21–38.
Sharma, P.K., Rao, K.H., Forssberg, K.S.E., Natarajan, K.A., 2001. Surface chemical characterisation of *Paenibacillus polymyxa* before and after adaptation to sulfide minerals. Int. J. Miner. Process. 62 (1–4), 3–25.
Shen, S., Rao, R., Wang, J., 2012. Application of indigenous sulfur-oxidizing bacteria from municipal wastewater to selectively bioleach phosphorus from high-phosphorus iron ore: effect of particle size. Environ. Technol. 34 (1–4), 173–180.
Smith, R.W., Miettinen, M., 2006. Microorganisms in flotation and flocculation: future technology or laboratory curiosity? Miner. Eng. 19 (6–8), 548–553.
Smith, R.W., Misra, M., Chen, S.Z., 1993. Adsorption of a hydrophobic bacterium onto hematite—implications in the froth flotation of the mineral. J. Ind. Microbiol. 11 (2), 63–67.
Solari, J.A., Huerta, G., Escobar, B., Vargas, T., Badilla-Ohlbaum, R., Rubio, J., 1992. Interfacial phenomena affecting the adhesion of *Thiobacillus ferrooxidans* to sulfide mineral surfaces. Colloids Surf. 69, 159–166.

Somasundaran, P., Deo, N., Deo, P., Natarajan, K.A., 2005. Role of biopolymers on bacterial adhesion and mineral beneficiation. Miner. Metall. Process. 22 (1), 1–11.

van der Mei, H.C., Bos, R., Busscher, H.J., 1998. A reference guide to microbial cell surface hydrophobicity based on contact angles. Colloids Surf. B Biointerfaces 11, 213–221.

Vasanthakumar, B., Ravishankar, H., Subramanian, S., 2012. A novel property of DNA—as a bioflotation reagent in mineral processing. PLoS One 7 (7), e39316.

Vijayalakshmi, S.P., Raichur, A.M., 2002. Bioflocculation of high-ash Indian coals using *Paenibacillus polymyxa*. Int. J. Miner. Process. 67, 199–210.

Vijayalakshmi, S.P., Raichur, A.M., 2003. The utility of *Bacillus subtilis* as a bioflocculant for fine coal. Colloids Surf. B Biointerfaces 29, 265–275.

Whitelaw, M., Harden, T., Heylar, K., 1999. Phosphate solubilisation in solution culture by the soil fungus *Penicillium radicum*. Soil Biol. Biochem. 31, 655–665.

Williams, P.J., Cloete, T.E., 2010. The use of *Aspergillus niger* for the removal of phosphorous and potassium from the iron ore concentrate of the Sishen Iron Ore Mine, South Africa. World J. Microbiol. Biotechnol. 2008 24, 2531–2538.

Xiao, C., Chi, R., Fang, Y., 2013. Effects of *Acidiphilium cryptum* on biosolubilization of rock phosphate in the presence of *Acidithiobacillus ferrooxidans*. Trans. Nonferrous Metals Soc. China 23, 2153–2159.

Yee, N., Fein, J.B., Daughney, C.J., 2000. Experimental study of the pH, ionic strength, and reversibility behaviour of bacteria–mineral adsorption. Geochim. Cosmochim. Acta 64 (4), 609–617.

Zheng, X., Arps, P.J., Smith, R.W., 2001. Adhesion of two bacteria onto dolomite and apatite: their effect on dolomite depression in anionic flotation. Int. J. Miner. Process. 62, 159–172.

Iron ore sintering

14

L. Lu[1], *O. Ishiyama*[2]
[1]CSIRO Mineral Resources Flagship, Pullenvale, QLD, Australia
[2]Nippon Steel & Sumitomo Metal Corporation, Futtsu, Chiba-Pref., Japan

14.1 Introduction

Sintering is a thermal process of converting loose fine particles into a solid coherent mass by heat and/or pressure without fully melting the particles to the point of melting. In the sintering process, the atoms in the materials and minerals move across the boundaries of the particles by either diffusion or assimilation, which are fused together to form one solid piece. Sintering happens naturally in mineral deposits under the impact of heat and pressure. It has been widely used as a manufacturing process in the field of materials science and a raw material preparation step in mineral processing. This chapter focuses on the application of the sintering process as an important raw material preparation step for the production of hot metal in blast furnaces in integrated steel mills, which account for about 70% of the world's steel production annually.

14.1.1 Sintering process for iron ore fines

Like other sintering processes, iron ore sintering converts iron ore fines of often −8 mm sizing into larger agglomerates, namely, sinter, between 5 and 50 mm particle size, which possess the physical and metallurgical characteristics and gas permeability required for efficient blast furnace operation. As shown in Figure 14.1, iron ore sintering is carried out in three stages: raw material preparation, ignition and firing, as well as cooling.

The sintering process begins with the preparation of a sinter mixture consisting of iron ore fines, fluxes, solid fuel (called bonding agents in Japan) such as coke breeze, and return fines from the sinter plant and blast furnace as well as recycled ferruginous materials from downstream iron and steelmaking processes. After being mixed in a rotating drum, water is then added to the mixture. Granulation is carried out in the same or a different rotating drum by controlling the moisture content and particle motion of the sinter mixture, sometimes with the help of binders, to form agglomerates of the sinter mixture or granules (also called micropellets, quasiparticles, or pseudoparticles). These granules are much coarser compared with the original sinter mixture and assist in obtaining optimum permeability of the sinter mixture during the sintering process.

The moistened granules of the sinter mixture are then loaded to a depth of typically 0.5–1 m on a sinter strand, which is a continuous grate moving continuously at typically 2–3 m/min. The sinter strand is normally about 4–6 m wide with

Iron Ore. http://dx.doi.org/10.1016/B978-1-78242-156-6.00014-9
© 2015 Elsevier Ltd. All rights reserved.

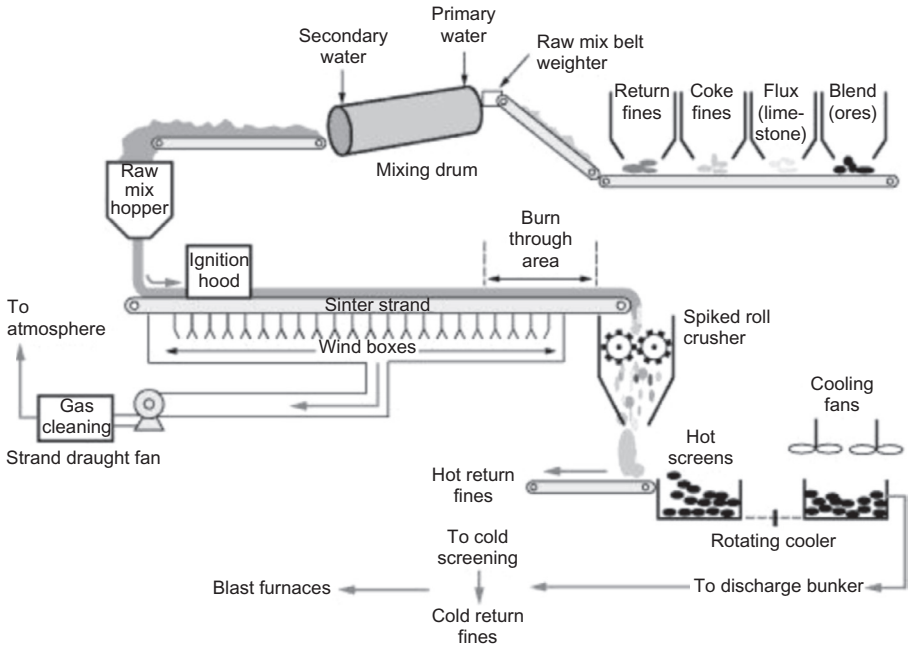

Figure 14.1 Schematic diagram showing the material flow in a sinter plant (Anon 1, 2014).

an effective sintering area of up to 600 m^2 and is covered generally with a layer of sized sinter screened out from the sinter product as a bedding material for the protection of the grates. After the granules are loaded and leveled on the sinter machine, the sinter bed passes a series of gas or oil burners, which heat the granules and ignite the coke particles at the surface of sinter bed. The heat generated from combustion of the coke particles continues to raise the temperature of successive layers of the sinter bed to generate a melt phase first from adhering fines and then by assimilation of coarse nucleus particles, which on cooling solidifies into a sinter matrix that bonds the initially loose iron ore particles into lumps of clinker-like material. The peak temperature of the burning coke layer (also called the flame front) reaches approximately 1300–1375 °C. The downdraft suction applied to the sinter bed helps to preheat the air sucked in from the top, to cool the sintered bed, and to heat and ignite the coke particles in the layer below the flame front. This allows the sintering of the iron ore granules on the grate to move downward with the flame front, while the grate proceeds horizontally toward the discharge point of the strand. The sinter strand speed and gas flow are so controlled that "burn through" (i.e., the point at which the flame front reaches the base of the strand) occurs just prior to the hot sinter being discharged.

At the end of the strand, the sintered product in the form of cake falls off the grate into a hot sinter breaker (primary crusher) where the hot sinter cake is crushed to a predetermined top particle size of typically 150–200 mm. The hot crushed sinter is

sometimes screened to remove hot return fines and then discharged onto a straight or annular cooler, which cools the sinter down to about 150 °C. After the cooler, coarse sinter particles of larger than 50–75 mm are usually crushed by a secondary crusher and conveyed to the screening station where the product sinter, hearth material, and return fines are separated. The return fines, which are too fine and not suitable for use in blast furnaces (generally 5 mm or under in particle size), are conveyed back to a bin for recycling in the sintering process.

The off-gas from selected zones of the sinter machine is sometimes mixed with cooler off-gas and/or ambient air and recirculated to the sinter machine by a sintering flue gas recirculation system or Emissions Optimized Sintering (EOS®) system. This process not only allows savings in bonding agents due to the contribution of CO postcombustion and recirculated heat but also reduces the volume of waste gas and emissions from a sinter plant. For detailed information on EOS® and sintering flue gas recirculation systems, please refer to Chapter 18 on sintering emissions and their mitigation technologies. The off-gas from other zones of the sinter machine is treated by a series of treatment steps after the primary dedusting step (e.g., an electrostatic precipitator or multi-cyclones) to reduce dust, acid gases, as well as harmful metallic and organic components. Selective catalytic reduction, where V_2O_5 is used as a catalyst to reduce NO_x into N_2, is often applied to remove NO_x in the off-gas. SO_x removal is achieved via installation of sintering flue gas desulfurization equipment. In addition to the conventional wet-type systems using limestone/lime, $Mg(OH)_2$, or ammonia as absorbent, dry-type desulfurizing systems utilizing activated coke adsorption are now used. These systems not only are effective for desulfurization but also are effective for the removal of NO_x and dioxins.

14.1.2 Application of iron ore sinter

Sintering is the most economic and widely used agglomeration process for preparing iron ore fines for blast furnace use. The product of the sintering process is conveyed and charged into the blast furnace for the production of hot metal. The countercurrent principle on which the blast furnace operates makes it heavily reliant on the quality and size of its burden materials to maintain a sufficient level of gas permeability in its upper shaft and liquid and gas permeability in its lower part. As shown in Figure 14.2, iron ore sinter typically constitutes more than 60% of the ferrous burden in modern blast furnaces in Japan and most of the blast furnaces in Europe.

Based on its chemistry, sinter is classified into acid, self-fluxing, and super-fluxed sinter. Self-fluxing sinter brings the lime required to flux its acid components (SiO_2 and Al_2O_3), while super-fluxed sinter contains extra CaO for the blast furnace. The majority of sinter currently being produced has a binary basicity of 1.7 or above. Compared with pellets, production of sinter is cheaper, while compared with lump ore, fluxed sinter is often more reducible with better softening characteristics. It brings the calcination reaction of limestone ($CaCO_3 \rightarrow CaO + CO_2$) outside the blast furnace, hence reducing the heat consumption of the blast furnace. Of course, sinter needs to meet a minimum quality for use in the blast furnace. This will be discussed in detail in Chapter 16 on the quality requirements of iron ore for iron production.

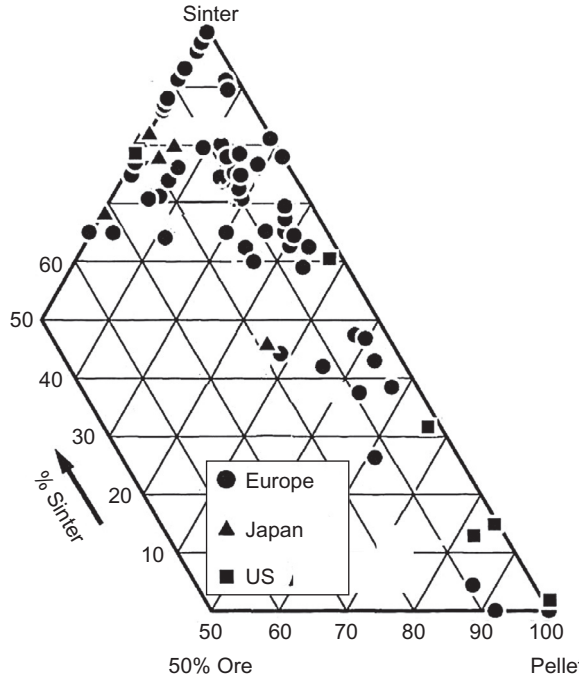

Figure 14.2 Burden compositions of various blast furnaces in Europe, Japan, and the United States.
Modified from the figure by Matsui et al. (2003).

14.2 Effect of iron ore characteristics on sintering

Granulation and thermal densification are two important steps of iron ore sintering and determine the quality of the resultant sinter and the performance of the sintering process. The effect of iron ore characteristics on sintering is mainly through their impact on the granulation and densification processes. Iron ore is typically characterized chemically, physically, and mineralogically. The following section is devoted to the effect of iron ore chemical, physical, and mineralogical characteristics on the granulation and thermal densification processes during sintering.

14.2.1 Influence of ore characteristics on granulation

Apart from the formation of granules in the sinter mixture to achieve better permeability, the granulation process also captures fine ores from dust emissions and facilitates the even distribution of bonding agents and fluxes required for the agglomerated product. The principal mechanism for the granulation process is the layering of adhering fine particles onto coarser nucleus particles (Litster and Waters, 1990). Initially, an inner layer of very fine material attaches to the nucleus particles and then an outer layer is added that contains some larger particles, intermediate between very fine material and nucleus particles (Roller, 1982).

The granulation efficiency is generally believed to be dependent on the raw material characteristics and operating conditions, such as moisture content (Furui et al., 1977; Litster and Waters, 1988; Waters et al., 1989), binder addition (Furui et al., 1977), granulation time (Litster and Waters, 1990), and the speed and occupancy of the rotating drum (Kano et al., 2005). The granulation rate was found to increase with a decrease in occupancy and an increase in the rotating speed of the drum mixer. Pilot-scale granulation studies (Litster and Waters, 1990) showed that granulation time had a significant effect on sinter pot productivity, which further confirmed the importance of the granulation kinetics of iron ore. When the operating conditions are fixed, the granulation efficiency is mainly related to the characteristics of iron ore. The granulation kinetics and behavior of iron ore particles have been studied both experimentally and using the discrete element method (Kano et al., 2005). The influence of iron ore characteristics on granulation efficiency has been studied by many authors (Kano et al., 2005; Khosa and Manuel, 2007; Litster and Waters, 1986, 1988, 1990; Lv et al., 2011; Maeda et al., 2005; Maki and Sekiguchi, 2009; Matsumura et al., 2005; Roller, 1982; Sakamoto, 2002; Waters et al., 1989). The role of iron ore characteristics in granulation is discussed below.

14.2.1.1 Physical characteristics of iron ore

Iron ore fines are characterized on a physical basis by variations in particle size, shape, density, porosity, surface area, roughness, and wettability. Furui et al. (1977) divided iron ore particles into nucleus particles of +0.7 mm size, intermediate particles of −0.7 + 0.2 mm size, and adhering particles of −0.2 mm size. As the intermediate particles can act as neither nucleus particles nor adhering particles, they suggested that the proportion of intermediate particles should be as low as possible while maintaining an appropriate proportion of adhering fines and nucleus particles. However, the boundary limits between the three size groups vary with individual ores. Litster and Waters (1988) defined a particle size ($X_{0.5}$) at which half the particles act as adhering fines and half act as nuclei particles. High values of $X_{0.5}$ correspond to large mean granule sizes. In addition, $X_{0.5}$ was found to decrease with increasing amounts of −0.25 mm particles, but it increases as the mass mean size of these particles decreases. $X_{0.5}$ is equivalent to the cutoff size between the nucleus and adhering particles and increases with the moisture available for granulation.

Figure 14.3 shows the mean size and morphology of green granules formed from the same iron ore fines, but with different loadings of ultrafine particles (−0.15 mm). It is clear that, while increasing the ultrafine particle loading does improve the morphology of the granules formed, it shifts the granule size distribution to finer sizes and reduces the mean granule size. Overall, increasing the loading of ultrafine particles from 20% to 40% results in severe deterioration in the structure and permeability of the green granule bed. This is in agreement with findings reported in the literature (Litster and Waters, 1988; Nagano et al., 1985) that granulation efficiency decreases with increasing amounts of fines.

Other physical characteristics, such as porosity, shape, and surface characteristics, can also affect granulation performance. Hida et al. (1982) found that surface roughness was also important. A rough surface of nucleus particles promotes layering of adhering fines. In addition, as the bonding forces in the adhering fines layer are

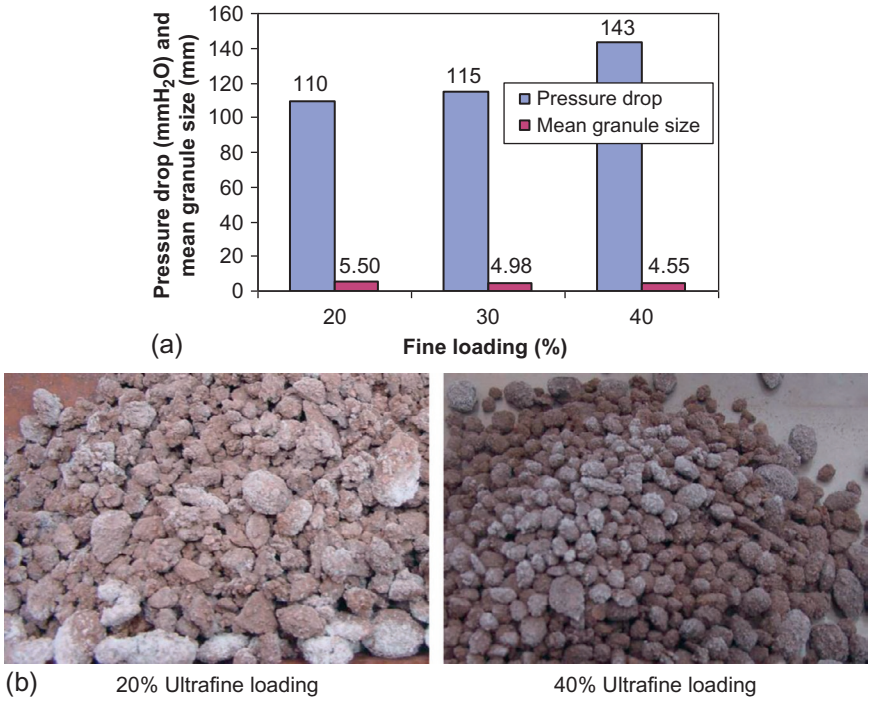

Figure 14.3 (a) Pressure drop across a 250 mm deep × 150 mm diameter bed at an airflow rate of 400 l/min and mean particle sizes and (b) morphology of green granules (+4 mm) formed from iron ore fines with different loadings of ultrafine particles.

primarily capillary forces due to the presence of water, interfacial phenomena, such as wettability and hydrophilicity, between iron ore particles and water are important. Mao et al. (2013) found that the granulation performance of iron ore improves as the contact angle between iron ore and water decreases. The effect of particle porosity and shape will be discussed together with the role of ore mineralogy, because they are both closely related to ore mineralogy.

14.2.1.2 Mineralogical characteristics of iron ore

Ore mineralogy affects the shape and size distribution of iron ore particles. In the same crushing circuit, friable ore textures tend to generate more fine materials. Ore particles of different mineralogical characteristics also tend to have different physical characteristics and are subject to different breakage mechanisms when crushed. As a result, some ore particles, such as Ore A (hard and uniform ore types, which tend to undergo brittle fracturing) in Figure 14.4, are found to be platy with angular edges, while others (including microporous textures, which tend to undergo size reduction by abrasion), such as Ore B in Figure 14.4, are often equigranular or well rounded. Hida et al. (1982) and Roller (1982) pointed out the importance of particle shape in granulation. As shown in Figure 14.4, Ores B and C have equigranular morphology and are relatively coarse with low amounts of ultrafine and intermediate particles, so

Figure 14.4 Effect of ore particle shape on the morphology and structure of green granules.

both ores granulate effectively with well-developed coatings. The platy, angular morphology of Ore A does not favor the embedding of adhering fines onto the surface of its particles, however, resulting in less distinct adhering fine coatings. While Ores A and C have a similar size distribution, Ore C also contains abundant goethitic ultrafine particles, which adhere effectively to the surface of large particles and bind other fine particles together.

The pore structure of ore particles plays an important role in determining granulation efficiency, because it influences their ability to absorb and hold moisture and the amount of moisture available for granulation at certain mix moisture contents. The porosity of iron ore particles is closely related to the mineralogical characteristics of iron ore, as evidenced in Figure 14.5a. The granulation efficiency is a strong function of the amount of moisture available for granulation, which is the total moisture present less the moisture absorbed and stored in the pores. The amount of moisture required for granulation was found to vary widely with ore type (Furui et al., 1977; Litster and Waters, 1988). The CSIRO moisture saturation measurement determines the capacity of an ore to hold water before dripping out, and therefore, it reflects the porosity of an ore. Based on the authors' studies in Figure 14.5b, it is clear that ores with a higher moisture saturation value need more water to achieve good granulation efficiency. This is because intraparticle pores need to be largely filled before surface water becomes available for interparticle adhesion. Therefore, the moisture saturation value of iron ore provides a good indication of the amount of water required for effective granulation.

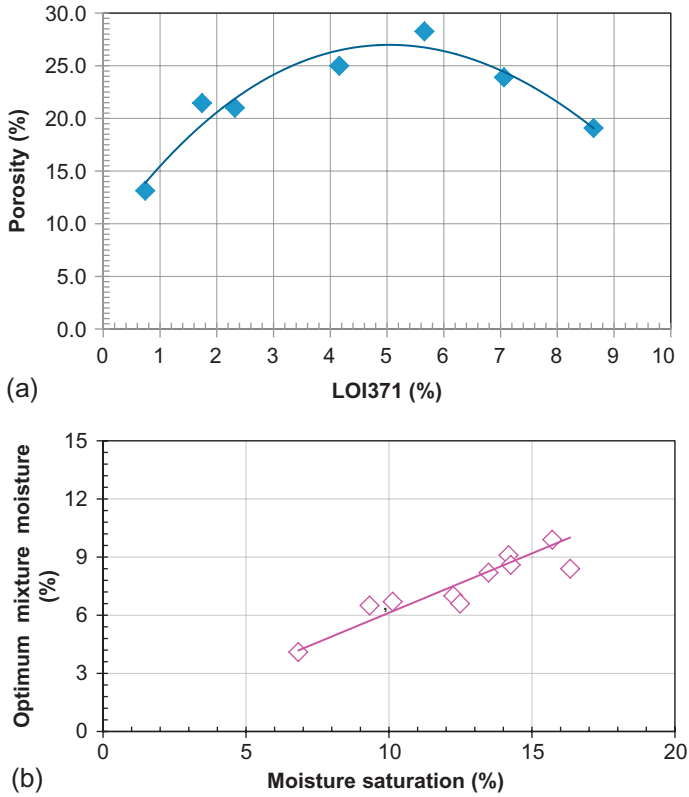

Figure 14.5 Influence of ore mineralogy on (a) particle porosity and (b) optimum mix moisture content for effective granulation.

14.2.1.3 Chemical characteristics of iron ore

Granulation is generally considered to be a physical process involving the physical interactions of particles mainly through capillary forces. The influence of ore chemical characteristics on granulation is therefore largely neglected in the literature. However, from the authors' experience on deslimed ores, the desliming process was found to affect the granulation efficiency of ore adversely. Apart from its impact on the amount of ultrafine particles, the desliming process also removes the aluminosilicates, which are predominantly present in the ultrafine particles. Both ultrafine particles and aluminosilicates are an integral part of the granulation process. As a result, deslimed ores granulate less effectively.

In summary, Figure 14.6 summarizes the Japanese permeability unit (JPU) versus mixture moisture content curves for various ores commercially available. While the ores show similar trends with mix moisture content, each ore achieves its distinct optimum permeability at its own specific mix moisture content. It is generally appreciated that the size distribution of an ore impacts more on permeability, while the porosity of an ore determines the optimum mixture moisture content where the optimum permeability is achieved.

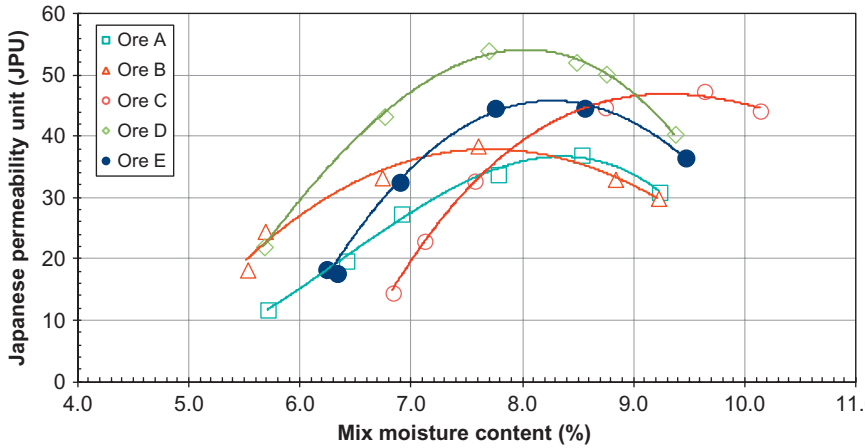

Figure 14.6 JPU permeability vs. mixture moisture curves for different ores.

14.2.2 Effect of ore characteristics on thermal densification

Unlike sintering of metallic powder in powder metallurgy where particles are bonded by solid diffusion at temperatures below the melting point, fluxes are added in iron ore sintering to react with fine iron ore particles at the flame front to form an initial melt of low melting point. The initial melt continues to react with nearby iron ore particles on heating and solidifies upon cooling to form a matrix to bond relict particles together. Densification is the act of reducing the porosity of a sample, thereby making it denser. Hence, densification enhances properties, for example, strength, of samples such as sinter. Densification occurs at the flame front during iron ore sintering via the following mechanisms:

- *Rearrangement* of granules packed at the flame front—as the initial melt forms, capillary action pulls the melt into pores and also causes unreacted particles to rearrange into a more favorable packing arrangement.
- *Assimilation–precipitation*—smaller and reactive particles are assimilated preferentially when in contact with the initial melt to contribute to the final melt, which precipitates on larger relict particles, leading to densification.
- *Final densification*—densification of the solid skeletal network, leading to melt movement from efficiently packed regions into pores.

Therefore, the densification process during iron ore sintering involves the creation of capillary pressure, which forces the sinter melt to spread into the pores within the packed granule bed. Therefore, granulation affects not only the airflow and efficiency of the sintering process but also the densification process in the granule bed during sintering. The effect of iron ore characteristics on granulation has been discussed in detail earlier. This section focuses on the effect of iron ore characteristics on the properties of the sinter melt, particularly melting temperature, viscosity, and surface tension, which are important to the densification process. The melting temperature, surface tension, and viscosity of the sinter melt are important because they affect the spread of the sinter melt. As the melt spreads, it assimilates the fine reactive ore particles.

Assimilation of ore particles will inevitably change the composition and properties of the sinter melt and consequently the spreading of the sinter melt. Of course, sintering temperature is also an important parameter in determining the densification process, because at higher temperatures, the melt viscosity decreases and the amount of melt increases. However, this is not within the scope of this chapter.

14.2.2.1 Chemical characteristics of iron ore

Chemically, iron ore fines consist mainly of various iron oxides, including hydrated oxides and oxyhydroxides, and small amounts of gangue minerals. While the majority of the iron present in iron ore fines is typically in the form of hematite (Fe_2O_3), some iron ore fines also contain a considerable amount of goethite (FeO(OH)), magnetite (Fe_3O_4), and other metastable forms of iron oxides. Key impurities in iron ore fines include SiO_2, Al_2O_3, S, P, MgO, and CaO, as well as varying amounts of components responsible for loss on ignition (LOI). The LOI components predominantly include hydrated iron oxides and to a lesser extent carbonates and other volatile minerals. Since the LOI components are closely related to the ore mineralogy, their impact is discussed in a later section on ore mineralogy. Iron ore fines from certain regions around the world may also contain certain amounts of minerals containing Ti, V, Cu, As, Cl, and alkali elements. Ti was found to have a deleterious impact on sinter quality (Bristow and Loo, 1992), while Cl can cause serious environmental problems during sintering (Ooi and Lu, 2011). The following discussion is focused on the key impurities, in particular SiO_2 and Al_2O_3.

From the data published (Tsukihashi and Kimura, 2003; Kongoli et al., 2003; Kimura et al., 2005), the chemical composition of melt formed during iron ore sintering is believed to fall within the range of the ferrous calcium silicate slag system. There has been a considerable amount of work on the physicochemical properties of different oxide melts based on the FeO_x–CaO–SiO_2 ternary system. While significant impacts of alumina on the properties of oxide melts have been reported (Tsukihashi and Kimura, 2003; Kongoli et al., 2003; Kimura et al., 2005; Pownceby and Clout, 2002; Kongoli, 2003; Machida et al., 2005), most of the data reported in the literature to date have been collected at compositions, thermal conditions, or oxygen partial pressures not relevant to the conditions encountered during the normal sintering process. According to Tsukihashi and coworkers (Kimura et al., 2005; Tsukihashi and Kimura, 2003), the addition of alumina up to 5% under oxygen partial pressures ranging from 1.8×10^{-3} to 10^{-1} Pa at 1573 K enlarges the liquid phase field slightly, which is particularly important for keeping the sinter mixture molten over a wide range (Figure 14.7a). This agrees with the results reported by other authors (Hino et al., 2003; Chen et al., 2010; Pownceby and Clout, 2002) that alumina in the ore lowers the temperature at which primary melt forms during sintering, but contrasts with the general belief that alumina is not a good flux based on the rationale that alumina behaves like a kind of refractory material with a high melting temperature. By using the computer package FLOGEN™, Kongoli et al. (Kongoli et al., 2003; Kongoli, 2003) tried to quantify the effect of alumina on the same system at 1523 K and 10^{-3} Pa, with alumina varying from 0% to 7%. As shown in Figure 14.7b, their results agree with the

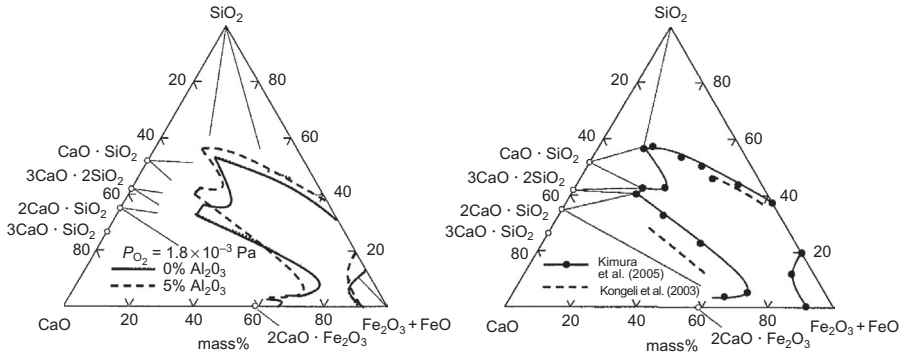

Figure 14.7 (a) Effect of alumina addition on the liquid field of the CaO–SiO_2–FeO_x system under $P_{O_2} = 1.8\times10^{-3}$ Pa at 1573 K (Kimura et al., 2005) and (b) comparison of observed (5% Al_2O_3, $P_{O_2} = 1.8\times10^{-3}$ Pa, 1573 K) and calculated (3% Al_2O_3, $P_{O_2} = 10^{-3}$ Pa, 1523 K) liquidus for the CaO–SiO_2–FeO_x–Al_2O_3 system (Kongoli et al., 2003; Kimura et al., 2005; Kongoli, 2003).

work conducted by Kimura and coworkers reasonably well (Tsukihashi and Kimura, 2003; Kimura et al., 2005).

Figure 14.8 shows the effect of SiO_2, Al_2O_3, and MgO on the viscosity of a simulated initial sinter melt formed from a low melting point composition within the Fe_2O_3–CaO binary system (Machida et al., 2005). It is clear that, at a constant temperature, the viscosity of the simulated melt increases with the addition of SiO_2, Al_2O_3, and MgO. At the sintering temperature of about 1300 °C, Al_2O_3 and MgO have a more profound effect on viscosity than SiO_2. The rapid increase in viscosity in Figure 14.8 is most likely related to the precipitation of solid phases. Figure 14.9 presents optical micrographs showing the effect of SiO_2, Al_2O_3, and MgO on the pore structure of laboratory sinters (Loo and Leung, 2003). Due to their impact on melt viscosity, the

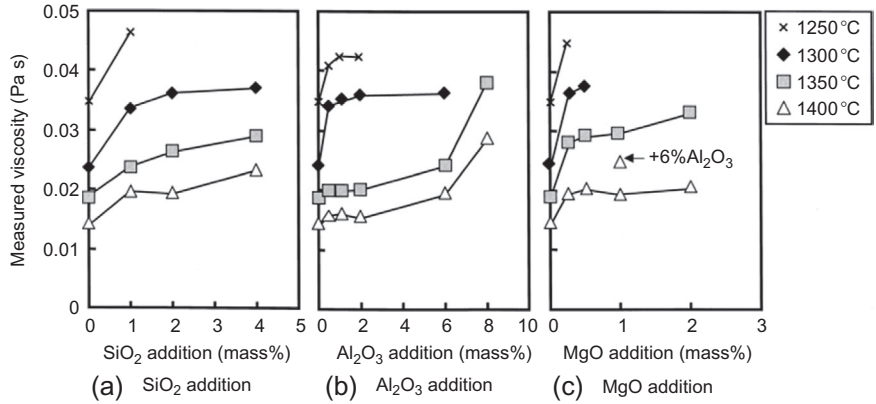

Figure 14.8 Effect of (a) SiO_2, (b) Al_2O_3, and (c) MgO on the viscosity of a simulated initial sinter melt generated from an 80% Fe_2O_3–20% CaO system (Machida et al., 2005).

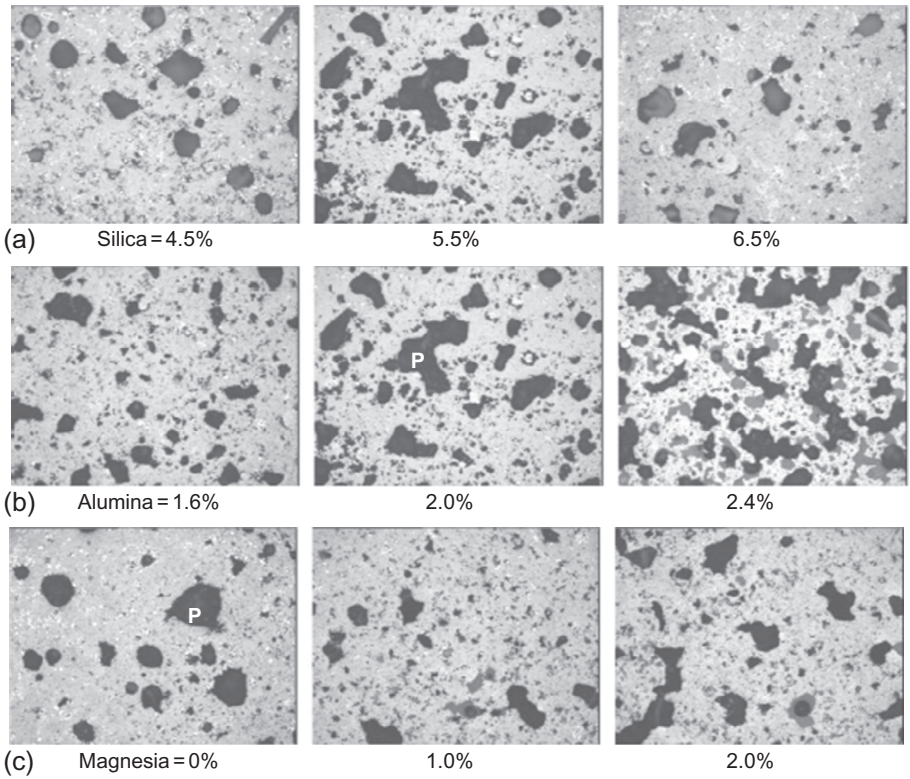

Figure 14.9 Optical micrographs showing the effect of (a) SiO_2, (b) Al_2O_3, and (c) MgO on the pore structure of laboratory sinters (Loo and Leung, 2003). The dark areas labeled as P in the images are pores.

gangue minerals therefore affect densification of the sintering mass and consequently the pore structure of the sinters. This will have a drastic impact on sinter strength, size, and yield. As shown in Figure 14.9a, the pore area was the highest at a silica content of 5.5%. When the silica content was increased or decreased from the base level of 5.5%, there was a greater degree of melt reshaping, resulting in more rounded pores. Figure 14.9b shows the effect of alumina on the pore structure of laboratory sinters. As the Al_2O_3 content increases, the pore area increases and the pore shape changes from well rounded, to irregular, to interconnected. It is apparent that as the Al_2O_3 content increases, the melt fluidity decreases, which reduces the ability of the bubbles in the melt to coalesce and of the melt to reshape. In Figure 14.9c, compared with the sinter containing 2.0% MgO, the sinter with no MgO shows relatively rounded, large discrete pores and a small amount of fine pores. There is reduced reshaping of pores at increasing MgO levels, probably due to changes in the melt liquidus temperature and viscosity as a result of the increasing MgO content.

Figure 14.10 shows the influence of Al_2O_3 content on the wetting width and apparent contact angle of CFS melt (calcium ferrite containing 6% SiO_2) spreading on a sintered hematite substrate 180 s after the sample is placed into the isothermal zone

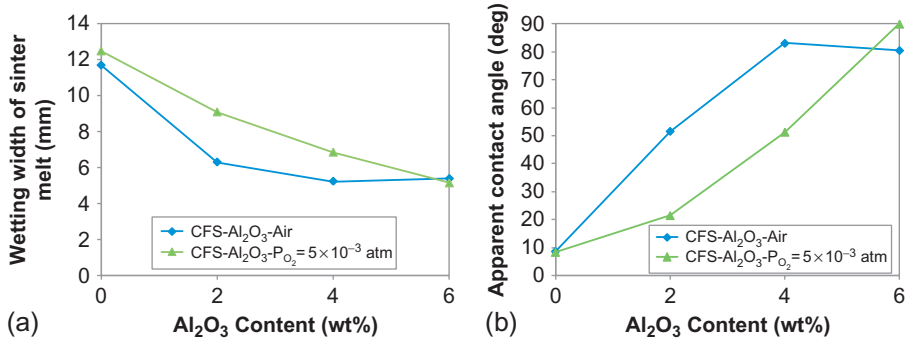

Figure 14.10 Effect of Al_2O_3 on (a) wetting width and (b) apparent contact angle of CFS (calcium ferrite containing 6% SiO_2) after 180 s at 1250 °C both in air and at $P_{O_2} = 5\times10^{-3}$ atm.

of a horizontal furnace at 1250 °C in air and at $P_{O_2} = 5\times10^{-3}$ atm, respectively. Under both gas atmospheres, the wetting width decreases and the contact angle increases with increasing alumina content in the melt. It is well known that a melt with better wetting characteristics spreads better on the substrate and is able to penetrate smaller pores in the substrate, leading to better densification. Also shown in Figure 14.10, the hematite substrate is better wetted by the CFS melt containing 2–4 wt% Al_2O_3 at $P_{O_2} = 5\times10^{-3}$ atm than in air. This suggests that decreasing oxygen partial pressure is beneficial to the wettability of CFS melt containing Al_2O_3 on the hematite substrate. The difference in wetting behavior observed in different atmospheres is believed to be due to the formation of a new interface under the reducing atmosphere.

Depending on their distribution, certain gangue minerals in coarse nucleus particles can affect nucleus stability, which influences the amount and properties of the final sinter melt. For example, our past experience has shown that ore particles from a higher alumina ore containing about 2.8% Al_2O_3 are not as reactive as ore particles of similar mineralogy from a lower alumina ore containing about 1.5% Al_2O_3. Gangue minerals in fine particles and reactive coarse particles, such as SiO_2, Al_2O_3, and MgO, readily enter the initial sinter melt formed mainly from fine Fe_2O_3 and CaO particles. This inevitably changes the composition and properties, such as viscosity and surface tension, of the final sinter.

In summary, ore chemistry, such as the SiO_2, Al_2O_3, and MgO contents, affects the composition and properties of sinter melt through either melt formation or assimilation of ore particles, which has important implications for the densification process and consequently the structure and quality of the resultant sinter. It is common for sinter plants to have fixed sinter chemistry targets in order to meet the subsequent chemistry targets required for their associated blast furnaces, in particular, the SiO_2 content, the CaO:SiO_2 ratio (basicity), and the MgO content. To achieve the same sinter chemistry targets, iron ore blends with lower SiO_2 and MgO contents require increased flux additions. Furthermore, as fluxing agents have a propensity to more readily enter the sinter melt phase, the melt formed from an iron ore blend with a lower

SiO_2 content will most likely form a sinter melt with a higher SiO_2 content than an ore blend with higher natural SiO_2 level, even at the same sinter chemistry targets, leading to quite different properties of the sinter melt.

14.2.2.2 Physical characteristics of iron ore

The size distribution of iron ore fines affects not only the granulation efficiency but also the formation of sinter melt, and the proportion and stability of coarse particles determine the number of relict ore nuclei in the sinter structure. Relatively stable coarse particles are unreacted or only partially assimilated and act as "spacers" in the sintering bed, helping to improve the bed permeability at the flame front, while reactive particles are fully assimilated and contribute to the sinter melt. As finer particles have a higher surface area and are in closer contact with fine flux particles, they react more readily with flux to form an initial sinter melt at a lower temperature. The proportion of fine particles and the stability of coarse nucleus particles therefore determine the volume, chemistry, and properties of the primary sinter melt formed during the sintering process. Figure 14.11 shows the strength and pore structure of laboratory sinters

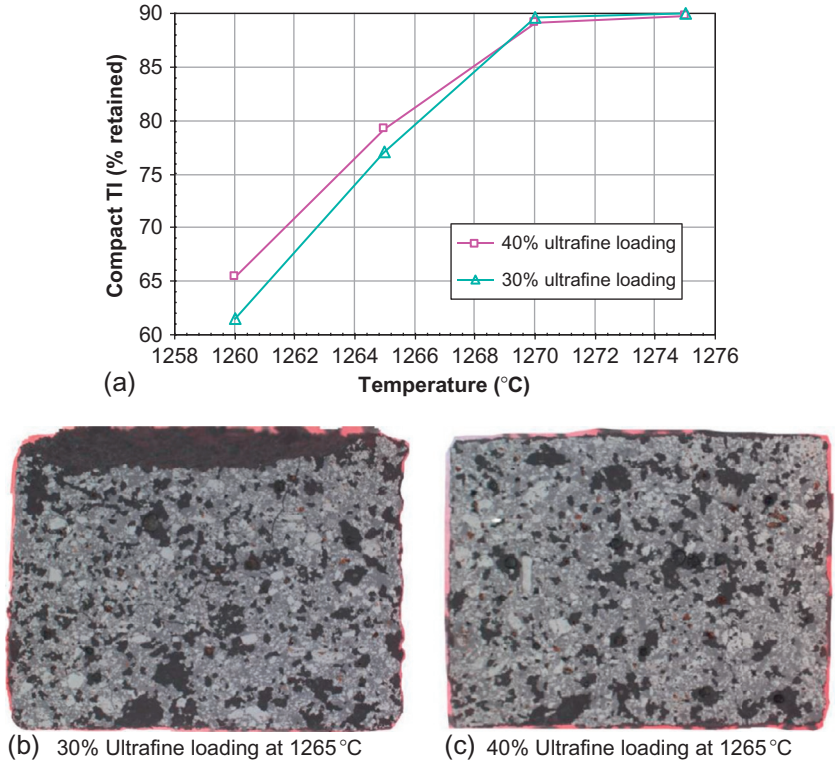

Figure 14.11 (a) Compact TI strength and (b and c) pore structure of laboratory sinters fired from the −1 mm fraction of the same iron ore fines containing different loadings of ultrafine particles.

fired from the −1 mm fraction of the same iron ore fines containing different loadings of ultrafine particles (−0.15 mm). The detailed experimental method used was described by Clout and Manuel (2003). While both sinters achieve similar strength at higher temperatures, the sinter from the mixture with a higher loading of ultrafine particles develops strength at slightly lower temperatures. From the pore structure shown in Figures 14.11b and c, both laboratory sinters have clearly started densification at 1265 °C. However, compared with the sinter with 40% ultrafine loading, the sinter with 30% ultrafine loading appears to be slightly less consolidated at the same temperature, with considerably more small angular pores interconnected by thinner necks.

Ideally, an ore or an ore blend should avoid too much material in the intermediate size range and contain appropriate proportions of coarse nucleus and adhering fine particles. Adhering fines will contribute not only to the granule coatings but also to the matrix formation.

14.2.2.3 Mineralogical characteristics of iron ore

Mineralogically, iron ore fines are characterized by the occurrence and abundance of different iron and gangue minerals and their associations and textures. The importance of ore mineralogy was demonstrated by recent modeling work that concluded that the inclusion of ore textural information can significantly improve model prediction of sinter quality (Donskoi et al., 2007, 2009).

Ore mineralogy and textural relationships determine the type and relative abundance of iron oxyhydroxides (e.g., dense, vitreous goethite vs. microporous, ochreous goethite) in an ore, which further determine the LOI components and bulk density of iron ore fines. The LOI components in iron ore fines are released as the temperature increases, leaving behind many secondary pores and cracks. The primary and secondary porosities strongly affect the stability of nucleus particles in contact with the gas and liquid phases. Therefore, the mineralogy and texture of ore particles also play an important role in melt formation and retention of nucleus particles. Figure 14.12 depicts the difference in the stability of typical hematitic and goethitic nucleus particles in a typical Japanese steel mill (JSM) sinter matrix. Ore A is composed largely of fine to very fine-grained microplaty hematite, which forms a moderately to highly microporous network. The microplaty hematite texture in Ore A is physically denser and harder than would otherwise be expected from its microporous microstructure. This explains the low nucleus assimilation rate and the high retention rate of nucleus particles from this ore (Figure 14.12a). Ore C has a uniform texture and mineralogy typical of channel iron deposit iron ores. The ore consists of concentrically zoned pisoliths of dense vitreous goethite, hydrohematite, and ochreous goethite, cemented together by porous vitreous-ochreous goethite. While this ore appears denser with some macropores but low microporosity, it consists predominantly of goethite, which generates large amounts of secondary porosity upon heating. Therefore, at the same firing temperature, the nucleus particles from Ore C are highly reactive and fully assimilated (Figure 14.12c). Ore B has the typical characteristics of a Marra Mamba ore and contains both stable nucleus particles (dense and harder ore textures dominated by martite-goethite associations) and reactive nucleus particles from vitreous and

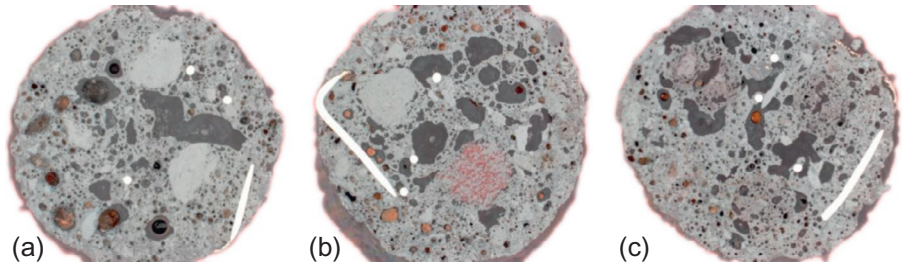

Figure 14.12 Stability of different types of nucleus particles at 1300 °C in the matrix of a typical Japanese steel mill (JSM) sinter blend. Relict ore particles are presented as dense gray particles in (a) and (b). (a) Nuclei from a dense hematitic ore (Ore A in Figure 14.4). (b) Nuclei from a Marra Mamba ore (Ore B in Figure 14.4). (c) Nuclei from a low alumina pisolitic ore (Ore C in Figure 14.4).

ochreous goethite types (Figure 14.12b). The release of the LOI components also increases the gas volume generated within the sinter matrix, which can result in a frothy texture, particularly where the melt viscosity is high, creating secondary porosity. This can have a negative impact on sinter strength.

Ideally, a sinter structure requires about 30% relict nuclei to avoid excess melting and densification and hence ensure sinter quality. Therefore, it is important when designing a sinter mixture to have an appropriate balance in mineralogy and sizing to maintain a sufficient amount of relict particles in the sinter structure but still generate sufficient sinter melt.

14.2.3 Summary

Granulation and densification are two important processes in iron ore sintering. The influence of the chemical, physical, and mineralogical characteristics of iron ore on granulation and densification, and therefore on the quality of the resulting sinter, has been discussed above.

Depending on their distribution within the ore and/or green bed, certain gangue phases such as Al_2O_3 in the coarse nucleus particles affect nucleus stability, although they may remain segregated from the matrix. The same phases in the ultrafine particles readily enter the initial sinter melt, formed mainly from fine Fe_2O_3 and CaO particles, and affect the chemistry and properties of the primary sinter melt and the final sinter structure formed. The influence of the chemical characteristics of the ore on granulation is largely neglected in the literature. However, it was found that some gangue minerals in iron ore can potentially act as a binder during granulation.

The shape, size distribution, and porosity of iron ore particles play an important role in determining the granulating characteristics of iron ore fines. The porosity of iron ore particles also affects the stability of nucleus particles and the reactivity of ultrafine particles, which, together with the size distribution of the iron ore fines, determines the volume of the sinter melt and the amount of relict nuclei. The size distribution of iron ore fines also influences the partitioning of potential nucleus particles and matrix forming material and therefore plays an important role in the formation of the primary sinter melt.

Ore mineralogy determines the primary porosity present in iron ore fines, which in turn determines the amount of water required for efficient granulation. There is a close link between ore mineralogy as reflected by the LOI and the amount of moisture required for efficient granulation. The release of the LOI components from iron ore fines generates secondary porosity, which, together with primary ore porosity, influences the reactivity of nucleus particles and distribution of retained porosity in the sinter matrix. As the release of LOI components is endothermic, iron ore fines with higher LOI often require more bonding agents to maintain the flame front temperature and sinter quality compared with those with lower LOI. For a given crushing flow sheet, ore mineralogy also affects the shape and size distribution of iron ore fines, both of which have important implications for the granulation and densification process during iron ore sintering.

14.3 Evaluation of iron ore for the sintering process

With the rapid change in iron ore supply and composition, steel mills now have to adjust the composition of ore blends for their sinter plants more frequently than ever before. Hence, test methods of different scales (Lu et al., 2007) have been developed to help the sinter plant evaluate new ore types in order to optimize ore blends. This allows the plant operator to maximize productivity and quality at the lowest cost through sinter blend optimization. This section highlights a variety of laboratory and pilot-scale testing methods for evaluation of iron ore for sintering.

14.3.1 Pilot-scale evaluation of iron ore

The advantage of pilot-scale sinter pot tests lies in their capability to simulate the two important steps in iron ore sintering, namely, granulation and thermal densification, as well as achieve a similar bed structure to a sinter strand consisting of zones of sintered, sintering (flame front), and unsintered (calcined, dry, and wet) materials from the top to the bottom of the bed. The sinter pot test method is therefore widely used in metallurgical laboratories and steel mills worldwide, and the test results are generally accepted by the steel industry. However, due to the complexity of the test method, there are no international standards for this purpose. Figure 14.13a shows the CSIRO pilot-scale multifunctional sinter pot testing facility, which was installed and commissioned in 2000. Over the last 15 years, it has evolved into a fully automated and sophisticated pilot-scale testing and research facility supported by a standard procedure covering preparation and characterization of raw materials, granulation, firing and sinter product evaluation, and sampling at various stages of the sinter pot test. The sinter pot testing facility consists of an ignition system, a data acquisition and control system, an online gas analyzer, and a variable depth sinter pot connected to a wet scrubber and sinter fan. The ignition system consists of multiple burners to form a horizontal vortex in the ignition chamber, producing a planar flame front to ignite the surface of the granulated sinter mix bed. The unique arrangement of the burners ensures a uniform flame front, which raises the surface of the bed quickly to the ignition

Figure 14.13 (a) CSIRO multifunctional pilot-scale sinter pot testing facility and (b) a fully charged sinter pot.

temperature without being significantly affected by the permeability of the granulated mix. This is important when the sintering characteristics of different ore blends are to be compared. The data acquisition and control system monitors and records important processing parameters to better understand the sintering process, such as the ignition temperature, pressure drop across the sintering bed, waste gas temperatures, inlet and outlet airflows, sinter fan speed, and waste gas composition from the online gas analyzer. The system also controls the ignition process, pot movement, cooling water, and pressure drop across the sintering bed. The sinter pot is uniquely designed to ensure that heat loss is minimized and is fitted with sensors to measure the temperature and permeability of the flame front during sintering. A specially designed feeder is used to ensure that the granulated mix is charged evenly and smoothly into the pot. The sinter pot has a grate area of 0.075 m^2 and a variable depth ranging from 0.5 to 0.86 m, which covers the bed depth found in most commercial sinter machines. The online gas analyzer enables the analysis and recording of the concentrations of CO_2, CO, NO_x, SO_x, O_2, hydrocarbons, and H_2O in the waste gas simultaneously, as well as collection of isokinetic samples for dioxin analysis and +10 µm particulates for dust emission analysis. Depending on the permeability of the granulated mix, the sinter fan installed is able to achieve a suction of up to 20 kPa across the sintering bed during the ignition, sintering, and cooling stages of the test run.

The standard pilot-scale sinter pot testing procedure at CSIRO uses about 65–120 kg of green granules for each test depending on the pot depth selected, which in turn generates enough product sinter for the evaluation of bulk sinter properties according to ISO or other relevant standards. After granulation, the sinter mixture is loaded into the cylindrical sinter pot (Figure 14.13b) and then ignited at the top typically for 90 s while air is drawn down through the bed at 6–8 kPa suction pressure. At the end of the ignition cycle of 90 s, the suction is then increased to values ranging

from 12 to 20 kPa to move the flame front down. The sintering process ends when the flame front travels through the bed, as evidenced by the peak temperature of the waste gas. The sinter plug is tipped out when it cools down below 200 °C for further processing and evaluation.

Sinter is often brittle and prone to degradation during handling. The sinter quality measured depends heavily on how the sinter plug is processed. Therefore, a standard procedure for processing sinter plugs is required to ensure that the sinter quality measured for a particular sinter run can be compared with that for other runs. Over the years, CSIRO has internally developed a standard sinter plug processing procedure that wherever possible utilizes automatic equipment to avoid human errors and ensure consistent handling. The sinter plug, which typically weighs 55–110 kg depending on pot height, is first automatically tipped out of the sinter pot at a fixed height and then stabilized using a drop tower by typically dropping the sinter four times from 2 m. The stabilization process, simulating breakdown during transport and handling, results in predominantly −40 mm material, which is then sized at 40, 25, 16, 10, and 5 mm using a set of trommel screens. The +5 mm fraction is weighed and termed "product sinter," while the −5 mm fraction is weighed and recorded as "sinter returns," which are deemed too fine for blast furnace use. The product sinter is then subsampled for chemical analysis, physical testing, and mineralogical examination. The following parameters are typically reported from sinter pot tests:

- Green bed permeability (JPU)—a measure of permeability calculated from the measured air flow across a 500 mm deep × 105.5 mm diameter pot at approximately 6 kPa. A high JPU indicates a low green bed resistance to airflow and therefore good voidage and permeability.
- Coke level—the percentage of coke added based on the total dry mix, %tdmb.
- Sinter returns level—the percentage of sinter returns added based on the total dry mix, %tdmb.
- Sintering time (s)—the time elapsed from the commencement of the ignition cycle to the time when the waste gas reaches a maximum temperature, which is used to calculate the sintering productivity.
- Yield—the ratio of the mass of product sinter (i.e., +5 mm sinter) to the total mass of sinter produced less the mass of the hearth layer sinter, %.
- Productivity—the amount of product sinter produced per day per unit grate area, t-sinter/d m^2.
- Bonding agent rate—the mass of coke in kilograms required to produce a tonne of product sinter, kg/t-sinter.
- Return fines balance (RFB)—the ratio of sinter returns generated to the sinter returns added to the sinter mix. A sinter plug is considered to be "balanced" if the RFB is within 1 ± 0.05. One of the key objectives of pilot-scale sinter pot tests is to achieve a balanced outcome.
- Sinter quality parameters, including tumble index (TI), reducibility index (RI), reduction disintegration index (RDI), and softening and melting characteristics, as well as size distribution and mean product sinter size. For detailed information on these quality parameters, readers can refer to Chapter 16 on the quality requirements of iron ore for iron production.

The pilot-scale sinter pot testing method has been widely used by CSIRO in its applied and fundamental sintering research to investigate

- the effect of ore characteristics, including ore mineralogy, chemistry, and sizing;
- the effect of sintering conditions, such as bed depth, moisture and bonding agent additions, fluxing, and suction;

- novel raw material preparation technologies;
- technoeconomic performance of iron ore fines individually or in simulated steel mill blends;
- emission and mitigation technologies for particulates, CO_2, SO_x, NO_x, and dioxins.

However, the sintering process for iron ore fines is very complex and involves many variables that are interdependent and hard to isolate. Therefore, the test results from sinter pot tests often reflect the overall impact of these interrelated parameters. Furthermore, for the same ores, the sinter quality and sintering performance can vary significantly with the scale at which the sinter pot tests are conducted. Research has been conducted to compare sinters fired from the same granules in the sinter plant and the laboratory (Loo and Wong, 2005). As shown in Table 14.1, compared with laboratory sinter, the plant sinter is stronger in terms of TI but has comparable RDI, RI, and chemistry. It has also been found that the RFB increases and the sinter TI decreases as the laboratory unit grate area is scaled down. Therefore, it is important to understand the effect of test scale on sintering performance and sinter quality when interpreting the test results (Lu et al., 2007). Finally, the sinter pot testing method requires a substantial amount of raw materials for the tests, and it is relatively expensive, time-consuming, and labor-intensive.

14.3.2 Laboratory-scale evaluation of iron ore

Pilot-scale sinter pot tests are good to simulate the sintering process and can generate a large quantity of sinter for bulk sinter quality assessment, but it is sometimes hard

Table 14.1 Comparison of plant and sinter pot test results from the same plant-granulated sinter mixture (Loo and Wong, 2005)

Sintering performance	Plant sinter	Laboratory sinter		
		0.2[a]	0.09[a]	0.05[a]
Productivity, t/m^2 d	29 (Average for day of sampling)	32	37	34
Return fines balance	1.00 (Assumed)	0.98	1.12	1.15
Sinter bulk properties				
ISO tumble index, mass% + 6.4 mm	71	69	65	65
RDI, mass% −2.8 mm	28	28	28	29
RI, %R	60	60	59	61
Sinter mineralogy				
Magnetite, vol%	19	20	22	22
Primary hematite, vol%	23	24	21	24
Secondary hematite, vol%	13	11	11	9
SFCA, vol%	33	32	33	33
Glass, vol%	5	5	5	4
Dicalcium silicate, vol%	5	6	6	7
Quartz, vol%	2	2	2	1

[a] Grate area of laboratory sinter pots (m^2).

to isolate the parameters to establish a fundamental understanding of the role of different ore characteristics in sintering. Therefore, a variety of laboratory-scale testing methods have been developed for iron ore evaluation, and important methods used in Australia and Japan are discussed below.

14.3.2.1 Fundamental granulation characteristics of iron ore

Water absorption capacity of iron ore

The water absorption capacity of iron ore is measured in Japan using the centrifugal moisture equivalent method (Okazaki and Higuchi, 2005). Ores of 2.0–2.8 mm and −1.0 mm particle sizes are used in the test. Similarly at CSIRO, the water-holding capacity of iron ore is measured to determine the ability of iron ore to absorb and hold water. Both head and −4 + 2 mm size fraction samples are used in the test. Ores with a high value for water absorption capacity/water-holding capacity require high moisture contents during granulation to provide water for efficient granulation.

Cohesive strength of fine ore

The cohesion force of fine particles is important for the growth and strength of green granules. The former affects the size distribution of final granules formed, while the latter has a direct impact on the permeability of a packed granule bed. Therefore, the cohesive strength of fine ore (Okazaki and Higuchi, 2005) is measured in Japan for evaluating iron ore granulation. The cohesive strength of fine ore is assessed by measuring the tensile strength of a packed bed of fine particles. The packed bed of fine ore comprises equivalent mass ratios of 5 size fractions of −1.0 mm material, namely, −0.063 mm, −0.125 + 0.063 mm, −0.25 + 0.125 mm, −0.5 + 0.25 mm, and −1.0 + 0.5 mm, and cohesive strength is measured as a function of the moisture content of the packed bed ranging between 0% and 15%. A high cohesive strength indicates good granulation ability, while the optimum moisture content is where the cohesive strength reaches its maximum.

14.3.2.2 Fundamental sintering characteristics of iron ore

Thermal cracks of coarse ore particles

The initial sinter melt of a $CaO–Fe_2O_3$ binary system forms at a temperature near 1200 °C during sintering. Therefore, the change in pore structure and formation of cracks while heating up the sinter mix to 1200 °C have a large influence on melt formation, due to the changes in the area available for sinter reactions. In addition, decrepitation of iron ore particles affects the physical stability of granules and consequently the permeability of the sintering bed. Figure 14.14a shows a schematic diagram of a heat treatment method to examine the structural change of ore particles during heating (Okazaki and Higuchi, 2005). Ore particles of −2.8 + 2.0 mm particle size are loaded in a Ni crucible 20 mm in diameter and 15 mm in height and subsequently heated in air in a vertical electric furnace. The sample is heated up to 1200 °C in 4 min. After being cooled, the thermally treated particles are mounted in resin and polished for microscopic evaluation to examine any change in pore structure and formation of cracks.

Melt penetration of fine ore particles

To simulate the interaction of melt formed from fine ore particles within the adhering layer of granules with nearby ore particles, melt penetration tests are carried out in Japan (Figure 14.14b; Okazaki and Higuchi, 2005; Okazaki et al., 2003). The penetration test uses two tablets, namely, one of ore and the other of primary melt-forming material. The ore tablet is made from a mixture of two size fractions of ore, that is, −0.25 mm and −0.5 + 0.25 mm, in equal mass ratio, which is then pressed into a cylindrical tablet of 15 mm diameter and 5 mm height. As an initial sinter melt source, a mixture consisting of 26% CaO and 74% Fe_2O_3 chemical reagents (the eutectic composition of the CaO–Fe_2O_3 system) is pressed into a cylindrical tablet of 5 mm diameter and 5 mm height. Both tablets are made using iron molds under a pressure of 4 MPa. The tablets are assembled as shown in Figure 14.14b in a Ni crucible and heated in air. The sample assembly is heated from 1100 to 1290 °C in 1 min and subsequently cooled down to 1100 °C in 3 min to simulate the heating and cooling conditions in sinter plants. After being cooled down to below 1100 °C, the tablet assembly is taken out of the furnace and cooled in air. The assembly is subsequently mounted in resin and polished to show the vertical section of the tablets. The penetration length of the melt is defined as the distance between the top surface of the ore tablet and the outer boundary of the interaction zone and is measured using image analysis at a magnification of 5. The penetration length of fine ore has been found to have a strong correlation with the strength of sinter and product yield in plant operations (Okazaki and Higuchi, 2005).

Assimilation behavior of coarse ore particles

To evaluate the stability or melting characteristics of coarse ore particles acting as nuclei, assimilation tests on a small packed bed consisting of granules comprising coarse ore particles coated by fine limestone are performed in Japan (Figure 14.14c; Okazaki and Higuchi, 2005). The granules are made from ore particles of −2.8 + 2.0 mm particle size as nuclei and limestone of less than 0.5 mm particle size as adhering fines at a CaO/ore mass ratio of 0.1 to simulate the blending conditions of materials in sinter plants. They are produced by hand granulation with the help of moisture and subsequently loaded into a Ni crucible to form a packed bed. The sample is heated in air from 1100 to 1300 °C in 1 min and subsequently cooled down to 1100 °C in 3 min. Polished blocks are made to reveal the horizontal cross-section of the sintered sample 5 mm from the bottom of the crucible. The assimilation behavior and microstructure are examined using an optical microscope.

In Australia, the former BHP Billiton Newcastle Technology Centre (NTC) developed a similar bench-scale technique to quantify the assimilation of iron ore by melt under a simulated sintering thermal profile (Loo, 2005). In the NTC assimilation test, tablets are made from a blend of very fine laboratory-grade reagents, namely, hematite, kaolinite (for silica and alumina), silica, limestone, and magnesia, to simulate the adhering fines layer of granules and iron ore particles (0.71–1.0 mm in size) to simulate nucleus particles. When the tablets are heated in an infrared rapid heating furnace under a simulated sintering thermal profile, the fines react to form an initial sinter melt encapsulating the nucleus particles. This initiates the assimilation of the

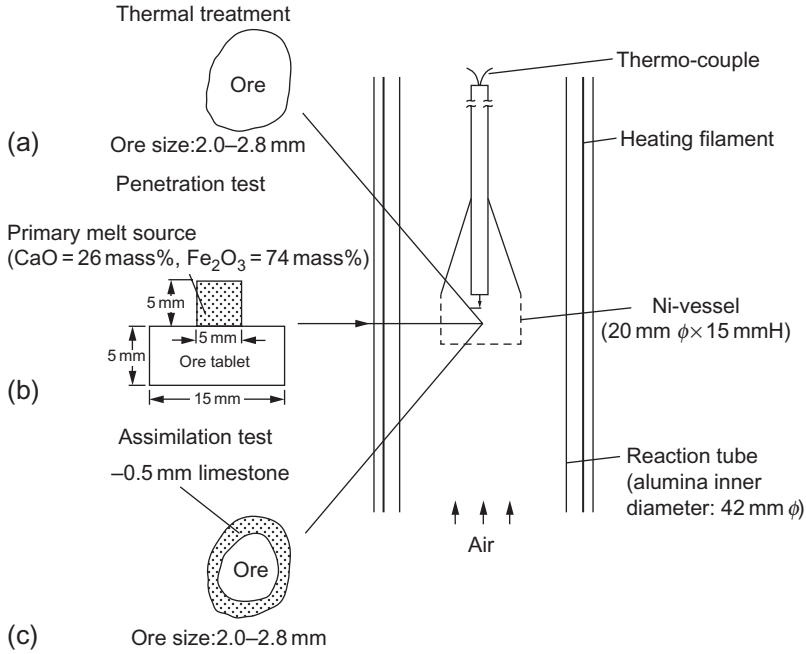

Figure 14.14 Experimental apparatus and sample assemblies used for thermal treatment, melt penetration, and assimilation tests in Japan.

nucleus particles by sinter melt, a process that continues until the tablet temperature drops below 1100 °C. Polished blocks are made to reveal the longitudinal cross section of the sintered tablets using optical microscopy. The volume percent of remnant ore in the sintered tablet, that is, the volume of nucleus particles that have not reacted over the sintering period, provides a measure of the "assimilability" of the ore nucleus particles. The results clearly demonstrate that ore mineralogy is important in determining the assimilation behavior of the coarse ore particles by the melt. Pisolitic ore particles assimilate at a much faster rate compared to porous or dense hematitic ore particles.

Compared with the Japanese assimilation test, the composition of the adhering fine layer in the NTC test better represents that of the adhering fine layer on granules. However, this method uses laboratory-grade reagents to simulate the adhering fine layer. The CSIRO laboratory-scale sintering tests are conducted on the fluxed −1 mm fraction of an ore blend consisting of natural ores. The finer ore particles in the −1 mm fraction readily react with fluxes to form the initial sinter melt during firing, while the relative coarser ore particles of the −1 mm fraction act as nucleus particles to react with the initial melt formed from the finer materials. Two cylindrical tablets of the fluxed −1 mm fraction of the ore blend are compacted and fired in a laboratory furnace under a simulated typical sintering temperature profile and an oxygen partial pressure of 0.005 atm. The two fired tablets are then tumbled together in a modified Bond abrasion tester for 8 min and screened to calculate the relative compact TI recorded as the percentage retained above 2 mm particle size. The tests are conducted in duplicate

and the arithmetic mean TI is calculated. Tablets are fired across a range of temperatures, in order to construct melting curves, to determine the temperature at which the optimum TI is obtained. For each temperature, a fired tablet is also set in epoxy resin, polished and examined to determine the level of melting and porosity under an optical petrographic microscope.

14.4 Recent developments in iron ore sintering

14.4.1 Background

Due to the depleting reserves of traditional high-grade iron ore, there have been considerable changes in iron ore resources available throughout the world, especially to steel mills in East Asia. Figure 14.15 shows the change in iron ore resources used by the Japanese steel industries during the period 1971–2007. The usage of Australian iron ores has been increasing over this period to reduce costs. Table 14.2 lists the chemical and physical characteristics of typical Australia iron ores used by Nippon Steel Corporation (now Nippon Steel & Sumitomo Metal Corporation) in 2008. The increase in the usage of Australian iron ores means that the ore resources changed from hard hematitic to more goethitic pisolitic or Marra Mamba ores.

Corresponding to the changes in the availability of iron ore resources, the amount of impurities in iron ore has been slowly increasing. Some of these impurities have been found to have deleterious impacts on sinter quality and sintering performance. In the meantime, an increasing number of large blast furnaces with inner volumes of more than 5000 m^3 have been built that require more sinter and are often more demanding in terms of the quality requirements of the ferrous materials. Finally, sinter plants are facing increasing pressure from more stringent regulations regarding their environmental impact. A variety of granulation and sintering technologies have therefore been developed worldwide to tackle the changing raw material characteristics (Table 14.2) and mitigate emissions from sintering operations.

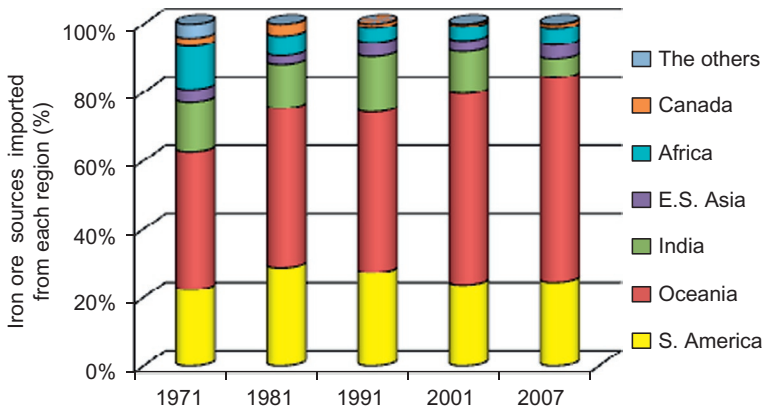

Figure 14.15 Change in iron ore resources used by the Japanese steel industries during the period 1971–2007.

Table 14.2 Fe grade, alumina content, % −0.15 mm adhering fines, and LOI of typical Australian iron ores used by Nippon Steel Corporation (now Nippon Steel & Sumitomo Metal Corporation) in 2008

	A	B	C (2007)	D	E
Ore type	Brockman	Brockman	Marra Mamba	Pisolite	Pisolite
T. Fe, %	62.40	61.80	61.78	56.40	58.30
Al_2O_3, %	2.47	2.24	2.26	2.79	1.52
−0.15 mm, %	12.10	13.10	28.08	3.20	4.58
LOI, %	3.20	5.20	5.98	9.40	10.00

14.4.2 *Selective granulation to address rising ore alumina content*

Selective granulation of fine clayish iron ores has been developed by Nippon Steel Corporation (now Nippon Steel & Sumitomo Metal Corporation, NSSMC) to improve the sintering performance of sinter mixtures containing higher proportions of limonitic ores. The key achievement of this technology is in sintering limonitic ore using low-energy input by inhibiting melt formation from high-alumina ores in the sintering reaction and by controlling the brittleness of the sintering ore texture formed during dehydration. These outcomes were achieved by preliminary granulation of a small portion of the fine high-alumina limonitic ore.

Figure 14.16 shows the material and process flow sheet for the selective granulation method. In this process, selected clayish ores are first screened at 2–4 mm to take out the fine material that often contains high alumina content. The undersized material is pelletized to make pseudoparticles, which are then mixed with the oversized and other raw materials. Therefore, the concentration of Al_2O_3 in the bonding material and the amount of fine material decreased, while the Fe_2O_3, CaO, and coke concentrations increased. This led to an increase in melt formation for the sinter products, which was confirmed by the observed increase in the ratio of open pores and pore size. Single-particle firing tests and small packed bed firing tests were carried out to evaluate the sintering characteristics of sinter mixtures containing such pseudoparticles (Haga et al., 1997a). From single-particle firing tests, the pseudoparticles using fine clayish iron ores as the adhering fines layer were strong both before and after firing. The results of small packed bed sintering tests showed that segregation of limestone in the sinter mix was effective in promoting melt formation. The increase in the limestone concentration of quartz-rich iron ore fines, which were adhering to coarse nucleus particles, was most effective for coalescing pseudoparticles and for generating a desirable pore network during sintering. From the plant test results (Haga et al., 1997b) on a commercial sintering machine in the NSSMC Oita Works in Japan, the green pseudoparticles prepared from fine clayish iron ores by selective granulation were found to be strong enough to retain their integrity during handling and effectively segregate the deleterious components from the bonding agents in the sinter mix. Furthermore, the increase in melt

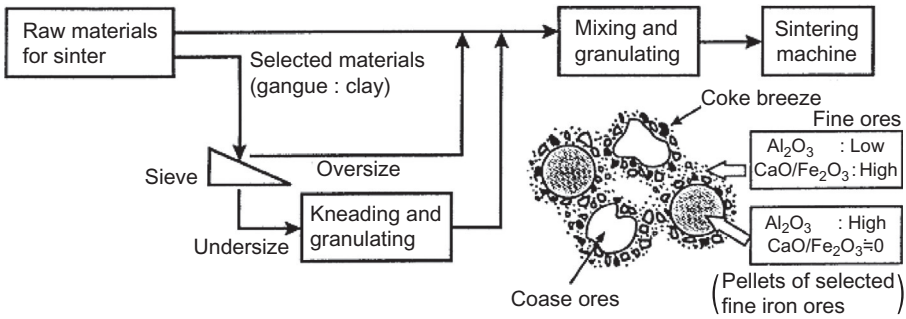

Figure 14.16 Concept and process description of the selective granulation method developed by Nippon Steel & Sumitomo Metal Corporation (Haga et al., 1997a).

formation of the sinter products was confirmed by the observed increase in the ratio of open pores and pore size. Finally, the coke consumption, permeability, and reducibility of the sinter were significantly improved.

14.4.3 Limestone and coke breeze coating for better combustion and melting

The effect of secondary mixing of coke breeze and limestone in a drum mixer on the permeability and reduction characteristics was investigated using sinter pot and laboratory scale tests (Oyama et al., 2004). The secondary mixing technique for the coke breeze enhanced the permeability in the wet zone by increasing the quasiparticle size and strength, while the secondary mixing technique for the limestone enhanced the permeability in the melting zone by improving the melt fluidity. The sinter reducibility was also improved by secondary mixing of the limestone and coke breeze, because of the increased microporosity arising from the relict ore. Based on the above laboratory tests, JFE Steel Corporation developed a new coke breeze and limestone coating granulation process for sinter feed pretreatment. Figure 14.17 shows the process flow sheet for the coating technology installed on the JFE Steel Corporation Kurashiki no. 2 sinter machine, as well as a schematic diagram of the granulated particle and sinter structure

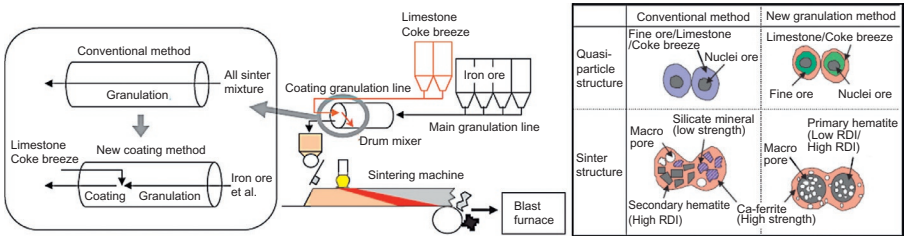

Figure 14.17 Process flow sheet for the limestone and coke breeze coating granulation technology installed on the JFE Steel Corporation Kurashiki no. 2 sinter machine and a schematic diagram of the granulated particle and sinter structure for this and conventional granulation methods (Oyama et al., 2005, 2008).

for this granulation and conventional methods. The technology controls the melting reactions of the iron ore and limestone by distributing the coke breeze on the surface of the quasiparticles and limestone in an appropriate ratio. This process improves the sintering productivity and sinter reducibility, because it retains finely porous and highly reducible primary hematite relict particles and maintains product yield by forming a strong calcium ferrite matrix that bonds together the primary hematite relict particles, as illustrated in Figure 14.17. This process has been installed on several JFE sinter machines achieving an annual throughput capacity of 19 million tonnes.

14.4.4 Improved charging methods for better permeability and segregation

Compared with the lower region of the sinter bed, more return fines are generated from the upper bed region because this part of the bed is sintered at a considerably lower temperature. Therefore, an appropriate segregation of bonding agents (coke breeze) is desirable to improve the sintering temperature of the upper bed region without overfiring the lower part of the sinter bed. Similarly, the lower region of the sinter bed is often less permeable compared with the upper bed region assuming uniform size distribution of feed material due to moisture condensation in the lower reaches of the bed during sintering and subsequent compression under the load of the upper region of the sinter bed. A coarse size distribution of feed material in the lower bed region is therefore desirable. Figure 14.18 shows different variants of conventional drum and chute-type charging systems. With the conventional charging systems, only limited segregation can be achieved due to the natural feed flow. An air nozzle to blow air at the point where raw material mix departs from a sloping chute (Figure 14.19a) was found to be effective in achieving particle size and coke segregation due to the density differences (Sasaki et al., 1980).

To enhance the segregation degree, some sinter machines have introduced multiple-layer charging methods, as shown in Figure 14.19b (Yoshinaga and Ichidate, 1982). However, such a system requires more than one charging unit for a single sintering machine. Therefore, systems such as slit bars (Fukuda et al., 1984), slit wires (Takai et al., 1993), intensified sifting feeder (ISF) (Inazumi et al., 1989, 1990), and segregation feeder (SF) (Sasaki et al., 1980) have subsequently been developed to enhance segregation. Figure 14.19 shows schematic diagrams depicting the size segregation achieved by these charging methods. As shown in Figure 14.19c, the "slit bars" charging system consists of several bars, which act as a mechanical screen to separate the feed material into oversized and undersized particles that flow onto the sinter strand at different locations to achieve vertical size segregation in the sinter bed.

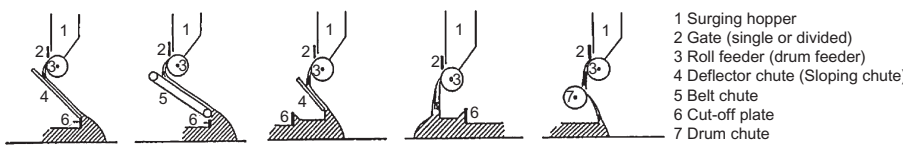

Figure 14.18 Different variants of conventional drum charging systems (Inazumi, 2000).

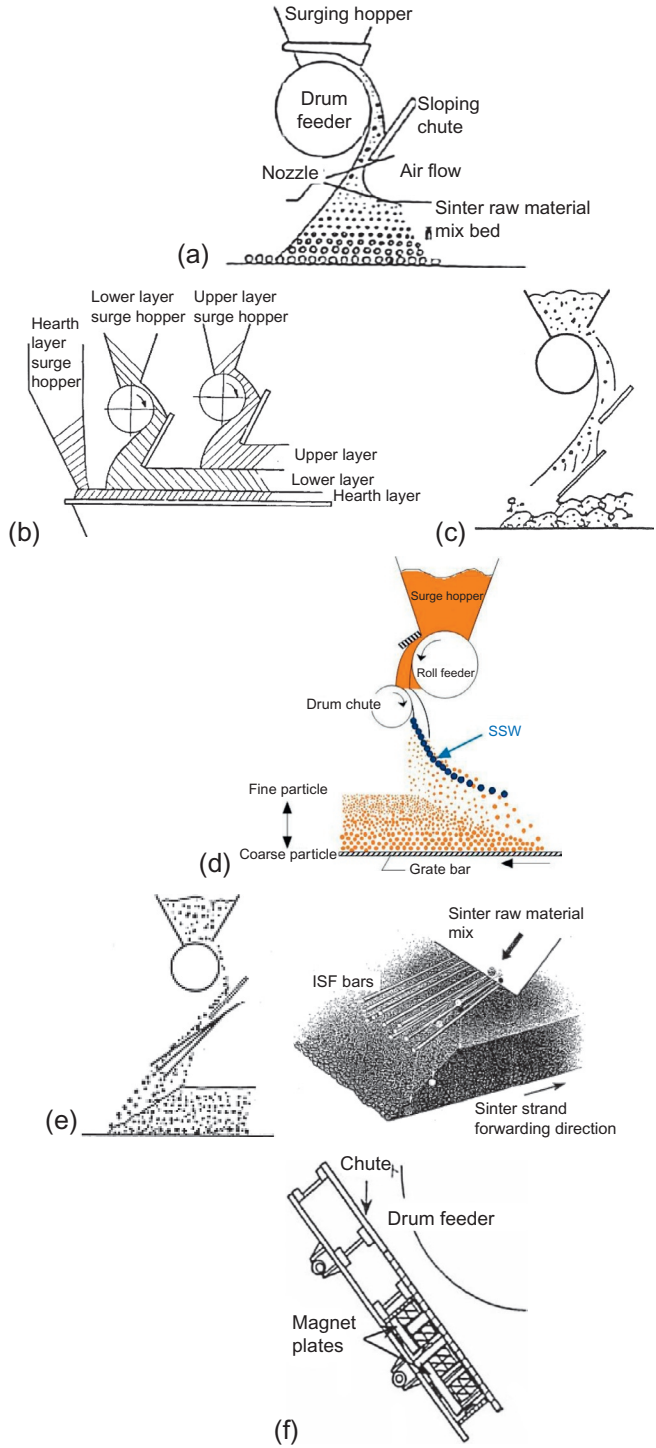

Figure 14.19 Different charging systems for segregated loading, i.e., (a) segregation feeder (SF) with an air nozzle (Sasaki et al., 1980), (b) multiple layer charging (Yoshinaga and Ichidate, 1982), (c) slit bars/wires (Fukuda et al., 1984; Takai et al., 1993), (d) segregation slit wires (SSW) with drum chute (Takeda and Oogami, 2008), (e) intensified sifting feeder (ISF) (Inazumi et al., 1988, 1989, 1990), and (f) magnetic brake feeder (MBF) (Takeda and Oogami, 2008; Oyama et al., 2000).

The "slit wires" charging system works essentially on the same principle, but it is easier to remove any adhered material by winding the wires using a mechanical reel. The slit bars and wires are now often coated with urethane to prevent abrasion and adhesion. The segregation slit wires (SSW) with a drum chute was developed and installed on the JFE Steel Corporation Fukuyama no. 5 sinter machine (Takeda and Oogami, 2008). The SSW charging system uses a curved screen and drum chute (Figure 14.19d) to improve screening efficiency and enhance particle size segregation further. Unlike slit bars, the intensified sifting feeder (ISF) (Figure 14.19e) consists of a set of bars distributed at different levels and rotating in opposite directions to maintain uniform friction and surface erosion to avoid sticking of material. These bars also move in the horizontal and diagonal directions to control, respectively, the contact point of the feed material and the distance between the bars and the surface of the mixture. The ISF feeder is reported to be effective in enhancing particle size segregation in the bed height direction and preventing avalanche phenomena, that decrease sinter yield due to inhomogeneous charging (Inazumi et al., 1989, 1990). The magnetic brake feeder (MBF) in Figure 14.19f, which has been developed and installed on the JFE Steel Corporation Kurashiki no. 3 sinter machine, is quite effective for concentrating high FeO material on the surface of the material bed to make up for the heat deficiency by increasing the proportion of material that oxidises exothermically in the upper bed region while simultaneously lowering charging density.

14.4.5 MEBIOS/HPS processes to address increasing finer materials

14.4.5.1 HPS process

The hybrid pelletized sinter (HPS) process, in which conventional processes for the production of both sinter and pellets are incorporated, was developed by NKK (now JFE Steel Corporation) to enable the use of large amounts of finer iron ores, including pellet feed with high iron content. Figure 14.20 shows schematically the material flow sheet for the HPS process. In contrast to the conventional sintering process, the blended ore, limestone, and burned lime are first mixed and pelletized in the HPS process using disk pelletizers to produce green pellets, which are then coated with coke breeze in a coating mixer before charging onto the sinter machine. Sinter pot tests have confirmed the benefits of the preferential addition of coke onto the surface of the green balls and the superior properties of the final agglomerates produced using the HPS process (Sakamoto et al., 1987).

Based on experimental studies and semicommercial plant trials, a commercial plant utilizing the HPS process with an annual capacity of 6 million tonnes per annum was constructed by remodeling the JFE Steel Corporation Fukuyama no. 5 sinter machine. It was confirmed that it was possible to operate the commercial plant at 4.7% silica content and 60% fine iron ore, including pellet feed, at a high productivity of 1.65 $t/m^2/h$. The HPS product had high reducibility (RI > 70%) and an acceptable reduction disintegration index (RDI < 40%) compared with conventional sinter produced at the plant (Niwa et al., 1993; Sakai et al., 2001). Hence, compared to the conventional sintering process,

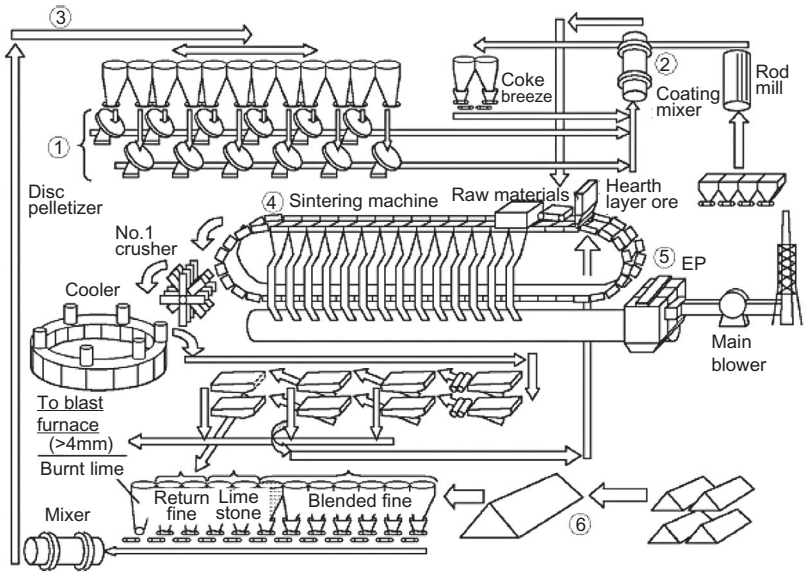

Equipment		Item and content
Sintering plant	① Pelletizer	Added disc pelletizer×2 7.5ϕm×H0.8m
	② Coating mixer	Enlarged coating mixer 4.4ϕm×L17.5m→ 5.5ϕm× L15.0m
	③ Belt conveyer	Increased capacity of belt conveyer
	④ Sinter pallet	Rose side-wall 620 mm→690 mm, Remodeled lower part of ignition furnance
	⑤ Measure for environment	Built a new EP
	Incidental construction	Remodeled controlling systems, Built a new electric source
Raw material treating plant	⑥ Blending pile (sinter feed)	Built new piling conveyers: 34→series Built new surge hopper and new CFW

Figure 14.20 Schematic diagram and outline of the hybrid pelletized sinter (HPS) process installed on the JFE Steel Corporation Fukuyama no. 5 sinter machine (Sakai et al., 2001) (Niwa et al., 1993).

the HPS process is capable of producing lower SiO_2 sinter of good strength due to the formation of solid diffusion bonding during sintering. Decreasing the sinter SiO_2 content is important for high pulverized coal injection (PCI) operation of blast furnaces.

14.4.5.2 MEBIOS process

Designing or controlling the position and size of voids formed in sinter cake is especially significant, because it affects the size distribution of the sinter product. However, an increase in the amount of fine ore, such as Marra Mamba fines or ultrafine Brazilian concentrate, in the raw material for sinter blends has been found to lower the permeability of the sintering bed and the sinter yield, probably due to the collapse of voids in the sintering bed. While some pregranulation techniques, such as selective granulation

and the HPS process, have been developed for utilizing these fine ores, the development of a sintering process that can control the void structure of the sintering bed to enable the use of a large amount of the fine ores is required. The *m*osaic *em*bedding *i*ron *o*re *s*intering (MEBIOS) process was recently developed as part of the Iron and Steel Institute of Japan (ISIJ) research project for the production of porous mesomosaic texture sinter.

The MEBIOS process is a multiple sintering process that arranges dense pregranulated pellets (called the aging bed), that do not easily deform during the sintering, in an ordinary sinter mixture (called the induction bed), which creates a ventilation route in the sinter bed (Otomo et al., 2009; Kamijo et al., 2013). As illustrated in Figure 14.21, pregranulated dense pellets are appropriately arranged in the induction bed, which provides an ideal void network under normal sintering conditions. In the research project, a pisolitic ore, which had a lot of coarse particles, was used for the induction bed and a Marra Mamba-type ore, which consisted of many fine particles, was used for the aging bed (Otomo et al., 2009). The aim of the MEBIOS process is the formation of a ventilation route in the sintering bed by creating a low-density area around the large pellets arising from a kind of wall effect and suppression of sinter bed shrinkage due to support of the load by the dense large pellets in the upper part of the sinter bed.

Small dry particles charged into the packed sinter bed were recently found to have a similar effect on controlling the bed structure due to friction between the dry and wet particles. Therefore, a process called "return fine-mosaic embedding iron ore sintering (RF-MEBIOS)" was developed to utilize return fines as the dry particles, because they are dry when produced by the sintering machine (Matsumura et al., 2013; Yamaguchi et al., 2013). Utilization of return fines as the dry particles eliminates the requirements for drying coarse ore particles. It was demonstrated through sinter pot tests that productivity increased at the same charging moisture content in the sinter mixture. This productivity increase is caused by the higher permeability of the packed sinter bed due to two major phenomena (Yamaguchi et al., 2013). The first is the increase in the pseudoparticle size during granulation, while the second is the decrease in the bulk density of the packed sinter bed after charging. The former is achieved due to the higher moisture content of the raw materials during granulation, which decreases the proportion

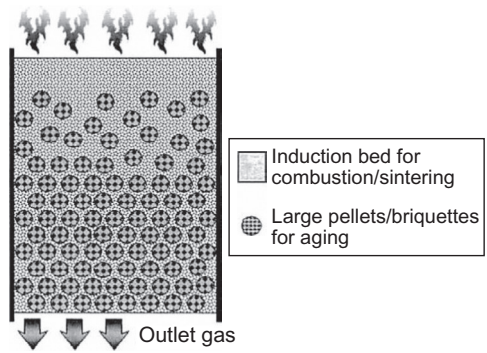

Figure 14.21 Conceptual illustration of the mosaic embedding iron ore sintering (MEBIOS) process.

of small pseudoparticles (−0.25 mm), while the latter is due to the higher friction in the packed bed composed of dry and wet particles, which decreases the bulk density.

The beneficial effect of RF-MEBIOS on sinter productivity was confirmed on no. 3 sinter plant in the NSSMC Kashima Steel Works (Matsumura et al., 2013). The RF-MEBIOS method has now been installed on three commercial sintering machines (Kashima, Wakayama, and Kokura) belonging to Sumitomo Metal industries, Ltd (now NSSMC). In all three sinter plants, a productivity increase was confirmed (Matsumura et al., 2013).

14.4.6 New binders for better permeability

Okada et al. (2006) had found that not only water bridges but also the behavior of microparticles, which are smaller than the fine particles, influences granulation. On the basis of their findings, Okada et al. had developed a new granulation technology using a dispersant, and Figure 14.22 shows a schematic diagram of the advanced granulation for innovation of sinter ore (AGIS) process. The microparticles in iron ore are dispersed in water by an anionic polymer dispersing (APD) agent, resulting in strengthening of the points of contact between the nucleus and fine particles or between the fine particles themselves. Laboratory granulation and pot-grate sinter test results by Nippon Steel Corporation (now NSSMC) (Okada et al., 2006; Kawachi and Kasama, 2009, 2011) showed that the use of APD agents increased the adhesion strength of pseudoparticles and pellet strength after drying, which consequently improved sintering productivity more than by using burned lime. Actual plant tests were also carried out, targeting a reduction in burnt lime addition through improved permeability of the sintering bed resulting from intensified granulation of the raw materials using this new dispersant and microparticle additives. The APD agent and additives were mixed with the other raw materials using a high-speed agitating mixer. A reduction of 10 kg/t-sinter in burnt lime consumption was confirmed while maintaining productivity and sinter strength, as well as stable operation. The granulation index (Hosotani et al., 1996) and therefore the preignition permeability of the granulated material were retained at levels equivalent to those for the base

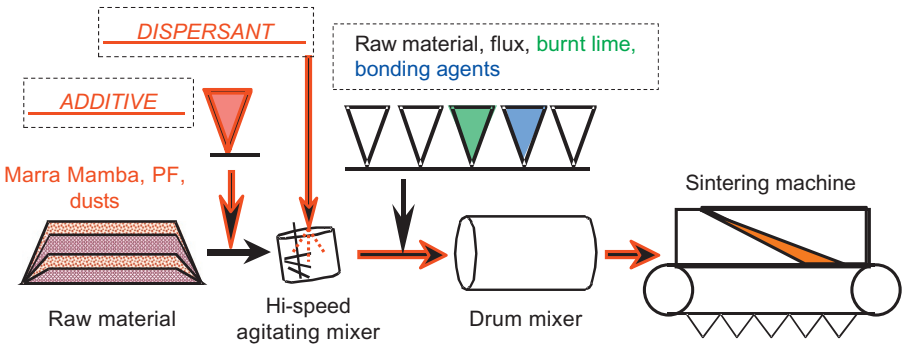

Figure 14.22 Process flow sheet for the advanced granulation for innovation of sinter ore (AGIS) process used on the NSSMC Tobata no. 3 sinter machine (Ishiyama et al., 2011).

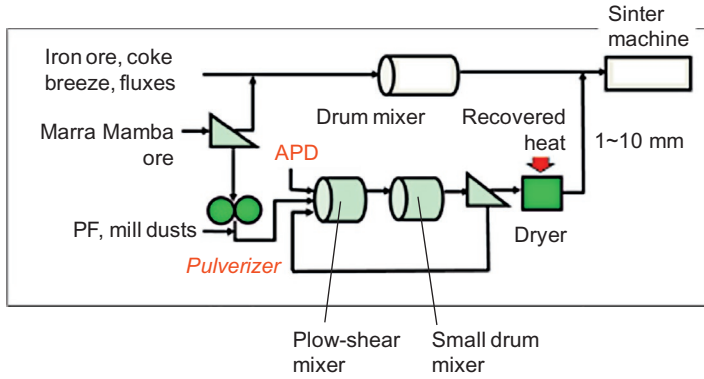

Figure 14.23 Process flow sheet for *s*emi*p*ellet *ex*pansion (SPEx) II adopted on the NSSMC Tobata no. 3 sinter machine (Takamatsu et al., 2011).

case, where a higher addition of burnt lime was applied but without the addition of APD agent. Furthermore, the total binder consumption, including the 4.3 kg/t-sinter of microparticle additives, was reduced by approximately 6 kg/t-sinter.

In response to the change in raw material characteristics, Nippon Steel Corporation (now NSSMC) has recently enhanced the AGIS process still further. Figure 14.23 shows the flow sheet for the *s*emi*p*ellet *ex*pansion (SPEx) II process used on the NSSMC Tobata no. 3 sinter machine. The enhanced process includes a pulverizer or roller press to generate microparticles from a Marra Mamba or high-phosphorus Brockman iron ore. With this process, stronger agglomerates of small pellets ("minipellets" or "semi-pellets") are produced to address the changing raw material characteristics while maintaining sinter quality and improving sinter productivity at deeper sinter bed depths.

14.4.7 Support stand for improved permeability in the lower part of the sinter bed

The sinter cake load on the combustion-melting zone has a large effect on the structure formation of sinter cake, especially in the lower part of the sinter bed. Stand-support sintering technology has been developed to improve bed permeability under the influence of gravity. With this technique, high sintering bed permeability is achieved in the lower part of the sinter bed as a result of reduced shrinkage due to gravity and suction by supporting the sinter cake load with the vertical plates, attached to the pallets, as shown in Figure 14.24. This technology has been adopted in several sintering machines operated by Nippon Steel Corporation (now NSSMC) since 1996 and has contributed to improved productivity with minimal effect on sinter quality.

14.4.8 Super-SINTER™ for energy and CO_2 reduction

JFE Steel Corporation has developed the "Super-SINTER™" (secondary-fuel injection technology for energy reduction) process (Oyama et al., 2011), which is illustrated in Figure 14.25. In this process, natural gas is blown in from the upper layer of

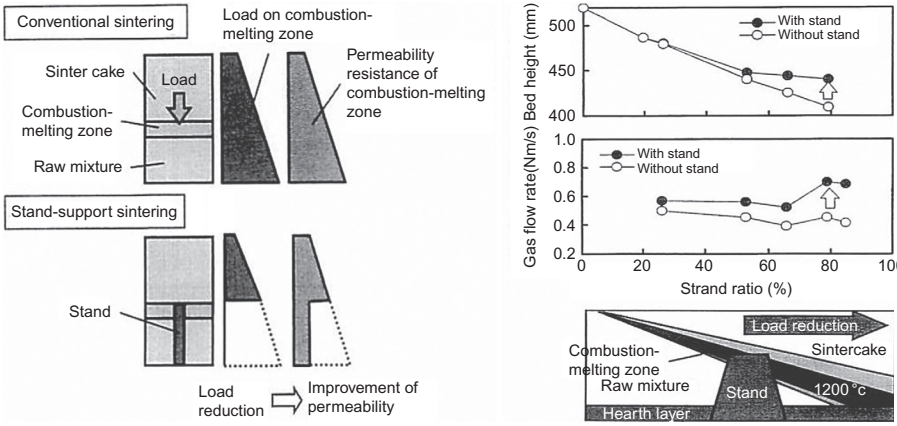

Figure 14.24 Schematic diagram showing the principle of stand-support sintering technology and actual plant data (no. 1 sinter machine, Kimitsu Steelworks, NSSMC) revealing improvement in the shrinkage behavior of the bed and gas flow distribution (Higuchi et al., 2006).

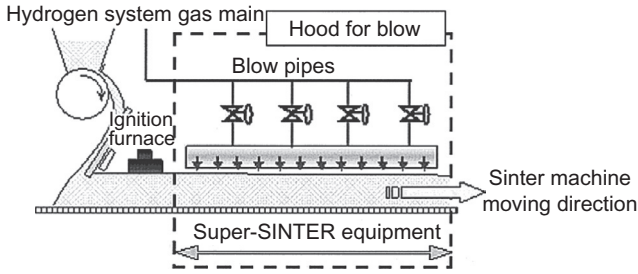

Figure 14.25 Schematic diagram of the Super-SINTER™ (secondary-fuel injection technology for energy reduction) process developed by JFE.

the sintering bed. With the "Super-SINTER™" process, it is possible to extend the zone in which the flame is in the optimum sintering temperature range, leading to the production of sinter with high strength and high reducibility. It also improves the energy efficiency, and the off-gas CO_2 emissions are decreased by about 60,000 ton per year.

14.5 Conclusions

Sintering is the most economic and widely used agglomeration process to prepare iron ore fines for blast furnace use. Compared with pellets, production of sinter is cheaper, and compared with lump ore, fluxed sinter is often more reducible with better softening characteristics. Iron ore sinter typically constitutes more than 60% of the blast furnace ferrous burden in modern blast furnaces in East Asia.

Granulation and thermal densification are two important steps in iron ore sintering and determine the quality of the resultant sinter and the performance of the sintering process. Iron ore is typically characterized chemically, physically, and mineralogically. The effect of iron ore characteristics on sintering is mainly through their impact on the granulation and densification processes.

With the rapid change in iron ore supplies and composition, steel mills now have to adjust the composition of the ore mixture to their sinter plants more frequently than ever before. Hence, different scales of test methods have been developed to help sinter plants evaluate new ore types and ore blends in order to optimize their ore mixtures. Pilot-scale sinter pot tests are good for simulating the sintering process and can generate a large quantity of sinter for bulk sinter quality assessment, but it is sometimes hard to isolate the parameters to establish a fundamental understanding of the role of different ore characteristics in sintering. For this purpose, a variety of laboratory-scale testing methods have also been developed for iron ore evaluation.

Due to the depleting reserves of high-grade iron ore around the world, the level of impurities in iron ore is increasing. Some of these impurities have been found to have deleterious impacts on sinter quality and sintering performance. In the meantime, an increasing number of large blast furnaces with inner volumes of more than 5000 m^3 have been built, which are often more demanding in terms of the quality requirements for ferrous feed materials. Finally, sinter plants are facing increasing pressure from more stringent regulations on their environmental impact. A variety of technologies have therefore been developed worldwide to tackle changing raw material conditions and mitigate emissions from sintering operations.

Acknowledgments

The authors wish to thank Dr. Ralph Holmes of CSIRO for reviewing the manuscript and his valuable comments and suggestions and the CSIRO sintering research team, in particular, Sarath Hapugoda, Matt Adam, Rodney Smith, Matt Kilburn, Alexander Edenton, and Natalie Ware, for their contributions to the results reported in this chapter.

References

Anon 1, 2014. How It Works—Iron Ore Sintering [Online]. Available: http://www.st-al.com/archive/sinteranlage/scheda.html (accessed 13 September 2014).

Bristow, N.J., Loo, C.E., 1992. Sintering properties of iron ore mixes containing titanium. ISIJ Int. 32, 819–828.

Chen, C., Zhang, L., Lu, L., Sun, S., 2010. Thermodynamic calculation of liquidus surface of FeO_x–CaO–SiO_2 System. ISIJ Int. 50, 1523–1531.

Clout, M.F., Manuel, J.R., 2003. Fundamental investigations of differences in bonding mechanisms in iron ore sinter formed from magnetite concentrates and hematite ores. Powder Technol. 130, 393–399.

Donskoi, E., Manuel, J.R., Clout, J.M.F., Zhang, Y., 2007. Mathematical modeling and optimization of iron ore sinter properties. Isr. J. Chem. 47, 373–379.

Donskoi, E., Manuel, J.R., Lu, L., Holmes, R.J., Poliakov, A., Raynlyn, T., 2009. Advances in mathematical modelling of sintering performance of iron ore fines. In: Iron Ore 2009, Perth, WA, Australia. The Australasian Institute of Mining and Metallurgy, pp. 341–349.

Fukuda, T., Himeda, M., Yoshida, H., Sasaki, N., Sato, M., Nasuno, T., Aso, S., Haga, R., 1984. The result of higher bed test operation in hirohata no. 1 sinter plant. Tetsu-to-Hagane 70, S30.

Furui, T., Kawazu, M., Sugawara, K., Fujiwara, T., Kagawa, M., Sawamura, A., Uno, S., 1977. Technology for preparation of raw materials to be sintered. Nippon Steel Technical Report, Overseas, 36–46.

Haga, T., Ohshio, A., Hida, Y., Fukuda, H., Ogata, N., 1997a. Improvement of the melting reaction in sintering process by the fine part selective granulation of clayish iron ores. Tetsu-to-Hagane 83, 233–238.

Haga, T., Ohshio, A., Nakamura, K., Kozono, T., Uekawa, K., 1997b. Control technique of the melting reaction in sintering process by the fine part selective granulation of clayish iron ores. Tetsu-to-Hagane 83, 103–108.

Hida, Y., Ito, K., Okazaki, J., Sasaki, M., Umezu, Y., 1982. Evaluation of coarse ores for sintering on the basis of their mineralogical properties. Tetsu-to-Hagane 68, 2166–2173.

Higuchi, K., Kawaguchi, T., Kobayashi, M., Toda, Y., Tsubone, Y., Ito, Y., Furusho, S., 2006. High-productivity operation in commercial machines by using stand-support sintering. Shinnittetsu-Giho 384, 28–32.

Hino, M., Kumano, A., Shimizuno, K., Nagasaka, T., 2003. Simulation on the formation, dripping and penetration behavior of primary oxide melt in the pyrometallurgical process. In: Kongoli, F., Itagaki, K., Yamauchi, C., Sohn, H.Y. (Eds.), Yazawa International Symposium: Metallurgical and Materials Processing: Principles and Technologies, 2003 San Diego, California, USA. In: Materials Processing Fundamentals and New Technologies, vol. 1. TMS, pp. 861–880.

Hosotani, Y., Konno, N., Yamaguchi, K., Orimoto, T., Inazumi, T., 1996. Reduction properties of sinter with fine dispersed pores at high temperatures of 1273 K and above. ISIJ Int. 36, 1439–1447.

Inazumi, T., 2000. Iron Ore Sinter (Review of Steps Taken to Overcome the Challenges Posed Japans Lack of Iron Ore Resources). The Iron and Steel Institute of Japan, Tokyo.

Inazumi, T., Fujimoto, M., Kasama, S., Sato, K., Shimozawa, E., Gushima, A., 1988. High permeability and high yield sintering operation by use of intensified sifting feeder. Zairyo-to-Process (CAMP-ISIJ) 1, 970.

Inazumi, T., Fujimoto, M., Sato, K., 1989. The mechanism of sintering reaction improvement with intensified sifting feeder (development of new feeding method of raw mix for sintering). Zairyo-to-Process (CAMP-ISIJ) 2, 940.

Inazumi, T., Fujimoto, M., Sato, K., 1990. Basic analysis of the influence of material grain size segregation on sintering. In: The Sixth International Iron and Steel Congress, October 21–26, 1990 Nagoya, Japan. ISIJ, pp. 110.

Ishiyama, O., Higuchi, K., Shinagawa, K., Ooyama, K., 2011. Granulation technology of raw material for sinter ore in Tobata no. 3 sinter plant. In: 2011 (8th) CSM Annual Meeting, October 26–28, 2011, Beijing, China. The Chinese Society for Metals, pp. 8.

Kamijo, C., Hara, M., Yamaguchi, Y., Yoshikawa, M., Kano, J., Matsumura, M., Kawaguchi, T., 2013. Technology for productivity improvement of sintering based on designing of composite granulation and bed structure of sinter mixture. ISIJ Int. 53, 1497–1502.

Kano, J., Kasai, E., Saito, F., Kawaguchi, T., 2005. Simulation model for granulation kinetics of iron ores. ISIJ Int. 45, 500–505.

Kawachi, S., Kasama, S., 2009. Quantitative effect of micro-particles in iron ore on the optimum granulation moisture. ISIJ Int. 49, 637–644.

Kawachi, S., Kasama, S., 2011. Effect of micro-particles in iron ore on the granule growth and strength. ISIJ Int. 51, 1057–1064.
Khosa, J., Manuel, J., 2007. Granulating behaviour of iron ores based on size distribution and composition. ISIJ Int. 47, 965–972.
Kimura, H., Ogawa, T., Kakki, M., Matsumoto, A., Tsukihashi, F., 2005. Effect of Al_2O_3 and MgO additions on liquidus for the CaO-SiO_2-FeO_x system at 1573 K. ISIJ Int. 45, 506–512.
Kongoli, F., 2003. Slags and fluxes in pyrometallurgical processes. In: Kongoli, F., Itagaki, K., Yamauchi, C., Sohn, H.Y. (Eds.), Yazawa International Symposium: Metallurgical and Materials Processing: Principles and Technologies, San Diego, California, USA. In: Materials Processing Fundamentals and New Technologies, vol. 1. TMS, pp. 199–210.
Kongoli, F., Mcbow, I., Yazawa, A., 2003. Phase relations during sintering of iron ore and fluxing effect of minor components. In: Kongoli, F., Itagaki, K., Yamauchi, C., Sohn, H.Y. (Eds.), Yazawa International Symposium: Metallurgical and Materials Processing: Principles and Technologies, March 2–6, 2003, San Diego, California, USA. In: Materials Processing Fundamentals and New Technologies, vol. 1. TMS, pp. 917–925.
Litster, J.D., Waters, A., 1986. Fundamentals of granulation of iron ore for ferrous sinter production. In: Fourteenth Australasian Chemical Engineering Conference: Chemeca 86, Adelaide, Australia. Institute of Chemical Engineers, Australia.
Litster, J.D., Waters, A.G., 1988. Influence of the material properties of iron ore sinter feed on granulation effectiveness. Powder Technol. 55, 141–151.
Litster, J.D., Waters, A.G., 1990. Kinetics of iron ore sinter feed granulation. Powder Technol. 62, 125–134.
Loo, C.E., 2005. A perspective of goethitic ore sintering fundamentals. ISIJ Int. 45, 436–448.
Loo, C.E., Leung, W., 2003. Factors influencing the bonding phase structure of iron ore sinters. ISIJ Int. 43, 1393–1402.
Loo, C.E., Wong, D.J., 2005. Fundamental factors determining laboratory sintering results. ISIJ Int. 45, 449–458.
Lu, L., Manuel, J.R., Khosa, J.S., 2007. Iron ore sintering research at different scales. In: Iron Ore 2007. AusIMM, Perth, WA, Australia.
Lv, X., Huang, X., Yin, J., Bai, C., 2011. Indication of the measurement of surface area on iron ore granulation. ISIJ Int. 51, 1432–1438.
Machida, S., Nushiro, K., Ichikawa, K., Noda, H., Sakai, H., 2005. Experimental evaluation of chemical composition and viscosity of melts during iron ore sintering. ISIJ Int. 45, 513–521.
Maeda, T., Fukumoto, C., Matsumura, T., Nishioka, K., Shimizu, M., 2005. Effect of adding moisture and wettability on granulation of iron ore. ISIJ Int. 45, 477–484.
Maki, T., Sekiguchi, I., 2009. Study for evaluation and optimization of iron ore granulation with consideration of dynamics and particle conditions. ISIJ Int. 49, 631–636.
Mao, H., Zhang, R., Lv, X., Bai, C., Huang, X., 2013. Effect of surface properties of iron ores on their granulation behavior. ISIJ Int. 53, 1491–1496.
Matsui, Y., Sato, A., Oyama, T., Matsuo, T., Kitayama, S., Ono, R., 2003. All pellets operation in Kobe no. 3 blast furnace under intensive coal injection. ISIJ Int. 43, 166–174.
Matsumura, T., Miyagawa, K., Yamagata, Y., 2005. Influence of the nuclei particle properties on granulability of marra mamba iron ore by high speed agitating mixer. ISIJ Int. 45, 485–491.
Matsumura, M., Yamaguchi, Y., Hara, M., Kamijo, C., Kawaguchi, T., Nakagawa, Y., 2013. Improvement of sinter productivity by adding return fine on raw materials after granulation stage. ISIJ Int. 53, 34–40.
Nagano, S., Noda, H., Yanaka, H., Shiobara, K., Yamaoka, Y., 1985. Characteristics of sinter feed and its influence on sintering. In: Capes, C.E. (Ed.), 4th International Symposium On Agglomeration. American Iron & Steel Society, Toronto, Canada, pp. 191–202.

Niwa, Y., Sakamoto, N., Komatsu, O., Noda, H., Kumasaka, A., 1993. Commercial production of iron ore agglomerates using sinter feeds containing a large amount of fine ores. ISIJ Int. 33, 454–461.

Okada, T., Okazaki, J., Nakano, M., Kawano, K., Miura, S., 2006. Influence of polymer dispersant on the granulation of raw materials for sintering process. Tetsu-to-Hagane 92, 735–741.

Okazaki, J., Higuchi, K., 2005. Marra Mamba ore, its mineralogical properties and evaluation for utilization. Isij International 45, 427–435.

Okazaki, J., Higuchi, K., Hosotani, Y., Shinagawa, K., 2003. Influence of iron ore characteristics on penetrating behavior of melt into ore layer. ISIJ Int. 43, 1384–1392.

Ooi, T.C., Lu, L., 2011. Formation and mitigation of PCDD/Fs in iron ore sintering. Chemosphere 85, 291–299.

Otomo, T., Takasaki, Y., Sato, H., 2009. Granule design for the sintering with less amount of liquid phase formation. ISIJ Int. 49, 659–666.

Oyama, N., Igawa, K., Nushiro, K., Fujii, N., 2000. Effects of the magnetic field exerted on the plate type feeder on the void fraction in the sintering bed and sinter productivity. Tetsu-to-Hagane 86, 309.

Oyama, N., Igawa, K., Takeda, K., Ariyama, T., Jinno, T., 2004. Influence of limestone and coke breeze distribution in the quasi-particle on permeability during sintering and sinter quality. Tetsu-to-Hagane 90, 546–553.

Oyama, N., Sato, H., Takeda, K., Ariyama, T., Masumoto, S., Jinno, T., Fujii, N., 2005. Development of coating granulation process at commercial sintering plant for improving productivity and reducibility. ISIJ Int. 45, 817–826.

Oyama, N., Takeda, K., Fujii, N., 2008. Development of new coating granulation technology of limestone and coke breeze. JFE Tech. Rep. 22, 32–37.

Oyama, N., Iwami, Y., Yamamoto, T., Machida, S., Higuchi, T., Sato, H., Sato, M., Takeda, K., Watanabe, Y., Shimizu, M., Nishioka, K., 2011. Development of secondary-fuel injection technology for energy reduction in the iron ore sintering process. ISIJ Int. 51, 913–921.

Pownceby, M.I., Clout, J.M.F., 2002. The importance of fine ore chemical composition and high temperature phase relations—applications to iron ore sintering and pelletising. In: Iron Ore 2002, 2002 Perth, Western Australia. The Australasian Institute of Mining and Metallurgy, pp. 209–215.

Roller, P.W., 1982. Granulation of iron ore. BHP Techn. Bull. 26, 44–45.

Sakai, A., Noda, H., Sato, H., Shiobara, M., Hashimoto, K., Yamashita, K., 2001. Technological improvements to attain high productivity at Fukuyama No.5 sintering machine (HPS). NKK Techn. Rep. 174, 34–38.

Sakamoto, N., 2002. Iron ore granulation model supposing the granulation probability estimated from both properties of the ores and their size distributions. ISIJ Int. 42, 834–843.

Sakamoto, N., Noda, H., Iwata, Y., Saito, H., Miyashita, T., 1987. Fundamental investigation on production conditions of new iron ore agglomerates for blast furnace burdens and evaluation of their properties. Tetsu-to-Hagane 73, 1504–1511.

Sasaki, M., Suga, Y., Fukuda, H., 1980. The air-segregated charging system in Sakai sinter plant. Tetsu-to-Hagane 66, S86.

Takai, C., Sakai, A., Sato, H., Komatsu, O., Noda, H., 1993. Feeding zone modification of fukuyama no. 4 sintering machine. Zairyo-to-Process (CAMP-ISIJ) 6, 916.

Takamatsu, N., Kurihara, K., Hatanaka, A., Saitoh, G., Kaku, H., 2011. Development of iron-making technology. Shinnittetsu-Giho 391, 79–87.

Takeda, K., Oogami, M., 2008. Recent development of iron making technology in JFE steel. JFE-Giho 22, 1–5.

Tsukihashi, F., Kimura, H., 2003. The effect of mgo and Al_2O_3 additions on the liquidus of the CaO-SiO_2-FeO_x system at various partial pressure of oxygen. In: Kongoli, F., Itagaki, K., Yamauchi, C., Sohn, H.Y. (Eds.), Yazawa International Symposium: Metallurgical and Materials Processing: Principles and Technologies, 2003, San Diego, California, USA. TMS, pp. 851–860.

Waters, A.G., Litster, J.D., Nicol, S.K., 1989. A mathematical model for prediction of granule size distribution for the multicomponent sinter feed. ISIJ Int. 29, 274–283.

Yamaguchi, Y., Kamijo, C., Matsumura, M., Kawaguchi, T., 2013. Improvement of permeability of sintering bed by adding dry particles to granulated raw materials. ISIJ Int. 53, 1538–1544.

Yoshinaga, M., Ichidate, M., 1982. Recent progress in iron ore sintering. Tetsu-to-Hagane 68 (15), 2156–2165.

Iron ore pelletization

15

D. Zhu[1], *J. Pan*[1], *L. Lu*[2], *R.J. Holmes*[3]
[1]Central South University, Changsha, Hunan, China
[2]CSIRO Mineral Resources Flagship, Pullenvale, QLD, Australia
[3]CSIRO Mineral Resources Flagship, Clayton South, VIC, Australia

15.1 Introduction

Iron ore lump, sinter, and pellets comprise the main burden of modern blast furnaces. However, sinter and pellets are now the dominant blast furnace burden, because the natural lump supply has declined dramatically due to depletion of the world's high-grade competent iron ore resources. In addition, more iron ore concentrates are being produced due to the increasing need for beneficiation to upgrade low-grade iron ore resources. Although iron ore concentrates are generally higher in iron grade and contain lower impurities, the finer size distribution of concentrates limits their usage in iron ore sintering. Therefore, pelletizing is needed to produce fired pellets from concentrates as burden materials for blast furnaces and direct reduction processes. The pelletization process is very widely used, particularly when burden materials must be shipped great distances between the mine and the blast furnace, because fired pellets are durable and easy to handle. Pellets also perform very well in the blast furnace, with good bed permeability and reducibility. There was an intensive study as early as in 1943 at the University of Minnesota on the pelletizing process given the necessity of using taconite (Ball et al., 1973). In 1955, two pelletizing plants commenced operation in the United States with an annual production rate of 12 Mt (Meyer, 1980; Jiang et al., 1996). Since then, various pelletizing technologies have been developed and the production of fired pellets has increased considerably (Jiang et al., 1996; Fu and Zhu, 2007).

The commercial large-scale production technologies for fired pellets currently available include the shaft furnace, the grate-kiln (GK), and the straight grate (SG) firing systems. The shaft furnace technology has advantages such as low capital and operating costs. However, it is only suitable for making fired pellets using magnetite concentrates as pellet feed and achieves relatively low productivity. The biggest annual capacity of shaft furnaces is reported to be about 600,000 tonnes per furnace in Benxi Steel, China (Qing and Li, 2000). Furthermore, the quality of fired pellets is not so uniform (Fu and Zhu, 2007). In contrast, the grate-kiln system has been demonstrated to be capable of producing fired pellets using a variety of pellet feeds, such as magnetite, hematite, specularite, goethite, pyrite cinder, and their mixtures (Fu and Zhu, 2007). The largest annual capacity of grate-kiln systems has reached 6–7 Mt. More importantly, the quality of product pellets fired using the grate-kiln system is much more uniform than that of shaft furnace and straight grate technologies. Furthermore, coal can be used in grate kilns as the fuel for firing the pellets, which makes the process much more flexible, leading to lower operating costs. The straight grate technology is characterized by an

Iron Ore. http://dx.doi.org/10.1016/B978-1-78242-156-6.00015-0
© 2015 Elsevier Ltd. All rights reserved.

annual capacity of as high as 9.25 Mt per system (Thomas and Collin, 2013), and it is suitable for various pellet feeds and the production of flexible product types, such as acid pellets, fluxed pellets, and high-MgO pellets (Chaigneau, 2013). Straight grate, grate-kiln, and shaft furnaces account for approximately 58%, 35%, and 6%, respectively, of world pellet production in 2013 (Oja, 2013). Therefore, the grate-kiln and straight grate systems are the dominant technologies currently being used in the iron ore pelletizing industry.

Figure 15.1 shows the flow sheets for modern straight grate and grate-kiln pelletizing processes. The straight grate process consists of a single furnace, which is divided into different zones for drying, preheating, and indurating green balls and zones for cooling the fired pellets. However, the grate-kiln system consists of three separate process units connected in series: a traveling grate for drying and preheating green balls, a rotary kiln for indurating preheated pellets, and an annular cooler for cooling the fired pellets. In Table 15.1, Mourão et al. compared the raw material requirements, unit capacity, fuel type, product quality, energy consumption, capital and operation

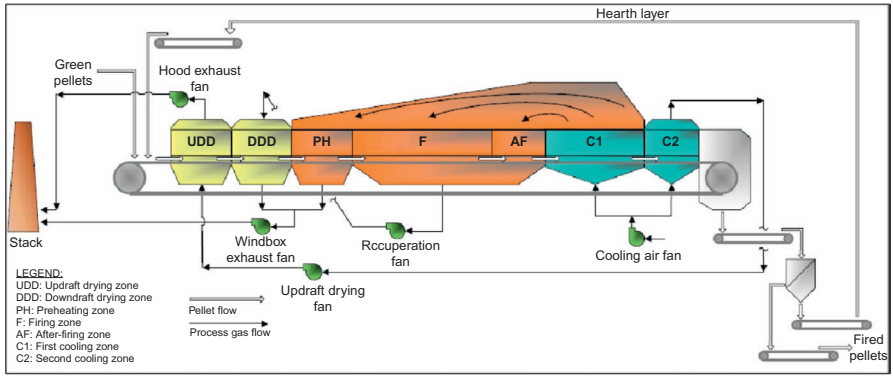

(a)

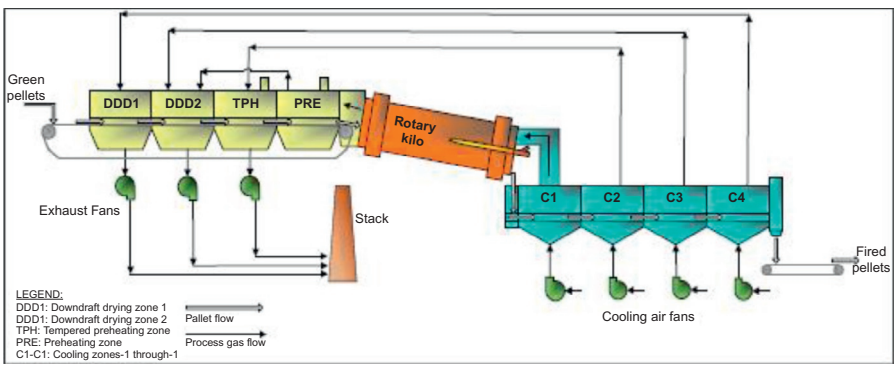

(b)

Figure 15.1 Schematic of the two main pelletizing processes: (a) straight grate pelletizing process; (b) grate-kiln pelletizing process (also known as the rotary-kiln process) (Mourão, 2012).

Table 15.1 Overall comparison of straight grate (SG) and grate-kiln (GK) pelletization (Mourão, 2012)

Variables		SG	GK	Remarks
(1)	Iron ore mineral			The grate-kiln is best suited for magnetite and magnetite/hematite mixtures, while the straight grate is suitable for all types of feed
	(a) Hematite	Yes[a]	Limited[b]	
	(b) Magnetite	Yes[a]	Yes[a]	
	(c) Hematite/ magnetite mixture	Yes[a]	Yes[a]	
(2)	Unit capacity			The grate-kiln has not demonstrated unit capacities beyond 7.0 Mtpa
	(a) 3–7 Mtpa	Yes[c]	Yes[c]	
	(b) 7–9 Mtpa	Yes[c]	No[c]	
(3)	Fuel type			The straight grate has not demonstrated operation with pulverized coal, while the grate-kiln can operate with all fuels. Furthermore, the straight grate can operate with high amounts of carbon addition to hematite ore mixes, whereas the use of the grate-kiln for this application is limited
	(a) Natural gas	Yes[a]	Yes[a]	
	(b) Fuel oil	Yes[a]	Yes[a]	
	(c) Pulverized coal	No[b]	Yes[a]	
	(d) Carbon addition to hematite ore mix	High amount[a]	Limited use[d]	
(4)	Thermal energy consumption	Slightly lower[a]	Slightly higher[c]	Slight advantage for the straight grate
(5)	Electrical energy consumption	Higher[d]	Lower[a]	Advantage for the grate-kiln due to smaller process fans
(6)	Product quality	Slightly lower[c]	Slightly higher[a]	Advantage for the grate-kiln due to more uniform pellet firing conditions
(7)	Fines generation	Less fines[a]	More fines[d]	Advantage for the straight grate due to fewer transfer points and no abrasion in the straight grate
(8)	Capex	Slightly higher[c]	Slightly lower[a]	Slight advantage for the grate-kiln in process fan cost, no hearth layer return system and potentially less building costs without abundant demands for high temperature alloy steel
(9)	Opex	Similar[c]	Similar[c]	Site specific
(10)	Environmental performance	Similar[c]	Similar[c]	More potential to reduce NO_x emissions for the grate-kiln, otherwise no obvious advantage

[a]Competitive advantage.
[b]Technical constraint.
[c]No advantage/disadvantage.
[d]Disadvantage.

costs, and environmental performance of straight grate and grate-kiln technologies (Mourão, 2012). The straight grate technology has been proved for all ore types and has achieved higher unit capacity, while the grate-kiln process is more flexible with respect to fuel type and produces pellets with slightly better quality.

The ratio in the output from the three main pelletizing technologies changes depending on practical circumstances, such as iron ore reserves, iron ore types, market demand, and required investment. The ratio for grate-kiln pellets has increased to 55.33% in 2011 from 7.21% in 2000, while the ratio for shaft furnace pellets has dropped to 42.05% in 2011 from 68.95% in 2000 in China (see Figure 15.2).

Iron ore pellets are essential burden materials to improve the performance of modern blast furnaces, because they possess high iron grade, low silica and alumina contents, excellent mechanical strength, and metallurgical performance with a uniform size distribution. The ratio of fired pellets in the burden of blast furnaces, particularly, in North America is as high as 100%. However, the use of pellets in East Asia is historically considerably lower. For example, the average percentage of fired pellets is only about 15% of the ferrous burden in blast furnaces in China (Zhu, 2013).

With the rapid development of the world steel industry, the world output of fired pellets has increased dramatically due to the increasing demand for fired pellets to improve the performance of blast furnaces. From 2010 to 2012, the global annual pellet production increased from 388 to 440 Mt (Narciso, 2013; Mendes, 2012; Zhang, 2012). Table 15.2 lists the key producers of iron ore pellets in the world between 2010 and 2012. China is the largest pellet producer and produced about 1.3–1.4 Mt fired pellets in 2012, accounting for approximately 30.7% of total world production (Narciso, 2013).

Of the pellets produced worldwide, about 30% are used in direct reduction processes to produce direct reduced iron, while the remainder are used in blast furnace iron making processes (Chaigneau, 2013). With the development of the world steel industry, the increasing need for beneficiation due to the depletion of high-grade iron

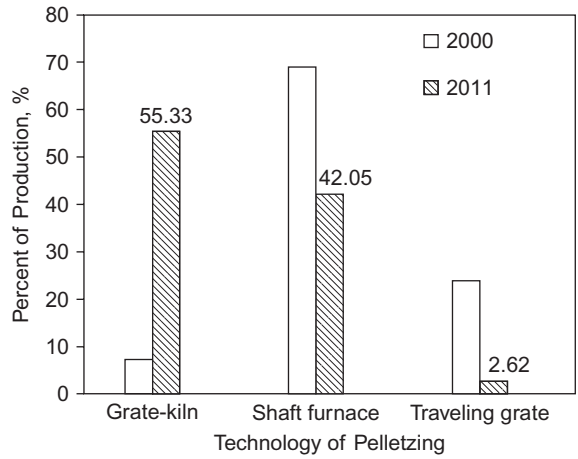

Figure 15.2 Ratios of pellets produced by different pelletizing processes in China in 2000 and 2011.

Table 15.2 Main producers of iron ore pellets in the world between 2010 and 2012 (Mt per year) (Narciso, 2013; Mendes, 2012; Zhang, 2012)

Company	Location	2010	2011	2012
Vale	Brazil, Oman	40.119	43.091	44.415
Cliffs	USA, Canada	32.446	34.892	33.068
Samarco	Brazil	21.508	21.452	21.305
LKAB	Sweden	22.100	22.900	23.800
Metalloinvest	Russia	21.971	22.409	22.629
Severstal	Russia	9.797	10.120	10.325
Metinvest	Ukraine	12.111	12.544	12.270
Evraz	Russia	5.616	5.907	6.051
US Steel	USA	18.144	19.142	19.414
ArcelorMittal	Canada, USA	12.000	12.100	11.910
Essar	India	5.400	4.7000	5.500
Tata	Netherlands, India	5.300	5.600	6.600
FMO	Venezuela	0.245	1.100	0.882
Huasco Valley	Chile	3.943	3.243	2.242
Sidor	Venezuela	4.110	5.144	4.326
Pena Colorada	Mexico	4.070	4.003	4.070
Erdemir	Turkey	1.493	1.495	1.543
Grange	Australia	2.205	1.978	2.005
Ternium	Mexico	1.757	1.699	1.872
Kobe	Japan	3.682	3.451	3.485
Zhuhai	China	1.200	1.200	1.200
Anyang	China	0	0	0.800
VTM Mining	China	0.713	0.613	0.499
Other China	China	122.087	129.387	132.901
JSW	India	1.425	0.963	0.934
JSPL	India	2.128	3.532	4.076
KIOCL	India	1.273	2.124	1.710
Bharat	India	0.800	0.800	0.800
Mobarakeh	Iran	5.200	6.200	7.200
Khouzestan	Iran	4.430	4.920	5.040
Go Gohar	Iran	1.278	2.889	4.500
Ardakan	Iran	2.255	2.953	3.438
Mandovi	India	0.600	0.600	0.600
AHMSA	Mexico	4.095	4.133	4.547
Hierro	Peru	3.021	3.505	3.342
Arrium	Australia	0.810	0.810	0.440

ore resources, and the strict requirements for environment protection, the production of fired pellets will have considerable room to increase, as predicted in Table 15.3 (Mendes, 2012).

By 2025, an estimated 500 Mtpa of new concentrate products will come onto the market and needs a means of consumption; currently, pelletizing is the only viable option (Chaigneau, 2013).

Table 15.3 Apparent and projected production of fired pellets (million tonnes)

Year	2006	2010	2011	2012	2013	2014	2015	2021
Sweden	15.85	20.49	24.78	25.95	26.24	26.50	26.60	28.11
CIS	64.15	64.93	61.72	61.46	65.33	69.91	67.88	78.22
Canada	26.78	24.94	26.33	26.43	26.43	26.43	26.43	28.91
Mexico	14.36	13.25	14.34	14.98	15.50	15.94	16.28	18.81
The United States	51.83	41.77	42.84	46.55	49.66	52.53	55.11	58.61
Brazil	51.00	55.76	59.10	63.72	65.70	68.61	72.44	83.98
China	75.47	124.50	128.37	142.53	157.39	171.58	185.86	202.13
India	9.86	18.19	23.81	32.72	38.50	46.34	54.75	92.99
Australia	2.88	4.44	4.87	4.84	5.32	6.35	8.39	6.45
Total	348.35	402.15	428.04	469.54	506.31	542.93	574.13	681.48

Production = (Total Consumption of Pellets + Pellet Exports) − Consumption of Imported Pellets.
Source: CRU Analysis (2011b).

The pelletizing process involves the preparation of raw materials; the proportioning and mixing of raw materials; the formation, preheating, and firing of green balls; and the cooling of the fired pellets. With the dramatic increase in pellet production, considerable progress has also been made in

- pelletizing difficult iron-containing feeds and wastes, such as specular hematite; high-sulfur-containing magnetite concentrates, and pyrite cinder;
- pretreating pellet feeds to improve their ballability and reduce the bentonite dosage;
- developing organic binders; and
- developing different types of fired pellets with better metallurgical performance, such as acid pellets, fluxed pellets, and high-MgO pellets.

Therefore, this chapter will focus on recent developments in the preparation of raw materials, balling, and firing for iron ore pellet production.

15.2 Specification requirements of pellet feed

Raw material characteristics are critical for the pelletizing process. The concentrate, together with other additives such as bentonite and fine coke, should meet certain specifications before they can be regarded as suitable pellet feed materials. Table 15.4 shows the chemistry of typical commercial pellets (Poveromo, 2014). To achieve the Fe grade and impurity levels required for pellets, a total Fe content of over 64% is preferred for pellet feed. The impurity specification of pellet feed is usually dictated by the intended application of the resultant pellets. Detailed discussion on the quality requirement of pellets can be found in Chapter 16.

While balling characteristics are less dependent on the chemical composition of concentrates, they are strongly affected by the physical properties of the concentrates, such

Table 15.4 Typical pellet chemistry (mass, %)

Chemistry	Blast furnace pellets				DR-grade pellets
	Acid		Fluxed	Low SiO_2, fluxed	
Fe	65.10	65.60	63.30	65.10	67.80
SiO_2	5.20	4.50	3.75	2.50	1.65
Al_2O_3	0.50	0.50	0.50	0.45	0.35
CaO/SiO_2	0.12	0.13	0.98	0.90	0.30
CaO	0.60	0.60	3.68	2.25	0.50
MgO	0.25	0.25	1.30	1.50	0.30

as size distribution, surface area, particle shape, porosity, roughness, and hydrophilicity. For example, specular hematite concentrates generally present more difficulties in green ball formation than magnetite concentrates because of the platelike shape and dense nature of their grains. Generally, any material being considered for pelletizing should contain at least 70%-44 μm material and have a specific surface area (Blaine index) of >1200 cm^2/g to ensure good balling characteristics (Poveromo, 2014; Indian Bureau of Mines, 2011). In practice, satisfactory green ball formation can usually be achieved by regrinding the material to achieve about 80–90% minus 44 μm material and a Blaine index of 1500–2100 cm^2/g. In China, the static ballability index, K_p, defined below is used to evaluate whether an iron ore concentrate can easily be pelletized or not:

$$K_p = W_m / (W_c - W_m) \tag{1}$$

where W_m and W_c are the saturated molecular moisture (%) and capillary moisture (%) of the iron ore concentrate, respectively. The ballability of iron ore concentrates is often poor when the value of K_p is less than 0.3 and acceptable when K_p is higher than 0.6.

In addition to the physical characteristics of pellet feed, the balling moisture content and binder addition also have a substantial impact on the quality of green balls formed. The optimum moisture content for good balling is usually in the range of 7–9% depending on the characteristics of the pellet feed. Different pellet feeds often require different bentonite additions to achieve the required green ball quality.

Good quality green balls are the basic requirement for manufacturing high-quality fired pellets, which require the green balls to remain intact and endure mechanical impact, pressure, and thermal impact during handling from the discharge from pelletizers, through roller screens, to drying and preheating on the straight grate. Therefore, a series of tests have been developed for the evaluation of green balls, such as size distribution, wet compressive strength, drop number, and thermal shock temperature. Table 15.5 summarizes the minimum quality generally required for green balls produced in laboratory balling tests. It is difficult to set an acceptable value for the thermal shock temperature of green balls, because the temperature varies greatly depending on the size distribution and surface properties of the pellet feed, the properties and dosage of bentonite used, and the amount of water added;

Table 15.5 Minimum quality requirements for green balls produced in the laboratory

Parameters	Size (mm, %)	Drop number (number of drops from 0.5 m)	Compressive strength (*N* per pellet)
Quality requirement	>85% 9–16 mm	5–6	>10

also, different pelletizing processes have very different requirements on the thermal shock temperature. Usually the higher the thermal shock temperature, the faster the permitted drying rate at higher drying temperatures or the larger the flow rate of drying medium.

15.3 Green ball formation and properties

15.3.1 Green ball formation

Good performance in green ball formation results in quality green balls, which is important for an efficient firing process and good pellet quality. In practice, the production of the pellets is carried out in pelletizing disks or drums. Figure 15.3 illustrates the formation mechanism for green balls, which is determined by a series of phenomenon involving the particles of the mixture and water (Meyer, 1980). For detailed information on green ball formation, readers can refer to the classic work by Meyer (1980).

Briefly, green balls of the finely ground iron-bearing materials, such as hematite and magnetite concentrates, are formed by the capillary and viscosity forces of the liquid between the concentrate particles, as well as the hydrogen bonding between the concentrate particles and water during rolling of the green balls in disk or drum

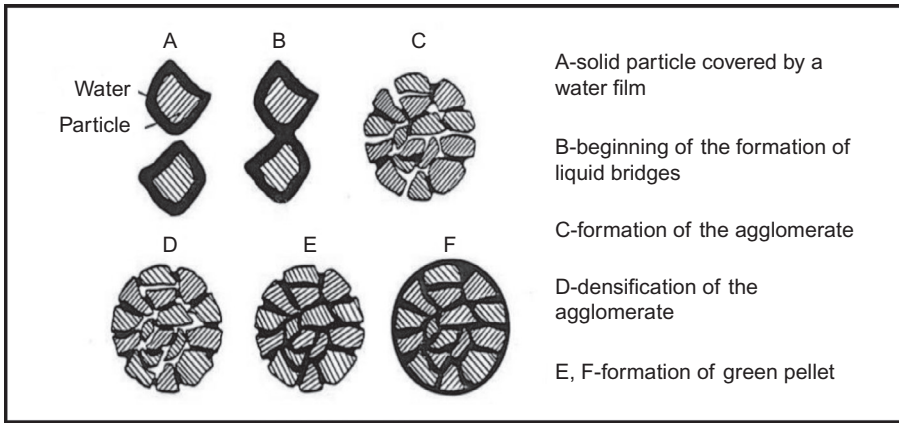

Figure 15.3 Steps in the formation of green pellets (Meyer, 1980).

pelletizers. Capillary forces between the concentrate particles are believed to be the dominant force during the formation of green balls (Zhu, 1994). Because the capillary force depends on the size distribution and hydrophilicity of pellet feed particles, factors influencing the formation and properties of green balls can be classified into the following three categories:

- Characteristics of the pellet feed, such as size distribution, specific surface area, surface morphology, hydrophilicity, and ore type
- Balling parameters, such as moisture, binder dosage and types, and balling time
- Operating conditions of the pelletizer, such as rotation speed, angle of inclination of the pelletizer, occupancy ratio, and circulation of the load

Therefore, under fixed balling conditions, the characteristics of the pellet feed play a key role in determining the formation and quality of green balls. The importance of pellet feed characteristics has been discussed in the proceeding section of this chapter on the specifications of pellet feed. Different material preparation methods have been developed to alter the characteristics of the pellet feed to improve its balling ability and consequently the quality of the resultant balls.

15.3.2 Pretreatment of pellet feed

With the rapid development of the pelletizing industry, new and more complicated raw materials, such as specularite, high-sulfur-containing magnetite concentrates, goethite, and pyrite cinder, are being used as pellet feed to supplement traditional hematite and magnetite feeds with good balling ability. These new materials often have coarser size distributions and very low specific surface areas even after being ground to 85% passing 74 μm and 60% passing 44 μm. On the other hand, some magnetite concentrates with fine size distributions and high specific surface areas have poor balling ability when reverse flotation is used to remove silica, because the surface of the magnetite particles is contaminated by surfactant during flotation, resulting in poor hydrophilicity. In such situations, pretreatments before balling are needed to improve the balling ability of the pellet feed by exposing more newly formed surfaces and achieving better hydrophilicity. Discussion here will be focused on pretreatment methods, including damp milling, ball milling, and high-pressure grinding rolls (HPGRs) processing or a combination of these processes (Fu and Zhu, 2007; Mendes, 2012). According to Pan et al. (2008), mechanical activation is an effective technique when the material is ground down into the brittle–ductile transition range. The wetting heat increases due to structural distortions such as material amorphization, changes in surface area, crystallite size and strain, and phase transformations. Such structural changes are essential factors in determining the reactivity of material (Boldyrev et al., 1996). Some research results have shown that the surface characteristics and sintering or crystallization capabilities of specularite can be improved through damp milling (He, 2005; Zhu et al., 2007). Some studies also indicate that green ball strength increased and bentonite consumption decreased when magnetite concentrates were treated with an HPGR, which occurred because the magnetite concentrates were activated with the change in structure (Wang et al., 2002, 2005; Zhang and Qi, 2005).

15.3.2.1 Damp milling

Damp milling with a rubber liner installed inside the mill is similar to dry ball milling in that wet raw materials, including magnetite concentrate and bentonite, are milled at 5–6% moisture. However, it differs from dry ball milling in that the physicochemical properties of the sample are changed during damp milling, such as hydrophilicity improved, wetting heat increased, and activation energy of the oxidation reaction decreased (Wang, 2003). The effectiveness of damp milling to improve balling ability depends on the milling time, moisture content of the feed, occupancy ratio, size distribution of the grinding medium, and rotation speed of the damp mill. Damp milling is widely used in shaft furnace pellet plants in China for improving the balling ability of magnetite concentrates and reducing the bentonite dosage (Wang, 2003).

In a study (Wang, 2003) to investigate the effect of damp milling on the balling ability of a magnetite concentrate, the drop number was found to increase first with milling moisture content and then declined after it reached a peak at 6% milling moisture content, as shown in Figure 15.4. Therefore, the optimum moisture content for damp milling is between 5% and 6% for this concentrate. In addition, once the moisture content was over 6%, more materials adhered onto the rubber liners inside the damp mill, leading to severe operational issues. After testing a series of rotation speeds, the critical rotation speed (at this rotation speed, outmost grinding media cannot fall off and start to rotate with the cylinder) of the laboratory damp mill was found to be 59.8 rpm. The recommended speed of operation was 70–80% of the critical rotation speed. Therefore, the damp mill was operated at 6% feed moisture content and a rotation speed of 45 rpm in subsequent tests to study the effect of milling time on green ball quality.

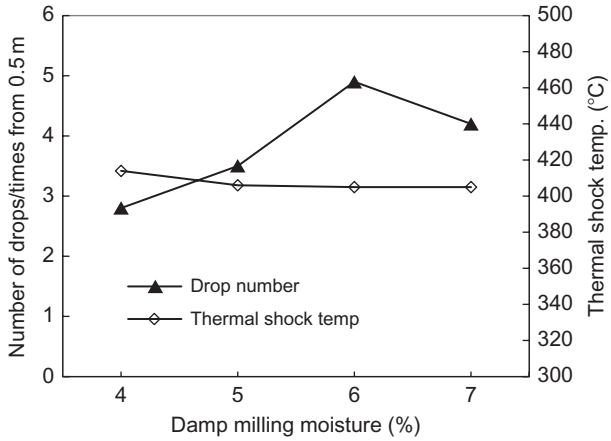

Figure 15.4 Effect of damp milling moisture content on the properties of green balls produced at 1.0% bentonite and 8.0% balling moisture content (the concentrate was milled at an occupancy rate of 17.36% and a rotation speed of 45 rpm in a damp mill for 6 min).

Table 15.6 Effect of damp milling time on the size distribution of a magnetite concentrate (mass, %)

Size fraction (mm)		+0.425	−0.425 +0.18	−0.18 +0.15	−0.15 +0.106	−0.106 +0.075	−0.075 +0.045	−0.045
Milling time (min)	0	0.80	0.35	6.25	14.50	9.10	18.15	50.85
	6	0.80	0.30	3.05	7.60	8.05	18.20	62.00
	10	0.15	0.30	2.15	9.40	7.00	15.40	65.60

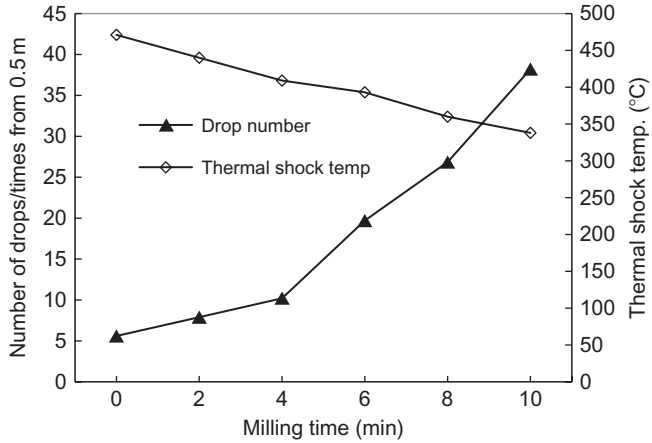

Figure 15.5 Effect of milling time on the properties of green balls produced at 2.5% bentonite and 8.0% balling moisture content (the concentrate was milled at 6% moisture content, an occupancy rate of 17.36% and a rotation speed of 45 rpm in a damp mill).

As shown in Table 15.6, the proportion of materials below 45 μm increased by approximately 11.2% after 6 min of damp milling. As the particle size decreased, the capillary radius of the concentrate particles reduced, leading to a higher capillary force.

The drop number for the green balls was found to increase dramatically with milling time (Figure 15.5), the drop numbers improving from 10 to over 20 when the milling time was increased from 4 to 6 min. By improving the balling ability, damp milling can therefore reduce the bentonite dosage. It was found that the green balls produced from the pretreated concentrate could still achieve a minimum drop number of 5 even when the dosage of bentonite was reduced to 1%. In contrast, the thermal shock temperature decreased with damp milling time due to the increased resistance to water transportation out of the green balls during drying. The thermal shock temperature dropped to below 350 °C when the milling time was over 6 min, which is below the minimum requirement for shaft furnaces. Therefore, a milling time of 4–6 min was recommended for this concentrate. The compressive strength of the green balls was found to be less dependent on the milling time and was consistently above 10 N per pellet over the range of milling times studied.

It is worth mentioning that damp milling is usually used in small pellet plants using shaft furnaces with an annual capacity of 300,000–800,000 tonnes per annum to produce fired pellets with magnetite as the feed. However, damp milling is not suitable for pretreating hard hematite fines prior to pelletizing.

15.3.2.2 HPGR

The HPGR is composed of two opposing rotating rolls, coupled with traction-resistant bearings, which provide a very robust structure. Through a pneumatic spring system, pressure is applied to one of the rolls, while the other remains in a fixed position (Figure 15.6). The two rolls are rotated by separate motors connected to the shafts of the rolls through a gear reducer (Klymowsky et al., 1998).

Use of HPGRs for grinding has gained considerable popularity over the last few years due to its potential for improving capacity and reducing energy consumption in grinding circuits (Norgate and Weller, 1994; Fuesternau et al., 1995; Pan et al., 2008). Comminution occurs in HPRGs due to the high interparticle stresses generated when a bed of solids is compressed as it moves down the gap between the two pressurized rolls. Such high interparticle stresses result in a much greater proportion of fines in comparison to conventional crushing methods. The HPGR has been widely used in the minerals and cement industries in the pregrinding stage prior to conventional ball milling. In this hybrid grinding configuration, the energy efficiency of HPGRs is combined with the ability of ball mills to achieve high size reduction ratios. Schönert (1988) pointed out that the success of the hybrid grinding mode depends on the efficiency of the HPGR in producing fractures within the product and weakening the particles that remain unbroken. Indeed, it is claimed that the Bond work index of the HPGR product is significantly lower than the product of conventional crushers (Norgate and Weller, 1994; Pazelt et al., 1995).

Brazilian hematite concentrates are quite different in terms of pelletizing behavior compared with Chinese domestic magnetite concentrates. These concentrates, especially the southern specular hematite concentrates, often have coarse grain sizes, low

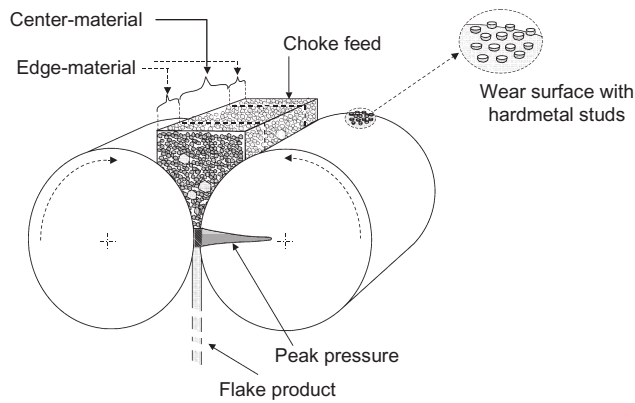

Figure 15.6 Diagram showing the grinding zones between the two rolls of a HPGR.

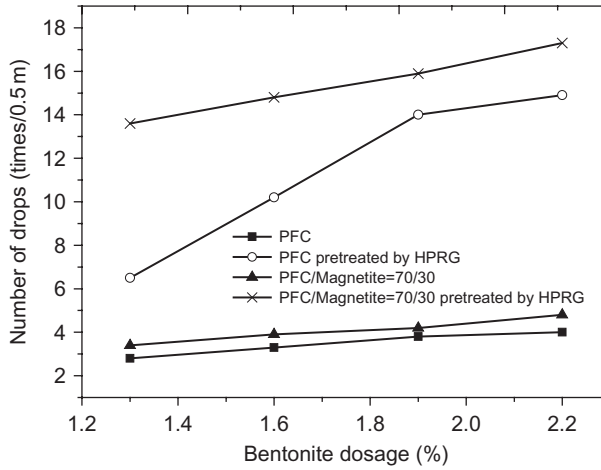

Figure 15.7 Effect of HPGR pretreatment on the drop number of green balls as a function of bentonite dosage (PFC—specularite and magnetite—Chinese domestic magnetite concentrate).

specific surface areas, poor wettability by water, and refractory firing characteristics, leading to weak green and fired pellets, high roasting temperatures, and low productivity. As shown in Figure 15.7, HPGR treatment is an effective process for greatly improving the drop strength of green balls, and HPGR-treated concentrates require much lower bentonite dosages to achieve the minimum required drop strength.

Apart from the increased specific surface area due to size reduction, the HPGR is also an effective technique for inducing mechanical activation when the material is ground down to the brittle–ductile transition region. The structural distortions occurring during the HPGR process, such as material amorphization, changes in surface area, crystallite size and strain, and phase transformations and internal fracture, increase the excess enthalpy leading to mechanical activation and a further increase in specific surface areas (Figure 15.8; Wang, 2003). Such structural changes were found to be essential factors in determining the reactivity of materials (Boldyrev et al., 1996).

The HPGR is now widely used for improving the balling characteristics of difficult pellet feeds, such as specularite and pyrite cinder, because it is very effective in increasing the specific surface area of pellet feeds at low production cost. Work on magnetite concentrates has revealed similar benefits. The green ball strength increases and the bentonite consumption decreases when magnetite concentrates are treated with HPGR (Zhu et al., 2004).

The efficiency of the HPGR process is affected by its processing parameters, such as feed moisture content, roll pressure and speed, and the feeding rate through the rolls. After examining various feeds, the authors found that each feed achieved its optimum specific surface area at its specific moisture content, as evidenced in Figure 15.9. Too high feed moisture content affects the specific surface area of HPGR ground products adversely, because the compression force imposed inside the feed bed between the rolls drops dramatically as the feed moisture content increases. This is due to that the

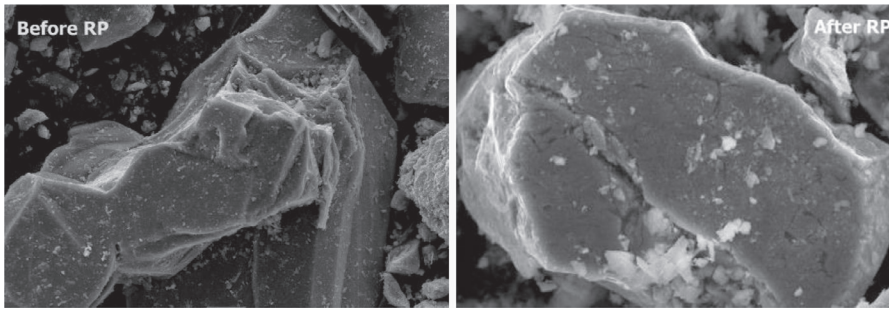

Figure 15.8 Change in surface morphology of concentrate particles as a result of HPGR pretreatment.

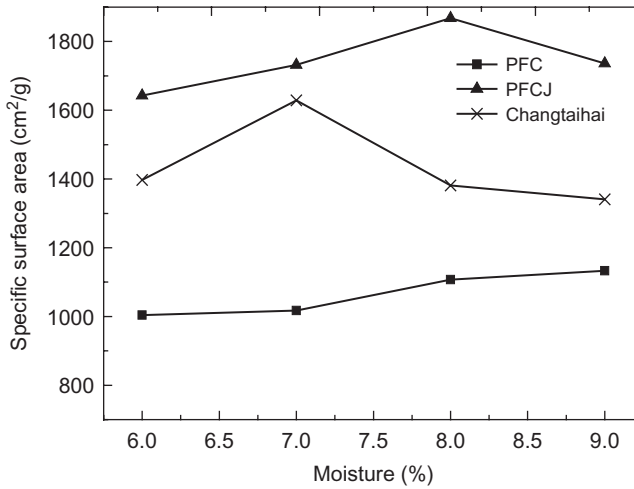

Figure 15.9 Effect of feed moisture content on the specific surface area of HPGR ground products (PFC and PFCJ are hematite concentrates, while Changtaihai is Chinese domestic magnetite concentrates) at a rolls speed of 168 r/min, a roller compaction force of 3.0 t, open circuit and one pass.

fact that the friction force between the particles inside the feed bed decreases and water is incompressible. The authors have also investigated the effect of the compression force between the rolls on the specific surface area of ground products. As shown in Figure 15.10, the higher the compression force, the greater the specific surface area achieved by the HPGR. However, too high a pressure requires more energy and a stronger machine structure, leading to higher capital investment.

The HPGR can be run in open or closed circuit. The open-circuit configuration usually consists of one or two stages of HPGR processing (Table 15.7). It can be found that the green balls' strength has been improved, while the concentrates pretreated by

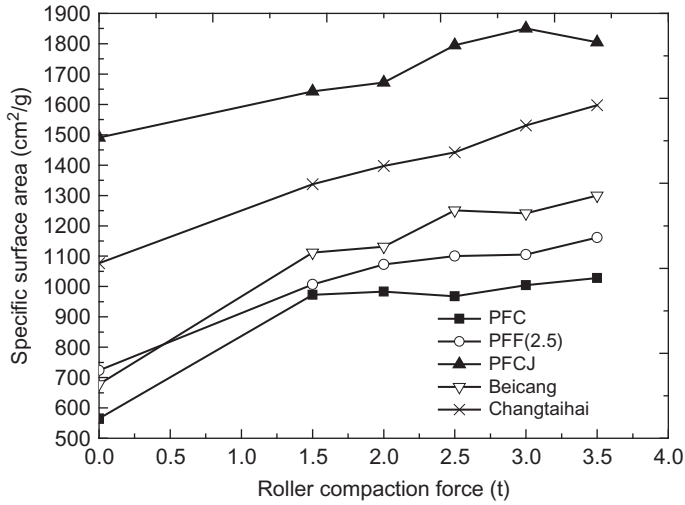

Figure 15.10 Effect of compaction force between the rolls on the specific surface area of HPGR ground products (PFC, PFF2.5, and PFCJ are hematite concentrates, while Beichang and Changtaihai are Chinese domestic magnetite concentrates), at 6% moisture content, a roller speed of 168 r/min, open circuit and one pass.

Table 15.7 Effect of high pressure roll grinding on the quality of green balls (two passes in open circuit at 7% moisture content, 3 t compaction force, 1.2% bentonite, and 7.8% moisture content for balling)

Samples	Wet compressive strength (*N* per pellet)	Drop number (number of drops from 0.5 m)	Thermal shock temperature (°C)
PFC hematite without HPGR pretreatment	4.9	1.0	355
PFC pretreated by HPGR	9.7	6.0	410
Mixture of PFC and magnetite 70/30) without HPGR pretreatment	4.7	2.0	454
Mixture of PFC and magnetite (70/30) pretreated by HPGR	10.3	4.5	455

HPGR; moreover, the thermal shock temperature of green balls has not deteriorated. On the other hand, in the closed-circuit configuration, the material from the roll edges is recirculated. In order to reduce capital investment and space, the closed-circuit configuration is often adopted, and the recirculation ratio is varied according to the targeted properties of the pellet feed required for balling.

Table 15.8 Effect of high pressure roll grinding on the size distribution and specific surface area (SSA) of iron ore concentrate mixtures

Size (mm)	+0.106	−0.106 +0.074	−0.074	−0.044	−0.0086	SSA ($cm^2 g^{-1}$)
PFC hematite without HPGR pretreatment	7.2	21.9	70.9	43.1	32.7	565
PFC pretreated by HPGR	3.5	9.4	87.1	70.5	54.5	1755
Mixture of PFC and magnetite (70/30) without HPGR pretreatment	6.5	22.8	70.8	48.1	35.8	785
Mixture of PFC and magnetite (70/30) pretreated by HPGR	3.5	13	83.6	61.8	43.6	1526

From Table 15.8, it can be seen that the fraction of material below 0.074 mm has increased from 70.9% and 70.8% to 87.1% and 83.6%, respectively, for the two concentrate mixtures after HPGR pretreatment. Accordingly, the fraction below 0.044 mm has increased from 43.1% and 48.1% to 70.5% and 61.8%, respectively, after HPGR pretreatment, while the specific surface area has increased from 565 and 785 to 1755 and 1525 cm^2/g, respectively.

Generally, a suitable pellet feed should contain 60–85% material passing 0.044 mm and more than 90% material passing 0.074 mm. Specific surface area is another critical parameter to evaluate the balling ability of pellet feeds. In order to make green balls from specularite concentrates at reasonable bentonite dosages, a specific surface area of over 1500–1700 cm^2/g is recommended. Concentrates with coarse size distributions and low specific surface areas have historically been used in China for pelletizing, but Wang (2003) suggested that the fraction of material over 200 µm in potential pellet feeds should be less than 20%. This is far from ideal conditions and requires high bentonite dosages and firing temperatures to achieve the minimum quality of green and fired pellets.

In some cases, ball milling is used before HPGR when the pellet feed is too coarse or too hard for saving grinding costs and improving balling characteristics of the pellet feed. For example, a wet ball mill plus an HPGR circuit was installed in WISCO Minerals' pellet plant in China to pretreat Brazilian specularite concentrates.

15.3.2.3 Ball milling

Ball milling is usually used to achieve a finely ground product for pelletizing when the pellet feed is too coarse. For example, if sintering fines are to be used for pelletizing, ball milling has to be utilized to prepare the raw material and achieve the required specific surface area. Before switching to magnetite pelletizing, Arrium Mining in South Australia ball-milled hematite/goethite fines for pelletizing. Similar procedures

are currently used in some pelletizing plants in India as well, especially in Tata Steel's 6 Mtpa straight grate pellet plant, which is the first in the world to use dry grinding to achieve specific surface areas of 2600–3000 cm^2/g (Paul et al., 2013). Closed-circuit dry ball milling is also used in Kobe Steel's Kakogawa grate-kiln pellet plant (Matsumura et al., 2013).

Many flow sheets have been developed and can generally be divided into wet or dry circuits based on the feed moisture and open or closed circuits based on material flow as follows:

- *Wet circuit*: the feed material is fed into the mill with water or in the form of a pulp.
- *Dry circuit*: this type of grinding requires a predrying step for the feed material, but it reduces the subsequent steps associated with handing wet material, such as thickening, homogenization, and filtering.
- *Open circuit*: the feed material passes through the mill only once and is fed at a low feed rate to ensure that all grains are broken. The regrinding of the feed material using the open-circuit configuration is unfavorable, because it can result in overgrinding and extra energy consumption (Chagas, 2008).
- *Closed circuit*: the feed material that does not have the appropriate particle size is returned to the mill for regrinding (Fonseca et al., 2007; Chagas, 2008). The moist and dry materials are classified using hydrocyclones, spiral classifier and air classifier, respectively, on the exit of the mill.

Table 15.9 shows the effect of fineness on the quality of green balls made from two ground hematite concentrates. Good overall green ball quality was achieved at 0.5% bentonite dosage when the fineness of the dry ground feed material was about 80–81% passing 74 μm. After being finely ground, the surface of the ore particles became very rough, as evidenced in Figure 15.11. This, together with size reduction, increased the specific surface area of the ground concentrates considerably, with both ground concentrates achieving a specific surface area of over 2000 cm^2/g. In contrast, specularite concentrate requires a finer size distribution to achieve the required specific surface area and green ball quality (see Table 15.10 and Figure 15.12).

Table 15.9 Effect of fineness on green ball properties (100%–8 mm feed material for grinding, 0.5% bentonite, 7.5% moisture, and 15 min for balling)

	Fineness (wt% passing 74 μm)	Drop number (number of drops from 0.5 m)	Wet compressive strength (*N* per pellet)	Thermal shock temperature (°C)
Ore A	90.8	23.7	22.3	305
	85.3	17.0	19.8	315
	81.6	14.6	18.3	326
Ore B	90.5	68.0	28.4	295
	85.1	35.3	26.7	307
	80.1	22.9	25.7	329

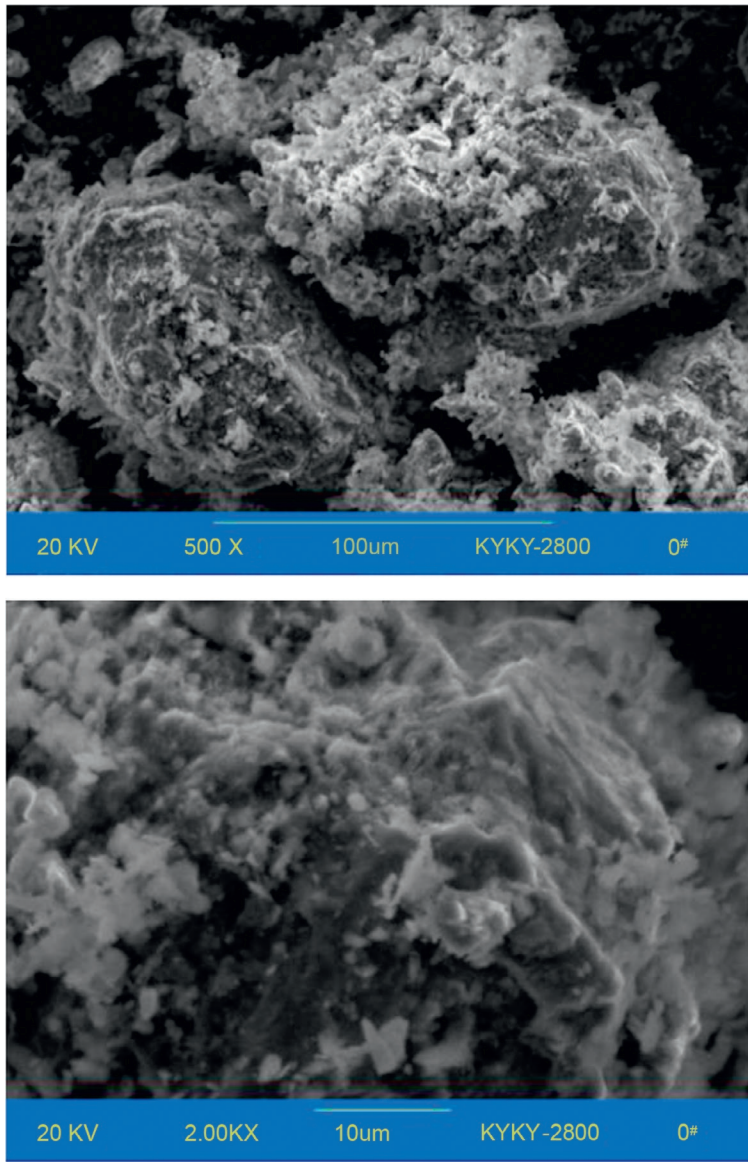

Figure 15.11 Morphology of ore A after being ground by dry ball milling to 80% passing 74 μm.

As shown in Table 15.11, the ball milling circuit did not obviously affect the green ball properties at similar fineness. Therefore, selection of the grinding circuit is based purely on technoeconomical analysis and operational convenience. Usually wet ball milling is suitable for pretreating magnetite concentrates, while dry ball milling is better for hematite concentrates because finely ground hematite concentrates are difficult

Table 15.10 Effect of grinding time on the particle size and specific surface area (SSA) of ground PFFT samples (one kind of specular hematite concentrate which produced from Tubarao, Brazil, similar as PFC)

Grinding time (min)	SSA (cm^2/g)	–74 μm (%)	–44 μm (%)
0	516	70.89	43.07
90	1300	93.95	78.30
120	1500	96.72	85.52
150	1700	97.83	88.97

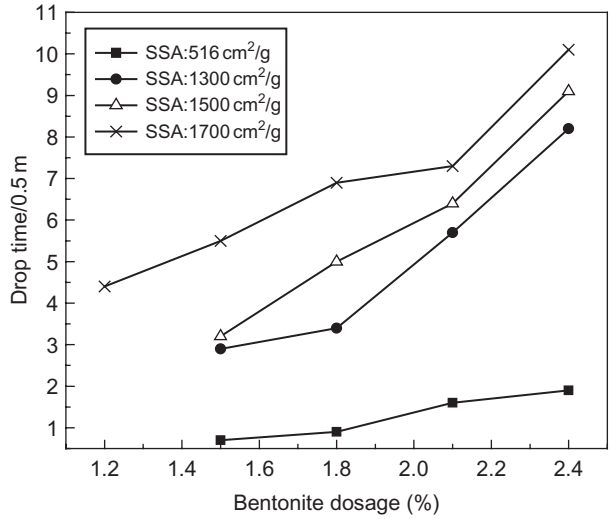

Figure 15.12 Effect of bentonite dosage and specific surface area on the drop number of green balls made from a Brazilian specularite concentrate pretreated by wet ball milling (balling conditions: 8.3–8.6% moisture for 12 min).

Table 15.11 Comparison of the properties of green balls made from ore A ground through different ball milling circuits (feed size of grinding circuit: 100%–8 mm; grinding product: 85% passing 74 μm; balling conditions: 0.5% bentonite and 7.5% moisture)

Grinding circuit	Drop strength (number of drops from 0.5 m)	Wet compressive strength (*N* per pellet)	Thermal shock temperature (°C)
Wet closed circuit	23.2	19.5	318
Wet open circuit	27.4	22.7	320
Dry open circuit	25.8	21.5	326

to filter. However, dry ball milling is confronted with difficulties in dust collection and high capital investment.

15.3.3 Blending hematite and pyrite cinder with magnetite

Unlike magnetite concentrates, hematite concentrates, especially specularite and pyrite cinder, are harder, denser with smooth surfaces, and less hydrophilic. Therefore, they are usually much more difficult to pelletize and require higher bentonite dosages and firing temperatures to achieve the minimum green and fired pellet quality. Therefore, the effect of adding magnetite concentrates on the pelletizing performance of a Brazilian specularite concentrate was investigated. As shown in Figure 15.13, blending the specularite concentrate with suitable magnetite concentrates has dramatically improved the properties of the green balls. As a result, less bentonite was needed for the mixed concentrates to achieve the green ball strength. For example, 1.8% bentonite was added to the feed comprising 100% PFFT (specularite) to achieve a drop strength of 5, while the bentonite dosage was reduced by half or more if one of the three Chinese magnetite concentrates in Figure 15.13 was blended at 30% with the specularite feed. It is worth mentioning that the benefit of blending magnetite concentrates varies considerably depending on the magnetite concentrate used.

Pyrite cinder is a by-product from the production of sulfuric acid, which comprises mainly hematite and silica. It is of significant importance to utilize it to both save resources and protect the environment. However, it is difficult to pelletize due

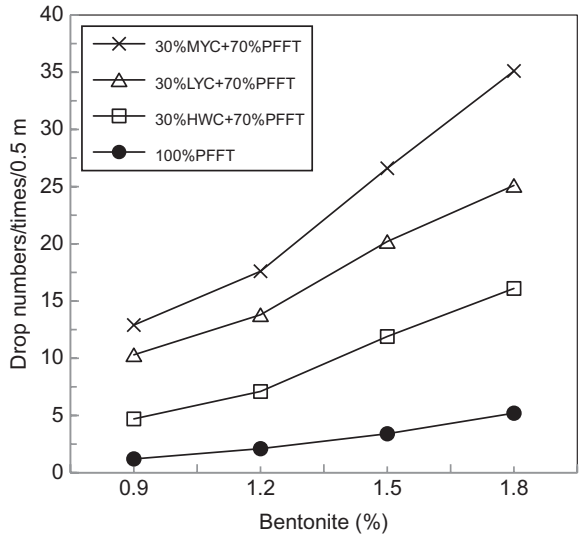

Figure 15.13 Effect of bentonite dosage and blending magnetite concentrates with a Brazilian specularite concentrate on the drop strength of green balls (PFFT is a specularite concentrate, while MYC, LYC, and HWC are Chinese magnetite concentrates). All blends had a similar SSA values of about 1500 cm^2/g and balling was conducted at 8.0% moisture.

Table 15.12 Effect of HPGR pretreatment on bentonite dosage and properties of green balls produced from pyrite cinder

Pretreatment	Bentonite (%)	Moisture content (%)	Drop strength (number of drops from 0.5 m)	Wet compressive strength (*N* per pellet)	Thermal shock temperature (°C)
Without pretreatment	2.3	22.8	6.0	6.1	>607
	2.6	22.8	9.0	7.2	>628
Pretreated by HPGR	0.9	18.7	6.9	7.2	>600
	1.2	18.6	9.2	7.9	>600
	1.5	18.8	11.6	8.3	>600
	1.7	18.9	15.7	9.6	>607
	2.0	18.9	17.5	9.0	>601
	2.3	18.9	30.0	10.6	>601
	2.6	18.9	31.9	13.2	587

to its low reactivity and high-sulfur content. An HPGR was therefore used to activate the particle surfaces and improve it pelletizing characteristics. As shown in Table 15.12, the compressive strength and drop strength of green balls were below 6.1 N per pellet and 6.0 drops from 0.5 m, respectively, which was achieved at 2.3% bentonite addition when the concentrate was not pretreated. However, the compressive strength and drop strength of green balls were increased considerably to 10.6 N per pellet and 30 drops from 0.5 m, respectively, after the concentrate was pretreated by HPGR.

15.3.4 New binders

Pelletizing differs from other agglomeration techniques in that the powdered ore is first formed into a "green" pellet or ball, which is then dried and hardened in a separate step, usually by heating. Green pellets are made by combining moist ore with a binder and rolling it into balls using either a pelletizing disk or a pelletizing drum. The green pellets are then dried, preheated, and finally heated to a temperature below the melting point of iron oxides, approximately 1300 °C, to achieve strength. The fired pellets are typically strengthened by recrystallization across the particle grain boundaries. Pelletizing has the following requirements:

- The ore being pelletized must have a sufficiently fine particle size distribution.
- Sufficient moisture needs to be added to make the ore sticky enough to pelletize, but not so much moisture that the ore becomes "muddy."
- A binder is required to hold the particle grains together before, when, and after the pellet is dried.

The pelletization process is the primary consumer of binders in the iron ore industry. The selection of an appropriate binder type and dosage is of critical importance

in producing good quality pellets at a reasonable price. Binders accomplish two very important functions in iron ore pelletization:

- The binder makes the moist ore plastic, so that it will nucleate seeds that grow at a controlled rate into well-formed pellets.
- During drying, the binder holds the grains in the agglomerates together while the water is removed and continues to bind them together until the pellet is heated sufficiently to sinter the grains together.

The suitability of a binder is determined by how well it can carry out each of these functions while at the same time not causing contamination or sintering problems.

Bentonite is a traditional binder used to improve the properties of green balls, such as drop strength, compressive strength, and thermal stability. However, it reduces the iron grade and adversely affects the metallurgical performance, especially reducibility, of fired pellets, because bentonite contains mainly aluminum silicate and contributes to slag formation after induration, which blocks the pores and retards the diffusion of reducing gases. Extensive studies have therefore been done to reduce bentonite dosage. Increasing the specific surface area of pellet feed by HPGR processing or other mechanical activations is by far the most effective way of reducing the bentonite dosage. The development of organic binders and organic/bentonite composite binders and the use of hydrated lime have also been widely reported in the literature (Eisele and Kawatra, 2010; Zhu et al., 2011b,c).

15.3.4.1 Organic binders

The main disadvantage of clays and other binders based on silicate minerals is that they add silica to the finished pellet. Since the purpose of iron ore processing is to remove silicate minerals from the ore, adding silicates back in the form of a binder is counterproductive. This has prompted long-term interest in developing or discovering binders that contain no silica. Particular attention has been devoted to organic binders, which include a variety of carbon-based polymeric or fibrous compounds. Investigators seeking new binders have tried everything from acrylamide polymers to cattle manure with mixed success. Extensive studies (Kater and Steeghs, 1984; Murr and Englund, 1988; Hanna, 1987; Qiu et al., 2003a,b; Eisele and Kawatra, 2010) were conducted in the 1980s and 1990s to substitute organic binders for bentonite. While commercial usage of Peridur in one Vale pellet plant was reported (Kater and Steeghs, 1984; Jiang et al., 1996; Eisele and Kawatra, 2010), no further reports were found on the commercial usage of organic binders until recently, namely, one of the Cliffs' grate-kiln pellet plants was using 100% organic binder to replace bentonite (Oja, 2013).

ArcelorMittal (Beaudin and Lucena, 2013) has been testing the substitution of bentonite with organic binders since the beginning of the 1990s for reducing the silica content of its direct reduction (DR) pellets. A full-scale plant trial of the substitution of a specific organic binder for bentonite was conducted in the company's straight grate pellet plant in Quebec, which produces 9.3 Mtpa of pellets, 36% of which are used as

Table 15.13 Results of ArcelorMittal's full scale pellet plant trial of an organic binder (Beaudin and Lucena, 2013)

Stages	First stage	Second stage	Third stage
Binder	0.6% bentonite	0.04% organic binder	0.6% bentonite
Trial test period (h)	48	48	48
Tonnage (t/h)	558	526	586
Cold compressive strength (kg)	309	295	318

feedstock for the DR process. The results of the full-scale pellet plant trial are given in Table 15.13.

It was found that the organic binder could fully replace bentonite to produce high-iron-grade and low-silica pellets for the DR process. However, the following issues need to be considered when evaluating and selecting organic binders for pelletizing applications:

- Water migration speed
- Surface moisture content after pelletizing
- Fresh feed sticks easily on green balls during pelletizing

The pellets produced during the plant trial (about 36,000 ton) were then tested in the ArcelorMittal Midrex DR plant in Montreal in November 2012. The use of the organic binder as a replacement for bentonite did not seem to affect the direct reduction process.

15.3.4.2 Organic/bentonite composite binders

Organic binders can no doubt improve the iron grade of fired pellets, because they decompose and release volatiles during firing. The typical organic binder in commercial use is Peridur (Fu and Zhu, 2007). However, organic binders are costly and difficult to mix into the pellet feed. Furthermore, organic binders have low thermal stability and lose their intended effects during drying and preheating, leading to low thermal shock temperatures and weak preheated and fired pellets. Therefore, considerable recent work has been focused on the combined use of organic binders and bentonite or limestone. The required dosage of bentonite was reported to drop by 50–0.5% bentonite (Penttinen, 2013) when 0.025% organic binder in solution was added. It has also been reported that dusting problems can be reduced by adding approximately 1.0% limestone along with Peridur (Murr and Englund, 1988). In addition, a new type of composite binder has been reported and used for DR pellet production in a coal-based grate-kiln process (Qiu et al., 2003a,b).

In order to tackle the lower thermal stability of pure organic binders, and the weak green ball strength and the decrease in iron grade of fired pellets when using bentonite as a binder, the authors have developed a new organic/bentonite composite binder

by inserting small organic molecules into the crystal layers of bentonite activated by sodium carbonate. Due to its improved thermal stability, the new binder resulted in stronger thermal shock resistance of the green balls. As shown in Figure 15.14 (Zhu et al., 2011b,c), the bentonite dosage is reduced to 1% from 3.2% to achieve the minimum drop strength of about 4 when organic binder is added. Similarly, the addition of organic binder in bentonite improved the thermal shock temperature to above 500 °C from about 350 °C at 1% organic bentonite composite binder. The results from successful commercial trial of the organic bentonite composite binder in WISCO

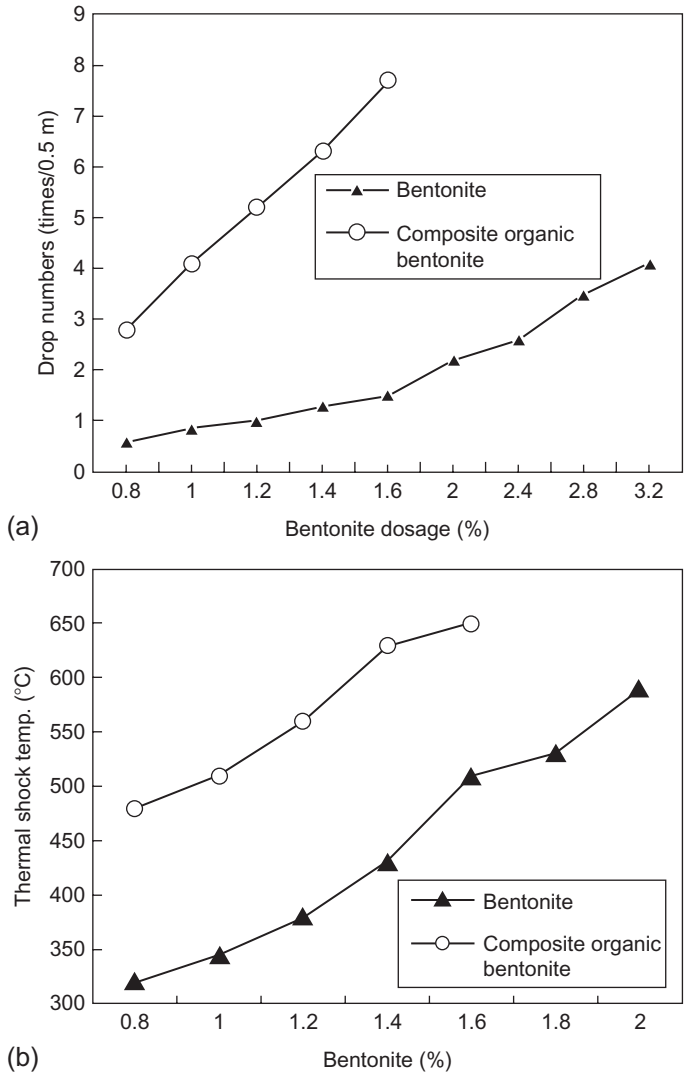

Figure 15.14 Effect on (a) drop strength and (b) thermal shock temperatures of green balls made with and without organic binder (Zhu et al., 2011a).

Minerals demonstrated that addition of organic binder (0.2–0.5% of bentonite mass) reduced the dosage of bentonite by over 50% from originally 3% to 1.4%. While the bentonite addition decreased, the drop number and thermal shock temperature of green balls improved by 0.9 times/0.5 m and 150 °C, respectively. This has resulted in an improvement in the overall iron grade of fired pellet by 1.02% and in CCS by 1000 N per pellet (Liu et al., 2005; Zhu et al., 2009).

15.3.4.3 Substitution of hydrated lime for bentonite in fluxed pellets

Hydrated lime ($Ca(OH)_2$) will harden when mixed with water and allowed to dry and recrystallize. It has a number of very appealing features for use as a pellet binder as follows:

- It contributes no silica to the final product.
- It acts as a silica flux when the pellet is reduced in the blast furnace and improves the metallurgical performance of the pellet.
- It is readily available, because limestone deposits suitable for lime production are widespread and readily accessible.

The use of hydrated lime as a binder is most attractive when fluxed pellets are being produced, which require several percent CaO and/or MgO to be added to the pellet. In traditional fluxed pellets, the flux is added as limestone ($CaCO_3$) or dolomite ($CaMg(CO_3)_2$), neither of which has any appreciable binding properties. However, if either of these flux components is calcined to either CaO or $CaMgO_2$ and then hydrated and added to the pellets, they can be quite effective binders. Hydrated lime was used as a binding agent for fluxed pellets in several plants as early as in the 1990s, including Algarrobo in Chile and both Fabrica and CVRD in Brazil (Eisele and Kawatra, 2010; de Souza, 1976; Bleifuss and Getzrnan, 1991; Mendes, 2012). It is technically feasible to produce a fully fluxed pellet that has acceptable physical and metallurgical qualities using hydrated lime. Substitution of hydrated lime significantly decreased the total energy requirement for the process, which provides direct cost savings (Mendes, 2012). Bentonite is a good binder and can improve the properties of green balls, namely, drop strength, compressive strength, and thermal shock temperature. However, when fluxed pellets are produced, hydrated lime can actually play two roles as both binder and fluxing agent. As fewer and less fluxes are used, hydrated lime can help improve the Fe grade and strength of preheated and fired pellets. As the raw materials available to produce fluxed pellets become more difficult, more attention is being paid to the use of hydrated lime in iron ore pelletizing.

The authors conducted a study comparing bentonite and hydrated lime as binders for manufacturing fluxed pellets from a hematite pellet feed. As shown in Figure 15.15, the green balls using hydrated lime as a binder had a similar drop strength and better compressive strength and thermal shock resistance, which was achieved at a dosage considerably higher than that generally required for bentonite. However, the higher dosage of hydrated lime did not adversely affect the firing of the fluxed pellets, because less limestone was required.

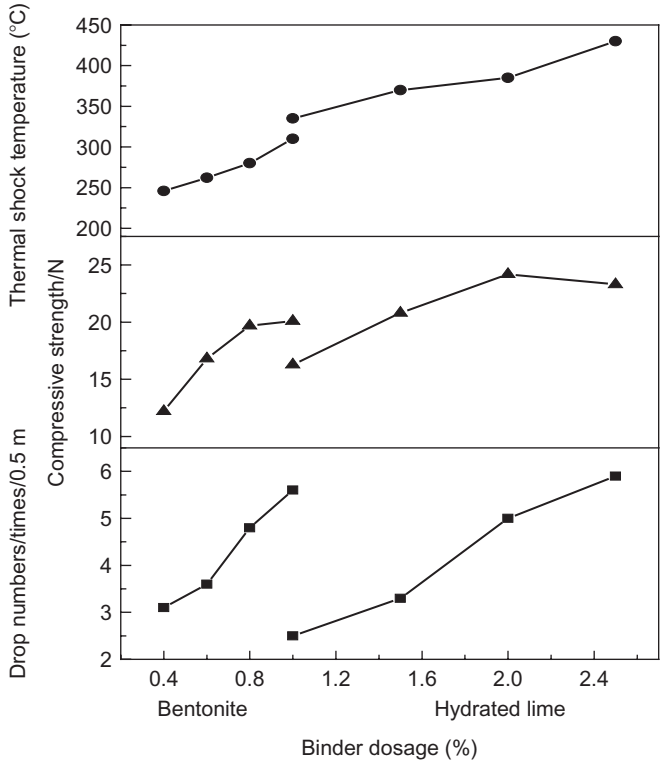

Figure 15.15 Effects of binder type and dosage on the green ball properties of a hematite pellet feed balled at 8.5% moisture content for 13 min. The pellet basicity was targeted at 1.0.

15.4 Induration of green pellets

15.4.1 Typical microstructures and bonding mechanisms of fired pellets

Induration involves drying, preheating, and firing green pellets in straight grate, grate-kiln, and shaft furnaces to produce fired pellets with desirable quality. The mechanical strength and metallurgical performance of fired pellets depend on the mineralogy of the fired pellets, which is formed through the reactions within and between ore particles as well as between ore particles and gangue or flux particles during induration. Therefore, the size, chemistry, and mineralogy of the pellet feed and the fluxing and firing conditions for the green pellets determine the mineralogy of the fired pellets. Due to the differences in mineralogy, different types of pellet feeds require very different fluxing and firing conditions, such as preheating temperature, preheating duration, oxygen potential, firing temperature, and firing duration. The oxygen potential is particularly important for the induration of green balls produced from magnetite concentrates. The full oxidation of the magnetite minerals determines not only the quality of the fired pellets but also the energy consumption of the induration process.

Because pellets are produced from different ore types under different conditions, they are expected to have distinct mineralogies to achieve the required quality. Table 15.14 lists the typical mineral phases present in iron ore pellets, while Figure 15.16 shows two typical microstructures of pellets produced from magnetite and hematite pellet feeds. While the main bonding phase of the pellets is recrystallized Fe_2O_3, there are

Table 15.14 Typical mineral phases present in iron ore pellets (%)

Minerals	Hematite	Magnetite	Ca-bearing ferrous fayalite ($CaO \cdot FeO \cdot SiO_2$)	Magnesium ferrite	Aluminum trioxide	Glass
Hematite concentrate feed	94.61	0.12	0.87	0.15	1.06	3.19
Magnetite concentrate feed	92.67	0.50	1.34	1.26	1.50	1.10

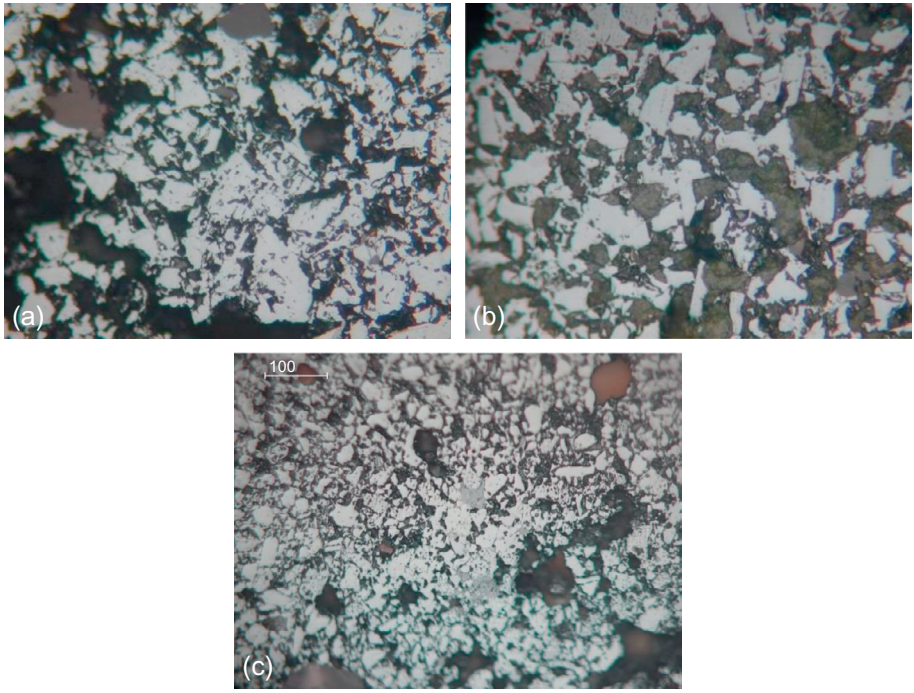

Figure 15.16 Typical microstructures of acid pellets made from (a) magnetite and (b) hematite pellet feeds and (c) one fluxed pellet at 0.83 basicity produced from hematite concentrate (×200; Fe_2O_3—white grains; Fe_3O_4—fine brown-yellow grains; SiO_2—grey/black grains; calcium ferrite—khaki grains; pores—black).

some key differences in the microstructures of pellets produced from magnetite and hematite concentrates. Pellets produced from magnetite may contain recrystallized Fe_3O_4 if the oxidation of magnetite is not complete. In addition, the recrystallization of hematite and therefore the diffusion bonds between the recrystallized hematite grains are often more extensive for the pellets produced from magnetite concentrates. Pellets are often fluxed to meet the chemistry and metallurgical performance required for the intended downstream processes. Acid pellets are bonded through diffusion between recrystallized hematite grains, while fluxed pellets are bonded via both recrystallization and diffusion of Fe_2O_3 and slag phases (normally below ~5–7% in volume), which includes fayalite, ferrite and silicate minerals.

The magnetite grains in the green pellets produced from magnetite pellet feeds are oxidized during preheating to form fresh hematite particles, which are more reactive than the hematite particles from hematite pellet feed and fused together through diffusion. This explains the different properties of pellets produced from different types of pellet feeds and why hematite pellet feed is more difficult to pelletize and often needs to be fluxed to achieve good quality fired pellets. Therefore, magnetite concentrates are ideal pellet feeds for making iron ore pellets. However, with the rapid development of the pelletizing industry and the shortage of good quality pellet feeds, feed materials like refractory hematite, specularite, goethite, and pyrite cinder need to be used to produce fired pellets. Apart from difficulties in balling mentioned earlier, these types of feed materials also present difficulties in induration due to the need for higher preheating and firing temperatures over longer durations, as well as less favorable metallurgical performance, such as reduction swelling, of the fired pellets. Therefore, many countermeasures have been developed to tackle these problems, such as the addition of magnetite concentrates and boron-containing additives, optimizing basicity and MgO content, and HPGR pretreatment.

15.4.2 Effect of blending magnetite concentrates and HPGR pretreatment

The compressive strength of preheated pellets is very important, particularly for the grate-kiln process, because the preheated pellets need to withstand compressive and impact stresses when they are transferred from the grate into the rotary kiln after preheating as well as abrasion inside the rotary kiln. The higher the compressive strength of the preheated pellets, the less fractures and fines generated in the rotary kiln, leading to higher availability of the rotary kiln and higher pellet output.

The authors investigated the effect of blending in magnetite concentrates and HPGR pretreatment on the compressive strength of preheated pellets produced from a Brazilian specularite concentrate (PFC). As shown in Figure 15.17a, the compressive strength of preheated pellets produced from 100% PFC without pretreatment is below 200 N per pellet, even at preheating temperatures up to 1100 °C. Blending 30% magnetite concentrate with the specularite concentrate improves the compressive strength of preheated pellets from 200 to 250 N per pellet. The compressive strength of preheated pellets is increased further to 500 N per pellet even at a lower preheating temperature

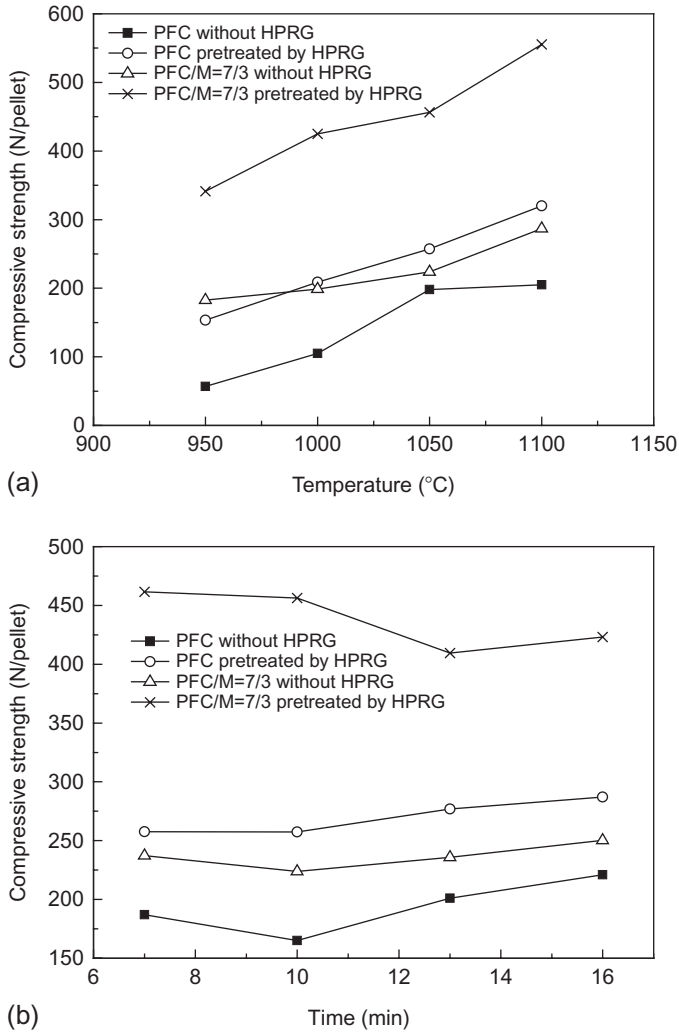

Figure 15.17 Effect of preheating conditions on the compressive strength of preheated pellets (preheating time in (a) 10 min; preheating temperature in (b) 1050 °C). The specific surface areas of the raw and treated samples are 565 cm^2/g for PFC without HPGR pretreatment, 1757 cm^2/g for PFC with HPGR pretreatment, 785 cm^2/g for blends comprising 30% magnetite and 70% PFC without HPGR pretreatment, and 1526 cm^2/g for blends comprising 30% magnetite and 70% PFC with HPGR pretreatment.

of 1050 °C when a blend comprising 30% magnetite concentrate and 70% specularite concentrate is pretreated using an HPGR. This meets the minimum requirement for a rotary kiln and the preheating time can be shortened. On the other hand, the compressive strength of preheated pellets produced from 100% HPGR-pretreated specularite (PFC) was less than 300 N per pellet. However, the preheating time has minor effect on the compressive strength of preheated pellets as shown in Figure 15.17b.

Figure 15.18 shows the effect of blending magnetite concentrates and HPGR pretreatment on the compressive strength of fired pellets. Compared with the compressive strength of 533 N for fired pellets produced from 100% specularite concentrate, HPGR pretreatment helped to increase the compressive strength of fired pellets considerably. The low compressive strength and higher firing temperatures reveal the

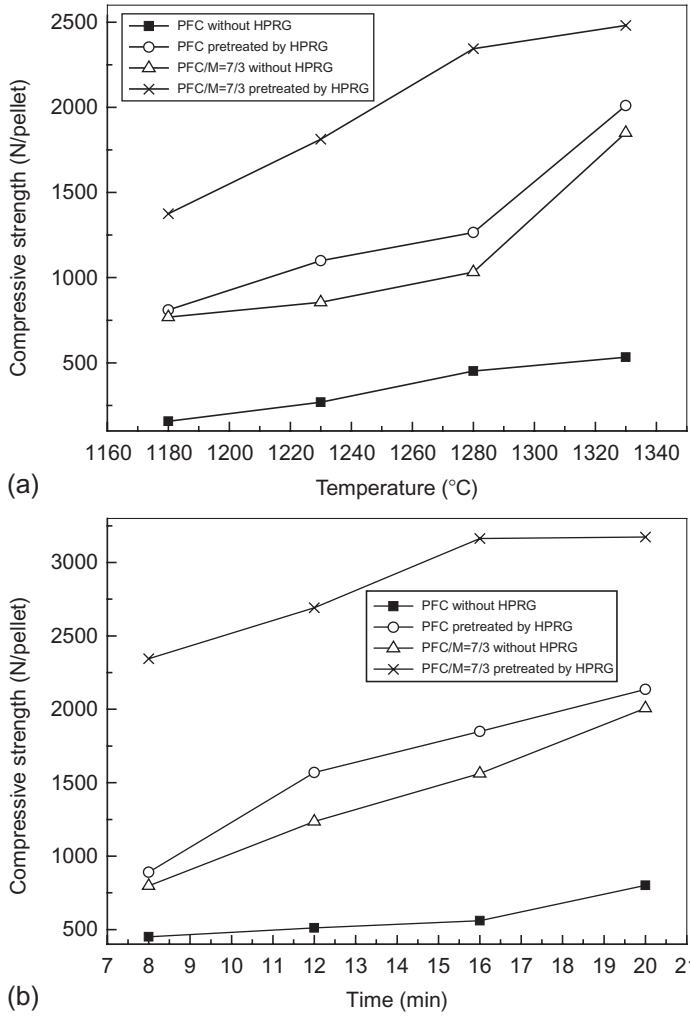

Figure 15.18 Effect of roasting conditions on the compressive strength of fired pellets (preheating for 10 min at 1050 °C and roasting for 8 min at different temperatures in (a), and preheating for 10 min at 1050 °C and roasting at 1280 °C for different times in (b)). The specific surface areas of the raw and treated samples are 565 cm^2/g for PFC without HPGR pretreatment, 1757 cm^2/g for PFC with HPGR pretreatment, 785 cm^2/g for blends comprising 30% magnetite and 70% PFC without HPGR pretreatment, and 1526 cm^2/g for blends comprising 30% magnetite and 70% PFC with HPGR pretreatment.

refractory nature of the PFC specularite concentrate even if an HPGR is used to pretreat the feed. The combination of HPRG pretreatment and magnetite addition was found to dramatically improve the firing performance of specularite concentrate. The compressive strength of pellets fired at 1280 °C for 16 min exceeded 3000 N per pellet when a blend comprising 30% magnetite and 70% specularite was pretreated using an HPGR.

Pyrite cinder is also difficult to pelletize, because it mainly comprises hematite. From Figure 15.19, it can be seen that the compressive strength of fired pellets reaches only 2858 N per pellet even at the firing temperature of over 1300 °C. However, the compressive strength of pellets fired at 1260 °C can be increased to over 3500 N per pellet when the pyrite cinder was pretreated using an HPGR (Zhu et al., 2011a).

15.4.3 Boron-containing additives

As shown in Figure 15.20, the authors found that, while the compressive strength of fired pellets increased with firing temperature, the compressive strength of fired pellets produced from 100% hematite feed was only 1865 N per pellet even if they were fired at 1300 °C for 15 min. Additives were therefore studied to improve the firing characteristics of difficult pellet feeds. The compressive strength of fired pellets was found to increase dramatically with the addition of a boron-bearing additive at 0.2–0.6%. The optimum dosage of the boron-bearing additive was 0.4%, where the compressive strength of the fired pellets was as high as 3096 N per pellet even if the firing temperature was only 1280 °C. Therefore, the boron additive not only improved the compressive strength of the fired pellets but also reduced the firing temperature.

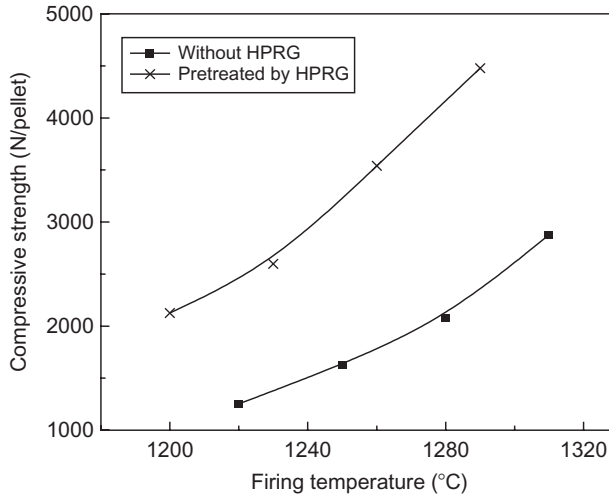

Figure 15.19 Effect of firing temperature on the compressive strength of fired pellets produced from 100% pyrite cinder without HPGR pretreatment (preheating for 6 min at 1100 °C and firing for 15 min) and HPGR pretreated pyrite cinder (preheating for 6 min at 1000 °C and firing for 15 min).

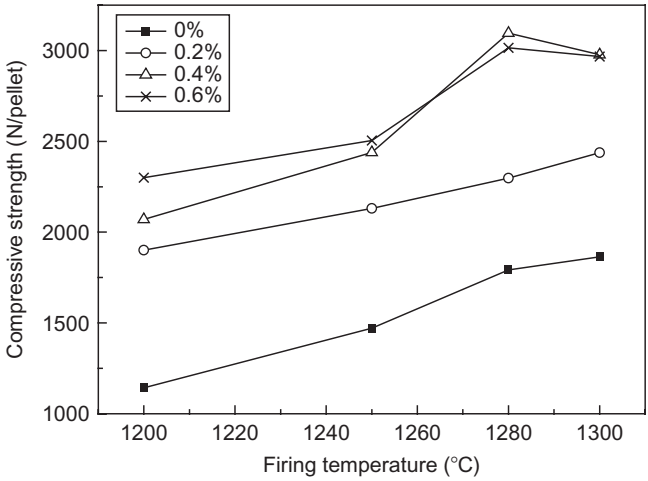

Figure 15.20 Effect of firing temperature on the compressive strength of fired pellets at various levels of a boron bearing additive (100% hematite feed, preheating at 1000 °C for 8 min and firing for 15 min).

To explain the role of the boron-bearing additive, the kinetics of hematite crystal growth was studied. It was found that the addition of the boron-bearing additive reduced the activation energy for hematite crystal growth from 277 to 167 kJ/mol. As a result, the average size of the hematite crystals in the fired pellets increased with the addition of the boron-bearing additive. For example, the average size of hematite crystals was about 15.10 μm for pellets fired at 1300 °C without any additives and 18.68 μm for pellets fired at only 1200 °C containing 0.4% boron additive. Therefore, the boron-bearing additive improved the induration of hematite pellets by catalyzing the recrystallization and growth of hematite crystals, leading to higher compressive strength of the fired pellets (Li, 2009).

15.4.4 Optimizing MgO and basicity

Fired pellets need to meet not only the mechanical strength but also the metallurgical characteristics, such as reducibility, reduction swelling, and degradation, required by their intended application. Poor metallurgical performance, especially high reduction swelling, has limited the usage of some pellets. Fluxes can be added to optimize the basicity and MgO content of fired pellets for improving their firing behavior and metallurgical performance. The type and amount of fluxes are vital to pellet quality, because they influence the bonding phases formed during pellet induration and their stability during reduction.

Figure 15.21 shows the effect of pellet basicity on the compressive strength of fired pellets produced from 100% specularite concentrate at various MgO contents. At the natural MgO content of 0.08%, the compressive strength of the fired pellets increased first with basicity and then decreased slightly after reaching a peak value

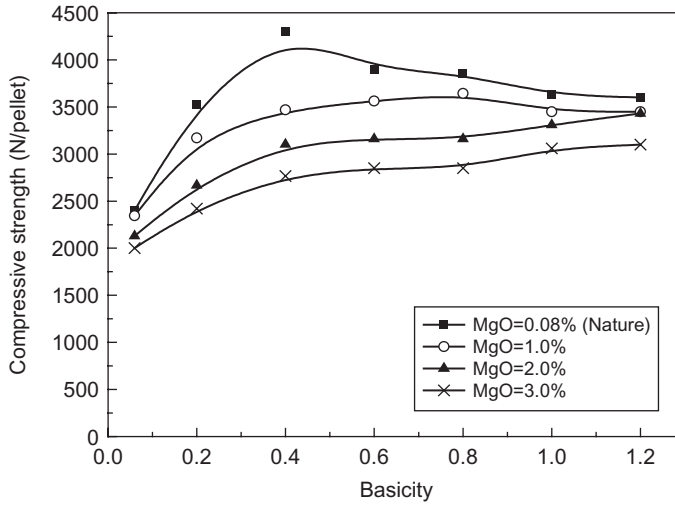

Figure 15.21 Effect of basicity on the compressive strength of fired pellets (3.0–3.1% SiO_2) produced from 100% specularite concentrate at various MgO contents.

of more than 3500 N per pellet at approximately a basicity of 0.4. At a fixed basicity, the compressive strength of fired pellets declined when the MgO content increased from 0.08% to 3%. At higher MgO contents, a higher basicity is required to achieve the required compressive strength of fired pellets. Therefore, increasing the MgO content is harmful to the compressive strength of fired pellets. This is probably due to the higher melting temperature of high MgO, which reduces liquid-phase formation and results in undesirable pore structures at fixed firing temperatures (Zhang, 2012).

The reducibility of fired pellets depends mainly on their mineralogy, particularly iron-bearing mineral phases and pore structure, which can be modified by adding fluxes in the pellet feed to adjust the MgO content and basicity. As shown in Figure 15.22, the reducibility index of fired pellets at natural basicity and MgO content is only 62.2%. However, the reducibility of fired pellets produced from the specularite concentrate was improved by increasing the basicity and MgO content. The reducibility of the fired pellets reached 68.0% at 3% MgO and natural basicity and 72.8% at 1.2 basicity and natural MgO content. The reducibility was improved further when both the MgO content and the basicity were increased and reached 76.9% for fired pellets containing 3% MgO at 1.2 basicity. The formation of greater porosity and reducible bonding phases is most likely responsible for the improved reducibility observed for fired pellets at higher basicity and MgO content.

It is normal for fired pellets to swell during reduction because of the phase transformation, and a reduction swelling index below 20% is generally permitted, which is unlikely to adversely affect the performance of the blast furnace. However, excessive swelling during reduction will lead to operational difficulties for blast furnaces, so a reduction swelling value lower than 15–20% is desirable for fired pellets. As shown in

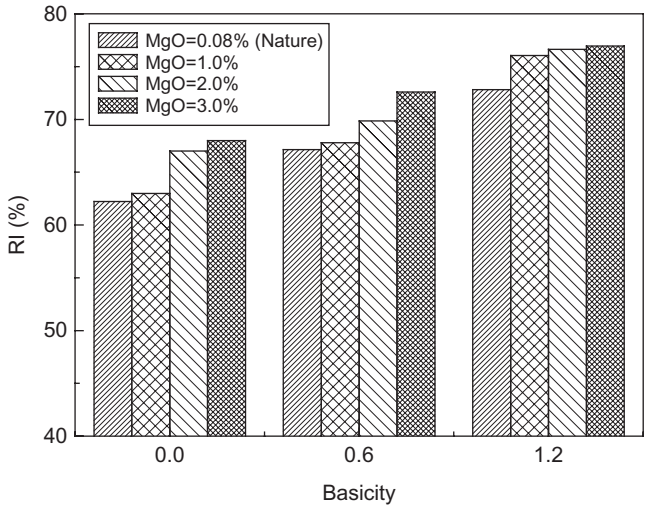

Figure 15.22 Effect of basicity on the reducibility of fired pellets (3.0–3.1% SiO_2) produced from 100% specularite concentrate at various MgO contents.

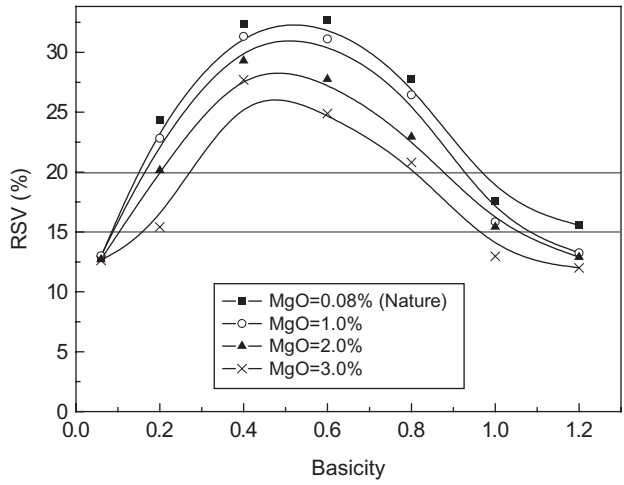

Figure 15.23 Effect of basicity on the reduction swelling index of fired pellets (3.0–3.1% SiO_2) produced from 100% specularite concentrate at various MgO contents.

Figure 15.23, the reduction swelling index can be improved by optimizing the basicity and MgO content of fired pellets. At a constant MgO content, the reduction swelling index increases with increased basicity and then falls after reaching a peak value at a basicity of between 0.4 and 0.6. On the other hand, MgO helps improve the reduction swelling index of fired pellets. The higher the MgO content, the lower the reduction swelling index. However, as mentioned earlier, MgO content is harmful to the compressive strength of fired pellets. Hence, both the compressive strength and the reduction

swelling index need to be considered when the MgO content of fired pellets is decided. Some research results (Dwarapudi et al., 2010, 2011, 2012) demonstrated that fired pellets exhibited optimum metallurgical performance at 1.0–1.5% MgO content. The formation of less liquid slag due to the presence of MgO is attributed to the improved reducibility of magnesite fluxed pellet properties, while the compressive strength of magnesite fluxed pellets is within the acceptable limits for blast furnace feed.

The basicity and MgO content of fired pellets are often adjusted by varying the amount of CaO- and MgO-bearing fluxes in the pellet feed mixture. The effects of MgO and CaO sources, such as limestone, dolomite, and pyroxenite, were also studied with respect to their suitability for producing quality pellets for blast furnaces (Dwarapudi et al., 2013). For pellets fluxed with limestone and dolomite, the amount of melt phase was found to increase with increasing basicity, while the FeO content of the silicate melt decreased. The swelling index of the limestone fluxed pellets reached its maximum at approximately 0.6 basicity, which is in good agreement with the observations in Figure 15.23.

Compared with fluxed pellets, acid pellets with natural basicity often have higher reduction swelling indexes. Once again, the addition of MgO was found to considerably reduce the swelling tendency of pellets due to the formation of stable high melting point slag that efficiently suppressed reduction swelling. Limestone pellets at 0.8 basicity and dolomite pellets at 0.4 basicity and 1.5% MgO exhibited optimum quality. Pyroxenite (olivine) was used as a Mg source to improve the metallurgical performance of fired pellets, but its usage was discontinued after 9 months of operation. It was observed during the commercial production of pyroxenite fluxed pellets that the quality of the fired pellets was very sensitive to firing temperature, most likely due to the very narrow temperature range of melt formation that resulted in a considerable variation in the amount of melt phase formed and therefore in the quality, especially cold compressive strength (CCS) and RDI, of fired pellets.

15.5 Quality requirements for fired pellets

Fired pellets are mainly used as feed materials for blast furnace and DR processes, about 30% of the pellets produced being currently used in DRI production. Due to the very different conditions pellets are subjected to, pellets used for blast furnace and DR processes require different specifications. The typical requirements of pellets for modern large blast furnaces and DR processes are discussed in Chapter 16.

15.6 Conclusions

A brief introduction to recent progress in iron ore pelletizing has been provided in this chapter, including the world output of fired pellets, the pellet production processes, preparation of pellet feed, organic binders, and new additives. Throughout the chapter, the authors used a difficult pellet feed, that is, a Brazilian specular hematite

concentrate, to illustrate different measures investigated by the authors for improving the pelletizing characteristics of such difficult pellet feeds. Based on the above discussion, the following conclusions can be made:

(1) The output of fired pellets has been increasing quickly and will continue to rise because of the increasing production and supply of concentrates' expanded capabilities in DRI production and increasing consumption of pellets to achieve better blast furnace performance and meet increasingly strict environmental regulations dictated by governments.

(2) The grate-kiln and straight grate routes will continue to be the dominant pellet production processes because of their advantages over the shaft furnace process in terms of capacity, energy efficiency, production cost, and pellet quality.

(3) The traditional hematite and magnetite concentrates are being depleted, but the newly available pellet feeds, such as specularite, pyrite cinder, and goethite, are often more complicated in mineralogy and less favorable for pelletizing. Many measures have been developed to improve the pelletizing performance of these types of pellet feeds and reduce the bentonite dosage, such as pretreatment using an HPGR; damp milling and ball milling, or alternatively a combination of these processes; using new binders; optimizing the basicity and MgO content of fired pellets; and adding boron-containing and other additives.

(4) More attention should be given to organic bentonite composite binders for partial or full substitution for bentonite to improve the quality of green balls and fired pellets.

References

Ball, D.F., Dartnell, J., Davidson, J., Grieve, A., Wild, L., 1973. Agglomeration of Iron Ores. Heinemann Education Books, London, pp. 3–9.

Beaudin, S., Lucena, G., 2013. AMEM experience with organic binder. In: 3rd Symposium on Iron Ore Pelletizing, Quebec, Canada, 29 September–2 October, 2013.

Bleifuss, R.L., Getzrnan, H.E., 1991. Replacement of limestone and dolomite with lime/dolomite hydrate for the production of fluxed pellets. In: Proceedings, Annual Meeting—Minnesota Section AIME, 64th Annual Meeting of the Society for Mining, Metallurgy, and Exploration, January 16–17, 1991. SME-AIME, Littleton, CO, pp. 195–206.

Boldyrev, V.V., Pavlov, S.V., Goldberg, E.L., 1996. Interrelation between fine grinding and mechanical activation. Int. J. Miner. Process. 44–45, 181–185.

Chagas, T.T.R., 2008. A moabilidade secundária de pellet feed de minérios de ferro em função da mineralogia, química e microestrutura *(Secondary Grinding of Pellet Feed of Iron Ores Due to Mineralogy, Chemistry and Microstructure)*. Master's Degree Thesis, Theme Network for Materials Engineering, Universidade Federal de Ouro Preto, Ouro Preto.

Chaigneau, R., 2013. A helicopter view on the future of pelletizing. In: 3rd Symposium on Iron Ore Pelletizing. Quebec, Canada. 29 September–2 October, 2013.

CRU Analysis, 2011. Iron Ore Market: Main Report 2011. CRU International Ltd, London.

de Souza, R.P., 1976. Production of pellets in CVRD using hydrated lime as binder, is growing up fast. In: Ironmaking Proceedings, Metallurgical Society of AIME Iron and Steel Division, 35th Annual Ironmaking Conference, March 29–April 1, St. Louis, MO, pp. 182–196.

Dwarapudi, S., Ghosh, T.K., et al., 2010. Effect of pyroxenite flux on the quality and microstructure of hematite pellets. Int. J. Miner. Process. 96 (1–4), 45–53.

Dwarapudi, S., Ghosh, T.K., et al., 2011. Effect of pellet basicity and MgO content on the quality and microstructure of hematite pellets. Int. J. Miner. Process. 99 (1–4), 43–53.

Dwarapudi, S., Ghosh, T.K., et al., 2012. Effect of MgO in the form of magnesite on the quality and microstructure of hematite pellets. Int. J. Miner. Process. 2012 (112–113), 55–62.

Dwarapudi, S., Banerjee, P.K., Chaudhary, P., Chakraborty, U., Prasad, P.R., 2013. Establishing right pellet chemistry for the 6 MTPA capacity iron ore pelletizing plant at Tata Steel, India. In: 3rd Symposium on Iron Ore Pelletizing. Quebec, Canada. 29 September–2 October, 2013.

Eisele, T.C., Kawatra, S.K., 2010. A review of binders in iron ore pelletization. Miner. Process. Extr. Metall. Rev. 24 (1), 1–90.

Fonseca, P.S.M., Alecrim, M.A., Silva, M.M., 2007. Siderurgia: Dimensionamento do Potencial de Investimento (Steelmaking: Sizing the Investment Potential). In: Perspectivas do Investimento 2007/2010 (Investment perspectives 2007/2010). Organizers: Ernani Teixeira Torres Filho, Fernando Pimentel Puga. Rio de Janeiro. BNDES, 2007, 328.

Fu, J.-y., Zhu, D.-g., 2007. Principle, Technology and Equipment of Iron Ore Pelletizing. Central South University Press, Changsha, 2007.

Fuesternau, D.W., De, A., Diao, J., Kapur, P.C., 1995. Fine grinding of coal in a two-stage high-pressure roll mill/ball mill hybrid mode. In: Kawatra, S.K. (Ed.), High Efficiency Coal Preparation. Society of Mining Engineers, Littleton, pp. 295–305.

Hanna Co. Research Center, 1987. Evaluation of solid fuels as pellet additives, final report for the Minnesota Department of Natural Resources, Contract No. 44516=44517.

He, A.-p., 2005. A Study of the Process and Mechanism of Pelletizing Brazilian Specularite. Master's Degree Thesis, Central South University, China.

Indian Bureau of Mines, 2011. Vision 2020 (Iron & Steel), Chapter4—Agglomeration.

Jiang, T., Fu, J.-y., Zhu, D.-q., 1996. Principle and Technology of Sintering and Pelletizing. Central South University Press, Changsha, 1996.

Kater, T., Steeghs, H.R.G., 1984. Organic binders for iron ore pelletization. In: Proceedings of the 57th Annual Meeting of the Minnesota Section of AIME, Duluth, MN, 1984, pp. 13.1–13.29.

Klymowsky, R., Patzelt, N., Knecht, J., Burchardt, E., 1998. Selection and sizing of high pressure grinding rolls. Krupp Polysius AG, Beckum, Germany.

Li, H.-m., 2009. A Study on the Pelletization of Brazilian Hematite by Composite Additive and Its Mechanism. Master's Degree Thesis, Central South University, China.

Liu, G.-y., Zhu, D.-q., Pan, J., Zhang, K.-c., Tian, F.-c., Hu, Y.-m., Liu, S.-l., 2005. Industrial tests on using modified bentonite to improve iron ore pelletizing. Sintering Pelletizing 30 (4), 13–16.

Matsumura, T., Amano, S., Yamada, K., 2013. Challenge of cost saving in pelletizing plant of Kakogawa works. In: 3rd Symposium on Iron Ore Pelletizing. Quebec, Canada. 29 September–2 October, 2013.

Mendes, V., 2012. Improvement of the Grate-Kiln Pelletization of Vale Hematite Fines and Its Industrial Practice. PhD Degree Thesis, Central South University, China.

Meyer, K., 1980. Pelletizing of Iron Ores. Springer Verlag, Berlin, ISBN: 3540102159, ISSN: 3514002460.

Mourão, J.M., 2012. Guidelines for selecting pellet plant technology. In: 6th International Congress on the Science and Technology of Ironmaking-ICSTI, Rio de Janeiro, RJ, Brazil, October 14–18, 2012, pp. 2162–2175.

Murr, D.L., Englund, D.J., 1988. Development and Production of Organic-Limestone Pellets. National Steel Pellet Co. and Hanna Research Center, Minnesota.

Narciso, J.J., 2013. A compilation of iron ore pellet production, volumes 2010–2012, Primarily from Public Domain Data. In: 3rd Symposium on Iron Ore Pelletizating, Quebec City, Canada, 30 September, 2013.

Norgate, T.E., Weller, K.R., 1994. Selection and operation of high pressure grinding rolls circuits for minimum energy consumption. Miner. Eng. 7, 1253–1267.

Oja, K., 2013. Straight grate vs grate kiln. In: 3rd Symposium on Iron Ore Pelletizing. Quebec, Canada. 29 September–2 October, 2013.

Pan, J., Zhu, D.Q., Xiong, S.A., Mendes, V., 2008. Improving the pelletization of refractory hematite by high pressure grinding rolls. In: Duo, W.D., Yao, S.C., Hang, W.F., Cheng, Z.L., Long, H. (Eds.), Proceedings of XXIV International Mineral Processing Congress, Beijing, China, pp. 2857–2865.

Paul, I., Reddy, A.S., Kumar, A., 2013. Pelletizing—an experience in Tata Steel. In: 3rd Symposium on Iron Ore Pelletizating, Quebec, Canada. 29 September–2 October 2013.

Pazelt, N., Knecht, H., Baum, W., 1995. Case made for high pressure roll grinding in gold plants. Min. Eng. 47, 524–529.

Penttinen, M., 2013. Optimizing iron ore pelletization with the use of custom-formulated binder compositions. In: 3rd Symposium on Iron Ore Pelletizing. Quebec, Canada. 29 September–2 October, 2013.

Poveromo, J.J., 2014. Future trends in Ironmaking, prepared for McMaster blast furnace ironmaking course, May 11–16, 2014.

Qing, H.-l., Li, X.-k., 2000. On the improvement and high yield of pelletizing shaft furnace. Sintering Pelletizing 25 (1), 47–48.

Qiu, G.-z., Jiang, T., Li, H.-x., Wang, D.-z., 2003a. Functions and molecular structure of organic binders for iron ore pelletization. Colloids Surf. A Physicochem. Eng. Asp. 224, 11–22.

Qiu, G.-z., Jiang, T., Huang, Z.-c., Zhu, D.-q., 2003b. Characterization of preparing cold bonded pellets for direct reduction using an organic binder. ISIJ Int. 43 (1), 20–25.

Schönert, K., 1988. A first survey of grinding with high-compression roller mills. Int. J. Miner. Process. 22, 401–412.

Thomas, S., Collin, B., 2013. Recent technological advancements in high capacity pellet plants. In: 3rd Symposium on Iron Ore Pelletizing, Quebec, Canada, 29 September–2 October, 2013.

Wang, C.-a., 2003. Study on the Improving Balling Technology and Mechanism of Mechanochemical Activation. Master's Degree Thesis. Central South University, China.

Wang, C.-a., Xiong, S.-a., Zhu, D.-q., 2002. Effect of high pressure roller mill pretreating concentrates on green ball properties. Sintering Pelletizing 27, 12–15.

Wang, C.-a., Wang, X.-j., Hu, C.-f., Huo, L.-c., 2005. Study of the activation mechanisms about pretreating magnetite concentrate by high pressure grinding. Sintering Pelletizing 30, 16–18.

Zhang, J.-l., 2012. A Study on the Firing Behaviours of Fluxed Pellets and Their Reduction Performance in Blast Furnace, Master's Degree Thesis. Central South University, China.

Zhang, H.-q., Qi, Y.-g., 2005. The application on improving the quality of iron ore pellets by roller press. Min. Eng. 3, 37–39.

Zhu, D., 1994. Study on mechanism of cold moulding of fine grinding concentrates and its application in direct reduction. Doctor's degree thesis, Central South University of Technology, China.

Zhu, D.-Q., 2013. Improving the pelletization of Brazilian hematite by HPRG. In: 3rd symposium on iron ore pelletizing, 29 September–2 October, 2013.

Zhu, D.-Q., Pan, J., Qiu, G.-z., 2004. Mechano-chemical activation of magnetite concentrate for improving its pelletability by high pressure roll grinding. ISIJ Int. 44 (2), 310–315.

Zhu, D.-g., Wang, Z.-y., Pan, J., Li, J., Xu, X.-f., 2007. Improvement of sintering behaviors of Brazilian specularite concentrate by damp milling. Iron Steel 42, 12–16.

Zhu, D.-Q., Li, H.-M., Yu, W., Wang, B., Pan, J., 2009. An organic activated bentonite mechanism for improving pelletization. J. Chongqing Univ. (Nat. Sci. Ed.), 32 (5), 582–588.

Zhu, D.-Q., Chen, D., Pan, J., 2011a. Comparison of pretreating pyrite cinder by high pressure roller grinding with damp milling to improve pelletization. J. Central South Univ. (Sci. Technol.), 42 (7), 1825–1832.

Zhu, D.-g., Yu, W., Chun, T.-j., Pan, J., 2011b. Improving the pelletization of fluxed hematite pellets by hydrated lime. In: 2011TMS. San Diego, USA, 27 February–3 March 2011.

Zhu, D.-q., Xiong, S.-a., Pan, J., Zhou, X.-l., 2011c. Improving pelletization of magnetite concentrate by organic complex bentonite and its industrial application. J. Cent. South Univ. 42 (2), 279–286.

Quality requirements of iron ore for iron production

16

L. Lu[1], *J. Pan*[2], *D. Zhu*[2]
[1]CSIRO Mineral Resources Flagship, Pullenvale, QLD, Australia
[2]Central South University, Changsha, Hunan, China

16.1 Introduction to ironmaking technologies

Nowadays, almost all the world's steel is produced via one of two main routes:

- The integrated iron- and steelmaking process
- The mini mill or electric arc furnace (EAF) process

The integrated iron- and steelmaking route involves blast furnace (BF) ironmaking followed by basic oxygen steelmaking (BOS). The BF uses sinter, pellet, and lump ore as the iron-bearing raw materials and coke and pulverized coal as reducing agents to produce hot metal with consistent quality for the BOS process. It produces more than 70% of the feed materials required for the BOS steelmaking process. The integrated process is the preferred route where the demand for steel is high and iron ore and coal are readily available.

Mini steel mills normally use the EAF to produce steel from scrap and direct reduced iron (DRI). Since the EAF uses scrap and DRI instead of molten iron, cokemaking and sintering operations are not required. The mini mill route can economically serve small, local markets where scrap is readily available and electric power is cheap. Due to the diminishing quality and supply of scrap, the consumption of DRI in EAFs is expected to increase. DRI is produced via a process called direct reduction (DR), one of the two main types of alternative ironmaking processes commercially available. The DR process involves the production of solid iron, DRI or sponge iron, from iron ore and a reducing agent (e.g., natural gas and noncoking coal). A variety of DR processes, such as MIDREX® and HYL, have been developed and commercialized since the 1970s.

Apart from DR, smelting reduction (SR) is the other alternative ironmaking technology commercially available. SR involves combining iron ore reduction with melting in a reactor, without the use of coke. The product is liquid pig iron, which can be treated and refined in the same way as hot metal from the BF. So far, only the COREX® process has been commercially proved, but a number of other variants are in an advanced stage of development.

As shown in Figure 16.1, world DRI production has seen constant growth since 1980 and reached over 75.2 million tonnes in 2013. Among the various DRI processes, MIDREX® dominates the market accounting for almost 63.2% of the total DRI production in 2013, followed by 21.2% for coal-based processes and 15.4% from the

Iron Ore. http://dx.doi.org/10.1016/B978-1-78242-156-6.00016-2
© 2015 Elsevier Ltd. All rights reserved.

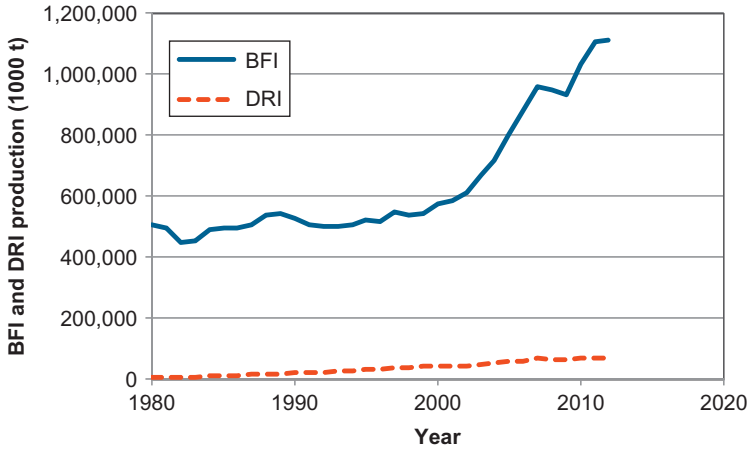

Figure 16.1 Global productions of blast furnace iron (BFI) and direct reduced iron (DRI) between 1980 and 2012 (Anon 1, 2014; Anon 2, 2014).

HYL/Energiron process (Anon 3, 2014). However, the BF ironmaking process is still the dominant process for providing steelmaking raw materials worldwide. The total share of DRI in world crude steel production is only about 4%, while BF hot metal accounts for about 61% and steel scrap for about 36% in 2005. However, the BF ironmaking process relies heavily on metallurgical coke and involves cokemaking and sintering operations, which are often related to serious environmental concerns. Therefore, DR and SR technologies using pulverized coal or other gases as reducing agents to replace metallurgical coke are expected to emerge as future alternative ironmaking processes.

16.2 Quality requirements of iron ore for the BF ironmaking process

16.2.1 BF ironmaking process

The BF is a countercurrent reactor with solid burden, ferrous materials and coke charged from the top of the furnace and oxygen enriched hot air and auxiliary fuel injected through the tuyeres located in the lower part of the furnace. Inside the BF, the solid burden descends while the reducing gases travel upwards. As the ferrous materials descend in the furnace, the iron oxides are dried, heated, and reduced by the ascending reducing gases. The chemical processes occurring in the BF are very complex. From the studies conducted on quenched BFs in Japan, five distinct zones have been identified from top to bottom of the furnace, that is, the lumpy zone, the cohesive zone, the active zone, the raceway, and the hearth, as shown in Figure 16.2 (Kanbara et al., 1976; Kojima et al., 1976; Sasaki et al., 1976; Shimomura et al., 1976).

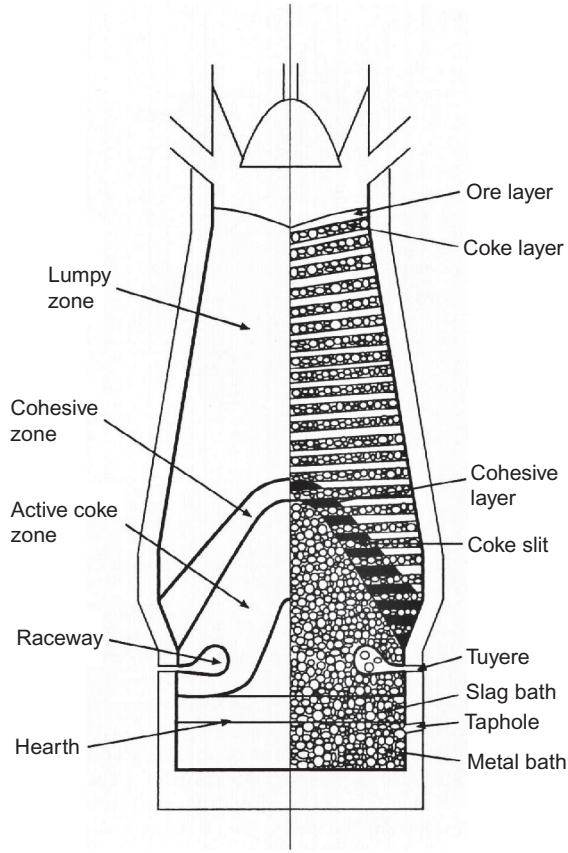

Figure 16.2 Schematic diagram of a blast furnace cross section showing the different zones (Loo and Bristow, 1998a).

Table 16.1 summarizes the key reactions occurring in the lumpy and cohesive zones of the furnace and the corresponding operational requirements for these zones, which largely determine the quality requirements for the burden material. Below the cohesive zone, the ferrous materials lose their identity due to the softening and melting (SAM) process resulting from heating and reduction. Therefore, the physical properties of ferrous materials will not have a significant impact on the phenomena occurring in the zones below the cohesive zone. However, the gangue minerals from the ferrous materials will partition either to the molten slag, if not reduced, or to the hot metal, if reduced, and are thus expected to impact on the chemistry and physicochemical properties of the BF slag and the chemistry and quality of the resultant hot metal.

16.2.2 Quality requirements

Sinter, pellet, and lump ore are typical ferrous raw materials for BFs worldwide. While the burden composition varies significantly from BF to BF, sinter is the predominant

Table 16.1 Key reactions, operational conditions, and ferrous burden quality requirements of different zones in the blast furnace

Zone	Description	Key reactions/ phenomena	Operational conditions	Quality requirements	Physical/chemical properties
Lumpy zone	From stockline to the surface of the cohesive zone	• Drying and preheating • Indirect reduction of iron ores • Carbon solution reaction	Permeable burden and even gas distribution to favor indirect reduction	• Appropriate size distribution • Resistance to breakdown during charging and due to compression in the furnace • Resistance to decrepitation due to thermal shock • Resistance to disintegration due to low-temperature reduction • High reducibility	• Size distribution and mean particle size • Tumble and abrasion indexes • Decrepitation index • Low-temperature reduction disintegration index • Reducibility index • Cold crushing strength • Swelling index

Cohesive zone (softened mass)	Starts when the ferrous material becomes softened and deformed and finishes when liquid starts dripping	• Indirect and direct reduction of FeO • Carburization of reduced iron by CO • Carbon solution reaction	As narrow as possible, and the root of the cohesive zone needs to be as low as possible	• High softening temperature • Low dripping temperature	• Softening temperature • Dripping temperature • Width of cohesive zone • *S* value
Lower part of blast furnace	Below the cohesive zone, including active zone, raceway as well as stagnant coke zone and hearth	• Coal and coke combustion in raceway • Gas/metal and slag drops and gas/coke reactions in active zone • Molten iron/coke, molten slag/coke, and molten slag/metal reactions in stagnant coke zone and hearth	Good slag chemistry	• Good slag fluidity and low viscosity	• Chemistry of ferrous materials to control impurities such as P, S, Al_2O_3, TiO_2, Zn, Na, and K

ferrous material for BFs particularly in countries in East Asia. However, the gradual increase in gangue minerals in iron ore fines in the last decade due to the depletion of high-grade iron ore resources has resulted in a considerable change in sinter chemistry, in particular alumina content and basicity (Lu et al., 2007). Since lump ore and pellets are more acidic and contain less alumina than iron ore sinter, their usage is tending to increase to help balance the chemistry of BF slag. Lump ore is also cheaper than iron ore pellets, which can help contain raw material costs for the BF. However, there have been long-standing concerns about lump ore decrepitation and low softening temperature, which have limited the usage of lump ore in the BF in the past (Wu et al., 2009). Nowadays, a typical modern BF burden in East Asia contains about 10–20% lump ore and 10–20% pellets.

The countercurrent principle of the BF makes it very efficient in transferring the heat and mass required to drive the reduction and smelting reactions inside the furnace. However, this does impose a stringent requirement on the permeability of the furnace shaft, that is, the stability and productivity of the BF are heavily dependent on the permeability of the furnace. To achieve good permeability, the ferrous burden materials need to meet specific criteria, in particular their resistance to fines generation and swelling/contraction. Excessive fines generation and swelling/contraction will lead to a significant loss in the permeability of the BF shaft.

As shown in Figure 16.3, the conditions the burden materials are subjected to, such as temperature, gas composition, and compressive load, vary widely both vertically and radially. Different quality requirements therefore need to be imposed on the burden materials, such as sinter, lump ore, and pellets, in different zones of the

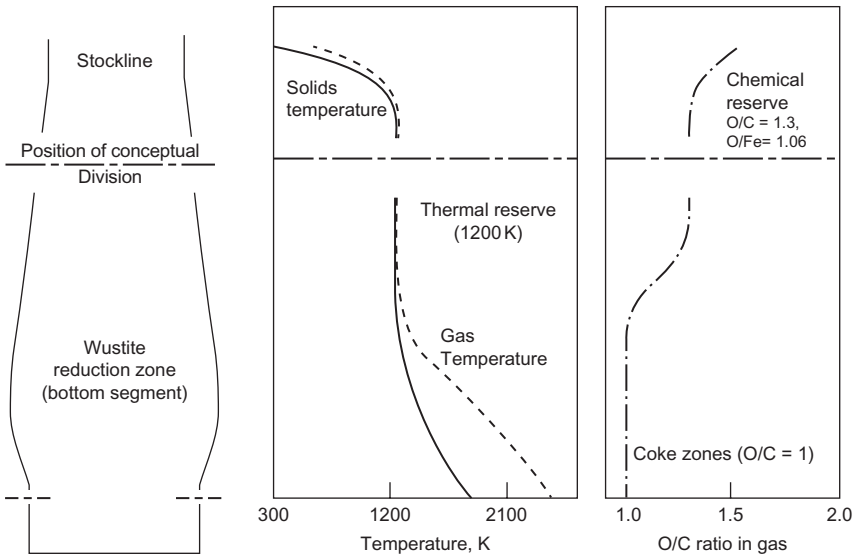

Figure 16.3 Thermal and chemical conditions the burden materials are subjected to inside the blast furnace (Cheng 2001).

furnace, as shown in Table 16.1. First of all, the ferrous material needs to be strong enough to avoid any significant size degradation, or generation of fines, during the charging operation at the top of the furnace. Then, the resistance to decrepitation and disintegration due to release of volatiles (loss on ignition (LOI)), thermal shock and low-temperature reduction in the upper part of the lumpy zone, and the swelling and reducibility of ferrous materials in the lower part of the lumpy zone are critical characteristics for stable BF operation. Finally, in the cohesive zone of the furnace, the SAM characteristics of the ferrous burden become extremely important. It is desirable to blend the ferrous materials available to formulate a ferrous burden of high softening temperature and low dripping temperature. Table 16.2 gives examples of typical quality requirements of ferrous materials for use in large BFs in China.

Below the cohesive zone, the ferrous materials are either reduced and carburized to form an Fe-C melt or fluxed to the molten slag if not reduced. Therefore, the chemistry of ferrous materials added, particularly the gangue minerals, becomes increasingly important as it will affect both the composition and properties of the molten slag and the composition and quality of the hot metal. The key gangue components in the ferrous materials include SiO_2, Al_2O_3, CaO, MgO, S, and P along with trace elements like Mn, Cu, Na, K, and Zn in the form of complex oxides. The majority of these components are fluxed into the molten slag. However, some of the gangue oxides are partially reduced and enter the hot metal as impurities, such as Si, Mn, and P. While S can be controlled inside the BF, an increase in burden S content necessitates an increase in the basicity and MgO of the slag and/or slag volume, leading to an increase in the hot metal production cost. Sulfur and phosphorus are both deleterious elements as they result in cold or hot brittleness of steel products. Alkalis (Na_2O and K_2O) and zinc are detrimental to furnace operation and can lead to higher fuel rates, a loss in productivity, and variable metal quality. Alkalis are also found to accelerate coke degradation by catalyzing the coke gasification reaction. In Japan, the alkali (Na + K) and Zn inputs from the ferrous materials are typically about 1.2 kg/t hot metal and 0.15 kg/t hot metal, respectively. As the gangue minerals in ferrous

Table 16.2 Typical quality requirements of ferrous materials for use in large blast furnaces in China

Burden materials	Units	Lump	Pellets	Sinter
TI (tumble index)	% + 6.3 mm	>80–85	>90	>65
AI (abrasion index)	%−0.5 mm	<10	<3	<7
CCS (cold crushing strength)	kg	N/A	>250	N/A
DI (decrepitation index)	% + 6.3 mm	<15	N/A	N/A
RDI (reduction disintegration index)	% + 2.8 mm	<25	N/A	<35
RI (reducibility index)	%	>60	>70	>65
SWI (swelling index)	%	N/A	<20	N/A

N/A, not applicable.

materials increase, attention also needs to focus on Al_2O_3 and TiO_2, which require fluxing. Al_2O_3 and TiO_2 affect the slag fluidity drastically.

16.2.3 Physical testing of BF ferrous burden materials

16.2.3.1 Standardized tests

Tumble and abrasion indexes

Ore degradation in transit can significantly reduce the amount of ferrous material available for charging into the BF and can have an adverse effect on BF operation if degradation occurs during the charging operation. ISO 3271:2007 was developed to assess the resistance to degradation of ferrous material during handling, transportation, and charging. In accordance with ISO 3271, the tumble (TI) and abrasion indexes (AI) are determined as the weight percentages of +6.3 and −0.5 mm materials present, respectively, after the tumble treatment in which 15 kg of sized ferrous material (−40 + 10 mm for sinter and lump and −40 + 6.3 mm for pellets) is tumbled in a 1 m diameter drum for 200 revolutions at a rotational speed of 25 rpm.

Two mechanisms are responsible for the mechanical degradation of individual particles in the BF, that is, impact and abrasion. If an individual particle is incapable of accommodating the energy due to impact during charging as well as the abrasion between particles and between the particles and the furnace wall, this individual particle is likely to break down to generate fines. These fines fill the voids in the packed burden material and reduce the permeability of the furnace shaft. The TI basically represents the resistance of ferrous material to volume breakage due to impact, while the AI gives an indication of the degree of fines generation due to abrasion. As shown in Figure 16.4, the permeability of BF improved considerably with the ferrous material TI.

The resistance of ferrous material to mechanical degradation is believed to be mainly determined by the mineralogy and texture of the material involved. After measuring the toughness of three lump ores using a combination of macro- and microfracture tests, Dukino and coauthors (Dukino et al., 1995) concluded that tough lump ores

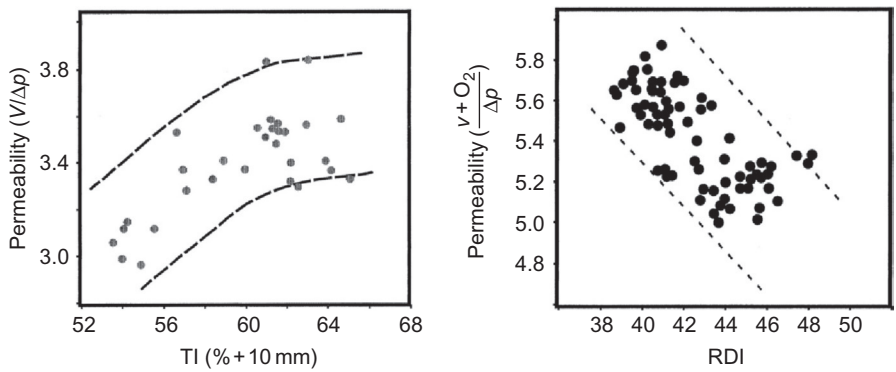

Figure 16.4 Effect of ferrous burden quality on blast furnace permeability (Ranade, 2000; Nishio et al., 1982).

with strong grain boundaries are more resistant to degradation and therefore generate a lower proportion of fines.

Compared to sinter, pellets and lump ore often have a better TI index, which is needed to resist mechanical degradation during transportation. Unlike sinter, which is produced on site, lump ore and pellets are often transported from site to site. However, compared with pellets and sinter, lump ore often has a higher AI.

Shatter index

Similar to ISO 3271, the Japanese Standards Association has developed a standard called the shatter test, JIS M8711:2011, to access the degradation of iron ore sinter due to drop during transportation from the sinter plant to the BF. In accordance with JIS M8711, the shatter index (SI) is determined as the weight percentage of +10 mm material remaining after four drops of a 20 kg sized sinter sample (−50 + 10 mm) from a height of 2 m. Unlike ISO 3271, the shatter test only simulates the degradation of sinter due to drops during transportation from the sinter plant to the BF.

Cold crushing strength

Unlike sinter, pellets are close to spherical in shape. Therefore, the mechanical property of pellets can readily be measured by a compression test. ISO 4700:2007 was developed to determine the CCS of iron ore pellets. In accordance with ISO 4700, the cold crushing strength (CCS) of pellets is the arithmetic mean of measurements of a test sample of at least 60 pellets of −12.5 + 10 mm particle size. From practical experience, a crushing strength of 200 kg, preferably 250 kg, is desirable for pellets to be used in large BFs.

Decrepitation index

As lump particles land on top of the hot burden in the furnace and descend, they are subjected to thermal shock, which may also cause breakdown of the lump particles. This behavior of lump ore is called decrepitation. The presence of hydrated and carbonate minerals as well as combined moisture is closely linked to the decrepitation of lump particles (Tenuta de Azevedo and Cardoso, 1983; Da Silva and Muniz, 2008). It is therefore not surprising that thermally processed ores, such as sinter and pellets, do not decrepitate.

ISO 8371:2007 was developed to assess this behavior for lump ore. Based on ISO 8371, the decrepitation index (DI) is defined as the weight percentage of −6.3 mm material generated after a sized, natural ore sample (−25 + 20 mm) of about 500 g is heated to 700 °C in 30 min. The DI quantifies the resistance of lump ore to thermal degradation. Ore texture has an important impact on the degree of decrepitation. As shown in Figure 16.5, porous ore does not decrepitate as much as dense ore even when it has a higher LOI.

A high DI indicates more Fe loss through dust and a negative impact on BF permeability. A DI value of less than 20, ideally 15, is desirable for lump ore to ensure the permeability of large BFs.

Low-temperature reduction disintegration index

As the burden material descends further in the furnace shaft, reduction of hematite (Fe_2O_3) to magnetite (Fe_3O_4) commences with the increase in temperature and decrease in oxygen partial potential in the shaft. ISO 4696-1 and 2:2007 were developed

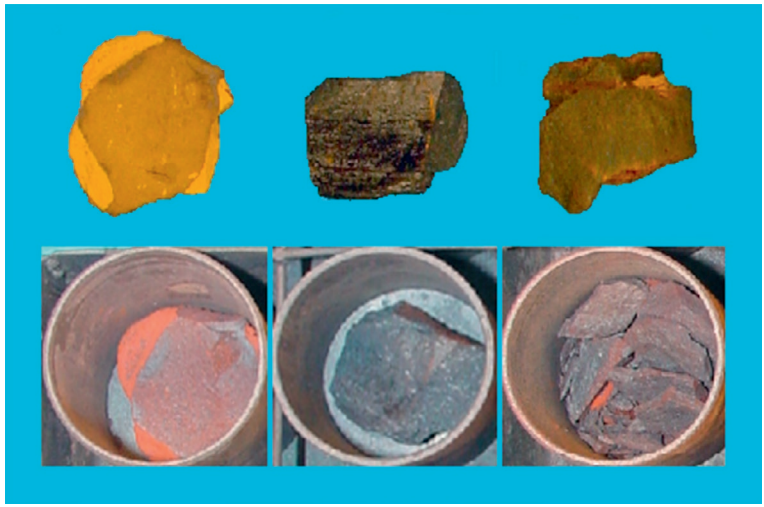

Figure 16.5 Effect of ore mineralogy and texture on the decrepitation tendency of −25 + 20 mm lump ore particles of highly microporous, ochreous goethite (left), microporous martite-goethite (center), and dense martite-goethite (right), before (top row) and after DI testing (bottom row). Images before and after DI testing are for the same particles.

to assess the behavior of ferrous material in this zone of the furnace. In accordance with ISO 4696-2, a sized sample of 500 g (−20 + 16 mm for lump ore and −12.5 + 10 mm for pellets) is reduced isothermally at 550 °C for 30 min in a fixed bed with a gas mixture of 30% CO + 70% N_2 flowing at 15 L/min. After cooling under N_2, the partially reduced sample is tumbled for 30 min at a speed of 30 rpm and then screened at 2.8 mm. The low-temperature reduction disintegration index (RDI-2) is the weight percentage of tumbled product passing 2.8 mm. A higher RDI-2 value corresponds to a greater amount of disintegration and therefore poorer quality product.

After considering European practice and the change in gas composition due to pulverized coal injection (PCI) operation, ISO 4696-1 was introduced using a gas mixture containing 2% H_2 and 20% CO_2. In accordance with ISO 4696-1, a sized sample of 500 g (−12.5 + 10 mm for lump, sinter, and pellets) is reduced isothermally at 500 °C for 60 min in a fixed bed with a gas mixture of 20% CO + 20% CO_2 + 58% N_2 + 2% H_2 flowing at 20 L/min. After cooling under N_2, the partially reduced sample is tumbled in a specific tumble drum for 300 revolutions at 30 rpm and then sieved at 6.30 mm, 3.15 mm, and 500 µm. Three reduction disintegration indexes (RDI-1) are calculated as the mass percentage of material greater than 6.30 mm, less than 3.15 mm, and less than 500 µm.

The RDI test is designed to evaluate the degree of fines generation from ferrous material when reduced under conditions similar to those prevailing in the low-temperature reduction zone of a BF. As shown in Figure 16.4, the permeability of the BF improved considerably as the ferrous material RDI value decreased. Detailed mechanisms responsible for this behavior have been previously reviewed (Dawson, 1993; Loo and Bristow, 1998b; Lu et al., 2007). The disintegration of ferrous material

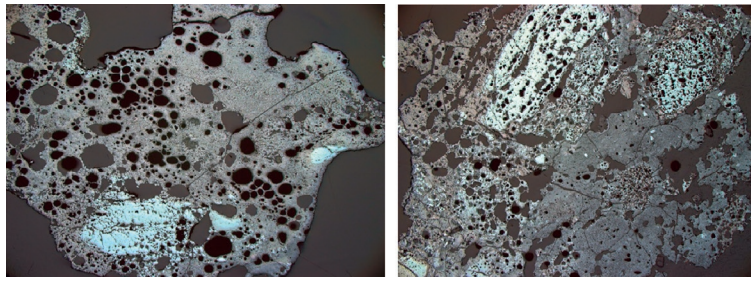

Figure 16.6 Photographs of sinter particles prior to (left) and after (right) RDI reduction.

is generally believed to be associated with crack initiation and propagation due to the volume change accompanying the reduction of hematite to magnetite and the inability of the hematite grains or sinter matrix to accommodate the strains resulting from changes in volume and crystal structure. As shown in Figure 16.6, sinter particles reveal more cracks after low-temperature reduction. Fe_2O_3 belongs to the hexagonal crystal system and has a theoretical density of 5.255 g/cm^3, while Fe_3O_4 has an octahedral spinel structure with a theoretical density of 5.200 g/cm^3. Solid-state reduction of hematite is therefore accompanied by both a change in crystal structure and volume expansion, generating strains. Cracks, believed to form initially at grain boundaries and propagate across the matrix, lead to disintegration of particles.

Compared with sinter, lump ore and pellets are generally much less affected by reduction disintegration. Typically, lump ores have RDI-2 values of <25, while pellets have excellent RDI-2 values of <5. However, as the alumina and LOI contents of sinter fines increase, the sinter RDI-2 values also increase from below 30 to 35 or even higher (Lu et al., 2007). Increasing sinter basicity and FeO and MgO contents has been found to improve sinter RDI.

Reducibility index

Two different types of reduction reactions occur simultaneously in the BF. Above the cohesive zone, the iron oxides are reduced to wüstite (FeO) by the reducing gases, including CO and H_2, while further reduction to iron occurs mainly in contact with solid fuel or coke in and below the cohesive zone. The former is called an indirect reaction, while the latter is termed a direct reaction. ISO 7215:2007, ISO 4695:2007, and ISO 7992:2007, which use distinct reducing gas compositions and reduction temperatures without (ISO 7215 and ISO 4695) or with a compression load (ISO 7992), are aimed at quantifying the reducibility of ferrous material under conditions resembling those prevailing in the indirect reduction zone of a BF. In accordance with ISO 7215, a sized sample of 500 g (−20 + 18 mm for sinter and lump ore and −12.5 + 10 mm for pellets) is reduced isothermally at 900 °C for 180 min in a fixed bed with a gas mixture of 30% CO + 70% N_2 flowing at 15 L/min. The reducibility index (RI) is determined from the extent to which oxygen is removed from iron ores within 180 min.

Reducibility is important to the BF, particularly in the lower part of the lumpy zone. It can affect utilization of the reducing potential of CO and H_2 in the furnace shaft and therefore the coke consumption of the furnace, as evidenced in Figure 16.7.

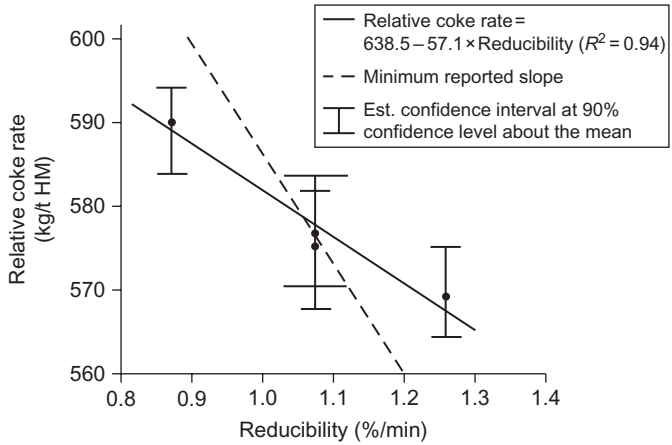

Figure 16.7 Effect of burden reducibility on blast furnace coke rate (Ranade, 2000; Blattner et al., 1984).

A highly reducible ore will also result in less FeO production as it descends into the high-temperature zone and, therefore, will improve the softening properties of the burden material. Ferrous materials with high reducibility are therefore desirable for efficient BF operation. During indirect reduction, iron oxides are reduced through a solid/gas reaction mechanism. At intermediate temperatures, the reduction rate is likely to be controlled by mixed gas diffusion and chemical reaction on the pore surface of the solid. The porosity of the solid phase is therefore expected to affect the reaction kinetics, as it changes the surface area available for chemical reaction.

Figure 16.8 shows the macrostructure of typical burden materials. Compared with lump ore, sinter and pellets, particularly fluxed pellets, are more porous and reducible with an RI value of often >65. Lump ores are often less porous and therefore lower in reducibility than sinter and most pellets. The RI value of lump ores varies widely from the middle forties to the low seventies. Comparing the two lump samples in Figure 16.8, lump A is denser and less porous compared with lump B. It is also worth mentioning that lump B has a higher LOI due to the presence of more goethite (FeOOH), which will generate more secondary porosity upon heating prior to indirection reduction. When reduced, lump B actually has a much better reducibility of about 65% compared with 41% for lump A.

Free swelling index

Practical experience shows that some pellets experience abnormal swelling during reduction at intermediate to high temperatures. Excessive swelling increases the pellet volume and reduces the pellet strength (Figure 16.9), leading to loss of furnace permeability and stable furnace conditions. ISO 4698:2007 was designed to quantify the swelling tendency of pellets under conditions resembling those prevailing in the indirect reduction zone of a BF. In accordance with ISO 4698, a test portion of 18 pellets of −12.5 + 10 mm particle size is reduced isothermally at 900 °C for 60 min

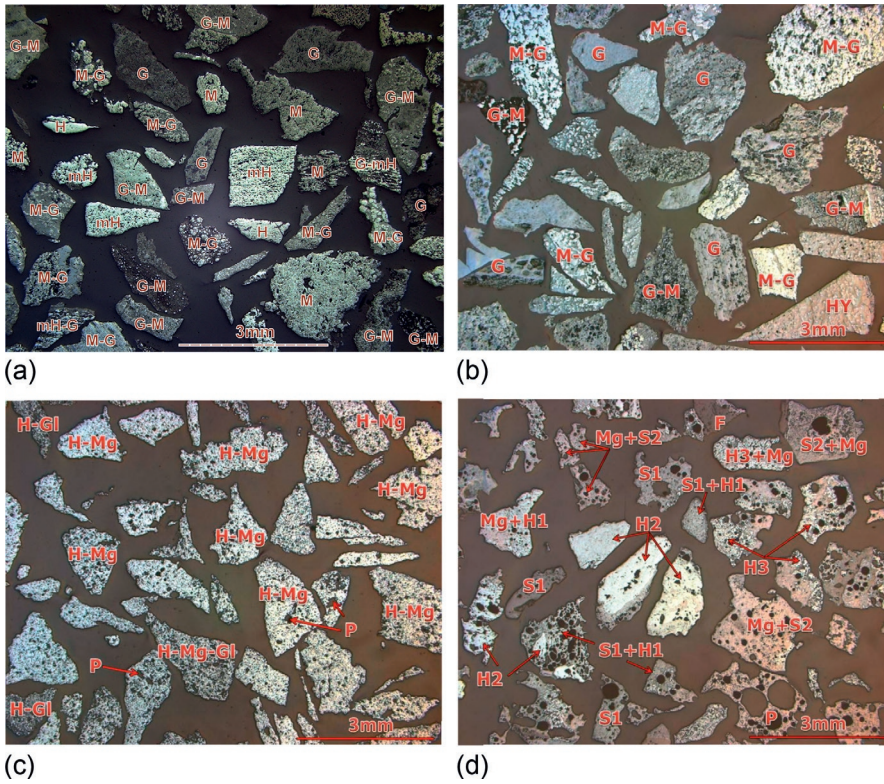

Figure 16.8 Reflected optical micrographs showing mineralogical characteristics of the burden materials tested (−2 + 1 mm fraction): (a) lump A, (b) lump B, (c) pellet, and (d) sinter. H-hematite (mH: microplaty hematite, H1: seconday subhedral hematite, H2: primary hematite, H3: secondary skeletal hematite), Mg: magnetite, M: Martite, G: Goethite, HY: Hydrohematite, S1: fibrous SFCA, S2: Prismatic SFCA, Gl: glass, P: pore, F: Flux.

under unconstrained conditions in a fixed bed with a gas mixture of 30% CO + 70% N_2 flowing at 15 L/min. The free swelling index (FSI) is calculated as the percentage of volume change of these pellets as a result of reduction.

Inside a BF, iron ore is reduced in three stages from mainly Fe_2O_3 to Fe through Fe_3O_4 and FeO. As mentioned earlier, there is about a 20% volume increase in the reduction of Fe_2O_3 to Fe_3O_4 due to the transformation of crystal lattices. However, there is negligible volume increase accompanying the reduction of Fe_3O_4 to FeO. In fact, the volume decreases, when FeO is reduced to Fe. Therefore, theoretically, pellets should not swell more than 20% during reduction. Extensive studies (Hayashi and Iguchi, 2003, 2005; Jiang et al., 2007; Dwarapudi et al., 2014; Xu et al., 2013; Zhu et al., 2012) have been conducted to understand the reduction swelling mechanisms for pellets and develop technologies to mitigate the abnormal swelling. The abnormal swelling is generally believed to occur in Stages 2 and 3 of reduction due to the anisotropy of hematite crystals during reduction, the presence of impurities like ZnO and some alkali metals, and the formation of iron whiskers. As discussed earlier, adding small

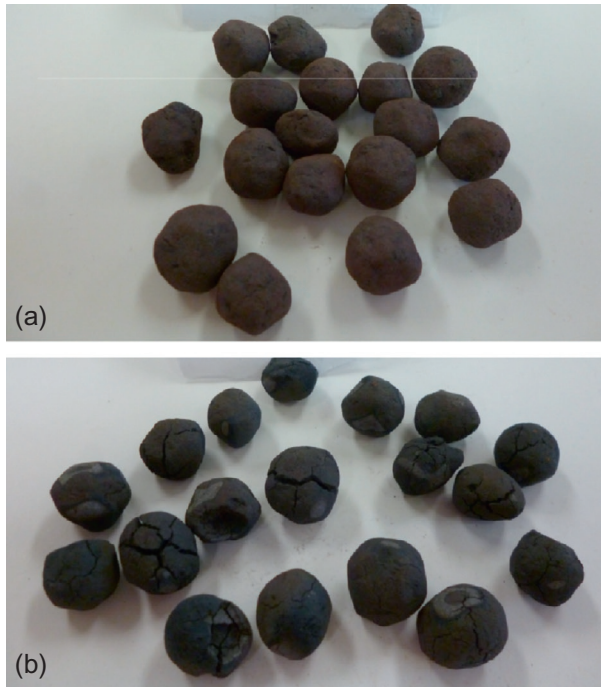

Figure 16.9 Pellets (−12.5 + 10 mm) (a) prior to and (b) after reduction.

amounts of impurities (Jiang et al., 2007; Dwarapudi et al., 2014; Xu et al., 2013; Zhu et al., 2012), such as MgO, and optimizing pellet basicity can effectively reduce the reduction swelling tendency of pellets. An FSI value of <20% is generally desirable for pellets in large BF applications.

16.2.3.2 Nonstandardized tests

Figure 16.10 shows the phase diagram of the Fe-C-O system showing the stability fields of Fe and various iron oxides (Ricketts, 2000). The conditions of various ISO standard physical tests and the working conditions measured for Japanese and German BFs are also shown in Figure 16.10. It is clear that the relationship between the gas composition and temperature inside the BF does not follow the equilibrium curves for either FeO or CO. The simple standardized tests are generally conducted at fixed conditions, which often represent the extreme situations encountered by ferrous material in the furnace. Therefore, the standard physical tests do not provide information on the behavior of the ferrous material in the BF, particularly in the cohesive zone of the furnace. For this purpose, more sophisticated, nonstandardized physical testing methods are needed to simulate the working conditions that the ferrous material encounters on its descent down the furnace. After reviewing the burden testing methods available, Chaigneau and coworkers (2001) suggested that standard physical tests are useful tools for quality control to ensure consistent quality of the raw materials, while nonstandard physical tests give better prediction when unfamiliar burden materials are used.

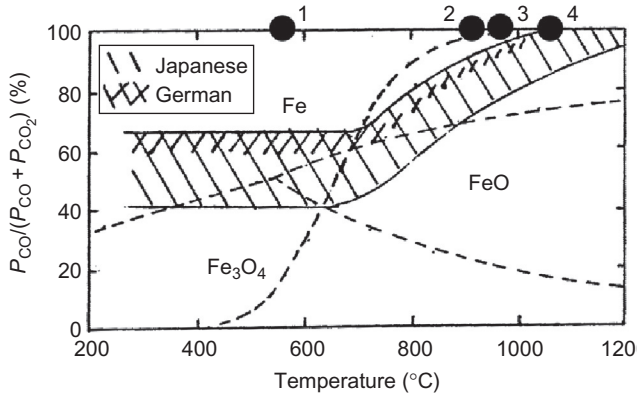

Figure 16.10 Phase stability fields of the Fe-C-O ternary system, Japanese and German blast furnace working conditions, and the conditions of different standard ISO physical tests: (1) ISO 4696-2, (2) ISO 7215, (3) ISO 4695, and (4) ISO 7992 (Ricketts, 2000).

The SAM test was therefore developed to simulate the physical and chemical changes occurring in a small volume of sample as it descends in a BF, particularly in the cohesive zone. During the test, the sample is sandwiched between two layers of graphite or coke particles and subjected to a programmed time-dependent variation of temperature, gas composition, and loading conditions. The physical and chemical changes occurring in the sample during the test are monitored continuously by measuring and recording changes in sample temperature, bed height, and pressure drop across the sample bed and by monitoring the dripping of melts.

As different BFs operate under distinct working conditions, and given the complexity of this test, there is no standard testing facility and procedure for the SAM test. Figure 16.11 presents a schematic diagram of the CSIRO SAM testing facility. It consists of a heating furnace, a gas distribution system, a loading system, and a data acquisition system. The heating furnace is capable of heating the test sample at required heating rates up to a temperature of 1550 °C. The gas distribution system enables simulation of the compositions of gaseous mixtures of N_2, CO, CO_2, and H_2 that are typically found in BFs. The loading system applies a fixed or variable load to the surface of the sample bed via an air cylinder and monitors the compaction of the sample bed. The data acquisition system is used to preset the initial values and ramping rates of the sample load and gas flow rates and record the changes in bed height and pressure drop across the sample bed, as well as sample and melt collector temperatures for analysis. Table 16.3 summarizes the typical testing conditions used in the CSIRO SAM test. While considerable differences exist in the crucible size and heating method between the various laboratories that conduct SAM tests, there is good consensus on the test sample particle size, gas composition, heating rate, and load.

Figure 16.12 shows SAM curves measured for a typical lump ore sample under CSIRO SAM testing conditions. The softening, melting, and dripping temperatures, as well as the other characteristics, are defined below and illustrated in Figure 16.12:

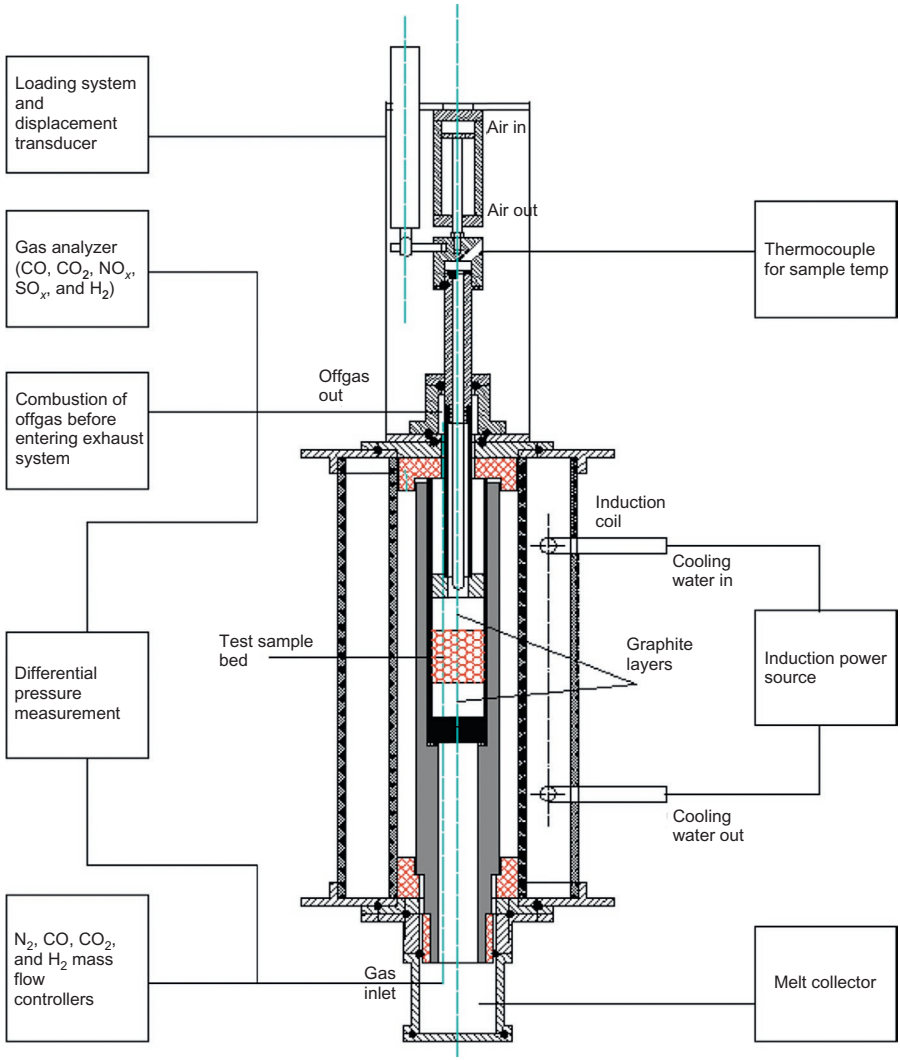

Figure 16.11 Schematic diagram of the CSIRO softening and melting test facility.

- *Softening temperature (°C),* T_s: the sample temperature where the pressure drop across the bed starts to increase rapidly. T_s usually coincides with the temperature at which DR starts and is defined as the start of the cohesive zone. However, in practice, the softening temperature is estimated as the sample temperature at 50% bed compaction, as shown in Figure 16.12. Some laboratories define T_s at a specific pressure drop value. However, due to the difference in the experimental setup, different values are specified for the pressure drop.
- *Dripping temperature (°C),* T_d: the sample temperature at which the first drop of molten material is recorded.
- *Melting temperature (°C),* T_m: the sample temperature at which the pressure drop across the sample bed returns to that at T_s or 1550 °C, whichever is lower, as shown in Figure 16.12.

Table 16.3 Summary of typical "CSIRO SAM" testing conditions

Parameter	Units	Variation range of key variables	Typical conditions
Sample mass	g	–	About 500
Sample size	mm	–	−12.5 + 10
Sample bed height	mm	–	65
Graphite layer depth	mm	–	45 bottom
	mm	–	40 top
Graphite size	mm	–	−12.5 + 10
Gas flow	L/min	Programmable N_2: 0–20 CO: 0–15 CO_2: 0–10 H_2: 0–3	11.3
Gas composition	Vol%	Programmable: four gas mixture of varying composition	30% CO + 70% N_2
Heating rate	°C/min	Programmable	10 at temperatures below 1000 °C and reduced to 5 at temperatures higher than 1000 °C
Load	kN/m^2	Programmable 0–250	98

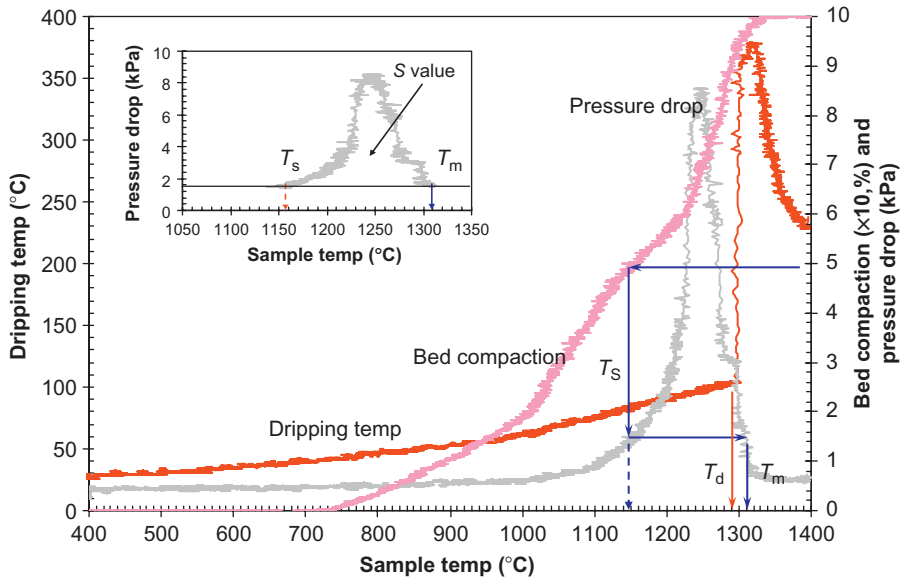

Figure 16.12 Typical softening and melting curves measured for a typical lump iron ore under "CSIRO SAM" testing conditions. $\Delta T = T_m - T_s$.

This indicates the end of meltdown and compaction of the bed. T_m can be either higher or lower than T_d depending on the difficulty in dripping out the melt.

- *Melting range (°C),* ΔT: the temperature interval ($T_m - T_s$) between the SAM temperatures, indicative of the thickness of cohesive zone.
- *S value (kPa°C)*: the area under the pressure drop curve, above the pressure drop at T_s, and bordered by the SAM temperatures. This is often referred to as the *S* value in Japan. As shown in the inset in Figure 16.12, the *S* value is calculated using the equation:

$$S = \int_{T_s}^{T_m} \left(\Delta P - \Delta P_{T_s} \right) \mathrm{d}T$$

where ΔP and ΔP_{T_s} are the pressure drops across the sample bed at temperatures T and T_s, respectively. The *S* value is a measure of resistance offered by the bed to the gas flow in the furnace.

In addition, the maximum pressure drop (ΔP_{max}) and metal drip ratio (MDR, percentage of metal dripped out at the end of test) can also be determined from the test.

The behavior of BF ferrous burden during reduction at high temperatures, or the softening and dripping temperatures, is believed to determine the configuration and location of the cohesive zone (Dawson, 1987; Higuchi et al., 2004), which has a profound impact on hot metal productivity and quality, fuel consumption, operational stability, and the lining life of the BF due to its effects on total gas flow and distribution of gas and temperature in the furnace burden (Dawson, 1987). The temperature interval between SAM of the ferrous burden gives the closest indication of the thickness of the cohesive zone in a BF and therefore the permeability of the furnace. The narrower the cohesive zone, the easier it is for the gases to flow through the bed resulting in better reduction kinetics of iron oxides. It is therefore important to ensure the temperature interval between SAM of the ferrous burden (higher softening temperature and lower dripping temperature) is as small as possible, preferably below 150–180 °C, for optimum BF performance.

While many factors, such as composition, pore structure, and mineralogy, can affect the softening and dripping characteristics of the ferrous material, it is thought that the reducibility of the material determines the amount of FeO in the sample during high-temperature reduction and therefore plays an important role in the softening characteristics of the material. On the other hand, the composition and properties of slag formed from the ferrous material determine the dripping temperature of the material (Lu et al., 2009). Different ferrous materials show distinct SAM characteristics. When measured individually, lump ores usually start to soften at lower temperatures and show higher pressure drop values than sinter and pellets. However, the T_s values of mixed burdens of varying proportions of sinter and lump ore are between the softening temperatures of the sinter and lump ore involved, indicative of improved softening characteristics of lump ore due to the interaction between lump and sinter particles. Results obtained for mixed burdens of sinter and lump ore show that the contraction behavior of a bed composed of 20% lump ore and 80% sinter is very similar to the results obtained for a 100% sinter bed (Loo et al., 2011). In fact, it has been reported that some of the BFs in China have been running efficiently at 20% lump ore in their burden (Wu et al., 2009).

16.3 Quality requirements of iron ore for alternative ironmaking processes

The BF ironmaking process relies heavily on metallurgical coke and involves coking and sintering operations, which are often related to serious environmental concerns. The complexity of modern blast furnaces and their associated infrastructure also has high capital requirements and often reduced operating flexibility. Alternative ironmaking processes address the key issues that currently confront the industry, such as high capital costs, environmental problems, and lack of production flexibility, so they have attracted increasing interest.

16.3.1 DR processes

16.3.1.1 Background

In a DR process, iron ore pellets and/or lump iron ores are reduced by a reducing gas to produce DRI or hot briquetted iron (HBI). Depending on the generation of the reducing gas, two different DR processes are commercially available: gas-based and coal/oil-based. In the gas-based DR process, the reducing gas is produced by chemically reforming a mixture of natural gas and off-gas from the reducing furnace to produce a gas that is rich in hydrogen and carbon monoxide. Typical examples of the gas-based DR process include MIDREX® and HYL, which are often the preferred technology in countries where natural gas is abundant. However in the coal/oil-based DR process, the reducing gas is generated from hydrocarbons (primarily coal, but sometimes oil and natural gas) in the reduction zone of the furnace, which is typically a rotary kiln. Typical examples of the coal-based process include the SL/RN and ACCAR processes. The coal-based DR process is more popular in India and China. Different types of reactors, such as shaft furnaces, fluidized beds, rotary kilns, and rotary hearth furnaces, have been used in different variations of the processe to achieve the metallization required.

Based on statistics (Anon 3, 2014), India is the world leader in DRI production producing about 17.8 Mt of DRI in 2013, approximately one-forth of world DRI production. The gas-based DR processes are producing almost 80% of the world's DRI. MIDREX® is the key variant of the gas-based DR processes accounting for about 63.2% of world DRI production in 2013, followed by HYL (15.4%). Therefore, the following discussion focuses mainly on the MIDREX® process.

16.3.1.2 MIDREX® process description

As shown in Figure 16.13, the MIDREX® process consists of three major stages: (1) reduction, (2) reforming, and (3) heat recovery. Iron oxide, in pellet or lump form, is introduced through a proportioning hopper at the top of the shaft furnace. As the ore descends through the furnace by gravity, it is heated and reduced by a counterflowing gas, which contains high contents of H_2 and CO. H_2 and CO gases react with Fe_2O_3 in the iron ore and convert it to metallic iron, generating H_2O and CO_2, which exit at the top of the

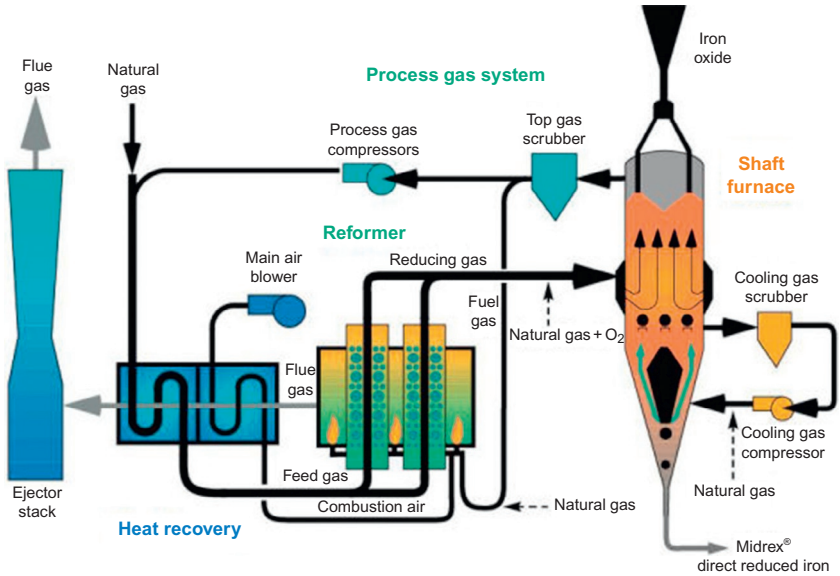

Figure 16.13 Schematic diagram of the MIDREX® process to produce DRI (Anon 5, 2008).

shaft furnace. For production of cold DRI, the reduced iron is cooled and carburized by counterflowing cooling gases in the lower portion of the shaft furnace. The reduced iron can also be discharged hot and fed to a briquetting machine for production of HBI, or fed hot, as hot DRI, directly to an EAF. To maximize the efficiency of reforming, off-gas from the shaft furnace is recycled and blended with fresh natural gas. The mixing gas is fed to the reformer, a refractory-lined furnace containing alloy tubes filled with catalyst. The gas is heated and reformed as it passes through the tubes. The newly reformed gas, containing 90–92% H_2 and CO, is then fed hot directly to the shaft furnace as the reducing gas. The thermal efficiency of the MIDREX® reformer is greatly enhanced by the heat recovery system. Sensible heat is recovered from the reformer flue gas to preheat the feed gas mixture, the burner combustion air, and the natural gas feed. In addition, depending on the economics, the fuel gas may also be preheated.

16.3.1.3 Raw material requirements

The MIDREX® shaft furnace is designed to operate with a combination of pellets and lump ores virtually in any proportion. This allows the plant operator to maximize productivity at the lowest cost. MIDREX® plants are reported to have processed iron oxide pellets and lump ores from over 50 sources around the world. Table 16.4 summarizes the preferred chemical, physical, and metallurgical characteristics required by the process for pellets and lump ores. Unlike BF ironmaking or SR processes, the MIDREX® process has no mechanism to achieve separation of gangue minerals and reduced iron. Therefore, DR pellets and lump ores are required to have a high Fe grade and low contents of gangue minerals. Sulfur and phosphorus are both deleterious elements for steel products and need to be controlled. In addition, sulfur when forming

Table 16.4 Preferred chemical, physical, and metallurgical characteristics of DR-grade pellets and lump ores

	Pellets	Lump
Chemical properties		
%Fe	67.0 minimum	67.0 minimum
%($SiO_2 + Al_2O_3$)	3.0 maximum	3.0 maximum
%S	0.008 maximum	0.008 maximum
%P	0.03 maximum	0.03 maximum
%TiO_2	0.15 maximum	0.15 maximum
Physical properties		
Nominal size	−16 + 6 mm	−35 + 10 mm
% −35 + 10 mm	–	85 minimum
% −16 + 9 mm	95 minimum	–
% −5 mm	3 maximum	5 maximum
Compression strength kg	250 minimum	–
% Less than 50 kg	2 maximum	–
Metallurgical properties		
MIDREX® Linder test (760 °C)		
% Metallization	93 minimum	93 minimum
% −3.36 mm	2 maximum	5 maximum
Hot load test (815 °C)		
Tumble strength (% +6.73 mm)	90 minimum	85 minimum
Compression strength (kg)	100 minimum	–
Clustering (% +25 mm after 10 revolutions)	0	0

Anon 4 (2014).

H_2S is known to deactivate nickel-based steam reforming catalysts by chemisorption on the metal surface during the steam reforming process.

Like the upper part of BFs, the MIDREX® shaft furnace is operated on the countercurrent principle. Therefore, a narrow and coarse size distribution of DR pellets and lump ores with minimum reduction degradation is important to ensure good permeability and even distribution of the reducing gas. Of course, for achieving the high metallization required by DRI, the DR pellets and lump ores must have a good reducibility. Increasing reducing temperatures can promote reduction kinetics and therefore increase the metallization and/or productivity. However, increasing temperature can lead to clustering of partially reduced products, resulting in serious operational problems. One of the most significant innovations in DR-grade iron ore has been oxide coating to overcome the clustering problem during shaft reduction at high temperatures. By coating pellets with a thin layer of limestone, cement, or bauxite, the reducing gas temperature can be increased significantly, resulting in a production increase of up to 20%. Many pellet suppliers are now coating DR-grade pellets, or this can be done by the DR plant operator.

16.3.1.4 Metallurgical testing of DR pellets and lump

As mentioned earlier, low-temperature disintegration, reducibility, and clustering are three key concerns for DR-grade lump and pellets. Historically, MIDREX® has developed and used two tests (Hot Load and Linder) to evaluate these parameters. There are also ISO standards corresponding to these two tests. A brief discussion on these testing methods is given below.

MIDREX Linder test

The MIDREX Linder test is designed primarily for accessing the low-temperature reducibility and disintegration of DR-grade pellets and lump and is essentially similar to ISO 11257:2007. In the Midrex Linder test, a sized test portion of 500 g is reduced isothermally at 760 °C for 5 h in a reduction tube rotating at 10 rpm with a gas mixture of 55% H_2 + 36% CO + 5% CO_2 + 4% CH_4 flowing at 15 L/min. The reduced product is sieved at 6.3 and 3.36 mm and analyzed for total iron and metallic iron. The RDI is calculated as the mass percentage of material less than 3.36 mm. The degree of metallization at 760 °C is calculated from the chemical analysis results.

Like the MIDREX Linder test, ISO 11257 is performed at the same temperature and gas composition. However, a lower flow rate of 13 L/min is used for the reducing gas and the reduced product is sieved at 3.15 mm rather than 3.36 mm.

MIDREX hot load test

The MIDREX hot load test simulates the increasing load experienced by the pellets as they descend through the shaft furnace. The test accesses the physical durability and clustering tendency of the DR-grade products during reduction under load. The test is performed at 815 °C, which is appropriate for DR operations. No detailed testing conditions are reported in the literature. As shown in Table 16.4, the DR-grade products need to demonstrate good strength and no clustering tendency during reduction under load.

For similar purpose, two ISO standards were also developed to access the clustering (ISO 11256:2007) and reducibility (ISO 11258:2007), respectively, for the DR-grade products. In accordance with ISO 11256, a sized test sample of 2000 g is reduced isothermally at 850 °C in a fixed bed with a gas mixture of 45% H_2 + 30% CO + 15% CO_2 + 10% N_2 flowing at 40 L/min, until a reduction degree of 95%. A constant load of 147 kPa is applied on the surface of the sample bed after 60 min of reduction. The clustered material from the reduced product is then subjected to seven disaggregation operations of five revolutions each inside a 1 m tumble drum rotating at 25 rpm. The clustering index is calculated as the mass percentage of the clustered material accumulated after the specific disaggregation operations.

The ISO 11258 reducibility test is performed on a sized test sample of 500 g, which is reduced isothermally for 90 min at 800 ° C, in a fixed bed, using a reducing gas consisting of 45% H_2, 30% CO, 15% CO_2, and 10% N_2 at a flow rate of 50 L/min. The rate of reduction is calculated at O/Fe ratios of 0.9 and 0.15, and the final degree of reduction is calculated from the oxygen mass loss after 90 min reduction (R_{90}). The degree of metallization is calculated either from the R_{90} or by chemical analysis of the reduced test portion.

16.3.2 Smelting reduction

16.3.2.1 Background

Smelting is a form of extractive metallurgy to produce a metal from its ore. Smelting uses heat and a chemical reducing agent to decompose the ore, driving off other elements as gasses or slag and leaving just the metal behind. The reducing agent is commonly a source of carbon such as coke, charcoal, and coal. The modern SR technologies aim at direct use of noncoking coal and therefore overcome the reliance of the existing BF ironmaking route on coking coal and prepared raw materials, which has attracted serious environmental concerns.

The SR processes that are commercially exploited or in development include COREX®, HISMELT, DIOS, AISI-DOE/CCF, and ROMELT. These processes differ in the number of reactors and the ore feed used (pellets, lump ore, or fines). For example, reduction and melting occur in two stages in two different vessels in COREX®, while in HISMELT, reduction and melting take place in the same vessel. COREX® is the key variant of the SR processes currently operating on a commercial basis. Therefore, the following discussion focuses mainly on the COREX® process.

16.3.2.2 COREX® process description

As shown in Figure 16.14, all metallurgical reactions in the COREX® process are carried out in two separate process reactors—the reduction shaft and the melter gasifier. In the first step, iron ore is reduced to sponge iron in a shaft furnace by means of reducing gas. In the second step, the reduced iron is completely reduced and melted in the melter-gasifier vessel. The combustion and gasification of the coal in the melter gasifier generate the heat to melt the reduced iron and the hot reducing gas containing

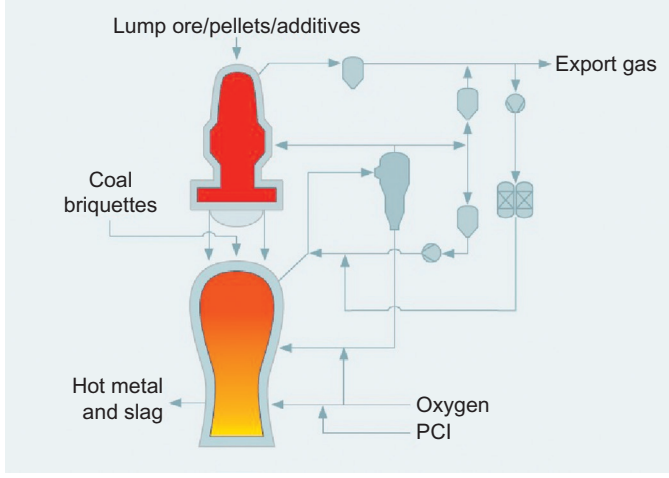

Figure 16.14 Schematic overview of the COREX® process flow sheet (Anon 6, 2014).

65–70% CO, 20–25% H_2, and 2–4% CO_2. After leaving the melter gasifier, the hot reducing gas is mixed with cooling gas to a gas temperature of approximately 850 °C. The gas mixture is then cleaned in hot cyclones and fed into the shaft furnace as the reducing gas. When the gas leaves the top of shaft furnace, it still has a relatively high calorific value and may be used as an export gas where the opportunity exists. Liquid iron and slag are discharged at the bottom of melter gasifier by a conventional tapping procedure similar to that used in BF operation.

Because of the separation of iron reduction and iron melting/coal gasification in two steps in the COREX® process, a high degree of flexibility is achieved and a wide variety of coals can be used. Since coking and sintering plants are not required for the COREX® process, substantial cost savings of up to 20% can be achieved in the production of hot metal. Regarding environmental concerns, COREX® plant emissions contain only insignificant amounts of NO_X, SO_2, dust, phenols, sulfides, and ammonia, which are well below the maximum limits allowed by future European standards. Furthermore, waste water emissions from the COREX® process are far less than those in the conventional BF route.

Following the first industrial application of a COREX® C-1000 plant with a nominal production of 1000 tHM/day at Iscor Pretoria, South Africa, four C-2000 plants (nominal production of 2000 tHM/day) were subsequently put into operation at POSCO in south Korea, Mittal Steel in South Africa, and JSW Limited in India. The first of the two planned COREX® C-3000 plants was started up in early November 2007 at Baosteel, China. It has a nominal production capacity of 1.5 million tHM/year. Recently, a variant of the COREX® process, FINEX, was codeveloped by VAI and POSCO for the production of hot metal based on the direct use of iron ore fines and noncoking coal. Unlike the COREX® process, fine iron ore is charged into a series of fluidized bed reactors together with fluxes. A commercial FINEX plant with a capacity of 1.5 million tHM/year started operation at Pohang Works, POSCO, in early 2007.

16.3.2.3 Raw material requirements

Like the MIDEX® process, the COREX® shaft furnace is also designed to operate with pellets and lump ore. Laboratory-scale and theoretical studies have been reported on the effect of raw materials on the operation of the COREX® process. Based on the statistical analysis of actual plant performance data, Kumar and coauthors (Kumar et al., 2009) discussed the impact of raw material characteristics such as physical, chemical, and high-temperature properties and their operational influence on the performance of the COREX® process. Table 16.5 summarizes the preferred chemical, physical, and metallurgical characteristics recommended by JWS Steel for pellets and lump ore.

Unlike the MIDEX® process, the reduced material is further discharged through discharge screws into the melter gasifier. In the melter gasifier, the material is further reduced, heated, and melted to achieve final separation of slag and melt. By optimizing the slag chemistry, some refining can also be achieved in the melter gasifier. Therefore, compared with the DR process, the COREX® process is less demanding

Table 16.5 Quality of iron-bearing materials recommended by JSW Steel for its COREX® plant

	Parameter	Preferred value
Chemical analysis	Fe (total), %	>64
	FeO, %	<0.5
	$SiO_2 + Al_2O_3$, %	<5.0
Physical properties	Size, mm	−16 + 8
Cold tumbling and crushing tests	Tumble index, % +6.3 mm	>95
	Abrasion index, % −0.5 mm	<3
	CCS, kg	>225
Static reduction test	Reducibility $(dR/dt)_{R=40}$, %/min	0.4
	Metallization, %	>90
	Reduction disintegration index, % −6.3 mm	<12
	Reduction disintegration index, % −0.5 mm	<4

Kumar et al. (2009).

on the chemical specification of its ferrous raw materials. However, appropriate raw materials still need to be selected to ensure high operational flexibility and lower operation costs. As shown in Table 16.5, the iron-bearing materials should preferably have an Fe (total) content above 64% and $Al_2O_3 + SiO_2$ content <5% to provide a low slag volume and high production rate. High slag volume operation demands high fuel rates and decreases productivity. The phosphorus and sulfur inputs are kept to a minimum to avoid high P and S contents in the hot metal.

Like other countercurrent reactors, the permeability of the burden inside the shaft furnace is one of the most important parameters in the COREX® process. In order to have a good permeable bed and uniform gas flow, the particle size range of the burden material, and the amount of fines generated before and after reduction, should be kept to a minimum. Therefore, the TI of iron-bearing materials should be >95% +6.3 mm and the RDI <12% −6.3 mm, as well as CCS >225 kg. More fines in the shaft furnace decrease the bed permeability, leading to nonuniform gas flow and temperatures in the shaft as well as difficulties in injecting the reducing gas through the bustle. This results in a low degree of reduction and metallization and serious operational problems, including hanging and slipping of the burden and shaft jamming.

For smooth material flow and high degree of reduction, the iron-bearing materials should have good reducibility (rate of reduction at 40% reduction) of >0.4% min^{-1} and achieve high metallization of >90% at the bottom of shaft furnace. If the reduced material is metallized at low levels, it will contain a high content of FeO, demanding high heat in the melter gasifier. It has been found that a decrease in metallization (high FeO in reduced pellets) demands more fuel in the melter gasifier and thereby increases the fuel rate. For every 10% drop in metallization, the fuel rate increases by 10 kg/tHM (Kumar et al., 2009).

16.3.2.4 Metallurgical testing for COREX® process

Like the MIDEX® process, disintegration, reducibility, and clustering are the key concerns of ferrous materials for use in the COREX® process. Apart from standard physical testing methods, the Linder test has been modified to assess the ferrous materials under the conditions resembling the COREX® reduction shaft furnace. In addition, Baosteel (Li et al., 2012) has been using a modified static load reduction test to evaluate these parameters. A brief discussion of these tests is given below.

COREX Linder test

The COREX Linder test is used to determine the percentage of metallization of pellets and lump ore under similar conditions to those experienced in the COREX® reduction shaft. In addition, the percentage of fine material generated during the dynamic test is measured. In the COREX Linder test (Van Der Vyver, 2008), a 500 g sample of −12.5 + 10 mm is heated to 800 °C in 30 min while the reduction tube is being rotated at 10 rpm. The reduction gas during the heat up stage consists of 30% CO, 50% CO_2, and 20% H_2 and is switched to 70% CO, 5% CO_2, and 25% H_2 when the sample reaches 800 °C. The sample is reduced at 800 °C for 4 h. At the end of the test, the reduced sample is cooled to room temperature under an inert gas atmosphere. The reduced sample is then sieved to determine the percentage of breakdown and analyzed for total Fe and FeO to determine the percentage of metallization.

Baosteel static load reduction test

The static load reduction test was developed based on two ISO standards, namely, the "low-temperature disintegration (ISO 4696-1)" and "reduction under load (ISO 7992)" tests aiming to test pellets and lump ore with respect to their disintegration and reducibility during reduction under conditions prevailing in the COREX® reduction shaft furnace. The test is carried out with a 2 kg sample of specified particle size range in a fixed bed under specific heating and gas composition. A constant load of 14 N/cm^2 is applied during the test onto the sample to simulate the burden pressure and to observe the appearance of sticking phenomena during the reduction procedure. The reduction procedure is terminated 360 min after start of the test. The reduced material, sized to +0.5 mm, is treated in a tumble drum for 30 min at 30 rpm and sieved at 6.3, 3.13, and 0.5 mm for evaluation of the reduction disintegration strength of the sample. The following test results are obtained for the sample:

- Degree of reduction
- Reducibility
- Metallization degree
- Disintegration and generation of fines
- Pressure drop
- Shrinkage or swelling properties
- Sticking behavior

The results from the static load reduction test provide an indication of the physical stability and chemical reducibility of ferrous materials under conditions resembling those in the COREX® shaft.

16.4 Summary

The BF ironmaking process is currently the dominant process for providing steelmaking raw materials worldwide. However, the BF process relies heavily on metallurgical coke and involves cokemaking and sintering operations, which often attract serious environmental concerns. Therefore, DR and SR technologies using noncoking coal or other gases as reducing agents to replace metallurgical coke are expected to emerge as future alternative routes for iron production. Due to the vast difference in operating conditions between these processes, different quality parameters are imposed by their operators on ferrous burden to ensure the efficiency and economics of the process. To quantify these quality parameters, a variety of standard and nonstandard physical tests have therefore been developed. The standardized tests are simple but generally are conducted at fixed conditions, which often represent the extreme situations encountered by ferrous materials. However, while nonstandardized physical testing methods are very sophisticated, they simulate the working conditions that the ferrous materials encounter more closely. Therefore, nonstandard physical tests are recommended in addition to standard physical tests when unfamiliar burden materials are used. Finally, because different ferrous materials have distinct characteristics, a comprehensive burden evaluation program allows the plant operator to maximize productivity at the lowest cost by optimizing the burden composition.

Acknowledgments

The authors wish to thank Dr Ralph Holmes and Mr Warren Bruckard of CSIRO for reviewing the manuscript and their valuable comments and suggestions.

References

Anon 1, 2014. Blast Furnace Iron (BFI) 1980–2012 [Online]. World Steel Association. Available: http://www.worldsteel.org/dms/internetDocumentList/statistics-archive/production-archive/iron-archive/iron-annually/BFI_yearly_19802012/document/BFI%20annual%201980-2012.pdf (accessed 15 August 2014).

Anon2, 2014. Direct Reduced Iron Production, 1980–2012 [Online]. World Steel Association. Available: http://www.worldsteel.org/dms/internetDocumentList/statistics-archive/production-archive/iron-archive/iron-annually/DRI_yearly_1980-2012/document/DRI%20annual%201980-2012.pdf (accessed 15 August 2014).

Anon 3, 2014. 2013 World Direct Reduction Statistics [Online]. Midrex Technologies Inc. Available: http://www.midrex.com/uploads/documents/Statsbook2013.6.5.14.pdf (accessed 15 August 2014).

Anon 4, 2014. The MIDREX® Process—The World Most Reliable and Productive Direct Reduction Technology [Online]. Midrex Technologies, Inc, Charlotte, NC 28217, USA. Available: http://www.midrex.com/pdfs/MIDREX_Process-Brochure.pdf (accessed 8 September 2014).

Anon 5, 2008. MIDREX® Process [Online]. Midrex Technologies, Inc, Charlotte, NC 28217, USA. Available: www.midrex.com (accessed 4 January 2008).

Anon 6, 2014. SIMETAL Corex Technology [Online]. Siemens VAI, Linz, Austria. Available: https://www.industry.siemens.com/datapool/industry/industrysolutions/metals/simetal/en/SIMETAL-Corex-technology-en.pdf (accessed 8 September 2014).

Blattner, J.L., Ranade, M.G., Ricketts, J., 1984. Evaluation of the effects of pellet properties on inland's 'A' blast furnace performance. In: The 43rd Ironmaking Conference, 1984 Chicago, IL, USA. Iron & Steel Soc of AIME, Warrendale, PA, USA, pp. 267–271.

Chaigneau, R., Bakker, T., Steeghs, A., Bergstrand, R., 2001. Quality assessment of ferrous burdens: utopian dream. In: 60th Ironmaking Conference Proceedings. Association for Iron and Steel Technology, Baltimore, MD, USA, pp. 689–703.

Cheng, A., 2001. Coke quality requirements for blast furnaces—part I: overview of the blast furnace process. Iron Steelmaker, 30–32.

Da Silva, E.M., Muniz, G.L.F., 2008. Pre drying of Rio Tinto Corumba's lump iron ore for direct reduction. In: 3rd International Meeting on Ironmaking and 2nd International Symposium on Iron Ore, 2008 Sao Luis. ABM Brazil, Maranhao, Brazil, pp. 416–427.

Dawson, P.R., 1987. Determination of the high temperature properties of blast furnace burden materials. SEAISI Q. J., 23–42.

Dawson, P.R., 1993. Recent developments in iron ore sintering. Ironmak. Steelmak. 20, 135–159.

Dukino, R.D., Swain, M.V., Loo, C.E., Bristow, N., England, B.M., 1995. Fracture behaviour of three Australian iron ores. Trans. Inst. Min. Metall., Sect. C 104, C11–C19.

Dwarapudi, S., Banerjee, P.K., Chaudhary, P., Sinha, S., Chakraborty, U., Sekhar, C., Venugopalan, T., Venugopal, R., 2014. Effect of fluxing agents on the swelling behavior of hematite pellets. Int. J. Miner. Process. 126, 76–89.

Hayashi, S., Iguchi, Y., 2003. Abnormal swelling during reduction of binder bonded iron ore pellets with CO–CO_2 gas mixtures. ISIJ Int. 43, 1370–1375.

Hayashi, S., Iguchi, Y., 2005. Influence of several conditions on abnormal swelling of hematite pellets during reduction with H_2-CO gas mixtures. Ironmak. Steelmak. 32, 353–358.

Higuchi, K., Naito, M., Nakano, M., Takamoto, Y., 2004. Optimization of chemical composition and microstructure of iron ore sinter for low temperature drip of molten iron with high permeability. ISIJ Int. 44, 2057–2066.

ISO 11256, 2007. Iron Ore Pellets for Shaft Direct-Reduction Feedstocks—Determination of the Clustering Index. ISO, Geneva.

ISO 11257, 2007. Iron Ores for Shaft Direct-Reduction Feedstocks—Determination of the Low-Temperature Reduction-Disintegration Index and Degree of Metallization. ISO, Geneva.

ISO 11258, 2007. Iron Ores for Shaft Direct-Reduction Feedstocks—Determination of the Reducibility Index, Final Degree of Reduction and Degree of Metallization. ISO, Geneva.

ISO 3271, 2007. Iron Ores for Blast Furnace and Direct Reduction Feedstocks—Determination of the Tumble and Abrasion Indices. ISO, Geneva.

ISO 4695, 2007. Iron Ores for Blast Furnace Feedstocks—Determination of the Reducibility by the Rate of Reduction Index. ISO, Geneva.

ISO 4696-1, 2007. Iron Ores for Blast Furnace Feedstocks—Determination of Low-Temperature Reduction-Disintegration Indices by Static Method—Part 1: Reduction with CO, CO_2, H_2 and N_2. ISO, Geneva.

ISO 4696-2, 2007. Iron ores for Blast Furnace Feedstocks—Determination of Low-Temperature Reduction-Disintegration Indices by Static Method—Part 2: Reduction with CO and N_2. ISO, Geneva.

ISO 4698, 2007. Iron Ore Pellets for Blast Furnace Feedstocks—Determination of the Free-Swelling Index. ISO, Geneva.

ISO 4700, 2007. Iron Ore Pellets for Blast Furnace and Direct Reduction Feedstocks—Determination of the Crushing Strength. ISO, Geneva.

ISO 7215, 2007. Iron Ores for Blast Furnace Feedstocks—Determination of the Reducibility by the Final Degree of Reduction Index. ISO, Geneva.
ISO 7992, 2007. Iron Ores for Blast Furnace Feedstocks—Determination of Reduction Under Load. ISO, Geneva.
ISO 8371, 2007. Iron Ores for Blast Furnace Feedstocks—Determination of the Decrepitation Index. ISO, Geneva.
Jiang, T., He, G.-Q., Li, G.-H., Fan, X.-H., Cui, Z.-X., 2007. Effect of gangue composition on reduction swelling of iron ore pellets. Kang T'ieh/Iron Steel (Peking) 42, 7–11.
JIS M8711, 2011. Iron Ore Sinter—Determination of Shatter Strength. Japanese Industrial Standards Committee (JISC), Tokyo.
Kanbara, K., Hagiwara, T., Shigemi, A., Kondo, S.-I., Kanayama, Y., Wakabayashi, K.-I., Hiramoto, N., 1976. Dissection of blast furnaces and their inside state—1. Report on the dissection of blast furnaces. Tetsu-To-Hagane/J. Iron Steel Inst. Jpn. 62, 535–546.
Kojima, K., Nisi, T., Yamaguchi, T., Nakama, H., Ida, S., 1976. Change of coke properties in the blast furnace—4. Report on the dissection of blast furnaces. Tetsu-To-Hagane/J. Iron Steel Inst. Jpn. 62, 570–579.
Kumar, P.P., Barman, S.C., Reddy, B.M., Sekhar, V.R., 2009. Raw materials for Corex and their influence on furnace performance. Ironmak. Steelmak. 36, 87–90.
Li, J., Zhu, J., Xiong, L., Zhao, X., Lin, J., Peng, X., 2012. Reduction behaviors of iron ore lump and pellets with H_2-CO gas. Baosteel Tech. Res. 6, 13–17.
Loo, C.E., Bristow, N.J., 1998a. Properties of iron bearing materials under simulated blast furnace indirect reduction conditions. I. Review and experimental procedure. Ironmak. Steelmak. 25, 222–232.
Loo, C.E., Bristow, N.J., 1998b. Properties of iron bearing materials under simulated blast furnace indirect reduction conditions. II. Reduction degradation. Ironmak. Steelmak. 25, 287–295.
Loo, C.E., Matthwes, L.T., O'dea, D.P., 2011. Lump ore and sinter behaviour during softening and melting. ISIJ Int. 51, 930–938.
Lu, L., Holmes, R.J., Manuel, J.R., 2007. Effects of alumina on sintering performance of hematite iron ores. ISIJ Int. 47, 349–358.
Lu, L., Holmes, R.J., Manuel, J.R., Edenton, A., Hapugoda, S., Adam, M., Smyth, R., 2009. CSIRO softening and melting facility and high temperature characteristics of blast furnace ferrous burdens. In: Asia Steel 2009, May 24–28, 2009 Busan, South Korea.
Nishio, H., Yamaoka, Y., Nakano, K., Yanaka, H., Shiohara, K., 1982. Testing methods of sinter. In: The 41st Ironmaking Conference, 1982 Pittsburgh, PA, USA. Iron & Steel Soc of AIME, Warrendale, PA, USA, pp. 90–97.
Ranade, M.G., 2000. Iron-bearing burden materials. In: Blast Furnace Ironmaking. McMaster University, Ontario, Canada.
Ricketts, J.A., 2000. Historical development and principles of the iron blast furnace. In: Blast Furnace Ironmaking. McMaster University, Ontario, Canada.
Sasaki, M., Ono, K., Suzuki, A., Okuno, Y., Yoshizawa, K.-I., Nakamura, T., 1976. Formation and melt-down of softening-melting zone in blast furnace furnaces—3. Report on the dissection of blast furnaces. Tetsu-To-Hagane/J. Iron Steel Inst. Jpn. 62, 559–569.
Shimomura, Y., Nishikawa, K., Arino, S., Katayama, T., Hida, Y., Isoyama, T., 1976. Inside state of the reducing zone of a blast furnace—2. Report on the dissection of blast furnaces. Tetsu-To-Hagane/J. Iron Steel Inst. Jpn. 62, 547–558.
Tenuta de Azevedo, A.L., Cardoso, M.B., 1983. Decrepitation of iron ores: a fracture-mechanics approach. Ironmak. Steelmak. 10, 49–53.
van der Vyver, W.F., 2008. Determination of Factors Influencing the Degree of Reduction Disintegration in Northern Cape Lump Ore and the Role of Gangue Minerals in the Propagation of Cracks. PhD, University of Pretoria.

Wu, S.L., Xu, H.F., Tian, Y.Q., 2009. Evaluation of lump ores for use in modern blast furnaces as part of mixed burden practice. Ironmak. Steelmak. 36, 19–23.

Xu, B., Hou, T., Chen, X.-L., Li, Q., Jiang, T., Li, P., 2013. Effect of dolomite on reduction swelling property of iron ore pellets. J. Cent. South Univ. 20, 2806–2810.

Zhu, D., Zhang, J., Pan, J., 2012. Effect of basicity and MgO on the pelletizing of specularite concentrate. In: 3rd International Symposium on High-Temperature Metallurgical Processing—TMS 2012 Annual Meeting and Exhibition. TMS, Orlando, FL, United States.

Recent developments in blast furnace iron-making technology

17

A. Babich, D. Senk
RWTH Aachen University, Aachen, Germany

17.1 Introduction

Iron making deals with the extraction of iron from ores because iron without processing is only available in meteorites. Iron is a principal component of steel (about 99.7%)—which is the most important construction material of today: world steel production made up in 2012 1548 Mt in comparison to 280 Mt of plastics and 58 Mt of aluminum (Stahl-Online, 2013).

There are four main steel production routes (Steel Institute VDEh, 2008):

- Blast furnace—oxygen converter (hot metal is produced in the BF, which is then refined in the oxygen converter, called BOF, to produce liquid crude steel)
- Smelting reduction—oxygen converter (liquid metal is produced in the melter gasifier without sinter step and almost without coke, which is also then refined in the converter)
- Direct reduction—electric arc furnace (sponge iron instead of liquid hot metal is produced, and then, this direct reduced iron is melted in electric furnace)
- Scrap—electric arc furnace (recycling-based route contrary to the three above mentioned ore-based routes)

The major part of metallic charge is hot metal from BF (64.7% in the year 2011); the rest is mainly steel scrap (30.6%); the share of DRI[1]/HBI[2] and hot metal from smelting reduction (Corex®/Finex®) makes up worldwide 4.3% and 0.4%, respectively (Peters and Schmoele, 2013).

BF exists about 700 years and remains the main aggregate for the reduction of iron ores due to its very efficient countercurrent flow principle (see Section 17.3). It has demonstrated flexibility and adaptability to changing conditions and produces today up to 10,000–13,000 tons of hot metal a day (Babich and Senk, 2013b). Reducing the carbon dioxide emissions is the biggest challenge facing currently the BF iron making. The CO_2 emission from the integrated steelworks based on the BF-BOF route is approximately 2 tons per ton of crude steel (Riley et al., 2010) and about 3/4 of this amount is accounted to hot metal production in the BF.

[1] Direct reduced iron.
[2] Hot briquetted iron.

Iron Ore. http://dx.doi.org/10.1016/B978-1-78242-156-6.00017-4
© 2015 Elsevier Ltd. All rights reserved.

17.2 Blast furnace design and facilities

17.2.1 Blast furnace profile and dimensions

The BF profile (inner shape) consists of five parts (Figure 17.1):

- Top or throat, which is a cylinder
- Shaft or stack, which tapers outward from the top
- Belly, which is a cylinder
- Bosh, which tapers inward toward its bottom
- Hearth, at the bottom of the furnace, which is a cylinder

Working height is a distance between the tuyere level and the stockline (more exactly 1 m below the rotating chute in vertical position in the case of bell-less-type charging system, right in Figure 17.1, or 1 m below the large bell in low position in the case of bell-type charging system, left). Corresponding furnace volume is working volume. Inner or useful height is a distance from the hot metal taphole level to the

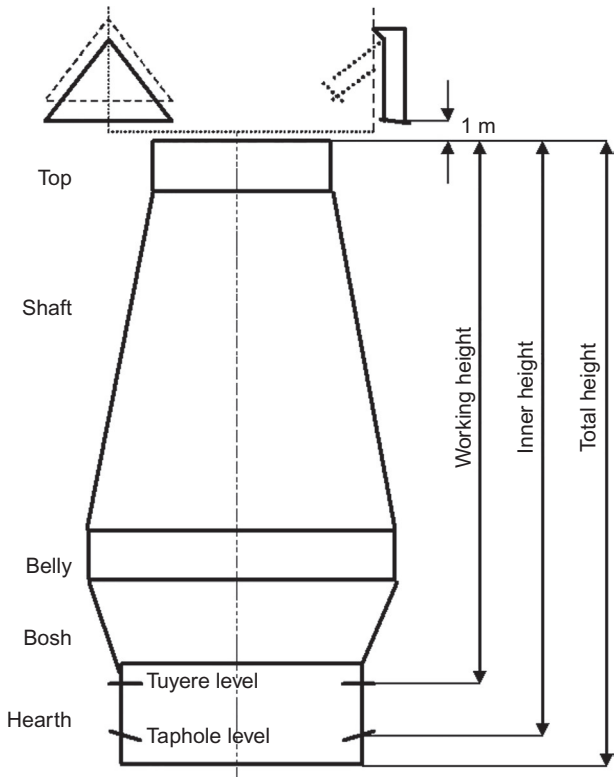

Figure 17.1 Blast furnace profile (Babich et al. 2008a).

stockline. Total height is a distance from the hearth bottom to the stockline. Above definitions are used in the EU countries.

The real BF lining wear profile, whose formation and stabilization depend on the operating conditions and constructive features such as a cooling system (see next sections), differs from the designed profile presented above.

It is considered that the BF was evolved in fourteenth century from the bloomery furnace. Figure 17.2 shows examples of inner shape for two German blast furnaces at the end of eighteenth to the beginning of the nineteenth centuries.

Figure 17.3 and Table 17.1 show evolution of blast furnace dimensions from 1860. Between the years 1860 and 1960, the diameter of the furnace hearth increased from 0.9 to 8–9 m with production of 25 and 1500–2000 tons of hot metal per day, respectively. From the 1960s to the 1980s, the hearth diameters have almost doubled, and the furnace volume and the productivity increased about 2.5- and 5-fold, respectively (Babich et al., 2008a).

Table 17.2 shows dimensions of some large blast furnaces.

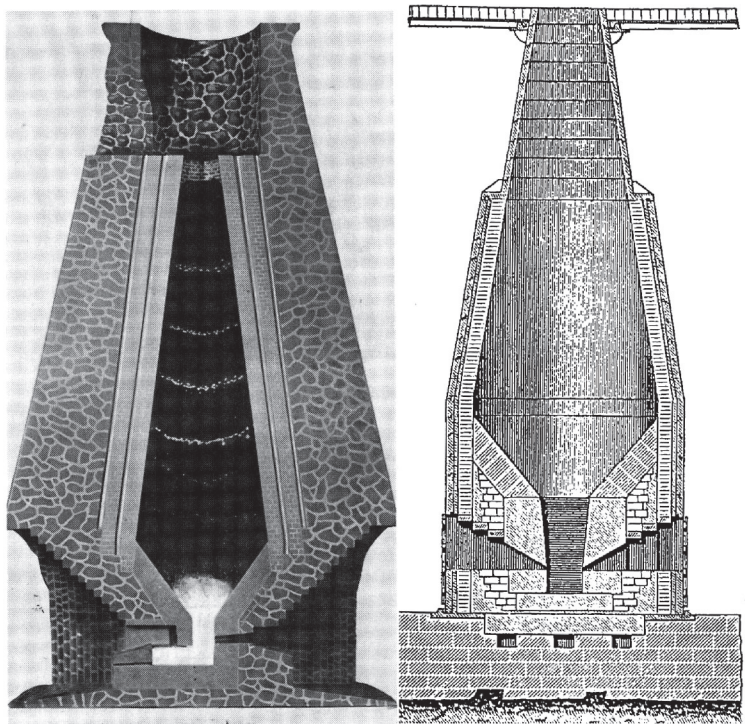

Figure 17.2 German blast furnaces: *left* BF in Gleiwitz/Oberschlesien, 1796, *right* BF Sayner works in Bendorf/Neuwied, 1828–1830 (Buschmann and Toncourt, 1989).

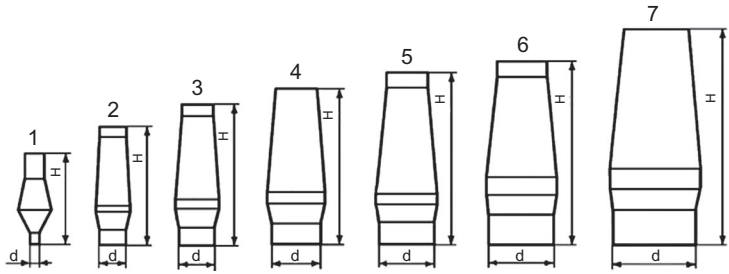

Figure 17.3 Development of blast furnace dimensions (Verein Deutscher Eisenhüttenleute, 1970/71).

Table 17.1 Development of blast furnace dimensions

BF no. in Figure 17.3	Region and period	Hearth diameter (m)	Height (m)	Useful volume (m^3)	Production capacity (t/24 h)
1	BF, 1861	0.9	15.3	64	25
2	West Germany, 1930s	4.5	20.0	425	450
3	West Germany, 1961	6.5	24.0	900	1200
4	West Germany, 1959	9.0	26.1	1424	>2000
5	USSR, 1960	9.8	29.4	1763	4000
6	Japan, 1968	11.2	31.5	2255	6000
7	West Germany, 1971/72	14.0	36.7	4100	≈10,000

Verein Deutscher Eisenhüttenleute (1970/71).

Large blast furnaces with an inner volume of about 5000 m^3 and more have a full height (including charging and off-gas systems; see Section 17.2) of about 100–130 m and production capacity approximately 11,000–13,000 tons of hot metal a day.

Two worldwide largest blast furnaces are BF 1, Shagang Group, China, with inner volume of 5800 m^3 and BF 1, Gwangyang, POSCO, South Korea, with inner volume of 6000 m^3 and hearth diameter of 16.1 m (Anon, 2013).

The BF is covered with a shell of steel plate and internally lined with refractories. The refractory structure is cooled by water-cooled metal components (the so-called staves), which are located between the shell and the refractories. Advanced refractory materials and effective furnace shell cooling along with technological advances in operation and maintenance enable campaign life of modern BFs over 15 years (Kawasaki Steel, 1997).

Table 17.2 Dimensions of large blast furnaces

Dimensions	Japan Fukuyama No. 4	Japan Fukuyama No. 5	Germany TKSE Schwelgern No. 2	Ukraine "ArcelorMittal Krivoy Rog" No. 9	Russia Severstal No. 5
Volume (m^3)					
Inner	4197	4617	5513	5037	5580
Working	3614	3923	4796	–	–
Diameter (m)					
Hearth	13.8	14.4	14.9	14.7	15.1
Belly	15.2	15.9	17.2	16.1	16.5
Top	10.5	10.7	11.0	10.8	11.2
Height (m)					
Hearth	5.75	6.2	6.6	4.4[a]	5.7[a]
Bosh	4.0	4.3	5.55	3.7	3.7
Belly	2.75	2.5	3.0	1.7	2.0
Shaft	16.75	17.0	17.7	20.7	20.4
Top	2.0	2.0	3.7	3.0	3.0
Inner	29.9	30.5	32.8	33.5	34.8
Shaft inclination angle	82°01′	81°18′	80°58′	82°42′17″	82°35′55″
Bosh inclination angle	80°04′	80°06′	73°47′	79°13′17″	79°17′15″
Number of tapholes	ND	ND	4	4 + 1[b]	4
Number of tuyeres	ND	ND	42	40	40
Production capacity ($10^3 \times$t/24 h)	~10	~11	~11	~12	~13

[a] From taphole.
[b] Taphole for slag.
Vegman et al. (2004) and Babich et al. (2008a).

17.2.2 Blast furnace plant layout and key equipment

A BF plant (Figure 17.4) typically comprises the following elements and equipment:

- Raw materials receiving, storage, and reclaiming (ore storage yard)
- Stockhouse equipped with bins
- Blast furnace with charging apparatus
- Casthouse
- Charging belt conveyor or skip hoist with skip cars for transporting raw materials to the furnace top
- Hot stoves
- Boilers and turbo blowers for feeding the blast
- Slag handling
- Hot metal handling
- Gas cleaning system (dust catcher, scrubber, and gas cooler)
- Control systems building
- Maintenance facilities

An ore *storage yard* (or an ore dock) serves to unload rail hoppers or ships with ore burden and flux raw materials. These materials and coke (from conveyor belts or rail hoppers) are transferred to the *stockhouse*. Each type of material (ore, pellet, sinter, coke, limestone, etc.) is dumped into separate bins. The raw materials are weighed by discharging from bins and transported to the furnace top by a belt conveyor or skip cars. Modern large blast furnaces are equipped with the conveyor belt.

The *BF itself* with charging apparatus and gas uptakes is shown in Figure 17.5. BFs are constructed to be mantle supported (see Figure 17.5) or freestanding.

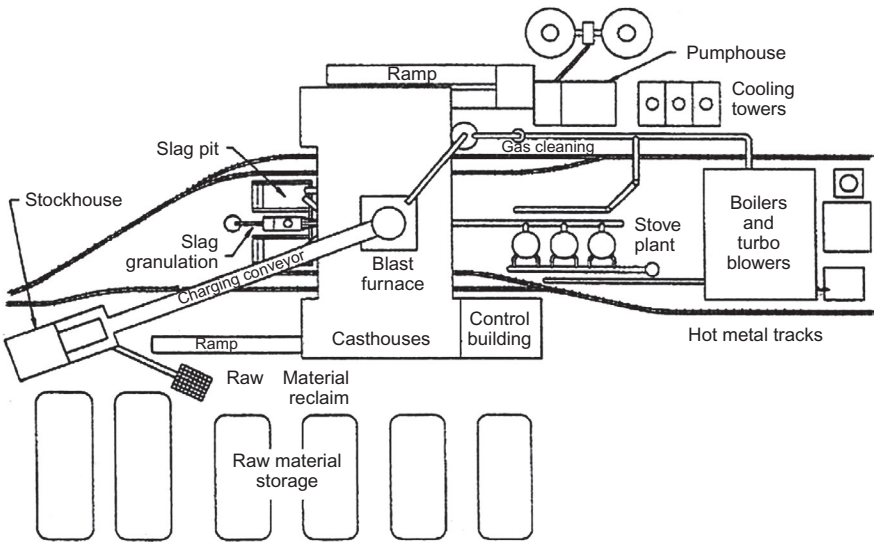

Figure 17.4 Layout of blast furnace plant (Carpenter, 2006).

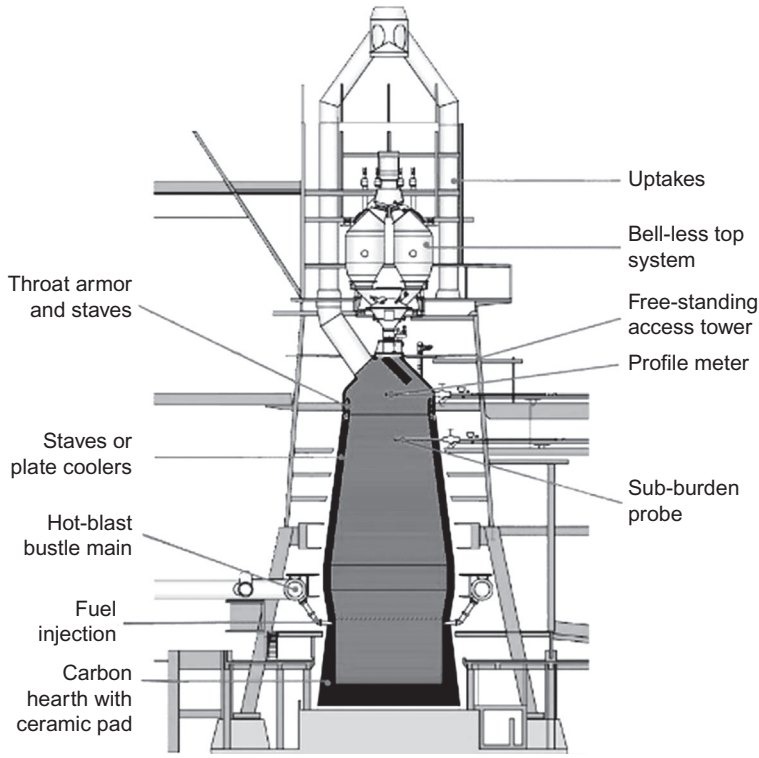

Figure 17.5 Scheme of a BF (VAI Industries, 2000).

Aside from the bell-less or no-bell *charging systems* such as shown in Figure 17.5, the raw materials can enter the furnace using bell-type charging equipment. A charging apparatus should also enable an appropriate distribution of the raw materials at the BF top.

The shaft, belly, and bosh are usually lined with chamotte bricks and silicon carbide bricks, and the hearth is lined with carbon bricks. Different cooling techniques can be applied in different BF zones to assist the lining to resist the specific deterioration factors, to maintain stability of the refractories, and to protect the furnace shell.

Depending on the size of the furnace, the side wall of the hearth is radially fitted with some 14–42 of water-cooled copper tuyeres, which are used to inject the hot blast into the furnace from the hot stoves through the hot-blast bustle main and blowpipes (Figure 17.5). A tuyere apparatus of a modern BF is fitted with special lances for the injection of auxiliary reducing agents and other additives (Babich et al., 2008a).

Tapholes for discontinued discharging hot metal and slag are also installed in the hearth. Modern large BFs have three to four tapholes (Figure 17.6). A taphole drill is used to bore a hole through the taphole clay into the hearth for tapping. A mud gun is used to close the taphole after the tapping with clay or with special high-temperature refractory compounds. Trough and runner systems serve to separate the hot metal and slag and to convey them to the torpedo and slag ladles.

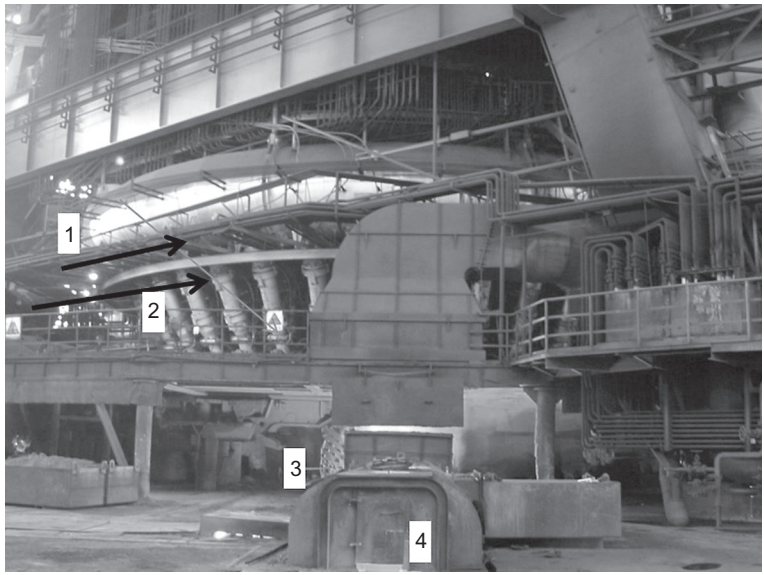

Figure 17.6 Lower zone of BF 4 Baosteel, Shanghai: 1—bustle pipe, 2—tuyere stock, 3—tapping, 4—runner cover.
Photo: A. Babich.

Hot stoves serve for heating the blast. It is a type of heat exchanger, in which the heat produced by combustion of the BF gas usually mixed with natural gas (NG) or coke oven gas (COG) is stored in the checkerwork chamber, after which cold air is blown through the hot checkerwork to produce the preheated hot air blast to the furnace. Three to four stoves are operated on alternate cycles, providing a continuous source of hot blast to the BF.

17.3 Blast furnace process

17.3.1 Principles of blast furnace operation

The BF is a continuously operating shaft reactor based on the countercurrent flow principle. At the top, coke and burden (sinter, pellets, lump ore, and flux) are charged in different layers (Figure 17.7, positions 1–3). Charge materials descend under the force of gravity. The raw materials require 5–8 h to descend to the bottom of the furnace where they become the final product. In the lower part of the furnace, hot blast (1000–1300 °C) that is produced in hot stoves is injected through tuyeres (Figure 17.7, position 4). Furthermore, auxiliary reducing agents and other injectants (see Section 17.4.4) enter the furnace tuyere apparatus (Figure 17.7, position 5). In front of each tuyere, the hot blast reacts with the coke and auxiliary reducing agents. Carbon monoxide is formed, ascends in the furnace, and reduces the iron ores. The reducing gas that was generated in the front of the furnace tuyeres ascends to the top in 5–20 s after going through numerous chemical reactions and leaves the furnace with a temperature of 100–200 °C (Figure 17.7, position 7). At the bottom, the molten

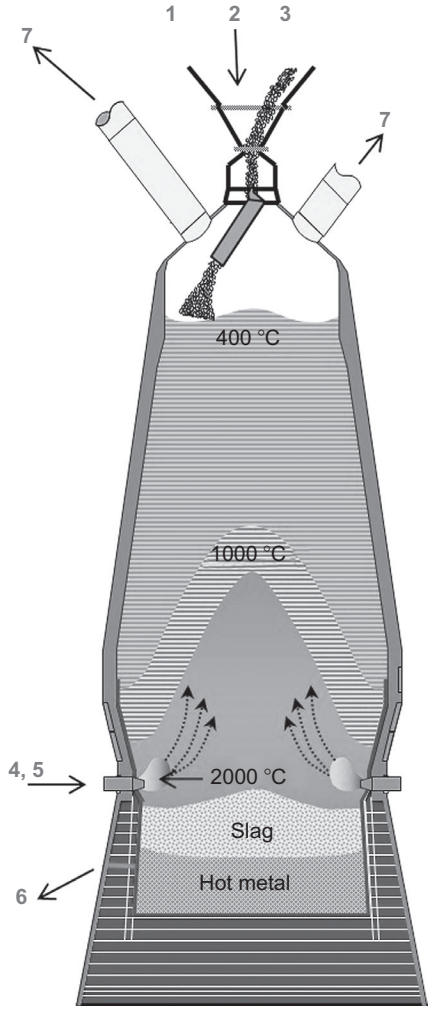

Figure 17.7 Blast furnace process: 1—iron burden, 2—flux and/or other additives, 3—coke, 4—hot blast with oxygen, 5—injectants, 6—taping of hot metal and slag, 7—top gas.

metal is collected. A slag formed from ore gangue, coke, coal, and other ashes and flux swims due to its lower density on the hot metal bath. Liquid hot metal and slag (about 1500 °C) are tapped regularly (Figure 17.7, position 6). The products of the blast furnace process are hot metal or pig iron, slag, top gas, and flue dust.

17.3.2 Streaming conditions and heat exchange

The BF process occurs in a counterflow of descending charge materials and ascending gases. Heat exchange between the descending materials and the ascending gases determines all the basic processes: heating of materials, decomposition of hydrates and carbonates, reduction of ore, and melting of metal and slag.

17.3.2.1 Motion of materials and gases

Material descending is caused by Babich et al. (2008a)

- coke burning in front of tuyeres;
- shrinkage in the material volume due to deposition of fines between the coarse pieces;
- change in the phase state of materials in the lower part of shaft, belly, and bosh (conversion of solids into liquids and gas) accompanied by volume reduction;
- tapping of hot metal and slag.

Materials descend due to the force of gravity. Carrying force of the gas flow, friction of materials at the walls, and some other forces counterbalance partially the gravity force. To maintain the smooth material descending, the sum of upward directed forces should be less than the weight of materials. The gradient of the opposite directed forces can be defined as a material effective weight (Efimenko et al., 1986):

$$P_a = P - \left(F_1 + F_2 + F_3\right) \tag{17.1}$$

where F_1 is the friction force of materials at the furnace wall, F_2 the carrying force of the gas flow, and F_3 the carrying force caused by rising level of accumulating liquid products.

The value of the effective weight has to be positive: $P_a > 0$. Otherwise, movement of materials will be stopped, and hanging of the stock will occur. It is hardly possible to calculate the value P_a under the real operating conditions. But the change in its value is mainly determined by F_2 because all other members in Equation (17.1) are virtually constant for a given BF under the assumption of the constant raw material quality. The value F_2 is proportional to static gas pressure drop:

$$\Delta P = P_{\mathrm{t}} - P_{\mathrm{h}}$$

where P_{t} is the top gas pressure and P_{h} the gas pressure at the tuyere level.

Darcy–Weisbach equation for pressure drop of the gas flow in a packed bed is typically used for calculation of ΔP (in N/m^2):

$$\Delta P = \psi \left(H / D\right)\left(1-\varepsilon\right) / \varepsilon^3 \left(w^2 \cdot \rho\right) \tag{17.2}$$

where ψ is the resistance coefficient; H the packed bed height, m; D the equivalent grain diameter, m; ε the voidage, m^3/m^3; w the gas velocity, m/s; and ρ the gas density, kg/m^3.

Resistance coefficient is

$$\psi = \mathrm{c} / Re^{\mathrm{m}}$$

where Re is the Reynolds number and c and m depend on the character of the movement: laminar or turbulent.

The analysis of Equation (17.2) shows that the pressure drop in the BF "dry" zone is mainly determined by the velocity and density of the gas, the grain size, the packed bed height, and voidage. The high gas permeability, that is, low pressure drop, is provided when ε is high, D is high, w is low, and ψ is low.

Gas velocity and voidage play the decisive role.

The gas amount per unit of time determines the furnace productivity. Under given conditions, the productivity increases as the blast volume per unit of time increases. But a rise in the blast volume is limited by an increase in the pressure drop. High-quality burden and coke regarding mechanical and physical properties, their appropriate distribution at the furnace top, and higher gas pressure in the furnace are prerequisites for keeping the pressure drop on a suitable level while the blast volume increases. The pressure drop is influenced considerably by the voidage of the packed bed. Not only absolute grain size of individual raw materials and its change in the furnace but also relationship between sizes of sinter, pellets, coke, and other materials has to be considered. For ensuring a suitable voidage and thus good gas permeability, it is also extremely important to exclude the charge and to avoid the generation of fines from the raw materials.

Upward *motion of gases* in the BF can be considered as movement in parallel vertical channels formed by particles of charged materials and having irregular shape and changeable cross-section and interacting between themselves. Gas pressure in the packed bed decreases continuously as the gas ascends, but not lineally along the furnace height. Gas pressure loss is the highest in the lower BF zone (at the tuyere level and in the dripping zone) and in the cohesive zone (softening and melting zone) and is low in the "dry" shaft (Figure 17.8).

Streaming conditions in the dripping zone are particularly complicated. As velocity of dropped liquids (metal and slag) or ascending gas is increased, the free area for gas decreases, and the pressure drop through the column increases. A point is finally reached when, through the smallest increase in gas velocity (e.g., due to increase in blast volume to raise the productivity), liquid is carried off mechanically (discharged) from the packing. This phenomenon is called flooding. Flooding can cause unstable operation (disturbance of smooth operation, irregular descent, hanging, or slipping), increases of pressure drop, and limits for productivity.

The cohesive zone is formed by the softening and melting of iron ore burden. It consists of permeable coke layers and viscous semifused burden materials and liquid drops; gases pass through the so-called coke windows. The cohesive zone, particularly its shape and position, affects significantly the gas flow distribution and operation efficiency (Figure 17.9).

17.3.2.2 Heat exchange

The two-stage heat exchange in the BF, proposed by Kitaev (1945) and Kitaev et al. (1967) and further developed by Yaroshenko, Michard, Rist, and other researchers, is worldwide recognized. According to this theory, heat transfer from the BF gases is accomplished in two successive steps, separated by a reserve zone of variable height. The temperature profile is illustrated in Figure 17.10.

In the upper zone of heat exchange (H_1), the temperatures of gas and solids increase longitudinally downward with decreasing difference between them. In the lower zone of heat exchange (H_3), both temperatures of gas and solids increase longitudinally downward with increasing difference between them. There is a region between the

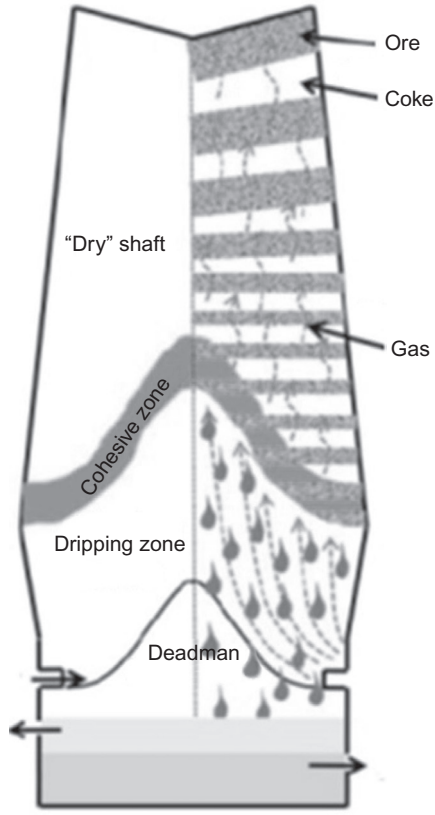

Figure 17.8 BF zones by motion of different phases.
Modified from Jin and Choi (2010).

upper and the lower regions where the temperature is kept almost constant around 900–1000 °C. This region is called the idle or thermal reserve zone (TRZ) in which heat exchange hardly occurs (H_2).

The thermal operation of upper and lower zones is independent, except that the temperature of gas reaching the upper zone is dependent on the temperature of the gas leaving the lower zone. The presence of a reserve zone indicates that heat transfer in a BF is completed.

It has to be noted that the existence of a TRZ was known before Kitaev and its first analysis was done by Reichardt (1927). Later on, it was shown that the reaction responsible for the thermal pinching in the BF is the solution loss reaction $\left(CO_2 + C = CO\right)$ (Michard, 1956). It is the reason why the temperature of the TRZ is determined by the temperature at which coke starts to react with CO_2 (around 950 °C for metallurgical coke). The possibility for decrease of carbon consumption in the BF by means of decreasing the TRZ temperature or the starting temperature of solution loss reaction is discussed in Section 17.4.2.

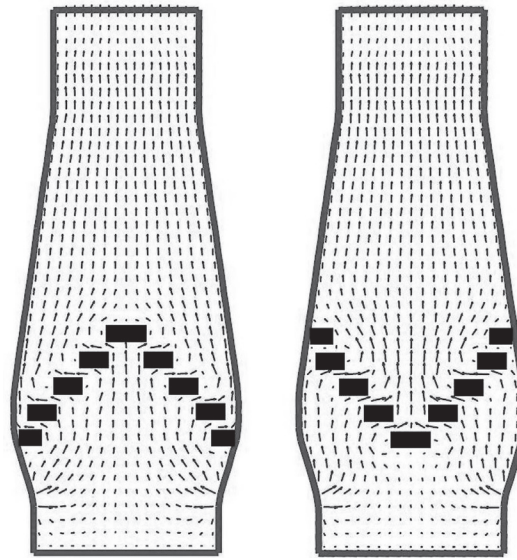

Figure 17.9 Gas velocity vectors under the conditions of inversed V-shaped cohesive zone (a) and V-shaped cohesive zone (b) (Zhou et al., 2003).

In accordance with the temperature profile (Figure 17.10), the intensity of heat transfer from gas to burden is decreasing from the top to the shaft and also from the tuyere level to the shaft, as shown in Figure 17.11 (the shaded area shows the total heat transferred from gases to burden in unit of time). In the BF, the maximum rate of heat exchange occurs at the tuyere level, and the minimum in the shaft. Thus, the maximum gas-material (hot metal and slag) temperature difference is about 400–500 °C at the tuyere level; the next largest temperature gradient is at the stockline (about 100–200 °C) and the minimum in TRZ in the shaft (10–30 °C).

A chemical reserve zone (wüstite zone) is located inside the TRZ.

17.3.3 Reduction processes

The reduction of iron and accompanying elements from their oxides is the main target of the BF operation. Due to the limited volume of this chapter, only fundamentals of reduction thermodynamics of iron oxides and accompanying elements are discussed here. Reduction kinetics and morphology as well as further chemical processes such as decomposition of materials are out of the scope of this chapter.

Reduction is defined as the release of oxygen from oxide (or other oxygen-containing compounds) with its conversion to the element or an oxide with less oxygen content than in the reduced oxide (Babich et al., 2008a).

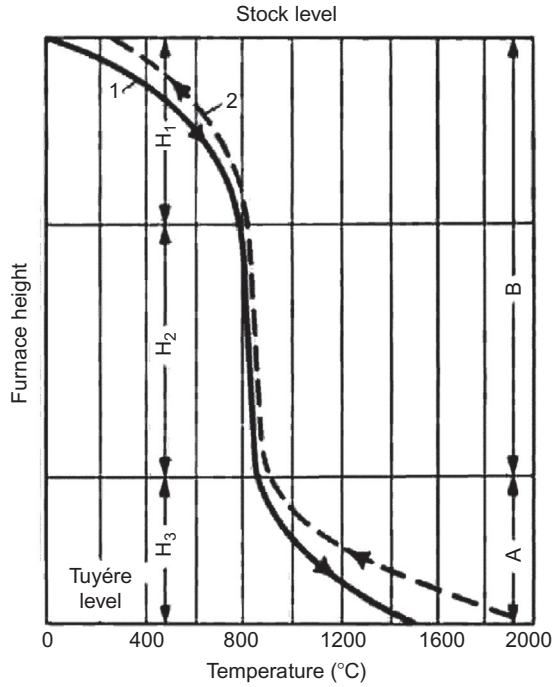

Figure 17.10 Scheme of heat exchange according to Kitaev et al. (1967): A—direct reduction; B—indirect reduction; H_1—upper zone of heat exchange; H_3—lower zone of heat exchange; H_2—idle or reserve zone (height not employed in heat exchange); 1—burden temperature; 2—gas temperature.

17.3.3.1 Reduction of iron oxides

Reduction of iron oxides by carbon monoxide and hydrogen with the formation of CO_2 and H_2O as final products is called indirect reduction. Reduction by carbon with the formation of CO as the final product is called direct reduction. The sum of direct and indirect reduction rates equals to unity or 100%, that is,

$$r_{id} = 1 - r_d \quad \text{or} \quad r_{id} = 100 - r_d\,(\%)$$

Reactions of *indirect reduction* can be represented as follows:

$$3Fe_2O_3 + H_2\,(CO) \rightarrow 2Fe_3O_4 + H_2O(CO_2), \quad \Delta H^0 < 0\ \left(\Delta H^0 < 0\right) \tag{17.3}$$

$$Fe_3O_4 + H_2\,(CO) \leftrightarrow 3FeO + H_2O(CO_2), \quad \Delta H^0 > 0\ \left(\Delta H^0 > 0\right) \tag{17.4}$$

$$FeO + H_2\,(CO) \leftrightarrow Fe + H_2O(CO_2), \quad \Delta H^0 > 0\left(\Delta H^0 < 0\right) \tag{17.5}$$

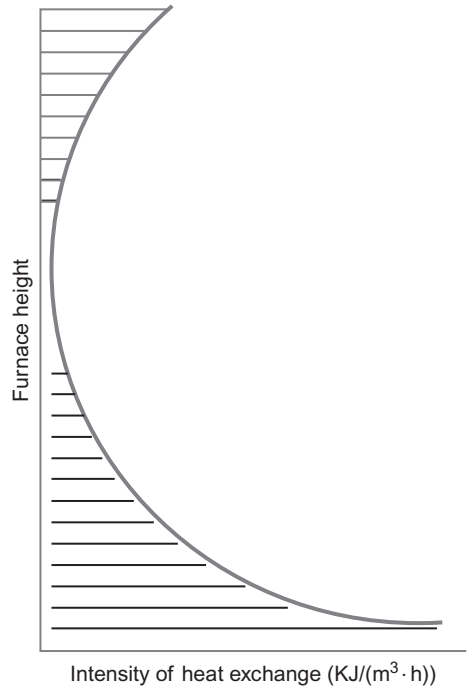

Figure 17.11 Intensity of heat exchange along the furnace height (Kitaev et al., 1967).

Reduction of magnetite to wüstite and then to metallic iron (Equations 17.4 and 17.5) is a reversible process that depends strongly on the temperature. To ensure the forward reactions, that is, reduction, the ratio of CO/CO_2 in gaseous phase has to exceed its stoichiometric value (Babich et al., 2008a).

At temperatures below 570 °C, magnetite is reduced directly to metallic iron because wüstite is unstable in this temperature range:

$$Fe_3O_4 + 4H_2\,(4CO) \rightarrow 3Fe + 4H_2O\,(4CO_2), \quad \Delta H^0 < 0\,(\Delta H^0 > 0) \tag{17.6}$$

Figure 17.12 shows equilibrium of iron–oxygen–carbon and iron–oxygen–hydrogen systems combined in one diagram. They were firstly represented by Baur and Glaessner (1903). At temperatures above 810 °C, hydrogen is thermodynamically stronger reductant as CO.

The reactions of *indirect reduction* are represented in Equations (17.3)–(17.5), and in Figure 17.12, the reduction scheme is simplified; wüstite is a solid solution of Fe_3O_4 in FeO, and its formula is FeO_{1-y}, where y may have a value of about 0.05−0.12. Furthermore, iron oxides are often present in burden materials in the form of compounds and solid solutions with accompanying oxides of Mn, Mg, Ca, and Si, which influence the iron reduction.

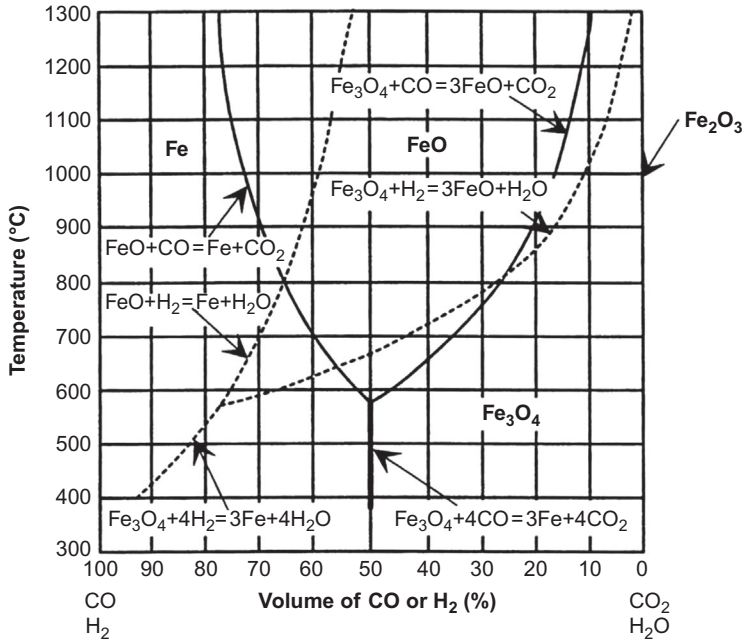

Figure 17.12 Combined equilibrium diagram of $CO–CO_2$ and $H_2–H_2O$ mixtures with iron oxides and iron (Edström, 1953).

In the BF, reduction reactions do not achieve equilibrium because of a short residence time of gases in the furnace and CO splitting according to solution loss reaction at $t < 900-1000°C:\ 2CO \rightarrow CO_2 + C$. Effect of solution loss reaction on reduction process depends not only on temperature but also on pressure.

At higher temperatures (above 900–1000 °C), carbon dioxide and/or water steam formed by reactions (17.3)–(17.5) reacts with coke according to the Boudouard reaction (reversible solution loss reaction (17.7) and/or water shift reaction (17.8)):

$$CO_2 + C \rightarrow 2CO, \quad \Delta H^0_{298} = 172.47\,\text{kJ/mol} \tag{17.7}$$

$$H_2O + C \rightarrow H_2 + CO, \quad \Delta H^0_{298} = 124.48\,\text{kJ/mol} \tag{17.8}$$

A total reaction comprising, for example, wüstite reactions (17.5) and (17.7 or 17.8) represents *direct reduction* and according to the Hess law can be written as

$$FeO + C \rightarrow Fe + CO, \quad \Delta H^0_{298} = 155.34\,\text{kJ/mol} \tag{17.9}$$

The minimum carbon consumption in the BF can be ensured by a certain balance between direct reduction and indirect reduction, which depends on operating parameters (Babich et al., 2008a).

17.3.3.2 Reduction of accompanying elements

Oxides that are present in BF burden can be divided into three groups (Babich et al., 2008a):

- Oxides with high oxygen potential like Cu_2O, P_2O_5, PbO, and NiO. They are reduced completely at relatively low temperatures by carbon monoxide and hydrogen (indirect reduction). The metal/slag distribution ratio of the abovementioned elements is close to 1.
- Oxides with lower oxygen potential than that for the corresponding iron oxides like V_2O, Cr_2O_3, MnO, SiO_2, and TiO_2. They are reduced in the lower BF zone at high temperatures by direct reduction. Distribution of these elements between metal and slag or reduction rate depends on the oxygen potential value: the lower the oxygen potential is, the less their rate in metal is. For example, chromium mainly enters the hot metal, and titanium is mainly lost as oxide in the slag.
- Oxides with lower oxygen potential than that for carbon at temperatures existing in the BF like CaO, MgO, and Al_2O_3. These oxides are not reduced in the BF and transfer completely into the slag.

There are elements such as zinc, sodium, and potassium, which are vaporized after reduction and ascend to low temperature zones in the BF where they are partly condensed on the surface of burden and coke. They descend then with charge materials to the belly or hearth, are reduced (after reoxidation by moving upward), and vaporize again. These circulating elements form circuits inside the furnace. Their accumulation causes decrease in furnace productivity, overconsumption of reducing agents, disturbances of smooth operation, building of scaffolds, and decrease in campaign life. Limiting the input of mentioned elements is important for a smooth blast furnace operation with high productivity. Some technological measures to reduce the harmful effect of the abovementioned elements can be undertaken as well (Babich et al., 2008a).

17.3.4 Oxidation processes

Oxidation processes take place in raceway zones in front of each tuyere where coke and injected auxiliary reducing agents burn in the oxygen of hot blast (see Sections 17.2.2 and 17.3.1). The total volume of the oxidizing zones or raceways usually does not exceed 1% of the inner BF volume (Babich et al., 2008a). Nevertheless, these zones are a vital region of the furnace because they supply the process with heat and reducing gases.

Within the raceway, there are two subzones (Figure 17.13):

– Inner zone A, where free oxygen exists and reacts with carbon:

$$C + O_2 = CO_2$$

– Outer zone B, where carbon reacts with carbon dioxide and water steam:

$$C + CO_2 = 2CO,\ C + H_2O = CO + H_2$$

While the oxygen disappears, the CO_2 content reaches a maximum (Figure 17.14). The CO_2 peak corresponds to a maximum gas temperature. The higher CO_2 content is, the higher the temperature due to the strongly exothermic reaction of carbon combustion. In subzone B, CO_2 disappears gradually with simultaneous increase in the CO content.

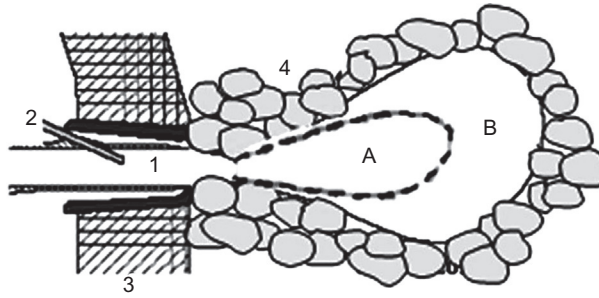

Figure 17.13 Schematic representation of oxidizing zone (raceway): 1—tuyere channel, 2—injection lance, 3—furnace wall, 4—coke packed bed, A—inner area of the raceway, B—outer space of the raceway.

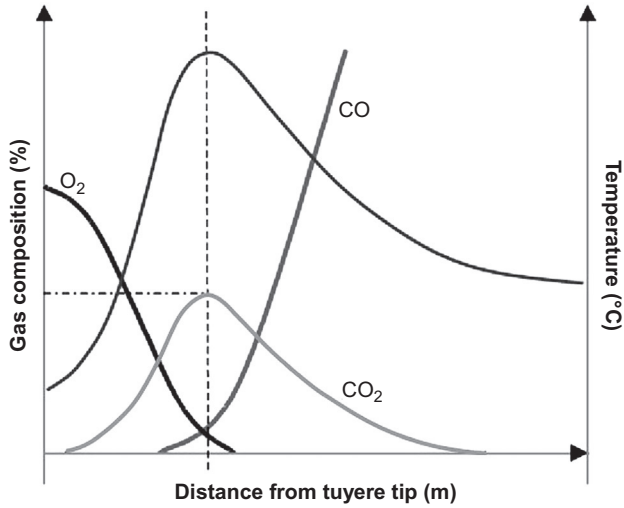

Figure 17.14 Gas composition and temperature along tuyere axis (schematic representation without hydrogen consideration).

Despite of numerous studies, knowledge on the raceway geometry (shape and extension) and processes inside are still not very clear. It is commonly believed that coke circulates in the raceway in both horizontal and vertical directions (Figure 17.15). As a part of coke is burning out, its new portions are being involved from more closely packed bed. There are experimental and modeling-based indications on the unstable and unsteady raceway motion and its fluctuations and partial collapses versus time (Babich et al. 2002; Yuu et al, 2005). Results of another study (Greuel et al., 1974) allowed for concluding that coke does not circulate in the raceway; it speeds away by the blast stream into the upper part of raceway cavity where the arch of burning coke is formed (zone "b" in Figure 17.16). The arch of zone "a" near the tuyere is unstable and periodically collapses as mentioned above; such a feeding of the raceway with

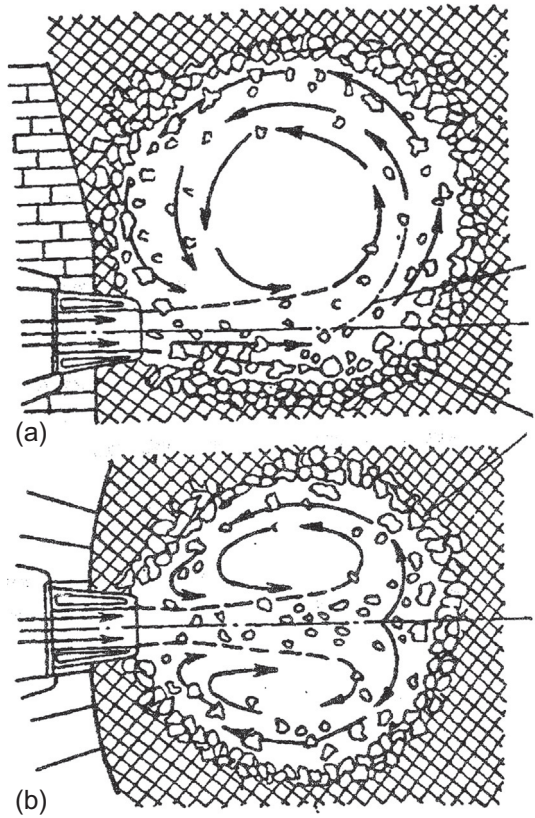

Figure 17.15 Scheme of coke circulation in the front of tuyere: (a) vertical section, (b) horizontal section.
Modified from Zylev et al. (1960), Jeschar et al. (1974), and Tovarovsky and Ljaljuk (2001).

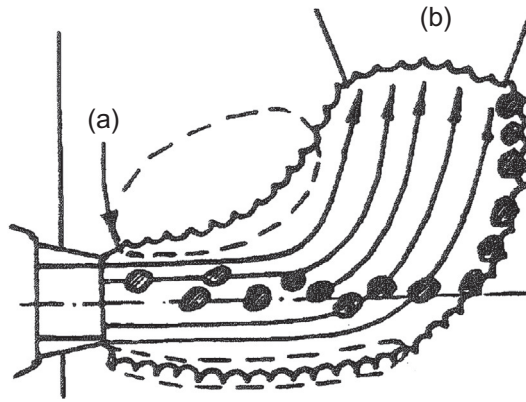

Figure 17.16 Scheme of the raceway with coke motion without circulation.
Modified from Greuel et al. (1974).

new coke portions that move then to the zone "b" causes, according to this theory, an illusion of coke circulation (Tovarovsky and Ljaljuk, 2001).

The raceway depth or its extension from the tuyere tip inward along the tuyere axis varies from 0.5 to 1.8 m according to different sources. Such a wide range of the raceway extension can be explained by several reasons (Babich et al., 2008a):

- Both measurement and calculation of its value are very complicated, and results obtained with various measuring tools and computational methods may differ significantly.
- Construction features like tuyere diameter and furnace operating parameters affect the dimensions of the raceways. In general, the kinetic energy or impulse of the blast, parameters of injectants, and coke properties in the BF lower zone influence the raceway dimension.
- There are different definitions of the raceway extension and corresponding methodologies for its determination. For instance, it can be defined as distance from the tuyere tip to the point where CO_2 content is 1% (it means where CO_2 is virtually disappeared) or as distance from the tuyere tip to the boundary of packed bed of the raceway coke, which can be hardly exactly fixed (Figure 17.17).
- Both the depth and the height of the raceway change periodically due to its dynamic nature, characterized by fluctuations and possible partial collapses.

Real gas temperature in the raceway, shown in Figure 17.14, is affected by numerous parameters including heat loss and reoxidation of the elements of hot metal dripped through the raceway. In the BF operational practice, the so-called flame temperature is commonly used; it is a calculated adiabatic temperature that is a function of blast parameters and characterizes the gas temperature before the beginning of mass and heat exchange.

The flame temperature can be expressed in generic form as follows (Ramm, 1980):

$$t_f = \frac{Q_c + Q_s + I_c + V_{bl} \cdot I_{bl}}{c_0 \cdot V_g}, \quad °C \tag{17.10}$$

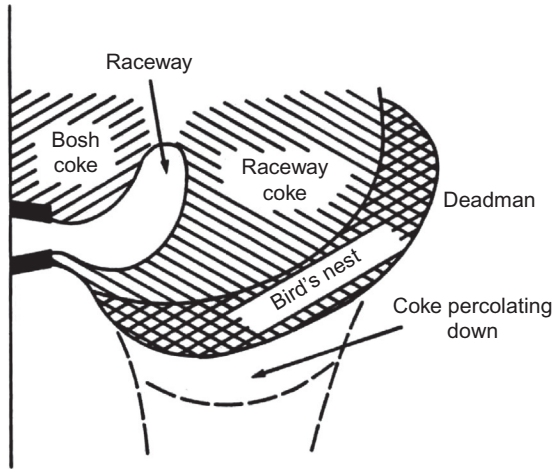

Figure 17.17 Schematic representation of coke behavior at the tuyere level.

where Q_c is the heat of incomplete combustion (or gasification) of carbon of coke, kJ/kg (typically $Q_c = 9800$ kJ / kg); Q_s the heat of incomplete combustion (or gasification) of hydrocarbons, kJ/kg; I_c the sensible heat of carbon in coke entering the raceway, kJ/kg; I_{bl} the sensible heat of blast minus heat of moisture decomposition, kJ/m^3, of dry blast; V_{bl} the blast volume, m^3/kg; c_0 the specific heat of two atomic gases, kJ/(m^3·°C); and V_g the bosh gas volume, m^3/kg.

Flame temperature ranges typically between 2000 and 2300 °C. An overview of the effect of different parameters on its value is given in Table 17.3.

17.3.5 Formation of metal and slag

Hot metal. Carburization of iron starts in the shaft by means of soot generated by carbon monoxide decomposition:

$$2CO \rightarrow CO_2 + C \tag{17.11}$$

$$3Fe + C \rightarrow Fe_3C \tag{17.12}$$

$$3Fe + 2CO \rightarrow Fe_3C + CO_2 \tag{17.13}$$

Carbon content in iron in the shaft usually does not exceed 1% because the reaction (17.12) takes place in the solid phase slowly.

Carbon lowers the melting point of iron. From the Fe–C phase diagram (Figure 17.18), the melting point of pure iron makes up 1537 °C; the eutectic temperature at (1146) 1152 °C contains about 4.3% C.

Table 17.3 The effect of various factors on the flame temperature (FT)

Parameter	Increase by	Change in FT (°C)
Blast temperature	100 °C	+60 … 80
Oxygen in blast	1%	+45 … 50
Moisture in blast:		
Range 1–9% H_2O	1%	−40 … 45
Range 10–20% H_2O	1%	−30 … 35
Natural gas	100 m^3/tHM	−320 … 450
	1%	−45 … 55
Coke oven gas	100 m^3/tHM	−200 … 250
Oil	100 kg/tHM	−270 … 340
	1 g/m^3	−4 … 6
Pulverized coal:		
Low-volatile matter	100 kg/tHM	−0 … 130
High-volatile matter	100 kg/tHM	−150 … 220

Modified from Babich et al. (2008a).

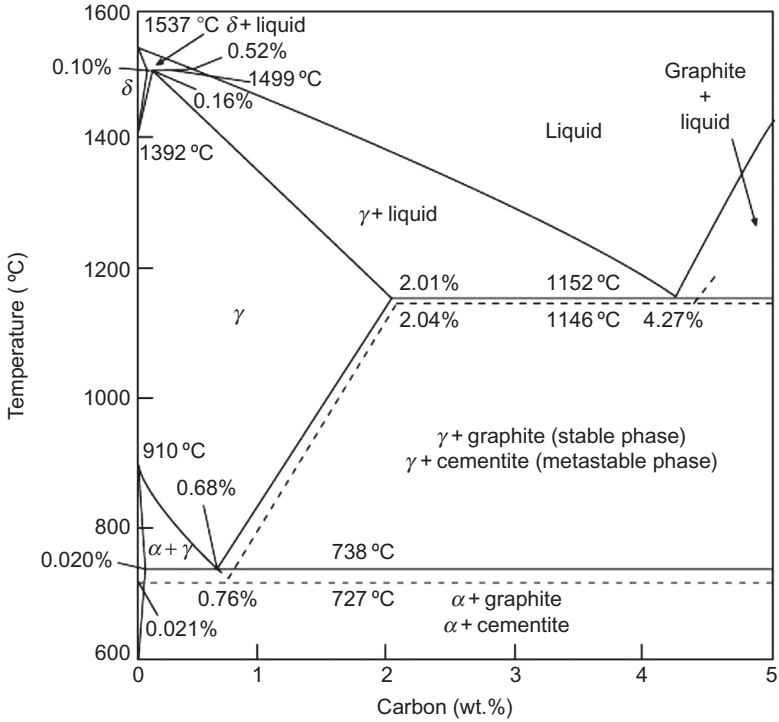

Figure 17.18 Iron–carbon phase equilibrium diagram; dashed lines represent phase boundary for metastable equilibrium with cementite (Fruehan, 1998).

In the liquid phase, iron reacts with carbon intensively and carbon content in the metal in the belly increases up to about 3.0–3.5%.

At $t > 1000\,°C$, the carbon of coke becomes a stronger carbonized agent than carbon monoxide. The final absorption of carbon to the tapping values occurs in the hearth where the metal is in intimate contact with the submerged coke column. The main reaction of carburization in the hearth is

$$Fe + C_{coke} \rightarrow Fe_3C \tag{17.14}$$

Carbon content in the hot metal does not depend on BF operating parameters unlike, for example, for Si and Mn but virtually only on the content of other elements in the hot metal and its temperature. For example, carbon-forming elements like manganese, chromium, vanadium, and titanium increase the carbon content. Silicon and phosphorus lower the carbon content because they build more stable compounds with iron than carbon.

The typical composition of different grades of hot metal, foundry or cast iron, and ferroalloys produced in the coke BF is given in Table 17.4. Nowadays, basic iron (hot metal) is almost unique grade of primary metal produced in BF because manufacturing of other grades, particularly ferroalloys, is beneficially in other aggregates.

Table 17.4 Typical composition of different grades of hot metal and ferroalloys (%)

Type	C	Si	Mn	P	S
Basic (nonphosphorus)	4.2–4.8	0.4–0.8	0.3–1.2	0.05–0.10	0.02–0.06
Foundry	3.5–4.2	2–3	0.5–1.0	0.07–0.30	0.02–0.06
Spiegel (mirror)	4.5–5.5	1–2	10–25	0.1–0.2	0.03–0.04
Ferromanganese	6.0–7.0	1.8–2.0	75–80	0.1–0.4	0.02–0.03
Ferrosilicon	1.5–2.0	9–14	0.5–1.0	0.1–0.2	0.02–0.03

Babich et al. (2008a).

Slag is formed from unreduced ore oxides, flux, and fuel ash. It is distinguished between the following:

- *Primary slag*. Its formation starts by sintering or sticking together of burden particles in the solid state. Slag softening and then melting occur during the descent and increase of the temperature. The location, extension, and shape of the softening and melting or cohesive zone depend on the burden and gas properties and distribution. The amount of primary slag is small. Its components (SiO_2, Al_2O_3, CaO, MgO, FeO, and MnO) are in proportions, which provide the formation of easily fusible eutectics. Content of MnO and FeO is high (about 5–10% and 20–30%, respectively) because of low melting point of their compounds.
- *Bosh slag*. Volume of slag becomes bigger, content of SiO_2, Al_2O_3, and CaO increases, and content of FeO and MnO decreases due to their reduction.
- *Final slag*. In the hearth, ash of coke and injected coal pass into the slag and sulfur content increases.

Slag volume, composition, and physical properties are of great importance for hot metal quality, furnace productivity, and its smooth operation.

Slag volume in the modern BFs producing basic hot metal is about 150–300 kg/tHM depending mostly on the burden composition.

The principal components of final slag are CaO (typically 37–42%), SiO_2 (32–38%), Al_2O_3 (10–15%), and MgO (6–12%), which make up over 95% of the total mass. The balance is made up of FeO, MnO, MnS, CaS, alkali silicates, etc. The FeO should be kept as low as possible (typically 0.3–0.5%) to obtain maximum yield of metal. An important characteristic of the slag is its basicity, which is usually determined as $B = CaO/SiO_2$. Further decisive slag properties are the melting point, the viscosity, the fusibility, and the desulfurizing capacity. The desulfurizing capacity of slag, which is decisive for the production of low sulfur hot metal, depends on slag basicity, viscosity, temperature, and volume.

The sulfur content of hot metal depends on the sulfur distribution ratio, sulfur load, and slag volume:

$$[S] = \frac{0.1 \cdot S}{1 + 0.001 \cdot L_s \cdot n}, \% \tag{17.15}$$

where S is the sulfur load (sulfur input minus sulfur leaving the furnace with the top gas), kg/tHM; $L_s = (S)/[S]$ the sulfur distribution ratio between slag and hot metal; and n the slag volume, kg/tHM.

In the BF, the sulfur distribution ratio is lower than its equilibrium value. Desulfurization potential of slag is characterized by the degree of approach to equilibrium of the reactions of desulfurization:

$$\sigma = \left(L_s / L_s^0\right) \times 100, \%$$

where L_s and L_s^0 are the real and the theoretical sulfur distribution ratios, respectively.

Low sulfur hot metal can be produced by the following:

- Controlling the BF process (Babich et al., 2008a)
- Lower sulfur load by decreasing the coke rate and using low sulfur coke, injectants, and burden materials
- Desulfurization of tapped metal in a runner or in a ladle

17.4 Key innovations and future trends

Looking at the long BF history, two key innovations should be mentioned:

- Introduction of coke instead of charcoal (firstly by A. Darby, Coalbrookdale, England, 1709)
- Introduction of preheating blast (firstly at Clyde plant, Scotland, and Alexandrovsk plant, St. Petersburg, Russia, both in 1829)

Nowadays, the specific productivity over 80 t/m²/24 h and the total reducing agent and coke rates below 500 and 300 kg/tHM, respectively, have been achieved at the best performing BFs due to numerous developments such as

- improvement of iron ore beneficiation and increasing use of high-quality sinter and pellets,
- increase of blast temperature and oxygen content,
- increase of top pressure,
- improvement of coke quality,
- improvement of burden distribution and gas flow control,
- partial coke replacement with auxiliary reducing agents,
- process monitoring using modern instrumentations and automatic control.

In this section, innovations and trends within last decades as well as running and possible future developments are discussed.

17.4.1 Unit size

Average production capacity of a BF unit increased in the past three decades enormously due to the following:

- An increase in average furnace size: many small BFs were shut down and large furnaces erected; worldwide, there are 21 BFs with a volume of over 5000 m³ (Anon, 2013).
- Improvement of operation efficiency.

For example, 15 BFs in Germany ensured 2010 almost the same annual hot metal production capacity (about 30 million tons) as the 34 BFs operated in 1985 (Schmoele et al., 2011).

The BF profile has a tendency for decreasing the height/diameter ratio with the rise of the furnace size (Table 17.5), particularly caused by coke destruction properties affecting along with primary slag characteristics prerequisitions for the smooth operation.

Considering production costs and requirements on material quality, there is no evidence on further increase in BF efficiency with raising size over 3000–6000 m³. It should also be mentioned that modern mini and compact blast furnaces became the competitive option for certain conditions (Yusfin et al., 2005; Das and Konar, 2007).

Table 17.5 Change in the blast furnace profile (rounded down typical values)

Inner volume (m³)	1000	2000	3000–3200	5000–5500
H/*D* ratio[a]	3.2	2.7	2.45–2.5	2.0–2.3

[a] *H*, inner height (m); *D*, belly diameter (m).

17.4.2 New burden components

Sinter and pellets are major iron carriers in the BF; lump iron ore with appropriate characteristics is also used. New burden materials—self-reducing pellets (SRP) and iron ore–carbon composites (shortly composites) with cold embedded reactive carbonaceous materials—have been proposed to decrease carbon consumption in the BF. The close arrangement of iron ore and carbonaceous materials should enable faster reduction and gasification reactions (Nakano et al., 2004; Yokoyama et al., 2012). The idea behind this is that FeO–Fe reduction equilibrium shifts to lower temperature (point W to W^1 in Figure 17.19), resulting in a decrease of TRZ temperature (see Section 17.3.2) or the starting temperature of solution loss reaction $\left(CO_2 + C = CO\right)$ in the BF. A decrease in the temperature of equilibrium between the reducing gas and wüstite would shift the composition of the reducing gas toward

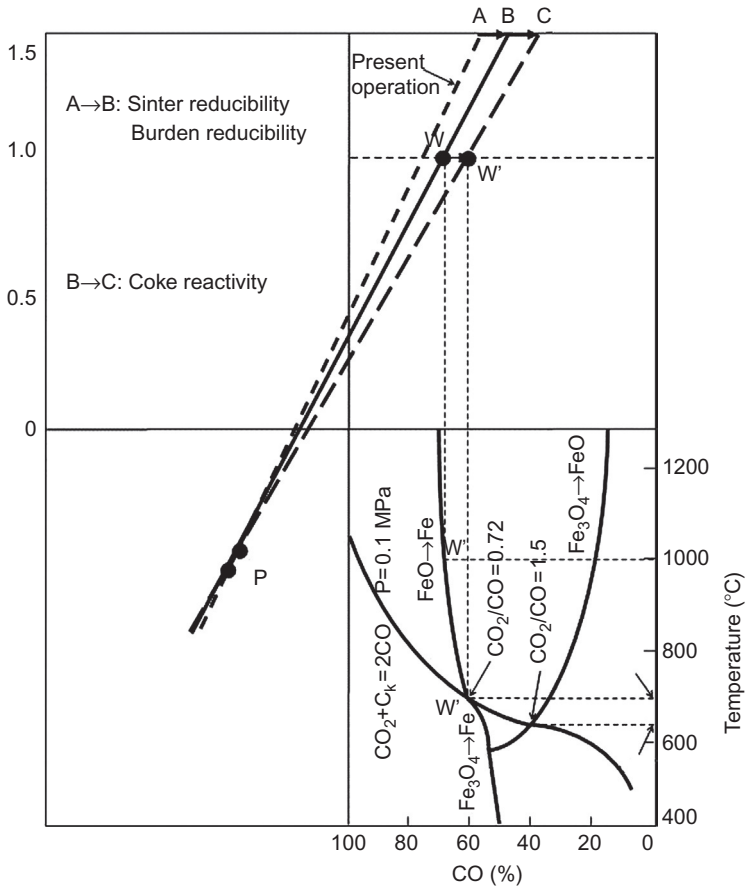

Figure 17.19 Rist operating diagram combined with Baur–Glaessner equilibrium diagram and Boudouard reaction at $P = 0.1$ MPa (Babich et al., 2009).

a lower CO and higher CO_2 content (Figure 17.19). This shift would improve the CO gas utilization efficiency, resulting in lower reducing agent consumption (Naito et al., 2001; Ariyama et al., 2005).

Numerous studies testified that SRP and composites are characterized indeed by higher reducibility as well as by improved volume change behavior (no swelling, typically shrinkage) and ability for carburization of hot metal, but these effects depend strongly on type and amount of embedded carbonaceous materials. Various carbon sources such as coal, coke, charcoal, and waste plastics have been investigated (Murakami and Kasai, 2011; Babich and Senk, 2013b; Ohno et al., 2012; Kowitwarangkul et al., 2012).

On the other hand, SRP and composites are characterized by lower crushing strength compared with, for example, conventional pellets. Appropriate methods for hardening these materials are still being investigated. An introduction of such new burden materials in a mini BF with lower strength requirements might be easier (Kowitwarangkul et al., 2012).

The commercial trials with the use of cement-bonded carbon–iron ore composites (the so-called reactive coke agglomerate with embedded coke) have been conducted at the Oita Works No. 2 BF in Japan with maximum rate of 54 kg/tHM (Yokoyama et al., 2012).

17.4.3 Beyond the BF coke

Coke constitutes a great portion of the production costs of hot metal, and its consumption is strongly related to the CO_2 emission. That is why, efficient and environmentally friendly production of high-quality coke and stable low-coke BF operation are key issues in the modern BF iron making. New coke-making technologies and use of additives to coal blends such as charcoal and waste plastics are summarized in Babich and Senk (2013b) and are out of the scope of this book. Partial replacement of coke with injected reducing agents is discussed in Section 17.4.4. In this section, top charging of supplementary energy carriers, which differs from metallurgical coke, is discussed.

17.4.3.1 Nut coke

The production of high-quality coke of a certain size (mainly 40–80 mm) causes the generation of big amount of undersieve product and therefore contributes to the raise of coke price. Charge of this undersieve material (commonly known as nut coke) into the BF in mixture with burden (different from layered charging, Figure 17.20) became a common practice at many BFs and proved the possibility for coke saving and increase of furnace productivity. The amount of used nut coke is very different: from 10 to 100 kg/tHM and more. It has to be mentioned that there is no clear definition of nut coke grain size; in different countries and even companies, its value is, for example, 10–30, 10–40, or 6–35 mm (Babich et al., 2008b). The positive effect of nut coke mixing with sinter (typically) or with pellets on the BF operation is caused mainly by the improvement of gas permeability in “dry zone” of a BF and by the improvement of reduction conditions of iron burden.

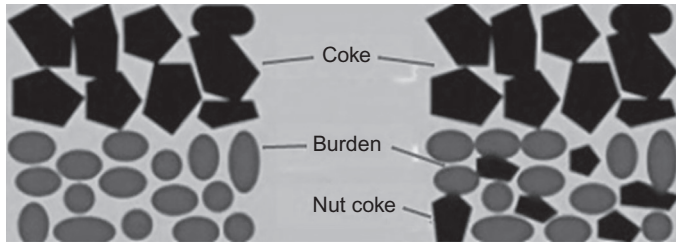

Figure 17.20 Conventional (left) and coke mixed (right) charging.
Modified from Satyendra (2013).

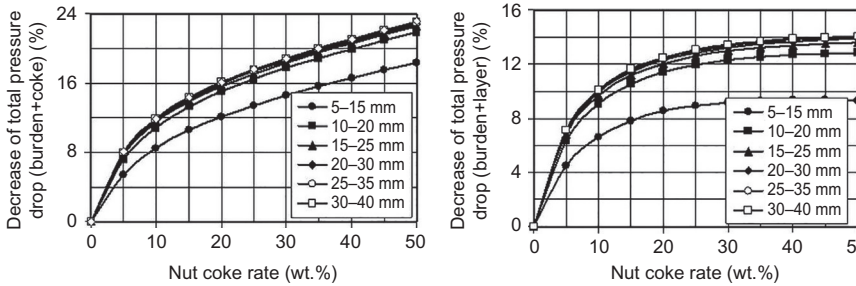

Figure 17.21 Change of pressure drop in BF "dry zone" when using nut coke of various grain sizes (Babich et al., 2008b).

Studies on shaft *gas permeability* showed that the pressure drop decreases as nut coke rate increases and nut coke effect becomes remarkable with increasing the gas flow rate. As the pressure drop decreases by nut coke application, the blast volume increases, and consequently, the furnace productivity increases. Effects of nut coke rate and layer thickness become apparent at increasing flow rate. The effect of nut coke on burden permeability is closed to exponential: it decreases with rising nut coke rate (Figure 17.21). The bigger grain size of nut coke, the stronger its influence on the change of gas permeability (Babich et al., 2008b; Mousa et al., 2011).

Studies on *reduction behavior of iron burden* showed that reducibility of sinter and pellets increases in the presence of nut coke by several mechanisms; particularly, the nut coke solution loss reaction improves the reducing gas diffusion, and contact between reducing gas and iron oxides as well as the mixing of nut coke with sinter inhibits the sticking between the sinter pieces (Figure 17.22) (Mousa et al., 2010a, b, 2011).

It was supposed that decrease in coke consumption while using nut coke may also be caused by higher reactivity of nut coke compared with metallurgical coke and that it reacts preferably with carbon dioxide and "protects" in this way bell coke from the solution loss reaction in the shaft. This possibility has not been proved so far. The results might also depend on the nut coke grain size (Mousa et al., 2011).

The optimum rate of nut coke seems to be 10–30 wt.% to total coke rate depending on various conditions.

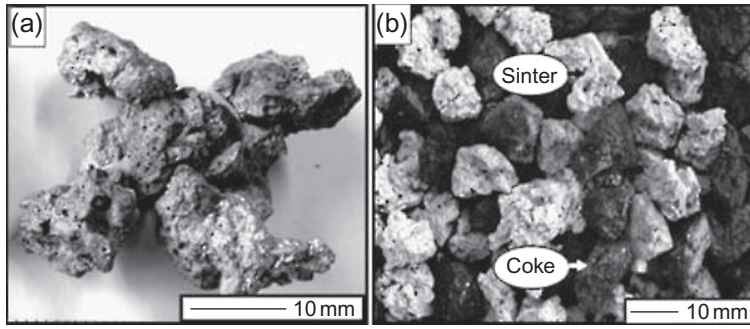

Figure 17.22 Sinter reduced without nut coke (a) and with nut coke in sinter bed (b) (Mousa et al., 2011).

17.4.3.2 Anthracite and charcoal charging

The BF technology with charging up to 40–70 kg/tHM of treated anthracite has been implemented at several small, medium, and large BFs including one with useful volume of 5000 m^3 (Lyalyuk et al., 2010). A technology to increase mechanical strength of anthracite has been developed. It includes two steps: anthracite treatment in an electromagnetic field to remove water and covering coal pieces by polymer film (by means of spraying) to protect them from secondary water penetration and to further improve their strength and other properties.

The introduction of small amounts (10–50 kg/tHM) of charcoal at the BF top was examined as another way to decrease the TRZ temperature (see Section 17.4.2) in a modern BF. Results showed that charging limited amount of high-reactivity charcoal should be sufficient for significant decrease of the TRZ temperature. The reduction kinetics and position of the cohesive zone at lower TRZ temperature were tested using lab facilities and mathematical modeling as well (Hanrot et al., 2011).

17.4.4 Injection technologies

17.4.4.1 Fossil auxiliary reducing agents

The tuyere injection of gaseous, liquid, and solid fuels, mostly pulverized coal (PC), NG, and heavy oil, became state of the art. About 64% of BFs worldwide use mentioned injectants; thereunder, 47.7% of BFs use PC (Stahlinstitut VDEh, 2009). A key trend is raising injection rates. Nowadays, about 40% of total reducing agent consumption can be replaced by injectants. Annual average PC injection rates of 215–235 kg/tHM have been reached, and a record of 255–265 kg/tHM has been reported; see Babich and Senk (2013b). An efficient BF operation at super high injection rates can only be achieved at high conversion degree of injected PC within the raceway. Measures for intensifying the PC conversion in the raceway have been summarized by Babich et al. (2008a) and listed in Babich and Senk (2013b). It is anticipated that PC injection rates "up to, and even above, 300 kg/tHM should be achievable" (Geerdes et al., 2011). Finally, it has to be mentioned that a part of the unburnt in the raceway

coal particles can be utilized by reactions of secondary gasification in deadman, shaft, or slag. In this context, char generation and its behavior in the BF are of great importance (Sahajwalla and Gupta 2005; Babich and Senk, 2013b).

17.4.4.2 Organic wastes, off-gases, and reducing gases

Injection of *waste plastics* is an appropriate way to recycle industrial and municipal wastes. Furthermore, the presence of hydrogen in this material may contribute to the CO_2 mitigation. This technology was implemented at several BFs since 1990s (Janz, and Weiss, 1996; Ariyama et al., 1997; Buergler et al., 2007). The injection rates are typically in the range of 30–60 kg/tHM. Figure 17.23 shows schematically an example of a plastics treatment and injection plant.

The limitation for the emissions of chlorine and heavy metals like Hg, Cd, Pb, and Zn with the BF gas is a decisive factor for the use of waste plastics (Buergler et al., 2007). Their conversion behavior is also of great importance. The study on reaction kinetics of waste plastics showed that despite of extremely high amount of volatile matters $(80-90\%)$, the reaction takes place almost only on the surface, and the complete conversion of injected plastics particles with grain size of about 5–8 mm can be hardly reached within the residence time of 20–30 ms (Knepper et al., 2011).

Injection of available free resources of *COG* contributes for decreasing the energy consumption and CO_2 emissions. The injection of hydrogen-rich COG (55–63% H_2, 22–28% CH_4, 6–8% CO, 2–4% CO_2, 2–3% C_mH_n, and the rest O_2, N_2, and H_2O) affects the raceway conditions and iron burden reduction. The high efficiency of COG use in the BF is caused by low hydrocarbon content (three to five times less than in NG)

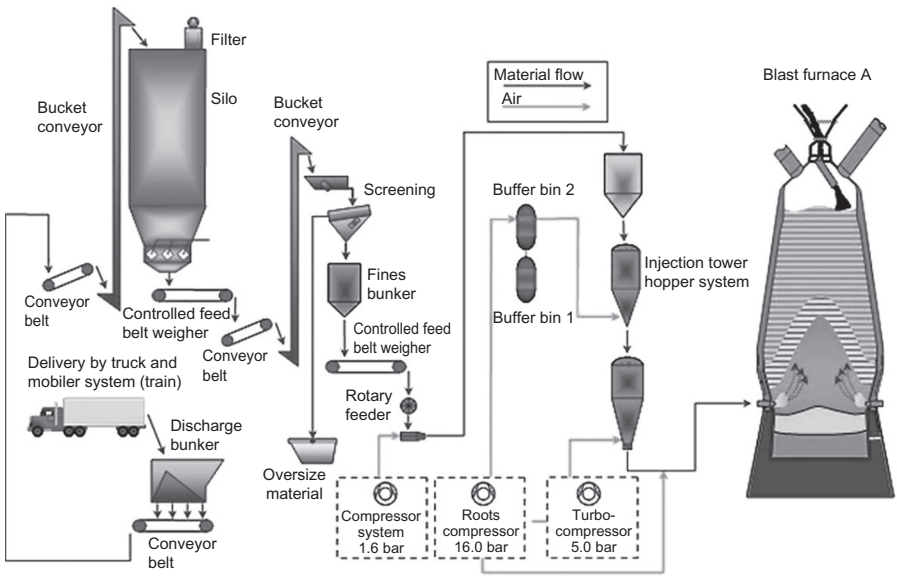

Figure 17.23 Layout of plastics injection at voestalpine Stahl BF A in Linz, Austria (Knepper et al., 2012).

along with high content of free hydrogen (Babich et al., 2008a). This improves its conversion, activates coke column, and increases gas utilization in the BF. Furthermore, iron ore sinter reducibility can be enhanced by COG injecting (Mousa et al., 2013). The injection rates of COG are in the range of 30–50 to 250–300 m^3/tHM; the coke replacement ratio makes up 0.4–0.45 kg/m^3 (Tovarovsky, 2006; Bürgler et al., 2004). Injection of further metallurgical *off-gases* such as BOF gas via BF tuyeres has also been studied.

Injection rate of fossil reducing agents and further hydrocarbons is limited by the processes in the raceway, deadman, and cohesive zone. To further save energy, increase in BF productivity and decrease in CO_2 emission might be achieved by the injection of *hot reducing gases* (*HRG*), which are produced outside of BF by low-grade coal or biomass and waste gasification, NG conversion (A), or top gas recycling after CO_2 removal (B); see Figure 17.24. Both tuyere and shaft injection technologies can be used for the introduction of HRG into the BF. BF operation with cold process oxygen instead of the hot blast (the so-called oxygen blast furnace) is possible when HRG is injected. Numerous investigations and industrial trials with HRG injection into the BF have been conducted since the 1960s and referenced in Babich et al., (2008a). A recently developed BF technology based on top gas regenerating and recycling is introduced in Section 17.4.6.

17.4.4.3 Renewable energy sources

Biomass sources, resources, processing, quality characteristics and requirements, and options for the use in the steel industry are summarized by Babich and Senk (Babich and Senk, 2013a) and also discussed in Chapter 19. Examples of biomass use in new burden materials and in coal blends for coke making are already mentioned in Sections 17.4.2 and 17.4.3. Here, only injection of biomass products (charcoals and torrefied materials) is discussed.

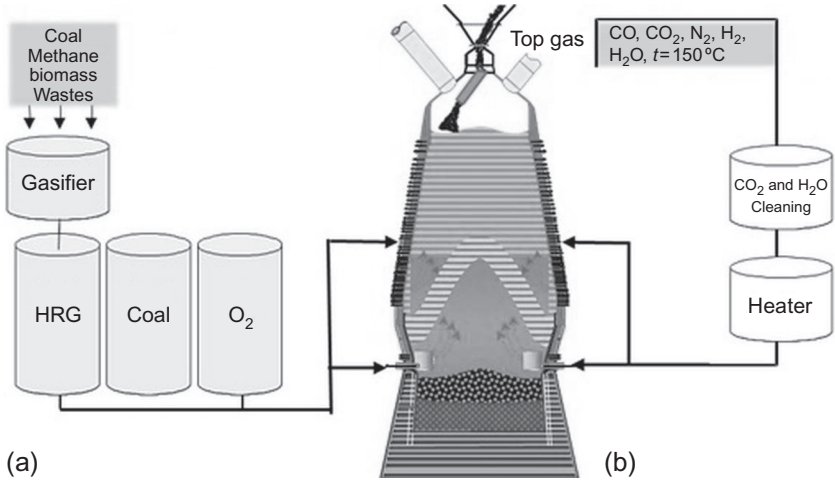

Figure 17.24 Different options for reducing gas generation and injection.

Charcoal injection is practiced in small BFs in Brazil with injection rate up to 100–190 kg/tHM (Mathieson et al., 2012), although its average value is about 80 kg/tHM (Assis, 2013).

The studies on charcoal injection under modern BF simulated conditions (Babich et al., 2009, 2010; Machado et al., 2010; Babich and Senk, 2013b) allow for concluding the following:

- Conversion behavior of charcoal under the raceway simulating conditions is comparable or even better than that for PC, particularly at high injection rates (conversion degree of charcoals is less dependent on its concentration in the blast than that for mineral coals; see Figure 17.25).
- Coarser grinding of charcoal compared to PC might be sufficient due to its large specific surface. This could lead to an increase of the dust yield and energy and cost saving.
- Solution loss reaction for unburnt charcoal particles goes on faster than for unburnt PC. Difference in reaction rates of charcoal and mineral coals lowers with rising temperature (the range of 900–1300 °C corresponding to temperatures in the cohesive zone was examined).

Conversion behavior of torrefied biomass materials, pyrolyzed at lower temperatures compared to charcoal (below 350 °C), is being investigated (Arnsfeld et al., 2012).

When injecting charcoals or torrefied biomass, BF operation results depend on ash content and composition and pyrolysis temperature of injectants. In case of constant injection rate, torrefied biomass materials require higher oxygen enrichment of blast and cause higher coke rate (Babich and Senk, 2013a).

17.4.4.4 Noncombustible materials

Injection of noncombustible additives, fluxes like

- BOF slag
- lime, dolomite and further CaO, MgO carriers
- titanium-containing materials
- catalysts

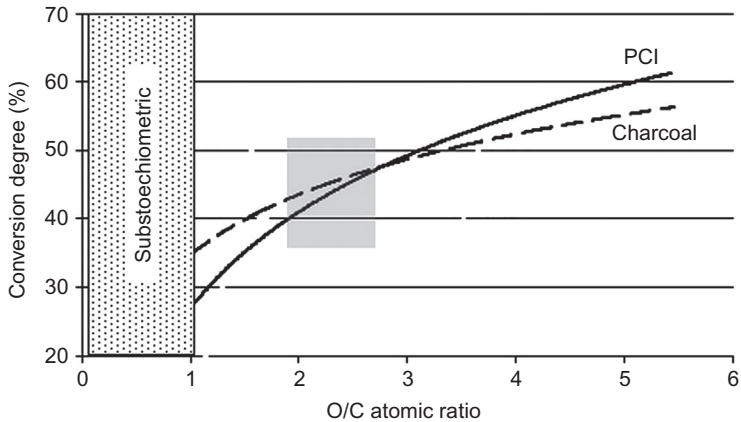

Figure 17.25 Conversion rate of charcoal and PC (Babich and Senk, 2013a).

as well as iron-containing materials like

- fine ores
- direct reduced iron/low reduced iron (DRI/LRI)
- own and external dusts and slurries (e.g., flue dust, BOF dust, mill scale)

has been investigated, tested, and partly used in order to improve hot metal quality, BF productivity and service life, environment, and auxiliary reducing agent conversion. Some of these substances are injected together with PC (see below).

17.4.4.5 Blends, coinjection, and flexible injection

Homogeneous *mixtures* of different coal types (typically high- and low-volatile coals), PC with catalysts, iron-containing materials, organic wastes, fluxes, slags, biomass, and other substances can be injected aiming at the following:

- Intensifying the coal conversion
- Controlling the hot metal quality
- Optimization of slag formation
- Improvement of desulfurization conditions
- Utilization of wastes

Coinjection of two or seldom even three reducing agents via separate inlets is practiced at a number of BFs. For example, 17 of the total 33 BFs in North America operated in 2011 with simultaneous injection of PC and NG (Poveromo and Rorick, 2012). Coinjection of NG + oil, PC + oil, PC + NG + oil, and HRG + PC is used, has been tested, or is being studied.

A new trend in philosophy of several steel producers consists in *flexible* use of various auxiliary reducing agents like oil, tar, NG, coke oven or BOF gases, biomass, and waste plastics depending on availability, costs, and other factors (Knepper et al., 2012).

17.4.5 Measurements, modeling, and automatic control

17.4.5.1 Measurements

High efficient operation of the modern BF, continuously operating for some 15–20 years and producing up to 11–13 Kt of hot metal a day, is impossible without continuous precise measurements of temperatures, pressures, flow rates, and gas composition at different positions, stockline level, and further parameters. Figure 17.26 shows typical BF instrumentation, which is a basis for process monitoring, control, investigation, model validation, and automation.

Some selected special instruments are listed below starting from BF top downward:

- Microwave, laser, and radar profile meters for the measurement of stockline level and burden profile; last two methods allow also for continuous online measurement of 3-D profile of the burden surface
- Acoustic temperature measurement at the BF top
- Movable probes above and in the burden (inclined, vertical, and horizontal) for the measurement of radial distribution of temperature, gas composition, pressure, dust content, and composition and for gas sampling (Figure 17.27)
- Helium tracing for direct measurements of the gas residence time, the deadman, and the shaft permeability and gas distribution by inoculation of the blast with helium or by He injection via horizontal tuyere probes

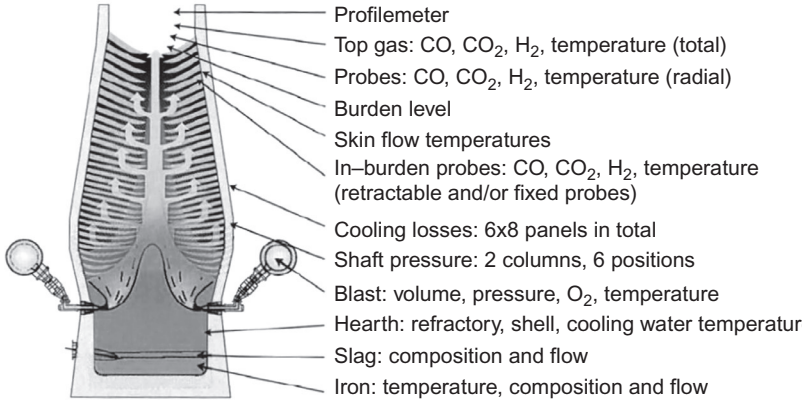

Figure 17.26 Overview of blast furnace instrumentation (Geerdes et al., 2009).

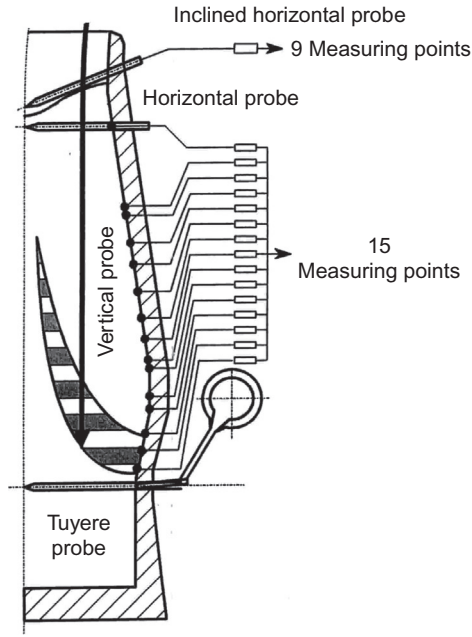

Figure 17.27 Probes for investigation of different zones (Bachhofen et al., 1998).

- Tuyere core drilling by movable probes for material sampling
- Nonintrusive measurements in the raceway and tuyere: new optical pyrometers, high-speed cameras like the CCD (Figure 17.28) and thermovision cameras, and laser, radar, and microwave instruments to determine the raceway depth
- Different kinds of instrumentation to control the accuracy of injected substance distribution around the furnace circumference
- Acoustic resonance for the evaluation of the hearth wear profile
- Measurement of the liquid level in the hearth, that is, level of hot metal and slag by EMF (electromotive force) technique

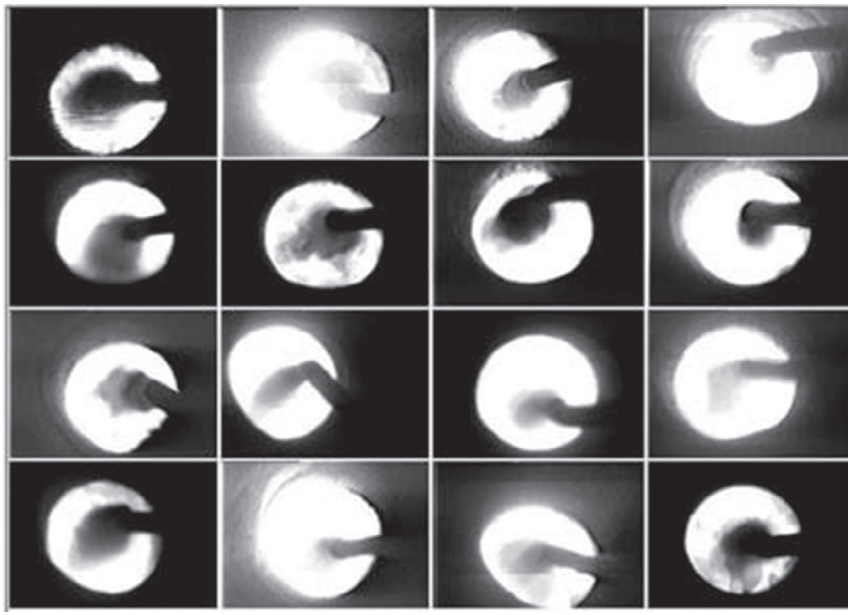

Figure 17.28 Image of the tuyere monitoring with a CCD camera (Sha et al., 2009).

17.4.5.2 Modeling

There are a huge number of mathematical models of the BF process, but an integrated global model of the BF process is not developed yet due to its enormous complexity and missing detail knowledge of some processes, phenomena, and their interrelationships.

According to the methods for process describing, mathematical models can be classified as follows (Babich et al., 2008a):

- Balance models (global and stage models, e.g., for upper and lower zones)
- Analytic or reaction kinetic models
- Numerical models
- Statistical models
- Artificial neural networks and fuzzy logic

Various BF models, particularly based on advanced numerical methods, have recently been developed. These methods are expected to be able to further improve model accuracy and optimize the BF operation.

17.4.5.3 Automatic control

Automatic control of the BF process has become an issue in past decades. Nowadays, the majority of automatic control systems (ACSs) are advisory expert systems. Closed-loop control systems are also being developed that go far beyond recommending actions for optimizing the process and control process parameters without any interaction with the operator. Both approaches can also be combined.

A mathematical model is a "brain" of any ACS. Due to the fact that no universal model has been established to date, the most effective way is the use of local ACSs for

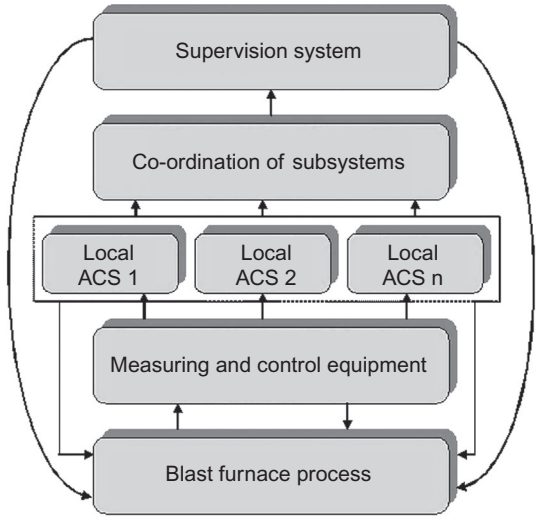

Figure 17.29 Hierarchical ACS (Babich et al., 2008a).

controlling local processes (e.g., burden distribution, hearth and taphole management, and raceway monitoring) and their subsequent integration into a hierarchical multifunctional decentralized ACS (Figure 17.29).

17.4.6 New BF technologies for energy saving and environmental

17.4.6.1 Top gas recycling BF

An oxygen BF with top gas recycling using the CCS technology (carbon capture and storage), which is one of the options for reducing gas injection presented in Figure 17.24, is being developing. This technology includes, along with reducing gas, coinjection of PC (Figure 17.30); the calculated coke/HRG replacement ratio, which is the ratio of the amount of coke saved to the amount of injected reducing gas, $k_r \approx 0.20-0.25\,\mathrm{kg/m^3}$, for HRG with low content of oxidizing components $(CO_2 + H_2O)$; and its achieved value at the experimental BF $k_r \approx 0.17\mathrm{kg/m^3}$ (Hirsch et al., 2012).

17.4.6.2 Coupling with other aggregates and use of prereduced ore

Smelting and direct reduction technologies are being typically indicated as alternatives to the BF; in the future, these processes might be complementary. For example, a process scheme for HRG injection based on the coupling of Corex® and BF was suggested (Figure 17.31). In this technology, the Corex® export gas after the removing of CO_2 is heated up and then injected into the BF (Wiesinger et al., 2001).

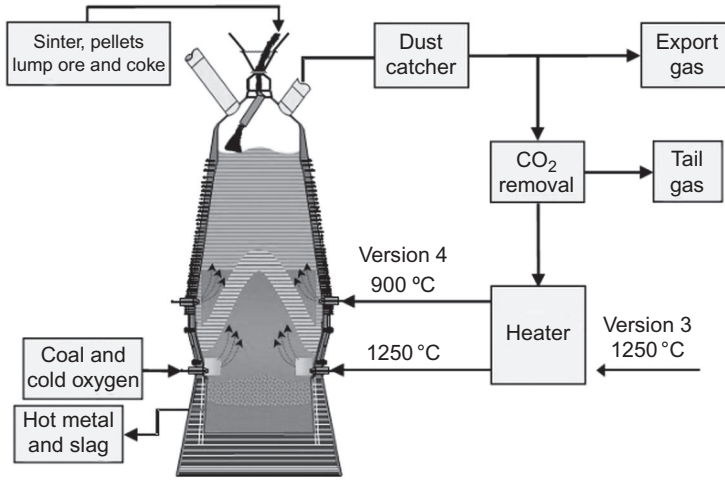

Figure 17.30 Process flow of the two versions of the top gas recycling BF (Zuo and Hirsch, 2009).

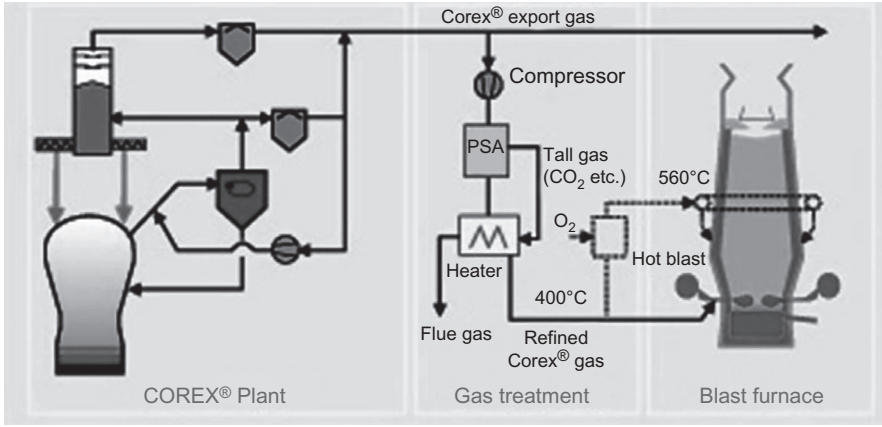

Figure 17.31 COREX export gas injection into the BF.
Modified from Wiesinger et al., (2001).

Looking at direct reduction processes, not only off-gases but also sponge iron in form of DRI or LRI might be used in the BF. Figure 17.32 shows a proposed and tested laboratory-scale operation modus of the Circofer® process (a coal-based direct reduction process using a CFB—circulating fluidized bed reactor), in which products DRI/LRI and char are used in the BF, for example, by means of injection via tuyeres (Born et al., 2012).

Injection of off-gases from aggregates of an integrated steel works such as COG or BOF gas, via BF tuyeres, was introduced in Section 17.4.4.

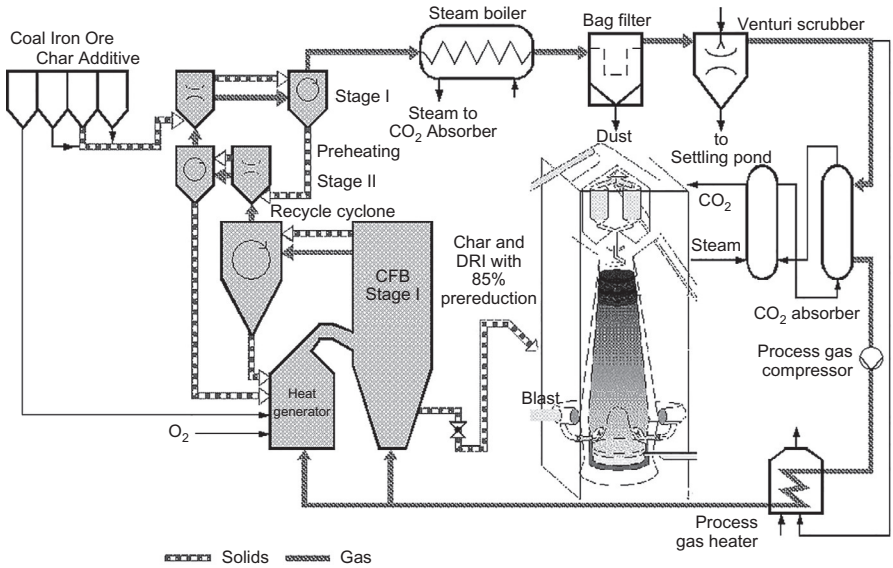

Figure 17.32 Fluidized bed direct reduction process Circofer® combined with the BF (Babich et al., 2008a).

17.4.6.3 Ways for long-term BF evolution

Further developments should target at a hydrogen-rich BF, where minimum coke amount will only be required as the burden supporter and perhaps carburizer. The crucial point thereby is the mass hydrogen production at a reasonable price. Therefore, aside from hydrogen generation using electrolysis, water steam reforming, partial oxidation of hydrocarbons, fermentation or photosynthesis, and available sources like NG or COG should be considered (Babich and Senk, 2013b).

Aside from hydrogen and renewables, other alternative energy sources, for example, electrical heat using plasma and microwave technologies, might be used in future.

The existing BF design makes an operation without coke impossible. Chernov suggested in 1940s to separate in the BF zone of solid-phase reduction and zone of melting without excess of solid carbon and developed a coke-less BF design (Chernov, 1950). Further iron-making development took the other way of alternative to the BF direct and smelting reduction processes. Later on, Tovarovsky developed further the Chernov's coke-less BF considering already the Corex® experience (Tovarovsky, 1994). In this BF, said the shaft-hearth aggregate, the iron oxides are reduced in solid phase up to metallization degree of 75–85% in shaft and bosh by reducing gas, introduced in shaft at $t < 900\,°C$ (Figure 17.33). Hot reducing gas from the tuyere zones 5 is mixed with cold reducing gas injected via tuyeres in shaft 6 to get the temperature of about 900 °C.

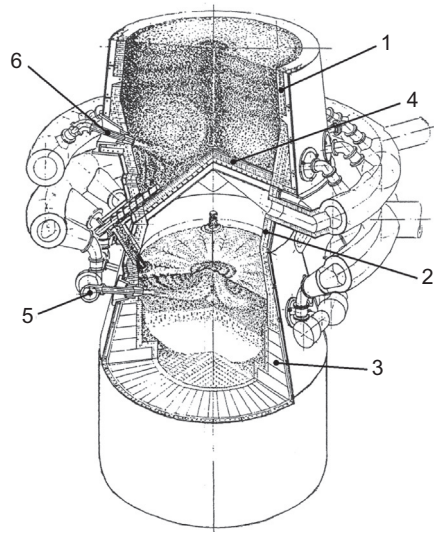

Figure 17.33 Expected material distribution and motion in the shaft-hearth aggregate (the upper part, which is not shown here, is the same as that the conventional BF): 1—shaft, 2—bosh, 3—hearth, 4—arch, 5, 6—tuyeres (Tovarovsky and Ljaljuk, 2001).

References

Anon, 2013. POSCO's Gwangyang blast furnace emerges as world's largest, http://english.donga.com/srv/service.php3?biid=2013060891448 (accessed 12 July 2013).

Ariyama, T., Matsuura, M., Noda, H., Asanuma, M., Shikada, T., Murai, R., Nakamura, H., Sumigama, T., 1997. Development of shaft-type scrap melting process characterized by massive coal and plastics injection. ISIJ Int. 37 (10), 977–985.

Ariyama, T., Murai, R., Ishii, J., Sato, M., 2005. Reduction of CO_2 emissions from integrated steel works and its subjects for a future study. ISIJ Int. 45 (10), 1371–1378.

Arnsfeld, S., Rodriguez Correa, C., Choi, S.-M., Babich, A., Senk, D., Gudenau, H.-W., 2012. Investigations of the reaction kinetics of torrefied biomass for metallurgical applications. In: Proc. 6th Int. Congress on the Science and Technology of Ironmaking (ICSTI), Rio de Janeiro, Brazil, pp. 1492–1502.

Assis, P.S., January 2013. Private communication.

Babich, A., Senk, D., 2013a. Biomass use in the steel industry: back to the future? Stahl Eisen 153 (5), 57–67.

Babich, A., Senk, D., 2013b. Coal use in iron and steel metallurgy. In: Osborne, D. (Ed.), The Coal Handbook: Towards Cleaner Production. Woodhead Publishing Ltd, UK.

Babich, A., Gudenau, H.-W., Senk, D., Formoso, A., Menendez, J.L., Kochura, V., 2002. Experimental modelling and measurements in the raceway when injecting auxiliary substances. In: Proc. Int. Blast Furnace Lower Zone Symposium, Wollongong, Australia, pp. 16.1–16.14.

Babich, A., Senk, D., Gudenau, H.-W., Mavrommatis, K., 2008a. Ironmaking Textbook. Mainz GmbH, Aachen.

Babich, A., Senk, D., Yaroshevskiy, S.L., Chlaponin, N.S., Kochura, V.V., Kuzin, A.V., 2008b. Effect of nut coke on blast furnace shaft permeability. In: Proc. 3rd Int. Conference on Process Development in Iron and Steelmaking (SCANMET III), Luleå, Sweden, vol. 2, pp. 227–236.

Babich, A., Senk, D., Gudenau, H.-W., 2009. Effect of coke reactivity and nut coke on the blast furnace operation. Ironmak. Steelmak. 36 (3), 222–229.

Babich, A., Senk, D., Fernandez, M., 2010. Charcoal behaviour by its injection into the modern blast furnace. ISIJ Int. 50 (1), 81–88.

Bachhofen, H.-J., Beppler, E., Janhsen, U., Kowalski, W., Peters, M., 1998. Measuring the coke properties in the tuyere level and the permeability of the dead man by means of tuyere probes. In: Proc. Measuring Techniques in Blast Furnace Ironmaking and Their Benefits for Industrial Practice, Düsseldorf, pp. 177–200.

Baur, E., Glaessner, A., 1903. Equilibrium between iron oxides and carbon monoxide and dioxide. Z. Phys. Chem. 43, 354–368, J. Chem. Soc., 84(2), 1903, p. 423.

Born, S., Senk, D., Babich, A., Gudenau, H.-W., Stefan, T., 2012. Investigations on the injection of DRI/LRI and char into the blast furnace. In: Proc. 6th Int. Congress on the Science and Technology of Ironmaking (ICSTI), Rio de Janeiro, Brazil, pp. 2301–2307.

Buergler, T., Brunnbauer, G., Pillmair, G., Ferstl, A., 2007. Waste okastucs as reducing agent in the blast furnace process—synergies between production and waste management processes. In: Proc. 3rd Int. Steel Conf. on New Developments in Metallurgical Process Technology, Düsseldorf, Germany, pp. 1037–1043.

Bürgler, T.-H., Brunnbauer, G., Ferstl, A., 2004. Operational results of a new blast furnace gas injection system. Stahl Eisen 124 (2), 39–42.

Buschmann (Publ.), W., Toncourt, M., 1989. Technik und Architektur der Hochöfen 1770–1970. Eisen und Stahl, Klartext.

Carpenter, J.A., 2006. In: Lecture#5 Blast Furnace Design 1, 19th Blast Furnace and Ironmaking, vol. 1. An Intensive Course McMaster University, pp. 5.1–5.87.

Chernov, D.K., 1950. About direct reduction of iron and steel in the blast furnace. In: Proc. GosNTI on Ferrous and Non-ferrous Metallurgy (in Russian), pp. 307–327.

Das, S.R., Konar (Consultant), S., 2007. Sustainability of small blast furnaces compared to larger one in Indian steel scenario. Steel Scenario 16 (Q3), 41–44.

Edström, J.O., 1953. The mechanism of reduction of iron oxides. J. Iron Steel Inst, 175, 289–304.

Efimenko, G.G., Gimmelfarb, A.A., Evchenko, V.E., 1986. Ironmaking. Vischa shkola, Kiev, p. 488.

Fruehan, R.J. (Ed.), 1998. The Making, Shaping and Treating of Steel—Steelmaking and Refining Volume. AISE Steel Foundation, Pittsburgh, PA, p. 761.

Geerdes, M., Toxopeus, H., Vliet, C., 2009. Modern Blast Furnace Ironmaking. IOS Press BV, The Netherlands, p. 154.

Geerdes, M., van Laar, R., Vaynshteyn, R., 2011. Low-cost hot metal: the future of blast furnace ironmaking. Iron Steel Technol. 51–56.

Greuel, M., Hillnhütter, F.W., Krüger, B., 1974. Untersuchung der Bewegungsvorgänge vor den Blasformen eines Hochofens mit einem Endoskop. Stahl Eisen 94 (12), 533–539.

Hanrot, F., Sert, D., Babich, A., Pietruck, R., Fernandez, M., Diez, M.A., Bürgler, T., Delinchant-Lété, J., 2011. Short Term CO_2 Mitigation for Steelmaking (SHOCOM). European Commission, Luxembourg, p. 108.

Hirsch, A., van der Stel, J., Sert, D., 2012. ULCOS top gas recycling blast furnace. Stahl Eisen 132 (4), 31–40.

Janz, J., Weiss, W., 1996. Injection of waste plastics into the blast furnace of Stahlwerke Bremen. In: Proc. 3rd European Ironmaking Congress, Gent, Belgium, pp. 114–119.

Jeschar, R., Pötcke, W., Ehlert, K.P., 1974. Modellversuche über die Ausbildung der Wirbelzone und über die Bewegungsvorgänge von den Blasformen im Hochofen. Stahl Eisen 94 (12), 525–532.

Jin, H., Choi, S., 2010. Numerical analysis of isothermal flow in lower part of blast furnace considering effect of cohesive zone. Ironmak. Steelmak. 37 (2), 89–97.

Kawasaki Steel, 1997. An introduction to iron and steel processing. http://www.jfe-21st-cf.or.jp/index2.html (accessed 11 July 2013).

Kitaev, B.I., 1945. Heat Exchange in Shaft Furnaces (in Russian). Metallurgizdat, Moscow.

Kitaev, B.I., Yaroshenko, Y.G., Suchkov, V.D., 1967. Heat Exchange in Shaft Furnaces. Pergamon Press, Oxford, London, p. 301.

Knepper, M., Babich, A., Senk, D., Schuster, S., Feilmayr, C., 2011. Characterisation of waste plastics for the injection into the blast furnace. In: Proc. METEC InSteelCon® 2011, 6th European Coke and Ironmaking Congress (ECIC), Düsseldorf, Germany, p. 8 (on CD-ROM).

Knepper, M., Babich, A., Senk, D., Buergler, T., Feilmayr, C., Kieberger, N., 2012. Waste plastics injection: reaction kinetics and effect on the blast furnace process. In: Proc. 6th Int. Congress on the Science and Technology of Ironmaking (ICSTI), Rio de Janeiro, Brazil, pp. 798–810.

Kowitwarangkul, P., Babich, A., Senk, D., 2012. In: Pellets mit eingebettetem Kohlenstoff für den Mini Hochofen, vol. 27. Aachener Stahlkolloquium, Aachen, Germany, pp. 17–28.

Lyalyuk, V., Scheremet, V., Otorvin, P., Tovarovskiy, I., Kassim, D., 2010. Entwicklungstrends bei Koks einsparenden Technologien für den Hochofenproress. Stahl Eisen 6 (130), 43–50.

Machado, J., Osório, E., Vilela, A., Babich, A., Senk, D., Gudenau, H.-W., 2010. Reactivity and conversion behaviour of Brazilian and imported coals, charcoal and blends in view of their injection into blast furnaces. Steel Res. Int. 81 (1), 9–15.

Mathieson, J.G., Rogers, H., Somerville, M., Jahanshahi, S., 2012. Reducing net CO_2 emissions using charcoal as a blast furnace tuyere injectant. ISIJ Int. 52 (8), 1489–1496.

Michard, J.A., 1956. Etude du haut fourneau. Cahiers du CESSID, Metz, France, 1964.

Mousa, E., Senk, D., Babich, A., Gudenau, H.-W., 2010a. Influence of nut coke on iron ore sinter reducibility under simulated blast furnace conditions. Ironmak. Steelmak. 37 (3), 219–228.

Mousa, E., Senk, D., Babich, A., 2010b. Reduction of pellets-nut coke mixture under simulating blast furnace conditions. Steel Res. Int. 81 (9), 706–715.

Mousa, E., Babich, A., Senk, D., 2011. Effect of nut coke-sinter mixture on the blast furnace performance. ISIJ Int. 51 (3), 350–358.

Mousa, E., Babich, A., Senk, D., 2013. Enhancement of iron ore sinter reducibility through coke oven gas injection into the modern blast furnace. ISIJ Int. 53 (8), 1372–1380.

Murakami, T., Kasai, E., 2011. Reduction mechanism of iron oxide–carbon composite with polyethylene at lower temperature. ISIJ Int. 51 (1), 9–13.

Naito, M., Okamoto, A., Yamaguchi, K., Yamaguchi, T., Inoue, Y., 2001. Advanced approach to intelligent ironmaking processes. Improvement of blast furnace reaction efficiency by use of high reactivity coke. Tetsu-to-Hagane 87 (5), 357–364.

Nakano, M., Naito, M., Higuchi, K., Morimoto, K., 2004. Non-spherical carbon composite agglomerates: lab-scale manufacture and quality assessment. ISIJ Int. 44 (12), 2079–2085.

Ohno, K., Babich, A., Mitsue, J., Maeda, T., Senk, D., Gudenau, H.-W., Shimizu, M., 2012. Effects of charcoal carbon crystallinity and ash content on carbon dissolution in molten iron and carburization reaction in iron-charcoal composite. ISIJ Int. 52 (8), 1482–1488.

Peters, M., Schmoele, P., 2013. Koksqualitaet und Hochofenleistung. Stahl Eisen 133 (6), 79–89.

Poveromo, J.J., Rorick, F.C., 2012. Developments in North American iron ore & ironmaking. In: Proc. 6th Int. Congress on the Science and Technology of Ironmaking (ICSTI), Rio de Janeiro, Brazil, pp. 597–608.

Ramm, A.N., 1980. A Modern Blast Furnace Process (in Russian). Metallurgiya, Moscow, p. 304.

Reichardt, P., 1927. Ein neues Wärmeschaubild des Hochofens. Archiv für das Eisenhüttenwesen 1, 77.

Riley, M.F., Rosen, L., Drnevich, R., 2010. Mitigating CO_2-emissions in the steel industry: a regional approach to a global need. Iron Steel Technol. 7 (2), 63–72.

Sahajwalla, V., Gupta, S., 2005. PCI coal combustion behaviour and residual coal char carry-over in the blast furnaces of three American steel companies during pulverized coal injection (PCI) at high rates. Final report, prepared by AISI, Washington, DC.

Satyendra, K.S., 2013. Use of nut coke in a blast furnace. http://ispatguru.com/use-of-nut-coke-in-a-blast-furnace (accessed 25 July 2013).

Schmoele, P., Peters, M., Luengen, H.B., 2011. Hot metal production in the blast furnace—development, status quo and outlook. In: Proc. METEC InSteelCon® 2011, 6th European Coke and Ironmaking Congress (ECIC), Düsseldorf, Germany, 8 p.

Sha, Y., Cao, J., Wang, F., 2009. Development of specific measuring techniques in ironmaking process. In: Proc. 5th Int. Congress on the Science and Technology of Ironmaking (ICSTI'09), Shanghai, China, pp. 933–936.

Stahlinstitut VDEh, 2009. Plantfacts-Datenbank. Stahlinstitut VDEh, Düsseldorf, Germany.

Stahl-Online, 2013. http://www.stahl-online.de/Deutsch/Linke_Navigation/Stahl_in_Zahlen/index.php (accessed 25 July 2013).

Steel Institute VDEh, 2008. Steel Manual. Stahleisen GmbH, Düsseldorf, Germany.

Tovarovsky, I.G., 1994. Evolution of the blast furnace process to the coke-less primary metal production. In: Proc. Ferrous Metallurgy in Russia and CIS Countries in XXI Century (in Russian), vol. 2, Metallurgiya, Moscow, pp. 105–108.

Tovarovsky, I.G. (Ed.), 2006. Coke Saving Technologies for the Blast Furnace (in Russian). Porogi, Dnepropetrovsk, p. 276.

Tovarovsky, I.G., Ljaljuk, V.P., 2001. Evolution of the Blast Furnace Process (in Russian). Porogi, Dnepropetrovsk, p. 424.

VAI Industries, 2000. The World of VAI Davy® Blast Furnace Technology. VAI Industries Ltd, UK, p. 12.

Vegman, E.F., Zherebin, B.N., Pochvisnev, A.N., Yusfin, Y.S., Kurunov, I.F., Parenkov, A.E., Chernousov, P.I., 2004. Ironmaking. Akademkniga, Moscow, p. 774.

Verein Deutscher Eisenhüttenleute (Publisher), 1970. Gemeinfassliche Darstellung des Eisenhüttenwesens, seventeenth ed. Stahleisen mbH, Düsseldorf, Germany.

Wiesinger, H., Eberle, A., Siuka, D., Freydorfer, H., Böhm, C., 2001. Status, realized improvements and future potentials of the Corex technology. Stahl Eisen 121 (11) I/26.

Yokoyama, H., Higuchi, K., Ito, T., Oshio, A., 2012. Decrease in carbon consumption of a commercial blast furnace by using carbon composite iron ore. ISIJ Int. 52 (11), 2000–2006.

Yusfin, Y.S., Chernousov, P.I., Golubev, O.V., 2005. The prospects for small blast furnaces. Steel Transl. 35 (10), 12–18.

Yuu, S., Umekage, T., Kadowaki, M., 2005. Numerical simulation of blast furnace raceway depth and height, and effect of wall cohesive matter on gas and coke particle flows. ISIJ Int. 45 (10), 1416–1425.

Zhou, Z.Y., Pinson, D., Zhu, H.P., Yu, A.B., Wright, B., Zulli, P., 2003. Discrete particle simulation of gas-solid flow in a blast furnace. In: Proc. 3rd Int. Conf. on CFD in the Minerals and Process Industries, CSIRO, Melbourne, Australia, pp. 455–460.

Zuo, G., Hirsch, A., 2009. The trial of the top gas recycling blast furnace at LKAB's EBF and scale-up. Revue de Metallurgie—Cahiers d'Informations Techniques 106 (9), 387.
Zylev, L.M., Ostrouxov, M.Y., Chodak, L.Z., 1960. Coke Combustion in the Blast Furnace (in Russian). Metallulgizdat, Moscow, p. 100.

Further Reading

Babich, A., Senk, D., Gudenau, H.W., Mavrommatis, K., 2008. Ironmaking Textbook. Mainz GmbH, Aachen, p. 402.
Omori, Y. (Ed.), 1987. Blast Furnace Phenomena and Modelling. Elsevier Applied Science, London and New York, p. 576.
Von Bogdandy, L., Engell, H.-J., 1971. The Reduction of Iron Ores. Springer Verlag, Stahleisen m.b.H, Berlin, Heidelberg, New York, Duesseldorf, p. 576.

Sintering emissions and their mitigation technologies

18

L. Lu[1], *T.C. Ooi*[2], *X. Li*[3]
[1]CSIRO Mineral Resources Flagship, Pullenvale, QLD, Australia
[2]Fortescue Metals Group Ltd, East Perth, WA, Australia
[3]University of Science and Technology Liaoning, Anshan, Liaoning, China

18.1 Introduction

18.1.1 Key gaseous emissions from sinter plants

Iron ore sintering is a material preparation process employed worldwide in the production of iron and steel. According to statistical data on pollution, sintering plants rank second in terms of toxic emissions, after the incineration of municipal solid waste (Menad et al., 2006; Remus et al., 2013). Of the eight CORINAIR (Core Inventory of Air Emissions (environment)) standard gaseous compounds, all except ammonia are known to be emitted by sinter plants. As described in Chapter 14 on iron ore sintering, sintering involves the combustion of fossil fuels like coal and coke breeze to generate the heat required for sintering reactions. Therefore, emissions from the sintering process arise primarily from the combustion reactions in the sintering bed on the traveling sinter strand. The off-gas from the combustion reactions contains dust entrained directly from the strand along with combustion products such as CO, CO_2, SO_x, NO_x, and particulate matter. The concentration of these substances varies with the quality of the fuel and raw materials used and the combustion conditions. Emissions also include volatile organic compounds (VOCs) formed from volatile material in the coke breeze and oily mill scale, and dioxins/furans formed in the presence of carbon, chlorine and metal catalysts, such as Cu, under certain operating conditions. While the majority of VOCs and dioxins/furans are vaporized, some of them may recondense and be trapped in the sinter bed. Metals are also volatilized from the raw materials used, and other acid vapors and high resistivity dusts are formed from the halides present in the raw materials. In addition, emissions also arise from material-handling operations, such as sinter discharge, crushing and screening, which result in airborne dust.

18.1.2 Secondary measures on sintering emissions

Typically, flue gas from sinter plants is cleaned in electrostatic precipitators (ESPs). The electrical precipitators significantly reduce dust emissions, but have minimal effect on the gaseous emissions. Therefore, wet scrubbers that have higher collection efficiency for gaseous emissions are often used in sinter plants. Sinter crushing and screening emissions are usually controlled by ESPs or fabric filters. Wastewater discharges, including runoff from the material storage areas, are treated in a wastewater treatment plant that

Iron Ore. http://dx.doi.org/10.1016/B978-1-78242-156-6.00018-6
© 2015 Elsevier Ltd. All rights reserved.

may also be used to treat blast furnace (BF) wastewater. However, as environmental regulations become increasingly stricter than those currently enforced, sintering plants are under increasing pressure to further minimize their emissions. Table 18.1 lists the upper limits of toxic emissions from existing sinter plants set by various countries. New efficient measures have therefore been developed for controlling and minimizing emissions from the sintering process. These include emission optimized sintering (EOS), activated carbon adsorption/absorption systems, fine wet scrubbing systems (such as Airfine system developed by Voest-Alpine Industrieanlagenbau GmbH in Linz, Austria), and KN-filter for more efficient separation of solid materials from gas at high temperatures. While significant reduction has been achieved (Table 18.2), these technologies require

Table 18.1 Upper limits of toxic emissions from existing sinter plants required by different countries

Toxic emissions	Unit	Japan	The United Kingdom	China
SO_x	mg/Nm^3	–	350–500 expressed as the SO_2 daily mean by way of limiting coke breeze, S in coke breeze, and S in iron fines, using activated carbon injection, 150 wet scrubber and regenerative activated carbon (RAC)	600
NO_x	mg/Nm^3	220 ppm	500 expressed as NO_2 daily mean value using process-integrated measures, 250 using RAC, and 120 using selective catalytic reduction (SCR)	500
Dust	mg/Nm^3	100–150	40 for advanced ESP, 15 for bag filters	130
Dioxins	ng-TEQ (toxicity equivalent)/ Nm^3	1.0	0.4 Polychlorinated dibenzo-*p*-dioxins and polychlorinated dibenzofurans (PCDD/Fs) <0.05–0.2 ng/Mm^3 for bag filter applications and <0.2–0.4 ng/Mm^3 for electrostatic precipitator applications	1.0

Table 18.2 Achievable levels of polychlorinated dibenzo-*p*-dioxin and polychlorinated dibenzofuran (PCDD/F) emissions from iron ore sintering plants (TEQ/Rm^3 stands for toxicity equivalent/ reference cubic meter)

Type of measures	Emission limit value
New plants	<0.2 ng-TEQ/Rm^3
Adsorption/absorption and high-efficiency dedusting	0.1–0.5 ng-TEQ/Rm^3
Fine wet scrubbing system	0.2–0.4 ng-TEQ/Rm^3

considerable capital investment and have not solved the fundamental emission problems as their intervention occurs only after emissions have been generated. Primary measures are therefore needed to prevent or minimize the formation and release of the identified pollutants and wastes. This chapter focuses on recent developments in preventing and therefore reducing sintering emissions by optimizing process variables, practices, raw materials, products, or energy consumption.

18.2 CO_2 emissions and their mitigation

18.2.1 Characteristics of CO_2 emissions

The steel industry is responsible for producing about 70% of the world's greenhouse gas emissions generated from primary metal production which contributes about 5% to total world's greenhouse gas emissions (Norgate et al., 2012). Global crude steel production in 2010 was 1410 Mt, of which the integrated BF/basic oxygen furnace (BF-BOF) route accounted for around 70% (Suopajärvi and Fabritius, 2012). According to Birat (2009), the BF-BOF route emits 1.97 tCO_2/t steel, and the biggest share of this (19%) comes from the BF where fossil-based reducing agents are used for reducing the iron oxides. The sintering process is energy-intensive and produces a considerable amount of CO_2 (~15%) from the combustion of coke breeze and calcination of carbonates. Based on an emission factor of 0.2 tonne of CO_2/tonne of sinter estimated by the Intergovernmental Panel on Climate Change (IPCC) (Anon, 2012) and the production of 13.3 Mt of sinter in 2007, CO_2 emissions are estimated to be 2.7 Mt per annum from iron ore sintering in the United States.

The CO_2 emissions from sinter plants vary widely over time and between sinter plants as a consequence of variations in fuel inputs, fluxes, and other feedstock, especially in the types and quantities of iron-bearing materials that are recycled. Figure 18.1 shows the CO_2 and CO concentrations measured in the waste gas during a sinter pot test on a typical East Asian sinter blend. CO_2 emissions occur across the entire sintering cycle from ignition to the burn-through point. This is because CO_2 is primarily formed from the combustion of fuel (coke oven gas (COG) or natural gas) during ignition and from the carbon in the feed material, including coke breeze and other carbonaceous materials such as limestone and dolomite, which are widely used as fluxing agents to adjust sinter chemistry. Therefore, measures that lead to reductions in fuel, limestone, and dolomite

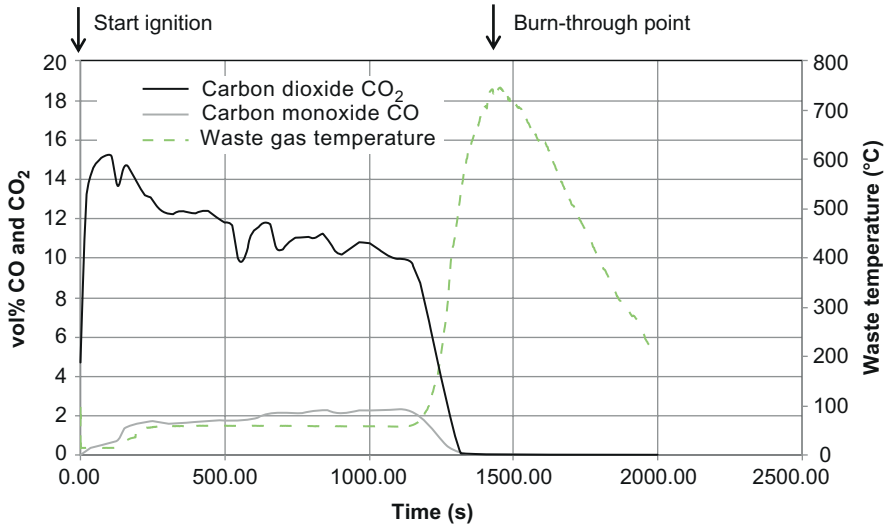

Figure 18.1 CO_2 and CO concentrations measured in the waste gas during a sinter pot test on a typical sinter blend.

consumption will result in the abatement of direct emissions of CO_2 from sinter plants. In addition to lowering fuel and flux consumption, reductions in electricity consumption, for example, to drive the downdraft and cooling fans during sintering will also result in the reduction of emissions indirectly.

18.2.2 Mitigation technologies for CO_2 emissions

18.2.2.1 Deep bed sintering

Deep bed sintering has been made possible by improved sinter feed preparation, in particular better granulation. Most sinter plants in East Asia now operate at bed heights in excess of 600 mm. Increasing the bed height will improve sinter yield since a significant amount of return fines is generated from the upper bed region, which is sintered at a lower temperature. Increasing the sinter yield will in turn lower fuel consumption as more sinter product is produced at the same fuel addition. In addition, compared with the temperature profile of conventional sintering, deep bed sintering allows the sinter bed to be kept at elevated temperatures for a longer time (Dawson et al., 1983; Lu et al., 2007). Increasing the time spent at temperatures above 1100 °C has been reported to be an effective way of improving the inherent strength of sinter and therefore enhancing its resistance to degradation (Dawson et al., 1983; Kumar et al., 1995). Therefore, increasing the bed depth in the sinter plant will not only lower fuel consumption but also improve product quality. It is estimated that fuel consumption will decrease by 0.3 kilogram (kg) of coke/tonne of sinter per 10 millimeters (mm) bed thickness increase (Anon, 2012). Electricity savings are expected to be 0.002 GJ/tonne of sinter. However, increasing the bed height does not necessarily increase productivity, because it also leads to prolonged sintering time.

18.2.2.2 Super-SINTER®

JFE Steel Corporation developed a technology for the injection of hydrogen-based gas fuel in sintering machines, that is, "Super-SINTER® (secondary-fuel injection technology for energy reduction)," which makes it possible to improve sinter quality while reducing the bonding agent (coke breeze) ratio and consequently greatly reducing CO_2 emissions from the sintering process (Oyama et al., 2011). In order to produce high-quality sinter, it is necessary to maintain the sintering temperature between 1200 and 1400 °C for a sufficient time.

With the "Super-SINTER®" technology, it is possible to extend the combustion zone in the optimum temperature range by injecting hydrogen-based gas fuel from the top side of the charged raw material to partially substitute for coke breeze. Figure 18.2 shows the effect of the gaseous fuel injection on the temperature distribution of a sintering bed measured by infrared thermography 250 s after ignition. Compared with the all coke sinter bed, gaseous fuel injection expands the combustion zone (the zone with temperature over 1200 °C) in the upper direction, although it slightly reduces the maximum sintering temperature achieved. Because the liquefied natural gas (LNG) was injected from the top surface of the sinter bed and ignites at a lower temperature of 650–750 °C, its combustion occurs at a location above the coke breeze combustion zone. Consequently, an expanded combustion zone comprising both the LNG and coke combustion zones is observed in Figure 18.2. Theoretical and experimental studies were carried out to verify the effect of the gaseous fuel injection technology on the pore structure of sinter cake produced in sinter pot tests using an X-ray CT scanner. The liquid phase ratio was found to increase with extension of the combustion zone by using gaseous fuel injection technology. The increase in liquid phase ratio promotes the consolidation of pores (1–5 mm) and improves the pore structure in the sinter cake and consequently sinter strength and reducibility.

This technology was successfully put into commercial operation at the Keihin No. 1 sinter plant for the first time in January 2009, and the plant has continued to perform

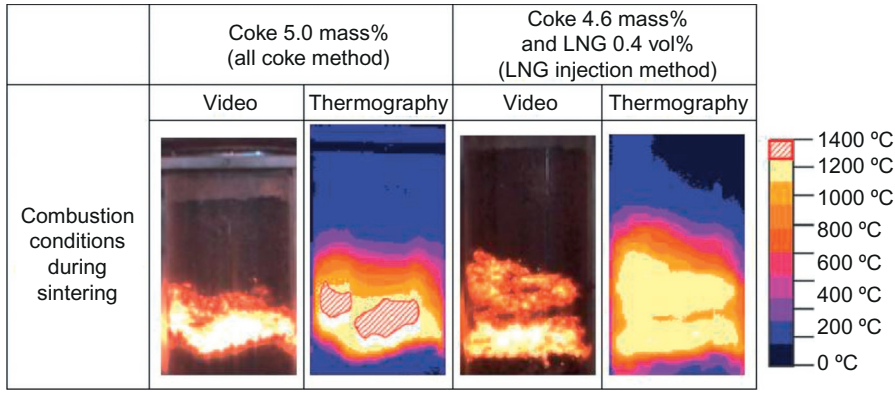

Figure 18.2 Effect of gaseous fuel injection on the temperature distribution of a sintering bed measured by thermography 250 s after ignition (Oyama et al., 2011).

smoothly. As a result, the energy efficiency of the sintering process was greatly improved, and CO_2 emissions were reduced by a maximum of approximately 60,000 t/year at the Keihin No. 1 sinter plant (Anon, 2010; Oyama et al., 2011).

18.2.2.3 Improved charging method

Increased demand and diminishing high-grade resources have resulted in a shift to increasing usage of low-grade iron ore in steel mills around the world. In response to the change in raw materials toward increasing usage of porous pisolite ore, various charging methods, including the segregating slit wires (SSW) feeder, the intensified sifting feeder (ISF), the magnetic braking feeder (MBF), and the deflector plate type feeder, were developed in Japan. The aim was to control the ore and coke segregation and improve the permeability of the charged bed by decreasing the bulk density of the bed due to the reduced impact pressure and introduction of particle size segregation while charging the sintering mixture (Machida et al., 2009). For detailed information on the improved charging methods available, readers can refer to Chapter 14 on iron ore sintering. For example, a charging system consisting of a drum chute and a segregation slit wires feeder (SSW) has been introduced in sinter plants in Japan. As shown in Figure 18.3, the drum chute is used to reduce the height difference (drop height) during material charging, while the SSW controls the particle size segregation. Because the preferred particle size segregation is achieved, the permeability of the sintering mixture is improved, resulting in improved sintering efficiency, and the ratio of return fines due to poor sintering is also reduced. Compared to a conventional charging system, the new drum chute and SSW system has led to a productivity improvement of ~5% and a decrease in energy consumption due to coke use of 0.08 GJ/tonne sinter (Anon, 2012).

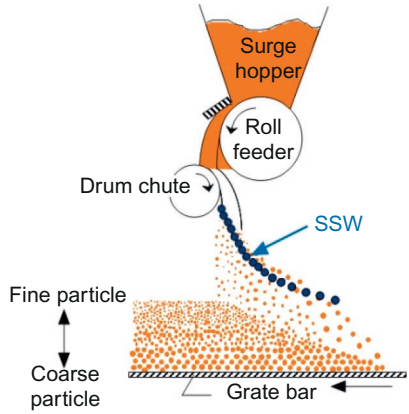

Figure 18.3 Charging method with a drum chute and a segregation slit wires feeder (SSW).

18.2.2.4 Use of metallic iron-bearing resources and waste fuels

Metallic iron-bearing resources (MIRs), such as mill scales, contain a high content of metallic iron that releases heat when oxidized and can be used to substitute for the primary fuel during sintering. Plant tests (Nakano et al., 1998) have been conducted at Nakayama Steel Works to clarify the effects of using resources containing metallic iron on the sintering process. An increase in MIRs in the sinter blend was found to reduce the fuel rate due to the exothermic oxidation of metallic iron during sintering. The emissions of NO_x and SO_x were also found to decrease due to the decrease in the N and S input from coke breeze. However, the sinter yield and productivity deteriorated with increasing MIRs in the sinter blend, while the sinter quality was found to depend on the kind of MIRs used.

The effect of substitution of metallic iron particles for coke on the structure and permeability of the sintering bed was analyzed in a laboratory-scale sintering simulator (Fujino et al., 2013). When using metallic iron particles in the sinter mixture, the pressure drop across the sintering bed shows a second peak after the rapid decrease stage of the initial peak often observed when coke is used. The decrease in permeability when metallic iron is used is attributed to blockage of the gas flow paths in the lower part of the bed due to the increasing amount of melt formed. However, increasing the CaO content of the sinter bed containing metallic iron particles was found to promote melt formation and accelerate changes in the structure of the sintering bed and improve bed permeability.

Waste materials with available caloric value, for example, oils from the cold rolling mill, can also be used as fuel to reduce the energy demand satisfied by the primary fuel. Based on data from European mills, the energy savings may amount to 0.18 GJ/tonne of sinter (Anon, 2012). However, the energy savings for this measure depend on the composition and quantity of lubricants and the installed gas cleanup system at the sinter plant. Use of waste material may be limited by permitted emission limits, because oils and other organics in the sinter feed increase emissions of organic compounds, including benzene, other VOCs, and dioxins.

18.2.2.5 Other CO_2 mitigation measures

18.2.2.5.1 Sinter plant heat recovery

Heat recovered from the waste gas of a sinter plant can be used to preheat the combustion air for the burners and to produce high-pressure steam, which can then be used in steam turbines to generate power. Various systems exist for new plants (e.g., the Lurgi EOS process) and can be retrofitted to existing plants. Based on a retrofitted facility in the Netherlands, fuel savings were estimated to be 0.55 GJ/tonne of sinter, and increased electricity generation was estimated to be 0.0056 GJ/tonne of sinter (Anon, 2012; Rengersen et al., 1995). Emissions of nitrogen oxide (NO_x), sulfur oxide (SO_x), and particulate matter were also reported to be reduced.

18.2.2.5.2 Improved ignition furnace efficiency

A large fuel and therefore CO_2 emission reduction can be achieved by improving the ignition furnace efficiency. A new multislit burner that can achieve rapid heating and uniform ignition across the sinter pallet width has been developed and introduced to

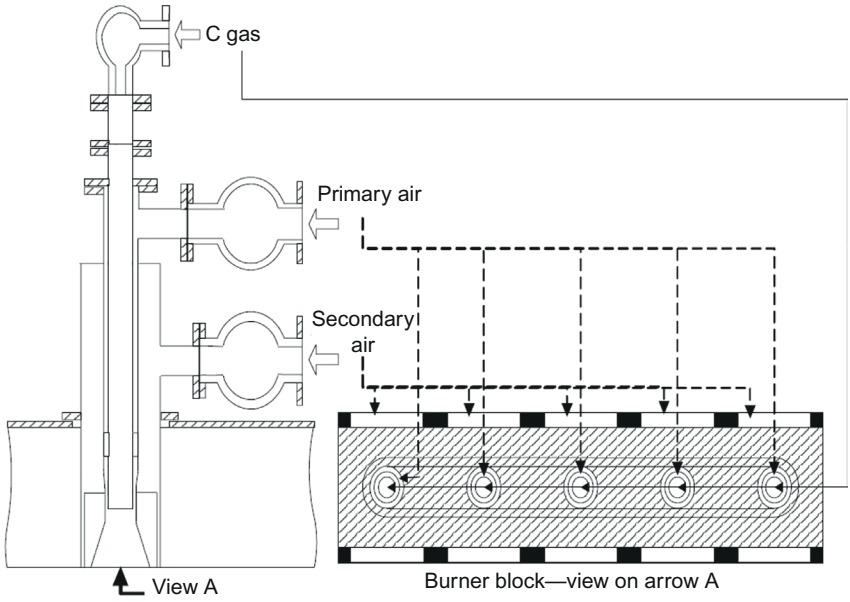

Figure 18.4 Outline of a multislit burner Lawrence Berkeley National Laboratory (Berkeley, CA and American Iron and Steel Institute (Washington, DC, 2007)).

realize large fuel reduction. Figure 18.4 shows an outline of the multislit burner. This burner consists of fuel exhaust nozzles located in the width direction of the sinter strand and a slit-like burner tile containing these fuel exhaust nozzles. The fuel supplied from the fuel exhaust nozzles reacts with the primary air inside the burner tile and then with the secondary air supplied to the flame through the outer periphery area. By using the slit-like burner tile, nonflamed areas are eliminated, and by controlling the ratio between the primary air and the secondary air, the length of the flame can be controlled to minimize the ignition energy. The total heat input for ignition was reduced by approximately 30% in the Wakayama Steel Works of Sumitomo Metals in Japan (Anon, 2012).

18.2.2.5.3 Reduction of air leakage

Reducing air leakage from a sinter plant reduces fan power consumption by approximately 0.011–0.014 GJ/tonne of sinter, which is expected to result in a reduction of indirect emissions from power generation (Anon, 2012).

18.3 SO_x emissions and their mitigation

18.3.1 Characteristics of SO_x emissions

Sulfur dioxide (SO_2) is one of the precursors of acid rain. According to Zhang et al. (2012), iron ore sintering accounts for 73.9% of the total 1.76 Mt SO_2 emissions from the iron and steel industry in 2010, which contributes to 7.5% of SO_2 emissions in China.

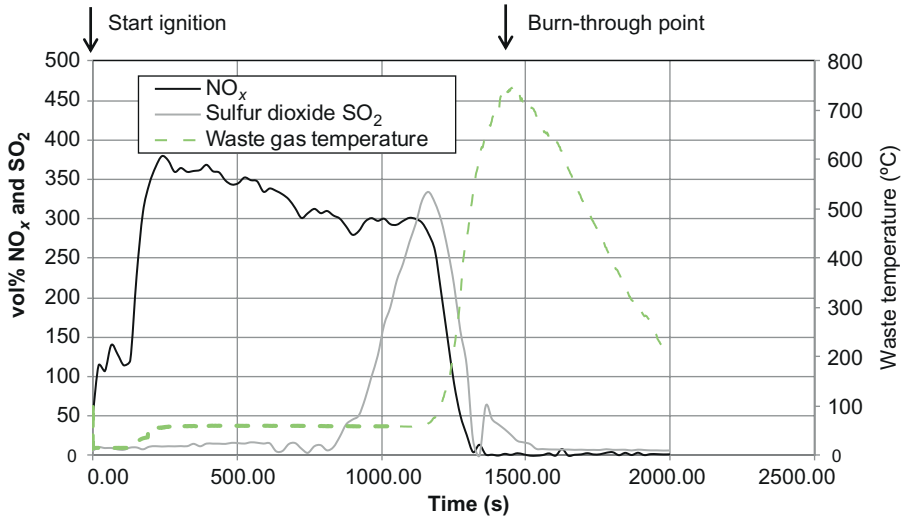

Figure 18.5 SO_2 and NO_x concentrates measured in the waste gas during a sinter pot test on a typical sinter blend.

Therefore, reducing SO_x emissions from sintering plants is important not only for the sustainable development of iron and steel industry but also for environmental protection. Figure 18.5 shows the SO_2 concentrate measured in the waste gas during a sinter pot test on a typical sinter blend. Unlike CO_2 and NO_x emissions occurring across the entire sintering cycle from ignition to the burn-through point, the major portion of total SO_2 emissions is generated near the burn-through point due to the condensation of SO_2 vapor in the wet zone of the sinter bed.

18.3.2 Mitigation of SO_x emissions

SO_x removal has been achieved by installing sintering flue gas desulfurization (SFGD) equipment. In addition to the conventional wet-type, dry-type desulfurizing systems, utilizing activated coke adsorption are now used. However, the low SO_2 content and large volume of sintering flue gas make it very difficult to capture SO_2, which leads to extremely high capital and operational costs in practice. Furthermore, complex by-products are also the bottlenecks for the existing SFGD processes. The Emission Optimized Sintering (EOS®) is a process developed by Outokumpu Technology in the 1990s where the entire sinter strand is housed within an EOS hood and the waste gases from the entire strand are partially recirculated back to the full surface of the strand. Figure 18.6 shows the difference in principle between the EOS® process and the conventional sintering process. As a result of the partial flue gas recirculation system, the EOS® process (Anon, 2014)

- minimizes off-gas volume by 50–60% and consequently cut off-gas cleaning investment costs,
- uses the CO content and heat from the recirculated gas as an energy source and consequently saves energy by up to 20% (in the form of coke) and reduces operational costs,
- significantly minimizes dust, NO_x, SO_x, CO, and CO_2 emissions.

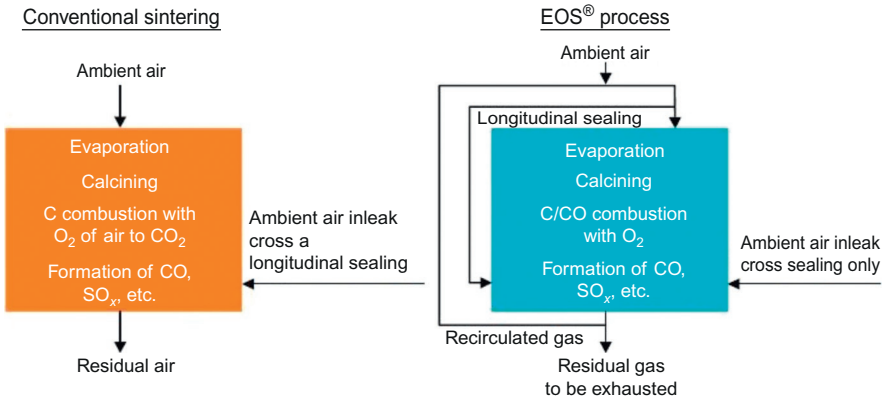

Figure 18.6 Comparison between the EOS process and conventional sintering processes. Outotec (2008).

While the EOS® system can be retrofitted to existing sintering strands with minimum production interference, it involves capital investment.

Almost the whole of the input sulfur from the sinter mix is thought to be oxidized and transferred to the gas phase in the form of SO_x, so SO_x emissions mostly originate from sulfur contained in the coke used as fuel and high sulfur-bearing ores. Therefore, SO_x emissions can be economically and effectively reduced via selective use of fuel with a low sulfur content. Compared with coke breeze, some biomass materials contain less S and have reportedly been used to substitute for coke breeze to reduce SO_x emissions (Gan et al., 2012). The application of biomass in iron ore sintering will be discussed separately. Similarly, the substitution of MIRs for coke has also been reported to be an effective SO_x mitigation measure, because most of the sulfur originates in the coke breeze (Nakano et al., 1998). Actual SO_x emissions from the sintering process may also depend on the basicity of the sinter mixture. With calcium oxide (CaO) dominated sinter mixtures, SO_2 production can be decreased by increasing the basicity (Mahmutović and Muhamedagić, 2009). For magnesium oxide (MgO)-dominated mixtures, about 97% of the sulfur content is converted to SO_2. Mo (1997) investigated the methods of depressing NO_x and SO_x formation in iron ore sintering rather than treating the waste gases and concluded that urea was a potential additive for in-bed de-SO_x. Charging 0.03 wt.% urea can lead to 85% depression of SO_x emissions. FTIR analysis of suspended particles collected from sinter pot waste gases also indicated that ammonium sulfate and bisulfate were formed when urea was added into the sinter mix.

18.4 NO_x emissions and their mitigation technologies

18.4.1 Characteristics of NO_x emissions

NO_x is associated with air pollution problems such as "photochemical smog." In Japan, the amount of NO_x emitted from sintering plants accounts for the majority of total NO_x emissions from integrated steelworks (Morioka et al., 2000). In China, the

NO_x produced in iron ore sintering also amounts to the major NO_x emissions from the integrated ironworks and steelworks, accounting for around 6% of total national NO_x emissions (Chen et al., 2009). Figure 18.5 also shows the NO_x concentration measured in the waste gas during a sinter pot test on a typical sinter blend. Like CO_2, NO_x emissions occur across the entire sintering cycle from ignition to the burn-through point, which is very different from that observed for SO_x emissions.

18.4.2 Mitigation of NO_x emissions

NO_x removal is achieved in various combustion plants by installing ammonia NO_x removal equipment. However, the huge reaction area required to treat the large waste gas volume and the huge construction cost make it uneconomical to install ammonia NO_x removal equipment for the treatment of waste gas from sintering plants. Considerable research has been conducted on the formation mechanism of NO_x within sintering beds. Research (Nakano et al., 1998; Mo et al., 1997) from Japanese steelworks indicated the following:

- There was almost no thermal NO_x (or prompt NO_x), but fuel NO_x was identified in the sintering process.
- The NO_x emitted was predominantly NO, while the NO_2 emitted was only minor at several ppm.
- The conversion ratio of nitrogen in coke to NO decreased with increasing CO/O_2 ratio in the gas boundary film on the surface of coke particles.
- The NO conversion ratio was found to decrease with increasing coke breeze consumption, minipellet granulation of coke, mixing coke with BOF dust, and the use of quicklime.

Therefore, like SO_x, NO_x emissions can be economically prevented via selective use of fuel with low-nitrogen content or control of the combustion process. As 80–90% of NO_x emissions originate from the combustion of fuel in iron ore sintering, selective use of fuel with low-nitrogen content is a practical measure for decreasing NO_x emissions. Compared with coke breeze, some biomass materials contain less N and have been used to substitute for coke breeze to reduce NO_x emissions (Gan et al., 2012). However, the availability of low-nitrogen fuel is very limited.

NO_x emissions can also be prevented via control of the combustion process. Instead of treating the waste gases, Mo et al. (1997) proposed a different approach, aimed at reducing the formation of NO_x during sintering. They found that rice husk and sugar had the potential to improve the sinter bed permeability and shorten the duration of high temperature in the combustion zone. The experimental results showed that the NO_x concentration was decreased from 223 to 160 ppm and emissions were decreased from 533.8 g/t sinter to 283.3 g/t sinter by adding 1% sugar. The addition of sugar was found to have no adverse impact on sinter quality, but it substantially improves the sintering productivity.

The NO_x emissions during coke combustion are greatly affected by the minerals present in coke; active components in the minerals (such as Na and Fe) suppress the conversion of fuel nitrogen to NO_x, while the inert component (such as Ca) can lead to an increase in the NO_x concentration (Kopsel and Halang, 1997; Zhao et al., 2006). In general, the coke mineral components suppress the conversion of fuel nitrogen to NO_x during coke combustion (Zhao et al., 2003). Based on this principle, a new NO_x

reduction method, named "In-bed-deNO_x," has been proposed to reduce the conversion ratio of fuel nitrogen to NO_x by using additives. Morioka et al. (2000) investigated the in-bed-deNO_x process by adding Ca and Fe oxides (CF) into the sinter mixture. The NO_x emissions were found to decrease with increasing levels of CF pellets charged into the sinter bed and with the substitution of fine limestone powder for coarse limestone. The addition of CF pellets is believed to play a role in eliminating NO_x production. NO_x emissions were also investigated by Chen et al. (2009) using a quartz fixed-bed reactor and sinter pot tests with CeO_2 modified coke. The results showed that CeO_2 was catalytically active in promoting not only coke combustion but also NO_x reduction. In coke combustion experiments, both NO_x and CO emissions were found to decrease with increasing CeO_2 loading up to 2.0 wt.% and decreasing CeO_2 particle size (28–150 μm), while sinter pot tests showed that NO_x emissions decreased by 18.8% with 2.0 wt.% CeO_2 modified coke as sinter fuel.

18.5 Dioxin emissions and their mitigation

18.5.1 Background

PCDD/Fs are reported to be linked to an increase in the occurrence rate of certain cancers in humans and a change in the sex ratio to an excess of female births from parents highly exposed to tetra-CDD (Anderson and Fisher, 2002). There is growing environmental concern worldwide about PCDD/Fs, the sources and fates of these compounds, and their effects on animal and human health. The dioxin formation potential of a simple sinter mixture composed of iron ore, coke, and limestone is lower than that of fly ash from a municipal solid waste incinerator (MSWI) (Suzuki et al., 2004). Nevertheless, the sintering process is identified as a significant source of PCDD/Fs after MSWIs. PCDD/Fs can be formed from chlorine and precursor compounds like oily additives during iron ore sintering. Potentially, PCDD/F emissions can be released from the sinter machine wind boxes close to the burnthrough point with SO*x*, the sinter machine discharge point, and sinter product processing operations (i.e., crushing, screening, and cooling). Because of the high temperatures used in sintering operations, it is probable that sinter plant PCDD/F emissions occur in both gaseous and particulate forms.

18.5.2 De novo formation characteristics of dioxins

The sintering bed can be divided into different reaction zones relative to the position of the flame front (the layer of burning coke particles) based on the physical and chemical changes of the sinter mixture due to the impact of heat generated from coke combustion at the flame front. Figure 18.7 shows a schematic diagram of the zone structure developed vertically through a sintering bed. There are essentially four zones from top to bottom: sintered material, sintering (flame front), calcined/dry, and wet zones. As a result of downdraft combustion, the moisture in the sinter mix vaporizes and migrates downwards with the airflow under suction, leading to the formation of the calcined/dry zone 20–30 mm ahead of the flame front. The wet zone develops as a

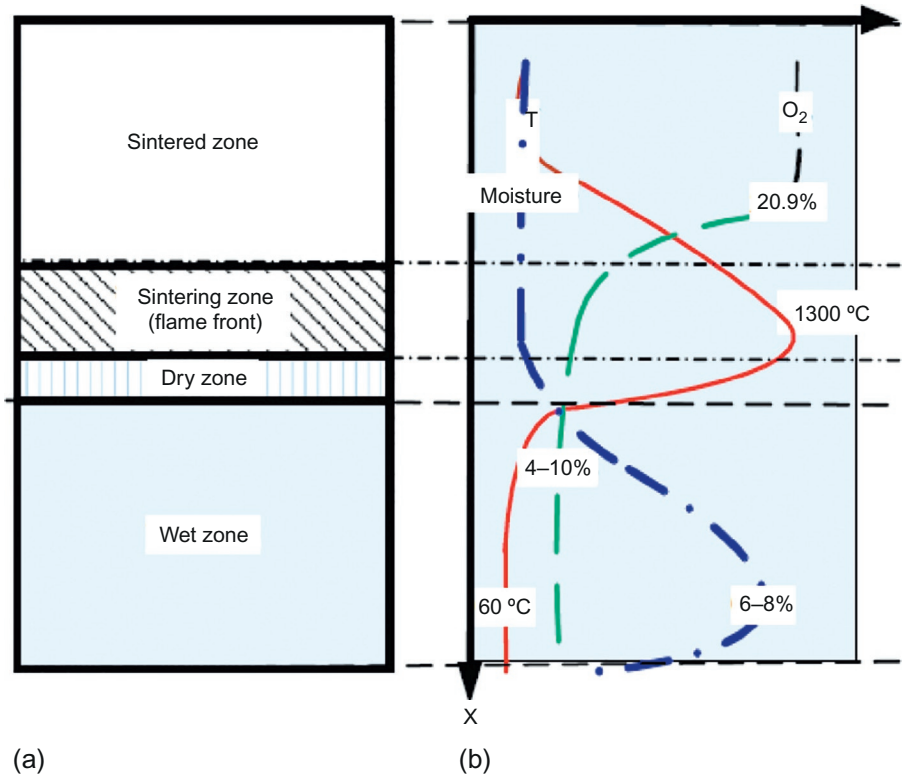

Figure 18.7 Schematic diagram of the zone structure developed vertically through a sintering bed Ooi and Lu (2011).

result of condensation of water vapor entrained in the downdraft airflow as the airflow passes through the calcined/dry zone. From the zone structure and concentrations of PCDD/Fs generated, Fisher et al. (1998) hypothesized that PCDD/Fs form via *de novo* synthesis inside the sintering bed. This was supported by experiments whereby the addition of urea to the sinter bed lowered PCDD/F emissions, while the injection of urea into the wind box produced no significant effect (Anderson et al., 2001; Kasai et al., 2001a). Nakano et al. (2005, 2009) observed high levels of PCDD/Fs in the dry zone of an interrupted sintering bed, 10–30 mm in front of the flame zone. This suggests that PCDD/Fs are possibly formed in the dry zone ahead of the flame front. Formation of PCDD/Fs in the dry zone has been attributed to the higher levels of carbon soot, chloride, and salts of transition metals in this zone as a result of migrations within the unfired portion of the sintering bed (Nakano et al., 2005).

In addition to moisture, there are a broad range of thermal and oxidizing conditions in the dry zone, which may be conducive for the *de novo* formation of PCDD/Fs (Suzuki et al., 2004; Ooi and Lu, 2011). Possible factors leading to the formation of dioxins in the dry zone are that the temperature of the dry zone ranges from 200 to 650 °C and the oxygen concentration of the gas flowing through the zone is about 10–15%.

The optimal temperature for the *de novo* formation of dioxins on incinerator fly ash is around 300 °C. There are also carbon and chlorine sources in the dry zone, which the *de novo* synthesis requires. Coke is a major carbonaceous material in the sintering bed, but soot in ESP dust can also act as a carbon source for dioxin formation, since it is usually recycled as a raw material for sintering. Furthermore, soot may form in the sintering bed and some of it may become trapped in the dry zone. The chlorine compounds in the sinter mixture are mainly alkali chlorides, such as KCl and NaCl, that are transformed by high-temperature reactions to gaseous species such as HCl and Cl_2 or minor vapors of various metallic chlorides. The mixture of raw materials may also contain a very small amount of copper compounds (usually less than 50 mg Cu/g) that are known to act as strong catalysts in the *de novo* synthesis of dioxins.

After examining the macroscopic behavior of dioxin formation in the sintering process of iron ores for two different sinter plants, Kasai et al. (2001a) found that PCDD/Fs possibly formed in the wind boxes and ESP as well as in the sintering bed and the dioxins formed in the sintering bed tend to be discharged in the later stage of sintering, similar to SO_x and HCl. As the flame front moves downwards in the sintering bed, some PCDD/Fs formed are thermally decomposed (or dechlorinated), particularly higher chlorinated congeners due to their proximity to the flame front, while other less chlorinated species are volatilized. The PCDD/Fs in the gas phase recondense as they migrate into the regions closer to the wet zone, which is approximately 60 °C. The vaporization and condensation process proceeds as the flame front travels downwards, resulting in PCDD/Fs being retained in the bed. Finally, PCDD/Fs are released into the exhaust gas as the flame front reaches the bottom of the sinter bed. Kasama et al. (2006) had conducted a detailed analysis of the exhaust gas at the NSSMC Oita No. 1 sinter plant to determine the strand positions where dioxins are released into the exhaust gas. The release of dioxins was detected at two different positions. The first release position was located at the point where the drying zone reached the hearth layer, showing a broad peak containing a large amount of furans. The second release position was located at the point where the melting zone reached the heath layer, showing a sharp peak. The difference in dioxin congeners between the release positions implies different mechanisms of dioxin formation. The dioxins collected at the second release point were considered to be formed in the wind boxes at temperatures of 300 °C or more (Kasama et al., 2006). Ensuring that the burn-through point is at the discharge end of the sinter strand is reported to be effective for mitigating dioxin emissions from the second release point.

18.5.3 Mitigation of dioxin emissions

PCDD/F emissions can be controlled and reduced to a certain degree by secondary measures (end-of-pipe treatments), that is, ESP or wet fine scrubbing systems. Guerriero et al. (2009) analyzed the performance of secondary measures such as an ESP and a wet fine scrubbing system (WS) in an iron ore sintering plant in Italy. Based on this study, the removal efficiencies of ESPs with respect to total PCDD/F concentration and total PCDD/F I-TEQ concentration are 44.3% and 41.4%, respectively, while those of the WS are 66.7% and 68.4%, respectively. However, the PCDD/F

distribution between the vapor and solid phases changes after the air pollution control devices (APCDs) are installed at sintering plants. By means of secondary measures, it appears that the pollutants are removed from the gases, but the total amount of PCDD/Fs entering the environment does not necessarily decrease in the process. As a consequence, the PCDD/Fs bearing wastes, usually dust and water, are often recycled to avoid disposal costs, to recover iron-bearing materials, and also to avoid additional emission burdens on the environment. However, this practice can increase the amount of PCDD/Fs present in the emissions by as much as a factor of 10^3 (Kasai et al., 2001a; Guerriero et al., 2009; Xhrouet and Pauw, 2004). For this reason, effective primary measures rather than end-of-pipe technologies are needed to reduce and suppress dioxin formation in the sintering bed.

The factors influencing the formation and emission of PCDD/Fs have been the subject of extensive investigations (Xhrouet and Pauw, 2004; Yu et al., 2012; Kawaguchi et al., 2002a,b,c; Matsumura et al., 2006a; Kasai et al., 2001b; Nakano et al., 2005; Suzuki et al., 2004; Ooi and Lu, 2011), and the measures for reducing dioxin emissions are as follows:

- Optimization of process variables to avoid conditions conducive to the formation of dioxins.
- Stable and consistent process conditions, that is, steady-state operations, minimization of process upsets, and minimization of strand stoppages.
- Minimization of feeding materials contaminated with persistent organic pollutants or contaminants leading to the formation of such pollutants, for example, minimization of chlorine input, mill scale deoiling, and avoiding processing of ESP sinter dusts.
- Feed material preparation, that is, agglomeration of fine materials, to minimize fugitive emissions in handling.
- Addition of inhibitors, such as urea, and partial replacement of coke with anthracite and biomass.

The following discussion will mainly focus on the effect of process variables, raw materials, and additives on the formation and emissions of dioxins.

18.5.3.1 Process variables

The dependence of PCDD/F formation on temperature during sintering is similar to that of *de novo* synthesis occurring during the incineration of municipal solid waste in that the highest level of PCDD/F formation occurs at approximately the same temperature of 300 °C (Ooi and Lu, 2011). A series of experiments were carried out by Suzuki et al. (2004) at four different temperatures between 300 and 550 °C using a sinter mixture impregnated with 0.1% $CuCl_2$. The total amounts of PCDDs, PCDFs, and coplanar polychlorinated biphenyls (Co-PCBs) appeared to be the highest at 300 °C in the experimental temperature range and decreased with further increase in temperature. The temperature distribution inside a sintering bed is dictated by the addition of fuel in the sinter mixture. The effect of coke rate on dioxin emissions was therefore investigated using pilot-scale sinter pot tests (Yu et al., 2012). The concentration of dioxins in the flue gas appeared to decrease with increasing coke rate most likely due to the less conducive temperature at the higher coke rate for the formation of dioxins.

Factors affecting dioxin emissions from iron ore sintering machines have been investigated by means of sinter pot tests (Nakano et al., 2009). The bed height, coke content, gas velocity, and afterburner were found to have insignificant effects. However, dioxin emissions were found to increase as the hearth layer increased and the distance of the burn-through point from the ignition hood decreased. Based on their observations, the authors further suggested that the hearth layer and wind boxes could be other synthesis sites in addition to the dry zone of the sintering bed, which was further confirmed by plant observations (Kasai et al., 2001a; Kasama et al., 2006). According to Kasama et al., setting the burn-through point at the sinter discharge point is effective for decreasing the emission of dioxins formed in the wind boxes (Kasama et al., 2006).

Dioxins are considered to form with oxidation of residual carbon particles formed from the solid fuels in the sintering process, and dioxin emissions were found to decrease with decreasing O_2 concentration (Matsumura et al., 2006a). The effect of H_2O concentration in the inlet gas on dioxin emissions was also studied by the same authors. Increasing the H_2O concentration by injecting steam into the inlet gas was found to decrease dioxin emissions (Matsumura et al., 2006a). However, in similar research by Suzuki and coworkers, moisture was found to have little effect on the total amount of dioxins emitted.

Therefore, controlling the processing variables and making them more consistent are effective mitigation measures to reduce the emission of dioxins formed in the sintering bed or in the wind boxes.

18.5.3.2 Raw materials

For sintering, it is generally accepted that PCDD/Fs are formed through *de novo* synthesis (Fisher et al., 1998; Kasai et al., 2001b; Ooi and Lu, 2011), because PCDD/Fs evolved from this process show the typical relative abundance or "fingerprint" of congeners developed from this pathway in waste incineration. The *de novo* synthesis firstly proceeds through the transfer of chloride (halide) to a macromolecular structure of the residual carbon, catalyzed by metal ions, followed by oxidative degradation of the carbon matrix, primarily to CO_2, with the release of aromatic halogens such as PCDD/Fs as by-products (Ooi and Lu, 2011; Stieglitz et al., 1989, 1991, 1993, 1997). Therefore, the carbon and Cl contents of the raw materials used for iron ore sintering are important to the formation of dioxins. This is supported by Kawaguchi et al. (2002a), who reported that the properties and contents of the solid fuels and chlorides in the raw mixture significantly affect dioxin emissions during the iron ore sintering process.

The behavior of trace Cl in the sintering bed and its effect on dioxin concentration in the flue gas from iron ore sintering were studied by Kawaguchi et al. (2002b). Sinter pot tests on sinter mixtures with the addition of Cl up to 500 mg/kg showed that the concentration of dioxins in the flue gas was proportional to the Cl content in the mixture. From their microscopic studies of dioxin emissions from two Japanese sinter plants, Kasai et al. (2001a) concluded that the PCDD/F concentrations in the exhaust gas of sintering machines were roughly related to the total chlorine content of the raw materials. The Cl source also affects the dioxin concentration in the flue gas

with sinter mixtures containing KCl reporting the highest dioxin concentration in the flue gas, followed by polyvinyl chloride, NaCl, $CaCl_2$, and high Cl ore in descending order. In their study of the *de novo* formation characteristics of dioxins in an iron ore sintering bed, Suzuki et al. (2004) investigated the effect of adding HCl through the inlet flow on the degree of chlorination and the total amount of dioxins formed in the outlet gas flow and in the sinter mixture, and found that the gaseous HCl contributed to chlorination during dioxin formation under their experimental conditions. It was concluded that not only the chlorine present in the sinter mixture but also HCl in the gas flowing through the sinter bed plays important roles as a chlorine source for the formation of dioxins in sinter mixtures.

Solid fuel is another important factor influencing dioxin formation as it constitutes the principal source of carbon for the *de novo* synthesis of PCDD/Fs in the sintering bed. Metallurgical coke has been reported to give higher dioxin emissions than other carbonaceous materials, such as anthracite, coal, and activated coke and coal (Kawaguchi et al., 2002c). The *de novo* synthesis of PCDD/Fs in the sintering process was simulated at the laboratory scale by thermal treatments of the samples (Xhrouet and Pauw, 2004). The authors found that the use of a particular coke as fuel does not drastically reduce the formation of PCDD/Fs. Actually, the global amounts of PCDD/Fs generated from graphite and two cokes tested in the study were very similar. Similarly, Suzuki et al. (2004) found that the total amounts of dioxins formed were nearly equal for sinter mixtures loaded with coke and activated coke. However, there was a large difference in the homologue distribution profiles of PCDD/Fs, especially PCDFs, observed for sinter mixtures containing coke and activated coke. No difference in the behavior of dioxins, Cl, and Cu in the dry zone were observed between the mixtures containing activated coke and metallurgical coke.

18.5.3.3 Additives

Kawaguchi and coworkers (Matsumura et al., 2006b; Kawaguchi et al., 2002a) studied the effect of additives on the formation of dioxins in the sinter process and found that some substances, especially copper and its compounds (Cu, CuO, and $CuCl_2$), act as catalysts to promote the formation of dioxins, while others, such as ammonia and nitrogen-bearing organic compounds, for example, urea, ethylene-*di*-amine, and monoethanolamine, act as inhibitors. As shown in Figure 18.8 (Matsumura et al., 2006b), the release of active nitrogen components like NH_i ($i = 1$–3) and CN at elevated temperatures in the dry zone from the decomposition of ammonia and its compounds is believed to suppress the formation of dioxins. Nakano et al. (2005) suggested that ammonia, urea, and monoethanolamine decrease the peak concentration of Cl in the dry zone and therefore inhibit the in-bed formation of dioxins. Matsumura et al. (2006b) reported 13-fold increases in penta-CDF formation as a result of a 400 mg/kg addition of CuO in raw sinter mixtures. The reactivity of Cu for *de novo* synthesis of dioxins decreases in the following order, that is, $CuCl_2 > CuO >$ metallic $Cu > CuSO_4$ (Matsumura et al., 2006b). $CuCl_2$ acts as both a catalyst and source of requisite Cl. The transition metals (e.g., Ni, Cu, Cr, and Ti) are believed to promote the formation of PCDD/Fs by catalyzing reactions preceding those suggested for the formation of

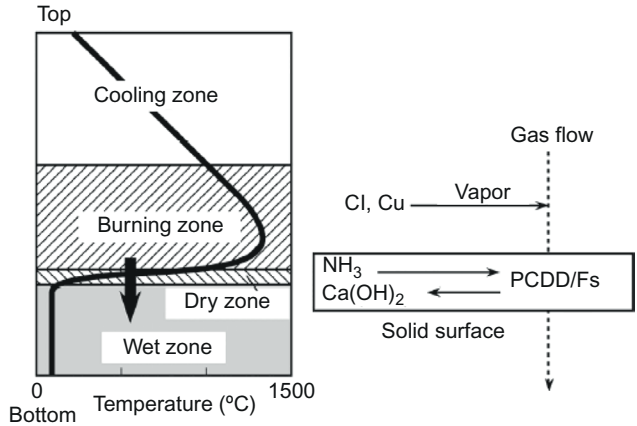

Figure 18.8 Behavior of Cu, NH_3, $Ca(OH)_2$, and PCDD/Fs in the sintering bed Matsumura et al. (2006b).

PCDD/Fs, viz., the Deacon and Ullmann reactions (Ooi and Lu, 2011). As shown in Figure 18.8, copper chlorides vaporizing in the flame front move to the dry zone with gas flow and are adsorbed at a solid surface, such as residual (unburned) carbon and soot in the dry zone, where the carbon oxidation reaction takes place in the presence of $CuCl_2$ as a catalyst, resulting in the formation of PCDD/Fs through *de novo* synthesis (Matsumura et al., 2006b; Nakano et al., 2005).

The effect of additives, namely, PVC, NaCl, oil, mill scale, anthracite, and dusts from steelworks, was evaluated using sinter pot tests (Kasai et al., 2001b). The additives were chosen in terms of organic/inorganic chlorine sources, volatile matters convertible to "soot" during combustion, and so forth. Significant increases in the discharged amount of PCDD/Fs were found with the addition of ESP dust. Similar results were also reported by Xhrouet and Pauw (2004) that the addition of 10 wt.% dust collected in the ESP leads to the formation of more than 1000 times the amount of PCDD/Fs. Factors affecting dioxin emissions from sintering machines were investigated by Nakano et al. (2009) using sinter pot tests and multiple regression analysis of commercial plant data. ESP dust, BF dust, and purchased scale were major dioxin accelerators, while quicklime was a dioxin suppressor.

In a study designed to clarify the influence of operating conditions on the formation and emissions of PCDD/Fs from sintering with hot flue gas recycling, Yu et al. (2012) found that the quality of quicklime used in the sinter mixture affected not only the sintering productivity but also the amount of PCDD/F emissions, which decreased markedly with improvement in quicklime quality. Quicklime is believed to reduce the chlorination atmosphere by reacting with HCl to suppress the formation of PCDD/Fs.

In summary, precautions are needed when waste materials such as ESP dust are recycled through the sintering process. However, the concentration of dioxins in the resultant sinter does not increase due to the recycling of EP dust, because dioxins initially contained in the raw materials are mostly decomposed during sintering (Kasai et al., 2001b).

18.6 Dust emissions and their reduction

18.6.1 Background

Sinter plants are the major contributor to dust emissions from integrated ironworks and steelworks. The dust emissions from sinter plants are generated from raw material handling, wind box exhausts, the discharge end of the sinter strand associated with sinter crushers and hot screens, the cooler, and cold screens. The wind box emissions represent about 60% of the total particulate emissions from the sinter plant, followed by discharge end emissions. As legislated limits become more and more stringent, sinter plants are under increasing pressure to further decrease emissions. One of the best available techniques for dedusting is the use of electrostatic precipitation plus fabric filter to remove particulate matter, which is associated with particulate matter emission concentrations of 10–20 mg/m^3 (UK Environment Agency, 2004). Other dedusting options that are commonly used for sinter plant off-gases include ESPs and wet scrubbers, but particulate removal efficiency is not as high as for fabric filters. ESPs and high-efficiency wet-gas scrubbers perform well with particulate matter concentrations of 30–50 mg/m^3 (William Lemmon and Associates Ltd., 2003). In addition to the control of dust emissions from the wind boxes, adequately sized capture and dedusting controls for both the feed and discharge ends of the sinter strand should be put in place. Crusher and hot screen emissions are usually controlled by hooding with a baghouse or scrubber, while emissions generated from other material handling operations are captured and vented to a baghouse.

18.6.2 Characteristics of dust emissions

The wind box off-gas is the primary source of particulate emissions, which are generally associated with black carbon (BC) and heavy metal (HM) emissions. BC can be formed in the sintering bed and entrained in the flue gas. During the sintering process, some of the HMs in the raw materials, such as zinc (Zn), lead (Pb), and cadmium (Cd), may be volatilized or converted into volatile compounds (e.g., chlorides) and can therefore be found in the flue gas. Arsenic (As) is emitted in gaseous form as As_2O_3, passing through the dry gas cleaning facilities, which are usually operated at 120 °C. In addition, the wind box off-gas also includes iron oxides, sulfides, carbonaceous material, and some hydrocarbons. The fine particles entrained in the sinter off-gas have extremely large surface areas for adsorption and condensation of gaseous pollutants, including PCDD/Fs. The fine particles collected in the filters contain a much higher content of HMs and other pollutants than the raw gas dust or the sinter mixture. Therefore, effective removal of dusts can help reduce emissions of HMs and PCDD/Fs. However, since hazardous volatile compounds are formed or adsorbed on the fine particles, they may be accumulated during the recycling of the fine particles that are captured by the gas cleaning facilities. The dust emissions at the discharge end and from raw material handling consist mainly of iron and calcium oxides.

18.6.3 Factors influencing dust emissions from iron ore sintering

Over the years, major efforts have been made in mitigating the dust emissions from the sinter plant and a number of different technologies are now available. However, most of these technologies are secondary measures and not the key focus of this chapter. The factors influencing the particulate emissions from the sintering bed have been investigated in detail by Debrubcat and Loo (2007). A blend fairly typical of that currently used in the Asia Pacific region, as well as another containing 30 mass% Marra Mamba ore, was tested. The authors (Debrubcat and Loo, 2007) found the following:

- Most particulate emissions had sizes less than 1.18 mm, indicating that they come mostly from the adhering fines layer of granules. Therefore, improving the adhesion between ore particles by increasing the moisture level (5.5–9.0%) decreased the particulate emission level. On the other hand, increasing the coke (5.5–7.5%) rate increased the particulate emission level.
- Decreasing the pressure drop just before the burn-through point led to a decrease in particulate emissions. The particulate emissions become coarser as the flame front moves further down the bed.
- Most particulate emissions originate from the calcination and dried zones. The production of KCl fume and the entrainment of particles by water flowing from the bed also contribute, but to a lesser extent. Most particulate emissions come from the bed at the end of sintering as the wet zone decreases in size until it cannot fully scrub the particles from the gas.
- The particulate emissions have higher coke levels than the 4.0 mass% in the raw sinter mixture. In addition, the Cl content is higher in the −0.3 mm fraction (0.18–0.26%) than the +0.3 mm fraction (0.036–0.11%) of the particulate emissions.

Therefore, optimizing the mixture moisture content, coke level, suction pressure, and burn-through point is an effective primary measure to mitigate particulate emissions from the sintering process.

18.7 Utilization of biomass materials in iron ore sintering

18.7.1 Background

From sinter pot tests carried out using raw biomass and biomass-derived char, Kawaguchi and Hara (2013) suggested that raw biomass is not suitable for direct use as a heat source for iron ore sintering. This is because raw biomass contains a high moisture content, low carbon content, and low specific energy. Therefore, pyrolysis is necessary to produce charcoals that are chemically more similar to coal/coke, which is widely used in the iron and steelmaking industry. Only limited work has been conducted to investigate the application of charcoal in the sintering process to replace coke breeze, with this work mainly focused on its environmental impacts and at low substitution rates.

18.7.2 Effect of substitution of biomass on CO_2 emissions

Biomass is carbon-neutral and renewable because the carbon cycle via wood (biomass) is very short (5–10 years) compared to fossil coal (approximately 100 million years).

Therefore, replacement of fossil fuel-based carbon with renewable carbon derived from biomass is seen as offering the greatest potential for reducing the greenhouse gas footprint of steel production (Norgate et al., 2012). The effect of substitution of charcoal for coke on CO and CO_2 emissions was investigated by Lu et al. (2013). As shown in Figure 18.9, both the CO and CO_2 concentrations in the sintering off-gas increased with increasing substitution of charcoal for coke breeze. This was further confirmed by Kawaguchi and Hara (2013). Therefore, substitution of charcoal does not lead to a reduction in CO_x emissions. In fact, it reduces the combustion efficiency as evidenced in Figure 18.9c. However, because it is carbon-neutral, substitution of charcoal for coke in sintering will potentially reduce the net CO_x emissions.

18.7.3 Effect of substitution of biomass on toxic emissions

Compared with coal and coke, charcoal is much lower in sulfur and nitrogen contents, which lowers SO_x and NO_x emissions. All research (Kawaguchi and Hara, 2013; Gan et al., 2012; Lu et al., 2013) has so far reported reduced concentrations of SO_x and NO_x in the sintering off-gas resulting from the substitution of charcoal for coke in sintering (Figure 18.10). Sinter pot tests with the addition of raw agriculture biomass (oil content: 0.55%) to a sinter mix containing anthracite and coke were carried out to investigate the effects of raw biomass on the dust concentration in sintering off-gas. The dust concentration in exhaust gas was found to increase with increasing addition ratios of raw biomass (Kawaguchi and Hara, 2013). However, the dust concentration in the case of biomass char is reduced compared with coke or anthracite. As Cl, S, and

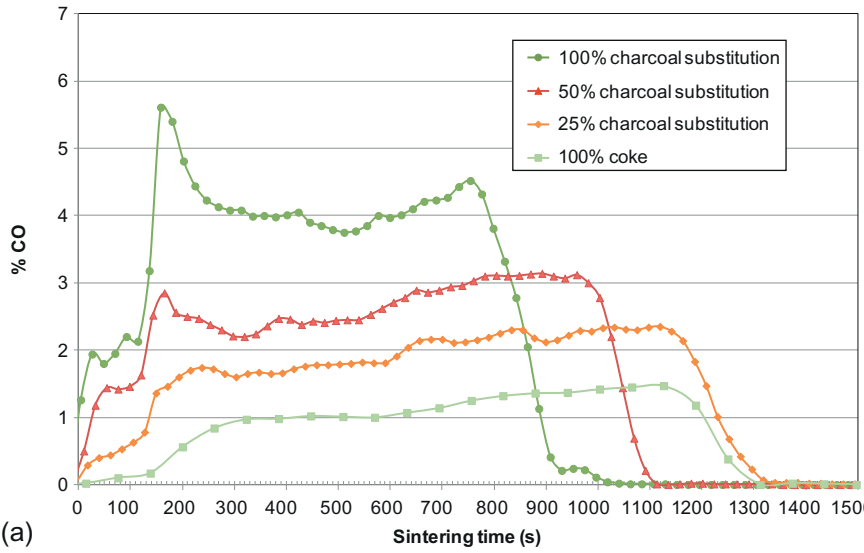

Figure 18.9 (a) CO and (b) CO_2 concentrations in the sintering off-gas and (c) combustion efficiencies during sintering of sinter mixtures with increasing charcoal substitution.

(Continued)

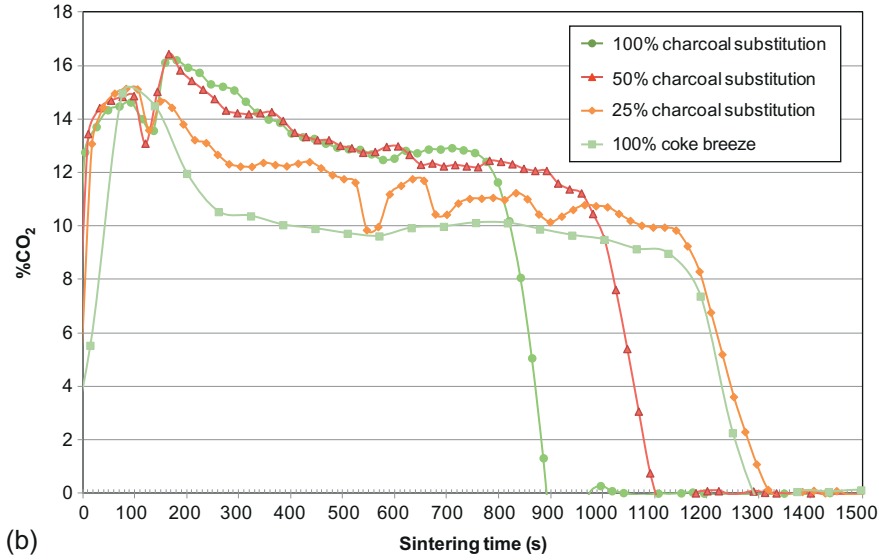

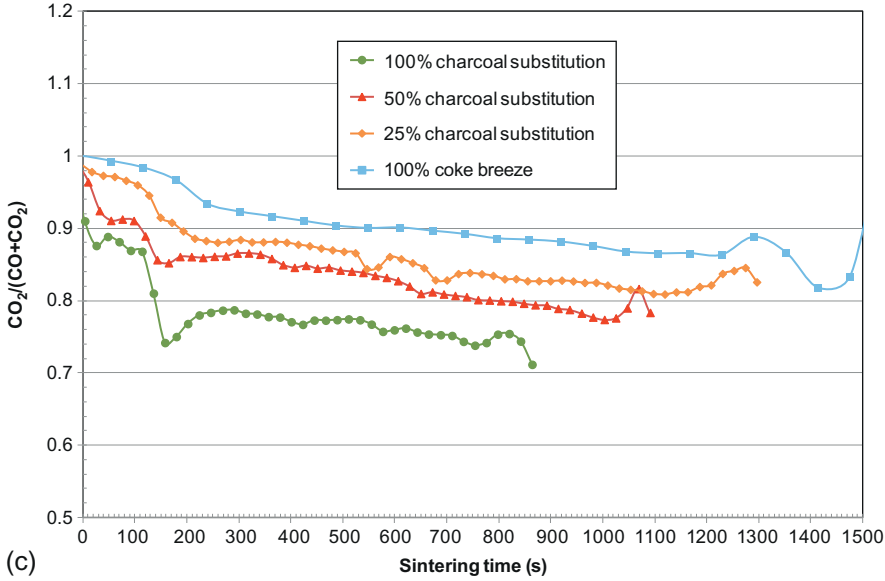

Figure 18.9 Continued

N compounds are the main factors that determine dust concentrations in the off-gas, the reduction in dust concentration is most likely due to the low N and S contents of the biomass char.

A study (Ooi et al., 2011) was carried out into the use of hardwood charcoal as a supplementary fuel in the sintering process. The primary fuel was coke breeze with 0%, 20%, 50%, and 100% replacement of the energy input by charcoal to produce raw

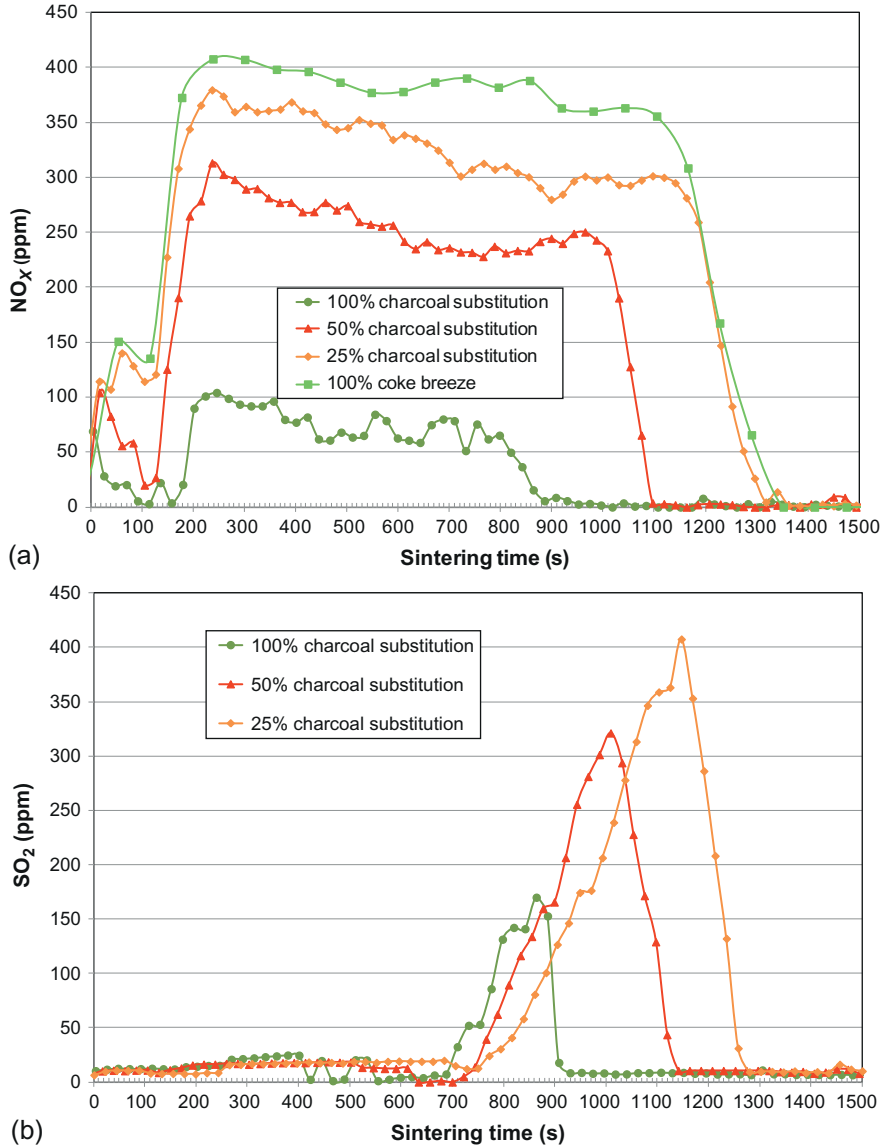

Figure 18.10 (a) NO_x and (b) SO_2 concentrations measured in the sintering off-gas of sinter mixtures with increasing charcoal substitution.

sinter mixtures with the same heat output as 4.0 wt.% coke breeze. At the optimum rate of 20% substitution of coke breeze energy input with charcoal, the emission of dioxins was similar to that observed with coke breeze alone as the fuel. The same authors (Ooi et al., 2008) have also tested sunflower seed husks as a supplementary fuel in the sintering process and achieved similar results. The replacement of 10% coke

breeze with an equivalent amount of energy from sunflower husks did not result in increased emissions of persistent organic pollutants such as PCDD/Fs and polycyclic aromatic hydrocarbons (PAHs).

18.7.4 Effect of substitution of biomass on sintering performance

The majority of previous work on the application of biomass in sintering has been focused mainly on its environmental impact at low substitution rates. Lu et al. (2013) studied the effect of substitution of treated charcoal on green bed permeability and found that substitution of treated charcoal for coke breeze in the sinter mixture increased the moisture requirement for optimum granulation. The green granules formed from the sinter mixture containing the treated charcoal were clearly less dense and formed a less compacted green bed as evidenced by the packing density. This together with its unique combustion characteristics results in a fast sintering speed, which is beneficial to sintering productivity. From small-scale sinter pot experiments with an inert bed, comparing coke breeze and 75% coke breeze and 25% biomass fuel (on a constant carbon content basis), Zandi et al. (2010) found that the temperature rise occurred earlier and the sintering time appeared to be shorter when the sinter mix contained biomass compared with coke breeze. Kawaguchi and Hara (2013) also found that the addition of raw biomass had a significant beneficial impact on the sintering speed and permeability of the sintering bed.

The effects of using biomass char with high levels of fixed carbon (>90%), which was carbonized at 900 °C, on sinter yield were investigated by Kawaguchi and Hara (2013). The sinter yield with biomass char was significantly lower than that of coke at the same fixed carbon level. Therefore, the substitution of biomass char for coke leads to a significant increase in energy consumption. An increase in the fuel addition level from 4% to 5% is required to ensure the same sinter yield. In a similar research on the substitution of charcoal for coke, Lu et al. (2013) reported that the fuel addition had to increase from 3.62% to 4.17% as the substitution of charcoal increased from 0% to 50% to retain the same sinter yield. Furthermore, compared with the sinter fired with coke breeze, the sinter from the mixtures containing up to 50% charcoal was marginally weaker in terms of sinter yield, tumble strength (TI), and reduction disintegration index (RDI). The authors (Lu et al., 2013) attributed this to the faster sintering speed, lower packing density, lower combustion efficiency, and more heat loss through the sintering off-gas from the sinter mixture with increasing substitution of charcoal for coke.

18.7.5 Challenges in the utilization of biomass in sintering

The use of charcoal as a fuel and reductant in ironmaking and steelmaking in place of fossil fuel-based carbon sources has been assessed from both an environmental and economic point of view using life-cycle assessment methodology (Norgate and Langberg, 2009; Norgate et al., 2012; Jahanshahi et al., 2014). Based on a long-term price of US$90/t for metallurgical coal, a carbon tax in the order of US$30–35/t CO_2 would be required for charcoal to be competitive with coal in steelmaking applications. In addition, currently, there is only a very limited worldwide charcoal-making capability

that supports silicon manufacture and the barbecue fuel market. However, the potential market within the steel industry is substantial if optimized products can be provided at prices competitive with their fossil-based equivalents. Therefore, there is an urgent need to identify sustainable renewable sources and develop a high-capacity production technology that produces charcoal from renewable sources identified at a low cost with low environmental impact. Finally, the potential biomass materials should achieve the qualities ideally suited to product applications, such as iron ore sintering and BF ironmaking. As discussed earlier, while substitution of charcoal increases the sintering speed, the sinter produced from the sinter mixtures containing high substitution levels of charcoal for coke is generally weaker even when fired at higher fuel rates. While raw biomass materials are not suitable for sintering applications, it is possible to produce optimized products through pyrolysis that either are superior to traditional fuels/reductants or minimize any weaknesses in physical properties. By fine-tuning the pyrolysis conditions and raw biomass materials, Lu et al. (2012) confirmed that the resultant sinter from two sinter blends containing specially designed charcoals had excellent RI, good RDI, and good to reasonable TI, which were all above the minimum quality required for sinter from pilot-scale pot tests.

18.8 Conclusions

Based on the emission characteristics of CO_2 and various toxic species, including SO_x, NO_x, dioxins, and particulate matter, some primary measures aimed at preventing and reducing the formation of these toxic species in the sintering bed have been discussed in this chapter and are summarized as follows:

- CO_2 emission occurs across the entire sintering cycle from ignition to the burn-through point. This is because CO_2 is primarily formed from the combustion of fuel (COG or natural gas) during ignition and carbon in the feed material, including coke breeze and other carbonaceous materials, such as limestone and dolomite. Therefore, measures that lead to a reduction in fuel, limestone, and dolomite consumption will result in the abatement of direct emissions of CO_2 from sinter plants. Of course, a reduction in electricity consumption during sintering will also result in a reduction of emissions indirectly.
- Like CO_2, NO_x emissions occur across the entire sintering cycle from ignition to the burn-through point. As 80–90% of the NO_x emissions originates from the combustion of fuel in iron ore sintering, selective use of the fuel and control of the combustion process are practical primary measures for decreasing NO_x emissions. Some additives, such as Ca and Fe oxides and CeO_2, have been tried to achieve in-bed reduction of NO_x emissions.
- Unlike CO_2 and NO_x emissions, the major fraction of the total SO_2 emission is generated near the burn-through point and mostly originates from sulfur contained in the coke used as fuel. Therefore, selective use of fuel with low sulfur content, including MIRs, can economically and effectively prevent SO_x emissions. Urea was also found to be a potential additive for in-bed reduction of SO_x emissions. Actual SO_x emissions from the sintering process may be further dependent on the basicity of the sinter mixture.
- Dioxins are most likely released from the sinter bed at the point where the drying zone reaches the hearth layer. There are a broad range of thermal and oxidizing conditions in the dry zone, which may be conducive for the *de novo* formation of PCDD/Fs. The formation

of dioxins can be effectively minimized by controlling the processing variables and making them more consistent, selective use of raw materials, and the addition of inhibitors.
- Most particulate emissions come from the bed at the end of sintering as the wet zone decreases in size until it cannot fully scrub the particles from the gas. Optimizing the mixture moisture content, coke level, suction pressure, and burn-through point is an effective primary measure to mitigate particulate emissions from the sintering process.
- While raw biomass materials are not suitable for direct utilization in iron ore sintering, charcoal from biomass materials has potential applications in iron ore sintering as a substitute for coke to reduce SO_x, NO_x, and dust emissions. However, more work is needed to develop potential biomass products to achieve the qualities required in iron ore sintering.

References

Anderson, D.R., Fisher, R., 2002. Sources of dioxins in the United Kingdom: the steel industry and other sources. Chemosphere 46, 371–381.

Anderson, D.R., Fisher, R., Roworth, M.C., Wilson, D.T., Southern, S.M., Fray, T.A.T., 2001. Formation and suppression of PCDD/F in iron-ore sintering. Organohalogen Compd. 54, 100–114.

Anon, 2010. Production and technology of iron and steel in Japan during 2009 (The Technical Society of the Iron and Steel Institute of Japan). ISIJ Int. 50, 777–796.

Anon, 2012. Available and Emerging Technologies for Reducing Greenhouse Gas Emissions from the Iron and Steel Industry. Research Triangle Park, North Carolina 27711: Sector Policies and Programs Division, Office of Air Quality Planning and Standards, U.S. Environmental Protection Agency.

Anon, 2014. Traveling grate sintering [Online]. Outotec. Available: http://www.outotec.com/en/About-us/Our-technologies/Agglomeration/Traveling-grate-sintering/#tabid-1 (accessed 10 September 2014).

Birat, J.P., 2009. Steel and CO_2—the ULCOS program, CCS and Mineral carbonation using steelmaking slag. In: Jones, P.T., Geysen, D., Guo, M., Blanpain, B. (Eds.), 1st International Slag Valorisation Symposium, Leuven, Belgium, pp. 15–26.

Chen, Y., Guo, Z., Wang, Z., 2009. Influence of CeO_2 on NO_x emission during iron ore sintering. Fuel Process. Technol. 90, 933–938.

Dawson, P.R., Ostwald, J., Hayes, K.M., 1983. Calcium ferrites in the new low silica sintering technology. BHP Tech. Bull. 27, 47–51.

Debrubcat, D., Loo, C.E., 2007. Factors influencing particulate emissions during iron ore sintering. ISIJ Int. 47, 652–658.

Fisher, R., Fray, T.A.T., Anderson, D.R., 1998. Investigation of the formation of dioxins in the sintering process. In: International Conference for the Science and Technology of Ironmaking (ICSTI'98), 22–25 March 1998, Toronto, pp. 1183–1193.

Fujino, K., Murakami, T., Kasai, E., 2013. Effect of utilization of metallic Fe particles as an agglomeration agent on the permeability of sintering bed. ISIJ Int. 53, 1617–1624.

Gan, M., Fan, X., Chen, X., Ji, Z., Lv, W., Wang, Y., Yu, Z., Jiang, T., 2012. Reduction of pollutant emission in iron ore sintering process by applying biomass fuels. ISIJ Int. 52, 1574–1578.

Guerriero, E., Guarnieri, A., Mosca, S., Rossetti, G., Rotatori, M., 2009. PCDD/Fs removal efficiency by electrostatic precipitator and wetfine scrubber in an iron ore sintering plant. J. Hazard. Mater. 172, 1498–1504.

Jahanshahi, S., Deev, A., Haque, N., Lu, L., Mathieson, J.G., Norgate, T.E., Ridgeway, P., Rogers, H., Somerville, M.A., Zughbi, H., Zulli, P., 2014. Recent progress in R&D on assessment of the use of biomass/designer chars for steel production. In: Innovation of Ironmaking Technologies and Future International Collaboration—To Overcome Energy & Resource Restrictions in Accordance with Environments, Tokyo, Japan.

Kasai, E., Aono, T., Tomita, Y., Takasaki, M., Shiraishi, N., Shinji, K., 2001a. Macroscopic behaviours of dioxins in the iron ore sintering plants. ISIJ Int. 41, 86–92.

Kasai, E., Hosotani, Y., Kawaguchi, T., Nushiro, K., Aono, T., 2001b. Effect of additives on the dioxins emissions in the iron ore sintering process. ISIJ Int. 41, 93–97.

Kasama, S., Yamamura, Y., Watanabe, K., 2006. Investigation on the dioxin emission from a commercial sintering plant. ISIJ Int. 46, 1014–1019.

Kawaguchi, T., Hara, M., 2013. Utilization of biomass for iron ore sintering. ISIJ Int. 53, 1599–1606.

Kawaguchi, T., Matsumura, M., Kasai, E., Ohtsuka, Y., Noda, H., 2002a. Promoter material and inhibitor material for dioxins formation in sintering process. Tetsu-to-Hagane 88, 370–377.

Kawaguchi, T., Matsumura, M., Hosotani, Y., Kasai, E., 2002b. Behavior of trace chlorine in sintering bed and its effect on dioxins concentration in exhaust gas of iron ore sintering. Tetsu-to-Hagane 88, 59–65.

Kawaguchi, T., Matsumura, M., Kasai, E., Noda, H., 2002c. Effect of properties of solid fuel on dioxin concentration of the exhaust gas in the iron ore sintering process. Tetsu-to-Hagane 88, 378–385.

Kopsel, R.F.W., Halang, S., 1997. Catalytic influence of ash elements on NO_x formation in char combustion under fluidized bed conditions. Fuel 76, 345–351.

Kumar, C.U., Ramana, R.V., Ali, S., Das, A.K., Kumar, A., De, A.K., Mukherjee, T., 1995. Quality of sinter in the light of blast furnace performance. Tata Search, 20–25.

Lawrence Berkeley National Laboratory, 2007. The State-of-the-Art Clean Technologies (SOACT) for Steelmaking Handbook. Lawrence Berkeley National Laboratory, American Iron and Steel Institute, Berkeley, CA, Washington, DC.

Lu, L., Holmes, R.J., Manuel, J.R., 2007. Effects of alumina on sintering performance of hematite iron ores. ISIJ Int. 47, 349–358.

Lu, L., Adam, M., Somerville, M., Hapugoda, S., Jahanshahi, S., Mathieson, J.G., 2012. Iron ore sintering with charcoal. In: 6th International Congress on the Science and Technology of Ironmaking, Rio de Janeiro.

Lu, L., Adam, M., Kilburn, M., Hapugoda, S., Somerville, M., Jahanshahi, S., Mathieson, J.G., 2013. Substitution of charcoal for coke breeze in iron ore sintering. ISIJ Int. 53, 1607–1616.

Machida, S., Higuchi, T., Oyama, N., Sato, H., Takeda, K., Yamashita, K., Tamura, K., 2009. Optimization of coke breeze segregation in sintering bed under high pisolite ore ratio. ISIJ Int. 49, 667–675.

Mahmutović, A., Muhamedagić, S., 2009. Reduction of SO_2 emissions in sinter plant steelwork zenica. In: 13th International Research/Expert Conference "Trends in the Development of Machinery and Associated Technology" TMT 2009 Hammamet, Tunisia.

Matsumura, M., Kawaguchi, T., Kasai, E., 2006a. Effect of inlet gas composition on dioxins emission in the iron ore sintering process. Tetsu-to-Hagane 92, 417–426.

Matsumura, M., Kawaguchi, T., Kasai, E., 2006b. Effects of promoting and suppressing materials on dioxin emissions in iron ore sintering process. In: Proc. Asia Steel International Conference 2006, May 9–11, 2006. Fukuoka, Japan. The Iron and Steel Institute of Japan (ISIJ), pp. 416–421.

Menad, N., Tayibi, H., Carcedo, F.G., Hernandez, A., 2006. Minimization methods for emissions generated from sinter strands: a review. J. Clean. Prod. 14, 740–747.

Mo, C.-L., 1997. A Study of In-Plant de-NO_x and de-SO_x in the Iron Ore Sintering Process. Doctor of Philosophy, University of Wollongong.
Mo, C.-L., Teo, C.-S., Hamilton, I., Morrison, J., 1997. Admixing hydrocarbons in raw mix to reduce NO_x emission in iron ore sintering process. ISIJ Int. 37, 350–357.
Morioka, K., Inaba, S., Shimizu, M., Ano, K., Sugiyama, T., 2000. Primary application of the "In-Bed-deNO_x" process using Ca–Fe oxides in iron ore sintering machines. ISIJ Int. 40, 280–285.
Nakano, M., Yamakawa, T., Hayakaw, N., Nagabuch, M., 1998. Effects of metallic iron bearing resources on iron ore sintering. ISIJ Int. 38, 16–22.
Nakano, M., Hosotani, Y., Kasai, E., 2005. Observation of behaviour of dioxins and some relating elements in iron ore sintering bed by quenching pot test. ISIJ Int. 45, 609–617.
Nakano, M., Morii, K., Sato, T., 2009. Factors accelerating dioxin emission from iron ore sintering machines. ISIJ Int. 49, 729–734.
Norgate, T., Langberg, D., 2009. Environmental and economic aspects of charcoal use in steelmaking. ISIJ Int. 49, 587–595.
Norgate, T., Haque, N., Somerville, M., Jahanshahi, S., 2012. Biomass as a source of renewable carbon for iron and steelmaking. ISIJ Int. 52, 1472–1481.
Ooi, T.C., Lu, L., 2011. Formation and mitigation of PCDD/Fs in iron ore sintering. Chemosphere 85, 291–299.
Ooi, T.C., Aries, E., Ewan, B.C.R., Thompson, D., Anderson, D.R., Fisher, R., Fray, T., Tognarelli, D., 2008. The study of sunflower seed husks as a fuel in the iron ore sintering process. Miner. Eng. 21, 167–177.
Ooi, T.C., Thompson, D., Anderson, D.R., Fisher, R., Fray, T., Zandi, M., 2011. The effect of charcoal combustion on iron-ore sintering performance and emission of persistent organic pollutants. Combust. Flame 158, 979–987.
Outotec, 2008. Recent developments in agglomeration technologies for iron ores. In: Pelletizing and Sintering Colloquium. SAIMM, Pretoria, South Africa.
Oyama, N., Iwami, Y., Yamamoto, T., Machida, S., Higuchi, T., Sato, H., Sato, M., Takeda, K., Watanabe, Y., Shimizu, M., Nishioka, K., 2011. Development of secondary-fuel injection technology for energy reduction in the iron ore sintering process. ISIJ Int. 51, 913–921.
Remus, R., Monsonet, M.A.A., Roudier, S., Sancho, L.D., 2013. Best Available Techniques (BAT) Reference Document for Iron and Steel Production. Joint Research Centre, Seville, Spain.
Rengersen, J., de Boer, W.F., Oosterhuis, E., Veel, T.J.M., Otto, J., 1995. First industrial experience with partial waste gas recirculation in a sinter plant. Revue de Métallurgie-CIT 92, 329–335.
Stieglitz, L., Zwick, G., Beck, J., Bautz, H., Roth, W., 1989. Carbonaceous particles in fly ash a source for the de-novo-synthesis of organochlorocompounds. Chemosphere 19, 283–290.
Stieglitz, L., Vogg, H., Zwick, G., Beck, J., Bautz, H., 1991. On formation conditions of organohalogen compounds from particulate carbon of fly ash. Chemosphere 23, 1255–1264.
Stieglitz, L., Eichberger, M., Schleihauf, J., Zwick, G., Will, R., 1993. The oxidative degradation of carbon and its role in the de novo synthesis of organohalogen compounds in fly ash. Chemosphere 27, 343.
Stieglitz, L., Bautz, W., Zwick, G., 1997. Investigation of precursor reactions in the de-novo synthesis of PCDD/PCDF on fly ash. Chemosphere 34, 1083–1090.
Suopajärvi, H., Fabritius, T., 2012. Effects of biomass use in integrated steel plant—gate-to-gate life cycle inventory method. ISIJ Int. 52, 779–787.
Suzuki, K., Kasai, E., Aono, T., Yamazaki, H., Kawamoto, K., 2004. De novo formation characteristics of dioxins in the dry zone of an iron ore sintering bed. Chemosphere 54, 97–104.

UK Environment Agency, 2004. Integrated Pollution Prevention and Control (IPPC) Guidance for the Coke Iron and Steel Sector. United Kingdom Environment Agency, Bristol, UK.

William Lemmon & Associates Ltd., 2003. Research on Technical Pollution Prevention Options for Iron Sintering, Draft of 2003/05/17 (Canada: Prepared for the Canadian Council of Ministers of the Environment).

Xhrouet, C., Pauw, E.D., 2004. Formation of PCDD/Fs in the sintering process: influence of the raw materials. Environ. Sci. Technol. 38, 4222–4226.

Yu, Y., Zheng, M., Li, X., He, X., 2012. Operating condition influences on PCDD/Fs emissions from sinter pot tests with hot flue gas recycling. J. Environ. Sci. 24, 875–881.

Zandi, M., Martinez-Pacheco, M., Fray, T., 2010. Biomass for iron ore sintering. Miner. Eng. 23, 1139–1145.

Zhang, H., Rao, M., Fan, Z., Zhang, Y., Li, G., Jiang, T., 2012. Effects of circulated flue gas components on iron ore sintering. ISIJ Int. 52, 2139–2144.

Zhao, Z., Li, W., Qiu, J., Li, B., 2003. Effect of Na, Ca and Fe on the evolution of nitrogen species during pyrolysis and combustion of model chars. Fuel 82, 1839–1844.

Zhao, Z., Li, W., Qiu, J., Chen, H., Li, B., 2006. Influence of Na and Ca on the emission of NO_x during coal combustion. Fuel 85, 601–606.

Utilization of biomass as an alternative fuel in ironmaking

19

J.G. Mathieson, M.A. Somerville, A. Deev, S. Jahanshahi
CSIRO Mineral Resources Flagship, Clayton South, VIC, Australia

19.1 Introduction

19.1.1 Challenges facing the steel industry in reducing CO_2 emissions

The steel industry is a significant contributor to global CO_2 emissions, and the World Steel Association has indicated this to be 6.7% of total emissions, based on 2010 data (WSA, 2014a). The Scope 1 and Scope 2 emissions from the iron ore-based integrated steelmaking route, the blast furnace (BF)–basic oxygen furnace (BOF) route, are typically around 2 t-CO_2/t-crude steel, while those from the scrap-based electric arc furnace (EAF) route are dominated by emissions from electrical power generation (85%) and are typically around 0.5 t-CO_2/t-crude steel where power is generated using black coal.

The steel industry has a large incentive to decrease energy usage and thereby reduce production costs, and is already very efficient, with advanced plants approaching theoretical minima (Fruehan et al., 2000). However, in order to combat anthropogenic global warming, the international steel industry has accepted the challenge to cut net CO_2 and other greenhouse gas (GHG) emissions by 50% or more. Major programs have been under way for a decade, for example, the European Union's Ultra-Low CO_2 Steelmaking project (ULCOS, 2014; Birat and Hanrot, 2005; Birat, 2011). Japan has its CO_2 Ultimate Reduction in Steelmaking Process by Innovative Technology for Cool Earth 50 project (COURSE50, 2014; Miwa and Okuda, 2010; Tonomura, 2013) and also a series of other initiatives (Takeda et al., 2011). South Korea, North America, and Australia (Mathieson et al., 2011; Jahanshahi et al., 2014) also have significant programs.

To date, most emphasis has been placed on the development of either (a) innovative new ironmaking processes or (b) major modifications to the BF, because it is the principal emitter. The new or modified processes either substitute H_2 for CO as the reductant (producing H_2O, rather than CO_2 in the evolved gases) or aim at producing very concentrated off-gas CO_2 streams, suitable for carbon capture and storage (CCS) (Birat and Hanrot, 2005).

As an alternative, the use of biomass-derived renewable fuels as substitutes for non-renewable fuels (coal, coke, natural gas, and oil) is also being investigated, particularly by researchers in Australia, Brazil, Canada, and Europe.

Iron Ore. http://dx.doi.org/10.1016/B978-1-78242-156-6.00019-8
© 2015 Elsevier Ltd. All rights reserved.

19.1.2 The biomass advantage

The utilization of biomass-derived materials can be considered to be part of a continuous balanced cycle of (a) biomass growing and absorbing CO_2 from the atmosphere, with storage of carbon as organic compounds; (b) harvesting and utilization of the biomass, for example, combustion of the stored carbon, emitting CO_2 to the atmosphere; and (c) recycling of the CO_2 back into storage as new growth. Cradle-to-gate life cycle assessment studies (Norgate et al., 2012) indicate that provided the biomass is grown sustainably, for example, in managed plantation forests, the production and utilization of the biomass-derived products either are near CO_2 neutral or can even be negative in the case where the pyrolysis by-products are beneficially utilized.

The biomass option is attractive, not only because such fuels can be CO_2 neutral but also because existing ironmaking and steelmaking plants can be retained with little or no need for modification and capital expenditure. In addition, key aspects have already been pioneered in Brazil, which has a significant ironmaking industry based on sustainably produced charcoal from eucalypt plantations (see Section 19.4).

19.1.3 Key requirements for biomass-derived fuels and reductants for the steel industry

Raw biomass, whether from trees, grasses, or algae, cannot be directly substituted for the conventional fossil-based fuels used in ironmaking because of its high moisture content, low carbon content, and low calorific value (CV). Pyrolysis (thermal decomposition in the absence of oxygen) is required to produce carbon-rich chars. Wood is the most commonly used form of biomass, and the resultant chars are named according to the degree of pyrolysis, for example, torrefied wood (produced at ~300 °C), semicharcoal (produced at ~400 °C), and various charcoal types (produced from 500 to 800 °C).

In general, the objective is to make the biomass-derived chars both chemically and physically similar to their conventional counterparts, that is, coal, coke, and coal-based chars. Theoretically, it may be possible to produce enhanced replicas of each of the conventional materials from biomass, but costs also need to be competitive. In practice, chemical similarity is relatively easy to achieve, but comparable physical properties such as density, mechanical strength, and reactivity may require prohibitive amounts of processing. It is usually conceded that a replica with the mechanical strength and structure of BF lump coke is currently unattainable at reasonable cost.

Although the need for processing raw biomass adds costs, three factors act in favor of biomass-derived chars. First, they normally have excellent chemical properties, that is, low ash, sulfur, and phosphorus contents (see Table 19.1). Second, by pyrolyzing at various temperatures from around 450 to 800 °C, key properties can be tailored to optimize use in each application, for example, volatile matter (VM) and CV (see Section 19.3). Last, the cost of processing can be partially offset if the pyrolysis co-products (bio-oil, combustible gases, and chemicals) are captured, processed, and sold or directly utilized (see Section 19.5). As mentioned above, achieving competitive cost structures for the manufacture of various charcoal types is a key requirement for biomass-based fuels and reductants to be utilized and is discussed in Section 19.4.

Table 19.1 Some relevant properties of charcoal

Property	Value
Ash content	Low (0.5–4%)
Sulfur content	Low (0.01–0.05%)
Apparent density	Low (600–1000 kg/m^3)
True density	Moderate (1300–1800 kg/m^3)
Reactivity to CO_2	High (0.3–3 g/s^2)

19.1.4 The pyrolysis of woody biomass

The chemical and physical characteristics of charcoal types are determined by the species of timber used (e.g., the density), the soil in which the trees were grown (e.g., ash composition), and the pyrolysis process, that is, whether fast or slow (product yield), and the highest temperature attained (the VM). The stages of charcoal formation are summarized in Table 19.2.

During pyrolysis, the molecular structures of cellulose, hemicellulose, and lignin are progressively rearranged to form aromatic carbon structures tending toward graphite. The pyrolysis of wood does not proceed through a liquid mesophase, as with coking coals, and the char retains the relict open cellular structure of the parent, albeit accompanied by a significant amount of shrinkage. The end result is a carbon structure that is very porous and reactive (Antal and Gronli, 2003).

Increasing the temperature of pyrolysis decreases the residual VM of the charcoal. The solid, liquid, and gaseous product yields and many of the charcoal properties are dependent on the fate of the volatiles evolved during pyrolysis. Slow heating, increased pressure, or larger particle size (allowing the pyrolysis vapors to be in contact with primary charcoal for longer periods) can result in decomposition of the vapors, the deposition of secondary chars, and a consequent increase in charcoal yield.

Table 19.2 Thermochemical stages of pyrolysis with increasing temperature

Temperature (°C)	Observation
20–110	Wood absorbs heat and progressively loses moisture to "bone-dry" state
110–270	Final traces of moisture are vaporized Endothermic decomposition commences, with the release of CO, CO_2, acetic acid, and methanol
270–290	Exothermic decomposition commences
290–400	Continued exothermic decomposition, with release of CO, CO_2, CH_4, and H_2 gases, acetic acid, methanol, and higher-chained hydrocarbons and tars
>400	The VM content and yield of the charcoal decrease and the fixed carbon content increases. Exothermic reactions decrease

The ash content of charcoal is determined by that of the parent and the net loss of VM during pyrolysis (Antal and Gronli, 2003). The VM content is determined by the maximum pyrolysis temperature. As temperature is increased, the size of graphite microcrystals increases (Kumar et al., 1993). This increasing graphitization increases the charcoal's true density. The decrease in volatile content increases porosity, while shrinkage of the charcoal matrix causes porosity to decrease. The net result is a minimum in charcoal apparent density at about 600 °C (Kumar and Gupta, 1993). Slow pyrolysis increases secondary charcoal deposition, therefore increasing apparent density and mechanical strength (Kumar et al., 1999).

The reactivity of carbons to CO_2 and O_2 gases is related to a combination of the intrinsic reactivity of the carbon structure, the surface area available for reaction, and catalysts in the carbon structure such as alkali and alkali earth compounds (Miura et al., 1989). Charcoal reactivity decreases with increasing pyrolysis temperature due to increasing graphitization, which reduces the number of reaction sites (Kumar et al., 1992; Kumar and Gupta, 1994).

19.1.5 Charcoal's strengths and weaknesses

The charcoal properties, which are most relevant to ironmaking, are shown in Table 19.3, along with how they may affect processing in an integrated steel plant, in comparison with conventional fuels and reductants.

Table 19.3 indicates some strategies to minimize charcoal's disadvantages. Charcoal's low density and high porosity adversely affect several areas, for example, mechanical strength, combustibility in sintering, reactivity as a coking component, high moisture absorption, and ease of contamination. Processing options that can increase the density of charcoal include conducting the pyrolysis under compression and pyrolyzing densified biomass, such as dense biomass fuel (DBF) pellets. Somerville et al. (2012) showed that the bulk density of charcoal made from DBF pellets can be up to 120% higher, at a given temperature, than charcoal made from conventional wood chips. This relationship is illustrated in Figure 19.1, which shows porosity plotted against pyrolysis temperature for the two types of charcoal. The production of DBF pellets is relatively inexpensive, and their use in charcoal making is particularly favorable for applications such as sintering solid fuel, coking blend component and as a steelmaking recarburizer.

19.2 Potential applications of biomass-derived materials and impact on net GHG emissions

Some potential applications of biomass-derived materials have already been mentioned, and Table 19.4 provides a full listing of applications that have been identified within integrated ironmaking operations (BF–BOF route). It also shows the extent of substitution that may be possible, based on the current status of research and industrial trials for each of the applications.

Table 19.3 Charcoal properties for ironmaking applications

Charcoal property	Advantages	Disadvantages
Low ash	Generally provides higher-value products	
Ash composition	CaO content may save on BF or sinter flux	If biomass is grown in saline soil, alkalis (reported as K_2O and Na_2O) may approach BF limits in rare circumstances, requiring selective sourcing or blending for CPI
Controlled VM	Flexibility. Allows graded properties, simulating coal types and coke	
High combustibility	Greater than coal for the same VM content, that is, improved heat balance as a BF injectant	May be too high for full coke substitution in sintering without modification (densification) Some propensity for spontaneous combustion of fines during storage, requiring safeguards
High reactivity to CO_2	Greater than coke in BF shaft, permitting lower temperature of thermal reserve zone (TRZ)	May lead to premature coke weakening in the BF if used as a high-percentage coking component
Low mechanical strength	Easier to grind for some applications	Unsuitable as a full substitute for top-charged coke in large BFs
Low density		Higher volumes for transport and manual handling
High moisture absorption		May require protection for some applications, for example, storage in airtight bags. Difficult to dry if saturated
Contamination		High surface area and high porosity promote contamination of charcoal fines by incidental contacts with dust and soil, requiring precautions

The emissions reduction percentages shown in Table 19.4 are based on total GHG emissions of 2.2 t-CO_2/t-crude steel for the BF–BOF route, which is the median for efficient operations (WSA, 2014b). Net CO_2 emissions from the utilization of the various charcoal types are assumed to be zero, and direct one-for-one fuel substitution is also assumed, that is, no efficiency gains or losses.

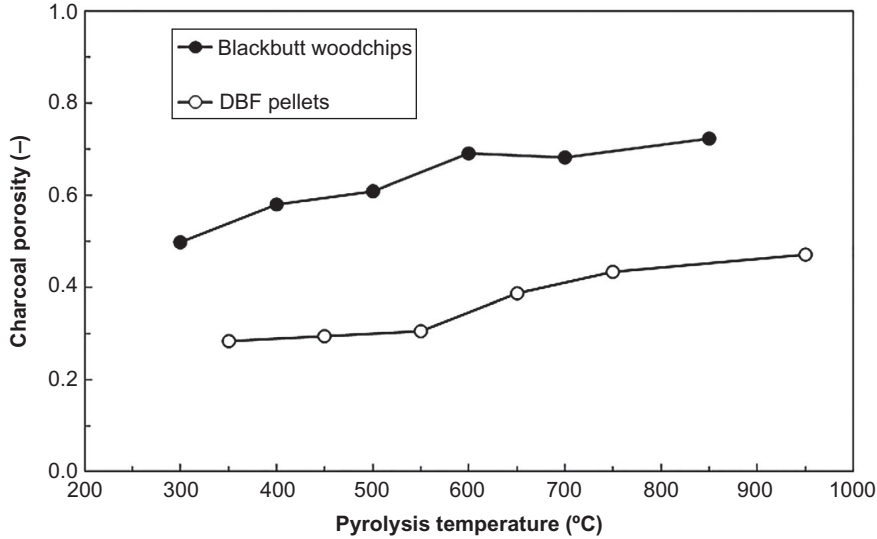

Figure 19.1 Charcoal porosity as a function of pyrolysis temperature for Blackbutt wood chips and hardwood DBF pellets.

Table 19.4 Proposed applications for biomass-derived chars in ironmaking operations and consequent CO_2 emissions reductions

		Net emissions reduction	
Application	**Basis**	**t-CO_2/t-crude steel**	**% of CO_2 emissions**
Sintering solid fuel	50–100% replacement of coke breeze or anthracite at 45–60 kg-coke or anthracite/t-sinter (and 1.7 t-sinter/t-HM)	0.12–0.32	5–15
Cokemaking blend component	2–10% of coking coal blend, with coke used at 300–350 kg-coke/t-HM	0.02–0.11	1–5
BF lump charcoal charge	Replace 2–10% of coke lump charge with coke used at 300–350 kg-coke/t-HM	0.02–0.11	1–5
BF nut coke replacement	50–100% replacement of 45 kg-nut coke/t-HM	0.08–0.16	3–7
BF carbon/ore composites (unreduced)	Replace 5–10% of iron charged to the BF by unreduced charcoal/ore briquettes	0.08–0.15	3–7
BF prereduced feed	Replace 5–10% of iron charged to the BF by prereduced charcoal/ore briquettes	0.09–0.18	4–8
BF tuyere fuel injectant	Full replacement of injected coal (PCI) at 150–200 kg-coal/t-HM	0.41–0.55	19–25
Totals		0.82–1.58	36–72

Assumption: Results are based on direct materials substitution.
Notes: HM is hot metal; PCI is pulverized coal injection; PCI coal assumed to be 75% C; Coke, coke breeze, anthracite, and recarburizer assumed to be 85% C.

Biomass-derived products have been tested in the laboratory to replace a minor proportion of the coking coal blend, for example, Sakurovs (2000) and MacPhee et al. (2009). However, new work has commenced at the CSIRO aimed at increasing the proportion to 10% or more. This application is discussed in more detail in Section 19.6.1.

With respect to sintering, pilot-scale testing has shown that low VM, or preferably dense, low-VM charcoal, can successfully substitute for coke breeze as the solid fuel, with higher productivity being possible, albeit at a slightly higher fuel rate (Chapter 18 and Lu et al., 2012). Although full substitution has been shown to be possible using pilot-scale testing, most integrated producers need to utilize indigenous coke breeze, so a more realistic limit for charcoal usage may be around 50% of the total solid sintering fuel.

It can be postulated that adding a small proportion of high-reactivity lump charcoal with the lump coke may lead to a lowering of the temperature of the thermal reserve zone in the BF by early commencement of the Boudouard reaction, that is, the reaction of CO_2 with charcoal to form CO (Equation 19.1). A key risk for this application is that a significant proportion of the charcoal may be lost to the gas stream as fines generated through crushing and abrasion. As there is no detailed information, this application is not discussed further in Section 19.6.

In modern BF practice, a small proportion of nut-sized coke is mixed within the ferrous burden layers to provide improved gas permeability and to more profitably utilize this material. It is possible that charcoal might replace coke in this application as it would not be load-bearing. Nonetheless, loss through fines generation remains a risk (see Section 19.6.3).

Several authors have proposed that unreduced carbon–ore composite pellets or briquettes be charged as BF feed, and Nakano et al. (2004), Ariyama and Sato (2006), and Konishi et al. (2009) suggested that the carbon source could be charcoal. Although the extent of this application is currently uncertain, it would be expected that perhaps 5–10% of the ferrous burden could be preprepared in this way. On the basis of their bench-scale experimental work, Nakano et al. (2004) predicted a BF coke rate reduction of about 9 kg/t of hot metal (HM) for a 10% addition. If the composites were prereduced as direct reduced iron (DRI) or hot briquetted iron (HBI), for example, using a rotary hearth furnace (RHF), they could also be used as BF feed, with additional fuel savings. See Section 19.6.4.

Pulverized coal injection (PCI), or the injection of other nonrenewable fuels such as oil or natural gas, is practiced on the vast majority of BFs. Replacement of these fuels by charcoal as the tuyere injectant is the application with the greatest potential for CO_2 mitigation (Mathieson et al., 2012a,b). Charcoal powder injection (CPI) is already practiced in mini-BFs in Brazil (Assis et al., 2009) at injection rates of 100–190 kg/t-HM (Babich et al., 2010). Others have estimated that CPI rates of 200–225 kg/t-HM may be feasible for large BFs (Nogami et al., 2004). Efficiency gains, for example, decreased coke rate, are expected for this application (Mathieson et al., 2011), and more details can be found in Section 19.6.5.

Table 19.4 shows that the aggregated potential for biomass-derived products to mitigate CO_2 emissions in integrated ironmaking is quite substantial (0.82–1.58 t-CO_2/t-crude steel or 36–72% for a typical plant), approaching or reaching the CO_2 reduction targets set for the year 2050.

Table 19.5 Proposed quality criteria for optimized charcoal types for ironmaking and steelmaking applications

Application	Optimized quality parameters[a]	Comments
Sintering solid fuel	Low VM: <3% High density[b]: >700 kg/m^3 Size: 0.3–3 mm	Protection of off-gas systems Preferable for reactivity control After crushing and screening
Cokemaking blend component	Low to mid VM: <10% High density[b]: >700 kg/m^3 Size: <1 mm Low alkalis	To reduce coke fissuring May help control reactivity Improve assimilation Check against BF limits
BF lump charcoal charge	Low to high VM: 0–25% Higher strength Size: 30–60 mm	Mini-BF charge material Via species selection (density) Nut coke size may also be useful
BF nut coke replacement	Low to mid VM: <7% Higher density Size: 20–25 mm	Combustibles loss to off-gas Probably an advantage Nut coke size
BF carbon/ore composites (unreduced)	Low VM: <5% Size: 80% passing 75 µm High strength: >500 N	May improve DRI strength Further optimization possible Minimize losses to dust stream
BF prereduced feed	High strength: >500 N High metallization: >95%	Minimize losses to dust stream Minimize coke rate
BF tuyere injectant	Higher VM: 10–20% Low ash: <5% Low alkalis	Optimizes BF heat balance Provides additional value Check against BF load limits
BOF prereduced feed (scrap substitute)	High strength: >500 N High metallization: >95%	Minimize losses to off-gas Minimize cooling effect
BOF fuel (scrap melting)	Low VM: <3% Low moisture: <2% High density[b]: >500 kg/m^3	Limits flames Limits H transfer to steel Implies additional strength
Liquid steel recarburizer	Low VM: <3% Low moisture: <2% High density[b]: >500 kg/m^3	Safety and high C recovery Limits H transfer to steel Less bags to handle

[a] Applications not requiring very low moisture levels require relatively dry charcoal, say <12% moisture.
[b] This is particle (not bulk) density, for example, made from DBF pellets.

For completeness, some BOF steelmaking applications will be briefly discussed. These are not shown in Table 19.4, but specifications for the designer chars required are shown in Table 19.5. Three applications have been identified.

BOF fuel. Some alternative ironmaking operations, for example, using a submerged arc furnace (SAF), produce HM with low carbon content, say, around 3.5%, rather than 4.5% from the BF. This leads to an energy shortage in the BOF process and the need for a solid fuel such

as coal char or coke. Similarly, fuels can be added to the BOF to enhance scrap melting, and charcoal is proposed as an alternative for both of these cases.
Scrap substitute. This could be either DRI or HBI made using charcoal as the reductant.
Liquid steel recarburizer. This is added into the steel ladle to provide and trim carbon content. Normally, a coal-based char is added, both to the ladle during furnace tapping and as a trimming addition during secondary metallurgy, for example, at a ladle metallurgy furnace. Charcoal has been shown to be suitable for this application by Wibberley et al. (2001) and in more detail by Somerville et al. (2010, 2011). Indeed, carbon recovery to steel appeared to be superior using low-VM charcoal.

19.3 Physical and chemical properties of biomass-derived chars to optimize ironmaking operations

Since charcoal is a manufactured product, this presents an opportunity for optimization. Physical and chemical properties can be tailored for each of the applications, a concept described as "designer char." The production of charcoal with specified properties requires careful control of the pyrolysis process via the selection of raw materials, for example, wood density and ash chemistry, and the use of processing temperatures from around 450 to 800 °C. As mentioned in Section 19.1.5, Somerville et al. (2012) had found that density can be usefully increased through the use of DBF pellets as the feed material for pyrolysis. Charcoal is a very porous material, and moisture levels as high as 50% are possible if saturated, meaning that good drainage, or preferably protection from rainfall, may be required to maintain normal air-dry moisture levels of around 10–12%. Table 19.5 summarizes the current state of our knowledge of quality criteria for each of the ironmaking and steelmaking applications.

19.4 Economic sources of biomass fuel

As part of the ULCOS project, Bellevrat and Menanteau (2009) have published results from an economic study that considered a number of energy-based scenarios for the future, under various carbon usage and pricing constraints. The modeling considered the steel industry over the period from the year 2000 to 2050. The most prospective future steelmaking technologies were incorporated, including the use of renewable fuels. In the desired scenario of a carbon-constrained world, where global CO_2 emissions had been halved by 2050 and reduced by three-quarters in Europe, key findings were as follows:

- Steel production via the BF (traditional and modified) was predicted to peak at 1100 Mt/year around 2025 and then decline slowly to 820 Mt/year by 2050. Its share of global steel production would decrease from about 60% to 35% over the same period.
- Very strong growth was predicted for the EAF sector, that is, steel scrap will be fully utilized as a first priority in reducing CO_2 emissions.
- The use of charcoal in the BF–BOF steelmaking route was predicted to grow very strongly and, in fact, becomes the dominant option within the BF categories, that is, the use of renewable carbon will be maximized.

- The new breakthrough ironmaking and steelmaking technologies that are currently being developed, such as smelting reduction (e.g., HIsarna) and iron electrolysis, will not be implemented before 2025 or 2030 and will remain a minor proportion of the mix in 2050 because of the capability to retrofit existing BF and DRI processes with new CO_2-efficient technologies.

The implied charcoal usage rates for the world steel industry, assuming an efficient BF fuel rate of 500 kg/t-HM, are approximately 45 Mt in 2030 and 135 Mt in 2050 (Bellevrat and Menanteau, 2009, Figure 8). This sets one view of the possible demand for sustainable biomass-derived fuels in the steel industry and assumes that charcoal provides 50% of the fuel for the BF route.

The ULCOS project studied the potential for charcoal supply from tropical eucalypt plantations as a way of reducing the net GHG emissions from steelmaking in Europe (Fallot et al., 2009), and surveys were conducted into the potential land availability for plantation forestry for charcoal supply. The combined requirements of land availability, high yield (t/ha), the best species with high productivity (short rotation), and suitable temperature and rainfall were found to occur in only a few locations, mostly in Central and East Africa and Latin America. Fallot et al. (2009) suggested that 400 Mha of land in these regions was available in 2000, but this could decrease to 175 Mha in 2050. However, these represent 25–100 times the land required (4–7 Mha) to fulfill the ULCOS aim of a 50% reduction in net CO_2 emissions from the European steel industry.

Three further examples of biomass resources, actual or potential supply of charcoal, and processing costs will now be discussed. These cover widely different geographies: Brazil, Australia, and Finland. Before moving to these examples, it is important to recognize that there may be conflicts with respect to water and land use if there is to be substantial growth in charcoal production. Consideration of many factors will be required and safeguards instituted. Such factors are biodiversity, monocultures, water supply, deforestation, air and water pollution, electricity generation, and the land required for food supply and other biofuels and biomaterials, for example, biochar for agriculture. It is worth noting that there is currently a decline in demand for biomass for pulp and paper production. This may provide an incentive for the growth of renewable carbon supply.

The first example is Brazil, which has the world's largest bioenergy industry and the most developed forestry/charcoal industry devoted to steelmaking. Piketty et al. (2009) used data from the Brazilian Association of Producers of Planted Forests (ABRAF) to show the state-by-state and total eucalypt and pine plantations in Brazil. The total eucalypt and pine plantation areas in 2006 were 3.55 and 1.82 Mha, respectively. With the productivity of eucalypt plantations presently at 40 m^3/ha/year, the wood generated from eucalypt plantations is about 142 Mm^3/year. For pine plantations, productivity is 28 m^3/ha/year, and the resultant softwood generation is about 51 Mm^3/year. Charcoal production represents around 22% of Brazilian wood consumption.

Figures published by the Brazilian Ministry of Mines (2007) indicate that charcoal production was around 10 Mt/year from 2004 to 2006 and that around three-quarters was used in the iron and steel industries. Although this is large by today's standards, it is relatively small compared with the 135 Mt demand predicted for the year 2050. Campos de Assis et al. (2008) and Valladares and Scherer (2012) showed that Brazilian pig iron production from charcoal-fired mini-BFs has varied somewhat in recent years but has averaged around 10 Mt/year, from up to 172 furnaces.

Pfeifer et al. (2012) indicated that the cost of lump charcoal from plantation eucalypts delivered to a mini-BF plant in northern Brazil was US$250/t in 2012, up from US$100 in 1990, with the cost of the wood being the largest item at US$104/t-charcoal. This relatively low cost indicates what can be achieved with large-scale production and could be improved considerably if the pyrolysis by-products were captured and/or utilized (see below).

The second example is Australia, where Haque et al. (2008) used data from industry sources to estimate the amount of sustainable biomass that could be available for a renewable carbon supply to the Australian steel industry. Three classes of biomass were considered: (a) forestry thinnings and harvest residues, (b) agricultural residues, and (c) residues from timber processing industries. Table 19.6 shows the amount of biomass available from each category and the amount of charcoal that could be produced. Mathieson et al. (2012a) had suggested that between 0.9 and 1.2 Mt of charcoal could be substituted for coal and coke in Australia, assuming the success of research and demonstration programs that are aimed at overcoming technical barriers to charcoal substitution. Even if only 50% of the potential biomass was available, Table 19.6 suggests there may be sufficient existing amounts to support a local charcoal industry that fully supplies the steel industry.

Jahanshahi et al. (2014) have reported a technoeconomic study of the hypothetical establishment of a charcoal making industry for BF tuyere injection (CPI) in Australia. The evaluation was based on a scenario where

- good-quality forest harvest residues were selected as the biomass source;
- raw biomass was collected, chipped, and dried close to the source and transported 100 km to newly built charcoal and by-product plants (AU$100 million investment for 100,000 t-charcoal per annum) that were located at a sawmill in order to share services;
- the charcoal was transported to an existing steel plant about 300 km from the charcoal plant;
- the bio-oil product had a value of AU$88/t-charcoal, based on energy content compared with crude oil (50%) (please note that if the diesel price was used, the value of bio-oil would almost be doubled);
- the value-in-use (VIU) of softwood charcoal as a BF injectant was taken into account and was 50% higher than the cost of the standard high-VM PCI coal, which had an assumed price of AU$135/t at the steel plant (see Mathieson et al. (2011) for the method);
- a carbon credit of AU$23/t-$CO_2$ was applied to the charcoal and the by-product bio-oil, reflecting the carbon price in Australia in 2012.

Table 19.6 Estimates of sustainable biomass and charcoal available in southeastern Australia

Resource category	Biomass (Mt/year dry)	Potential charcoal[a] (Mt/year dry)
Forestry harvesting residues	3.4	1.0
Wood processing residues	2.3	0.7
Nonforestry residues	1.9	0.6
Total	7.6	2.3

[a] Charcoal yield during pyrolysis is assumed to be 30% (dry basis).

Table 19.7 Estimated charcoal production costs based on biomass collected from the Finnish forestry industry

Operation	Cost of biomass (€/m³)	Cost of charcoal[a] (€/t)
Stumpage price	1	7.8
Forest haulage	6	47
Chipping	6	47
Transport (70 km)	7.5	58.7
Management	3.5	27.4
Pyrolysis	23–37	80–290
Total	47–61	268–478

[a] The conversion of forest logs into charcoal assumes that the density of the logs is about 860 kg/m³; the logs contain 50% water and the charcoal yield in pyrolysis is 30%.

On the basis of the assumptions above, the net cost of charcoal at the steel plant was estimated to be AUS$169/t, which was considered to be comparable with the cost of the normal PCI coal. This cost would increase with decreasing carbon price and decrease as the price of PCI coal increases due to the VIU factor. It should be noted that the excess combustible gas from pyrolysis was not valued as quantities were uncertain.

The final example is from Finland, where Suopajärvi and Fabritius (2013) investigated the resources and economics of biomass supply and charcoal production. They estimated the total charcoal production costs by adding the costs of the component operations as shown in Table 19.7. The total cost was estimated to be between €268 and €478/t-charcoal. However, this did not consider the capture and utilization of the pyrolysis by-products or a VIU component, which could be significant, as indicated in the Australian study.

Suopajärvi and Fabritius (2013) showed that logging residues available in Finland amounted to 7.4 Mm³. Although these materials were the cheapest for forest chip production, and hence for charcoal production, their availability could be limited due to competition from other industrial users.

The overall conclusions from this examination of the economics of charcoal supply are that the volumes required appear to be feasible, despite environmental concerns, competition from other land uses, and the need to ensure food and water supplies. The full cost of charcoal production appears to be already competitive with the cost of BF coke and can approach that of PCI coal when by-products are captured and their value is realized (Suopajärvi and Mikko, 2011).

19.5 Pyrolysis of biomass for ironmaking applications

Charcoal is produced from biomass via pyrolysis as outlined in Section 19.1.3. Of the important properties of optimized charcoal types for the steel industry (i.e., VM content, particle density, ash content, ash composition and particle size), only the amount of VM is primarily controlled by the conditions of pyrolysis, namely, by the maximum temperature reached. The other properties are largely determined by the properties of the feed material. For example, Somerville et al. (2012)

demonstrated that the density of charcoal particles can be increased by a factor of two or more if compacted raw materials are utilized, for example, DBF pellets.

The VM requirements for the designer charcoals listed in Table 19.5 can be satisfied by processing biomass at maximum temperatures in the range from 450 to 800 °C, which does not impose a significant engineering challenge. For charcoal to be competitive with conventional fuels and reductants, the choice of pyrolysis technology will be governed by the need to minimize net product costs while maintaining high environmental standards.

The major charcoal making industry in Brazil uses logs as feed to traditional large batch-based pyrolysis kilns. The charcoal typically has around 25% VM, which is too high for several applications, and is divided into lump and fine products. The by-product gases are typically flared, and product yields can be affected if there is air ingress into the kilns.

A future that may require 135 Mt of charcoal per annum (see Section 19.4) would benefit from a new approach to large-scale pyrolysis. Key design factors include the following:

- Scalable modules capable of producing charcoal at 100 kt/year or more
- Continuous highly automated processing with low labor requirements
- Versatile wood chip or pellet feed
- The ability to produce consistent products with varying VM and densities
- High yield of charcoal products
- Low or zero need for process heat during steady-state operation
- Full recovery and utilization of by-products (bio-oil, combustible gases, and chemicals), to reduce the net cost of charcoal
- Capability to meet the highest environmental standards

Among existing continuous wood pyrolysis technologies, the Lambiotte carbonization process (FAO, 1985) is probably the most efficient and can achieve the highest production from a single reactor unit. The feed is heated by the flow of hot gases generated in a burner fired by the pyrolysis by-products, and the maximum temperature of the material can be up to 800 °C.

Although the Lambiotte process can be recommended as the best available option for the production of large volumes of charcoal, feed is restricted to reasonably large pieces of wood, since the gas permeability of the bed in the retort needs to be high in order to facilitate heating by the forced circulation of hot noncombustible gases. Most wood wastes and residues are smaller in size than required for this process and hence cannot be carbonized using this technology. Additionally, a consequence of gas circulation through the material is that the gaseous pyrolysis products are diluted by noncombustible heat carrier gases, which lowers their CV.

Presently, there are few continuous wood carbonization processes that can process smaller-sized feeds such as residues and wastes. Such processes are based on rotary kilns (e.g., DGEngineering, 2013), multi-hearth furnaces (FAO, 1985), or auger pyrolysis reactors (tubular reactors with internal screw transport) (Riegel and Kent, 1962). The reactors are normally heated externally by combusting pyrolysis gases, but in some cases, the combustion of gases is designed to occur inside the reactors. Like the Lambiotte reactor, these processes can readily reach a temperature of 800 °C.

Although these technologies are available for the production of charcoal from wood fines, including chipped wood wastes and high-density pellets, they have some

intrinsic limitations. External heating of the reactor is neither effective nor efficient due to the low thermal conductivity of the feed. As a result, externally heated pyrolysis reactors processing small-sized biomass have limited scalability, requiring a large number of reactors to achieve required production volumes. Some processes have introduced moving parts within their high-temperature zones to accelerate heating by stirring, but the increased mechanical complexity increases the demand for maintenance. Internal combustion of a fraction of the biomass feed or pyrolysis products as the means of heating can marginally improve the scalability of these reactors but at the expense of burning valuable materials (lower charcoal yield).

As indicated above, the competitiveness of charcoal will improve if more efficient charcoal making technologies are developed. Several shortcomings of the existing pyrolysis technologies can be overcome if an autothermal or autogenous principle is used (Stafford, 1921). A process based on this principle does not need either an external source of heat to bring the feed to the required maximum temperature or the supply of air or hot gases to the reactor, thereby avoiding yield loss from combustion of the feed or the pyrolysis products. In an autogenous process, the feed is heated by the exothermic pyrolysis reactions naturally occurring within the material, resolving difficulties in heating smaller-sized feed.

A commercial autogenous pyrolysis process currently does not exist, but the CSIRO is working to revitalize and to improve the concept (Deev, 2012). Its advantages are as follows: reactors are readily scalable as there are no heat transfer limitations restricting the size of the reactors, the yield of charcoal is high, and the process is highly energy efficient (Deev and Jahanshahi, 2012). In addition, the by-products of pyrolysis have a higher CV than those for existing technologies as they are not diluted either by noncombustible gas or by free moisture (bone-dry feed is used), and the feed is not burned by free oxygen during processing. Such a process can be continuous and arranged in a vertical shaft reactor with material descending under gravity, that is, the pyrolysis reactor is mechanically simple and suitable for automation. However, it should be mentioned that the maximum pyrolysis temperature that can be reached spontaneously by dry wood is limited to approximately 520 °C (Deev, 2012). Nevertheless, the VM content of charcoal treated to such a temperature is expected to be 10–15% (FAO, 1987), which satisfies many ironmaking applications (see Table 19.5) without further treatment. Production of dense charcoal from DBF pellets is also possible with this technology.

The development of the CSIRO's continuous autogenous charcoal process has reached pilot scale, and a process flow diagram of the plant is shown in Figure 19.2.

19.6 Applications in ironmaking

19.6.1 The production of biocoke

The feasibility of making high-quality BF coke from coking coal blends containing additions of raw biomass, torrefied wood, or charcoal with medium or high VM has been assessed in Japan, Canada, Brazil, Europe, and Australia.

Additions of untreated wood particles or densified wood pellets to a coking coal blend were found to reduce the cold strength of the resultant biocoke substantially

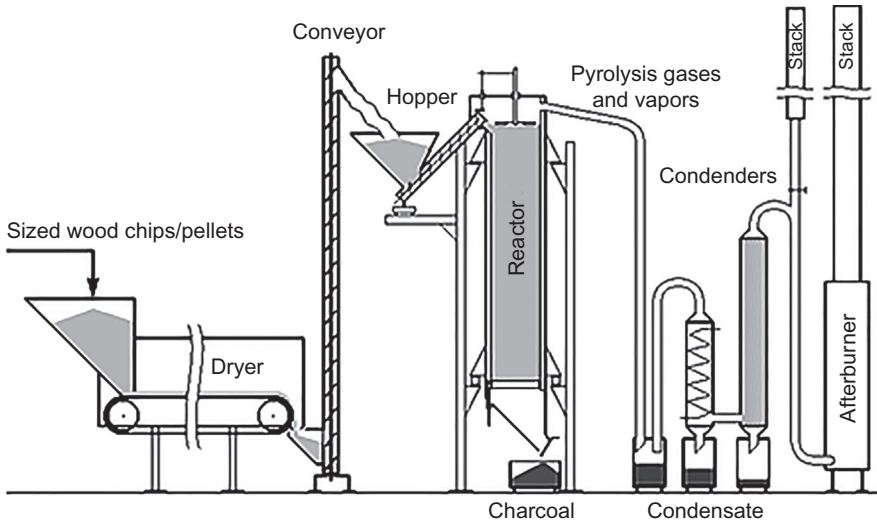

Figure 19.2 Process flow diagram of the pilot-scale wood pyrolysis plant at the CSIRO. Reactor shaft height: 2750 mm. Reactor internal diameter: 600 mm. Reactor volume: 0.78 m^3. Feed rate: Up to 300 kg/h (dry).

when the rates of biomass additions exceed 2% (Ota et al., 2006; Matsumura et al., 2008). According to Nishimura et al. (2004), thermally pretreated wood at 300–500 °C, prior to mixing it with coal, had smaller negative effects on coke strength than untreated wood, so that a 3% addition of pretreated wood was possible without a major deterioration of cold strength. The reactivity of the resultant biocokes was not evaluated in these tests.

The substitution of 5% of coking coal by finely ground charcoal (<0.063 mm) with medium VM content (9.5%) did not reduce the cold strength of coke (Ng et al., 2011a,b). However, when larger particles of charcoal were used, for example, up to 2 mm in size (Wibberley et al., 2001), or up to 9.5 mm (Ng et al., 2011a,b), the cold strength of coke fell below an acceptable level. Also, when 10% of the coal blend was substituted by low-VM charcoal, the cold strength of the coke was unsatisfactory (Wibberley et al., 2001). Da Silva et al. (2008) demonstrated that pelletized charcoal was distinctly more dense than conventional charcoal and had a positive effect on the cold strength of biocoke. These results suggest that other means of densification of charcoal may extend the limits of the substitution of coal by renewable carbon.

Coke performance in the BF is also judged by hot tests, such as its reactivity to CO_2 at 1100 °C (by the coke reactivity index (CRI) test) and its consequent loss of physical strength (by the coke strength after reaction (CSR) test) (ISO, 2006). These tests have been conducted for biocoke samples by Wibberley et al. (2001), MacPhee et al. (2009), and Hanrot et al. (2011) and recently by the CSIRO. All have found that charcoal addition leads to progressive deterioration in both the CRI and CSR. Figure 19.3 shows results for coke made in a retort (1 kg charge), where the deteriorations in the CRI and CSR with the amount charcoal added were the least reported

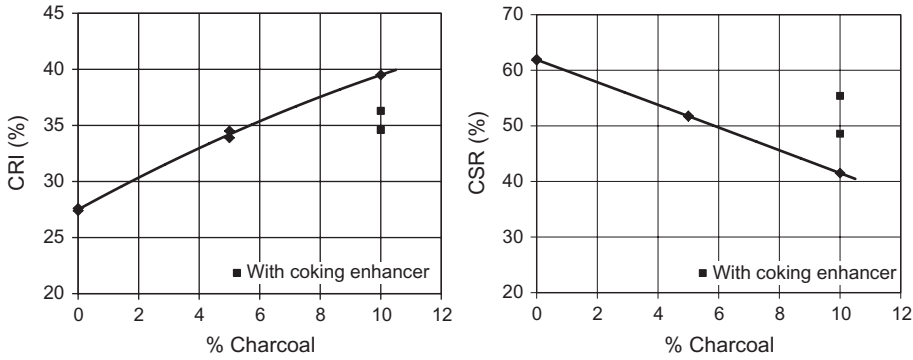

Figure 19.3 Coke reactivity index (CRI) and coke strength after reaction (CSR) for coke containing various amounts of charcoal and 2% of an organic coking enhancer.

to date. The optimized charcoal used was low-VM (5.8%), high-density (from DBF pellets), and sized from 0.5 to 1.0 mm. It should be noted that coke made in the laboratory has slightly different properties than that made in full-scale commercial ovens. For example, the base coking coal blend used in these experiments produced a CSR of 72% in commercial coke ovens.

In similar experiments, MacPhee et al. (2009) found that an increase in the particle size of the charcoal to a few millimeters had a positive effect, and when combined in a high-fluidity coal blend, the substitution of 3–5% of the coal by charcoal was possible with only modest deterioration in the CSR.

In summary, the following properties of charcoal have been found to affect its performance as a component of a coking coal blend:

- *Combined oxygen*. Charcoal inherits a substantial amount of oxygenated chemical compounds from the parent wood. These are distributed within its structure and in tars deposited in pores. Oxygen-containing compounds are known to reduce the coking ability of coal, which affects both the strength and reactivity of the coke (Sakurovs, 2000).
- *Low mechanical strength*. Charcoal does not become part of the liquid mesophase during coking and appears in the coke structure in a similar way to inert coal macerals, that is, recognizable as being relatively unchanged. If the charcoal inclusions are large, their low strength may lead to a decreased ability of the coke to bear loads. Additionally, cracking is often evident in biocoke structures, indicating that the charcoal facilitated some weakening of the original coke matrix.
- *High reactivity*. Charcoal's high reactivity to CO_2 is due to several factors. Probably, the most important are (a) its very high specific surface area (Diez and Borrego, 2013) and (b) the catalytic effect of its mineral matter. This mineral matter has significant amounts of active Na, K, and Ca compounds, which catalyze the Boudouard reaction (Equation 19.1), as shown by Ng et al. (2011b, 801–804). The combination of the catalytic effect and high surface area results in a tendency for the charcoal inclusions to be preferentially removed from the coke matrix when exposed to high-temperature BF gases. In addition, the volatile catalysts may diffuse into the adjacent coke structure and accelerate its gasification, tending to weaken the entire biocoke matrix.

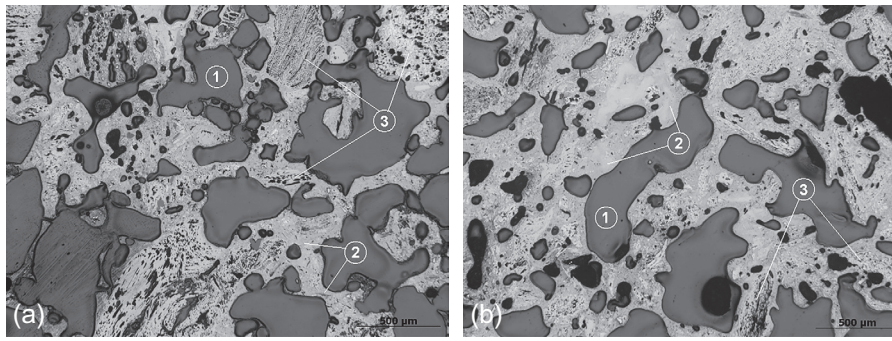

Figure 19.4 Optical micrographs of biocoke: (a) coke with 10% charcoal; (b) coke with 10% charcoal and a coking enhancer. 1—Voids; 2—coke matrix; 3—charcoal particle inclusions.

The extent of substitution of charcoal for coal achieved so far, without compromising the quality of the resultant coke, is moderate. However, the positive trends observed give rise to optimism that a viable rate of substitution can be attained, hopefully at around 10%. The way forward is seen as using dense and perhaps demineralized charcoal (Ng et al., 2011a,b) to assist the base coking coal blend to be more tolerant of the presence of charcoal inclusions (MacPhee et al., 2009; Hanrot et al., 2011) or by using coking enhancers.

Coking enhancers improve the cokability of a coal blend and thus may partially compensate for the negative effects of charcoal additions. This is demonstrated in Figure 19.4 from recent work at the CSIRO. The left-hand micrograph (Figure 19.4a) relates to biocoke obtained without the addition of a coking enhancer. It shows that the surfaces of the relict charcoal particles are poorly assimilated into the coke matrix, evidenced by the well-defined boundaries of the charcoal inclusions. The encapsulation of charcoal particles into the coke matrix was considerably improved when 2% of an organic coking enhancer was added to the blend (Figure 19.4b). The CRI and CSR also improved, as shown in Figure 19.3. Additional optimization of the chemical composition of the charcoal to better suit cokemaking, for example, demineralization, may also help to increase the amount of charcoal that can be added to the coking coal blend.

19.6.2 Sintering solid fuel

The possible contribution of this application to CO_2 emissions reduction is covered in Section 19.2 and Table 19.4. Details of the science of this application are the subject of Chapter 18.

19.6.3 BF nut coke replacement

Nut coke is typically the size fraction between 10 mm and 25 or 30 mm. The finer fraction, coke breeze, is normally utilized in sintering, while the larger lump coke fraction is the main fraction charged at the top of the BF. Nut coke would

significantly lower the gas permeability of the lump coke if incorporated in the main coke charge. However, it has been found to improve the permeability of the ferrous burden layers and is typically incorporated at around 45 kg/t-HM, as shown in Table 19.4.

Since the nut coke is not load-bearing in this application, it has been proposed that lump charcoal may be a suitable substitute. This would not only introduce a renewable fuel/reductant but also may be beneficial to lowering the temperature of the thermal reserve zone and thereby reduce overall fuel rate.

The theory of this application is described in detail by Babich et al. (2009b). Kunitomo et al. (2013) had conducted pilot-scale testing in the BIS furnace (BF inner reaction simulator) and have noted a large decrease in thermal reserve zone temperature. Also, this application has been practiced in a 700 m^3 BF, operated by Aperam in Brazil, at a rate of 25–30 kg-charcoal/t-HM, with the charcoal being 13–32 mm nominal size. Good operational results were reported, for example, improved permeability and decreased heat losses, albeit at the cost of a slightly increased top gas dust loading (Gonçalves et al., 2012).

19.6.4 BF reducible and prereduced composite feeds

Composite pellets or briquettes are formed from intimate mixtures of finely ground iron oxide (iron ore) and carbon (coal or charcoal). When heated to 1250–1400 °C, the iron oxides are reduced to form metallic sponge iron, and the other mineral components form a slag phase. Fast reduction kinetics is achievable because of the close proximity of the carbon and iron oxide particles. Depending on the raw materials, reduction can be complete in as little as 10 min at 1300 °C.

Unreduced composites (green) may be charged into the BF as part of the ferrous burden. They are also the feed material for a new generation of ironmaking processes that use an RHF to produce DRI, such as the FASTMET or ITmk3 processes. Reduced composites have applications as a metallized feed to an EAF, BOF, or BF or in other melting operations such as a SAF, where pig iron is produced.

For practical operations, both the green composites and the DRI are required to have significant physical strength to withstand abrasion and impacts, for example, compressive strength minima of 500 or 1000 N before yield or fracture.

As indicated in Section 19.2, composites containing charcoal as the carbon source can be a convenient way of introducing renewable carbon into the ironmaking process. However, a number of challenges need to be overcome. For example, during investigations into the reduction of composite pellets containing charcoal, coal, or coke, Gupta and Misra (2001) found that charcoal resulted in higher reduction rates and higher extents of reaction, but the pellets tended to break open due to the formation of iron whiskers.

The reduction of iron oxide in composite mixtures is believed to occur via a two-stage process. First, carbon is gasified by CO_2 to produce CO gas (Equation 19.1), the Boudouard reaction. In the second stage, CO gas reduces iron oxides to produce CO_2. These reactions are shown as Equations (19.2–19.4) (after Ghosh (1999)). Hence, the reduction occurs via CO and CO_2 gaseous intermediates.

$$C(s) + CO_2(g) = 2CO(g) \tag{19.1}$$

$$3Fe_2O_3(s) + CO(g) = 2Fe_3O_4(s) + CO_2(g) \tag{19.2}$$

$$Fe_3O_4(s) + CO(g) = 3FeO(s) + CO_2(g) \tag{19.3}$$

$$FeO(s) + CO(g) = Fe(s) + CO_2(g) \tag{19.4}$$

Several other workers have observed an increase in the rate of reduction of composites when charcoal is substituted for coal or coke. Halder and Fruehan (2008) and Fortini and Fruehan (2005) showed that the rate constants for carbon oxidation were an order of magnitude higher for charcoal than for coal char. They attributed this increase to the higher reactivity of charcoal with CO_2 caused by higher internal pore surface area. The rate-determining step in the reduction process is usually the gasification of carbon by CO_2 (Equation 19.1).

The reduction of composites occurs as a nonisothermal system or process. Temperature gradients occur within the briquettes/pellets because of many factors, for example, uneven heating, slow heat transfer, and the endothermic Boudouard and metal reduction reactions. These can limit briquette internal heating and hence the overall reduction rate. The use of charcoal as a reductant in composite briquettes or pellets increases the reduction rate through the enhancement of the Boudouard reaction. However, in some cases, the reduction limitation can change from carbon gasification to heat transfer.

Recent work conducted at the CSIRO has been aimed at determining the factors that affect the strength of both the green (unreduced) and the fired composite briquettes made with coal and charcoal.

The strength and density of green composite briquettes increased with die pressure and starch binder content. For briquettes made with coal, the optimum moisture content was about 10%, but with charcoal, it rose to between 20% and 25%. Also, 2% binder in the mix and a C/Fe ratio of about 0.25 were found to maximize the green strength. Under these conditions, composite green briquettes were produced with a compressive strength of 6 kN and a density of about 2000 kg/m^3.

For composites made with charcoal, the density of fired briquettes increased with increasing furnace temperature (1250–1350 °C). Figure 19.5a shows that the strength of briquettes fired at either 1300 or 1350 °C was satisfactory, but at 1300 °C, strength tended to decrease with increasing time at temperature. The strength of briquettes fired at 1350 °C was independent of time. Figure 19.5b indicates that the degree of iron metallization was high at both temperatures and at all times studied.

An examination of the microstructures of the fired briquettes showed that the dominant phases were metallic iron, which can be seen as rounded globules, and a continuous slag phase often containing secondary crystal phases such as spinel and wüstite dendrites. The slag phase forms from the fusion of the nonferrous components of the iron ore, the charcoal ash, unreduced iron oxides, and any flux added to the briquette mix. The strength of the fired briquettes is largely due to the formation of a continuous and coherent slag phase. This slag layer is most apparent near the outer surface of the briquette. The center regions of the briquettes contain many pores and generally lack the coherent nature of the outer region. The changes of strength with

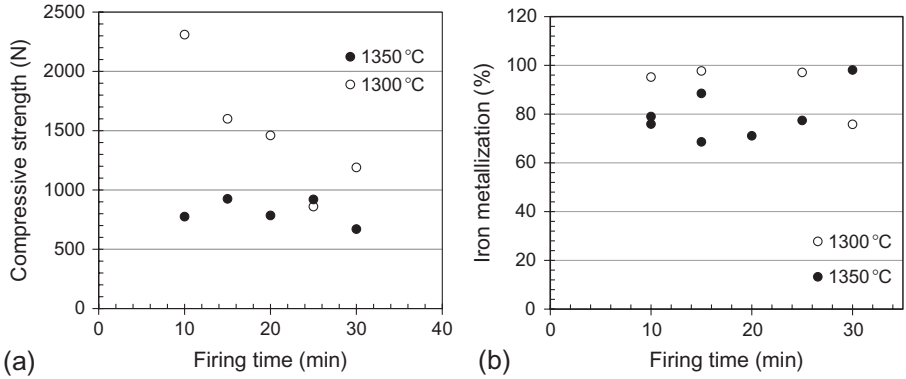

Figure 19.5 Relationships of (a) fired briquette strength and (b) iron metallization as a function of firing time at 1300 and 1350 °C.

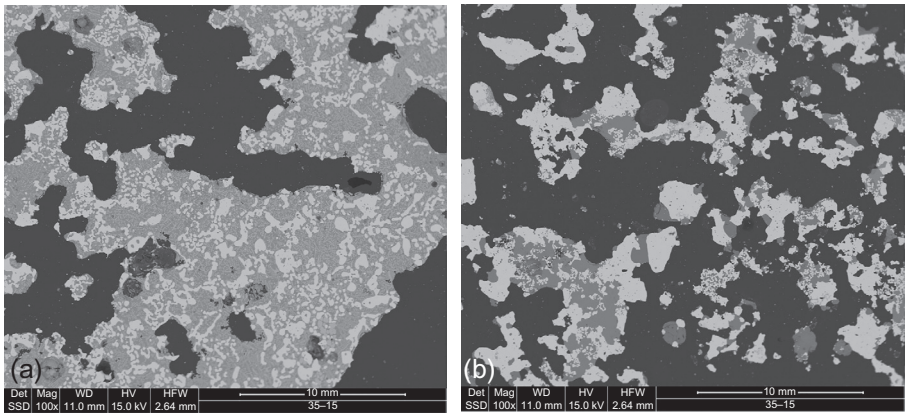

Figure 19.6 Microstructures of (a) the outer region and (b) the central region of a fired composite briquette (1300 °C for 5 min) showing a coherent and continuous slag phase.

firing time at 1300 °C (Figure 19.5a) are attributed to ongoing annealing processes of both the slag and iron phases. At 1350 °C, it appears that the final microstructure and strength have already been reached at 10 min. Figure 19.6 shows typical microstructures of (a) the dense outer region and (b) the porous central region of a fired briquette made with charcoal.

19.6.5 BF charcoal injection at the tuyeres

Table 19.4 indicates that BF charcoal injection potentially can yield the largest decrease in net CO_2 emissions. Since charcoal must be finely ground for injection, for example, to 80% <90 µm, its lack of mechanical strength may be an advantage. CPI is already practiced in Brazil on mini-BFs up to 700 m^3 inner volume (Assis et al., 2009), where fines arising from the handling of the top-charged lump charcoal are collected, pulverized, and injected at the tuyeres at rates of up to 190 kg/t-HM (Babich et al., 2010).

For injection in large BFs, the key technical and economic questions are the following:

- Can charcoal chemistry and thermochemistry be optimized to minimize the fuel rate and improve BF productivity?
- Are charcoal combustion rates under BF raceway conditions greater than those for PCI coals, thereby minimizing the amount of unburned char entering the cohesive zone and shaft?
- Are there any technical limitations concerning the grinding and pneumatic conveying of charcoal or charcoal–coal mixtures?

The first question has been answered principally through the use of heat and mass balance modeling by workers in Germany, Japan, Canada, and Australia. As an example of this work, Table 19.8 shows compositions for some coal and charcoal types, and Table 19.9 summarizes key results calculated for injection at a rate of 140 kg/t-HM for all fuel types (Mathieson et al., 2011).

Since fuel rate is coke rate plus injection rate, clearly, CPI offers potential for lower overall fuel rates, saving some fossil-derived CO_2 in addition to the benefit of using the renewable injectant. This is exemplified in Table 19.9 via the lowered coke rate and percentage fuel rate changes for the three charcoal types. Compared with the standard PCI coal (reference), charcoal theoretically has the ability to lower coke rate (and thereby fuel rate and CO_2 emissions) by 20–30 kg/t-HM, that is, 4–6%, in good agreement with similar studies (e.g., Babich et al., 2010; Ng et al., 2011a,b). However, Babich et al. (2010) predicted small increases in coke and fuel rates in a situation where the ash content (6.8%) was higher. Presumably the VM was also higher. For example, perhaps similar to the semicharcoal shown in Table 19.9.

Table 19.9 shows that torrefied wood and semicharcoal are not predicted to perform as well as the three charcoal types but would retain the benefit of the near-zero CO_2 emissions associated with the use of renewable fuels. This is illustrated in Figure 19.7.

The second question, regarding charcoal's combustion performance, has been studied by groups in Japan, Germany, Brazil, Canada, and Australia. For example, the Australian pilot-scale combustion studies (Mathieson et al., 2012b) were conducted under simulated BF raceway conditions and indicated that charcoal's combustibility is superior to that of coal at the same VM content (see Figure 19.8), in general agreement with other studies, for example, Hanrot et al. (2011) and Babich et al. (2010).

Noting the lower predicted fuel rates and, therefore, bosh gas volumes, improved BF productivity has been predicted for low-ash charcoals with 25% VM or less. The "burnout" or "combustion efficiency" shown in Figure 19.8 is the percentage of the organic material combusted in the 20 ms available in the simulated BF raceway. The combustibility improvement was approximately 40% (absolute), and this means that lower-VM charcoals, with higher CVs, theoretically can be used to enable the overall fuel rate reductions shown in Table 19.9. The compositions of the charcoals tested are given in Table 19.10 along with definition of the sample symbols shown in Figure 19.8.

Each of the pulverized charcoals and several of the combustion chars were mounted for optical microscopy. Micrographs of the medium-VM softwood charcoal (Ch-SwM) and low-VM hardwood charcoal (Ch-HwL) and the corresponding combustion chars obtained under air-cooled coaxial lance injection and fuel-lean combustion conditions

Table 19.8 **Key injectant parameters (ad, air-dried)**

	BF tuyere injectant[a]	Inherent moisture (% ad)	Volatile matter (% ad)	Ash (% ad)	S (% ad)	P (% ad)	$K_2O + Na_2O$ (% ad)	$CV_{g\,ad}$[b] (kJ/kg)
Coals	Subbituminous	16.0	29.5	6.5	0.65	0.06	0.03	23 305
	High-VM (reference)	2.5	34.5	9.0	0.40	0.01	0.15	30 543
	Semianthracite	1.5	12.5	7.5	0.60	0.07	0.12	32 844
	Anthracite	2.0	6.5	9.0	0.50	0.01	0.48	31 882
Chars	Torrefied softwood	2.0	69.1	0.5	0.02	0.01	0.05	23 000
	Semicharcoal (hardwood)	0.7	33.1	2.3	0.05	0.07	0.20	29 500
	Charcoal (softwood)	1.0	6.2	0.9	0.05	0.02	0.11	35 100
	Charcoal (hardwood)	1.8	7.6	3.4	0.09	0.10	0.35	33 500
	Charcoal (mallee)	1.6	0.3	3.4	0.04	0.0	0.73	32 000

[a] All materials were injected at 1.4% moisture in the model.
[b] CV_g is the gross calorific value or combustion enthalpy.

Table 19.9 Key calculated blast furnace operating parameters for substitution of various tuyere injectants for the reference coal (high-VM) and injected at 140 kg/t-HM

	Fuel injectant	Coke rate (kg/t-HM)	Change in fuel rate (%)	Slagrate (kg/t-HM)	Coke replacement ratio[a] (kg-coke/kg-injectant)	Top gas energy (GJ/t-HM)	Blast oxygen enrichment (%)	Hot metal			Alkali oxide load[b] (kg/t-HM)
								Si (%)	S (%)	P (%)	
Coals	Subbituminous	370	3.7	245	0.68	5.14	2.9	0.41	0.023	0.080	0.35
	High-VM (reference)	**352**	**0.0**	**246**	**0.81**	**5.13**	**3.2**	**0.41**	**0.017**	**0.070**	**0.41**
	Semianthracite	335	−3.5	239	0.92	4.92	1.9	0.37	**0.020**	0.078	0.37
	Anthracite	334	−3.7	242	0.94	**4.79**	1.0	0.38	0.019	0.069	0.86
Chars	Torrefied softwood	**409**	**11.6**	236	**0.39**	**5.57**	5.6	0.41	0.016	0.072	0.43
	Semicharcoal (hardwood)	355	0.6	228	0.78	4.98	0.8[c]	0.35	0.015	0.078	0.44
	Charcoal (softwood)	321	**−6.3**	223	1.06	4.84	**0.7**[c]	**0.32**	**0.014**	0.069	0.40
	Charcoal (hardwood)	331	−4.3	225	1.02	4.92	**0.7**[c]	0.33	0.015	**0.081**	0.58
	Charcoal (mallee)	331	−4.3	226	**1.03**	4.83	**0.7**[c]	0.33	**0.014**	0.067	**1.03**

[a] Calculated at the injection rate, that is, 140 kg/t-HM, by the tangent method, with raceway adiabatic flame temperature (RAFT) maintained constant by oxygen enrichment.
[b] This is shown to indicate cases where BF load limits for alkalis may be exceeded.
[c] Requires additional steam (cooling) to maintain RAFT.

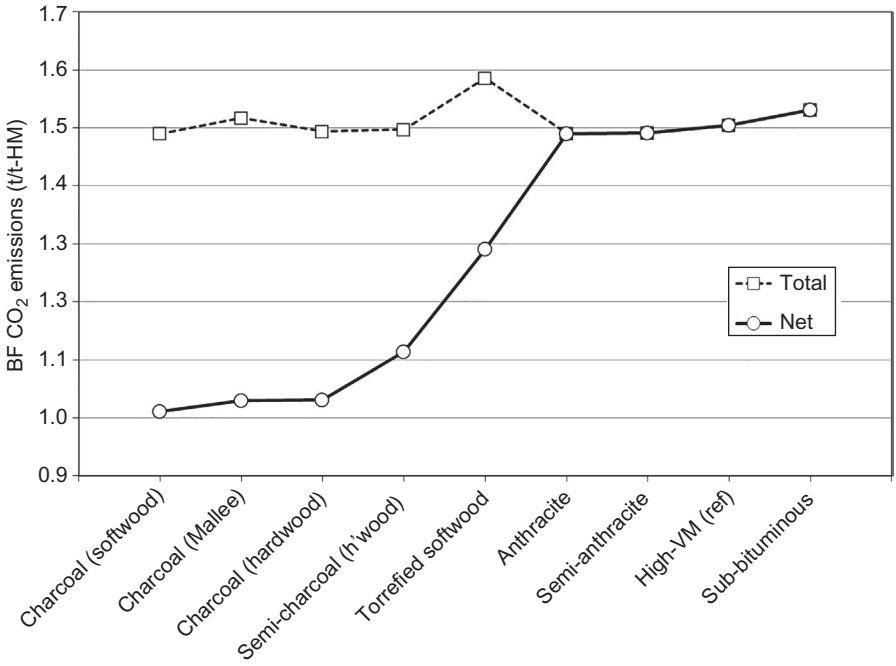

Figure 19.7 Calculated CO_2 emissions from the blast furnace (excluding the stoves) for a series of renewable and nonrenewable injectants. The net emissions assume that CO_2 generated from the renewable fuels is zero. Order: Increasing net CO_2 emissions.

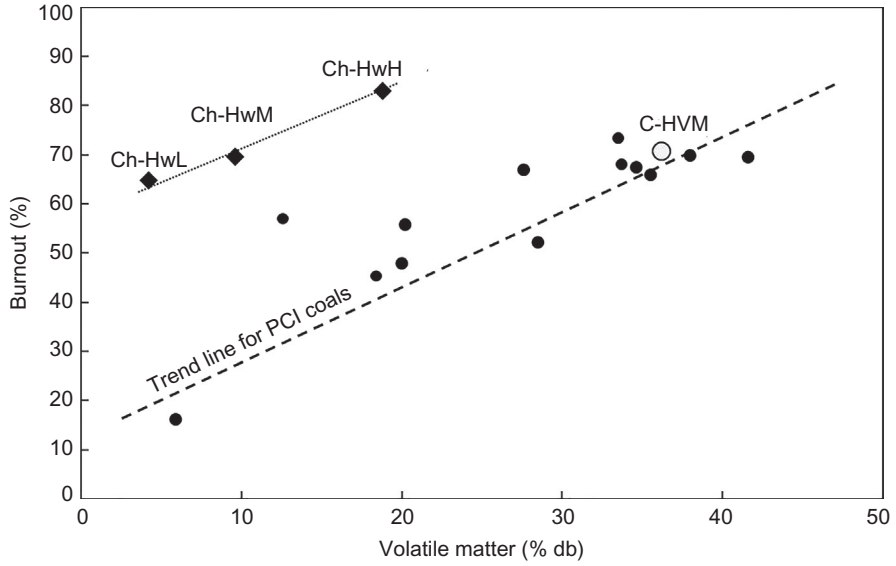

Figure 19.8 Combustion efficiency of hardwood charcoal types under simulated BF raceway conditions as a function of VM and comparison with PCI coals (the sample symbols are defined in Table 19.10).

Reproduced with the permission of the Steel Institute VDEh and the Iron and Steel Institute of Japan.

Table 19.10 Key properties of the coal and charcoal samples used in the combustion study

Parameter	PCI coal C-HVM	Medium-volatile softwood charcoal Ch-SwM	Medium-volatile hardwood charcoal Ch-HwM	Low-volatile hardwood charcoal Ch-HwL	High-volatile hardwood charcoal Ch-HwH
Proximate analysis					
Moisture % (ad)	3.5	8.1	8.6	4.1	6.8
Ash, % (db)	8.2	1.6	2.4	2.8	2.7
Volatile matter, % (db)	36.2	7.4	9.6	4.2	18.8
Fixed carbon, % (db)	55.6	91.0	88.0	93.0	78.5
Total sulfur, % (db)	0.50	nd	0.03	0.02	0.02
Phosphorus in coal, % (db)	0.003	0.052	0.118	0.014	0.022
Calorific value, MJ/kg (db)	31.81	33.14	32.20	32.48	31.00
Hardgrove grindability index	50	89	107	80	100
Crucible swelling no.	7	0	0	0	0
Ultimate analysis, % (daf)					
C	83.76	94.20	92.40	95.06	84.84
H	5.53	1.61	1.69	0.80	2.53
N	1.94	0.22	0.34	0.45	0.30
S_o	0.48	nd	0.03	0.0	0.01
O + errors	8.3	4.0	5.5	3.7	12.3

Notes: nd, not determined; ad, air dried; db, dry basis; daf, dry ash free.

(O/C = 2.4–2.7) are presented in Figure 19.9 and are representative of the full range of observations (Mathieson et al., 2012b).

The preinjection samples shown in Figure 19.9a and c were as expected from the work of Babich et al. (2010, 2011) and Ng et al. (2011a,b), with the charcoals retaining much of the cellular structure of the source wood. The distinction between softwood and hardwood structures is recognizable. The relict wood structures show significant microscopic porosity, unlike pulverized coals, where the particles appear as solid grains (Babich et al., 2009a,b, 2010), presumably with submicroscopic porosity.

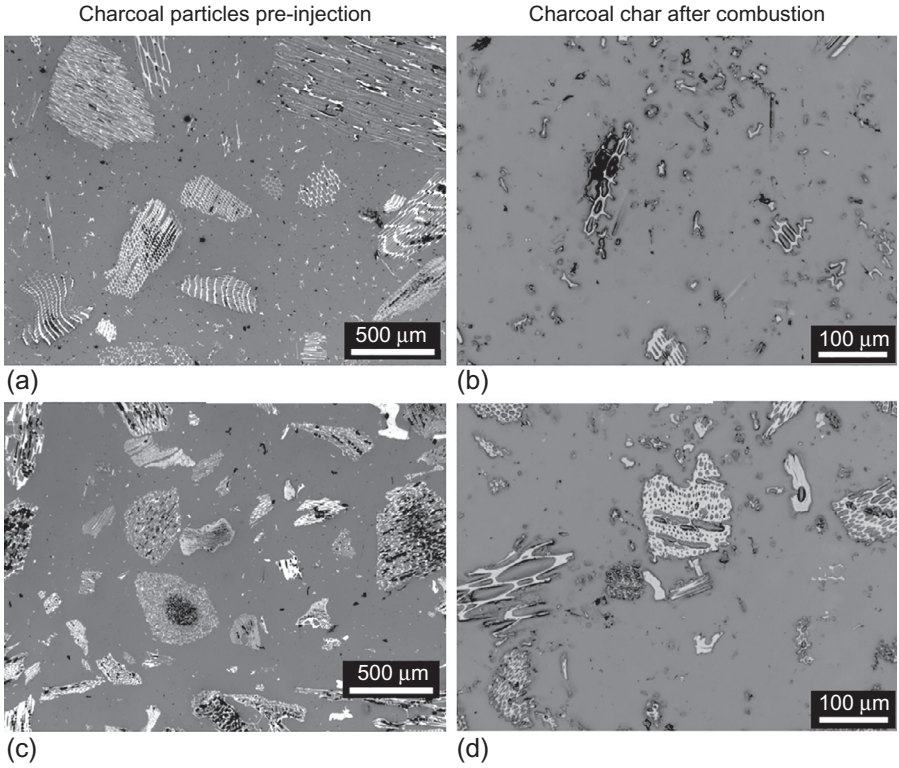

Figure 19.9 Reflected light optical micrographs of charcoal before injection and combustion chars: (a) and (b) medium-VM softwood charcoal (Ch-SwM); (c) and (d) low-VM hardwood charcoal (Ch-HwL). The uniform gray material is the mounting resin.
Reproduced with the permission of the Iron and Steel Institute of Japan.

The micrographs of the postcombustion chars (e.g., Figure 19.9b and d) indicate significant fragmentation of the charcoals during combustion (note the scale differences). Although both combustion chars contained some coarse grains, there was a predominance of smaller grains down to a few micrometers. For the softwood charcoal combustion chars (Figure 19.9a and b), the coarse grains tended to be elongated in outline, while the hardwood combustion chars (Figure 19.9d) tended to be equant to rounded. In both combustion chars, many of these finer grains were of lower reflectivity relative to the original charcoal samples, suggesting extensive heterogeneous reaction, while for the largest grains, patchy reaction was evident at the edges.

The overall impression from this study was that, unlike coals (Rogers et al., 2011), volatile release from charcoals is accompanied by significant fragmentation, creating additional surface area, and that the heterogeneous reactions of O_2 and CO_2 with the char are not pervasive but occur on the exposed surfaces. The increased combustibility of charcoals can be reasonably attributed to the heterogeneous reaction of the gases with the combustion chars. This is most likely due to the greater reaction surface presented, rather than the intrinsic chemical reactivity of the surfaces, in agreement with the findings of Ng et al. (2011a,b), Machado et al. (2010), and Babich et al. (2009a,b, 2010, 2011).

On the third question, although CPI has been successfully practiced in Brazil for many years (Campos de Assis et al., 2008; Machado et al., 2010), using conventional grinding equipment and both dense- and lean-phase pneumatic conveying, uncertainties remain regarding the introduction of charcoal into existing pulverized coal preparation plants. For example, Mathieson et al. (2012b) found that a persistent small proportion of larger particles was produced in small-scale grinding, necessitating removal via sieving. In commercial practice, this behavior may indicate that pendulum mills are preferred over table mills to minimize recirculation of oversize lamellar and acicular particles.

The injection of charcoal/coal mixtures (15%) is practiced at ArcelorMittal's Monlevade plant in Brazil, and Marques and Pepper (2010) have described the approaches developed to make this both an economic and technical success.

Overall, provided the charcoal selected for injection is optimized for ash and VM contents (see Table 19.5), the adoption of CPI should provide the following advantages:

- Major decrease in net CO_2 emissions
- Decreased BF fuel rate (and decreased CO_2 emissions specific to the decrease in coke rate)
- Improved BF gas permeability, allowing for higher productivity and/or increased injection rates
- Improved HM chemistry (lower Si, S, and P).

19.6.6 Applications in alternative and emerging ironmaking processes

Charcoal types generally should have good applicability to the updated, alternative, and emerging coal-based direct reduction and smelting-reduction processes, except perhaps for the kiln-based direct reduction processes, where low strength may lead to high levels of fines and loss of carbon via the off-gas stream. Table 19.11 provides a summary of potential applicability.

19.7 Future trends

Currently, only Brazil has a large biomass-based ironmaking industry. Despite the possibility of some local conflicts with other land and water uses, there is clearly potential for the growth of charcoal industries in many countries because of the potential effectiveness of using biomass-based fuels and reductants for net CO_2 emissions reduction (0.82–1.58 t-CO_2/t-crude steel). In fact, the worldwide demand could reach 135 Mt/year by the year 2050 if the steel industry is to achieve projected CO_2 emissions reduction targets.

The economics of charcoal supply appear to be favorable, especially in the situation where carbon pricing exists internationally. Probably, the greatest difficulty lies in the establishment of new large-scale pyrolysis industries because current process options appear to be suboptimal on yield, efficiency, product versatility, or environmental aspects, and there is a particular need to capture and realize the value of pyrolysis by-products.

Table 19.11 Likely applicability of charcoal types in alternative and emerging ironmaking and steelmaking processes

	Process	Potential substitution	Comments
Direct reduction	Rotary hearth furnace with carbon/ore briquettes/pellets, for example, FASTMET and ITmk3	Full	Requires low-VM charcoal and higher moisture levels; see Section 19.6.4
	Kiln-based, for example, SL/RN, CODIR	Partial	Not suitable as lump feed due to likely high fines loss to the off-gas; suitable as pulverized feed from the discharge end central burner
Smelting reduction	ULCOS top gas recirculation (TGR) or oxygen blast furnace (OBF)	Partial	Similar to normal blast furnace (see Table 19.4), with tuyere injection as the largest application
	COREX and FINEX	At least partial	Suitable as tuyere injectant; dense forms or briquettes may be suitable for the melter gasifier top charge
	HIsmelt and HIsarna	Full	All coal is pulverized, so pulverized charcoal should be a suitable substitute

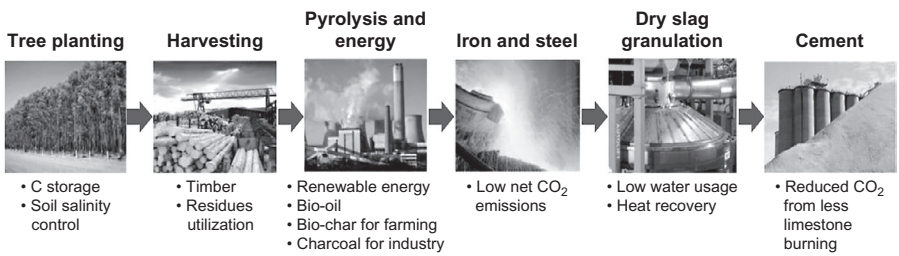

Figure 19.10 Conceptual integrated value chain for decreased net CO_2 emissions and other benefits.

Beyond the steel and metal industries, the production of biomass and resultant biochars can provide benefits more broadly, for example, to agriculture, the cement industry, and electrical power generation. An integrated value chain is illustrated in Figure 19.10 (also see Jahanshahi et al., 2014).

19.8 Sources of further information and advice

Babich and Senk (2013) give excellent background material on the use of biomass in the steel industry. Hanrot et al. (2011) provide a comprehensive survey of options for short-term CO_2 mitigation for steelmaking in a major study for the European community.

Issues related to biomass conversion technologies and sustainability assessments are reviewed by Suopajärvi et al. (2013). Suopajärvi and Fabritius (2013) exemplify a layered sustainability assessment framework for the use of charcoal in the steel industry.

An overview of the roles for biochar in environmental management has been provided in a monograph edited by Lehmann and Joseph (2009).

References

Antal, M.J., Gronli, M., 2003. The art, science and technology of charcoal production. Ind. Eng. Chem. Res. 42, 1619–1640.

Ariyama, T., Sato, M., 2006. Development of ironmaking process for reducing CO_2 emissions in the integrated steel works. ISIJ Int. 46, 1736–1744.

Assis, P.S., Campos de Assis, C.F., Mendes, H.L., 2009. Effect of charcoal physical parameters on the blast furnace powder injection. In: AISTech Proceedings—Volume 1, St. Louis, May, pp. 345–353.

Babich, A., Senk, D., 2013. Biomass use in the steel industry: back to the future? Stahl Eisen 133, 57–67.

Babich, A., Senk, D., Fernandez, M., 2009a. Blast furnace technology with charcoal injection: technological and ecological aspects. In: 5th International Congress on the Science and Technology of Ironmaking (ICSTI'09), Shanghai, October, pp. 762–766.

Babich, A., Senk, D., Gudenau, H.W., 2009b. Effect of coke reactivity and nut coke on blast furnace operation. Ironmak. Steelmak. 36, 222–229.

Babich, A., Senk, D., Fernandez, M., 2010. Charcoal behaviour by its injection into the modern blast furnace. ISIJ Int. 50, 81–88.

Babich, A., Ohno, K., Senk, D., Gudenau, H.W., Kowitwarangkul, P., Ueki, Y., Shimizu, M., 2011. Use of charcoal, biomass and waste plastics for reducing CO_2 emission in Ironmaking. In: EECR-METEC InSteelCon 2011, Dusseldorf June, Session 9, CD-ROM.

Bellevrat, E., Menanteau, P., 2009. Introducing carbon constraint in the steel sector: ULCOS scenarios and economic modelling. Rev. Metall. Paris 9, 318–324.

Birat, J.-P., 2011. CO_2-lean steelmaking: ULCOS, other international programs and emerging concepts. In: EECR-METEC InSteelCon 2011, Dusseldorf June, Session 1, CD-ROM.

Birat, J.-P., Hanrot, F., 2005. ULCOS—European steelmakers' efforts to reduce greenhouse gas emissions. In: 5th European Coke and Ironmaking Congress, Swedish Steel Producers' Association, Stockholm, June, We7: 4-1 to 4-12.

Brazilian Ministry of Mines, 2007. Brazilian Energy Balance. Brazilian Federal Government Ministry of Mines and Energy, Brasilia, p. 65.

Campos de Assis, C.F., Mendes, H.L., Cordeiro, F.C.M., Assis, P.S., 2008. Effect of charcoal physical parameters on blast furnace powder injection. In: 7th Japan-Brazil Symposium on Dust Processing–Energy-Environment in Metallurgical Industries, Sao Paulo, September, pp. 236–244.

COURSE50, 2014. See http://www.jisf.or.jp/course50/outline/index_en.html (accessed June 2014).

da Silva, A.M., de Oliveira, A.T., Medrado, S.B., de Oliveira, P.R., 2008. Study concerning the influence of adding biomass and increasing the coal blending bulk density over the quality of hard coke produced in the pilot coking oven. In: 3rd International Meeting on Ironmaking and 2nd International Symposium on Iron Ore, San Luis City, Brazil, September. pp. 1214–1226.

Deev, A.V., 2012. Apparatus and Process for Continuous Carbonisation of Wood Chips or Wastes and Other Charring Organic Materials for Charcoal Production. International Patent Application WO 2012174587, A1.

Deev, A., Jahanshahi, S., 2012. Development of a pyrolysis technology to produce large quantities of charcoal for the iron and steel industry. In: 6th International Congress on the Science and Technology of Ironmaking (ICSTI'12), Rio de Janeiro, October, pp. 1132–1142.

DGEngineering, 2013. Indirect heated rotary kiln plants for pyrolysis/thermolysis. Available from: http://www.dgengineering.de/Rotary-Kiln-Reference-Plants.html (accessed June 2014).

Diez, M.A., Borrego, A.G., 2013. Evaluation of CO_2-reactivity patterns in cokes from coal and woody biomass blends. Fuel 113, 59–68.

Fallot, A., Saint-Andre, L., Le Maire, G., Laclau, J.-P., Ouvellon, Y.N., Marsden, C., Bouillet, J.-P., Silva, T., Piketty, M.G., Hamel, O., 2009. Biomass sustainability, availability and productivity. Rev. Metall. Paris 106, 410–418.

FAO, 1985. Modern carbonising retort systems. In: Industrial Charcoal Making. FAO forestry paper 63. Food and Agriculture Organization of the United Nations, Mechanical Wood Products Branch. Available from: http://www.fao.org/docrep/x5555e/x5555e04.htm#chapter3.Moderncarbonisingretortsystems (accessed June 2014).

FAO, 1987. Carbonisation processes. In: Simple Technologies for Charcoal Making. FAO forestry paper 41. Food and Agriculture Organization of the United Nations. Mechanical Wood Products Branch. Available from: http://www.fao.org/docrep/x5328e/x5328e05.htm (accessed June 2014).

Fortini, O.M., Fruehan, R.J., 2005. Rate of reduction of ore-carbon composites: part 1. Determination of intrinsic rate constants. Metall. Mater. Trans. B 36B, 865–872.

Fruehan, R.J., Fortini, O., Paxton, H.W., Brindle, R., 2000. Theoretical minimum energies to produce steel for selected conditions. Consultant report for the U.S. Department of Energy, Office of Industrial Technologies, Washington, DC, 33pp.

Ghosh, A., 1999. Kinetics and mechanisms of reduction in composite iron ore-reductant pellets. In: International Conference on Alternative Routes of Iron and Steelmaking, AusIMM, Perth, Australia, September, pp. 71–78.

Gonçalves, L.J., de Oliveira, V.M., da Silva, F.R., 2012. Consumption of small charcoal in blast furnace 2 of APERAM South America. In: 6th International Congress on the Science and Technology of Ironmaking (ICSTI'12), Rio de Janeiro, October. pp. 1765–1776.

Gupta, R.C., Misra, S.N., 2001. Composite pre-reduced pellet quality as affected by reductant reactivity. ISIJ Int. 41 (Suppl.), S9–S12.

Halder, S., Fruehan, R.J., 2008. Reduction of iron oxide-carbon composites: part 1: estimation of the rate constants. Metall. Mater. Trans. B 39B, 784–795.

Hanrot, F., Sert, D., Babich, A., Pietruck, R., Fernandez, M., Diez, M.A., Bürgler, T., Delinchant-Lété, J., 2011. Short term CO_2 mitigation for steelmaking (SHOCOM). Final report to European Commission Directorate-General for Research and Innovation, EUR 24989 EN, 101pp.

Haque, N., Somerville, M., Jahanshahi, S., Mathieson, J.G., Ridgeway, P., 2008. Survey of sustainable biomass resources for the iron and steel Industry. In: 2nd Annual Conference of the Centre for Sustainable Resource Processing, Brisbane, November.

ISO, 2006. Determination of Coke Reactivity Index (CRI) and Coke Strength After Reaction (CSR). International Standards Organisation ISO Standard 18894:2006.

Jahanshahi, S., Deev, A., Haque, N., Lu, L., Mathieson, J.G., Norgate, T.E., Pan, Y., Ridgeway, P., Rogers, H., Somerville, M.A., Xie, D., Zulli, P., 2014. Current status and future direction of low emission integrated steelmaking process. In: Celebrating the Megascale: An EPD Symposium in Honor of David G. C. Robertson, TMS, San Diego, pp. 303–316, February.

Konishi, H., Usui, T., Harada, T., 2009. The preparation and behaviour of charcoal composite iron ore pellets. J. High Temp. Soc. 34, 14–19.

Kumar, M., Gupta, R.C., 1993. Influence of carbonization conditions on physical properties of acacia and eucalypt wood chars. Trans. Indian Inst. Metals 46, 345–352.

Kumar, M., Gupta, R.C., 1994. Influence of carbonization conditions on the gasification of acacia and eucalypt wood chars by carbon dioxide. Fuel 73, 1922–1925.

Kumar, M., Gupta, R.C., Sharma, T., 1992. Influence of carbonization temperature on the gasification of Acacia wood chars by carbon dioxide. Fuel Process. Technol. 32, 69–76.

Kumar, M., Gupta, R.C., Sharma, T., 1993. X-ray diffraction studies of acacia and eucalypt wood chars. J. Mater. Sci. 28, 805–810.

Kumar, M., Verma, B.B., Gupta, R.C., 1999. Mechanical properties of acacia and eucalypt wood chars. Energy Sources 21, 675–685.

Kunitomo, K., Ohno, K., Yokota, K., Okazaki, J., Nishimura, T., Kogure, S., 2013. Reduction behaviour of Iron oxide using woody biomass. In: IEAGHG/IETS Iron and Steel Industry CCUS and Process Integration Workshop, Tokyo, November. Available from: http://www.ieaghg.org/ccs-resources/technical-workshops/19-ccs-resources/technical-workshops/392-iron-steel-workshop (accessed June 2014).

Lehmann, J., Joseph, S. (Eds.), 2009. Biochar for Environmental Management: Science and Technology. Earthscan, London.

Lu, L., Adam, M., Hapugoda, S., Jahanshahi, S., Mathieson, J.G., 2012. Iron ore sintering with charcoal. In: 6th International Congress on the Science and Technology of Ironmaking (ICSTI'12), Rio de Janeiro, October, pp. 1121–1131.

Machado, J.G.M.S., Osorio, E., Vilela, A.C.F., Babich, A., Senk, D., Gudenau, H.W., 2010. Reactivity and conversion behaviour of Brazilian and imported coals, charcoal and blends in view of their injection into blast furnaces. Steel Res. Int. 81, 9–16.

MacPhee, J.A., Gransden, J.F., Giroux, L., Price, J.T., 2009. Possible CO_2 mitigation via addition of charcoal to coking coal blends. Fuel Process. Technol. 90, 16–20.

Marques, M.B., Pepper, F.V., 2010. Injeção de moinha de carvão vegetal no alto-forno A. In: 40th Seminar on the Reduction of Iron Ore and 11th Brazilian Symposium on Iron Ore, ABM, Belo Horizonte, April.

Mathieson, J.G., Rogers, H., Somerville, M., Ridgeway, P., Jahanshahi, S., 2011. Use of biomass in the iron and steel industry—an Australian perspective. In: EECR-METEC InSteelCon, Dusseldorf, June, paper 252, CD-ROM.

Mathieson, J.G., Norgate, T., Jahanshahi, S., Somerville, M.A., Haque, N., Deev, A., Ridgeway, P., Zulli, P., 2012a. The potential for charcoal to reduce net greenhouse emissions from the Australian steel industry. In: 6th International Congress on the Science and Technology of Ironmaking (ICSTI'12), Rio de Janeiro, October. pp. 1602–1613.

Mathieson, J.G., Rogers, H., Somerville, M., Jahanshahi, S., 2012b. Reducing CO_2 emissions using charcoal as a blast furnace tuyere injectant. ISIJ Int. 52, 1489–1496.

Matsumura, T., Ichida, M., Nagasaka, T., Kato, K., 2008. Carbonization behaviour of woody biomass and resulting metallurgical coke properties. ISIJ Int. 48, 572–577.

Miura, K., Hashimoto, K., Silverston, P.L., 1989. Factors affecting the reactivity of coal chars during gasification, and indices representing reactivity. Fuel 68, 1461–1475.

Miwa, T., Okuda, H., 2010. CO_2 ultimate reduction in steelmaking process by innovative technology for cool earth 50. J. Jpn. Inst. Energy 86, 28–35.
Nakano, M., Naito, M., Higuchi, K., Morimoto, K., 2004. Nonspherical carbon composite agglomerates: lab-scale manufacture and quality assessment. ISIJ Int. 44, 2079–2085.
Ng, K.W., Giroux, L., MacPhee, T., 2011a. Biofuel ironmaking strategy from a Canadian perspective: short-term potential and long-term outlook. In: EECR-METEC InSteelCon 2011, Dusseldorf, June, Session 9, CD-ROM.
Ng, K.W., MacPhee, J.A., Giroux, L., Todoschuk, T., 2011b. Reactivity of bio-coke with CO_2. Fuel Process. Technol. 92, 801–804.
Nishimura, M., Nishibata, Y., Matsudaira, K., 2004. Effect of waste wood addition to coal on coke quality. In: 21st Annual International Pittsburgh Coal Conference, Osaka, Paper 54-3.
Nogami, H., Yagi, J., Sampaio, R.S., 2004. Exergy analysis of charcoal charging operation of blast furnace. ISIJ Int. 44, 1646–1652.
Norgate, T., Haque, N., Somerville, M., Jahanshahi, S., 2012. Biomass as a source of renewable carbon for iron and steelmaking. ISIJ Int. 52, 1472–1481.
Ota, K., Nishibata, Y., Nishimura, M., 2006. Effect of waste wood addition to coal on coke quality. In: 4th International Congress on the Science and Technology of Ironmaking (ICSTI'06), Osaka, November, pp. 129–132.
Pfeifer, H.C., de Sousa, L.G., da Silva, T.T., 2012. Design of the charcoal blast furnace: difference to the coke blast furnace. In: 6th International Congress on the Science and Technology of Ironmaking (ICSTI'12), Rio de Janeiro Charcoal Ironmaking Course, Lecture 4, CD-ROM.
Piketty, M.-G., Wichert, M., Fallot, A., Aimola, L., 2009. Assessing land availability to produce biomass for energy: the case of Brazilian charcoal for steel making. Biomass and Bioenergy 33, 180–190.
Riegel, R., Kent, J.A., 1962. In: Kent, J.A. (Ed.), Industrial chemistry of wood, Chapman & Hall Ltd, London, pp. 591.
Rogers, H., Mathieson, J.G., Mason, M.B., 2011. The impact of coal petrographic composition on the combustion of pulverised coals under simulated blast furnace tuyere injection conditions. In: CHEMECA 2011, Sydney September, Paper 248, CD-ROM.
Sakurovs, R., 2000. Some factors controlling the thermoplastic behaviour of coals. Fuel 79, 379–389.
Somerville, M.A., Jahanshahi, S., Davies, M., Ridgeway, P., Mathieson, J.G., 2010. Sustainable carbon in steelmaking—plant trials at the Sydney Steel Mill. In: Sustainable Mining Conference, AusIMM, Kalgoorlie, Australia, pp. 38–52.
Somerville, M.A., Davies, M., Mathieson, J.G., Ridgeway, P., Jahanshahi, S., 2011. Addition of renewable carbon to liquid steel: plant trials at OneSteel Sydney Steel Mill. In: CHEMECA 2011, Sydney September, Paper 223, CD-ROM.
Somerville, M.A., Mathieson, J.G., Ridgeway, P., 2012. Overcoming problems of using charcoal as a substitute for coal and coke in iron and steelmaking operations. In: 6th International Congress on the Science and Technology of Ironmaking (ICSTI'12), Rio de Janeiro, October. pp. 1056–1057.
Stafford, O.F., 1921. Destructive Distillation Process. US Patent No. 1,380,262.
Suopajärvi, H., Fabritius, T., 2013. Towards more sustainable ironmaking—an analysis of energy wood availability in Finland and the economics of charcoal production. Sustainability 5, 1188–1207.
Suopajärvi, H., Mikko, A., 2011. Layered sustainability assessment framework. In: EECR-METEC InSteelCon 2011, Dusseldorf, June, Session 10, CD-ROM.

Suopajärvi, H., Pongracz, E., Fabritius, T., 2013. The potential of using biomass-based reducing agents in the blast furnace: a review of thermochemical conversion technologies and assessments related to sustainability. Renew. Sust. Energ. Rev. 25, 511–528.

Takeda, K., Anyashiki, T., Sato, T., Oyama, N., Watakabe, S., Sato, M., 2011. Recent developments in mid- and long-term CO_2 mitigation projects in ironmaking. Steel Res. Int. 82, 512–520.

Tonomura, S., 2013. Outline of course 50. Energy Procedia 37, 7160–7167.

ULCOS, 2014. See http://www.ulcos.org/en/index.php (accessed June 2014).

Valladares, S.K., Scherer, S.W.G., 2012. Brazilian green pig iron industry. In: 6th International Congress on the Science and Technology of Ironmaking (ICSTI'12), Rio de Janeiro October, Plenary Lecture, CD-ROM.

Wibberley, L., Nunn, J., Scaife, P., Zivals, A., Andrews, L., Coomber, B., Dickson, R., Gardner, D., Cowie, A., 2001. Large scale use of forest biomass for iron and steelmaking, NSW Government Sustainable Energy Research Development Fund (SERDF). Report by BHP Minerals Technology and State Forests, 109pp.

WSA, 2014a. Steel's Contribution to a Low Carbon FutureWorldsteel Position Paper. World Steel Association. June. Available from: http://www.worldsteel.org/publications/position-papers/Steel-s-contribution-to-a-low-carbon-future.html (accessed June 2014).

WSA, 2014b. CO_2 Emissions Data Collection. World Steel Association. Available from: http://www.worldsteel.org/steel-by-topic/climate-change/data-collection.html (accessed June 2014).

Life cycle assessment of iron ore mining and processing

20

N. Haque, T. Norgate
CSIRO Mineral Resources Flagship, Clayton South, VIC, Australia

20.1 Introduction

20.1.1 Principles of LCA

Life cycle assessment (LCA) is a recognized method for assessing the environmental impacts of products, processes, and services. It provides a scientifically sound method for comparing products and processes on common grounds and to identify so-called hot spots and provide opportunities for reducing environmental impacts. Ideally, LCA should be used to evaluate the total environmental burdens and benefits over the entire life cycle for a product from "cradle" to "grave" including material and energy used during extraction and processing of raw materials, manufacturing, transportation, reuse, recycling, and end-of-life disposal. Depending on the scope of a study, the LCA boundary sometimes is restricted to only a part of the full life cycle, for example, "cradle to gate." In a commercial sense, LCA assists environmental assessments such as ecolabeling, environmental product declarations (EPD), so-called carbon footprints, and GHG accounting and management. In the applications, the aim is to implement the principles of ecoefficiency, design for environment, or the discipline of industrial ecology that tries to mimic closed loop processes of natural ecology. Recently, some conceptual guides have been developed with the title life cycle sustainability assessment (LCSA), which covers conventional environmental LCA, life cycle costing (LCC), and social LCA (s-LCA) following the framework of international standards (UNEP/SETAC LCI, 2011). For these studies, environmental, cost, and social data of relevant unit processes are collected, impact indicators are selected, and overall sustainability is assessed. In this chapter, only environmental LCA is considered and global warming potential (GWP) is the impact indicator of the focus for iron ore.

Adequate primary process data (including databases) for industry sectors, such as energy, transport, mining and metals, agriculture, building construction, materials, and chemicals, are essential to LCA studies. There are initiatives in various countries to collect such data or develop databases (often referred to as life cycle inventories (LCI)) for LCA, which are sometimes under the leadership of government or private organizations or learned societies. One such initiative in Australia is called the Australian National Life Cycle Inventory Database Initiative (AusLCI), led by the Australian Life Cycle Assessment Society (ALCAS, 2012). Because of the complexity of many interlinked processes, an enormous amount of resources is required for the development of such databases.

There has been significant LCI data development for several thousand industrial processes in Europe. There was also an attempt to make some datasets of "world

Iron Ore. http://dx.doi.org/10.1016/B978-1-78242-156-6.00020-4
© 2015 Elsevier Ltd. All rights reserved.

average" technology for particular processes and customize these data sources for various regions of the world, including North America. One such database is called "Ecoinvent" (SCLCI, 2012). These databases have been packaged in standard LCA software, such as SimaPro developed by the Dutch company, PRé Consultants bv (PRe, 2012), and can be adjusted for specific regions. Ecoinvent Centre owns, maintains, and updates the Ecoinvent database and sells licenses as part of LCA software sales. Another LCA software, GaBi (PE International, 2012), also contains similar datasets, which are maintained and owned by the company. Given that LCA is an evolutionary methodology, any LCA study can be revised as more precise data become available for a specific technology or geographic location.

It can be expected that the environmental impacts, particularly energy consumption and greenhouse gas (GHG) emissions, of mining and mineral processing for many metals will become much more significant in the future than they currently are. It is therefore critical that the contributions of the various processing steps that make up these stages be quantified, with the major contributing steps being identified in order for efforts to reduce these environmental impacts be focused on these steps. With this objective in mind, LCA of the mining and mineral processing of iron ore was carried out in Australia.

20.1.2 Current status of LCA application in mining and mineral processing

The ever-increasing global demand for consumer goods means that the production of primary metals can be expected to increase well into the future, despite society's best efforts in recycling and dematerialization. The mining, mineral processing, and metal production sector, like other industrial sectors, is coming under increased pressure to reduce the amount of energy it consumes and GHGs it emits. This has led to the application of LCA methodology (discussed later) to the production life cycles of most metals (Norgate et al., 2007). However, most LCAs of metal production processes do not consider the mining and mineral processing stages in any detail, largely due to a lack of publicly available data. This generally means that mining and mineral processing are lumped together as a single stage in the metal LCA. This approach can often be justified by the relatively small contribution that the mining and mineral processing stages make to the "cradle-to-gate" environmental impacts of many metal production processes, particularly with regard to impacts such as embodied energy and GHG emissions. This is illustrated in Figure 20.1, which compares the embodied energy of the mineral processing to the downstream metal extraction (smelting and refining or hydrometallurgy) stages for iron, aluminum, and copper (Norgate et al., 2007). The life cycle-based GHG emissions have been estimated for iron ore, bauxite ore, and copper concentrate and published (Norgate and Haque, 2010) showing the contributions from the various unit processes of the mining and mineral processing stages. Part of this latter study has been modified for this book chapter.

Iron ore was chosen for this study due to the significant amount of this ore mined annually in Australia, as shown in Figure 20.2 over time. Since 2009, the production of

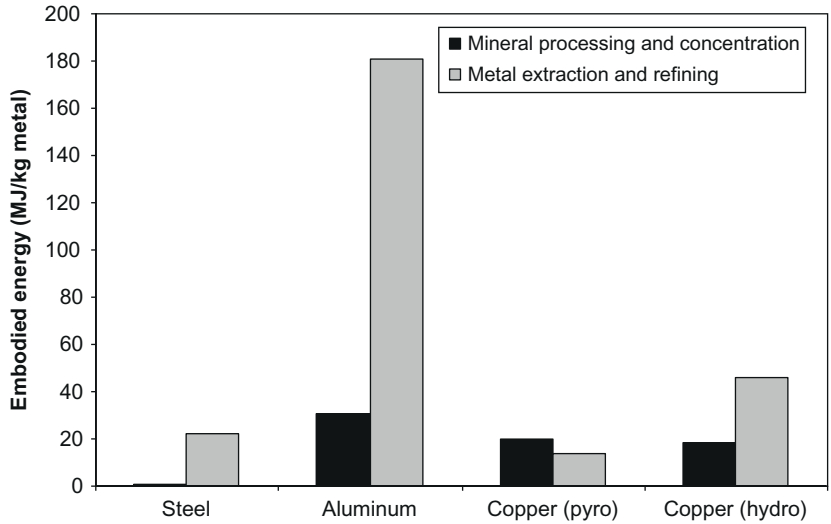

Figure 20.1 Mineral processing stage contributions to embodied energy of steel, aluminum, and copper production.

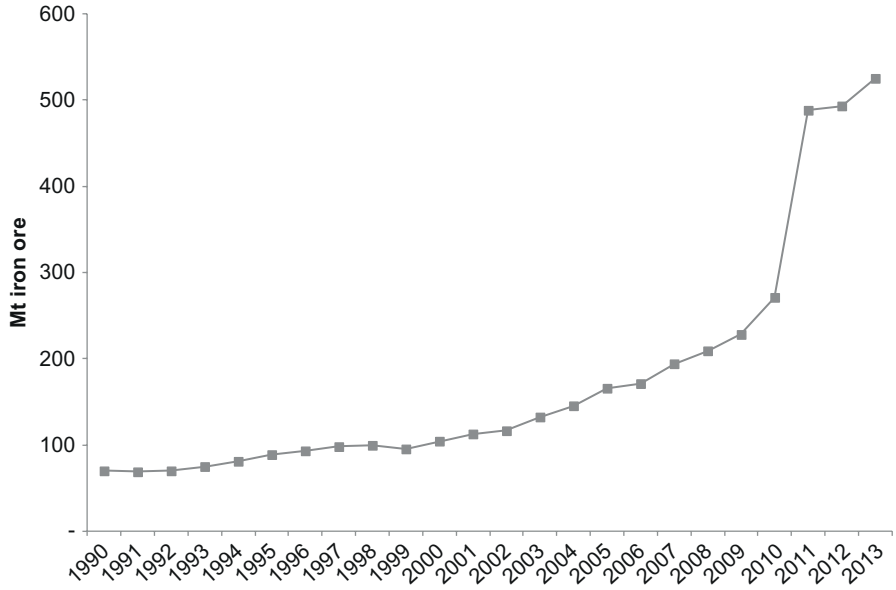

Figure 20.2 Historical annual tonnages of iron ores mined in Australia (2012 and 2013 forecast production (Curtis, 2013; Geoscience Australia, 2012)).

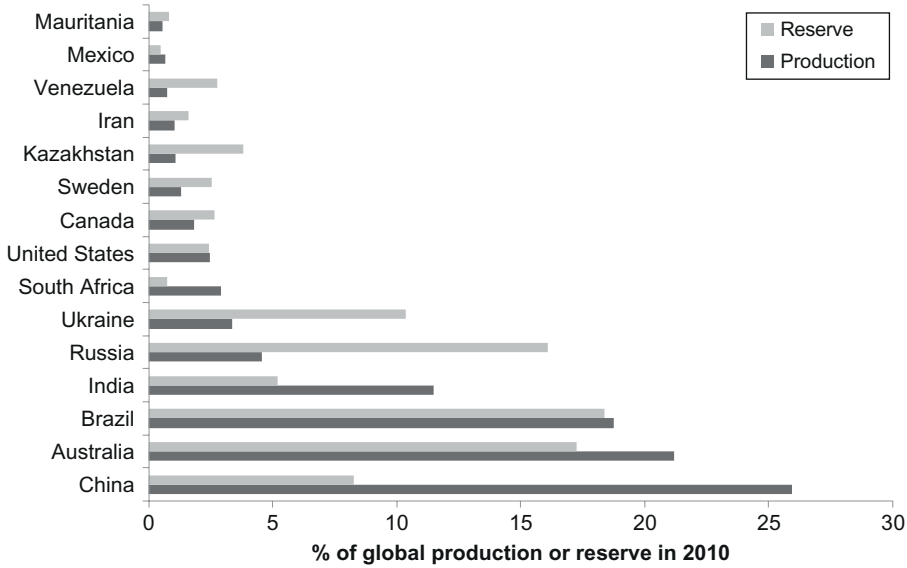

Figure 20.3 Percent of global production and reserve for major iron ore-producing countries in 2010 (data compiled by Curtis (2013) but reanalyzed for this chapter).

iron ore from Australia has risen significantly. The percentage of global production and reserves for the major iron ore-producing countries for 2010 is shown in Figure 20.3. It is evident from this figure that top four iron ore-producing countries are mining more than the percentage of global reserves they have. In contrast, the remaining countries in general are mining less than their percentage of global reserves. Iron ore is commonly transported to downstream metal extraction plants with minimum beneficiation because of their relatively high ore grades as mined (e.g., typically 60% for iron ores from Australia).

However, it was reported (Norgate and Jahanshahi, 2006; Mudd, 2007) that the grades (i.e., metal content) of metallic ores have been falling globally for some time and that this will have a significant effect on the amount of energy required for mining and processing of these lower-grade ores due to the additional amount of material that must be treated in these stages and additional processing steps to achieve optimum concentrate grades required for downstream smelting and refining. Therefore, lower ore grades will not significantly increase the energy consumption of the downstream metal extraction and refining stages of many metals (e.g., copper), as a concentrate of fixed grade is produced for downstream processing, irrespective of the initial ore grade.

In addition to falling ore grades, many of the newly discovered ore deposits are more fine-grained, requiring grinding to finer sizes in order to liberate the valuable or waste minerals in order to achieve separation and concentration. This will also increase the energy consumption of the mineral processing and the combined effects of declining ore grades and finer grind sizes on the embodied energy of metal. The status of iron ore resources has been discussed in detail in Chapter 1 (Holmes and Lu, 2015).

Many minerals contain iron, but the primary sources of iron ore minerals used to make iron and steel are hematite, magnetite, goethite, siderite, and pyrite. Hematite and goethite ores are most desirable because of their high iron content and ease of processing. Magnetite ore is increasingly being mined as more preferable deposits are becoming scarcer. Other less common iron-bearing minerals include pyrite, siderite, and titanomagnetite in mineral sand resources in some countries (e.g., iron sand in New Zealand). In terms of mining, there are six significant iron-containing mineral deposit types, but only three are generally considered to be viable for mining. Chapter 2 provides detail information about iron-bearing minerals (Clout and Manuel, 2015).

CSIRO sponsored the Mineral Futures Collaboration Cluster in 2009, which brought together researchers from the university sector in Australia and CSIRO to explore future sustainability issues in the minerals industry across regional, national, and global scales. The institutions brought in-depth knowledge about, and links into, a diversity of mining regions and communities in both the west and the east of Australia. CSIRO's partners in the cluster were the University of Queensland (Centre for Social Responsibility in Mining), Curtin University of Technology, the University of Technology, Sydney (Institute for Sustainable Futures), Australian National University, and Central Queensland University. In addition, researchers from Monash University also provided key research inputs to the cluster through the University of Technology, Sydney.

Among other areas, this cluster program focused on commodity futures and investigated the macroscale challenges, dynamics, and drivers of change facing the Australian minerals industry through scenarios and monitoring of peak minerals. The technology futures focus investigated the potential social and environmental impacts of, and community responses to, innovative new technologies being developed through the Minerals Down Under Flagship program. There were several reports produced on the sustainability and life of metals particularly focusing on iron ore, copper, and gold resources and production in Australia and with global comparisons. It was reported that there is a complex interrelationship between production technologies, consumption patterns, and the domestic and global infrastructure of the steel sector. Iron ore production globally was 2.3 Bt in 2013. The cluster research has used a model called Geological Resources Supply-Demand Model (GeRs-DeMo), which optimistically predicts that iron ore production in Australia would peak to 900 Mt in 2050 (Yellishetty et al., 2012a). It is possible that metals will not physically run out but will peak and then production will decline and be severely constrained by the challenges of lower grades, higher specific energy, carbon and water footprints, and cost of production.

20.2 Iron ore mining and processing

The extraction of iron ore involves surface (open-pit) or underground mining techniques (please refer to Chapter 7 (Stace, 2015) on Iron Ore Extraction Techniques). The LCA boundary used in this study is shown in Figure 20.4. The mining method selected depends on a variety of factors, including the nature and location of the deposit and the size, depth, and grade of the deposit. Underground mining requires more energy than

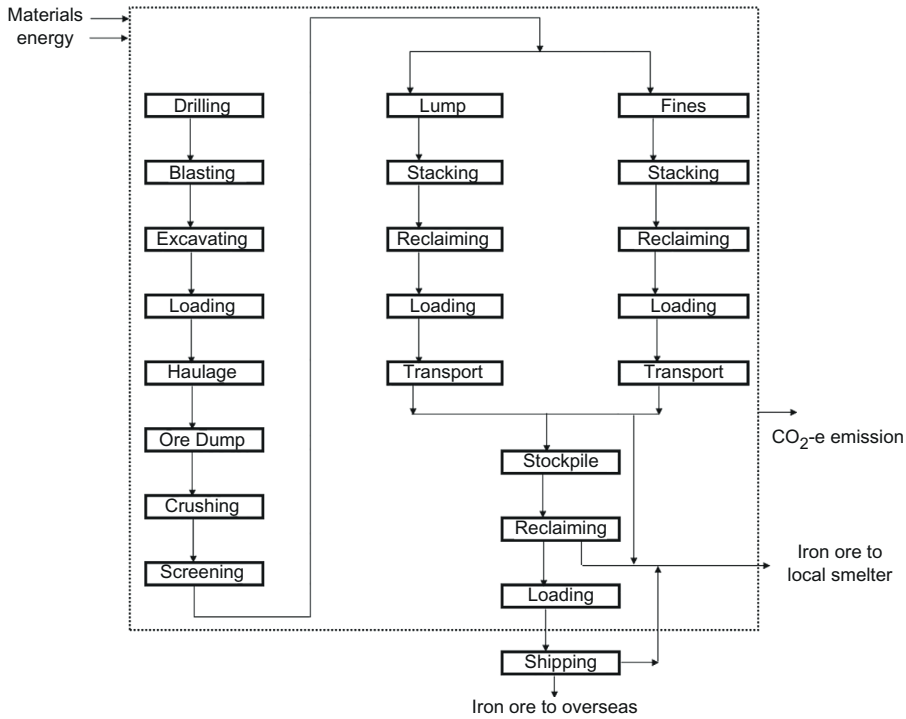

Figure 20.4 The boundary used for this GHG impact assessment using LCA.

surface mining due to greater requirements for hauling, ventilation, water pumping, and other operations. Surface mining accounts for the majority of iron ore being produced worldwide. The various mining and processing stages in Figure 20.4 are described briefly below and the readers can refer to earlier chapters for detailed description.

20.2.1 Drilling

Drilling is the act or process of making a cylindrical hole with a tool for the purpose of exploration, blasting preparation, or tunneling. Drilling equipment includes explosive loader trucks, diamond drills, rotary drills, percussion drills, and drill boom jumbos. Drills are run from electricity and diesel power and, to a lesser extent, indirectly from compressed air. The energy is used to power components of the drill that perform tasks such as hammering and rotation. The number of drilling machines on site is about two to six depending on the mine production capacity.

20.2.2 Blasting

Blasting uses explosives to aid in the extraction or removal of to be mined material by fracturing rock and ore using the energy released during the blast. The energy consumed in the blasting process is derived from the chemical energy contained in

the blasting agents. This sets blasting apart from other processes, which are powered by traditional energy sources, such as electricity and diesel fuel. A common explosive used for blasting operations is ammonium nitrate/fuel oil (ANFO) mixture. The powder factor is the amount of explosives used per unit of rock blasted and varies depending on the rock type and strength. Data were collected on the powder factor for various mine blasting operations. The explosive is detonated with a nonel (nonelectric) device for firing. Blasting reduces the size of ore before it undergoes crushing and grinding, thereby reducing the energy consumption of crushing and grinding processes. Therefore, optimizing blasting techniques will produce downstream energy savings.

20.2.3 Loading and haulage

In open-pit mines, the broken rocks are excavated by a front-end loader and loaded onto a dump truck for haulage to the processing plant. Most mines have a loading fleet including wheel loaders, shovel units, and excavators. The wheel loaders have a capacity ranging from 50 to 90 t, while the shovel units and excavators have capacities ranging from 200 to 250 t. The haulage units typically include off-road dump trucks with carrying capacities ranging from 150 to 300 t of rocks. Typical numbers of these haul trucks can be from 10 to 22 depending on the mine size.

Typical energy consumption data for the loading and hauling fleet were collected as part of this study. Much of the equipment used in the transfer or haulage of materials in mining is powered by diesel engines. Diesel technologies are highly energy-intensive, accounting for 87% of the total energy consumed in materials handling (US Department of Energy, 2007).

20.2.4 Crushing

Crushing is the process of reducing the size of run-of-mine material into coarse particles (typically coarser than 5 mm). The efficiency of crushing depends on the efficiency of upstream processes (rock fragmentation due to blasting or digging in the extraction process) and, in turn, has a significant effect on downstream processes (grinding or separations).

20.2.5 Screening and separations

Screening is an important step for dry beneficiation of iron ore. Crushing and screening is typically the first step of iron ore beneficiation processes. In most ores, including iron ore, valuable minerals are usually intergrown with gangue minerals, so the minerals need to be separated in order to be liberated. This screening is an essential step prior to their separation into ore product and waste rock. Secondary crushing and screening can result in further classification and grading of iron ore. The fines fraction is usually of lower grade compared with lump ore.

20.2.6 Stacking and stockpiling

Stackers are used for stockpiling so that bulk goods can later be reclaimed for loading onto a truck or rail containers for transporting to another stockpile in the port or steelworks or for shiploading. Mechanical stackers are operated using diesel fuel-based machinery or electricity.

20.2.7 Reclaiming and loading on container/vessel

Iron ores, either fines or lumps, are reclaimed from a stockpile for loading onto a vessel, container, truck, or ship for transport. Reclaimers use diesel fuel for their energy source.

20.2.8 Transport

Iron ores are transported from the mine site to the port for overseas export or to a local steelworks for making iron in a blast furnace. Ore is usually transported by either rail or truck to a port. Sometimes, ships are used for transporting ores to the port or a local steelworks. Transport fuel is diesel for both truck and rail. Diesel consumption for transporting iron ore was also sourced for this study.

Multitrailer trucks are also used for road transport to the nearest port for shipping. The transport distance by rail from the mine site to ports can be appreciable, for example, from a particular mine in Western Australia to the port at Dampier is about 200–300 km.

20.2.9 Auxiliary equipment

On most mine sites, there are other equipments used for road construction, maintenance, and dust suppression within the mine site, such as dozers, graders, excavators, and water tankers. These units use diesel fuel for their operation.

20.3 Application of LCA to iron ore mining and processing

LCA is a relatively new methodology that can be used to assess the environmental impact of various activities, products, and processes objectively. LCA covers the consecutive and interlinked stages of a product or process system, from raw material acquisition or generation from natural resources to final disposal. It essentially involves the compilation of an inventory of relevant environmental exchanges during the life cycle of a product and evaluation of the potential environmental impacts associated with those exchanges. The full product life cycle is usually divided into the following stages:

- Cradle to entry gate (raw material extraction and refining).
- Entry gate to exit gate (product manufacture).
- Exit gate to grave (product use, recycling, and disposal).

Based on impact assessment, two types of LCA can be distinguished, problem-oriented (midpoints) and damage-oriented (end points). The LCAs of iron ore mining and processing operations described in this chapter were all based on the problem-oriented approach and were carried out in accordance with the international standard LCA guidelines (ISO 14044, 2006) using the SimaPro software package.

20.3.1 Goal and scope

The goal of this study was to determine the energy consumption and associated carbon footprint of selected mining and mineral processing operations to assist the iron ore industry in identifying potential areas for improvement of their environmental performance, particularly as ore grades fall in the future. The study used typical iron ore mining and processing operations in Pilbara, Western Australia, as a case study and covers the upstream part of the cradle-to-gate life cycle of steel: the mining and processing of iron ore. Transport of lump and fines to the shipping port was also included, as these mines are usually located some distance inland in Australia. The iron ore mines were open-pit (i.e., surface) mines. The functional unit assumed for the study was 1 t of ore ready for shiploading. The impact categories considered were gross energy requirement (or embodied energy) and GHG emissions (expressed as GWP). The Australian impact method with normalization (version 1) has been used for calculation of the results based on Australian data. The assessment of other impact categories and various impact methods for this dataset has been published elsewhere (Yellishetty et al., 2012b).

20.3.2 Inventory data

There is not a great deal of published data in this area. The LCA inventory data used in the study were derived from a number of published sources, supplemented by other mining inventory data collected by the authors. Calculations were made by the authors and described below. All the inventory data used in the study are tabulated in Table 20.1. There was no need for any coproduction allocation, since all mine sites considered produced only one product (i.e., iron ore). Given the limited amount of publicly available data in this area, this study is considered to be a preliminary, or first-approach, investigation to assess the relative contributions of the various stages of the selected mining and mineral processing operations to the energy consumption and GHG footprints. It is anticipated that the inventory data will be refined further over time, with the LCA results being progressively updated as industry stakeholders become increasingly engaged.

20.3.3 Calculation procedure

Four Australian mine sites (i.e., Brockman, Paraburdoo, Hopes Down, and Yandicoogina) were chosen for this analysis to derive representative information for the iron ore mining and processing operations in Australia. These mine sites were chosen as they range from small to large iron ore mine sites in terms of production

Table 20.1 Inventory data for mining and ore processing operations used in study

Ore mined	Mining method	Stage	Inventory		
			Item	Value	Units
Iron ore	Open-cut	Drilling	Diesel	0.03	kg/t ore
		Blasting	Explosives[a]	0.5	kg/t ore
		Loading and hauling	Diesel	2.2	kg/t ore
		Crushing and screening	Electricity	2.5	kWh/t ore
		Stacking and reclaiming	Electricity	0.5	kWh/t ore
		Rail transport	Diesel	0.5	kg/t ore
		Port operations[b]	Electricity	0.8	kWh/t ore
		Overall	Water	0.21	m^3/t ore
			Diesel[c]	3.4	kg/t ore
			Electricity	135	MJ/t ore
			Explosives	3.8	kWh/t ore
			Waste rock	0.5	kg/t ore
					t/t ore

[a] Ammonium nitrate/fuel oil (ANFO)—94% AN and 6% FO. Production of AN = 7.1 MJ/kg, 1.2 kg CO_2-e/kg; ANFO = 7.6 MJ/kg, 1.4 kg CO_2-e/kg.
[b] Includes train unloading, stacking, reclaiming, and shiploading.
[c] Includes 0.7 kg/t ore from miscellaneous equipment.

capacity. Production data (i.e., the number of machines and annual production) for each mine site were collected from company websites and a published survey of each mine site (Mineral Processing Survey, 2008).

From the respective mining and mineral processing flowsheets, each processing unit was identified. Material and equipment required for each unit were then derived from published data. The number of the various equipment items, their capacities, and energy consumption were collected for each mine site from several sources, including mining and equipment manufacturing company websites and published survey (Mineral Processing Survey, 2008). Data for each mine site were weighted according to production tonnage to give the mean values per ton of iron ore produced, as shown in Table 20.1. As an additional cross-check, the calculated results were compared with published values where available.

20.3.4 Impact assessment of iron ore mining and processing stages

The energy and GHG results from the LCA study of the four iron ore mining and processing operations in Australia are given in Table 20.2 and shown graphically in Figure 20.5. The total GHG emissions and embodied energy value were 11.9 CO_2-e/t

Table 20.2 Energy and greenhouse gas results from the LCA study for iron ore mining and processing

Unit processes	Energy (MJ/t ore)	GWP (kg CO_2-e/t ore)
Drilling	1.3	0.1
Blasting	3.3	0.7
Loading and hauling	92.1	6.0
Crushing and screening	23.1	2.5
Stacking and reclaiming	4.6	0.5
Rail transport	20.9	1.3
Port operations	7.4	0.8
Total	152.7	11.9

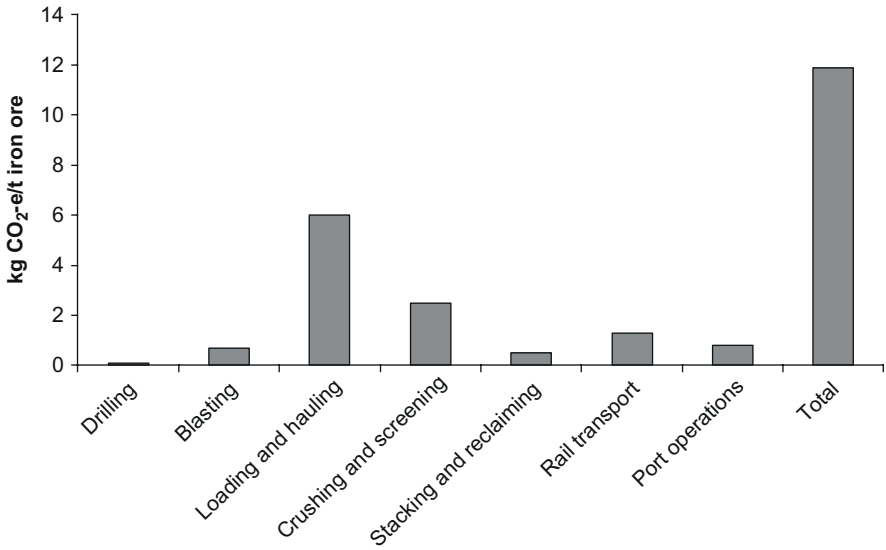

Figure 20.5 Stage contributions to GWP for iron ore production.

ore and 153 MJ/t ore for iron ore, respectively. These results show that loading and hauling made the largest contributions (approximately 50%) to the total GHG emissions from the mining and processing of iron ore. Explosives made only a small contribution to the overall GHG emissions, amounting to 0.7 kg CO_2-e/t iron ore. The annual GHG emissions resulting from the mining and processing of iron ore in Australia were also estimated in broad terms as 5.8 Mt for year 2011.

Yellishetty et al. (2010) reported a wide variation in the primary energy footprint of 1 t of iron ore for various countries (Figure 20.6). The data presented were reported to be an average of iron ore mining operations from India, Australia, Brazil, and Canada. However, the methodology used by Yellishetty et al. (2010) combined all energy types into one category without any correction for electrical or thermal energy type. Despite the efficiency factor for electricity, the variation would still be large. There would be

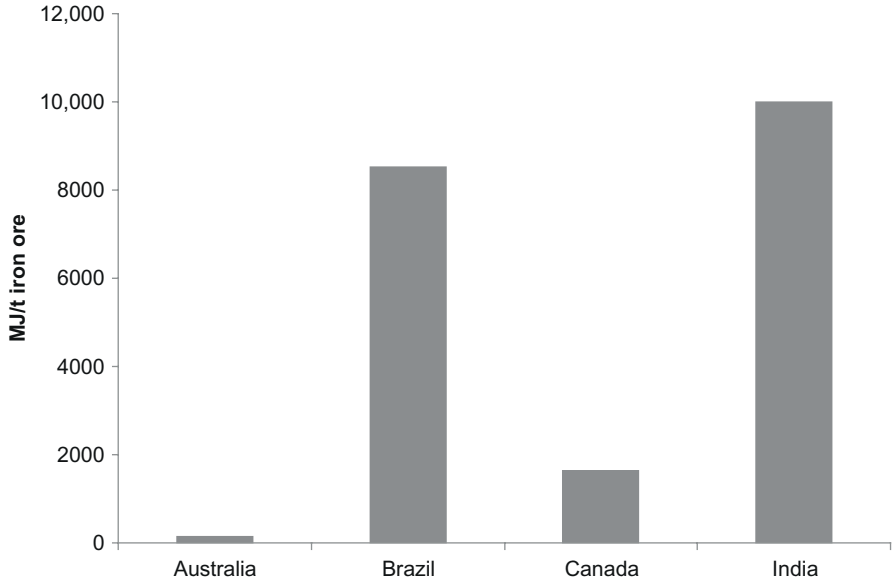

Figure 20.6 Primary energy footprint of iron ore production in various countries Yellishetty et al. (2010).

some differences due to the mining methods and technologies used and the type and grade of iron ore; however, the large differences between the countries seem unlikely and need further investigation.

20.4 Using LCA to reduce energy and GHG impacts

As loading and hauling followed by crushing and screening are the two main stages contributing to the energy and GHG footprints of iron ore mining and processing, it is these stages that offer the greatest potential for reducing the energy and GHG footprints. Likely approaches include the implementation of current best practice where feasible and the utilization of new and emerging technologies that reduce energy consumption and the associated GHG emissions of these stages.

Hauling trucks at mine site with larger payload (e.g., MT5500 AC 326 t mining truck, ultra class dump truck with 360 t payload, and BelAZ's 400 t dump truck with 3.3 MW engine power) to up to 400 t are becoming the newest addition by the equipment suppliers and used by the mining companies (Australian Mining, 2012). Although the engine power requirements are slightly higher compared with conventional trucks, the overall specific energy per unit of load is smaller for new trucks due to increase in efficiency. Some of these trucks can run on biodiesel or renewable fuel with lower carbon footprints. The development of electric mining shovels and trucks in some sites for loading and hauling system can have potential benefit if the electricity is sourced from renewable sources. This may lead to the reduction of an overall

emission footprint. These new innovative mine site vehicles and integrated system tools are expected to reduce the GHG footprint of iron ore when used.

It has been reported (US Department of Energy, 2007) that the metal mining industry in the United States has the potential to reduce energy consumption by about 61% from current practice to the best-estimated practical minimum energy consumption. This reduction was made up of a 21% reduction by implementing best practices and a 40% reduction from research and development that improves energy efficiency of mining and mineral processing technologies. Reported (US Department of Energy, 2007) current and practical minimum energy consumptions, including potential percentage energy savings for the various stages of the mining and mineral processing life cycle, are given in Table 20.3. Assuming these energy savings will be realized in the future, their effects on the greenhouse gas and embodied energy impacts of mining were estimated by incorporating these energy savings into the respective LCAs,[1] and the results are shown in Figure 20.7. As a conservative approach, no energy savings were assumed for those processing stages listed in Table 20.1 but not included in Table 20.3. The results in Figure 20.6 indicate potential reductions in the embodied energy and GHG footprints in the order of 30–40%.

Some of the new and emerging technologies that could contribute to these energy reductions also include high-pressure grinding rolls (Tavares, 2005) and stirred mills (Sinnott et al., 2006) for grinding, as well as more advanced blasting techniques (Brent, 2008) and further advances in diesel engine technology for loading and hauling applications (US Department of Energy, 2007). Another possible approach to improving the energy efficiency of loading and hauling is by optimizing pit and mine design to reduce haulage requirements. In some situations, the in-pit crushing and conveying (IPCC) system has potential to reduce GHG footprint of mining (Norgate and Haque, 2013) particularly for mines with high annual throughput and longer mine to mill

Table 20.3 Potential energy savings proposed for mining and mineral processing stages

Stage	Current energy consumption[a] (MJ/t ore)	Practical minimum energy consumption[a] (MJ/t ore)	Potential energy savings (%)
Drilling	2.7	1.5	43
Blasting	11.5	4.8	59
Loading and hauling[b]	87.2	41.5	52
Ventilation	17.5	13.6	23
Crushing	6.9	3.6	48
Crushing and grinding	220.6	63.2	71

[a]Primary energy (i.e., all electrical energy converted to thermal energy).
[b]Diesel equipment.
US DoE (2007).

[1] By applying the % energy savings in Table 20.3 to the respective energy inputs in Table 20.1.

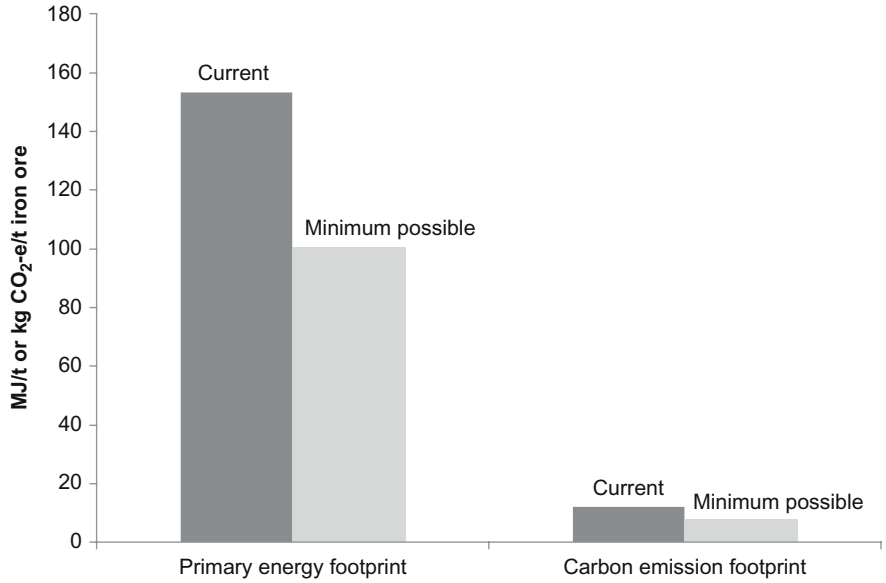

Figure 20.7 Comparison of current and best practical minimum primary energy and GWP of iron ore mining and processing.

transport distance employing conventional haul truck and shovel system. Furthermore, for example, in-pit mobile crushing and conveying systems for open-pit mining reportedly eliminate the need for trucks by having the shovel feed the run-of-mine ore directly to a continuous and dedicated belt conveyor handling system. Potential GHG savings of 100,000–133,000 t CO_2/year have been reported for these systems compared to a conventional shovel/truck operation.

20.5 Conclusions

Most LCAs of metal production processes do not consider the mining and mineral processing stage in any detail, largely due to a lack of publicly available data. This approach can often be justified by the relatively small contribution that the mining and mineral processing stages make to the "cradle-to-gate" environmental impacts of many metal production processes, particularly with regard to impacts such as embodied energy and GHG emissions. However, falling ore grades together with the likelihood of more finely grained deposits in the future will increase the energy and greenhouse gas impacts of these stages. It is therefore critical that the contributions of the various processing steps that make up these stages be quantified, with the major contributing steps being identified in order for efforts to reduce these environmental impacts be focused on these steps.

Based on the inventory data used in the study, it was observed that loading and hauling made the largest contributions (approximately 50%) to the total GHG emissions

from the mining and processing of iron ore (11.9 kg CO_2-e/t). These results indicate that efforts to reduce the GHG emissions should focus on loading and hauling for iron ore. There are a number of new and emerging technologies that could be expected to assist in this task, which includes further advances in diesel engine technology for loading and hauling applications.

20.6 Sources of further information and advice

There are other similar LCA software packages such as OpenLCA and databases available that readers can explore further (OpenLCA, 2015). The LCA discipline has publications covering relevant studies in established scientific journals, predominantly in the International Journal of Life Cycle Assessment, the Journal of Cleaner Production, and the Journal of Industrial Ecology.

International standards (ISO 14044, 2006) provide principles and framework for undertaking LCAs. LCA should include definition of goal and scope, inventory analysis, impact assessment, and interpretation of results, as its phases are illustrated in ISO 14044 (2006). International Standards series (ISO14041:1999, ISO14042:2001, and ISO14043:2001) provide further details on each of the steps and stages. Recently published ISO 14046:2015 provides guidelines for undertaking water footprints in LCA.

References

ALCAS, 2012. Australian Life Cycle Assessment Society and AusLCI Database Initiative. Available from: http://www.alcas.asn.au (accessed 23 August 2012).

Australian Mining, 2012. Minesite vehicles. Australian Mining 104/11 (November).

Brent, G., 2008. Reducing energy and greenhouse gas intensities of mining through blasting. In: Sustainable Development Conference, Darwin, September 2008. Minerals Council of Australia. Available from: www.sd08.com.au (accessed 17 March 2009).

Clout, J.M.F., Manuel, J.R., 2015. Mineralogical, chemical, and physical characteristics of iron ore. In: Lu, L. (Ed.), Iron Ore: Mineralogy, Processing and Environmental Sustainability. Woodhead publications, Elsevier, Cambridge, pp. 45–84.

Curtis, E., 2013. Sustainability Assessment of Key Metal Production and Predicted Exhaustion. CSIRO, Australia, EP133973.

Geoscience Australia, 2012. Australia's Identified Mineral Resources 2012. Commonwealth of Australia, Canberra. Available from: www.ga.gov.au (accessed 8 May 2013).

Holmes, R., Lu, L.,, 2015. Introduction: overview of the global iron ore industry. In: Lu, L. (Ed.), Iron Ore: Mineralogy, Processing and Environmental Sustainability. Woodhead publications, Elsevier, Cambridge, pp. 1–42.

ISO 14044, 2006. Environmental Management—Life Cycle Assessment—Requirements and Guidelines. International Organization for Standardization, ISO, Geneva, Switzerland.

OpenLCA, 2015. The Open LCA Project. Available from: http://www.openlca.org (accessed 31 March 2015).

Mineral Processing Survey, 2008. Plants in 2008 survey. Mining Monthly (May), 91–123.

Mudd, G., 2007. An analysis of historic production trends in Australian base metal mining. Ore Geol. Rev. 32, 227–261.

Norgate, T., Haque, N., 2010. Energy and greenhouse gas impacts of mining and mineral processing operations. J. Clean. Prod. 18, 266–274.
Norgate, T., Haque, N., 2013. The greenhouse gas impact of IPCC and ore-sorting technologies. Miner. Eng. 42, 13–21.
Norgate, T., Jahanshahi, S., 2006. Energy and greenhouse gas implications of deteriorating quality ore reserves. In: 5th Australian Conference on Life Cycle Assessment, Melbourne, November.
Norgate, T., Jahanshahi, S., Rankin, W.J., 2007. Assessing the environmental impact of metal production processes. J. Clean. Prod. 15, 838–848.
PE International, 2012. GaBi Software—A Software Solution by PE International. Available from: http://www.gabi-software.com (accessed 23 August 2012).
PRe, 2012. Life Cycle Consultancy and Software Solutions, SimaPro Software. Available from: http://www.pre.nl (accessed 23 August 2012).
SCLCI, 2012. Swiss Centre for Life Cycle Inventories Ecoinvent Database. Available from: http://www.ecoinvent.ch (accessed 23 August 2012).
Sinnott, M., Cleary, P., Morrison, R., 2006. Analysis of stirred mill performance using DEM simulation: part 1—media motion, energy consumption and collisional environment. Miner. Eng. 19, 1537–1550.
Stace, R., 1995. Iron ore extraction techniques. In: Lu, L. (Ed.), Iron Ore: Mineralogy, Processing and Environmental Sustainability. Woodhead publications, Elsevier, Cambridge, pp. 231–250.
Tavares, L., 2005. Particle weakening in high-pressure rolls grinding. Miner. Eng. 18, 651–657.
UNEP/SETAC LCI, 2011. Towards a life cycle sustainability assessment: making informed choices on products. Job Number DTI/1412/PA, Stockholm, pp. 1–33.
US Department of Energy, 2007, Industrial Technologies Program. Mining Industry Energy Bandwidth Study, June 2007.
Yellishetty, M., Ranjitha, P.G., Tharumarajah, A., 2010. Iron ore and steel production trends and material flows in the world: is this really sustainable? Resour. Conserv. Recycl. 54, 1084–1094.
Yellishetty, M., Haque, N., Dubreuil, A., 2012a. Issues and challenges in life cycle assessment in the minerals and metals sector: a chance to improve raw materials efficiency. In: Non-Renewable Resource Issues: Geo-scientific and societal challenges. Series of Books as Part of the International Year of Planet Earth, Springer, Heidelberg, Germany, pp. 229–246.
Yellishetty, M., Mudd, G., Mason, L., Mohr, S., Prior, T., Giurco, D., 2012a. Iron resources and production: technology, sustainability and future prospects. Prepared for CSIRO Minerals Down Under Flagship, by the Department of Civil Engineering (Monash University) and the Institute for Sustainable Futures (University of Technology, Sydney).

Index

Note: Page numbers followed by *f* indicate figures and *t* indicate tables.

A

Abrasion index (AI), 71*t*, 72, 482–483
Acidiphilium cryptum, 379
Acidithiobacillus caldus, 376
Acidithiobacillus ferrooxidans, 375–376, 378–379, 380, 381–382
Acid leaching, 357, 359, 360, 366, 369
Acidophilic bioleaching microorganisms, 378–379
Advanced granulation for innovation of sinter ore (AGIS) process, 426–427, 426*f*
Advanced Spaceborne Thermal Emission and Reflection Radiometer (ASTER), 199
AGIS process. *See* Advanced granulation for innovation of sinter ore (AGIS) process
Aguas Claras mine, 60
Algoma-type BIF, 51
Allflux, 324, 325*f*
  and gaustec testwork, 326, 327*t*
  and spiral concentrators, 325, 326*f*
Alljig, 318, 319–320, 319*f*
Allmineral allflux upflow classifier, 324, 325*f*
Aluminum-bearing clay minerals, 206–207
Amorphous phase, 90
Amphiboles, 208
Analytical spectral device (ASD), 195–196, 197–198
Anionic polymer dispersing (APD) agent, 426–427
Anti-Stokes Raman-shifted frequency, 195
Apatite, 358
Apurimac-Cusco porphyry-skarn belt, 48
ArcelorMittal's Mont-Wright project, 335
Archaean iron formation, 51
Arrium's Iron Duke Ore Beneficiation Plant, 335
Aspergillus niger, 378
Australian Pilbara operations, 38–39
Australia's iron ore
  BHP Billiton Iron Ore, 16, 17*f*, 18*f*
  Christmas Creek mine, 16–17, 19*f*
  FMG's Cloudbreak, 16–17, 19*f*
  location of, 11–12, 14*f*
  Pilbara region, 13–15, 14*f*
  producing and exporting, 3*t*, 7*t*, 11–12
  production tonnages, 13–15, 15*t*
  Rio Tinto, 16, 17*f*, 18*f*
Autogenous grinding (AG), 262, 265, 341
Automated optical image analysis (OIA)
  advantage, 153–154
  BMI sample (*see* Martite/kenomagnetite ore (BMI sample))
  compact sinter grain, 153–154, 154*f*, 155*f*
  correction of mineral maps, 131*f*, 133–135, 134*f*, 135*f*, 136*f*
  image processing, 136–141, 138*f*, 140*f*
  nonopaque minerals, 118–124, 120*f*, 122*f*, 123*f*
  particles and opaque minerals, 114–118, 115*f*, 116*f*, 117*f*, 119*f*
  particle separation, 124–128, 124*f*, 126*f*, 127*f*
  porosity identification, 128–129, 129*f*
  RM1 sample, 150
  unidentified minerals identification, 129–133, 131*f*, 132*f*, 133*f*, 134*f*
Automatic control systems (ACS), 539–540, 540*f*
Auto-SEMs technology
  advantages, 185
  disadvantages, 181*t*, 185–186
  EDS detectors, 165–166
  grain size, 173
  hematite-quartz binary particle, 173–174
  iron oxide discrimination, 167
  liberation, 173–174
  lithotyping/microlithotyping, 173
  locking, 173–174
  magnetite/hematite distinction, 171–173
  mineral abundance, 171, 172*t*
  mineralogical system, 170

Auto-SEMs technology *(Continued)*
morphological classification, 166, 166*f*
"one-button" approaches, 187
smarter, 186, 187
textural analysis, 171, 176*f*
uses of, 161–162, 163*t*
XRMs, 187
ZAF correction factors, 166

B

Bacillus circulans, 381
Bacillus subtilis, 384
Backscattered electron (BSE), 162, 164
Ball milling
bentonite dosage, 451, 453*t*
blending hematite and pyrite cinder, magnetite, 454–455, 454*f*
blending magnetite concentrates, effect of, 452*f*
closed circuit, 451
dry circuit, 451
fineness effect, 451, 451*t*
full-scale pellet plant trial, 452–454, 453*t*
open circuit, 451
wet circuit, 451
Ball mills, 263, 265–266, 266*f*, 270, 277
Banana screens, 256, 256*f*
Banded iron formations (BIFs)
abrasion properties, 72
CWi, 70
high-grade hematite ores, 58–60, 59*t*
magmatic and contact metasomatic deposits, 340–341
martite-goethite ore, 47*f*, 49*t*, 55–58, 56*f*, 58*f*
mesobands and microbands, 53–54, 53*f*
phosphorus, 357, 369
sedimentary rock, 340
texture and geologic age, 51
unenriched iron formation ores, 52*t*, 54–55, 55*t*, 56*f*, 57*f*
Baosteel static load reduction test, 500
Batac jig, 316, 316*f*
Baum jig, 316, 316*f*
Baur–Glaessner equilibrium diagram, 530–531, 530*f*
Beeshoek mine, 30
Beneficiation. *See also* Biobeneficiation
Arrium low-grade beneficiation plants, 321, 322*f*
in China, 18*f*, 349–350
flotation cell in, 13*f*
jigging (*see* Jigging)
LIMS, 306
physical beneficiation, 360
screening (*see* Screening)
separation medium, 310
spiraling, 328–337
sulfide ores, biobeneficiation of (*see* Sulfide ores, biobeneficiation)
Bentonite, 441–442, 445, 447, 449*f*, 453*t*, 454, 456, 457–459, 460*f*
Bézier–Spline curve, 337
BHP Billiton Iron Ore, 16, 17*f*
BIFs. *See* Banded iron formations (BIFs)
Biobeneficiation, 373
commercial bioleaching acidophilic bacteria, 381–382
soil bacteria, 382–384
sulfide ores, 380–381
Bioflocculation, 373–374, 380, 381
Bioflotation, 373–374, 381, 386
Bioleaching
commercial bioleaching acidophilic bacteria, 378–379
phosphorus bioleaching fungi, 378
soil bacteria, 379
sulfide ores, 380
Biomass
advantage, 582
charcoal's advantages and disadvantages, 584, 585*t*, 586*f*
chemical properties, 582, 583*t*
CO_2 emissions, 570–571, 571*f*
environmental impacts, 570
fuel (*see* Economic sources)
GHG (*see* Greenhouse gas (GHG) emission)
integrated value chain, 608, 608*f*
life-cycle assessment methodology, 574–575
low substitution rates, 570
NO_x emissions, 571–572, 573*f*
physical and chemical properties, 588*t*, 589
pyrolysis, 588*t*, 592–594
raw biomass and biomass-derived char, 570

reduction disintegration index, 574
sinter yield, 574
sources, 609
SO_x emissions, 571–572, 573*f*
steel industry, 581
tumble strength, 574
Blaine index, 440–441
Blast furnace—basic oxygen furnace (BF-BOF) route, 252
Blast furnace (BF) iron-making technology
ACS, 539–540, 540*f*
anthracite and charcoal charging, 533
bell-less/no-bell charging systems, 511, 511*f*
burden components, 530–531, 530*f*
bustle pipe, 511, 512*f*
CCS, 483
charging apparatus and gas uptakes, 510, 511*f*
chemical processes, 476–477
in China, 481*t*
COREX export gas injection, 540, 541*f*
decrepitation index, 483, 484*f*
dimensions, 507, 508*f*, 508*t*, 509*t*
flexibility and adaptability, 505
fluidized bed direct reduction process, 541, 542*f*
free swelling index, 486–488, 488*f*
German blast furnaces, 507, 507*f*
hot stoves, 511*f*, 512
injection (*see* Injection technology)
instrumentation, 537, 538*f*
long-term BF evolution, 542, 543*f*
low-temperature reduction disintegration index, 483–485
mantle support/freestanding, 510, 511*f*
mathematical models, 539
nonstandardized tests, 488–492, 489*f*, 490*f*, 491*f*
nut coke, 531–532, 532*f*, 533*f*
operational conditions, and ferrous burden quality requirements, 478*t*
ore storage yard, 510, 510*f*
principles of, 480, 512–513, 513*f*
probes, 537, 538*f*
profile, 506, 506*f*
reducibility index, 485–486, 486*f*, 487*f*
runner cover, 511, 512*f*
shatter index, 483
staves, 508
steel production routes, 505
stockhouse, 510, 510*f*
tapping, 511, 512*f*
thermal and chemical conditions, 480–481, 480*f*
top gas recycling, 535*f*, 540, 541*f*
tumble and abrasion indexes, 482–483, 482*f*
tuyere monitoring, 538, 539*f*
tuyere stock, 511, 512*f*
unit size, 529, 529*t*
water-cooled copper tuyeres, 511, 511*f*
Blasting, 233, 234*f*, 235, 239, 245
Bond abrasion index (Ai), 72
Bragg–Brentano geometry, 87, 87*f*
Brazil's iron ore, 349
production of, 18, 20*t*
Samarco's pelletizing complex, 21, 23*f*
Vale's Carajás mine, Para, 17–18, 19*f*
Vale's iron ore, 19–21, 21*f*, 22*t*
Brockman Iron Formation ore, 363–366
Brockman 2 processing plant, 257, 258*f*
Bureau of Mines Experimental Station, 344, 345, 346
Burkholderia caribensis, 379
Burkholderia cepacia, 379
Bustle pipe, 511, 512*f*

C

Calibration procedure, 138–139, 140*f*
Canada's Labrador province, 334–335
Candida albicans, 376
Carajás system in Brazil, 3–4
Carbonates, 208
Carbon dioxide (CO_2) emissions
air leakage reduction, 558
biomass, 570–571, 571*f*
characteristics, 553–554, 554*f*
charging method, 556, 556*f*
deep bed sintering, 554
MIRs, 557
multislit burner, 557–558, 558*f*
sinter plant heat recovery, 557
Super-SINTER® technology, 555–556, 555*f*
waste fuels, 557
Carburization, 525, 526
Carol Lake operation, Canada, 33–35, 34*f*

Casa de Pedra mine
open pit view, 245–247, 246*f*
stockpiles, 245–247, 247*f*
Terex 503 haul truck, 247, 247*f*
US Geological Survey report, 245
Cationic flotation, 346–347
Caustic leaching, 357, 360, 366, 369
Chadormalu iron ore, Iran, 35, 36*f*, 37*f*
Channel iron deposits (CIDs), 15, 48, 61–62, 62*f*
Charcoal injection
blast furnace operating parameters, 601, 603*t*, 604*f*
burn-out/combustion efficiency, 601, 602*t*
CO_2 emissions reductions, 586*t*, 600
combustibility improvement, 601, 603*t*
compositions, 601, 605*t*
injectant parameters, 601, 602*t*
low-VM hardwood charcoal, 601–605, 606, 606*f*
medium-VM softwood charcoal, 601–605, 606, 606*f*
optimized quality parameters, 588, 588*t*, 607
sample symbols, 601, 604*f*
Charcoal powder injection (CPI), 587
Chemical separation
phosphorus removal (*see* Phosphorus removal)
silicon, aluminum, and sulfur minerals, removal of, 367–368
China's iron ore
average in situ analyses, 8, 10*t*
beneficiation plant, 9–11, 12*f*
flotation cell, 9–11, 13*f*
formations, and mining areas, 8, 9*t*
iron ore-producing companies, 9, 11*t*
LIMS, 9–11, 12*f*
occurrence, 8, 8*f*
production, 2*f*, 5–8, 7*t*
provinces, 8, 9*t*, 10*f*
SLon WHIMS, 9–11, 13*f*
trade, 3*t*, 5–8
Worldsteel Association, 1, 2*f*
Chip scanning systems, 196–198, 196*f*
Chlorite, 207
Christmas Creek deposit, 242
Circofer® process, 541, 542*f*
Circular motion screens, 255, 256*f*
CITIC Pacific Mining's Sino Iron project, 13–15
Citric acid, 378
Clay minerals, 206–207
Cleveland ironstone mines, 233–234
Cliffs Natural Resources iron ore operations, United States, 31–32, 32*f*
Cloudbreak mine, 242
Cluster analysis, 92, 93*f*
Coarse-grained specular hematite, 32–33, 34*f*
Coarse ore stockpile (COS), 259
CO_2 emissions. *See* Carbon dioxide (CO_2) emissions
Coke oven gas (COG), 534–535
Cold crushing strength, 483
Comminution and classification technology
banana/multislope screens, 256, 256*f*
BHP Billiton Newman iron ore handing hub, 259, 260*f*
CAPEX and OPEX considerations, 279–280, 280*f*, 281*f*
cone and gyratory crushers, 253, 254, 254*f*
fine screening technologies, 272–274, 273*f*, 274*f*
grinding (*see* Grinding)
grizzly screen, 255, 256*f*
horizontal low-head/linear vibrating screens, 256, 256*f*
hydrocyclone separators, 267–268, 267*f*, 268*f*
inclined/circular motion screens, 255, 256*f*
jaw crushers, 252–253, 252*t*, 253*f*
low-grade hematite ores, 251
mobile crushing and screening plant systems, 261–262
Rio Tinto iron ore processing plants, 257, 258*f*
rotary scrubbers, 257
Roy Hill operation, 259, 261*f*
Vale S11D project, 261
vibrating screen, 255, 256*f*
VRM, 275–276, 275*f*
Companhia Siderúrgica Nacional (CSN), 18, 244–245, 247–248
Computational fluid dynamics (CFD), 336–337
Cone crusher, 253, 254, 254*f*
Conglomerate, 171, 176*f*
COREX export gas injection, 540, 541*f*
COREX Linder test, 500
COREX® process, 497–498, 499*t*

CO_2 Ultimate Reduction in Steelmaking Process, 581
Crushability work index (CWi), 70, 71*t*
Crushing
  BHP Billiton Newman iron ore handing hub, 259, 260*f*
  cone and gyratory crushers, 253, 254, 254*f*
  crusher types, 252, 252*t*
  jaw crushers, 252–253, 252*t*, 253*f*
  mobile crushing plant systems, 261–262
  Rio Tinto iron ore processing plants, 257, 258*f*
  Roy Hill operation, 259, 261*f*
  Vale S11D project, 261
CSIRO Mineral4 OIA software, 106, 118, 121, 123, 131, 136*f*
CSIRO point analysis scanning robot, 198
Cyclone efficiency, 268*f*

D

de Broglie wavelength equation, 162
Debye–Waller factor, 86
Decrepitation index (DI), 483, 484*f*
Deep bed sintering, 554
Deep mining of iron ore, 231
Dense medium separation (DMS)
  medium density considerations, 315
  medium recovery, 315
  Mount Tom Price plant, 312, 313*f*
  particle size limit, 315
  performance measurement, 313–314, 314*f*
  principle, 310
  Sishen plant, 310–311, 311*f*, 312*f*
Denver jig, 316, 317*f*
Derrick screens, 272, 273*f*, 274, 274*f*
Desliming, 345–347
Desulfovibrio desulfuricans, 382
Detrital iron deposits (DIDs), 15, 48
Dioxin emissions
  additives, 567–568, 568*f*
  calcined/dry zone, 562–563, 563*f*
  de novo formation characteristics, 562–563, 563*f*
  emissions reduction, 565
  MSWI, 562
  optimal temperature, 563–564
  process variables, 565–566
  raw materials, 566–567
  sintered material zone, 562–563, 563*f*
  sintering (flame front) zone, 562–563, 563*f*
  thermal and oxidizing conditions, 563–564
  upper limits, 551–553, 552*t*
  vaporization and condensation process, 564
  wet zone, 562–563, 563*f*
Direct reduced iron (DRI), 475, 476*f*
Direct reduction (DR), 456–457
  chemical characteristics, 495*t*
  metallurgical characteristics, 495*t*
  MIDREX Hot Load test, 496
  MIDREX Linder test, 496
  MIDREX® process description, 493–494, 494*f*
  physical characteristics, 495*t*
  raw material requirements, 494–495, 495*t*
Direct shipping ore (DSO), 12–13, 33–35, 35*f*, 200, 202*f*, 241–242, 251, 252
Disk magnetic scavenger, 288–289, 289*f*
DMS. *See* Dense medium separation (DMS)
Dodecylamine, 346
Donganshan processing plant, 350
Double toggle crusher, 252–253, 253*f*
DR. *See* Direct reduction (DR)
Drum low-intensity magnetic separators (drum LIMS), 293–294, 293*f*
  and magnetic column flow sheet, 294, 295*f*
  and reverse flotation flow sheet, 294, 296*f*
  and SLon magnetic separator flow sheet, 296–297, 297*f*
Dry magnetic separators, 306
DSO. *See* Direct shipping ore (DSO)
Dust emissions
  characteristics, 569
  factors, 570
  upper limits, 551–553, 552*t*
DVLO theory, 383

E

Ecart probable (E_p), 314
Eccentric shaft, 252–253, 253*f*
Economic sources
  actual/potential supply, 590
  biomass resources, 590
  charcoal usage rates, 590
  cost estimation, 592, 592*t*
  eucalypt and pine plantations, 590
  evaluation, 591
  forestry harvesting residues, 591, 591*t*
  nonforestry residues, 591, 591*t*

Economic sources *(Continued)*
processing costs, 590
ULCOS project, 589, 590
wood processing residues, 591, 591*t*
Electric arc furnace (EAF) process, 475
Electronic spectroscopy, 194
Electron probe microanalysis (EPMA), 105, 165
Electrophoretic mobility, 342, 343*f*
Electrostatic precipitators (ESPs), 551–553
Elutriation, 323–324, 324*f*
Emissions Optimized Sintering (EOS®) system, 397
Empire Mines, 262–263
Energy-dispersive (EDS) detectors, 165–166
Equivalent circular diameter (ECD) values, 173
Ernest Henry Mining, 13–15
Extracellular polymeric substance (EPS), 376–377, 377*f*, 380, 381, 384, 386
EZRaman-I Series, 196*f*, 199–200

F

Field emission gun (FEG) platforms, 167
Field spectroradiometer, 195–196
FLOGEN™, 404–405
Flotation, 374
aluminum removal, 347–348
challenges, 352–353
Donganshan processing plant, 350
equipment, 348–349
hematite and quartz, 343*f*
Paenibacillus polymyxa, 383–384
phosphorus removal, 348
Republic Mine, 351, 352*f*
reverse anionic flotation, 346–347, 349–350
reverse cationic flotation, 346–347, 349–350
silica separation, 343–347
sulfur removal, 348
Tilden Mine, 350, 351*f*
Fluidized bed direct reduction process, 541, 542*f*
Fluorapatite, 358
Fortescue Metals Group (FMG), 16–17
Fortescue's Christmas Creek operation, 335*f*
Fossil auxiliary reducing agents, 533–534
Fourier transform infrared (FTIR) spectrometer, 197–198
Frodingham Ironstone bed, 234–235
Fundamental parameters approach, 88–89

G

Gangue minerals, 285–286, 292
amphiboles, 208
carbonates, 208
characteristic absorption features, 201*t*, 205
chlorite, 207
clay minerals, 206–207
electronic and vibrational processes, 194*f*, 202*f*, 205
hydroxyl-bearing silicates, 205
quartz, 205–206
talc, 207–208
German blast furnaces, 507, 507*f*
GHG emission. *See* Greenhouse gas (GHG) emission
Gibbsite, 200, 201*t*, 202*f*, 340, 348, 352
Goethite, 220
B3LYP, 362–363
chemical composition, 45, 46*t*
CIDs, 61–62, 62*f*
forms of, 46–47, 47*f*
lattice constant refinement, 94–97
metasedimentary iron ore deposits, 46–47, 47*f*
points of zero charge, 342, 342*t*
reflectance spectroscopy, 200, 202, 202*f*
reflected light photomicrograph, 108–110, 110*f*
Gohar Zamin iron ore mine, 35
Gol Gohar iron ore, Iran, 35, 37*f*
Gongchangling deposit, 55
Granular iron formations (GIFs), 51, 52*t*
Granulation, 398–402
alumina content, 419–420, 420*f*
assimilation behavior, 416–418, 417*f*
chemical characteristics of iron ore, 402, 403*f*
coarse ore particles, thermal cracks, 415, 417*f*
cohesive strength, 415
melt penetration, 416, 417*f*
mineralogical characteristics of iron ore, 400–401, 401*f*, 402*f*
physical characteristics of iron ore, 399–400, 400*f*
water absorption capacity, 415

Grate-kiln (GK) system, 435–438, 450–451, 460, 462, 470
Gravity separation techniques
  DMS, 310–315
  jigging, 315–322
  spiraling, 328–337
  upflow classification/hindered bed settling (*see* Upflow classification)
Green balls
  ball milling, 450–454, 451*t*, 452*f*, 453*f*, 453*t*
  damp milling, 444–446, 444*f*, 445*t*
  formation mechanism, 442–443, 442*f*
  HPGR, 446–450, 446*f*, 447*f*, 448*f*, 449*f*, 449*t*, 450*t*
  hydrated lime, fluxed pellets, 459, 460*f*
  organic/bentonite composite binders, 457–459, 458*f*
  organic binders, 456–457
  quality requirement, 440*t*
Greenhouse gas (GHG) emission, 616
  applications, 584, 586*t*, 588
  BOF fuel, 588–589, 588*t*
  CPI, 587
  emissions reduction, 585, 586*t*
  liquid steel recarburizer, 588*t*, 589
  PCI, 587
  pilot-scale testing, 587
  scrap substitute, 588*t*, 589
Green pellets
  blending magnetite concentrates and HPGR pretreatment, 462–465, 463*f*, 464*f*, 465*f*
  boron-containing additives, 465–466, 466*f*
  MgO and basicity, 466–469, 467*f*
  microstructures and bonding mechanisms, fired pellets, 460–462, 461*f*
Grinding
  equipment, 264
  gangue minerals, 292
  HPGRs, 262–263
  stirred milling, 269–272, 270*f*, 271*f*, 271*t*
  tumbling mills, 264–266
  typical Empire grinding—concentrating line, 262, 263*f*
  Vertimill® fine grinding technology, 262–263
  VRM, 275–276
Grizzly screen, 255, 256*f*
Gyratory crusher, 253, 254, 254*f*

H

Hamersley-type BIFs, 51
Harz jig, 316, 317*f*
Haver & Boecker Latinoamericana (HBL), 261
Hazardous minerals, 199
HCI-3 SystemT, 196–197, 196*f*
HDPE piping, 332*f*
Heat exchange
  idle/thermal reserve zone, 515–516, 518*f*
  intensity of heat transfer, 517, 519*f*
  lower zone of heat exchange (H_3), 515–516, 518*f*
  temperature profile, 515, 517, 518*f*
  upper zone of heat exchange (H_1), 515–516, 518*f*
Heating treatment, 357, 363, 367
Hematite
  BIF (*see* Banded iron formations (BIFs))
  blast furnace lump quality, 66*t*, 75–78, 76*f*, 77*t*
  bulk density, 74, 74*t*
  chemical composition, 45, 46*t*, 65–68, 66*t*, 67*t*
  electrophoretic mobility, 342, 343*f*
  frictional properties, 72, 72*t*, 73*f*
  iron formation-hosted iron ore deposits, 51–53, 52*t*
  lattice constant refinement, 94–97
  lump decrepitation index (DI) and ore groups, 78, 78*f*, 79*f*
  lump material-handling properties, 64*f*, 69, 70*f*
  microplaty hematite ore, 56*f*, 58*f*, 60–61
  Mycobacterium phlei, 382
  oxidation of magnetite, 45
  phosphorus removal, 360
  points of zero charge, 342, 342*t*
  product particle size, 74, 75*f*
  reflectance spectroscopy, 200, 202, 202*f*
  reflected light photomicrograph, 108, 109*f*
  relative hardness, 64*f*, 68–69
  specific gravity, 70, 71*t*
  textural classification, 50*t*, 56*f*, 58*f*, 62–65, 63*t*, 64*f*
Hematite-goethite mixtures, 203, 204*f*
Hematite thresholding segmentation, 114–116, 115*f*

Hibbing taconite mining operations in United States, 31–32, 32*f*
High-grade Simandou deposit in Guinea, 3–4, 5*f*
High-pressure grinding rolls (HPGRs), 262–263, 341
  advantages, 278
  Arrium Whyalla magnetite grinding circuit, 277
  bentonite dosage, 447–448, 448*f*, 453*t*
  Blaine improvement, 277
  COMFLEX® plant flowsheet, 279
  components and grinding mechanism, 276–277, 276*f*
  efficiency of, 447–448
  feed moisture, 446–447, 447*f*
  green pellets, quality of, 442*t*
  Los Colorados, 277
  open-circuit configuration, 448–449, 449*t*
  ore texture, changes in, 446, 446*f*
  for pellet production, 277
  pilot-scale testing, 279
  size and SSA, PFFT samples, 450, 450*t*
  size distribution, 445*t*
  specific surface areas, 447, 448*f*
  Zourerat iron ore mine, 277, 278*f*
HORIBA Scientific LabRAM HR Evolution Raman microscope, 199–200
Horizontal screens, 256, 256*f*
Hot briquetted iron (HBI), 493
Hot reducing gases (HRG), 535, 535*f*
HPGRs. *See* High-pressure grinding rolls (HPGRs)
Hybrid pelletized sinter (HPS) process, 423–424, 424*f*
Hydrocyclone separators, 267–268, 267*f*, 268*f*
Hydrohematite
  chemical composition, 45, 46*t*
  reflected light photomicrograph, 108, 109*f*
  solid solution structure, 47
Hydrous iron oxides, 220
HyLoggingT systems, 196–198, 196*f*
HyMap, 199
Hyperspectral drill core, 196–198, 196*f*
Hyperspectral imaging systems, 198, 198*f*
Hypothetical DMS partition curves, 314, 314*f*

I

iDiscover software, 173
Idle/thermal reserve zone, 515–516, 518*f*
India's iron ore
  characteristics of, 22–23, 24*t*
  economic deposits, 21, 23*f*
  estimation, 4*t*, 21
  exports, 25, 26*t*
  installed pelletizing capacity, 25, 26*t*
  production, 7*t*, 25
  SAIL iron ore mining operations, 23–25, 25*f*
Injection technology
  COG, 534–535
  coinjection, 537
  flexible injection, 537
  fossil auxiliary reducing agents, 533–534
  homogeneous mixtures, 537
  HRG, 535, 535*f*
  noncombustible materials, 536
  renewable energy sources, 535–536
  waste plastics, 534, 534*f*
Integrated mine and beneficiation plant in Liaoning Province, 9–11, 12*f*
Intensified sifting feeder (ISF), 421–423, 422*f*
Interparticle crushing, 253
Iran Central Iron Ore, 35
Ironmaking applications
  alternative and emerging processes, 607, 608*t*
  BF charcoal injection (*see* Charcoal injection)
  BF nut coke replacement, 586*t*, 597–598
  BF reducible and prereduced composite feeds, 598–600, 600*f*
  biocoke production, 594–597, 596*f*, 597*f*
  pyrolysis, 588*t*, 592–594
  sintering solid fuel, 586*t*, 597
Iron ore-producing countries, 7*f*, 191, 192*t*
  in Australia (*see* Australia's iron ore)
  in Brazil (*see* Brazil's iron ore)
  in Canada, 32–35, 33*f*, 34*f*, 35*f*
  in China (*see* China's iron ore)
  geologic formations, 3–4, 6*f*
  higher-cost iron ore producers, 40–41, 41*f*
  high-grade Simandou deposit, 3–4, 5*f*
  in India (*see* India's iron ore)

in Iran, 35, 36*f*, 37*f*
prices fluctuation, 40–41, 41*f*
in Russia, 26–27, 27*f*, 28*t*
in South Africa, 29–30, 29*f*, 30*f*
in Sweden, 35–37, 38*f*
technology status and challenges, 38–40
in Ukraine, 27–29, 28*f*
in United States, 31–32, 31*f*, 32*f*, 33*t*
in West Africa, 3–4, 5*f*, 6*t*
Iron ore shiploading at Saldanha Bay in South Africa, 29, 30*f*
Iron oxide Cu-Au (IOCG) deposits, 48
Iron–oxygen–carbon system, 519
Iron–oxygen–hydrogen system, 519
Iron sands, 62
Ironstone bands, 232
IsaMill™, 271–272, 271*f*
ISO RDI test, 484–485
Itabirite, 19, 51, 60
ITmk3® process, 31–32

J

James mine, 33–35
Japanese permeability unit (JPU), 402, 403*f*
Japanese steel mill (JSM), 409–410
Jaw crushers, 252–253, 252*t*, 253*f*
JFE Steel Corporation Kurashiki no. 2 sinter machine, 420–423, 420*f*
Jigging
advantages, 322, 322*t*
assessment of, 321–322, 322*f*, 322*t*
Baum and Batac jigs, 316, 316*f*
disadvantages, 322, 322*t*
Harz and Denver jigs, 316, 317*f*
jig bed, layer thickness, 318–319, 319*f*
Kelsey jig, 320, 321*f*
movable bed, 319, 319*f*
principle of, 316–318, 316*f*, 317*f*
product extraction, 318–319, 319*f*
ragging deck, 319–320, 320*f*
variable speed star gate, 319, 319*f*
water column movement, 317–318, 317*f*
JKTech, 167–170

K

Kaolinite, 200, 201*t*, 202*f*, 347, 352, 377, 377*f*, 383–384
Kelsey jig, 320, 321*f*
Kenomagnetite
chemical composition, 45, 46*t*
metal-deficient spinel phases, 45
reflected light photomicrograph, 108, 109*f*
Khumani mine, 30
Kiruna-type iron oxide-apatite ores, 48
Kiruna underground mine, 35–36, 38*f*
location and geology, 236–237
1365 m level, 240–241
sublevel caving, 237–240, 238*f*, 239*f*
worldwide iron ore market, 236
KMAruda iron ore mine, 272, 273*f*
Kolomela mine, 29
Kumba Iron Ore operations in South Africa, 29, 29*f*, 30, 30*f*

L

Labrador Iron Mines (LIM), 33–35
Labrador Trough, 32–33, 33*f*, 34*f*
Lake Superior-type BIF-GIF taconite, 54–55
Lambiotte carbonization process, 593
"Large section stereological correction,", 136–137
Laser power, 200
LCA. *See* Life cycle assessment (LCA)
Leaching, 369
acid leaching, 357, 359, 360, 366, 369
caustic leaching, 357, 360, 366, 369
and heating temperature, 364*t*
microbial leaching, 373
nitric acid, 367
percolation, 359
Lepidocrocite, 220
Leptospirillum ferriphilum, 376
Life cycle assessment (LCA)
auxiliary equipment, 622
blasting, 620–621
calculation procedure, 623–624
crushing, 621
drilling, 620–621
goal and scope, 623
inventory data, 623
loading and haulage, 621
principles, 615–616
reduce energy and GHG impacts, 626–628
screening and separations, 621
stacking and stockpiling, 622
transport, 622
Limonite, 46–47, 360–362

LIMS. *See* Low-intensity magnetic separators (LIMS)
Lincolnshire mines, 234–236
Lisakovsky iron ore, 360–361
LKAB. *See* Luossavaara-Kiirunavaara Aktiebolag (LKAB)
Load-Haul-Dump (LHD), 235, 239–240, 239*f*
Loss on ignition (LOI), 404, 409–410, 411, 480–481
Low-intensity magnetic separators (LIMS), 9–11, 12*f*. *See also* Drum low-intensity magnetic separators (drum LIMS)
  disk magnetic scavenger, 288–289, 289*f*
  magnetic column separator, 287–288, 287*f*
  magnetic thickener, 288, 288*f*
  permanent magnetic drum separator, 286–287, 286*f*
Low-VM hardwood charcoal (Ch-HwL), 601–605
Luossavaara-Kiirunavaara Aktiebolag (LKAB), 35–36, 37, 38*f*, 39*f*, 236, 237–240, 262

M

Maghemite
  alluvial deposits, 47
  chemical composition, 45, 46*t*
  reflected light photomicrograph, 108, 109*f*
Magnetic brake feeder (MBF), 421–423, 422*f*
Magnetic column separator, 287–288, 287*f*
Magnetic separation
  ball mill grinding, 293–294
  dry magnetic separators, 306
  gangue minerals, 285–286
  iron and ceramic balls, 283, 284*f*
  iron ore-related minerals, magnetic susceptibility, 284–286, 285*t*
  Jones wet high-intensity magnetic separator, 289–290, 290*f*
  large magnetic separator models, 305–306
  low-intensity magnetic separators, 286–289
  magnetic force on particles, 283–284, 284*f*
  magnetite ores, flow sheets for (*see* Magnetite)
  oxidized iron ores, flow sheets (*see* Oxidized iron ores)
  principles, 292
  SLon vertical ring and pulsating high-gradient magnetic separator, 290–292, 291*f*
  subeconomic iron ores, utilization of, 306
Magnetic thickener, 288, 288*f*
Magnetite
  abrasion properties, 71*t*, 72
  AG mills, 262
  Arrium Whyalla magnetite grinding circuit, 277
  blast furnace lump quality, 66*t*, 75–78, 76*f*, 77*t*
  blending hematite and pyrite cinder, 454–455, 454*f*
  bulk density, 74, 74*t*
  chemical composition, 45, 46*t*, 65–68, 66*t*, 67*t*
  cyclone efficiency, 267–268, 268*f*
  drum LIMS flow sheet, 292–294
  energy-efficient magnetite processing flowsheet, 280*f*
  frictional properties, 72, 72*t*, 73*f*
  grains in green pellets, 462
  iron sands, 62
  lump decrepitation index (DI) and ore groups, 78, 78*f*, 79*f*
  metasedimentary and magmatic origin, 45
  OPEX and NPV for, 281*f*
  phosphorus removal, 358–359
  points of zero charge, 342, 342*t*
  product particle size, 74, 75*f*
  reflectance spectroscopy, 200–201, 203*f*
  reflected light photomicrograph, 108, 109*f*
  Sino iron magnetite concentration plant, 263, 264*f*
  specific gravity, 70, 71*t*
  spinel structure, 45
  unenriched iron formation ores, 52*t*, 54–55, 55*t*, 56*f*, 57*f*
Main Seam, 233, 234
Marcona Mine, 348
Marra Mamba fine ore, 15, 150, 151*f*
Martite
  chemical composition, 45, 46*t*
  hematite pseudomorphs, 45
Martite-goethite ores, 47*f*, 49*t*, 55–58, 56*f*, 58*f*
Martite/kenomagnetite ore (BMI sample)
  liberation analysis, 141–144, 145*t*

liberation histogram, 144, 146*f*
mineral association analysis, 144–146, 146*f*, 147*t*
mineral maps, 141, 142*f*
"modal analysis,", 141–144, 143*t*
statistical processing and output, 150
textural classification, 146–150, 148*t*, 149*t*
Medium-VM softwood charcoal (Ch-SwM), 601–605
Melt penetration, 416
Metal
carburization, 525, 526
iron–carbon phase equilibrium diagram, 525, 526*f*
typical composition, 526, 527*t*
Metallic iron-bearing resources (MIRs), 557
Metalloinvest's iron ore operations in Russia, 26, 27*f*
Metalloinvest's Lebedinsky iron ore mine in Russia, 26, 27*f*
Metamict zircon, 171
Michigan iron ore deposits in United States, 31–32, 31*f*
Microbial leaching, 373
Microorganisms, 373
adhesion mechanisms, 375–376
growth conditions, cell surface, 376
mineral selectivity, microbial adaptation, 377–378
mineral surface, microbial adhesion, 376–377
sulfur-oxidizing microorganisms, 373
Microplaty hematite replacement ore, 51, 60–61
Mid infrared (MIR), 194*f*, 199, 206*f*
clay minerals, 206–207
mineralogy and composition, 209, 210*f*
quartz, 205–206
MIDREX Hot Load test, 496
MIDREX Linder test, 496
MIDREX® process, 494*f*
shaft furnace, 494–495
stages, 493–494
Minas Gerais Province, Brazil, 244–248
Mineral properties
liberation, 341
mineralogy and occurrence, 340–341
surface and electrokinetic properties, 341–342
Mineral4/Recognition4 software, 146
Minnesota iron ore deposits in United States, 31–32, 31*f*
Mitigation. *See* Sintering
Mont-Wright Mining Complex operation, 33–35
Mosaic embedding iron ore sintering (MEBIOS) process, 424–426, 425*f*
Mount Newman Mining Co. Pty Ltd, 12–13
Mount Tom Price DMS plant, 312, 313*f*
Mount Whaleback mine, 15, 16*f*, 61
Mt Moss Mining in Queensland, 13–15
Multiple-stage elutriation circuit, 324, 324*f*
Municipal solid waste incinerator (MSWI), 562
Mycobacterium phlei, 375, 382

N

National Mineral Development Corporation (NMDC), 23–25
NEO HySpex, 196–197, 196*f*
Net present value (NPV), 280, 281*f*
Newcastle Technology Centre (NTC), 416–417
Newman Hub, 259, 260*f*
New Millennium Iron Corporation, 33–35
Ningxiang ore, 360
Nippon Steel Corporation (NSSMC), 426–427, 426*f*, 427*f*, 428*f*
Nitric acid, 358–359, 360, 361, 367, 369
Nitrogen oxide (NO_x) emissions
biomass, 571–572, 573*f*
characteristics, 560–561
mitigation, 561–562
upper limits, 551–553, 552*t*
Nonstandardized tests
CSIRO softening and melting test facility, 489, 490*f*, 491*f*, 491*t*
Fe-C-O ternary system, 488, 489*f*
North Lincolnshire mines, 234–236

O

Ochreous goethite, 56*f*, 57
Off-line data mining, 165–166
OIA. *See* Optical image analysis (OIA)
Oolitic hematite ores, 360
Opencast methods, 232

Optical image analysis (OIA)
automated OIA (*see* Automated optical image analysis (OIA))
automated segmentation of imaged objects, 105
EPMA, 105
image acquisition, 104–105
image improvement, 105
iron oxides and oxyhydroxides, 107–110
manual check and correction, 106
measurements, 106, 107*f*
mineral identification, 106
nonidentified minerals, 105–106
object separation, 105
porosity identification, 105
reflected light microscopy, 102
sinter, 110–114, 112*f*, 113*f*
transmitted light microscopy, 101
Optical remote sensing technologies, 199
Oxidation processes
coke behavior, 524, 524*f*
coke circulation, 522–524, 523*f*
flame temperature, 524, 525, 525*t*
gas composition and temperature, 521, 522*f*, 524
oxidizing zone, 521, 522*f*
raceway with coke motion without circulation, 522–524, 523*f*
Oxidized iron ores, 295–305
drum LIMS, 296–297, 297*f*
reverse flotation flow sheet, 298–299, 299*f*, 300–301, 300*f*, 304*f*
SLon magnetic separator flow sheet (*see* SLon magnetic separator)

P

Paenibacillus polymyxa, 377, 377*f*, 379–380, 381, 383–384
Paraburdoo processing plant, 257, 258*f*
Pebble mills, 266
Pelletization
in China, 436–438, 436*f*
fired pellets, 438, 439*t*, 455, 469
green balls (*see* Green balls)
milling time, effect of, 441*t*
pellet feed, requirements of, 440–442
pretreatment of pellet feed, 443–454
production, 436–438, 437*t*
Penicillium citrinum, 378
Percolation leaching, 359
Permanent magnetic drum separator, 286–287, 286*f*
Phase quantification, 85, 90
Phosphorus removal
bioleaching, 378–380
goethite-hematite ores, 362–367
magnetite ores, 358–359
oolitic hematite ores, 360
oolitic limonite ores, 360–362
Photochemical smog, 560–561
Physical separation
magnetic separation (*see* Magnetic separation)
nonmagnetic physical separation technologies, hematitic/goethitic iron ore (*see* Dense medium separation (DMS); Jigging; Spiraling; Upflow classification)
Pico Mine, 60
Pilbara deposit, Western Australia, 241–244, 243*f*
Pilbara martite-goethite ores, 56*f*, 57
Pilot-scale sinter pot tests, 411–415, 412*f*
Pilot-scale testing, 279
Pisolite deposit, 61–62
Point-counting technique, 166, 178–180, 182*t*, 183*t*
Pointe-Noire near Sept-Iles, 33–35
Point of zero charge (pzc), 342, 342*t*
Polychlorinated dibenzo-*p*-dioxin and polychlorinated dibenzofuran (PCDD/F) emissions. *See* Dioxin emissions
Powder X-ray diffraction (XRD)
applicability, 92–93
Bragg-Brentano geometry, 87, 87*f*
cluster analysis, 92, 93*f*
crystal structure and chemistry, 85
diffraction patterns, 87
error in, 91–92
goethitic iron ore, 87, 88*f*
intensity$_{Ihkl}$ of a diffraction peak, 86
iron ore characterization, 94
lattice constant refinement, 94–97, 97*t*
mass balancing, 93–94, 95*t*
minerals and phases, 94, 96*t*
phase quantification, 85
Rietveld analysis, 88–91, 89*f*, 91*f*
sintering and pelletizing, 97–98, 98*f*, 99*f*

structure factor, 86
temperature factor, 86
Primary gyratory crushers, 254
Proterozoic iron formation, 51
PulseTor, 170
Pulverized coal injection (PCI), 484, 587
Pyrolysis
ash content, 584
auger pyrolysis reactors, 593
autogenous process, 594
by-product gases, 593
commercial autogenous pyrolysis process, 594
design factors, 593
Lambiotte carbonization process, 593
multi-hearth furnaces, 593
rotary kilns, 593
thermochemical stages, 583, 583*t*
VM requirements, 588*t*, 593
wood carbonization processes, 593

Q

QEMSCAN system
clast size distribution, 175, 177*f*
conglomerate textural images, 171, 176*f*
different platforms, 167, 169*t*
hematite clasts, 175, 175*f*
hematite granulation, BIF samples, 175, 176*f*
hematite macroband profile, 178, 179*f*
hematite standard measured, 167, 168*f*
magnetite/hematite distinction, 171–173
micro-bandwidth distribution, 175, 178*f*
mineral distinction, 178–180, 182*t*
minimum and maximum bandwidths, 178, 180*t*
point-counting, 178–180, 183*t*
SFCA modal, 178–180
textural map, 178, 180*f*
Topas and Autoquan results, 178–180, 184*t*
X-ray collection, 167
zircon and metamict zircon, 171
Quadrilátero Ferrífero, 60, 244
Quality requirements
alternative ironmaking processes, 493–500
BF ironmaking process, 476–492
Quantum mechanical modeling, 362–363
Quantum theory, 162

R

Raman-shifted frequency, 195
Raman spectroscopy
anti-Stokes Raman-shifted frequency, 195
diagnostic iron ore mineralogy, 200, 201*t*
HyLoggingT scanning platform, 220–221
iron ore minerals, 209–220, 211*f*, 212*t*, 215*t*, 218*f*
microscope, 200
monochromatic radiation, 195
polymers and superconductors/semiconductors, 195
portable Raman spectroscope, 199–200
Rayleigh scattering, 195
reflectance spectroscopy, 200, 202*f*, 203, 204*f*, 205*f*
Rapitan iron formations (RIFs), 51, 52*t*
Rayleigh scattering, 195
Reducibility index (RI), 485–486, 486*f*, 487*f*
Reduction disintegration index (RDI), 483–485, 496, 499, 574
Reduction processes
definition, 517
direct reduction, 520
indirect reduction, 518, 519, 520*f*
iron–oxygen–carbon and iron–oxygen–hydrogen systems, 519
oxides, 521
Reference reflectance standard, 195–196
Reflectance spectroscopy
binary mixtures of iron oxides, 203, 204*f*, 205*f*
diagnostic iron ore mineralogy, 200, 201*t*
face mapping system, 198
field spectroradiometer, 195–196
fundamental bending vibrations, 194
gangue minerals (*see* Gangue minerals)
goethite and hematite, 202, 203*f*
hyperspectral drill core and chip scanning systems, 196–198, 196*f*
magnetite and maghemite, 200–201, 203*f*
MIR wavelength range, minerals, 209, 210*f*
remote sensing technology, 199
spectral signature, mineral, 194–195, 194*f*
spectral variation, 194–195
vibrational modes, molecules, 194, 194*f*
visible and infrared wavelength range, 193, 193*f*, 194

Reflected light microscopy, iron ore and iron ore sinter
epoxy blocks, 102, 103*f*
mineral composition, 102–104, 103*f*
polished blocks, 104
Reoxidation, 359
Republic Mine, 351, 352*f*
Resources Supply-Demand Model (GeRs-DeMo), 619
Return fine-mosaic embedding iron ore sintering (RF-MEBIOS), 425–426
Return fines balance (RFB), 413, 414
Reverse flotation
drum LIMS, 294, 296*f*
SLon magnetic separator, 298–299, 299*f*, 300–301, 300*f*, 303, 304*f*
RGB thresholding, 119, 120–122, 120*f*
Rhizobium, 379
Rhodococcus opacus, 383
Rietveld analysis, 88–91, 89*f*, 91*f*
Rio Tinto iron ore processing plants
Brockman 2 processing plant, 257, 258*f*
crusher amps, 257
crusher bowl level, 257
crusher product tons per hour, 257
feeder speed, 257
feed type, 257
gap setting, 257
Paraburdoo processing plant, 257, 258*f*
Rio Tinto's Parker Point port, Western Australia, 16, 17*f*
Rod mills, 344
ROM. *See* Run-of-mine (ROM) ore
Rotary drilling method, 235
Rotary scrubbers, 257
Roy Hill operation, 259, 261*f*
Run-of-mine (ROM) ore, 51
characteristic, 46*t*, 48
impact crushability, 70, 71*t*
uniaxial compressive strength, 69–70, 71*t*

S

SAIL iron ore mining operations, India, 23–25, 25*f*
Samarco Alegria mine, 17–18
SAM process. *See* Softening and melting (SAM) process
Sandvik Jumbo drills, 238
Scalping screens, 259
Scanning electron microscope (SEM)-based technologies
atomic number, 164
auto-SEM technologies (*see* Auto-SEMs technology)
characteristic X-ray spectra, 164
electron beam-specimen interaction, 162, 164*f*
electron probe microanalysis, 165
MLA, 167–170
QEMSCAN system (*see* QEMSCAN system)
sample preparation techniques, 164–165
TIMA, 170
Schefferville area, Canada., 33–35, 35*f*
Screening
banana/multislope screens, 256, 256*f*
BHP Billiton Newman iron ore handing hub, 259, 260*f*
grizzly screen, 255, 256*f*
horizontal low-head/linear vibrating screens, 256, 256*f*
mobile screening plant systems, 261–262
Rio Tinto iron ore processing plants, 257, 258*f*
rotary scrubbers, 257
Roy Hill operation, 259, 261*f*
Vale S11D project, 261
vibrating screen, 255, 256*f*
Seaborne-traded iron ores, 46–47, 47*f*
Segregation feeder (SF), 421–423, 422*f*
Segregation slit wire (SSW), 421–423, 422*f*, 556, 556*f*
Selective flocculation, 342, 345, 346–347, 350, 352
SEM-based technologies. *See* Scanning electron microscope (SEM)-based technologies
Semiautogenous (SAG) mills, 265, 265*f*
Semipellet expansion (SPEx) II process, 427
SFCA. *See* Silicoferrite of calcium and aluminum (SFCA)
Shaft furnace
advantages, 435–436
ratio for, 438
Shale-like mesobands, 53–54
Shatter index (SI), 483
Shortwave infrared (SWIR)
amphiboles, 208

carbonates, 206*f*, 208
chlorite, 207
clay minerals, 206–207
hydroxyl-bearing silicates, 205
magnetite, 203
talc, 207–208
Silica-induced cell surface protein (SIP), 385–386
Silicoferrite of calcium and aluminum (SFCA)
fibrous and columnar types, 111, 113*f*
hematite nuclei, 110–111, 111*f*
larnite area, 111–114, 112*f*, 113*f*
prismatic, acicular, dendritic, 111
200x magnification, 111, 112*f*
Single-particle firing tests, 419–420
Single-shaft screens, 255
Single toggle jaw crusher, 252–253, 253*f*
Sino iron project, 263, 264*f*
Sintering
blast furnaces, 397, 398*f*
bonding agent rate, 413
carbon adsorption/absorption systems, 551–553, 553*t*
CO_2 (*see* Carbon dioxide (CO_2) emissions)
coke level, 413
CSIRO multifunctional pilot-scale sinter pot testing facility, 411–413, 412*f*
dioxin (*see* Dioxin emissions)
dust, 569–570
energy and CO_2 reduction, Super-SINTER™ for, 427–428
EOS® system, 397
fine wet scrubbing system, 551–553, 553*t*
flame front, 395–396, 403, 411
granulation characteristics of iron ore (*see* Granulation)
green bed permeability, 413
high-efficiency dedusting, 551–553, 553*t*
HPS process, 423–424, 424*f*
Japanese steel industries, 418, 418*f*
JPU permeability *vs.* mixture moisture curves, 402, 403*f*
laboratory-scale evaluation of iron ore, 414–418
limestone and coke breeze coating, 420–421, 420*f*
material flow, sinter plant, 396*f*
MEBIOS process, 424–426, 425*f*
NO_x emissions, 560–562
off-gas, 397
permeability and segregation, 421–423, 421*f*, 422*f*
productivity, 413
return fines balance, 413
self-fluxing sinter, 397
sintering time, 413
sinter returns level, 413
SO_x emissions, 558–560
super-fluxed sinter, 397
thermal densification, ore characteristics on (*see* Thermal densification)
volatile organic compounds, 551
yield, 413
Sishen DMS plant
cyclone plant sinks and floats, 311, 312*f*
DMS cyclone plant, 310–311, 311*f*
drum plant sinks and floats, 311, 312*f*
WEMCO drums, 310–311, 311*f*
Sishen hematite deposit, 59–60
SisuROCK, 196–197, 196*f*
Skanska Raise Drilling, 237
Slag formation, 528
SLon magnetic separator
centrifugal separator flow sheet, 301–303, 302*f*
and drum LIMS, 296–297, 297*f*
limonitic ore, 303–305, 305*f*
pulsating mechanism, 290–292, 291*f*
and reverse flotation flow sheet, 298–299, 299*f*, 300–301, 300*f*, 303, 304*f*
specularite ore, 297–298, 298*f*, 303, 304*f*
spiral separators, 300–301, 300*f*
Smelting reduction (SR), 475
Baosteel static load reduction test, 500
COREX Linder test, 500
COREX® process, 497–498, 497*f*
Softening and melting (SAM) process, 476–477, 489
dripping temperature, 490
melting range, 492
melting temperature, 490–492
softening temperature, 490
S value, 492
Soil bacteria, 379, 381, 382–384
Spaceborne hyperspectral sensors, 199
Spectral Geologist (TSGT), 197–198

Specularite, 53–54
Spiraling
  advancements in, 336
  advantages, 329*t*
  disadvantages, 329*t*
  flanged feed inlet and antisiphon HDPE piping, gravity distributor, 330, 332*f*
  historical gravity separation and modern-day spirals, 328
  offtake piping and dart valves, gravity distributor, 330, 332*f*
  operating criteria, 331–333
  primary and secondary flow properties, 333, 333*f*
  single, double and triple start units, 329, 330*f*
  spiral assembly, general arrangement of, 330, 331*f*
  spiral suppliers, 334
  testwork design, 334
  trough profiles, 330
Spiral separators, 300–301, 300*f*
SR. *See* Smelting reduction (SR)
Stack Sizer fine-screening machine, 272
Starch, 347
Static ballability index, 440–441
Stirred milling
  IsaMill™, 271–272, 271*f*
  Vertimill®, 270–271, 270*f*, 271*t*
Straight grate (SG) systems, 435–438, 441–442, 450–451, 456–457, 460
Streaming conditions
  cohesive zone, 515, 517*f*
  material descending, 514
  motion of gases, 515, 516*f*
Sublevel caving, 237–240, 238*f*, 239*f*
Sulfide ores, biobeneficiation
  commercial bioleaching acidophilic bacteria, 380
  soil bacteria, 381
Sulfur oxide (SO_x) emissions
  biomass, 571–572, 573*f*
  characteristics, 558–559, 559*f*
  EOS process *vs.* conventional sintering processes, 559, 560*f*
  upper limits, 551–553, 552*t*
Super-SINTER™ process, 427–428
Super-SINTER® technology, 555–556, 555*f*
Super Swellex, 240

T

Taconite iron ore deposits, 33–35, 35*f*
Talc, 207–208
Tata Steel Minerals Canada, 33–35
TESCAN integrated mineral analyzer (TIMA), 170
Thermal densification
  assimilation-precipitation, 403
  chemical characteristics of iron ore, 404–408
  final densification, 403
  mineralogical characteristics of iron ore, 409–410, 410*f*
  physical characteristics of iron ore, 408–409, 408*f*
  rearrangement of granules, 403
Tilden Mine, 350, 351*f*
Timmins mine, 33–35
Titanomagnetite, 62
Tumble index (TI), 482–483, 482*f*
Tumbling mills
  autogenous and semiautogenous mills, 265, 265*f*
  ball mills, 265–266, 266*f*
  types of, 264
Tuyere stock, 511, 512*f*

U

Underground mining
  in Cleveland ironstone mines, 233–234, 234*f*
  in Kiruna, Sweden (*see* Kiruna underground mine)
  in North Lincolnshire mines, 234–236
Uniaxial compressive strength (UCS), 69–70, 71*t*
Unpolarized Raman spectra, 199–200
Upflow classification, 323*f*
  advantages, 327*t*
  assessment, 327, 327*t*
  disadvantages, 327*t*
  elutriation, 323–324, 324*f*
  multiple stage, 324, 324*f*, 325*f*
  spiral concentrators, 325, 326*f*
  spirals, 325, 326*f*
  WHIMS, 325–327, 327*t*

V

Vale's Carajás mine, Para, 17–18, 19*f*
Vale S11D project, 261

Vale's iron ore operations, Brazil, 19–21, 21*f*, 22*t*
Vertical roller mills (VRM), 275–276, 275*f*
Vertimill®, 270–271, 270*f*, 271*t*, 274*f*
Vibrating screens, 293–294
Vibrational spectroscopy, 194
VideoPro, 104
Visible and near-infrared (VNIR), 194, 194*f*
  carbonates, 206*f*
  goethite and hematite, 202
  magnetite and maghemite, 200–201
  quartz, 205–206

W

Wabush and Bloom Lake operations, 33–35
Water absorption capacity, 415
Watershed separation approach, 126, 126*f*, 127*f*
Wavelength-dispersive spectroscopy, 165
Wet fine scrubbing system (WS), 564–565
Wet high-intensity magnetic separators (WHIMS), 9–11, 13*f*, 289–290, 290*f*, 325–327, 327*t*
WHIMS. *See* Wet high-intensity magnetic separators (WHIMS)
Wirtgen surface mining machines, 242–243, 243*f*
World iron ore production, 1, 2*f*
World iron ore trade, 1, 3*f*, 3*t*, 4*f*
World Steel Association, 1, 2*f*

X

X-ray diffraction (XRD), 209, 216, 217. *See also* Powder X-ray diffraction (XRD)
X-ray microtomography (XRMs), 187

Y

Yellow ochreous goethite, 46–47, 47*f*

Z

Zeiss Axioplan microscope, 101, 102*f*
Zircon, 171